Published in Journals: Energies, Mathematics,
Fluids, Applied Sciences and Materials

Topic Reprint

Fluid Mechanics

Volume II

Edited by
Vasily Novozhilov and Cunlu Zhao

mdpi.com/topics

MDPI

Fluid Mechanics—Volume II

Fluid Mechanics—Volume II

Editors

Vasily Novozhilov
Cunlu Zhao

MDPI

Basel • Beijing • Wuhan • Barcelona • Belgrade • Novi Sad • Cluj • Manchester

Editors

Vasily Novozhilov
Victoria University
Melbourne, VIC
Australia

Cunlu Zhao
Xi'an Jiaotong University
Xi'an
China

Editorial Office
MDPI AG
Grosspeteranlage 5
4052 Basel, Switzerland

This is a reprint of articles from the Topic published online in the open access journals *Energies* (ISSN 1996-1073), *Mathematics* (ISSN 2227-7390), *Fluids* (ISSN 2311-5521), *Applied Sciences* (ISSN 2076-3417), and *Materials* (ISSN 1996-1944) (available at: https://www.mdpi.com/topics/fluid).

For citation purposes, cite each article independently as indicated on the article page online and as indicated below:

Lastname, A.A.; Lastname, B.B. Article Title. *Journal Name* **Year**, *Volume Number*, Page Range.

Volume II
ISBN 978-3-7258-1465-7 (Hbk)
ISBN 978-3-7258-1466-4 (PDF)
doi.org/10.3390/books978-3-7258-1466-4

Set
ISBN 978-3-7258-1461-9 (Hbk)
ISBN 978-3-7258-1462-6 (PDF)

Contents

fluids

MDPI

Article

Numerical Simulation of Carbon Dioxide–Nitrogen Mixture Dissolution in Water-Saturated Porous Media: Considering Cross-Diffusion Effects

Saeed Mahmoodpour [1,*], Mrityunjay Singh [2,*], Ramin Mahyapour [3], Sina Omrani [4] and Ingo Sass [2,5]

[1] Group of Geothermal Technologies, Technische Universitat Munchen, 80333 Munich, Germany
[2] Institute of Applied Geosciences, Geothermal Science and Technology, Technische Universitat Darmstadt, 64287 Darmstadt, Germany
[3] Department of Petroleum Engineering, Sharif University of Technology, Tehran 11155-9161, Iran
[4] Institute of Petroleum Engineering, College of Engineering, University of Tehran, Tehran 4563-1115, Iran
[5] Geoenergy Section, GFZ, 14473 Potsdam, Germany
* Correspondence: saeed.mahmoodpour@tum.de (S.M.); mrityunjay.singh@tu-darmstadt.de (M.S.)

Highlights:

1. What are the main findings?

- CO_2–N_2 mixture dissolution in brine is examined by considering the cross-diffusion effect for CO_2 sequestration in a deep storage reservoir.
- Heterogeneity lowers the average dissolved CO_2 and impedes the onset of convection.

2. What is the implication of the main finding?

- Correlations are developed to predict the transition time between the dissolution regimes.

Abstract: The possibility of impure carbon dioxide (CO_2) sequestration can reduce the cost of these projects and facilitate their widespread adoption. Despite this, there are a limited number of studies that address impure CO_2 sequestration aspects. In this study, we examine the convection–diffusion process of the CO_2–nitrogen (N_2) mixture dissolution in water-saturated porous media through numerical simulations. Cross-diffusion values, as the missing parameters in previous studies, are considered here to see the impact of N_2 impurity on dissolution trapping in more realistic conditions. Homogeneous porous media are used to examine this impact without side effects from the heterogeneity, and then simulations are extended to heterogeneous porous media, which are a good representative of the real fields. Heterogeneity in the permeability field is generated with sequential Gaussian simulation. Using the averaged dissolved CO_2 and dissolution fluxes for each case, we could determine the onset of different dissolution regimes and behaviors of dissolution fluxes in CO_2–N_2 mixture dissolution processes. The results show that there is a notable difference between the pure cases and impure cases. Additionally, a failure to recognize the changes in the diffusion matrix and cross-diffusion effects can result in significant errors in the dissolution process. At lower temperatures, the N_2 impurity decreases the amount and flux of CO_2 dissolution; however, at higher temperatures, sequestrating the CO_2–N_2 mixture would be a more reasonable choice due to enhancing the dissolution behavior and lowering the project costs. The results of the heterogeneous cases indicate that heterogeneity, in most cases, reduces the averaged dissolved CO_2, and dissolution flux and impedes the onset of convection. We believe that the results of this study set a basis for future studies regarding the CO_2–N_2 mixture sequestration in saline aquifers.

Keywords: CO_2 sequestration; impurity; dissolution trapping; heterogeneity; convection–diffusion

Citation: Mahmoodpour, S.; Singh, M.; Mahyapour, R.; Omrani, S.; Sass, I. Numerical Simulation of Carbon Dioxide–Nitrogen Mixture Dissolution in Water-Saturated Porous Media: Considering Cross-Diffusion Effects. *Fluids* **2023**, *8*, 22. https://doi.org/10.3390/fluids8010022

Academic Editor: Mehrdad Massoudi

Received: 30 November 2022
Revised: 20 December 2022
Accepted: 31 December 2022
Published: 6 January 2023

1. Introduction

The continuous and significant increase in greenhouse gas emissions due to the excessive use of fossil fuels in the industrial production, power, and transportation sectors

has caused global warming and climate change [1–3]. In order to control greenhouse gas emissions and prevent global warming, carbon dioxide (CO_2) capture and storage (CCS) in geological formations is considered a viable tool for reducing atmospheric CO_2 concentrations [4–11]. Saline aquifers, depleted oil and gas reservoirs, unmineable coal seams, hydrate storage of CO_2 within the subsurface environment, and CO_2-based enhanced geothermal systems are the main CO_2 storage options in underground geological formations [12,13]. Among these options, saline aquifers have attracted more attention due to their chemistry, permeability, porosity, temperature, pressure, massive capacity for the storage of CO_2, wide distribution, and vicinity to the sources of production [6,14–20]. Involved processes during CCS happen in a fully coupled framework, which is one of the main challenges in this regard. Examining such a complex problem requires a multidisciplinary approach. Here, detailed numerical simulations, which consider these coupled processes, could be helpful, and they supported us in the underlying gaps in our knowledge for a successful CCS project [21,22].

The high cost of CCS in saline aquifers is a barrier to the implementation of these projects, and the possibility of impure CCS (CO_2 + impurities) is proposed as a solution to reduce the project cost [23]. Currently, the three main CO_2 capture technologies used in large-scale power plants are post-combustion, pre-combustion, and oxyfuel combustion, all of which produce CO_2-dominant streams containing impurities [24,25]. It was indicated that impurities have an influence on all types of geological CO_2 storage mechanisms [26,27]. Although permitting the existence of impurities in the CO_2 streams decreases the cost of CCS projects, it can have undesirable and unknown effects, such as decreased CO_2 storage capacity, corrosion, and so on [28].

Nitrogen (N_2) is an abundant species in impure CO_2 streams [29–31]. Accordingly, various studies have been performed to investigate the feasibility of the sequestration of CO_2–N_2 mixtures in saline aquifers [28,32–39]. From some aspects, N_2 injection alongside CO_2 is examined, and it seems a suitable solution. For example, N_2 is a non-toxic and inert gas that is not present in most aquifers. Previous studies showed that the lower viscosity and water solubility of N_2 in comparison to CO_2 cause N_2 to move in the leading edge of the injected gas, which can be used as a safety signal against leakage in the long-term by monitoring N_2 [32,33]. Additionally, during the injection period, N_2 increases gas mobility and plume propagation. Hence, the surface area between the injected gas mixture and brine could increase and subsequently enhance the solubility trapping [36,40,41]. The corrosion effects of N_2 on the equipment used in the CCS project are negligible. Therefore, there are no safety concerns about damage to equipment with the N_2 co-injection [42]. In the CO_2–N_2-brine system, experimental studies show that N_2 increases capillary trapping and causes a reduction in leakage risks through this mechanism [35]. Despite the mentioned advantages, like other impurities, it is believed that N_2 reduces the storage capacity of saline aquifers due to the possible reduction of the solubility ratio [43,44] and requires additional investigations on the other aspects.

The estimation of dissolution flux during different dissolution regimes is one of the most significant aspects of the studies mentioned in previous experimental and numerical studies [16,45–51]. These estimations provide a pragmatic tool for policy and engineering applications to have an initial knowledge about the efficiency of the dissolution process and, consequently, of the storage capacity and project safety in different time scales [52]. During various time scales of CCS, the diffusion coefficient plays an important role. In the injection phase, it controls the viscous fingering and, consequently, the capillary trapping mechanism [8]. Moreover, it is a vital factor for dissolution trapping and, because of that, for mineralization trapping [53,54]. All of these trapping mechanisms are essential to a project's safety [55]. In previous studies, researchers ignored the impurity effects on the diffusion coefficient due to the complexity of its direct measurement and used the diffusion coefficient of the pure case [28,36,40,41,53,56] to simulate the dissolution process during the impure CCS.

Recently, Omrani et al. [57] provided a data set for the diffusion coefficient of CO_2–N_2–water systems through the molecular dynamics simulation (shown in Methodology section). These data are validated based on the experimental tests for pure CO_2 [57]. However, for the CO_2–N_2–water systems, there are no experimental data about the cross-diffusion values for validation. However, the data set generally follows up a trend that is observed during our previous experimental tests for the overall effects of the impurity on the diffusion and, consequently, on the onset of convection and dissolution flux [38,39]. Furthermore, we have observed such changes in the diffusion coefficient values, which are measured for specific three-component mixtures (not for impure CO_2 in water) [58–60].

We considered the effects of heterogeneity in porous media to examine the process in a more realistic condition. Heterogeneity can be examined from structural heterogeneity resulting from fault, fold, or salt diapirs and stratigraphic heterogeneities within facies [61]. Here, we focus on heterogeneous stratigraphic structures within facies. The coupled effect of the gas impurity and heterogeneity in porous media is studied by creating a permeability field through the sequential Gaussian simulation (SGS) [62–64].

To the best of the authors' knowledge, no simulation study has investigated the convective dissolution behavior of complex CO_2–N_2–water systems by considering the cross-diffusion effects. In this study, we tried to examine the effect of cross-diffusion on convective dissolution behavior in the CO_2–N_2-water system. We conducted this evaluation based on the amount of dissolved CO_2 and the dissolution flux rate through three sets of experiments with mixtures of pure CO_2, 90% CO_2 + 10% N_2, and 80% CO_2 + 20% N_2. In addition to the homogeneous porous media, which enables us to track the effect of impurity separately, the simulations are followed up on heterogeneous porous media, which are good representatives of the real field conditions. Although great achievements have been made through previous studies on solubility trapping, in this study, we intend to examine the role of N_2 impurity in the diffusion–convective dissolution in both homogeneous and heterogeneous porous media. The findings of this study are supposed to provide insights into impure CO_2 geological storage and show whether the composition of impurity can be engineered to control the dissolution process, which may be beneficial to the practical deployment of CCS technology.

2. Methodology

To capture the CO_2 or CO_2 + N_2 dissolution in a water-saturated porous medium, a rectangular system away from the injection well was selected as the domain of interest. At distances far enough from the injection well, it can be assumed that the gas-brine contact is horizontal. To examine the behavior of the system through a high-resolution simulation framework, it is essential to use a small-scale domain from the computational costs aspect. A thickness of 10 m is used as the most frequent thickness between the reported aquifers data [60]. The length of the domain is 20 m here. A sharp interface is considered for the gas–water contact, which is a valid assumption for aquifers deeper than 1 km [61,62]. The no-flow boundary conditions are imposed on the side and bottom boundaries of the model. Initial CO_2 and N_2 concentrations in water are set to zero, and the presence of CO_2 or CO_2+N_2 at the top boundary is represented by the fixed concentrations based on the solubility of CO_2 and N_2 in brine.

The governing equations in the ternary system are as follows (derived from Kim et al. [54]):

$$\nabla . U = 0 \tag{1}$$

$$\varphi \frac{\partial C_1}{\partial t} = \varphi \left(D_{11} \nabla^2 C_1 + D_{12} \nabla^2 C_2 \right) - U . \nabla C_1 \tag{2}$$

$$\varphi \frac{\partial C_2}{\partial t} = \varphi \left(D_{22} \nabla^2 C_2 + D_{21} \nabla^2 C_1 \right) - U . \nabla C_2 \tag{3}$$

The first equation is the continuity equation, and Equations (2) and (3) are the mass transfer equations for each gas. In these equations, φ and C are porosity and the concen-

tration of dissolved gases, respectively. D_{11} and D_{22} are the main diffusion coefficients, and D_{12} and D_{21} are the cross-diffusion coefficients. Here, U is the velocity vector that can be calculated through Darcy's law, which describes the motion of Newtonian fluid in the porous medium.

$$U = -\frac{k}{\mu}(\nabla P - \rho g) \tag{4}$$

In which k, μ, and ρ are permeability, viscosity, and density, respectively. The mentioned equations are coupled and solved by the finite element method through the COMSOL Multiphysics software to catch the behavior of CO_2 or CO_2 + N_2 dissolution in water. The density of the aqueous phase is calculated by the below equation:

$$\frac{M_{aq}}{\rho_{aq}} = \frac{x_w M_w}{\rho_w} + \sum_{i=1}^{NCG} V_i x_i \tag{5}$$

In this equation M, ρ, x, and V stand for the molecular weight, density, mole fraction, and partial molar volume, respectively. Furthermore, subscripts aq, w, and i are used for the resulting solution, water, and dissolved gases. Table 1 lists the model parameters that are used during the simulation. The involved parameters are updated based on pressure and temperature during the simulation. In order to better interpret the convection–diffusion problems, the Rayleigh number is used, which is a dimensionless number and is defined as follows [63]:

$$Ra = \frac{\Delta\rho k g H}{\mu D \varphi} \tag{6}$$

Table 1. The model parameters.

Pressure (bar)	Temperature (K)	Porosity (-)	Permeability (mD)
100	323.15	0.25	250
200	373.15		
300	423.15		

To distinguish the different regimes in the dissolution process, we plotted the dissolution flux versus the logarithm of dimensionless time (t_D). The t_D is defined as tD/H^2 where t, D, and H are the time, diffusion coefficient, and height of the system, respectively. Further analyses were performed on these plots to determine the start of the quasi-steady state regime, its dissolution flux, and the starting time of the shut-down regime.

Table 2 lists Fick's diffusion matrix elements. D_{11} and D_{22} are the main diffusion coefficients, and D_{12} and D_{21} are the cross-diffusion coefficients. The main diffusion coefficients express the section of the component diffusion that depends on its own concentration gradient, and the cross-diffusion coefficients provide the molar flux of one component driven by the concentration gradient of another component. We applied the molecular dynamic simulation to evaluate the CO_2–N_2-water diffusion matrix for the first time. For more detail on how these values are calculated, we refer you to our previous work [57].

Table 2. Fick diffusion coefficients of CO_2–N_2–water system [57].

Temperature (K)	Pressure (bar)	CO_2 Mole Fraction	D_{11} ($\times 10^{-9}$ m^2/s)	D_{12} ($\times 10^{-9}$ m^2/s)	D_{21} ($\times 10^{-9}$ m^2/s)	D_{22} ($\times 10^{-9}$ m^2/s)
323	100	1	3.453	-	-	-
323	100	0.9	2.3119	0.2616	0.0495	39.715
323	100	0.8	1.8604	−0.4292	−0.0033	26.108
373	100	1	6.983	-	-	-
373	100	0.9	4.3614	-1.0323	0.0061	89.2921
373	100	0.8	6.5221	−0.5939	−0.0024	55.8109
423	100	1	10.716	-	-	-
423	100	0.9	8.976	-1.3035	0.0133	130.0136
423	100	0.8	10.0413	−0.1552	0.0578	54.9741
323	200	1	3.7	-	-	-
323	200	0.9	1.4821	−0.146	0.0149	13.15855
323	200	0.8	1.946	−0.3165	−0.0368	9.3242
373	200	1	6.73	-	-	-
373	200	0.9	3.3163	−0.8697	−0.019	39.4697
373	200	0.8	3.76365	−0.84585	−0.0085	49.32485
423	200	1	11.033	-	-	-
423	200	0.9	5.7988	−0.9622	0.1099	76.7250
423	200	0.8	5.52505	−0.24735	0.0503	33.1235
323	300	1	3.683	-	-	-
323	300	0.9	1.3997	−0.4567	−0.0383	9.9591
323	300	0.8	1.6961	−0.3346	−0.0718	6.1526
373	300	1	6.633	-	-	-
373	300	0.9	2.7572	−0.1616	0.0411	24.0971
373	300	0.8	2.8922	−0.2709	−0.0625	14.6273
423	300	1	11.1	-	-	-
423	300	0.9	4.1235	−1.0655	−0.0414	34.9856
423	300	0.8	5.0785	−0.0885	0.0638	20.1737

In order to investigate the effect of heterogeneity, a random permeability field is created by applying the sequential Gaussian simulation (SGS) algorithm. The SGeMS software was used to generate a normal random distribution in the range of $0-1$. The following equation is used to create a log-normal permeability distribution based on the normal random distribution.

$$k_{log-normal} = k_{average} \times exp(\sigma \times k_{SGeMS}) \quad (7)$$

where $k_{log-normal}$, $k_{average}$, σ, and k_{SGeMS} are the permeability field in the log-normal distribution, the average permeability of the reservoir, the standard deviation of the permeability field, and the permeability field in the standard normal distribution obtained from the SgeMS software, respectively. Each random permeability value generated by this method is assigned to a point in the simulation domain at a specified distance in length, and the permeability between these points is interpolated to reach a continuous field. The average permeability of the reservoir is 250 mD (Table 1), the standard deviation of the permeability field is 1, and the distance length is 1 m in both the x and y directions. Due to the high difference in distribution pattern from one realization to another, repetition of the simulations for each case is necessary for the results to be reliable. In this regard, considering the computational limitations, we chose 20 realizations for each case.

We conducted a mesh sensitivity analysis to ensure that our results were mesh independent. We selected the most difficult case with the highest Rayleigh number for this purpose. We found that a triangular mesh with a maximum size of 0.1 m is a good choice for this case (and other cases with lower Rayleigh numbers). We considered 4 different triangular meshes: maximum mesh sizes of 0.08, 0.1, and 0.12 m and an adaptive meshing with a maximum size of 0.1 m. Moreso, except for the case with a maximum size of 0.12 m, the average dissolved CO_2 for all the other cases overlapped with each other. It should be noted that for the case with a maximum size of 0.1 m, we used 55294 elements to mesh the system, while for the case with a maximum size of 0.08 m, we used 84942 elements. However, we employed an adaptive meshing option in all the simulations to capture the

fingers' movements with a high resolution in some of the high permeability zones of the heterogeneous porous media. We employed adaptive time stepping through the second-order backward differentiation formula (which is a linear multi-step implicit method) to increase the computational speed. To do this, we used 4.375×10^{-4} years as the first-time step to reach the convergence. Additionally, we used the absolute tolerance of 0.001. The consistent initialization was completed through the backward Euler methodology with 0.001 as the fraction of the initial step. To solve the fully coupled equations, we used the automatic highly nonlinear Newton method with an initial damping factor of 10^{-4} and a minimum damping factor of 10^{-8}. We restricted the update for step size by a factor of 10. The solver in this numerical model is the Multi-frontal Massively Parallel sparse direct Solver (MUMPS). Here, the recovery damping factor is 0.75. Furthermore, due to the computational restrictions for the gas mixture dissolution process in a 3D heterogeneous porous structure, we used 2D simulations. For the discretization of pressure in Darcy's law, we used the quadratic approach, and for the concentration values in the mass transfer equation, we employed the linear discretization approach.

3. Results and Discussion

At the beginning of this section, the results of the pure CO_2 cases are presented. Then, we discuss the impure cases and the changes that N_2 will impose on the dissolution behavior. The simulations are conducted to represent up to 7 years, which is sufficient to catch all the regimes that appear in a dissolution process. For analyzing the CO_2 or CO_2 + N_2 dissolution process, the total concentration of the dissolved gas and dissolution flux, and the dissolution patterns, number, and shape of the convective fingers are considered. Figure 1 shows a schematic of the dissolution behavior. The dissolution process starts with a diffusion-dominated regime. CO_2 diffuses into the water due to the concentration gradient. The dissolution flux slows down because of the reduction of the concentration gradient at the interface. The dissolved CO_2 + water has a higher density than pure water. This initiates instabilities that lead to the downward motion of dissolved gas and water. As the fingers grow and descend to the bottom, freshwater moves up to the interface to improve the dissolution process. This process continues until the bottom water that moves up to the interface contains dissolved gas. From this stage, the dissolution process moves toward the shut-down regime until a point where the system can no longer dissolve more gas and reaches its maximum capacity. Table 3 lists the details of the pure cases at different temperatures and pressures. Figure 2 illustrates the average dissolved CO_2 and dissolution flux for all the pure cases. As was expected, the case with the highest Rayleigh number reaches the higher dissolution flux, and the case with the lowest Rayleigh number ends with the lowest dissolution flux among all the cases. Three cases of 7-p, 8-p, and 9-p almost have the same Rayleigh number; however, the case with a lower diffusion coefficient ends in the higher dissolution flux. This behavior can be seen by comparing the 2-p and 3-p cases. Furthermore, based on the lower solubility of case 3-p, this case would finally result in a lower dissolution capacity. By comparing the dissolution flux curves, it can be interpreted that with the increase of the Rayleigh number, the onset of the quasi-steady and shut-down regimes happens faster, and the dissolution flux of the quasi-steady state regime raises. We fitted and proposed some correlations that relate these parameters to the Rayleigh number. These equations are as follows:

$$t_D^{Onset} = (64,491)Ra^{-2.487} \tag{8}$$

$$t_D^{QS} = (1320.5)Ra^{-1.744} \tag{9}$$

$$F = \left(2 \times 10^{-10}\right)Ra^{1.5517} \tag{10}$$

$$t_D^{SD} = (1925.1)Ra^{-1.629} \tag{11}$$

where t_D^{Onset}, t_D^{QS}, t_D^{SD}, and F are the non-dimensional time of onset of convection, the onset of the quasi-steady state, the onset of the shut-down regime, and the dissolution flux during the quasi-steady regime, respectively.

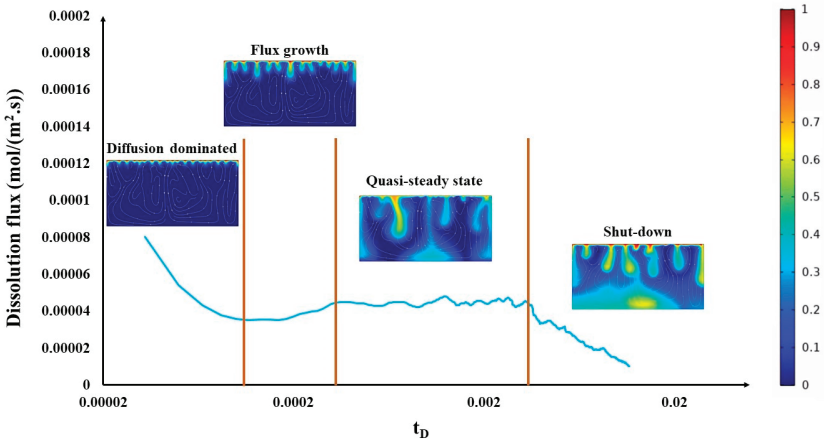

Figure 1. A schematic of different regimes in a dissolution process.

Table 3. Details of the pure cases.

Case Name	Temperature (K)	Pressure (bar)	t_D^{Onset}	t_D^{QS}	F	t_D^{SD}	Ra
1-p	323	100	0.00015	0.00091	4.0329	0.00443	2555
2-p	373	100	0.00066	0.00284	2.7641	0.00839	1691
3-p	423	100	0.00071	0.00392	1.9180	0.00135	1527
4-p	323	200	0.00007	0.00098	5.3417	0.00383	2790
5-p	373	200	0.00028	0.00168	5.1562	0.00558	2522
6-p	423	200	0.00038	0.00253	3.4526	0.01040	2325
7-p	323	300	0.00017	0.00108	6.6560	0.00301	3058
8-p	373	300	0.00015	0.00128	5.7127	0.00497	3029
9-p	423	300	0.00025	0.00157	5.4777	0.00535	2906

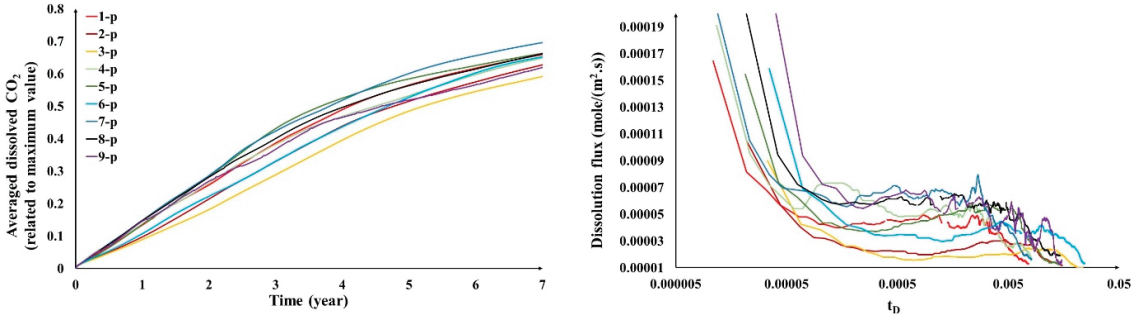

Figure 2. The averaged dissolved CO_2 and dissolution flux for the pure case. Legends for left- and right-hand subplots are same.

For a ternary system of CO_2–N_2–water, a 2 × 2 matrix of the diffusion coefficient was needed to describe the diffusion behavior. The diagonal elements are the main diffusion coefficients, and the cross-diagonal elements are the cross-diffusion coefficients. In previous studies, for analyzing impure cases, researchers either used the pure diffusion coefficient

or the effective diffusion coefficient that was calculated from experimental data, and it was assumed to be independent of concentration for the diluted solution [38,64]. In this study, wherever the diffusion coefficient was needed, we used the summation of the main diffusion coefficient and cross-diffusion coefficient of each component. In other words, $D_{CO_2} = D_{11} + D_{12}$ for analyzing the CO_2 dissolution and $D_{N_2} = D_{21} + D_{22}$ for the N_2 dissolution behavior (see Equations (2) and (3)) are the effective conditions.

The details on the impure cases of CO_2 are listed in Table 4. These data indicate that impure cases do not exactly follow what was expected based on pure cases. The dissolution flux does not act in accordance with the Rayleigh number. In the pure cases, we observed a relation between the increase of the Rayleigh number and the dissolution flux, yet there are contradictions of this relation in the impure cases. In comparison to the pure cases, it seems that at higher pressure, there is no noticeable reduction in the dissolution flux, and it is either the same as the pure cases or has a higher value. However, at lower pressure, the change in dissolution flux can be considerable. Other than the dissolution flux, there are special relations between the Rayleigh number with t_D^{Onset}, t_D^{QS}, and t_D^{SD}. The cases with a higher Rayleigh number have a faster onset of convection, quasi-steady and shut-down regimes. We proposed the following correlations for predicting the t_D^{Onset}, t_D^{QS} and t_D^{SD} of impure cases:

$$t_D^{Onset} = (0.1575)Ra^{-0.812} \tag{12}$$

$$t_D^{QS} = (2.7486)Ra^{-0.945} \tag{13}$$

$$t_D^{SD} = (18.325)Ra^{-1.013} \tag{14}$$

Table 4. Details of the impure CO_2 cases.

Case Name	Temperature (K)	Pressure (bar)	CO_2 Mole Fraction (-)	t_D^{Onset} (-)	t_D^{QS} (-)	F (-)	t_D^{SD} (-)	Ra (-)
1-i	323	100	0.9	0.00022	0.00064	2.19	0.00446	3215
2-i	323	100	0.8	0.0001	0.00087	1.88	0.00255	5384
3-i	373	100	0.9	0.00019	0.00161	2.13	0.00383	3341
4-i	373	100	0.8	0.00043	0.00264	1.45	0.0095	1765
5-i	423	100	0.9	0.00024	0.00184	2.31	0.0075	2005
6-i	423	100	0.8	0.00053	0.00365	1.61	0.01553	1458
7-i	323	200	0.9	0.00009	0.00043	2.74	0.00221	7903
8-i	323	200	0.8	0.00012	0.00048	2.14	0.00251	6100
9-i	373	200	0.9	0.00014	0.00074	3.08	0.00334	6672
10-i	373	200	0.8	0.00021	0.00072	3.00	0.00287	5284
11-i	426	200	0.9	0.00018	0.00103	5.37	0.00311	5263
12-i	426	200	0.8	0.00013	0.00103	4.47	0.00341	4451
13-i	323	300	0.9	0.00007	0.00034	3.05	0.00125	12,664
14-i	323	300	0.8	0.000099	0.000717	2.67	0.00198	8169
15-i	373	300	0.9	0.00022	0.0009	4.68	0.0023	7521
16-i	373	300	0.8	0.00011	0.0007	4.01	0.0022	7184
17-i	423	300	0.9	0.00008	0.00043	7.13	0.00155	10,628
18-i	423	300	0.8	0.00011	0.00071	4.90	0.00324	6064

These equations are in good agreement with our previous studies that show impurities in the system of CO_2–water (such as different types of gases and salts) and demonstrate a drastic impact on the CO_2 dissolution parameters [48]. We conducted all simulations with and without considering cross-diffusion to check the influence of the diffusion coefficient on the dissolution behavior. Figure 3 shows the averaged dissolved CO_2 and dissolution flux of all the impure cases. It is obvious that there is a clear difference between these two sets of simulations. It can be implied that ignoring the changes in the diffusion coefficient can cause significant errors in the dissolution process parameters. For example, if we do not consider the change in the diffusion matrix, case 1-i reaches the average dissolved CO_2 of about 0.3 (Figure 3c); however, by applying these changes, it reaches the final value of

almost 0.4 (Figure 3a). Moreover, by looking at the dissolution flux curves, the noticeable alteration of the onset of different regimes and dissolution flux is indisputable. Referring to the impure cases with consideration given to cross-diffusion (Figure 3, first and third rows), higher or lower Rayleigh numbers do not necessarily lead to higher or lower dissolved CO_2 or dissolution flux. Furthermore, these results imply that reducing the CO_2 main diffusion coefficient at higher temperatures results in a higher amount of dissolved CO_2 and dissolution flux. By comparing cases 13-i and 17-i, we can see that case 17-i, even with a lower Rayleigh number than case 13-i, has the highest amount of dissolved CO_2 and dissolution flux among all impure cases, with 90% CO_2-10% N_2.

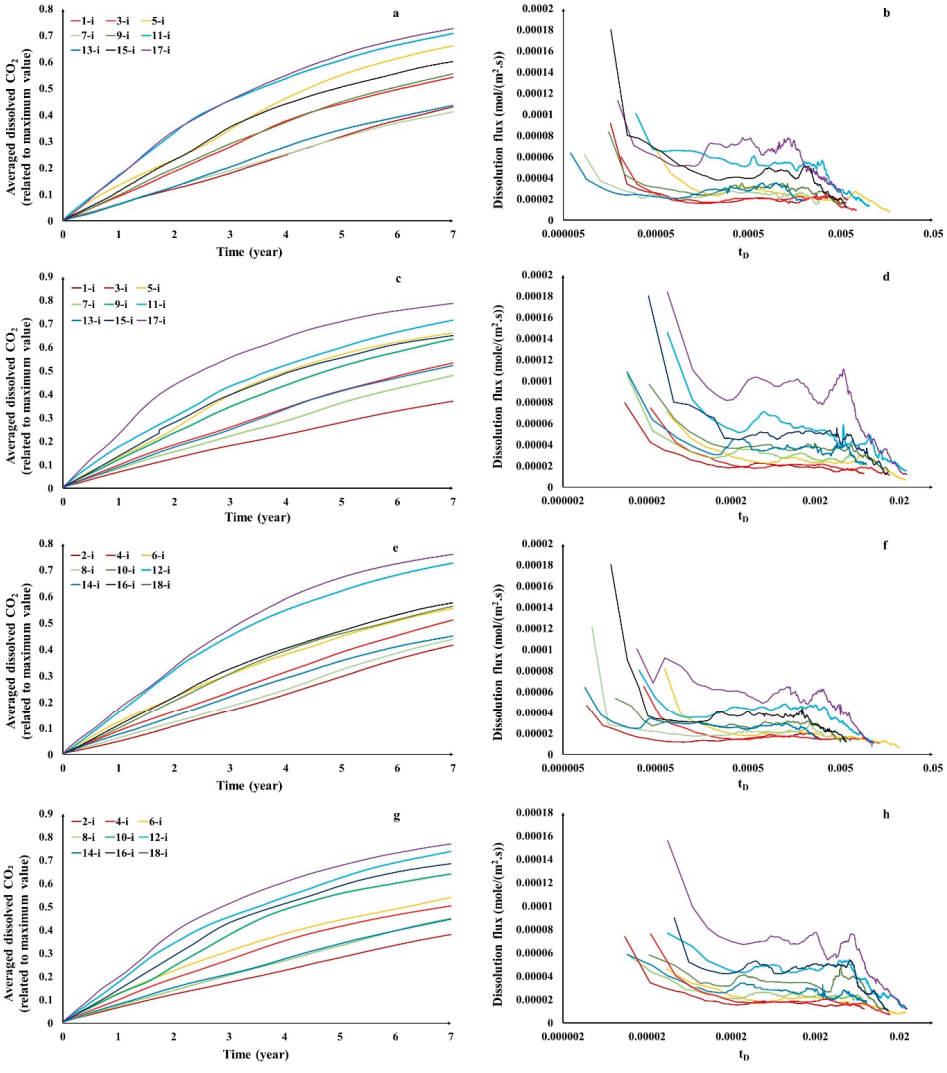

Figure 3. The averaged dissolved CO_2 and dissolution flux for the systems of 90% CO_2-10% N_2 with considering cross-diffusion (**a**,**b**) and without considering cross-diffusion (**c**,**d**); the systems of 80% CO_2-20% N_2 with considering cross-diffusion (**e**,**f**) and without considering cross-diffusion (**g**,**h**). Legends for left- and right-hand subplots are same.

Suppose we consider cases based on their temperature, as in Figure 4, at 323 K, then the difference between the pure and impure cases is obvious, both in the average dissolved CO_2 and dissolution flux. This suggests that in a reservoir with lower temperatures, it is probably better to sequester pure CO_2. At a temperature of 373 K, the pure cases show a higher amount of dissolved CO_2 and dissolution flux than the impure cases, but the differences are insignificant. Due to the high costs of purifying the injection stream, impure CO_2 storage can be a more reasonable choice. At 423 K, the 90% CO_2-10% N_2 cases reach higher dissolved CO_2 and dissolution flux than the pure cases. Therefore, injection of CO_2 with N_2 in reservoirs with high temperatures can lead to higher dissolved CO_2, higher dissolution flux, and a faster onset of quasi-state and shut-down regimes in the dissolution process. Figure 5 illustrates the dissolved CO_2 pattern at the times of the onset of convection, flux growth, the onset of a quasi-steady state, and the onset of the shut-down regime for 7-p, 13-i, 9-p, and 18-i. At early times, the activation of the convective flow holds the intense decrease of dissolution flux, and the convective fingers grow independently; however, as time progresses, these fingers grow and interact with each other in different patterns, which are discussed in our previous work [48]. The higher number and faster descending motion of convective fingers bring more freshwater to the interface, which leads to the enhancement of the diffusion–convection mass transfer rate and CO_2 dissolution flux. In Figure 5, if we compare cases with higher dissolved CO_2 (cases 7-p and 18-i) with lower ones, a special pattern can be identified in the number and interaction of convective fingers. Due to the restriction of lateral movement at the side boundaries, the downward finger motion at these sites may be faster. The comparison of cases 7-p and 13-i confirm the reduction of dissolved CO_2 and dissolution flux due to the addition of 10% N_2 into the injection stream. Despite this, case 18-i has the highest dissolved CO_2 ratio among the impure cases, appears to have more convective fingers, and, therefore, has a stronger convection flow than its pure case (9-p). These patterns, alongside the previous findings, show the effects and importance of N_2 impurity on the CO_2 dissolution process. Figure 6 shows the averaged dissolved N_2 and dissolution flux for the impure cases. It can be seen that, in most cases, there is no convection regime, and there is only a monotonic downward trend. At lower pressures, the N_2 diffusion coefficient drastically increases, leading to a stronger diffusion-dominated flow, but at higher pressures, there are indications of a convective flow.

We developed the dissolution model to include the reservoir heterogeneity in permeability in the presence of the fluid's cross-diffusion effect. We chose five cases of 1-i, 2-i, 3-i, 4-i, and 9-i (see Table 4). Figures 7–11 display these cases. We depicted all the realizations for each case (dotted lines) beside the curves for the homogeneous system with and without considering the cross-diffusion (solid line and dashed line, respectively). Almost in all cases, heterogeneity decreases the averaged amount of dissolved CO_2. Furthermore, it can be seen that it impedes the onset of the convective regime and lowers the dissolution flux. Intuitively, heterogeneity increases the uncertainty and complexity of a system. To demonstrate a clearer picture, we averaged the results of all the realizations for each case (Figure 12). Detecting the onset of convection in Figure 12 is indistinct visually. However, it is well known that the onset of convection corresponds to the minimum dissolution flux, and we can estimate this point from Figure 12 or measure it from the dissolution flux data. It should be noted that this behavior comes from the combined effect of heterogeneity in porous media and cross-diffusion from the impurity. By comparing the homogeneous and heterogeneous cases of 3-i and 9-i (Figures 3a and 12), it can be inferred that heterogeneity increases the separation between these two cases and has a stronger impact at lower pressures.

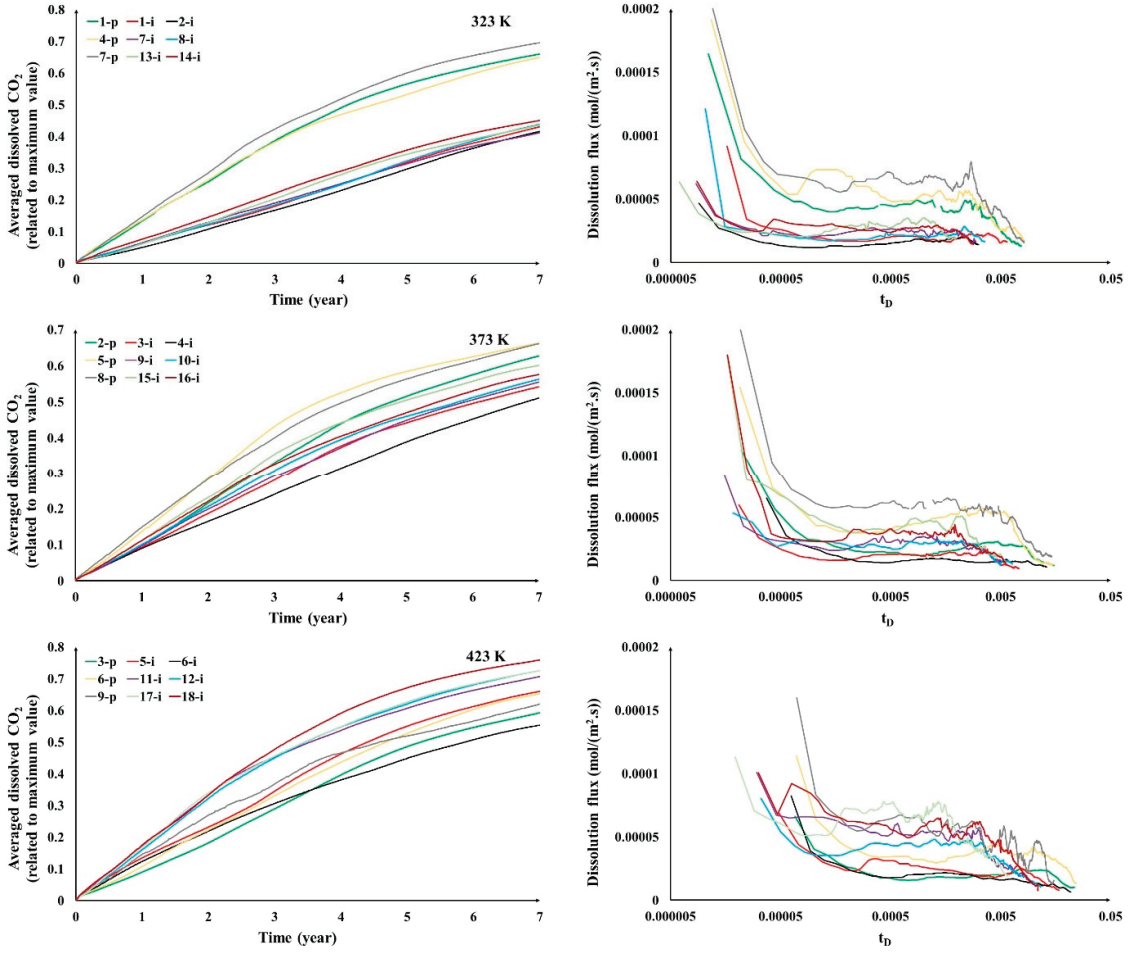

Figure 4. The averaged dissolved CO_2 and dissolution flux for pure and impure cases classified based on temperature. Legends for left- and right-hand subplots are same.

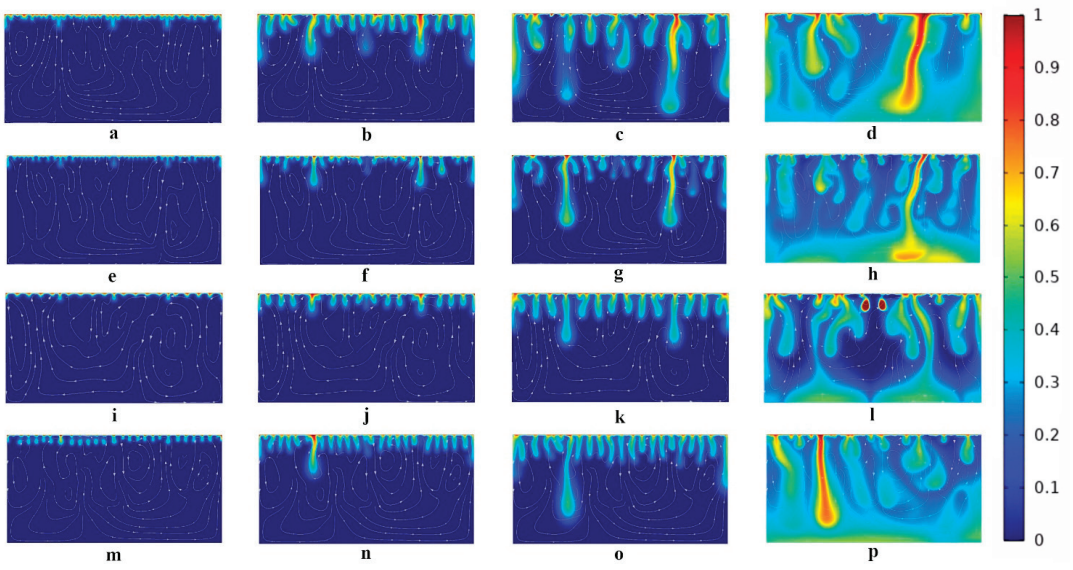

Figure 5. Dissolved CO_2 patterns for cases 7-p (first row), 13-i (second row), 9-p (third row), and 18-i (fourth row): (**a**) case 7-p at $t_D = 0.00017$; (**b**) case 7-p at $t_D = 0.00055$; (**c**) case 7-p at $t_D = 0.00108$; (**d**) case 7-p at $t_D = 0.00301$; (**e**) case 13-i at $t_D = 0.00007$; (**f**) case 13-i at $t_D = 0.00017$; (**g**) case 13-i at $t_D = 0.00034$; (**h**) case 13-i at $t_D = 0.00125$; (**i**) case 9-p at $t_D = 0.00025$; (**j**) case 9-p at $t_D = 0.0007$; (**k**) case 9-p at $t_D = 0.00157$; (**l**) case 9-p at $t_D = 0.00535$; (**m**) case 18-i at $t_D = 0.00011$; (**n**) case 18-i at $t_D = 0.00036$; (**o**) case 18-i at $t_D = 0.00071$; (**p**) case 18-i at $t_D = 0.00324$.

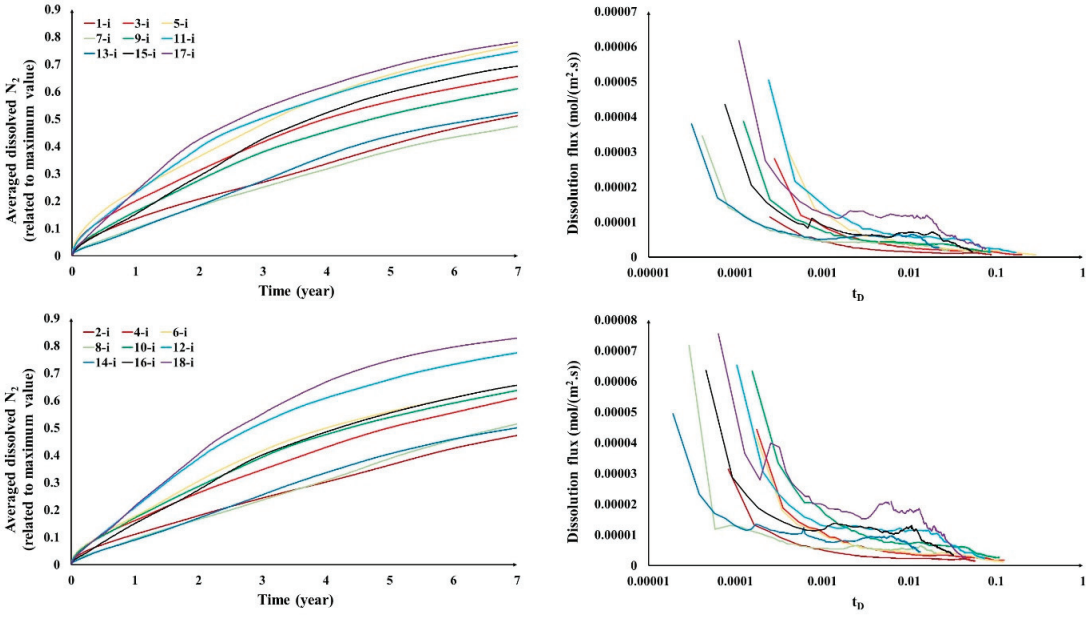

Figure 6. The averaged dissolved N_2 and dissolution flux for impure cases. Legends for left- and right-hand subplots are same.

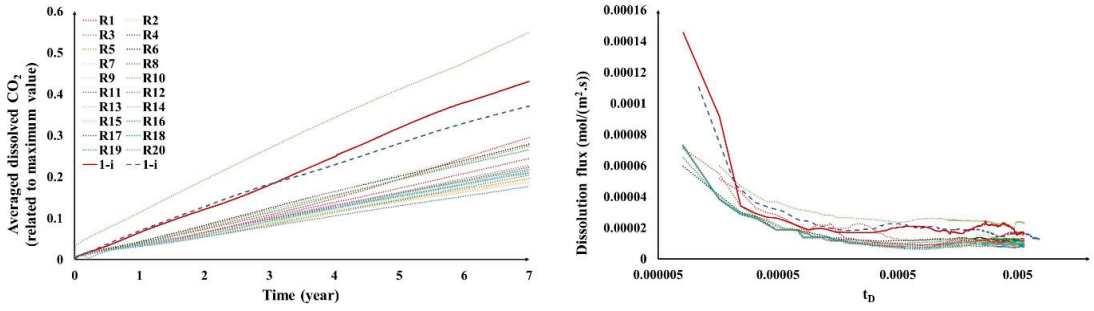

Figure 7. The heterogeneous realizations (dotted lines), homogeneous with considering cross-diffusion (solid line), and homogeneous without considering cross-diffusion (dashed line) averaged dissolved CO_2 and dissolution flux for case 1-i. Legends for left- and right-hand subplots are same.

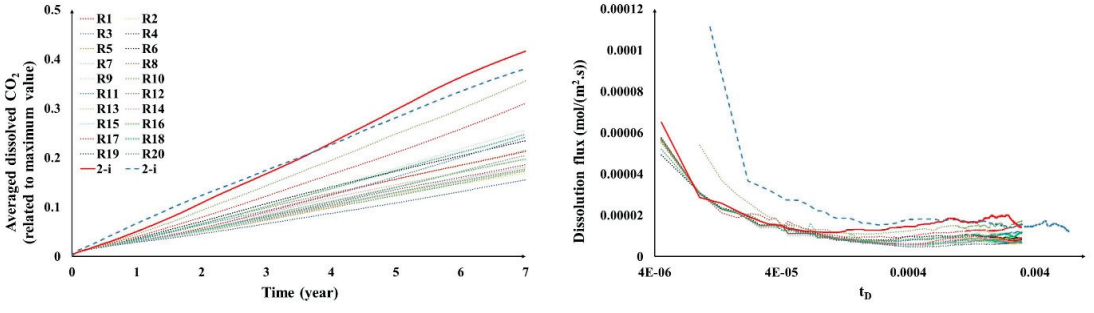

Figure 8. The heterogeneous realizations (dotted lines), homogeneous with considering cross-diffusion (solid line), and homogeneous without considering cross-diffusion (dashed line) averaged dissolved CO_2 and dissolution flux for case 2-i. Legends for left- and right-hand subplots are same.

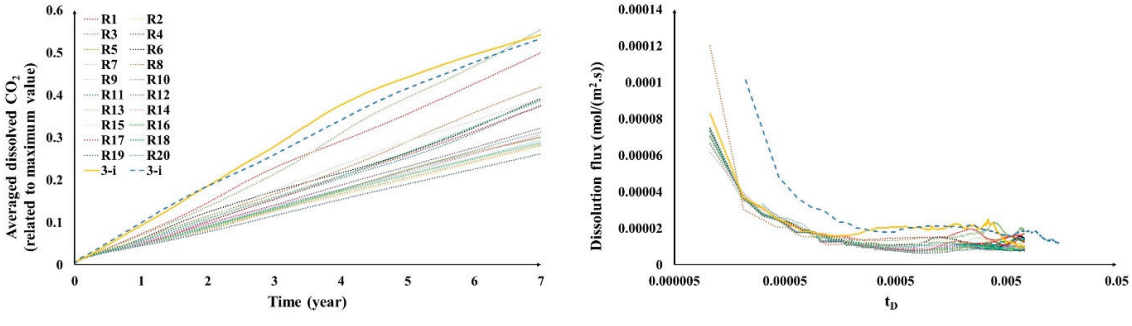

Figure 9. The heterogeneous realizations (dotted lines), homogeneous with considering cross-diffusion (solid line), and homogeneous without considering cross-diffusion (dashed line) averaged dissolved CO_2 and dissolution flux for case 3-i. Legends for left- and right-hand subplots are same.

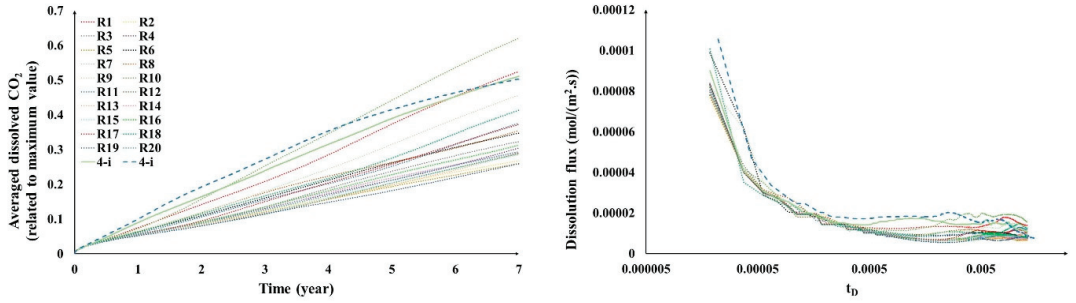

Figure 10. The heterogeneous realizations (dotted lines), homogeneous with considering cross-diffusion (solid line), and homogeneous without considering cross-diffusion (dashed line) averaged dissolved CO_2 and dissolution flux for case 4-i. Legends for left- and right-hand subplots are same.

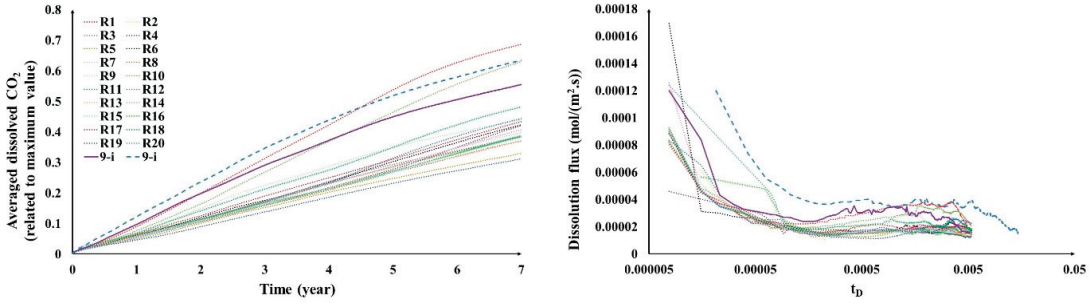

Figure 11. The heterogeneous realizations (dotted lines), homogeneous with considering cross-diffusion (solid line), and homogeneous without considering cross-diffusion (dashed line) averaged dissolved CO_2 and dissolution flux for case 9-i. Legends for left- and right-hand subplots are same.

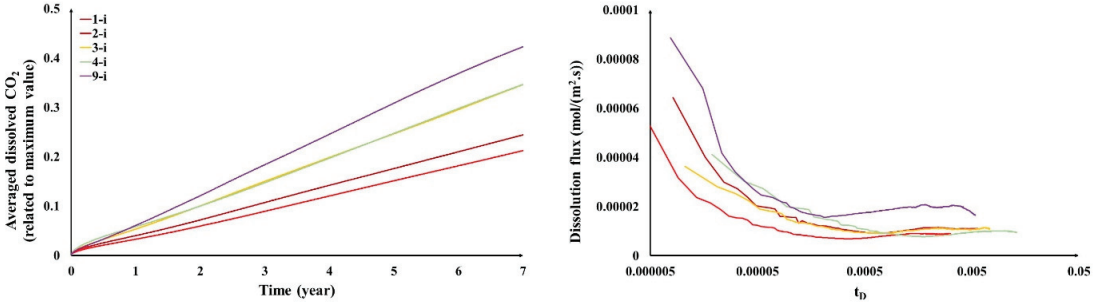

Figure 12. The averaged dissolved CO_2 and dissolution flux averaged for all the realizations of heterogeneous cases. Legends for left- and right-hand subplots are same.

4. Conclusions

In this study, we examined the CO_2–N_2 mixture dissolution in water-saturated porous media by considering the cross-diffusion effects through numerical simulations. Furthermore, we extended our study by including permeability heterogeneity in our simulations. The analysis of pure CO_2 dissolution reveals a relationship between the Rayleigh number and different quantification parameters of the dissolution process, including the dissolution flux and transition time. We proposed some correlations to predict the onset of convection, the onset of a quasi-steady state, the onset of a shut-down regime, and the dissolution flux of pure cases. The key takeaway point is that, despite the pure CO_2 in which the dissolution

flux could be estimated based on the Rayleigh number, more complexity arises from the cross-diffusion in the CO_2–N_2–water system. It seems that at lower temperatures, the N_2 impurity highly impacts and lowers the CO_2 dissolution; however, at higher temperatures, sequestrating the CO_2–N_2 mixture could be a more reasonable choice, either because of being an economically more feasible option or enhancing the CO_2 dissolution behavior. We also proposed some relations based on the Rayleigh number to predict the onset of convection, the onset of the quasi-steady state, and the onset of the shut-down regime for CO_2–N_2 cases. The interpretation of the heterogeneous cases implies that heterogeneity, in most cases, decreases the averaged dissolved CO_2, weakens the convective flow, and lowers the dissolution flux. Moreover, a stronger influence on the dissolution process at lower pressures is possible. The outcomes of this study declare that ignoring the changes in the diffusion matrix and cross-diffusion effects can cause major errors in predicting CO_2–N_2 mixture dissolution behavior. We hope that the results of this study pave the way for future studies regarding impure CO_2 sequestration in saline aquifers.

Author Contributions: Conceptualization, S.M., M.S., R.M., S.O. and I.S.; Methodology, S.M., M.S., R.M. and S.O.; Software, S.M. and M.S.; Validation, S.M., M.S., R.M. and S.O.; Formal analysis, S.M., M.S., R.M. and S.O.; Investigation, S.M., M.S., R.M., S.O. and I.S.; Resources, I.S.; Data curation, S.M., M.S. and R.M.; Writing—original draft, S.M., M.S., R.M. and S.O.; Writing—review & editing, S.M., M.S., R.M. and I.S.; Visualization, S.M., M.S. and R.M.; Supervision, I.S.; Project administration, I.S.; Funding acquisition, I.S. All authors have read and agreed to the published version of the manuscript.

Funding: The work has received funding from the FiF with project number 40101383. Authors have received support from the Group of Geothermal Science and Technology, Institute of Applied Geosciences, Technische Universität Darmstadt.

Acknowledgments: Authors have received support from the Group of Geothermal Science and Technology, Institute of Applied Geosciences, Technische Universität Darmstadt. We acknowledge support by the Deutsche Forschungsgemeinschaft (DFG, German Research Foundation) and the Open Access Publishing Fund of Technical University of Darmstadt.

Conflicts of Interest: On behalf of all authors, the corresponding authors states that there is no conflict of interest.

References

1. Rubin, E.; De Coninck, H. *IPCC Special Report on Carbon Dioxide Capture and Storage*; Cambridge University Press: Cambridge, UK, 2005; p. 14.
2. Wang, K.; Xu, T.; Wang, F.; Tian, H. Experimental study of CO_2–brine–rock interaction during CO_2 sequestration in deep coal seams. *Int. J. Coal Geol.* **2016**, *54*, 265–274. [CrossRef]
3. Ajayi, T.; Awolayo, A.; Gomes, J.; Parra, H.; Hu, J. Large scale modeling and assessment of the feasibility of CO_2 storage onshore abu dhabi. *Energy* **2019**, *185*, 653–670. [CrossRef]
4. Bradshaw, J.; Bachu, S.; Bonijoly, D.; Burruss, R.; Holloway, S.; Christensen, N.P.; Mathiassen, O.M. CO_2 storage capacity estimation: Issues and development of standards. *Int. J. Greenh. Gas Control.* **2007**, *1*, 62–68. [CrossRef]
5. Talebian, M.; Al-Khoury, R.; Sluys, L. A computational model for coupled multiphysics processes of CO_2 sequestration in fractured porous media. *Adv. Water Resour.* **2013**, *59*, 238–255. [CrossRef]
6. Soltanian, M.R.; Amooie, M.A.; Dai, Z.; Cole, D.; Moortgat, J. Critical dynamics of gravito-convective mixing in geological carbon sequestration. *Sci. Rep.* **2016**, *6*, 1–13. [CrossRef]
7. Du, S.; Su, X.; Xu, W. Assessment of CO_2 geological storage capacity in the oilfields of the Songliao Basin, North Eastern China. *Geosci. J.* **2016**, *20*, 247–257. [CrossRef]
8. Singh, M.; Chaudhuri, A.; Chu, S.; Stauffer, P.; Pawar, R. Analysis of evolving capillary transition, gravitational fingering, and dissolution trapping of CO_2 in deep saline aquifers during continuous injection of supercritical CO_2. *Int. J. Greenh. Gas Control* **2019**, *82*, 281–297. [CrossRef]
9. Singh, M.; Chaudhuri, A.; Stauffer, P.; Pawar, R. Simulation of gravitational instability and thermo-solutal convection during the dissolution of CO_2 in deep storage reservoirs. *Water Resour. Res.* **2020**, *56*, e2019WR026126. [CrossRef]
10. Amarasinghe, W.; Fjelde, I.; Rydland, J.-A.; Guo, Y. Effects of permeability on CO_2 dissolution and convection at reservoir temperature and pressure conditions: A visualization study. *Int. J. Greenh. Gas Control* **2020**, *99*, 103082. [CrossRef]
11. Amarasinghe, W.; Fjelde, I.; Giske, N.; Guo, Y. CO_2 convective dissolution in oil-saturated unconsolidated porous media at reservoir conditions. *Energies* **2021**, *14*, 233. [CrossRef]

12. Riaz, A.; Cinar, Y. Carbon dioxide sequestration in saline formations: Part 1—Review of the modeling of solubility trapping. *J. Pet. Sci. Eng.* **2014**, *124*, 367–380. [CrossRef]
13. Emami-Meybodi, H.; Hassanzadeh, H.; Green, C.; Ennis-King, J. Convective dissolution of CO_2 in saline aquifers: Progress in modeling and experiments. *Int. J. Greenh. Gas Control* **2015**, *40*, 238–266. [CrossRef]
14. Mahmoodpour, S.; Rostami, B. Design-of-experiment-based proxy models for the estimation of the amount of dissolved CO_2 in brine: A tool for screening of candidate aquifers in geo-sequestration. *Int. J. Greenh. Gas Control* **2017**, *56*, 261–277. [CrossRef]
15. Soltanian, M.; Amooie, M.; Cole, D.; Darrah, T.; Graham, D.; Pfiffner, S.; Phelps, T.; Moortgat, J. Impacts of methane on carbon dioxide storage in brine formations. *Groundwater* **2018**, *56*, 176–186. [CrossRef] [PubMed]
16. Jun, Y.-S.; Giammar, D.; Werth, C. Impacts of Geochemical Reactions on Geologic Carbon Sequestration. *Environ. Sci. Technol.* **2013**, *47*, 3–8. [CrossRef]
17. Soltanian, M.R.; Hajirezaie, S.; Hosseini, S.A.; Dashtian, H.; Amooie, M.A.; Meyal, A.; Ershadnia, R.; Ampomah, W.; Islam, A.; Zhang, X. Multicomponent reactive transport of carbon dioxide in fluvial heterogeneous aquifers. *J. Nat. Gas Sci. Eng.* **2019**, *65*, 212–223. [CrossRef]
18. Zhang, W.; Xu, T.; Li, Y. Modeling of fate and transport of coinjection of H_2S with CO_2 in deep saline formations. *J. Geophys. Res. Solid Earth* **2011**, *116*. [CrossRef]
19. Davison, J.; Thambimuthu, K. An overview of technologies and costs of carbon dioxide capture in power generation. *Proc. Inst. Mech. Eng. Part A J. Power Energy* **2009**, *223*, 201–212. [CrossRef]
20. Jacquemet, N.; Picot-Colbeaux, G.; Vong, C.Q.; Lions, J.; Bouc, O.; Jérémy, R. Intrusion of CO_2 and impurities in a freshwater aquifer—Impact evaluation by reactive transport modelling. *Energy Procedia* **2011**, *4*, 3202–3209. [CrossRef]
21. Bachu, S. CO_2 storage in geological media: Role, means, status and barriers to deployment. *Prog. Energy Combust. Sci.* **2008**, *34*, 254–273. [CrossRef]
22. Jiang, X. A review of physical modelling and numerical simulation of long-term geological storage of CO_2. *Appl. Energy* **2011**, *88*, 3557–3566. [CrossRef]
23. Li, D.; Jiang, X.; Meng, Q.; Xie, Q. Numerical analyses of the effects of nitrogen on the dissolution trapping mechanism of carbon dioxide geological storage. *Comput. Fluids* **2015**, *114*, 1–11. [CrossRef]
24. Wilkinson, M.; Boden, J.; Panesar, R.; Allam, R. CO_2 capture via oxyfuel firing: Optimisation of a retrofit design concept for a refinery power station boiler. In Proceedings of the First National Conference on Carbon Sequestration, Washington DC, USA, 15–17 May 2001; Volume 5, pp. 15–17.
25. Pipitone, G.; Bolland, O. Power generation with CO_2 capture: Technology for CO_2 purification. *Int. J. Greenh. Gas Control* **2009**, *3*, 528–534. [CrossRef]
26. Porter, R.T.; Fairweather, M.; Pourkashanian, M.; Woolley, R. The range and level of impurities in CO_2 streams from different carbon capture sources. *Int. J. Greenh. Gas Control* **2015**, *36*, 161–174. [CrossRef]
27. Bachu, S.; Bennion, B. Chromatographic partitioning of impurities contained in a CO_2 stream injected into a deep saline aquifer: Part 1. effects of gas composition and in situ conditions. *Int. J. Greenh. Gas Control* **2009**, *3*, 458–467. [CrossRef]
28. Wei, N.; Li, X.; Wang, Y.; Wang, Y.; Kong, W. Numerical study on the field-scale aquifer storage of CO_2 containing N_2. *Energy Procedia* **2013**, *37*, 3952–3959. [CrossRef]
29. Ziabakhsh-Ganji, Z.; Kooi, H. Sensitivity of joule–Thomson cooling to impure CO_2 injection in depleted gas reservoirs. *Appl. Energy* **2014**, *113*, 434–451. [CrossRef]
30. Wu, B.; Jiang, L.; Liu, Y.; Yang, M.; Wang, D.; Lv, P.; Song, Y. Experimental study of two-phase flow properties of CO_2 containing N_2 in porous media. *RSC Adv.* **2016**, *6*, 59360–59369. [CrossRef]
31. Li, D.; Jiang, X. Numerical investigation of the partitioning phenomenon of carbon dioxide and multiple impurities in deep saline aquifers. *Appl. Energy* **2017**, *185*, 1411–1423. [CrossRef]
32. Wu, B.; Jiang, L.; Liu, Y.; Lyu, P.; Wang, D.; Li, X.; Song, Y. An experimental study on the influence of co2 containing N_2 on CO_2 sequestration by x-ray CT scanning. *Energy Procedia* **2017**, *114*, 4119–4128. [CrossRef]
33. Mahmoodpour, S.; Rostami, B.; Emami-Meybodi, H. Onset of convection controlled by N_2 impurity during CO_2 storage in saline aquifers. *Int. J. Greenh. Gas Control* **2018**, *79*, 234–247. [CrossRef]
34. Mahmoodpour, S.; Amooie, M.A.; Rostami, B.; Bahrami, F. Effect of gas impurity on the convective dissolution of CO_2 in porous media. *Energy* **2020**, *199*, 117397. [CrossRef]
35. Lei, H.; Li, J.; Li, X.; Jiang, Z. Numerical modeling of co-injection of N_2 and O_2 with CO_2 into aquifers at the tongliao ccs site. *Int. J. Greenh. Gas Control* **2016**, *54*, 228–241. [CrossRef]
36. Li, D.; Zhang, H.; Li, Y.; Xu, W.; Jiang, X. Effects of N_2 and H_2S binary impurities on CO_2 geological storage in stratified formation—A sensitivity study. *Appl. Energy* **2018**, *229*, 482–492. [CrossRef]
37. Talman, S. Subsurface geochemical fate and effects of impurities contained in a CO_2 stream injected into a deep saline aquifer: What is known. *Int. J. Greenh. Gas Control* **2015**, *40*, 267–291. [CrossRef]
38. Wang, J.; Wang, Z.; Ryan, D.; Lan, C. A study of the effect of impurities on CO_2 storage capacity in geological formations. *Int. J. Greenh. Gas Control* **2015**, *42*, 132–137. [CrossRef]
39. Ershadnia, R.; Hajirezaei, S.; Gershenzon, N.; Ritzi, R., Jr.; Soltanian, M.R. Impact of methane on carbon dioxide sequestration within multiscale and hierarchical fluvial architecture. In Proceedings of the 2019 AAPG Eastern Section Meeting: Energy from the Heartland, Columbus, OH, USA, 12–16 October 2019.
40. Neufeld, J.; Hesse, M.; Riaz, A.; Hallworth, M.; Tchelepi, H.; Huppert, H. Convective dissolution of carbon dioxide in saline aquifers. *Geophys. Res. Lett.* **2010**, *37*. [CrossRef]

41. Taheri, A.; Torsaeter, O.; Wessel-Berg, D.; Soroush, M. Experimental and simulation studies of density-driven-convection mixing in a Hele-Shaw geometry with application for CO_2 sequestration in brine aquifers. In Proceedings of the SPE Europec/EAGE Annual Conference, Copenhagen, Denmark, 4–7 June 2012; Society of Petroleum Engineers: Richardson, TX, USA, 2012.
42. MacMinn, C.; Neufeld, J.; Hesse, M.; Huppert, H. Spreading and convective dissolution of carbon dioxide in vertically confined, horizontal aquifers. *Water Resour. Res.* **2012**, *48*. [CrossRef]
43. Mahmoodpour, S.; Rostami, B.; Soltanian, M.R.; Amooie, M.A. Convective dissolution of carbon dioxide in deep saline aquifers: Insights from engineering a high-pressure porous visual cell. *Phys. Rev. Appl.* **2019**, *12*, 034016. [CrossRef]
44. Mahmoodpour, S.; Rostami, B.; Soltanian, M.R.; Amooie, M.A. Effect of brine composition on the onset of convection during co2 dissolution in brine. *Comput. Geosci.* **2019**, *124*, 1–13. [CrossRef]
45. Tang, Y.; Li, Z.; Wang, R.; Cui, M.; Wang, X.; Lun, Z.; Lu, Y. Experimental study on the density-driven carbon dioxide convective diffusion in formation water at reservoir conditions. *ACS Omega* **2019**, *4*, 11082–11092. [CrossRef] [PubMed]
46. Fu, B.; Zhang, R.; Liu, J.; Cui, L.; Zhu, X.; Hao, D. Simulation of CO_2 rayleigh convection in aqueous solutions of NaCl, KCl, $MgCl_2$ and $CaCl_2$ using lattice boltzmann method. *Int. J. Greenh. Gas Control* **2020**, *98*, 103066. [CrossRef]
47. Soltanian, M.R.; Amooie, M.A.; Gershenzon, N.; Dai, Z.; Ritzi, R.; Xiong, F.; Cole, D.; Moortgat, J. Dissolution trapping of carbon dioxide in heterogeneous aquifers. *Environ. Sci. Technol.* **2017**, *51*, 7732–7741. [CrossRef] [PubMed]
48. Raad, S.M.J.; Hassanzadeh, H. Does impure CO_2 impede or accelerate the onset of convective mixing in geological storage? *Int. J. Greenh. Gas Control* **2016**, *54*, 250–257. [CrossRef]
49. Kim, M.C.; Song, K.H. Effect of impurities on the onset and growth of gravitational instabilities in a geological CO_2 storage process: Linear and nonlinear analyses. *Chem. Eng. Sci.* **2017**, *174*, 426–444. [CrossRef]
50. Bachu, S.; Bonijoly, D.; Bradshaw, J.; Burruss, R.; Holloway, S.; Christensen, N.P.; Mathiassen, O.M. CO_2 storage capacity estimation: Methodology and gaps. *Int. J. Greenh. Gas Control.* **2007**, *1*, 430–443. [CrossRef]
51. Raad, S.M.J.; Hassanzadeh, H. Prospect for storage of impure carbon dioxide streams in deep saline aquifers—A convective dissolution perspective. *Int. J. Greenh. Gas Control* **2017**, *63*, 350–355. [CrossRef]
52. Omrani, S.; Mahmoodpour, S.; Rostami, B.; Sedeh, M.S.; Sass, I. Diffusion coefficients of CO_2–SO_2–water and CO_2–N_2–water systems and their impact on the CO_2 sequestration process: Molecular dynamics and dissolution process simulations. *Greenh. Gases: Sci. Technol.* **2021**, *11*, 764–779. [CrossRef]
53. Rives, R.; Mialdun, A.; Yasnou, V.; Shevtsova, V.; Coronas, A. Experimental determination and predictive modelling of the mutual diffusion coefficients of water and ionic liquid 1-(2-hydroxyethyl)-3-methylimidazolium tetrafluoroborate. *J. Mol. Liq.* **2019**, *296*, 111931. [CrossRef]
54. Mialdun, A.; Bataller, H.; Bou-Ali, M.M.; Braibanti, M.; Croccolo, F.; Errarte, A.; Ezquerro, J.M.; Fernández, J.J.; Gaponenko, Y.; García-Fernández, L.; et al. Preliminary analysis of diffusion coefficient measurements in ternary mixtures 4 (dcmix4) experiment on board the international space station. *Eur. Phys. J. E* **2019**, *42*, 1–9. [CrossRef]
55. Mialdun, A.; Bou-Ali, M.M.; Braibanti, M.; Croccolo, F.; Errarte, A.; Ezquerro, J.M.; Fernandez, J.J.; García-Fernández, L.; Galand, Q.; Gaponenko, Y.; et al. Data quality assessment of diffusion coefficient measurements in ternary mixtures 4 (dcmix4) experiment. *Acta Astronaut.* **2020**, *176*, 204–215. [CrossRef]
56. Lengler, U.; De Lucia, M.; Kühn, M. The impact of heterogeneity on the distribution of CO_2: Numerical simulation of CO_2 storage at Ketzin. *Int. J. Greenh. Gas Control* **2010**, *4*, 1016–1025. [CrossRef]
57. Delbari, M.; Afrasiab, P.; Loiskandl, W. Using sequential gaussian simulation to assess the field-scale spatial uncertainty of soil water content. *Catena* **2009**, *79*, 163–169. [CrossRef]
58. Safikhani, M.; Asghari, O.; Emery, X. Assessing the accuracy of sequential gaussian simulation through statistical testing. *Stoch. Environ. Res. Risk Assess.* **2017**, *31*, 523–533. [CrossRef]
59. Jia, W.; McPherson, B.; Pan, F.; Dai, Z.; Moodie, N.; Xiao, T. Impact of three-phase relative permeability and hysteresis models on forecasts of storage associated with CO_2-EOR. *Water Resour. Res.* **2018**, *54*, 1109–1126. [CrossRef]
60. Bachu, S.; Nordbotten, J.; Celia, M. Evaluation of the spread of acid-gas plumes injected in deep saline aquifers in western canada as an analogue for CO_2 injection into continental sedimentary basins. In *Greenhouse Gas Control Technologies 7*; Elsevier: Amsterdam, The Netherlands, 2005; pp. 479–487.
61. Ennis-King, J.; Preston, I.; Paterson, L. Onset of convection in anisotropic porous media subject to a rapid change in boundary conditions. *Phys. Fluids* **2005**, *17*, 084107. [CrossRef]
62. Islam, A.; Lashgari, H.R.; Sephernoori, K. Double diffusive natural convection of CO_2 in a brine saturated geothermal reservoir: Study of non-modal growth of perturbations and heterogeneity effects. *Geothermics* **2014**, *51*, 325–336. [CrossRef]
63. Lapwood, E. Convection of a fluid in a porous medium. In *Mathematical Proceedings of the Cambridge Philosophical Society*; Cambridge University Press: Cambridge, UK, 1948; Volume 44, pp. 508–521.
64. Raad, S.M.J.; Hassanzadeh, H. Onset of dissolution-driven instabilities in fluids with nonmonotonic density profile. *Phys. Rev. E* **2015**, *92*, 053023. [CrossRef]

energies

MDPI

Article

A Numerical Study on the Characteristics of the Pressurized Water Reactor's (PWR) Primary Moisture Separator Using the Particle Tracking Method

Hongwu Zhao [1], Jun-Ho Jeon [2], Dong-In Yu [3] and Yeon-Won Lee [3,*]

[1] Department of Mechanical Design Engineering, Graduate School of Pukyong National University, Busan 48513, Republic of Korea
[2] PIBEX Inc., CAE Team, Pohang 37668, Republic of Korea
[3] School of Mechanical Engineering, Pukyong National University, Busan 48513, Republic of Korea
* Correspondence: ywlee@pknu.ac.kr; Tel.: +82-51-629-6162

Abstract: The primary moisture separator—a key component in the PWR nuclear power plant—determines the quality of supplied steam to a turbine. Investigating its characteristics is important because supplying steam with excessive droplet entrainment results in damages to pipes, valves, and turbines in power plant circuits. In this numerical study, the particle tracking method in the Eulerian–Lagrangian methodology is used to investigate the characteristics of a primary moisture separator. Various swirl vanes with different bending angles, vane quantities, and vane locations are chosen to investigate the effect of design parameters on characteristics of the primary moisture separator. Additionally, the water droplet size is considered to vary from 0.01 to 50 μm in this study. The pressure drop between the inlet and outlet, the steam quality at the orifice outlet, and the particle collection ratio are discussed in this paper. The results show that steam quality increases as the bending angle decreases, and increasing the number of swirl vanes increases both the pressure drop and the steam quality.

Keywords: primary moisture separator; swirl vane; droplet size; particle tracking method; CFD

Citation: Zhao, H.; Jeon, J.-H.; Yu, D.-I.; Lee, Y.-W. A Numerical Study on the Characteristics of the Pressurized Water Reactor's (PWR) Primary Moisture Separator Using the Particle Tracking Method. *Energies* **2023**, *16*, 1310. https://doi.org/10.3390/en16031310

Academic Editor: Bjørn H. Hjertager

Received: 30 December 2022
Revised: 19 January 2023
Accepted: 20 January 2023
Published: 26 January 2023

1. Introduction

Nuclear power plants, when compared with coal-fired power plants, do not emit carbon dioxide, sulfur dioxide, nitrogen oxides, and other environmentally damaging emissions. They can be considered as one of the alternatives to traditional fossil fuel power plants in terms of environmental protection. There has been little growth in fossil fuel power plants in the past ten years. On the contrary, the development of nuclear power is gaining importance all over the world [1]. Therefore, research on nuclear power has become a popular research project in many countries. In this study, the PWR's primary moisture separator is the target of this investigation. The primary moisture separator, located in the upper part of the steam generator, plays a key role in the system [2]. The mixture flow into the moisture separator becomes the swirl flow after the swirl vane. The swirl flow is generated by a swirling motion that imparts a swirl velocity component to the flow, by using an axial-plus-tangent entry into the vortex generator, or by tangential entry into the chamber [3]. This swirl flow makes the droplets migrate towards the wall of the riser and forms a thin water film on the wall. Due to the density differences between the water droplet and the vapor, the water droplets are separated from the mixture. More than 80% of the droplets generated in the steam generator should be separated by the primary moisture separator [4].

Numerous researchers have studied the characteristics of the primary moisture separator. Several scholars have focused on the theoretical study of the separator. Qu et al. [5],

Najafi et al. [6], and Saqr et al. [7] mainly investigated the importance of the swirl intensity in the process of separating. Liu et al. [8] developed a mechanistic model for the prediction of swirling annular flow pattern transitions. Based on their investigation, they concluded that the annular flow property was related to the critical film thickness and critical gas/liquid velocity. These scholars' results illustrated that the newly developed correlation yielded a more accurate transition flow pattern prediction for swirl flows. Additionally, Liu et al. [9] mathematically investigated separators and proposed a scaling law that enabled a comparison between the reduced and full-scale model. Based on the scaling theory, several scholars investigated the separator through the experimental method. Matsubayashi et al. [10], Kataoka et al. [4], and Funahashi et al. [11,12] studied the boiling water reactor's (BWR) separator by changing the geometry, including the bending angle and the vane quantity, and by adding pick-off rings. The pressure drop or separation was related to these parameter designs. Furthermore, Nishida et al. [13] developed a new design with a swirl vane hub with a small diameter and horizontal slits at the riser barrel. This design could also strongly prevent vane damage. Nevertheless, Xiong et al. [14], Kataoka et al. [15], and Funahashi et al. [16] experimentally investigated the separator by changing the mixture velocity or single phase flux. Their experimental studies were mostly focused on the geometry design or the changing inlet conditions.

In comparison to the experimental approach, which always needs to consider the scaling law, the numerical approach can easily overcome this scaling problem. Due to the development of computer technology in the past few decades, the numerical analysis has sufficient robustness for determining the characteristics of the moisture separator, as long as the appropriate model is selected [17]. Tamrina et al. [18] concluded that the higher-order discretization scheme yielded a better result compared to the first-order scheme. Zhang et al. [19,20] numerically studied both primary and secondary separators of the AP1000 geometry. Their results illustrated the primary stage separation efficiency with different inlet humidity values. Tian et al. [21] numerical studied a new structure of separators. They concluded that reducing the cylinder diameter could increase the separation effect. Kataoka et al. [22] used numerical methods to investigate the pressure drop and film thickness in a moisture separator. After changing the gas and liquid volume fluxes, the results illustrated that the pressure drop with a swirling flow was about five times that with a nonswirling flow. Huang et al. [20] and Song et al. [23] numerically studied the separation process of the moisture separator. They verified the feasibility of the numerical analysis and concluded that the data matched the experiment. Fang et al. [2,24] studied a full-scale numerical model regarding the process from the moisture separator to the dryer and then compared the difference between the moisture separator and the dryer. Their conclusions showed that the separator simulation should consider the cold leg and hot leg in the steam generator. Saito et al. [25] numerically analyzed the droplet behavior of the BWR's moisture separator. They concluded that the deposition coefficient would increase by adding the swirl intensity. Katono et al. [26] numerically and experimentally studied the down-scale moisture separator characteristics by moving the swirl vane section. The results showed that a modified separator could reduce the pressure drop by more than 50%. Xiong et al. [27] developed an experiment and simulation on a 1:3.5 scale swirl vane separator and investigated both the separation efficiency and pressure drop. The conclusions illustrated that the pressure was mainly affected by the airflow rate and water droplet size. Rocha et al. [28] developed an axially induced swirling pipe flow through numerical and experimental studies. They concluded that smaller gap widths and larger deflection angles could provide more swirls. This result can be beneficial for applications that require swirling over a longer pipeline distance.

Based on the above literature review, we found that most numerical investigations on moisture separators used the volume of fluid (VOF) method. However, we know that the approach to dealing with numerically capturing interfaces is an established field in CFD communities [29]. Logically, this kind of multiphase flow problem can be classified as a continuity phase and a dispersed phase, which are solved through Eulerian and

Lagrangian approaches, respectively [30,31]. Zhang et al. [19,21,27] used the VOF method. However, the particle tracking multiphase model mentioned in Fang et al. [29,32,33] was used for a bubble flow. The target in this study focused on capturing droplet particles in moisture separators. Judging from the property of moisture flow, the droplets are transported by the steam. In order to classify the process of capturing particles during the moisture flow through the moisture separator, a suitable approach should be considered. The particle tracking method is suitable for this study, even though it is simple. The particle tracking model based on the Lagrangian–Eulerian methodology is used here to study the characteristics of the primary moisture separator. Since the droplet particles follow the steam flow during the flow process, the effect of the droplet particles on the steam flow is ignored, and a one-way coupling is applied in the simulation process.

Although previous researchers have made many research contributions in this field, the research on moisture separators is still insufficient. Here, we focus on the moisture separator's droplet-capturing process by using the particle tracking method. In addition, we investigate the effects of different moisture separator models aiming to increase the separator's outlet steam quality and decrease the pressure drop. We also aim to improve the separation efficiency of the moisture separators. This study can act as a relevant reference for future designs and research. In this numerical study, the particle tracking method in the Eulerian–Lagrangian methodology is used to investigate the characteristics of the primary moisture separator. Different swirl vane bending angles, different quantities of swirl vanes, and different swirl vane locations are chosen to investigate the characteristics of the primary moisture separator. Moreover, various water droplet sizes—from 0.01 to 50 μm—are also considered in this study.

2. Numerical Analysis

The moisture separator model comes from the general model of the steam generator of the pressurized water reactor in a nuclear power plant [34]. Figure 1 shows the schematic of the computational domain used and the mesh generation in this study. It includes a tangent nozzle outlet, an orifice outlet, a downcomer outlet, a riser, swirl vanes, and an inlet.

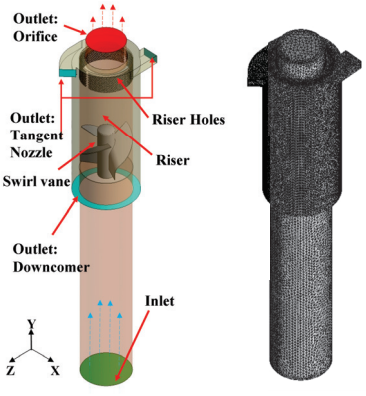

Figure 1. Schematic of the computational domain and the mesh generation.

2.1. Governing Equations

2.1.1. Continuous and Dispersed Fluid

The process of moisture flow in the separator was considered adiabatic so that we only needed to calculate the continuity and momentum equation. The moisture flow was

classified into a continuous fluid-steam and dispersed fluid–water particle. The governing equations that describe the flow of the continuous fluid are given below [30,35,36].

$$\frac{\partial \rho}{\partial t} + \frac{\partial \rho u_i}{\partial x_i} = 0 \tag{1}$$

$$\frac{\partial (\rho u_i)}{\partial t} + \frac{\partial (\rho u_i u_j)}{\partial x_j} = -\frac{\partial p}{\partial x_i} + \frac{\partial}{\partial x_j}[\mu(\frac{\partial u_i}{\partial x_j} + \frac{\partial u_j}{\partial x_i})] + S_M \tag{2}$$

where ρ, u, p, μ, and S_M are the density, velocity, pressure, viscosity, and the sum of body force, respectively. For turbulence models, the $k-\epsilon$ model, the baseline (BSL) $k-\omega$ model, and the shear stress transport (SST) $k-\omega$ model were compared. The simulation results showed that the BSL model was not suitable for the particle tracking model when compared to the results of the $k-\epsilon$ model and the SST $k-\omega$ model. Previous researchers compared the model simulations, and the results showed that the SST $k-\omega$ model had stronger adaptability to the swirl flow compared to the $k-\epsilon$ model [17,21]. The BSL model failed to predict the onset and the amount of flow separation from the smooth surfaces, despite combining the Wilcox and the $k-\epsilon$ model. This is why these models do not account for the transport of the turbulent shear stress and overpredict the eddy viscosity [30]. For these reasons, the SST $k-\omega$ model was applied in this study. The SST $k-\omega$ model solves the two transport equations, namely, one for the turbulent kinetic energy and the other for the turbulent frequency. The stress tensor is computed from the eddy viscosity equation [30]. The SST $k-\omega$ model assumes that the turbulence viscosity is linked to the turbulence kinetic energy k and the turbulent frequency ω through the equations.

$$\mu_t = \rho \frac{k}{\omega} \tag{3}$$

$$\frac{\partial (\rho k)}{\partial t} + \frac{\partial}{\partial x_j}(\rho u_j k) = \frac{\partial}{\partial x_j}[(\mu + \frac{\mu_t}{\sigma_k})\frac{\partial k}{\partial x_j}] + P_k - \beta' \rho k \omega + P_{kb} \tag{4}$$

$$\frac{\partial (\rho \omega)}{\partial t} + \frac{\partial}{\partial x_j}(\rho u_j \omega) = \frac{\partial}{\partial x_j}[(\mu + \frac{\mu_t}{\sigma_\omega})\frac{\partial \omega}{\partial x_j}] + \alpha \frac{\omega}{k} P_k - \beta \rho \omega^2 + P_{\omega b} \tag{5}$$

where μ_t, k, and ω are the turbulence viscosity, kinetic energy, and turbulence frequency, respectively. σ, β, and P are the constant coefficients for the turbulence model. Their specific expression can be found in [30].

2.1.2. Particle Tracking Methodology

In the process of Lagrange particle implementation, a specified portion of particles represents all of the particles in the flow through the continuum fluid during particle transport. The discrete particle moves in the continuous fluid medium. Such a particle's motion is driven by the force exchange between the continuum and discrete media. The process equations are derived from Basset, Boussinesq, and Oseen [30]. The equations are as follows:

$$\frac{dx_p}{dt} = U_p \tag{6}$$

$$x_p^n = x_p^o + U_p^o \delta_t \tag{7}$$

$$m_p \frac{dU_p}{dt} = F_D + F_B + F_R + F_{vm} + F_P + F_{BA} \tag{8}$$

$$m_p = \frac{\pi}{6} d_p^3 \rho_p \tag{9}$$

where x_p, U_p^o, and m_p are the particle displacement, the initial particle velocity, and the mass of the particle, respectively. The superscripts o and n refer to old and new values, respec-

tively. These equations describe the method to calculate the particle variables and the realization of the interphase transfer through the particle transport model. Equations (6) and (7) illustrate the calculation of the new value of one particle during the simulation, and δ_t represents the timestep. The variables F_D, F_B, F_R, F_{VM}, F_P, and F_{BA} in Equation (8), respectively, represent the drag force acting on the particle, the buoyancy force due to gravity, the forces due to domain rotation, the virtual mass force, the pressure gradient force, and the Basset force or history term that accounts for the deviation in flow pattern from a steady state.

2.2. Modeling and Analysis

The mixture in the moisture separator is swirled by a swirl vane in the moisture separator. Due to the differences in density, the droplet particles with a larger mass are subjected to more centrifugal force, leading to a move towards the riser wall. Several droplets in the mixture are captured and separated by the riser wall and become the reflux of the downcomer. Some of the droplets come out of the separator's tangent nozzle into the steam generator's gravity space. The particles are returned to the steam generator for further separating due to the action of gravity.

According to the automatic near-wall treatment method requirements of the CFX [30], the first node distance should avoid the buffer layer. The solver will choose a suitable treatment based on the detection Y-plus value. For this study case, a Y-plus value between 30 and 200 was chosen, which means the Y-plus was located at the log-law layer of the boundary layer. This solution approach used a fully implicit discretization of the equations at any given time scales—set as 0.04 s. Since the particle tracking method selected a certain number of particles to substitute for all the droplet particles in the simulation [30], a particle-quantity-sensitive study became necessary. The particle numbers were chosen from 100 to 20,000, which were distributed randomly in the geometry inlet to inspect the influence of the particle numbers. When the number of particles exceeded 1000, the result of the steam quality at the orifice outlet tended to be constant. Nevertheless, in order to test sufficient particles, the number of particles in different cases was chosen as 10,000 to represent all the water particles in this study.

When the particles collide with each other and with the separator wall, we considered the exchange momentum only with the wall. During such collisions, the momentum loss is controlled by constant or time-dependent coefficients of restitution. In the case of a fully inelastic collision, the particles are collected on the wall. Generally, the droplets will migrate to the wall and become a film after contact with the separator surface. The model enforced that all particles hitting the wall became part of the wall film, regardless of their impact velocity or impact angle. To terminate the tracking of particles when they hit a wall boundary, both the perpendicular and parallel coefficients could be set to zero. The particle then came to a stop regardless of what was set for the parallel coefficient of restitution.

Figure 2 shows the schematic of the wall treatment method described above. When the parallel and perpendicular restitution coefficient is set to 1, the particle fully rebounds, and when both the coefficients are set to 0, the particles do not rebound because they are captured by the wall when they are in contact. The restitution coefficient was set to 0 in this study.

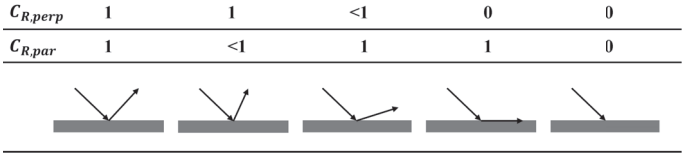

Figure 2. The schematic of the wall treatment method [30].

Since the separator consists of many curved surfaces and small holes, the tetra/mixed type meshing was used to better fit the mesh with the model. For the partitioning methods, the robust mode by which sufficient parts are divided was used. To accurately capture the

boundary layer flow during the simulation process, all parts of the wall were added to the prism mesh in this study, and the grid was set to 5 layers. Before the particle quantity sensitivity analysis, we also completed a mesh independence study. The nodes' quantities were, respectively, from 1.3 million to 6.3 million. The three-dimensional computational domain was discretized to an unstructured grid using the ICEM CFD meshing tool. As shown in Figure 3, with the number of nodes at more than 4.2 million, the result of the steam quality at the orifice outlet changed within 3% from 4.2 million nodes to 6.3 million nodes. The changes were calculated by the function $C_{change} = (SQ_2 - SQ_1)/SQ_1$, where SQ represents the steam quality with different mesh quantities. Thus, the study simulation of different conditions used the same order of magnitude as for node quantities over 4 million.

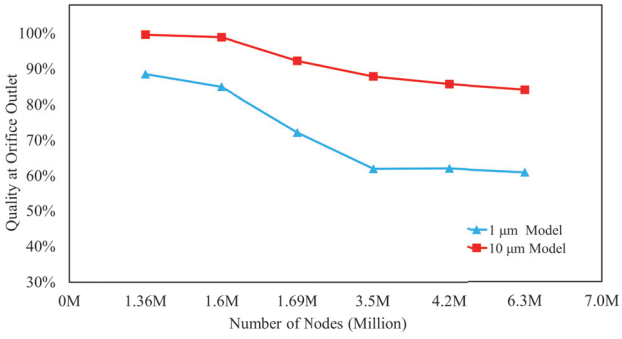

Figure 3. Results of mesh independence.

Generally, this study was based on a well-known moisture separator model. Most work was completed in the ANSYS platform. The preprocessing was based on the ANSYS ICEM CFD. The solving process applied was ANSYS CFX, which is known as a fully implicit coupled solver. As mentioned before, the turbulence model applied was the SST $k - \omega$ model, and the multiphase model was based on the particle transport theory. The discretization schemes in this study were chosen using the high-resolution method in CFX. The linear equations were solved using an algebraic multigrid method (AMG). Additionally, postprocessing was applied via ANSYS CFD-post.

2.3. Problem Description

To study the influence of different structures of the swirl vane separator, three different geometries—with different vane bending angles, different vane quantities, and different vane locations—were used. Figures 4–6 show the schematics of these different structures, respectively.

Figure 4 shows the vane bending angle α as the angle between the curved line of the swirl vane and the horizontal line. Four angle cases, namely, 20°, 30°, 40°, and 50°, were chosen. Figure 5 shows the variation in swirl vane quantities from 3 to 6. Figure 6 shows the different vane locations, where Y denotes the distance from the outline of the vane bottom to the original vane bottom outline. The reference model origin point was defined as the distance between the orifice outlet plane and the swirl start plane, which was equal to 1400 mm. The case with a bending angle of 30°, 4 vanes, and Y = 0 was taken as the reference model.

The physical parameters and boundary conditions used in this study are shown in Table 1. The real operation conditions of the power plant were applied as the simulation conditions. The steam inlet mass flow rate and pressure were fixed as 30 kg/s and 6.9 MPa. The droplet particle size ranged from 1 to 50μm for all cases to investigate the influence on particle size. Forty-five cases were analyzed in this study and were divided into 4 groups. The pressure drop results were classified into 3 groups to visualize the effect of different

geometries. The classification details are shown in Table 2. Related discussions are provided

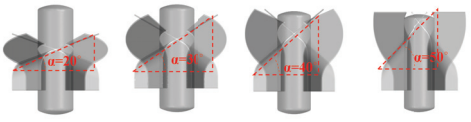

Figure 4. Schematic of different vane bending angles.

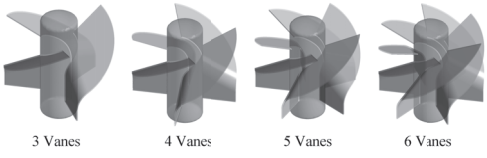

Figure 5. Schematic of different swirl vane quantities.

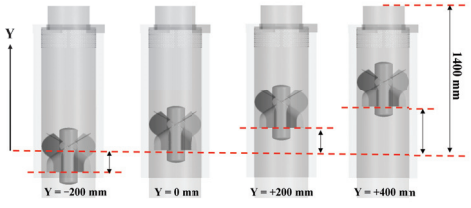

Figure 6. Schematic of the different swirl vane locations from the origin.

Table 1. Summary of input parameters.

Properties	Values	Units
Inlet steam mass flow rate	30	kg/s
Inlet particle mass flow rate	90	kg/s
Inlet pressure	6.9	MPa
Inlet temperature	300	°C
Outlet pressure	0	MPa
Bending angle of swirl vane	20, 30, 40, 50	deg
Swirl vane quantity	3, 4, 5, 6	-
Swirl vane location	−200, 0, 200, 400	mm
Particle size	0.01, 0.1, 1, 10, 30, 50	μm
Injected particle quality	25	%

The information about the droplet particle size distribution could be obtained from relevant references [37–40], and the following conclusions could be made. When the number of droplet particles was large enough, the droplet size followed the law of a normal distribution, which is a continuous probability distribution of a random variable whose logarithm is normally distributed. Through this theory, we could further analyze the steam quality difference in this paper. The mathematical relationship between the steam quality result under a specific particle size and the real steam quality result could be determined. We provide the expression of the droplet size normal distribution as follows:

$$f(D) = A\frac{1}{D\sigma\sqrt{2x}}exp - (\frac{(\ln D - \ln D_{av})^2}{2\sigma^2}) \quad (10)$$

where D represents the diameter of the droplet, D_{av} represents the average droplet size in this paper, and σ represents the standard deviation of the droplet size. The average droplet size was set to be 138 µm, the standard variance $\sigma = 0.5514$, and the amplitude coefficient $A = 530$ [40]. The droplet particle size normal distribution is shown in Figure 7.

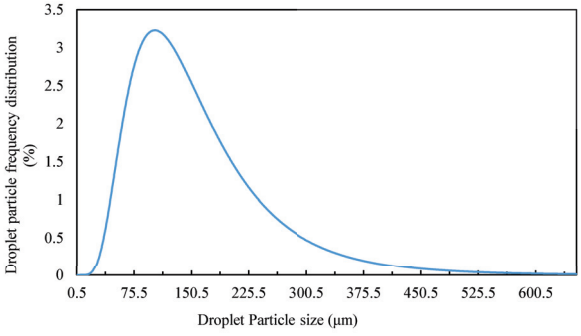

Figure 7. Droplet particle size normal distribution.

After integrating the equation, the cumulative distribution function could be obtained. After multiplying and summing the result of the numerical solution in this paper and the result of the distribution function, we obtained the theoretical real steam quality at the outlet of the moisture separator. The function was as follows:

$$Q_{total} = \sum_{0}^{Maxsize}(Q_n F_n) \quad (11)$$

Q_{total} represents the steam quality after the separator, Q_n represents the simulated results of the steam quality after the steam separator at a specific droplet size n, and F represents the percentage of the corresponding droplet size n obtained by the distribution function. Through this formula, we could calculate the real outlet steam quality of moisture separators of different structures.

Table 2. Classification groups of the pressure drop results.

	Case 1	Case 2	Case 3	Case 4
Bending angle	20 deg	30 deg	40 deg	50 deg
Vane quantity	3	4	5	6
Vane location	−200 mm	0	200 mm	400 mm

3. Results and Discussion

In this section, several flow fields are presented to briefly describe the separator flow. These results are based on the reference model with a bending angle of 30°, four swirl vanes, and a reference swirl vane location.

Figure 8 shows the pressure and velocity distribution of the reference model. The pressure decreased when the mixture flowed through swirl vanes. The velocity magnitude distribution had a different trend when the mixture flowed through the swirl vanes. The maximum velocity could be found at the bending point of the swirl vanes. The velocity magnitude of moisture was at a relatively low level compared to the location after the swirl vanes. On the contrary, when moisture flowed through the swirl vane, the velocity was significantly rotated. Finally, the fluid entered the downcomer through the holes in the riser, and the remaining part flowed into the tangent nozzle outlet and the orifice

outlet. The reason for the sudden change in velocity and pressure was that the flow section area shrunk at the swirl vane. Similar results were found by He et al. [41] and Fang et al. [24]. The distribution of velocity in the separator changed sharply near the swirl vane. The corresponding visualizations can be seen in Figure 9 for different locations along the Y axis. Y = −150 mm and Y = 1400 mm represent the moisture separator's bottom and top, respectively. The figure at −150 mm shows that the mixture flow had no swirl before the swirl vane. As the flow went up to 200 mm, a strong swirling flow was generated. At 1000 mm, it was clear that part of the mixture would flow out of the riser holes. Tian et al. [21] found a similar distribution in sectional views. The above shows that the particle separated from the mixture process. Because of the swirl generated, several particles moved toward the wall and were captured by the wall. Several particles flowed out from the riser holes.

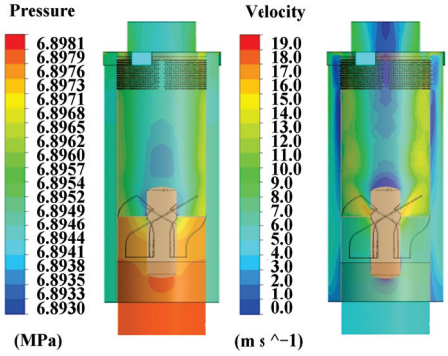

Figure 8. Pressure and velocity magnitude distribution of the reference model.

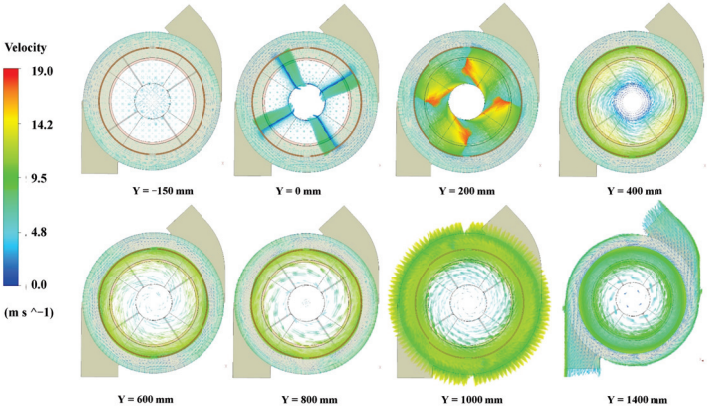

Figure 9. Velocity vector contours from Y = −150 mm to Y = 1400 mm in the reference model.

3.1. Droplet Separation Process

In this section, the effect of different structures on the droplets captured on the separator wall is considered . The results are summarized based on the reference model. Using the particle tracking method to simulate the process provided a simple way of capturing the water droplets' motion features during the process of the steam flow [31]. It allowed us to understand the correlation principle of the particles being captured by the wall in the separator.

Firstly, in Figure 10, the streamline and velocity isosurface of the moisture flow are shown. It is obvious that the moisture obtained a swirl component during the process of

passing through the swirl vanes. This caused the moisture to flow in the vertical direction with a tangential velocity. The droplet particles in the mixture fluid were collected by the riser wall when they encountered it. For the mixture, the density gap between the vapor and droplet particles were utilized for this process. As the density of the droplets was greater than that of the steam, the particles were subjected to a greater centrifugal force. Based on this principle, the swirl velocity in the separator needed to be increased if the droplets were to easily migrate to the wall.

The results related to the particle size are summarized in the following sections. When the droplet particle diameter increased, the mass of the droplets was continuously increased. This led to an increase in the centrifugal force of the droplet particles. The particles moved in the direction of the center of the cut surface and were captured by the wall. All three structures made use of this centrifugal force. As in the other two sections, the results show that the change in the swirl vane angle had the highest influence on particle capture.

In contrast, Fang et al. [23] concluded that, when the particle diameter exceeded 102 μm, all droplet particles were separated from the steam, and Matsubayashi et al. [8] illustrated that the critical particle size was 25 μm. These different results are due to the different inlet steam velocity in these investigations. Our results showed a critical particle size of around 50 μm because the inlet velocity was higher than in previous studies. It is understood that different researchers have different critical particle sizes due to the particle collection rate. The results came from different kinds of geometries and various definition conditions in the simulations.

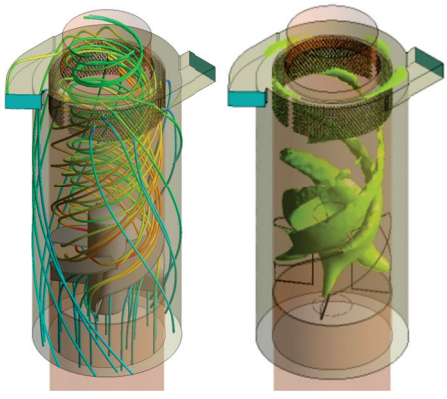

Figure 10. The streamline and velocity isosurface of the moisture flow.

3.2. Effect of the Vane Bending Angle

Figure 11 shows the rate of particles collected on the wall with changing vane angles and droplet sizes. The vertical axis is the ratio of water droplets removed by wall collisions. As the droplet size increased, the rate of particles collected on the wall increased. A vane bending angle from 20° to 50° maintained a constant collection rate if the droplet size was less than 1μm. A vane angle of 20° had the highest particle collection rate, and a vane bending angle of 50° had the lowest collection rate, even at 50 μm. Moreover, the critical particle size, which is a collection rate on the wall of 100% at a certain particle size, was 10∼30 μm in the 20° model, 30∼50 μm in the 30° model, and over 50 μm in the 40° model.

Figure 12 shows the pressure drop between the inlet and orifice outlet for various bending angles. With the bending angle changing from 20° to 50°, the pressure dropped by 6444, 3035, 1579, and 820.5 Pa, respectively, which implied that the pressure of the separator decreased gradually as the bending angle increased. As the vane angle decreased by 10°, the pressure drop increased to nearly twice that of the higher angle. The figure shows that a vane angle of 50° had the lowest pressure drop. Because the swirl vanes were fixed in the moisture separator, the flow section areas decreased in the axis direction. This caused

the local friction to increase, meaning that the pressure drop increased at the same time. It can be understood from the conservation of energy that the reduction of the pressure term would result in an increase in the velocity term and the internal energy.

The steam that passes through the orifice outlet directly passes through the secondary moisture separator and then flows to the turbine. As the steam quality in a moisture separator outlet should be at least 80% [34], the steam that flows out of the primary moisture separator should maintain a high quality to ensure the stability and efficiency of the turbine. The steam quality can be calculated by using Equation (12).

$$\chi = \frac{\dot{m}_{steam}}{\dot{m}_{steam} + \dot{m}_{waterdroplet}} \tag{12}$$

Figure 13 shows the steam quality at the orifice outlet for various swirl vane bending angles. The size of the droplet had no effect if the bending angle was 20°. The steam quality in the direction of the orifice outlet was 100%, which implied that all water droplets were separated from the steam. When the vane angle was 30°, the steam quality began at 62% at a particle size of 1 μm and was 100% at 50 μm. For a vane angle of 40°, the steam quality began at 32.3% at a particle size of 1 μm and reached 100% at over 50 μm. The geometry with a vane angle of 50° yielded the lowest efficiency in terms of steam quality; even for a particle size of 50 μm, the orifice steam quality was only 40%. There were two reasons for this. Firstly, reducing the bending angle increased the resistance. This increased the local velocity. Secondly, the increase in particle diameter directly caused the mass of the droplet particles to increase. From the centrifugal force formula, the centrifugal force increased as the speed increased, and the mass increased. Fang et al. [2] illustrated a separation efficiency change from 98.2% to 99.4% during a steam velocity increase from 2.5 m/s to 6 m/s. As our inlet velocity was greater than that, an orifice outlet steam quality of 100% was acceptable.

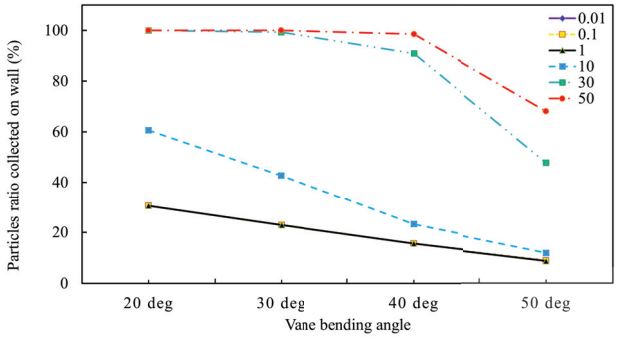

Figure 11. Effect of vane bending angles with different particle sizes.

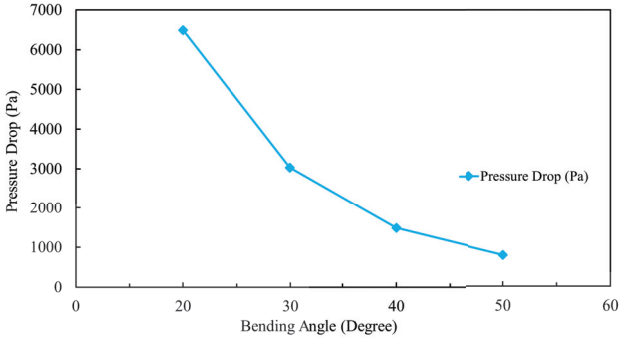

Figure 12. Pressure drop between the inlet and orifice outlet for various bending angles.

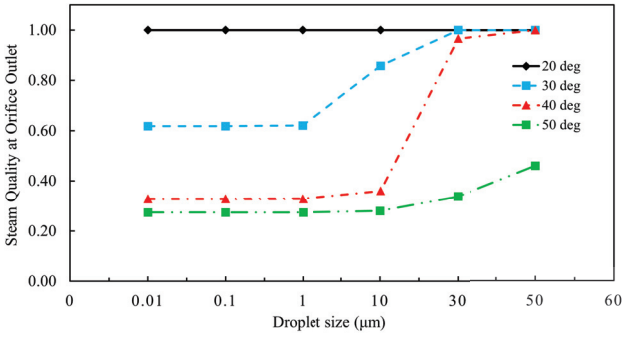

Figure 13. Steam quality at the orifice outlet for various droplet sizes and vane bending angles.

3.3. Effect of Vane Quantity

The probability of trapping droplet particles on the wall increased as the swirl vane quantities increased, as shown in Figure 14. The vane quantity had little effect on particle collection. The particles were all captured by the wall when the diameter of the particles reached 30 μm, implying that all particles were separated from the steam if the diameter exceeded 30 μm.

Figure 15 shows the pressure drop between the inlet and outlet pressure of the moisture separator for various vane quantities. The pressure drop increased as the swirl vane quantity increased, implying that the resistance along the inside of the separator increased significantly. However, compared with the previous changing bending angle, the result was not as obvious. Thus, the flow section areas reduced more slowly as swirl vane quantities changed.

Figure 16 shows the steam quality at the orifice outlet for various swirl vane quantities. For six vanes, the steam quality in the direction of the orifice outlet exceeded 95%, which means that almost all water droplets were separated from the steam. For 3–6 vanes, the steam quality started from 56%, 62%, 74%, and 93%, respectively. Thus, the steam quality increased as the vane quantity increased. Similar results were found when more swirl vanes were fixed in the separator. As a result, the local resistance increased, which immediately led to a significant increase in speed. The droplet particles were subjected to more centrifugal force in this process, which was why the steam quality increased.

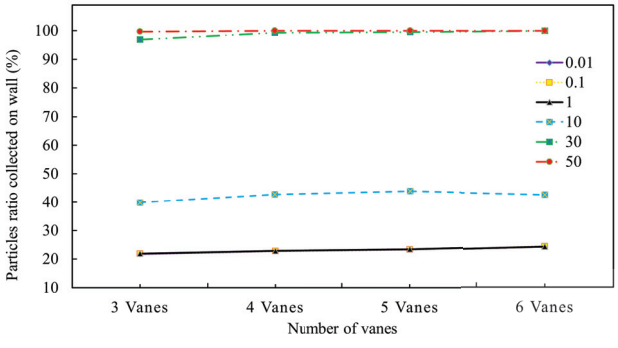

Figure 14. Effect of vane quantities with different particle sizes.

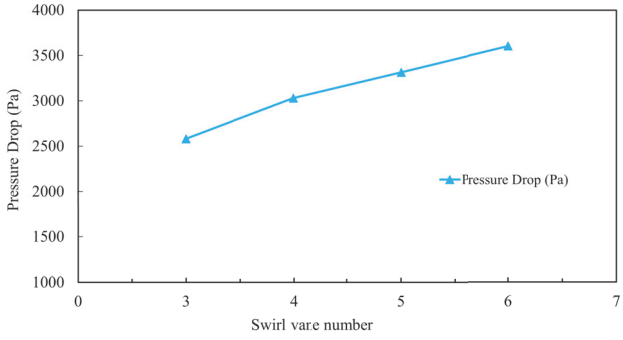

Figure 15. Pressure drop between the inlet and outlet for various vane quantities.

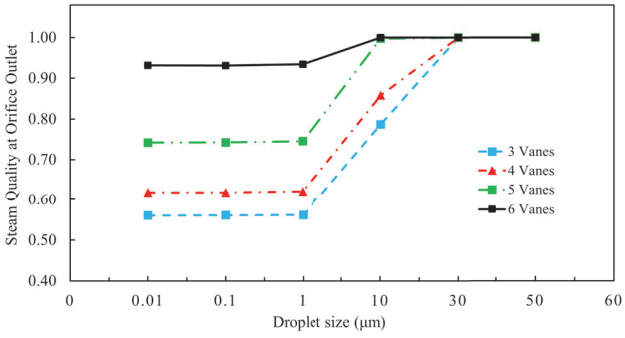

Figure 16. Steam quality at the orifice outlet for various droplet sizes and vane quantities.

3.4. Effect of Vane Location

Figure 17 shows the simulation results of the particle collection rate at different vane locations and for different droplet sizes. The figure shows that the particle collection rate increased as the droplet size increased. However, the particle collection rate changes were not very significant at different vane positions. Nevertheless, raising the vane location increased the particle collection rate. This implied that when the location of the swirl vane was close to the orifice outlet, a higher particle collection rate was found.

Figure 18 shows the pressure drop between the inlet and outlet pressure of the moisture separator at various vane locations. There was no significant pressure drop at various swirl vane locations, except for the location near the orifice outlet, as shown in the figure. Even this pressure increase near the orifice added only about 100 Pa. This pressure drop seems reasonable when compared with the case where the vane bending angle and the swirl vane quantity changed. Changing the swirl vane location did not increase the local resistance.

Figure 19 shows the steam quality at the orifice outlet at various vane locations. The steam quality changed from 37% to 91%, respectively, when the vane location changed from −200 to 400 mm. The greater the distance between the swirl vane and the orifice outlet plane, the higher the steam quality at the outlet. In addition, when the particle size was larger than 30 microns, the quality of the steam became 100%, implying that all droplets were being separated from the steam. This result is consistent with previous results shown in Figures 15 and 17. The reason for this is mainly that the droplet particles were subjected to centrifugal force, and it took a certain amount of time to move from the inside of the separator to the riser wall. When the position of the swirl vanes was raised, the droplet particles were not captured by the wall collision, and they flowed directly out of the moisture separator. This caused the increase in the position of the rotor, which reduced the steam quality.

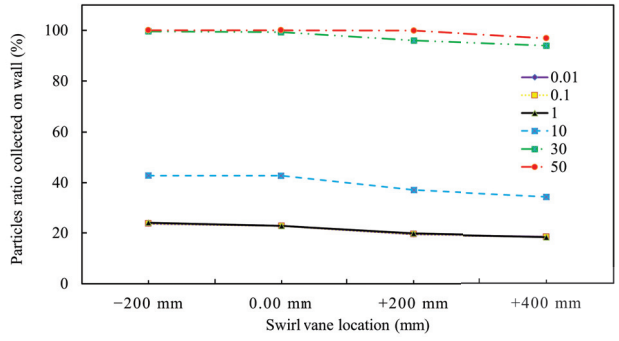

Figure 17. Effect of vane location with different particle sizes.

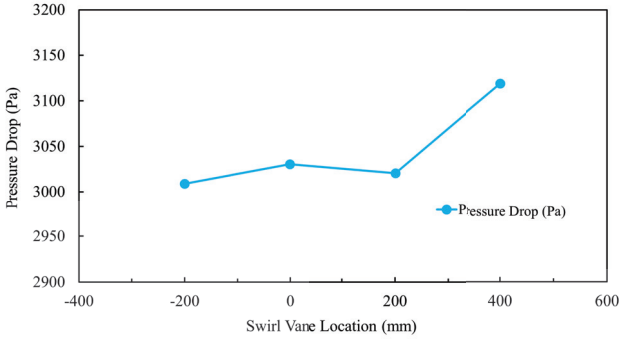

Figure 18. Pressure drop between the inlet and outlet at various vane locations.

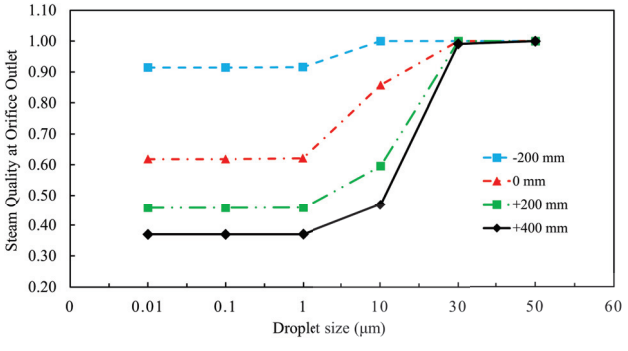

Figure 19. Steam quality at the orifice outlet for various droplet sizes and vane locations.

Figure 20 shows the classification and comparison of the pressure drop results for the three different structures, respectively. In Figure 13, the swirl vane bending angle had the highest impact on the pressure drop, whereas the swirl vane location changes had the weakest effect. The changes in the drag factor of various structures increased the local resistance. The separator design specifications of Westinghouse indicate that the pressure drop of the swirl vane separator should be less than 2.8 psi (19.3 kPa) [42]. Thus, although decreasing the angle of the swirl vanes caused a substantial pressure drop, the result met the requirements of the design specification (in this study, a maximum of 7 kPa).

From the above results, changing the bending angle of the swirl vane had the greatest effect on steam quality. When the bending angle of the vane was 50°, the steam quality of the orifice outlet only reached 46%. In the process of changing the number of swirl vanes and their positions, the steam quality could be maximized when the droplet size was

greater than 30μm. In these three structures, the purpose of changing the bending angle, quantities, and locations was to increase the swirling velocity of the moisture, subjecting the particles to more centrifugal force. While changing the position of the swirl vanes from 400 to −200 mm, the particles took more time moving from the inside to the riser surface. All three of the above methods could effectively improve the steam quality at the orifice outlet.

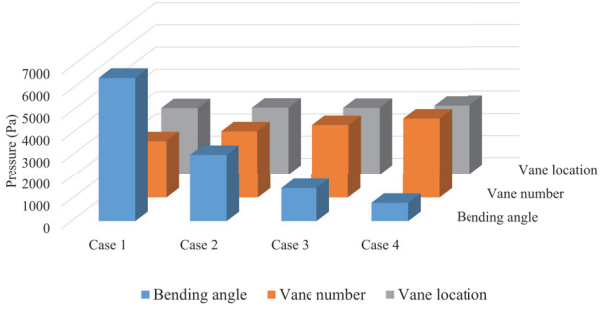

Figure 20. Comparison of different structure effects on pressure drop.

In Figure 13, the steam qualities with a bending angle of 30° were 0.62, 0.62, 0.62, 0.86, 1, and 1, respectively, with different droplet particle sizes. The total steam quality was 99.99% based on Equation (11). Applying a similar method to other cases, the total steam quality was 100%, 99.99%, 99.54%, and 44.49% as the bending angle changed from 20° to 50°. In addition, the total steam quality values with changing swirl vane quantities and locations were all over 99%. This showed that changes in the droplet particle size within 50 microns did not have a significant impact on the total steam quality. The reason for this can be attributed to the fact that most of the droplet particles are larger than 50 microns in size [43].

4. Conclusions

The characteristics of a PWR's primary moisture separator were analyzed in this study. A study was conducted on three parameters affecting the quality of the steam: swirl vane angle, swirl vane quantity, and swirl vane location. Different water droplet sizes from 0.01 to 50 μm were also considered. The results of a pressure drop between the inlet to the outlet, the steam quality at the orifice outlet, and the particle collection rate on the wall of the moisture separator were analyzed. The results were as follows:

Firstly, the steam quality increased as the bending angle decreased. However, the pressure drop between the inlet to the outlet increased during this process. When the vane angle decreased by 10°, the pressure drop increased nearly twice as much. This showed that changing the vane bending angle had the greatest influence on the pressure drop.

Secondly, when the swirl vane quantity increased, both the pressure drop and steam quality increased. In addition, increasing the distance between the swirl vane location and the reference line increased the steam quality significantly but involved a relatively small pressure drop. The simulation results thus showed that a new moisture separator design that improved steam quality at the orifice outlet involved a significant pressure drop. However, even a pressure drop in a model with a bending angle of 20° could provide results that met the Westinghouse design specifications.

Finally, these three moisture separator structure changes had an effect only when the particle size was below 50 μm, because all particles were collected on the wall if the particle size was over 50 μm.

Author Contributions: H.Z.: conceptualization, methodology, investigation, visualization, and writing—original draft; J.H.J.: investigation, writing—review and editing; D.I.Y.: methodology, writing—review and editing; Y.W.L.: conceptualization, supervision, project administration, funding

acquisition, writing—review and editing. All authors have read and agreed to the published version of the manuscript.

Funding: This work was supported by the Human Resources Program in Energy Technology of the Korea Institute of Energy Technology Evaluation and Planning (KETEP), granted financial resources from the Ministry of Trade, Industry & Energy, Republic of Korea (no. 20184010201700), and by a National Research Foundation of Korea (NRF) grant funded by the Korean Government (MSIT) (NRF-2019R1F1A1062140).

Data Availability Statement: Data available on reasonable request from the corresponding author.

Conflicts of Interest: The authors declare that they have no conflicts of interest.

References

1. Exxonmobil. 2018 Outlook for Energy: A View to 2040. Report, 2018. Available online: https://www.aop.es/wp-content/uploads/2019/05/2018-Outlook-for-Energy-Exxon.pdf (accessed on 1 July 2019).
2. Fang, D.; Li, L.; Li, J.; Wang, M.; Yu, H.; Zhang, J.; Qiu, S.; Tian, W.; Su, G.H. Full-scale numerical study on the thermal-hydraulic characteristics of steam-water separation system in an advanced PWR UTSG. Part two: Droplets separation process. *Prog. Nucl. Energy* **2020**, *118*, 103139. [CrossRef]
3. Gupta, A.K.; Lilley, D.G.; Syred, N. *Swirl Flows*; Abacus Press: Tunbridge Wells, UK, 1984; 488p.
4. Kataoka, H.; Shinkai, Y.; Tomiyama, A. Effects of Swirler Shape on Two-Phase Swirling Flow in a Steam Separator. *J. Power Energy Syst.* **2009**, *3*, 347–355. [CrossRef]
5. Qu, J.; Yan, T.; Sun, X.; Li, Z.; Li, W. Decaying Swirl Flow and Particle Behavior through the Hole Cleaning Device for Horizontal Drilling of Fossil Fuel. *Energies* **2019**, *12*, 336. [CrossRef]
6. Najafi, A.F.; Mousavian, S.M.; Amini, K. Numerical investigations on swirl intensity decay rate for turbulent swirling flow in a fixed pipe. *Int. J. Mech. Sci.* **2011**, *53*, 801–811. [CrossRef]
7. Saqr, K.M.; Wahid, M.A. Effects of swirl intensity on heat transfer and entropy generation in turbulent decaying swirl flow. *Appl. Therm. Eng.* **2014**, *70*, 486–493. [CrossRef]
8. Liu, L.; Bai, B. A mechanistic model for the prediction of swirling annular flow pattern transition. *Chem. Eng. Sci.* **2019**, *199*, 405–416. [CrossRef]
9. Liu, L.; Bai, B. Scaling laws for gas-liquid flow in swirl vane separators. *Nucl. Eng. Des.* **2016**, *298*, 229–239. [CrossRef]
10. Matsubayashi, T.; Katono, K.; Hayashi, K.; Tomiyama, A. Effects of swirler shape on swirling annular flow in a gas-liquid separator. *Nucl. Eng. Des.* **2012**, *249*, 63–70. [CrossRef]
11. Funahashi, H.; Hayashi, K.; Hosokawa, S.; Tomiyama, A. Study on two-phase swirling flows in a gas-liquid separator with three pick-off rings. *Nucl. Eng. Des.* **2016**, *308*, 205–213. [CrossRef]
12. Funahashi, H.; Hayashi, K.; Hosokawa, S.; Tomiyama, A. Improvement of separator performance with modified pick-off ring and swirler. *Nucl. Eng. Des.* **2017**, *322*, 360–367. [CrossRef]
13. Nishida, K.; Mizutani, T.; Suzuta, T.; Kondo, Y.; Hirao, Y. Development of Moisture Separator With High Performance of Steam Generator. In Proceedings of the 12th International Conference on Nuclear Engineering, Arlington, VI, USA, 25–29 April 2004; Volume 3, pp. 545–550. [CrossRef]
14. Xiong, Z.; Lu, M.; Li, Y.; Gu, H.; Cheng, X. Effects of the slots on the performance of swirl-vane separator. *Nucl. Eng. Des.* **2013**, *265*, 13–18. [CrossRef]
15. Kataoka, H.; Tomiyama, A.; Hosokawa, S.; Sou, A.; Chaki, M. Two-Phase Swirling Flow in a Gas-Liquid Separator. *J. Power Energy Syst.* **2008**, *2*, 1120–1131. [CrossRef]
16. Funahashi, H.; Vierow Kirkland, K.; Hayashi, K.; Hosokawa, S.; Tomiyama, A. Interfacial and wall friction factors of swirling annular flow in a vertical pipe. *Nucl. Eng. Des.* **2018**, *330*, 97–105. [CrossRef]
17. Versteeg, H.K.; Malalasekera, W. *An Introduction to Computational Fluid Dynamics: The Finite Volume Method*; Pearson Education: London, UK, 2007.
18. Tamrina, K.F.; Sheikhb, N.A.; Rahmatullaha, B.; Malim, T. Numerical Analysis of Swirl Intensity in Turbulent Swirling Pipe Flows. *J. Teknol.* **2015**, *76*, 362–372.
19. Zhang, H.; Liu, Q.; Qin, B.; Bo, H.; Chen, F. Study on working mechanism of AP1000 moisture separator by numerical modeling. *Ann. Nucl. Energy* **2016**, *92*, 345–354. [CrossRef]
20. Zhang, H.; Bo, H.; Chen, F. Numerical Simulation of Separation Efficiency and Pressure Drop of AP1000 Swirl-Vane Moisture Separator. *Nucl. Power Eng.* **2015**, *36*, 75–79. [CrossRef]
21. Tian, Z.; Yang, L. Numerical Investigation on a New Type of Two-Stage Steam Separator in Pressurized Water Reactors. *Energy Procedia* **2017**, *142*, 3962–3967. [CrossRef]
22. Kataoka, H.; Shinkai, Y.; Tomiyama, A. Pressure Drop in Two-Phase Swirling Flow in a Steam Separator. *J. Power Energy Syst.* **2009**, *3*, 382–392. [CrossRef]
23. Song, J.; Guo, H.; Yao, Q.; Jiang, R. The modeling and simulation analysis on steam generator working process. *Chin. J. Nucl. Sci. Eng.* **2007**, *27*, 27–31.

24. Fang, D.; Wang, M.; Duan, Y.; Li, J.; Qiu, G.; Tian, W.; Zuo, C.; Su, G.H.; Qiu, S. Full-scale numerical study on the flow characteristics and mal-distribution phenomena in SG steam-water separation system of an advanced PWR. *Prog. Nucl. Energy* **2020**, *118*, 103075. [CrossRef]
25. Saito, Y.; Aoyama, G.; Souma, H.; Nakao, T.; Sumida, I. Analysis of Droplet Behavior in BWR Separator. *J. Nucl. Sci. Technol.* **1994**, *31*, 349–351. [CrossRef]
26. Katono, K.; Ishida, N.; Sumikawa, T.; Yasuda, K. Air-water downscaled experiments and three-dimensional two-phase flow simulations of improved steam separator for boiling water reactor. *Nucl. Eng. Des.* **2014**, *278*, 465–471. [CrossRef]
27. Xiong, Z.; Lu, M.; Wang, M.; Gu, H.; Cheng, X. Study on flow pattern and separation performance of air-water swirl-vane separator. *Ann. Nucl. Energy* **2014**, *63*, 138–145. [CrossRef]
28. Rocha, A.D.; Bannwart, A.C.; Ganzarolli, M.M. Numerical and experimental study of an axially induced swirling pipe flow. *Int. J. Heat Fluid Flow* **2015**, *53*, 81–90. [CrossRef]
29. Fang, J.; Cambareri, J.J.; Brown, C.S.; Feng, J.; Gouws, A.; Li, M.; Bolotnov, I.A. Direct numerical simulation of reactor two-phase flows enabled by high-performance computing. *Nucl. Eng. Des.* **2018**, *330*, 409–419. [CrossRef]
30. ANSYS, Inc. *ANSYS CFX-Solver Theory Guide*; Release 16.2; ANSYS, Inc.: Canonsburg, PA, USA, 2015.
31. ANSYS, Inc. *ANSYS CFX-Solver Modeling Guide*; Release 16.2; ANSYS, Inc.: Canonsburg, PA, USA, 2015.
32. Fang, J.; Cambareri, J.J.; Li, M.; Saini, N.; Bolotnov, I.A. Interface-resolved simulations of reactor flows. *Nucl. Technol.* **2020**, *206*, 133–149. [CrossRef]
33. Afrasiabi, M.; Roethlin, M.; Wegener, K. Thermal simulation in multiphase incompressible flows using coupled meshfree and particle level set methods. *Comput. Methods Appl. Mech. Eng.* **2018**, *336*, 667–694. [CrossRef]
34. Kolev, N.I. *Multiphase Flow Dynamics 5: Nuclear Thermal Hydraulics*; Springer Science & Business Media: Berlin, Germany, 2007; Volume 5.
35. Blazek, J. *Computational Fluid Dynamics: Principles and Applications*; Elsevier Science: Amsterdam, The Netherlands, 2015.
36. Masatsuka, K. *I Do Like CFD*, 2nd ed.; Lulu Press, Inc.: Morrisville, NC, USA, 2013; Volume 1.
37. ZHOU, X.; Gao, S. Confidence intervals for the log-normal mean. *Stat. Med.* **1997**, *16*, 783–790. [CrossRef]
38. Katolicky, J.; Jicha, M.; Mares, R. Droplets deposition in steam piping connecting steam generator and steam turbine in nuclear plant. *Nucl. Eng. Des.* **2007**, *237*, 1534–1549. [CrossRef]
39. Olsson, U. Confidence intervals for the mean of a log-normal distribution. *J. Stat. Educ.* **2005**, *13*, 1–9. [CrossRef]
40. Jin, Y.; Miller, D.J.; Qiao, S.; Rau, A.; Kim, S.; Cheung, F.B.; Bajorek, S.M.; Tien, K.; Hoxie, C.L. Uncertainty analysis on droplet size measurement in dispersed flow film boiling regime during reflood using image processing technique. *Nucl. Eng. Des.* **2018**, *326*, 202–219. [CrossRef]
41. He, X.; Liu, Q.; Zhang, H.; Kui, M.Q.; Tan, X.H.; Li, X.P. Numerical investigation of the performance of moisture separators based on two-way coupling model by Lagrangian-Eulerian methodology. *Ann. Nucl. Energy* **2019**, *124*, 407–417. [CrossRef]
42. Commission, U.S.N.R. Delta 53 RSG Thermal Hydraulic Design Analysis Report for UCN1&2 RSG, 2021. Available online: https://www.nrc.gov/docs/ (accessed on 10 February 2021).
43. Jun-Ho, J.; Hong-Wu, Z.; Young-Kyu, P.; Yeon-Won, L. Numerical Analysis of Swirl-Vane Separator Using Particle Tracking Method. *J. Power Syst. Eng.* **2020**, *24*, 30–36. [CrossRef]

energies

MDPI

Article

Study of the Influence of Dynamic and Static Capillary Forces on Production in Low-Permeability Reservoirs

Yuanzhang Zhang [1,2,3], Youqi Wang [1,2], Jianwen Gao [4], Yuehua Cui [4] and Shuoliang Wang [3,*]

[1] State Key Laboratory of Shale Oil and Gas Enrichment Mechanisms and Effective Development, China Petroleum and Chemical Corporation, Beijing 100083, China
[2] Research and Development Center for the Sustainable Development of Continental Sandstone Mature Oilfield by National Energy Administration, SINOPEC, Beijing 102206, China
[3] School of Energy Resources, China University of Geosciences (Beijing), Beijing 100083, China
[4] Exploration and Development Research Institute of PetroChina Changqing Oilfield Company, Xi'an 710018, China
* Correspondence: wangshuoliang@cugb.edu.cn

Abstract: Low-permeability reservoirs have strong heterogeneity, and the production prediction based on traditional seepage model is not accurate enough. The dynamic capillary-force seepage model can characterize the dynamic heterogeneity of seepage and more accurately describe the oil–water flow process. In this paper, the calculation formula of the dynamic capillary force is obtained through a real low-permeability core experiment, and the seepage model of dynamic capillary force is established. Based on the model, the authors quantitatively study the effects of formation pressure, heterogeneity and production speed on dynamic capillary force through numerical solutions. It is found that compared with the traditional static capillary-force seepage model, the dynamic capillary-force seepage model makes the predicted water cut increase and the recovery factor decrease. With the increase in development time, formation pressure and production rate will make the effect of dynamic capillary force more obvious. According to the comparison of heterogeneous reservoir models, results show that the horizontal heterogeneity will strengthen the dynamic capillary-force effect, while the vertical heterogeneity will weaken the dynamic capillary-force effect. In the range of research parameters, the recovery ratio predicted by the dynamic capillary-force seepage model can be reduced by 4.7%. A new oil–water seepage model is proposed, which can characterize the spatial difference and dynamic change of low-permeability reservoirs with time. It is of great significance for describing the remaining oil distribution of low-permeability reservoirs in detail and making decisions on efficient EOR measures.

Keywords: dynamic capillary force; low-permeability reservoir; production rate; heterogeneity; oil recovery

Citation: Zhang, Y.; Wang, Y.; Gao, J.; Cui, Y.; Wang, S. Study of the Influence of Dynamic and Static Capillary Forces on Production in Low-Permeability Reservoirs. *Energies* **2023**, *16*, 1554. https://doi.org/10.3390/en16031554

Academic Editor: Reza Rezaee

Received: 14 November 2022
Revised: 19 December 2022
Accepted: 20 January 2023
Published: 3 February 2023

1. Introduction

Low-permeability reservoirs have a small pore throat radius and obvious capillary force. The water-injection mode has achieved good results in the development of low-permeability reservoirs. How to further improve the production of low-permeability reservoirs is the research hotspot. With the development process of low-permeability reservoirs entering the middle and late stage, it is found that the predictive distribution of remaining oil from numerical simulation is different from the actual situation. The actual development effect is worse than that predicted by numerical simulation. The inaccurate description of capillary force is one of the important reasons for this situation [1,2]. In traditional seepage theory, capillary force is a function of wetting-phase saturation, and its value is equal to the pressure difference between oil and water in equilibrium state. However, under the actual reservoir conditions, oil and water are always in flowing states. Research has confirmed that the value of the capillary force is not only related to the

saturation (static factor) but also related to the flow velocity (dynamic factor) [3,4]. In high-permeability reservoirs, pore radius is large and capillary force is small, so the influence of dynamic capillary force is usually ignored. However, in low-permeability reservoirs, pore radius is small and capillary force is large. The dynamic capillary force caused will have a certain impact on the seepage. Therefore, using the traditional static capillary force to describe the reservoir seepage will produce error, which will affect the distribution of remaining oil and development parameters. To improve the development effect of low-permeability reservoirs, it is necessary to systematically study the impact of dynamic capillary force on the production of low-permeability reservoirs [5,6].

Scholars have carried out some theoretical research work around dynamic capillary force. Hassanizadeh proposed the dynamic capillary force first [7]; he found that if the contact surface of oil and water is not balanced, the value of dynamic capillary force is constantly changing. The dynamic capillary force is not only related to the saturation of the wetting fluid but also to the velocity [8]. Joekarniasar, V. found that the viscosity ratio between two-phase fluids can affect dynamic capillary forces [9]. Wang, S. analyzed the influence of formation pressure on dynamic capillary force [10] and Helmig, R. studied the influence of heterogeneity on dynamic capillary force [11]. These studies confirm that velocity, formation pressure, and heterogeneity are important factors affecting dynamic capillary force, but the mechanism of dynamic capillary force is complex. It is better to describe dynamic capillary force based on a specific type of reservoirs [12,13].

The current theories of dynamic capillary force do not pay enough attention to the low-permeability reservoir [14,15]. It is necessary to study dynamic capillary force based on low-permeability reservoirs. Therefore, the authors tested the dynamic and static capillary forces through low-permeability cores from the Changqing oilfield and established a seepage model considering the dynamic capillary force. Then, the numerical simulation method is used to systematically analyze the influence of dynamic capillary force on water cut and oil recovery in a low-permeability reservoir.

2. Methodology

2.1. Calculation Method of Dynamic and Static Capillary Force

The capillary force is determined by the interfacial tension, reservoir wettability, and pore throat radius, and its calculation formula is:

$$P_c = \frac{2\sigma \cos\theta}{r}, \tag{1}$$

where the oil–water interface is in equilibrium state, and the capillary force is static. According to the traditional capillary force theory, the static capillary force is a function of the saturation of the wetting phase [16,17], that is:

$$P_{\mathrm{c}} = P_o - P_w = f(S_{wet}), \tag{2}$$

where the oil–water interface is in non-equilibrium state, that is, the oil and water are flowing. Then the capillary force is not only a function of the saturation of the wetting fluid, but also is affected by the change velocity of the saturation of the wetting-phase fluid with time [18,19]. That is:

$$P_{\mathrm{c}} = P_o - P_w = f(S_{wet}, \frac{\partial S_{wet}}{\partial t}), \tag{3}$$

Some authors with a view to accommodating a more complete description of the system under non-equilibrium conditions established a new formula [14,20]:

$$P_{c,dyn} = P_o - P_w = P_{c,stat} + \tau \frac{\partial S_{wet}}{\partial t}, \tag{4}$$

where $p_{c,dyn}$ is the dynamic capillary force, and $p_{c,stat}$ is the static capillary force. According to Equation (4), $P_{\mathrm{c,dyn}} - P_{\mathrm{c,stat}}$ and $\frac{\partial S_w}{\partial t}$ conform to a linear relationship. When they are fitted

as a straight line, the slope of this line is the dynamic capillary-force coefficient (τ) [21], which is related to the rock and fluid properties, such as permeability, porosity, viscosity, density, wettability, matrix type, and so on. Due to the complexity of τ, its value is usually determined by fitting the experimental results [15].

2.2. Measuring Method of Static and Dynamic Capillary Force

The static capillary force's measuring methods include the mercury intrusion method, semi-permeable diaphragm method, etc. It is measured when oil and water reach equilibrium, there is no seepage, and the saturation no longer changes with time. Traditional numerical simulations use the static capillary-force curve. On the contrary, the dynamic capillary force is measured under the nonequilibrium condition that the fluid is flowing. Influenced by the flow, the saturation is changing with time and its value is different from that in the equilibrium state. Reservoir development is a process of fluid flowing at all times. The closer to the wellbore, the higher the fluid flow velocity. So, there is no doubt that the dynamic capillary force is more consistent with the real state of the reservoir. A dynamic capillary-force model used in reservoir numerical simulation will make the description of the remaining oil more accurate.

The capillary force experimental cores are from the Chang 8 reservoir of the Xifeng Oilfield, Changqing, China, with a length of 7.00 cm and a diameter of 2.54 cm. They are weak water-wetness and their permeability and porosity are 41.71 mD and 18.86%, respectively. The experiments were carried out at 25 °C. The viscosity of oil is 4.0 mPa·s, and the salinity of water is 38,000 mg/L.

In this paper, the semi-permeable diaphragm instrument is used to measure the static capillary force, as shown in Figure 1. Based on the basic principle of semi-permeable diaphragm method, we designed experimental equipment with semi-permeable membranes and pressure sensors to measure the dynamic capillary force, as shown in Figure 2.

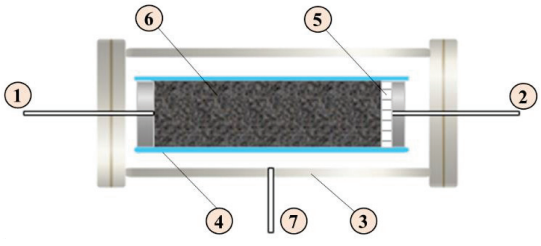

Figure 1. Static capillary-force tester based on semi-permeable membrane. ①. Fluid inlet; ②. wetting-phase outlet; ③. core holder; ④. rubber sleeve; ⑤. water wet diaphragm; ⑥. core; ⑦. confining pressure inlet.

First, we saturated the core with water. We weighed the core before and after the saturation operation to obtain the initial water volume. Then, we put the core into the experimental device with a semi-permeable membrane (Figure 1) and displaced the water with oil under the designed pressure until it reached the equilibrium state (no water was produced for 12 h). At this time, we recorded the produced water volume and calculated the water saturation of the core. Then, the pressure was raised for the next experiment to get the water saturation and the static capillary force under each pressure and finally drew the static capillary-force curve.

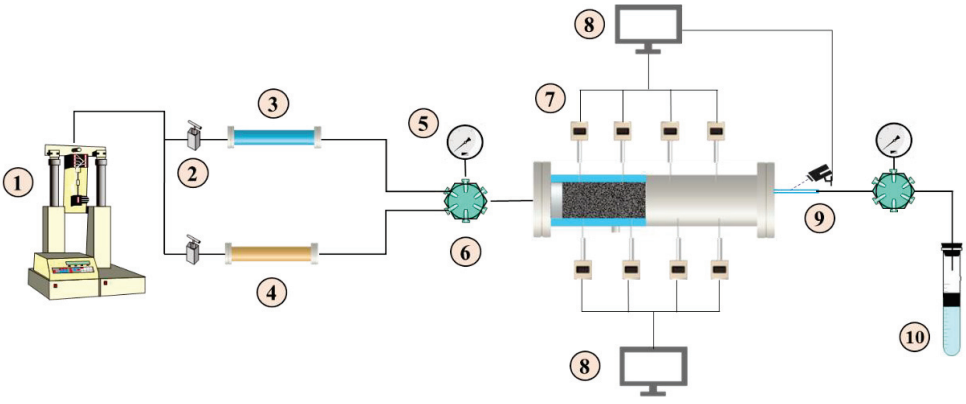

Figure 2. Dynamic capillary-force monitoring experimental equipment. ①. Pump; ②. valves; ③. intermediate container (water); ④. intermediate container (oil); ⑤. pressure gauge; ⑥. six-way valve; ⑦. multifunction sensor; ⑧. monitoring system; ⑨. real-time metering device; ⑩. metering device.

The pressure resistance of the pump can reach 35.0 MPa, and the accuracy of the monitoring system can reach 0.0001 mL. Eight small pressure sensors with semi-permeable membrane are uniformly arranged along the core holder, which can measure the saturation and pressure of points. In Figure 2, for the semi-permeable membrane sensor on one side, the oil phase can pass through but the water phase cannot, so they can measure the pressure of the oil phase, but another semi-permeable membrane sensor is opposite and they can measure the pressure of the water phase. It should be noted that to avoid the influence of gravity, the sensors are connected horizontally rather than vertically during the actual experiment.

Next, the core is placed in the core holder; the experimental equipment is connected. The confining pressure is increased to 8.00 MPa; the core is vacuumized and saturated with water and oil in turn. Based on the testing principle of the non-equilibrium state method, the constant velocity water displacement is carried out, and the saturation and corresponding dynamic capillary force at different sections and times are monitored with the sensors. We changed the displacement flow rate from 0.01 mL/min to 0.03 mL/min and 0.05 mL/min, calculated the water saturation and corresponding dynamic capillary force at different flow rates, and drew the dynamic capillary-force curve at different flow rates.

2.3. Capillary-Force Test Results

According to the measured static capillary-force curve and dynamic capillary-force curve, Figure 3 can be obtained by using Equation (4):

According to the displacement theory, oil and water saturation in cores is a function of distance and time in dynamic capillary test experiments. Therefore, with the increase in flow velocity, the change velocity of water saturation (dSw/dt) increases. The scatter plot, displayed in Figure 3, with $\frac{\partial S_w}{\partial t}$ exhibited in the x axis and $P_{c,dyn} - P_{c,stat}$ shown in the y axis. Based on the slope of the fitting line, the dynamic capillary-force coefficient τ= 0.00334592 could be obtained.

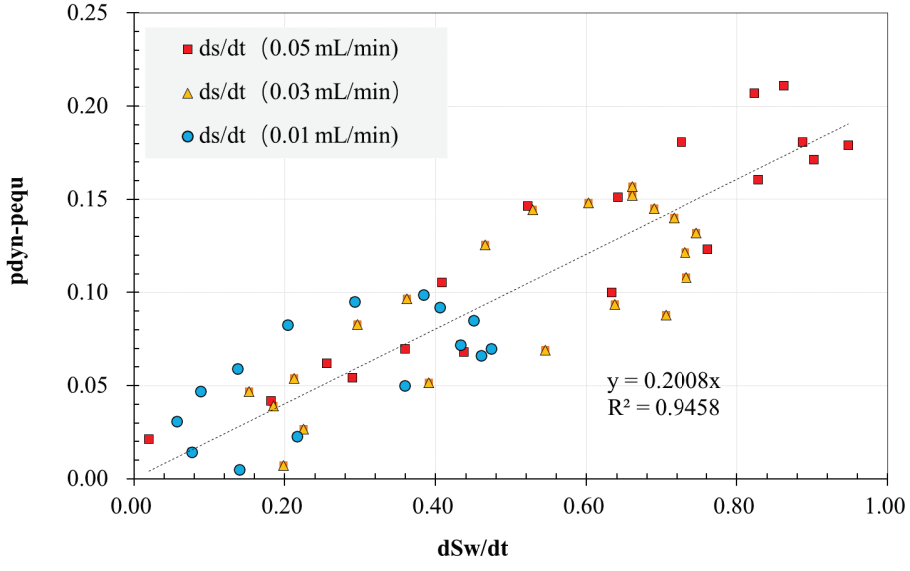

Figure 3. Linear fitting of experimental data.

3. Numerical Model of Low-Permeability Reservoir Considering Dynamic Capillary Force

Reservoir pressure, heterogeneity, and production influence most the development of low-permeability reservoirs [22,23]. A three-dimensional two-phase mathematical model is established. The finite difference numerical method is used to solve the mathematical model. By changing the above three factors, the influence of dynamic capillary force on reservoir recovery and water cut is studied [24–26].

The assumptions of the numerical model are:

(1) The fluid in the reservoir is the oil and the water phase and the wetting phase is water and the oil phase is non-wetting phase.
(2) The seepage process conforms to the Darcy law.
(3) The fluid in the reservoir is isothermal seepage; the temperature does not change with time.
(4) Pressure gradient affects the seepage process.
(5) Dynamic capillary force and gravity affect the seepage process.

Based on oilfield reservoir characteristics and experimental parameters, set reservoir model parameters as in Table 1.

Table 1. Reservoir basic parameters.

Parameter	Value	Parameter	Value
Thickness of reservoir (m)	10	Oil viscosity (mPa·s)	10
Well spacing (m)	200	Formation water viscosity (mPa·s)	1
Porosity (%)	20	Initial oil saturation (%)	85
Permeability (mD)	40	Initial water saturation (%)	15

The continuity equation of two-phase seepage flow is established:

$$\begin{cases} \nabla\left[\frac{kk_{ro}\rho_o}{\mu_o}(\nabla\rho_o - \rho_o\nabla D)\right] + q_o = \frac{\partial(\varphi\rho_o S_o)}{\partial t} \\ \nabla\left[\frac{kk_{rw}\rho_w}{\mu_w}(\nabla\rho_w - \rho_w\nabla D)\right] + q_w = \frac{\partial(\varphi\rho_w S_w)}{\partial t} \end{cases}, \quad (5)$$

Auxiliary equation:

$$S_o + S_w = 1, \tag{6}$$

Considering the dynamic capillary force:

$$p_c^{dyn} - p_c^{equ} = p_c^{dyn}\left(S_w \frac{\partial S_w}{\partial t}\right) = \tau \frac{\partial S}{\partial t}, \tag{7}$$

$$\tau = 0.00334592, \tag{8}$$

Get the discretization equation in cartesian coordinates:

$$\begin{cases} \frac{\partial}{\partial x}\left[\frac{kk_{ro}\rho_o}{\mu_o}\left(\frac{\partial p_o}{\partial x} - \rho_o g \frac{\partial D}{\partial x}\right)\right] + \frac{\partial}{\partial y}\left[\frac{kk_{ro}}{\mu_o}\left(\frac{\partial p_o}{\partial y} - \rho_o g \frac{\partial D}{\partial y}\right)\right] \\ + \frac{\partial}{\partial z}\left[\frac{kk_{ro}}{\mu_o}\left(\frac{\partial p_o}{\partial z} - \rho_o g \frac{\partial D}{\partial z}\right)\right] + q_o = \frac{\partial(\varphi\rho_o S_o)}{\partial t} \\ \frac{\partial}{\partial x}\left[\frac{kk_{rw}}{\mu_w}\left(\frac{\partial p_w}{\partial x} - \rho_w g \frac{\partial D}{\partial x}\right)\right] + \frac{\partial}{\partial y}\left[\frac{kk_{rw}}{\mu_w}\left(\frac{\partial p_w}{\partial y} - \rho_w g \frac{\partial D}{\partial y}\right)\right] \\ + \frac{\partial}{\partial z}\left[\frac{kk_{rw}}{\mu_w}\left(\frac{\partial p_w}{\partial z} - \rho_w g \frac{\partial D}{\partial z}\right)\right] + q_w = \frac{\partial(\varphi\rho_w S_w)}{\partial t} \end{cases}, \tag{9}$$

Solve the equation:

$$\begin{cases} \Delta T_o \Delta p^{n+1} - \Delta T_o \gamma_o \Delta D + q_o V_{ijk} = \frac{V_{ijk}}{\Delta t}\left[(\varphi\rho_o S_o)^{n+1} - (\varphi\rho_o S_o)^n\right] \\ \Delta T_n \Delta p^{n+1} - \Delta T_w \Delta p_{dyn}^{n+1} - \Delta T_w \gamma_w \Delta D + q_w V_{ijk} = \frac{V_{ijk}}{\Delta t}\left[(\varphi\rho_w S_w)^{n+1} - (\varphi\rho_w S_w)^n\right] \end{cases}, \tag{10}$$

$$V_{ijk} = \Delta x_i \Delta y_j \Delta z_k, \tag{11}$$

4. Results and Discussion

4.1. Effect of Formation Pressure

A homogeneous model was constructed as shown in Figure 4. It used five spot pattern water injection. The main parameters are considered as shown in Table 2.

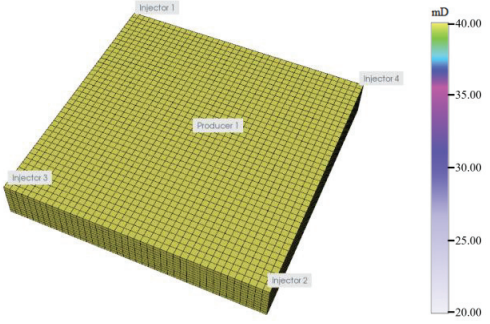

Figure 4. 3D homogeneous reservoir model containing five-spot well pattern.

Table 2. Numerical model parameters.

Parameters	Value	Parameters	Value
Horizontal permeability	40.0 mD	Formation pressure	10/15/25 MPa
Vertical permeability	4.0 mD	Production velocity	8.0 m^3/d
Porosity	20.0%	Injection velocity	2.0 m^3/d

Reservoir exploitation is then simulated for 15 years. The effect of dynamic capillary force on the oil recovery and water cut is compared and analyzed [19].

Dynamic capillary force takes into account the dynamic effect; its value is greater than the static capillary force. Due to the influence of dynamic factors, the value of

dynamic capillary force is different in different production stages and different spatial positions [23–27].

Dynamic capillary force will increase the seepage resistance and enhance the heterogeneity of the reservoir. Therefore, compared with the traditional numerical simulation method, the development effect of the low-permeability reservoir becomes worse. Figure 5 shows that compared with the traditional static capillary force, the water cut of low-permeability reservoirs increases faster under the consideration of dynamic capillary force, but the degree is different under different formation pressures. When the initial formation pressure is 10.0 MPa, the water cut will increase by 2.4% after 15 years of development. Under the initial formation pressure of 15.0 MPa, the water cut finally increases by 4.65%; under the initial formation pressure of 25.0 MPa, the water content finally increases by 5.72%. This is a big impact, and with the increase in formation pressure, the degree of water-cut increase caused by dynamic capillary force will be more obvious.

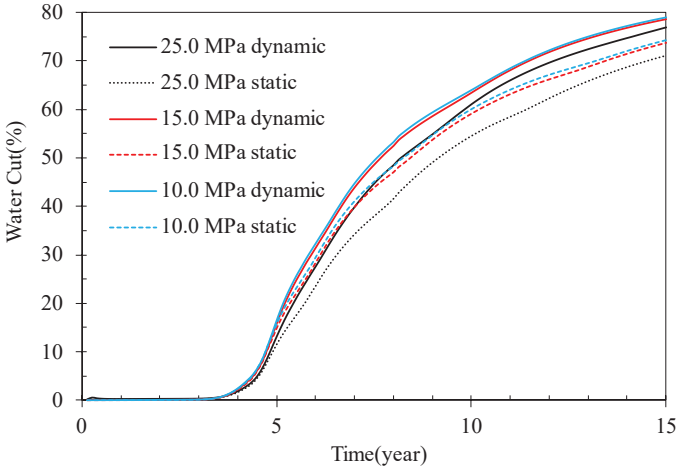

Figure 5. Water cut under different formation pressures.

Figure 6 shows the recovery curves of the dynamic capillary-force seepage model and static capillary-force seepage model under different formation pressures. The higher the formation pressure is, the more abundant the reservoir energy and the higher the oil recovery [21]. Compared with the static capillary-force seepage model, the dynamic capillary-force seepage model will cause the decline of oil recovery. This difference is not significant in the first 6 years of development, but, in the middle and later stages of development, the difference between the two capillary-force seepage models will gradually become prominent, and the greater the original formation pressure, the more obvious the decline in oil recovery. When the formation pressure is 10.0 MPa, the dynamic capillary-force model predicts that the oil recovery will decrease by 1.21% in 15 years. When the formation pressure is 15.0 MPa, the predicted oil recovery decreases by 1.29%. When the formation pressure is 25.0 MPa, the predicted oil recovery decreases by 1.69%.

4.2. Influence of Heterogeneity

To analyze the influence of the dynamic capillary-force seepage model on the development effect of heterogeneous reservoirs, the authors designed a horizontal heterogeneous reservoir model and a vertical heterogeneous reservoir model, as displayed in Figure 7. The volumes of the high-permeability parts and low-permeability parts of these two models both account for 50%. Other parameters are the same. The main parameters are considered as shown in Table 3.

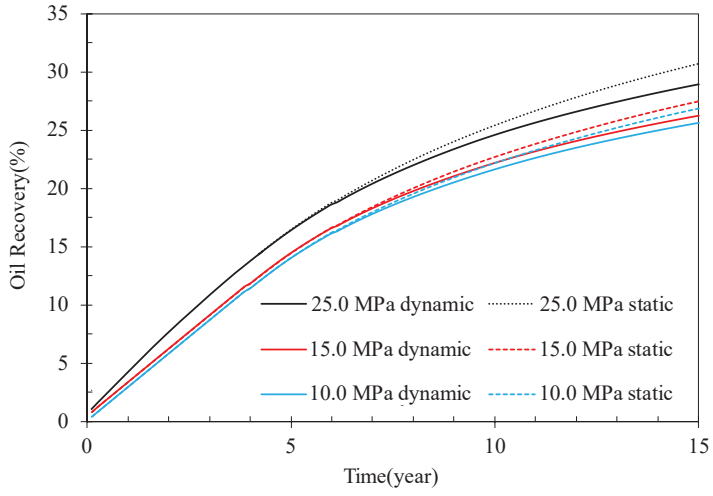

Figure 6. Oil recovery under different formation pressures.

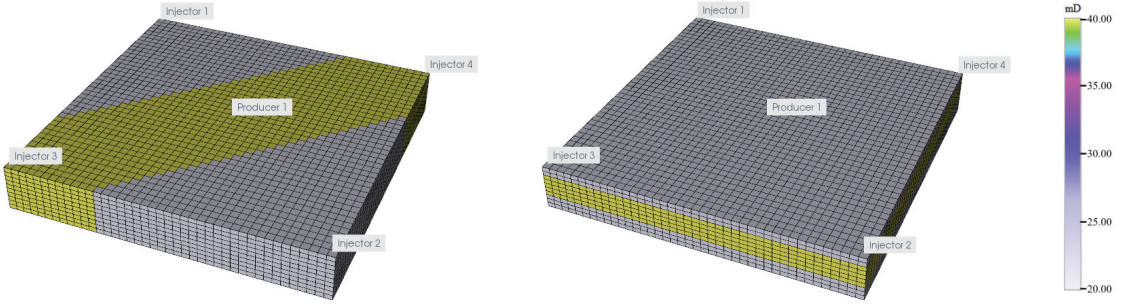

Figure 7. Heterogeneous reservoir models where a five-spot well pattern is implemented: (**a**) horizontal heterogeneous model; (**b**) vertical heterogeneous model.

Table 3. Parameters of heterogeneous reservoir model.

Reservoir Parameters	Value	Reservoir Parameters	Value
Formation pressure (MPa)	10	High permeability (mD)	40
Well spacing (m)	400	Low permeability (mD)	20
Production rate (m^3/d)	14	Porosity	0.18

Based on the above different reservoir geological settings, the difference of dynamic capillary force seepage model and static capillary force model on the recovery of low-permeability reservoirs are compared.

Figure 8 shows that under the same production rate, dynamic capillary force seepage models will reduce the predicted oil recovery in the three geological settings of low permeability, but they differ at different stages. For the homogeneous model, the effect of dynamic capillary force begins to appear when the model is developed until the fifth to sixth years. The horizontal heterogeneous model accelerates this process, showing obvious differences in the second year of development, and the subsequent differences continue to increase. However, the vertical heterogeneous model weakens this difference, and only in the 8th to 9th years does it show a certain difference.

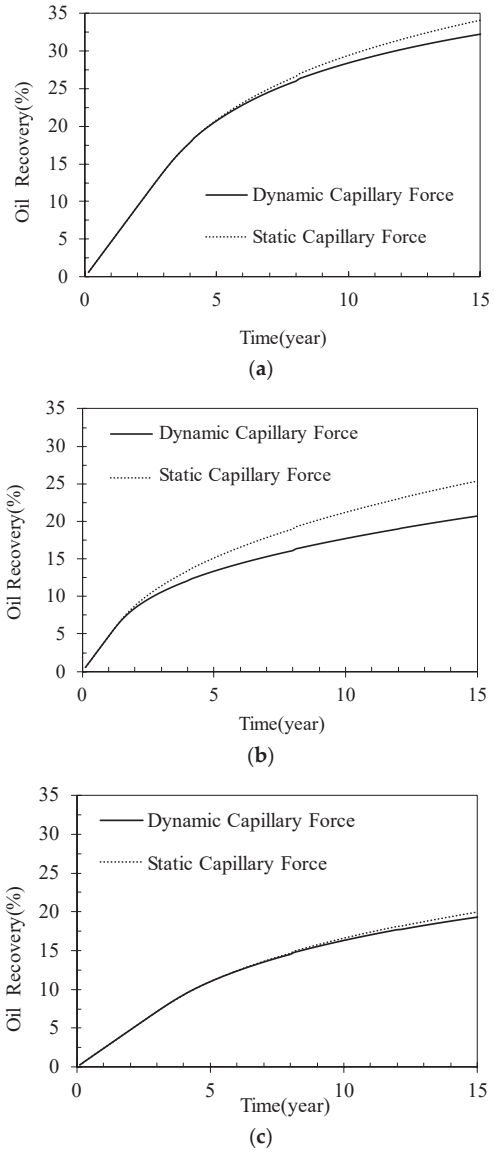

Figure 8. Oil recovery curves of the three different reservoir permeability distributions. (**a**) Oil recovery curves of the homogeneous reservoir. (**b**) Oil recovery curves of horizontal heterogeneous reservoir. (**c**) Oil recovery curves of vertical heterogeneous reservoir.

The numerical simulation results show that after using the dynamic capillary-force seepage model, the final recovery ratio of homogeneous reservoir changes from 34.0% to 32.1%, decreasing by 1.9%. The final recovery ratio of the horizontal heterogeneous reservoir changed from 25.3% to 20.6%, decreasing by 4.7%; the final recovery ratio of vertical heterogeneity changes from 19.9% to 19.8%, and the decline of recovery ratio is exceedingly weak. Therefore, the above data show that the horizontal heterogeneity has more obvious influence on the dynamic capillary force than the vertical heterogeneity of a low-permeability reservoir.

4.3. Influence of Development Intensity

The effect of dynamic capillary force is closely related to the flow rate. To study the difference between the dynamic capillary force and the static capillary-force seepage model under different development strategies, the authors conducted research on the geological models of homogeneous reservoirs, horizontal heterogeneous reservoirs, and vertical heterogeneous reservoirs. The model formation pressure is set as 10 MPa, and the production rates are 8 m^3/d, 11 m^3/d, and 14 m^3/d, respectively. The recovery curves predicted by the dynamic capillary-force seepage model and static capillary-force seepage model are obtained as displayed in Figure 9.

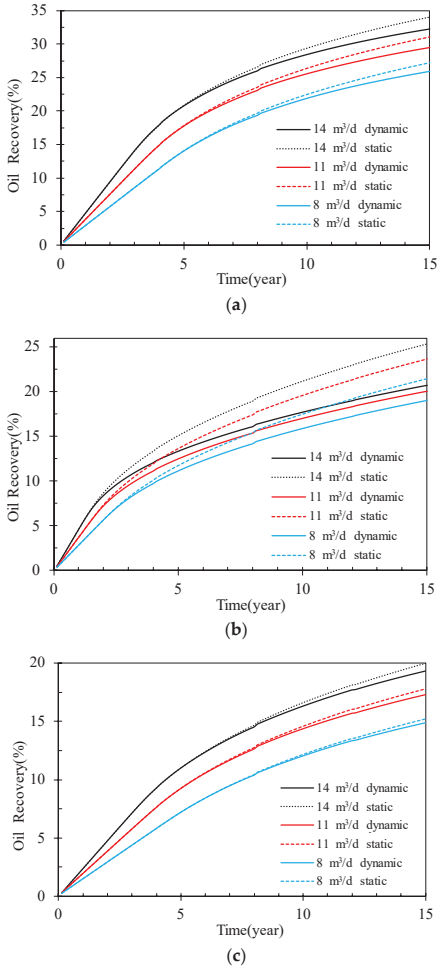

Figure 9. Comparison of oil recovery curves at different production rates of three types of geological reservoirs. (**a**) Oil recovery under different development strategies in the homogeneous reservoir. (**b**) Oil recovery under different development strategies in the horizontal heterogeneity reservoir. (**c**) Oil recovery under different development strategies in the vertical heterogeneity reservoir.

Figure 9a shows the oil recovery efficiency at different development rates in homogeneous reservoirs. We can see that with the increase in the oil production rate, the oil recovery will increase significantly in a short time. At a high production rate, the phenomenon of dynamic capillary force leading to the decline of oil recovery will be more

obvious. It can be seen from the data that when the production rate is 8 m^3/d, 11 m^3/d, and 14 m^3/d, the dynamic capillary force will reduce the recovery efficiency by 1.21%, 1.56%, and 1.85%, respectively, after 15 years, and increase the production intensity by 75% and the dynamic capillary force effect by 52.89%, from 8m^3/d to 14m^3/d.

In the comparison of Figure 9a,b: in horizontal heterogeneous reservoirs, the overall recovery ratio of the reservoir will decrease at the same production rate. When the production rate is 8 m^3/d, 11 m^3/d, and 14 m^3/d, the dynamic capillary force will reduce the recovery efficiency by 2.45%, 3.50%, and 4.71%, respectively, 15 years later. Compared with homogeneous reservoirs, the effect of dynamic capillary force will increase by 102.4%, 124.1%, and 154.1%, respectively, at the same production rate. From 8 m^3/d to 14 m^3/d, the production intensity is increased by 75% and the dynamic capillary force effect is increased by 92.24%. In addition, the comparison shows that the static capillary-force seepage model magnifies the effect of improving the production rate in low-permeability reservoirs. In the static capillary-force seepage model, the predicted oil recovery will be changed from 21.45% to 25.35%, and the oil recovery will be increased by 3.9% when it is increased from 8 m^3/d to 14 m^3/d, but in the dynamic capillary-force seepage model, the predicted oil recovery will be increased from 19.00% to 20.64%, and the oil recovery will only be increased by 1.64% when it is increased from 8 m^3/d to 14 m^3/d. This can explain why for low-permeability reservoirs with dominant seepage channels, it is often impossible to obtain good results predicted by traditional numerical simulation methods simply by increasing the production rate [24–27].

Figure 9c shows that compared with the above two types of models, the recovery ratio of vertically heterogeneous low-permeability reservoirs is lower at the same production rate. When the production rate is 8 m^3/d, 11 m^3/d, and 14 m^3/d, the dynamic capillary force will reduce the recovery efficiency by 0.07%, 0.47%, and 0.67%, respectively, 15 years later. Compared with homogeneous reservoirs, the effect of dynamic capillary force will decrease by 94.6%, 69.8%, and 63.7%, respectively, at the same production rate [28–38].

According to the above comparison in Figure 10, it can be found that the greater the production rate is, the more the difference between the dynamic and static capillary force seepage models becomes obvious. The horizontal heterogeneity will strengthen this difference, while the vertical heterogeneity will weaken this difference.

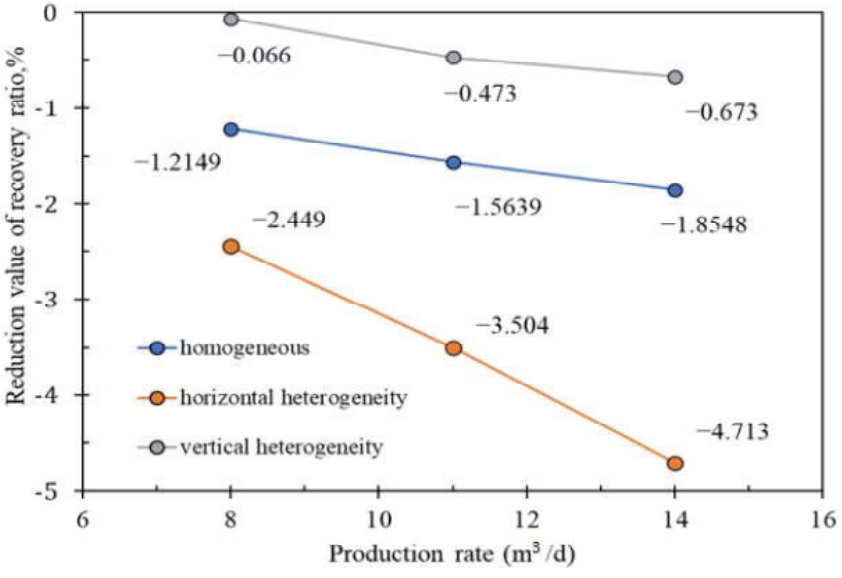

Figure 10. Reduction in dynamic capillary force for predicting oil recovery under different production rates.

5. Conclusions

1. The capillary force of the reservoir is not only related to the static factor of wetting-phase saturation, but also to the dynamic factor of the change of saturation with time. The experiment proves that dynamic capillary force is greater than static capillary force, and there is a linear relationship between $P_{c,dyn} - P_{c,stat}$ and $\frac{\partial S_w}{\partial t}$. The dynamic capillary force coefficient $\tau = 0.2008$ is obtained by fitting the experimental data.
2. In low-permeability reservoirs, there are differences between the predicted results of dynamic and static capillary-force seepage models. Compared with the static capillary force, the dynamic capillary force will continuously enhance the heterogeneity of the reservoir and increase the oil-phase seepage resistance. The predicted water cut will increase faster, and the recovery ratio will decrease.
3. Initial formation pressure and development time have influence on the effect of dynamic capillary force. With the increase in reservoir burial depth and formation pressure, the effect of dynamic capillary force is more obvious. As the reservoir enters the middle and late development stages, the effect of dynamic capillary force is gradually highlighted.
4. The effect of dynamic capillary force is different in different heterogeneous reservoirs. The horizontal heterogeneity of a reservoir will strengthen the effect of the dynamic capillary force, while the vertical heterogeneity will weaken the effect of dynamic capillary force. In other words, in the process of water flooding in low-permeability reservoirs, when the horizontal spread range is inhomogeneous, the dynamic capillary force effect is obvious; when the vertical spread range is inhomogeneous, the effect of dynamic capillary force is not obvious.
5. The greater the production rate, the greater the prediction error of static capillary force seepage model, which is more obvious in horizontal heterogeneous reservoirs. After using the dynamic capillary-force seepage model, the predicted recovery error of horizontal heterogeneous reservoir can reach 2.4%, 3.5%, and 4.7% at the production rate of 8, 11, and 14 m^3/d, respectively. Therefore, the low-permeability reservoir with strong horizontal heterogeneity should pay more attention to the dynamic capillary force.

Author Contributions: As the first author, Y.Z. established the seepage model, carried out numerical simulation research, and wrote the main manuscript. As the corresponding author, S.W. has made significant contributions to the design of the works; Y.W. processed and analyzed the experimental data; J.G. and Y.C. provided real low-permeability core and carried out core experimental research. All authors discussed the results and critically reviewed the manuscript. All authors have read and agreed to the published version of the manuscript.

Funding: This research was supported by the 2021 open funding of the Research and Development Center for the Sustainable Development of Continental Sandstone Mature Oilfield by National Energy Administration (No. 33550000-22-ZC0613-0021).

Informed Consent Statement: Not applicable.

Data Availability Statement: Not applicable.

Acknowledgments: The authors thank the financial and technical support of SINOPEC petroleum exploration and production research institute and PetroChina Changqing Oilfield. We would like to express our gratitude to the senior engineer Liu Ping for guiding us to complete the fund research.

Conflicts of Interest: The authors declare no competing interest.

Nomenclature

P_c	capillary force, MPa
σ	oil–water interfacial tension, N/m
θ	wetting angle, degree
r	pore radius, mm
P_o	oil-phase pressure, MPa
P_w	water-phase pressure, MPa
S_{wet}	wetting-phase saturation, decimal
t	time, s
$P_{c,dyn}$	dynamic capillary force, MPa
$P_{c,stat}$	static capillary force, MPa
τ	dynamic capillary-force coefficient, MPa·s
k	formation permeability, mD
k_{ro}	relative permeability of oil phase, decimal
k_{rw}	relative permeability of oil phase, decimal
ρ_o	density of oil phase, kg/m^3
ρ_w	density of water phase, kg/m^3
q_o	rate of oil phase, m^3/d
φ	porosity, decimal
S_o	saturation of oil phase, decimal
S_w	saturation of water phase, decimal

References

1. Abbasi, J.; Ghaedi, M.; Riazi, M. A new numerical approach for investigation of the effects of dynamic capillary pressure in im-bibition process. *J. Pet. Sci. Eng.* **2018**, *162*, 44–54.
2. Tian, S.; Lei, G.; He, S.; Yang, L. Dynamic effect of capillary pressure in low permeability reservoirs. *Pet. Explor. Dev.* **2012**, *39*, 405–411. [CrossRef]
3. Civan, F. Temperature dependency of dynamic coefficient for nonequilibrium capillary force-saturation relationship. *Aiche J.* **2012**, *58*, 2282–2285.
4. Sander, G.C.; Glidewell, O.J.; Norbury, J. Dynamic capillary pressure, hysteresis and gravity-driven fingering in porous media. *J. Phys. Conf. Ser.* **2008**, *138*, 012023. [CrossRef]
5. Korayem, M.; Kavousi, A.; Ebrahimi, N. Dynamic analysis of tapping-mode AFM considering capillary force interactions. *Sci. Iran.* **2011**, *18*, 121–129. [CrossRef]
6. Yan, C.Z.; Xiu-Sheng, L.I.; Chang, Y.W.; Li-Jun, Y.U.; Shi, J.Z. Development of low permeability reservoir with closely-spaced wells. *Petrol. Explor. Dev.* **2005**, *32*, 105–107.
7. Hassanizadeh, S.M.; Gray, W.G. Toward an improved description of the physics of two-phase flow. *Adv. Water Resour.* **1993**, *16*, 53–67. [CrossRef]
8. Hassanizadeh, S.M.; Celia, M.A.; Dahle, H.K. Dynamic effects in the capillary force–saturation relationship and its impact on unsatuvelocity d flow. *Vadose Zone J.* **2002**, *1*, 38–57.
9. Joekar-Niasar, V.; Hassanizadeh, S.M.; Dahle, H.K. Non-equilibrium effects in capillarity and interfacial area in two-phase flow: Dynamic pore-network modelling. *J. Fluid Mech.* **2010**, *655*, 38–71. [CrossRef]
10. Wang, S.; Liu, P.; Zhao, H.; Zhang, Y. A novel method for calculating the dynamic capillary force and correcting the pressure error in micro-tube experiment. *Sci. Rep.* **2017**, *7*, 16590. [CrossRef]
11. Helmig, R.; Weiss, A.; Wohlmuth, B.I. Dynamic capillary effects in heterogeneous porous media. *Comput. Geosci.* **2007**, *11*, 261–274. [CrossRef]
12. Hassanizadeh, S.; Gray, W.G. Mechanics and thermodynamics of multiphase flow in porous media including interphase boundaries. *Adv. Water Resour.* **1990**, *13*, 169–186. [CrossRef]
13. Barenblatt, G.I.; Patzek, T.W.; Silin, D.B. The Mathematical Model of Nonequilibrium Effects in Water-Oil Displacement. *SPE J.* **2003**, *8*, 409–416. [CrossRef]
14. Das, D.B.; Mirzaei, M. Dynamic effects in capillary force relationships for two-phase flow in porous media: Experiments and numerical analyses. *Aiche J.* **2012**, *58*, 3891–3903. [CrossRef]
15. Li, Y.; Liu, C.; Li, H.; Chen, S.; Lu, K.; Zhang, Q.; Luo, H. A review on measurement of the dynamic effect in capillary pressure. *J. Pet. Sci. Eng.* **2022**, *208*, 109672. [CrossRef]
16. Bear, J. *Dynamics of Fluids in Porous Media*; American Elsevier Publishing Company Inc.: New York, NY, USA, 1988; ISBN-13: 978-0-486-65675-5.
17. Das, D.B.; Hanspal, N.S.; Nassehi, V. Analysis of hydrodynamic conditions in adjacent free and heterogeneous porous flow domains. *Hydrol. Process.* **2005**, *19*, 2775–2799. [CrossRef]

18. Kalaydjian, F. Effect of the Flow rate on an imbibition capillary pressure curvetheory versus experiment. In *SCA European Core Analysis Symposium*; Institute Francais du Petrole: Rueil-Malmaison, France, 1992; pp. 175–194.
19. Bhusan, D.; Mirzaei, M. Experimental measurement of dynamic effect in capillary pressure relationship for two-phase flow in weakly layered porous media. *AIChE J.* **2013**, *59*, 1723–1734.
20. Bottero, S.; Hassanizadeh, S.M.; Kleingeld, P.J.; Heimovaara, T.J. Non-equilibrium capillarity effects in two-phase flow through porous media at different scales. *Water Resour. Res.* **2011**, *47*, 10. [CrossRef]
21. Hanspal, N.S.; Das, D.B. Dynamic effects on capillary pressure–Saturation relationships for two-phase porous flow: Implications of temperature. *AIChE J.* **2011**, *58*, 1951–1965. [CrossRef]
22. Blank, L.; Rioseco, E.M.; Caiazzo, A.; Wilbrandt, U. Modeling, simulation, and optimization of geothermal energy production from hot sedimentary aquifers. *Comput. Geosci.* **2020**, *25*, 67–104. [CrossRef]
23. Salimi, H.; Bruining, J. Upscaling of fractured oil reservoirs using homogenization including non-equilibrium capillary force and relative permeability. *Computat. Geosci.* **2012**, *16*, 367–389. [CrossRef]
24. Mikelić, A. A global existence result for the equations describing unsatuvelocity flow in porous media with dynamic capillary force. *J. Differ. Equ.* **2010**, *248*, 1561–1577.
25. Camps-Roach, G.; O'Carroll, D.M.; Newson, T.A.; Sakaki, T.; Illangasekare, T.H. Experimental investigation of dynamic effects in capillary force: Grain size dependency and upscaling. *Water Resour. Res.* **2010**, *46*, 863.
26. Juanes, R. Nonequilibrium effects in models of three-phase flow in porous media. *Adv. Water Resour.* **2008**, *31*, 661–673. [CrossRef]
27. Fuík, R.; Mikyka, J.; Sakaki, T.; Bene, M.; Illangasekare, T.H. Significance of dynamic effect in capillarity during drainage experiments in layered porous media. *Vadose Zone J.* **2010**, *9*, 697–708.
28. Hajibeygi, H.; Lunati, I.; Lee, S.H. Accuvelocity and efficient simulation of multiphase flow in a heterogeneous reservoir with error estimate and control in the multiscale finite-volume framework. *SPE J.* **2012**, *17*, 1071–1083.
29. Manthey, S.; Hassanizadeh, S.M.; Helmig, R. Macro-Scale Dynamic Effects in Homogeneous and Heterogeneous Porous Media. *Transp. Porous Media* **2005**, *58*, 121–145. [CrossRef]
30. Mirzaei, M.; Das, D.B. Dynamic effects in capillary force–saturations relationships for two-phase flow in 3D porous media: Implications of micro-heterogeneities. *Chem. Eng. Sci.* **2007**, *62*, 1927–1947. [CrossRef]
31. Peszyńska, M.; Yi, S.-Y. Numerical methods for unsatuvelocity d flow with dynamic capillary force in het-erogeneous porous media. *Int. J. Numer. Anal Mod.* **2008**, *5*, 126–149.
32. Lv, C.; Wang, J.; Sun, Z.G. An experimental study on starting pressure gradient of fluids flow in low permeability sandstone porous media. *Petrol. Explor. Dev.* **2002**, *29*, 86–89.
33. Xu, M.A.; Tian, S.B.; Zhou, S.W.; Lei, G. Investigation of the effect of dynamic capillary force on water flooding in ultra-low permeability reservoirs. *Sci. Technol. Eng.* **2015**, *15*, 153–155.
34. Liu, P.; Yuan, Z.; Li, K. An improved capillary force model using fractal geometry for coal rock. *J. Pet. Sci. Eng.* **2016**, *145*, 473–481.
35. Beliaev, A.Y.; Hassanizadeh, S.M. A Theoretical Model of Hysteresis and Dynamic Effects in the Capillary Relation for Two-phase Flow in Porous Media. *Transp. Porous Media* **2001**, *43*, 487–510. [CrossRef]
36. Beliaev, A.Y.; Schotting, R.J. Analysis of a new model for unsatuvelocity d flow in porous media including hysteresis and dynamic effects. *Computat. Geosci.* **2001**, *5*, 345–368.
37. O'Carroll, D.M.; Phelan, T.J.; Abriola, L.M. Exploring dynamic effects in capillary force in multistep outflow experiments. *Water Resour. Res.* **2005**, *41*, 312–329.
38. Abidoye, L.K.; Das, D.B. Scale dependent dynamic capillary force effect for two-phase flow in porous media. *Adv. Water Resour.* **2014**, *74*, 212–230. [CrossRef]

fluids

MDPI

Article

Detailed Analysis of Airflow Generated by High Voltage on a Point-Tube Electrode Geometry

Jiří Primas [1,*], Michal Malík [1], Pavel Pokorný [2], Josef Novák [1], Petr Parma [1], Filip Sanetrník [2] and Petr Schovanec [1]

[1] Faculty of Mechatronics, Technical University of Liberec, Hálkova 6, 461 17 Liberec, Czech Republic; michal.malik@tul.cz (M.M.)
[2] Faculty of Textile Engineering, Technical University of Liberec, Studentská 2, 461 17 Liberec, Czech Republic
* Correspondence: jiri.primas@tul.cz; Tel.: +420-485-353-608

Abstract: This paper is focused on the research of airflow generating through the use of high-voltage electrohydrodynamic devices. For this purpose, the authors built several electrohydrodynamic airflow generators with one point electrode and one tube electrode of varying dimensions and compared their efficiency in generating the airflow in order to find an optimal design. The character of the flow was also analyzed with the help of particle image velocimetry, and velocity vector maps and velocity profile were acquired. In addition, a possible practical cooling application was proposed and realized with positive results. Lastly, the products present in the generated airflow were tested for ozone and nitrogen oxides, which could have detrimental effects on human health and material integrity. In both cases, the concentration has been found to be below permissible limits.

Keywords: electrohydrodynamics; high voltage; generated airflow; ozone concentration; electrode geometry

Citation: Primas, J.; Malík, M.; Pokorný, P.; Novák, J.; Parma, P.; Sanetrník, F.; Schovanec, P. Detailed Analysis of Airflow Generated by High Voltage on a Point-Tube Electrode Geometry. *Fluids* **2023**, *8*, 115. https://doi.org/10.3390/fluids8040115

Academic Editors: Vasily Novozhilov, Cunlu Zhao and D. Andrew S. Rees

Received: 6 March 2023
Revised: 27 March 2023
Accepted: 28 March 2023
Published: 31 March 2023

1. Introduction

Flow generation and control are rapidly developing as key technological areas relevant to several engineering sectors with the main goal of transport of mass or energy. There are many ways of generating and controlling flow, which include propellers, pumps, valves, turbines, synthetic jets, and magnetohydrodynamic and electrohydrodynamic generators. The main question is which one of these is the most appropriate for a given application. For some of them, the reason for implementation can be simply cost effectiveness and general availability, while others are reserved for special conditions. At the Technical University of Liberec, production of nanofibers is a very important research area. During the nanofiber production process, it is beneficial to use an external airflow to deposit the nanofibers to the desired location. The electrospinning process [1], which is commonly used as the main production method, already uses high voltage (in the range of tens of kilovolts). This special situation offers the opportunity to apply the present strong electric field to also generate the airflow via electrohydrodynamic devices.

It is well known that around an asymmetrical system of electrodes connected to high voltage, two interconnected phenomena arise. The first one is a mechanical force (called after its discoverers, Biefeld–Brown force [2]) affecting the whole system of electrodes in the same direction, commonly observed on a device called "lifter", where a lightweight system of asymmetrical electrodes is able to lift itself against gravity [3]. The second one is an airflow generated around the electrodes with the opposite orientation to the direction of the force [4]. Since their discovery, many scientists have tried to use both phenomena in practical and also in somewhat unconventional applications, e.g., bladeless fans, air purifiers, ionic wind propulsion, reduction of drag on wings, electrospinning of nanofibers, flow control, and various military and space applications [5–8].

One of these is the possibility to generate and control airflow using these phenomena. This application has many advantages—very simple in design, no moving parts, little

to no noise and very low power consumption [9]. Since the airflow is generated by the interaction of a very strong electric field with the surrounding medium, the phenomena cannot be studied only from the point of view of physics. The fact that is in this case often neglected is the presence of chemicals generated during the process. This was studied only in some special cases, where corona discharge is used for commercial applications—e.g., air cleaners [10,11]. However, this has to be taken into account whenever corona discharge is used, since these chemicals can have negative consequences on both materials and health [12,13]. The novelty of this study lies in measuring the generated airflow using two independent methods—particle image velocimetry and hot-wire anemometry—comparing the results, especially in the analysis of possibly harmful chemical products in the airflow.

2. Theory

This article is focused on the properties of the airflow generated on the system of asymmetrical high-voltage electrodes. Most serious studies agree on the fact that the physical principle of the airflow generation is a continuous movement of ions and their interaction with neutral particles of the surrounding medium [3].

On the system of two strongly asymmetrical electrodes (where the smaller electrode is connected to high voltage and the larger one is grounded), several basic postulates, which are the basis for the theory behind the phenomenon, can be stated:

(1) In the immediate vicinity of the small electrode, after it is connected to high voltage (in the range of kV), a strong electric field (in the range of MV/m) is generated. If the surrounding medium is air, a large number of charged particles of both polarities are formed in the vicinity of the small electrode at such high electric field strength.

(2) Charged particles with the opposite charge to the small electrode are immediately attracted to it and discharged. Conversely, particles with the same polarity (in the air primarily N_2^+ ions) are accelerated in the direction of the electric field strength vector to a drift velocity and move from the equally charged smaller electrode to the grounded larger electrode (see Figure 1).

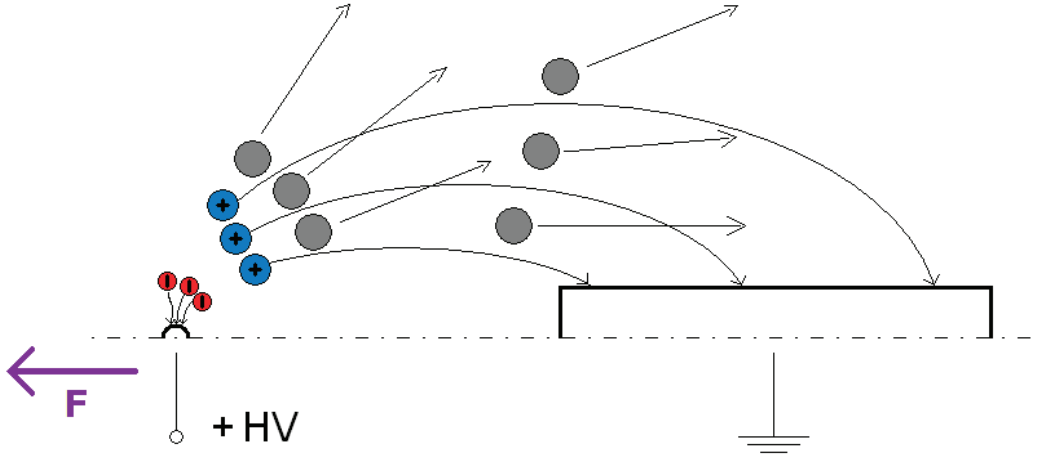

Figure 1. Diagram of the basic principle.

(3) Since the charged particles move through an environment in which they are surrounded by a large number of electrically neutral molecules of the surrounding air, during their journey from one electrode to another, they collide with them many times (approximately 10^7 collisions per second).

(4) If the kinetic energy of charged particles accelerated by the electric field is not sufficient to ionize neutral air molecules, only momentum is transferred during collisions.

(5) Neutral particles can be considered stationary until the collision, because the speed of thermal motion is negligible compared with the speed of charged particles, which is induced by the electric field.

(6) It follows from the law of conservation of momentum that after a collision, neutral particles and charged particles should fly in opposite directions. Before the collision, the charged particle was accelerated by the electric field away from the equally charged smaller electrode. This means that after the collision with a neutral molecule, it should move back towards the smaller electrode. However, since it is still in the presence of the electric field, it is not allowed to move in this direction, and instead, it is again accelerated in the direction away from the equally charged electrode. However, the momentum that the charged particle gained by colliding with the neutral particle is transferred back to the source of the field, i.e., to the entire system of electrodes.

(7) A neutral molecule, which, after the collision, gained momentum of the same magnitude but in the opposite direction, gradually loses this momentum through further collisions with neutral molecules of the surrounding air. However, since neutral molecules are neither attracted nor repelled by either of the electrodes, their momentum is not transferred to the electrodes, but this movement of neutral particles is observed as an oriented airflow.

This mechanism works only if the region around the small electrode in which ionization takes place is sufficiently narrow. If the value of the electric field strength in the space between the electrodes increases enough to allow avalanche ionization, the airflow will decrease significantly, because the principle of its generation depends on the fact that the neutral air particles remain neutral even after a collision with a charged particle. If the voltage between the electrodes comes near the breakdown voltage of the given dielectric (in our case air), the characteristics of the discharge significantly changes. First, the intense corona discharge with ionized streamers is generated; then a spark discharge appears, and if the power supply allows, arc forms. However, neither of these generate continuous oriented airflow.

Furthermore, it is assumed that the cause of the current that flows through the circuit is only accelerated ions that move without recombination and other losses from one electrode to another.

There are many known electrode shapes for which the airflow has been studied [14–16]. For practical reasons, the authors chose to use an electrohydrodynamic (EHD) generator with a tubular grounded electrode and a single-point positive high-voltage electrode. This design offers several advantages—the generated airflow is canonical, well defined, and focused on a small area; the device itself is very simple to build; and most of its dimensions can be very easily adjusted.

The authors built several EHD airflow generators with different electrode dimensions. The single-point wire electrode is made of a stainless steel wire with a 1 mm diameter sharpened into a point with a slope of 45°. To restrict unwanted corona discharge along the wire length, it is fitted into a plastic cylinder with a diameter 30 mm so that just the pointed part of the wire extends. The only mechanical parameters that are changed during the experiments are the length of the larger electrode a and the gap between the electrodes g (see Figure 2). The length (120 mm) and the diameter (70 mm) of the isolating plastic tube remain the same so that changing the length of the larger electrode a does not change the aerodynamic conditions in the experiments.

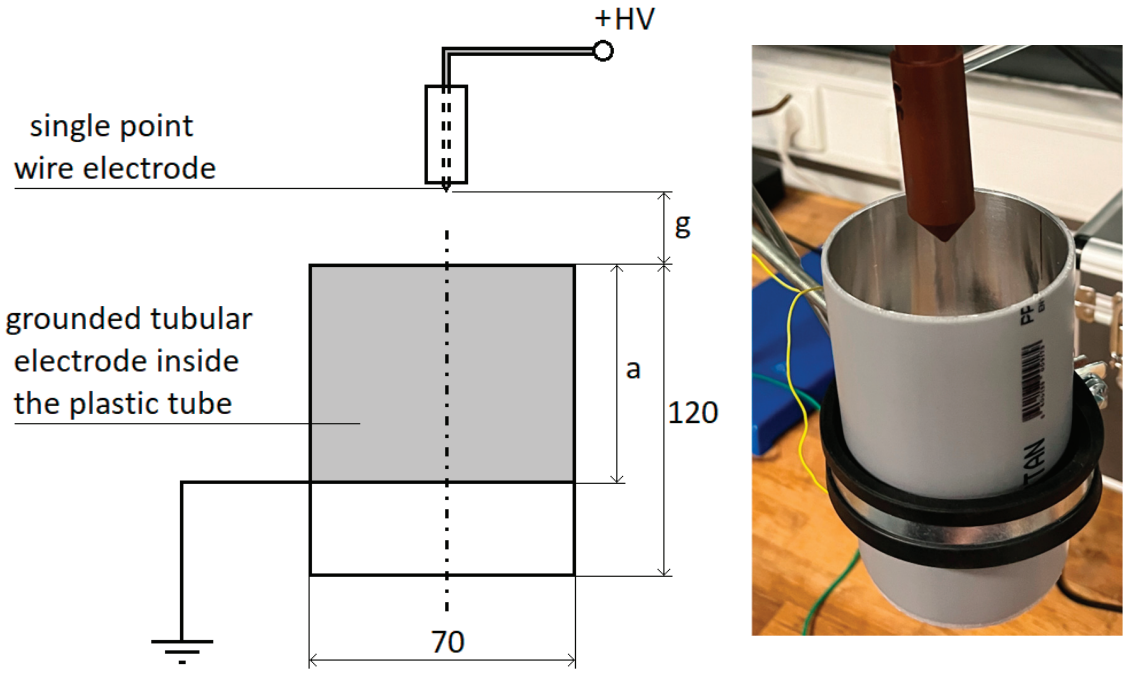

Figure 2. Diagram (**left**) and photography (**right**) of EHD generator design and its dimensions.

During the measurements, the pointed electrode is always connected to positive high voltage U (power supply Glassman FX series, maximum voltage 50 kV, current limitation was set during all measurements to 5 mA), and the larger electrode is grounded. On the grounded side, the electric current I through the device is measured for each corresponding voltage. Electric current was measured using a digital multimeter, Agilent U1252B, set to the range of microamperes.

The airflow velocities were acquired using the Voltcraft hot-wire anemometer PL-135HAN. A hot-wire anemometer works on the principle of heating a thin metal wire by passing electric current through it and observing changes in temperature caused by the movement of the surrounding medium. If the temperature of the medium is known, it is then possible to calculate its velocity from the temperature changes in the heated wire. The hot-wire sensor was placed directly in the middle of the bottom end of the airflow generator. This placement ensures the electrical safety of the hot-wire sensor, since the electric field in this location (well below the grounded electrode) is approaching zero. Any charged particles moving from the pointed positive electrode are attracted to the grounded electrode and immediately discharged, so they cannot reach the hot-wire sensor. Therefore, the sensor measures only the velocity of the neutral airflow.

Since the velocities are changing dynamically around a central value, the measured data were averaged over 30 s for each measurement, and the mean velocity $\overline{v}$ was obtained. All measured data were acquired for six different voltages, 10, 12, 14, 16, 18, and 20 kV. Ambient temperature (21 °C) and relative humidity (40%) were constant during all measurements.

3. Numerical Simulation

To obtain a more precise image of electric field strength around EHD generator electrodes, it is necessary to calculate it using numerical methods—in our case, finite element method (FEM). The behavior of the electric field in the $\Omega \subset R^3$ region with the boundary Γ is described by the elliptical partial differential equation—Gauss law of electrostatic field:

$$\nabla \cdot \boldsymbol{D} = \frac{\partial D_{\mathrm{i}}}{\partial x_i} = \sigma \text{ on } \Omega, \text{ for } i = 1,\ 2,\ 3, \tag{1}$$

where $\boldsymbol{D}$ is the electric displacement vector, and σ is the electric charge density. It is assumed that the boundary of the region is divided into two parts, $\Gamma = \Gamma_1 \cup \Gamma_2$, on which the boundary conditions are given. On the part of the boundary Γ_1, the Dirichlet boundary condition is defined (denoted by the index D); on the part of the boundary Γ_2, the Neumann boundary condition is defined (denoted by the index N); n_k is the k-th component of the external normal unit vector on the boundary of the region Ω.

$$\varphi = \varphi_D \text{ on } \Gamma_1, \tag{2}$$

$$\mathrm{D}_k n_k = \mathrm{D}_{\mathrm{N}} \text{ on } \Gamma_2. \tag{3}$$

The model is implemented in the ANSYS computing software. The PLANE121 element is used for electrostatic field analysis and implements Gauss law with boundary conditions. The geometry of the FEM model is a region approximately 3 times larger than the characteristic dimension of the experimental device in order to limit the influence of boundary conditions. The homogeneous Neumann boundary condition $\mathrm{D_N} = 0$ is given on the whole boundary of the region. The electrodes are represented by the Dirichlet boundary condition, where the value of the electric potential is given. Figure 3 shows the distribution of the electric potential and the electric field strength vector in the region bounded by the central axis and the tubular grounded electrode (electrode geometry corresponding to the built EHD generator, with zero gap g between electrodes and U = 18 kV).

As can be seen in Figure 3, the maximum electric field strength is around the positive sharp wire electrode, as was expected. It decreases very rapidly with distance from the positive electrode. Thus, it is obvious that the ionization of air, which is the basis of the EHD generator operation, occurs only in the vicinity of the positive electrode. This is in accordance with the postulates presented in the Theory section. As the ionized particles move away from this very small ionization region, while being attracted to the grounded larger electrode, they collide along their path with electroneutral molecules in the surrounding air without any further ionization. This process, in turn, generates the examined airflow.

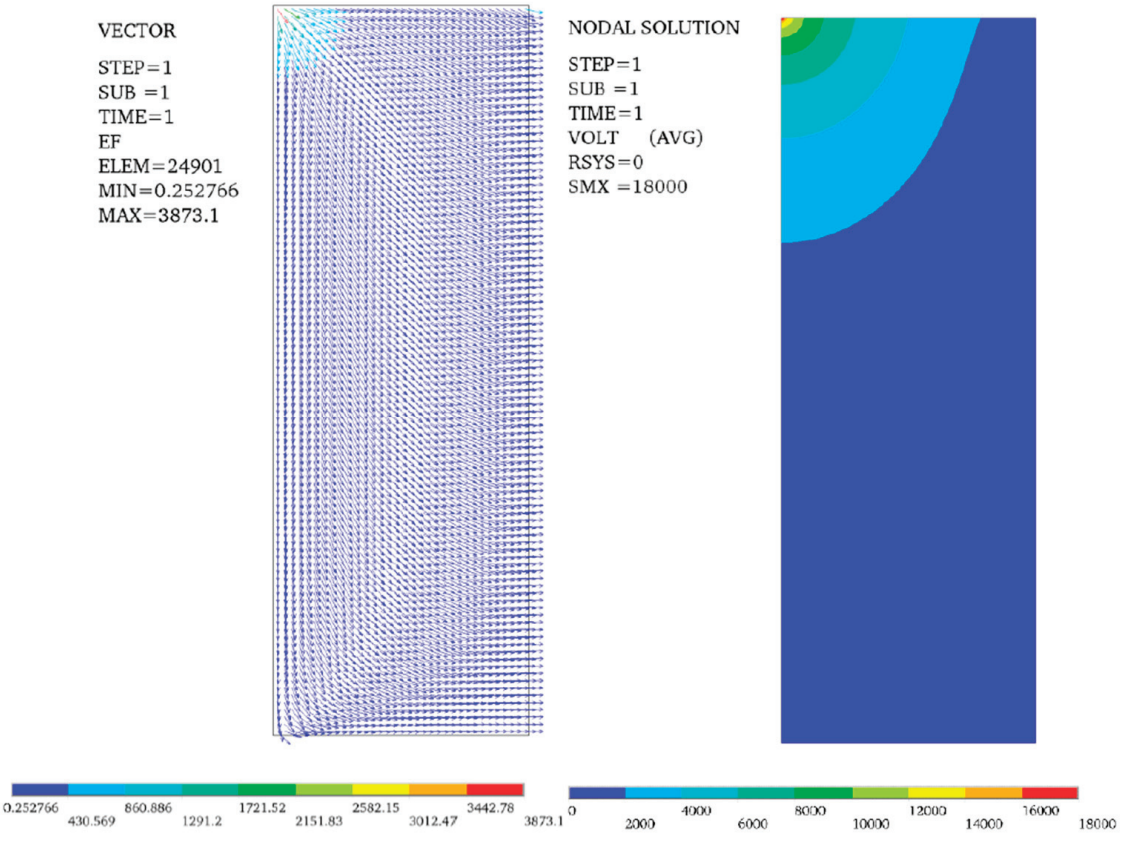

Figure 3. Results of FEM calculated model of electric field strength vector field (**left**) and electric potential (**right**) in EHD generator geometry.

4. Measurements

To find the optimal design for generating the airflow, it was necessary to consider both electrical parameters (U, I) as a single variable—power consumption P, defined for direct current as $P = U \cdot I$ and to measure its relation to the value of the mean velocity $\overline{v}$ for each airflow generator geometry (see Figures 4–7).

As can be seen, the maximal value of averaged velocities (around 2 $m \cdot s^{-1}$) is generated on an EHD generator with the longest grounded electrode (a = 100 mm). The second very important observation is that the airflow generation falls off at higher voltages for the majority of measured cases, because the electric current is consumed more and more on other types of discharge (first, corona discharge, and later, spark) and less on airflow generation. During spark discharge, the postulates stated in the Theory section are no longer valid, and for this reason, the working voltage range can be limited for this EHD generator's geometries to 16 kV maximum. Another important fact shown in the graphs is that in the vast majority of measurements, the gap g = 40 mm is too big (affecting both electric field intensity vector and aerodynamic conditions), thus generating the least airflow velocities. Therefore, any practical applications of this type of EHD generator can be limited to 16 kV maximum working voltage and to 30 mm as the maximum electrode gap g.

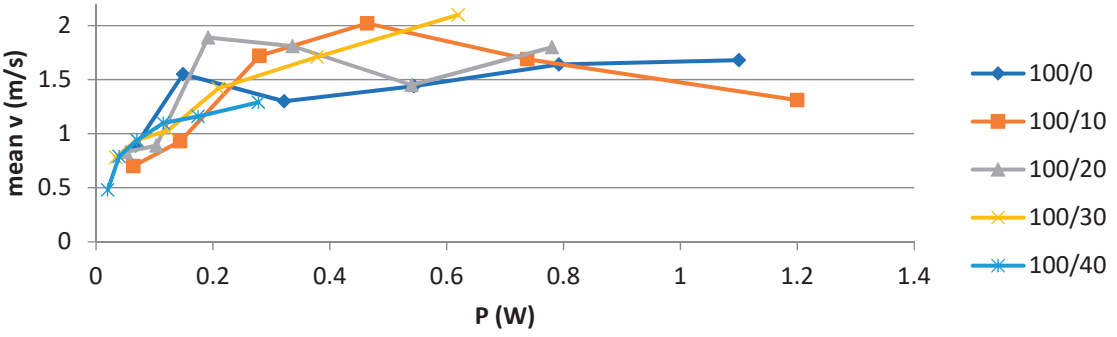

Figure 4. Measured mean velocity in the relation to the power consumption on the airflow generator with a = 100 mm for five different electrode gaps g = 0–40 mm.

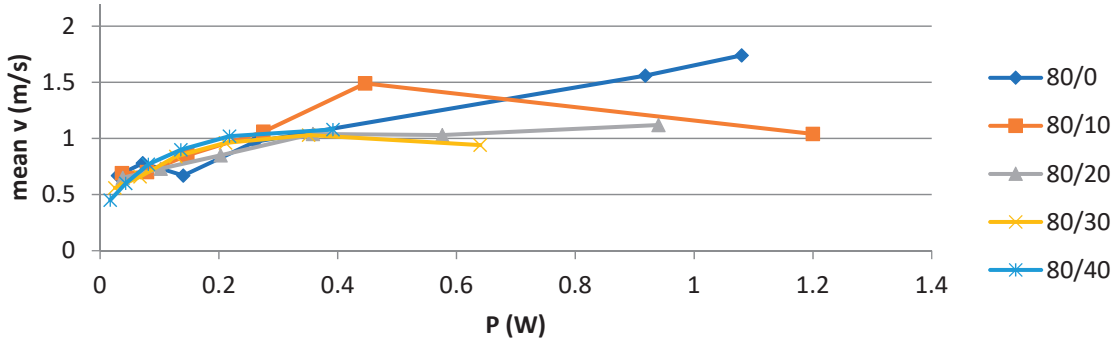

Figure 5. Measured mean velocity in the relation to the power consumption on the airflow generator with a = 80 mm for five different electrode gaps g = 0–40 mm.

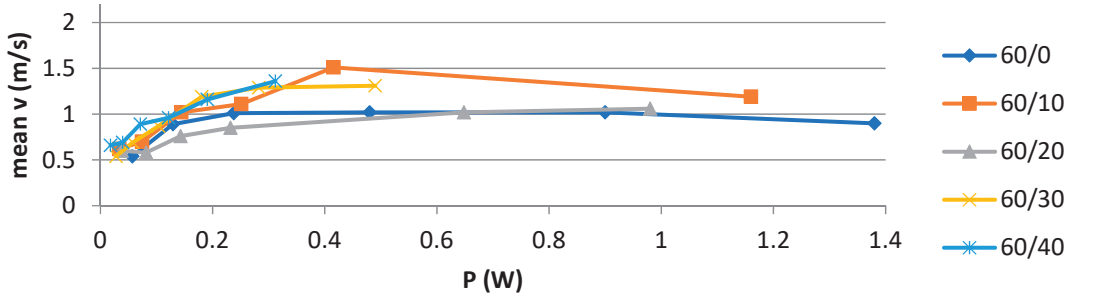

Figure 6. Measured mean velocity in the relation to the power consumption on the airflow generator with a = 60 mm for five different electrode gaps g = 0–40 mm.

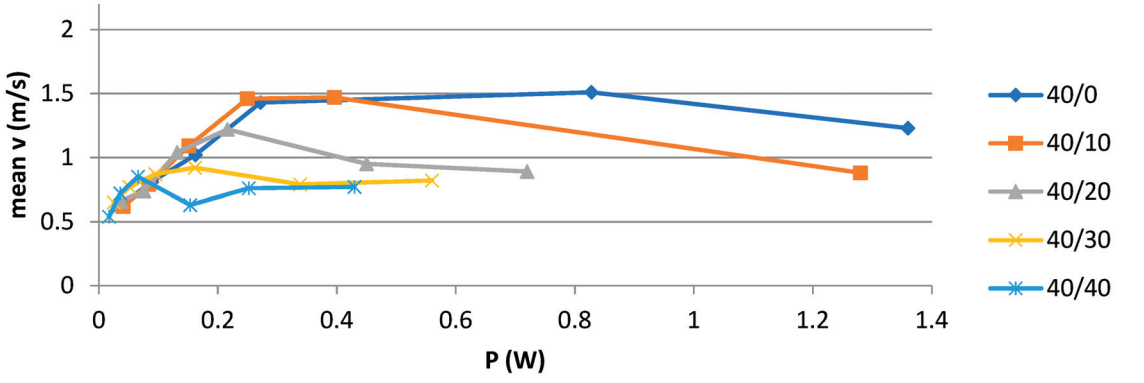

Figure 7. Measured mean velocity in the relation to the power consumption on the airflow generator with a = 40 mm for five different electrode gaps g = 0–40 mm.

For the sake of completeness, the V-A characteristic of one of the measured devices (a = 100 mm) with several electrode gaps is also included (see Figure 8). As expected, the typical V-A characteristics of high-voltage corona discharge are shown. Because the device is working in the region of corona discharge only, the V-A characteristic includes the appropriate voltage ranges. For this reason, other discharge modes (e.g., spark discharge, arc) are not included.

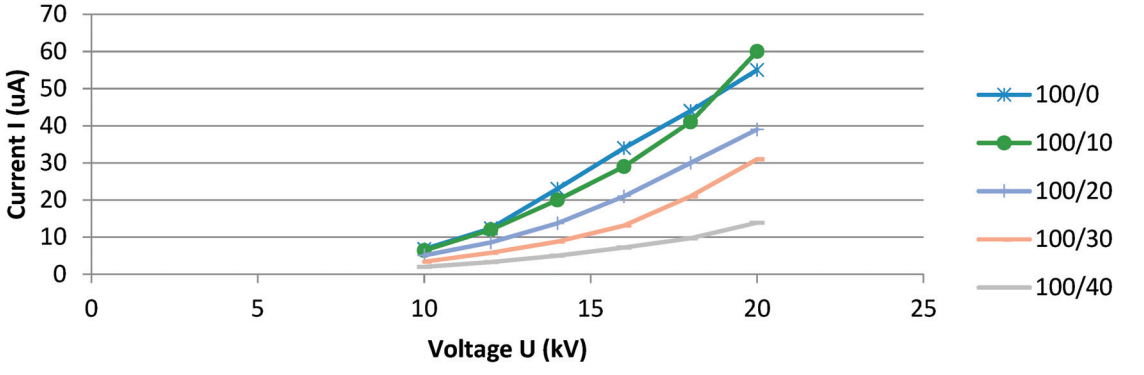

Figure 8. Measured V-A characteristic of the airflow generator with a = 100 mm for five different electrode gaps g.

To further examine the generated airflow, the authors used the particle image velocimetry (PIV) method [17], which can be successfully used even in these specific conditions, where the strong electric field is present [18]. The PIV method begins with seeding the examined flowing medium with tracer particles with a very similar density to the medium to ensure that the particles follow the measured flow faithfully. Then the particles are illuminated by two pulses of laser light in immediate succession optically expanded into a plane, which the tracer particles reflect. The scene is captured using a high-speed digital camera, and the two images are compared through digital image analysis (using specialized software), where, from the position of the particles in both images, the velocity vector map can be calculated.

The PIV measuring setup consisted of the Nd:YAG green pulse laser Quantel Ever-Green (wavelength of 532 nm, pulse frequency of 15 Hz, length of pulse of 10 ns, and energy of 25 mJ) and the digital camera HiSense Neo (resolution of 2260 × 2160, 12 bits/pixel, maximal capture rate of 50 frames/s), with Nikkor 60 mm f/2.8 D AF Microlens connected through a measurement card to a PC with Dantec Dynamics Studio software. The fog fluid SAFEX standard (according to DIN/VDE 0700 part 245 # 32.1) with an average particle size of 1 μm was used as a source of tracer particles, which were generated using a SAFEX Fog Generator.

PIV images were processed as follows: masking, cross-correlation, moving average filter, and vector statistics. The result can be seen in Figure 9, showing the detailed characteristic of the measured airflow and also showing a very good agreement with previously measured results using hot-wire anemometry.

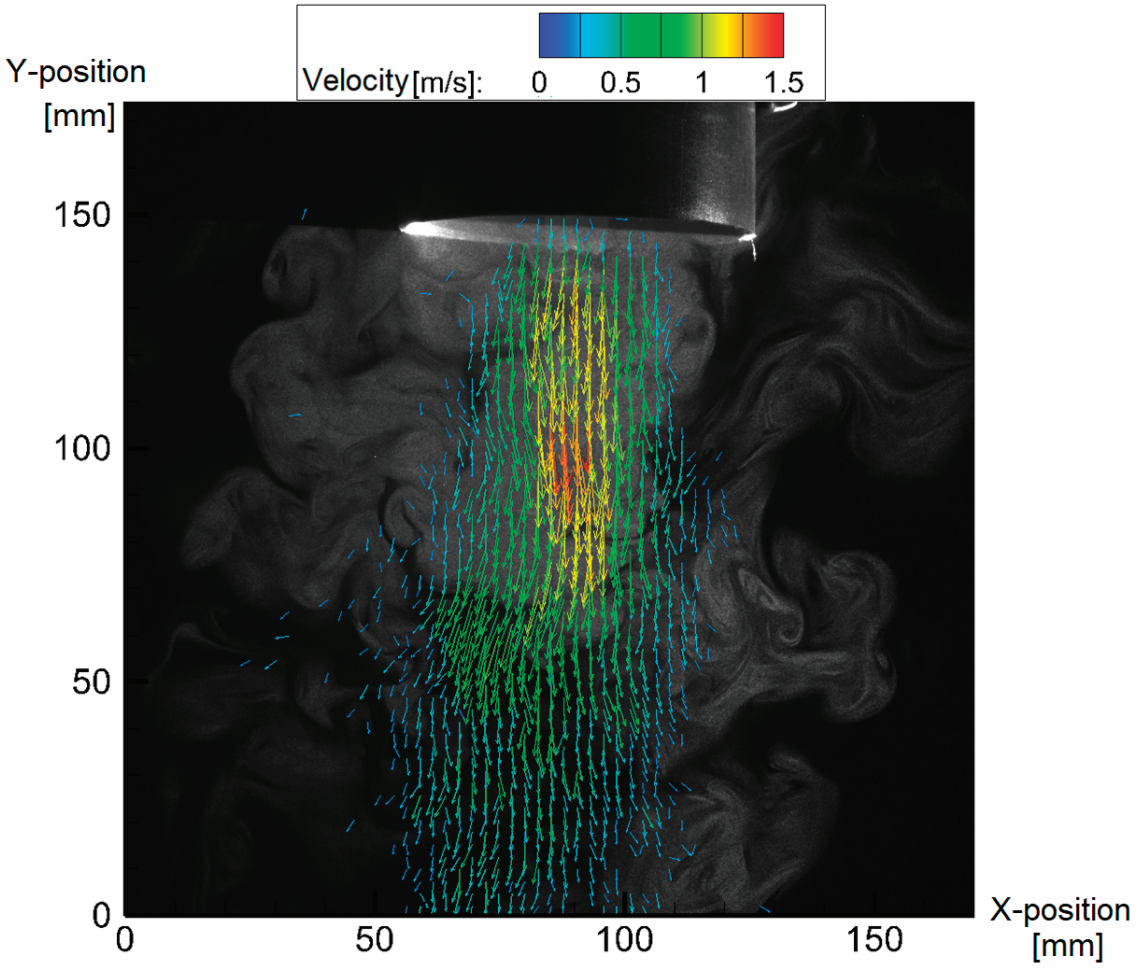

Figure 9. Flow velocity vector map measured using the PIV method on the bottom end of the EHD generator (a = 80 mm, g = 10 mm) connected to the working voltage U = 16 kV.

It is also interesting to note that the measured airflow is mostly focused in the center of the tube around the axis. This was further proven by the velocity profile of the examined airflow at a distance of 40 mm from the bottom edge of the EHD generator, as can be seen in Figure 10. From this velocity profile, the approximate volumetric flow rate Q as 0.9 $dm^3 \cdot s^{-1}$ was calculated. This value is indeed interesting for practical applications of the EHD flow generator, since the volumetric flow rate in the range of liters per second is not negligible and can be used, e.g., for the cooling of an individual power electric component.

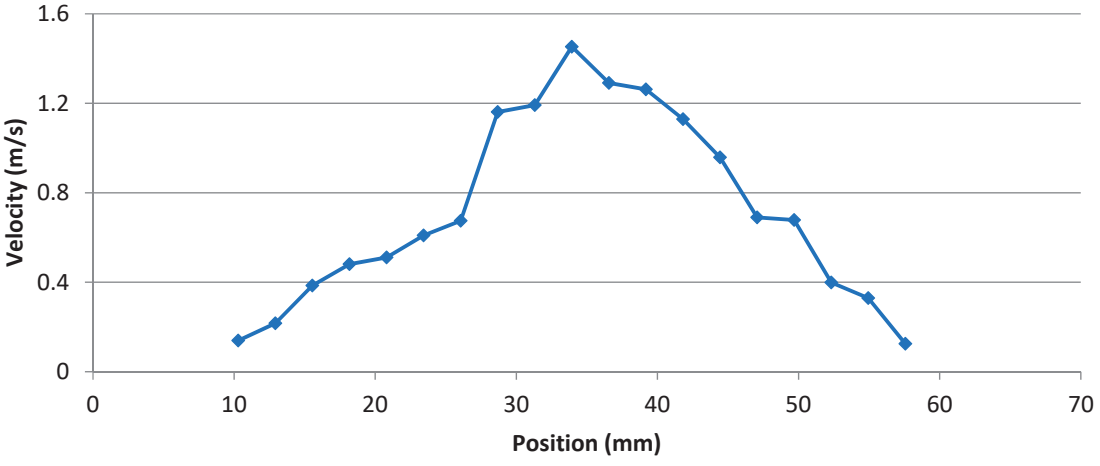

Figure 10. Flow velocity profile acquired from measured PIV data.

5. Possible Practical Application

To demonstrate the practical viability of EHD generated airflow, a very simple experiment was designed. The power resistor TESLA TR 108 (R = 820 Ω ± 1%) was placed 50 mm below the grounded tubular electrode of the airflow generator and powered by the direct current power supply SEFRAM 6136 set to U = 17 V (current flowing through the resistor was then I = 20 mA). The resistor was mounted on a Styrofoam block to prevent unwanted losses by heat conduction (see Figure 11).

In this simple electrical circuit, the resistor generated Joule heat with P = 0.35 W, and its temperature increased until thermal equilibrium was reached. This, in our conditions, resulted in a stable temperature, T = 48.9 °C. Temperature was measured using an FLIR-E63900 thermal camera directly on the surface of the power resistor using the "hot-spot" function to find the point with the highest temperature. The EHD generator was then turned on, and the high voltage was increased. In accordance with all the previous observations, the temperature of the power resistor decreased for increasing the EHD flow generator working voltage, thus increasing airflow velocities. At the voltage U = 20 kV, the temperature stabilized at T = 36 °C, as can be seen in Figure 12.

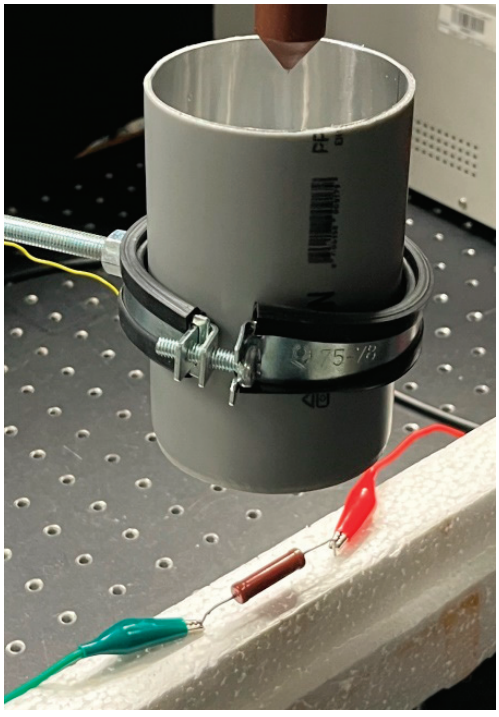

Figure 11. Experimental setup of power resistor cooled by EHD airflow generator.

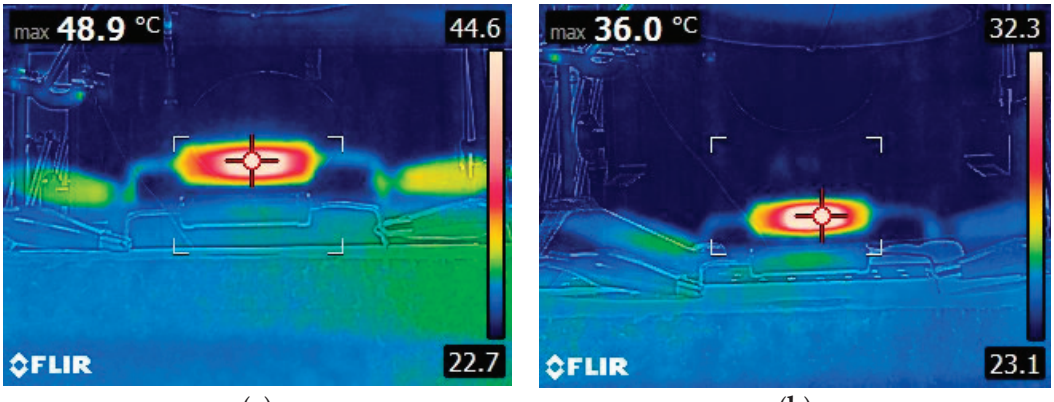

(**a**) (**b**)

Figure 12. Thermal image of the power resistor at a stabilized temperature (**a**) with no cooling, (**b**) cooled with EHD airflow at U = 20 kV.

These results prove the viability of using the EHD-generated airflow in practical power cooling applications.

6. Determination of Ozone and Nitrogen Oxides in the Generated Airflow

Because the airflow is generated using high voltage, it can be expected that it may contain harmful chemical products, especially ozone (O_3) and nitrogen oxides (NO_X). To measure the concentrations of both products, the following procedures were used.

The sampling conditions and the method of determination of ozone were based on the Occupational Safety and Health Administration [19] method. The air sample was collected using a pump sampling probe, passed through two glass fiber filters impregnated with sodium nitrite (together with potassium carbonate and glycerine) at a flow rate of 200 mL·min^{-1}. Each filter was analyzed separately using ultraviolet molecular absorption spectrometry (UV-MAS) [20], specifically the UV–VIS spectrometer PerkinElmer model Lambda 25. The entire ozone concentration measurement was performed twice in immediate succession.

The method used for the determination of nitrogen oxides was based on the methodological regulations of the Office of Public Health. The sampled air was sieved through an oxidation cartridge to ensure oxidation of the other nitrogen oxides to nitrogen dioxide. The nitrogen dioxide was subsequently absorbed in two series-connected frit impingers. Each impinger contained 10 mL of absorbent solution (containing 15 g of triethanolamine and 3 mL of n-butanol in 1000 mL). The nitrite formed was subsequently determined photometrically.

The measured concentration of ozone was 4.5 ± 0.4 μg·m^{-3}. The US health exposure permissible limit for ozone is set to 200 μg·m^{-3}. The measured concentration of nitrogen oxides was below 10 μg·m^{-3}. The health exposure permissible limit for nitrogen oxides is set to 20 mg·m^{-3}. It is obvious that in both cases, the generated products are well below the permissible limits. However, it is very important to emphasize that even minuscule amounts of ozone over a long time period can have detrimental effects on many technical materials (especially polymers), even if they pose no health hazards.

7. Conclusions

The authors examined the airflow generated by a high voltage connected to an EHD generator with point-tube geometry. Several models with different electrode dimensions were built, and experiments were made to measure the generated airflow velocity. These measurements were used to find the optimal geometrical dimensions, where the highest airflow velocity is achieved in relation to the power consumption. Because of the stochasticity of the examined phenomena, it is impossible to find the exact optimum for both working voltage and gap between the electrodes, but it is possible to find the working voltage interval for our geometry (max 16 kV) and maximum gap g = 30 mm for this working voltage and EHD generator geometry. The PIV measurements for a selected EHD generator model showed the detailed characteristic of the flow, especially its focusing around the axis. This was also confirmed by the measured velocity profile, which was used to calculate the approximate volumetric flow rate Q = 0.9 dm^3·s^{-1}. This value shows the practical usability of this principle in airflow generation above all, considering its very low power consumption (below 1 W) and the absence of any moving parts. The authors also examined the part of the phenomenon that is often neglected, the chemical products present in the generated airflow—ozone and NO_X. In both cases, the concentration of the products is well below human-exposure-permissible limits, but has to be taken into consideration for the longevity of technical materials in prolonged use. This analysis and its results are essential for any study pertaining to corona discharge and its possible practical applications.

The novelty and main contribution of this study lies in measuring the generated airflow using two independent methods, comparing the results, especially in the quantitative analysis of possibly harmful chemical products in the airflow. The authors have also demonstrated that the generated airflow can be used in practical cooling applications, as shown in the case study of power resistor cooling. The research of EHD generators at the Technical University of Liberec will follow the direction of using generators in a cascade with the aim of increasing the generated airflow velocity.

Author Contributions: Conceptualization, M.M. and J.P.; Methodology, P.P. (Petr Parma) and F.S.; Software, J.N.; Validation, P.P. (Pavel Pokorný); Formal analysis, J.P.; Investigation, M.M., J.P. and P.P. (Petr Parma); Resources, F.S.; Data curation, P.P. (Pavel Pokorný) and P.S.; Writing—original draft, M.M. and J.P.; Writing—review & editing, M.M.; Visualization, P.S.; Supervision, P.P. (Pavel Pokorný); Project administration, J.N.; Funding acquisition, J.N. All authors have read and agreed to the published version of the manuscript.

Funding: This research was funded solely by the Technical University of Liberec, Grant Number PURE-2020-6009 and received no external funding.

Conflicts of Interest: Authors have no competing interests to declare.

References

1. Tucker, N.; Stanger, J.J.; Staiger, M.P.; Razzaq, H.; Hofman, K. The history of the science and technology of electrospinning from 1600 to 1995. *J. Eng. Fibers Fabr.* **2012**, *7*, 63–73. [CrossRef]
2. Brown, T.T. A Method of and an Apparatus or Machine for Producing Force or Motion. British Patent 300311, 15 August 1928.
3. Ianconescu, R.; Sohar, D. An analysis of the Brown-Biefeld effect. *J. Electrost.* **2011**, *69*, 512–521. [CrossRef]
4. Tajmar, M.; Schreiber, T. Put Strong Limits on All Proposed Theories so far Assessing Electrostatic Propulsion. *J. Electrost.* **2020**, *107*, 103477. [CrossRef]
5. Matsoukas, G.; Ahmed, N. Investigation of Ionic Wind as a Means of Generating Propulsive Force. *Int. Rev. Aerosp. Eng.* **2012**, *5*, 35–39.
6. Jiang, X.; Zhao, C. Nonlinear electrohydrodynamic ion transport in graphene nanopores. *Sci. Adv.* **2022**, *8*, eabj2510. [CrossRef] [PubMed]
7. Vu, T.; Nguyen, H. Enhanced Electrohydrodynamics for Electrospinning a Highly Sensitive Flexible Fiber-Based Piezoelectric Sensor. *ACS Appl. Electron. Mater.* **2022**, *4*, 1301–1310. [CrossRef]
8. Guan, X.; Wang, Z. Interfacial electrohydrodynamic solitary waves under horizontal electric fields. *J. Fluid Mech.* **2022**, *940*, A15. [CrossRef]
9. Zhao, L.; Adamiak, K. EHD flow in air produced by electric corona discharge in pin–plate configuration. *J. Electrost.* **2005**, *63*, 337–350. [CrossRef]
10. Dorsey, J.A.; Davidson, J.H. Ozone Production in Electrostatic Air Cleaners with Contaminated Electrodes. *IEEE Trans. Ind. Appl.* **1994**, *30*, 370–376. [CrossRef]
11. Tanasomwang, L.; Lai, F.C. Long-Term Ozone Generation from Electrostatic Air Cleaners. In Proceedings of the 1997 IEEE Industry Applications Society 32nd IAS Annual Meeting, New Orleans, LA, USA, 5–9 October 1997; Volume 3, pp. 2037–2044.
12. Bo, Z.; Yu, K.; Lu, G.; Mao, S.; Chen, J.; Fan, F.-G. Nanoscale Discharge Electrode for Minimizing Ozone Emission from Indoor Corona Devices. *Environ. Sci. Technol.* **2010**, *44*, 16. [CrossRef] [PubMed]
13. Health and Safety Executive. *Control of Substances Hazardous to Health*; HSE Books: Sudbury, UK, 2013; ISBN 978-0717665822.
14. Dau, V.T.; Dinh, T.X.; Bui, T.T.; Tran, C.-D.; Phan, H.T.; Terebessy, T. Corona based air-flow using parallel discharge electrodes. *Exp. Therm. Fluid Sci.* **2016**, *79*, 52–56. [CrossRef]
15. Brindle, I.W.; Lai, F.C. Experimental Study of Corona Jet Produced from a Circular Tube Fitted with a Nozzle. *J. Electrost.* **2017**, *90*, 15–22. [CrossRef]
16. Birhane, Y.T.; Woldemariam, M.W.; Lai, F.C. Numerical Study of Corona Jet Produced from a Circular Tube Fitted with a Nozzle. *IEEE Trans. Ind. Appl.* **2022**, *58*, 2444–2451. [CrossRef]
17. Raffel, M.; Willert, C.E. *Particle Image Velocimetry*; Springer: New York, NY, USA, 2018; ISBN 978-3-319-68852-7.
18. Malík, M.; Primas, J.; Schovanec, P.; Novák, J.; Pokorný, P.; Sanetrník, F. Possible Limitations of the Particle Image Velocimetry Method in the Presence of Strong Electric Fields. *Processes* **2021**, *9*, 1790. [CrossRef]
19. Occupational Safety and Health Administration Salt Lake Technical Center. Ozone in workplace atmospheres (impregnated glass fiber filter). *Method ID-214* **1995**.
20. Krýsl, S.; Lexa, J. Determination of ozone in air. In Proceedings of the Occupational Hygiene Laboratory Personnel, Lúčany, Czech Republic, 7–9 May 2007.

applied sciences

MDPI

Technical Note

Hydraulic Performance of Wave-Type Flow at a Sill-Controlled Stilling Basin

Yu Zhou [1], Jianhua Wu [2,*], Hai Zhao [3], Jianyong Hu [4] and Fuqing Bai [5]

[1] Key Laboratory for Technology in Rural Water Management of Zhejiang Province, Zhejiang University of Water Resources and Electric Power, Hangzhou 310018, China; zhouyu@zjweu.edu.cn
[2] College of Water Conservancy and Hydropower Engineering, Hohai University, Nanjing 210098, China
[3] Fuyang Forest and Water Conservancy Hydropower Bureau, Hangzhou 310018, China
[4] Zhejiang Institute of Water Resources and Ocean Engineering, Zhejiang University of Water Resources and Electric Power, Hangzhou 310018, China
[5] College of Water Conservancy and Environmental Engineering, Zhejiang University of Water Resources and Electric Power, Hangzhou 310018, China
* Correspondence: jhwu@hhu.edu.cn

Abstract: Downstream of the sluice gate or weir, wave-type flows inevitably occur in stilling basins with no tailwater. This paper aims to investigate the hydraulic performance of wave-type flows at a sill-controlled stilling basin through experimental research. The flow pattern, bottom pressure profiles along the stilling basin, and the air concentrations on the bottom and the sidewall were examined in five sill-controlled stilling basins by altering the sill position and the height. The results show that wave-type flow patterns contain submerged and non-submerged jumps, which are relevant to ambient pressure head and air entrainment. The bottom pressure profiles are related to larger pressure fluctuations at large unit discharges and two peak pressure values in the vicinity of the sill. The air concentrations on the bottom and the sidewall decrease with the increasing unit discharge. The flow zone in the vicinity of the sill should be focused upon concerning protection against cavitation damage because of the slight air entrainment and significant pressure fluctuations. These findings advance our understanding of wave-type flows, and their ambient pressure heads and air entrainment are useful for designing the sill-controlled stilling basin in hydraulic engineering.

Keywords: air entrainment; flow pattern; pressure head; sill-controlled stilling basin; wave-type flow

Citation: Zhou, Y.; Wu, J.; Zhao, H.; Hu, J.; Bai, F. Hydraulic Performance of Wave-Type Flow at a Sill-Controlled Stilling Basin. *Appl. Sci.* **2023**, *13*, 5053. https://doi.org/10.3390/app13085053

Academic Editors: Vasily Novozhilov and Cunlu Zhao

Received: 4 April 2023
Revised: 15 April 2023
Accepted: 17 April 2023
Published: 18 April 2023

1. Introduction

A hydraulic jump is a phenomenon that occurs by converting supercritical to subcritical flow regimens downstream of hydraulic structures. Hydraulic jumps mostly occur in stilling basins with sills or blocks after the sluice gates or weirs. For a sill-controlled stilling basin, the flow passing over the sill changes with the supercritical Froude number, and the relevant hydraulic characteristics (i.e., the hydraulic jump performance) are strongly influenced by the position and height of the sill [1–4]. In the stilling basin, hydraulic jumps can be classified successively into five types—namely A, B, minimum B, C, and wave-type flow—as the tailwater decreases, as illustrated in Figure 1 [5]. The A-jump corresponds practically to a classical jump as the sill position is at the end of the surface roller, and the sill has no effect on the jump (Figure 1a). The B-jump occurs when the tailwater depth decreases, the jump toe moves toward the sill and the deflection of the bottom stream occurs (Figure 1b). Consequently, the minimum B-jump is the formation of a second roller at the downstream of the sill and a C-jump forms when the maximum difference between the flow depth over the sill and the tailwater depth is realized (Figure 1c,d). As the tailwater is gradually reduced, eventually reaching the point of no tailwater, a wave-type flow will occur in the vicinity of the sill, and the resulting downstream flow is characterized by supercritical flow conditions. Distinct from other types of flow, wave-type flows result in

excessive standing waves and highly erosive supercritical flow downstream of the sill; thus, this type of flow should be generally avoided (Figure 1e). In the design of stilling basins or energy dissipators, it is very important to make sure that a hydraulic jump occurs for all possible tailwater depths. Thus, according to the practical engineering design of the sill-controlled stilling basin (i.e., an abrupt bottom rise), wave-type flow inevitably occurs when there is no tailwater [6,7].

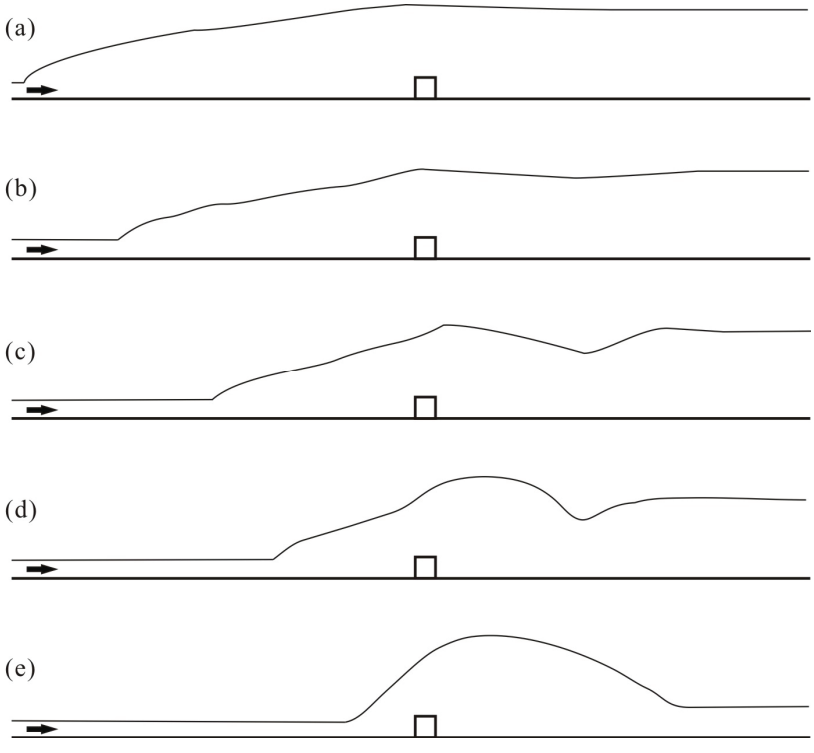

Figure 1. Sill-controlled flow: (**a**) A-jump; (**b**) B-jump; (**c**) minimum B-jump; (**d**) C-jump; (**e**) wave-type flow.

In the literature, much attention has been given to wave formation in different types of hydraulic jumps [8–10]. Different cases of wave-type flows resulting from abrupt bottom changes have been studied under supercritical downstream conditions. Kawagoshi and Hager [11] investigated the wave formation at an abrupt drop and examined various parameters, such as the sequent depth ratio, the maximum height, the location of the plunging point, the length of the downstream jump, and the resultant surface roller. Hager and Li [5] conducted an analysis on the impact of a continuous, transverse sill on the hydraulic jump in a rectangular channel. The study revealed that the jump controlled by the sill was a perturbed classical jump, as evident from the overall jump pattern. A significant reduction in the energy dissipation of the wave-type flow was observed compared to other patterns. Eroğlu and Tokyay [12] presented a simple empirical expression for determining the hydraulic characteristics of wave-type flows at abrupt bottom drops. Eroğlu and Taştan [13] analyzed the flow pattern and energy dissipation of wave-type flow when the basin bottom both rose and fell. Huang et al. [14] conducted an experimental study on wave characteristics in stilling basins with negative steps. The study describes wave height, period, probability density, and power spectrum in different stilling basins. It establishes relationships between characteristic wave heights and provides an empirical formula

for relative characteristic wave height. Zhou et al. [15] studied the energy dissipation of wave-type flow caused by a sill in the stilling basin and compared them with the data of energy dissipation by using a positive step. Moreover, a better agreement with respect to energy dissipation curves can be obtained by considering both upstream and downstream conditions.

Previous research has investigated different cases involving wave-type flows, including energy dissipation and hydraulic variables such as sequent depth ratios, maximum wave height, and wave profile. However, the effect of wave-type flows on the ambient pressure head and air entrainment has not been analyzed thoroughly. In this study, we aim to examine the hydraulic characteristics of wave-type flows, with a special focus on the bottom pressure profile along the stilling basin and the concentration of air on the bottom and sidewall. By gathering this data, it will be possible to improve the accuracy of computational fluid dynamics (CFD) models used to predict the hydraulic behavior of wave-type flows. Furthermore, the findings of this research can expand the application of sill-controlled stilling basins by developing new relationships based on the data collected.

2. Experimental Setup and Methodology

The experiments were conducted in the High-Speed Flow Laboratory at Hohai University in Nanjing, China. The experimental setup consisted of a large feeding basin, a pump, an approach conduit, a rectangular flume, a stilling basin model, and a flow return system (Figure 2). The rectangular flume made of Perspex was 25.00 m in length, 0.50 m in width, and 0.60 m in height. The stilling basin model consisted of a weir and a sill. The height of the weir P was 0.36 m. The weir was a standard Waterways Experiment Station (WES) weir with a crest profile of $y = 1.81x^{1.85}$ and a chute with an angle of 57° relative to the basin bottom. The sill in the stilling basin had a thickness and width of 0.01 m and 0.50 m. Wave-type flow was observed downstream of the weir by a sill with no tailwater conditions, and downstream flows were also supercritical.

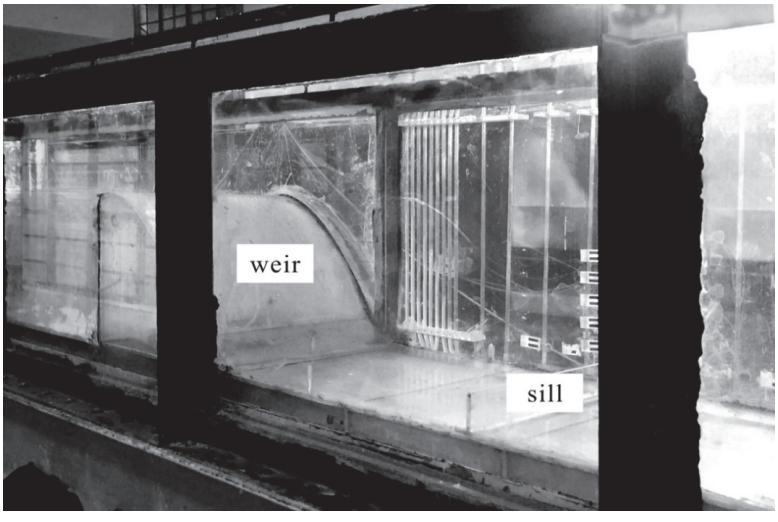

Figure 2. Experimental setup.

Figure 3 shows the experimental variables for submerged and non-submerged jumps, including the upstream flow depth, y_0; the approaching supercritical flow depth, y_1 upstream of the sill; the inflow discharge Q; the sill height, s, the length of the stilling basin, l_s (i.e., the sill position), from the weir toe (Station 0.0 m) to the upstream face of the sill; and the downstream depth, y_2. The inflow discharge, Q, was measured using a 90° V-notch weir

with an accuracy of ±1%, and flow depths y_0 and y_2 were measured using point gauges with an accuracy of ±1%. Due to the effect of free-surface instability, y_2 was measured 10 m downstream of the sill, where the free-surface undulations diminished.

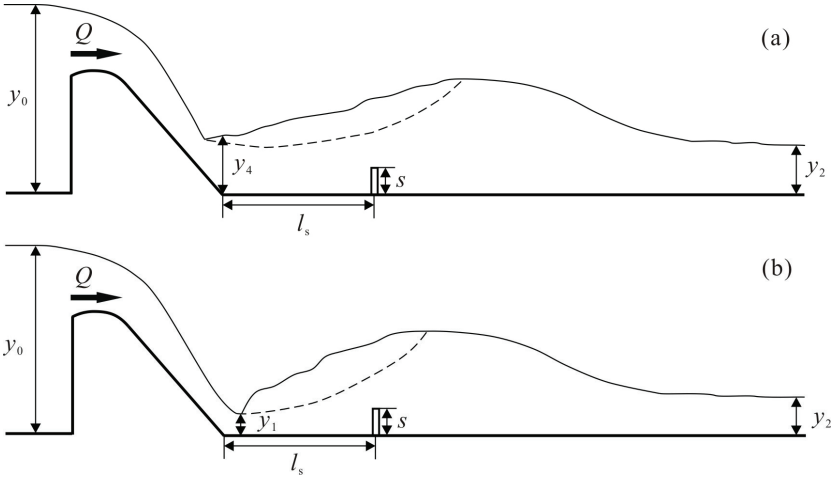

Figure 3. Experimental variables for submerged and non-submerged jumps: (**a**) submerged jump; (**b**) non-submerged jump.

Since a submerged jump may occur under certain conditions, a different method was used to calculate the flow depth y_1 and velocity v_1. For non-submerged jumps (Figure 3b), flow depth y_1 was calculated by means of an energy balance (i.e., $y_1 = E_0 - \frac{Q^2}{2gB^2\varphi^2 y_1^2}$, where E_0 is the total energy upstream of the weir, g is the acceleration of gravity, B = 0.50 m is the basin width, and φ = 0.95 is the coefficient of velocity), and velocity v_1 was calculated by means of the continuity law. For submerged jumps (Figure 3a), v_1 was calculated as $\sqrt{2g(y_0 - y_4)}$, where y_4 denotes the flow depth at the terminal section of the weir [16], and y_1 was calculated by means of the continuity law.

Figure 4 shows the layout of the air concentration and pressure measurement points. The pressure measurement points were placed at the centerline of the bottom (Figure 4b) corresponding to station 0 m, 0.05 m, 0.15 m, … , and 1.85 m (from the second to the last for every 0.1 m interval). The pressure on the bottom was measured with piezometric tubes with an error of ±0.5 mm. The air concentration measurement points were placed both 0.1 m off the centerline on the bottom (Figure 4b) and 0.05 m above the bottom on the sidewall at the same station (Figure 4a), which corresponds to station 0.35 m, 0.45 m, … , and 1.05 m (from the first to the last for every 0.1 m interval). The air concentrations both on the bottom and the sidewall were measured by using a CQ6-2005 aeration apparatus with a sampling rate of 1020 Hz, a time period of 10 s, and an error of ±0.3% [17].

For this study, the experiments were conducted for inflow unit discharges $0.102\ m^2/s \leq q_w \leq 0.230\ m^2/s$ (i.e., 0.102, 0.154, 0.188, 0.205 and 0.230), equaling Reynolds numbers of $3.97 \times 10^5 \leq Re \leq 9.14 \times 10^5$. Hence, the Reynolds numbers were large enough to avoid significant scale effects as identified in air-water flows in the stilling basin [18]. The experiments encompassed five sill-controlled stilling basins by altering the position (l_s) and height (s) of the sill. Table 1 lists the experimental flow conditions for all sill configurations comprising the upstream and downstream Froude numbers F_1 ($F_1 = v_1/\sqrt{gy_1}$) and F_2 ($F_2 = v_2/\sqrt{gy_2}$).

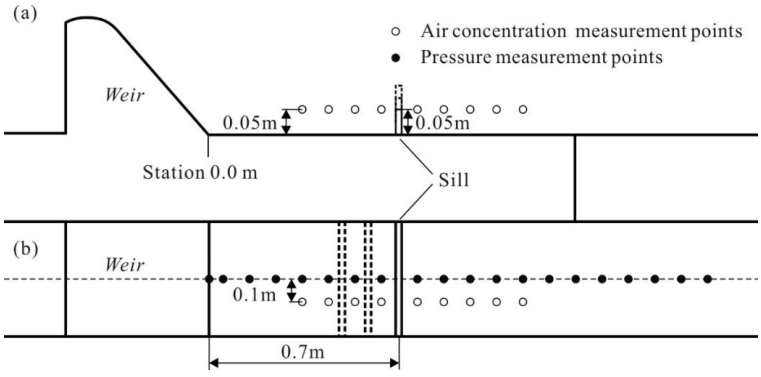

Figure 4. Layout of air concentration and pressure measurement points: (**a**) sideview; (**b**) plain view.

Table 1. Hydraulic and geometrical parameters of the sill-controlled stilling basin.

Cases	l_s (m)	s (m)	F_1	F_2	Jump Type
M12-1	0.5	0.065	5.12	1.93	SWTF
M12-2	0.5	0.065	4.21	1.65	SWTF
M12-3	0.5	0.065	3.86	1.62	SWTF
M12-4	0.5	0.065	3.77	1.72	SWTF
M12-5	0.5	0.065	3.70	1.91	SWTF
M22-1	0.6	0.065	5.18	1.66	SWTF
M22-2	0.6	0.065	4.29	1.79	SWTF
M22-3	0.6	0.065	4.13	1.87	SWTF
M22-4	0.6	0.065	3.82	1.95	SWTF
M22-5	0.6	0.065	3.74	1.77	NSWTF
M32-1	0.7	0.065	5.31	1.97	SWTF
M32-2	0.7	0.065	4.30	1.82	SWTF
M32-3	0.7	0.065	4.08	1.76	NSWTF
M32-4	0.7	0.065	3.93	2.79	NSWTF
M32-5	0.7	0.065	3.74	2.96	NSWTF
M31-1	0.7	0.050	5.26	1.44	NSWTF
M31-2	0.7	0.050	4.43	2.89	NSWTF
M31-3	0.7	0.050	4.08	3.10	NSWTF
M31-4	0.7	0.050	3.93	3.19	NSWTF
M31-5	0.7	0.050	3.74	3.13	NSWTF
M33-1	0.7	0.080	4.96	2.07	SWTF
M33-2	0.7	0.080	4.13	1.94	SWTF
M33-3	0.7	0.080	3.77	1.95	SWTF
M33-4	0.7	0.080	3.62	2.10	SWTF
M33-5	0.7	0.080	3.47	1.99	SWTF

NSWTF and SWTF are the abbreviations for non-submerged and submerged wave-type flow, respectively.

3. Results and Discussion

3.1. Flow Pattern

In most practical cases, the stilling basin with a positive step or a sill (i.e., abrupt bottom rise) was constructed to grant a forced jump inside the basin [2]. Figure 5 illustrates the wave-type flow for both Case M31 and M32 at different inflow unit discharges.

As the unit discharge increased, implying a decrease in F_1, the beginning of the jump roller moved downstream. The wave type flow exhibited a significant wave height in the vicinity of the sill, a significant water drop downstream of the sill, and the resultant downstream supercritical flow ($F_2 > 1$), as listed in Table 1. In addition, air entrainment occurred at the toe of the jump, and entrained bubbles were transported into the downstream zone.

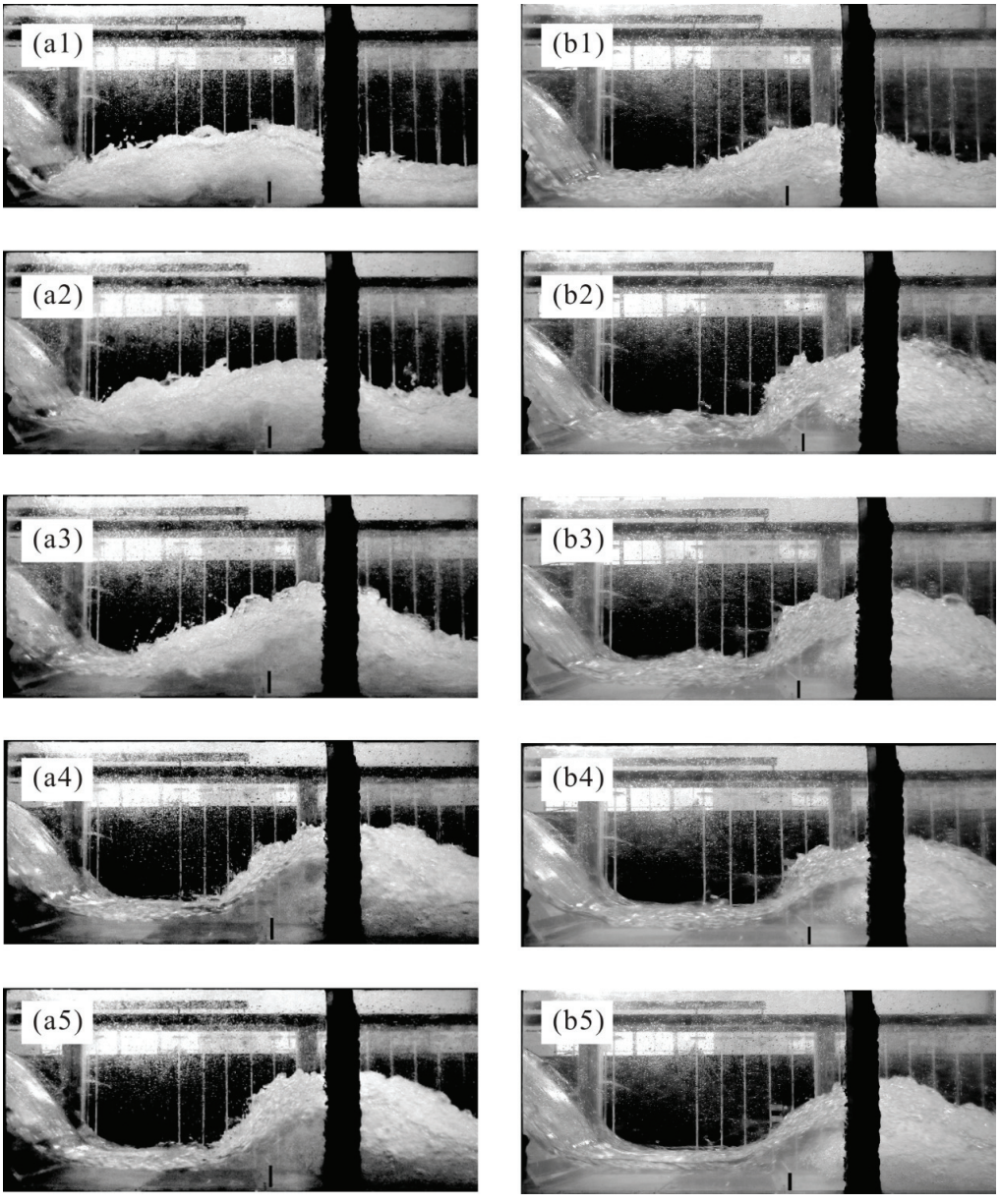

Figure 5. Wave flow pattern at different inflow unit discharges (q_w = 0.102, 0.154, 0.188, 0.205 and 0.230): (**a**) Case M31; (**b**) Case M32.

For comparison purposes, the beginning of the jump roller in Case M32 moved downstream more clearly, presenting a distinct transition from the submerged jump to the non-submerged jump, especially when the unit discharge varied from 0.154 m^2/s to 0.205 m^2/s. Moreover, the visual observations suggested a more significant amount of air in the submerged jump in Case M32, and even the entrained air could reach the stilling basin bottom.

In addition to the wave type flow, a jet flow may occur, and the curvature of the streamline approaching the sill became larger. The supercritical flow would splash over the sill and a cavity formed between the jet flow and the downstream depth [7]. Because the splash flow occurred when the relative sill height of s/y_1 was larger than its critical value, the flow pattern was closely related to inflow conditions and the sill height.

In Figure 6, the relative sill height S (i.e., $S = s/y_1$) is plotted against the upstream Froude number F_1. The data for the critical splash flow conditions are also illustrated in this figure. The relative sill height, s/y_1, in this study conformed to the wave-type flow conditions found in a previous study [7]. When wave-type flow occurred with a positive step, the flow zone behind the step could be classified into aerated or nonaerated flow. The main difference between these two wave types was that the aerated wave-type flows were associated with a better aeration effect and higher wave heights due to the subatmospheric pressure at the horizontal step surface [19].

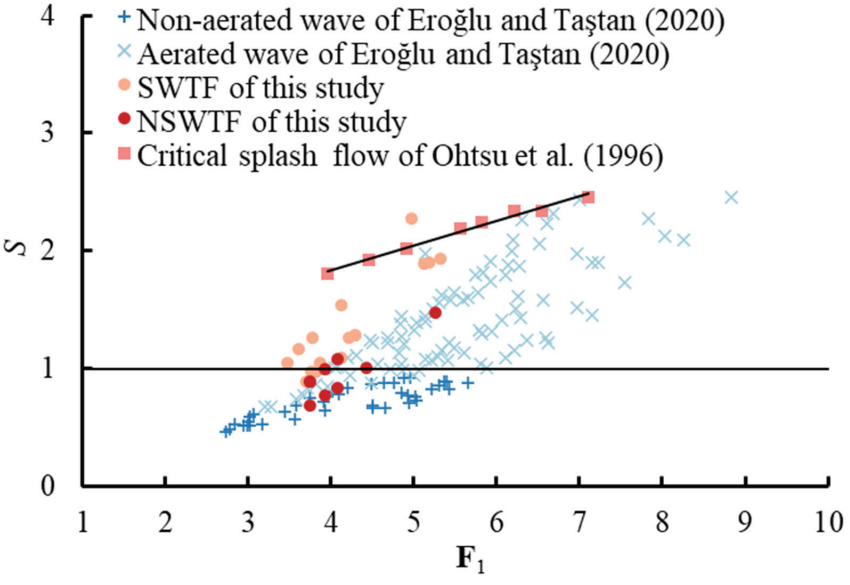

Figure 6. Relative sill height S against the upstream Froude number F_1 [7,13].

For these two wave types, the data for the relative positive step height h_s/y_1 against F_1 are also plotted in Figure 6 [13], and the line, $S = 1$, was referred to as the limit between non-wave and wave-type flows. For wave-type flow occurring with a sill in this study, the data for S against F_1 also suggest that a higher relative sill height corresponding to submerged wave-type flows is relevant for a better aeration effect, as observed in Figure 5.

3.2. Pressure Head

Figure 7 shows the maximum, mean, and minimum pressure head, H_p, on the bottom along the stilling basin starting at the weir toe (Station 0.0 m) at different unit discharges for Case M32 and a CHJ (a classical hydraulic jump). It can be observed that the bottom pressure varied greatly along the stilling basin for each unit discharge and reached a peak both at the location upstream and downstream of the sill (Figure 7a–e). Moreover, these peak values all increased with an increasing unit discharge due to the increase in water surface elevation. The maximum, mean, and minimum pressure head of a CHJ is also shown in Figure 7f, where the depth of supercritical flow (y_1) and its subcritical conjugate depth (y_2) are 0.17 m and 0.92 m, respectively, when $q_w = 0.93$ m^2/s [20]. For comparison purposes, the pressure profiles of a CHJ increased monotonically along the stilling basin,

except at its beginning. As observed in Figure 7a–e, for a small unit discharge (e.g., q_w = 0.102 m^2/s, and 0.154 m^2/s), the values of the maximum, mean, and minimum pressure were nearly the same; i.e., the pressure fluctuation along the stilling basin bottom is small. However, as the unit discharge q_w increased (q_w = 0.188 m^2/s, 0.205 m^2/s and 0.230 m^2/s, pressure fluctuations became greater in the vicinity of the sill, particularly at q_w = 0.205 m^2/s. This was attributed to the turbulent roller region of the jump, which was closer to the sill related to the transition from a submerged jump to a non-submerged jump. However, the pressure fluctuation of the classic hydraulic jump was more distinct at a near prototype scale. In order to prevent erosion below overflow spillways, chutes, and sluices, the pressure peak of wave-type flows should be carefully focused upon in this study.

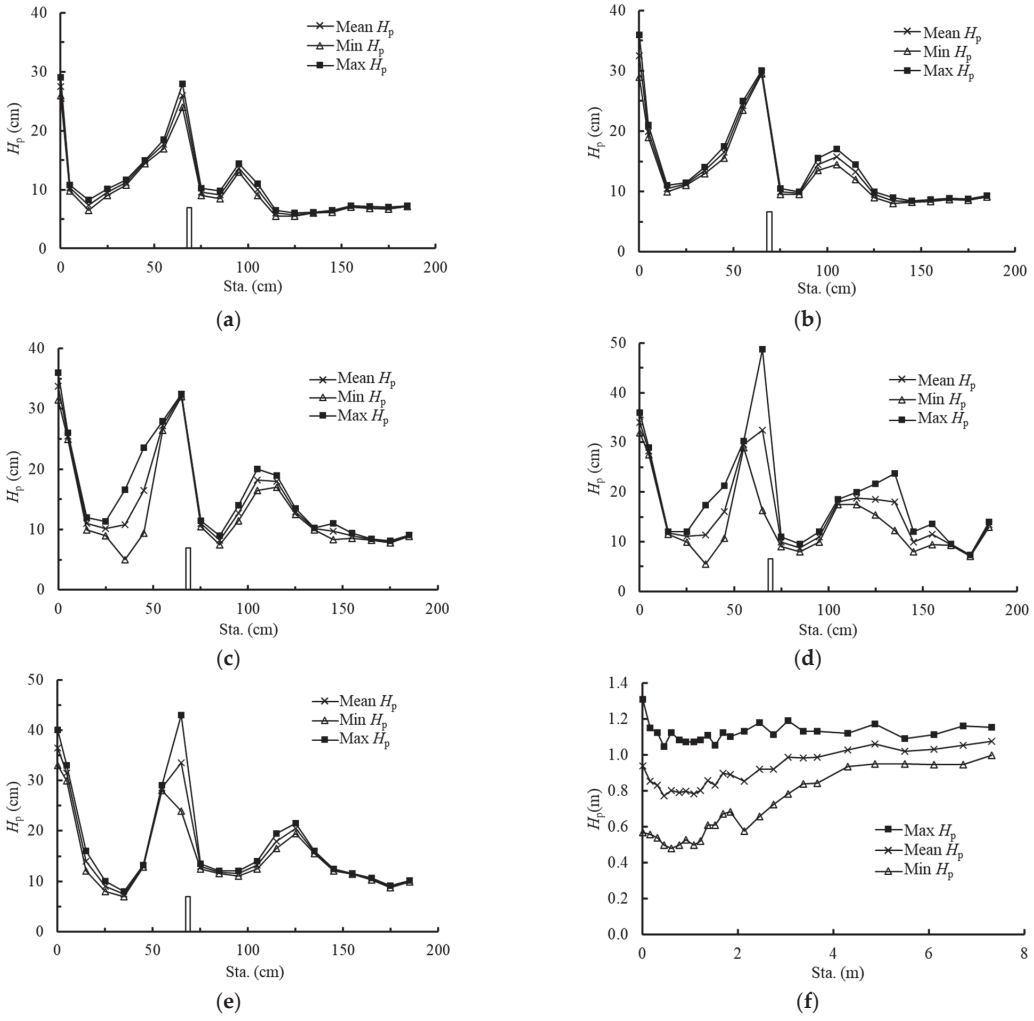

Figure 7. Maximum, mean and minimum pressure head on the bottom along the stilling basin at different unit discharges for Case M32 and a CHJ: (**a**) q_w = 0.102 m^2/s; (**b**) q_w = 0.154 m^2/s; (**c**) q_w = 0.188 m^2/s; (**d**) q_w = 0.205 m^2/s; (**e**) q_w = 0.230 m^2/s; (**f**) q_w = 0.93 m^2/s for a classical hydraulic jump [16].

Figure 8 illustrates the normalized mean pressure heads (H_p/y_2) along the stilling basin at different unit discharges (q_ws) for each case and a CHJ. In this figure, the down-

stream flow depth, y_2, was used to normalize H_p. In general, the streamwise dimensionless mean pressure heads H_p/y_2s for each case (Figure 8a–e) exhibited a similar trend at different unit discharges, with two distinct peak values observed along the stilling basin. For a CHJ in Figure 8f, H_p/y_2 typically decreased initially and then increased along the stilling basin. A larger H_p/y_2 could be obtained for a smaller q_w until the end of the jump, except for the beginning of the stilling basin. According to the existence of pressure peaks and the sill position in Figures 7 and 8, the streamwise dimensionless mean pressure indicated the following flow zones: (1) deflection zone, (2) jump zone, and (3) wave impact zone.

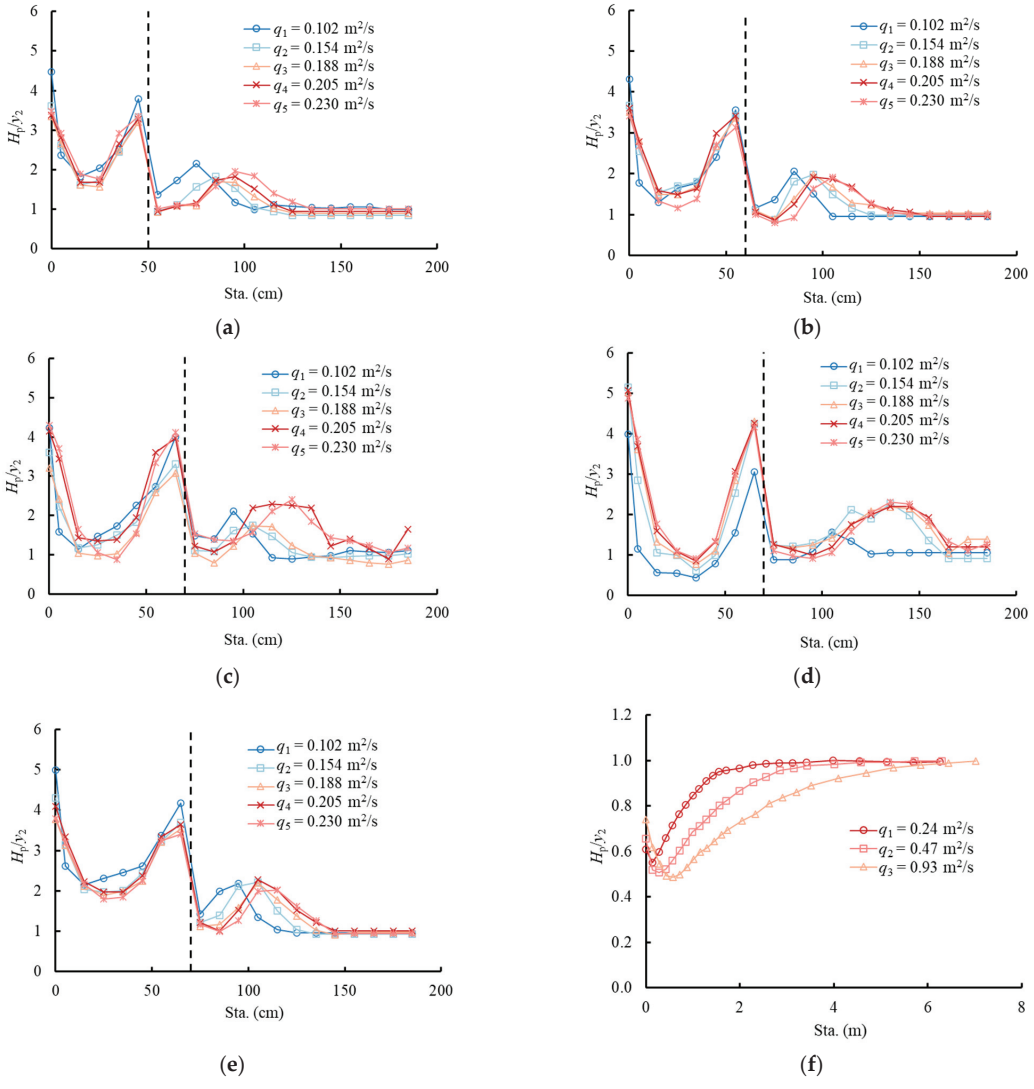

Figure 8. Normalized mean pressure head along the stilling basin for the range of q_w tested for each case: (**a**) Case M12; (**b**) Case M22; (**c**) Case M32; (**d**) Case M31; (**e**) Case M33; (**f**) Classical hydraulic jump [16].

The defection zone was characterized by the pronounced mean pressures due to the impact and curvature of the flow. In this zone, the pressure head decreased, and the

dimensional impact pressure H_p/y_2s was determined using the upstream weir flow. In the jump zone, the jump formation involved a strong pressure variation. The pressure head increased continually and reached the maximum closest to the upstream face of the sill. The resultant first peak value was much larger than the downstream depth. For the wave impact zone, wave-type flows induced a significant water drop downstream of the sill and resulted in a sudden pressure decrease and a secondary peak. The peak pressure value is still very high compared to downstream stable flow conditions y_2 (e.g., H_p/y_2 approximates 2.0 times y_2 when q_w = 0.205 m^2/s for Case M31). After the wave impact, the pressure head gradually decreased to a constant value. The pressure profile for a classical hydraulic jump by a sill—for which its position was at sta./y_2 = 5.71, 5.79, 5.87 at a unit discharge of 0.24 m^2/s, 0.46 m^2/s, and 0.93 m^2/s, respectively—is also illustrated in Figure 8f. Apart from the apparent pressure drop and wave impact in the vicinity of the sill, the mean pressure downstream of the sill was quasi-hydrostatic [21].

Generally, the designers and contractors should reinforce the stilling basin with concrete and steel to prevent the scouring of the bedrock, particularly for the local peak pressure [22]. The relative first and second peak pressure head in the vicinity of the sill normalized by the sill height H_p/s can be expressed in terms of dimensionless variables as

$$\frac{H_p}{s} = aF_1^b L^c S^d, \tag{1}$$

where $L = l_s/y_1$ and S = s/y_1 denote the relative length and height of the stilling basin, respectively; a, b, c, and d are constants. The relative first and second pressure peak values for sill configurations can be expressed with the following equations.

$$\frac{H_{p1}}{s} = 2.165F_1^{0.970} L^{0.182} S^{-0.718}, \tag{2}$$

$$\frac{H_{p2}}{s} = 3.010F_1^{0.346} L^{0.204} S^{-0.506}, \tag{3}$$

The graphs of Equations (2) and (3) are plotted in Figure 9. Equations (2) and (3) also reflected the relationships among the peak pressure heads, inflow conditions, and the sill configurations; i.e., the relative peak pressure increased with an increasing F_1 and the relative length of the stilling basin l_s/y_1 but decreased with increasing sill height s/y_1.

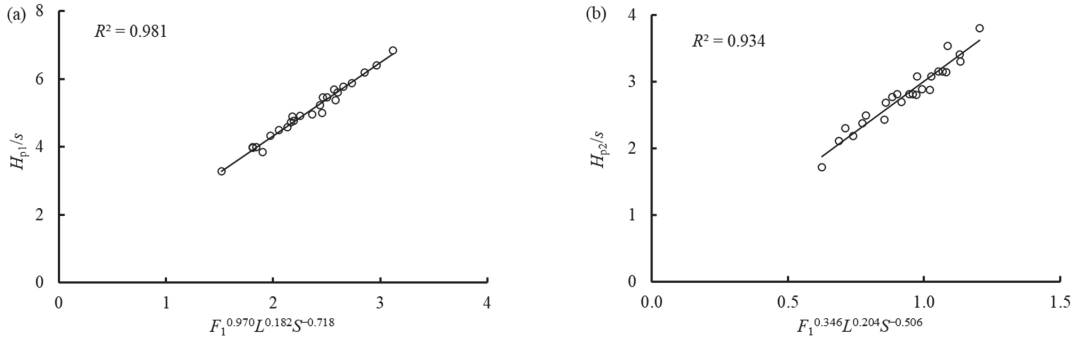

Figure 9. The relative first and second pressure peak: (**a**) first peak; (**b**) second peak.

3.3. Air Entrainment

The jump formation in the stilling basin would result in extreme water turbulence and pressure fluctuations on the bottom or the sidewall (e.g., with a restricted width) [23]. Due to the structural vibration caused by these pressure fluctuations and high velocity near the bottom of the basin, the risk of cavitation increases.

The cavitation damage can be greatly reduced by introducing enough air, and more attention should be focused upon the air concentration of the flow (i.e., the ratio of air volume to the sum of the air and water volumes) on the bottom and the sidewall. Air concentrations on the bottom (C_b) and the sidewall (C_s) in the vicinity of the sill at different inflow unit discharges q_ws for both Case M32 and M31 are highlighted in Figure 10. In this figure, $X = (x - l_s)/l_s$ represents the location of the measuring point relative to the sill position along the stilling basin floor.

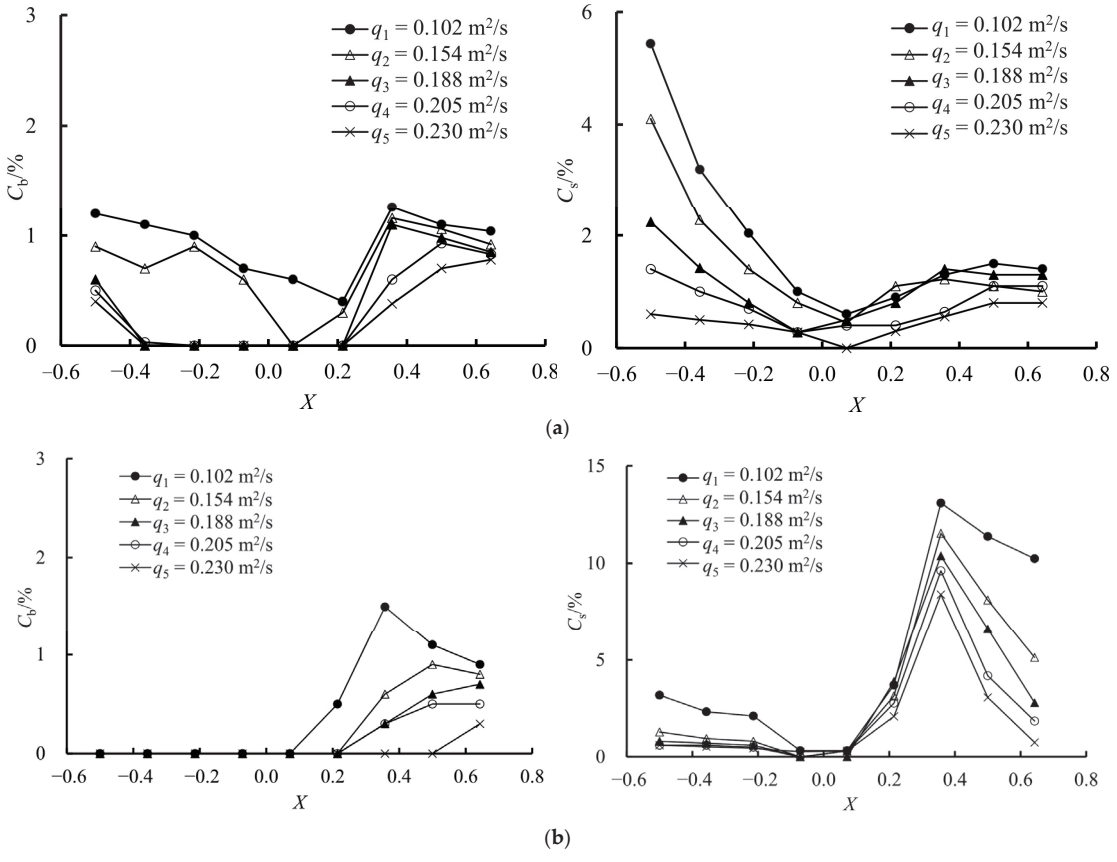

Figure 10. Air concentrations on the bottom (C_b) and the sidewall (C_s) for both Case M32 and M31 at different q_w values: (**a**) Case M32; (**b**) Case M31.

As shown in Figure 10a, air concentrations (C_b and C_s) decreased with an increasing q_w for M32. At each q_w value, a decreasing trend was observed in the upstream flow zone of the sill, and an opposite trend was found downstream of the sill. The data for M31 also exhibited the same trend at most of the flow zone in Figure 10b, but most bottom air concentrations upstream of the sill measured as zero due to the flow pattern of wave-type flows. For instance, with the increase in q_w for Case M32, the jump type changed from submerged to non-submerged, and the amount of entrained air was gradually transported downstream of the sill. At a small q_w value, entrained air resulting from the submerged jump at the toe of the weir reached the stilling basin bottom (e.g., q_w = 0.102 m^2/s and 0.154 m^2/s in Figure 5a). The blackwater zone close to the stilling basin bottom gradually enlarged with an increase in the unit discharge. In contrast, for Case M31, the flow zone upstream of the sill was always characterized by the blackwater in this study (Figure 5b).

Table 2 shows the air concentrations on the bottom and the sidewall along the stilling basin for all cases. Generally, air concentrations on the sidewall (C_s) were higher than that on the bottom (C_b). Peterka [24] proved that when the air concentration on the structure's surface was 1.0–2.0%, the cavitation damage could be considerably reduced. It was worth noting that the flow zone in the vicinity of the sill had a relatively small air concentration value (i.e., the value is below 1%) both on the bottom and the sidewall. Within these zones, the pressure profiles obviously fluctuated, especially for the location upstream of the sill, as observed in Figure 7. Thus, the resultant slight air entrainment and large pressure fluctuation should be focused upon in future work.

Table 2. Air concentrations on the bottom and the sidewall (%).

	Station (m)								
Case	**0.35**	**0.45**	**0.55**	**0.65**	**0.75**	**0.85**	**0.95**	**1.05**	**1.15**
M12-1	0.3/3.0	0/0.6	0/0	1.0/1.8	0.6/1.9	0.8/2.7	0.6/2.1	1.0/2.0	1.5/2.1
M12-2	0/1.5	0/0.3	0/0	0.7/1.0	0.5/3.4	1.1/1.1	0.7/1.5	1.0/1.8	1.8/2.2
M12-3	0/0.4	0/0	0/0	0/0.8	0.5/3.0	0.6/1.0	1.0/1.0	1.1/1.5	1.6/2.0
M12-4	0/0.3	0/0	0/0	0.3/0.8	0.6/1.1	0.8/1.0	1.3/1.4	1.4/1.6	1.5/1.8
M12-5	0/0	0/0	0/0	0/0.3	0.4/0.8	0.5/1.6	0.7/1.3	0.9/1.2	1.0/1.4
M22-1	0.6/4.4	0/2.5	0.4/1.0	0.4/0.6	1.0/1.1	0.9/0.9	1.1/2.1	0.7/8.1	0.7/1.0
M22-2	0.5/3.6	0/1.5	0.3/1.2	0/0.3	0.6/0.6	0.8/1.2	1.3/1.3	0.7/1.0	0.7/0.7
M22-3	0.4/1.5	0.3/1.7	0.3/1.0	0/0	0.4/0.4	0.9/1.2	1.0/1.0	0.7/1.1	0.7/0.7
M22-4	0/1.2	0/0.9	0/0	0/0	0/0.6	0.9/1.1	0.8/0.8	0.6/0.7	0.3/0.4
M22-5	0/1.9	0/0.4	0/0	0/0	0/0	0/1.2	0.8/1.6	0.7/1.2	0.5/0.5
M32-1	1.2/5.4	1.1/3.2	1.0/2.0	0.7/1.0	0.6/0.6	0.4/0.9	1.3/1.3	1.1/1.5	1.0/1.4
M32-2	0.9/4.1	0.7/2.3	0.9/1.4	0.6/0.8	0/0.5	0.3/1.1	1.2/1.2	1.1/1.1	0.9/1.0
M32-3	0.6/2.2	0/1.4	0/0.8	0/0.3	0/0.5	0/0.8	1.1/1.4	1.0/1.3	0.9/1.3
M32-4	0.5/1.4	0/1.0	0/0.7	0/0.3	0/0.4	0/0.4	0.6/0.6	0.9/1.1	0.8/1.1
M32-5	0.4/0.6	0/0.5	0/0.4	0/0.3	0/0	0/0.3	0.4/0.6	0.7/0.8	0.8/0.8
M31-1	0/3.2	0/2.3	0/2.1	0/0.3	0/0.3	0.5/3.7	1.5/13.1	1.1/11.4	0.9/10.2
M31-2	0/1.3	0/0.9	0/0.8	0/0	0/0.3	0/3.1	0.6/11.5	0.9/8.1	0.8/5.1
M31-3	0/0.8	0/0.7	0/0.6	0/0	0/0	0/3.9	0.3/10.4	0.6/6.6	0.7/2.8
M31-4	0/0.6	0/0.6	0/0.5	0/0	0/0.3	0/2.8	0.3/9.6	0.5/4.2	0.5/1.8
M31-5	0/0.6	0/0.5	0/0.4	0/0.3	0/0.3	0/2.1	0/8.4	0/3.1	0.3/0.7
M33-1	0.8/2.9	0.8/2.2	0.7/1.9	0.3/0.6	0.6/0.7	1.2/2.1	1.6/2.2	1.7/1.9	1.3/1.6
M33-2	0.7/2.4	0.8/1.9	0.6/1.7	0/0	0.5/0.6	1.0/1.9	1.6/2	1.6/1.7	1.2/1.4
M33-3	0.6/1.9	0.6/1.6	0.5/1.4	0/0.3	0.4/0.5	0.8/1.6	1.4/1.7	1.4/1.5	1.1/1.2
M33-4	0.6/1.3	0.6/1.2	0.5/1.3	0/0.3	0.3/0.5	0.7/1.3	1.2/1.5	1.3/1.4	1.0/1.2
M33-5	0.6/1.2	0.6/1.0	0.5/1.1	0/0	0.3/0.4	0.7/1.2	1.2/1.3	1.2/1.2	1.0/1.1

In the term "x/y" of the air concentration data, x and y are experimental data on the bottom and the sidewall, respectively.

4. Conclusions

Downstream of the sluice gate or weir, wave-type flows may occur under no tailwater conditions in a stilling basin. Experimental tests were conducted on five different sill configurations, including the sill position and the sill height. Five test unit discharges between 0.154 m^2/s and 0.230 m^2/s were conducted. The main findings are summarized as follows:

(1) When a sill is located near the upstream weir flow (i.e., the weir toe in this study), the jump types of the wave flow can be classified as submerged and non-submerged. The submerged wave type flow corresponding to a higher relative sill height was relevant for obtaining a better aeration effect.

(2) The ambient pressure head of the wave-type flow (i.e., the bottom pressure of the stilling basin) is strongly influenced by the flow pattern. Pressure fluctuations were more significant in the vicinity of the sill, and these are caused by the movement of the turbulent region of the jump, especially for the change in wave-type flow from a submerged jump to a non-submerged jump. The streamwise mean bottom pressure

profile revealed the existence of three distinct flow zones: (1) deflection zone, (2) jump zone, and (3) wave impact zone. There were two peak pressure points along the stilling basin, and these values can be distinguished by the upstream Froude number and the position and height of the sill.

(3) The air concentrations on the bottom and the sidewall were also affected by the flow pattern. For a given sill-controlled stilling basin, the air concentrations on the bottom and the sidewall decreased with increasing unit discharges. The flow zone within the vicinity of the sill had slight air entrainment and significant pressure fluctuations, which may be prone to cavitation. Thus, this region near the sill should be focused upon in order to provide protection.

The findings from this study have the potential to expand the application of sill-controlled stilling basins in hydraulic engineering by establishing new relationships. Additionally, the results can be used to improve the accuracy of CFD models in predicting wave-type flow behavior.

Author Contributions: Conceptualization, Y.Z.; methodology, Y.Z.; validation, H.Z.; formal analysis, J.H.; investigation, F.B.; resources, Y.Z.; data curation, Y.Z.; writing—original draft preparation, Y.Z.; writing—review and editing, H.Z. and Y.Z.; visualization, J.H.; funding acquisition, Y.Z. and J.W. All authors have read and agreed to the published version of the manuscript.

Funding: This research is supported by the Chinese Scholarship Council (CSC), National Natural Science Foundation of China (Grant No. 51809079), the Scientific and Technological Program of Zhejiang Water Resources Department (RB2119, and RC2143), the Joint Funds of the Zhejiang Provincial Natural Science Foundation of China (Grant No. LZJWY23E090002), the Nanxun Young Scholar, and the Research Center for Digital Economy and Sustainable Development of Water Resources, Zhejiang University of Water Resources and Electric Power (xrj2022012).

Institutional Review Board Statement: Not applicable.

Informed Consent Statement: Not applicable.

Data Availability Statement: All data, models, and code generated or used during the study are available from the corresponding author by request.

Conflicts of Interest: The authors declare no conflict of interest.

Notations

The following symbols are used in this paper:

P	weir height (m)
l_s	length of the stilling basin from the weir toe (m)
s	sill height (m)
h_s	positive step height (m)
Q	inflow discharge (m^3/s)
q_w	inflow unit discharge (m^2/s)
y_0	upstream flow depth (m)
y_1, y_2	supercritical flow depth upstream and downstream of the sill (m)
y_4	flow depth at the terminal section of the weir (m)
v_1, v_2	supercritical flow velocity upstream and downstream of the sill (m/s)
H_p	pressure head (m)
C_b, C_s	air concentrations on the bottom and the sidewall
F_1	upstream Froude number
F_2	downstream Froude number

References

1. Carvalho, R.F.; Lemos, C.M.; Ramos, C.M. Numerical computation of the flow in hydraulic jump stilling basins. *J. Hydraul. Eng.* **2008**, *46*, 739–752. [CrossRef]
2. Manoochehr, F.M.; Sadegh, H.; Babak, L.A.; Peyman, A. Reduction of stilling basin length with tall end sill. *J. Hydrodyn.* **2011**, *23*, 498–502. [CrossRef]

3. Tajabadi, F.; Jabbari, E.; Sarkardeh, H. Effect of the end sill angle on the hydrodynamic parameters of a stilling basin. *Eur. Phys. J. Plus.* **2018**, *133*, 10. [CrossRef]
4. Zhou, Y.; Wu, J.H.; Qian, S.T.; Ding, C.M.; Pan, G.Y. Discussion of "Types I, II, III, and IV Stilling Basin Performance for Stepped Chutes Applied to Embankment Dams" by Sherry L. Hunt and Kem C. Kadavy. *J. Hydraul. Eng.* **2023**, *149*, 07022008. [CrossRef]
5. Hager, W.H.; Li, D. Sill-controlled energy dissipator. *J. Hydraul. Res.* **1992**, *30*, 165–181. [CrossRef]
6. Kang, J.G.; Yeo, H.K.; Lee, K.C.; Choi, N.J. Experimental study on flow characteristic and wave type flow at downstream of stepped weir. *J. Korea Water Resour. Assoc.* **2010**, *43*, 41–49. [CrossRef]
7. Ohtsu, I.; Yasuda, Y.; Hashiba, H. Incipient jump conditions for flows over a vertical sill. *J. Hydraul. Eng.* **1996**, *122*, 465–469. [CrossRef]
8. Eldesoky, I.M.; Abdelsalam, S.I.; Abumandour, R.M.; Kamel, M.H.; Vafai, K. Interaction between compressibility and particulate suspension on peristaltically driven flow in planar channel. *Appl. Math. Mech.* **2017**, *38*, 137–154. [CrossRef]
9. Mossa, M.; Petrillo, A.; Chanson, H. Tailwater level effects on flow conditions at an abrupt drop. *J. Hydraul. Res.* **2003**, *41*, 39–51. [CrossRef]
10. Ferreri, G.B.; Nasello, C. Hydraulic jumps at drop and abrupt enlargement in rectangular channel. *J. Hydraul. Res.* **2002**, *40*, 491–505. [CrossRef]
11. Kawagoshi, N.; Hager, W. Wave type flow at abrupt drops: I. Flow geometry. *J. Hydraul. Res.* **1990**, *28*, 235–252. [CrossRef]
12. Eroğlu, N.; Tokyay, N. Statistical approach to geometric properties of wave-type flow occurring at an abrupt drop. *J. Fac. Eng. Archit. Gazi Univ.* **2012**, *27*, 911–919.
13. Eroğlu, N.; Taştan, K. Local Energy Losses for Wave-Type Flows at Abrupt Bottom Changes. *J. Irrig. Drain. Eng.* **2020**, *146*, 04020029. [CrossRef]
14. Huang, G.; Diao, M.; Jiang, L.; Wang, C.A.; Jia, W. Experimental Study on Wave Characteristics of Stilling Basin with a Negative Step. *Entropy* **2022**, *24*, 445. [CrossRef]
15. Zhou, Y.; Wu, J.H.; Qian, S.T.; Ma, F.; Hu, J.Y. Discussion of "Local Energy Losses for Wave-Type Flows at Abrupt Bottom Changes" by Nihat Eroglu and Kerem Tastan. *J. Irrig. Drain. Eng.* **2021**, *147*, 07021007. [CrossRef]
16. Padulano, R.; Fecarotta, O.; Del Giudice, G.; Carravetta, A. Hydraulic design of a USBR Type II stilling basin. *J. Irrig. Drain. Eng.* **2017**, *143*, 04017001. [CrossRef]
17. Zhou, Y.; Wu, J.H.; Ma, F.; Qian, S.T. Experimental investigation of the hydraulic performance of a hydraulic-jump-stepped spillway. *KSCE J. Civ. Eng.* **2021**, *25*, 3758–3765. [CrossRef]
18. Hager, W.H.; Bremen, R. Classical hydraulic jump: Sequent depths. *J. Hydraul. Res.* **1989**, *27*, 565–585. [CrossRef]
19. Hager, W.H.; Bretz, N.V. Hydraulic jumps at positive and negative steps. *J. Hydraul. Res.* **1986**, *24*, 237–253. [CrossRef]
20. Hunt, S.L.; Kadavy, K.C. Types I, II, III, and IV stilling basin performance for stepped chutes applied to embankment dams. *J. Hydraul. Eng.* **2021**, *147*, 06021004. [CrossRef]
21. Stojnic, I.; Pfister, M.; Matos, J.; Schleiss, A.J. Effect of 30-degree sloping smooth and stepped chute approach flow on the performance of a classical stilling basin. *J. Hydraul. Eng.* **2021**, *147*, 04020097. [CrossRef]
22. Hager, W.H.; Sinniger, R. Flow characteristics of the hydraulic jump in a stilling basin with an abrupt bottom rise. *J. Hydraul. Res.* **1985**, *23*, 101–113. [CrossRef]
23. Sobani, A. Pressure fluctuations on the slabs of stilling basins under hydraulic jump. In Proceedings of the 11th International Conference on Hydroinformatics, New York, NY, USA, 17–21 August 2014.
24. Peterka, A.J. The effect of entrained air on cavitation pitting. In Proceedings of the Proceedings: Minnesota International Hydraulic Convention, Minneapolis, MN, USA, 1–4 September 1953; pp. 507–518.

applied sciences

MDPI

Article

Effects of "S"-Type Bowed Guide Vanes on Unsteady Flow in 1.5-Stage Axial Compressors

Yupeng Liu [1], Guangqing Liao [2], Yunzhu Li [1], Yonghui Xie [1,*] and Di Zhang [2]

[1] State Key Laboratory of Strength and Vibration of Mechanical Structures, School of Energy and Power Engineering, Xi'an Jiaotong University, Xi'an 710049, China
[2] MOE Key Laboratory of Thermo-Fluid Science and Engineering, School of Energy and Power Engineering, Xi'an Jiaotong University, Xi'an 710049, China
* Correspondence: yhxie@mail.xjtu.edu.cn

Abstract: In axial compressors, the unsteady flow caused by the interaction between dynamic and static cascades will make the moving vanes subject to periodic forces and increase the risk of high-cycle fatigue fractures. In this study, an "S"-type bowed guide vane was designed and a 1.5-stage axial compressor model was established. For five guide vanes with different bending coefficients, unsteady numerical simulation was carried out under design conditions and near-blockage conditions. The influence of the guide vane bending coefficient on the pressure ratio and efficiency is analyzed, and the aerodynamic exciting force on moving vanes is analyzed by using the fast Fourier transform. The study shows that the model with an "S"-type bowed guide vane can greatly reduce the amplitude of aerodynamic exciting force on moving vanes. The model with a guide vane bending coefficient of −10 mm can reduce the tangential and axial aerodynamic exciting force amplitudes at the first-order blade-passing frequency by 90.82% and 90.39% under the design conditions, respectively. Under the near-blockage condition, the tangential and axial aerodynamic exciting force amplitudes can be reduced by 85.84% and 86.58%, respectively. This can greatly improve the vibration safety of the moving vane.

Keywords: axial compressor; unsteady flow; aerodynamic exciting force; "S"-type bowed; guide vane

Citation: Liu, Y.; Liao, G.; Li, Y.; Xie, Y.; Zhang, D. Effects of "S"-Type Bowed Guide Vanes on Unsteady Flow in 1.5-Stage Axial Compressors. *Appl. Sci.* **2023**, *13*, 5071. https://doi.org/10.3390/app13085071

Academic Editors: Vasily Novozhilov and Cunlu Zhao

Received: 1 April 2023
Revised: 15 April 2023
Accepted: 17 April 2023
Published: 18 April 2023

1. Introduction

The unsteady flow caused by the relative motion between the moving and static vanes is an intrinsic unsteady phenomenon in fluid machinery, and has certain periodic laws. The outlet aerodynamic parameters of the upstream vane are not uniform, but show a periodic distribution [1], so the downstream moving vane will bear the high-frequency periodic aerodynamic exciting force during rotation. For axial flow compressors, the high-frequency aerodynamic exciting force on the moving vane will increase the high-cycle fatigue fracture risk and reduce the compressor service life. It is also an important part of the compressor aerodynamic noise. Therefore, it is very important to study the unsteady flow phenomena in axial flow compressors and explore efficient measures to reduce the flow exciting force of moving vanes for safe and stable operations [2].

Many scholars have carried out detailed research on unsteady flow in axial flow compressors. Gallus et al. [3,4] experimentally measured the pressure fluctuation on the surface of the moving and stator blades in the subsonic compressor as well as the shape of the moving wake. The results show that the higher-order harmonics of potential flow interaction attenuate very quickly. In most cases, the amplitude of the second harmonic is only 20% to 40% of the first harmonic, and the influence of the higher harmonic on the blade vibration is very small. When the axial clearance of the cascade row is small, the potential flow interference and the wake maintain the same order of magnitude. Thus, increasing the axial clearance can reduce the discrete tone level. The research by Gorrell [5] shows that, in transonic compressors, with a smaller axial clearance between moving and stator blades,

the aerodynamic loss caused by stator–rotor interactions increases gradually, resulting in the decline of axial compressor performance. Douglas et al. [6] studied the unsteady flow characteristics generated by the interaction between guide vane wakes and moving blades of axial compressors through experiments, and analyzed the probability distribution of the wake characteristics. The results indicate that the relative position between the moving and stator blades have a strong correlation with unsteady aerodynamic response of the moving vanes, but this correlation would be weakened with the decrease of the flow rate under working conditions. Burkhardt et al. [7] conducted the unsteady measurements of the moving and stator blades for the high load 1.5-stage axial compressor and studied the influence of different working conditions on boundary layer transition. Smith et al. [8] explored the influence of the interaction between upstream blades on the downstream blade boundary layer transition position through a 3-stage axial compressor test rig.

The research on unsteady aerodynamic exciting forces can be traced back to the 1960s. Lefcort [9] used a simple analysis model to predict the pressure fluctuation of adjacent blades. However, due to the lack of cognition at that time, the author could only make rough assumptions about the research model, which pose a limitation on its adaptability. Daigji et al. [10] studied the correlation between wake and unsteady aerodynamic forces, and the influence of wake on moving cascades is studied through the combination of the finite element method and the finite difference method. Mailach et al. [11] studied the influence mechanism of unsteady blade row interference on unsteady aerodynamic forces of a 4-stage compressor. In this research, the time and frequency domain distribution of aerodynamic forces are analyzed. It is pointed out that the amplitude and shape of aerodynamic forces are not only related to the wake strength and flow field potential, but also affected by the interaction between the wake and the potential flow field. Smith et al. [12] set up a three-stage axial compressor test platform and used high-frequency response pressure sensors to conduct tests. The results show that the rotor wake and tip clearance flow are the main reasons for the unsteady load fluctuation of the downstream stator blades. The two rows of moving vanes adjacent to the stator blade have a significant effect on the unsteady pressure fluctuation on its surface, and the timing effect has obvious effects on the dynamic–static interference.

It can be found that the unsteady flow in the compressor is mainly caused by the interference of the potential flow field and wake. The stator–rotor interaction plays a decisive role in the unsteady force on the blade. Many scholars have designed the structure of the blade in an effort to improve the unsteady aerodynamic performance as well as reduce the aerodynamic exciting force and noise. Monk et al. [13] analyzed the effect of asymmetric stator distribution on unsteady flow by researching a three-stage compressor. It can be found from Fourier transform results that the number of stator blades is asymmetric, which reduces the amplitude of aerodynamic excitation and deflects the excitation frequency. Wenjie et al. [14] studied the method of reducing the dynamic and static interference noise using nonuniform trailing edge blowing. Through numerical simulation, they found that the axial force amplitude of the moving vane at the first-order blade-passing frequency can be reduced by 63.83%. Milidonis et al. [15] studied the effects of clocking on acoustic noise-generation characteristics in a 1.5-stage axial compressor using high-fidelity and low-order numerical methods. It is found that stator clocking has little effect on compressor efficiency and tonal acoustic noise levels in the far field but the amplitude varies differently when the clocking position varies in the near field. Asymmetric stator distribution and nonuniform trailing edge blowing can play a better role in reducing the amplitude of the airflow exciting force. However, the structure of these designs is very complex and the cost is greatly increased.

Improving unsteady performance by changing the vane stacking in space is also a research direction. Weir et al. [16] measured the influence of forward swept rotors and inclined guide vane on rotor–stator interaction noise. The results show that the noise of the improved fan model is lower than that of the original model in most conditions. Bamberger et al. [17] changed the sweep strategy and geometrical parameters to optimize

the sound emission and efficiency of a low-pressure axial fan using the simplex method, and verified it via experiments and numerical methods. Bohn et al. [18] compared the 3D unsteady flow field of a cylindrical-designed blade and bow-blade with numerical calculations, and found that bow-blades can reduce the wake intensity and the unsteady profile pressure fluctuations. Laborderie et al. [19] established a two-stagger-angle method to predict the vane camber effects on fan noise. It has been shown that the interaction noise sources are predominant in the leading-edge region. Ling et al. [20] optimized the stacking line of the compressor curved vane of a linear compressor, analyzed the influence of a stack line on aerodynamic loss, and obtained the optimum stack line under different geometric parameters and aerodynamic conditions. Rajesh et al. [21] proposed a variable camber inlet guide to increase the stable operating range of a low-speed axial compressor and analyzed its stable operating range and efficiency at an off-design point using numerical simulation. Wadia et al. [22] designed a swept and leaned-outlet guide vane. Through numerical calculation, it is found that it can reduce the potential flow interaction of stators and rotors and reduce the back-pressure disturbance. Keke et al. [23] studied the influence of a stator blade camber on the unsteady performance of axial turbines, and found that a bowed stator can effectively reduce the airflow exciting force amplitude of rotor blades. Xiangyi et al. [24] studied the effect of variable-camber inlet guide vanes on the performance of compressors using a numerical method. Results show that the stall margin and the total pressure rise of the compressor rotor are sensitive to the span range of the variable-camber. Lei et al. [25] studied the effect of bowed outlet guide vanes in gas turbines on the heat conduction and aerodynamic performance near the endwall using numerical simulations. It was found that the bowed vanes can effectively reduce the endwall heat transfer. Niu et al. [26] found that forward-swept and positive-leaned vanes can reduce the exciting force and make the output power more stable for gas turbines using numerical calculations. Liu et al. [27] conducted numerical and aeroacoustic studies on axial flow compressors with different lean angles of the stator, and found that a positive leaned stator has better noise reduction effect than the negative. Zhu et al. [28] found that the combination of blade lean and blade clocking can improve unsteady aerodynamic performance and adiabatic efficiency through the numerical simulation of 1.5-stage axial turbines.

Through the above research, it can be found that most of the researches are aimed at improving unsteady aerodynamic performance or reducing aerodynamic noise. However, in order to ensure the safe and stable operation of the compressor, the unsteady force on the vane is also very important. In addition, changing the vane stacking line in the tangential direction has a greater impact on the unsteady aerodynamic performance of fluid machinery, and the effect of reducing unsteady aerodynamic force is more obvious. However, most of the designs are leaned vanes and "C"-type bowed vanes. This study improved the structure of the guide vane of the axial compressor with an "S"-type bowed guide vane, and the improvement is validated on a 1.5-stage axial compressor model. For five guide vane models with different bending coefficients, the unsteady numerical simulation was carried out under design conditions and near-blockage conditions, respectively. The influence of the "S"-type bowed guide vane on the aerodynamic performance and the aerodynamic exciting force on moving vanes are both studied to explore the optimal structure of the guide vane of the 1.5-stage axial compressor.

2. Methods

2.1. The 1.5-Stage Axial Compressor with the "S"-Type Bowed Guide Vane

In this study, based on a civil axial compressor, a numerical calculation model of a 1.5-stage full three-dimensional axial compressor including a guide vane, moving vane, and stator vane was established. The structural parameters of the compressor model are shown in Table 1.

Table 1. Structure parameters of the 1.5-stage axial compressor.

Parameters	Guide Vane	Moving Vane	Stator Vane
number of blades	54	36	45
inner diameter of vane/mm	260	260	260
outer diameter of vane/mm	447	445	442
rated speed/rpm	—	4830	—

The guide vane of the original model is straight. We fix the endwall sections and ensure that the profiles at different blade height positions are the same. The stacking line is bent into the "S"-type in the form of a sine function in the tangential direction and its position in the axial direction is unchanged. The stacking line of the "S"-type bowed curved guide vane can be expressed as shown in Equation (1) in the cylindrical coordinate system:

$$c = a \sin\left(\frac{2\pi}{R_1 - R_0}(r - R_0)\right) \tag{1}$$

where a is defined as the guide vane bending coefficient, which represents the maximum distance of the "S"-type bowed guide vane from the original vane in the tangential direction. R_1 is the outer diameter of the guide vane, R_0 is the inner diameter of the guide vane, r is the radial coordinate of the stacking line, and c is the tangential coordinate of the stacking line. Figure 1 shows the guide vanes with different bending coefficients.

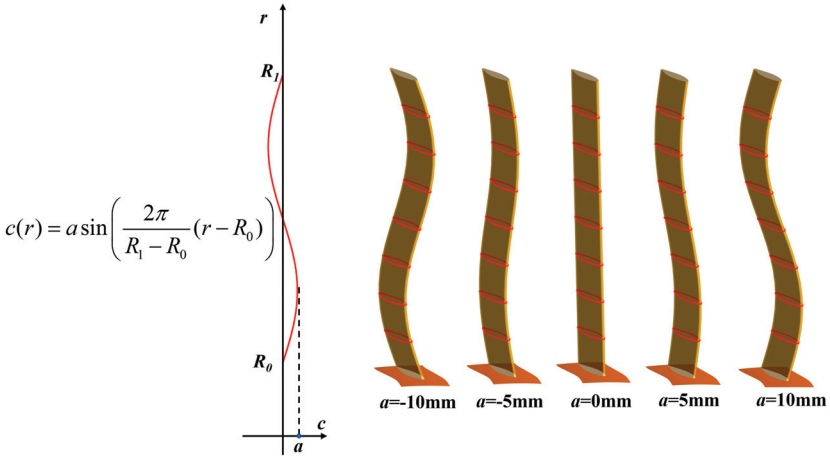

Figure 1. Guide vanes with different bending coefficients.

In this study, the 1.5-stage axial compressor with different bending coefficient a is numerically simulated under the design condition and near-blockage condition, respectively. The boundary conditions of the two working conditions are shown in Table 2.

Table 2. Boundary conditions of the design condition and near-blockage condition.

Parameters	Design Condition	Near-Blockage Condition
inlet total pressure/kPa	101.32	101.32
inlet total temperature/K	288.15	288.15
outlet flow rate/kg·s^{-1}	48.75	56

2.2. Numerical Method

The full three-dimensional unsteady Navier–Stokes equations are used for numerical calculation, while real air is used as the working medium. The SST k-ω turbulence model

is selected for unsteady aerodynamic analysis in this study. The computational domain of aerodynamic analysis is established with the number of guide vanes, moving vanes, and stator vanes being 6, 4, and 5, respectively. The computational domain is one-ninth of the whole axial compressor model. The computational domains extend two times of the guide vane chord ahead of the guide vane and three times of the stator chord length behind the stator vane to improve the computational accuracy. Taking the a = 0 mm model as an example, the geometric model of the aerodynamic computational domain is shown in Figure 2.

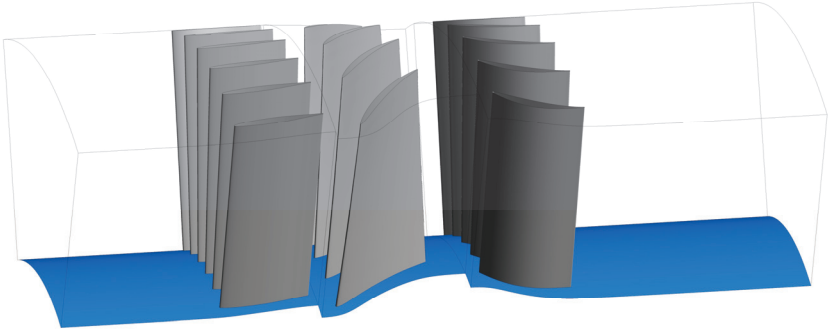

Figure 2. Full geometry of the investigated case. The gray parts are the vanes and the blue parts are the hubs.

The numerical analysis is completed using the ANSYS CFX 16.0 software. The transient rotor stator method [29,30] is adopted for dynamic and static interfaces. The transient rotor stator method can well simulate the relative motion between the guide vane and the moving vane as well as the relative motion between the moving vane and the stator vane by using a sliding interface. The relative position of the grids on each side of the interface is updated each timestep with the rotation of the moving vane. A high accuracy difference scheme is adopted for convection terms and a second-order upwind scheme is adopted for time-term discretization. The inlet turbulence intensity is 5% for a fully developed flow. The time step equals 7.668×10^{-6} s, which means it takes 30-time steps for a moving vane to sweep through a guide vane. In the unsteady calculation, the axial force and the tangential force of a single moving vane are detected. When there are more than 10 regular cycles, the calculation is considered to be convergent.

The frequency-domain distribution of unsteady aerodynamic exciting forces is obtained using fast Fourier transform, and the frequency-domain distribution law of unsteady aerodynamic forces can be obtained, including excitation amplitude and excitation frequency, so as to further reveal the mechanism of aerodynamic excitation. In this study, the function $f(t)$ with a period of 2π is used to express the unsteady force of the moving vane, as shown in Equation (2) [23].

$$f(t) = \sum_{k=-\infty}^{+\infty} a_k e^{ikt} \tag{2}$$

The spectrum function can be obtained using Fourier transformation of Equation (1), as shown in Equation (3) [23].

$$a_k = \frac{1}{2\pi} \int_0^{2\pi} f(t) e^{-ikt} dt \tag{3}$$

For the overall quantities, we validated the numerical calculation method through the numerical analysis of NASA Rotor 67. Strazisar et al. [31] gave detailed test measurement values of the blade. For the blade of Rotor 67, the number of grid nodes of the single channel numerical model is 0.921 million, and the number of elements is 0.854 million. The grid is densified at the tip clearance and the blade surface. Parameter settings for

numerical analysis are as follows: (1) The calculation domain is set as the rotation domain, the rotational speed is 16,043 rpm, and the working medium is ideal gas. The turbulence model is SST *k*-*ω*; (2) The total inlet pressure is set to 101,325 Pa, and the total temperature is set to 288.15 K; (3) By adjusting the back pressure at the outlet, the pressure ratio and efficiency under various flow conditions are calculated; (4) The position of the inner wall of the hub and the gearbox is under the condition of a no-slip wall. Based on the above settings, the aerodynamic performance of the R67 fan blade is calculated. At 100% speed, the blockage flow of the fan blade is 34.56 kg·s^{-1}, the test data are 34.96 kg·s^{-1}, and the relative error of numerical simulation is 1.1%. In order to facilitate the comparison, the flow results under all calculation conditions are dimensionless treated with the blockage flow, and the change curve of performance parameters under the dimensionless flow rate is obtained. The pressure ratio of fan blades is defined as:

$$P_r = \frac{P_o^t}{P_i^t} \tag{4}$$

where P_o^t is the total outlet pressure, and P_i^t is the total inlet pressure. The isentropic efficiency of fan blades is defined as:

$$\eta = \frac{H_{2s} - H_1}{H_2 - H_1} \tag{5}$$

where H_{2s} is the outlet enthalpy value of the compressor under isentropic compression, H_1 is the inlet enthalpy value of the compressor, and H_2 is the actual outlet enthalpy of the compressor.

Figure 3 shows the pressure ratio and efficiency obtained via numerical calculation with the experimental data. The red curve is the fitting result of numerical calculations, and the black point is the test result. The pressure ratio and efficiency obtained using numerical calculations are in good agreement with the experimental data. In the whole flow rate range, the maximum error of the pressure ratio obtained via experiments and numerical simulations is less than 2.0%, and the maximum error of efficiency is less than 3.0%, which verifies the accuracy of the numerical method for the overall quantities analysis of compressor blades.

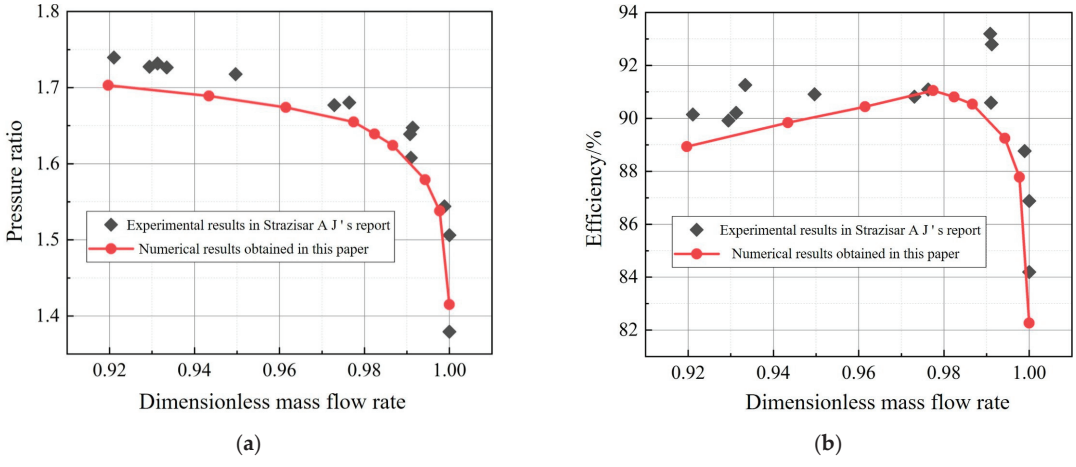

Figure 3. Calculation result verification of a R67 fan blade. (**a**) Comparison of pressure ratio results; (**b**) Comparison of isentropic efficiency results.

For an unsteady computation method, Zhu et al. [32] performed unsteady aerodynamic analysis on a 1.5-stage subsonic axial compressor through the same turbulence model

and numerical method and compared it with experimental data [33,34]. The average error of efficiency between CFD and the experimental results is about 4%, while the maximum error of total pressure coefficients is about 0.8%. In addition, the main frequencies of the flow field obtained using CFD are consistent with experimental data. Therefore, the unsteady numerical method used in this study is appropriate and accurate.

2.3. Numerical Validation

The whole fluid domain is divided into high-quality hexahedral grids. The O-type grid is applied around vanes and the H-type grid is mainly applied in the flow channels. The grids near the wall are densified to ensure the accuracy of the aerodynamic parameter calculations of the boundary layer. The value of y^+ near the wall is less than 1. The grid is also densified at the trailing edge and leading edge to fully reflect the geometric characteristics. Taking the a = 0 mm model as an example, Figure 4 shows the unsteady tangential force on the moving vane with different grid numbers under design condition. When the grid numbers increase from 6.7 million to 8.2 million, the maximum relative error of the tangential force is less than 0.1%. The number of grids is determined to be 6.7 million. Figure 5 shows the grids used in this study.

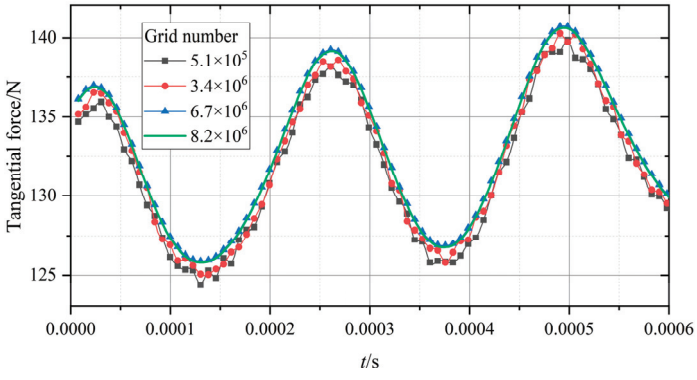

Figure 4. Grid independence verification.

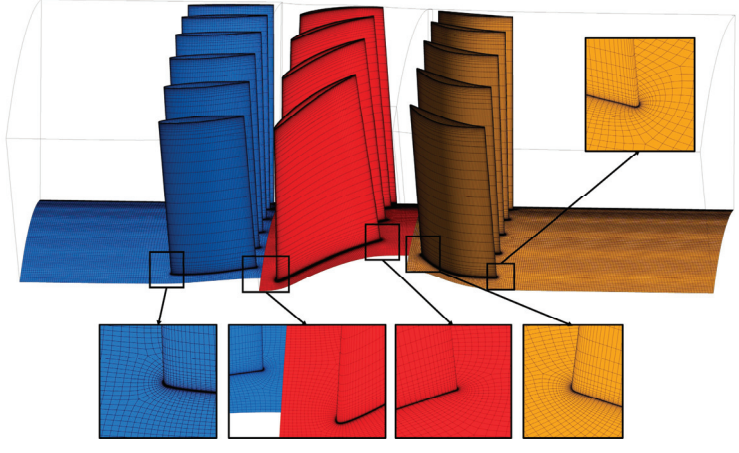

Figure 5. Aerodynamic analysis grids. The blue parts show the guide vanes grids, the red parts show the moving vanes grids, and the yellow parts show the stator vanes grids.

The time step used in the unsteady calculation is also verified. Taking the a = 0 mm model as an example, Figure 6 shows the unsteady tangential force on the moving vane

with different time steps under the design condition. The maximum error of the model with time steps of 7.668×10^{-6} s and 5.751×10^{-6} s is less than 0.2%. Therefore, setting the time step to 7.668×10^{-6} s can not only accurately show the unsteady parameters, but also do not increase the unnecessary calculation.

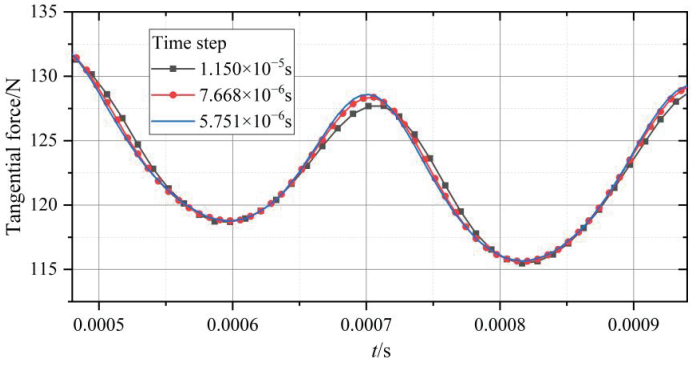

Figure 6. Time step verification.

3. Results and Discussion

3.1. Unsteady Aerodynamic Results under the Design Condition

Table 3 shows the pressure ratio and total efficiency of different guide vane bending coefficients under the design condition. It can be seen that the guide vane bending coefficient has little effect on the overall aerodynamic performance. The pressure ratio decreases with the increase of a. The pressure ratio of the a = 10 mm model decreases by 0.18% compared with the a = 0 mm model. The total efficiency of the "S"-type bowed models is reduced. The total efficiency of the structure with the $a = -10$ mm decreases the most, which is 0.57%.

Table 3. Overall aerodynamic performance under the design condition.

Bending Coefficient *a*/mm	**−10**	**−5**	**0**	**5**	**10**
pressure ratio	1.1908	1.1904	1.1903	1.1901	1.1882
total efficiency/%	82.39	82.66	82.93	82.64	82.51

Figure 7 shows the turbulent kinetic energy distribution of models with different bending coefficients at different axial positions under the design condition at the time t = 0 T. The left figure is the front 2 mm position of the moving vane, which is the inflow of the moving vane. The middle figure is the middle position of the moving vane passage. The right figure is the back 2 mm position of the moving vane, which is downstream of the moving vane. It can be seen that, although the flow channels are geometrically symmetrical, the turbulent kinetic energy distribution of different flow channels is different, which is caused by the inherent unsteadiness of turbulence. At the inflow of the moving vane, the distribution of the high turbulent kinetic energy region is the same as the guide vane shape. This is because as the fluid flows downstream, the guide vane surface boundary layer changes to the turbulent boundary layer. The flow in the turbulent boundary layer is disordered. The turbulent boundary layers on both sides fall off and converge at the guide vane trailing edge, forming a wake area with higher turbulence intensity and more vortices. In addition, there are also regions with higher turbulent kinetic energy near the endwall, where the turbulent kinetic energy intensity near the hub is higher than that near the shroud. The area with higher turbulence kinetic energy regions near the shroud of the $a = -5$ mm model is very small while that of the other models is large.

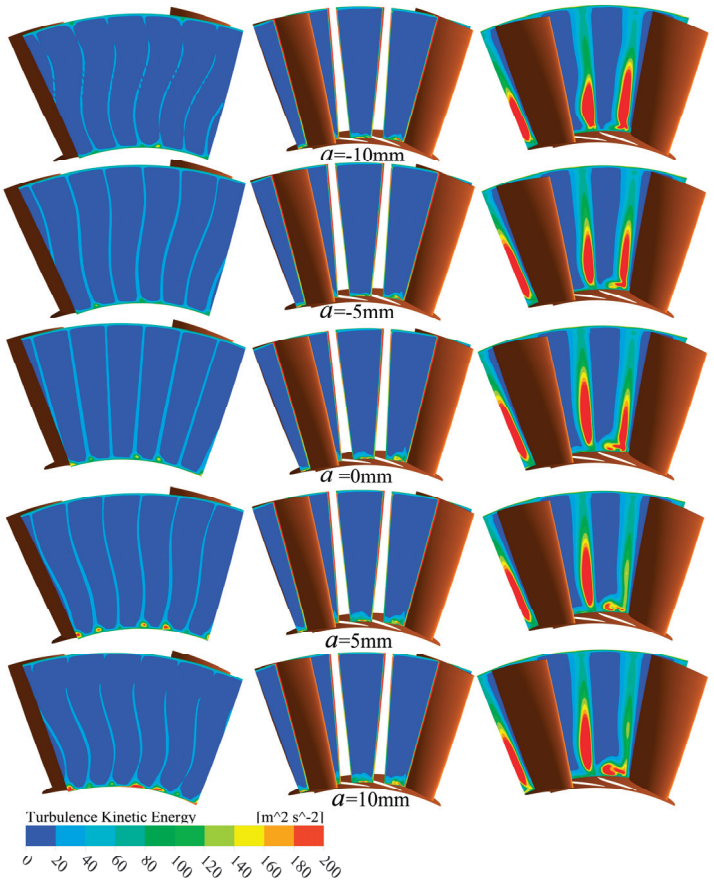

Figure 7. Turbulent kinetic energy distribution of the different models under design conditions.

In the moving vane channel, the turbulent kinetic energy of the main flow area is low, and the areas with high turbulent kinetic energy are mainly concentrated on the moving vane surface and endwall, which is caused by the boundary layer. Among them, the turbulent kinetic energy near the hub is significantly higher. This is because the fluid domain of the moving vane is a rotating domain. Under the effect of centrifugal forces, the fluid in the moving vane channel tends to move in the radial direction, so the fluid near the hub is easier to perform flow separation. Among them, the turbulent kinetic energy of the $a = -5$ mm model is the smallest near the hub. With the increase of a, the turbulent kinetic energy near the hub shows an increasing trend. In addition, the intensity of turbulent kinetic energy near the suction surface of the moving vane is also significantly higher than that near the pressure surface. This is depended by the shape of the vane. The pressure surface is concave while the suction surface is convex. Fluid flow separation is more likely to occur when flowing through a convex surface.

Turbulent kinetic energy distribution downstream of the moving vane is also uneven in the circumferential direction according to the shape of the moving vane. The turbulent kinetic energy intensity is high in the wake area near the moving vane trailing edge, and low in the mainstream area near the middle of the moving vane channel. In the wake of the moving vane, the turbulent kinetic energy distribution along the blade height is also uneven. The turbulent kinetic energy intensity is higher at the position with a lower blade height. In the $a = 0$ mm, $a = 5$ mm, and $a = 10$ mm models, the area near the hub with high

turbulent kinetic energy is separated from the moving vane wake area, which has a great impact on the mainstream.

Figures 8 and 9 show the tangential and axial exciting force–time domain distribution on moving vanes of different bending coefficient models under the design condition. It can be seen that the tangential and axial aerodynamic exciting forces show obvious periodicity. In the $a = -5$ mm, $a = 0$ mm, $a = 5$ mm, and $a = 10$ mm models, the time domain distribution of the exciting force is close to the form of sine functions. The time domain distribution of the aerodynamic exciting force of the $a = -10$ mm model is very different from other models. Although the exciting force of the $a = -10$ mm also shows a certain periodicity, its distribution is not in the form of a sine function, and the amplitude is significantly reduced compared with other models. The periodic aerodynamic exciting force will easily cause high-cycle fatigue fracture of the moving vane, reducing the service life of the blade. In addition, the phases of axial force and tangential force of different models are almost the same, which indicates that the tangential force and axial force reach the maximum and minimum values almost simultaneously. It means that the amplitude of the resultant force of the moving vane is larger, which is more unfavorable to the vibration safety of the blade.

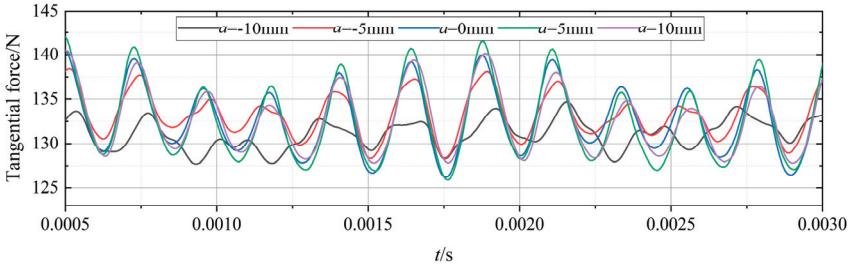

Figure 8. Tangential force–time domain distribution under design conditions.

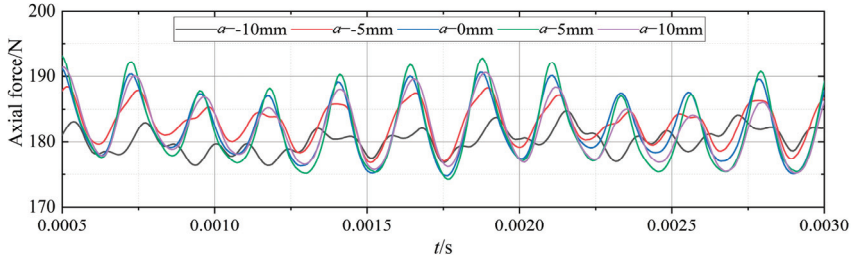

Figure 9. Axial force–time domain distribution under design conditions.

Theoretically, the frequency of a high-frequency aerodynamic exciting force should be equal to the first-order blade-passing frequency. The number of guide vanes is 54 and the speed is 4830 rpm, so the time for a single moving vane to sweep through a guide vane channel is 2.3×10^{-4} s, and the first order blade-passing frequency is 4347 Hz.

The time domain distribution of aerodynamic exciting forces is analyzed by using fast Fourier transform, and the frequency–domain distribution under design conditions shown in Figure 10 is obtained. It can be seen that, for models with different bending coefficients, there is a high local amplitude at the first-order blade-passing frequency, but the magnitude of the amplitude is very different. Table 4 shows the time mean value and the amplitude value at the first-order blade-passing frequency of aerodynamic exciting forces with different bending coefficients. Compared with the $a = 0$ mm model, the aerodynamic exciting force amplitude of the $a = 5$ mm model increases, in which the tangential exciting force amplitude increases by 14.89% and the axial exciting force amplitude increases by 14.35%. The aerodynamic exciting force amplitudes of the other models decreased, of

which the $a = -10$ mm model decreased the most, the tangential exciting force amplitude decreased by 90.82%, and the axial exciting force amplitude decreased by 90.39%.

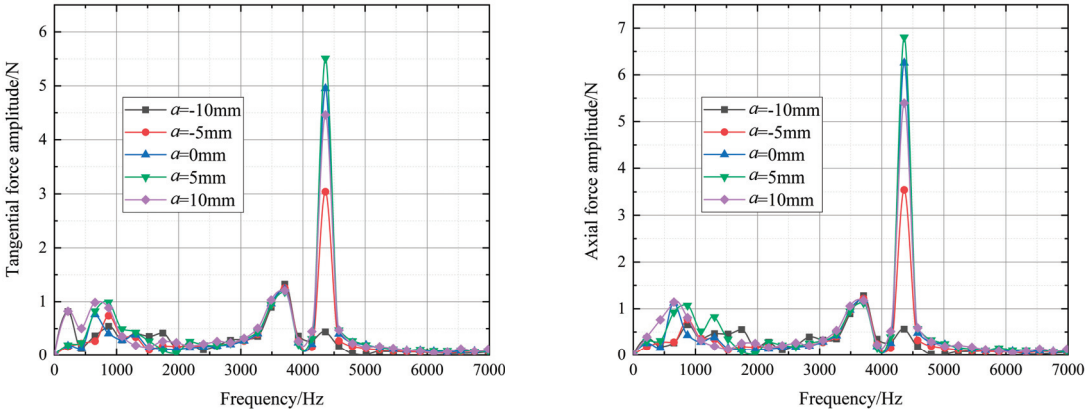

Figure 10. Frequency domain distribution of aerodynamic exciting force under design conditions. (**a**) Tangential aerodynamic exciting force; (**b**) Axial aerodynamic exciting force.

Table 4. Exciting force under design conditions.

Bending Coefficient *a*/mm	**−10**	**−5**	**0**	**5**	**10**
tangential exciting force mean value/N	131.2	132.8	131.9	131.4	132.2
axial exciting force mean value/N	181.1	182.3	182.2	181.6	180.7
tangential exciting force amplitude value/N	0.448	3.033	4.882	5.609	4.460
axial exciting force amplitude value/N	0.578	3.722	6.013	6.876	5.423

Since the time–domain distribution of the air flow exciting force has obvious periodicity, the time when a single moving vane sweeps through a guide vane channel is taken as a period, and four times are selected in each period to analyze the flow field characteristics. The time selection method is shown in Figure 11a, where 0.25 T is the time when the exciting force is the maximum and 0.75 T is the time when the aerodynamic exciting force is the minimum. In space, three section locations with different blade heights are selected for flow-field analysis. The selection method of blade–height section is shown in Figure 11b. For the "S"-type bowed guide vanes, 0.25 H and 0.75 H blade–height sections are the locations where the guide vane deviates most from the original model.

Figure 12 shows the Mach number distribution of different positions at different times of the model with a guide vane bending coefficient $a = 0$ mm under the design condition. The moving vane with a black outline is the moving vane monitored in the unsteady aerodynamic calculation. The fluid forms a boundary layer on the guide vane surface. When the fluid flows out of the guide vane passage, the boundary layers on both sides fall off and converge at the trailing edge, forming a vortex zone with low velocity behind. The velocity of the mainstream near the middle of the guide vane channel is high, which results in uneven velocity distribution at the guide vanes outlet. The moving vanes will be alternately impacted by the high-speed fluid in the mainstream area and the low-speed fluid in the vortex area, so they will be subject to the periodic unsteady aerodynamic exciting force.

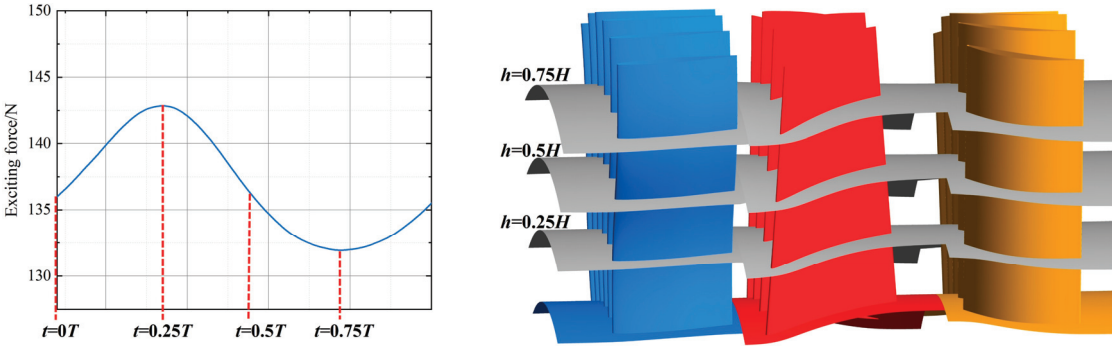

(**a**) (**b**)

Figure 11. Selection of location and time of unsteady flow field. (**a**) Time selection; (**b**) Blade–height location selection. The blue parts show the guide vanes, the red parts show the moving vanes, and the yellow parts show the stator vanes.

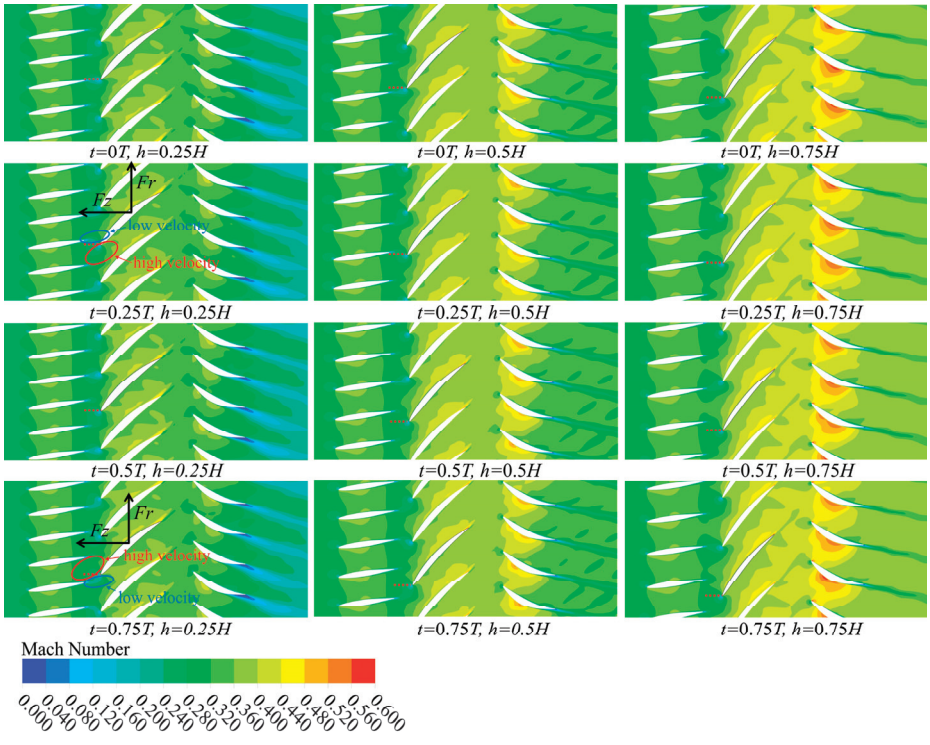

Figure 12. Mach number distribution of the a = 0 mm model under design conditions.

At the position of h = 0.25 H, the overall Mach number changes little from the inlet to the outlet of the guide vane. In the moving vane passage, the Mach number increases significantly. The Mach number near the pressure surface is relatively low while the Mach number near the suction surface is high. The maximum Mach number at the blade height of h = 0.25 H appears near the suction surface trailing edge. After the fluid flows through the stator vane passage, the Mach number gradually decreases along the flow direction,

and a vortex zone with a lower flow velocity is formed behind the stator vanes trailing edge. The Mach number at the stator outlet is also relatively low, even lower than that at the guide vane inlet.

At the h = 0.5 H position, the flow field distribution in the guide vane and moving vane passage is similar to that at the position of h = 0.25 H, but the maximum Mach number appears at the stator vanes suction surface. The Mach number at the stator outlet is lower than that in the moving vane passage, but slightly higher than that at the guide vane inlet. At the h = 0.75 H position, the Mach number in the stator passage is further increased, a large area of the high Mach number appears on the pressure stator surface side, and the Mach number at the stator outlet is also significantly increased compared with that at the inlet of the guide vane. In summary, the Mach number tends to increase with the increase of the blade height. The increase at the downstream position is more obvious.

The red dotted line marks the relative position of the moving vane leading edge and the guide vane. For the a = 0 mm model, although the guide vane is straight, the moving vane is designed to be twisted, so the relative position at different blade heights is slightly different. At t = 0.25 T, the moving vane leading edge is roughly at the position just passing the guide vane trailing edge, although relative positions of different blade heights are slightly different. We analyze the influence of the guide vane wake on the exciting force of the moving vane at this time. If there is no guide vane in this compressor stage, the moving vane incoming flow is uniform along the tangential direction. The flow force acting on the moving vane should be constant. The direction of the force is indicated by the black arrows in the figure. When the guide vane exists, the moving vane incoming flow is uneven. At the time t = 0.25 T, the low-speed fluid from the guide vane wake impacts the suction surface of the moving vane as shown in the blue circle, while the high-speed fluid from the main flow area of the guide vane impacts the pressure surface of the moving vane as shown in the red circle. Since the higher the speed, the higher the momentum, so the fluid force on both sides of the moving vane is different, and the fluid force on the pressure surface is higher than the suction surface. Since the direction of force caused by the uneven incoming flow is consistent with the direction of the aerodynamic force originally received by the moving vane, the aerodynamic force received by the moving vane reaches the maximum value at t = 0.25 T.

At the time t = 0.5 T, the moving vane leading edge rotates to the middle position of the guide vane channel, and the tangential force and axial force decrease. At time t = 0.75 T, with the rotation of the moving vane, the moving vane leading edge is close to the wake area of the next guide vane. The low-speed fluid in the guide vane wake area impacts the pressure surface of the moving vane, and the high-speed fluid in the main flow area of the guide vane impacts the suction surface. The fluid force on the suction surface is higher than that on the pressure surface. Since the direction of the force caused by the uneven incoming flow is opposite to the direction of the aerodynamic force originally received by the moving vane, the aerodynamic force received by the moving vane reaches the minimum value at t = 0.75 T.

Since the aerodynamic exciting force amplitude of the a = 5 mm model is the largest, the unsteady flow field distribution of the a = 5 mm model is analyzed in detail. Figure 13 shows the Mach number distribution of different positions at different times of the model with a guide vane bending coefficient a = 5 mm under the design condition. The overall distribution of the Mach number is basically consistent with that of the a = 0 mm model. The Mach number tends to increase with the increase in blade height. The increase at the downstream position is more obvious. This shows that the a = 5 mm model will not have too much deviation from the a = 0 mm model in overall aerodynamic parameters.

The red dotted line marks the relative position of the moving vane leading edge and the guide vane. It can be seen that, at different blade heights, the relative position of the moving vane leading edge and the guide vane is almost the same. This results in that, at the same time, the influence of uneven flow field on the moving vane is almost the same at different blade heights.

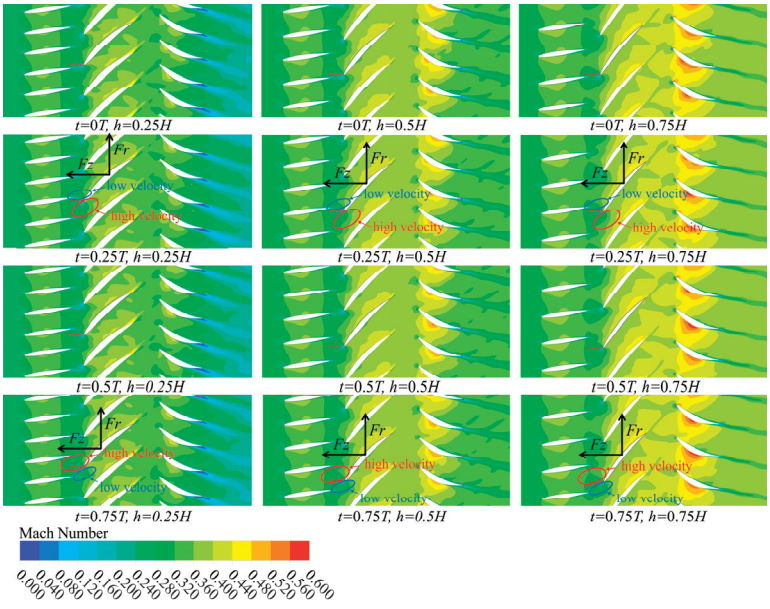

Figure 13. Mach number distribution of the a = 5 mm model under design conditions.

At t = 0.25 T, the moving vane leading edge is roughly at the position just passing the guide vane trailing edge. The low-speed fluid from the guide vane wake impacts the suction surface of the moving vane as shown in the blue circle, while the high-speed fluid from the main flow area of the guide vane impacts the pressure surface of the moving vane as shown in the red circle. The fluid force on the pressure surface is higher than that on the suction surface. The direction of the force caused by the uneven incoming flow is consistent with the direction of the aerodynamic force originally received by the moving vane. Moreover, at different blade heights, the effect of increasing aerodynamic force is almost the same, which further increases the aerodynamic force.

At t = 0.75 T, the moving vane leading edge is roughly close to the trailing edge of the other guide vane. A low-speed fluid from the guide vane wake impacts the pressure surface of the moving vane as shown in the blue circle, while the high-speed fluid from the main flow area of the guide vane impacts the suction surface of the moving vane as shown in the red circle. The fluid force on the suction surface is higher than the pressure surface. The direction of the force caused by the uneven incoming flow is opposite to the direction of the aerodynamic force originally received by the moving vane. Furthermore, at different blade heights, the effect of reducing the aerodynamic force is almost the same, which further reduces the aerodynamic force at this time. Therefore, the a = 5 mm model will increase the aerodynamic exciting force amplitude on the moving vane.

Since the aerodynamic exciting force amplitude of the $a = -10$ mm model is minimal, the unsteady flow field distribution of the $a = -10$ mm model is analyzed in detail. Figure 14 shows the Mach number distribution of different positions at different times of the model with a guide vane bending coefficient $a = -10$ mm under design conditions. The overall distribution of the Mach number is basically consistent with that of the a = 0 mm model. This shows that the $a = -10$ mm model will also not have too much deviation from the a = 0 mm model in overall aerodynamic parameters.

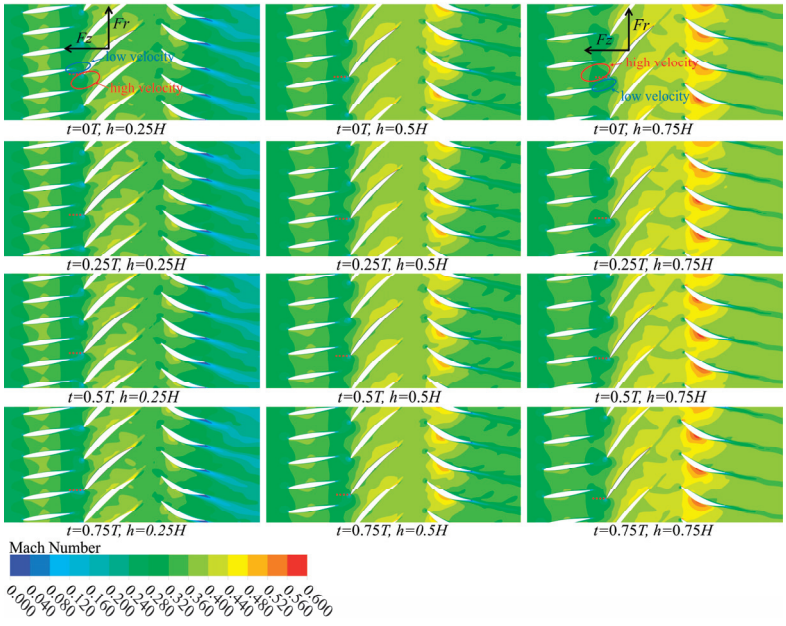

Figure 14. Mach number distribution of the $a = -10$ mm model under design conditions.

The red dotted line marks the relative position of the moving vane leading edge and the guide vane. It can be seen that, at different blade heights, the relative position difference between the moving vane leading edge and the guide vane is very large. Taking the time $t = 0$ T as an example, at $h = 0.25$ H, the moving vane leading edge is at the position just passing the trailing edge of the guide vane. A low-speed fluid from the guide vane wake impacts the suction surface of the moving vane, as shown in the blue circle, while the high-speed fluid from the main flow area of the guide vane impacts the pressure surface of the moving vane, as shown in the red circle. The fluid force on the pressure surface is higher than that on the suction surface. The direction of the force caused by uneven incoming flow is consistent with the direction of the aerodynamic force originally received by the moving vane. This increases the aerodynamic force on the moving vane.

At $t = 0.75$ T, the moving vane leading edge is roughly close to the trailing edge of the other guide vane. A low-speed fluid from the guide vane wake impacts the pressure surface of the moving vane, as shown in the blue circle, while the high-speed fluid from the main flow area of the guide vane impacts the suction surface of the moving vane, as shown in the red circle. The fluid force on the suction surface is higher than that on the pressure surface. The direction of the force caused by the uneven incoming flow is opposite to the direction of the aerodynamic force originally received by the moving vane. This will reduce the aerodynamic force on the moving vane. This means that, at different blade heights, the uneven flow field at the guide vane outlet may have the opposite effect on the force of the moving vane. Therefore, the amplitude of the exciting force on the moving vane of the $a = -10$ mm model is very small, and the time–domain distribution curve of the exciting force is not like other models showing regular sine-like curves.

3.2. Unsteady Aerodynamic Results under Near-Blockage Conditions

Table 5 shows the pressure ratio and total pressure of different guide vane bending coefficients under near-blockage conditions. The effect of the guide vane bending coefficient on the overall aerodynamic performance is consistent with that of the design condition under the condition of near-blockage. The pressure ratio decreases with the increase in

bending coefficients. When the bending coefficient a = 10 mm, the pressure ratio decreases by 0.22% compared with the prototype. The total efficiency of the "S"-type bowed models is reduced. The total efficiency of the structure with $a = -10$ mm decreases the most, which is 0.87%. In addition, the pressure ratio and total efficiency under the near-blockage condition are generally lower than that in the design condition.

Table 5. Overall aerodynamic performance under near-blockage conditions.

Bending Coefficient *a*/mm	**−10**	**−5**	**0**	**5**	**10**
pressure ratio	1.1651	1.1637	1.1636	1.1632	1.1610
total efficiency/%	80.87	81.59	81.74	81.72	81.21

Figure 15 shows the turbulent kinetic energy distribution of models with different bending coefficients at different axial positions of the moving vane under near-blockage conditions at the time t = 0 T. The left figure is the front 2 mm position of the moving vane, which is the inflow of the moving vane. The middle figure is the middle position of the moving vane passage. The right figure is the back 2 mm position of the moving vane, which is downstream of the moving vane.

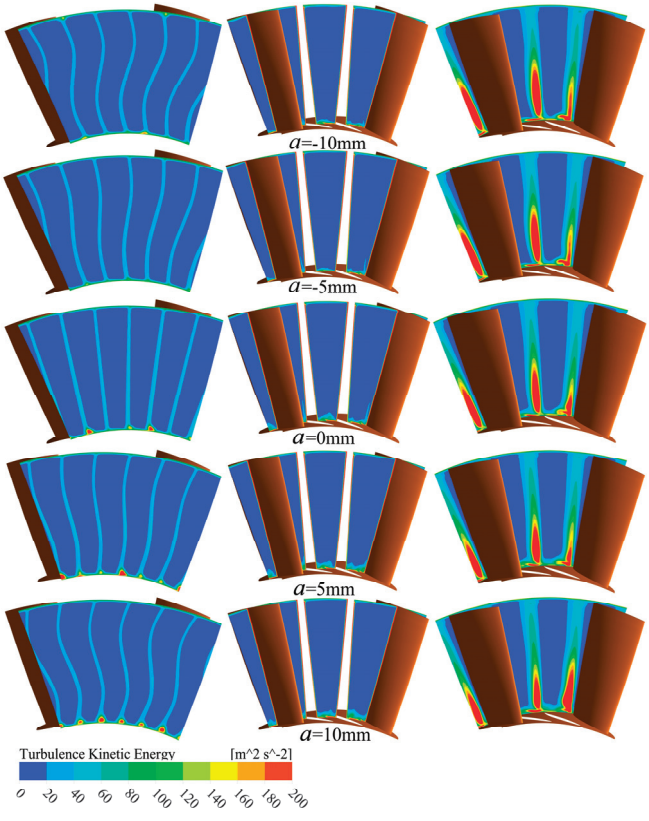

Figure 15. Turbulent kinetic energy distribution of different models under near-blockage condition.

The turbulent kinetic energy distribution of the near-blockage condition is similar to that of the design condition on the whole, but it is different locally. The difference is that the turbulent kinetic energy intensity in the guide vane wake region under the near-blockage condition is higher than that under design conditions. This is due to the

greater flow of near-blockage conditions. When the boundary layer on the guide vane surface is transformed into a turbulent boundary layer, the turbulence intensity is higher, which leads to higher turbulent kinetic energy of the guide vane wake.

In addition, the turbulent kinetic energy intensity downstream of the moving vane under near-blockage conditions is obviously lower than that under the design conditions. This is because for the 1.5-stage axial compressor, the pressurization process is mainly completed in the rotor passage. Therefore, the flow in the moving vane channel is inverse the pressure gradient flow, which will cause more serious flow separation on the moving vane surface, making the turbulent kinetic energy of the moving vane wake larger. The pressure ratio of the near-clogging condition is smaller, so the flow separation caused by the inverse pressure gradient is lighter.

Figures 16 and 17 show the tangential and axial exciting force–time domain distribution on the moving vane of different models under near-blockage conditions. In the $a = -5$ mm, $a = 0$ mm, $a = 5$ mm, and $a = 10$ mm models, the time–domain distribution is close to the form of the sine function. The time–domain distribution of the aerodynamic exciting force of the $a = -10$ mm model is very different from other models.

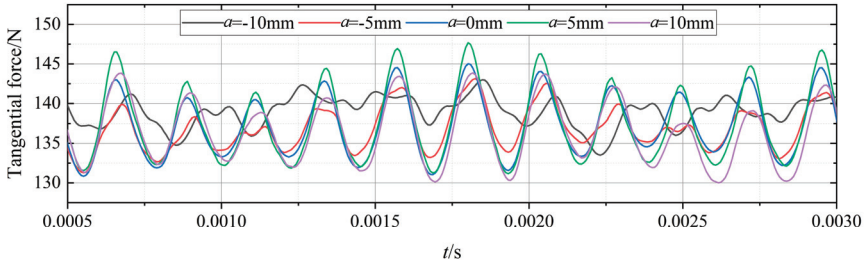

Figure 16. Tangential force–time domain distribution under near-blockage conditions.

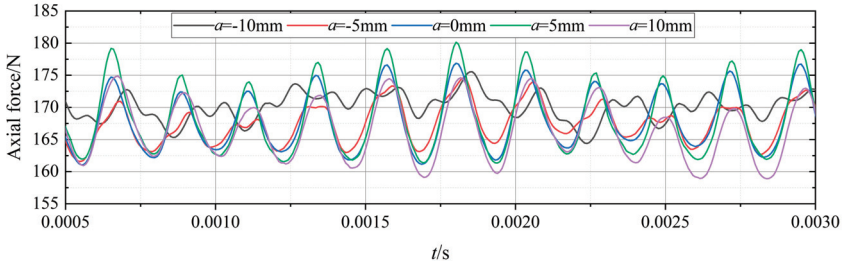

Figure 17. Axial force–time domain distribution under near-blockage conditions.

The time–domain distribution of the air flow exciting force under near-blockage conditions is analyzed using a fast Fourier transform, and the spectrum distribution is obtained as shown in Figure 18. The amplitude of the $a = -10$ mm model is much lower than that of other models.

Table 6 shows the time mean value and the amplitude value at the first-order blade-passing frequency of the aerodynamic exciting force with different bending coefficients. Compared with the design condition, the mean value of the tangential force increased slightly, the mean value of the axial force decreased, and the amplitude of the exciting force under each model increased compared with the design condition. It can be seen that, compared with the $a = 0$ mm model, the aerodynamic exciting force amplitude of the $a = 5$ mm model increases, in which the tangential exciting force amplitude increases by 19.09% and the amplitude of the axial exciting force increases by 17.19%. The aerodynamic exciting force amplitudes of the other models decreased, of which the $a = -10$ mm model decreased the most, the tangential exciting force amplitude decreased by 85.84%, and the axial exciting force amplitude decreased by 86.58%.

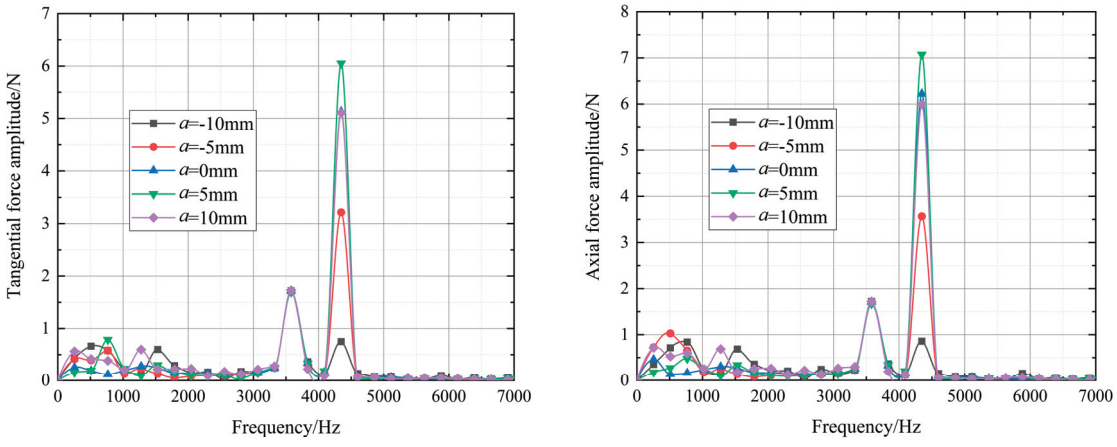

Figure 18. Frequency domain distribution of the aerodynamic exciting force under near-blockage conditions. (**a**) Tangential aerodynamic exciting force; (**b**) Axial aerodynamic exciting force.

Table 6. Exciting force under near-blockage conditions.

Bending Coefficient *a*/mm	**−10**	**−5**	**0**	**5**	**10**
tangential exciting force mean value/N	138.2	136.1	137.3	137.9	136.1
axial exciting force mean value/N	169.7	167.2	168.3	168.7	166.6
tangential exciting force amplitude value/N	0.719	3.114	5.081	6.051	5.223
axial exciting force amplitude value/N	0.823	3.641	6.133	7.184	6.010

Figure 19 shows the Mach number distribution for the a = 0 mm model under the near-blockage conditions. The overall Mach number of the near blocking condition is higher than that of the design condition. At the position of h = 0.25 H, the Mach number of the stator outlet is almost the same as the inlet Mach number of the guide vane in the near-blockage condition, which is different from the design condition.

In addition, at the position of h = 0.75 H, the Mach number in the stator passage is not much higher than that in the guide vane and moving vane passage. The Mach number difference of different blade heights is reduced in the near-blockage condition compared to the design condition. At the time t = 0.25 T, the exciting force on the moving vane is the largest, and the leading edge of the moving vane is at the position just passing the guide vane trailing edge. At the time t = 0.75 T, the exciting force on the moving vane is the smallest, and the leading edge of the moving vane is at the position near the trailing edge of the next guide vane. The relative position of the moving vane and guide vane is consistent with that under the design condition.

Under the near-blockage condition, the aerodynamic exciting force amplitude of the a = 5 mm model is the highest and the aerodynamic exciting force amplitude of the a = −10 mm model is the lowest. Figures 20 and 21 show the Mach number distributions of a = 5 mm and a = −10 mm under near-blocking conditions. The Mach number distribution of different models is not much different. It shows that the "S"-type bowed guide vane will not have a great impact on the overall aerodynamic performance under near-blockage conditions. The reason for the increase and decrease of the aerodynamic exciting force amplitude is the same as that of the design condition, which is determined by the relative position of the moving vane and the guide vane of different blade heights. The reason for the change of the aerodynamic exciting force amplitude is the same as that of the design

condition, which is determined by the relative position of the moving vane and the guide vane at different blade heights.

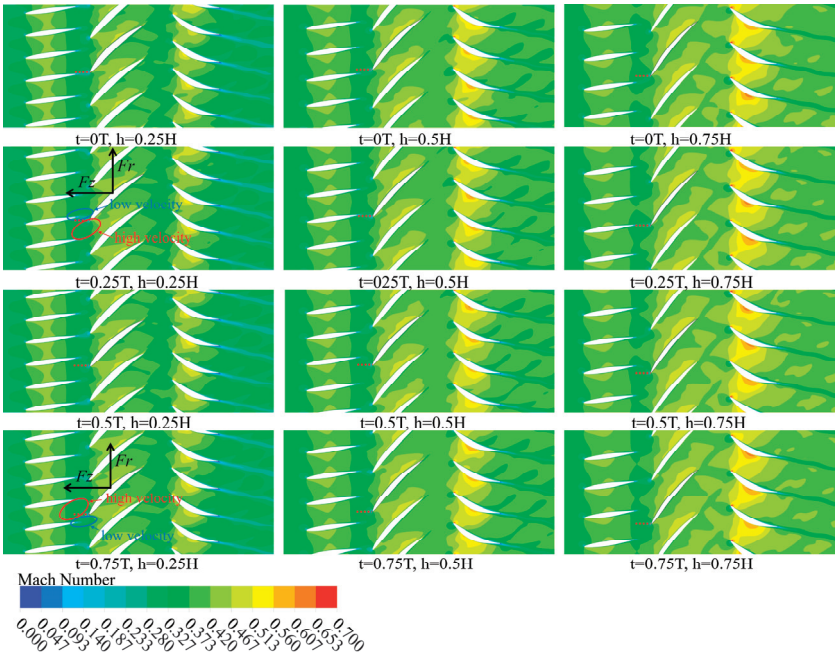

Figure 19. Mach number distribution of the a = 0 mm model under near-blockage conditions.

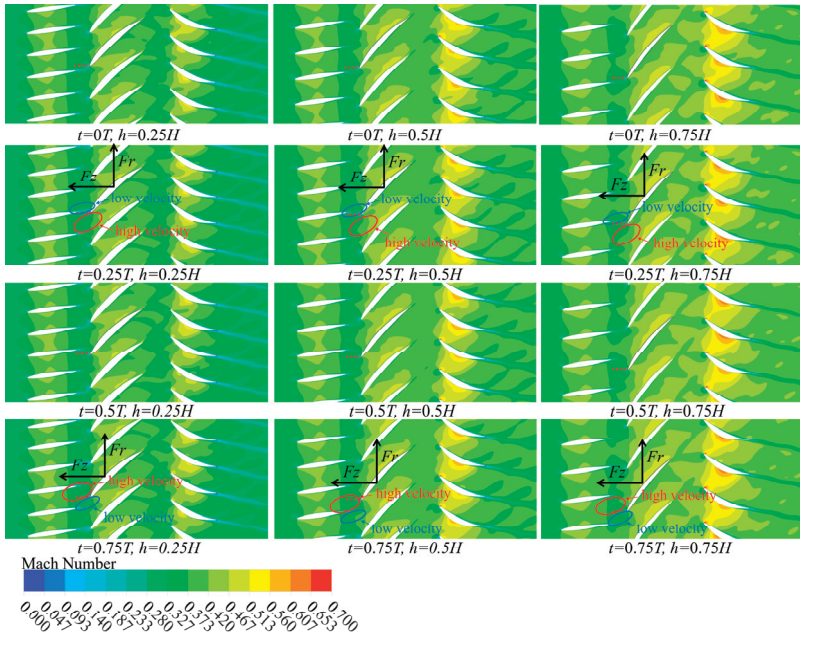

Figure 20. Mach number distribution of the a = 5 mm model under near-blockage conditions.

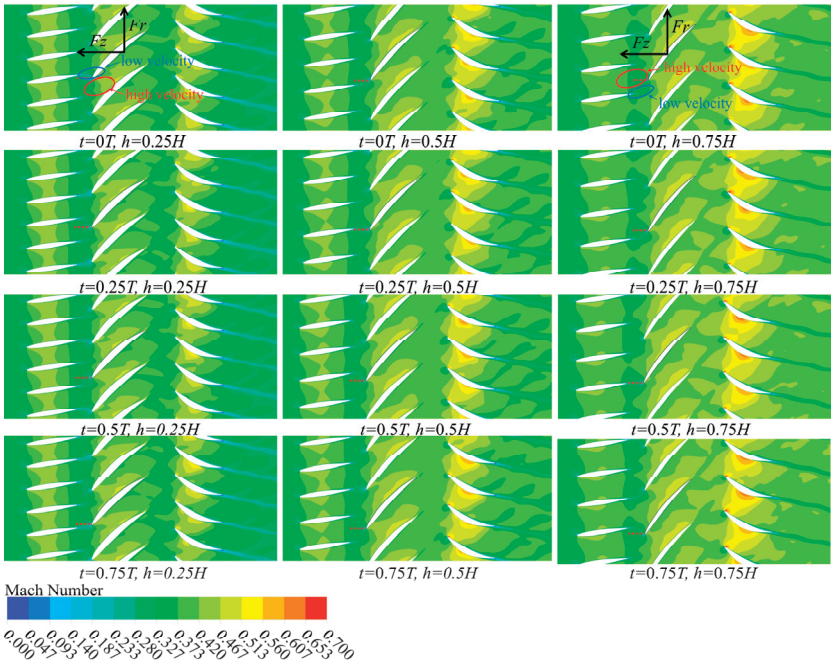

Figure 21. Mach number distribution of the $a = -10$ mm model under near-blockage conditions.

4. Conclusions

In this study, an "S"-type bowed guide vane was designed, and a 1.5-stage axial compressor model was established. For five guide vane models with different bending coefficients, an unsteady numerical simulation was carried out under the design condition and the near-blockage condition. The influence of the "S"-type bowed guide vane on the overall aerodynamic performance, unsteady flow field distribution, and air flow exciting force is analyzed. The main conclusions are as follows:

(1) The pressure ratio decreases with the increase in the guide vane bending coefficient. Compared with the original straight vane, the pressure ratio under the design condition and the near-blockage condition decreases by 0.18% and 0.22%, respectively, in the $a = 10$ mm models. The total efficiency of the model with the "S"-type bowed guide vane is reduced. The total efficiency of the $a = -10$ mm model decreases the most, which is 0.57% and 0.87% in the design condition and near-blockage condition, respectively.

(2) The turbulence kinetic energy near the hub of the guide vane will increase with the increase in the absolute value of the bending coefficient. The turbulence kinetic energy of the guide vane wake under the near-blockage condition is higher than that under the design condition due to the higher velocity. However, in the moving vane passage and the wake of the moving vane, due to the low-pressure ratio under the near-blockage condition, the flow separation caused by the inverse pressure gradient is relatively small.

(3) The $a = 5$ mm model will increase the aerodynamic exciting force amplitude on the moving vane. The $a = -10$ mm model can reduce the tangential and axial aerodynamic exciting force amplitudes under the first-order blade-passing frequency of the moving vane by 90.82% and 90.39% under the design condition, respectively. Under the near-blockage condition, the reduced values are 85.84% and 86.58%, respectively. This is because, for the $a = -10$ mm model, at different blade heights, the relative position difference between the moving vane leading edge and the guide vane is very large.

This means the uneven flow field at the guide vane outlet may have the opposite effect on the force of the moving vane at different blade heights.

This shows that the "S"-type bowed guide vanes can greatly reduce the aerodynamic exciting force amplitude under the premise of reducing aerodynamic efficiency, which provides an idea for compressor design under some conditions with extremely high requirements for vibration safety. Subsequently, we can consider the design of the moving vane near the end wall to improve the efficiency of the compressor with the "S"-type bowed guide vanes.

Author Contributions: Each author has contributed to different work in this study. Y.L. (Yupeng Liu) is mainly responsible for data curation, methodology and writing—original draft. The validation and visualization were completed by Y.L. (Yunzhu Li); G.L., Y.X. and D.Z. undertook the task of writing—review and editing. All authors have read and agreed to the published version of the manuscript.

Funding: This research was funded by the National Science and Technology Major Project grant number [J2019-IV-0022-0090].

Institutional Review Board Statement: Not applicable.

Informed Consent Statement: Not applicable.

Data Availability Statement: Data sharing is not applicable to this article.

Acknowledgments: All the authors in the paper express great gratitude for the financial support by the National Science and Technology Major Project (J2019-IV-0022-0090).

Conflicts of Interest: The authors declare that they have no known competing financial interest or personal relationships that could have appeared to influence the work reported in this paper.

References

1. Matsunuma, T. Unsteady flow field of an axial-flow turbine rotor at a low Reynolds number. *J. Turbomach.* **2007**, *129*, 360–371. [CrossRef]
2. Maroldt, N.; Amer, M.; Seume, J.R. Forced Response Due to Vane Stagger Angle Variation in an Axial Compressor. *J. Turbomach.* **2022**, *144*, 081011. [CrossRef]
3. Gallus, H.E.; Lambertz, J.; Wallmann, T. Blade-Row Interaction in an Axial-Flow Subsonic Compressor Stage. *J. Eng. Power* **1980**, *102*, 169–177. [CrossRef]
4. Gallus, H.E.; Grollius, H.; Lambertz, J. The Influence of Blade Number Ratio and Blade Row Spacing on Axial-Flow Compressor Stator Blade Dynamic Load and Stage Sound Pressure Level. *J. Eng. Power* **1982**, *104*, 633–641. [CrossRef]
5. Gorrell, S.E.; Okiishi, T.H.; Copenhaver, W.W. Stator-Rotor Interactions in a Transonic Compressor—Part 1: Effect of Blade-Row Spacing on Performance. *J. Turbomach.* **2003**, *125*, 328–335. [CrossRef]
6. Douglas, M.B.; Sanford, F. Axial Compressor Blade-to-Blade Unsteady Aerodynamic Variability. *J. Propuls. Power* **2015**, *19*, 242–249.
7. Burkhardt, O.; Nitsche, W.; Goller, M.; Swoboda, M.; Guemmer, V. Rotor-stator interaction in a highly-loaded, single-stage, low-speed axial compressor: Unsteady measurements in the rotor relative frame. In *Unsteady Aerodynamics, Aeroacoustics and Aeroelasticity of Turbomachines*; Hall, K.C., Kielb, R.E., Thomas, J.P., Eds.; Springer: Dordrecht, The Netherlands; Berlin/Heidelberg, Germany, 2006; pp. 603–614.
8. Smith, N.R.; Key, N.L. Unsteady vane boundary layer response to rotor–rotor interactions in a multistage compressor. *J. Propuls. Power* **2014**, *30*, 416–425. [CrossRef]
9. Lefcort, M.D. An Investigation into Unsteady Blade Forces in Turbomachines. *J. Eng. Power* **1965**, *87*, 345–354. [CrossRef]
10. Daigji, H.; Shirahara, H. A finite element solution of cascade flow in a large-distorted periodic flow. *Bull. JSME* **1978**, *21*, 824–831. [CrossRef]
11. Mailach, R.; Müller, L.; Vogeler, K. Rotor-stator interactions in a four-stage low-speed axial compressor—Part II: Unsteady aerodynamic forces of rotor and stator blades. *J. Turbomach.* **2004**, *126*, 519–526. [CrossRef]
12. Smith, N.R.; Key, N.L. Blade-row interaction effects on unsteady stator loading in an embedded compressor stage. *J. Propuls. Power* **2017**, *33*, 248–255. [CrossRef]
13. Monk, D.J.; Key, N.L.; Fulayter, R.D. Reduction of aerodynamic forcing through introduction of stator asymmetry in axial compressors. *J. Propuls. Power* **2016**, *32*, 134–141. [CrossRef]
14. Wenjie, W.; Peter, J.T. Acoustic Improvement of Stator-Rotor Interactionwith Nonuniform Trailing Edge Blowing. *Appl. Sci.* **2018**, *8*, 994–1004.
15. Milidonis, K.; Semlitsch, B.; Hynes, T. Effect of Clocking on Compressor Noise Generation. *AIAA J.* **2018**, *56*, 4225–4231. [CrossRef]

16. Weir, D.S.; Podboy, G.G. Flow Measurements and Multiple Pure Tone Noise from a Forward Swept Fan. In Proceedings of the 43rd AIAA Aerospace Sciences Meeting and Exhibit, Reno, NV, USA, 10–13 January 2005.
17. Bamberger, K.; Carolus, T. Optimization of axial fans with highly swept blades with respect to losses and noise reduction. *Noise Control. Eng. J.* **2012**, *60*, 716–725. [CrossRef]
18. Bohn, D.E.; Ren, J.; Tümmers, C.; Sell, M. Unsteady 3D-numerical investigation of the influence of the blading design on the stator-rotor interaction in a 2-stage turbine. In Proceedings of the ASME Turbo Expo 2005: Power for Land, Sea, and Air, Reno, NV, USA, 6–9 June 2005.
19. Laborderie, J.D.; Blandeau, V.; Node-Langlois, T.; Moreau, S. Extension of a Fan Tonal Noise Cascade Model for Camber Effects. *AIAA J.* **2015**, *53*, 863–876. [CrossRef]
20. Ling, J.; Du, X.; Wang, S.; Wang, Z. Relationship between optimum curved blade generate line and cascade parameters in subsonic axial compressor. In Proceedings of the ASME Turbo Expo 2014: Turbine Technical Conference and Exposition, Düsseldorf, Germany, 16–20 June 2014.
21. Rajesh, E.; Roy, B. Numerical study of variable camber inlet guide vane on low speed axial compressor. In Proceedings of the ASME 2015 Gas Turbine India Conference, Hyderabad, India, 2–3 December 2015.
22. Wadia, A.R.; Szucs, P.N.; Gundy-Burlet, K.L. Design and Testing of Swept and Leaned Outlet Guide Vanes to Reduce Stator–Strut–Splitter Aerodynamic Flow Interactions. *J. Turbomach.* **1999**, *121*, 416–427. [CrossRef]
23. Keke, G.; Yonghui, X.; Di, Z. Effects of stator blade camber and surface viscosity on unsteady flow in axial turbine. *Appl. Therm. Eng.* **2017**, *118*, 748–764.
24. Chen, X.; Chu, W.; Wang, G.; Yan, S.; Shen, Z.; Guo, Z. Effect of span range of variable-camber inlet guide vane in an axial compressor. *Aerosp. Sci. Technol.* **2021**, *116*, 106–136. [CrossRef]
25. Luo, L.; Wang, C.; Wang, L.; Sundén, B.; Wang, S. Endwall heat transfer and aerodynamic performance of bowed outlet guide vanes (OGVs) with on- and off-design conditions. *Numer. Heat Transf. Part A Appl.* **2016**, *69*, 352–368. [CrossRef]
26. Niu, X.; Wang, L.; Li, D.; Du, Q. Reduction of Turbine Blade Unsteady Forces by Shape Modification of Vanes for Industrial Gas Turbines. In Proceedings of the ASME Turbo Expo 2016: Turbomachinery Technical Conference and Exposition, Seoul, South Korea, 13–17 June 2016.
27. Liu, H.J.; Ouyang, H.; Tian, J.; Wu, Y.D.; Du, Z.H. Aeroacoustics benefit of stator lean effect for rotor-stator interactions. *Noise Control. Engr. J.* **2013**, *61*, 389–399. [CrossRef]
28. Zhu, Y.; Luo, J.; Liu, F. Influence of blade lean together with blade clocking on the overall aerodynamic performance of a multi-stage turbine. *Aerosp. Sci. Technol.* **2018**, *80*, 329–336.
29. Hwang, S.; Son, C.; Seo, D.; Rhee, D.H.; Cha, B. Comparative study on steady and unsteady conjugate heat transfer analysis of a high pressure turbine blade. *Appl. Therm. Eng.* **2016**, *99*, 765–775. [CrossRef]
30. Cornelius, C.; Biesinger, T.; Galpin, P.; Braune, A. Experimental and computational analysis of a multistage axial compressor including stall prediction by steady and transient CFD methods. *J. Turbomach.* **2014**, *136*, 061013. [CrossRef]
31. Strazisar, A.J.; Powell, J.A. Laser Anemometer Measurements in a Transonic Axial Flow Compressor Rotor. *J. Eng. Gas Turbines Power* **1981**, *103*, 430–437. [CrossRef]
32. Zhu, G.; Liu, X.; Yang, B.; Song, M. A Study of influences of inlet total pressure distortions on clearance flow in an axial compressor. *J. Eng. Gas Turbines Power* **2021**, *143*, 101010. [CrossRef]
33. Song, M.R.; Yang, B.; Dong, G.M.; Liu, X.L.; Wang, J.Q.; Xie, H.; Lu, Z.H. Research on Accuracy of Flowing Field Based on Numerical Simulation for Tonal Noise Prediction in Axial Compressor. In Proceedings of the ASME Turbo Expo 2018: Turbomachinery Technical Conference and Exposition, Oslo, Norway, 11–15 June 2018.
34. Yang, B.; Gu, C.G. The Effects of Radially Distorted Incident Flow on Performance of Axial-Flow Fans with Forward-Skewed Blades. *J. Turbomach.* **2013**, *135*, 011039. [CrossRef]

fluids

MDPI

Article

Bifurcation Analysis and Propagation Conditions of Free-Surface Waves in Incompressible Viscous Fluids of Finite Depth

Arash Ghahraman * and Gyula Bene

Department of Theoretical Physics, Institute of Physics, Eötvös Loránd University, Pázmány Péter Sétány 1/A, 1117 Budapest, Hungary; bene.gyula@ttk.elte.hu

* Correspondence: ghahraman.arash@ttk.elte.hu

Abstract: Viscous linear surface waves are studied at arbitrary wavelength, layer thickness, viscosity, and surface tension. We find that in shallow enough fluids no surface waves can propagate. This layer thickness is determined for some fluids, water, glycerin, and mercury. Even in any thicker fluid layers, propagation of very short and very long waves is forbidden. When wave propagation is possible, only a single propagating mode exists for a given horizontal wave number. In contrast, there are two types of non-propagating modes. One kind of them exists at all wavelength and material parameters, and there are infinitely many such modes for a given wave number, distinguished by their decay rates. The other kind of non-propagating mode that is less attenuated may appear in zero, one, or two specimens. We notice the presence of two length scales as material parameters, one related to viscosity and the other to surface tension. We consider possible modes for a given material on the parameter plane layer thickness versus wave number and discuss bifurcations among different mode types. Motion of surface particles and time evolution of surface elevation is also studied at various parameters in glycerin, and a great variety of behaviour is found, including counterclockwise surface particle motion and negative group velocity in wave propagation.

Keywords: shallow water; viscose fluid; surface waves; bifurcation analysis

PACS: 47.10.-g; 47.11.-j

Citation: Ghahraman, A.; Bene, G. Bifurcation Analysis and Propagation Conditions of Free-Surface Waves in Incompressible Viscous Fluids of Finite Depth. *Fluids* **2023**, *8*, 173. https://doi.org/10.3390/fluids8060173

Academic Editors: D. Andrew S. Rees and Vasily Novozhilov

Received: 21 March 2023
Revised: 23 May 2023
Accepted: 25 May 2023
Published: 31 May 2023

1. Introduction

Although capillary gravity surface waves have been studied for a long time, they are still a fascinating and interesting subject [1–15]. The dispersion of linear and nonlinear waves, wave damping in deep water owing to viscosity, and weakly nonlinear waves in shallow water are classic problems that have long been studied [16]. Comprehending the dissipation and dynamics of internal waves occurring at the boundary between viscous fluids holds significant importance. Surfactant, pollutant, and fluid film impacts at interfaces are now hot subjects [17–35]. Current research on surface waves remains ongoing, with a predominant emphasis on multi-layer models [18], damping rate [2,5,7,17–20,36,37], and experimental verifications [17,20]. The majority of research endeavours in this particular domain are founded upon the utilization of viscoelastic fluids [17,21]. Hence, the constancy of surface tension is no longer maintained. The Marangoni number has been identified as a significant factor in the determination of a fluid's surface behaviour, owing to its ability to characterize the fluid's tendency to flow as a result of surface tension gradients [20,22,23]. The aforementioned phenomenon exhibits potential practical implications in the field of hydrodynamics, particularly in microfluidics and the study of nanoscopic capillary waves. This assertion is supported by various scholarly sources [24–28]. Whilst recent theoretical and experimental investigations [29,30] have primarily focused on fluid in deep layers,

it is important to note that the structure and velocity of surface waves are significantly impacted by finite depth.

It is noteworthy that the uncomplicated scenario of linear surface waves in a viscous fluid possessing a clean surface and finite depth has not yet been fully explored. Only few works have been identified that address this problem, as documented in the references [33,36,38,39]. References [36,38] exclusively examined the scenario where surface tension was absent. The reference [39] incorporated surface tension, although the dispersion relation it obtained did not align with those presented in references [36,38] under the condition of zero surface tension. The appendix of reference [33] examines linear surface waves in finite depth, neglecting surface tension, and providing an approximation that is valid only under weakly damped conditions. Additionally, it should be noted that the dispersion relations derived in the works [36,38] exhibit dissimilarities.

The current investigation involves the derivation of the dispersion relation for surface waves that are both viscous and gravity-capillary in nature. This is achieved for fluid depths that are arbitrary. The outcome of our study in the limit of zero surface tension concurs with the dispersion relation derived in Hunt's work [38]. As far as current understanding allows, the present work contains the first correct dispersion relation for viscous surface waves, which also incorporates the influence of surface tension and finite fluid depth. The present study demonstrates concurrence with prior research [17,21] in the context of the deep water regime. Upon examining the implications of the dispersion relation, it becomes apparent that a multitude of over-damped modes exist across all parameter values in an infinite fashion. There exist two distinct types of over-damped modes, characterized by either monotonic or oscillatory behaviour along the vertical axis. The latter category is a perpetual presence (in actuality, there are an infinite number of such modes at a specified wave number), whereas there may be zero, one, or two modes of the former category at a given wave number.

It has been observed that a single propagating mode can exist in a specific direction. This mode experiences a bifurcation at both long and short wavelengths, resulting in the emergence of two over-damped modes. The parameter space wave number versus layer thickness (we actually use the parameter p, which is related to layer thickness, cf. Equation (23)) can be thus partitioned according to the presence or absence of propagating modes and types and number of over-damped modes. The present study includes a discussion, primarily through numerical demonstration, of the bifurcations that occur at the boundaries of the distinct parameter space regions.

This paper is organized in the subsequent fashion: In Section 2, a derivation and discussion of the dispersion relation is presented, which serves as the basis for our subsequent investigations. Section 3 of the paper investigates various modes, their dependence on parameters, and bifurcations. Section 4 is dedicated to analysing the minimum layer thickness required for wave propagation. Section 5 delves into the examination of particle motion at the surface, and Section 6 scrutinizes the temporal progression of surface elevations. Section 7 of the paper offers a comprehensive analysis of the findings.

2. Dispersion Relation

The propagation of surface waves in deep water has been studied by several works, with results that generally agree with each other [17,21,24,40,41]. They are based on linearization of the Navier–Stokes equation. Here, we also consider linear surface waves on a viscous, incompressible fluid layer of finite, constant depth h. The coordinates x and y are horizontal, z is vertical. The origin lies at the undisturbed fluid surface. Suppose that the flow corresponding to the surface wave does not depend on y.

The linearized Navier–Stokes equation may be written as

$$\frac{\partial \mathbf{V}}{\partial t} - \nu \triangle \mathbf{V} = \nabla \left(-\frac{P}{\rho} - gz \right). \tag{1}$$

where g indicates acceleration due to gravity, $\mathbf{V}$ is velocity vector, P is pressure, ν is viscosity, and ρ is fluid density. Since the right hand side is a full gradient, we have

$$\frac{\partial}{\partial z}\left(\frac{\partial u}{\partial t} - \nu\triangle u\right) = \frac{\partial}{\partial x}\left(\frac{\partial w}{\partial t} - \nu\triangle w\right) . \tag{2}$$

Due to linearity, we may search for the horizontal u and vertical w velocity components in the following form:

$$u(x,z,t) = f'(z)e^{i(kx-\omega t)} \tag{3}$$

$$w(x,z,t) = -ikf(z)e^{i(kx-\omega t)} \tag{4}$$

here the prime denotes derivative with respect to the argument. Further, k is a real, positive wave number, while ω is in general complex frequency, its imaginary part describing the damping. The specified x and t dependence is due to translational symmetry in horizontal direction and time, respectively, while the specific form of z dependence is forced by the incompressibility condition $\nabla\cdot\mathbf{V} = 0$. Note that the stream function is given by $f\exp(i(kx-\omega t))$.

Putting Ansatz (3), (4) into Equation (2), we obtain

$$f'''' + \left(i\frac{\omega}{\nu} - 2k^2\right)f'' - \left(i\frac{\omega}{\nu} - k^2\right)k^2 f = 0 . \tag{5}$$

Equation (5) has exponential solutions $f = \exp(\kappa z)$. For the exponent κ we get

$$\kappa^4 + \left(i\frac{\omega}{\nu} - 2k^2\right)\kappa^2 - \left(i\frac{\omega}{\nu} - k^2\right)k^2 f = 0 . \tag{6}$$

The solutions are

$$\kappa_{1,2} = \pm k , \tag{7}$$

$$\kappa_{3,4} = \pm\sqrt{k^2 - i\frac{\omega}{\nu}} . \tag{8}$$

For brevity, we shall use the notation κ for $\kappa_3 = -\kappa_4$ and k for $\kappa_1 = -\kappa_2$. The general solution for f may be given as

$$f = a_1\cosh[k(z+h)] + a_2\sinh[k(z+h)] + b_1\cosh[\kappa(z+h)] + b_2\sinh[\kappa(z+h)] , \tag{9}$$

where a_1, a_2, b_1, b_2 are the integration constants and h stands for the fluid depth. Then boundary conditions at the bottom,

$$u(z=-h) = w(z=-h) = 0 , \tag{10}$$

imply

$$a_1 = A , \quad b_2 = B , \quad b_1 = -A , \quad a_2 = -\frac{\kappa}{k}B , \tag{11}$$

expressed in terms of the new constants A and B. Hence for f we get

$$f = A\cosh[k(z+h)] - \frac{\kappa}{k}B\sinh[k(z+h)] - A\cosh[\kappa(z+h)] + B\sinh[\kappa(z+h)] . \tag{12}$$

Upon integrating the x component of the Navier–Stokes equation with respect to x, we get the pressure as

$$P = P_o - \rho gz - \rho e^{i(kx-\omega t)}\left(-\frac{\omega}{k}f' - i\nu kf' + i\frac{\nu}{k}f'''\right) . \tag{13}$$

At the fluid surface we have zero boundary conditions, therefore (in linear approximation) we have

$$\frac{\partial u}{\partial z} + \frac{\partial w}{\partial x} = 0 \tag{14}$$

for the shear and

$$P - 2\rho\nu\frac{\partial w}{\partial z} = P_0 - \sigma\frac{\partial^2\eta}{\partial x^2} \tag{15}$$

for the pressure. Here $\eta = \eta(x,t)$ stands for the deviation of the fluid surface from equilibrium and σ is the surface tension.

Equation (14) implies

$$f'' + k^2 f = 0 \tag{16}$$

at $z = 0$, while Equation (15) implies

$$-g\eta + \frac{\sigma}{\rho}\frac{\partial^2\eta}{\partial x^2} - e^{i(kx-\omega t)}\left(-\frac{\omega}{k}f' - i\nu k f' + i\frac{\nu}{k}f'''\right) + 2i\nu k f' e^{i(kx-\omega t)} = 0\,. \tag{17}$$

In linear approximation, we have at the surface

$$\frac{\partial\eta}{\partial t} = w\,. \tag{18}$$

Note that on the right hand side we may set $z = 0$. Putting here the expression of w (i.e., Equation (4)) and combining the result with Equation (17), in terms of κ (cf. Equation (8)), we have

$$\left(1 + \frac{\sigma}{g\rho}k^2\right)k^2 f + \frac{\nu^2}{g}(\kappa^2 - k^2)(\kappa^2 + 2k^2)f' - \frac{\nu^2}{g}(\kappa^2 - k^2)f''' = 0\,. \tag{19}$$

Here, again, $z = 0$. By now inserting the solution (12) into Equations (16) and (19) we obtain a linear homogeneous system of equation for the quantities A and B. A non-trivial solution can be found only if the determinant of the 2×2 matrix formed out of the coefficients of A and B is zero. The resulting dispersion relation, expressed in terms of dimensionless quantities, sounds

$$\begin{aligned} &K(Q\sinh K\cosh Q - K\cosh K\sinh Q)(1 + sK^2) + p\left[-4K^2Q\left(K^2 + Q^2\right)\right. \\ &\left.+Q\left(Q^4 + 2K^2Q^2 + 5K^4\right)\cosh K\cosh Q - K\left(Q^4 + 6K^2Q^2 + K^4\right)\sinh K\sinh Q\right] = 0 \end{aligned} \tag{20}$$

Here

$$K = kh \tag{21}$$

$$Q = \kappa h \tag{22}$$

$$p = \frac{\nu^2}{gh^3} \tag{23}$$

$$s = \frac{\sigma}{\rho g h^2} \tag{24}$$

Given parameters p and s, and scaled wave number K, a solution Q of Equation (20) yields the angular frequency (cf. Equations (8) and (22))

$$\omega = -i\frac{\nu}{h^2}\left(K^2 - Q^2\right)\,. \tag{25}$$

For the ratio of the coefficients A and B we get (cf. Equations (12) and (16))

$$\frac{B}{A} = \frac{2K^2\cosh(K) - (K^2+Q^2)\cosh(Q)}{2QK\sinh(K) - (K^2+Q^2)\sinh(Q)} \,. \tag{26}$$

Let us compare dispersion relation (20) with those available in the literature. The dispersion relation (20) for $\sigma = 0$ coincides with the result of Hunt [38], albeit he used different notations. Meur [36] derived the dispersion relation

$$\begin{aligned} &4K^2Q(K^2+Q^2) + 4QK^3[Q\sinh(K)\sinh(Q) - K\sinh(K)\cosh(Q)] \\ &-(K^2+Q^2)^2[Q\cosh(K)\cosh(Q) - K\sinh(K)\sinh(Q)] \\ &-KRe^2[Q\sinh(K)\sinh(Q) - K\cosh(K)\sinh(Q)] = 0 \end{aligned} \tag{27}$$

for $\sigma = 0$. Here $Re = \frac{hc}{\nu}$ where $c = \sqrt{gh}$, hence, according to Equation (23),

$$p = \frac{1}{Re^2} \,. \tag{28}$$

Note that Re looks formally like a Reynolds number, but it has a quite different physical meaning. Reynolds number traditionally means the ratio of the nonlinear term to the viscous term in the Navier–Stokes equation. Now, there is no nonlinear term present. Further, in the definition of the present Re, the velocity c is not the fluid velocity but the propagation velocity of waves in shallow fluid.

Equation (27) is almost identical with (20), but there is a difference in the the bracket of $KRe^2[\ldots]$. The first term should be $Q\sinh(K)\cosh(Q)$. Sanochkin [39] also introduced a dispersion relation. All terms in [39] are the same as Equation (20) if $\cosh(a\sqrt{q})$ and $\sinh\left(\frac{a}{\sqrt{1+q}}\right)$ change to $\cosh(a\sqrt{1+q})$ and $\sinh(a\sqrt{1+q})$, respectively. Note that q in his notation represents $\frac{Q^2}{K^2} - 1$ and $a \equiv K$.

In the limit of $K \to \infty$, the dispersion relation (20) agrees with [21]. The author studied the dispersion relation in terms of dimensionless variables in three layers.

$$K\left(1 + sK^2\right) + p(Q-K)\left(Q^3 + Q^2K + 3K^2Q - K^3\right) = 0 \tag{29}$$

Parameters p and s may be expressed in terms of the viscous length scale and the capillary length scale, which is related to surface tension, respectively. These parameters characterize the physical mechanisms that govern the oscillatory motion of capillary waves.

$$\ell_\nu = \left(\frac{\nu^2}{g}\right)^{1/3} \tag{30}$$

$$\ell_\sigma = \left(\frac{\sigma}{\rho g}\right)^{1/2}, \tag{31}$$

namely,

$$p = \left(\frac{\ell_\nu}{h}\right)^3 \tag{32}$$

$$s = \left(\frac{\ell_\sigma}{h}\right)^2 . \tag{33}$$

It is obvious that the ratio

$$\mu = \frac{\ell_\sigma}{\ell_\nu} = \frac{s^{1/2}}{p^{1/3}} \tag{34}$$

is a material parameter (apart from g), and does not depend on the layer thickness. On the other hand, when parameter dependence is studied, often this is done by changing the layer thickness of a given material. In that case it is advisable to use parameters μ and p, while

$$s = \mu^2 p^{2/3} \,. \tag{35}$$

Rajan [21] also utilizes dimensionless variables in dispersion relation that involve the properties of the fluid and of the interface. We are interested in comparing wave-Reynolds σ_{Rajan} number with s and p

$$\sigma_{Rajan} = \frac{(1-R)+sK^2}{(1+R)pK^3} \tag{36}$$

where $R = \frac{\rho_{upper}}{\rho_{lower}}$. The density ratio R is restricted to take values less than or equal to unity due to the requirement of static stability. As $R \to 1$ in the fluid system, the effects of gravity tend to vanish [21]. In the case $R = 0$, Equation (36) reduces to the well-known form of free fluid surface if the Marangoni number is zero. Therefore, we have

$$\sigma_{Rajan} = \frac{1+sK^2}{pK^3} \tag{37}$$

In this study the Marangoni number P equals to zero, which represents zero interfacial elasticity and implies that the interface is clean.

Note that if Q is a solution of Equation (20), then so is $-Q$. On the other hand, this sign does not matter when calculating ω or f (cf. Equation (12)). Henceforth we assume that the real part of Q is positive, and thus $\tanh Q \to 1$ when $|Q| \to \infty$.

The dispersion Equation (20) is valid for waves in a general system of fluids with arbitrary density, viscosity, surface tension, and depth. Here we modify Equation (20) for small viscosity and large wavelength cases that are applicable to specific systems. We also obtain numerical solutions. To this end, Equation (20) was expanded as a 50-order polynomial and all roots were found. The non-physical roots arising from the expansion were eliminated by the requirements that ω satisfy the original equation. Our analyses reveal the presence of bifurcation in some physical solutions, which are discussed in Section 2.4.

2.1. Small Viscosity Case

In the small viscosity case, Equation (20) may be solved approximately. In that case $p \to 0$ and $|Q| \to \infty$. This implies that in leading order Equation (20) reduces to

$$K \tanh K \,(1+sK^2) + pQ_0^4 = 0 \,, \tag{38}$$

or

$$Q_0^2 = -i\sqrt{\frac{K \tanh K \,(1+sK^2)}{p}} \,. \tag{39}$$

Here the negative sign has been chosen in order to get a positive real part of angular frequency via Equation (25). Further, according to the convention mentioned above, we have

$$Q_0 = \frac{1-i}{\sqrt{2}}\left(\frac{K \tanh K \,(1+sK^2)}{p}\right)^{1/4} \,. \tag{40}$$

A systematic expansion in terms of $p^{1/4}$ leads in the next two orders to [38]

$$Q = Q_0 - \frac{K}{2\sinh(2K)} - \frac{K^2}{2Q_0}\frac{Y^2+6Y+5}{Y(Y+4)}\,. \tag{41}$$

Here $Y = 4\sinh^2 K$. To this order we have for the angular frequency

$$\begin{aligned}\omega &= \left[\sqrt{\left(gk+\frac{\sigma k^3}{\rho}\right)\tanh(kh)} - \frac{\sqrt{2\nu k^2\sqrt{\left(gk+\frac{\sigma k^3}{\rho}\right)\tanh(kh)}}}{2\sinh(2kh)}\right]\\ &-i\left[\frac{\sqrt{2\nu k^2\sqrt{\left(gk+\frac{\sigma k^3}{\rho}\right)\tanh(kh)}}}{2\sinh(2kh)} + 2\nu k^2\frac{Y^2+5Y+2}{Y(Y+4)}\right].\end{aligned} \tag{42}$$

The first term of the real part is the well-known dispersion relation of surface waves in ideal fluids. As for damping, the leading term is the first one in the second bracket, proportional to $\sqrt{\nu}$, except in deep fluid. In deep fluid ($K \to \infty$) this term vanishes and one gets the well-known damping exponent $2\nu k^2$ [17,19]. The result (42) was first published (for $\sigma = 0$) in reference [42] and then to higher orders in reference [38]. Note that taking into account surface tension is formally equivalent with replacing p with $p/(1+sK^2)$.

2.2. Behaviour at Large Wavelengths

At $K = 0$ Equation (20) reduces to

$$Q^5\cosh(Q) = 0 \tag{43}$$

(independently of p and s), which can be solved analytically: either

$$Q = 0 \tag{44}$$

or

$$Q = i(2n+1)\frac{\pi}{2}\,,\ n = 0,1,2,\ldots \tag{45}$$

The corresponding frequencies are $\omega = 0$ and

$$\omega = -i\frac{\nu\pi^2}{4h^2}(2n+1)^2\,. \tag{46}$$

Note that the order of the limits $\nu \to 0$ and $K \to 0$ does matter. If we take the limit $\nu \to 0$ first, we get ideal fluid, and if we take $K \to 0$ first, we get a limit where viscosity dominates and no wave propagation is possible.

2.3. Numerical Methods for Finding Roots

Equations (44) and (45) proved to be important technically, as solutions of Equation (20) could be obtained numerically from the differential equation (obtained directly by differentiating Equation (20) with respect to K)

$$\frac{dQ}{dK} = -\frac{\partial D/\partial K}{\partial D/\partial Q} \tag{47}$$

where D stands for the left hand side of Equation (20). Then Equations (44) and (45) play the role of initial conditions at $K = 0$. At bifurcations we get singular behaviour, which is

avoided on the complex K plane, afterwards we return to real K values. This method worked, and one could even choose different branches by going around the singularity from left or right on a half circle, yet it was somewhat in a state-of-art, as we had to experiment to get the correct radius of the half-circles. Another method we applied to get Q was direct numerical solution of Equation (20). In this case, bracketing solutions were a nontrivial task. Note that we compared the results obtained with these two different methods, and found an excellent agreement. A graphical solution was also helpful in locating roots.

2.4. Numerical Results for Frequencies

Having obtained Q for parameters p, s and K one may calculate mode frequencies. We present such results for a given material—glycerine—at some selected p values and as a function of scaled wave number K. The grand picture is this: at any given parameter settings one obtains infinitely many solutions, organized into branches as K changes (cf. Figure 1). In the following, the mode frequencies belonging to branch n will be denoted by $\Omega^{(n)}(K)$. They emanate from values (46) or from zero. Most of them remain purely imaginary, but the lowest two may collide when increasing K. At such a collision, a bifurcation takes place, as in Figures 1 and 2a, and two imaginary solutions Q may combine to complex solutions with non-zero real parts. Note that this bifurcation is also present in the parameters of Figure 3, but cannot be seen at the given resolution (it happens at very small wave numbers). The presence of complex Q solutions manifests itself in the appearance of a real part for the frequency. This means that wave propagation becomes possible. In that case the imaginary parts are the same, and the real parts differ in their signs only. As the value of p is increased, after a while such a collision no longer occurs, as in Figure 2c. This means that no wave propagation is possible because all modes are over-damped. The intermediate situation is approximately shown in Figure 2b. The mechanism of this possible bifurcation will be studied in more details in the next section (cf. Figures 4 and 5). A bifurcation that is closely related to the one we find here at short wavelengths has already been found by Refs. [21,37]. In those works an infinitely deep fluid was studied.

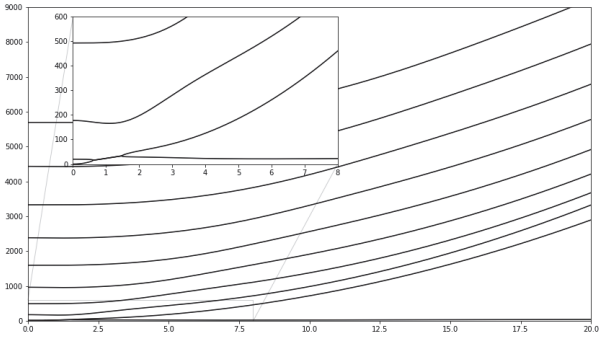

Figure 1. First, we find 10 branches of solutions for glycerin at $p = 0.077$. The majority of the frequencies remain purely imaginary, but the two lowest branches intersect when the value of K is increased.

In contrast, the bifurcation at long wavelength has been found explicitly here, and can be seen in Figures 1 and 2a, where imaginary parts of the two lowest branches collide at a small wave number or long wavelength (we consider the wave number to be the control parameter when we speak about bifurcations). Below that wave number, all frequencies are purely imaginary, while above that wave number a real part arises (not shown in the figures), hence wave propagation becomes possible, as mentioned above. This bifurcation is also shown in Figure 6 on the $p - K$ parameter plane. There, wave propagation is possible in region IV, and a bifurcation at low wave numbers takes place when for a sufficiently low parameter p the red line between region I and region IV is crossed. For small wave numbers

this line is parabolic, as quantified by Equation (75). This equation readily implies that the critical wavelength is $\lambda_c \propto h^{5/2}$, hence this bifurcation appears only in fluids of finite depth. The physical reason why this bifurcation happens can be understood from a simple order of magnitude estimate as follows. Let us consider a finite volume of the fluid, vertically from top to bottom, horizontally from a trough to the nearest crest. The main restoring force is gravity. If η is the surface elevation, the pressure difference between the two vertical sides of the fluid volume is $\propto g\rho\eta$, and the restoring force (per unit perpendicular horizontal distance) is $\propto -g\rho h\eta$. Friction with the bottom is $\rho\nu du/dz \propto \rho\nu u/h$ per unit surface (the characteristic vertical length scale is h, cf. Equation (74)), or $\propto \lambda\rho\nu u/h$ for the whole segment (numerical factors are neglected), where λ is the wavelength. The mass of the fluid segment is $\rho h\lambda$. Hence, Newton's second law reads in this case as

$$\rho h\lambda\dot{u} = -\lambda\rho\nu u/h - g\rho h\eta \; . \tag{48}$$

Further, we have the kinematic condition at the surface, $w = \dot{\eta}$, and the condition of incompressibility, $\partial u/\partial x + \partial w/\partial z = 0$. The partial derivatives may be estimated as $\partial u/\partial x \propto u/\lambda$ and $\partial w/\partial z = w/h$. By inserting these relations into Equation (48), we have

$$\ddot{\eta} + \frac{\nu}{h^2}\dot{\eta} + \frac{gh}{\lambda^2}\eta = 0 \; . \tag{49}$$

It is clear that for long waves friction prevails and the wave becomes over-damped. Indeed, the Ansatz $\eta = \eta_0 \exp(-i\omega t)$ leads to

$$\omega = -i\frac{\nu}{2h^2} \pm \sqrt{\frac{gh}{\lambda^2} - \frac{\nu^2}{4h^4}} \; . \tag{50}$$

This shows that for very long waves frequencies are purely imaginary. When wavelength λ is decreased, at around

$$\lambda_c \propto \frac{g^{1/2}h^{5/2}}{\nu} \tag{51}$$

a non-zero real part of the frequencies emerges. Note that Equation (51), obtained from rough order of magnitude estimates for the bifurcation point, agrees well with Equation (75).

There are a number of works where the bifurcation phenomena in surface waves were studied [23,43–47]. All these works considered the infinite depth fluid case. They fall into three categories: (1) a non-viscous case where bifurcation is due to nonlinearity [45,46]. (2) The presence of a surfactant where an interplay between dilational and capillary waves takes place [21,23,47]. (3) The presence of elastic membrane at the surface of the ideal fluid [43,44].

A further work, not belonging to the above categories, contains an ingenious application of bifurcation theory in order to prove the existence of linear waves and find the dispersion relation [48]. The system considered is a finite depth ideal (non-viscous) fluid without surface tension. Laminar rotational flow is assumed with constant vorticity (i.e., horizontal velocity is changing linearly with depth), and linear surface gravity waves at a fixed wavelength are considered. Stationary solutions are sought for in a coordinate system moving horizontally with constant speed compared to the fluid. This speed is considered to be the control parameter (in fact, the equivalent mass flux is used). Now, if the speed of the coordinate system is not equal to the phase speed of the waves, only the trivial, zero amplitude stationary solution exists, since the linear wave is a travelling wave as seen from that coordinate system. If, however, the speed of the coordinate system is equal to the phase speed, a further, nontrivial stationary solution emerges, whose existence is proved with mathematical exactitude under quite general circumstances. This technique has also been applied to study linear capillary waves in the same system, by neglecting gravity [49].

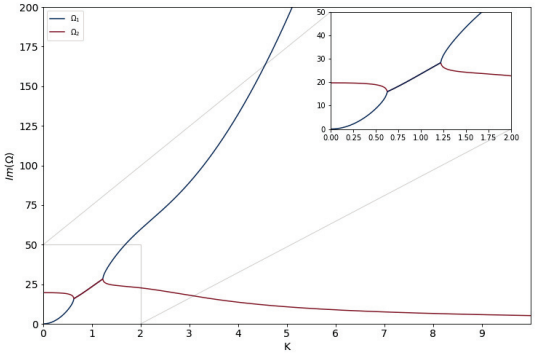

(**a**)

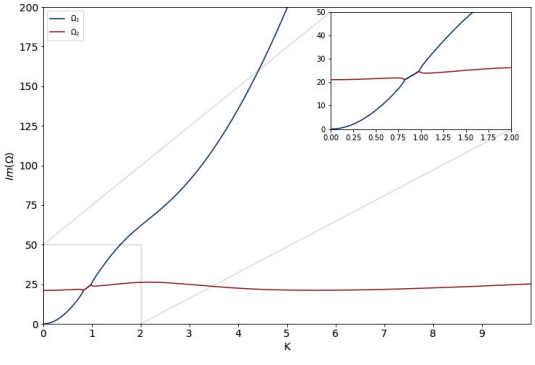

(**b**)

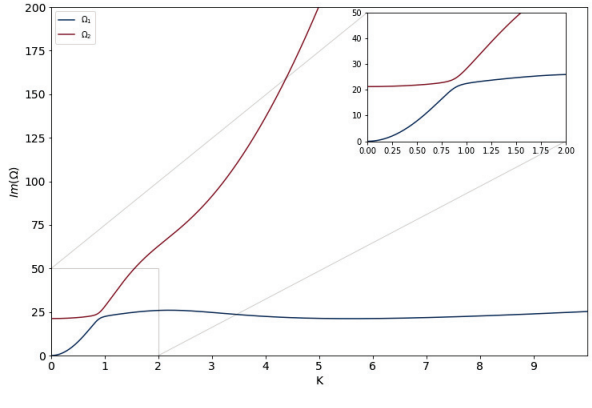

(**c**)

Figure 2. Two lowest branches of solutions for glycerin at different p values. Moduli of imaginary parts of frequencies are displayed. (**a**) Two lowest branches of solutions for glycerin at $p = 0.077$. (**b**) Two lowest branches of solutions for glycerin at $p = 0.085$. (**c**) Two lowest branches of solutions for glycerin at $p = 0.086$. The collision no longer occurs by increasing the value of p.

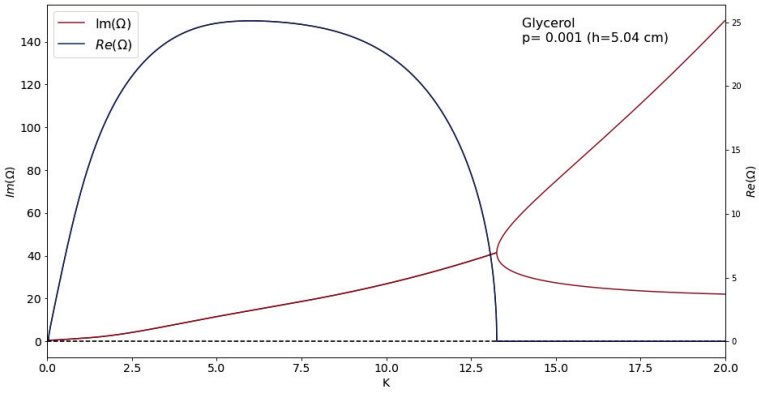

Figure 3. The real and imaginary parts of frequencies corresponding to the lowest lying branches versus K for glycerin at $p = 0.001$ ($h = 5.04$ cm).

3. Parameter Dependence

3.1. Wave Modes

Plotting the real and imaginary parts of Equation (20) on the complex Q plane one usually observes several intersections, i.e., roots. They can be real, purely imaginary, or complex with non-zero real and imaginary parts (henceforth we shall use the term "complex" as an equivalent with "complex with non-zero real part and non-zero imaginary part"). In the first two cases the angular frequency (25) is purely imaginary, so these modes decay exponentially with time. Propagating modes are only possible if Q is complex.

3.1.1. Modes with Real Q

In this case, Equation (25) implies that $Q < K$, since the decay rate cannot be negative. We have found numerically that at a given parameter settings (s, p, and K) there can exist zero, one, or two real modes (due to the symmetry of the solutions, we consider roots only in the first quadrant). There is always a trivial solution $Q = K$. Then, we get $f = 0$ from Equation (12), so this solution is irrelevant.

In case of nontrivial real solutions, the decay rate is always smaller than νk^2. Velocity components may be calculated from Equations (3), (4), (12) and (26). Provided that coefficient A is real, u is real, too, while w is purely imaginary, so there is a 90° phase shift in their x-dependent oscillations.

3.1.2. Modes with Imaginary Q

In this case the decay rate is always larger than νk^2. Such modes exist at any parameter setting, moreover, there are infinitely many of them. Indeed, if Q is purely imaginary as $Q = i\beta$ and its modulus is large, Equation (20) reduces to

$$p\left[Q^5 \cosh K \cosh Q - KQ^4 \sinh K \sinh Q\right] = 0\,, \tag{52}$$

or, substituting $Q = i\beta$,

$$\beta \cosh K \cos\beta - K \sinh K \sin\beta = 0\,. \tag{53}$$

Now, if $\beta = 2n\pi$ (n being an integer), the left hand side is positive, and if $\beta = 2n\pi + \pi/2$, the left hand side is negative. Therefore, between these values there is a root for any (arbitrarily large) n. The distance between imaginary roots is approximately constant and independent of viscosity.

As before, the phase of velocity components does not change with depth, while there is a 90° phase shift between the x and z components. It is interesting that imaginary Q causes an oscillatory behaviour with depth.

3.1.3. Modes with Complex Q

On the basis of our numerical investigations, we believe that at a given parameter setting at most one such mode can exist. If there exists one, then at the same parameter setting no mode with real Q can exist. This time the phases of velocity components do change with depth. An oscillatory dependence on depth is in principle present, but much less pronounced than in the imaginary case.

3.2. Bifurcations

If, at the given s and p parameters one adjusts K, the type and number of solutions changes. This is shown in Figure 4a–i where $s = 7.44$ and $p = 2.0$. The left hand side of Equation (20) divided by $K^2 Q \cosh(K) \cosh(Q)$ is plotted (this factor is chosen to avoid exponential growth.) on the complex Q plane, the zero level lines of the real part in blue, and those of the imaginary part in red. Hence, intersections of red and blue curves are solutions of Equation (20). As wave number K grows, these solutions are moving on that plain and display bifurcations. Since there are other (sometimes non-physical) solutions present, we denoted by black arrows the solutions we wish to focus on. In Figure 4a one can see a real solution. A bifurcation is shown in Figure 4b, where the real solution and its mirror image collide at the origin, and a further increase of the wave number gives rise to an imaginary solution (cf. Figure 4c, lower arrow) and its mirror image.

Increasing the scaled wave number K further, one can observe that that two imaginary solutions in Figure 4c collide (see Figure 4d) and give rise to a complex solution (see Figure 4e). This complex solution gradually goes down to the real axis (cf. Figure 4e–h) and decays to two real solutions (Figure 4i) which survive any further increase of K.

Choosing the parameter values $s = 7.44$ and $p = 3.0$, one has a different scenario, see Figure 5a–c. This time only a single bifurcation takes place, namely, an imaginary solution and its mirror image collide at the origin (see Figure 5b) and give rise to a (second) real solution (cf. Figure 5c).

These observations allow us to find the mathematical conditions of the bifurcations, which mean transitions among different types of possible modes. These conditions appear as curves on the K-p plane and partition that plane according to the types of possible solutions. Since the p-dependence is simpler than the K-dependence, we find these curves at constant K by varying p, rather than varying K at constant p, as has been done above when demonstrating the bifurcations. The curves are certainly the same.

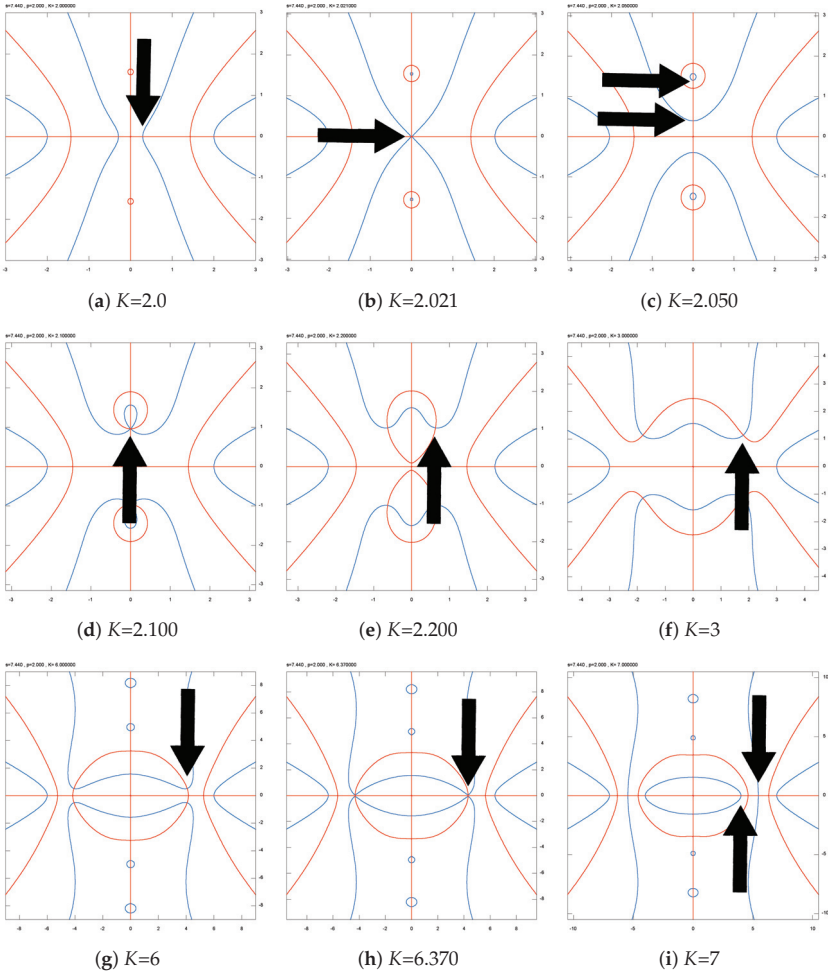

(**a**) K=2.0 (**b**) K=2.021 (**c**) K=2.050

(**d**) K=2.100 (**e**) K=2.200 (**f**) K=3

(**g**) K=6 (**h**) K=6.370 (**i**) K=7

Figure 4. Zero level lines of the real (blue) and imaginary (red) part of Equation (20) divided by $K^2Q\cosh(K)\cosh(Q)$ plotted on the complex Q plane at parameter values $p = 2.0$ and $s = 7.44$.

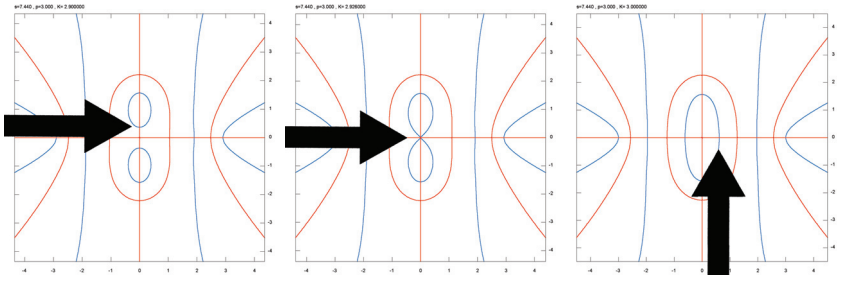

(**a**) (**b**) (**c**)

Figure 5. Zero level lines of the real (blue) and imaginary (red) part of Equation (20) divided by $K^2Q\cosh(K)\cosh(Q)$ plotted on the complex Q plane at parameter values $p = 3.0$ and $s = 7.44$. (**a**) $K = 2.900$. (**b**) $K = 2.926$. (**c**) $K = 3.00$.

In all the above numerically discussed cases (Figures 4 and 5) at the birth of new solutions one can observe that by approaching the critical parameter the zero level lines of the real part of Equation (20) develop an edge, and at bifurcation they become (locally) two straight lines crossing each other on the real and/or the imaginary axis (Figures 4b,d,h and 5b). This means that at the bifurcation point the derivative of the line is undetermined, i.e., it has a form $\frac{0}{0}$. Note in passing that it is equivalent with the condition that the second derivative becomes infinite. Let us denote for brevity the real part of Q with α and its imaginary part with β (i.e., $Q = \alpha + i\beta$), further, the left hand side of Equation (20), divided by $K^2 Q \cosh(K) \cosh(Q)$ be $D(\alpha + i\beta)$. Then the zero level line of the real part of D is given by

$$\Re(D(\alpha + i\beta)) = 0\,. \tag{54}$$

Here $\Re$ stands for the real part. Taking its derivative with respect to α, we get

$$\Re\left(D'(\alpha + i\beta) + iD'(\alpha + i\beta)\frac{d\beta}{d\alpha}\right) = 0\,, \tag{55}$$

hence the derivative of the curve is written as

$$\frac{d\beta}{d\alpha} = \frac{\Re(D'(\alpha + i\beta))}{\Im(D'(\alpha + i\beta))}\,. \tag{56}$$

Here $\Im$ stands for the imaginary part (without i). It follows that at bifurcation

$$D'(\alpha + i\beta) = 0 \tag{57}$$

must be satisfied, together with $D(\alpha + i\beta) = 0$. Now it is easily seen that $D(\alpha + i\beta)$ is real along both the real and the imaginary axis, while $D'(\alpha + i\beta)$ is real along the real axis and imaginary along the imaginary axis. Therefore, in case of a bifurcation on the real axis we have

$$D(\alpha) = 0 \tag{58}$$
$$D'(\alpha) = 0\,, \tag{59}$$

i.e., two real equations for the two real parameters α and p (at constant K and μ). Similarly, in case of a bifurcation on the imaginary axis we have

$$D(i\beta) = 0 \tag{60}$$
$$iD'(i\beta) = 0\,, \tag{61}$$

again two real equations for the two real parameters β and p.

Equation (20) shows that $D(Q)$ may be expressed as

$$D(Q) = \left(1 + sK^2\right)F(Q) + p\,G(Q) \tag{62}$$

where

$$F(Q) = \frac{\tanh K}{K} - \frac{\tanh Q}{Q}\,, \tag{63}$$

$$G(Q) = -4\frac{K^2 + Q^2}{\cosh K \cosh Q} + \left(\frac{Q^4}{K^2} + 2Q^2 + 5K^2\right) - \left(Q^4 + 6K^2Q^2 + K^4\right)\frac{\tanh K}{K}\frac{\tanh Q}{Q}. \tag{64}$$

In terms of these functions we have (cf. Equations (58) and (59))

$$F(\alpha)G'(\alpha) - G(\alpha)F'(\alpha) = 0 \tag{65}$$

$$\frac{p}{1+sK^2} = -\frac{F(\alpha)}{G(\alpha)} \tag{66}$$

and (cf. Equations (60) and (61))

$$F(i\beta)G'(i\beta) - G(i\beta)F'(i\beta) = 0 \tag{67}$$

$$\frac{p}{1+sK^2} = -\frac{F(i\beta)}{G(i\beta)} \tag{68}$$

for bifurcations on the real and imaginary axis, respectively. In these cases, Equation (65) or Equation (67) is solved numerically to get α or β, respectively, then the solution is inserted into Equations (66) and (68), respectively, which in turn are solved for p at constant K and μ, taking into account Equation (35).

As for the transformation of an imaginary solution to a real one at the origin, mentioned above, for the critical $p(K)$ line one obtains

$$\frac{p}{1+sK^2} = -\frac{F(0)}{G(0)} = \frac{1-\frac{\tanh K}{K}}{5K^2 - 4\frac{K^2}{\cosh(K)} - K^3\tanh K} \,. \tag{69}$$

Since both $F(Q)$ and $G(Q)$ are even functions of Q, it follows that $F'(0) = G'(0) = 0$, hence Equations (65) and (67) are automatically satisfied for $\alpha = 0$ and $\beta = 0$, respectively. The results are plotted in Figure 6a,b for glycerin and water, respectively. These two figures are very much different, not only in the shape of the curves, but in their vertical scales, in the first place. The values in Figure 6b are of order 10^9. Such a huge difference needs an explanation. When we solve the Equations (66), (68), or (69) for p, we actually solve an equation

$$\frac{p}{1+\mu^2K^2p^{2/3}} = a \,, \tag{70}$$

where a is a function of K alone and is of order 0.1. The solution of Equation (70) is

$$p = \frac{1}{\mu^3K^3}\Phi^{-1}(\mu^3K^3a) \,, \tag{71}$$

where $\Phi^{-1}(x)$ stands for the inverse of function $\Phi(x) = x/(1+x^{2/3})$. It is easily seen that

$$\Phi^{-1}(x) \approx x, \text{ if } x \ll 1 \,, \tag{72}$$

and

$$\Phi^{-1}(x) \approx x^3, \text{ if } x \gg 1 \,. \tag{73}$$

Therefore, when $\mu^3K^3a \ll 1$, the solution is approximately $p = a$, as is the case for glycerin. In contrast, if $\mu^3K^3a \gg 1$, then the solution is $p = \mu^6K^6a^3$. This happens in the case of water and mercury, and we get huge values for p, except for very small K values. These large p values are equivalent with extremely small layer widths (cf. Section 4). In fact, they are so small that the bifurcations in question are hardly observable in case of water or mercury as well as other fluids with low viscosity. They might be observable, however, in more viscous fluids such as glycerin.

In short, the physical reason of the difference between Figure 6a,b is that in case of water the viscosity is much smaller than in the case of glycerin (the surface tensions in the two cases are comparable) and this is reflected in the corresponding μ values (58.40 for

water and 0.45 for glycerin). The two order of magnitude difference in the values of μ for water and glycerin is further magnified by the cubic functional dependence (73).

On the other hand, for small enough K values, condition $\mu^3 K^3 a \ll 1$ is satisfied, hence in that limiting case the parameter space regions become independent of μ. This is natural, since in the long wavelength limit the impact of the surface tension vanishes.

In Figure 6 the red line means the onset of the creation of a complex solution at the imaginary line, i.e., the solution of Equations (67) and (68). The bue line is the same at the real line (cf. Equations (65) and (66)), while the black line is the onset of the crossover from the imaginary to the real solution at the origin (Equation (69)). It is obvious that these lines must have a common point. The lines partition the $K - p$ parameter space to four regions, denoted in the figures by Roman numbers:

I. Only imaginary solutions (infinitely many of them) are present;
II. There is a single real solution and there are infinitely many imaginary solutions;
III. There are two real solutions and there are infinitely many imaginary solutions;
IV. There is a single complex solution and there are infinitely many imaginary solutions.

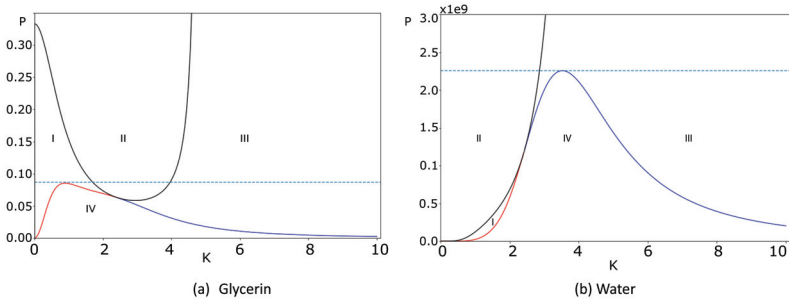

Figure 6. The maximal parameters p versus the scaled wave-number K for glycerin (**a**) and water (**b**). Note the vertical scale in (**b**). The red line signifies the emergence of complex solutions at the imaginary line, while the blue line represents the real solutions obtained from Equations (65) and (66). The black line denotes the onset of the crossover from imaginary to real solutions at the origin.

Asymptotics and some special cases of the bifurcation curves are the following.

1. Imaginary to complex Q (border between regions I and IV, the red curve in Figure 6): For small K ($K \ll 1$) we have

$$Q = (1.1127 + 0.2509\ K^2)i \tag{74}$$

$$p = 0.53667\ K^2\Big(1 + (s - 3.8674)K^2\Big) \tag{75}$$

2. Complex to real Q (border between regions IV and III, the blue curve in Figure 6): For large K we have

$$Q = 0.6823\ K \tag{76}$$

$$p = \frac{1.7200(1 + sK^2)}{K^3} \approx \frac{1.7200s}{K}\ . \tag{77}$$

This implies (cf. Equations (21)–(24) and Equations (30) and (31)) that the transition to the over-damped mode happens at wavelength

$$\lambda = 3.6530\ \frac{\rho\nu^2}{\sigma} = 3.6530\ \frac{\ell_\nu^3}{\ell_\sigma^2}\ . \tag{78}$$

It is remarkable that this value does not depend on layer thickness h or gravity of Earth g, as it is a purely material constant. Numerically, we get $\lambda = 5 \times 10^{-8}$ m for water, 7×10^{-4} m for glycerin and 10^{-9} m for mercury. In our opinion, this effect cannot be

observed in water or mercury, but might be observed in glycerin. It is questionable if hydrodynamics are applicable at the scales obtained for water and mercury, albeit at least one study states that it is applicable down to the nanoscales [28]. It is obvious that in case of these short waves gravity does not play a role. Here we demonstrate, that our more general setup leads to the right results in this limiting case. There are other situations, however, when gravity becomes important. This happens, e.g., at the bifurcation at long wavelengths. Gravity and surface tension become equally important when the two bifurcations (at large and small wavelength) are close to each other, as in Figure 2a.

3. Imaginary to real Q (borders between regions I, II, and III, the black curve in Figure 6): For small K we have

$$p = \frac{1}{3}\left[1 + \left(s - \frac{7}{5}\right)K^2\right] . \tag{79}$$

At $K \approx 4.9435$ parameter p diverges as

$$p = \frac{0.8452 + 20.654\, s}{4.9435 - K} , \tag{80}$$

For a given material this implies (cf. Equation (35))

$$p = \frac{8.8 \times 10^3\, \mu^6}{(4.9435 - K)^3} . \tag{81}$$

4. The common point of the bifurcation parameter curves (red, blue, and black lines in Figure 6 satisfies

$$\frac{F(0)}{G(0)} = -\frac{p}{1 + sK^2} = \lim_{Q \to 0} \frac{F'(Q)}{G'(Q)} = \frac{F''(0)}{G''(0)} , \tag{82}$$

since $F'(0) = G'(0) = 0$. This implies

$$F(0)G''(0) - G(0)F''(0) = 0 . \tag{83}$$

The solution of this equation yields for the coordinates of the common point

$$K = 2.4152 \tag{84}$$

$$p = 0.05307(1 + 5.8332\, s) . \tag{85}$$

4. Minimal Layer Thickness Necessary for Wave Propagation

Viscosity not only damps waves, but it can even prevent their propagation. Indeed, propagation, mathematically, a real part of the complex angular frequency, appears only in region IV (cf. Figure 6). This implies that no gravity-capillary waves can propagate if p is large enough (or, equivalently, if the layer width is small enough). Further, even if the layer thickness is larger than the critical value, neither very long, nor very short waves can propagate.

The critical layer thickness is found from the maximum point of the curves bordering region IV in Figure 6 (cf. Equations (65)–(68)). This depends on the material parameter μ, so we present the results in Table 1. Clearly, for water and mercury the critical layer width is so extremely small that at such scales even the applicability of standard hydrodynamics is more than questionable.

Table 1. Material parameters l_ν, l_σ and μ for some fluids.

Material	l_ν	l_σ	μ	p_{max}	h
water	4.67×10^{-5}	2.73×10^{-3}	58.40	2.255×10^{9}	3.561×10^{-8}
glycerin	5.04×10^{-3}	2.27×10^{-3}	0.45 [1]	0.085	1.146×10^{-2}
mercury	1.09×10^{-5}	1.90×10^{-3}	174.86	1.625×10^{12}	9.271×10^{-10}

[1] Properties are at 20 °C.

5. Particle Motion at Surface

In this section, we focus on the numerical simulation of particle trajectories associated with wave patterns at the surface of the fluid. Since we are considering linear waves, both the horizontal and vertical motion is that of a damped harmonic oscillator. If we neglect damping, the resulting motion due to these two perpendicular harmonic oscillations results in a general elliptical motion. Note that in the presence of damping, the actual motion will be a spiral. The parameters of the ellipse (see Figure 7), main axis a, small axis b, and angle of the main axis made with x direction, φ are related to the horizontal and vertical amplitudes and phase difference. The relevant relations are the following:

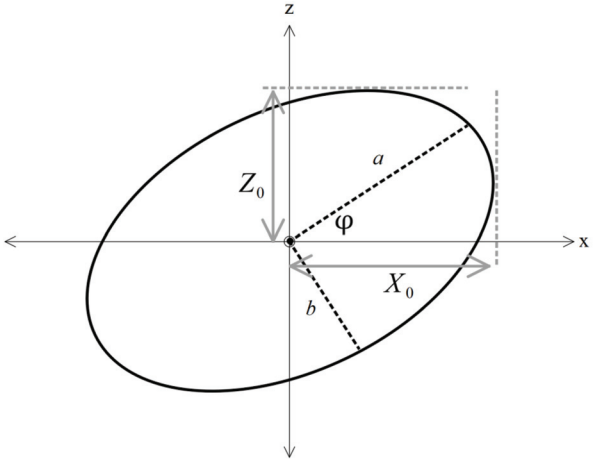

Figure 7. Motion of the particles at the surface.

$$a^2 = \frac{X_o^2 \cos^2\varphi - Z_o^2 \sin^2\varphi}{\cos^2\varphi - \sin^2\varphi}\,, \tag{86}$$

$$b^2 = \frac{Z_o^2 \cos^2\varphi - X_o^2 \sin^2\varphi}{\cos^2\varphi - \sin^2\varphi}\,. \tag{87}$$

Angle of main axis compared to horizontal, φ, is given by

$$\tan\varphi = \frac{c^2 - 1 + \sqrt{(c^2+1)^2 - 4c^2\sin^2\gamma}}{2c\cos\gamma}\,. \tag{88}$$

Here

$$c = \left|\frac{Z_o}{X_o}\right| \tag{89}$$

and

$$\gamma = \xi - \chi\,, \tag{90}$$

where ξ and χ are phases of the horizontal and the vertical oscillations, respectively:

$$x = X_o e^{i\chi} \cdot e^{-i\omega t} \tag{91}$$

$$z = Z_o e^{i\xi} e^{-i\omega t} \tag{92}$$

Explicitly,

$$\begin{aligned} X_o e^{i\chi} = &\frac{i}{\omega} K[Q(Q^2 + 3K^2) \cdot (\cosh(Q)\cosh(K) - 1) \\ &- K \cdot (K^2 + 3Q^2)\sinh(Q)\sinh(K)] \end{aligned} \tag{93}$$

and

$$\begin{aligned} Z_o e^{i\xi} = &\frac{1}{\omega} K(Q^2 - K^2) \cdot [K\cosh(K)\sinh(Q) \\ &- Q \cdot \cosh(Q)\sinh(K)] \, . \end{aligned} \tag{94}$$

According to Equations (93) and (94), when Q is a real, the value of γ is $-\frac{\pi}{2}$, but if Q is purely imaginary, then the value of γ is $\frac{\pi}{2}$.

These parameters are plotted versus scaled wave number K in Figure 8 at $p = 0.001$. Wave propagation is permitted from $K = 0$ to $K = 13$, as seen in Figure 3 (Except for very small K values where the motion always becomes damped. At the resolution of the figure, this regime can not be seen). The motion is virtually linear ($\frac{b}{a} \ll 1$) for small values of K but quickly transforms into a circle with $\frac{b}{a}$ close to unity at $K \approx 1$. The angle that the main axis makes with the horizontal, φ, is almost zero up to this point, then it rapidly takes 90 degree turn and remains around that. The ellipse gets narrower for wave numbers greater than unity ($K > 1$) and at wave number $K = 7.5$, it degenerates into a linear segment. The corresponding motion is nearly perpendicular to the surface. The ellipse then gets a little bit thicker. Both the horizontal and vertical motion are excessively over-dampened at $K \approx 13$. The change in the phase difference between horizontal and vertical motion is also displayed. It is clear that with K being approximately 1, the phase difference is approximately $\pi/2$. When the ellipse degenerates into a line segment at $K \approx 7.5$, the phase difference reaches π. At the $K \approx 13$ bifurcation point, the phase difference γ hits $-\pi/2$.

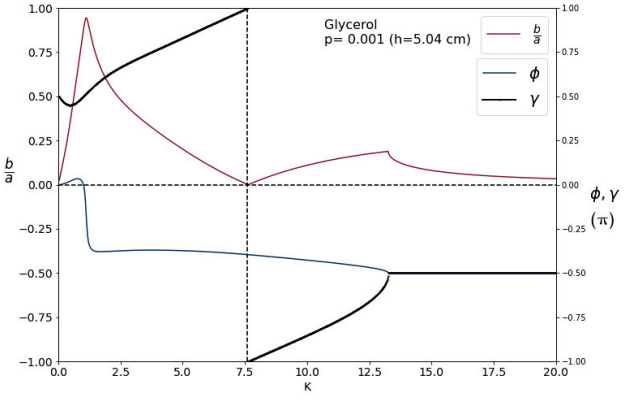

Figure 8. The ratio of $\frac{b}{a}$ and the angles ϕ and γ in terms of K are presented for glycerin at $p = 0.001$ (cf. Figure 3). Angles are given in π units.

6. Time Evolution of Surface Elevations

Figures 9–15 demonstrate the time evolution of a propagating wave in a fluid, along with the associated dispersion relations. We have chosen glycerin as the fluid medium due to its physical properties, as other fluids may require a thinner layer for observation of the

phenomena. Then, the critical thickness for glycerin is 1.1 cm, for water is 3.6×10^{-8} m, and for mercury is 9.3×10^{-10} m, which is the reason we have chosen the glycerin for simulation. We limit our study to the lowest two branches of the dispersion relation, because, as shown in Figure 1 these branches have the longest lifetime and, i.e., they are the least damped.

We aim to establish a correlation between theoretical predictions and empirical observations. The findings indicate that wave propagation is detected at a particular wavenumber of $K = 1$, within a narrow range, when $p = 0.077$, which is in proximity to the critical value of $p = 0.086$. Conversely, no propagation is observed at longer wavelengths, such as $K = 0.62$, or at shorter wavelengths, such as $K = 2$, as illustrated in Figures 9–11. Figure 9 depicts the over-damped mode characterized by a long wavelength. At a specific wavelength of $\lambda = 12$ cm, a wavenumber of $K = 0.62$, it can be observed that wave propagation is not feasible due to the nodes remaining in the unchanged position (cf. Figure 2a). It should be noted that surface tension plays a minor role in this context. The nodes in Figure 10 are observed to be in motion due to the occurrence of wave propagation at a wavenumber of $K = 1$. This is in agreement with Figure 2a. At $K = 2$, the wave in Figure 11 exhibits over-damping. Surface tension is a dominant phenomenon in this particular regime.

At $p = 0.001$, the range of wavelengths that undergo propagation is wider. However, it is worth noting that a non-propagating long-wave mode develops at a wavelength of 8 m in a fluid layer of 5 cm, which poses a challenge for observation (refer to Figure 12). Figure 13 illustrates the observation of a travelling wave with a shorter wavelength of $\lambda = 6.33$ m. The demonstration shows the limited wavenumber spectrum within which long wavelength over-damped modes exist. Figure 14 shows the propagation of waves at the same layer width, with a wavelength of $\lambda = 3.16$ cm. It should be noted that the velocity is significantly greater, as evidenced by the time labels. The propagation of waves with a shorter wavelength, specifically those with a wavelength of $\lambda = 2.11$ cm, is prohibited, as shown in Figure 15.

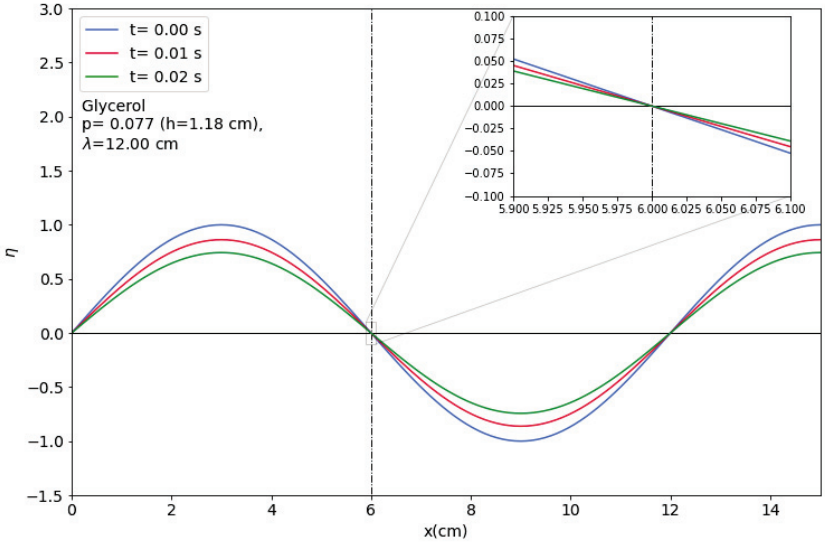

Figure 9. Time evolution of surface elevation in glycerin at parameter $p = 0.077$ and wave number $K = 0.62$.

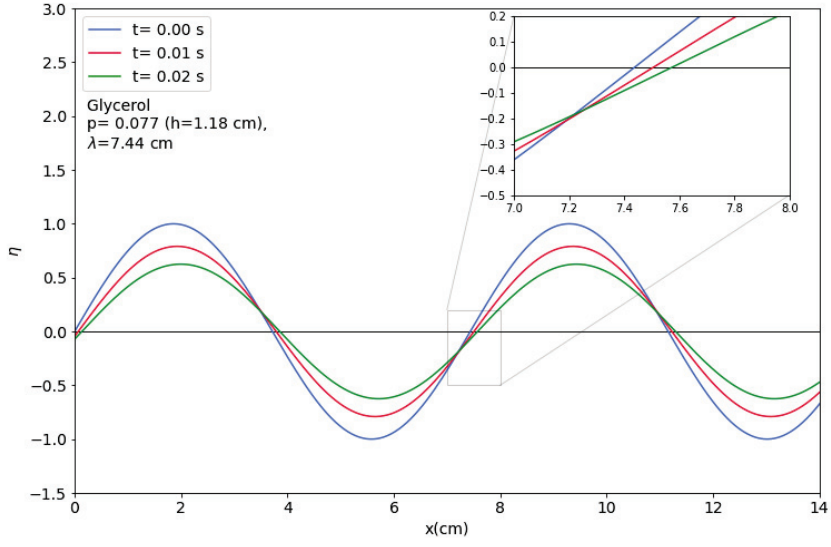

Figure 10. Time evolution of surface elevation in glycerin at parameter $p = 0.077$ and wave number $K = 1.00$.

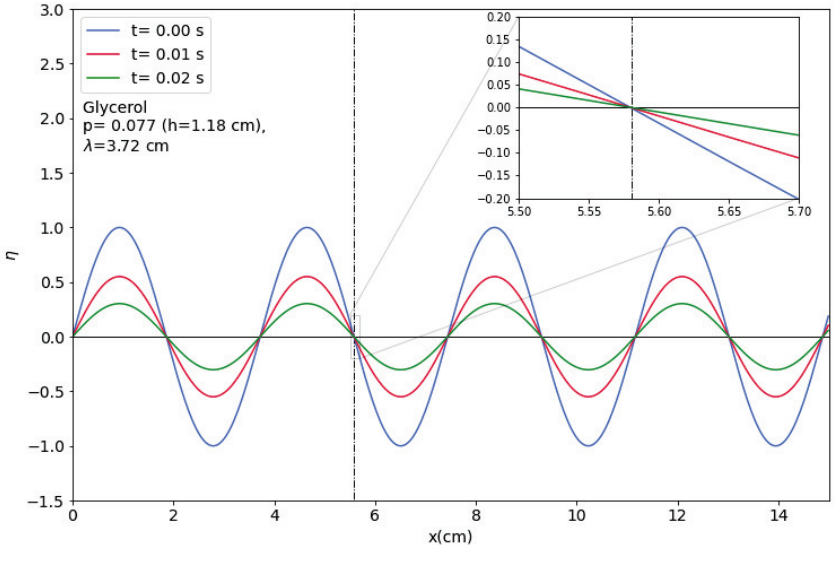

Figure 11. Time evolution of surface elevation in glycerin at parameter $p = 0.077$ and wave number $K = 2.00$.

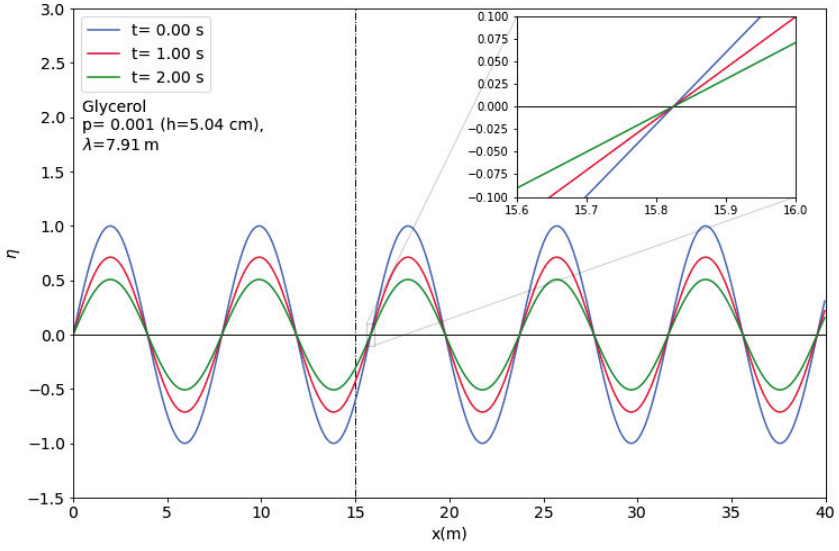

Figure 12. Time evolution of surface elevation in glycerin at parameter $p = 0.001$ and wave number $K = 0.04$.

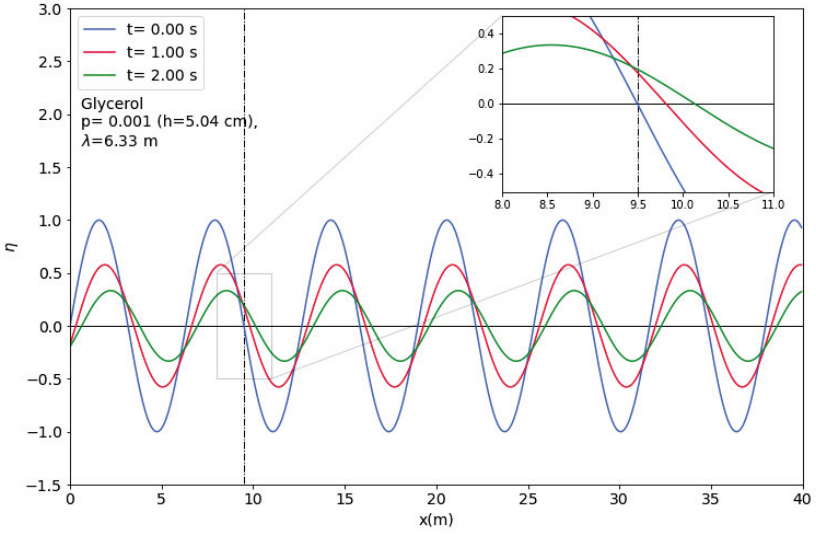

Figure 13. Time evolution of surface elevation in glycerin at parameter $p = 0.001$ and wave number $K = 0.05$.

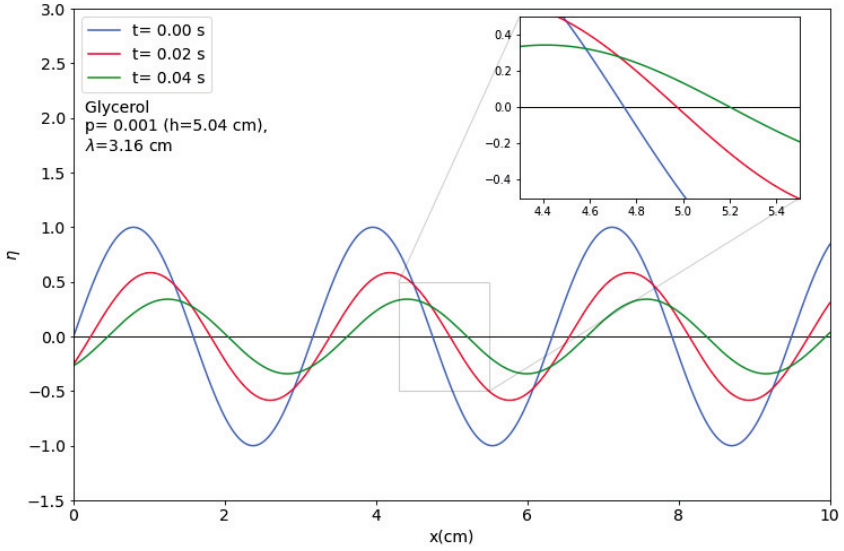

Figure 14. Time evolution of surface elevation in glycerin at parameter $p = 0.001$ and wave number $K = 10.0$.

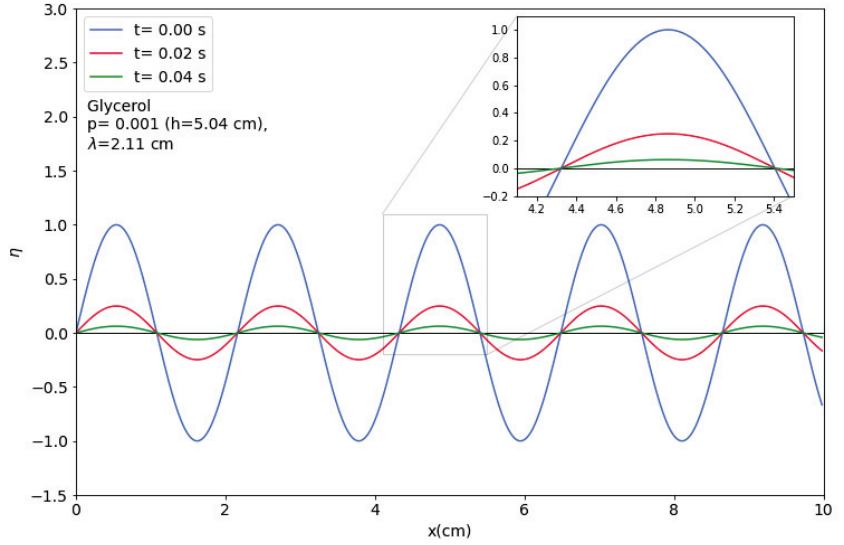

Figure 15. Time evolution of surface elevation in glycerin at parameter $p = 0.001$ and wave number $K = 15.0$.

For the purpose of demonstrating the group velocities present in the propagating modes, we overlay two wavelengths that are in close proximity. Specifically, we consider the expression $\sin(k_1(x - x_o) - \Omega^{(1)}t) - \sin(k_2(x - x_o) - \Omega^{(2)}t)$, where both waves are propagating towards the right. Nevertheless, the direct observation of this phenomenon appears improbable due to significant damping. In order to show the motion of the envelope, the superposition is amplified at a rate of $e^{(|\gamma|t)}$, where γ denotes the lesser decay rate. Figure 16 illustrates the superposition of two waves with two nearby wavenumbers

($K = 0.75$ and $K = 0.76$) at three consecutive time intervals. The direction of their travel is towards the right. At the onset, the envelope exhibits a node. At a subsequent time interval, the node expands to form a bottleneck. The position of the bottleneck is moving to the right, which indicates that the group velocity is also positive in this scenario. The phenomenon of broadening can be attributed to the disparate damping exhibited by two modes that are superimposed. Figure 17 describes the superimposition of two waves with closely spaced wavenumbers at the same fluid depth as previously. The present instance involves a reduction in wavelength, specifically with values of K equal to 0.94 and 0.95. Although the phase velocity retains a positive value, the position of the envelope remains unaltered in implying zero group velocity. The phenomenon of bottleneck widening persists due to the dissimilar damping exhibited by the two modes. Figure 18 illustrates the presence of two superimposed modes, which exhibit a comparatively reduced wavelength of $K = 1.2$ and $K = 1.21$. At present, although the phase velocity remains positive, the retrograde motion of the envelope indicates a negative group velocity. It should be noted that the frequency's real part exhibits a negative slope versus K in this instance.

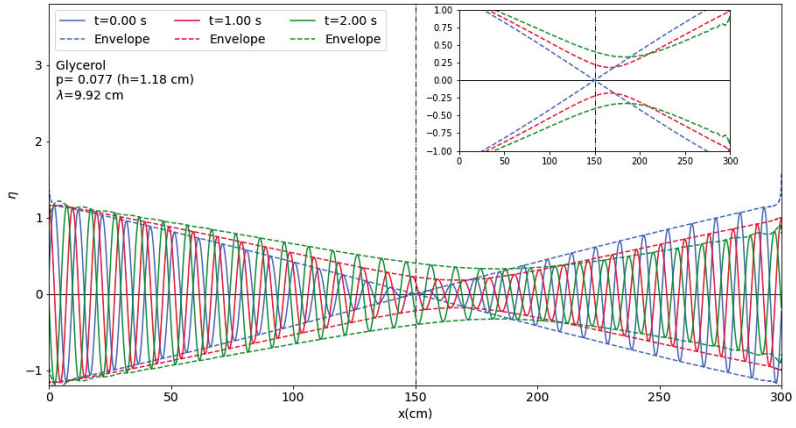

Figure 16. Time evolution of surface elevation in glycerin at parameter $p = 0.077$ with two nearby wave numbers at $K = 0.75$ ($\Delta K = 0.01$).

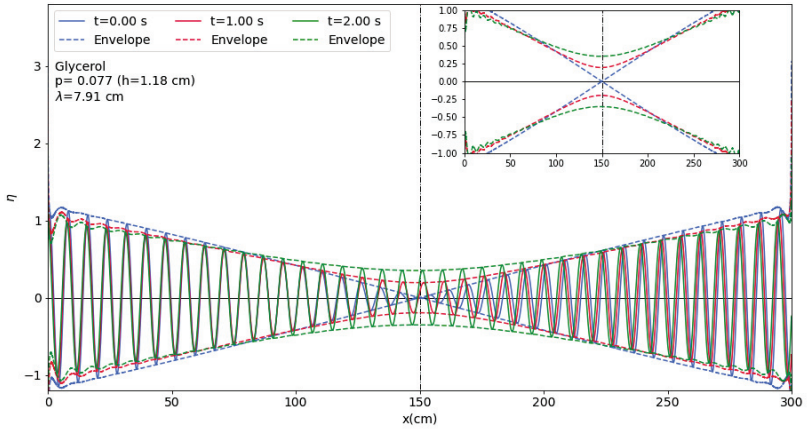

Figure 17. Time evolution of surface elevation in glycerin at parameter $p = 0.077$ with two nearby wave numbers at $K = 0.94$ ($\Delta K = 0.01$).

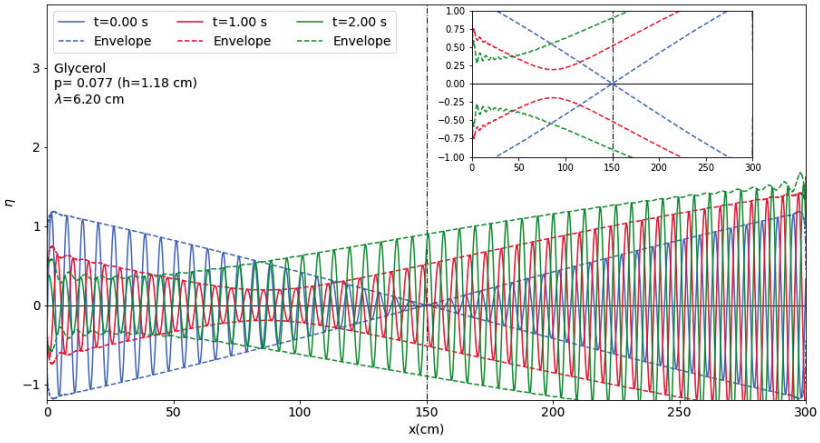

Figure 18. Time evolution of surface elevation in glycerin at parameter $p = 0.077$ with two nearby wave numbers at $K = 1.20$ ($\Delta K = 0.01$).

An arbitrary initial condition means specifying the velocity field at an instant of time everywhere within the fluid layer. In linear approximation one may decompose such an initial condition in terms of modes:

$$\mathbf{V}(x,z,t=0) = \int_{-\infty}^{\infty} dk \sum_{n=1}^{\infty} a_n(k)\mathbf{V}_n(k,z)e^{ikx} \tag{95}$$

Here $a_n(k)$ stands for suitable expansion coefficients, while

$$\mathbf{V}_n(k,z) = \begin{pmatrix} Ak\sinh[k(z+h)] - B\kappa\cosh[k(z+h)] - A\kappa\sinh[\kappa(z+h)] + B\kappa\cosh[\kappa(z+h)] \\ -iAk\cosh[k(z+h)] + iB\kappa\sinh[k(z+h)] + iAk\cosh[\kappa(z+h)] - iBk\sinh[\kappa(z+h)] \end{pmatrix} \tag{96}$$

is the velocity field of a mode (cf. Equations (3), (4) and (12)). Note that $\kappa = \kappa_n(k)$ corresponds to the n-th solution of Equation (20), while the ratio of A and B is specified by Equation (26) (The quantities A and B are thus specified up to an arbitrary normalization factor), hence they also depend on κ, and thus on n and k.

If we take the Fourier transform of both sides of Equation (95) with respect to the x variable, we get

$$\tilde{\mathbf{V}}(k,z,t=0) = \sum_{n=1}^{\infty} a_n(k)\mathbf{V}_n(k,z)\,, \tag{97}$$

where

$$\tilde{\mathbf{V}}(k,z,t) = \frac{1}{2\pi}\int_{-\infty}^{\infty} dx\; e^{-ikx}\mathbf{V}(x,z,t)\,. \tag{98}$$

For arbitrary later times t we have

$$\tilde{\mathbf{V}}(k,z,t) = \sum_{n=1}^{\infty} a_n(k)\mathbf{V}_n(k,z)e^{-i\Omega^{(n)}(k)t}\,. \tag{99}$$

Most modes are strongly damped. Therefore, leaving them out of the decomposition (99) may not lead to a significant error, except initially for a very short time. If we keep only the lowest two branches, it is possible to formulate the initial value problem in terms of the surface profile and its time derivative. Note that in the range of wave numbers where

propagation is possible, the two branches differ only in the sign of the real part of the frequency, allowing a description of both directions of propagation. Explicitly, we may formulate the initial value problem in wave number space (Fourier space) as follows. At a given wave number we have two modes, therefore the decomposition (99) reduces to

$$\tilde{\eta}(k,t) = c_1(k)e^{-i\Omega^{(1)}t} + c_2(k)e^{-i\Omega^{(2)}t} \tag{100}$$

for surface elevation at time t, where (cf. Equation (18))

$$c_n(k) = a_n(k)\frac{k}{\Omega^{(n)}}\left\{A\cosh[kh] - B\frac{\kappa}{k}\sinh[kh] - A\cosh[\kappa h] + B\sinh[\kappa h]\right\}, \tag{101}$$

and

$$\tilde{\eta}(k,t) = \frac{1}{2\pi}\int_{-\infty}^{\infty} dx\, e^{-ikx}\eta(x,t)\,. \tag{102}$$

If the initial surface profile is $\tilde{\eta}(k, t = 0)$, then

$$\tilde{\eta}(k,t=0) = c_1 + c_2 \tag{103}$$

should hold. Similarly, given the initial vertical velocity profile $\tilde{\eta}_t(k, t = 0)$ we have

$$\tilde{\eta}_t(k,t=0) = -i\Omega^{(1)}c_1 - i\Omega^{(2)}c_2 \tag{104}$$

From this we get for the coefficients c_1 an c_2

$$c_1 = \frac{i\tilde{\eta}_t - \Omega^{(2)}\tilde{\eta}}{\Omega^{(1)} - \Omega^{(1)}} \tag{105}$$

$$c_2 = \frac{i\tilde{\eta}_t - \Omega^{(1)}\tilde{\eta}}{\Omega^{(2)} - \Omega^{(1)}} \tag{106}$$

This allows one to solve the initial value problem within the limits of the approximation sketched above. On the other hand, such an approximation is completely equivalent with a second order differential equation for the surface elevation

$$\frac{\partial^2\tilde{\eta}}{\partial t^2} + i(\Omega^{(1)}(k) + \Omega^{(2)}(k))\frac{\partial\tilde{\eta}}{\partial t} - \Omega^{(1)}(k)\Omega^{(2)}(k)\tilde{\eta} = 0 \tag{107}$$

As an application of Equations (100)–(107), a narrow initial Gaussian profile (blue line) encompassing both propagating modes and over-damped modes is chosen (cf. Figure 19). Time evolution can be seen on the displayed profiles with different colours.

It is seen that the two peaks develop and radiate off symmetrically due to the propagating modes. Since there is no initial velocity, the peaks are in the same weight. Gradually, the Gaussian wave gives way to a much broader Gaussian shape profile, composed of non-propagating over-damped modes (yellow line). It is worth mentioning that in this example over-damped modes have a much smaller damping rate than the propagating ones. Therefore, the contributions of the propagating modes, the peaks, decay, and the longer living over-damped mode content of the initial profile becomes visible.

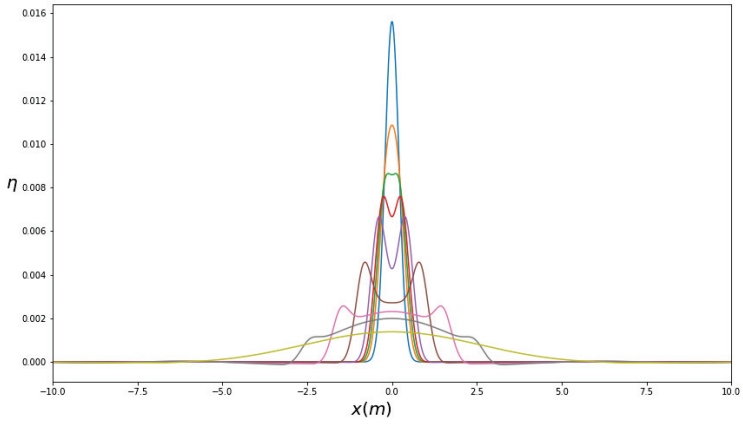

Figure 19. Time evolution of an initial Gaussian wave for glycerin at $p = 0.001 (h = 5.04$ cm) presented. Time values are t = 0., 0.3, 0.4, 0.5, 0.7, 1.4, 2.5, 4, and 10 s. A slim initial Gaussian wave (blue line) containing both propagating modes and over-damped modes spreads outwards and gradually diminishes and leaves behind a broader Gaussian shape profile due to non-propagating modes at long wavelengths (yellow line).

7. Conclusions

Linear viscous capillary-gravity waves were studied in a channel of constant depth, without restricting the parameters. The resulting dispersion relation is published for the first time. We explored all the modes numerically. Modes were labelled by horizontal wave number K, a continuous parameter, and vertical wave number Q, a discrete, complex quantity. We found that there were always infinitely many non-propagating (over-damped) modes. Propagation can only occur in the two modes with the smallest decay. In a sufficiently thin layer no propagation occurs at all. When increasing layer thickness, a bifurcation occurs, which shows up in the plot of imaginary parts of frequencies, such as a collision of the lowest lying branches of modes. After that collision, at increasing wave numbers, one can observe a merging and a subsequent split of these branches. The wave number range of the merged section frequencies have a non-zero real part (propagation). We stress that even at those depths where propagation becomes possible, propagation at very low and very high wave numbers is still prohibited. The over-damping at large wave numbers is already known [21,37]. The over-damping at small wave numbers has been discussed in Section 2.4. This is due to the fact that by increasing the wavelength, the restoring force (due to gravity) does not change, but the friction increases significantly. We also determined the minimal layer thickness necessary for wave propagation. Further, we studied surface motion. Assuming a monochromatic wave propagating to the positive x direction, we found that a surface particle in a viscous fluid could rotate both clockwise or counterclockwise, depending on the wave number. We also demonstrated the propagation or non-propagation of waves in a few cases. In order to illustrate that both positive, zero, or even negative group velocities can occur, the beat of two nearby wave numbers was displayed at a few consecutive time instants. Finally, with the assumption that the effect of fast decaying high lying branches was negligible, we kept the lowest two modes and formulated the solution of the initial value problem of surface motion in wave number space. As an application, the time evolution of a narrow initial Gaussian surface elevation with zero velocity was studied and a radiation of propagating modes in the form of two oppositely travelling bumps was observed. A slowly decaying wide Gaussian was left behind, consisting of large wavelength non-propagating modes.

It is remarkable how many interesting phenomena occur in this simple setup. It is an intriguing question what happens in the presence of an elastic surface at finite fluid depth, since two propagation modes, a capillary mode and a dilational mode, exist in deep water [23].

It is a natural question whether and how these results can have practical applications. As we already noted, in water most of the phenomena discussed are unobservable, because its viscosity is small and surface tension is large. In thick oils, however, these phenomena might be observed. For actual applications (industrial, or perhaps biological) one has to consider thin layers, but then other surface effects, such as pollution or surface elasticity, should be included, as well. It is tempting to think of the effect of the surfactant because they clearly decrease surface tension and with that μ. However, with surfactants a wealth of new phenomena appear, e.g., the possibility of a dilational wave due to the presence of surface elasticity and interplay between this propagating mode with capillary waves (cf. [21,23,47]). Such phenomena are certainly not covered by the current paper.

Another potential application might be in geology (lava flows, glaciers) with especially large viscosity or planetology with different g parameters. In the first case, however, many other effects can be important, too, so the results of the present work could be used as the order of magnitude estimates at best. In case of other planets, a larger g decreases μ, since it is proportional to $g^{-1/6}$, but at the same time parameter p is decreased, so an even thinner fluid layer (or larger viscosity) is necessary to prevent wave propagation, than in Earth. However, the minimal layer thickness was determined numerically, so it is not straightforward to predict the effect of changing g. It may happen that under suitable planetary circumstances the minimal layer thickness for some fluid that is present in abundance will be significantly larger than that for water on Earth.

Author Contributions: Conceptualization, A.G. and G.B.; methodology, A.G. and G.B.; formal analysis, A.G. and G.B.; investigation, A.G. and G.B.; writing—original draft preparation, A.G. and G.B.; writing—review and editing, A.G. and G.B.; visualization, A.G. and G.B.; supervision, G.B. All authors have read and agreed to the published version of the manuscript.

Funding: This research received no external funding.

Acknowledgments: This research was supported by the Ministry of Culture and Innovation and the National Research. A.G. greatly acknowledges the support from Stipendium Hungaricum. We are indebted to our reviewers for their many helpful comments and suggestions.

Conflicts of Interest: The authors declare no conflict of interest.

References

1. Naeser, H. The Capillary Waves' Contribution to Wind-Wave Generation. *Fluids* **2022**, *7*, 73. [CrossRef]
2. Berhanu, M. Impact of the dissipation on the nonlinear interactions and turbulence of gravity-capillary waves. *Fluids* **2022**, *7*, 137. [CrossRef]
3. Gnevyshev, V.; Badulin, S. Wave patterns of gravity–capillary waves from moving localized sources. *Fluids* **2020**, *5*, 219. [CrossRef]
4. Bongarzone, A.; Gallaire, F. Numerical estimate of the viscous damping of capillary-gravity waves: A macroscopic depth-dependent slip-length model. *arXiv* **2022**, arXiv:2207.06907.
5. Behroozi, F.; Smith, J.; Even, W. Effect of viscosity on dispersion of capillary–gravity waves. *Wave Motion* **2011**, *48*, 176–183. [CrossRef]
6. Lu, D.; Ng, C.O. Interfacial capillary–gravity waves due to a fundamental singularity in a system of two semi-infinite fluids. *J. Eng. Math.* **2008**, *62*, 233–245. [CrossRef]
7. Denner, F.; Gounsetti, P.; Zaleski, S. Dispersion and viscous attenuation of capillary waves with finite amplitude. *HAL* **2017**, *226*, 1229–1238. [CrossRef]
8. Shen, L.; Denner, F.; Morgan, N.; van Wachem, B.; Dini, D. Marangoni effect on small-amplitude capillary waves in viscous fluids. *Phys. Rev. E* **2017**, *96*, 053110. [CrossRef]
9. Kim, N.; Debnath, L. Motion of a buoy on weakly viscous capillary gravity waves. *Int. J. Nonlinear Mech.* **2000**, *35*, 405–420. [CrossRef]
10. Lu, D.Q. Analytical solutions for the interfacial viscous capillary-gravity waves due to an oscillating Stokeslet. *J. Hydrodyn.* **2019**, *31*, 1139–1147. [CrossRef]
11. Young, I.R.; Babanin, A.V. Spectral distribution of energy dissipation of wind-generated waves due to dominant wave breaking. *J. Phys. Oceanogr.* **2006**, *36*, 376–394. [CrossRef]

12. Babanin, A.; Young, I. Two-phase behaviour of the spectral dissipation of wind waves. In Proceedings of the 5th International Symposium Ocean Wave Measurement and Analysis, Madrid, Spain, 3–7 July 2005.
13. Sutherland, B.R.; Balmforth, N.J. Damping of surface waves by floating particles. *Phys. Rev. Fluids* **2019**, *4*, 014804. [CrossRef]
14. Sutherland, B.R. Finite-amplitude internal wavepacket dispersion and breaking. *J. Fluid Mech.* **2001**, *429*, 343–380. [CrossRef]
15. Babanin, A.V.; Tsagareli, K.N.; Young, I.; Walker, D.J. Numerical investigation of spectral evolution of wind waves. Part II: Dissipation term and evolution tests. *J. Phys. Oceanogr.* **2010**, *40*, 667–683. [CrossRef]
16. Lamb, H. *Hydrodynamics*; Cambridge University Press: Cambridge, UK, 1924.
17. Ermakov, S.; Sergievskaya, I.; Gushchin, L. Damping of gravity-capillary waves in the presence of oil slicks according to data from laboratory and numerical experiments. *Izv. Atmos. Ocean. Phys.* **2012**, *48*, 565–572. [CrossRef]
18. Rajan, G.K. A three-fluid model for the dissipation of interfacial capillary-gravity waves. *Phys. Fluids* **2020**, *32*, 122121. [CrossRef]
19. Rajan, G.K. Damping rate measurements and predictions for gravity waves in an air–oil–water system. *Phys. Fluids* **2022**, *34*, 022113. [CrossRef]
20. Kalinichenko, V. Standing Gravity Waves on the Surface of a Viscous Liquid. *Fluid Dyn.* **2022**, *57*, 891–899. [CrossRef]
21. Rajan, G.K. Solutions of a comprehensive dispersion relation for waves at the elastic interface of two viscous fluids. *Eur. J. Mech. B Fluids* **2021**, *89*, 241–258. [CrossRef]
22. Sergievskaya, I.; Ermakov, S. Damping of gravity–capillary waves on water surface covered with a visco-elastic film of finite thickness. *Izv. Atmos. Ocean. Phys.* **2017**, *53*, 650–658. [CrossRef]
23. Earnshaw, J.; McLaughlin, A. Waves at liquid surfaces: Coupled oscillators and mode mixing. *Proc. R. Soc. Lond. Ser. A Math. Phys. Sci.* **1991**, *433*, 663–678.
24. Lucassen-Reynders, E.; Lucassen, J. Properties of capillary waves. *Adv. Colloid Interface Sci.* **1970**, *2*, 347–395. [CrossRef]
25. Denner, F. Frequency dispersion of small-amplitude capillary waves in viscous fluids. *Phys. Rev. E* **2016**, *94*, 023110. [CrossRef]
26. Shen, L.; Denner, F.; Morgan, N.; van Wachem, B.; Dini, D. Capillary waves with surface viscosity. *J. Fluid Mech.* **2018**, *847*, 644–663. [CrossRef]
27. Sauleda, M.L.; Hsieh, T.L.; Xu, W.; Tilton, R.D.; Garoff, S. Surfactant spreading on a deep subphase: Coupling of Marangoni flow and capillary waves. *J. Colloid Interface Sci.* **2022**, *614*, 511–521. [CrossRef]
28. Delgado-Buscalioni, R.; Chacon, E.; Tarazona, P. Hydrodynamics of nanoscopic capillary waves. *Phys. Rev. Lett.* **2008**, *101*, 106102. [CrossRef]
29. Bühler, O. *Waves and Mean Flows*; Cambridge University Press: Cambridge, UK, 2014.
30. Rajan, G.K.; Henderson, D.M. The linear stability of a wavetrain propagating on water of variable depth. *SIAM J. Appl. Math.* **2016**, *76*, 2030–2041. [CrossRef]
31. Sergievskaya, I.; Ermakov, S.; Lazareva, T.; Guo, J. Damping of surface waves due to crude oil/oil emulsion films on water. *Mar. Pollut. Bull.* **2019**, *146*, 206–214. [CrossRef]
32. Sergievskaya, I.; Ermakov, S. A phenomenological model of wave damping due to oil films. In Proceedings of the Remote Sensing of the Ocean, Sea Ice, Coastal Waters, and Large Water Regions 2019, Strasbourg, France, 9–10 September 2019; Volume 11150, pp. 153–158.
33. Henderson, D.M.; Segur, H. The role of dissipation in the evolution of ocean swell. *J. Geophys. Res. Ocean.* **2013**, *118*, 5074–5091. [CrossRef]
34. Henderson, D.; Miles, J. Surface-wave damping in a circular cylinder with a fixed contact line. *J. Fluid Mech.* **1994**, *275*, 285–299. [CrossRef]
35. Henderson, D.M. Effects of surfactants on Faraday-wave dynamics. *J. Fluid Mech.* **1998**, *365*, 89–107. [CrossRef]
36. Le Meur, H.V. Derivation of a viscous Boussinesq system for surface water waves. *Asymptot. Anal.* **2015**, *94*, 309–345. [CrossRef]
37. Armaroli, A.; Eeltink, D.; Brunetti, M.; Kasparian, J. Viscous damping of gravity-capillary waves: Dispersion relations and nonlinear corrections. *Phys. Rev. Fluids* **2018**, *3*, 124803. [CrossRef]
38. Hunt, J. The viscous damping of gravity waves in shallow water. *Houille Blanche* **1964**, *6*, 685–691. [CrossRef]
39. Sanochkin, Y.V. Viscosity effect on free surface waves in fluids. *Fluid Dyn.* **2000**, *35*, 599–604. [CrossRef]
40. Lucassen, J. Longitudinal capillary waves. Part 1.—Theory. *Trans. Faraday Soc.* **1968**, *64*, 2221–2229. [CrossRef]
41. Kramer, L. Theory of light scattering from fluctuations of membranes and monolayers. *J. Chem. Phys.* **1971**, *55*, 2097–2105. [CrossRef]
42. Biesel, F. Calculation of wave damping in a viscous liquid of known depth. *Houille Blanche* **1949**, *4*, 630–634. [CrossRef]
43. Baldi, P.; Toland, J.F. *Steady Periodic Water Waves under Nonlinear Elastic Membranes*; De Gruyter: Berlin, Germany, 2011.
44. Baldi, P.; Toland, J.F. Bifurcation and secondary bifurcation of heavy periodic hydroelastic travelling waves. *Interfaces Free Boundaries* **2010**, *12*, 1–22. [CrossRef]
45. Toland, J.F.; Jones, M. The bifurcation and secondary bifurcation of capillary-gravity waves. *Proc. R. Soc. Lond. A Math. Phys. Sci.* **1985**, *399*, 391–417.
46. Jones, M.T.J. Symmetry and the bifurcation of capillary-gravity waves. *Arch. Ration. Mech. Anal.* **1986**, *96*, 29–53. [CrossRef]
47. Brown, S.; Triantafyllou, M.; Yue, D. Complex analysis of resonance conditions for coupled capillary and dilational waves. *Proc. R. Soc. Lond. Ser. A Math. Phys. Eng. Sci.* **2002**, *458*, 1167–1187. [CrossRef]

48. Constantin, A.; Varvaruca, E. Steady periodic water waves with constant vorticity: Regularity and local bifurcation. *Arch. Ration. Mech. Anal.* **2011**, *199*, 33–67. [CrossRef]
49. Martin, C.I. Local bifurcation for steady periodic capillary water waves with constant vorticity. *J. Math. Fluid Mech.* **2013**, *15*, 155–170. [CrossRef]

fluids

MDPI

Article

Compressible and Viscous Effects in Transonic Planar Flow around a Circular Cylinder—A Numerical Analysis Based on a Commercially Available CFD Tool

Jana Hoffmann * and Daniel A. Weiss

Institute of Thermal and Fluid Engineering, University of Applied Sciences and Arts Northwestern Switzerland, Klosterzelgstrasse 2, 5210 Windisch, Switzerland; daniel.weiss@fhnw.ch
* Correspondence: jana.hoffmann@fhnw.ch

Abstract: Transonic planar flows around a circular cylinder are investigated numerically for laminar and turbulent flow conditions with Reynolds numbers of $50 \leq Re_D \leq 300$ and $8890 \leq Re_D \leq 80{,}000$ and free stream Mach numbers in the range of $0.2 \leq Ma_\infty \leq 2$. A commercially available CFD tool is used and validated for this purpose. The results show that the flow phenomena occurring can be grouped into eight regimes. Compared to the incompressible flow regimes, several new phenomena can be found. In contrast, at higher Ma_∞ of $0.6 \leq Ma_\infty \leq 0.8$ vortices in the wake of the cylinder are suppressed for $Re_D = 50$. In some cases, $Ma_\infty = 0.8$ and $Re_D \geq 300$, λ-shocks are formed in the near cylinder wake. For supersonic Ma_∞, two different phenomena are observed. Beside the well-known oblique and detached shocks, for $50 \leq Re_D \leq 300$ a wake with instabilities is formed downstream of the cylinder. Furthermore, the temporal mean drag coefficient $\overline{C}_D$, the Strouhal number Str, as well as the critical Mach number Ma_{crit} are calculated from the simulation results and are interpreted.

Keywords: transonic flow; circular cylinder; Kármán vortex street; Computational Fluid Dynamics (CFD); shock waves; tangential discontinuity; Laval nozzle

Citation: Hoffmann, J.; Weiss, D.A. Compressible and Viscous Effects in Transonic Planar Flow around a Circular Cylinder—A Numerical Analysis Based on a Commercially Available CFD Tool. *Fluids* **2023**, *8*, 182. https://doi.org/10.3390/fluids8060182

Academic Editors: Vasily Novozhilov, Cunlu Zhao and D. Andrew S. Rees

Received: 27 April 2023
Revised: 6 June 2023
Accepted: 9 June 2023
Published: 14 June 2023

1. Introduction

The flow around a circular cylinder is encountered in many engineering applications as well as in nature and in fundamental research. Some examples are the air flow around a cooling tower, as well as missiles and aircrafts in the transonic regime. In transonic flows and fluid dynamical situations in general, a variety of typical phenomena, such as shock waves, vortices, boundary layers, flow separation and shear layers, arise. Studying the interaction of those phenomena is of large interest in fluid–structure interactions, because resonance frequencies can be excited by flow instabilities. The question arises as to what frequency is triggered by the flow around a cylinder, which could provoke an oscillation. In dimensionless terms, this means that the Strouhal number Str becomes a function not only of the Reynolds number Re_D, but also of the Mach number Ma_∞. In practical situations embedded in a larger project context, where questions like the mentioned one arise, one often does not have the time nor the resources to develop one's own numerical tool for simulation and calculation. Rather, one has to refer to methods and tools available on the market; that is why the investigation described here is based on a commercially available CFD tool. It is clear, though, that such a tool has to be checked appropriately before the corresponding findings can be used.

There are various studies describing the flow phenomena occurring in incompressible flow. For small Reynolds numbers in the range of $80 \leq Re_D \leq 300$, a Kármán vortex street is formed in the wake of the cylinder described by Schlichting and Gersten [1]. Although the flow around a circular cylinder has received a lot of attention in recent decades, very few experimental and numerical studies are available about the compressible and in particular transonic flow around a circular cylinder. One of the reasons might be the difficulties

in performing experiments of simple flow situations such as the planar flow around a circular cylinder. However, planar aerodynamical investigations are also of interest, as they allow one, for example, to estimate in a simplified manner the force on a body in a surrounding transonic flow. The most important experimental studies and their findings are summarised below.

Macha [2] performed wind tunnel tests in order to determine the drag coefficient $\overline{C}_\mathrm{D}$ for a Reynolds number range of $5 \times 10^4 \leq Re_D \leq 8.7 \times 10^6$ and a Mach number range of $0.2 \leq Ma_\infty \leq 1.4$. One of the most important findings is the reduction in $\overline{C}_\mathrm{D}$ from $Ma_\infty = 0.7$ to 0.8, caused by the formation of shock waves. In addition, Murthy and Rose [3] performed a series of wind tunnel tests with $0.25 \leq Ma_\infty \leq 1.2$ and $3 \times 10^4 \leq Re_D \leq 5 \times 10^5$. The increase in $\overline{C}_\mathrm{D}$, as Ma_∞ reaches sonic conditions and agrees with the findings of Macha [2]. Furthermore, it was found that the detectable vortex shedding ceases at $Ma_\infty \geq 0.9$. The ranges $0.4 \leq Ma_\infty \leq 0.85$ and $1.7 \times 10^5 \leq Re_D \leq 3.4 \times 10^5$ were investigated by Rodriguez [4] using a wind tunnel. It was found that the coupling between the near wake and the vortex street increases with increasing Ma_∞. As soon as local regions of the flow reach sonic conditions and λ shocks occur, the coupling between the vortex street and the near wake is cut off. The upstream flow field is now independent of the vortex street. In addition, the Strouhal number Str is approximately 0.2, except for a rise when the quasi-steady regime is reached. In addition, the drag and lift coefficients, C_D and C_L, were calculated from the pressure measurements. Ackerman et al. [5] experimentally investigated time-resolved pressure distributions at $0.1 \leq Ma_\infty \leq 0.9$ and $Re_D = 6.83 \times 10^5$. From these measurements, the surface pressure fluctuations, $\overline{C}_\mathrm{D}$, Str and the occurring flow regimes were evaluated. For $Ma_\infty = 0.4$, local regions of flow around the cylinder reach sonic conditions, but only on one side of the cylinder at a time. The flow enters the intermittent shock wave regime. As Ma_∞ increases beyond 0.4, $\overline{C}_\mathrm{D}$ increases. The region downstream of the cylinder, in which the vortices are formed, shortens. Beyond around $Ma_\infty = 0.65$, the flow enters the permanent shock wave regime and $\overline{C}_\mathrm{D}$ decreases. Once the flow enters the wake shock wave regime below $Ma_\infty = 0.8$, the vortex formation region becomes elongated. A normal shock grows at the point of vortex roll up and $\overline{C}_\mathrm{D}$ increases. Nagata et al. [6] used a low-density wind tunnel with time-resolved Schlieren visualisations, pressure and force measurements, in order to characterise the flow for $1000 \leq Re_D \leq 5000$ and $0.1 \leq Ma_\infty \leq 0.5$. The trend of the Ma_∞ effect on the flow field, Str and the maximum width of the recirculation change at approximately $Re_D = 3000$. Str increases as Re_D increases and the increment becomes larger as Ma_∞ increases. For $Ma_\infty < 0.3$, Str is independent of Ma_∞. For $Re_D \leq 3000$ and $Re_D \geq 4000$ at $Ma_\infty > 0.3$, Str decreases and increases, respectively. Furthermore, it is observed that $\overline{C}_\mathrm{D}$ increases as Ma_∞ or Re_D increase. Gowen and Perkins [7] measured the pressure distribution around a circular cylinder in subsonic and supersonic flows and calculated $\overline{C}_\mathrm{D}$ for $5 \times 10^4 \leq Re_D \leq 10^6$ and $0.3 \leq Ma_\infty \leq 2.9$. It is shown that $\overline{C}_\mathrm{D}$ is not influenced by Re_D under the supersonic conditions investigated.

In addition to the experimental investigations, numerical simulations of the compressible flow around a circular cylinder have been increasingly carried out over the last few decades. Some examples of numerical investigations are described below. Botta [8] integrated the Euler equations numerically to investigate the inviscid flow for $0.38 \leq Ma_\infty \leq 0.98$, that means for a Reynolds number $Re_D \to \infty$. The time-dependent C_D and C_L are evaluated in order to determine Str. Furthermore, the distributions of the vorticity, the entropy deviation, pressure coefficient, as well as the velocity fields are provided. Two transitions over the investigated Ma_∞ range were observed, the transition to a chaotic turbulent regime and from this to a quasi-steady flow. In the range $0.5 \leq Ma_\infty \leq 0.6$, the solution shows a periodic behaviour. Bobenrieth Miserda and Leal [9] performed numerical Detached Eddy Simulations of the unsteady transonic flow at $Ma_\infty = 0.8$ and $Re_D = 500{,}000$, where several complex viscous shock interactions were observed. The frequency of C_L corresponds to the vortex-shedding frequency, whereas the frequency of the C_D characterises the viscous shock interaction. In addition, Xu et al. [10] performed Detached Eddy Simulations for

$Re_D = 2 \times 10^5$ and various Mach numbers $0.85 \leq Ma_\infty \leq 0.98$. Two flow states are found, an unsteady one for $Ma_\infty < 0.9$ and a quasi-steady flow state for $Ma_\infty > 0.9$. The unsteady flow state is characterised by the interaction of moving shock waves, the turbulent boundary layer on the cylinder wall and the vortex shedding in the cylinders near the wake. In the quasi-steady flow state, strong oblique shock waves are formed and the vortex shedding is suppressed. Furthermore, the local supersonic zone, the separation angle and $\overline{C}_\mathrm{D}$ are evaluated and analysed. Hong et al. [11] studied $0.1 \leq Ma_\infty \leq 0.95$ and $Re_D = 2 \times 10^5$ using constrained Large Eddy Simulations. The effects of Ma_∞ on the flow patterns and state variables such as the pressure, the skin friction, C_D and the cylinder surface temperature are studied. Non-monotonic behaviour of the pressure and skin friction distributions are observed with increasing Ma_∞. The minimum mean separation angle occurs at $0.3 \leq Ma_\infty \leq 0.5$. Canuto and Taira [12] performed Direct Numerical Simulations of $20 \leq Re_D \leq 100$ and $0 \leq Ma_\infty \leq 0.5$. The wake is characterised using different lengths and $\overline{C}_\mathrm{D}$, and Str and some examples of the pressure distribution are provided. Furthermore, a stability analysis is performed. It is shown that $\overline{C}_\mathrm{D}$ increases and Str decreases with increasing Ma_∞ for constant Re_D. Xia et al. [13] performed constrained Large Eddy Simulations for $Re_D = 4 \times 10^4$ and $Re_D = 10^6$ and various Mach numbers of $0.5 \leq Ma_\infty \leq 0.95$. The separation angle, $\overline{C}_\mathrm{D}$, the pressure distribution and the skin friction coefficient were evaluated and analysed. Furthermore, the density gradient $|\nabla\rho|$ was used to identify four different flow regimes. Shirani [14] simulated $0.1 \leq Ma_\infty \leq 0.9$ and $10^3 \leq Re_D \leq 8.4 \times 10^6$ solving the two-dimensional time averaged Navier–Stokes equations numerically. The behaviour of the time averages of C_D and C_L and their fluctuation frequencies were evaluated. Matar et al. [15] investigated the real gas flow around a circular cylinder at high Reynolds numbers Re_D and Mach numbers Ma_∞ between 0.7 and 0.9 using wall-resolved implicit Large Eddy Simulations (iLESs). For experimental validation at $Ma_\infty = 0.7$, Background Oriented Schlieren (BOS) visualisations are used. The flow phenomena of a Kármán vortex street, acoustic waves and compression waves are observed. In addition, the Strouhal number Str, the wall pressure and the mean pressure drag coefficients are provided and are compared with literature and URANS simulation results. In addition, Linn and Awruch [16] performed Large Eddy Simulations (LESs) of the two- and three-dimensional flow around a circular cylinder at $Re_D = 500{,}000$ and $Ma_\infty = 0.8$ using various tetrahedron-adapted meshes. The density gradient $|\nabla\rho|$, the streamlines and Q-criterion isosurfaces are used to visualise the flow behaviour. Moreover, the drag and the lift coefficients C_D and C_L, the Strouhal number Str_L, the mean surface pressure coefficient and the angle of the boundary layer separation point are provided.

The present study describes the transonic planar flow around a circular cylinder at conditions Ma_∞ and Re_D where only a few investigations have been carried out (Figure 1). The investigation of the planar situation enables one to analyse the phenomena uncoupled from the influence of potential three-dimensional effects. This investigation gives an overview of the flow phenomena occurring in a wide range of Mach numbers of $Ma_\infty = 0.2$ to 2 and Reynolds numbers of $Re_D = 50$ to 80,000. Within the first few chapters, the fundamentals and the numerical implementation are briefly introduced. The simulations of the compressible flow around a circular cylinder are verified by applying the code used to the flow in a Laval nozzle. For validation, the results obtained for the flow around a cylinder are compared to the results from other authors. Different regimes with phenomena such as shock waves, sound waves, flow separation, vortex shedding, shear layers and tangential discontinuities are identified and some of them are analysed in more detail. To capture the different flow phenomena, different regions of interest are used for the numerical procedure. This investigation focuses on the behaviour in the wake of the cylinder. In addition, the critical Mach number Ma_crit is evaluated and the averaged drag coefficient $\overline{C}_\mathrm{D}$ and the Strouhal number Str are provided. Finally, polar diagrams are presented, that means the time-resolved drag and lift coefficients, C_D and C_L, are plotted as a function of time in a C_D-C_L-diagram, to analyse their phase shift and their frequency ratio.

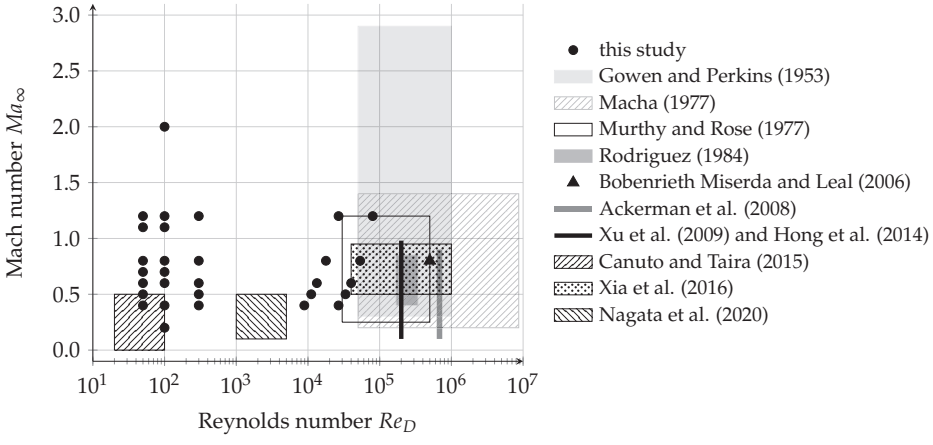

Figure 1. Conditions investigated in previous studies and in this study [2–7,9–13].

2. Fundamentals

Within this chapter, the most important fundamentals such as the governing equations solved in CFD and the dimensionless numbers used within this study are introduced.

2.1. Governing Equations

The three transport equations of mass, momentum and energy are called the Navier–Stokes equations, where only momentum and energy can be transported via conduction in all directions x, y and z. The general transport equation is shown in Equation (1) where φ is the transported property. In Table 1, the transport property φ, the diffusion coefficient Γ_φ and the source, loss and production term S_φ are specialised for the mass, momentum and energy transport equations.

$$\frac{\partial \varphi}{\partial t} = -\nabla \cdot (\varphi \vec{u}) + \nabla \cdot \left(\Gamma_\varphi \nabla \varphi\right) + S_\varphi \tag{1}$$

The terms of Equation (1) can be described in words as follows.

- $\frac{\partial \varphi}{\partial t}$: Accumulation of φ in the control volume.
- $\nabla \cdot (\varphi \vec{u})$: Convective flux of φ across the surfaces of the control volume.
- $\nabla \cdot \left(\Gamma_\varphi \nabla \varphi\right)$: Conductive flux of φ across the surfaces of the control volume.
- S_φ: Production and/or loss of φ in the control volume + external supply of φ in the control volume.

The fluid air is assumed to behave as an ideal gas; thus, the corresponding equation follows

$$p = \rho R T \tag{2}$$

where R denotes the specific gas constant, expressed in $\mathrm{J\,kg^{-1}\,K^{-1}}$ and T the absolute temperature. Turbulence effects are described by means of the Shear Stress Transport (SST) model; see Section 3.1.

Table 1. Specialisation for mass, momentum and energy for the Navier–Stokes equations

	Transport Property φ	**Diffusion Coefficient Γ_φ in $\mathrm{m^2\,s^{-1}}$**	**Source, Loss and Production S_φ**
Mass	Density ρ in $\mathrm{kg\,m^{-3}}$	0	0
Momentum	Specific momentum ρu_i in $\mathrm{N\,s\,m^{-3}}$	Kinematic viscosity ν	$S_{\rho u_i}$ in $\mathrm{N\,m^{-3}}$
Energy	Specific enthalpy h in $\mathrm{J\,m^{-3}}$	Thermal diffusivity α_{th}	S_h in $\mathrm{W\,m^{-3}}$

2.2. Classification of the Flow Regimes

The fluid flow is classified by means of the Reynolds and the Mach numbers Re_D and Ma_∞. The Reynolds number Re_D defined in Equation (3) describes the ratio of inertial forces to viscous forces and is used to predict the flow regime of laminar, transitional or turbulent flow. It is defined using the free stream density ρ_∞ of the fluid, the free stream velocity u_∞, the cylinder diameter D and the free stream dynamic viscosity μ_∞.

$$Re_D = \frac{\rho_\infty \cdot u_\infty \cdot D}{\mu_\infty} \tag{3}$$

For the Reynolds numbers above a critical Reynolds number Re_{crit}, which depends on the flow situation (flow over a flat plate, pipe flow, etc.), the flow becomes turbulent, which means it behaves in a chaotic way and underlies random fluctuations. Nevertheless, it has to be said that Re_{crit} is only a guiding value; there is no abrupt transition from laminar to turbulent at a certain Reynolds number.

The free stream Mach number Ma_∞ is the ratio between the free stream velocity u_∞ and the speed of sound a_∞ in the far field.

$$Ma_\infty = \frac{u_\infty}{a_\infty} \tag{4}$$

According to the local Mach number Ma, the flow is called subsonic if $Ma < 1$, supersonic if $Ma > 1$ and hypersonic if $Ma > 5$. Transonic flows have regions of both types, subsonic and supersonic.

2.3. Further Dimensionless Numbers

The behaviour of the fluid flow can then further be characterised by additional dimensionless numbers, which are described in this chapter.

The Strouhal number Str in Equation (5) describes periodically oscillating flow phenomena using the frequency of the particular oscillation f, the cylinder diameter D and the free stream velocity u_∞.

$$Str = \frac{f \cdot D}{u_\infty} \tag{5}$$

The drag and the lift coefficients C_D and C_L, respectively, are defined in Equations (6) and (7) as the ratio of the particular component of the force acting on the cylinder, drag or lift force, F_D or F_L, and the product of the dynamic pressure $\frac{\rho_\infty}{2} \cdot u_\infty^2$ and the cylinder's front face A.

$$C_D = \frac{F_D}{\frac{\rho_\infty}{2} \cdot u_\infty^2 \cdot A} \tag{6}$$

$$C_L = \frac{F_L}{\frac{\rho_\infty}{2} \cdot u_\infty^2 \cdot A} \tag{7}$$

3. Numerical Simulation

Simulations in the laminar and turbulent regimes have been performed. Figure 2 shows Ma_∞ and Re_D of those simulations. Therefore, the simulations are carried out in groups with constant Reynolds number Re_D or constant cylinder diameter D. The Re_D range of the laminar simulations is chosen in accordance with the Kármán vortex street in order to investigate the influence of the increase in Ma_∞ on the vortices. In addition, two simulations with $Ma_\infty = 0.2$ and 2 at $Re_D = 100$ were performed for validation with Burbeau and Sagaut [17]. The turbulent regimes are chosen with a constant cylinder diameter D in view of an upcoming experimental validation in a transonic wind tunnel.

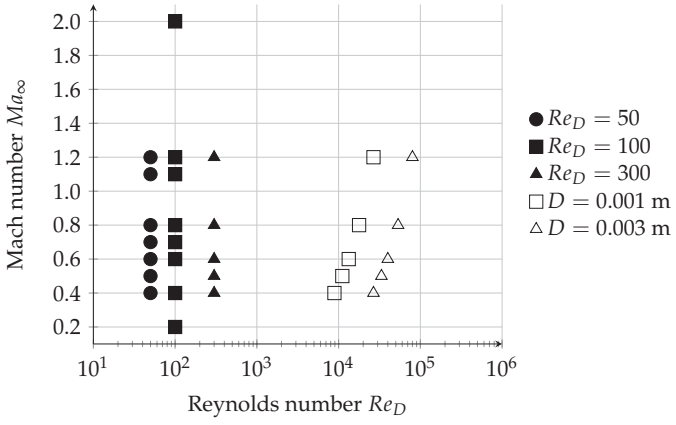

Figure 2. Simulation points at different Mach and Reynolds numbers, Ma_∞ and Re_D, for constant Reynolds number (black) and constant diameter (white).

3.1. Numerical Method and Model

The simulations were performed using the commercial software tool Ansys CFX 19.0. In Ansys CFX, the Navier–Stokes equations are solved using the Element-Based Finite-Volume Method. Depending on the Mach number Ma_∞ and whether the flow is stationary or transient, etc., the partial differential equations that are solved are elliptic, parabolic, hyperbolic or even of mixed-type.

The transport equations are solved in an implicit way. In general, the transient scheme of "Second Order Backward Euler" and the advection scheme of "High Resolution", respectively, are chosen. The "High Resolution" advection scheme is based on the boundedness principles used by Barth and Jesperson [18]. The pressure–velocity coupling proposed by Rhie and Chow [19] and modified by Majumdar [20] is used.

The heat transfer is chosen to be "Total Energy", which is necessary for high-speed flows at flow velocities u near the speed of sound a. Using "Total Energy", the transport equation for total enthalpy h^0 is solved, which is related to the static enthalpy h according to Equation (8).

$$h^0 = h + \frac{1}{2}\vec{u}^2 \tag{8}$$

Turbulence is modelled using the Shear Stress Transport (SST) model. It is a suitable trade-off between quality and computational time. One of its strengths is the accuracy of the prediction of the onset and the amount of flow separation under adverse pressure gradients. In contrast with the Direct Numerical Simulation (DNS), in which the turbulent structures of all length scales are resolved with a fine computational mesh, all length scales are modelled in this turbulence model. For this reason, the flow variables are split into their time-averaged values and their fluctuating components and the Reynolds-Averaged Navier–Stokes (RANS) equations have to be solved. In order to do so, models for the computation of the Reynolds stresses and the Reynolds fluxes are provided. The SST turbulence model was first presented by Menter [21] and combines the advantages of the k-ω turbulence model near the wall and the k-ϵ turbulence model in the bulk flow. Based on the distance of a node to the nearest wall, blending functions are used to ensure a smooth transition between the two models.

Because the near wall formulation determines the accuracy of the wall shear stress, "automatic wall functions" are used. Depending on the y^+-value, switching occurs between the low-Reynolds near wall approach and the wall-function approach, which is logarithmic for higher y^+-values. [22]

3.2. Description of the Computational Domain

Figure 3 shows the computation domain of the cylinder and its surroundings. Different computational domains with different values of $x_{\min}$, $x_{\max}$, $y_{\min}$ and $y_{\max}$ were carried out for the different simulation conditions depending on Re_D and Ma_∞. This leads to various cylinder diameters D.

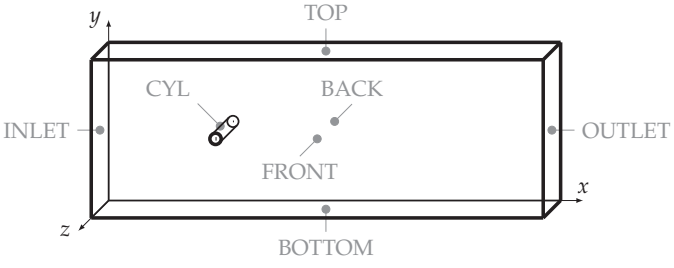

Figure 3. Computational domain with the locations of the boundary conditions in capital letters.

3.3. General Simulation Parameters

The geometries and the meshes were created with Ansys ICEM CFD. The simulations were performed as transient with a steady-state solution as the initial condition. To speed up the solving process, the steady-state solution of the laminar regimes was set up with a rotating cylinder $\Omega = \frac{2 \cdot u_\infty}{D}$ in order to obtain unsteady behaviour in shorter time steps. This idea follows those proposed by Shirani [14] and Braza et al. [23]. Furthermore, simulations with coarser meshes were used as initial conditions, the final simulations were carried out with finer meshes. Three different considerations are made regarding the time step size Δt. Firstly, an estimation of the time step size based on the vortex shedding frequency f assuming $Str \approx 0.21$ is made with one oscillation period being resolved with 16 time steps. Secondly, the time step size is calculated from a mean cell dimension of the free stream according to $\Delta t \sim \frac{\Delta x_{\text{cell}}}{u_\infty}$. Thirdly, the time step size can be calculated using the acoustic Courant number. Since the present work involves transonic conditions with velocities u_∞ close to the speed of sound a_∞, the time step size $\Delta t \sim \frac{\Delta x_{\text{cell}}}{a_\infty}$ is of the same order of magnitude as the previously mentioned one. The time step $\Delta t \sim \frac{\Delta x_{\text{cell}}}{u_\infty}$ was the smallest one in all the simulations; this one was chosen. The time steps Δt of the final simulations lie in the range of micro- to nanoseconds.

3.4. Mesh Generation

Some phenomena of compressible flow are more strongly influenced by the selected flow region or the boundary conditions than others. For this reason, a combined geometry and mesh study was performed to assess and minimise the influence of the mesh and the geometry dimensions. It was carried out for different Mach numbers Ma_∞ and for the Reynolds number of $Re_D = 100$, as well as the constant cylinder diameter of $D = 0.003$ m in an iterative manner. The mesh was refined step by step and the relative deviations of Str, $\overline{C}_{\text{D}}$ and $Ma_{\max}$ were calculated between two meshes. If the relative deviation in these quantities of the respective mesh from the next finer mesh is less than 2.5 %, where most of the deviations are even below 1 %, then the mesh is considered to be sufficiently fine. The mesh quality of each mesh was determined according to the requirements in Table 2, where the minimum and maximum values over all the meshes are listed. Most of the criteria are within the required range, only a few cells exceed the criteria of the mesh expansion factor. Table 3 shows the result of the mesh study with the corresponding domain sizes and the number of cells for each simulation.

The general mesh, which is shown in Figure 4, consists of sixteen mesh blocks with a square O-grid with an overall dimension of $3 \cdot D$ around the cylinder. A second O-grid within the first one was created to better resolve the boundary layer around the

cylinder surface. It is ensured that the y^+-value is $y^+ < 300$ to model the boundary layer with automatic wall function. The y^+-value amounts to $5 < y^+ < 35$ for the turbulent simulations. The z-direction is resolved with one cell; the dimension of this cell is scaled with the smallest cell dimension near the cylinder wall. The cell sizes in the x- and y-directions increase with increasing distance from the cylinder with a maximum growth rate of 1.2 to have a trade-off between computational time and accuracy.

Table 2. Mesh quality requirements based on several criteria and min./max. values of all the meshes.

Criteria	Requirement	Min./Max. Value
Aspect ratio	<1000 "double precision" [24]	1.41 to 140.5
Orthogonal quality (numerical accuracy, robustness)	>1/3 [24], >0.1 [25]	0.72 to 1
Skewness	<0.95 [25]	0 to 0.5
Smoothness	1 to 1.5 [25]	1 to 1.47
Angle	20 to 160 [26]	45 to 134.4
Mesh expansion factor	<1.2	1 to 1.5

Table 3. Size of the computational domain (min. and max. values of x and y) and number of mesh cells for different simulations based on Re_D and Ma_∞.

Re_D	Ma_∞	Range x	Range y	Number of Cells
50	0.4 to 1.1	$-50 \cdot D \leq x \leq 50 \cdot D$	$-50 \cdot D \leq y \leq 50 \cdot D$	323,304
	1.2			1,290,432
100	0.2 to 2.0	$-50 \cdot D \leq x \leq 50 \cdot D$	$-50 \cdot D \leq y \leq 50 \cdot D$	1,290,432
300	0.4 to 0.5	$-50 \cdot D \leq x \leq 50 \cdot D$	$-50 \cdot D \leq y \leq 50 \cdot D$	1,290,432
	0.6 to 0.8	$-25 \cdot D \leq x \leq 100 \cdot D$	$-25 \cdot D \leq y \leq 25 \cdot D$	3,547,380
	1.2	$-50 \cdot D \leq x \leq 50 \cdot D$	$-50 \cdot D \leq y \leq 50 \cdot D$	1,290,432
8890	0.4	$-50 \cdot D \leq x \leq 50 \cdot D$	$-50 \cdot D \leq y \leq 50 \cdot D$	1,307,732
11,100	0.5			
13,300	0.6			
17,800	0.8			
26,700	1.2			
26,700	0.4	$-25 \cdot D \leq x \leq 100 \cdot D$	$-25 \cdot D \leq y \leq 25 \cdot D$	3,547,380
33,400	0.5	$-50 \cdot D \leq x \leq 50 \cdot D$	$-50 \cdot D \leq y \leq 50 \cdot D$	1,307,732
40,000	0.6	$-25 \cdot D \leq x \leq 100 \cdot D$	$-25 \cdot D \leq y \leq 25 \cdot D$	3,547,380
53,400	0.8			
80,000	1.2	$-50 \cdot D \leq x \leq 50 \cdot D$	$-50 \cdot D \leq y \leq 50 \cdot D$	1,307,732

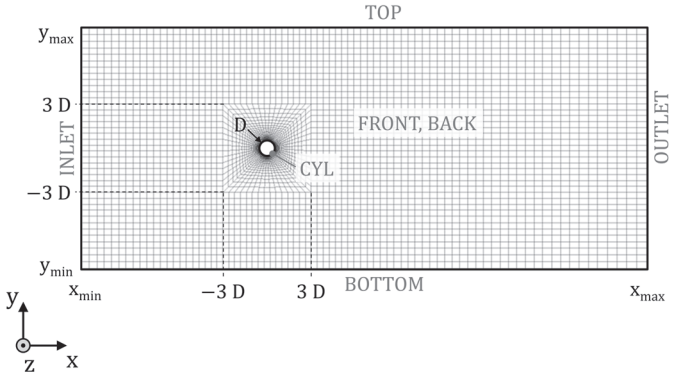

Figure 4. Domain and general mesh showing the dimensions of the mesh blocks and in capital letters the locations of the boundary conditions

3.5. Boundary Conditions

The boundary conditions shown in Table 4 are given separately for $Ma_\infty < 1$ and $Ma_\infty > 1$. The pressures for the subsonic and supersonic simulations were set to $p = 0$ bar(g) and $p = 8$ bar(g), respectively.

Table 4. Boundary conditions for $Ma_\infty < 1$ and $Ma_\infty > 1$; positions of the boundary conditions according to Figure 3.

Position	**Boundary Condition**	
	$\boldsymbol{Ma_\infty < 1}$	$\boldsymbol{Ma_\infty > 1}$
CYL	No slip wall	
FRONT, BACK	Symmetry	
INLET	u_∞, T	p, u_∞, T
OUTLET	p	Outlet
TOP, BOTTOM	Free slip wall	Outlet

4. Verification and Validation

In addition to the mesh and the parametrical study, the numerical procedure was verified and validated for selected cases of planar transonic flow situations. The Laval nozzle was used to analyse the flow phenomenon of the straight shock wave more precisely regarding the numerics. Furthermore, the results were validated with results from other investigations.

4.1. Laval Nozzle for Verification

The planar Laval nozzle with air assumed as ideal gas shown in Figure 5 was simulated for verification. The boundary conditions defined are either Dirichlet or Neumann boundary conditions, as shown in Figure 5. Symmetry boundary conditions were chosen in the direction perpendicular to the drawing plane and on the middle axis of the Laval nozzle, which are basically zero-gradient conditions. Different boundary conditions were specified for the wall in two simulations, no slip ($u = 0\ \mathrm{m\,s^{-1}}$) and free slip in order to analyse the influence of the wall on the flow phenomena. Three different meshes with 3125, 12,500 and 50,000 elements were used to investigate the influence of mesh resolution on the shock, where a sufficient mesh quality is ensured using the criteria listed in Table 2. The solver process is started with the advection schemes "Upwind" and "High Resolution", respectively, for comparison purposes with a maximum number of 10,000 iterations.

One result of the Mach number *Ma* from the CFD simulation of the Laval nozzle described above is shown in Figure 5. The subsonic flow from the inlet is accelerated to a Mach number of around 1.8 along the Laval nozzle. Further downstream follows a shock and a strong reduction of *Ma* to about 0.6. Downstream, the flow is slightly decelerated until it finally reaches the outlet.

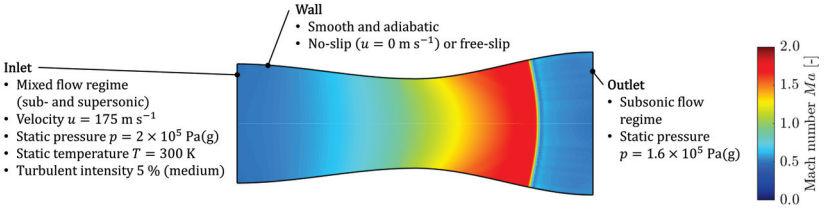

Figure 5. Planar Laval nozzle (length 0.84 m) coloured by the Mach number *Ma* including the boundary conditions for the inlet, the outlet and the wall. The inlet (dimension of 0.14 m) of the Laval nozzle is on the left-hand side; the outlet (dimension of 0.17 m) is on the right-hand side. Only the upper half of the Laval nozzle is simulated resolved with 12,500 elements due to the x-axis symmetry.

In a next step, the behaviour of the Mach number *Ma* along the Laval nozzle is examined in more detail. In order to do so, Figure 6 shows *Ma* along the central axis of the Laval nozzle for different simulation setups with the three different meshes. The result of a simplified calculation is also shown in black colour for comparison. For this calculation, the flow is assumed to be one-dimensional, steady-state, compressible and adiabatic with air as ideal gas and with a shock wave expansion which is infinitesimally small. It is an iterative calculation, whereby the exact shock position of $x = 0.6979$ m is calculated. Figure 6 shows two different curves for each simulation; these are the area-averaged Mach number over the respective position in blue colour and *Ma* evaluated on the central axis of the Laval nozzle in red colour. The reason for this is the better comparability with the one-dimensional calculation. However, due to the two-dimensional simulation, comparability is only guaranteed to a limited extent. It is obvious that at *Ma* on the central axis (red curves) the shock can be depicted more precisely with a finer mesh resolution. In the simulation with "High Resolution" and the free-slip wall, the shock occurs further downstream, which seems plausible. As a result of the higher-order advection scheme, the gradient at the shock position can be depicted better, resulting in a steeper curve. After the decrease of *Ma* as a result of the shock, there is a non-physical undershoot. Compared to a higher-order scheme, the first-order scheme "Upwind" suffers from numerical diffusion. Therefore, the higher-order scheme "High Resolution" should be chosen in order to sufficiently resolve the shocks. In the case of the area-averaged curves, the gradient at the shock position is almost identical for the different mesh resolutions. The reason for that is, as Figure 5 shows, that the shock is not completely straight, it is curved. However, the shock position of the different meshes differs only slightly. Detailed analyses of the flow variables, such as pressure p, temperature T and the Mach number *Ma* show that there are about eight to nine elements needed to resolve the shock. In reality, the extent of shock waves in the stream-wise direction amounts to only a few mean free paths of the molecules, so this must be taken into account.

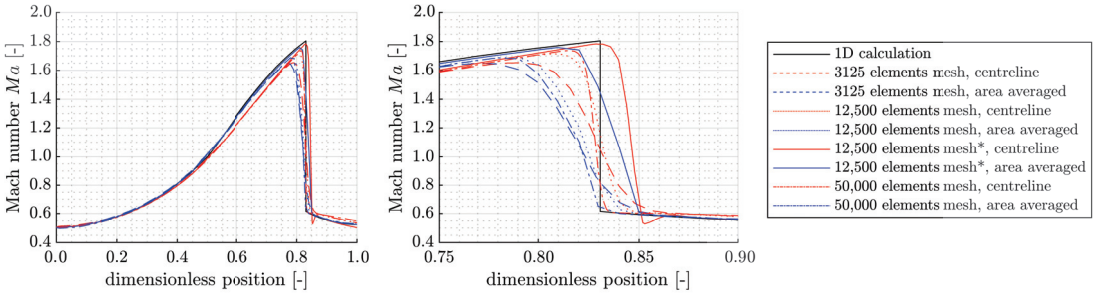

Figure 6. Mach number *Ma* along the planar Laval nozzle from the one-dimensional calculation and the two-dimensional simulation results. Full range (**left**) and zoomed region of interest (**right**). The simulation results indicated with * were performed using a free-slip wall instead of a no-slip wall and an advection scheme of "High Resolution" instead of "Upwind".

4.2. Validation with Literature

In addition to the verification using the Laval nozzle, some points were also simulated based on Ma_∞ and Re_D, for which results from other work [17,27,28] are available. The compressible and the incompressible flow around a planar circular cylinder at $Re_D = 100$ and $Ma_\infty = 0.2$ and the compressible flow at $Re_D = 100$ and $Ma_\infty = 2$ are investigated.

Figure 7a,b show the velocity component u_x of the compressible flow at $Re_D = 100$ and $Ma_\infty = 0.2$, in which the advection schemes "Upwind" and "High Resolution" are compared with each other. The results show that a higher-order advection scheme is necessary for the adequate prediction of the periodic vortex shedding, a so-called Kármán vortex street. In addition, Table 5 shows the time-averaged drag coefficient $\overline{C}_D$ and the Strouhal number *Str* for the incompressible and compressible cases, including a comparison with the literature. A good agreement of $\overline{C}_D$ and *Str* with the literature can be seen with a maximum deviation of approximately 2% and 4%, respectively.

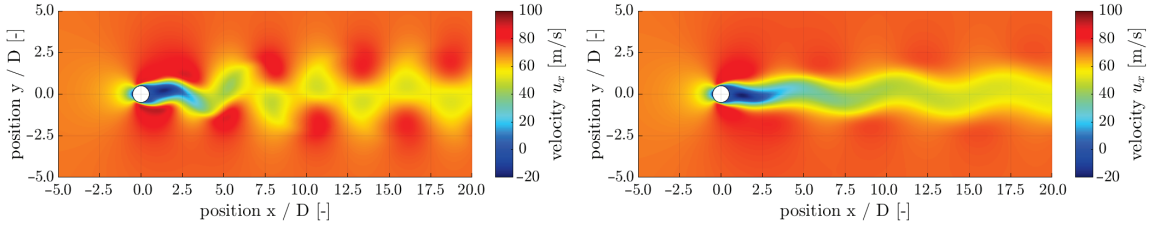

(**a**) (**b**)

Figure 7. Transient result of velocity in *x*-direction u_x at $Re_D = 100$ and $Ma_\infty = 0.2$ with a time step size of 10^{-8} s. (**a**) Advection scheme "High Resolution"; (**b**) Advection scheme "Upwind".

Table 5. Comparison of the Strouhal number *Str* and the time-averaged drag coefficient $\overline{C}_D$ at $Re_D = 100$ and $Ma_\infty = 0.2$ with other studies [17,27,28].

	Compressibility	***Str***	$\overline{C}_D$
This study	incompressible	0.176	1.396
This study	compressible	0.162	1.419
Burbeau and Sagaut [17] and Lesaint and Raviart [27]	incompressible	0.173	1.411
Burbeau and Sagaut [17] and Oden Tinsley et al. [28]	compressible	0.165	1.370

In addition,the supersonic flow at $Re_D = 100$ and $Ma_\infty = 2$ was also considered. For this purpose, the boundary conditions are chosen according to Table 4 . Figure 8a shows

the Mach number Ma distribution, in which the detached shock position corresponds very precisely to that from Burbeau and Sagaut [17] (dashed black line). Figure 8b shows a simulation result with extended flow area in the positive x- and y-axis directions. The symmetry is assumed in the simulation with respect to the x-axis, because the flow in Figure 8b is also symmetric with respect to the x-axis. The flow phenomena at $Re_D = 100$ and $Ma_\infty = 2$ can be clearly seen in Figure 8a,b. A detached shock forms upstream of the cylinder. This detached shock turns into a Mach cone along the shock front with increasing distance in the y-direction. The opening angle of $\alpha = 32°$ from Figure 8b agrees well with the theoretical angle of $\alpha = 30°$ according to Equation (10); for more details, see Section 5.4.

In Figure 8a, a weak reflection of the detached shock at the boundary conditions in the y-direction downstream from around $x/D = 7$ can also be seen. In comparison to Figure 8b, the influence of the boundary condition is clearly visible. For this reason, when simulating the flow around the planar circular cylinder, it must be ensured that the limitation of the flow region in the y-direction is chosen sufficiently. In addition to the detached shock, two oblique shocks form downstream of the cylinder or obliquely away from the cylinder. Analogously to the detached shock, this is followed by an abrupt change or a discontinuity of the flow variables. A wake with a very small velocity $u \approx 0$ forms downstream of the cylinder. This wake is separated from the rest of the flow area by a tangential discontinuity; for more details, see Section 5.1.

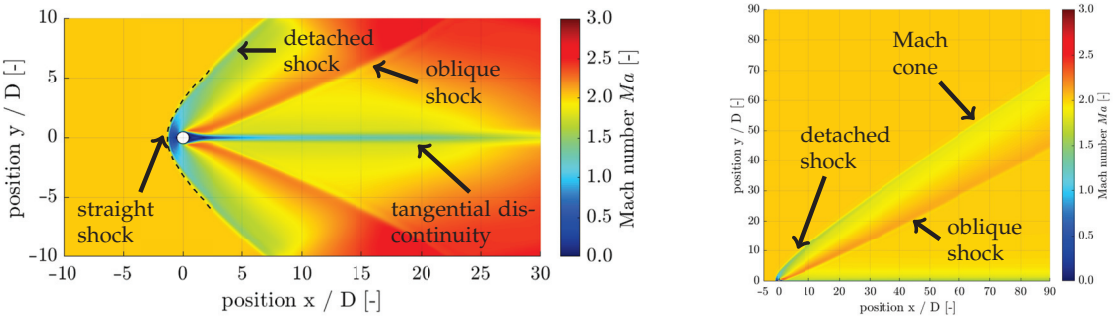

(**a**) (**b**)

Figure 8. Mach number Ma distribution showing the flow phenomena at $Re_D = 100$ and $Ma_\infty = 2$ for two geometries. (**a**) Shock wave position from Burbeau and Sagaut [17] (dashed line); (**b**) Extended geometry.

5. Results and Discussion

In the first subsection of this chapter, the way different flow phenomena are identified is described. The eight flow regimes obtained are then described in a general way and classified, based on Ma_∞ and Re_D. The flow structures of the regimes are discussed in more detail and compared to other authors. After that, the straight and the λ shocks are evaluated. Finally, the critical Mach number Ma_{crit}, the Strouhal number Str, the drag coefficient $\overline{C}_D$ and the polar diagrams are presented.

5.1. Identification of Flow Phenomena

Inspired by the experimental Schlieren flow visualisation techniques, the modulus of the dimensionless density gradient $\frac{D \cdot |\nabla \rho|}{\rho_\infty^0}$ is used to visualise all relevant flow phenomena.

Various shock waves can be observed in compressible flows such as detached shocks, normal shocks, oblique shocks and λ shocks. Shocks are irreversible discontinuities in the flow variables over a few mean free-path lengths of the molecules. If the plane of the discontinuity is perpendicular to the flow or the streamlines, it is a straight shock wave. The streamlines are not deflected and the flow is supersonic upstream of the shock and subsonic downstream. In the case of an oblique shock, however, the streamlines are kinked and the normal component of the velocity is supersonic upstream of the shock and subsonic

downstream. The magnitude of the tangential velocity component is constant across the shock and the flow downstream of the shock can be either subsonic or supersonic. In addition to the density gradient, shocks can be identified by a discontinuous change in other flow variables. An example is the Mach number Ma shown in Figure 9a, which decreases over the detached shock as well as the oblique shock (Figure 10). Across the detached shock, the flow regime changes from supersonic to subsonic and over the oblique shock from supersonic to a lower velocity in the supersonic range. The streamlines in Figure 9a are kinked across the shock waves away from the x-axis, but not on the symmetry axis in the y-direction, where the detached shock is normal to the streamlines. Furthermore, the pressure p increases across both the detached and the oblique shocks, as shown in Figure 9c. As can be seen in Figure 9d, there is a discontinuous reduction in the total pressure p^0 across the shocks.

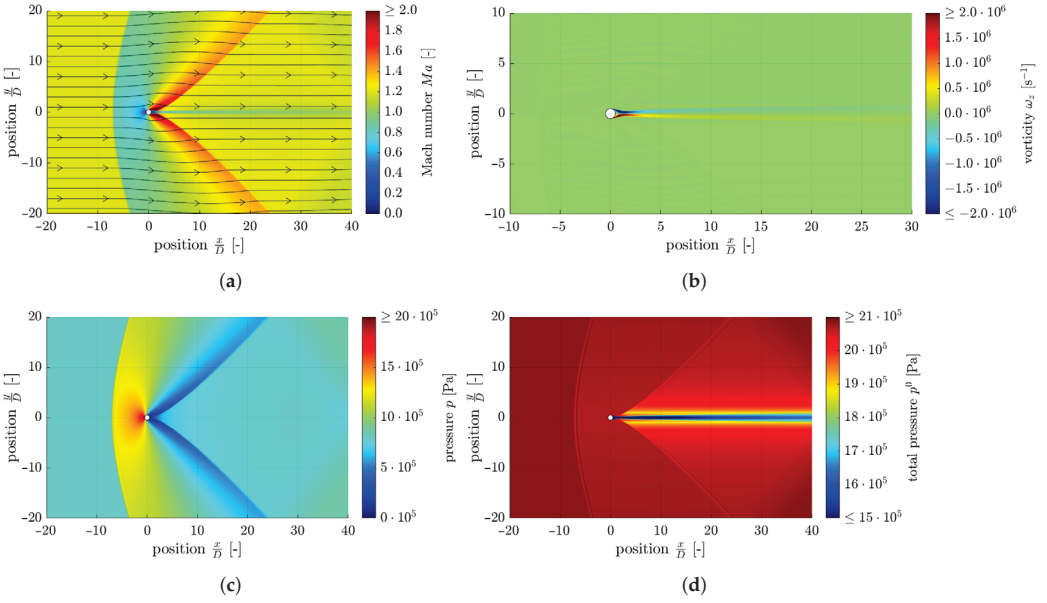

Figure 9. Shocks and tangential discontinuities at $Ma_\infty = 1.2$ and $Re_D = 26{,}700$ visualised by Ma, ω_z, p and p^0. (**a**) Mach number Ma field with streamlines in black colour; (**b**) Vorticity component ω_z distribution; (**c**) Pressure p distribution; (**d**) Total pressure p^0 distribution.

In the wake of the cylinder, a detachment forms at $Ma_\infty = 1.2$ and $Re_D = 26{,}700$, which is characterised by two converging shear layers further downstream of the cylinder. There is no mass flow across this tangential discontinuity (Figure 10) and because of that the normal velocity component on both sides of the tangential discontinuity must be zero. Therefore, the streamlines are parallel in the area of the tangential discontinuity, which can be seen in Figure 9a. As shown in Figure 9a, there is a discontinuity in the Mach number Ma and in the tangential velocity component. Due to this change in the tangential velocity, a theoretically diverging vorticity ω (see Equation (9)) results, which can be used to identify the tangential discontinuity. Due to the mesh resolution, which is finite, there is no abrupt discontinuity in the tangential velocity component; however, the value of the corresponding vorticity component still becomes very large.

$$\vec{\omega} = \vec{\nabla} \times \vec{u} \tag{9}$$

Across such a tangential discontinuity, the pressure p, however, must be continuous (see Figure 9c). The total pressure p^0 (Figure 9d) in turn may be and in general will be discontinuous, as can be concluded from the momentum balance.

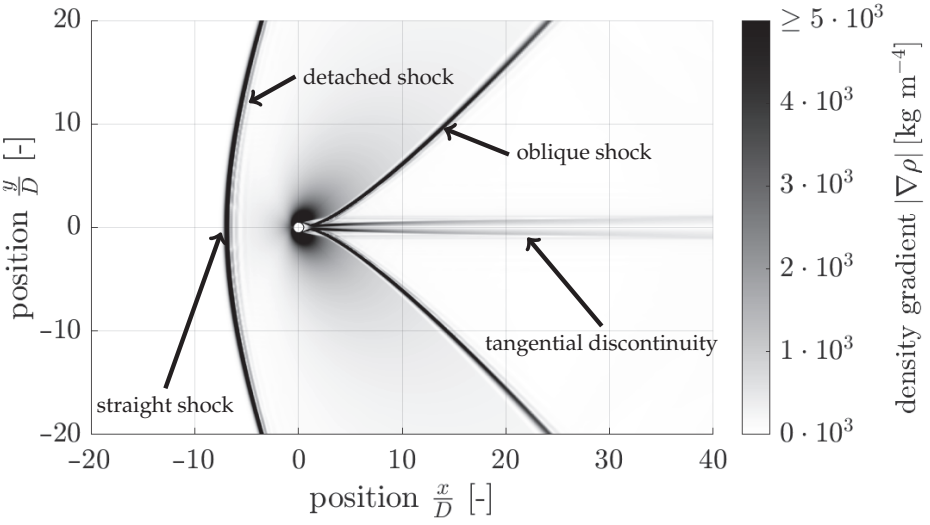

Figure 10. Density gradient $|\nabla\rho|$ at $Ma_\infty = 1.2$ and $Re_D = 26,700$ showing the different phenomena.

The question arises, how the vortices can be distinguished from other flow phenomena. The z-component of the vorticity ω_z is shown in Figure 11a, whereby the left-turning and right-turning vortices have a different sign. In contrast to the tangential discontinuity, the streamlines cross areas of different orders of magnitude of the vorticity. Vortices are rather smeared out compared to shocks and tangential discontinuities. In addition, vortices are decently visible in the swirling strength ζ, as shown in Figure 11b (the swirling strength ζ denotes the imaginary part of the pair of complex-conjugated eigenvalues of the velocity gradient tensor. Thus, in the case where the velocity gradient tensor is symmetric, the swirling strength is zero).

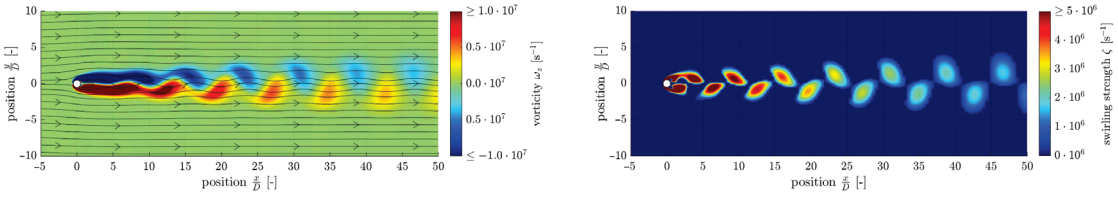

(**a**) (**b**)

Figure 11. Shedding vortices at $Ma_\infty = 0.4$ and $Re_D = 50$ visualised by ω_z and ζ; (**a**) Vorticity component ω_z; (**b**) Swirling strength ζ

5.2. Classification of Flow Regimes

The eight flow regimes, denoted by (a) to (h), are shown in Figure 12 and compared to the incompressible regimes from Schlichting and Gersten [1]; incompressible flow is assumed as $Ma_\infty < 0.3$. The occurring compressible regimes (a) to (c) at $Re_D = 50$ to 100 and $0.2 \leq Ma_\infty \leq 0.8$ are similar to the incompressible regimes. It is observed that subsonic Ma_∞ of $0.6 \leq Ma_\infty \leq 0.8$ suppress the vortices in the wake of the cylinder for $Re_D = 50$, whereas the incompressible flow regime at $Re_D = 50$ shows an onset of the Kármán vortex street. Increasing Re_D with subsonic $0.4 \leq Ma_\infty \leq 0.6$ and $Re_D \geq 300$ leads to regime (d), which is similar to the incompressible subcritical regime. In contrast, sound wave propagation is shown in compressible flow. The regimes (e) to (h) differ from the incompressible regimes, because the Ma_∞ is far away enough from the incompressible flow. For $Ma_\infty = 0.8$ and $Re_D \geq 300$, λ shocks as well as vortices are formed. In the

supersonic regimes, it is observed that a detached shock upstream of the cylinder and two oblique shocks downstream of the cylinder are formed. In addition, for $50 \leq Re_D \leq 300$ and $1.1 \leq Ma_\infty \leq 2$, regime (g) occurs and vortices in the wake of the cylinder are formed. For higher Mach numbers Ma_∞, the wake of the cylinder is steady and symmetric; this corresponds to regime (h).

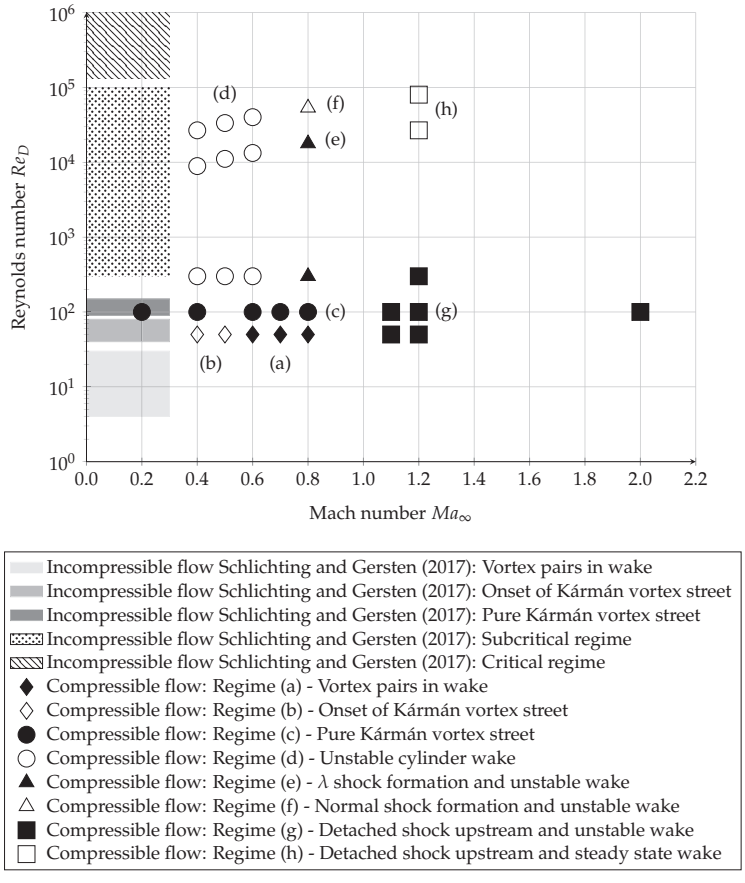

Figure 12. Flow regimes based on Re_D and Ma_∞ occurring in the compressible flow compared to the results of Schlichting and Gersten [1].

5.3. In-Depth Analysis of the Eight Flow Regimes

Basically, the dimensionless density gradient $\frac{D \cdot |\nabla \rho|}{\rho_\infty^0}$ consists of the density gradient $|\nabla \rho|$ multiplied with the cylinder diameter D divided by an averaged total free stream density ρ_∞^0. Typical results including only the most interesting areas of the simulation domain are shown for the different regimes in Figures 13–21.

Regime (a) in Figure 13 belongs to a steady symmetric separation downstream of the cylinder. The flow detaches symmetrically on the upper and lower sides of the cylinder surface, whereby a shear layer (tangential discontinuity) forms due to the two different tangential velocities. This is in good agreement with the findings from Nagata et al. [6], where the experimental investigation for $Ma_\infty = 0.2$ to 0.5 at $Re_D = 1000$ (slightly larger Re_D compared to Figure 13) shows very similar behaviour. The shear layers that form at the detachment point are more pronounced at larger Ma_∞ due to the increasing density gradient $|\nabla \rho|$. Furthermore, Nagata et al. [6] investigate the dependence on the Reynolds number Re_D in the range from 1000 to 5000 at $Ma_\infty = 0.5$. The flow detaches at the

poles of the cylinder surface and a backflow area forms immediately downstream of the cylinder, which becomes more unstable and shorter with increasing Re_D, the flow starts to develop swirl.

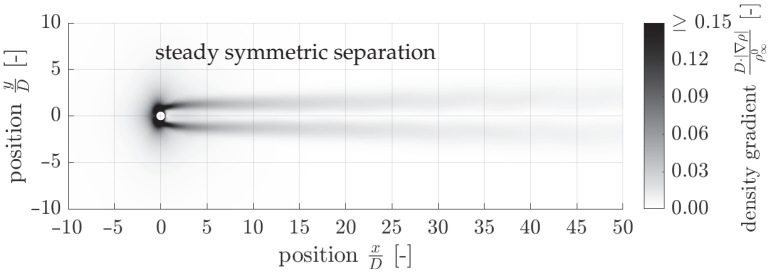

Figure 13. Regime (a), example $Re_D = 50$ and $Ma_\infty = 0.6$, distribution of $\frac{D\cdot|\nabla\rho|}{\rho_\infty^0}$.

Regime (b) is shown in Figure 14, where in comparison to the stable wake in Figure 13, an unstable wake with periodical vortex shedding forms. The vortex street is not fully developed; it is an onset of a Kármán vortex street. This flow regime can be validated using the results of Canuto and Taira [12], whereby the simulation results at $Ma_\infty = 0, 0.3$, and 0.5 and $Re_D = 50$ show less pronounced vortices with increasing Ma_∞. In particular, when looking at Figures 13 and 14, it is noticeable that with a Reynolds number of $Re_D = 50$ and $Ma_\infty = 0.4$, an unstable wake with periodic vortices results, whereas an increase in the Mach number to $Ma_\infty = 0.6$ results in a symmetrical, stationary cylinder wake. In the investigations by Canuto and Taira [12], the maximum Mach number is $Ma_\infty = 0.5$, with weak eddies still occurring, which could also be observed in this study.

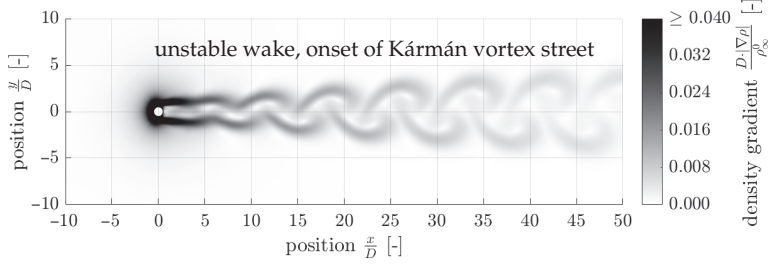

Figure 14. Regime (b), example $Re_D = 50$ and $Ma_\infty = 0.4$, distribution of $\frac{D\cdot|\nabla\rho|}{\rho_\infty^0}$.

Regime (c) in Figure 15 shows a periodical vortex shedding, a so-called Kármán vortex street, where the oscillation amplitude of the vortices is growing downstream of the cylinder over approximately the first four pairs of vortices. The Kármán vortex street can be compared with the results from Van Dyke [29] (Figures 94 to 96) for the Reynolds numbers $Re_D = 105, 140$, and 200. Despite the incompressible flow, the qualitative pattern fits with the behaviour shown in Figure 15. Comparing the vortices in Figure 15 with Figure 14, it can be noticed that an increase in Re_D from 50 to 100 at a constant Mach number of $Ma_\infty = 0.4$ leads to stronger vortices. These vortices turn more and more into a Kármán vortex street. This influence of the Reynolds number is studied by Canuto and Taira [12] using Reynolds numbers of $Re_D = 60, 80$, and 100, where the vortices are also more pronounced with higher Re_D and the distance between two consecutive vortices decreases. The results in Figures 14 and 15 agree very well with the experimental results of Canuto and Taira [12] in a qualitative manner.

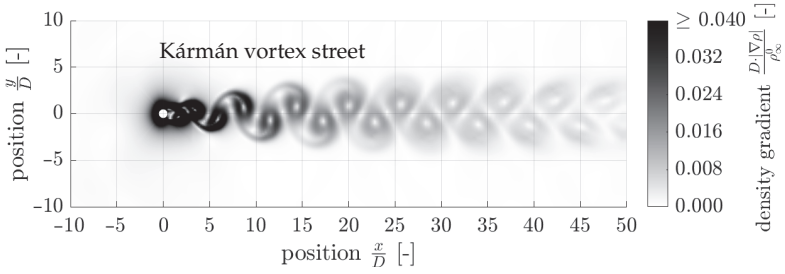

Figure 15. Regime (c), example $Re_D = 100$ and $Ma_\infty = 0.4$, distribution of $\frac{D\cdot|\nabla\rho|}{\rho_\infty^0}$.

Regime (d) in Figure 16 is similar to regime (c); vortices are shed periodically. However, the wake further downstream of the cylinder is unstable and there is a sound wave propagation. The sound waves are present in the compressible simulations for the Reynolds numbers $100 \leq Re_D \leq 80{,}000$ with a subsonic free stream Mach number $0.4 \leq Ma_\infty \leq 0.8$. Müller [30] found that each time a vortex is shed from the cylinder, a sound wave is emitted. Further numerical investigations on the sound wave propagation from a circular cylinder in a wide range of Reynolds numbers for $Re_D = 150$ and $Ma_\infty = 0.1$ and 0.2 [30,31], $Re_D = 200$ and $Ma_\infty = 0.3$ [32], $Re_D = 1000$ and $Ma_\infty = 0.27$ [33], as well as $Re_D = 1.58 \times 10^4$ [34] are presented in the literature. The results of Dumbser [35] at $Re_D = 150$ and $Ma_\infty = 0.2$ show a flow behaviour very similar to Figure 16. Although no sound waves are observed in this study at low Mach numbers, below $Ma_\infty = 0.4$, the results of Dumbser [35] make regime (d) appear more plausible. The reason that no sound waves can be observed might be the small density gradient or the too small flow domain for the prediction of sound waves. However, since the results from Khalili et al. [31], Dumbser [35] and Müller [30] are obtained using high-order numerical simulations, it is questionable whether the advection scheme "High Resolution" can sufficiently predict the sound waves. Due to this, the phenomena are analysed as in Figure 17, which shows the example of $Re_D = 300$ and $Ma_\infty = 0.5$. The so-called Doppler effect occurs. Thereby, the sound source's location is almost constant and lies near the cylinder. The wave fronts upstream of the sound source are compressed and those downstream are thinned. The thinning and compressing increase with increasing Mach numbers Ma_∞ until $Ma_\infty = 1$ is reached. Some representative points are chosen for every sound wave and circles with centre on the x-axis are fitted through the points in Figure 17. Finally, the Mach number can be calculated from the difference in the circle centres and radii $Ma = \frac{u}{a} = \frac{\Delta x}{\Delta r}$. Using the differences of each circle to the first one and calculating the arithmetic mean, a Mach number of $Ma = 0.48$ is obtained. This Mach number has a relative deviation of -4% compared to the free stream Mach number $Ma_\infty = 0.5$.

Regime (e) is shown in Figure 18a and consists of a wake with instabilities downstream of the cylinder and two λ shocks immediately downstream of the cylinder. Regime (f) in Figure 19 basically is analogous to regime (e), but the λ shocks turn into a normal shock wave further away from the cylinder. However, the transition of the λ shocks into normal shocks might be a result of an intersection with the boundary conditions. Various investigations from other works at higher Reynolds numbers Re_D, such as Linn and Awruch [16] at $Re_D = 5 \times 10^5$, support this conclusion. Therefore, it is assumed that regime (e) occurs in a wide range of $Re_D \geq 300$ at $Ma_\infty = 0.8$. Figure 18b shows the contour diagram of the simulation with $Re_D = 300$ and $Ma_\infty = 0.8$; at this point, several phenomena of interest occur. Starting from the free stream, the fluid slows down on the symmetry x-axis owing to the stagnation point. Above and below the x-axis, the fluid is accelerated. Downstream of the cylinder, two λ shocks occur, which consist of compression waves and a main shock wave. Compression waves lead to a continuous increase in the Mach number Ma; this is indicated with the Contour lines, which are parallel to each other. Through the main shock wave, the Ma is decreased from supersonic to subsonic regime, passing multiple contour lines. The

λ shocks in Figure 19 interact with the flow separation. Bobenrieth Miserda and Leal [9] investigated these complex viscous shock interactions using basically a Detached Eddy Simulation. They observed λ shocks associated with the boundary layer separation point, quasi-straight shocks that are normal to shear layers and connecting shocks between vortices at $Ma_\infty = 0.8$ and $Re_D = 500{,}000$ (higher Re_D compared to this study). The overall flow behaviour of Bobenrieth Miserda and Leal [9] is similar to this study with the development of the two λ shocks and the vortex street. However, the simulation results of Bobenrieth Miserda and Leal [9] show the flow phenomena in more detail, because of the numerical method and the higher mesh resolution. Comparable experimental results can also be found in the study of Van Dyke [29] (Figure 222) for $Ma_\infty = 0.8, 0.9, 0.95$, and 0.98 and a small Reynolds number Re_D. The results of Van Dyke [29] at $Ma_\infty = 0.8$ are identical to the results shown in Figure 18a and therefore the simulation results seem plausible. The experimental results found by Rodriguez [4] support the simulation results in Figure 18a as well, where the two λ shocks and the instabilities downstream of the cylinder were found at $Ma_\infty = 0.75$ and $Re_D = 10^5$.

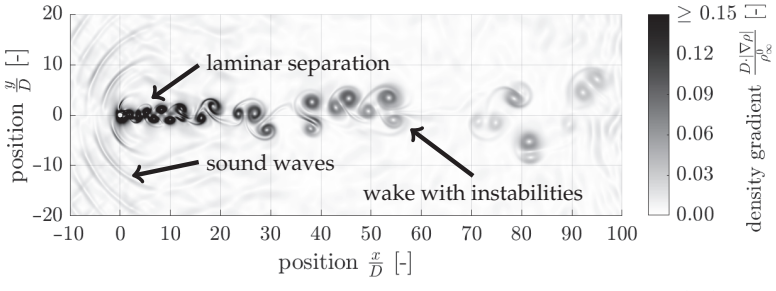

Figure 16. Regime (d), example $Re_D = 300$ and $Ma_\infty = 0.6$, distribution of $\frac{D\cdot|\nabla\rho|}{\rho_\infty^0}$.

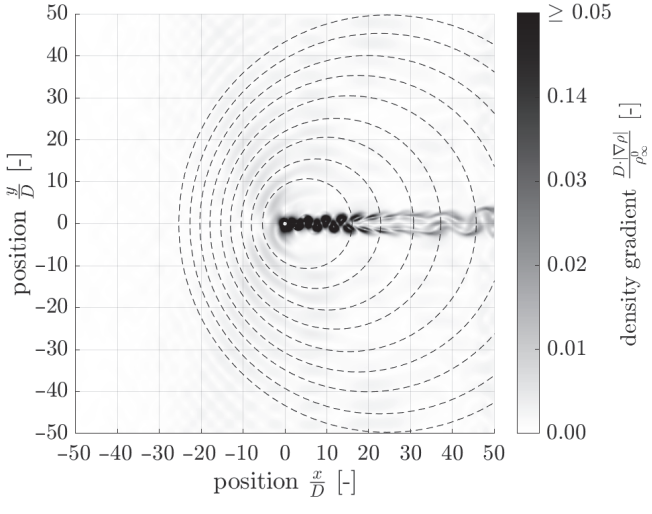

Figure 17. Sound wave propagation, $Re_D = 300$ and $Ma_\infty = 0.5$, distribution of $\frac{D\cdot|\nabla\rho|}{\rho_\infty^0}$.

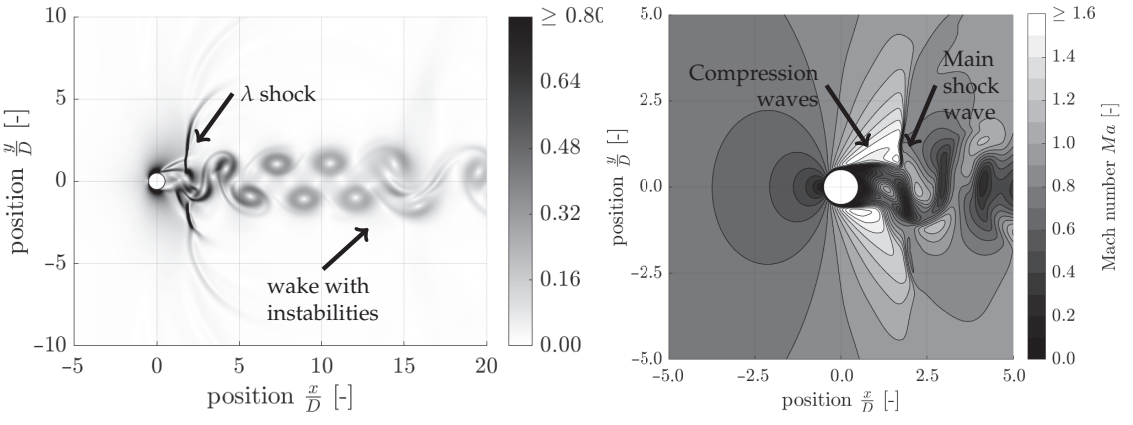

(**a**) (**b**)

Figure 18. Regime (e), example $Re_D = 300$ and $Ma_\infty = 0.8$. (**a**) Distribution of $\frac{D \cdot |\nabla \rho|}{\rho_\infty^0}$; (**b**) Contour plot of the Mach number Ma.

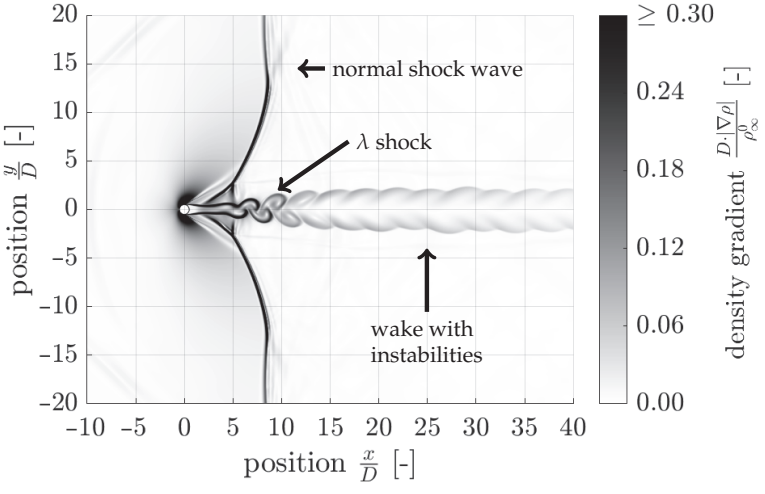

Figure 19. Regime (f), example $Re_D = 53{,}400$ and $Ma_\infty = 0.8$, distribution of $\frac{D \cdot |\nabla \rho|}{\rho_\infty^0}$.

Regime (g) in Figure 20 shows a detached shock upstream of the cylinder, two oblique shocks downstream of the cylinder and a wake with vortices. The only difference between the flow situation at a higher Reynolds number of $Re_D = 26{,}700$ in Figure 21 is the cylinder wake which is unstable with the lower Reynolds number of $Re_D = 100$. Because of the identical Mach numbers $Ma_\infty = 1.2$, the oblique shock upstream of the cylinder is equal in both regimes (g) and (h), which seems plausible.

Regime (h) shown in Figure 21 is similar compared to regime (g), but there are no instabilities in the cylinder's wake, as it is steady and symmetric. Because of the difference in the tangential velocities of the cylinder wake and the surrounding fluid, a tangential discontinuity is formed. This shear layer can be seen in the density gradient above and below the axis of symmetry in the y-direction downstream of the cylinder; there is no fluid passing these shear layers. Numerical results similar to regime (h) are obtained by de Tullio et al. [36], where $Ma_\infty = 1.7$ and $Re_D = 200{,}000$ is investigated. However, Ma_∞ and Re_D are higher compared to Figure 21. Despite this, the flow phenomena are very similar, which leads to the conclusion that this regime extends over a much larger range

of Mach and Reynolds numbers. The flow phenomena of a detached shock upstream of the cylinder, the supersonic flow region between the cylinder, the detached shock, the subsonic recirculation region behind the cylinder and the two symmetrical oblique shocks, which are formed at the end of the recirculation region, are present in both the study from de Tullio et al. [36] and Figure 21. Obviously, an increase in the Mach number Ma_∞ leads to a higher curvature of the detached shock. Hinman et al. [37] performed numerical simulations at an even higher Mach number $Ma_\infty = 10$ and $Re_D = 5.5 \times 10^4$, where the flow structure is somehow similar compared to Figure 21. However, there are noticeable differences in the flow structure, namely the lid separation shock, which connects the recirculation region with the oblique shock and there is more curvature in the detached shock due to the high Mach number.

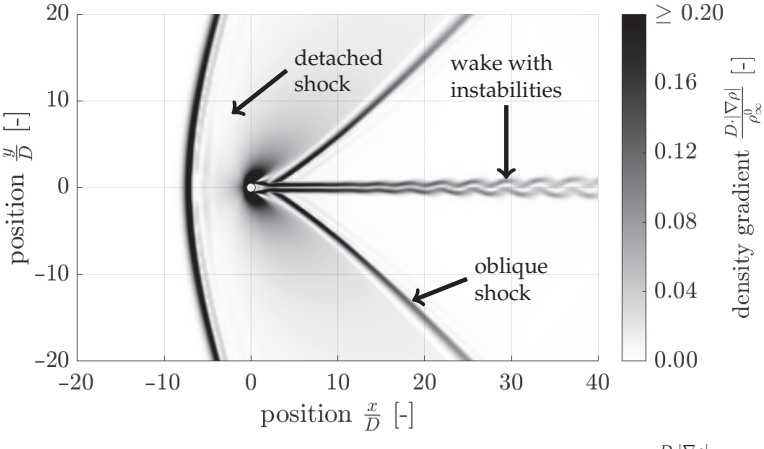

Figure 20. Regime (g), example $Re_D = 100$ and $Ma_\infty = 1.2$, distribution of $\frac{D\cdot|\nabla\rho|}{\rho_\infty^0}$.

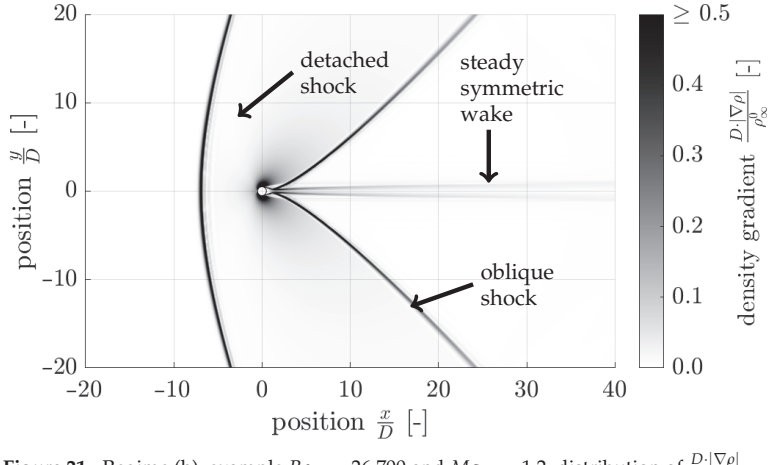

Figure 21. Regime (h), example $Re_D = 26{,}700$ and $Ma_\infty = 1.2$, distribution of $\frac{D\cdot|\nabla\rho|}{\rho_\infty^0}$.

5.4. Analysis of the Shock Waves

For Mach numbers $Ma_\infty > 1.0$, a detached shock is formed upstream of the cylinder. This shock consists of three different phenomena. Near the cylinder symmetry x-axis, an

oblique shock is formed. Further away from the cylinder, a weaker oblique shock turns into a Mach cone, whose angle α can be calculated with Equation (10).

$$\sin(\alpha) = \frac{1}{Ma} \tag{10}$$

Figure 22a shows this situation for $Ma_\infty = 1.2$ and $Re_D = 100$. However, the shock angle of 65° is larger than the angle of the Mach cone of $\alpha = 56.4°$. This is due to the fact that the geometry is not sufficiently large to depict the transition to the Mach cone. Different calculations of the normal shock wave on the x-axis have been done. The state upstream of the shock is indicated as 1 and the state downstream of the shock is indicated as 2. The simulation quantities were compared to the ones calculated from the theory. The results are shown in Table 6 and fit well with the calculations, the maximum deviation is about -4%.

In addition, the λ-shock wave is analysed in a similar way for the simulation with $Re_D = 300$ and $Ma_\infty = 0.8$. The flow regime as well as the states upstream and downstream of the shock are shown in Figure 22b. The calculations in Table 7 show that the simulation results fit well with the calculations. The maximum deviation is about -7.6%. The calculation of the different quantities shown in Table 7 is based on the upstream Mach number $Ma_\infty = 1.1258$ from the simulation results.

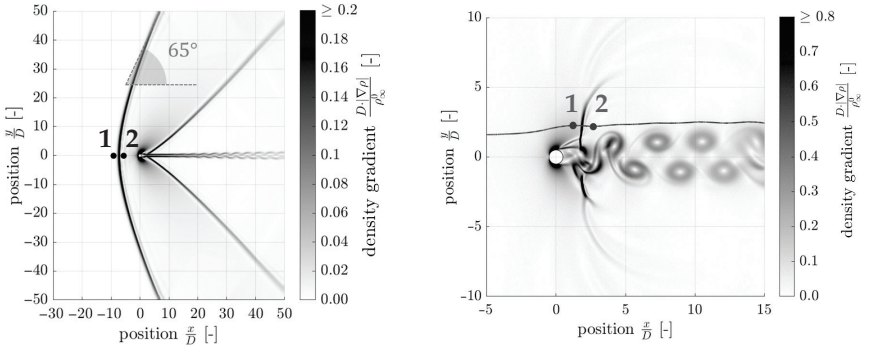

(**a**) (**b**)

Figure 22. Analysis of shocks, distribution of $\frac{D\cdot|\nabla\rho|}{\rho_\infty^0}$. The states upstream and downstream of the shock are indicated as 1 and 2. (**a**) $Re_D = 100$ and $Ma_\infty = 1.2$, detached shock; (**b**) $Re_D = 300$ and $Ma_\infty = 0.8$, λ shock.

The Mach number downstream of the shock Ma_2 can be calculated from the Mach number upstream of the shock Ma_1 and the heat capacity ratio $\kappa = 1.4$ for air.

$$Ma_2^2 = \frac{Ma_1^2 + \frac{2}{\kappa-1}}{\frac{2\kappa}{\kappa-1}Ma_1^2 - 1} \tag{11}$$

The pressure ratio $\frac{p_2}{p_1}$ is calculated from the two Mach numbers Ma_1 and Ma_2 and the heat capacity ratio κ as follows.

$$\frac{p_2}{p_1} = \frac{1 + \kappa Ma_1^2}{1 + \kappa Ma_2^2} \tag{12}$$

Table 6. Analysis of the detached shock for $Re_D = 100$ and $Ma_\infty = 1.2$.

Quantity	Calculation	Simulation
Ma_1	1.200	1.1999
Ma_2	0.8422	0.8082
p_2/p_1	1.5133	1.5675
T_2/T_1	1.1280	1.1392
p_2^0/p_1^0	0.9928	0.9936
ρ_2/ρ_1	1.3416	1.3760
u_2/u_1	0.7454	0.7189
T_2^0/T_1^0	1.0000	1.0000

Table 7. Analysis of the λ shock for $Re_D = 300$ and $Ma_\infty = 0.8$.

Quantity	Calculation	Simulation
Ma_2	0.8081	0.8102
p_2/p_1	1.6801	1.5522
T_2/T_1	1.1645	1.1403
p_2^0/p_1^0	0.9859	0.9122
ρ_2/ρ_1	1.4428	1.3613
T_2^0/T_1^0	1.0000	0.9797

5.5. Critical Mach Number

The critical Mach number of the inflow Ma_{crit} shown in Figure 23 was determined. This corresponds to the lowest Mach number of the inflow Ma_∞, at which the flow near the cylinder reaches the speed of sound a. Polhamus [38] discovered the critical Mach number for very large Reynolds numbers $Re_D \to \infty$ to be $Ma_{\text{crit}} = 0.4$. This agrees with the critical Mach number found in this study at a Reynolds number of $Re_D = 26{,}683$.

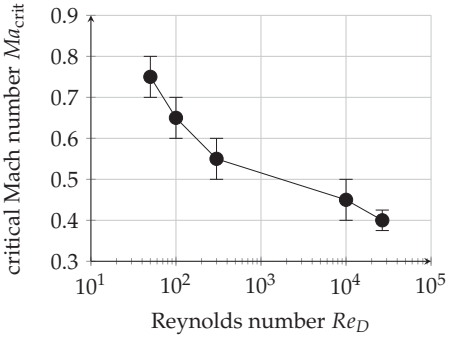

Figure 23. Critical Mach number Ma_{crit} vs. Reynolds number Re_D.

5.6. Strouhal Number and Drag Coefficient

Table 8 shows an overview for the Strouhal number Str and the mean drag coefficient $\overline{C}_D$ of all simulation points; the Strouhal numbers are in the range of $0.1 < Str < 0.25$.

Drag forces F_D occur in flows around objects and act opposite to the relative motion of the object with respect to the surrounding fluid. F_D basically consists of three forces: pressure drag, friction drag and wave drag. The friction drag is produced by the viscous momentum exchange; in addition, the drag force corresponds to the sum of all forces parallel to the flow. The wave drag is created when the velocity is close to the speed of sound a, which means the Mach number Ma_∞ exceeds the critical Mach number Ma_{crit}. Reaching the critical Mach number Ma_{crit} leads to an increase in the mean drag coefficient $\overline{C}_D$.

For the subsonic regimes, the mean drag coefficient lies in the range of $1.3 < \overline{C}_D < 1.61$. For higher Ma_∞ in the transonic regimes, which means where the critical Mach number Ma_{crit} is reached, the wave drag increases and the mean drag coefficient is in the range of $1.6 < \overline{C}_D < 2.5$. Increasing the free stream Mach number to supersonic leads to very large $\overline{C}_D$ of $12.5 < \overline{C}_D < 14.5$; the reason for this is the compression fronts which lead to higher wave drag. The wave drag then decreases again in the supersonic range. The values of the drag coefficient $\overline{C}_D$ and the Strouhal number Str for $Re_D = 50$ to 100 in a Mach number range $0 \leq Ma_\infty \leq 0.5$ are in good agreement with the values from Canuto and Taira [12].

Table 8. Mean drag coefficient $\overline{C}_D$ and Strouhal number Str.

Re_D	Ma_∞	$\overline{C}_D$	Str
50	0.4	1.471	0.1143
	0.5	1.517	0.1080
	0.6	1.609	0.1075
	0.7	1.760	
	0.8	2.069	
	1.1	14.43	0.2128
	1.2	13.85	0.2279
100	0.2	1.319	0.1582
	0.4	1.410	0.1565
	0.6	1.648	0.1559
	0.7	1.847	0.1550
	0.8	1.877	0.1383
	1.1	13.822	0.2378
	1.2	13.453	0.2408
	2.0	12.970	
300	0.4	1.483	0.1983
	0.5	1.623	0.2048
	0.6	1.781	0.2083
	0.8	2.380	0.2238
	1.2	13.46	0.2444
8890	0.4	1.603	
11,100	0.5	1.726	
13,300	0.6	1.834	
17,800	0.8	1.860	
26,700	1.2	14.145	
26,700	0.4	1.614	
33,400	0.5	1.717	
40,000	0.6	1.873	
53,400	0.8	2.171	
80,000	1.2	13.808	

5.7. Polar Diagrams

So-called polar diagrams, i.e., the lift coefficient C_L versus the drag coefficient C_D plotted, were evaluated. In some cases, the polar diagrams correspond to a closed curve, so-called Lissajous figures. In this case, the oscillations correspond to a single respectively finite number of frequencies involved. The frequency ratio as well as the phase shift can be determined analysing these closed curves. For the Kármán vortex street or similar phenomena, the drag coefficient C_D oscillates at double the frequency of the lift coefficient C_L. This confirms the rough idea that the drag is basically a quadratic effect compared with lift, in agreement with the fact that drag is generally positive, whereas lift can be of

either sign. For some simulation points, especially when vortex shedding occurs in the subsonic and supersonic regimes, closed curves are observed; typical results are shown in Figure 24a–d. Figure 24a corresponds to the subsonic simulation at $Re_D = 100$ and $Ma_\infty = 0.4$ with the phenomena shown in Figure 15. The Lissajous figure shows that the lift coefficient C_L oscillates at half the frequency of the drag coefficient C_D. The phase shift of the drag coefficient C_D is $\frac{\pi}{4}$ and $\frac{3\cdot\pi}{4}$, respectively. Figure 24b shows the supersonic simulation point $Re_D = 100$ and $Ma_\infty = 1.2$, the corresponding flow phenomena are shown in Figure 20. The frequency ratio is equal to Figure 24a; the phase shift of the drag coefficient C_D is $\frac{5\cdot\pi}{4}$ and $\frac{7\cdot\pi}{4}$, respectively. Figure 24c shows the transonic simulation point $Re_D = 300$ and $Ma_\infty = 0.6$, related to the flow regime in Figure 16. The frequency ratio is equal to the previous Figure 24a,b; the phase shift of the drag coefficient C_D is $\frac{\pi}{2}$. Figure 24d shows the supersonic simulation point $Re_D = 13{,}300$ and $Ma_\infty = 0.6$ and Figure 25 shows the corresponding flow phenomena in the distribution of the dimensionless density gradient $\frac{D\cdot|\nabla\rho|}{\rho^0_\infty}$. Looking at the density gradient, the phenomena sound waves and vortex shedding are observed. However, the vortices shed randomly, which does not lead to a closed curve in the polar diagram. That means that several frequencies are involved in the oscillations. These random oscillations are observed for all the high Reynolds numbers Re_D where the flow is turbulent.

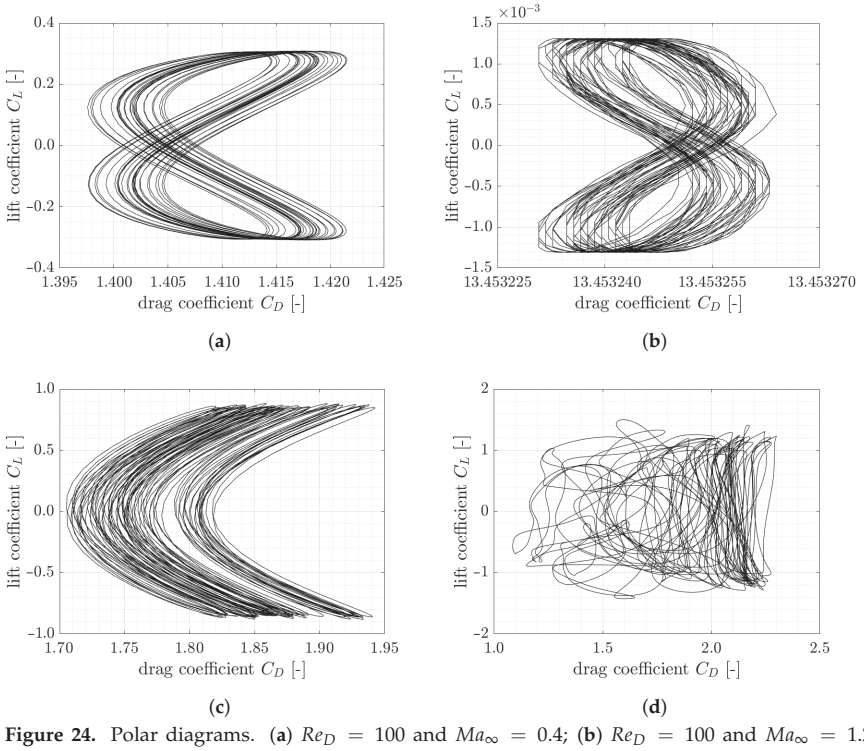

Figure 24. Polar diagrams. (**a**) $Re_D = 100$ and $Ma_\infty = 0.4$; (**b**) $Re_D = 100$ and $Ma_\infty = 1.2$; (**c**) $Re_D = 300$ and $Ma_\infty = 0.6$; (**d**) $Re_D = 13{,}300$ and $Ma_\infty = 0.6$.

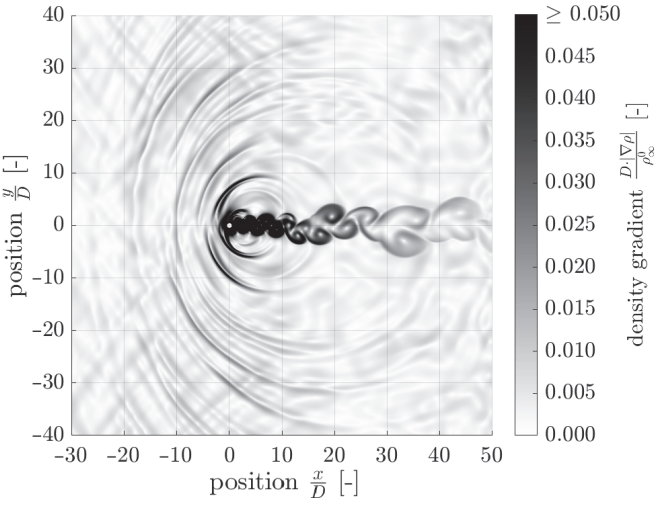

Figure 25. $Re_D = 13{,}300$ and $Ma_\infty = 0.6$, distribution of $\frac{D\cdot|\nabla\rho|}{\rho^0_\infty}$.

6. Conclusions

The applicability of the commercially available tool Ansys CFX was verified and validated. The distribution of the Mach number *Ma* along a planar Laval nozzle showed that there are about eight to nine cells necessary to resolve a shock wave in comparison to the abrupt transition over a few mean free paths of the molecules. For validation, the Strouhal number *Str* and the drag coefficient $\overline{C}_\mathrm{D}$ at $Ma_\infty = 0.2$ and 2 at $Re_D = 100$ are compared to Burbeau and Sagaut [17] and they are in good agreement with a maximum deviation of 4%. In addition, even the detached shock wave position and the flow phenomena at the conditions investigated agree well with Burbeau and Sagaut [17]. Moreover, the validation showed that a higher-order advection scheme is necessary for adequate prediction of periodic vortex shedding and shock waves. Eight flow regimes were found in the planar flow around a circular cylinder for $50 \leq Re_D \leq 300$ and $8890 \leq Re_D \leq 80{,}000$ and $0.2 \leq Ma_\infty \leq 2$. The modulus of the dimensionless density gradient $\frac{D\cdot|\nabla\rho|}{\rho^0_\infty}$ has proven to be suitable for identifying and distinguishing between different flow phenomena, such as vortices, shocks, tangential discontinuities and sound waves. The simulation results at low Ma_∞ are found to be in similar flow regimes compared to the incompressible flow. At higher velocity near the speed of sound *a*, shocks occur. The cylinder wake in the turbulent regime behaves in a steady state and symmetrically and for $50 \leq Re_D \leq 300$ vortices are formed in the cylinder wake. For some conditions in the transonic regime, for example $Re_D = 300$ and $Ma_\infty = 0.5$, sound wave propagation occurs. The sound waves were identified by retracing the free-stream Mach number Ma_∞ from circles, which are fitted through the sound waves. Furthermore, the critical Mach number Ma_crit, the lowest Ma_∞ where the flow around the cylinder reaches the speed of sound, decreases with increasing Reynolds number Re_D and for $Re_D \to \infty$ it is $Ma_\mathrm{crit} = 0.4$ from Polhamus [38]. The C_D-C_L-diagram shows a close curve in cases of laminar vortex shedding, but not for turbulent vortex shedding. A close curve corresponds to a given frequency ratio and a given phase shift of C_D and C_L.

Author Contributions: Conceptualization, J.H. and D.A.W.; methodology, J.H. and D.A.W.; software, D.A.W.; validation, J.H.; formal analysis, J.H.; investigation, J.H.; resources, D.A.W.; data curation, J.H.; writing—original draft preparation, J.H.; writing—review and editing, J.H. and D.A.W.; visualization, J.H.; supervision, D.A.W.; project administration, J.H. All authors have read and agreed to the published version of the manuscript.

Funding: This research received no external funding.

Data Availability Statement: Data sharing not applicable.

Acknowledgments: Useful comments by Christoph Gossweiler, Markus Kerellaj and Walter Vera-Tudela on different versions of the manuscript are gratefully acknowledged.

Conflicts of Interest: The authors declare no conflict of interest.

Nomenclature

Symbol	Unit	Description
		Dimensionless numbers
C_D		Drag coefficient
C_L		Lift coefficient
Ma		Mach number
Re_D		Reynolds number based on the cylinder diameter D
Str		Strouhal number (determined from the lift coefficient in this study) C_L
y^+		Dimensionless distance from the wall
		Latin letters
A	m^2	Cylinder's front face
a	$m\,s^{-1}$	Speed of sound
D	m	Cylinder diameter
F	N	Force
f	Hz	Frequency
h	$J\,kg^{-1}$	Specific enthalpy
p	Pa	Pressure
R	$J\,kg^{-1}\,K^{-1}$	Specific gas constant, $R = 287\,J\,kg^{-1}\,K^{-1}$ for air
r	m	Radius
S_φ	$N\,m^{-3}$, $W\,m^{-3}$	Source, loss and production of the transport properties $\varphi = \rho u_i$ and $\varphi = h$
T	K	Temperature
t	s	Time
u	$m\,s^{-1}$	Velocity
x	m	Cartesian coordinate
x_{cell}	m	Cell dimension of the computational mesh
y	m	Cartesian coordinate
z	m	Cartesian coordinate
		Greek letters
α	°	Opening angle of Mach cone
α_{th}	$m^2\,s^{-1}$	Thermal diffusivity
Γ_φ	$m^2\,s^{-1}$	Diffusion coefficient of the transport properties $\varphi = \rho u_i$ and $\varphi = h$
ζ	s^{-1}	Swirling strength
κ	-	Heat capacity ratio
μ	Pa s	Dynamic viscosity
ν	$m^2\,s^{-1}$	Kinematic viscosity
ρ	$kg\,m^{-3}$	Density
φ	$kg\,m^{-3}$, $N\,s\,m^{-3}$, $J\,m^{-3}$	Transport property of mass, momentum and energy
Ω	$rad\,s^{-1}$	Rotational velocity
ω	s^{-1}	Vorticity
		Subscripts, superscripts, etc.
X_D		Drag component
X_L		Lift component
X_{crit}		Critical property
X_{max}		Maximum property
X_{min}		Minimum property
X_i		i-component of the corresponding property with $i = x, y, z$

X_∞	Free-stream property
X_1	Upstream of the shock
X_2	Downstream of the shock
X^0	Total property
$\overline{X}$	Averaged property
$\vec{X}$	Vectorial property
ΔX	Difference in property

References

1. Schlichting, H.; Gersten, K. *Boundary-Layer Theory*, 9th ed.; Springer: Berlin/Heidelberg, Germany, 2017.. [CrossRef]
2. Macha, J.M. Drag of circular cylinders at transonic Mach numbers. *J. Aircr.* **1977**, *14*, 605–607. [CrossRef]
3. Murthy, V.; Rose, W. Form drag, skin friction and vortex shedding frequencies for subsonic and transonic crossflows on circular cylinder. In Proceedings of the 10th Fluid and Plasmadynamics Conference, Albuquerque, NM, USA, 27–29 June 1977; p. 687. [CrossRef]
4. Rodriguez, O. The circular cylinder in subsonic and transonic flow. *AIAA J.* **1984**, *22*, 1713–1718. [CrossRef]
5. Ackerman, J.; Gostelow, J.; Rona, A.; Carscallen, W.E. Base Pressure Measurements on a Circular Cylinder in Subsonic Cross Flow. In Proceedings of the 38th Fluid Dynamics Conference and Exhibit, Seattle, WA, USA, 23–26 June 2008; p. 4305. [CrossRef]
6. Nagata, T.; Noguchi, A.; Kusama, K.; Nonomura, T.; Komuro, A.; Ando, A.; Asai, K. Experimental investigation on compressible flow over a circular cylinder at Reynolds number of between 1000 and 5000. *J. Fluid Mech.* **2020**, *893*, A13. [CrossRef]
7. Gowen, F.E.; Perkins, E.W. Drag of circular cylinders for a wide range of Reynolds numbers and Mach numbers. *NACA TN* **1953**, *2960* .
8. Botta, N. The inviscid transonic flow about a cylinder. *J. Fluid Mech.* **1995**, *301*, 225–250. [CrossRef]
9. Bobenrieth Miserda, R.F.; Leal, R.G. Numerical Simulation of the Unsteady Aerodynamic Forces over a Circular Cylinder in Transonic Flow. In Proceedings of the 44th AIAA Aerospace Sciences Meeting and Exhibit, Reno Hilton, NV, USA, 9–12 January 2006; p. 1408. [CrossRef]
10. Xu, C.Y.; Chen, L.W.; Lu, X.Y. Effect of Mach number on transonic flow past a circular cylinder. *Chin. Sci. Bull.* **2009**, *54*, 1886–1893. [CrossRef]
11. Hong, R.; Xia, Z.; Shi, Y.; Xiao, Z.; Chen, S. Constrained large-eddy simulation of compressible flow past a circular cylinder. *Commun. Comput. Phys.* **2014**, *15*, 388–421. [CrossRef]
12. Canuto, D.; Taira, K. Two-dimensional compressible viscous flow around a circular cylinder. *J. Fluid Mech.* **2015**, *785*, 349–371. [CrossRef]
13. Xia, Z.; Xiao, Z.; Shi, Y.; Chen, S. Mach number effect of compressible flow around a circular cylinder. *AIAA J.* **2016**, *54*, 2004–2009. [CrossRef]
14. Shirani, E. Compressible Flow Around A Circular Cylinder. *Pak. J. Appl. Sci.* **2001**, *1*, 472–476. [CrossRef]
15. Matar, C.; Cinnella, P.; Gloerfelt, X. Sundermeier, S.; Hake, L.; aus der Wiesche, S. Numerical investigation of the transonic non-ideal gas flow around a circular cylinder at high Reynolds number. In Proceedings of the Workshop Direct and Large-Eddy Simulation (DLES13), Udine, Italy, 26–29 October 2022.
16. Linn, R.V.; Awruch, A.M. Adaptative finite element simulation of unsteady turbulent compressible flows on unstructured meshes. *Comput. Fluids* **2023**, *254*, 105816. . [CrossRef]
17. Burbeau, A.; Sagaut, P. Simulation of a viscous compressible flow past a circular cylinder with high-order discontinuous Galerkin methods. *Comput. Fluids* **2002**, *31*, 867–889. [CrossRef]
18. Barth, T.J.; Jesperson, D.C. The Design and Application of Upwind Schemes on Unstructured Meshes. *AIAA Pap.* **1989**, *27*, 366. [CrossRef]
19. Rhie, c.M.; Chow, W.L. A Numerical Study of the Turbulent Flow Past an Isolated Airfoil with Trailing Edge Separation. *AIAA Pap.* **1982**, *21*, 1525–1532. [CrossRef]
20. Majumdar, S. Role of Underrelaxation in Momentum Interpolation for Calculation of Flow with Nonstaggered Grids. *Numer. Heat Transf.* **1988**, *13*, 125–132. [CrossRef]
21. Menter, F.R. Zonal Two Equation $k-\omega$ Turbulence Models for Aerodynamic Flows. *AIAA J.* **1994**, *32*, 1598–1605. [CrossRef]
22. Ansys Inc. and Ansys Europe. *Ansys CFX-Solver Modeling Guide*; Ansys Inc. and Ansys Europe: Canonsburg, PA, USA; 2022 .
23. Braza, M.; Chassaing, P.H.H.M.; Minh, H.H. Numerical study and physical analysis of the pressure and velocity fields in the near wake of a circular cylinder. *J. Fluid Mech.* **1986**, *165*, 79–130. [CrossRef]
24. Ansys Inc. *Ansys Documentation*; Ansys Inc.: Canonsburg, PA, USA , 2022 .
25. Ansys Inc. GroupoSSC. 2014. Available online: https://www.gruposssc.com/ponencias/ponencia_39114164442.pdf (accessed on 8 July 2020).
26. Ansys Inc. Ansys Customer Portal. 2010. Available online: https://support.ansys.com/staticassets/ANSYS%20UK/staticassets/Reliable%20and%20Accurate%20CFD%20Solutions,%20Mark%20Keating.pdf (accessed on 8 July 2020).
27. Lesaint, P.; Raviart, P.A. *On a Finite Element Method to Solve the Neutron Transport Equation*; Partial Differentiel Equations. C. de Boor; Academic Press: New York, NY, USA, 1974. [CrossRef]

28. Oden Tinsley, J.; Babuška, I.; Baumann, C.E. A discontinuoushpfinite element method for diffusion problems. *J. Comput. Phys.* **1998**, *146*, 491–519. [CrossRef]
29. Van Dyke, M. *An Album of Fluid Motion*; Parabolic Press Stanford: Stanford, CA, USA, 1982.
30. Müller, B. Towards high order numerical simulation of aeolian tones. *PAMM* **2005**, *5*, 473–474. [CrossRef]
31. Khalili, M.E.; Larsson, M.; Müller, B. High-order ghost-point immersed boundary method for viscous compressible flows based on summation-by-parts operators. *Int. J. Numer. Methods Fluids* **2019**, *89*, 256–282. [CrossRef]
32. Seo, J.H.; Moon, Y.J. Perturbed compressible equations for aeroacoustic noise prediction at low mach numbers. *AIAA J.* **2005**, *43*, 1716–1724. [CrossRef]
33. Tsutahara, M.; Kataoka, T.; Shikata, K.; Takada, N. New model and scheme for compressible fluids of the finite difference lattice Boltzmann method and direct simulations of aerodynamic sound. *Comput. Fluids* **2008**, *37*, 79–89. [CrossRef]
34. Cheong, C.; Joseph, P.; Park, Y.; Lee, S. Computation of aeolian tone from a circular cylinder using source models. *Appl. Acoust.* **2008**, *69*, 110–126. [CrossRef]
35. Dumbser, M. Arbitrary high order PNPM schemes on unstructured meshes for the compressible Navier–Stokes equations. *Comput. Fluids* **2010**, *39*, 60–76. [CrossRef]
36. de Tullio, M.D.; De Palma, P.; Iaccarino, G.; Pascazio, G.; Napolitano, M., Immersed boundary technique for compressible flow simulations on semi-structured grids. In *Compitational Fluid Dynamics 2006, Proceedings of the Fourth International Conference on Computational Fluid Dynamics, ICCFD, Ghent, Belgium, 10–14 July 2006*; Springer: Berlin/Heidelberg, Germany, 2009; pp. 365–370. 10.1007/978-3-540-92779-2_56 [CrossRef]
37. Hinman, S.W.; Johansen, C.T.; Arisman, C.J.; Galuppo, W.C. Numerical investigation of laminar near wake separation on circular cylinders at supersonic velocities. In Proceedings of the Congress of the International Council of the Aeronautical Sciences, St. Petersburg, Russia, 7–12 September 2014.
38. Polhamus, E.C. A review of some Reynolds number effects related to bodies at high angles of attack. *NASA Contract. Rep.* **1984**, *3809* .

fluids

MDPI

Article

Experimental Detection of Organised Motion in Complex Flows with Modified Spectral Proper Orthogonal Decomposition

Nick Schneider, Simon Köhler * and Jens von Wolfersdorf

Institute of Aerospace Thermodynamics (ITLR), University of Stuttgart, 70569 Stuttgart, Germany
* Correspondence: simon.koehler@itlr.uni-stuttgart.de

Abstract: Spectral proper orthogonal decomposition (SPOD) has seen renewed interest in recent years due to its unique ability to decouple organised motion at different timescales from large datasets with limited available information. This paper investigated the unsteady components of the flow field within a simplified turbine centre frame (TCF) model by applying SPOD to experimental, time-resolved flow speed data captured by particle image velocimetry (PIV). It was observed that conventional methods failed to capture the two significant active bands in the power spectrum predicted by preliminary hot wire anemometry measurements. Therefore, a modification to the SPOD procedure, which employs subsampling of the time sequence recorded in the experiment to artificially lower the PIV data acquisition frequency, was developed and successfully deployed to analyse the TCF flow field. The two dynamically active bands were identified in the power spectra, resulting in a closer match to the preceding analyses. Within these bands, SPOD's ability to capture spatial coherence was leveraged to detect several plausible coherent, fluctuating structures in two perpendicular planes. A partial three-dimensional reconstruction of the flow phenomena suggested that both bands were associated with a distinct mode of organised motion, each contributing a significant percentage of the system's total fluctuating energy.

Keywords: spectral proper orthogonal decomposition; spectral analysis; organised motion; experimental fluid dynamics; particle image velocimetry; turbine centre frame

Citation: Schneider, N.; Köhler, S.; von Wolfersdorf, J. Experimental Detection of Organised Motion in Complex Flows with Modified Spectral Proper Orthogonal Decomposition. *Fluids* **2023**, *8*, 184. https://doi.org/10.3390/fluids8060184

Academic Editors: Vasily Novozhilov, Cunlu Zhao and D. Andrew S. Rees

Received: 3 May 2023
Revised: 7 June 2023
Accepted: 14 June 2023
Published: 17 June 2023

1. Introduction

In recent years, the improved availability of complex hardware and computational capacity has made applying more demanding data-driven methods in experimental fluid mechanics more feasible. It is a competitive and rapidly progressing space in which a number of different methods vie for the limelight. The space-only formulation of proper orthogonal decomposition (POD) [1] has long remained the default option, benefiting from denser datasets due to improvements in high-speed imaging and simulation, which allowed expanding its domain of possible applications to more complex turbulent flows and heat transfer problems [2,3]. Other popular methods include dynamic mode decomposition (DMD) [4] and its derivatives [5], wavelet analysis [6,7], and independent component analysis (ICA) [8,9]. This work's focus lied in spectral proper orthogonal decomposition (SPOD), which has recently enjoyed more attention due to its unique capability to optimally represent spatiotemporal coherence in flow data [10–12]. While the method is proven to be a valuable tool mainly in rather idealised scenarios, its applications as an investigative aid in exploring the dynamics of complex systems remain largely unexplored in the literature.

One such system, which, due to technical relevance, warrants closer examination, is the turbine centre frame (TCF)—a single module connecting the low- and high-pressure turbines of twin spool gas turbine engines, which forms the gas duct between the two sections, while also providing internal channels for hydraulics, the transfer of structural loads, and cooling air exchange between the hub and the exterior of the engine. Contemporary TCFs incorporate aggressive geometries to accommodate the rapidly diverging gas duct,

complicating the design of the struts that house the service channels. Consequently, the flow of cooling air through the structure, which maintains safe operating temperatures of the TCF itself and is also supplied to the neighbouring turbine disks, is profoundly complex: large pressure gradients and narrow channels produce high local flow speed spikes, which result in a convoluted series of unsteady flow structures spanning the TCF's multiple internal cavities.

This paper documented the use of SPOD to process flow data acquired in a high-speed particle image velocimetry (HSPIV) experiment on a simplified TCF model. The objective was two-fold: first, to assess the utility of SPOD as a tool to detect yet-unknown coherent structures in a complex fluid system, and second, if the first step proves a success, to obtain a result with the potential for immediate technical application. The dynamics analysis can, for instance, be used to gauge the performance of a numerical solver used to design a TCF interior in an engineering context.

Sections 2 and 3 provide a brief overview of the theoretical framework of POD and the fluids' experimental setup, respectively. Section 4 details the necessary preliminary steps to contextualise the modal decomposition results. This includes a discussion of the topology of the mean flow through the model, as well as insights into the fluid system's dynamics obtained through hot wire anemometry. The results of an analysis of the experimental data with conventional SPOD are presented in Section 5; as the base, the SPOD algorithm was found to perform poorly with the available data. Section 6 proposes and validates a modification, which involves the use of subsampling to lower the effective data acquisition frequency of the input. The results obtained with the updated method are presented thereafter.

2. Spectral Proper Orthogonal Decomposition

Modal decomposition produces a set of deterministic modes that capture dynamically significant patterns in the energy distribution of stochastic data. One such technique, known as spectral proper orthogonal decomposition, was the primary analytic instrument employed in this work.

2.1. Background

POD is a family of decomposition algorithms that contains several distinct techniques. Its inception lies in the work of Lumley [13,14], who first proposed the use of the Karhunen–Loève (K-L) theorem as a tool for analysing turbulent flows. Though its initial formulation was deliberately agnostic towards the nature of the kernel, the field was long dominated by an exclusively spatial form of POD popularised by Sirovich [1], which produces spatially orthogonal modes and, therefore, only represents spatial coherence. Our focus lied in *spectral* proper orthogonal decomposition, which is geared specifically towards the optimal representation of spatiotemporal coherence. The concept was coined by Picard and Delville [15] and recently applied widely by Towne et al. [10], Schmidt et al. [11], Schmidt and Colonius [16], and others. Note that this algorithm is distinct from the procedure by the same name proposed by Sieber et al. [17].

The fundamental principle of POD lies in computing a set of deterministic functions $\boldsymbol{\phi}(z)$ that are the optimal representation of a zero-mean stochastic process $\{\boldsymbol{q}(z;\xi)\}$ with respect to the inner product $\langle\cdot,\cdot\rangle$ of the Hilbert space $\mathcal{H}$ that each realisation of $\boldsymbol{q}$ inhabits; $z \in \Omega$ denotes a set of independent variables, whereas ξ parameterises the probability space. The zero-mean property of $\boldsymbol{q}$ can be expressed as $\mathrm{E}\{\boldsymbol{q}(z;\xi)\} = 0$, with $\mathrm{E}\{\cdot\}$ being the expectation operator within the probability space.

The desired qualities of $\boldsymbol{\phi}(z) \in \mathcal{H}$ can be expressed through the maximisation problem:

$$\lambda = \frac{\mathrm{E}\{|\langle \boldsymbol{q}(z;\xi), \boldsymbol{\phi}(z)\rangle|^2\}}{\langle \boldsymbol{\phi}(z), \boldsymbol{\phi}(z)\rangle}. \tag{1}$$

(1) can be intuitively contextualised as an effort to optimise $\boldsymbol{\phi}$ such that the expectation value of the projection of the stochastic process onto a deterministic modal function is

maximal. The expression is normalised to decouple λ from the magnitude of $\boldsymbol{\phi}$. The desired functions can be shown to be the eigenfunctions of the Fredholm integral equation:

$$\int_{\Omega} \mathbf{R}(z, z')\boldsymbol{\phi}(z')\,\mathrm{d}z' = \lambda\boldsymbol{\phi}(z) \tag{2}$$

whose kernel is the two-point correlation tensor across Ω:

$$\mathbf{R}(z, z') = \mathrm{E}\{\boldsymbol{q}(z;\xi)\boldsymbol{q}^*(z';\xi)\}. \tag{3}$$

The K-L theorem states that (2) is solved by a infinite set of functions $\{\boldsymbol{\phi}_k, \lambda_k\}, k \in \mathbb{N}$, which are mutually orthonormal (i.e., $\langle\boldsymbol{\phi}_j, \boldsymbol{\phi}_k\rangle = \delta_{jk}$) and can be ranked by the magnitude of their eigenvalue, $\lambda_1 \geq \lambda_2 \geq \ldots \geq 0$. The eigenfunctions form an energy-optimal (proper) basis for each realisation of $\boldsymbol{q}$.

Space-only POD, as typically employed in statistical fluid mechanics, defines $\boldsymbol{q}(\boldsymbol{x}, t)$ as a finite set of fields of scalar (e.g., pressure, vorticity) or vector (e.g., velocity) properties, i.e., snapshots of a fluid flow. These can be understood as independent realisations of a stochastic process. The domain Ω of the statistical ensemble, therefore, consists of a bounded control volume $V \subseteq \mathbb{R}^n, \boldsymbol{x} \in V$, and a temporal component. The definition of the latter is quite elastic [18], though for most purposes, the temporal domain constitutes discrete, uniformly sampled times t_j.

In contrast, the objective that informs SPOD is to generalise the decomposition to enable the detection of temporally coherent structures within the flow. This requires a different definition of the stochastic ensemble $\boldsymbol{q}$: instead of viewing individual snapshots as a realisation, we considered a series of correlated snapshots. The inner product associated with $\mathcal{H}$ is defined as

$$\langle\boldsymbol{q}_1, \boldsymbol{q}_2\rangle_{x,t} = \int_{-\infty}^{\infty}\int_{V} \boldsymbol{q}_2^*(\boldsymbol{x}, t)\mathbf{W}(\boldsymbol{x})\boldsymbol{q}_1(\boldsymbol{x}, t)\,\mathrm{d}\boldsymbol{x}\,\mathrm{d}t, \tag{4}$$

where $\mathbf{W}$ is the weight tensor, which further specifies the properties of the norm. Under these parameters, the kernel introduced in (3) becomes

$$\mathbf{R}(\boldsymbol{x}, \boldsymbol{x}', t, t') = \mathrm{E}\{\boldsymbol{q}(\boldsymbol{x}, t)\boldsymbol{q}^*(\boldsymbol{x}', t')\}\mathbf{W}. \tag{5}$$

However, the eigenmodes produced by (5) have some inconvenient properties; POD only considers statistically stationary flows, which are unbound in time and, therefore, have infinite energy in the space–time norm. One solution relies on the ergodicity assumption, instead formulating a cross-correlation tensor, which only considers differences between points in time:

$$\mathbf{R}(\boldsymbol{x}, \boldsymbol{x}', t, t') \to \mathbf{R}(\boldsymbol{x}, \boldsymbol{x}', \tau), \tag{6}$$

with $\tau = t - t'$. The cross-spectral density tensor $\mathbf{S}$, which serves as the kernel of the SPOD, is the Fourier transform of $\mathbf{R}$:

$$\mathbf{S}(\boldsymbol{x}, \boldsymbol{x}', f) = \int_{-\infty}^{\infty} \mathbf{R}(\boldsymbol{x}, \boldsymbol{x}', \tau)e^{-\mathrm{i}2\pi f\tau}\,\mathrm{d}\tau \tag{7}$$

We can construct the spectral eigenvalue problem:

$$\int_{V} \mathbf{S}(\boldsymbol{x}, \boldsymbol{x}', f)\mathbf{W}(\boldsymbol{x}')\boldsymbol{\psi}_k(\boldsymbol{x}', f)\,\mathrm{d}\boldsymbol{x} = \lambda(f)\boldsymbol{\psi}_k(\boldsymbol{x}, f), \tag{8}$$

to produce modes $\{\boldsymbol{\psi}_k(\boldsymbol{x}, f), \lambda_k(f)\}$, which both satisfy the space–time eigenvalue problem once transformed back into the time domain and maintain properties equivalent to space-only POD modes. While these spectral eigenfunctions are frequency-dependent, they are spatially orthonormal ($\langle\boldsymbol{\psi}_j, \boldsymbol{\psi}_k\rangle_x = \delta_{jk}$) and serve as an optimal basis for Fourier modes of the flow.

In essence, spectral POD may be applied in fluid mechanics to decompose a statistically stationary flow into a series of characteristic eddies [14], which oscillate at a single frequency and optimally capture a space–time energy distribution.

2.2. Computational Algorithms for SPOD

In practice, the successful application of POD relies on algorithms that efficiently perform modal decomposition from large amounts of discrete flow data, whether of experimental or numerical origin. A thoroughly documented spectral scheme termed batch SPOD was presented by Schmidt and Towne [19]. For reproducing a functional SPOD scheme, this work also benefited from the open SPOD repository generously provided by Schmidt and the California Institute of Technology [20]. What follows briefly presents the core data processing methods used in this work.

As discussed in Section 2.1, the individual realisations forming the basis of the statistical analysis must be time-resolved. While the definitive method of obtaining such data is to run the same experiment multiple times, this approach is typically impractical, especially when working with pre-existing sets of data generated for purposes other than SPOD. Additionally, more complex experiments may be impossible to replicate with sufficient precision to be considered the same process. An alternative solution is Welch's method [21], a spectral estimation technique in which a single long recording of an ergodic signal is separated into blocks whose spectra are then evaluated statistically. Crucially, it can be demonstrated that the spectral estimates computed with this method converge for an increasing number of snapshots n_t, unlike those directly evaluated from the time series. Batch SPOD transplants this idea onto continuous recordings of flow data.

Consider a set of n_t 2D flow data snapshots $\boldsymbol{q}(\boldsymbol{x}, t_j)$ with $N = n_x n_y$ discrete, equidistant points in the control volume V, where each instance is a vector field representing the instantaneous velocity distribution of the flow. For the purposes of POD, the exact nature of the spatial grid is immaterial; it suffices to sequentially index each vector in the field as $\boldsymbol{u}_j^k$, i.e., the velocity at the jth position and the kth time step. We first reorganised the dataset: the x- and y-components of the velocity vectors were separated and each assembled into an $N \times n_t$ matrix. These were then vertically concatenated to produce $\mathbf{U}$, an array containing all input data for the decomposition. $\mathbf{U}$ was then sectioned into n_{blk} blocks $\mathbf{U}_m$ of length n_{FFT}. These blocks may overlap to a certain extent to decrease the variance of the power spectral density (PSD) estimate, though in practice, overlaps larger than 50% yield greatly diminishing returns as the independence of the realisations is increasingly compromised [16,21].

The next step applies a row-wise discrete Fourier transform (DFT) to each block, specifically the DFT algorithm known as the fast Fourier transform (FFT). This produces a set of matrices $\hat{\mathbf{U}}_m \in \mathbb{C}^{n_f \times N}$, n_f being the number of frequencies resolved by the FFT, which now contain the transformed data sampled at discrete frequencies. SPOD solves the eigenvalue problem (8) one frequency at a time, by rearranging the rows of $\hat{\mathbf{U}}_m$ into a different set of n_f data matrices $\mathbf{X}_f \in \mathbb{C}^{N \times n_{\text{blk}}}$, which groups the data from each block by frequency. Given this, the cross-spectral density tensor is

$$\mathbf{S}_f = \mathbf{X}_f^* \mathbf{W} \mathbf{X}_f. \tag{9}$$

(9) produces a small $n_{\text{blk}} \times n_{\text{blk}}$ tensor, for which the eigenvalue problem is computationally inexpensive to solve. Consequently, modes $(\boldsymbol{\theta}_m)_f$ obtained in the eigendecomposition:

$$\mathbf{S}_f = (\boldsymbol{\Theta} \boldsymbol{\Lambda} \boldsymbol{\Theta}^{-1})_f \tag{10}$$

must be transformed before interpretation in the physical flow domain:

$$\boldsymbol{\Psi}_f = (\mathbf{X} \boldsymbol{\Theta} \boldsymbol{\Lambda}^{-1/2})_f = \begin{bmatrix} \boldsymbol{\psi}_1 & \boldsymbol{\psi}_2 & \cdots & \boldsymbol{\psi}_{n_{\text{blk}}} \end{bmatrix}_f \tag{11}$$

After assembly into 2D fields, the modes $(\boldsymbol{\psi}_m)_f$, represent characteristic eddies of the flow that evolve coherently in time, i.e., oscillate at a single discrete frequency f.

3. Experimental Approach

This section introduces the rig on which the experiments were conducted and briefly details the equipment used for recording PIV and other experimental data.

3.1. TCF Model

The data used in this work were recorded on the TCF test rig assembly, located at the University of Stuttgart's Institute for Aerospace Thermodynamics. The setup is described in detail by Köhler et al. [22]; we limit ourselves to briefly introducing the relevant elements.

The centrepiece of the rig was a machined PERSPEX® (acrylic glass) model of a TCF ring segment (illustrated in Figure 1), the flow through which was examined by PIV. Its geometry was scaled and simplified to improve optical access to the interior: curved surfaces, such as the vane and hot gas duct walls, were generally approximated with flat panels to avoid unnecessarily complex reflections. The block on the air inflow side mimicked a segment of the hollow outer ring, which was connected to the hub cavity of the inner ring on the opposite side of the hot gas duct by a symbolic load-carrying strut. The strut was encased in a fairing, under which the cooling air passed between the cavities.

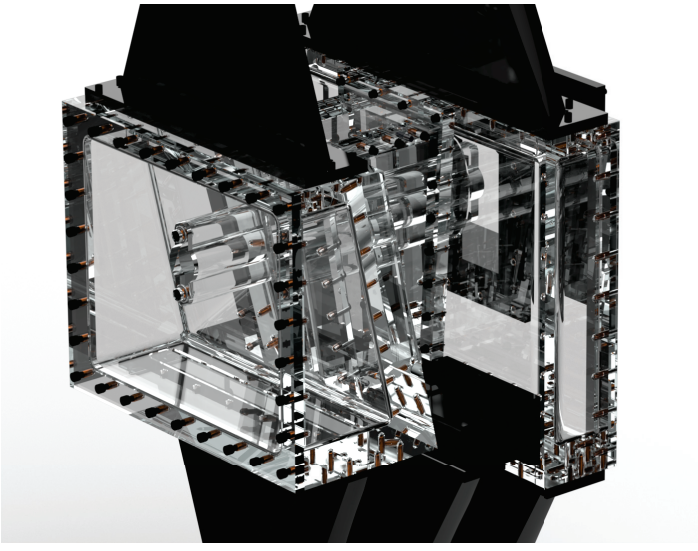

Figure 1. The TCF model and outlet diffusers.

Air for the experiment was taken from the environment, pumped into a plenum chamber at a constant, adjustable mass flow rate and homogeneously seeded with droplets of di-ethyl-hexyl-sebacate, which acted as the tracer particles for PIV. The air entered the model through an elliptical inlet gap with a hydraulic diameter of $d_\mathrm{h} = 26.9\,\mathrm{mm}$, forming an annular jet, passed through the model, and exited through five outlets, three of which were situated around the tip cavity and two around the hub cavity. The flow conditions in the model were adjusted by modulating the mass flow rate through the air supply duct until the desired Reynolds number at the elliptical inflow gap was obtained.

The control volume of the experiment was the TCF model's interior (hereafter referred to as the fluid domain), shown in Figure 2. Its maximum dimensions were $400\,\mathrm{mm} \times 500\,\mathrm{mm} \times 430\,\mathrm{mm}$. PIV was performed through the transparent walls of the model, with the laser and camera installed outside at different positions. As 2D PIV only captures the velocity distribution within a planar section of the control volume, measurements were confined to a single plane at a time. The two relevant planes for this work were Y00, the symmetry plane, and Z15, both highlighted in Figure 2; the latter derives its name from being the XY plane situated at 15% along the z-length of the fluid domain.

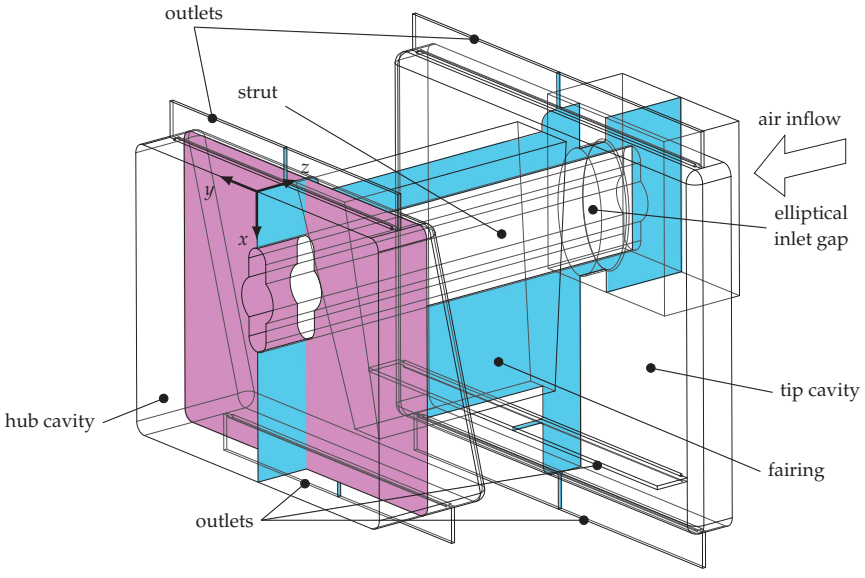

Figure 2. An isometric view of the fluid domain. The areas where the relevant planes intersect the fluid domain are highlighted in colour: Y00 in blue; Z15 in violet. The orientation of the fluid domain's local coordinate system is shown at the tip of the hub cavity.

Figure 3 shows the Y00 and Z15 slices in more detail. As the camera field of view (FOV) was limited, making it impossible to capture the entire domain in a single run, the bottom of the hub cavity (highlighted in grey for each plane) was chosen as the focus area.

While measuring in Y00 is best suited to creating an overview of the dynamics, the evaluation of Z15 allows for better understanding of the spatial characteristics of the flow phenomena. Using the information from both angles, the modal behaviour can be partially interpreted in 3D, which aids in the understanding of three-dimensional flow structures.

3.2. Measuring Equipment

The PIV method employed in this work was a high-speed 2D approach, in which the laser and camera were triggered to produce double images at a prescribed frequency. These images were interpreted by software, which matched the 32×32 pixel interrogation windows in two successive frames to produce vector fields representing the instantaneous velocity distribution in the flow. The specifics of PIV are beyond the scope of this work; while the choice of operating parameters affects the evaluation and will be discussed in Section 5.1, we must accept that the raw images can be reliably processed into instantaneous vector fields if the parameters are well chosen. For more technical insight, the statistical background and application of PIV are explored thoroughly by Raffel et al. [23].

The laser employed in the PIV was an INNOSLAB IS200-2-L single-cavity green short-pulse Tm:YLF unit manufactured by EdgeWave GmbH. The laser pulse frequency can be adjusted up to a maximum of 10 kHz. The images were recorded with a Photron FASTCAM SA-X2, which was triggered at the data acquisition frequency f_s to produce two consecutive images. This resulted in a maximum total of 5000 velocity snapshots per measurement. The commercial software LaVision DaVis 10.2 was used for post-processing.

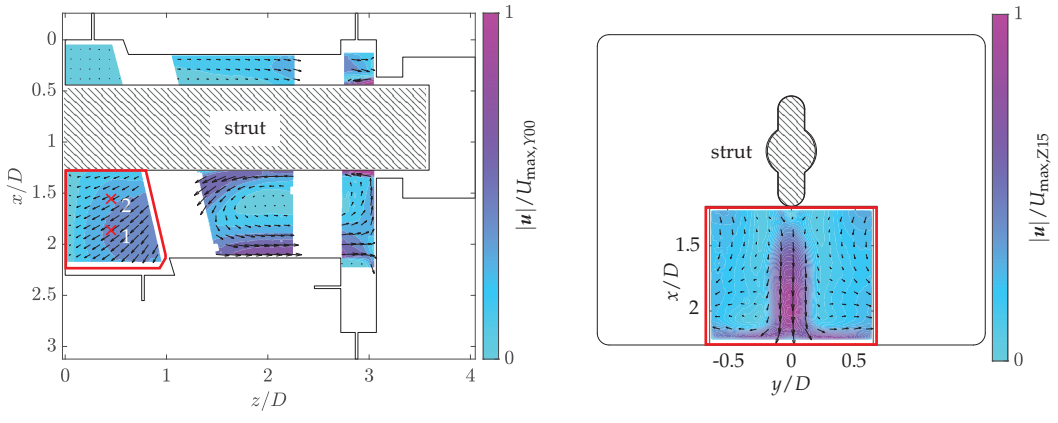

(**a**) (**b**)

Figure 3. The two measurement planes with overlaid mean flow speed distribution. Coordinate axes are normalised by the major axis of the elliptical inflow slit D, and the velocity field is normalised by the highest measured flow speed $U_{\max}$. The areas in which HSPIV data were recorded, as well as the locations of the hot wire anemometer probes are highlighted with markers 1 and 2 for the locations $x_{\mathrm{HW},1}$ and $x_{\mathrm{HW},2}$ respectively. (**a**) Y00, evaluated from 8 Hz PIV. (**b**) Z15, evaluated from high-speed PIV data.

Aside from PIV, a hot wire anemometer was deployed inside the fluid domain to record 1D velocities. The hardware used was an SVMtec GmbH SVM-4CTA-DAQ anemometry system coupled with HWP10/90 10 µm gold-plated wolfram wire probes. The probe calibration data suggested an error of roughly 1% in the detected velocity in the relevant range.

Due to its low bandwidth and storage requirements, the 1D signal can be written at extremely high sampling frequencies for a long time, allowing highly resolved PSDs to be obtained. The probe was inserted into the hub cavity at the base of the exhaust funnel; measurements were conducted at different depths of insertion, as indexed in Figure 3a, as well as different Reynolds numbers. The positions denoted by 1 and 2 were at $x_{\mathrm{HW}} = [60, 100]$ mm, respectively, as measured from the inner wall of the cavity.

4. Initial Analysis

While high-speed PIV is by far the most-powerful available tool for experimental analysis of fluid systems, the necessary equipment is expensive and, therefore, in high demand. Gathering information about the behaviour of the system in advance, using more accessible methods, helps ensure the effective use of the equipment later on. At the same time, obtaining similar results through functionally diverse avenues of analysis serves to validate the involved methods.

In this section, several available sources of data were invoked to narrow down the spatial locations and spectral range of the characteristic structures within the TCF model. This information can be used to set the operational parameters of the PIV, such as the image acquisition frequency, as well as hone the post-processing algorithms used to evaluate the recordings.

4.1. Mean Flow

The baseline for understanding the dynamics of any fluid system is examining the time-averaged conditions. Fortunately, low-speed PIV data recorded at $f_{\mathrm{s}} = 8$ Hz are abundant from previous investigations of the same model [22]. While these recordings proved unhelpful in exploring the time evolution of the system, they were useful for gaining

an overview of the mean flow through the fluid domain. The time-averaged flow speed for $\mathrm{Re} = 37{,}000$ is presented in Figure 3a.

Köhler et al. [22] provide a comprehensive overview of the topology of the mean flow field. The most-dominant structure in the fluid domain was a jet that remains attached to the strut approximately halfway along the fairing, before separating, crossing the hub cavity diagonally and impacting the inner wall in the bottom left corner, where a stagnation area developed. At the same time, it featured sufficiently low velocities to be examined by PIV. The anemometer probe locations and PIV windows detailed in Figure 3 were defined to most-effectively capture it.

The mean flow in the transverse Z15 plane, as computed from PIV, is depicted in Figure 3b. Unsurprisingly, the topology was largely symmetrical along the y-axis. It was dominated by the footprint of the hub cavity jet, whose elliptical shape was owed to the orientation of the plane; from comparisons with Figure 3a, we can infer that it intersected the jet at an angle of roughly 45°. Consequently, the section contained the vertical component of the jet's velocity vector. The most-energetic region was found at $x/D = 2$, very close to the bottom wall; in fact, the jet already experienced significant deflection this far downstream, as evidenced by the stagnation point and higher speed outwash regions along the boundary of the camera window. Towards the top, the shape split in two, where the flow separated around the central strut. The lowest flow speeds were found in the shear layer on either side of the jet; beyond it, the field showed air symmetrically moving slightly inwards at $x/D = 1.2$ before being deflected straight down and finally outward by $x/D = 1.8$. This suggested the presence of larger vortical structures that extended beyond the camera FOV.

4.2. Hot Wire Anemometry

As laid out in Section 3.2, a hot wire anemometer was used in the early stages of the work to gather some information about the dynamics of the internal flow field with a method that is well-understood, reliable, and simple to deploy. The main objectives for this step were to identify dynamically active ranges in the PSD and establish that they are robust towards changes in the Reynolds number. These data were used later as a direct reference to validate the PSDs obtained through more sophisticated post-processing (see Sections 5.2 and 6.2).

The data were recorded at every position and mass flow rate with a sampling frequency of $f_\mathrm{s} = 5\,\mathrm{kHz}$ for $T_\mathrm{HW} = 60\,\mathrm{s}$. The three flow regimes that were investigated were $\mathrm{Re}_j = [37, 55.5, 74] \times 10^3$. We interpreted the data by performing a Fourier transform and examining the resulting PSDs. Keeping with established practises in signal processing [21], the PSD was constructed as the average of n_blk blocks of length n_FFT; a block size of $n_\mathrm{FFT} = 2^{15}$ was selected as a suitable compromise between conclusive averaging and sufficiently informative spectral resolution.

The results of this evaluation are presented in Figure 4. The PSDs at different flow regimes Re_j were grouped by position $x_{\mathrm{HW},k}$; the raw spectra are each shown in grey along with a smoothed spectrum, depicted in red, obtained by applying a Savitzky–Golay finite impulse response filter (SGF) of order three with a frame length of 31 data points. The SGF is based on low-order polynomial fits and the linear least-squares method and is commonly used to smooth 1D data in signal processing and experimental applications such as spectroscopy [24,25]. The filter is a convenient tool to identify trends in an otherwise noisy spectrum, which establishes an overview of the flow dynamics; at the same time, the spectral clarity in low frequency bands remains superior to simply evaluating the FFT with smaller block sizes. The frequency axis was nondimensionalised as the Strouhal number $\mathrm{Sr} = fD/U_0$ to ease the comparison of the data at different Reynolds numbers, where U_0 is the nominal inlet flow speed.

As expected, the absolute amount of energy in the flow rose with increasing Reynolds number regardless of position. As our primary concern was the shape of the spectrum, the results at both positions were normalised to the highest detected amplitude for the sake of clarity.

The initial analysis of the results was encouraging. At Re_1, both Figure 4a,b feature a pair of distinct peaks at roughly $Sr = 0.014$ and 0.07. A third peak emerged after an increase in Reynolds number to Re_2, though the general structure of the spectrum was preserved: for $x_{HW,1}$, we observed peaks at 0.012 and 0.149, as well as a broad elevation between 0.056 and 0.093. At Re_3, the same pattern appeared at 0.012, 0.07–0.091 and 0.119. A very similar structure was observed at $x_{HW,2}$, where, for Re_2, the three peaks were registered at 0.013, 0.07–0.084, and 0.131 before shifting to 0.012, 0.053–0.084, and 0.116 after an increase in Reynolds number to Re_3.

In summary, we concluded that, for $Re \geq 37{,}000$, the system exhibited strong organised unsteady behaviour in the $Sr = 0$ to 0.2 range, which can be clearly separated from broadband turbulence in the spectra derived from hot wire anemometry. In this range, the general structure of the PSD was invariant to changes in Reynolds number when presented in nondimensional space, which suggested stable oscillating behaviour. Peaks at higher Strouhal numbers notably exhibited bigger shifts. The spectra did not differ significantly based on the position of the probe, suggesting that the dominant motion was sufficiently extensive to cover both examined locations. For future reference, the two frequency bands in which the reference signal was most active at Re_1 will be referred to as Band 1 between $Sr = 0.01$ and 0.03 and Band 2 between $Sr = 0.07$ and 0.1.

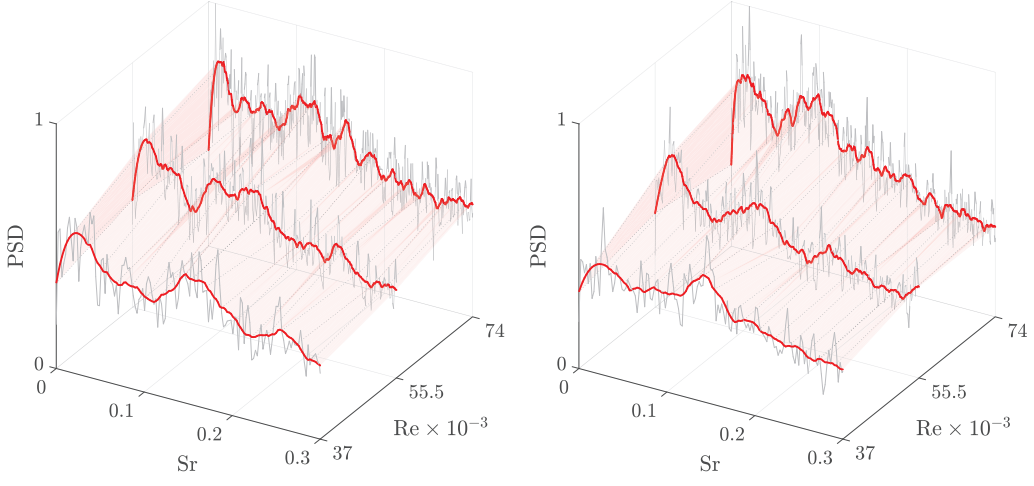

(**a**) (**b**)

Figure 4. Normalised power spectra of 1D hot wire anemometer signals at different positions (see Figure 3a). The black lines are the raw PSD interpreted with $n_{FFT} = 2^{15}$, while the red lines are the PSD smoothed with a 3rd-order SGF, computed over a window of 31 sample points. (**a**) $x_{HW,1} = 60$ mm. (**b**) $x_{HW,2} = 100$ mm.

5. Conventional SPOD

Section 4.2 presents us with strong evidence for stable, coherent structures in the fluid system, which was essential to justify further analysis. The combined anemometry data also provided an estimate of the dynamically active range of the system, which we captured with HSPIV.

5.1. Data Acquisition

A PIV experiment can be tailored to optimally resolve any system by adjusting several process parameters. The first barrier is the successful evaluation of the images recorded through PIV, which provides the instantaneous velocity fields that form the basis for all further post-processing. The experiments showed that the maximum particle displacement,

beyond which the DaVis cross-correlation algorithm failed to reliably converge, was reached if the inflow Reynolds number meaningfully exceeded $\mathrm{Re}_1 = 37{,}000$. This flow regime was, thus, chosen for the HSPIV measurements, as the analysis of anemometry data in Section 4.2 suggested that strong fluctuations were already present in the system at this point, and the behaviour showed significant commonality with higher Reynolds number regimes.

However, while a high pulse frequency was necessary to produce the velocity fields, single-pulse PIV at $f_{\mathrm{s,max}} = 10\,\mathrm{kHz}$ would fill the camera's internal storage after a mere second of operation. Such a brief run would include too few cycles of the organised motion in the system's dynamically active range to be statistically meaningful. We, thus, opted for simulated double-pulse operation to produce snapshots at $f_\mathrm{s} = 500\,\mathrm{Hz}$, which resulted in a total of 5000 snapshots per measurement run, produced over a period of $T_\mathrm{s} = 10\,\mathrm{s}$. This approach maintained a time step of $\Delta t = 10^{-5}\,\mathrm{s}$ between frames, which was necessary to correlate the snapshots.

With this setup, four independent runs were performed in the Y00 plane, referred to as $\mathrm{Y00_I}$ through $\mathrm{Y00_{IV}}$, as well as a run in the Z15 plane. An additional Y00 recording was performed with different parameters, that is a sampling frequency of $f_\mathrm{s} = 125\,\mathrm{Hz}$. The rationale for this decision was that the resulting cutoff frequency $f_\mathrm{N} = 62.5\,\mathrm{Hz}$ was the lowest possible choice of f_N that did not infringe upon the dynamically relevant range. The immediately apparent drawback of this approach is that the laser must still fire continuously at a rate of 10 kHz; the energy input would inevitably damage the TCF model if it were subjected to it for too long, which limited the maximum measurement period to $T_\mathrm{s} = 20\,\mathrm{s}$. This setup can, therefore, only produce 2500 snapshots. It is henceforth referred to as $\mathrm{Y00_{125}}$.

5.2. Evaluation

As with the anemometry data, we begin our discussion of the SPOD results with spectral analysis. The individual measurements were characterised primarily by their leading modes; the energy in the remaining modes was distributed near-uniformly across the frequency spectrum and trailed the leading mode's amplitude by roughly an order of magnitude. We, thus, focused on the leading modes when discussing parallels and differences between measurements.

Figure 5 shows the leading modes of the runs introduced in Section 5.1, as well as the Strouhal number bands obtained from evaluating the hot wire data at Re_1 in which the reference exhibited increased activity. The filtered hot wire spectrum at $x_{\mathrm{HW},1}$ and Re_1 was included as a prediction for the shape of the PSD distribution. For the sake of simpler qualitative analysis, the spectra were normalised by the tallest detected peak in each measurement. Additionally, in working with the PIV data, PSD information below $\mathrm{Sr} = 0.01$ was consistently chaotic and unrepeatable. This likely was a result of a very small number of full cycles being included in the recording; consequently, these data were excluded from the following analysis. Note that, due to the complexity of the signal, each individual measurement was unlikely to produce the exact desired result. Instead, we chose to evaluate the superposition of $n = 5$ measurements, as with $n \to \infty$, we expected the cumulative spectrum to approach the reference.

The takeaways from Figure 5 are mixed. While it is encouraging that the dominant peaks in all PIV-derived spectra occurred between $\mathrm{Sr} = 0.01$ and $\mathrm{Sr} = 0.1$, which matched the reference, they failed to replicate the twin peak clusters around $\mathrm{Sr} = 0.02$ and $\mathrm{Sr} = 0.08$ present in the hot wire spectra. Instead, the tallest peaks of several measurements, including $\mathrm{Y00_{II}}$, Z15, and notably, $\mathrm{Y00_{125}}$, were located between $\mathrm{Sr} = 0.03$ and $\mathrm{Sr} = 0.06$, a range in which the reference displayed much lower amplitudes. Evidently, simply lowering f_s did not immediately yield favourable results.

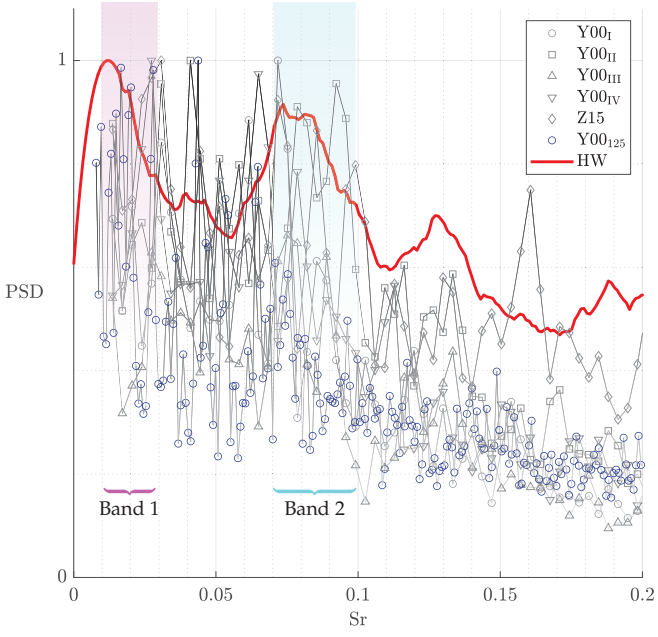

Figure 5. Normalised PSD of the SPOD solutions for the high-speed PIV experiments. The red line represents a reference based on filtered hot wire data at $x_{\mathrm{HW},1}$ and Re_1.

6. S2POD

The results presented above failed to capture the dynamics identified in the reference. The options for continued analysis with conventional SPOD were unpromising: an increase in data acquisition frequency f_s would inevitably lead to even poorer spectral resolution, while the physical barrier of a maximum recording time T_s caused measurements with decreased f_s to produce less data overall. Faced with this dilemma, we propose a novel preprocessing method termed spectral subsampling POD (S2POD).

6.1. Establishing Ideas

Section 2.2 introduced the idea of the subdivision of the data into blocks, then processed separately using Welch's method. To reduce the effective sampling frequency f_s^*, we created the blocks $\mathbf{U}_m$ by subsampling the original sequence: assembling every other frame into a block created a realisation of the process over the same length of physical time, but halved the sampling frequency. We can increase the subsampling factor C_sub further until we obtain enough blocks to compute a statistically satisfactory number of modes with $f_\mathrm{s}^* = f_\mathrm{s}/C_\mathrm{sub}$.

Figure 6 demonstrates the subsampling method for a fictional scalar value at a single point in the control volume, $|\boldsymbol{u}_j|$. The progression through time corresponded to the column index k. For illustrative purposes, a low base sampling frequency was chosen.

Aside from the sample rate, the four sequences created by this method varied from the original in several ways. We observed a shift in the absolute beginning and end times as a result of the frames being discarded, though absolute time was irrelevant, as most further computation occurred in the frequency domain. A distortion of the signal was avoided, as we assumed that the base sampling frequency was much higher than the most-energetic components of the flow; f_s^* can be lowered significantly before they begin approaching the Nyquist limit f_N.

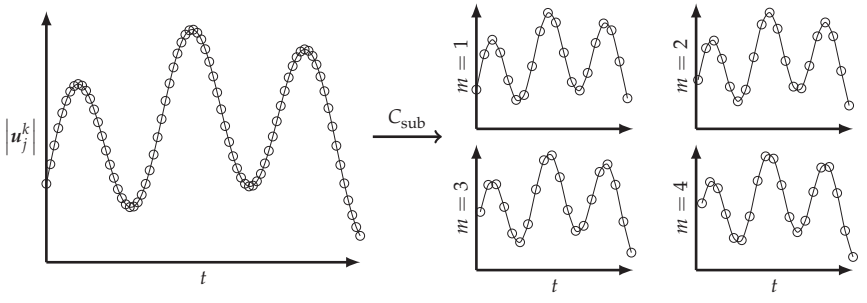

Figure 6. A 1D demonstration of creating several realisations $\mathbf{U}_m$ from a single sequence through subsampling at $C_{\text{sub}} = 4$. The line through the samples denotes a reconstruction of the continuous signal rather than the ground truth.

This approach offers certain advantages. Selecting parameters for traditional SPOD involves a compromise between the number of modes n_{blk} and the frequency resolution, characterised by n_{FFT}, while the subsampling approach always yields the optimal frequency resolution for a given set of data $\Delta f = f_{\text{s}}/n_t$. The decision was instead made between a larger number of modes $n_{\text{blk}} = C_{\text{sub}}$ and a broader frequency domain:

$$f_{\text{N}} = \frac{f_{\text{s}}}{2C_{\text{sub}}} \tag{12}$$

As this method is primarily geared towards applications where the sampling rate is so high that frequency resolution in the dynamically active range is poor, the top end of the spectrum rarely contains relevant information. Consequently, we traded a lower f_{N} for improved statistical convergence. However, it must be noted that realisations created through subsampling were strongly correlated, and the variation of the system was, therefore, largely captured by the leading mode.

A simple numerical simulation demonstrated the effectiveness of the procedure. Using an SMAC Navier–Stokes solver [26], we computed snapshots of the flow around a cylinder with the boundary conditions tuned to produce a Kármán vortex street at a cylinder with a Reynolds number of $\text{Re} = 100$. The complete dataset, trimmed to only contain fully developed flow, comprised 10,000 vector fields with $\Delta t = 0.02\,\text{s}$, i.e., sampled with $f_{\text{s}} = 500\,\text{Hz}$.

Without subsampling, as seen in Figure 7a, the spectrum contained a single broad peak at $f = 0.2441\,\text{Hz}$—even with the balance shifted heavily towards the frequency resolution, as n_{FFT} was so large that the data yielded only three modes. The results were drastically more favourable once subsampling was applied: Figure 7b shows a a clear peak at $f = 0.25\,\text{Hz}$, as well as a series of progressively weaker harmonics at $f = 0.25n\,\text{Hz}$, $n = 2, 3, \ldots$, which was consistent with the results obtained by other analyses of the dynamics of the Kármán vortex street [27]. Simultaneously, $n_{\text{blk}} = 10$ and low amplitudes for the lesser modes showed the reliable statistical convergence of the process.

Of course, as a consequence of the method, f_{N} dropped from 250 Hz to just 25 Hz. However, as displayed in the PSD graphs, even a much lower limit still allowed us to draw informative conclusions about the dynamics of the flow.

The plausibility of the result can be verified by estimating the main frequency of the vortex shedding: Schlichting and Gersten [28] suggest that, for flows around a cylinder, the Strouhal number $\text{Sr} = fd/u_\infty$ is correlated with the Reynolds number, which was known to be $\text{Re} = 100$ in the simulation. Thus, with $\text{Sr} \approx 0.15$, as well as cylinder diameter $d = 0.5625\,\text{m}$ and $u_\infty = 1\,\text{m/s}$, we obtained $f \approx 0.2667\,\text{Hz}$ for the main shedding frequency. This aligned with the peaks observed in Figure 7.

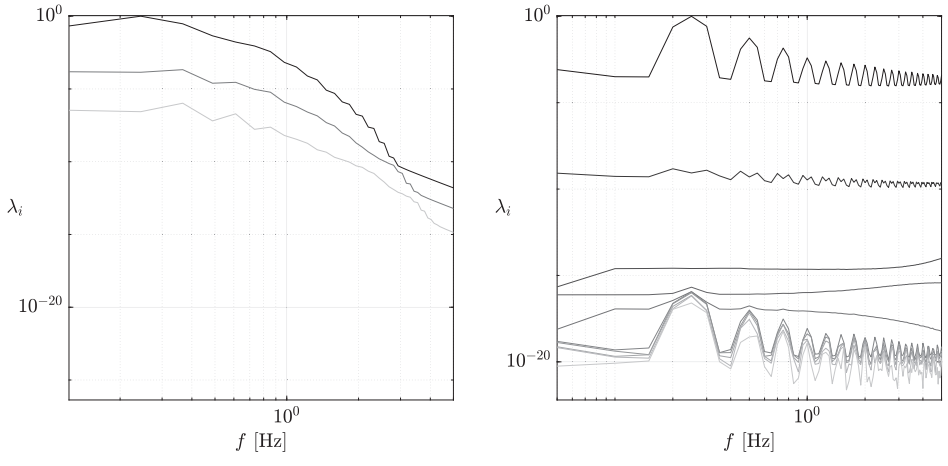

(**a**) (**b**)

Figure 7. Normalised power spectra of the numerical simulation of a Kármán vortex street. (**a**) No subsampling, $n_{\mathrm{FFT}} = 4096$. (**b**) $C_{\mathrm{sub}} = 10$, $n_{\mathrm{FFT}} = 1000$.

Another issue to be addressed is the aliasing error, which inevitably contaminated the downsampled signal. Signal components oscillating at frequencies exceeding the new effective maximum frequency f_{N}^* can no longer be resolved by the Fourier transform. If left unheeded, this would result in a higher overall noise background and artificially inflated eigenvalues on secondary modes. A distortion of the downsampled signal was prevented by applying a lowpass filter at f_{N}^* before breaking the data up into blocks, discarding the energy contribution of the high-frequency components. This basic level of post-processing was applied whenever subsampled data are discussed within this work.

6.2. Results

Having demonstrated the effectiveness of S2POD on a predictable, simulated system, we shall attempt to improve upon the analysis presented in Section 5. The PSDs computed through S2POD with $C_{\mathrm{sub}} = 8$ for the 500 Hz HSPIV measurements are showcased in Figure 8. $\mathrm{Y00}_{125}$ is not included; any downsampling with $C_{\mathrm{sub}} > 2$ would reduce f_{N} below the acceptable threshold.

Figure 8 significantly improves upon Figure 5. We can identify several key differences. A brief glance reveals that the noise background was substantially lower, even at low frequencies. This was owed primarily to the improved spectral resolution, allowing for a greater dynamic range. The energy distribution of the superimposed S2POD solutions matched the hot wire reference spectrum very well. The highest observed peaks of each measurement, with the exception of $\mathrm{Y00}_{\mathrm{I}}$, fell within a $\Delta\mathrm{Sr} = \pm 0.01$ window of the dominant peaks in the reference: $\mathrm{Y00}_{\mathrm{II}}$ and Z15 matched the identified bands very well at $\mathrm{Sr} = 0.072$ and $\mathrm{Sr} = 0.092$, respectively. As a result, the trough between the two band boundaries at $\mathrm{Sr} = 0.03$ and $\mathrm{Sr} = 0.06$, which failed to materialise in Figure 5, was clearly identifiable. While the tallest peaks in Band 1 in the measurements fell somewhat higher on the spectrum than the peak of the reference curve, this can be attributed to overall poorer performance at low frequencies.

These positive findings allowed us to realise the key advantage SPOD offers over conventional methods, i.e., the production of spatial modes that directly magnify the utility of spectral analysis. To elaborate on the brief introduction given in Section 2.2, the modes were spatial representations of the characteristic eddies, which the decomposition algorithm identified as energy-optimal basis vectors of the original sequence. Each mode oscillated

periodically at a specific Strouhal number; the PSD supplied information regarding which frequencies and, consequently, which modes contained the highest energy content. We can, thus, reconstruct a reduced-order model of the fluctuating component of the fluid system by superimposing the leading mode at several peaks in the power spectrum.

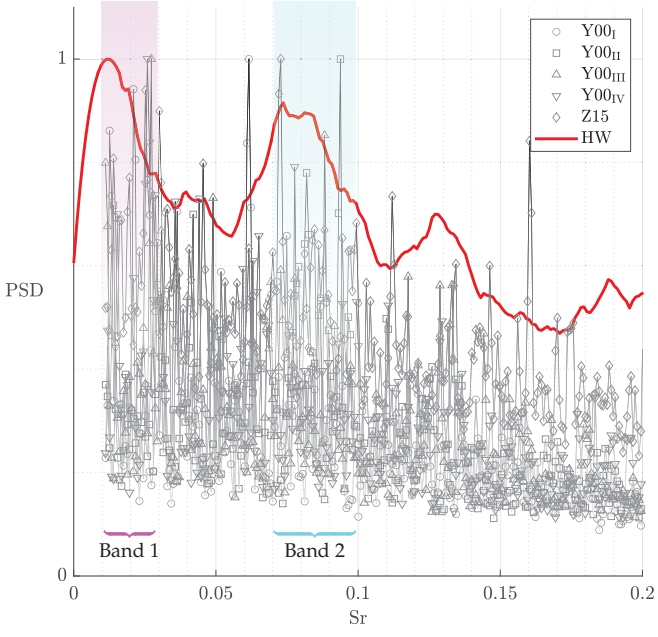

Figure 8. Normalised PSD of the S2POD solutions for the high-speed PIV experiments. The red line represents a reference based on filtered hot wire data at $x_{\mathrm{HW},1}$ and Re_1.

The decomposition algorithm produced the spatial modes at a random phase φ_0. This instantaneous slice frequently failed to convey the topology of the mode; it was, therefore, preferable to inspect the modes at different phase shifts $\Delta\varphi$. As we considered only the absolute magnitude of the velocity, the period of the oscillation was reduced from 2π to π, which we discretised into steps of $\pi/3$ for the visual presentation. Such a discrete progression of each mode through their π-periodic cycle is presented in Figures 9–12.

The two dynamically active bands detected, through spectral analysis of each feature, a geometrically distinct characteristic eddy, which repeatedly emerged at significant peaks. Data in the Y00 and Z15 planes can be combined for a more complete phenomenological description of the three-dimensional fluid flow.

Representative spatial modes for the first band are presented in Figures 9 and 10. The Y00 section was characterised by two parallel lobes, which roughly followed the contour of the annular jet with a clearly defined trough between them. While the bottom lobe, most prominently visible at $\Delta\varphi = 2\pi/3$, remained predominantly straight, the top lobe fanned out and formed an identifiable stagnation area at the wall between $x/D = 1.8$ and 2.2. Most importantly, the phase evolution of the structure was clearly alternating: the top and bottom lobes swelled and receded periodically, one giving way to the other.

The Z15 section revealed a complementary image. For most of its cycle, the eigenmode evolved within the jet's outer layer, i.e., the tall elliptical structure between $y/D = -0.2$ and 0.2 that surrounded the core and featured the greatest mean flow speed gradient in the domain. The mode's cycle began with an elongated lobe stretching along the shear layer to the right of the core; see Figure 10a. As the phase advanced, the lobe migrated upward and

to the left, where it assumed a more compact, rounded shape at $\Delta\varphi = \pi/3$. By $\Delta\varphi = 2\pi/3$, the lobe moved to the shear layer to the left of the core.

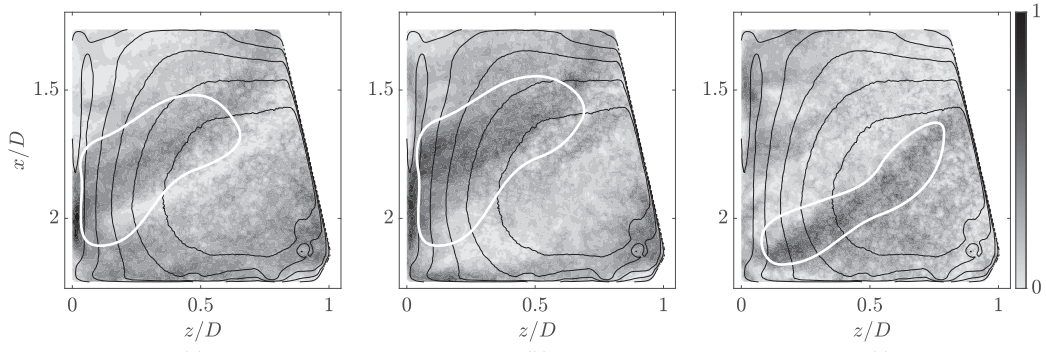

Figure 9. Normalised leading S2POD spatial eigenmode for $Y00_{II}$ at $Sr = 0.029$, evaluated at different phase shifts; the overlaid isocontours represent the mean flow's velocity distribution. The white outlines highlight relevant flow structures. (**a**) $\Delta\varphi = 0$. (**b**) $\Delta\varphi = \pi/3$. (**c**) $\Delta\varphi = 2\pi/3$.

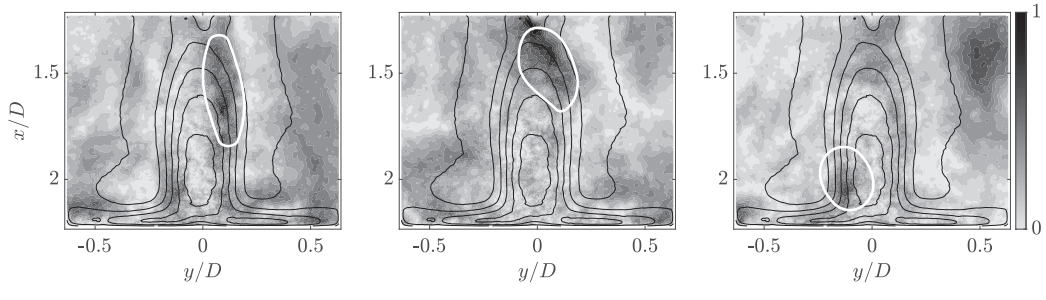

Figure 10. Normalised leading S2POD spatial eigenmode for Z15 at $Sr = 0.025$, evaluated at different phase shifts. (**a**) $\Delta\varphi = 0$. (**b**) $\Delta\varphi = \pi/3$. (**c**) $\Delta\varphi = 2\pi/3$.

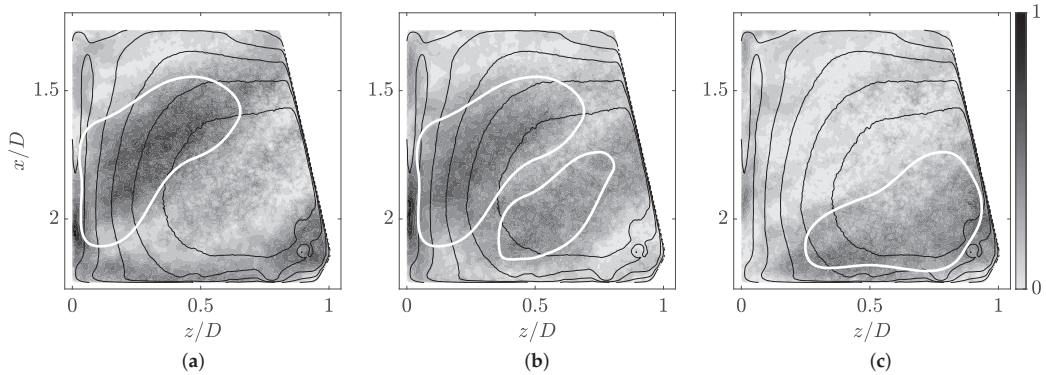

Figure 11. Normalised leading S2POD spatial eigenmode for $Y00_{II}$ at $Sr = 0.094$, evaluated at different phase shifts. (**a**) $\Delta\varphi = 0$. (**b**) $\Delta\varphi = \pi/3$. (**c**) $\Delta\varphi = 2\pi/3$.

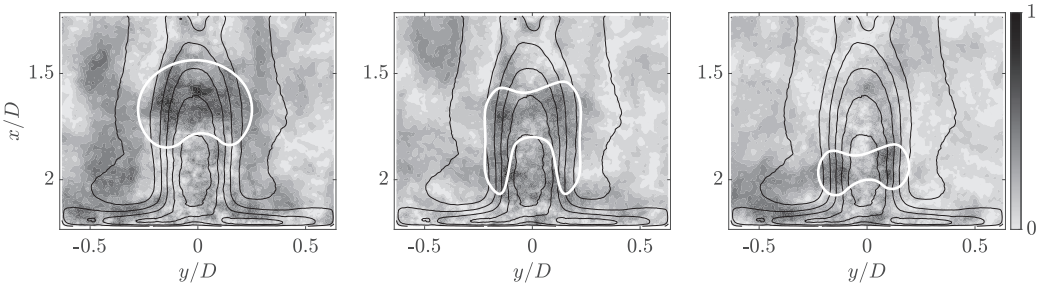

Figure 12. Normalised leading S2POD spatial eigenmode for Z15 at Sr $= 0.112$, evaluated at different phase shifts. (**a**) $\Delta\varphi = 0$. (**b**) $\Delta\varphi = \pi/3$. (**c**) $\Delta\varphi = 2\pi/3$.

Having gathered information about the spatial characteristics of the oscillations in this frequency band in two perpendicular planes, we may attempt to reconstruct the three-dimensional structure of the phenomenon at hand. Both spatial modes in Y00 and Z15 exhibited decidedly directional motion surrounding the jet; while the analysis in Y00 consistently found elongated lobes moving perpendicular to the jet, emerging in the shear layer and dissipating in it again after traversing the core, Z15 indicated that the dominant motion in the cross-section plane was counterclockwise rotation throughout the shear layer. These factors aligned with the suggested presence of a counterclockwise precessing component of the jet, induced by the transition from an annular structure at the inflow gap. Cafiero et al. [29], in their investigation of a three-dimensional turbulent jet, registered precession at Strouhal numbers between 0.01 and 0.025; this aligned with the range detected in our experiment.

The modes associated with the second band differed significantly from the patterns discussed above. In Figure 11, the domain is split into two wide, staggered bands along the core of the jet. The bands progressively expanded, achieving their maximum amplitude at different $\Delta\varphi$; while the top band was most prominent at $\Delta\varphi = 0$, the bottom band dominated at $\Delta\varphi = 2\pi/3$. The corresponding structure in Z15 was found largely in the shear layer, though it expanded into the core of the jet further than the lobes seen in Figure 10. We can successfully match the lobe position in Z15, where the Y00 lobes intersected the perpendicular plane, e.g., Figures 11a and 12a.

The most-notable difference from the previous three peaks was the directionality of the time evolution. While the spatial patterns of the first band exhibited predominantly rotary motion, modes in Band 2 exhibited cyclic growth parallel to it. This observation helped substantiate the hypothesis that the higher frequency peaks belonged to a distinct flow phenomenon from the previously discussed patterns.

7. Concluding Remarks

The focus of this work was an exploration of the utility of spectral proper orthogonal decomposition (SPOD) as an instrument for primary analysis of complex flow fields and the detection of organised motion therein. As an example of a largely unknown system, with practical engineering applications in mind, an abstracted model of a radial slice of a turbine centre frame (TCF) was selected to investigate its internal flow structures.

As a first measure of gauging the system's dynamics, a hot wire anemometer was deployed in the hub cavity. Spectral analysis of the 1D signal at various positions confirmed the existence of organised motion outside of the range typically associated with turbulence mechanisms in open jets, justifying further investigation with more sophisticated equipment. Beyond that, the dominant unsteady structures were found to be stable throughout the entire range of Reynolds numbers at which the experiment was conducted.

The base procedure was found to perform poorly in scenarios where the sample rate was high while the total length of the recorded sequence was short; this excess in time resolution led to unnecessarily wide frequency ranges in spectral analysis, i.e., power spectra that were dominated by broadband turbulence, while the regions of interest were represented by only a few sample points. To remedy this shortcoming, a modification of the batch SPOD algorithm was developed. Instead of conducting Welch averaging with blocks split from the original sequence, the blocks were assembled by subsampling, i.e., assembling every nth frame into a series of new sequences with a lower effective sampling frequency $f_s^* = f_s/n$. This procedure achieved maximum possible spectral resolution at the expense of a lower Nyquist frequency, which in most applications is a favourable trade-off.

Armed with S2POD and high-speed particle image velocimetry (PIV) data in two perpendicular planes, we successfully identified two distinct flow phenomena:

1. A precessing structure in the shear layer surrounding the hub cavity jet, characterised by counterclockwise motion at several peaks between $\mathrm{Sr} = 0.01$ and 0.03.
2. A modulation of the jet's flow speed at several peaks between $\mathrm{Sr} = 0.07$ and 0.1.

This analysis suggested that the inclusion of subsampling successfully broadens the applicability of SPOD. The dilemma between sampling frequency and recording time is inherent to all PIV experiments, even though it can be amortised through more sophisticated equipment in some cases. S2POD offers a way out without the need for hardware upgrades. Similarly, existing experimental or numerical data may not have ideal parameters for decomposition if they were originally recorded with different post-processing methods in mind. Δt tends to be very small, especially in numerical solutions, making it time-consuming and expensive to compute for extended periods of physical time. Gaining insight into the dynamics of such approaches through S2POD allows it to be tuned to resemble real systems beyond matching time-averaged conditions.

Author Contributions: Conceptualisation, S.K.; formal analysis, N.S., S.K. and J.v.W.; funding acquisition, J.v.W.; investigation, N.S. and S.K.; methodology, N.S. and S.K.; data curation, N.S.; project administration, J.v.W.; resources, J.v.W.; software, N.S.; supervision, J.v.W.; validation, N.S., S.K. and J.v.W.; visualisation, N.S.; writing—original draft, N.S.; writing—review and editing, S.K. and J.v.W. All authors have read and agreed to the published version of the manuscript.

Funding: The research was carried out as part of the joint research programme ECOFLEX-turbo by AG Turbo. The work was funded by the Federal Ministry for Economic Affairs and Climate Action as per the resolution of the German Federal Parliament under Grant Number 0324358I.

Data Availability Statement: Data sharing not applicable.

Acknowledgments: The authors gratefully acknowledge AG Turbo and MTU Aero Engines AG for their support.

Conflicts of Interest: The authors declare no conflict of interest. The funders had no role in the design of the study; in the collection, analyses, or interpretation of the data; in the writing of the manuscript; nor in the decision to publish the results.

Abbreviations

The following abbreviations are used in this manuscript:

DFT	Discrete Fourier transform
FFT	Fast Fourier transform
FOV	Field of view
(HS)PIV	(High-speed) particle imagine velocimetry
K-L	Karhunen–Loève
PSD	Power spectral density
SGF	Savitzky–Golay finite impulse response filter
(S2)POD	(Spectral subsampling) proper orthogonal decomposition

TCF	Turbine centre frame
Latin Symbols	
C_{sub}	Subsampling factor (-)
d	Diameter (m)
D	Major axis of elliptical inflow slit (m)
f	Frequency (Hz)
$\mathcal{H}$	Hilbert space (-)
n	Natural number, No. of data points (-)
N	No. of spatial points (-)
$\boldsymbol{q}$	Vector function (-)
$\mathbf{R}$	Correlation tensor (-)
Re	Reynolds number (-)
$\mathbf{S}$	Cross-spectral density tensor (-)
Sr	Strouhal number (-)
t	Time (s)
T	Period, measurement duration (s)
$\boldsymbol{u} = [u, v, w]$	Cartesian velocity vector ($\mathrm{m\,s^{-1}}$)
U	Reference flow speed ($\mathrm{m\,s^{-1}}$)
$\mathbf{U}$	Input data array (-)
V	Control volume/spatial domain (-)
$\mathbf{W}$	Weight tensor (-)
$\boldsymbol{x}$	Spatial coordinates (m)
x, y, z	Cartesian coordinates (m)
$\mathbf{X}$	Fourier coefficient matrix (-)
$\boldsymbol{z}$	Set of independent variables (-)
Greek Symbols	
δ	Kronecker delta (-)
Δ	Delta operator or difference (-)
λ	Eigenvalue (-)
$\mathbf{\Lambda}$	Eigenvalue matrix (-)
ξ	Stochastic variable (-)
τ	Time shift (s)
φ	Phase (rad)
$\boldsymbol{\phi}$	Eigenfunction (-)
$\mathbf{\Phi}$	Eigenfunction matrix (-)
$\boldsymbol{\psi}$	Spectral eigenfunction (-)
$\mathbf{\Psi}$	Spectral eigenfunction matrix (-)
Ω	Variable domain (-)
Subscripts	
0	Nominal, initial
∞	Far-field condition
blk	Block
f	Frequency index
FFT	No. of data points used in FFT
h	Hydraulic diameter
HW	Local hot wire coordinate system
max	Maximum occurring value
N	Nyquist
s	Sampling

t	Time steps
x	Related to x-axis
y	Related to y-axis
Operators	
$\mathrm{E}\{\cdot\}$	Expectation operator (-)
$\bar{\cdot}$	Expectation value
$\hat{\cdot}$	Fourier-transformed
$\cdot^*$	Conjugate transpose, effective
$\langle \cdot, \cdot \rangle$	Inner product

References

1. Sirovich, L. Turbulence and the dynamics of coherent structures. I–III. *Q. Appl. Math.* **1987**, *45*, 561–590. [CrossRef]
2. Wang, Y.; Yu, B.; Wu, X.; Wei, J.J.; Li, F.C.; Kawaguchi, Y. POD study on the mechanism of turbulent drag reduction and heat transfer reduction based on Direct Numerical Simulation. *Prog. Comput. Fluid Dyn.* **2011**, *11*, 149–159. [CrossRef]
3. Wang, Y.; Yu, B.; Wu, X.; Wang, P.; Li, F.C.; Kawaguchi, Y. POD Study on Large-Scale Structures of Viscoelastic Turbulent Drag-Reducing Flow. *Adv. Mech. Eng.* **2014**, *6*, 574381. [CrossRef]
4. Schmid, P.J. Dynamic mode decomposition of numerical and experimental data. *J. Fluid Mech.* **2010**, *656*, 5–28. [CrossRef]
5. Wynn, A.; Pearson, D.S.; Ganapathisubramani, B.; Goulart, P.J. Optimal mode decomposition for unsteady flows. *J. Fluid Mech.* **2013**, *733*, 473–503. [CrossRef]
6. Farge, M. Wavelet transforms and their applications to turbulence. *Annu. Rev. Fluid Mech.* **1992**, *24*, 395–457. [CrossRef]
7. Wang, Y.; Yu, B.; Wu, X.; Wang, P. POD and wavelet analyses on the flow structures of a polymer drag-reducing flow based on DNS data. *Int. J. Heat Mass Transf.* **2012**, *55*, 4849–4861. [CrossRef]
8. Carassale, L. Analysis of aerodynamic pressure measurements by dynamic coherent structures. *Probabilist. Eng. Mech.* **2012**, *28*, 66–74. [CrossRef]
9. Wu, T.; He, G. Independent component analysis of streamwise velocity fluctuations in turbulent channel flows. *Theor. Appl. Mech. Lett.* **2022**, *12*, 100349. [CrossRef]
10. Towne, A.; Schmidt, O.T.; Colonius, T. Spectral proper orthogonal decomposition and its relationship to dynamic mode decomposition and resolvent analysis. *J. Fluid Mech.* **2018**, *847*, 821–867. [CrossRef]
11. Schmidt, O.T.; Towne, A.; Rigas, G.; Colonius, T.; Brès, G.A. Spectral analysis of jet turbulence. *J. Fluid Mech.* **2018**, *855*, 953–982. [CrossRef]
12. Araya, D.; Colonius, T.; Dabiri, J. Transition to bluff-body dynamics in the wake of vertical-axis wind turbines. *J. Fluid Mech.* **2017**, *813*, 346–381. [CrossRef]
13. Lumley, J.L. The structure of inhomogeneous turbulent flows. In *Atmospheric Turbulence and Radio Propagation*; Yaglom, A.M., Tatarski, V.I., Eds.; Nauka: Moscow, Russia, 1967; pp. 166–178.
14. Lumley, J.L. *Stochastic Tools in Turbulence*; Academic Press: New York, NY, USA, 2007.
15. Picard, C.; Delville, J. Pressure velocity coupling in a subsonic round jet. *Int. J. Heat Fluid Flow* **2000**, *21*, 359–364. [CrossRef]
16. Schmidt, O.T.; Colonius, T. Guide to Spectral Proper Orthogonal Decomposition. *AIAA J.* **2020**, *58*, 1023–1033. [CrossRef]
17. Sieber, M.; Paschereit, O.C.; Oberleithner, K. Spectral proper orthogonal decomposition. *J. Fluid Mech.* **2016**, *792*, 798–828. [CrossRef]
18. Aubry, N. On the hidden beauty of the proper orthogonal decomposition. *Theor. Comput. Fluid Dyn.* **1991**, *2*, 339–352. [CrossRef]
19. Schmidt, O.T.; Towne, A. An efficient streaming algorithm for spectral proper orthogonal decomposition. *Comput. Phys. Commun.* **2018**, *237*, 98–109. [CrossRef]
20. Schmidt, O.T. Spectral Proper Orthogonal Decomposition in Matlab. 2018. Available online: https://github.com/SpectralPOD/spod_matlab (accessed on 13 January 2022).
21. Welch, P. The use of fast Fourier transform for the estimation of power spectra: A method based on time averaging over short, modified periodograms. *IEEE Trans. Audio Electroacoust.* **1967**, *15*, 70–73. [CrossRef]
22. Köhler, S.; Stotz, S.; Schweikert, J.; Wolf, H.; Storm, P.; von Wolfersdorf, J. Aerodynamic study of flow phenomena in a turbine center frame. In Proceedings of the GPPS Chania22, Chania, Greece, 12–14 September 2022.
23. Raffel, M.; Willert, C.E.; Scarano, F.; Kähler, C.J.; Wereley, S.T.; Kompenhans, J. *Particle Image Velocimetry: A Pratical Guide*, 3rd ed.; Springer: Berlin, Germany, 2018.
24. Savitzky, A.; Golay, M.J.E. Smoothing and Differentiation of Data by Simplified Least Squares Procedures. *Anal. Chem.* **1964**, *36*, 1627–1639. [CrossRef]
25. Orfanidis, S.J. Introduction to Signal Processing. 2010. Available online: https://www.ece.rutgers.edu/~orfanidi/intro2sp/ (accessed on 10 July 2022).
26. Nakabayashi, T. Solving 2D Navier-Stokes Equations with SMAC Method. 2020. Available online: https://github.com/taku31/NavierStokes2D-with-SMAC-method (accessed on 8 October 2021).

27. Bardera-Mora, R.; Barcala-Montejano, M.A.; Rodríguez-Sevillano, A.A.; de Sotto, M.R.; de Diego, G.G. Frequency prediction of a Von Karman vortex street based on a spectral analysis estimation. *Am. J. Sci. Technol.* **2018**, *5*, 26–34.
28. Schlichting, H.; Gersten, K. *Boundary-Layer Theory*, 9th ed.; Springer: Berlin, Germany, 2017.
29. Cafiero, G.; Ceglia, G.; Discetti, S.; Ianiro, A.; Astarita, T.; Cardone, G. On the three-dimensional precessing jet flow past a sudden expansion. *Exp. Fluids* **2014**, *55*, 1677. [CrossRef]

applied sciences

MDPI

Article

Aerodynamic Characteristics Analysis of Rectifier Drum of High-Speed Train Environmental Monitoring Devices

Baowang Li [1], Xiaobing Wang [2], Junqiang Wu [2], Yang Tao [2,*] and Neng Xiong [2,*]

[1] CRRC, Tangshan Co., Ltd., Tangshan 063000, China; libaowang@crrc.cn
[2] High-Speed Aerodynamics Institute, China Aerodynamics Research and Development Center, Mianyang 621000, China; wangxiaobing@cardc.cn (X.W.); cardc_wujunqiang@163.com (J.W.)
* Correspondence: taoyang@cardc.cn (Y.T.); xiongneng@cardc.cn (N.X.); Tel.: +86-13628081890 (Y.T.)

Abstract: To study the aerodynamic characteristics of the convex structure of a surface-monitoring device on a high-speed train and to evaluate its impact on the aerodynamic performance of the high-speed train, numerical simulation research was conducted on three different layouts of the monitoring device. The computational fluid dynamics (CFD) method was used for the simulation study, and the unsteady compressible NS equation was used as the control equation. Hexagonal grid technology was used to reduce the demand for the grid quantity. The rationality of the grid size and layout was verified through grid independence research. To increase the accuracy of the numerical simulation, the γ-Re_θ transition model and improved delayed detached eddy simulation (IDDES) method were coupled for the simulation research. The aerodynamic characteristics of the different operation directions and configurations were compared and analyzed. The research results showed that the windward side of the single pantograph detection device experienced positive pressure, and the sideline and leeward sides experienced negative pressure. Increasing the fillet radius of the sideline could appropriately reduce the aerodynamic resistance. When the speed was about 110 m/s, the drag force coefficient of the detection device was 210~410 N, and the lateral force was small, which means that it had little impact on the overall aerodynamic force of the train. According to the results of the unsteady analysis of the layout with a large space, the resistance during forward travel was greater than that during negative travel. The streamlined upwind surface was conducive to reducing the scope of the leeward separation zone and the amplitude of the pressure fluctuation in the leeward zone, and it thus reduced the resistance. For the running trains, a vortex was formed on their leeward surface. The pressure monitoring results showed that the separated airflow had no dominant frequency or energy peak. The possibility of the following train top and other components experiencing resonance damage is low.

Keywords: state detection; aerodynamic force; numerical simulation; high-speed railway; faults locating; monitoring device of operation state

Citation: Li, B.; Wang, X.; Wu, J.; Tao, Y.; Xiong, N. Aerodynamic Characteristics Analysis of Rectifier Drum of High-Speed Train Environmental Monitoring Devices. *Appl. Sci.* **2023**, *13*, 7325. https://doi.org/10.3390/app13127325

Academic Editors: Vasily Novozhilov, Junhong Park and Cunlu Zhao

Received: 11 April 2023
Revised: 30 May 2023
Accepted: 15 June 2023
Published: 20 June 2023

1. Introduction

China's high-speed railway operation mileage ranks first in the world, reaching 40,000 km, and the high-speed railways annually transport 2.5 billion passengers [1,2]. The rapid development of the high-speed railway means that more requirements are needed for the safe and stable operation of the trains. The online monitoring device used to determine the high-speed train operation status (hereinafter referred to as the device) is a device that is installed on the top of the power car and is exposed to the air to optically monitor the operation status of the high-speed train by using infrared technology [3–5]. The monitoring device is the key equipment that provides power to the locomotive in high-speed railways. Its reliability is related to the safety and efficiency of the entire railway transportation system. It has six characteristics: a complex space environment, a large impact on climate conditions, no standby, uncertain load, a huge space mechanical system,

and a multidisciplinary complex. The monitoring device completes the extraction of the geometric parameters of the catenary along the route; the analysis of the current collection parameters; and the accurate positioning of the fault points and bird's nest early warning by using a video detection camera, a pillar number plate camera, and a scene camera on the operating electric multiple units (EMUs), and then it finally dynamically detects the operation status of the high-speed railway catenary. For running trains, the aerodynamic load cannot be ignored. In addition, because the outer layer of the device is a shell, whether its rigidity, strength, and stability meet the design requirements also needs to be carefully verified. All these require the aerodynamic characteristics of the device to be analyzed under rated conditions.

When the EMU runs at a low speed, the proportion of air resistance in the overall EMU resistance is very small. With the increase in the train speed, the proportion of aerodynamic resistance in the total resistance will exponentially increase. When the speed reaches 200 and 300 km/h, the proportion will increase by 70 and 85%, respectively [4,5]. China is developing and constructing new technologies, such as side-suspension high-speed trains with speeds up to 400~600 km/h. The detection device installed on the top of the train will inevitably affect the aerodynamic performance of the whole vehicle. Given the impact of monitoring devices, the researchers conducting aerodynamic research on high-speed EMUs at home and abroad are mainly focused on model tests [6] (including wind tunnels, dynamic models, etc.), numerical simulations [7–10], and real-vehicle aerodynamic tests [11]. The model test is not limited by the tunnel, vehicle head shape, external meteorological conditions, etc. Still, the construction cost is high, and the test accuracy and model speed are limited by the model material and launching device, which makes meeting the test requirements for higher vehicle speeds difficult. The real vehicle test is the most direct and reliable test used to study the tunnel pressure wave and verify the theoretical model. The test is limited by the test environment, personal safety, resource investment, test cycle, and many other limitations. With the continuous development of numerical simulation technology, many simulation analyses on the aerodynamic performance of high-speed multiple units have been conducted. Han Sports et al. [12,13] simulated the air distribution in an equipment cabin under an open-line meeting of an EMU. Zhu C. [14] simulated and analyzed a scaled model of a high-speed train that included the monitoring device, and they found that the separation of the air boundary layer of the monitoring device produced relatively atmospheric dynamic resistance, and the numerical calculation results agreed with the wind tunnel test data. According to the results of our literature search, the aerodynamic characteristics of the detection device when the vehicle is running at high speed have seldom been studied [15].

We took the detection device of a high-speed train as the research object; conducted a comparative study on three types of monitoring devices with different aerodynamic configurations; analyzed the pressure and velocity distribution and aerodynamic, pressure, and velocity pulsation effects of the detection device under different operating directions; and put forward the corresponding optimization scheme, which can guide the structural design of high-speed trains and their on-board equipment.

2. Calculation Model and Numerical Method

2.1. Model Introduction

Three device configurations were involved in this calculation (see Figure 1). Among them, configurations 1 and 2 were both C-type buckles with left and right raised ears that were slightly different at the inlet, and configuration 3 was the clean shape of the C-type buckles.

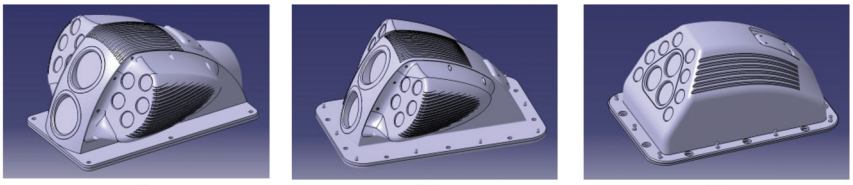

(**a**) (**b**) (**c**)

Figure 1. Outline diagram of the monitoring device; (**a**) Configuration 1; (**b**) Configuration 2; (**c**) Configuration 3.

2.2. Calculation Condition

The normal speed range of high-speed trains is about 55~140 m/s. The higher the speed, the greater the aerodynamic load on the device. Therefore, we considered the aerodynamic force on the train at the highest speed. With the viewing window of the device facing the positive airflow direction, the aerodynamic characteristics of the three model configurations at a vehicle speed V = ±110 m/s were investigated, and the force and moment coefficients and surface pressure on the body surface and its ears were mainly calculated. Six calculation conditions were used in total (see Table 1).

Table 1. Working condition comparison table.

Working Condition	Model	Velocity
1	1	110 m/s
2	1	−110 m/s
3	2	110 m/s
4	2	−110 m/s
5	3	110 m/s
6	3	−110 m/s

2.3. Computational Grid

Unstructured grids were used for this investigation. The calculation model is shown in Figure 2. Considering that the device was installed on the top of the train and was far away from the head and tail of the train, the influence of the train shape on the flow field was ignored, and only the installation plane of the device was set as the fixed wall plane and as the boundary condition of the influence of the train roof; that is, the influence of the shape on the flow field could be simplified as the flow around the device installed on the fixed wall plane. Because the device was symmetrical and the incoming flow had no sideslip angle, the semi-model calculation could be adopted, whereby we took a distance that was 20 times the reference distance as the far-field pressure boundary, P = 101,325 Pa, and the temperature was 300 K. The calculation grid is shown in Figure 2. Among the grids, the positive grid quantity of configuration 1 was about 16 million, and the negative grid quantity of the form was about 15 million. The wake area was encrypted according to the different driving directions.

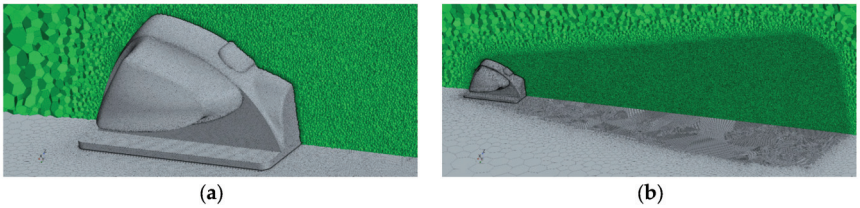

(**a**) (**b**)

Figure 2. *Cont*.

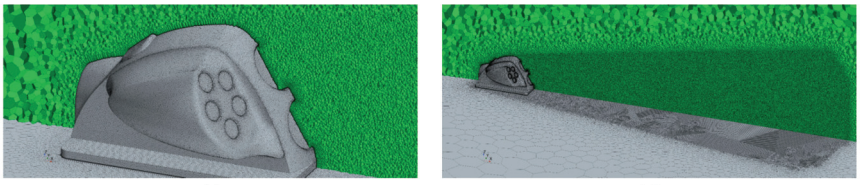

(**c**) (**d**)

Figure 2. Computing grid; (**a**) Grid near the wall; positive operation: condition 1; (**b**) Grid far field; positive operation: condition 1; (**c**) Grid near the wall; negative operation: condition 2; (**d**) Grid far-field; negative operation: condition 2.

2.4. Control Equations and Discretization Schemes

The train was assumed to operate at a speed of V = 110 m/s and a temperature of T = 300 K (27 °C). At this time, the Mach number of the incoming flow relative to the train was about M = 0.32, which belonged to the subsonic range of aerodynamics. The compressibility of the air needed to be considered, so the complete gas model was adopted. If the length of the device in the x direction was taken as the reference length of the Reynolds number L = 0.5 m, then Re = 3.54×10^6, which belongs to the turbulent flow.

Because the Mach number of the incoming flow was M = 0.32, which belongs to the subsonic category, the air followed the complete gas model, and the Reynolds number corresponding to the flow was about Re = 3.54×10^6. Therefore, the control equation of the problem was the compressible Reynolds average Navier–Stokes equation (RANS equation), in which the shear stress transfer (SST) turbulence model was used to treat the turbulence. The three-dimensional conservative RANS equations follow the computational coordinate system. For the specific meaning of each item, please refer to books on computational fluid mechanics.

$$\frac{\partial \boldsymbol{Q}}{\partial t} + \frac{\partial \boldsymbol{E}}{\partial x} + \frac{\partial \boldsymbol{F}}{\partial y} + \frac{\partial \boldsymbol{G}}{\partial z} = \frac{\partial \boldsymbol{E}_v}{\partial x} + \frac{\partial \boldsymbol{F}_v}{\partial y} + \frac{\partial \boldsymbol{G}_v}{\partial z} \tag{1}$$

The finite volume method was used to discretize the N-S equation [16–18], a practical and widely used method in engineering. The bounded central differencing (BCD) scheme was used to discretize the flux terms; with this scheme, we adopted a blended coefficient (φ) to adjust the numerical accuracy and stability. For the present simulation, the coefficient (φ) was set to 0.15 to reduce the numerical dissipation considerably. This calculation is unsteady, and we finally obtained steady results with a high convergence rate. The implicit scheme with dual-time steps was adopted, the physical time step was 0.00005 s, and 10,000-time steps were iteratively calculated.

2.5. Turbulence and Transition Model

Because the Reynolds number of the monitoring device was medium, to accurately evaluate the aerodynamic resistance, the transition impact needed to be considered. Additionally, a large range of separated flows exists when operating high-speed trains. To increase the accuracy of the numerical simulation, we used a coupling γ-Re_θ transition model and IDDES method.

The γ-Re_θ transition model not only includes the intermission factor transport equation [19–22], but it also uses the momentum thickness Reynolds number as a transport scalar and establishes the transport equation for it; this allows the momentum thickness Reynolds number of the incoming flow to be used for the boundary layer due to convection, which thus allowed us to obtain the local transition initial momentum thickness Reynolds number. Then, we could judge the beginning of the transition by comparing the Reynolds number of the vortex and momentum thickness. The intermittent factor (γ) and the trans-

port equation of the Reynolds number of the transition initial momentum thickness ($\overline{\mathrm{Re}_{\theta t}}$) was as follows:

$$\frac{\partial(\rho\gamma)}{\partial t} + \frac{\partial(\rho U_j\gamma)}{\partial x_j} = P_\gamma - E_\gamma + \frac{\partial}{\partial x_j}[(\mu + \frac{\mu_t}{\sigma_\gamma})\frac{\partial\gamma}{\partial x_j}] \tag{2}$$

$$\frac{\partial(\rho\overline{\mathrm{Re}_{\theta t}})}{\partial t} + \frac{\partial(\rho U_j\overline{\mathrm{Re}_{\theta t}})}{\partial x_j} = P_{\theta t} + \frac{\partial}{\partial x_j}[\sigma_{\theta t}(\mu + \frac{\mu_t}{\sigma_\gamma})\frac{\partial\gamma}{\partial x_j}] \tag{3}$$

$$P_\gamma = F_{length}C_{a1}\rho S[\gamma F_{onset}]^{0.5}(1 - C_{e1}\gamma) \tag{4}$$

$$E_\gamma = \mathrm{C}_{a2}\rho\Omega\gamma F_{turb}(C_{e2}\gamma - 1) \tag{5}$$

$$F_{onset} = \frac{\mathrm{Re_v}}{2.193\mathrm{Re}_{\theta c}} \tag{6}$$

$$P_{\theta t} = \mathrm{C}_{\theta t}\frac{\rho}{t}(\mathrm{Re}_{\theta t} - \overline{\mathrm{Re}_{\theta t}})(1.0 - F_{\theta t}) \tag{7}$$

$$\mathrm{Re}_{\theta t} = \mathrm{F(Tu)F}(\lambda_\theta) \tag{8}$$

$$F_{length} = \mathrm{f}_1(\overline{\mathrm{Re}_{\theta t}}) \tag{9}$$

$$\mathrm{Re}_{\theta c} = \mathrm{f}_2(\overline{\mathrm{Re}_{\theta t}}) \tag{10}$$

$$\overline{P_k} = \lambda P_k \tag{11}$$

$$\overline{\mathrm{D}_k} = \min[\max(\gamma, 0.1), 1.0]D_k \tag{12}$$

where P_γ and E_γ are the generation and destruction terms of the γ equation, respectively; $P_{\theta t}$ is the generation terms of the $\overline{\mathrm{Re}_{\theta t}}$ transport equation; $\mathrm{Re}_{\theta t}$ is the Reynolds number of the momentum thickness outside the boundary layer, which is related to the turbulence intensity and pressure gradient of the incoming flow; and λ_θ is the parameter representing the pressure gradient. Two key factors influence the term P_γ and determine the threshold function (F_{onset}) at the beginning of the transition and the parameters of the transition region length (F_{length}). In the upstream laminar flow region, the value F_{onset} is 0. When the Reynolds number (Re_v) of the ground vortex is greater than 2.193 times the critical momentum thickness Reynolds number ($\mathrm{Re}_{\theta c}$), F_{onset} is activated, the intermittent factor γ gradually increases, and the $\mathrm{Re}_{\theta c}$ and F_{length} of the flow gradually changes from determining the laminar flow to turbulence. Both parameters are related to the Reynolds number ($\overline{\mathrm{Re}_{\theta t}}$) of the initial momentum thickness of the transition. Langtry successfully associated these two parameters by analyzing many plate test data. These two correlations contain the internal physical mechanism of transition, and many modified versions based on the transition model have modified these two correlations accordingly. The above two transport equations modify the generation and destruction terms of the k equation in the SST model through the intermittent factor, where P_k and D_k represent the generation and destruction terms of the k equation in the SST model, respectively. $\overline{P_k}$ and $\overline{D_k}$ represents the generation and destruction terms of the k equation after coupling with the transition model, respectively.

2.6. Combination of IDDES Method and Transition Model

The γ-Re_θ model solves the intermission factor γ by adding two transport equations and combines the SST turbulence model by causing γ to act on the generation and destruction terms of the k equation. In terms of form, adding the IDDES method based on the

SST model is simpler, and this can be performed by modifying the length scale function of the damage term of the turbulent kinetic energy transport equation in the SST turbulence model. The turbulent kinetic energy equation in the SST model is

$$\frac{D(\rho k)}{Dt} = \tau_{ij}\frac{\partial u_i}{\partial x_j} - \beta^*\rho\omega k + \frac{\partial}{\partial x_j}\left[(\mu + \sigma_k\mu_t)\frac{\partial k}{\partial x_j}\right] \tag{13}$$

where $D = \beta^*\rho\omega k$ is the damaged item, which should actually be $D = \rho k^{3/2}/\widetilde{l}$. Because $\widetilde{l} = k^{1/2}/(\beta^*\omega)$ in the RANS model, the equation is finally displayed as $D = \beta^*\rho\omega k$, where $\beta^* = 0.09$. For the IDDES method, $\widetilde{l} = l_{IDDES}$. To combine the IDDES method with γ-Re_θ, if the transition model is combined, it needs to be solved by using γ-Re_θ, and the four-equation transition model is obtained by modifying the length scale function of the damage term of the turbulent kinetic energy equation. The turbulent kinetic energy transport equation in the four-equation model is

$$\frac{D(\rho k)}{Dt} = \gamma\tau_{ij}\frac{\partial u_i}{\partial x_j} - \gamma\rho k^{3/2}/\widetilde{l} + \frac{\partial}{\partial x_j}\left[(\mu + \sigma_k\mu_t)\frac{\partial k}{\partial x_j}\right] \tag{14}$$

For the traditional γ-Re_θ transition model, $\widetilde{l} = k^{1/2}/(\beta^*\omega)$ in the IDDES framework based on the γ-Re_θ transition model, and $\widetilde{l} = l_{IDDES}$. So far, whether the pure IDDES method or framework based on γ-Re_θ is used, the transition model only needs l_{IDDES} to be provided, and then the equation can be used.

For details on developing the length-scaling function from DES to IDDES, please refer to the literature. We only provide the calculation of l_{IDDES} related to the grid scale:

$$\Delta = \min\{\max[C_w d_w, C_w h_{\max}, h_{\min}], h_{\max}\} \tag{15}$$

Here, $h_{\max} = \max(\Delta_x, \Delta_y, \Delta_z)$ and $h_{\min} = \min(\Delta_x, \Delta_y, \Delta_z)$. d_w is the distance from the wall and C_w is an empirical constant that is independent of the sublattice model and is generally taken as $C_w = 0.15$.

l_{IDDES} is in the form of

$$l_{IDDES} = \widetilde{f}_d l_{RANS} + (1 - \widetilde{f}_d) l_{LES} \tag{16}$$

Here, $l_{RANS} = k^{1/2}/(\beta_k\omega)$, $l_{LES} = C_{DES}\Delta$, $C_{DES} = (1 - F_1)C_{DES}^{k-\varepsilon} + F_1 C_{DES}^{k-\omega}$, and $C_{DES}^{k-\varepsilon} = 0.61$, $C_{DES}^{k-\omega} = 0.78$.

$$\widetilde{f}_d = \max\{(1 - f_{dt}), f_B\} \tag{17}$$

$$f_{dt} = 1 - \tanh[(C_{dt} r_{dt})^3] \tag{18}$$

$$r_{dt} = \frac{\nu_t}{\max\{\sqrt{U_{ij}U_{ij}}, 10^{-10}\}\kappa^2 d_w{}^2} \tag{19}$$

where ν_t is the turbulent viscosity coefficient and $U_{ij} = \frac{\partial U_i}{\partial x_j}$. $\kappa = 0.41$ is the Karman constant. C_{dt} is the empirical constant, which is taken as 20 in IDDES based on the SST model. f_B is defined as follows:

$$f_B = \min\{2\exp(-9\alpha^2), 1.0\} \tag{20}$$

Here, $\alpha = 0.25 - d_w/h_{\max}$, and l_{IDDES} was determined.

2.7. Numerical Validation

The case of square cylinder flow at a high Reynolds number was adopted to validate the numerical method. The Reynolds number was 2.2×10^4 based on the side length of the

square, and the Mach number was 0.2. A set of grids contained 2.8 million cells, refined near the wall to ensure the $y^+ \approx 1$ for the first grid spacing. The physical time step was 0.005 s, and the Courant number during the inner iteration was 10. Figure 3 illustrates the computational field and grid distribution.

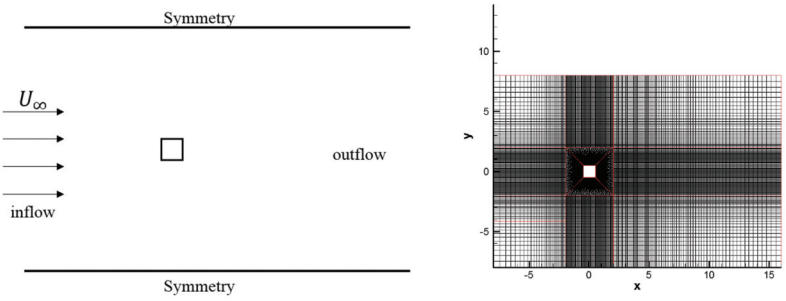

Figure 3. Computational field (**left**) and grid distribution (**right**) of the square cylinder flow.

The Q criterion is commonly used to depict the coherent structures of the intricate wake flow. A detailed definition is provided in reference [23]. Figure 4 provides the Q isosurface distribution with a nondimensional Q = 0.45. The large-scale, three-dimensional vortex alternately shed in the wake. The quantitative results are provided and compared with the experiment results in Figure 5, which includes the time-averaged streamwise velocity and the Reynolds stress. The simulation results agreed with the experimental ones well, and we concluded that the numerical IDDES model provided higher numerical accuracy than the RANS model.

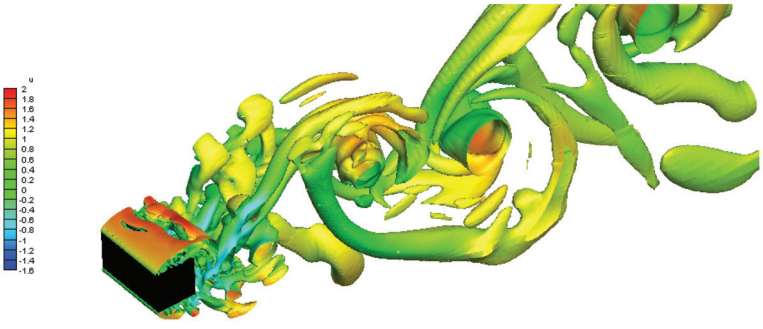

Figure 4. Q isosurface of the square cylinder flow.

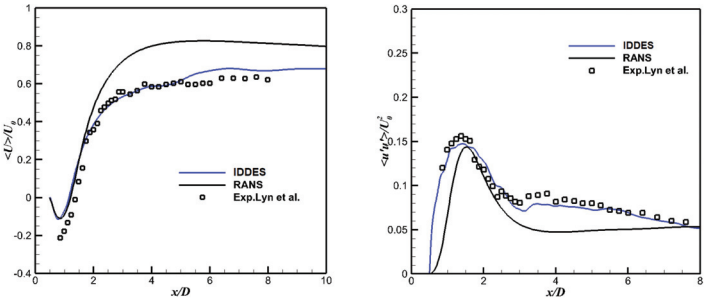

(**a**) Velocity. (**b**) Reynolds stress <*u*′*u*′>.

Figure 5. *Cont*.

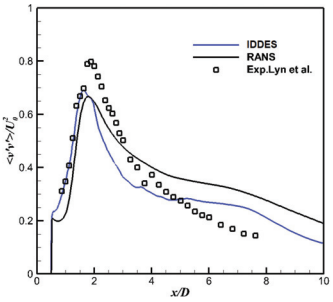

(**c**) Reynolds stress <*v'v'*>.

Figure 5. The time averaged results along the centerline of square cylinder flow [24].

3. Result Discussion

3.1. Aerodynamic Comparison

The results of the aerodynamic force and moment coefficient calculations are provided in Table 2, which were nondimensionalized based on the inflow density (ρ), velocity (V), characteristic area, and device length, as defined in Equation (21):

$$\begin{aligned} C_x &= F_x/\left(0.5\rho V^2 S_c\right) \\ C_y &= F_y/\left(0.5\rho V^2 S_c\right) \\ C_z &= F_z/\left(0.5\rho V^2 S_c\right) \\ m_x &= M_x/\left(0.5\rho V^2 S_c L_c\right) \\ m_y &= M_y/\left(0.5\rho V^2 S_c L_c\right) \\ m_z &= M_z/\left(0.5\rho V^2 S_c L_c\right) \end{aligned} \tag{21}$$

where ρ = 1.225 kg·m^3, V = 110 m/s, S_c = 0.149 m^2, and L_c = 0.5 m. Because the stress of the components (ears), the moment characteristics, and the other parameters of the swing ears need to be considered, the lift and drag were used for the full-mode results, and all the moments and lateral forces were used for the half-mode integration results.

Table 2. Force and moment coefficients for the three grids used in the convergence study.

Working Condition	Component	Cx	Cy	Cz	mx	my	mz
1	body	−0.227	0.302	0.426	0.0159	−0.0147	0.0114
	ear	−0.141	0.559	−0.272	−0.1083	0.0170	0.0389
	total	−0.369	0.862	0.154	−0.0924	0.0024	0.0503
2	body	0.142	0.204	0.356	0.0109	−0.0071	−0.0096
	ear	0.056	0.446	−0.026	−0.0650	0.0134	0.0176
	total	0.197	0.650	0.330	−0.0542	0.0063	0.0080
3	body	−0.263	0.290	0.529	0.0491	−0.0101	0.0205
	ear	−0.106	0.582	−0.215	−0.1065	0.0259	0.0435
	total	−0.368	0.872	0.314	−0.0574	0.0158	0.0639
4	body	0.157	0.186	0.415	0.0315	−0.0350	−0.0078
	ear	0.062	0.420	−0.050	−0.0638	0.0165	0.0197
	total	0.219	0.606	0.365	−0.0322	−0.0183	0.0120
5	body	−0.195	0.836	0.640	−0.0446	0.0007	0.0540
6	body	0.193	0.687	0.545	−0.0286	−0.0069	−0.0143

Note: (1) The moment reference point is the origin of the digital-analog coordinate system; (2) All moments and lateral forces were calculated with a half model to represent the stress of parts (ears) accurately.

Because some common characteristics were present in the flow field of the three configurations, we mainly analyzed the aerodynamic characteristics under the two conditions of configuration 1. We only described the conclusions for configurations 2 and 3.

Figures 6–11 show the pressure distribution and streamlines on the surface of the device, as well as the off-surface streamlines around the device under different working conditions. An evident high-pressure zone appeared on the windward side because the blockage effect of the device reduced the flow velocity; additionally, the low-pressure belt at the shoulder was induced by the flow acceleration when it bypassed the large-curved corner, and a reverse pressure gradient was formed because of the intense flow acceleration and the relatively higher pressure downstream of the shoulders. Then, the flow separated near the shoulders, forming a recirculation zone on the leeward side. The separation slowed down the pressure recovery and induced a pressure difference between the opposite sides, which contributed to the drag force of the device.

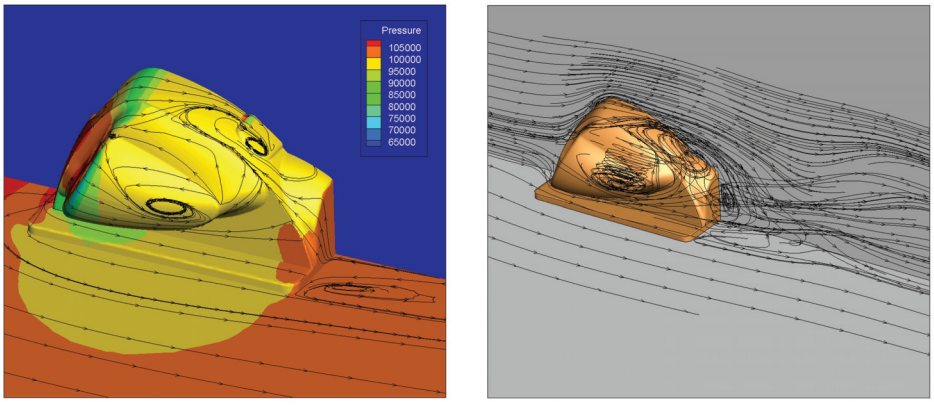

Figure 6. Condition 1 surface and space streamline.

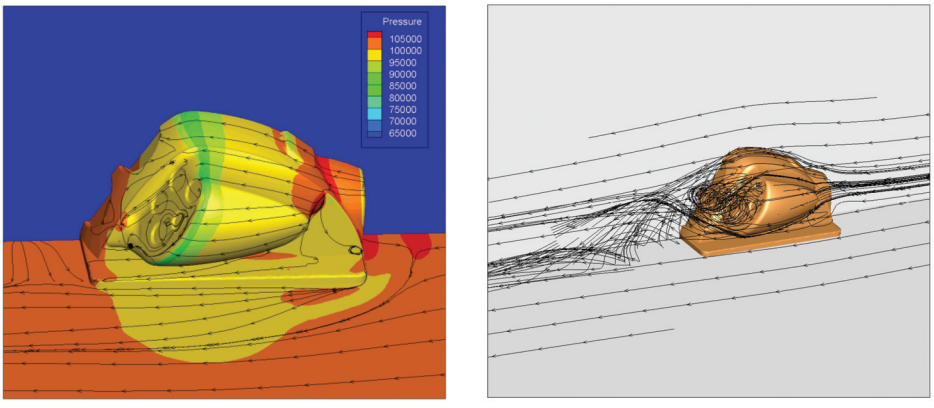

Figure 7. Condition 2 surface and space streamline.

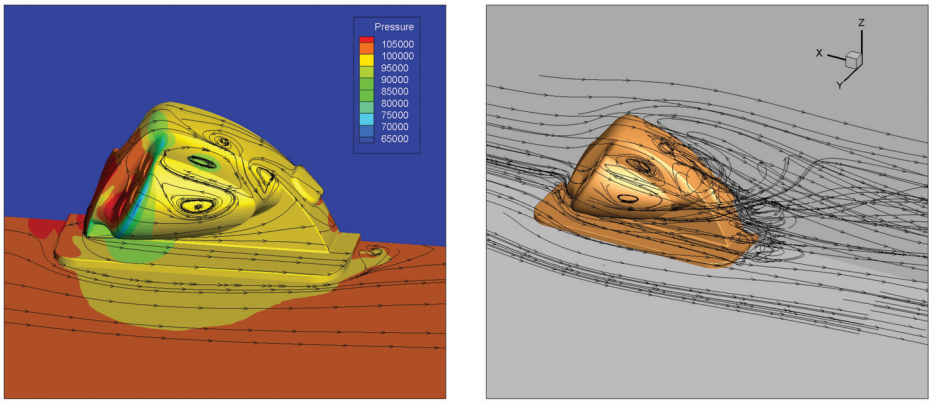

Figure 8. Condition 3 surface and space streamline.

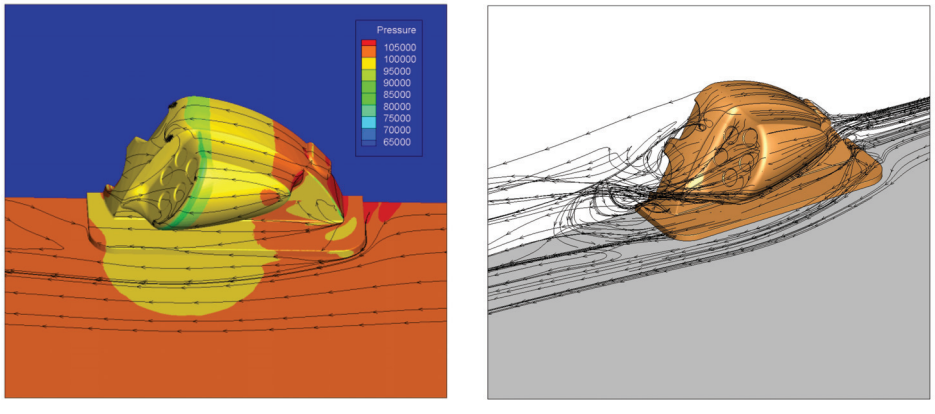

Figure 9. Condition 4 surface and space streamline.

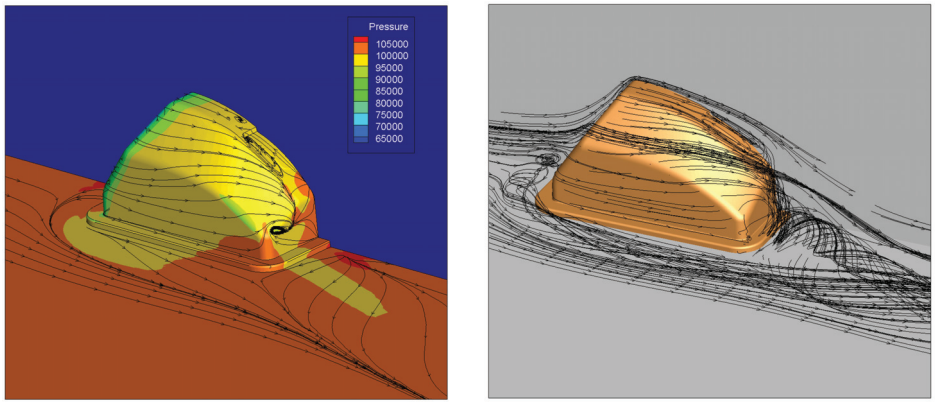

Figure 10. Condition 5 surface and space streamline.

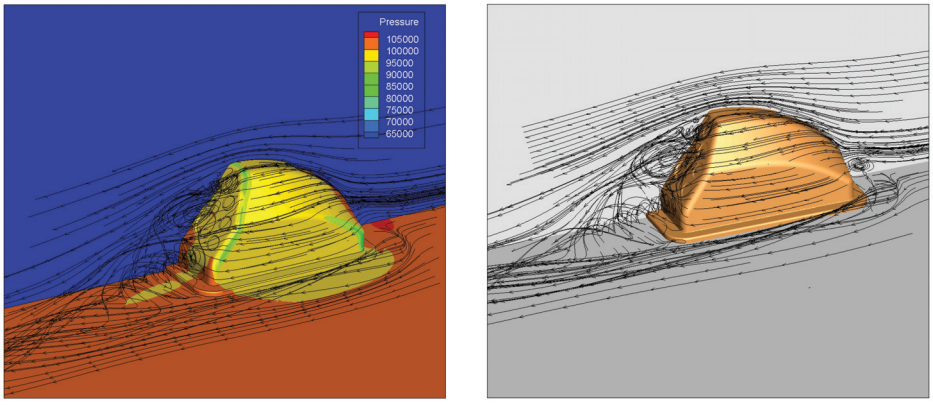

Figure 11. Condition 6 surface and space streamline.

As shown in Figure 6, the area of the high-pressure zone on the windward side of configuration 1 was large under operating conditions. It was mainly distributed in the lower half of the two observation windows and the windward side of the two ears. About 1/3 of the total drag was caused by the two ears. Reducing the windward area of the two ears is appropriate when ignoring other design constraints. For example, increasing the sweep angles of the two sides of the ears can reduce the drag during forward driving. Figure 6 shows three dominant eddies downward from the leeward side of configuration 1 under operating conditions. They formed a large recirculation zone near the leeward side of the ear and the leeward area at the upper part of the inlet and behind the inlet. Therefore, the resistance under condition 1 was large. When driving in the reverse direction (condition 2), a similar pressure distribution existed as when driving in the forward direction. The area of the high-pressure zone at the two ears was smaller than that in condition 1. The relative position of the separation point was behind, and the backflow zone at the leeward side was also smaller. Therefore, the total drag was considerably reduced by about 50% compared with the reduction in the total drag in the forward direction.

The configuration 2 situation was similar to that of configuration 1, and the resistance under the two conditions was equivalent to that of configuration 1. The third configuration was clean and had no strong blocking effect when the ear drove forward. The resistance magnitude of forward and reverse driving was the same, and reverse driving was slightly slower than forward.

The ear of configurations 1 and 2 was subjected to a large negative lift when driving in the forward direction (in modes 1 and 3, respectively). This was because the air separation occurred above the two ears, and the pressure was high, whereas the flow near the ears induced a lower pressure. The pressure difference produced about 0.27 (condition 1) and 0.22 (condition 3) downward resultant force coefficients on a single ear and a remarkable rolling moment. Thus, one must pay considerable attention to the strength of the connection between the ears and the body during the design stage.

3.2. Unsteady Flow Analysis of Wake

A large, separated flow in the leeward area of the surface-monitoring device on the high-speed train was present. To evaluate its unsteady aerodynamic characteristics, the unsteady aerodynamic characteristics of configuration 1 with a large separation area were analyzed. According to the flow characteristics of the leeward area of the monitoring device, two rows of monitoring points were arranged. One row was on the symmetry plane, starting 10 cm away from the object surface and with an interval of 10 cm from each point, resulting in six monitoring points. The other row was near the Guangyuan glass; it

also started 10 cm away from the object's surface and had an interval of 10 cm from each point, resulting in seven monitoring points. See Figure 12 for the detailed layout.

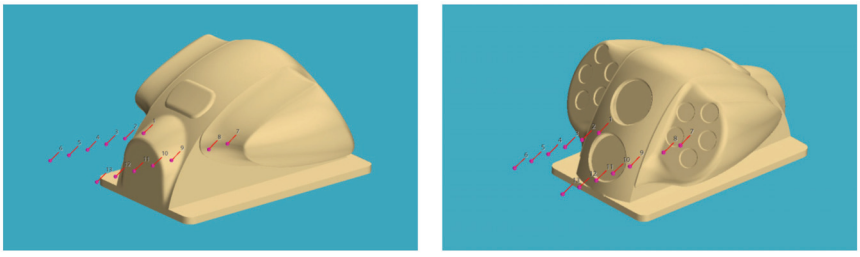

(**a**) (**b**)

Figure 12. Distribution of monitoring points in the wake area of the detection device; (**a**) Positive operation (condition 1); (**b**) Negative operation (condition 2).

Figure 13 compares the pressure pulsations at different monitoring points during positive and negative operations. Figure 13a shows that the pressure pulsation at the center line of the forward operation was smaller than that of the negative operation, whether the point near the wall (point 1) or far away from the wall (point 6) was used. Figure 13b shows that the contrast between the positive and negative movement at the right monitoring point was consistent with the law at the center line. The overall pressure fluctuation of the right monitoring point was larger than that of the monitoring point at the center line. This was mainly because the right monitoring point was closer to the boundary of the external high-speed airflow and the airflow stagnation zone at the rear of the monitoring device and because the relationship between the mass transfer effect between different areas was more intense.

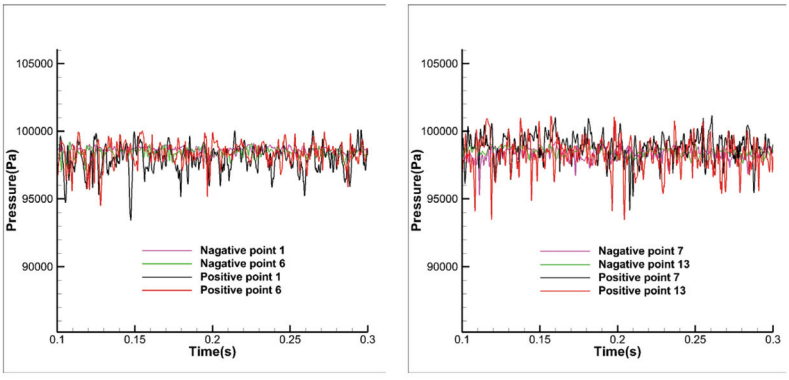

(**a**) (**b**)

Figure 13. Comparison of pressure at different detection points; (**a**) Centerline detection point; (**b**) Right detection point.

Figure 14 compares the pressure and velocity combinations at different monitoring points during the positive and negative operations. Figure 14a shows that at the center line, a large positive velocity was present at the point close to the wall (point 1), and a large reverse velocity was present at the point far away from the wall (point 6), which indicates that a small separation zone was present at the center line. During the reverse operation, a large positive velocity was also present at the point near the wall (point 1). In contrast, the velocity at the point far away from the wall (point 6) was 0, which indicated that this area was the velocity stagnation region. This could be mutually verified with the flow field structure shown in Figure 13. Figure 14a shows that the pressure pulsation at the monitoring point on the right

side was consistent with the law of the pressure pulsation at the monitoring point during the positive and negative operation, both of which formed reflux near the wall; additionally, the velocity in the area far away from the wall was consistent with the outflow, which indicated that a certain separation flow area was also present on the right side, which is consistent with the spatial streamline shown in Figures 6 and 7.

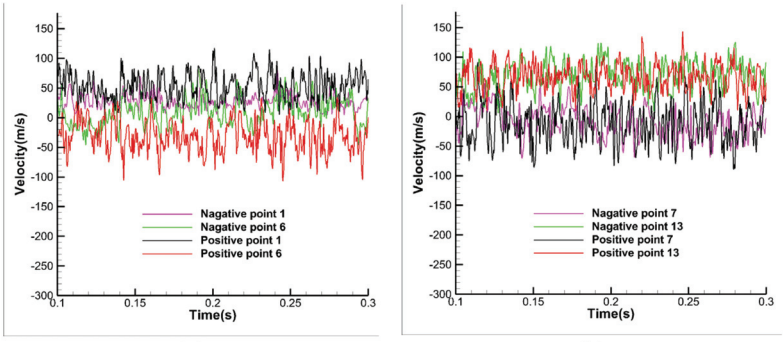

Figure 14. Comparison of velocity at different detection points (**a**) Centerline detection point; (**b**) Right detection point.

A power spectrum density (PSD) analysis was conducted to analyze the pressure time history. Figure 15 compares the power density spectra, whereby the pressure fluctuations at different monitoring points during the positive and negative operations are compared. The pressure fluctuation at the monitoring points in the wake area had no obvious peak value, and the PSD values of the points (points 1 and 7) close to the wall during the negative operation were considerably reduced, which showed that the flow near the wall in the leeward area was relatively stable during the negative operation.

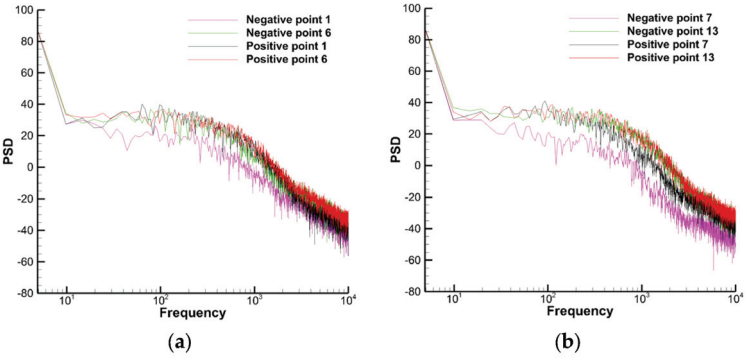

Figure 15. Comparison of power density spectra of pressure fluctuation at different detection points; (**a**) Centerline detection point; (**b**) Right detection point.

Figure 16 shows the characteristics of the wake separation using the *Q* isosurface colored according to the pressure. More abundant leeward vortex structures were present in the forward operation, and the influence of the separation zone was also wider, which was consistent with the performance of the overall aerodynamic drag.

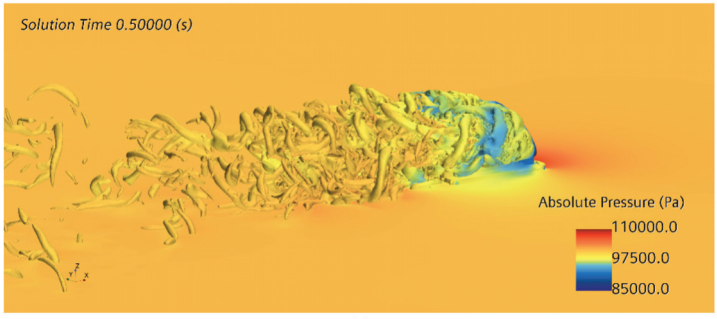

(**a**)

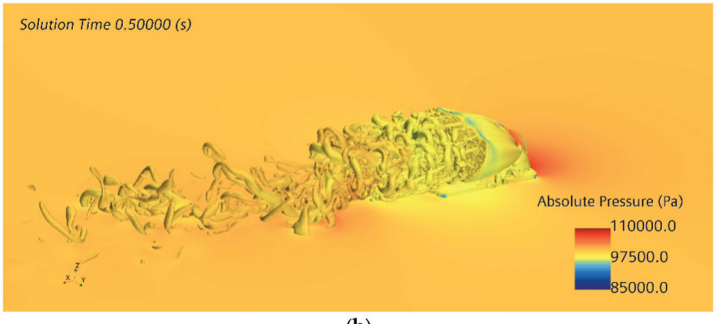

(**b**)

Figure 16. *Q* isosurface of wake under different operating conditions; (**a**) Positive operation; (**b**) Negative operation.

Figure 17 compares the symmetry plane's pressure and Mach number distribution under different operation conditions. The separation area and influence range of the wake flow during the forward operation was larger than those during the negative operation, and the wake flow was partially far away from the top of the train, which was also the reason for the greater resistance during the forward operation.

(**a**)

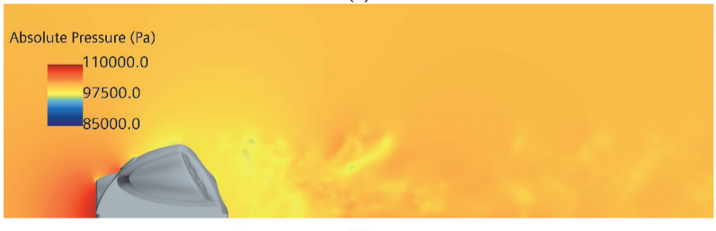

(**b**)

Figure 17. *Cont.*

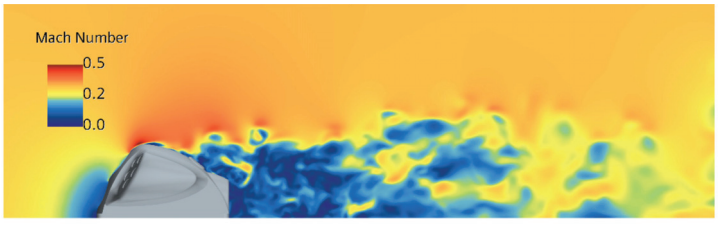

(**c**)

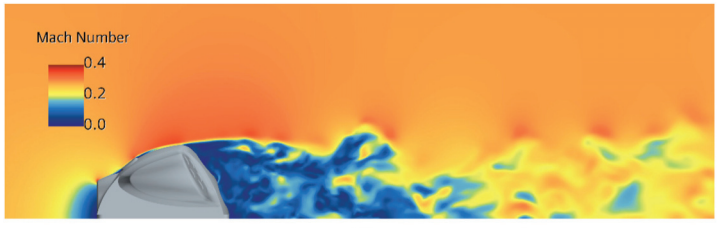

(**d**)

Figure 17. Comparison of pressure and Mach number distribution on symmetry plane under different operating conditions; (**a**) Pressure distribution during positive operation; (**b**) Pressure distribution during negative operation; (**c**) Mach number during positive operation (**d**) Mach number during negative operation.

4. Conclusions

Numerical simulation research on the operation-condition monitoring device of a high-speed train was conducted. The calculation accuracy was increased by using the IDDES method. By conducting an analysis of the aerodynamic force, surface flow pattern, and space wake structure, the following conclusions were obtained:

(1) The windward side of the detection device experienced positive pressure, and the sideline and leeward sides experienced negative pressure. Increasing the fillet radius of the sideline can appropriately reduce the aerodynamic resistance.

(2) The shaping of the downstream flow in the leeward area can effectively reduce the resistance of the monitoring device. The resistance of configurations 1 and 2 in the reverse direction was about 1/2 of that in the forward direction, and the resistance of configurations 3 in the forward and reverse directions was the same. The streamlined upwind surface was conducive to reducing the scope of the leeward separation area and the amplitude of the pressure fluctuation in the leeward area and thus reduced the resistance;

(3) The monitoring device had a certain height and formed a vortex on its leeward side when the train was running at high speed. From the results of the analysis on the pressure monitoring, we found that the separated airflow did not have an obvious dominant frequency and energy peak, and the possibility of resonance damage occurring to the following parts, such as the top of the train, was small.

Author Contributions: Methodology, B.L., X.W. and N.X.; Software, B.L. and X.W.; Validation, X.W. and N.X.; Formal analysis, Y.T. and N.X.; Investigation, B.L. and J.W.; Resources, J.W.; Data curation, J.W.; Writing—original draft, Y.T. All authors have read and agreed to the published version of the manuscript.

Funding: This work was funded by the National Natural Science Foundation of China, grant number 11372337.

Conflicts of Interest: The authors declare no conflict of interest.

References

1. Zhou, N.; Yang, W.; Liu, J.; Zhang, W.; Wang, D. Investigation of a pantograph-catenary monitoring system using condition-based pantograph recognition. *Sci. Sin. Technol.* **2021**, *51*, 23–34.
2. Xiukun, W.; Da, S.; Dehua, W.; Xiaomeng, W.; Siyang, J.; Ziming, Y. A survey of the application of machine vision in rail transit system inspection. *Control. Decis.* **2021**, *36*, 257–282.
3. Han, Z.; Liu, Z.; Zhang, G.; Yang, H.M. Overview of non-contact image detection technology for pantograph-catenary monitoring. *J. China Railw. Soc.* **2013**, *35*, 40–47.
4. Hongqi, T. *Train aerodynamics*; China Railway Press: Beijing, China, 2007.
5. Zhenxu, S.; Yongfang, Y.; Dilong, G.; Guowei, Y.; Shuanbao, Y.; Ye, Z.; Dawei, C.; Guibo, L.; Keming, S.; Ling, J. Research progress in aerodynamic optimization of high-speed trains. *Chin. J. Theor. Appl. Mech.* **2021**, *53*, 51–74.
6. Jiqiang, N.; Xifeng, L.; Dan, Z. Equipment cabin aerodynamic performance of electric multiple unit going through tunnel by dynamic model test. *J. Zhejiang Univ. Eng. Sci.* **2016**, *50*, 1258–1265.
7. Liu, T.; Chen, Z.; Zhou, X.; Zhang, J. A CFD analysis of the aerodynamics of a high-speed train passing through a windbreak transition under crosswind. *Eng. Appl. Comput. Fluid Mech.* **2018**, *12*, 137–151. [CrossRef]
8. Xu, J.L.; Sun, J.C.; Mei, Y.G.; Wang, R.L. Numerical Simulation on crossing pressure wave characteristics of two high-speed trains in tunnel. *J. Vib. Shock.* **2016**, *35*, 184–191.
9. Weibin, M.A.; Qianli, Z.H.N.; Yanqing, L.I. Study evolvement of high-speed railway tunnel aerodynamic effect in China. *J. Traffic Transp. Eng.* **2012**, *12*, 25–32.
10. Niu, J.Q.; Zhou, D.; Liu, T.H.; Liang, X.F. Numerical simulation of aerodynamic performance of a couple multiple units high-speed train. *Veh. Syst. Dyn.* **2017**, *55*, 681–703. [CrossRef]
11. Kim, H.; Hu, Z.; Thompson, D. Effect of cavity flow control on high-speed train pantograph and roof aerodynamic noise. *Railw. Eng. Sci.* **2020**, *28*, 54–74. [CrossRef]
12. Ko, Y.Y.; Chen, C.H.; Hoe, T.; Wang, S.T. Field measurements of aerodynamic pressures in tunnels induced by high speed trains. *J. Wind Eng. Ind. Aerodyn.* **2012**, *100*, 19–29. [CrossRef]
13. Yundong, H.; Dawei, C.; Peng, L. Air distribution simulation study of EMU equipment bay under passing by each other on open track. *Railw. Locomot. Car* **2013**, *33*, 22–26.
14. Zhu, C.; Hemida, H.; Flynn, D.; Baker, C.; Liang, X.; Zhou, D. Numerical simulation of the slipstream around a high-speed train with pantograph system. *J. Railw. Sci. Eng.* **2016**, *13*, 1447–1456.
15. Wang, S.; Bell, J.R.; Burton, D.; Herbst, A.H.; Sheridan, J.; Thompson, M.C. The performance of different turbulence models (URANS, SAS and DES) for predicting high-speed train slipstream. *J. Wind Eng. Ind.* **2017**, *165*, 46–57. [CrossRef]
16. Barman, P.C. Introduction to computational fluid dynamics. *Int. J. Inf. Sci. Comput.* **2016**, *3*, 117–120. [CrossRef]
17. Hill, D.J.; Pantano, C.; Pullin, D.I. Large-eddy simulation and multiscale modeling of a Richtmyer-Meshkov instability with reshock. *J. Fluid Mech.* **2006**, *557*, 29–61. [CrossRef]
18. Baorui, F. *Aero-Configuration Design of Aero Plan*; Beijing Aviation Industry Publishing Company: Beijing, China, 1997. (In Chinese)
19. Viswanathan, A.; Squires, K.D.; Forsythe, J.R. Detached-Eddy Simulation around a forebody at high angle of attack. In *AIAA Aerospace Sciences Meeting*; AIAA Paper 2003-0263; AIAA: Reston, VA, USA, 2003.
20. Forsythe, J.R.; Squires, K.D.; Wurtzler, K.E.; Spalart, P.R. Detached-eddy simulation of the F-15E at high alpha. In *AIAA Aerospace Sciences Meeting*; AIAA Paper 2002-0591; AIAA: Reston, VA, USA, 2002.
21. Morton, S.A.; Steenman, M.B.; Cummings, R.M.; Forsythe, J.R. DES grid resolution issues for vertical flows on a delta wing and an F-18C. In *41st Aerospace Sciences Meeting and Exhibit*; AIAA Paper 2003-1103; AIAA: Reston, VA, USA, 2003.
22. Denning, R.M.; Allen, J.E.; Armstrong, F.W. The broad delta airliner. *Aeronaut. J.* **2003**, *107*, 547–558. [CrossRef]
23. Jeong, J.; Hussain, F. On the identification of a vortex. *J. Fluid Mech.* **1995**, *285*, 69–94. [CrossRef]
24. Lyn, D.A.; Einav, S.; Rodi, W. A laser-Doppler velocimetry study of ensemble-averaged characteristics of the turbulent near wake of a square cylinder. *J. Fluid Mech.* **1995**, *304*, 285–319. [CrossRef]

applied sciences

MDPI

Article

Numerical Investigation of the Cavitation Characteristics in Venturi Tubes: The Role of Converging and Diverging Sections

Yi Liu * and Bin Li

Faculty of Mechanical Engineering & Automation, Zhejiang Sci-Tech University, Hangzhou 310018, China
* Correspondence: yi.liu@zstu.edu.cn

Abstract: Cavitation is a typical physical process that has shown to be highly valuable in the wastewater treatment field. This study aims to investigate the effects of the converging and diverging sections of a Venturi tube on the cavitation flow field. Multiphase flows in tubes are presented using the mixture model and the standard k-ε model. And the Schnerr and Sauer cavitation model is employed to simulate the vapor–liquid phase transition process. Both grid independence and the numerical method's feasibility were validated before the research. The results showed that the influence of the divergence section length on Venturi cavitation characteristics depends on the provided pressure conditions. As the pressure increases, shorter divergence sections result in more significant cavitation effects. The length of the convergence section displays various cavitation behaviors under different pressure situations. A small contraction section length can achieve better cavitation effects in high-pressure applications, whereas the opposite is true in low-pressure cases. Within the scope of this study, it was observed that the Venturi tube with a divergent section of 14 Lt and a convergent one of 2.4 Lt provided enhanced cavitation performance when subjected to inlet pressures ranging from 0.8 to 1.2 MPa. Our findings indicate that the selection of converging and diverging section lengths in Venturi tubes should consider the corresponding operational pressure conditions, which provides valuable guidance and engineering significance in the research and development of Venturi cavitation devices in hydraulic engineering.

Keywords: Venturi tube; cavitation; vapor volume fraction; low-pressure zone

Citation: Liu, Y.; Li, B. Numerical Investigation of the Cavitation Characteristics in Venturi Tubes: The Role of Converging and Diverging Sections. *Appl. Sci.* **2023**, *13*, 7476. https://doi.org/10.3390/app13137476

Academic Editor: Ricardo Castedo

Received: 8 May 2023
Revised: 18 June 2023
Accepted: 19 June 2023
Published: 25 June 2023

1. Introduction

Cavitation is a typical vapor–liquid phase change mechanism that is commonly found in throttling structures. When the liquid's local static pressure is lower than the saturated vapor pressure at a reference temperature, the tiny gas nuclei in the liquid or the gap at the solid–liquid interface gradually grow under the action of internal and external pressure differences, and finally collapse and release a large amount of energy after pressure recovery [1–4]. Currently, cavitation plays an important role in addressing the issue of wastewater [5,6]. The localized high temperature and high-pressure environment created by cavitation bubble collapse can cause the water molecules near the bubble surface to pyrolyze into hydroxyl and hydrogen free radicals, which then have the effect of oxidizing organic pollutants in the water body through the diffusion of hydroxyl free radicals in the liquid medium [7]. Various studies have assessed the efficacy of cavitation in wastewater treatment: Innocenzi et al. [8] carried out laboratory-scale research on the effectiveness and possibility of treating methyl orange solution with cavitation of the Venturi tube; their results demonstrated that the cavitation induction into the oxidation process can improve dye degradation under regulated operating settings. Bagal et al. [9] investigated the degradation effect of the residual pharmaceutical diclofenac sodium in wastewater using a novel approach combining hydraulic cavitation and heterogeneous photocatalysis and discovered that, under ideal conditions, the combined treatment had an advantage over the single treatment scheme. Mezule et al. [10] developed a rotational cavitation device that

generates cavitation in a thin water layer in order to investigate the effect of hydrodynamic cavitation on the disinfection of E. coli. Experiments have demonstrated that hydrodynamic cavitations are particularly efficient in reducing bacterial division capacity. Badve et al. [11] used a cavitation device that included a stator and a rotor assembly to clean effluent from the wood finishing sector within a specific rotating speed range, and they discovered that the chemical oxygen demand (COD) in real wastewater may be significantly lowered. Therefore, it is evident that hydraulic cavitation has shown considerable promise in the realm of wastewater treatments.

However, the design of hydrodynamic cavitation reactors has a substantial impact on their cavitation performance. At present, there exist four main types of cavitation reactors that are typically utilized in a laboratory setting: the orifice plate, the Venturi tube, vortex, and rotary types [12,13]. While the latter two types exhibit low pressure loss, their intricate structure and high maintenance costs serve as limiting factors for their widespread adoption. In contrast, both the orifice plate and Venturi tube cavitation reactors operate on similar principles of cavitation and offer the advantages of simple design, ease of use, and strong controllability. Nevertheless, the orifice plate cavitation reactors are more prone to blockages at sudden changes in the flow channel section and experience greater pressure losses than the Venturi tube counterparts. Therefore, the Venturi tube cavitation reactors are more widely applied in the field of hydraulic cavitation.

Until recently, researchers' interest in Venturi cavitation characteristics has not waned. Most of them focus on the cavitation inception, evolution process, cavitation instability, and the structural parameters of Venturi tubes. Simpson et al. [14] analyzed the effect of key geometric parameters, such as the throat length and diffuser angle of Venturi tubes on cavitation inception. Further, Li et al. [15] investigated the impact of various geometric parameters on cavitation inception using a numerical simulation and experimental methods and discovered that flow resistance determines cavitation inception. Sato et al. [16] used a high-speed video camera to visualize the behavior of a moving bubble cavitation in a Venturi from the inception to collapse process. Brunhart et al. [17] verified two mechanisms of vapor shedding (re-entrant jet and condensation shock) and offered more information on vapor shedding using the computational fluid dynamics (CFDs) method. Fang et al. [18] investigated the primary features and physical signals of two vapor-shedding mechanisms in Venturi tubes using a self-developed compressible cavitation phase change solver. Long et al. [19] evaluated the global cavitation behavior in a Venturi tube and found that the inlet pressures had no effect on the cavity length, which was only a function of the pressure ratio or the cavitation number. Kuldeep et al. [20] optimized the structural characteristics of various types of Venturi tubes (such as slit, circular, and elliptical), and they came to the conclusion that the optimal geometry for cavitational activity has a throat height/diameter to length ratio of 1:1 and a divergence angle of 6.5°. Shi et al. [21] carried out two-dimensional (2D) CFD simulations using a two-phase mixture model to investigate the impact of the convergent angle on the cavitation performance in the Venturi tube; the numerical findings revealed that a larger convergent angle enhances the cavitation yield but requires more power. In addition, they developed a semi-empirical model for predicting cavitation in the Venturi tubes. In a study by Zhao et al. [22], experiments were conducted to identify the role of the Venturi divergent angle in bubble breakup and showed that the divergent angle had a significant influence on the deceleration process. The larger the divergent angle, the shorter the distance and time, which is required for bubble deceleration.

While much research has been conducted on the inception, evolution, and structural parameters of Venturi-induced cavitation, there remains a lack of discussion on the influence of converging and diverging section lengths of a Venturi on cavitation characteristics under varying operating pressure. Furthermore, in this study, the convergence and divergence angles of the Venturi tube, which are significant factors influencing cavitations, were not altered. This provided a favorable starting point for conducting such research. Additionally, the Venturi cavitation reactors are often subject to different pressure conditions in various

application scenarios, such as wastewater treatment, organic compound synthesis, and biodiesel production [23–25]. Therefore, we focus our attention on an investigation of the effect of diverging and converging section lengths on cavitation characteristics at different pressure conditions. In this study, several Venturi devices with varying converging and diverging section lengths were simulated with a two-phase mixture model and the standard k-ε turbulence model, and the simulated results were validated using an actual pressure drop and flow rate data. Additionally, changes in the cavitation flow field within the Venturi under different pressure conditions were also investigated. Other flow field characteristics in the Venturi, such as the maximum throat velocity, mass flow rate, and vapor volume, were also measured and analyzed. The findings and conclusions from this study can provide insights for the design and application of Venturi cavitation devices.

2. Materials and Methods

2.1. Governing Equation and Turbulence Model

The governing equation can be utilized to elucidate the liquid flow behavior in a Venturi tube. In the presence of cavitation, the flow in a Venturi tube is a combination of vapor and liquid phases. To describe the two-phase flow of vapor and liquid in a Venturi tube, the mixture model is applied [7,15,21,26]. Based on this, a hypothesis is proposed, which assumes that the vapor and liquid phases are homogeneously mixed and able to permeate each other, regardless of their relative velocities. Moreover, it is assumed that the fluid is continuous during the flow process and the impact of volume force on fluid movement is negligible. The continuity and momentum equations of the mixture phase are provided as follows:

$$\nabla \cdot (\rho_{\mathrm{m}} v_{\mathrm{m}}) = 0 \tag{1}$$

$$\nabla \cdot (\rho_{\mathrm{m}} v_{\mathrm{m}} v_{\mathrm{m}}) = -\nabla p + \nabla \cdot \left[\mu_{\mathrm{m}} \left(\nabla v_{\mathrm{m}} + \nabla v_{\mathrm{m}}^{T} \right) \right] \tag{2}$$

where ρ_{m}, v_{m}, and μ_{m} denote the mixed phase's density, mass-averaged velocity, and viscosity, respectively. p is pressure; ∇ is the nabla symbol.

The phenomenon of cavitation is often accompanied by significant turbulence and the formation of cavities within the fluid flow, which grow, merge, collapse, and ultimately affect the performance and durability of engineering devices. The complex nature of cavitation events, which exhibit different time-scales and are influenced by various flow parameters, poses significant challenges for accurate and efficient numerical simulation. Although Direct Numerical Simulation (DNS) can be used to simulate the details of cavitation flows, it is computationally expensive and impractical for most actual engineering applications. Consequently, the Reynolds-averaged Navier–Stokes (RANS) equations are widely accepted to model the time-averaged variables of such a turbulent flow in the Venturi device. According to the calculations performed using the Reynolds number formula,

$$\mathrm{Re} = \frac{\rho_{\mathrm{w}} v d}{\mu_{\mathrm{w}}} \tag{3}$$

where ρ_{w} denotes water density, v represents the average flow velocity at the inlet of the Venturi tube, d is the diameter at the inlet of the Venturi tube, and μ_{w} represents the viscosity of water.

The Reynolds numbers for all investigated operating conditions in this study fall within the range of 34,174 to 141,767. These values significantly exceed the widely accepted critical Reynolds number threshold of 5000 for lamina flow in pipes. Hence, it can be inferred that the flow inside the Venturi tube exhibits turbulent characteristics. To account for the turbulence, the standard k-ε model is employed, which has been extensively vali-

dated by previous researchers [20,27,28]. The transport equations for the turbulence kinetic energy (k) and its dissipation rate (ε) are expressed as follows:

$$\frac{\partial}{\partial t}(\rho k) + \frac{\partial}{\partial x_i}(\rho k u_i) = \frac{\partial}{\partial x_j}\left[\left(\mu + \frac{\mu_t}{\sigma_k}\right)\frac{\partial k}{\partial x_j}\right] + G_k + G_b - \rho\varepsilon - Y_M + S_K \quad (4)$$

$$\frac{\partial}{\partial t}(\rho \varepsilon) + \frac{\partial}{\partial x_i}(\rho \varepsilon u_i) = \frac{\partial}{\partial x_j}\left[\left(\mu + \frac{\mu_t}{\sigma_\varepsilon}\right)\frac{\partial \varepsilon}{\partial x_j}\right] + C_{1\varepsilon}\frac{\varepsilon}{k}(G_k + C_{3\varepsilon}G_b) - C_{2\varepsilon}\rho\frac{\varepsilon^2}{k} + S_\varepsilon \quad (5)$$

where ρ denotes fluid density; k is turbulent kinetic energy; ε is turbulent kinetic energy dissipation rate. x and the subscripts i and j represent the coordinate direction; u_i is the component of the velocity vector in the i direction; G_k represents the generation of turbulence kinetic energy due to the mean velocity gradients; G_b is the generation of turbulence kinetic energy due to buoyancy; Y_M represents the contribution of the fluctuating dilatation in compressible turbulence to the overall dissipation rate; S_K and S_ε are user-defined source terms; σ_k and σ_ε are the turbulent Prandtl numbers of turbulent kinetic energy k and dissipation rate ε, which are 1.0 and 1.3, respectively. $C_{1\varepsilon}$, $C_{2\varepsilon}$, and $C_{3\varepsilon}$ are model constants, which are 1.44, 1.92, and 0.09, respectively. μ_t is turbulent viscosity.

2.2. Cavitation Model

The Rayleigh–Plesset equation and its variations are commonly employed to simulate mass transfer in the cavitation phenomena. Within the Ansys Fluent software package, three prevailing cavitation models are available, namely, the Singhal, Schnerr and Sauer, and Zwart–Gerber–Belamri models. Among these models, the Singhal model is the most comprehensive, considering the effects of phase transition, bubble motion, turbulent pressure fluctuations, and non-condensable gases on vapor phase formation and condensation. However, its numerical stability is inferior to that of the Schnerr and Sauer model and the Zwart–Gerber–Belamri model. In addition, prior studies [21,28,29] have utilized the Schnerr and Sauer model to analyze Venturi cavitation, making it a suitable choice for simulating vapor–liquid mass transfer in Venturi tubes. The rate of evaporation (Re) and the rate of condensation (Rc) of vapor in the Schnerr and Sauer models can be expressed as follows:

When $P \leq P_V$

$$R_e = F_{vap}\frac{\rho_v \rho_l}{\rho_m}\alpha_v(1-\alpha_v)\frac{3}{\Re_B}\sqrt{\frac{2}{3}\frac{(P_V - P)}{\rho_l}} \quad (6)$$

When $P \geq P_V$

$$R_c = F_{cond}\frac{\rho_v \rho_l}{\rho_m}\alpha_v(1-\alpha_v)\frac{3}{\Re_B}\sqrt{\frac{2}{3}\frac{(P - P_V)}{\rho_l}} \quad (7)$$

where ρ_v is the density of vapor; ρ_l is the density of liquid phase; P is the pressure in the liquid surrounding the bubble; P_V is the saturated vapor pressure of water; F_{vap} and F_{cond} are empirical calibration coefficients for evaporation and condensation, which are 1.0 and 0.2, respectively. α_v is the vapor volume fraction; $\Re_B$ is the bubble radius; α_v is a function of $\Re_B$

$$\alpha_v = \frac{n_b \frac{4}{3}\pi \Re_B^3}{1 + n_b \frac{4}{3}\pi \Re_B^3} \quad (8)$$

where n_b is the bubble number density, and the default value of $n_b = 1 \times 10^{13}$ m^{-3} is taken in Fluent.

2.3. Geometric Model

Figure 1 shows the geometric structure of a Venturi tube. Based on the Venturi pipe designed by Long et al. [19], the straight pipe of the inlet and outlet sections is adequately extended. The entrance straight pipe is $5D_t$, and the outlet straight pipe is $35D_t$. Meanwhile,

in order to investigate the impact of the lengths of converging and diverging sections on Venturi cavitation characteristics, a series of 15 Venturi models were constructed under varying operational conditions, as outlined in Table 1. The models maintained a consistent throat diameter (L_t = D_t = 10 mm), convergence angle (α = 45°), and divergence angle (β = 12°). In addition, the dimensionless parameter cavitation number is also included in Table 1, which reflects the cavitation flow state inside the Venturi tube, which is obtained from the following equation:

$$\sigma = \frac{P_{out} - P_V}{\frac{1}{2}\rho_l U_{th}{}^2} \quad (9)$$

where P_{out} is the outlet pressure, and U_{th} is the average velocity at the throat of the Venturi tube.

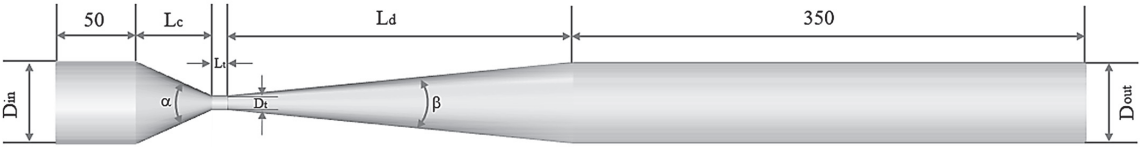

Figure 1. The geometry of the Venturi tube.

Table 1. Structural and operational parameters of Venturi model.

Cases	P_{in} (MPa)	σ	L_C (mm)	D_{in} (mm)	L_C/D_{in}	L_d (mm)	D_{out} (mm)	L_d/D_{out}
1	0.4	0.2595	48	50.00	0.960	140	39.42	3.55
2		0.2603	48	50.00	0.960	190	50.00	3.80
3		0.2608	48	50.00	0.960	240	60.46	3.97
4		0.2480	24	29.88	0.803	190	50.00	3.80
5		0.2678	72	69.64	1.030	190	50.00	3.80
6	0.8	0.1294	48	50.00	0.960	140	39.42	3.55
7		0.1298	48	50.00	0.960	190	50.00	3.80
8		0.1299	48	50.00	0.960	240	60.46	3.97
9		0.1236	24	29.88	0.803	190	50.00	3.80
10		0.1328	72	69.64	1.030	190	50.00	3.80
11	1.2	0.0860	48	50.00	0.960	140	39.42	3.55
12		0.0863	48	50.00	0.960	190	50.00	3.80
13		0.0865	48	50.00	0.960	240	60.46	3.97
14		0.0823	24	29.88	0.803	190	50.00	3.80
15		0.0881	72	69.64	1.030	190	50.00	3.80

2.4. Solution Strategy and Grid Independence

In the present study, 2D axi-symmetric models of Venturi tubes were simulated using a pressure-based solver. The working fluids considered were water and vapor, and the surrounding environment was maintained at 25 °C. The specific boundary conditions used for calculations in this study are listed in Table 2. For pressure solution, the PRESTO scheme was selected, and the first-order upwind discretization scheme was employed to discretize turbulent kinetic energy and turbulent dissipation rates. The momentum and vapor were discretized using the second-order upwind discretization scheme and QUICK scheme, respectively. Pressure–velocity coupling was carried out using the SIMPLE algorithm. To ensure convergence, the consistency of mass flow rates at the inlet and outlet was checked, and a convergence criterion of residual of the continuity equation below 10^{-5} was set. All CFD simulations were performed under steady-state conditions.

Table 2. Boundary conditions applied to the calculation.

Section	Boundary Conditions	Remark
Working fluid	-	Primary phase: water Second phase: vapor
Inlet	Pressure inlet	Table 1 (0.4–1.2 MPa)
Outlet	Pressure outlet	0.1 MPa
Wall	No slip condition	The wall treatment method: standard wall functions
Turbulence	Intensity and hydraulic diameter	Intensity: 3% Hydraulic diameter: 50 mm

Accurate simulations in computational fluid dynamics (CFDs) require careful consideration of the mesh size used. Therefore, conducting a sensitivity analysis is crucial to evaluate the impact of varying grid sizes on the accuracy and consistency of simulation results. As shown in Figure 2, ANSYS ICEM was employed to generate a structural mesh and apply local refinement to create half of two-dimensional Venturi geometric model, given its axial symmetry characteristics. Additionally, initial grid layers were positioned within the turbulent core region to ensure that most wall-adjacent grids had Y+ values exceeding 30. The heights of the first layer of grids were set to 0.1 mm, 0.08 mm, and 0.05 mm for model circumstances of 0.4 MPa, 0.8 MPa, and 1.2 MPa, respectively. The Y+ distribution of the Venturi tube is depicted in Figure 3 across three distinct pressure conditions. It is evident that the Y+ values for all pressure conditions predominantly reside within a reasonable range of 30 to 300 (suitable for standard wall functions). For the Venturi geometric model with a divergence segment length of 190 mm, four different grid sizes were generated with respective cell counts of 21,064, 41,584, 80,804, and 121,211. Figure 4 displays the absolute pressure profile along the Venturi wall for four distinct mesh sizes. It is evident that no significant deviation in the pressure distribution occurs upon further grid refinement beyond a certain point when using 80,804 grid cells. Therefore, it can be asserted that a grid containing 80,804 cells is sufficient to conduct the present simulation. The identical mesh generation approach was also utilized for both the model parameters of 140 mm and 240 mm divergence section lengths, resulting in mesh element counts of 74,632 and 87,484, respectively.

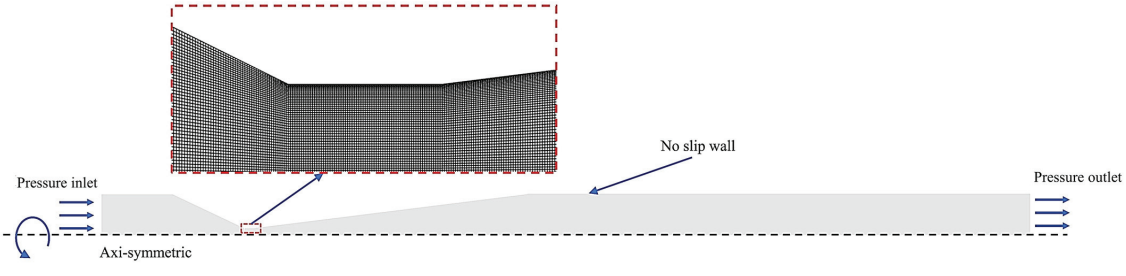

Figure 2. The refinement of the Venturi tube throat.

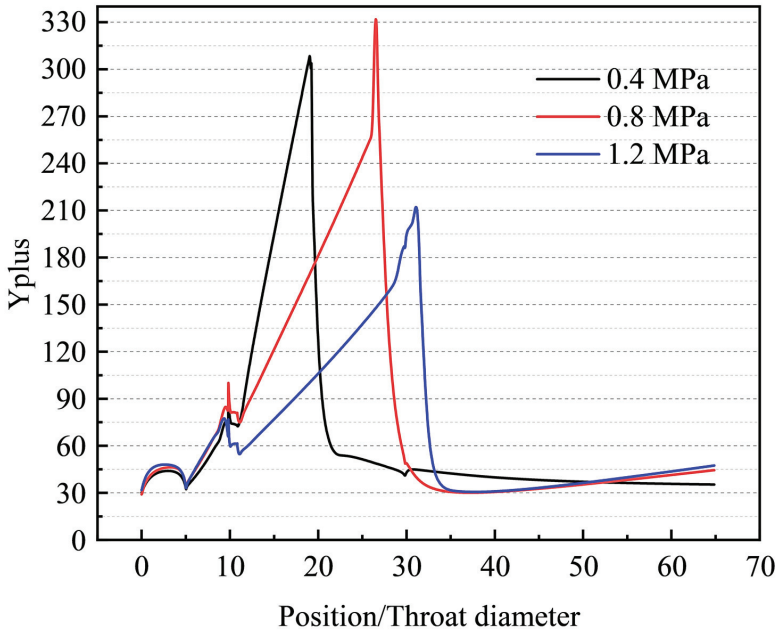

Figure 3. Distribution of Y plus at different inlet pressures.

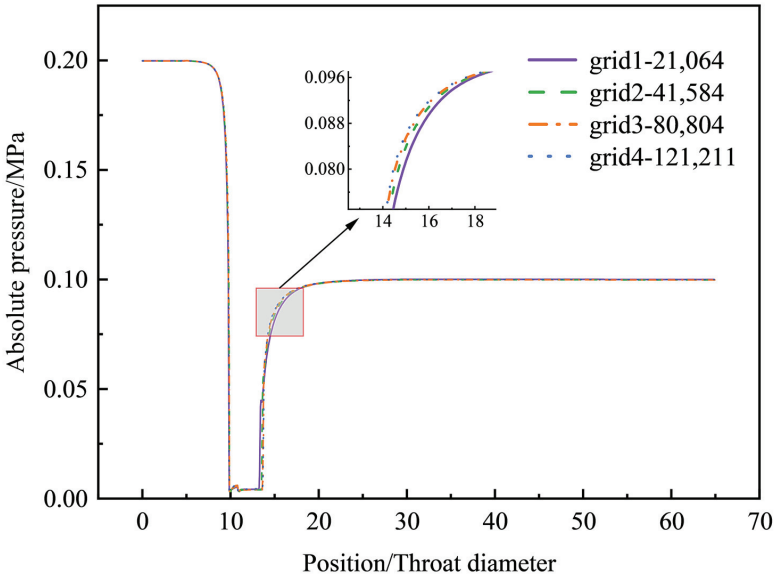

Figure 4. Absolute pressure profile of Venturi in four different mesh sizes.

3. Results and Discussion

3.1. Verification of the Simulation Method

In order to verify the reliability of the proposed numerical method, the Venturi tube geometry model utilized in the Long et al. [19,30] experiment was employed as the CFD calculation model. The inlet pressure was fixed at 0.4 MPa, whereas the outlet pressure ranged between 0.091 MPa and 0.378 MPa, with the temperature set at 19 °C, resulting in a

saturation vapor pressure of 2200 Pa. In addition, the pressure ratio is defined as the ratio of outlet pressure to inlet pressure, which can be written as follows:

$$\mathrm{P}_{\mathrm{ratio}} = \frac{P_{\mathrm{out}}}{P_{\mathrm{in}}} \tag{10}$$

where P_{in} is the inlet pressure.

The simulated flow rate results were subsequently compared with the experimental data. Figure 5 displays a comparison between the measured flow rate and the predicted values obtained from numerical simulations using the Venturi tube model employed in the experiment. As depicted in the figure, while there exists a discrepancy of 4.49% between the critical pressure ratio prediction from numerical simulation and its corresponding experimental value at the inception of cavitation, the numerical simulation results agree well with the experimental values for pressure ratios below 0.8. Figure 6 shows a comparison of the distribution of the vapor phase obtained from the experiment [30] and numerical simulations at an outlet pressure value of 0.188 MPa. It is noteworthy that there is a high degree of consistency in the extent of cavity development between the two approaches. And from the detailed local flow streamlines, it can be observed that there is a recirculation region at the downstream end of the cavitation region. The emergence of this structure effectively inhibits further extension of the cavity. This observation indicates a good agreement between the numerical simulation results and the experimental measurements under cavitation conditions.

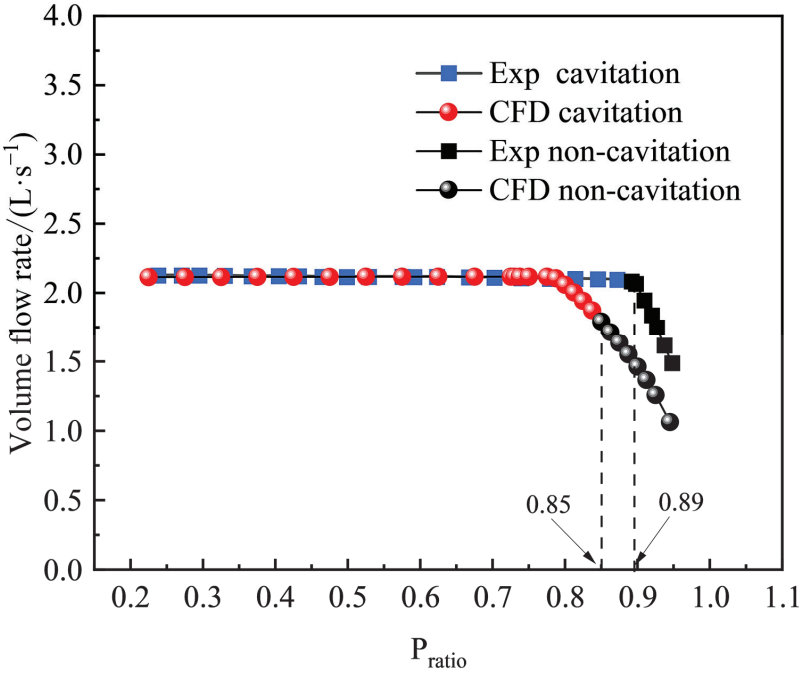

Figure 5. Comparison of experimental flow rate and simulation results.

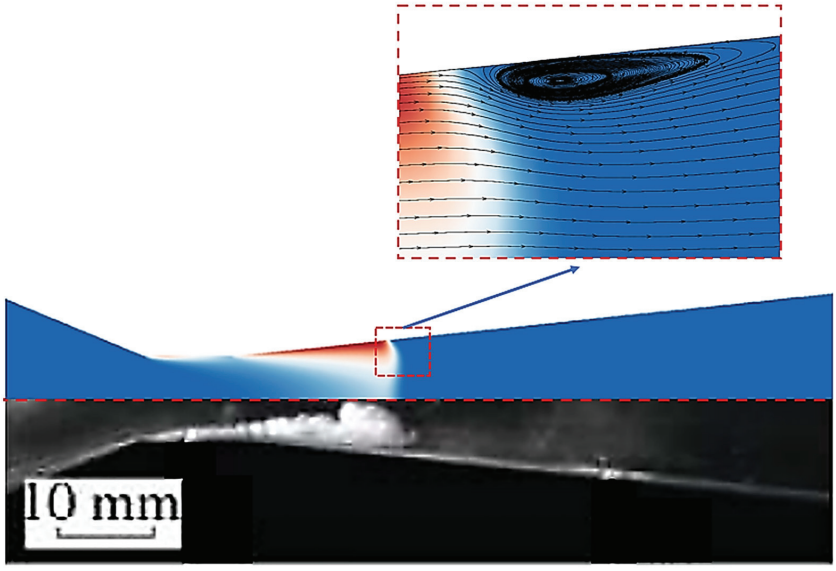

Figure 6. Comparison of the distribution of vapor phase between the experiment and the numerical results.

3.2. Effects of Divergent Length on Cavitation Characteristics

3.2.1. Analysis of Pressure and Vapor Volume Fraction

Figures 7 and 8 depict the changes in the absolute pressure and vapor volume fraction for varying divergence lengths of Venturi tubes at inlet pressures of 0.4 MPa, 0.8 MPa, and 1.2 MPa. The results indicate that the absolute pressure variation profile is similar across all three operating conditions, characterized by a sudden drop in pressure, followed by the lowest pressure in the throat, and eventually rebounding to the outlet pressure. The aforementioned process was also reported in a study conducted by Hwang et al. [28], who observed that the pressure flatness at the throat of the Venturi indicates the occurrence of a phase transition. However, our current study reveals that the influence of the divergence length on the absolute pressure is contingent upon the inlet pressure. Specifically, when the inlet pressure is 0.4 MPa, as depicted in Figure 7a, the curves representing the absolute pressure variation for the three different divergence lengths show a remarkable overlap, suggesting that the length of the divergence section has a negligible effect on the absolute pressure under these conditions. In Figure 7b,c, the effect of the length of the divergence section on the absolute pressure becomes more prominent when the inlet pressure is either 0.8 or 1.2 MPa. It is observed that shorter divergence sections in Venturi tubes result in longer low-pressure zones, which promote bubble formation. This distinction becomes increasingly apparent with higher inlet pressures. The rationale behind this phenomenon can be ascribed to the synergistic impact of two key factors: the inlet pressure and the expansion of the diameter in the diverging section. In the context of higher pressure conditions, the length of the low-pressure zone within the Venturi tube is not solely determined by the magnitude of the inlet pressure but is also influenced by the degree of diameter expansion in the diverging section. Venturi tubes with shorter diverging sections exhibit a relatively smaller increase in diameter. As a result, the velocity decay inside the tube is gradual, leading to an extended low-pressure zone. Figure 8 exhibits a rising trend in the vapor volume fraction within the Venturi's throat, which is aligned with the previously discussed pressure variation. These findings indicate that the low-pressure region in the throat plays a significant role in generating cavities. Furthermore, it has been observed that there exists a certain degree of overlap in the ascending segment of the

vapor phase curve under varying pressure conditions, suggesting that alterations in the length of the divergent section do not impact the cavitation characteristics of the throat. Moreover, at an inlet pressure of 0.4 MPa, the distribution of vapor volume fraction remains consistent across different divergence section lengths. However, at inlet pressures of 0.8 MPa and 1.2 MPa, this consistency is broken, and an increasing trend is observed in both the amplitude and coverage area of the vapor volume fraction with a decreasing divergence section length. This shows that shorter divergence section lengths under higher pressure circumstances are beneficial to enhance the cavitation effect in the Venturi tube.

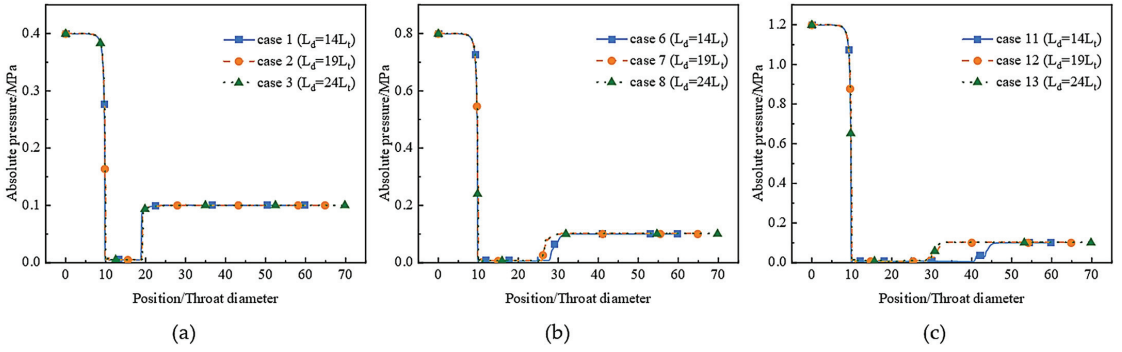

Figure 7. Absolute pressure variation along Venturi wall with different divergence lengths under varying inlet pressure: (**a**) 0.4 MPa, (**b**) 0.8 MPa, and (**c**) 1.2 MPa.

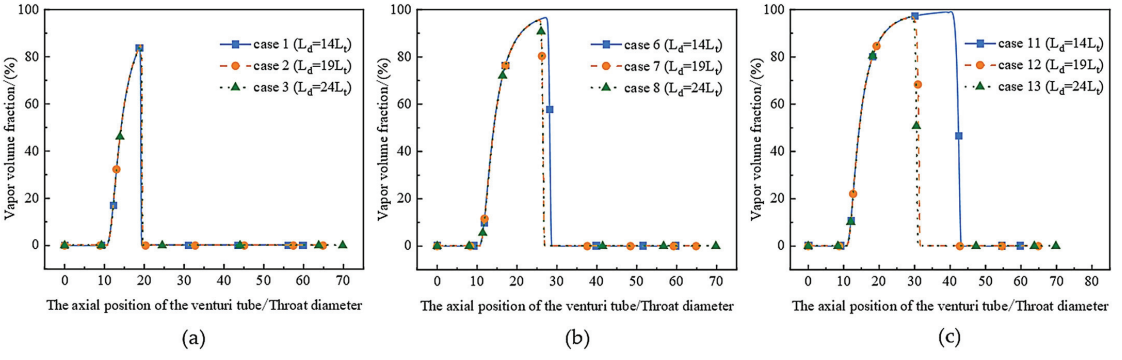

Figure 8. Vapor volume fraction variation in Venturi tube with different divergence lengths under varying inlet pressure: (**a**) 0.4 MPa, (**b**) 0.8 MPa, and (**c**) 1.2 MPa.

Figure 9 presents a comparison of the vapor volume fraction contours for three divergence lengths of the Venturi at various inlet pressures. The figure illustrates that vapor initially appears in the neck of the Venturi and then develops further in the divergence section. Furthermore, it is worth noting that the sensitivity of the vapor volume fraction exhibits variations under different pressure conditions. When the inlet pressure is 0.4 MPa, the cavity lengths of the Venturi with different divergence lengths are very similar, as demonstrated in Figure 9a. This can be attributed to the relatively small pressure difference in the Venturi at this point, resulting in a shorter low-pressure zone formed in the Venturi throat compared to the 0.8 and 1.2 MPa conditions. According to the research by Bashir et al. [31], the extent of cavity growth is determined by the residence time of the cavity within the low-pressure region. Thus, under the pressure condition of 0.4 MPa, the generated cavity has a shorter residence time in the throat and collapses in the diffusion section before it fully develops to the outlet. So, the cavity length is weakly influenced by the length of the divergence section in this situation. Figure 9b,c show that the Venturi

with a shorter divergence length has a broader coverage of the cavitation region when the inlet pressure is 0.8 or 1.2 MPa. This variation can be attributed to the fact that the shorter divergence section reduces the cross-sectional area of the outlet, which in turn reduces the pressure recovery rate in the Venturi and lengthens the cavitation coverage area. This is also confirmed by the work of Kuldeep et al. [20], which shows that the pressure recovery rate in the downstream section has a significant impact on the growth of these generated cavities.

3.2.2. Analysis of Cavitation Collapse Strength

Figure 10 depicts the profiles of the turbulence kinetic energy (TKE) along the axis of a Venturi tube for various inlet pressures, which reveals two conspicuous spikes in TKE within the Venturi tube, corresponding to the inception of cavitation at the throat and the subsequent collapse of bubbles in the divergence section. Notably, the surge in the TKE during the collapse of cavitation bubbles surpasses that during the throat cavitation inception, which is indicative of a pronounced release of energy during bubble collapse. Upon comparing Figure 10a–c, it is evident that changes in the length of the divergence segment do not significantly impact the fluctuation behavior of the first turbulent kinetic energy inside the Venturi tube, which can be attributed to the fact that variations in the length of the divergent section have no impact on the cavitation characteristics at the throat of the Venturi tube. Nonetheless, there are noticeable differences in the variations of the second turbulent kinetic energy within the tube due to changes in the length of the Venturi tube divergence under various inlet pressures.

To gain further insights into the fluctuation characteristics of the turbulent kinetic energy, Figure 11 exhibits the trends in the variation at two distinct locations of peak turbulent kinetic energy across diverse pressure conditions. It can be seen that the turbulent kinetic energy peak values at the throat of the Venturi tube are consistent for different divergence lengths at different inlet pressures, and the peak values show a linear relationship with the inlet pressure. In addition, as the inlet pressure increases from 0.4 to 1.2 MPa, the turbulent kinetic energy peak in the divergence section of the Venturi tube undergoes two stages of growth. In the first stage, a short divergence section results in fast peak growth. In the second stage, the slow growth of the peak value can be attributed to the fact that as the cavities develop closer to the exit straight section under higher pressure conditions, the variation in the cross-sectional area at the diffuser section is minimal, leading to a slow enhancement of the cavitation collapse intensity. Furthermore, the maximum diameter that the cavities can achieve imposes a limitation on further improvements in the cavitation collapse intensity.

3.2.3. Analysis of Flow Field Parameters

Several significant flow field parameters at three different pressure conditions were collected in Table 3 to assess the impact of divergence section length on the cavitation flow field more accurately. The table shows that for the inlet pressure of 0.4 MPa, the variation of the cavitation volume of Venturi with different divergence section lengths is very tiny. However, at the inlet pressure of 0.8 and 1.2 MPa, Venturi tubes with shorter divergence section lengths obviously have higher cavitation volumes, which is consistent with the analysis in Figure 8. Furthermore, the maximum velocity of the throat increases slightly as the length of the divergence section decreases under varied inlet conditions. Another fact we may observe is that with the same inlet pressure, the outlet mass flow rate of Venturi tubes with various diffusion lengths is nearly identical, indicating that the diffusion length has no significant impact on the outlet mass flow rate.

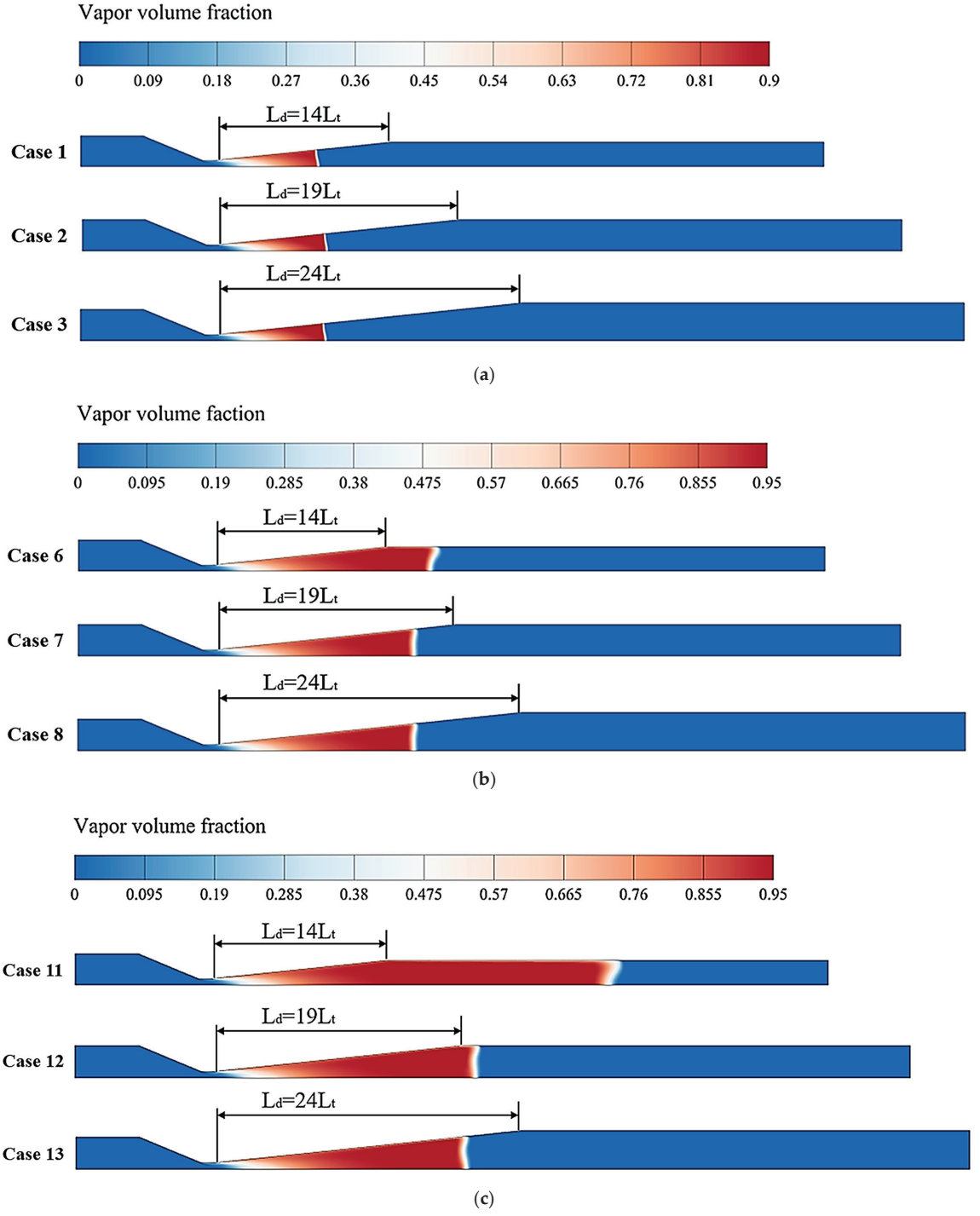

Figure 9. Vapor volume fraction contour of Venturi tubes at various inlet pressures and divergence lengths: (**a**) 0.4 MPa, (**b**) 0.8 MPa, and (**c**) 1.2 MPa.

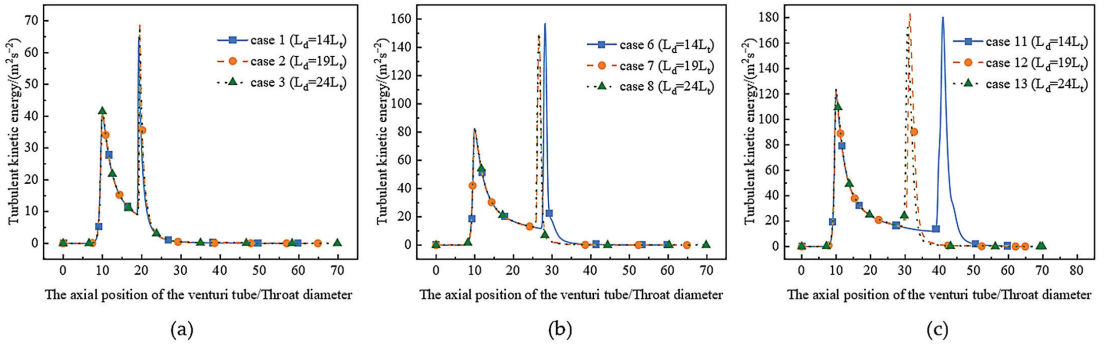

Figure 10. The variation of turbulent kinetic energy along the axis of the Venturi tube under varying pressure conditions: (**a**) 0.4 MPa, (**b**) 0.8 MPa, and (**c**) 1.2 MPa.

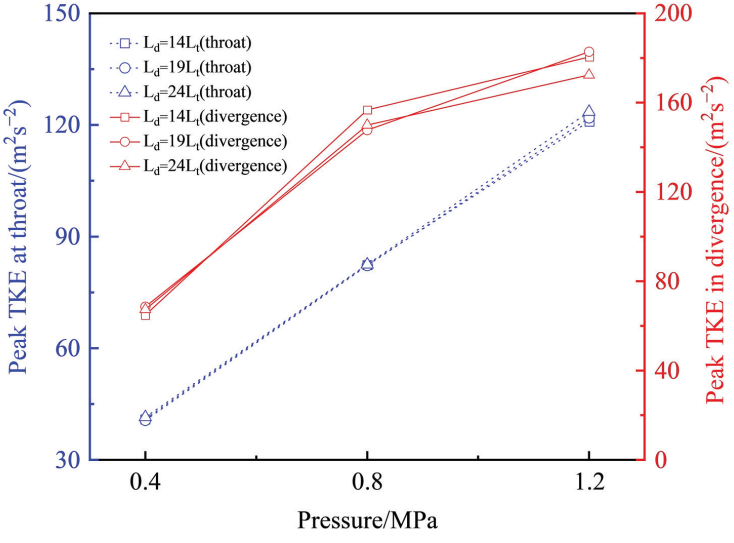

Figure 11. Variations of turbulence kinetic energy peaks at two locations (throat and divergence) in a Venturi tube under different pressures.

Table 3. Comparison of Venturi tubes' flow field characteristics at various pressures and diffusion lengths.

Cases	P_{in} (MPa)	σ	L_d (mm)	Q (kg·s^{-1})	V_t (m·s^{-1})	Vol (mm^3)	Vap_m
1	0.4	0.2595	140	1.88831842	27.29931	17,694.4	0.8916025
2		0.2603	190	1.88298337	27.26803	18,965.5	0.8933302
3		0.2608	240	1.88450754	27.23960	18,932.1	0.8932120
6	0.8	0.1294	140	2.67930270	38.68253	106,551	0.9799927
7		0.1298	190	2.67167545	38.62886	85,491.1	0.9747809
8		0.1299	240	2.67394078	38.60078	85,072.4	0.9747983
11	1.2	0.0860	140	3.29722403	47.45741	268,358.5	0.9915485
12		0.0863	190	3.28465412	47.39365	162,272.6	0.9926510
13		0.0865	240	3.28479553	47.33728	149,088.7	0.9912778

V_t represent the maximum velocity of the Venturi throat; Vol is the volume of the cavity in the Venturi; Vap_m is the maximum vapor holdup.

3.3. Effects of the Convergent Length on Cavitation Characteristics

3.3.1. Analysis of Pressure and Vapor Volume Fraction

Figures 12 and 13 disclose the influence of the convergence section length on the absolute pressure and vapor volume fraction at various inlet pressures. Figure 12 indicates that the impact of the convergence section length on the absolute pressure of the flow field depends on the inlet pressure. Specifically, when the inlet pressure is 0.4 MPa, a slower pressure recovery rate is observed for the Venturi with a 24 mm convergence section length. These results suggest that a contraction section length of 24 mm results in a higher throat velocity and slower velocity reduction, potentially impacting the intensity of cavitation. However, for inlet pressures of 0.8 or 1.2 MPa, a shorter convergence section length leads to a longer low-pressure region, with greater differences observed as the inlet pressure increases. Furthermore, changes in the absolute pressure can affect the volume fraction of vapor, as depicted in Figure 13. The coverage and amplitude of the vapor volume fraction decrease as the length of the convergence section decreases when the inlet pressure is 0.4 MPa. Conversely, when the inlet pressure is 1.2 MPa, the coverage area of the vapor volume fraction increases with decreasing convergence section lengths. These findings indicate that the impact of the convergence section length on the cavitation characteristics of the Venturi tube is non-monotonic and also dependent on the inlet pressure conditions.

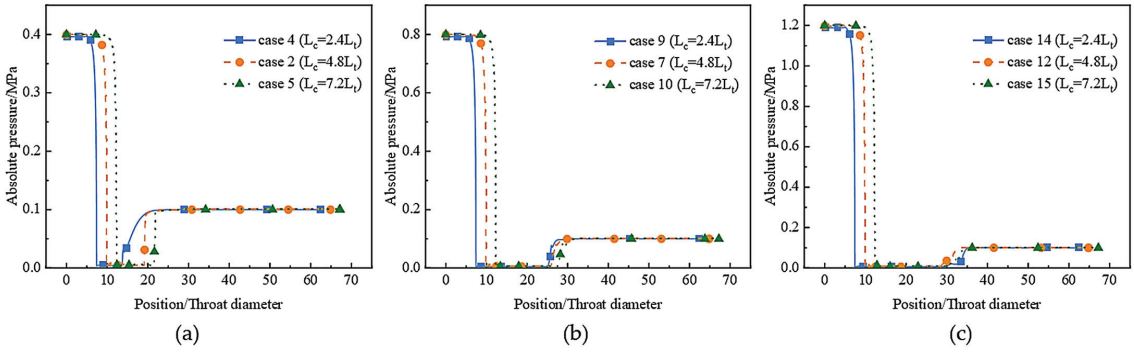

Figure 12. Absolute pressure variation along Venturi wall with different convergence lengths under varying inlet pressure: (**a**) 0.4 MPa, (**b**) 0.8 MPa, and (**c**) 1.2 MPa.

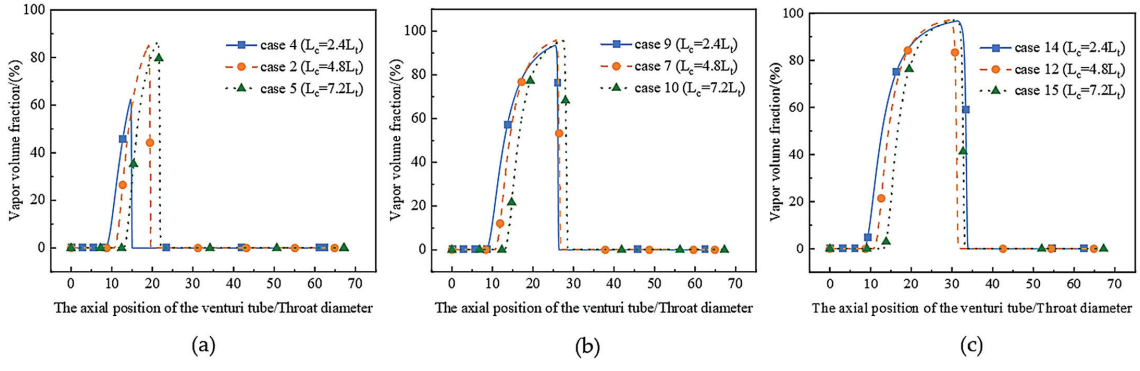

Figure 13. Vapor volume fraction variation in Venturi tube with different convergence lengths under varying inlet pressure: (**a**) 0.4 MPa, (**b**) 0.8 MPa, and (**c**) 1.2 MPa.

Figure 14 compares the effect of the length of the convergence section on the distribution of the vapor phase under different pressure conditions in a more visible way. It can be observed that the cavitation cloud within the Venturi tube, characterized by a 24 mm

convergence section length, exhibits a distinct "jet" shape under an inlet pressure of 0.4 MPa. Furthermore, it is noteworthy to mention that the length of the cavitation cloud is comparatively shorter compared to other convergence length scenarios. The observed phenomenon can be ascribed to the direct impact of the length of the convergence section on the cross-sectional area of the inlet. The Venturi tube with a small cross-sectional area of the inlet has a higher inflow velocity under the same inlet pressure. Cavities in the throat may have a shorter residence time due to the higher flow velocity, and they are carried into the divergence section by the flow before they fully develop and are pushed to both sides of the tube axis by the flow. As a result, cavitation clouds develop into the shape of jets. However, when the inlet pressure is 0.8 or 1.2 MPa, the shorter convergence length of the Venturi tube has a longer cavitation cloud. There are two potential causes for this. On the one hand, as depicted in Figure 12, a bigger pressure difference causes the low-pressure area with a shorter contraction section length to be longer, which is beneficial to the development of the cavity. Furthermore, fluid impinging on the wall of the convergence section will result in a significant flow loss at high-pressure differentials. Shorter convergence structures reduce the flow loss in the convergence section, improve the throat velocity, and extend the cavitation cloud's coverage area.

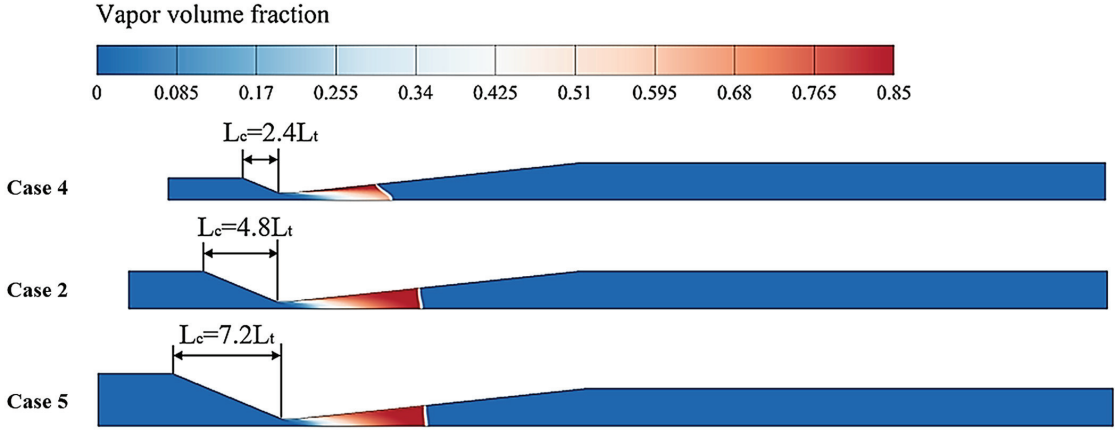

(**a**)

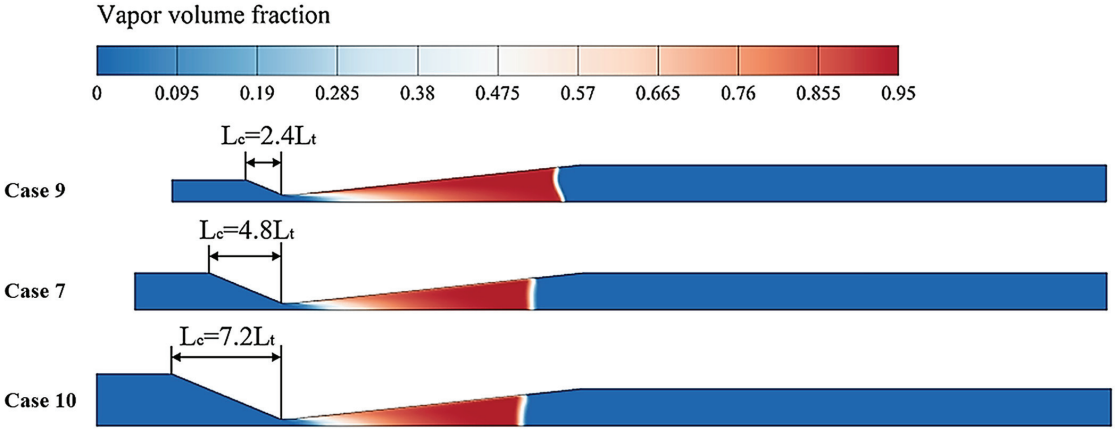

(**b**)

Figure 14. *Cont.*

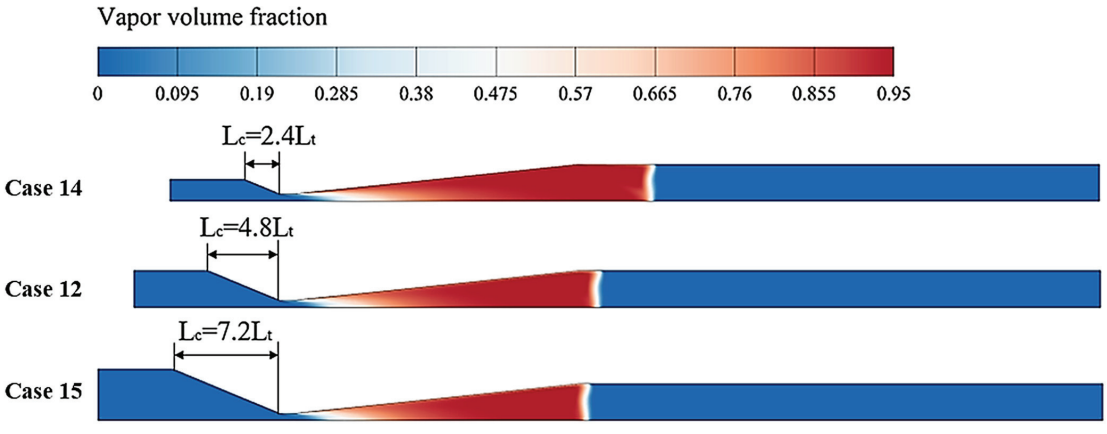

(**c**)

Figure 14. Vapor volume fraction contour of Venturi tubes at various inlet pressures and convergence lengths: (**a**) 0.4 MPa, (**b**) 0.8 MPa, and (**c**) 1.2 MPa.

3.3.2. Analysis of Cavitation Collapse Strength

The formation and collapse of cavities often lead to changes in the local turbulent kinetic energy [14,20]. Figure 15 depicts the profile of turbulent kinetic energy distribution within the Venturi tube under varying inlet pressures. The plot effectively captures the discernible alterations in turbulent kinetic energy resulting from the inception of cavitation at the throat region and the subsequent bubble collapse in the divergence segment. In contrast to Venturi tubes with varying divergence lengths, alterations in the convergence length of a Venturi tube exert an influence on the turbulent kinetic energy at both the throat and diffuser sections. Comparing the profiles of the turbulent kinetic energy in Figure 15a–c, it is evident that the effect of the convergence length on the turbulence kinetic energy at the throat is consistent, regardless of the pressure conditions. Clearly, the peak value of the turbulent kinetic energy at the throat increases with the increasing convergence length. The turbulent kinetic energy distribution at the divergence section of a Venturi tube varies differently under varying pressure conditions. Specifically, at an inlet pressure of 0.4 MPa, it is apparent from Figure 15a that Venturi tubes with longer convergence lengths exhibit higher peak turbulent kinetic energy and stronger bubble collapse intensity at the divergence section. Conversely, at an inlet pressure of 1.2 MPa, the peak turbulent kinetic energy at the divergence section of Venturi tubes with different convergence lengths is similar, and the intensity of the bubble collapse is comparable as well. These observations suggest that the variations in the turbulent kinetic energy at the divergence section of the Venturi tube are more sensitive to pressure conditions than the convergence length.

Figure 16 presents the trends in the variations of the two locations of turbulent kinetic energy peaks within the Venturi tube. In general, both peaks show an increase as the inlet pressure rises. The growth trend of the peak at the throat is relatively stable. Longer convergent sections in the Venturi tube lead to higher turbulent kinetic energy peaks. However, the impact of the convergent section length on the turbulent kinetic energy peak in the divergence section depends on the inlet pressure. As the inlet pressure increases, the effect of the convergent section length on the turbulent kinetic energy peak in the divergence section gradually diminishes. This indicates that the effect of the Venturi tube convergence section length on the downstream bubble collapse strength is limited, and this effect gradually weakens as the inlet pressure increases.

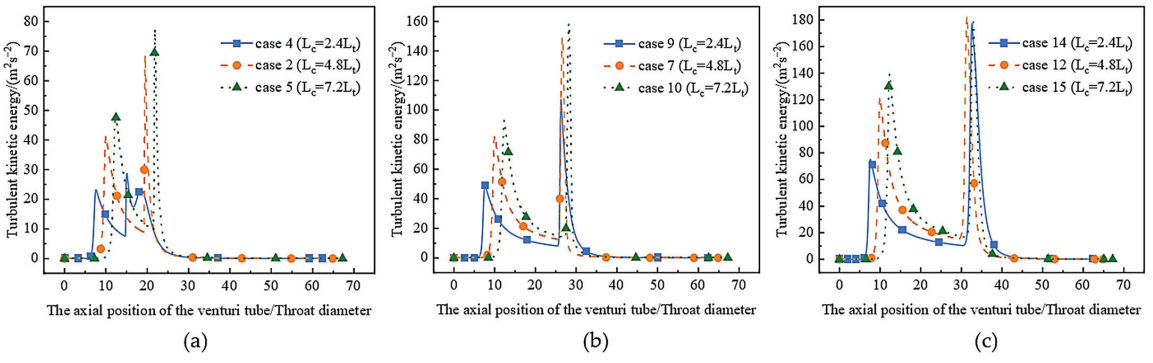

Figure 15. Variation of turbulence kinetic energy along the axis of the Venturi tube under different inlet pressures: (**a**) 0.4 MPa, (**b**) 0.8 MPa, and (**c**) 1.2 MPa.

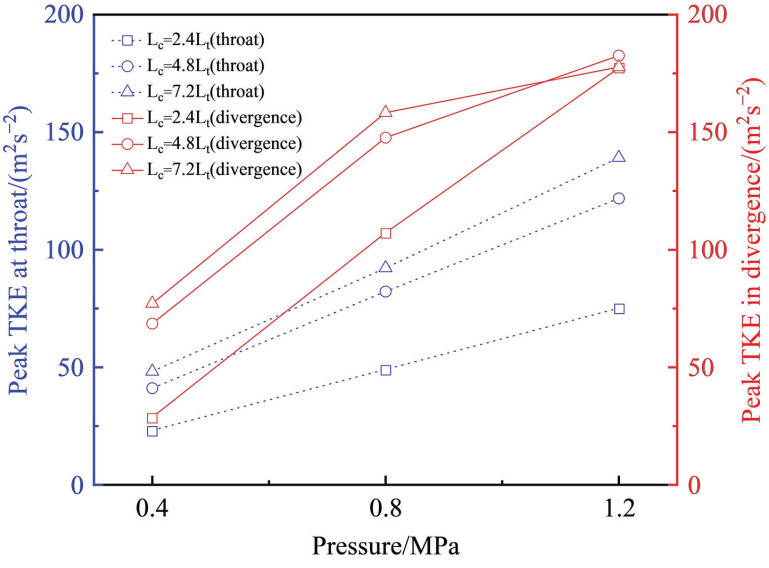

Figure 16. Variations of turbulence kinetic energy peaks at two locations (throat and diffuser) in a Venturi tube under different pressures.

3.3.3. Analysis of Flow Field Parameters

Table 4 presents the variations in several flow field parameters for each Venturi model across different inlet pressure conditions. According to the data in the table, under different inlet pressures, the mass flow rate and the maximum velocity of the throat show different degrees of decrease with an increase in the length of the convergence section. This indicates that the maximum velocity of the throat and the mass flow of the Venturi are not only related to the inlet pressure but also to the length of the convergence section. In addition, the variation in the cavitation volume observed in the table indicates that the effect of the convergence section's length on the cavitation characteristics depends on the provided inlet pressure. When the inlet pressure is low, a short convergence section length does not improve the cavitation effect of the Venturi tube. When the inlet pressure is high, a small convergence section length can significantly improve the cavitation effect, and the cavitation effect becomes more significant as the inlet pressure rises. Thus, the specified pressure conditions should be considered while determining the length of the convergence section.

Table 4. Comparison of Venturi tubes' flow field characteristics at various pressures and convergence lengths.

Cases	P_{in} (MPa)	σ	L_C (mm)	Q ($kg \cdot s^{-1}$)	V_t ($m \cdot s^{-1}$)	Vol (mm^3)	Vap_m
4	0.4	0.2480	24	1.92805647	28.05349	8058.9	0.9013388
2		0.2603	48	1.88341402	27.27604	19,173.1	0.8957157
5		0.2678	72	1.86739731	26.88531	19,232.4	0.8973735
9	0.8	0.1236	24	2.72222116	39.70596	110,433.2	0.9740466
7		0.1298	48	2.67167545	38.62886	85,491.1	0.9747809
10		0.1328	72	2.65792438	38.19953	77,281.3	0.9731250
14	1.2	0.0823	24	3.34104545	48.63226	253,014.8	0.9919481
12		0.0863	48	3.28465412	47.39365	162,272.6	0.9926510
15		0.0881	72	3.26788526	46.89446	146,933.8	0.9918739

V_t represent the maximum velocity of the Venturi throat; Vol is the volume of the cavity in the Venturi; Vap_m is the maximum vapor holdup.

4. Conclusions

In this study, the CFD method was used to study the Venturi tube's cavitation phenomenon. The effects of convergence and divergence segment length on Venturi tube cavitation characteristics are investigated and discussed. The findings provide useful guidance for designing and studying Venturi structures under various pressure conditions. The present work leads to the following conclusions:

The cavitation characteristics around the throat region are generally unaffected by changes in the divergence section's length. In addition, the influence of the divergent section length on Venturi cavitation characteristics relies on the pressure conditions provided. With the increase in pressure drop, the Venturi tubes with shorter divergence section lengths have longer low-pressure areas, which can yield greater cavitation zones. The peak turbulence kinetic energy at the divergence section of the Venturi tube shows a two-stage growth. In the first growth stage, the Venturi tubes with shorter divergence sections have a faster growth rate of the turbulence kinetic energy, resulting in a significant enhancement of the bubble collapse strength. In the second growth stage, the growth rate of the turbulence kinetic energy peak slows down due to the limited development space of the straight section, leading to a suppression of the enhancement of bubble collapse strength.

Unlike the divergence section, the length of the convergence section has a more profound impact on the cavitation behavior in the Venturi tube. Under different pressure conditions, the length of the convergence section exhibits varied cavitation behavior. The cavitation effect in the Venturi tube is not enhanced by shortening the length of the convergence section when the inlet pressure is low. In contrast, a shorter convergence section length can extend the low-pressure area and promote the formation of longer cavitation clouds when the inlet pressure is high. The amplification of turbulent kinetic energy induced by the inception of a cavity at the throat of the Venturi tube increases as the length of the tube's contraction section grows. However, the primary factor influencing turbulence kinetic energy at the diffuser section is the inlet pressure conditions. With increasing inlet pressure, the effect of changing the contraction section length on turbulence kinetic energy at the diffuser section gradually diminishes.

Under the same inlet pressure, the effect of Venturi tube divergence section lengths on the outlet mass flow rate and maximum throat velocity is minor, whereas the length of the convergence section has some discernible impact on these parameters. As the convergent section increases, the outlet mass flow rate and the maximum throat velocity exhibit a decreasing trend.

Author Contributions: Conceptualization, Y.L. and B.L.; methodology, Y.L.; software, B.L.; validation, B.L.; formal analysis, Y.L.; investigation, B.L.; resources, Y.L.; writing—original draft preparation, B.L.; writing—review and editing, Y.L.; supervision, Y.L.; project administration, Y.L.; funding acquisition, Y.L. All authors have read and agreed to the published version of the manuscript.

Funding: This research was funded by the Scientific Research Start-up Fund of Zhejiang Sci-Tech University, grant no.11132932619106.

Institutional Review Board Statement: Not applicable.

Informed Consent Statement: Not applicable.

Data Availability Statement: Not applicable.

Acknowledgments: The authors would like to thank the editor and anonymous reviewers for their constructive suggestions, which comprehensively improved the quality of the paper. The authors would also like to thank the support from Zhejiang Sci-Tech University.

Conflicts of Interest: The authors declare no conflict of interest.

References

1. Carpenter, J.; Badve, M.; Rajoriya, S.; George, S.; Saharan, V.K.; Pandit, A.B. Hydrodynamic cavitation: An emerging technology for the intensification of various chemical and physical processes in a chemical process industry. *Rev. Chem. Eng.* **2017**, *33*, 433–468. [CrossRef]
2. Sarvothaman, V.P.; Simpson, A.; Ranade, V.V. Comparison of Hydrodynamic Cavitation Devices based on Linear and Swirling Flows: Degradation of dichloroaniline in water. *Ind. Eng. Chem. Res.* **2020**, *59*, 13841–13847. [CrossRef]
3. Sarvothaman, V.P.; Simpson, A.T.; Ranade, V.V. Modelling of vortex based hydrodynamic cavitation reactors. *Chem. Eng. J.* **2018**, *377*, 119639. [CrossRef]
4. Gogate, P.R.; Pandit, A.B. Hydrodynamic Cavitation Reactors: A state of the art review. *Rev. Chem. Eng.* **2001**, *17*, 1–85. [CrossRef]
5. Rajoriya, S.; Bargole, S.; George, S.; Saharan, V.K. Treatment of textile dyeing industry effluent using hydrodynamic cavitation in combination with advanced oxidation reagents. *J. Hazard. Mater.* **2018**, *344*, 1109–1115. [CrossRef]
6. Wang, C.; Jin, R.; He, Z.; Qiao, Y.; Wang, Y.; Wang, K.; Lu, Y.; Wang, X.; Liu, D. A new water treatment technology for degradation of B[a]A by Hydrodynamic Cavitation and Chlorine Dioxide Oxidation. *Ultrason. Sonochem.* **2020**, *61*, 104834. [CrossRef] [PubMed]
7. Abbas-Shiroodi, Z.; Sadeghi, M.T.; Baradaran, S. Design and optimization of a cavitating device for Congo red decolorization: Experimental investigation and CFD simulation. *Ultrason. Sonochem.* **2021**, *71*, 105386. [CrossRef]
8. Innocenzi, V.; Prisciandaro, M.; Vegliò, F. Study of the effect of operative conditions on the decolourization of azo dye solutions by using hydrodynamic cavitation at the lab scale. *Can. J. Chem. Eng.* **2020**, *98*, 1980–1988. [CrossRef]
9. Bagal, M.V.; Gogate, P.R. Degradation of diclofenac sodium using combined processes based on hydrodynamic cavitation and heterogeneous photocatalysis. *Ultrason. Sonochem.* **2014**, *21*, 1035–1043. [CrossRef]
10. Mezule, L.; Tsyfansky, S.; Yakushevich, V.; Juhna, T. A simple technique for water disinfection with hydrodynamic cavitation: Effect on survival of Escherichia coli. *Desalination.* **2009**, *248*, 152–159. [CrossRef]
11. Badve, M.; Gogate, P.; Pandit, A.; Csoka, L. Hydrodynamic cavitation as a novel approach for wastewater treatment in wood finishing industry. *Sep. Purif. Technol.* **2013**, *106*, 15–21. [CrossRef]
12. Wang, B.; Su, H.; Zhang, B. Hydrodynamic cavitation as a promising route for wastewater treatment—A review. *Chem. Eng. J.* **2021**, *412*, 128685. [CrossRef]
13. Wang, B.; Liu, Y.; Zhang, H.; Shi, W.; Xiong, M.; Gao, C.; Cui, M. Hydrodynamic cavitation and its application in water treatment combined with ozonation: A review. *J. Ind. Eng. Chem.* **2022**, *114*, 33–51. [CrossRef]
14. Simpson, A.; Ranade, V.V. Modeling Hydrodynamic Cavitation in Venturi: Influence of Venturi Configuration on Inception and Extent of Cavitation. *AIChE J.* **2019**, *65*, 421–433. [CrossRef]
15. Li, M.; Bussonnière, A.; Bronson, M.; Xu, Z.; Liu, Q. Study of Venturi tube geometry on the hydrodynamic cavitation for the generation of microbubbles. *Miner. Eng.* **2019**, *132*, 268–274. [CrossRef]
16. Sato, K.; Hachino, K.; Saito, Y. Inception and Dynamics of Traveling-Bubble-Type Cavitation in a Venturi. *Nippon. Kikai Gakkai Ronbunshu B Hen* **2004**, *70*, 69–76. [CrossRef]
17. Brunhart, M.; Soteriou, C.; Gavaises, M.; Karathanassis, I.; Koukouvinis, P.; Jahangir, S.; Poelma, C. Investigation of cavitation and vapor shedding mechanisms in a Venturi nozzle. *Phys. Fluids.* **2020**, *32*, 083306. [CrossRef]
18. Fang, L.; Li, W.; Li, Q.; Wang, Z. Numerical investigation of the cavity shedding mechanism in a Venturi reactor. *Int. J. Heat Mass Transf.* **2020**, *156*, 119835. [CrossRef]
19. Long, X.; Zhang, J.; Wang, J.; Xu, M.; Lyu, Q.; Ji, B. Experimental investigation of the global cavitation dynamic behavior in a Venturi tube with special emphasis on the cavity length variation. *Int. J. Multiphase Flow.* **2017**, *89*, 290–298. [CrossRef]
20. Kuldeep; Saharan, V.K. Computational study of different Venturi and orifice type hydrodynamic cavitating devices. *J. Hydrodyn.* **2016**, *28*, 293–305. [CrossRef]

21. Shi, H.; Li, M.; Nikrityuk, P.; Liu, Q. Experimental and numerical study of cavitation flows in Venturi tubes: From CFD to an empirical model. *Chem. Eng. Sci.* **2019**, *207*, 672–687. [CrossRef]
22. Zhao, L.; Sun, L.C.; Mo, Z.Y.; Du, M.; Huang, J.; Bao, J.J.; Tang, J.G.; Xie, G. Effects of the divergent angle on bubble transportation in a rectangular Venturi channel and its performance in producing fine bubbles. *Int. J. Multiphase Flow.* **2019**, *114*, 192–206. [CrossRef]
23. Kim, H.J.; Nguyen, D.X.; Bae, J.H. The performance of the sludge pretreatment system with Venturi tubes. *Water Sci. Technol.* **2008**, *57*, 131–137. [CrossRef]
24. Ramisetty, K.A.; Pandit, A.B.; Gogate, P.R. Novel Approach of Producing Oil in Water Emulsion Using Hydrodynamic Cavitation Reactor. *Ind. Eng. Chem. Res.* **2014**, *53*, 16508–16515. [CrossRef]
25. Maddikeri, G.L.; Gogate, P.R.; Pandit, A.B. Intensified synthesis of biodiesel using hydrodynamic cavitation reactors based on the interesterification of waste cooking oil. *Fuel* **2014**, *237*, 285–292. [CrossRef]
26. Dastane, G.G.; Thakkar, H.; Shah, R.; Perala, S.; Raut, J.; Pandit, A.B. Single and multiphase CFD simulations for designing cavitating Venturi. *Chem. Eng. Res. Des.* **2019**, *149*, 1–12. [CrossRef]
27. Chitsaz, H.R.; Omidkhah, M.R.; Ghobadian, B.; Ardjmand, M. Optimizing Different Angles of Venturi in Biodiesel Production Using CFD Analysis. *Iran. J. Chem. Chem. Eng.* **2019**, *38*, 285–295.
28. Hwang, H.J.; Park, J.; Min, J.K. A numerical study on the flow control characteristic of a cavitating Venturi with one- and two-stage diffusers. *J. Mech. Sci. Technol.* **2021**, *35*, 1463–1472. [CrossRef]
29. Ashrafizadeh, S.M.; Ghassemi, H. Experimental and numerical investigation on the performance of small-sized cavitating Venturis. *Flow Meas. Instrum.* **2015**, *42*, 6–15. [CrossRef]
30. Long, X.P.; Wang, J.; Zuo, D.; Zhang, J.Q.; Ji, B. Experimental investigation of the instability of cavitation in veturi tube under different cavitation stage. *J. Mech. Eng.* **2018**, *54*, 209–215. [CrossRef]
31. Bashir, T.A.; Soni, A.G.; Mahulkar, A.V.; Pandit, A.B. The CFD driven optimisation of a modified Venturi for cavitational activity. *Can. J. Chem. Eng.* **2011**, *89*, 1366–1375. [CrossRef]

materials

MDPI

Article

Investigation the Effect of MR Fluid Composition on Properties at Low Strain Ranges

Anna Fenyk [1,*], Wojciech Horak [2] and Marek Zieliński [1]

[1] Department of Inorganic and Analytical Chemistry, Faculty of Chemistry, University of Lodz, Tamka 12, 91-403 Lodz, Poland; marek.zielinski@chemia.uni.lodz.pl
[2] Faculty of Mechanical Engineering and Robotics, AGH University of Science and Technology, al. A. Mickiewicza 30, 30-059 Kraków, Poland; horak@agh.edu.pl
* Correspondence: anna.fenyk@chemia.uni.lodz.pl; Tel.: +48-42-635-57-80

Abstract: The paper presents the results of eight magnetorheological (MR) fluids of different compositions. Magnetite and carbonyl iron were used as magnetic particles. MR fluids based on glycerin and OKS 352 oil were produced using stabilizers in the form of oleic acid and Aerosil 200 (Evonik Resource Efficiency GmbH, Hanau, Germany) silica; additives such as graphite and yellow dextrin were also used. The aim of the study was to determine the properties of various combinations of components on the dynamic properties of MR fluids, i.e., properties characterizing the fluid within the range of low deformations, as well as to investigate the effect of different compositions on structural yield stress and flow stress prepared MR fluids at different magnetic field induction values.

Keywords: magnetorheological fluids; carbonyl iron; magnetite; magnetic field; DMA; rheology

Citation: Fenyk, A.; Horak, W.; Zieliński, M. Investigation the Effect of MR Fluid Composition on Properties at Low Strain Ranges. *Materials* **2023**, *16*, 5730. https://doi.org/10.3390/ma16175730

Academic Editor: Michal Sedlačík

Received: 12 July 2023
Revised: 17 August 2023
Accepted: 18 August 2023
Published: 22 August 2023

1. Introduction

Rapid development of science, technology, and industry has resulted in the emergence of a new class of materials often referred to as "smart". They are characterized by the fact that they can change their properties under the influence of external physical factors, e.g., electric or magnetic fields, mechanical stress, light intensity, temperature, pH etc. These include, among others, magnetorheological (MR) materials, whose rheological and viscoelastic properties, such as the flow limit, shear stress, dynamic modules, and damping properties, can be quickly and reversibly controlled using an external magnetic field [1]. Fluids, elastomers, gels, lubricants, and foams can be distinguished as MR materials [2]. Previous works [3–6] proved that the factors that affect the rheological properties of MR fluids can be divided into intrinsic, such as the concentration, particle shape and size, the viscosity of the carrier fluid, and the type of additives used. and extrinsic ones, i.e., the value and direction of magnetic field, the shear rate, the temperature. The interdependence of all these factors is very complex and at the same time important when selecting the composition and parameters for a specific application. The flow limit value is one of the main parameters that can be determined from the flow curves [7,8] and which are critical for most applications of MR fluids.

Mineral, silicone, and hydraulic oils, silicone copolymers, polyester, diesters, polyoxyalkylenes, glycols, as well as water are most often used to produce MR fluids [9,10]. In the article by [11], two organic oils (cotton oil and sunflower oil) were used as carrier liquids for the research. Additionally, magnetic particles in the form of carbonyl iron were coated with guar rubber, which ensured better sedimentation stability. It was also found that cottonseed oil-based fluid demonstrates better sedimentation resistance when compared to sunflower oil-based fluid. In the work by [12], the experimental results indicated that ionic liquid carrier-based MR fluids had a higher flow limit and a more significant MR effect than those based on silicone oil with a higher magnetic field induction value. The obtained result was associated with the phenomenon of surface tension of ionic liquids. Since ion

fragments are small compared to the size of magnetic particles, they are easily absorbed on their surface, forming an ionic layer. The van der Waals force between them strengthens the interaction between the particles, thus creating a more stable structure. Using silicone oil as a carrier liquid, as in the publication by [13], the MR fluid was prepared. The flow limit was higher in a silicone oil-based fluid when compared to conventional synthetic fluid.

According to Iglesias et al. [14] and Harsh et al. [15], MR fluids consist of magnetizable particles, among others of carbonyl iron, iron oxide, cobalt, nickel, with micron dimensions and a non-magnetizable carrier liquid. They also contain additives affecting their rheological, tribological properties, as well as anti-sedimentation and agglomeration of magnetic particles [16–18]. To maximize the MR effect, the base liquid should have low viscosity. In a publication by [19], it was observed that due to the application of an external magnetic field, magnetic particles are aggregated along the direction of the field lines, forming a chain-like structure. The chain structures increase the apparent viscosity of the fluid, causing a change from a liquid state to a solid-like state within milliseconds. The magnetic particles, under the influence of a magnetic field, form chain-shaped structures, which affects the flow limit in the MR fluid [20,21]. In recent years, significant progress has been made in understanding the effect of particle size on the rheological behavior of the material under study [22]. The larger the particles, the greater their magnetization, and therefore the higher the yield stress [23]. A liquid containing colloidal silica and polyethylene glycol mixed with different mass fractions of iron powder was tested, and then the rheological behavior of the obtained substance was analyzed in a publication by [24]. It was observed that the increasing content of carbonyl iron powder effectively increased the viscosity of the fluid under weak magnetic field conditions. According to [25,26], shear stress is an important indicator for the assessment of the rheological properties of liquids, and this important parameter is also influenced by the type of additives used. In the experiment, carbonyl iron particles, two methylsilicone oils, and an additive in the form of stearic acid were used. In a study of the correlation between shear stress and shear rate, it was demonstrated that, under the influence of a magnetic field, the shear stress decreases slightly at the beginning and then gradually increases with a tendency to stabilize, confirming the fact that the larger the magnetic field, the stronger the force of interaction between the chains of particles in the MR fluid, and thus the greater the shear stress. Rheological analysis was carried out on liquids containing carbonyl iron particles, silicone oil, liquid paraffin, graphite, and various additives, including stearic acid, sodium dodecyl sulfate (SDS), and their mixture, as seen in the work of [27]. The results indicated that the rheological properties of MR fluids are affected, in particular, by the mass fraction of magnetic particles. When the mass share of CI was 40–50%, the shear stress first increased and then decreased as the magnetic field strength increased. In contrast, at 60–70% CI mass share, the shear stress of the MR fluid first increased and then stabilized with an increase in magnetic field strength. The authors of [28] presented the results of tests on the rheological properties of magnetorheological fluids with different physicochemical compositions. The tests concerned both the complete compositions of MR fluids and the base liquids (the samples containing no particles with ferromagnetic properties). The paper shows the influence of the selection of individual components of MR fluids on their rheological properties, paying attention to the interaction of the base liquid with particles of the solid phase of the MR fluid. Under magnetic field conditions, the type of ferromagnetic particles (their magnetic properties) have a decisive impact on the MR response of the fluid (change in rheological properties due to the impact of the magnetic field on the fluid).

This article is a more detailed supplement to the work conducted in [28]. The main objective of the work included the assessment of the influence of selected components on one of the key properties of MR fluids, which is the yield stress. The value of this parameter is essential for almost all MR fluid applications, including shock absorbers, brakes, and valves [29–32]. The problem of determining limit stress values is a complex issue [33,34]. Moreover, in the case of MR fluids, these stresses can be significantly dependent on the deformation conditions, in particular when working in compression mode [35].

The paper focuses on the study of limit stress values of several MR fluids operating in the shear mode, i.e., the mode characteristic of most of the currently known technical applications. It should be noted that the complexity of determining and interpreting limit stresses in MR fluids applies to a large group of liquids with complex composition, in particular non-colloidal suspensions. In such cases, the presence of two characteristic points associated with liquid deformation limit states can be identified. The first of them, referred to as yield stress, corresponds to the value of stress at which the internal structure of the liquid is violated. In this work, the stress corresponding to the linear-elastic range of deformations of the sample was assumed to be this value. In turn, the second characteristic point is flow stress, i.e., the stress value at which the internal structure of the liquid is destroyed. This corresponds to the total flow of the liquid. In the work, the value of tangential stresses corresponding to the equilibrium point of the elasticity and damping moduli was assumed as the flow stress.

Due to the direct relationship of each flow limit with the structural changes occurring in the volume of the MR fluid, the effects of the individual components of the fluid can be expected to be visible in the results of measurements. This paper highlights that individual components can influence the behavior of MR fluids, with differences particularly noticeable at very low deformations. The observed changes can be related to the chemical phenomena described in the paper. It can be also possible to hypothesize that there is a change in the friction coefficient within the fluid. Conclusions about possible changes at the structural level were drawn based on the variability of the measured parameters. If the magnetorheological effect is due to a change in the structure of the fluid, then by observing the rheological quantities it is possible to deduce what is happening inside a suspension.

2. Materials and Methods

2.1. Preparation of MR Sample

This paper presents the results of investigations into the properties of eight MR fluid samples that differed in composition. The samples were prepared using two types of ferromagnetic particles (magnetite and carbonyl iron), two types of carrier liquid (glycerin and OKS 352 synthetic oil), and two types of stabilizers (oleic acid and Aerosil 200 silica). In addition, Graphite EG 290 and Active carbon and yellow dextrin were added to two samples. All the samples contained a small (0.5%) addition of alumina.

The materials used for preparation of the samples were purchased from commercial sources and used without further purification or chemical treatment. The manufacturers of chemical reagents were: glycerin (Chempur, Piekary Śląskie, Poland), OKS 352 oil (OKS Spezialschmierstoffe GmbH, Maisach—Gernlinden, Germany), Fe_3O_4 (magnetite) (Alfa Aesar GmbH, Kandel, Germany), carbonyl iron (Libra, Trzebinia, Poland), oleic acid (Chempur, Piekary Śląskie, Poland), SiO_2 (Aerosil 200) (Evonik Resource Efficiency GmbH, Hanau, Germany), Al_2O_3 (Wolem GmbH, Eschwege, Germany), Graphite EG 290 (3D Nano, Krakow, Poland), $Mg(OH)_2$ (Acros Organics, Morris Plains, NJ, USA), activated carbon (Chempur, Piekary Śląskie, Poland), and yellow dextrin (Biomus, Lublin, Poland). Each of the prepared samples contained in its composition respectively: 59 wt.% base liquid, 40 wt.% magnetic particles, 0.5 wt.% each. stabilizer and 5 wt.% of additives, except for samples CM7 and CM8, which contained 54 wt.% base liquid, because they contained that additionally 5 wt.% ingredients in the form of graphite, $Mg(OH)_2$ or activated carbon and yellow dextrin. The total was 100% by weight. The procedure consisted in measuring the appropriate amount of a given component and then manually mixing it for about 30 min to obtain a uniform consistency.

The samples produced were marked as CM1 to CM8; the composition of the samples has been presented in detail in Table 1.

Table 1. Composition of MR fluids samples with the content of magnetic particles.

	Magnetic Powder (40% wt.)	Carrier Fluid	Stabilizer (0.5% wt.)	Addition (0.5% wt.)	Addition (5% wt.)
CM1	Magnetite	glycerine (59% wt.)	Oleic acid	Al_2O_3	-
CM2	Carbonyl iron				
CM3	Carbonyl iron				
CM4	Magnetite	OKS 352 (59% wt.)	SiO_2 (Aerosil 200)		Graphite EG 290
CM5	Carbonyl iron				$Mg(OH)_2$
CM6	Magnetite	OKS 352 (54% wt.)			Active carbon, yellow dextrin
CM7	Carbonyl iron				
CM8	Carbonyl iron				

The CM7 and CM8 samples contained 54% w/w of the base liquid in their composition due to the fact that they additionally contained 5% w/w of components in the form of graphite, $Mg(OH)_2$, or activated carbon and yellow dextrin. The whole constituted 100% mass. Some of the chemical components that are a part of MR fluids can be characterized as follows: OKS 352 oil is a synthetic hydrocarbon oil, resistant to high operating temperatures. SiO_2 (Aerosil 200) is a matted colloidal silica, with hydrophilic properties, synthetic, amorphous silicon dioxide with a very fine structure, produced by burning silicon tetrachloride in hydrogen furnaces, with 99.8% content of SiO_2, specific surface area of 200 m^2/g, bulk density of 0.05 g/cm^3 and particle diameter of 7–40 nm.

The so-called base liquids were selected for their different properties. OKS 352 synthetic oil protects against oxidation very well, is resistant to high temperatures with optimal wear protection, including under the influence of moisture, prevents corrosion, as well as shows minimal losses due to evaporation (samples C3–C8). Glycerin ($C_3H_8O_3$) has hygroscopic and hydrophilic properties (samples C1 and C2).

On comparison of the two base liquids with the magnetite (Fe_3O_4) content, some differences can be observed. The sample C4 (OKS 352 oil and magnetite) does not change its properties and consistency. The situation is different with the sample C1 (glycerin and magnetite). Glycerin easily absorbs water and is oxidized with oxygen from the air. The magnetite present in the mixture catalyzes the glycerin oxidation reaction, with its decomposition into glyceraldehyde and dihydroxyacetone according to the following Equation (1):

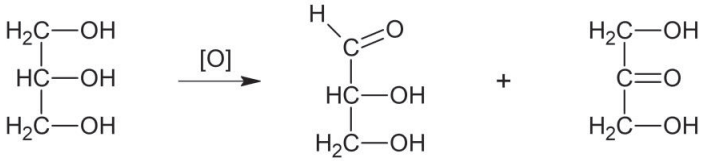

(1)

However, in the environment of glycerin, magnetite itself decomposes into hematite and iron(II) oxide according to Equation (2):

$$Fe_3O_4 \rightarrow Fe_2O_3 + FeO \quad (2)$$

Hematite under the influence of moisture (water) forms iron(III) hydroxide according to Equation (3):

$$Fe_2O_3 + 3\ H_2O \rightarrow 2\ Fe(OH)_3 \quad (3)$$

whereas iron(II) oxide forms iron(II) hydroxide according to Equation (4):

$$FeO + H_2O \rightarrow Fe(OH)_2 \quad (4)$$

The sequence of these reactions affects the change in the density of magnetic particles from 5.2 g/cm^3 to 3.4 g/cm^3 and the change in the consistency of the whole mixture.

Magnetorheological fluids have been selected so as to contain two different carrier liquids, with different viscosities, two different types of magnetic particles, with different structures, two different types of stabilizers and various additives to change the properties of these liquids, e.g., graphite (EG 290) for thermal conductivity, $Mg(OH)_2$ for non-flammable properties, activated carbon to CO_2 and the other impurities capture properties, or yellow dextrin resulting in biodegradable properties of the liquids.

The graphite used for the CM7 sample is expanded graphite EG 290, with a density of 1.46 g/cm^3 (bulk density 0.64 g/cm^3 only) and a granulation of 200–600 μm. The density is identical to that of carbonyl iron with 5–6.5 μm granulation (1.46 g/cm^3). Expanded graphite (also referred to as intumescent graphite) is graphite modified for the needs of industry. It has a fluffy texture (specific surface area of 100 m^2/g) and is one of the most delicate minerals.

2.2. Characterization of Obtained MRs

The scope of the research included conducting dynamic tests (DMA) to analyze the properties of the produced fluids within the low deformation range, with a specific focus on determining the stress limits (yield stress and flow stress). The scope of research included conducting Amplitude Sweep tests with controlled deformation. In this method, the yield stress is defined as the value of the shear stress at the end of the LVE regime. Here, we define this stress as the point where G′ differs by more than 5% from its strain-independent value in the LVE regime [36–39]. The flow stress is defined as the value of shear stress at the crossover point where the storage modulus is equal to the loss modulus (G′ = G″) (Figure 1).

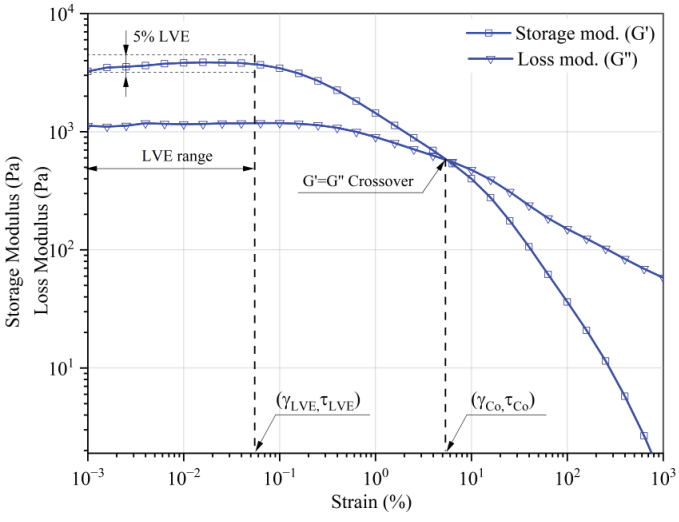

Figure 1. Storage modulus (G′) and loss modulus (G″) vs. strain (γ). Method of determining the yield stress (τ_{LVE}) and flow stress (τ_{Co}).

The research was carried out on the Physica MCR 301 (Anton Paar) rotational rheometer, equipped with an MRD-180 magnetic field test cell. The plate-plate geometry (d = 20 mm) was used, the height of the measuring gap (h = 0.5 mm), the volume of the sample (v = 175 μL). The test parameters were as follows: strain (γ = 0.001 to 1000%), changed according to the logarithmic profile (5 points/dec), angular velocity (ω = 101/s), value of the applied magnetic induction (B = 0, 50, 100, 200, 400, and 500 mT). The mag-

netic field induction values were selected on the basis of previous studies discussed in the paper [28].

The main part of the research was preceded by Frequency Sweep tests, which was the basis for the adoption of a value of angular velocity. The adopted values ensure that tests are carried out both within the scope of controllability of the tested MR fluids, as well as under magnetic saturation conditions. The tests were conducted at t = 25 °C.

3. Results and Discussion

3.1. Studies of Dynamic Properties of the Examined Mr Fluids

Figure 2 presents the results of oscillatory tests of produced MR liquids not subjected to magnetic field (in the so-called zero conditions (B = 0 mT)). For all MR fluids tested, a clear linearly elastic range (LVE) was observed. This unexpected behavior of the liquid at zero conditions indicated that all tested MR liquids showed stable elastic properties even before the application of the magnetic field. Under zero conditions, three characteristic groups were distinguished: CM1 liquid, a group of MR liquids containing magnetite and carbonyl iron powder.

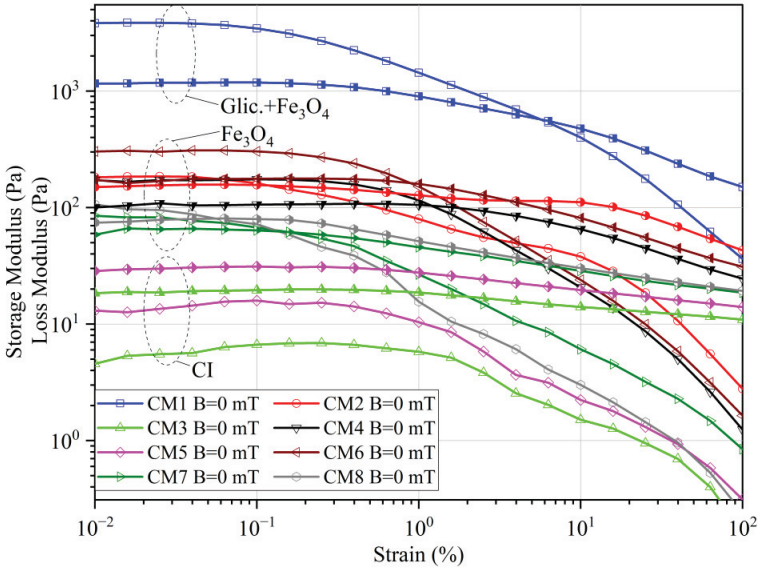

Figure 2. Storage (open symbols) and loss (half empty symbols) modulus at zero state (B = 0 mT).

CM1 liquid stood out from all tested liquids with high values of elastic moduli ($G' \approx 3800$ Pa), with the second liquid (CM6) characterized by more than 10 times lower elasticity ($G' \approx 310$ Pa).

All liquids assigned to the second group, containing magnetite, have similar properties (G' ranges from 80 to 310 Pa). As for CM1, there is a clear LVE range and an intersection point of the elastic moduli.

The samples prepared on the basis of carbonyl iron (CI), CM3, and CM5, regardless of additional components, showed the lowest elastic properties (G = 5–12 Pa) among the tested MR fluids. Additionally, only for these two fluids (CM3 and CM5), the value of the loss modulus exceeded the value of the modulus of elasticity, and no intersection point of the curves G' and G'' was observed. This behavior can be explained by the physicochemical properties of magnetic particles, i.e., carbonyl iron.

Figure 3 shows examples of results obtained in the presence of a magnetic field. Two ranges were selected: the first one for the lowest analyzed magnetic field induction, i.e., B = 50 mT (Figure 3a), and the second for the highest magnetic induction: B = 500 mT

(Figure 3b). In either case, very high values of the elasticity modulus were obtained, which is related to the magnetorheological effect. The value of G′ already at a relatively low magnetic induction was in the order of 6.5–29 kPa, reaching over 730 kPa at B = 500 mT.

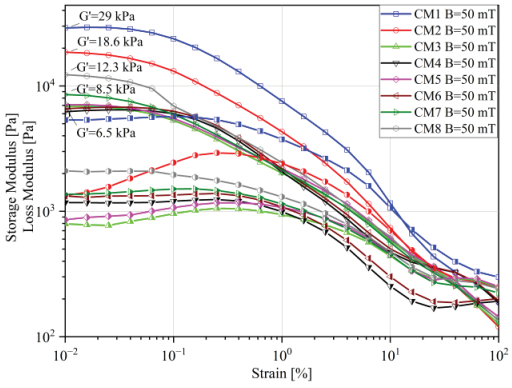

(**a**)

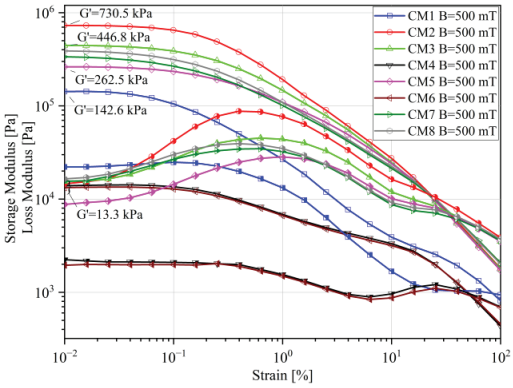

(**b**)

Figure 3. Storage (open symbols) and loss (half empty symbols) modulus: (**a**) B = 50 mT, (**b**) B = 500 mT.

Even within the low magnetic induction range (B = 50 mT), the CM1 sample had the highest modulus of elasticity among all tested samples. However, at the highest analyzed magnetic induction value (B = 500 mT), the highest storage modulus values were obtained for the CM2 fluid, i.e., that prepared on the basis of glycerin like CM1, but containing carbonyl iron. In the first case, the high elasticity of the sample in the zero-state turned out to be decisive, while at higher magnetic induction values the effect of the magnetic properties of ferromagnetic particles prevails.

In the context of the loss modulus (G″), a significant intensification of nonlinearity of changes in this parameter is visible with the increase in the value of the applied magnetic field. Greater fluctuations are observed for the samples produced with the use of carbonyl iron (CI).

Differences are noticeable between the CM1 and CM2 samples, considering that the same base liquid was used to produce them, but they differ in the magnetic particles used. These differences, resulting from the physicochemical properties of magnetic particles, may explain the discrepancies in the test results and also affect the form and consistency of the CM1 and CM2 samples. Magnetite is an inorganic chemical compound from the group of

oxides with a density of ρ = 5.2 g/cm^3 and a particle diameter < 45 μm, in which iron is present in the +2 and +3 oxidation states. Smaller fluctuations in the loss modulus (G″) are observed for the samples produced using magnetite (CM4 and CM6). The CM7 fluid differs from other samples containing carbonyl iron. It contains the addition of graphite, which reduced friction between carbonyl iron particles. This was due to the physicochemical properties of the added graphite.

To characterize the dynamic properties of the tested MR fluids, the damping factor tan δ = G″/G′ was determined. For the purposes of comparison, the value of tan δ in the middle LVE range (γ = 0.01%) was recorded; the results are summarized in Figure 4. In the zero state, the CM3 and CM5 samples exhibited the highest damping values, with tan(δ) approximately 4 and just over 2.8, respectively. This indicates a clear advantage of viscous properties over elastic ones. The results suggest that the components used to produce these fluids resulted in the formation of a liquid structure with relatively high internal damping or low elasticity. Notably, only these samples contained carbonyl iron (CI). For the remaining samples, under zero conditions, the values of this parameter were 0.3 for CM1, whereas for samples CM2, CM4, CM6, CM7, CM8, they were similar and fell within the range of 0.6–0.8.

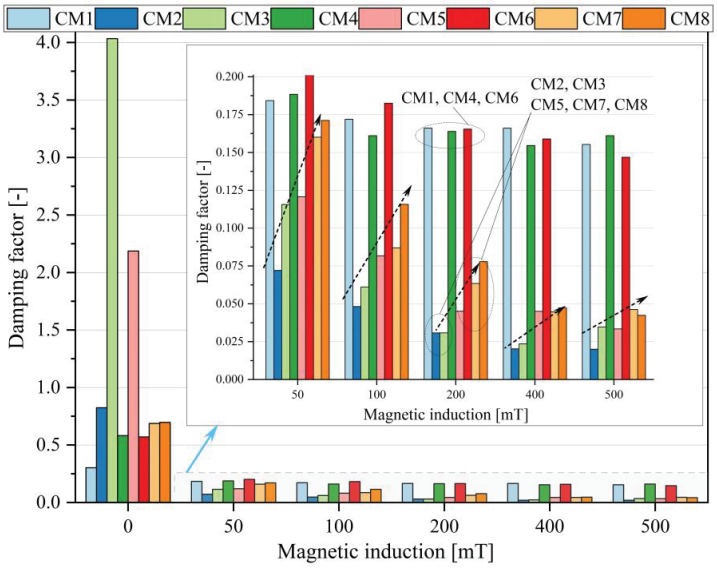

Figure 4. The damping factor at LVE (gamma = 0.01%).

In the case of application of a magnetic field, there is a significant reduction in the damping factor value, which results from the magnetorheological effect and the associated significant increase in the G′ value. The tan(δ) values for all tested samples are within the range of 0.0–0.2. The thumbnail (Figure 4) shows the obtained results on a graph with a scaled ordinate axis. Regardless of the magnetic induction value, the qualitative change in the damping factor is similar for all tested samples. The samples containing magnetite (CM1, CM4, CM6) show relatively high damping, while for other samples (containing carbonyl iron), a trend (marked with arrows) is visible, showing an increase in the damping factor in the individual samples depending on the use of individual additives. The lowest values are visible for the glycerin-based sample (CM2), followed by pure OKS 352 oil (CM3), silica addition (CM5 sample), and graphite and dextrin in the CM7 and CM8 samples, respectively. At the same time, for the highest values of magnetic field induction, the differences in the results between CM7 and CM8 begin to blur.

3.2. Studies of the Yield Stresses and Flow Stresses

Figure 5 illustrates the yield stress as a function of the set value of magnetic field induction. The values were determined to correspond to a 5% change of G′ in the LVE (Linear Viscoelastic) range. To distinguish the range of low magnetic field values, the diagrams are presented in semi-logarithmic (Figure 5a) and linear (Figure 5b) systems.

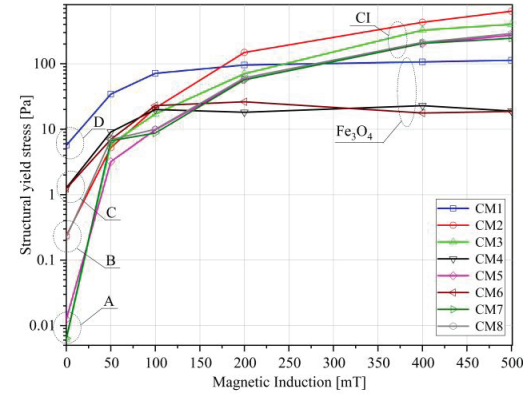

(**a**)

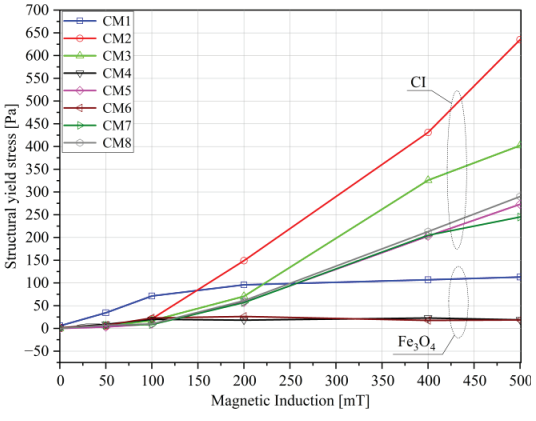

(**b**)

Figure 5. Structural yield stress versus magnetic induction (**a**) in a semi-logarithmic system, (**b**) in a linear system.

In the zero state (Figure 5a), a clear division of the tested liquids into four groups is observed: group A, represented by CM5 and CM7 liquids, exhibiting the lowest limit stress values (approximately 0.01 Pa); group B, represented by CM2 and CM3 liquids, showing more than 10× higher values (about 0.11 Pa); group C, represented by CM4 and CM6 liquids, demonstrating another nearly 10-fold increase in stress (to about 1.05 Pa); and the sample with the highest flow stress in the zero state, CM1 (5.7 Pa). Samples from groups A and B were prepared based on carbonyl iron, while groups C and D were based on magnetite.

The samples with magnetite show significantly higher structural yield stress only in the zero state. However, at higher magnetic field induction values (Figure 5b), significantly higher limit stress values are observed for samples with carbonyl iron due to the higher saturation magnetization. There is also a visible saturation of structural yield stress values

in the case of liquids produced based on magnetite (CM1, CM4, CM6), beyond which, at B ≈ 100 mT, no further increase in the flow limit is observed.

In the case of carbonyl iron fluids, an increase in shear stress is observed over the entire range of the applied magnetic field induction. There are three groups of liquids: CM2 and CM3 with the highest limit stress values, and CM5, CM7, and CM8, for which similar limit stress values have been obtained. The highest structural yield stress values were obtained for the samples containing the fewest additives. It should be emphasized here that the differences in the value of this parameter are visible only at very low deformations and indicate the effect of the individual components at the level of interactions of the MR fluid molecules.

Figure 6 shows the flow stress measurement results. The value of the parameter is determined as the G′ = G″ intersection point. In contrast to structural yield stress, the value of this parameter is determined under the conditions of greater deformation, and its physical sense can be referred to the situation in which the internal structure of the MR fluid is broken.

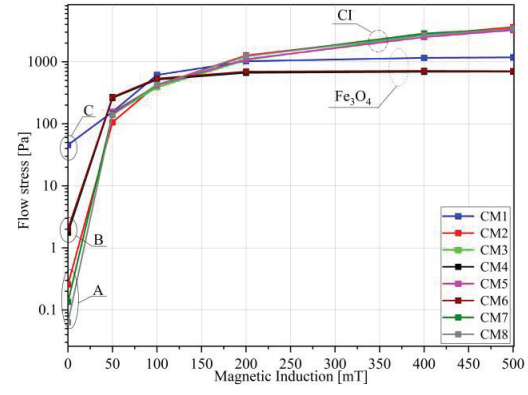

(**a**)

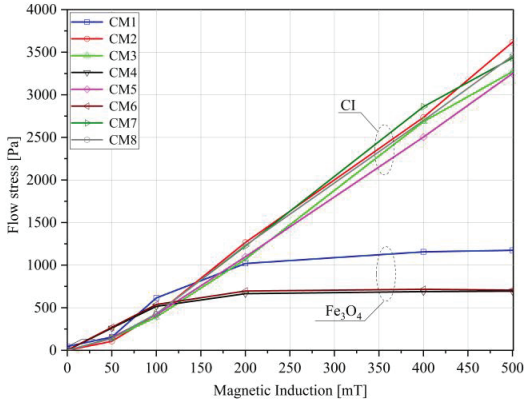

(**b**)

Figure 6. Flow stress versus magnetic induction (**a**) in a semi-logarithmic system, (**b**) in a linear system.

To better illustrate the results for B = 0 and B ≠ 0, the data are presented on both logarithmic and linear scales. In the zero state, three groups were distinguished: Group A (CM2, CM7, and CM8) with the lowest flow stress (ranging from 0.05–0.2 Pa) (see Figure 6a). The results obtained for CM3 and CM5 also align with the curves of this group, with the

difference that no flow stress was recorded for these two liquids under zero conditions. All the Group A fluids were manufactured using carbonyl iron. The other two groups (Group B and Group C) include magnetite-based fluids, and similarly to the structural yield stress, much higher flow stresses were obtained for them in the absence of a magnetic field.

When magnetic induction was applied (Figure 6b), a clear distinction in the samples' reactions is evident based on the utilized magnetic powder. The higher values of the yield stress were observed for the fluids containing carbonyl iron. This is related to the higher magnetization capability of this material. Therefore, it can be seen that, in the range of low deformations, the influence of the analyzed components on the flow limit is noticeable and can be associated with interactions at the structural level. However, within the range of large deformations, the magnetic properties of ferromagnetic particles come to the forefront.

4. Conclusions

The paper presents research results on various MR fluids with differing compositions, types of magnetic particles, viscosity of the carrier liquid, stabilizers, and additives. The study aimed to analyze how the composition affected the dynamic properties and flow limits of the liquids. The differences in physicochemical properties of the magnetic particles explained the discrepancies in test results and influenced the sample's form and consistency. Dynamic tests (DMA) were conducted to determine the properties of the produced liquids, focusing on structural yield stress and flow stress.

The most significant differences in the behavior of the tested liquids were observed under zero conditions. In the absence of a magnetic field, the rheological behavior of MR fluids depended on the carrier liquid properties and particle properties (number and size). MR fluids with magnetite exhibited higher structural yield stress values under zero conditions. However, at higher magnetic field induction values, samples with carbonyl iron showed much higher stress values due to higher saturation magnetization.

Notably, CM3 and CM5 fluids (differing only in the stabilizer used) exhibited significant differences in behavior only concerning structural yield stress, within the range of very low deformations. Which indicates the apparent impact of the used stabilizer.

The influence of individual additives on rheological properties primarily appeared at low deformations (moduli of elasticity and structural yield stress), indicating their effect near the flow stress. Within the range of higher deformations corresponding to flow stress, differences in the behavior of individual MR fluid samples were much smaller. The main distinctions in the obtained results in this case, were related solely to the type of ferromagnetic powders used.

Author Contributions: Conceived and designed the research, A.F., W.H. and M.Z.; coordinated the study, W.H.; writing, review and editing, A.F. and M.Z. All authors have read and agreed to the published version of the manuscript.

Funding: The paper was prepared as part of the project: "InterChemMed—Interdisciplinary doctoral studies of Lodz public universities" conducted at the Lodz University of Technology, the University of Lodz and the Medical University of Lodz, implemented under the Operational Programme Knowledge Education Development 2014–2020, co-financed by the European Social Fund (No POWR. 03.02.00-00-I029/16).

Institutional Review Board Statement: Not applicable.

Informed Consent Statement: Not applicable.

Data Availability Statement: Not applicable.

Acknowledgments: This work was supported by the Lodz University.

Conflicts of Interest: The authors declare no conflict of interest.

References

1. Kang, S.S.; Choi, K.; Nam, J.; Choi, H.J. Magnetorheological Elastomers: Fabrication, Characteristics, and Applications. *Materials* **2020**, *13*, 4597. [CrossRef]
2. Carlson, J.D.; Jolly, M.R. MR fluid, foam and elastomer devices. *Mechatronics* **2000**, *10*, 555–569. [CrossRef]
3. Maurya, C.S.; Sarkar, C. Dynamic and creep and recovery performance of Fe_3O_4 nanoparticle and carbonyl iron microparticle water-based magnetorheological fluid. *J. Intell. Mater. Syst. Struct.* **2020**, *33*, 743–755. [CrossRef]
4. Pei, P.; Peng, Y. Constitutive modeling of magnetorheological fluids: A review. *J. Magn. Magn. Mater.* **2022**, *550*, 169076. [CrossRef]
5. Ji, J.; Wu, X.; Tian, Z.; Xie, F.; Chen, F.; Li, H. A Novel Magnetorheological Fluid with High-Temperature Resistance. *Materials* **2023**, *16*, 4207. [CrossRef]
6. Sedlacík, M.; Pavlínek, V.; Saha, P.; Svrcinova, P.; Filip, P.; Stejskal, J. Rheological properties of magnetorheological suspensions based on core–shell structured polyaniline-coated carbonyl iron particles. *Smart Mater. Struct.* **2010**, *19*, 115008. [CrossRef]
7. Devol, A.; Kumar, C. Preparation of Magnetorheological fluids: A Research. *Int. J. Recent Technol. Eng.* **2019**, *8*, 2277–3878.
8. Gutiérrez, J.; Vadillo, V.; Gómez, A.; Berasategi, J.; Insausti, M.; Gil de Muro, I.; Mounir Bou-Ali, M. Aspects Concerning the Fabrication of Magnetorheological Fluids Containing High Magnetization FeCo Nanoparticles. *Fluids* **2021**, *6*, 132. [CrossRef]
9. Lita, M.; Han, A.; Susan-Resiga, D. Characterization of sedimentation and high magnetic field flow behavior of some magnetorheological fluids. *J. Phys. Conf. Ser.* **2009**, *149*, 012071. [CrossRef]
10. Goteti, C.; Sreenivasulu, R. A review on magneto rheological fluids and their applications. *Sigma J. Eng. Nat. Sci.* **2023**, *41*, 613–624. [CrossRef]
11. Jinaga, R.; Jagadeesha, T.; Kolekar, S.; Choi, S.B. The Synthesis of Organic Oils Blended Magnetorheological Fluids with the Field-Dependent Material Characterization. *Int. J. Mol. Sci.* **2019**, *20*, 5766. [CrossRef] [PubMed]
12. Tong, Y.; Li, X.; Zhao, P.; Dong, X.; Wu, Z.; Qi, M. Improved Magnetorheological Properties by Using Ionic Liquid as Carrier Liquid of Magnetorheological Fluids. *Front. Mater.* **2021**, *29*, 659998. [CrossRef]
13. Kumbhar, B.K.; Patil, S.; Sawant, S.M. Full length article synthesis and characterization of magneto-rheological (MR) fluids for MR brake application. *Eng. Sci. Technol. Int. J.* **2015**, *18*, 432–438. [CrossRef]
14. Iglesias, G.R.; Ruiz-Morón, L.F.; Durán, J.D.G.; Delgado, A.V. Dynamic and wear study of an extremely bidisperse magnetorheological fluid. *Smart Mater. Struct.* **2015**, *24*, 127001. [CrossRef]
15. Harsh, P.K.R.; Sankar, D.N.; Luitel, A.K.; Nerusu, P. Change in sedimentation rate of MR fluid with different base fluids. *J. Emerg. Technol. Innov. Res.* **2021**, *8*, 464–468.
16. Gopinath, B.; Sathishkumar, G.K.; Karthik, P.; Charles, M.M.; Ashok, K.G.; Ibrahim, M.; Akheel, M.M. A systematic study of the impact of additives on structural and mechanical properties of Magnetorheological fluids. *Mater. Today Proc.* **2021**, *37*, 1721–1728. [CrossRef]
17. Kaide, A.; Kanda, M.; Tochigi, H.; Saeki, T. Preparation of Magnetorheological Fluid Using Stabilizing Additives. *MATEC Web Conf.* **2021**, *333*, 02005. [CrossRef]
18. Milde, R.; Moucka, R.; Sedlacik, M.; Pata, V. Iron-Sepiolite High-Performance Magnetorheological Polishing Fluid with Reduced Sedimentation. *Int. J. Mol. Sci.* **2022**, *23*, 2187. [CrossRef]
19. Fonseca, H.A.; Gonzalez, E.; Restrepo, J. Study of a magnetorheological fluid submitted to a uniform magnetic field. *J. Phys. Conf. Ser.* **2017**, *935*, 012038. [CrossRef]
20. Raju, K.M.; Varma, D.V. Developments in vibration control of structures and structural components with magnetorheological fluids. *Curr. Sci.* **2017**, *112*, 499–508. [CrossRef]
21. Qiu, J.; Luo, Y.; Li, Y.; Luo, J.; Su, Z.; Wang, Y. Research on a mechanical model of magnetorheological fluid different diameter particles. *Nanotechnol. Rev.* **2022**, *11*, 158–166. [CrossRef]
22. Gwon, H.; Park, S.; Lu, Q.; Choi, H.J.; Lee, S. Size effect of iron oxide nanorods with controlled aspect ratio on magneto-responsive behavior. *J. Ind. Eng. Chem.* **2023**, *124*, 279–286. [CrossRef]
23. Morillas, J.R.; de Vicente, J. Magnetorheology: A review. *Soft Matter* **2020**, *16*, 9614–9642. [CrossRef]
24. Sanfeng, Y.; Xiangming, H.; Yang, M.; Wei, L.; Qing, Z. Rheological behavior of a magnetorheological shear-thickening fluid (MRSTF) and dynamic characteristics of an MRSTF damper. *Chin. J. Mech. Eng.* **2022**, 2–19.
25. Mangal, S.; Kataria, M. Characterization of magnetorheological finishing fluid for continuous. *J. Appl. Fluid Mech.* **2018**, *11*, 1751–1763. [CrossRef]
26. Xie, J.; Liu, C.; Cai, D. Analysis and Experimental Study on Rheological Performances of Magnetorheological Fluids. *Mechanika* **2020**, *26*, 31–34.
27. Zhang, X.; Liu, X.; Ruan, X.; Zhao, J.; Gong, X. The Influence of Additives on the Rheological and Sedimentary Properties of Magnetorheological Fluid. *Front. Mater.* **2021**, *7*, 631069. [CrossRef]
28. Fenyk, A.; Horak, W.; Zieliński, M.; Miękoś, E.; Chrześcijańska, E.; Sroczyński, D. Investigation of the properties of selected magnetorheological fluids. *J. Intell. Mater. Syst. Struct.* **2022**, *33*, 2294–2304. [CrossRef]
29. Giorgetti, A.; Baldanzini, N.; Biasiotto, M.; Citti, P. Design and testing of a MRF rotational damper for vehicle applications. *Smart Mater. Struct.* **2010**, *19*, 065006. [CrossRef]
30. Sapiński, B.; Gołdasz, J. Development and performance evaluation of an MR squeeze-mode damper. *Smart Mater. Andstructures* **2015**, *24*, 115007. [CrossRef]

31. Thakur, M.K.; Sarkar, C. Experimental and numerical study of magnetorheological clutch with sealing at larger radius disc. *Def. Sci. J.* **2020**, *70*, 575–582. [CrossRef]
32. Gołdasz, J.; Sapiński, B.; Kubík, M.; Macháček, O.; Bańkosz, W.; Sattel, T.; Suryadi Tan, A. Review: A survey on configurations and performance of flow-mode MR valves. *Appl. Sci.* **2022**, *12*, 6260. [CrossRef]
33. Barnes, H.A. The yield stres—A review or 'παντα ρει'—Everything flows? *J. Non-Newton. Fluid Mech.* **1999**, *81*, 133–178. [CrossRef]
34. Khajehsaeid, H.; Alaghehband, N.; Bavil, P.K. On the yield stress of magnetorheological fluids. *Chem. Eng. Sci.* **2022**, *256*, 117699. [CrossRef]
35. Horak, W. Modeling of magnetorheological fluid in quasi-static squeeze flow mode. *Smart Mater. Struct.* **2018**, *27*, 065022. [CrossRef]
36. Horak, W.; Stępień, B.; Sapiński, B. Experiment and analysis of the limit stresses of magnetorheological fluid. *Acta Mech. Et Autom.* **2022**, *16*, 408–416. [CrossRef]
37. Wereley, N.M.; Chaudhuri, A.; Yoo, J.H.; John, S.; Kotha, S.; Suggs, A.; Radhakrishnan, R.; Love, B.J.; Sudarshan, T.S. Bidis-perse Magnetorheological Fluids using Fe Particles at Nanometer and Micron Scale. *J. Intell. Mater. Syst. Struct.* **2006**, *17*, 393–401. [CrossRef]
38. Kannappan, K.T.; Laherisheth, Z.; Parekh, K.; Upadhyay, R.V. The effect of spherical nanoparticles on rheological properties of bi-dispersed magnetorheological fluids. *AIP Conf. Proc.* **2015**, *1665*, 130020.
39. Leong, S.A.N.; Mazlan, S.A.; Samin, P.M.; Idris, A.; Ubaidillah. Performance of bidisperse magnetorheological fluids utilizing superparamagnetic maghemite nanoparticles. *AIP Conf. Proc.* **2016**, *1710*, 030050. [CrossRef]

fluids

MDPI

Communication

Hagen-Poiseuille Flow in a Quarter-Elliptic Tube

Mateus D. Bacelar [1], Hugo C. M. G. Ferreira [2], Rajai S. Alassar [3] and André B. Lopes [2,*]

[1] Departament of Science and Aerospace Technology, Aeronautics Institute of Technology, São José dos Campos 12228-900, SP, Brazil; mateusdutra@outlook.com
[2] Departament of Mechanical Engineering, Faculty of Technology, University of Brasília, Brasília 70910-900, DF, Brazil; hcmgf1@gmail.com
[3] Interdisciplinary Research Center for Renewable Energy and Power Systems, Department of Mathematics, King Fahd University of Petroleum & Minerals, Dhahran 31261, Saudi Arabia; alassar@kfupm.edu.sa
* Correspondence: andre.lopes@unb.br

Abstract: We present a rare exact solution of the Navier–Stokes equations for the Hagen–Poiseuille flow through a quarter-elliptic tube. Utilizing the separation of variables method, we derive the solution and report expressions for both the volumetric flow rate and the friction factor–Reynolds number product.

Keywords: laminar flow; internal viscous flow; pipe flow; exact solution; Navier–Stokes equations

Citation: Bacelar, M.D.; Ferreira, H.C.M.G.; Alassar, R.S.; Lopes, A.B. Hagen-Poiseuille Flow in a Quarter-Elliptic Tube. *Fluids* **2023**, *8*, 247. https://doi.org/10.3390/fluids8090247

Academic Editors: Vasily Novozhilov, Cunlu Zhao and D. Andrew S. Rees

Received: 30 May 2023
Revised: 28 August 2023
Accepted: 29 August 2023
Published: 7 September 2023

1. Introduction

Fluid flow through a tube with an elliptic geometry is of significant interest in fluid mechanics due to its relevance in various industrial and biological applications, including its widespread use in the heating, ventilation, and air-conditioning industry, particularly in finned-tube heat exchangers [1] and the flow of cerebrospinal fluid in perivascular spaces [2]. The Hagen–Poiseuille flow, a fundamental laminar flow regime, describes the steady flow of an incompressible fluid through a tube under the influence of a constant pressure gradient. The understanding of Hagen–Poiseuille flow in elliptic tubes has evolved over the years through the works of pioneering researchers.

The solution for Hagen–Poiseuille flow in elliptic tubes was first derived in 1868 by Joseph Boussinesq, who found a closed-form analytical expression for the velocity distribution over the elliptic cross-section and for the volumetric flow rate [3]. In 1879, Greenhill resolved the Hagen–Poiseuille flow through confocal elliptic cylinders [4]. After over 13 decades, Alassar and Abushoshah [5] solved the problem of Hagen–Poiseuille flow in wide semielliptic tubes using separation of variables. This work was later complemented by Wang [6], who derived the corresponding expressions for deep semielliptic tubes, and more recently by Kundu and Sakar [7], who analytically and numerically investigated the Hagen–Poiseuille flow through wide and narrow semielliptic annuli. Other notable related works include those of Lal [8] and Chorlton and Lal [9], who explored Couette-Poiseuille flow through a channel with a cross-sectional area bounded by two ellipses of the same ellipticity. Additionally, a recent study by Lopes and Siqueira [10] presented solutions for two related problems: Couette flow and Couette–Poiseuille flow in semielliptic tubes. However, despite significant progress in solving this problem for these various elliptic configurations, the analysis of a pressure-driven flow through a quarter-elliptic tube remains to be explored.

The purpose of this work is to solve the Hagen–Poiseuille flow through a quarter-elliptic tube and to report analytical expressions for the volumetric flow rate and the friction factor–Reynolds number product. This solution represents a rare exact solution of the Navier–Stokes equations. Bazant [11] emphasized the analogies between this phenomenon and sixteen others, spanning six broad fields: fluid mechanics, solid mechanics, heat and mass transfer, stochastic processes, electromagnetism, and electrokinetic phenomena. Thus,

by establishing appropriate correspondences, the presented solution holds the potential to elucidate various physical phenomena, such as the torsion or bending of a beam and the electrostatic potential in a charged cylinder with a quarter-elliptic cross-section.

This work is presented as follows. In Section 2, the governing equation and the boundary condition for this flow are presented and written in dimensionless form. The problem is solved in Section 3 using separation of variables in elliptic coordinates. Qualitative and quantitative results regarding are presented and discussed in Section 4. Section 5 provides a summary of the main contributions of this communication.

2. Formulation

Consider the steady Hagen–Poiseuille (pressure-driven) flow of an incompressible Newtonian liquid in a tube of quarter-elliptic cross-section, as depicted in Figure 1. In the sketch, a and b are the lengths of the semimajor and semiminor axes of the corresponding full elliptic cross-section. The flow is governed by the Poisson equation

$$\boldsymbol{\nabla}^{*2} w^* = -\frac{G^*}{\mu}, \tag{1}$$

where $w^* = w^*(x^*, y^*)$ is the fluid velocity in the flow direction, $G^* = -\mathrm{d}p^*/\mathrm{d}z^*$ is the constant pressure gradient, μ is the dynamic viscosity, and $\boldsymbol{\nabla}^{*2}$ is the Laplacian operator.

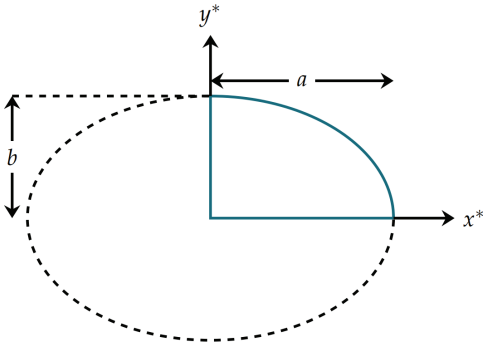

Figure 1. Sketch of the quarter-elliptic cross-section.

In the present work, we use a and $a^2 G^*/\mu$ as length and velocity scales, respectively. Therefore, by defining

$$w = \frac{w^*}{\frac{a^2 G^*}{\mu}}, \quad x = \frac{x^*}{a}, \quad y = \frac{y^*}{a}, \quad \boldsymbol{\nabla}^* = a\boldsymbol{\nabla},$$

Equation (1) becomes

$$\boldsymbol{\nabla}^2 w = -1. \tag{2}$$

The aspect ratio,

$$\alpha = \frac{b}{a}, \tag{3}$$

is the only resulting dimensionless parameter. Furthermore, due to the no-slip boundary condition, $w = 0$ on any wall.

3. Solution

Introducing elliptic coordinates (ξ,θ) [5,10], Equation (2) takes the form

$$\frac{\cosh^2 \xi_0}{\cosh^2 \xi - \cos^2 \theta}\left(\frac{\partial^2 w}{\partial \xi^2} + \frac{\partial^2 w}{\partial \theta^2}\right) = -1, \tag{4}$$

where $\xi_0 = \tanh^{-1} \alpha$ represents the curved boundary. The boundary conditions are

$$\begin{cases} w = 0 & \text{at} \quad \theta = 0, \\ w = 0 & \text{at} \quad \theta = \dfrac{\pi}{2}, \\ w = 0 & \text{at} \quad \xi = 0, \\ w = 0 & \text{at} \quad \xi = \xi_0. \end{cases} \tag{5}$$

After Alassar and Abushoshah [5], we introduce the following change of variables:

$$w(\xi, \theta) = W(\xi, \theta) - \frac{1}{2}\frac{\sinh^2 \xi \sin^2 \theta}{\cosh^2 \xi_0}. \tag{6}$$

Substituting into Equations (4) and (5), we obtain the Laplace equation:

$$\frac{\partial^2 W}{\partial \xi^2} + \frac{\partial^2 W}{\partial \theta^2} = 0. \tag{7}$$

subject to

$$\begin{cases} W = 0 & \text{at} \quad \theta = 0, \\ W = \dfrac{1}{2}\dfrac{\sinh^2 \xi}{\cosh^2 \xi_0} & \text{at} \quad \theta = \dfrac{\pi}{2}, \\ W = 0 & \text{at} \quad \xi = 0, \\ W = \dfrac{1}{2}\tanh^2 \xi_0 \sin^2 \theta & \text{at} \quad \xi = \xi_0. \end{cases} \tag{8}$$

The problem described by Equations (7) and (8) can be solved by separation of variables. The solution is

$$W(\xi, \theta) = \frac{1}{2\pi}\frac{\sinh \xi_0 \sinh(2\xi) \sin(2\theta)}{\cosh^3 \xi_0} + \sum_{n=1}^{\infty} A_n \sin\left(\frac{n\pi\xi}{\xi_0}\right) \sinh\left(\frac{n\pi\theta}{\xi_0}\right) + \sum_{n=2}^{\infty} B_n \sinh(2n\xi) \sin(2n\theta), \tag{9}$$

where

$$A_n = \frac{(-1)^n\left(2\xi_0^2 - \pi^2 n^2 \sinh^2 \xi_0\right) - 2\xi_0^2}{n\pi\left(4\xi_0^2 + \pi^2 n^2\right) \cosh^2 \xi_0 \sinh\left(\dfrac{n\pi^2}{2\xi_0}\right)}$$

and

$$B_n = \frac{\tanh^2 \xi_0\left[(-1)^n - 2(-1)^n n^2 - 1\right]}{2\pi(n-1)n(n+1)\sinh(2n\xi_0)}.$$

Thus,

$$w(\xi, \theta) = -\frac{1}{2}\frac{\sinh^2 \xi \sin^2 \theta}{\cosh^2 \xi_0} + \frac{1}{2\pi}\frac{\sinh \xi_0 \sinh(2\xi) \sin(2\theta)}{\cosh^3 \xi_0} + \sum_{n=1}^{\infty} A_n \sin\left(\frac{n\pi\xi}{\xi_0}\right) \sinh\left(\frac{n\pi\theta}{\xi_0}\right) + \sum_{n=2}^{\infty} B_n \sinh(2n\xi) \sin(2n\theta). \tag{10}$$

For the dimensionless volumetric flow rate, we have

$$Q = -\frac{(\pi^2 - 8)}{32\pi}\tanh^3\xi_0 + \frac{\xi_0^2}{\cosh^2\xi_0}\sum_{n=1}^{\infty} A_n C_n + \frac{1}{8\cosh^2\xi_0}\sum_{n=2}^{\infty} B_n D_n, \tag{11}$$

where

$$C_n = \frac{(-1)^n\left[\sinh^2\xi_0 - \cosh\left(\frac{\pi^2 n}{2\xi_0}\right)\cosh^2\xi_0\right] + \cosh\left(\frac{\pi^2 n}{2\xi_0}\right)}{4\xi_0^2 + \pi^2 n^2}$$

and

$$D_n = \frac{2n(-1)^n - \sinh(2\xi_0)\sinh(2\xi_0 n)\left[1-(-1)^n\right] - 2n\cosh(2\xi_0 n)\left[(-1)^n\cosh^2\xi_0 - \sinh^2\xi_0\right]}{(n-1)n(n+1)}.$$

Note that the friction factor–Reynolds number product is related to Q by [12]

$$fRe = \frac{8A^3}{P^2 Q}. \tag{12}$$

Here,

$$A = \frac{\pi\tanh\xi_0}{4} \tag{13}$$

is the dimensionless cross-sectional area of the flow,

$$P = 1 + \tanh\xi_0 + E(\operatorname{sech}^2\xi_0) \tag{14}$$

is the dimensionless wetted perimeter of the cross-section, and $E(k)$ denotes the complete elliptic integral of the second kind (see, e.g., [13]). It should be noted that $\tanh\xi_0 = \alpha$ and $\operatorname{sech}^2\xi_0 = 1 - \alpha^2$.

In the limiting case of $\alpha \to 1$, it can be shown that

$$Q = \frac{\pi}{24} - \frac{\ln 2}{2\pi}, \tag{15}$$

in agreement with the solution reported by Lopes and Alassar [14], and that

$$fRe = \frac{12\pi^4}{(\pi^2 - 12\ln 2)(\pi+4)^2}. \tag{16}$$

In the limit of $\alpha \to 0$, it is possible to show that the following relationship holds:

$$fRe = 2\pi^2. \tag{17}$$

It is possible to demonstrate that this limit also holds true for elliptic and semielliptic tubes. This finding is noteworthy as it appears to be a novel contribution to the literature. Shah and London [12] previously reported an approximate value of fRe when $\alpha = 0$ as 19.739 for elliptic tubes and observed that it did not approach the parallel plate geometry. However, they did not acknowledge the possibility of determining its exact value. Furthermore, it is important to note that the results obtained for the velocity field, flow rate, and fRe (as described by Equations (10)–(12)) have been validated through independent methods, namely, finite differences and Rayleigh–Ritz.

Intuitively, one might think that the methodology employed in this section could be extended to any elliptic sector, as previously performed for the elliptic tube [15], for the wide semielliptic tube [5], and for the deep semielliptic tube [6]; however, this is not true. The curves of constant ξ and η in elliptic coordinates are, respectively, confocal ellipses and hyperbolas. In addition, the x-axis and y-axis are also part of this family of orthogonal

curves. Thus, it is not possible to use the method of separation of variables a priori for any elliptic sector, as it cannot be described using the curves of constant ξ and η, except in cases where the opening angle of the elliptic sector is $\pi/2$, π, $3\pi/2$, or 2π. Furthermore, even though elliptic sectors with an opening angle of $3\pi/2$ and 2π can be formulated in elliptic coordinates (see Appendix A), their boundary conditions are rather exotic, presenting a challenge that makes finding solutions through the method of separation of variables unlikely to work. Thus, it is possible that our work concludes the investigation into tubes whose cross-sections are elliptic sectors that can be analytically solved through the method of separation of variables.

4. Results

The dimensionless velocity contours for $\alpha = 0.6$ are shown in Figure 2. The contours span from $0.2u_{\max}$ to $0.8u_{\max}$ in increments of $0.2u_{\max}$, with $u_{\max}$ representing the maximum dimensionless velocity in the sector.

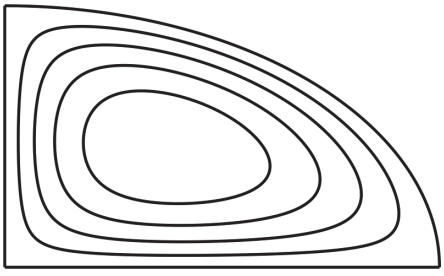

Figure 2. Dimensionless velocity contours for $\alpha = 0.6$, showing normalized velocity contour lines ranging from 0.2 to 0.8 with increments of 0.2.

Figure 3 shows the dimensionless volumetric flow rate as of the aspect ratio. The curve is a smooth and gradually increasing function, with flow rate starting at zero and finishing at $\pi/24 - \ln 2/(2\pi) \approx 0.0205$ in the limits of $\alpha \to 0$ and $\alpha \to 1$ (quarter-circular tube), respectively. As the aspect ratio increases, the flow rate rises slowly at first, then more steeply, due to the nonlinear relationship between the two variables. When compared to a circular tube, which has a maximum dimensionless flow rate of $\pi/8 \approx 0.3926$ [3], the flow rate in the quarter-circular tube is much lower, with a ratio of approximately 1:19. This large difference can be attributed not only to the fact that the cross-sectional area of the circular tube is four times larger than that of the quarter-circular tube, but also to the additional retardation in fluid velocity caused by the no-slip condition at the horizontal and vertical walls, as well as the curved wall of the quarter-circular tube.

The relationship between the friction factor–Reynolds number product (fRe) and the aspect ratio α for the quarter-elliptic tube is displayed in Figure 4 and can also be found in Table 1. For comparison purposes, the friction factor–Reynolds number product of the semielliptic tube (inferred from Alassar [16] and Abushoshah [5]) and that of the elliptic tube (cf. Shah and London [12]) were added to the plot. The solid curve depicts the friction factor–Reynolds number product for the quarter-elliptic tube, the dashed curve represents it for the semielliptic tube, and the dotted curve corresponds to the elliptic tube. All three curves exhibit a similar trend, with the friction factor–Reynolds number product decreasing as the aspect ratio increases. It is worth noting that they all start at $fRe = 2\pi^2$, which is the limit when the aspect ratio approaches zero. However, when the aspect ratio is greater than zero, the quarter-elliptic tube consistently displays a lower friction factor–Reynolds number product than semielliptic and elliptic tubes for all aspect ratios. Interestingly, when the aspect ratio of the quarter-elliptic tube is approximately equal to 0.42, the friction factor–Reynolds number product is equal to 16, which is the friction factor–Reynolds number product of the circular tube. A parallel behavior is observed in semielliptic tubes when the

aspect ratio approaches around 0.90. It is also interesting to note that Equation (16) provides the lower limit for the friction factor–Reynolds number product in quarter-elliptic tubes.

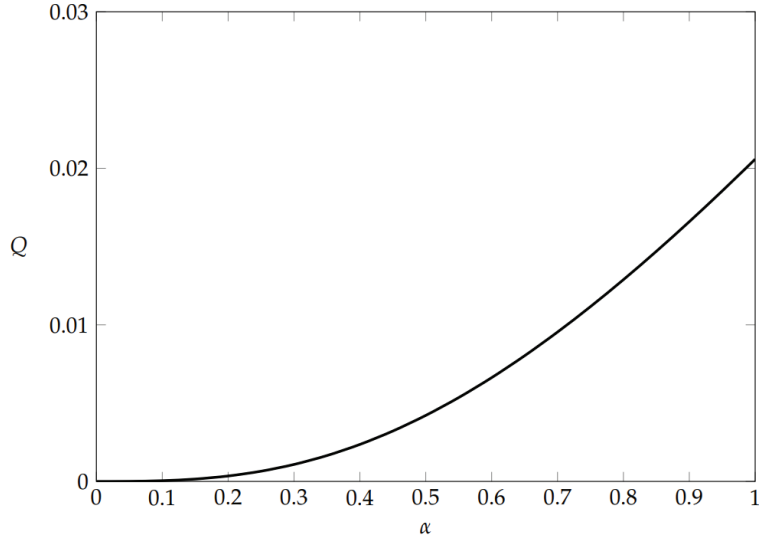

Figure 3. Dimensionless volumetric flow rate (Q) as a function of the aspect ratio α.

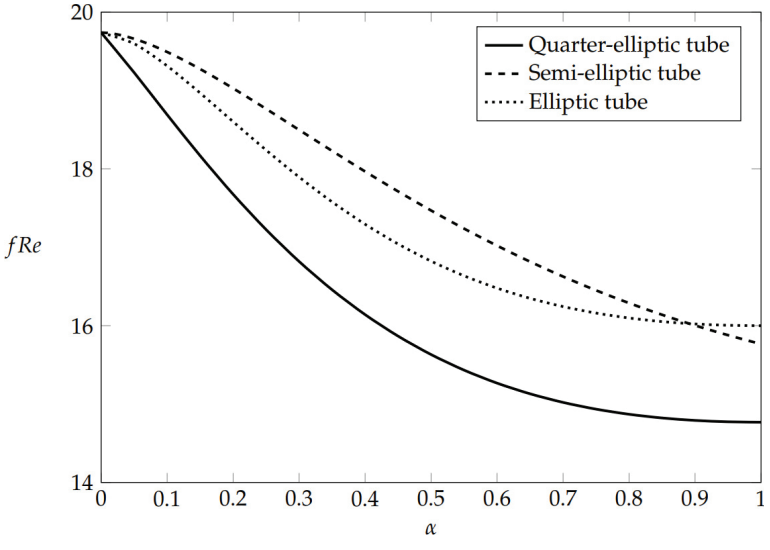

Figure 4. Friction factor–Reynolds number product (fRe) as a function of the aspect ratio α for the quarter-elliptic tube (solid line), for the semielliptic tube (dashed line), and for the elliptic tube (dotted line).

The fRe factors presented in Table 1 can be approximated (within $\pm 0.05\%$) by

$$fRe = 2\pi^2\left(1 - 0.5309\alpha - 0.1839\alpha^2 + 1.4313\alpha^3 - 1.4616\alpha^4 + 0.4933\alpha^5\right). \quad (18)$$

We observe that the coefficients of this fifth-degree polynomial equation, which was derived using the least squares method, were chosen to satisfy Equation (17).

Table 1. fRe values for quarter-elliptic tubes of aspect ratio α.

α	fRe
0	19.7392 *
0.1	18.6916
0.2	17.6764
0.3	16.8191
0.4	16.1413
0.5	15.6318
0.6	15.2672
0.7	15.0214
0.8	14.8700
0.9	14.7916
1	14.7687 *

Closed forms are indicated by asterisks.

5. Conclusions

In conclusion, by using the method of separation of variables, we derived analytical expressions that describe the behavior of fluid flow through a quarter-elliptic tube. The volumetric flow rate increases as the aspect ratio increases, but it is much lower than that of a circular tube due to the smaller cross-sectional area and the no-slip condition at the walls. The friction factor–Reynolds number product decreases as the aspect ratio increases, and, except for in the limit where the aspect ratio approaches zero, it is always lower for the quarter-elliptic tube than for the elliptic tube. In this limit, the friction factor–Reynolds number product of both tubes is the same, equal to $2\pi^2$. A fifth-degree polynomial equation was derived to approximate the fRe factors with high accuracy. Overall, the results of this study offer valuable insights into the fluid dynamics of quarter-elliptic tubes and can be useful for the design and optimization of microfluidic devices [17]. Additionally, the study sheds light on the application of wedge-shaped passages, which have been utilized in conventional heat-exchanger applications [18].

Author Contributions: Conceptualization, A.B.L. and R.S.A.; methodology, A.B.L. and R.S.A.; software, H.C.M.G.F. and M.D.B.; validation, H.C.M.G.F. and M.D.B.; formal analysis, A.B.L. and R.S.A.; investigation, H.C.M.G.F. and M.D.B.; resources, A.B.L. and R.S.A.; data curation, A.B.L.; writing—original draft preparation, A.B.L.; writing—review and editing, A.B.L., M.D.B. and R.S.A.; visualization, M.D.B.; supervision, A.B.L.; project administration, A.B.L.; funding acquisition, R.S.A. All authors have read and agreed to the published version of the manuscript.

Funding: André B. Lopes would like to express his gratitude to the support provided by the Fundação de Apoio à Pesquisa do Distrito Federal (Nº FAPDF: 473/2022, Edital—09/2022 Demanda Induzida).

Data Availability Statement: Not applicable.

Conflicts of Interest: The authors declare no conflict of interest.

Appendix A

In this appendix, we formulate the problem of Hagen–Poiseuille flow in two distinct tubes whose cross-section is an elliptic sector. The first tube features a three-quarter elliptic tube (Figure A1a), while the second tube is referred to as a "four-quarter elliptic tube" (Figure A1b) due to a lack of a better term. This particular tube represents the limiting scenario where the opening angle of the elliptical cross-section is equal to 2π, and it is characterized by an infinitely thin wall along the positive x-axis. Note that, in all that follows, the variables are presented in a dimensionless form, following the nondimensionalization presented in Section 2.

We begin by noting that Cartesian coordinates (x, y) are related to the elliptic coordinates (ξ, θ) introduced in Section 3 by

$$x = c\cosh\xi\cos\theta \quad \text{and} \quad y = c\sinh\xi\sin\theta, \tag{A1}$$

where $c = \operatorname{sech}\xi_0$. In the case of the three-quarter-elliptic tube, it follows from Figure A1a and the relations in Equation (A1) that the appropriate boundary conditions for w are

$$\begin{cases} w = 0 & \text{at} \quad \theta = 0, \\ w = 0 & \text{at} \quad \theta = \dfrac{3\pi}{2}, \\ w = 0 & \text{at} \quad \xi = 0 \quad \text{for} \quad 0 < \theta \leq \dfrac{\pi}{2}, \\ w = F & \text{at} \quad \xi = 0 \quad \text{for} \quad \dfrac{\pi}{2} < \theta < \dfrac{3\pi}{2}, \\ w = 0 & \text{at} \quad \xi = \xi_0. \end{cases} \tag{A2}$$

Here, $F = F(\theta)$ is an unknown 2π-periodic function such that $F(\frac{\pi}{2}) = F(\pi) = 0$. As for the case of the cross-section depicted in Figure A1b, the boundary conditions are

$$\begin{cases} w = 0 & \text{at} \quad \theta = 0, \\ w = 0 & \text{at} \quad \theta = 2\pi, \\ w = 0 & \text{at} \quad \xi = 0 \quad \text{for} \quad 0 < \theta \leq \dfrac{\pi}{2}, \\ \dfrac{\partial w}{\partial \xi} = 0 & \text{at} \quad \xi = 0 \quad \text{for} \quad \dfrac{\pi}{2} < \theta < \dfrac{3\pi}{2}, \\ w = 0 & \text{at} \quad \xi = 0 \quad \text{for} \quad \dfrac{3\pi}{2} \leq \theta < 2\pi, \\ w = 0 & \text{at} \quad \xi = \xi_0. \end{cases} \tag{A3}$$

In both problems, a similar feature occurs at $\xi = 0$. More precisely, in the range where $\pi/2 < \theta < 3\pi/2$, the boundary condition is not of Dirichlet type but, rather, periodic in (A2) and Neumann in (A3). This boundary segment corresponds to $-1 < x < 0$ at $y = 0$, a segment in the interior region of the fluid domain in the x-y plane, which renders the application of the method of separation of variables more challenging, if not impossible.

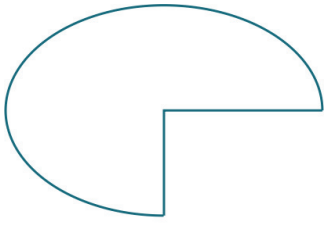

(a)

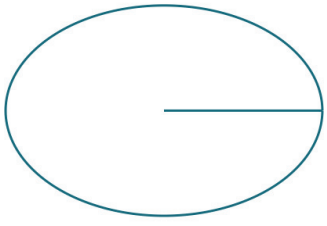

(b)

Figure A1. Sketch of the (**a**) three-quarter-elliptic and (**b**) four-quarter-elliptic cross-sections.

References

1. Sun, L.; Zhang, C.L. Evaluation of elliptical finned-tube heat exchanger performance using CFD and response surface methodology. *Int. J. Therm. Sci.* **2014**, *75*, 45–53. [CrossRef]
2. Thomas, J.H. Fluid dynamics of cerebrospinal fluid flow in perivascular spaces. *J. R. Soc. Interface* **2019**, *16*, 20190572. [CrossRef] [PubMed]
3. Boussinesq, J. Mémoire sur l'influence des frottements dans les mouvements réguliers des fluids. *J. Mathématiques Pures Appliquées* **1868**, *13*, 377–424.
4. Greenhill, A. Fluid motion between confocal elliptic cylinders and confocal ellipsoids. *Q. J. Pure Appl. Math.* **1879**, *16*, 227–256.
5. Alassar, R.S.; Abushoshah, M. Hagen–Poiseuille flow in semi-elliptic microchannels. *J. Fluids Eng.* **2012**, *134*, 124502. [CrossRef]
6. Wang, C.Y. On viscous flow in semi-elliptic ducts. *J. Fluids Eng.* **2015**, *137*, 114502. [CrossRef]
7. Kundu, K.; Sarkar, U.K. Analytical and numerical investigation of Poiseuille flow through semi-elliptic annulus. *Phys. Fluids* **2022**, *34*, 083603. [CrossRef]
8. Lal, K. On the steady laminar flow of a viscous incompressible fluid through a channel bounded by two ellipses having same ellipticity. *Z. Angew. Math. Mech.* **1963**, *43*, 507–508. [CrossRef]
9. Lal, K.; Chorlton, F. A new approach to flow through a region bounded by two ellipses of the same ellipticity. *Wear* **1981**, *68*, 249–252. [CrossRef]
10. Lopes, A.B.; Siqueira, I. Couette–Poiseuille Flow in Semi-Elliptic Channels. *J. Fluids Eng.* **2022**, *144*, 101302. [CrossRef]
11. Bazant, M.Z. Exact solutions and physical analogies for unidirectional flows. *Phys. Rev. Fluids* **2016**, *1*, 024001. [CrossRef]
12. Shah, R.K.; London, A.L. *Laminar Flow Forced Convection in Ducts: A Source Book for Compact Heat Exchanger Analytical Data*; Academic Press: New York, NY, USA, 1978.
13. Abramowitz, M.; Stegun, I.A.; Romer, R.H. *Handbook of Mathematical Functions with Formulas, Graphs and Mathematical Tables*; Dover Publications: New York, NY, USA, 1965; Volume 55.
14. Lopes, A.B.; Alassar, R.S. Comment on "Newtonian Poiseuille flow in ducts of annular-sector cross-sections with Navier slip". *Eur. J. Mech.-B/Fluids* **2022**, *96*, 105–107. [CrossRef]
15. Jog, C.S. *Fluid Mechanics: Foundations and Applications of Mechanics*, 3rd ed.; Cambridge University Press: Cambridge, UK, 2015; Volume 2. [CrossRef]
16. Alassar, R. Hagen-Poiseuille flow in tubes of semi-circular cross-sections. In Proceedings of the 2011 Fourth International Conference on Modeling, Simulation and Applied Optimization, Kuala Lumpur, Malaysia, 19–21 April 2011; pp. 1–2.
17. Kyritsi-Yiallourou, S.; Georgiou, G.C. Newtonian Poiseuille flow in ducts of annular-sector cross-sections with Navier slip. *Eur. J. Mech.-B/Fluids* **2018**, *72*, 87–102. [CrossRef]
18. Trupp, A.C.; Lau, A.C.Y. Fully Developed Laminar Heat Transfer in Circular Sector Ducts With Isothermal Walls. *J. Heat Transf.* **1984**, *106*, 467–469. [CrossRef]

energies

MDPI

Review

Under-Expanded Jets in Advanced Propulsion Systems—A Review of Latest Theoretical and Experimental Research Activities

Francesco Duronio [1], Carlo Villante [1,*] and Angelo De Vita [1,2]

[1] Department of Industrial Engineering, Information and Economics, Università degli Studi dell'Aquila, Piazzale Ernesto Pontieri, Monteluco di Roio, 67100 L'Aquila, Italy; francesco.duronio@univaq.it (F.D.); angelo.devita@univaq.it (A.D.V.)
[2] Consiglio Nazionale delle Ricerche, Istituto di Scienze e Tecnologie per l'Energia e la Mobilità Sostenibili (STEMS), Via G. Marconi 4, 80125 Napoli, Italy
* Correspondence: carlo.villante@univaq.it; Tel.: +39-0862434302

Abstract: The current ongoing rise in environmental pollution is leading research efforts toward the adoption of propulsion systems powered by gaseous fuels like hydrogen, methane, e-fuels, etc. Although gaseous fuels have been used in several types of propulsion systems, there are still many aspects that can be improved and require further study. For this reason, we considered it important to provide a review of the latest research topics, with a particular focus on the injection process. In advanced engine systems, fuel supply is achieved via enhanced direct injection into the combustion chamber. The latter involves the presence of under-expanded jets. Under-expanded jets are a particular kind of compressible flow. For this reason, the review initially provides a brief physical explanation of them. Next, experimental and numerical CFD investigation techniques are discussed. The last section of this manuscript presents an analysis of the jet's structure. The injection parameters commonly used are examined; next, the characteristics of the near-nozzle field are reviewed and finally, the far-field turbulent mixing, which strongly affects the air–fuel mixture formation process, is discussed.

Keywords: under-expanded; CFD; compressible flow; supersonic flow; gaseous injection

Citation: Duronio, F.; Villante, C.; De Vita, A. Under-Expanded Jets in Advanced Propulsion Systems—A Review of Latest Theoretical and Experimental Research Activities. *Energies* **2023**, *16*, 6471. https://doi.org/10.3390/en16186471

Academic Editors: Vasily Novozhilov and Cunlu Zhao

Received: 29 July 2023
Revised: 27 August 2023
Accepted: 4 September 2023
Published: 7 September 2023

1. Introduction

One of the essential actions for mitigating current climate change risks is to significantly reduce transport sector emissions [1–4]. As a consequence, over the last few years, an increasing number of researchers have focused on the development of advanced propulsion systems [5]. In particular, powering Internal Combustion engines (ICEs) with gaseous or strong evaporative fuels (like hydrogen, propane or methane gas) may be introduced in the near future and also maintained for a longer period (especially if equipping heavy-duty long-range transport applications) to achieve the aforementioned goal [6]. Furthermore, these fuels may also be completely renewable and/or have zero emissions on a WTW (well-to-wheel) evaluation approach, therefore leading to zero-impact transportation solutions to be compared with all those based on pure electric traction [7].

When using gaseous fuels, the injection process plays the most crucial role in defining ICE environmental performance, affecting mixture formation, its combustion, and, therefore, production of pollution. Moreover, in advanced ICEs, the fuel is Directly Injected (DI) inside the cylinder, calling for more rapid, controlled and efficient mixture formation processes [8–10].

High-injection pressures are typically used for gaseous fuelling in order to achieve the required mass flow rates and promote air/fuel mixing [11–17], typically leading to the formation of highly under-expanded jets (UEJ) at the injector outlet, when the fuel jet faces surrounding airflow.

Under-expanded jets are complex high-speed flows, which are also formed in many other engineering applications and devices such as exhaust aircraft plumes (rockets and missiles), supersonic combustion chambers, actuators, etc. [18–20]. This type of jet can also be observed in geophysical systems (volcanic eruption) and in the accidental release of hazardous gases (such as hydrogen) from tiny cracks in high-pressure pipelines and reservoirs [21–23]. For these reasons, under-expanded jets were historically investigated, especially for aerospace applications. At the same time, there are a paucity of studies examining their presence and influence in automotive advanced propulsion systems, being a newer topic in fluid-dynamic and engine-related research.

However, in recent years, following the great interest shown by political institutions in fuels like hydrogen, a multitude of scientific studies were conducted [24–28]. The authors propose that it could be important to provide researchers with a quick and, as far as possible, complete reference guide to under-expanded jets in ICEs, highlighting the most interesting topics and the most relevant works undertaken in recent years.

To this aim, this review paper firstly focuses on a brief physical and phenomenological discussion of these complex flows and then reports on the main literature results in the sector, subsequently dividing them into two main sections concerning, respectively, experimental and mathematical investigation methodologies usually adopted for studying UEJ. Each cited research study will be introduced and briefly discussed, highlighting the most important outcomes from a fluid-dynamic perspective and final engine application.

2. Physics of Under-Expanded Jets

An under-expanded jet may appear when a high-pressure fluid is connected through a convergent or a convergent–divergent nozzle within an environment where much lower pressure conditions are created. As well known, two possible scenarios can be identified depending on the total pressure ratio between the inlet and outlet of the nozzle.

$$\eta_0 = \frac{P_0}{P_\infty} \tag{1}$$

Figures 1 and 2 report the pressure ratio and the mass flow rate evolution as a function of the axial distance for a convergent nozzle.

The first regime depicts a subsonic flow (cases a and b); the mass flow increases as the downstream pressure decreases, and the exit pressure is equal to the ambient one. Critical conditions are reached if the upstream pressure increases and the nozzle is choked (cases c and d). The outflow pressure is equal to the critical pressure (P^*), and the mass flow cannot increase more; it is called indeed choked as reported in Figure 2.

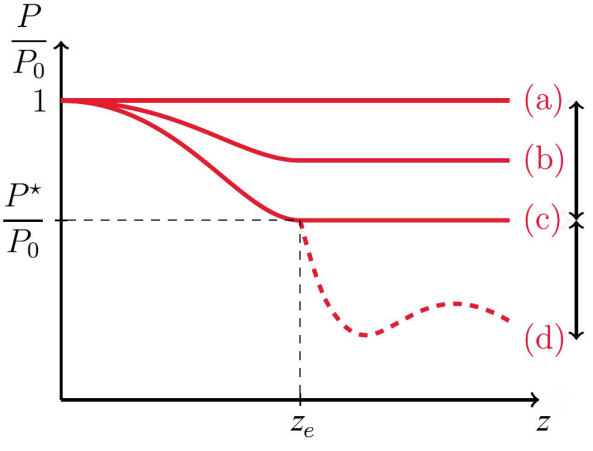

Figure 1. Pressure evolution along nozzle axis for various pressure ratios.

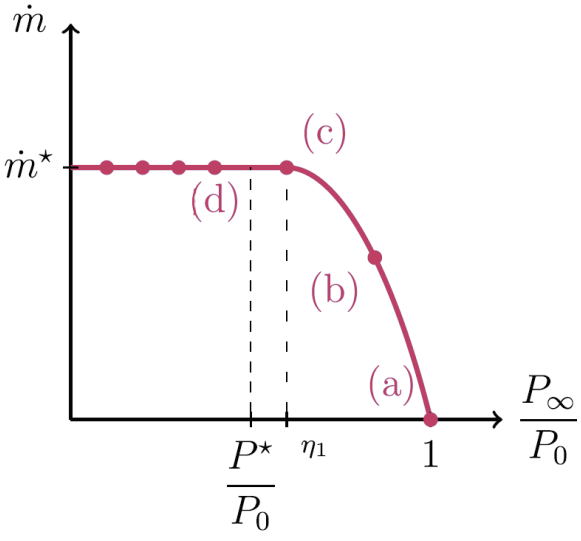

Figure 2. Mass flow rate for various pressure ratios.

It follows that, an the exit section, the pressure is greater than the ambient one and to achieve pressure equilibrium, under-expanded jets arise.

In choked conditions, the pressure waves cannot travel back upstream, and the mass flow rate is no longer dependent on downstream conditions ($\dot{m}^*$). The flow characteristics inside the nozzle, in fact, only depend only on the upstream boundary conditions.

As represented in Figure 3, it is common practice to divide the jet into three zones [29]:

- the near-nozzle zone;
- the transition zone;
- the far-field zone;

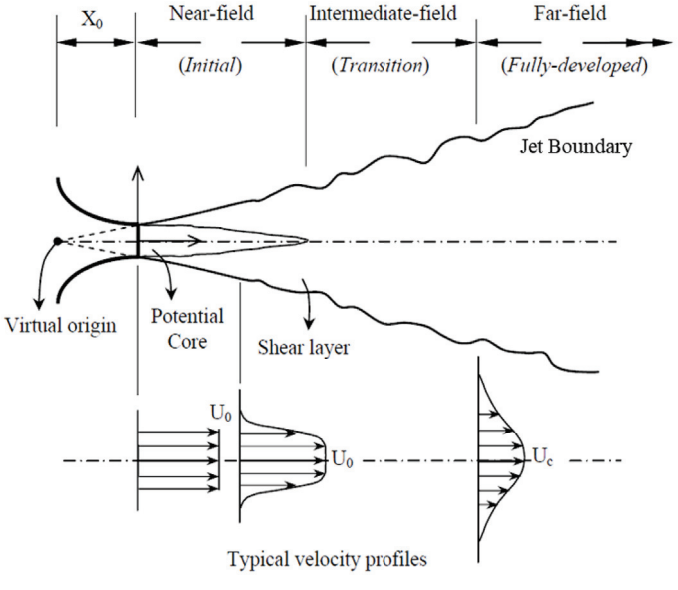

Figure 3. Under-expanded jet zones.

The near-nozzle zone is split into two sections: the core and the mixing layer. In the former, also called the gas-dynamic area, the flow is separated from the environment, and its behaviour is governed mostly by compressible effects and is rather steady. The fluid expands iso-entropically until it is re-compressed by shock waves.

In the mixing layer, turbulence causes an interaction between the injected fluid and the surrounding environment, which is characterized by huge turbulent structures (vortices) that are formed within the fluid flow downstream of the nozzle outlet. A shearing zone between the frontier of the potential core of the jet and the constant pressure line can be distinguished.

Depending on the pressure ratio, different under-expanded jet configurations can be observed in the near-nozzle zone:

- The jet is weakly under-expanded, a normal shock appears in the exit plane.
- The jet is moderately under-expanded and has a "diamond" or "X" structure, depicted in Figure 4, $2 < \eta_0 < 4$ [30,31]. In the exit plane (marker A), a Prandtl–Meyer expansion fan (marker C) expands the fluid downstream of the device's edges up to the jet boundary that corresponds to the external surface of the mixing layer (marked JB). The expansion waves are reflected as compression waves when they reach the constant pressure streamline (marker D), where the pressure matches the ambient pressure. They converge on the inner jet and merge to produce an oblique shock (marker E), commonly referred to as the intercepting shock.
- The jet is highly under-expanded, $4 < \eta_0 < 7$ [32,33]. It has a "barrel" or "bottle" structure, shown in Figure 5, Mach disc appears (due to a singular reflection). When the pressure ratio grows, the regular reflection of the intercepting shock on the axis is no longer possible. As a result, above the critical angle, this reflection becomes singular, resulting in the appearance of a normal shock-denominated Mach disc (marker F). The triple point is defined as the intersection of the intercepting shock, the Mach disc and the reflected shock (marker G). A slipstream (marker H) develops at this point: this is an embedded shear layer that divides the flow upstream of the Mach disc (subsonic) from the flow downstream of the reflected shock (supersonic).
- The jet is extremely (or very highly) under-expanded, $\eta_0 > 7$ [34,35]. As depicted in Figure 6, the structure is dominated by a unique barrel. In this case, the Mach disc is no longer considered as a normal shock, and its curvature must be considered. Due to the momentum exchange generated by the ambient fluid's entrainment, the jet's overall diameter will decrease, resulting in an extremely long plume.

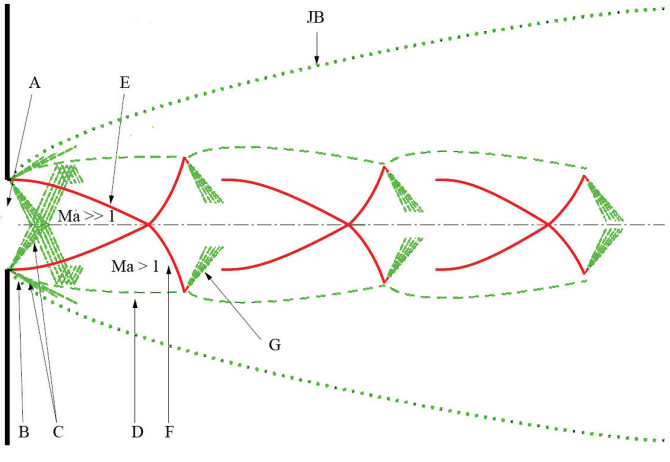

Figure 4. Structure of a moderately under-expanded jet.

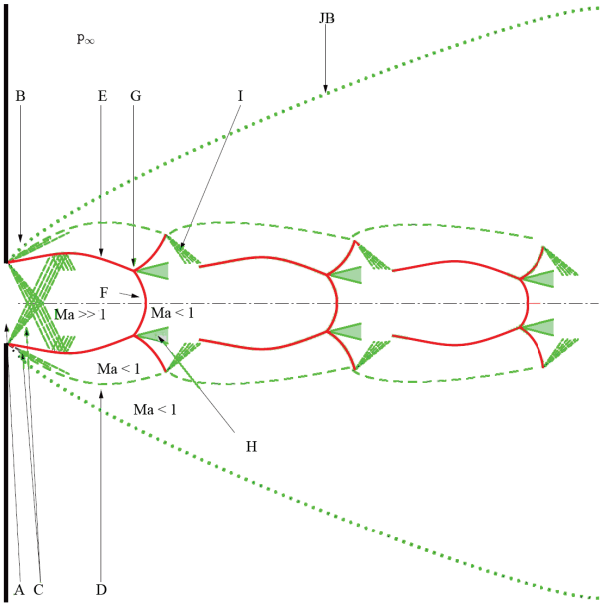

Figure 5. Structure of a highly under-expanded jet.

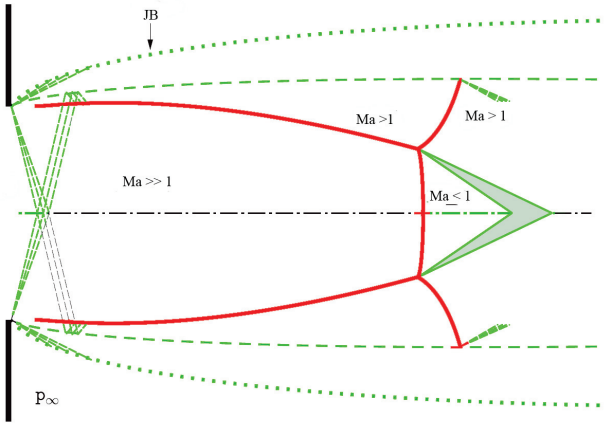

Figure 6. Structure of a very highly under-expanded jet.

Nevertheless, the Mach disc is undoubtedly one of the most studied features of under-expanded jets Moreover, there is still significant ongoing discussion regarding the transition from a regular reflection to a singular reflection, accompanied by the appearance of the Mach disc. This phenomenon is currently quantitatively not well known, particularly the dependence (and interactions) on pressure range and exit Mach number, fluid characteristics (i.e., the polytropic coefficient), nozzle shape, and exit nozzle angle [36].

The Mach disc location is primarily governed by the pressure ratio, increases with the Mach number and, among the many, a good estimation of the position is given by the following relation:

$$\frac{H_d}{D} = 0.67\sqrt{\eta_0} \tag{2}$$

with H_d Mach disc height, D outlet section diameter [34,36,37].

The Mach disc width or diameter was clearly less investigated than the Mach disc length. However, it appears that it is also mainly governed by the pressure ratio and strongly dependent on the nozzle geometry and shape [38–40].

Towards the end of the near-nozzle zone, the sonic line reaches the axis, indicating that the mixing layer has fully replaced the inner region. This marks the beginning of the transition zone, where variations in variables, both longitudinally and radially, become minimal. In this region, a more effective mixing of the two fluids, the ejected fluid and the ambient fluid, takes place. As a result, the pressure field becomes more homogenized as entrainment occurs throughout the transition zone.

In the far-field zone, the jet exhibits self-similarity, but compressible effects may still be present if the Mach number is above 0.3 and may even be supersonic. Qualitatively, the normalized radial profiles of the mean variables follow the same pattern, typically characterized by a Gaussian profile.

3. Experimental Observation of Under-Expanded Jets

The observation of under-expanded jets can be performed both with quantitative and qualitative techniques. Among the first category, schlieren and shadowgraph imaging surely can be mentioned, adopted for capturing images of both near and far field zones [13,41–43].

High-speed schlieren imaging is a robust diagnostic technique capable of visualizing optical in-homogeneities of transparent media, otherwise not visible to the human eye [44–46]. The method is sensitive to changes in the refractive index of a light beam travelling through a heterogeneous medium. For this reason, Schlieren diagnostic is frequently adopted for the observation of compressible flows, such as under-expanded jets, in which the difference in refractive index is caused by the gradient of density between the injected fuel and the ambient gas [44].

Figure 7 shows the schematic diagram of a typical experimental setup for schlieren imaging.

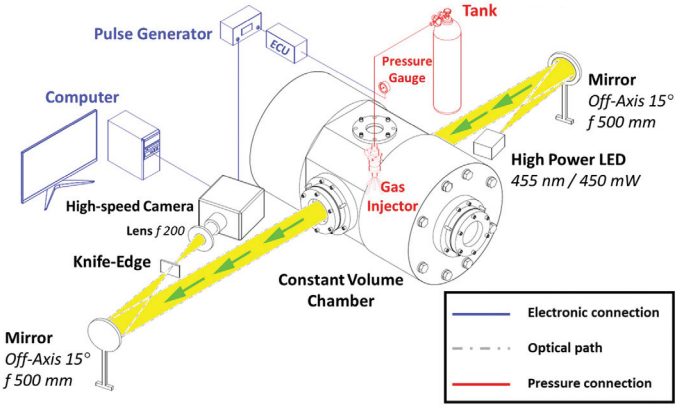

Figure 7. Experimental optical setup of schlieren technique with z-type configuration (reproduced with permission from Ref. [47]. Copyright 2020 SAE International).

The Schlieren light source is usually a high-power LED lamp. A series of lenses and glasses modify the beam characteristics. The main difference between Schlieren and shadowgraph is the presence of a knife-edge in the first case to regulate the percent of light cutoff, obtaining the desired contrast for the Schlieren images. High-speed cameras are adopted for recording images with frame rates of the order of thousands of frames per second. Depending on the magnification system, different spatial resolutions can be achieved.

The injection system usually consists of a pressurized fuel tank, a pressure transducer and a pressure regulator to ensure the desired value for the test conditions. The

transistor–transistor logic (TTL) triggering signal produced by a pulse generator is used by an Electronic Control Unit (ECU) to control the injection events and to guarantee proper synchronization and delay between the injection and acquisition chain.

Under-expanded jets are almost always being observed in Constant Volume Chambers (CVC), optically accessible through quartz windows with the injector fixed in a customized holder.

The images recorded with these techniques provide a proficient visualization of the near field zone, and so of the barrel shocks, the Mach discs, etc., as well as the overall spray structure, allowing the evaluation of macroscopic parameters such as the Mach disc height, width, the jet tip penetration, the jet angle, the volumetric growth, the tip speed, radial expansion, etc. Figure 8 depicts some classical visualization of the under-expanded jets obtained with schlieren imaging and regarding various jet's characteristics [48].

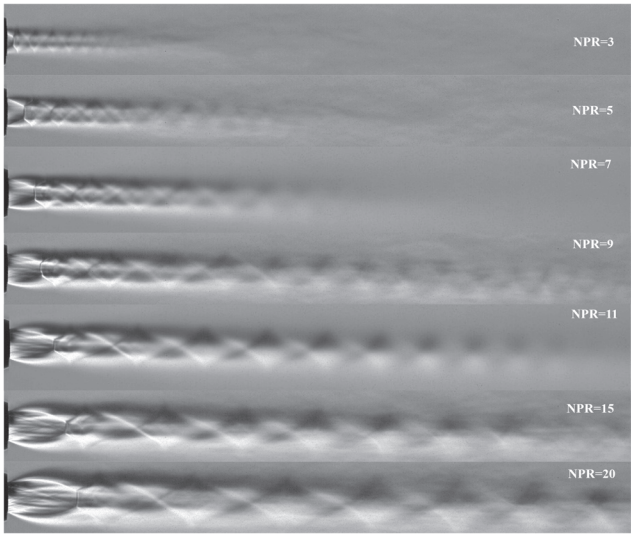

Figure 8. Visualization of under-expanded jets by means of schlieren optical technique (reproduced with permission from Ref. [48]. Copyright 2022 Elsevier).

These information are of relevant importance for verifying and validating CFD simulation codes by comparison of the aforementioned parameters but, at the same time, do not allow to evaluate microscopic features of the jet or give a quantitative estimation of local fuel concentration, jet temperature or velocity. To obtain some of these information other experimental techniques are required. They are Planar Laser-Induced Fluorescence (PLIF) or Particle Image Velocimetry (PIV) [43,49–53].

The PIV technique is a non-intrusive diagnostic technique that allows the velocity field to be measured on a two-dimensional plane. The measurement principle is based on determining the distance the tracer particles cover in a known time interval [54,55]. The typical elements of a PIV system are a laser source (typically a pulsed Nd-YAG laser with a wavelength of 532 nm), an optical system, a camera and a data acquisition system (DAQ).

The PLIF technique allows the measurement of the concentration of species and the temperature in the flow field of a fluid. It is based on the process of photon absorption–emission, and therefore, on the phenomenon of natural fluorescence of molecules and atoms. Through the PLIF technique, it is possible to obtain visualization with high spatio-temporal resolution. Although the instantaneous (temporally based) quantitative measurement of the parameters of interest remains complex, it is still possible to obtain quantitative measurements of concentration, temperature, pressure and speed based on an average of consecutive sequences (time-averaged).

Figure 9 depicts some results regarding the fuel concentration of under-expanded jets [53].

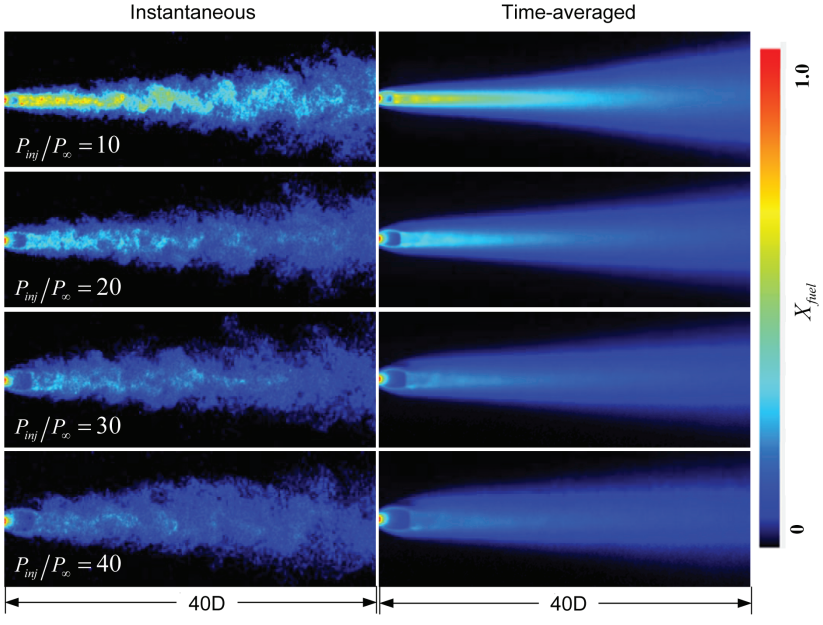

Figure 9. Visualization of under-expanded jets by means of PLIF optical technique for different P_{inj}/P_{amb} ratios (reproduced with permission from Ref. [53]. Copyright 2013 SAE International).

Table 1 summarizes the papers regarding experimental investigations of under-expanded jets.

Table 1. Experimental Techniques Jets Summary Table.

Technique	Measurement Zone	Fuel	NPR	Reference
Schlieren	Developed Spray	CH_4	$P_{inj} = 300 \quad bar$ $P_{amb} = 60, 12, 30 \quad bar$	[56]
	Developed Spray	He	$NPR = 2, 3, 4, 5$	[13]
	Near-nozzle/ Mach Disc	N_2	$NPR = 20$	[57]
	Developed Spray	CH_4	NPR = 190, 220, 250, 280, 310	[43]
	Developed Spray	CH_4	$NPR = 60, 11, 16, 21, 26$	[41]
	Developed Spray	CH_4	$P_{inj} = 10, 14, 18 \quad bar$ $P_{amb} = 3, 5 \quad bar$	[42]
PLIF	Near-nozzle/Mach Disc	N_2	$NPR = 10, 20, 30, 40$	[50]
	Developed Spray	N_2	$NPR = 10, 40$	[53]
	Developed Spray	CH_4	$NPR = 20, 60$	[51]
PIV	Developed Spray	N_2	$NPR = 20$	[57]
	Developed Spray	Ar	$NPR = 12$	[58]

4. CFD Simulation of Under-Expanded Jets

Computational fluid dynamic codes (CFD) are undoubtedly the other powerful tool broadly adopted to investigate under-expanded jets. The advantages of developing a virtual model of this engineering problem are quite obvious not only to understand the

underlying physics of these flows but also with the perspective of the application to the propulsion system.

This paragraph aims to illustrate, in a synthetic but also organized fashion, the main characteristics of the CFD codes used by researchers to study the aforementioned problem. Further than in-house developed codes, basically three finite volume CFD codes were used. They are OpenFOAM, CONVERGE and STAR-CCM+ [59–61]. It should also be mentioned that some studies use the Lattice Boltzmann method [62,63]. The following two sub-sections report the main characteristics of the discretization schemes adopted and of the turbulence modelling selected.

4.1. Discretization Schemes and Solution Algorithms

The simulation of under-expanded jets requires the adoption of high-order numerical schemes able to describe flow-field discontinuities along with avoiding undesired oscillations. High-order schemes are required both for spatial discretization and temporal integration.

Methodologies, based on Riemann solvers, such as the Weighted Essentially Non-Oscillatory schemes (WENO) or the Piecewise Parabolic Method (PPM), give the best reproduction of compressible flow but have relevant limitations. These approaches involve characteristic decomposition and Jacobian evaluation, and so they were implemented only for structured grids. The adaptive central-upwind sixth-order weighted essentially non-oscillatory (WENO-CU6) scheme with low dissipation was used by Ren Z et al. [64] to achieve a proper resolution of the flow properties around the shock waves. Seventh-order accurate weighted essentially non-oscillatory (WENO7) reconstruction of the characteristic fluxes was also adopted for simulating under-expanded jets. The shocks and discontinuities can be resolved using highly accurate and low-dissipation hybrid ENO schemes with shock detectors [65–67].

Contrarily, unstructured grids are far more flexible than structured grids and can easily discretize complex geometries [68–70]. One of the principal methods developed for unstructured grids uses the so-called central schemes formulations of Kurganov (KNP) and Kurganov and Tadmor (KT) [71,72]. These are non-staggered second-order central methods that use the cell centres' values to evaluate the cell faces' fluxes. The cell-to-face flow interpolation is divided into inward and outward directions with respect to the face owner cell. An extensive and detailed description can be found in [68]. Considering the intrinsic geometrical complexity of the injector's nozzles, these schemes are broadly adopted for this kind of simulation in union with flux limiters of Minmod or of Van Leer to ensure stability and convergence of the computation [68,73]. This discretization method, initially implemented in OpenFOAM's solver *rhoCentralFoam*, was exploited in various other solvers purposely developed to study under-expanded jets [74–80]. Another proficient scheme used is the Advection Upstream Splitting Method (AUSM^{+}-up). AUSM+-up is accurate and reliable in solving fluid flows with any arbitrary range of velocities, but it excels at high-velocity flows with strong discontinuities like shock waves [81,82]. AUSM+-up avoids explicit artificial dissipation by using a separate splitting for the pressure terms of the governing equations; the mass flux and pressure flux are calculated on the basis of local flow characteristics (including the speed of sound) to ensure precise information propagation inside the fluid for convective and acoustic processes [83]. This minimizes numerical dissipation, especially in high-velocity flows, and prevents wiggles at flow discontinuities like shocks.

The solution methods commonly used involve both explicit (density-based) [84–86] and Pressure Implicit Split Operator (PISO) algorithms [56,87–90]. The density-based approach proved to be the best choice for reproducing under-expanded jet features. Implicit (or pressure-based) methods for solving fluid-flow governing equations were historically employed for incompressible flows and only recently adapted to account for compressible flows. However, as broadly demonstrated in the literature [84–86,89], the best choice in terms of results accuracy is represented by explicit methods (or density-based). The reason

for that is intrinsically contained in the algorithm procedure. The temporal integration is usually performed using high-order schemes such as explicit Runge–Kutta 4th (RK4) [84].

Another relevant aspect of under-expanded jet simulation is the computation of the thermo-physical properties for the species involved in the fluid flow. The equation of state (EoS) (for a description of the pressure–volume–temperature (P-V-T) relationship) is crucial to the accuracy of the solution. Further than the ideal-gas EoS, Cubic EoS such as Soave–Redlich–Kwong (SRK) and Peng–Robinson (PR) were widely applied due to their simplicity and reasonable accuracy [56,61,76,77,91–94].

4.2. Turbulence Modelling

The numerical solution of the fluid-dynamic problem is valid when the computational grid is fine enough to resolve all the flow scales [85]. This would be a Direct Numerical Simulation (DNS) of the flow, which is now unaffordable due to its complexity and resource demands. So, turbulence modelling techniques, such as Reynolds Averaged Navier Stokes (RANS) or Large Eddy Simulation (LES), are preferred for under-expanded jet simulations [78,85,86,95].

Among the many simulation approaches regarding under-expanded jets, just a few use RANS, while most adopt LES models. The LES technique is based on modelling the lower scales, which are universal and unaffected by flow geometry, while explicitly solving the larger ones. This is done by mathematically filtering the governing equations and introducing the Sub-Grid Stress (SGS) tensor (τ_{sgs}) [96]. The SGS term modelling involves an eddy viscosity approximation. Various SGS closure models can be found in the literature. In some cases, LES WALE model is used, both without wall functions or applying global damping functions. The model produces an efficient and fast-solving scheme due to its algebraic formulation. This approach also showed some promising results in predicting the transition from laminar to turbulent regimes [97].

The Yoshizawa model is another common choice. It is a one-equation eddy viscosity model for compressible flows [98,99], which is different from zero equation models such as the Smagorisky model. It exploits a transport equation to compute the local SGS kinetic energy k_{sgs}. Then, the sub-grid scale eddy viscosity ν_{sgs} is calculated using the k_{sgs} field and the filter dimension Δ (usually evaluated from the grid size) according to the following relation:

$$\nu_{sgs} = C_k \Delta \sqrt{k_{sgs}} \tag{3}$$

where C_k is a model constant whose default value is 0.094.

The scale selective discretization (SSD) technique proposed by Vuorinen et al. relates to the so-called implicit LES (ILES) modelling category [84,100–102]. However, unlike ILES, the SSD approach targets the dissipative effects exclusively to the flow's smallest scales via scale separation procedure. A Laplacian filter separates the scales by splitting the convection term into low and high-frequency components for which centred and upwind-biased techniques can be used individually.

Table 2 summarizes the papers regarding CFD simulations of under-expanded jets.

Table 2. CFD Simulations Summary Table.

Numerical Approach	Code	Turbulence Modeling	Fuel	Reference
WENO/ENO	In-house	LES	Air	[65]
	In-house	LES	Air	[66]
	In-house/Finite Differences	LES	Reactive jet	[67]
	In-house	LES	H_2	[64]
AUSM	STAR CCM+	LES WALE	H_2	[60,82,89,103]
		LES WALE	N_2	[60,103]
		LES WALE	CH_4	[89,103]

Table 2. *Cont.*

Numerical Approach	Code	Turbulence Modeling	Fuel	Reference
KNP/KT	OpenFOAM	LES, RANS k-ω	H_2	[74,86]
	OpenFOAM	LES k-Eqn	N_2	[77,86]
	OpenFOAM	LES k-Eqn	CH_4	[47,75,104,105]
Bulk Viscosity Method	OpenFOAM	LES Scale Selective Method	N_2	[53,85]
			CH_4	[84]
			H_2	[53]
Hybrid KNP/KT	OpenFOAM	LES	CH_4	[56,106,107]
	OpenFOAM	LES, RANS	H_2	[61,108]
MUSCL	CONVERGE	LES	CH_4	[61,109]
Lattice Boltzmann	In-house	LES	N.A.	[62,63]

5. Jet Structure Analysis

Although we are considering pure experimental research or a CFD investigation, the information provided can be classified and subdivided in the following paragraphs.

First of all, the main parameters of the injection process are reviewed and discussed; then, the features of the Mach discs and, generally, of the near field flow are presented accordingly with the outcomes of the works considered. Finally, the characterization of the turbulent mixing zone and of the far-field zone are discussed being of central importance in propulsion systems applications.

5.1. Characteristics and Parameters of the Injection

The injectors investigated in the literature are mainly single-hole prototype devices. These usually have round holes with a diameter of about 1 mm [41,60,78]. Some other authors investigated hollow cone outwardly opening devices [52,88,109,110]. One of these is produced by Continental (Figure 10), and it was characterized both numerically and experimentally.

Commercially available injectors were also modified to inject gaseous fuels generating multi-hole patterned sprays [13,43,57].

Very few works were found concerning multi-hole injectors purposely designed for gaseous injection. A 50 bar maximum injection pressure device with inter-changeable nozzles was investigated experimentally and numerically in a series of publications [104,105].

When working with gaseous injection, typically, Net Pressure Ratio (NPR), the ratio between the injection and the environment pressure, is conveniently used as a reference to classify the resulting jets, more so than using injection pressure. In particular, common NPR values range from 4 to 5 to around 40–50 [42,43,104]. The ambient pressure is usually kept equal to 1 bar. Some works explore injection pressures up to 200 bar [51].

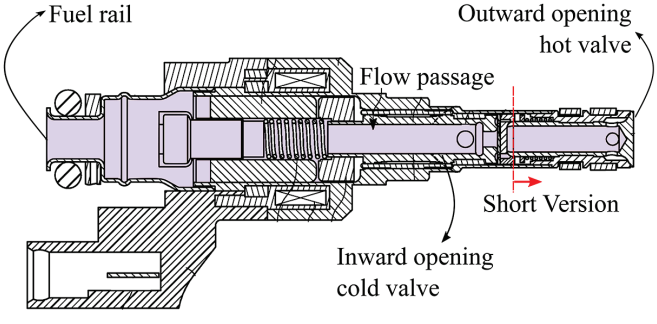

Figure 10. Outwardly opening injector for gaseous injections (reproduced with permission from Ref. [109]. Copyright 2020 The University of Queensland).

In the investigation of under-expanded jets, the characteristics of the injected fluid play a very important role, strongly influencing resulting jet conditions. However, due to security issues, experimental investigations are normally realized with inert gases like N2, argon or helium [52,58,92,111]. Moreover, some papers examine methane or hydrogen injections, the latter especially considering the latest interest in this fuel shown by many research groups. From the perspective of potential application in propulsion systems, testing inert gas is mainly used to validate and calibrate numerical CFD approaches, which can afterwards be extended to flammable fluid injections and mixture formation processes.

5.2. Near Field—Mach Disc Features

The investigation of the near nozzle flow field of under-expanded jets is mainly focused on Mach discs, barrel shocks or converging shocks that appear in this flow just downstream of the injector nozzle. Schlieren imaging is undoubtedly the most adopted technique to record them. The pictures obtained are a powerful tool to validate the CFD codes. Further than a visual comparison of the Schlieren measurements with the gradient of the density field computed with CFD, the Mach disc's height and width represent quantitative parameters that can be used for an actual comparison. An investigation using the PLIF technique was instead performed by Yu et al. [50]. The following Figure 11 depicts a comparison between LES simulation and PLIF visualization of the Mach disc issued from a methane injection.

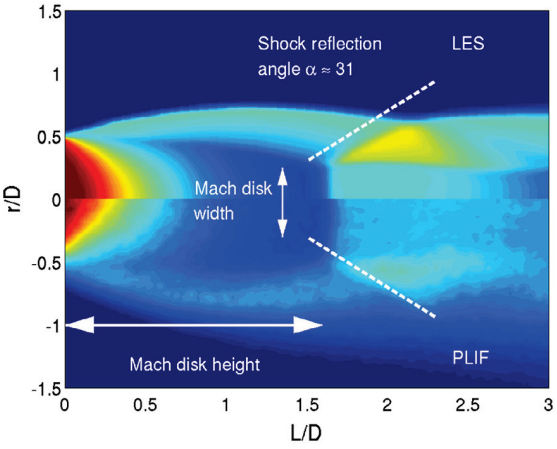

Figure 11. Mach disc: comparison of experimental PLIF images with LES CFD simulation (reproduced with permission from Ref. [50]. Copyright 2013 Elsevier).

The computational requirements for under-expanded jets simulations are very high. Grid sensitivity analysis performed by various authors demonstrated that to have a proficient representation of the near nozzle shocks mesh dimensions must be of the order of D/20–D/50 or, in dimensional terms, of tens of micro-meter [84,85,89,103]. This, together with the time step of the order of 10^{-8} s, requires relevant computational resources.

From a modelling point of view interesting comparisons between different CFD codes (such as OpenFOAM, Star CCM+ and CONVERGE) were carried out by various authors [61,112].

The equation of state was also investigated. Redwlich-Kwong and Peng-Robinson real gas EoS give different configurations of under-expanded jets with respect to ideal gas EoS especially when the jets are issued in critical conditions [106,107]. Other fluid properties, such as specific heat or viscosity are also objects of interest. Chung relation and Chapman–Enskog theory were used for the viscosity while the Janaf pressure-corrected relation for C_p and C_v [58,113].

The effect of the NPR on the characteristics of the Mach disc is one of the most investigated physical parameters demonstrating how, depending on the value assumed, the jet configuration significantly changes. Figure 12 shows the different shock structures obtainable accordingly with the net pressure ratio.

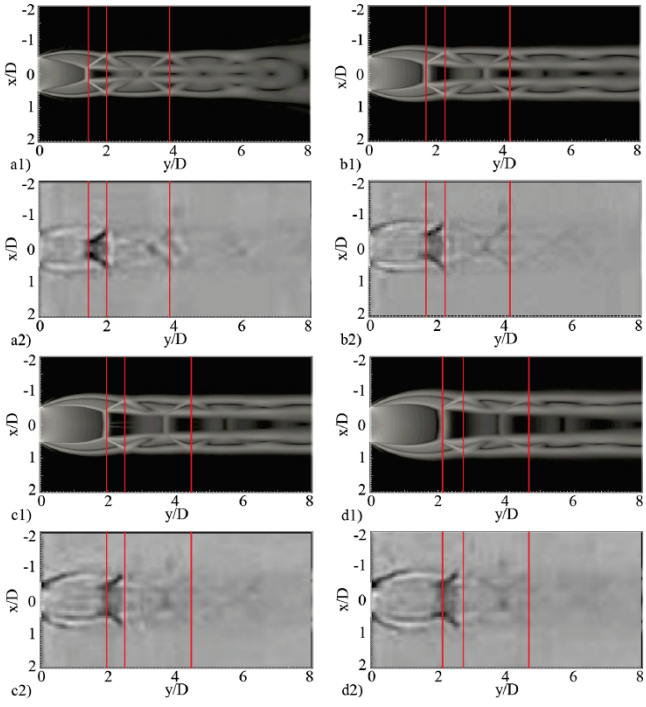

Figure 12. Mach discs: comparison of different pressure ratios. (**a1**,**a2**) NPR = 5.60, (**b1**,**b2**) NPR = 7.47, (**c1**,**c2**) NPR = 9.34, and (**d1**,**d2**) NPR = 11.2 (reproduced with permission from Ref. [77]. Copyright 2016 American Institute of Aeronautics and Astronautics).

The effect of the fuel characteristics was also an important research topic treated by Hamzehloo et al. comparing mach discs produced with hydrogen and methane [89,103]. The near-nozzle shock structure of the methane jet displayed a slightly different pattern compared to the hydrogen jets. The methane jet exhibited intense expansion fans right from the early stages of its formation, resulting in a normal shock that was wider than the nozzle diameter and resembled a Mach disc. On the other hand, the hydrogen jets were associated with a slim Mach disc. For methane, mixing occurs only downstream of the Mach disc while, for hydrogen, high momentum exchange and mixing was observed at the boundaries of the jet.

5.3. Far Field—Turbulent Mixing

Jet area, volumetric growth and tip penetration are the main parameters used to describe the characteristics of the far field and especially to validate the CFD approach exploiting schlieren images [43,53,56].

PLIF and PIV measurements also make it possible to characterize the mixing process, providing detailed information about the local fuel concentration and about the velocity field [49,53]. Axial and transverse density concentration profiles are also common plots produced from both simulation results and experimental measurements.

Two main approaches are used to characterize the mixing process: Scalar Dissipation Rate (SDR) and the development of a Probability density function (PDF).

The SDR is a measure of the mixing activity. Higher SDR values indicate more significant fuel concentration gradients. Low SDR values, on the other hand, indicate a very homogeneous spatial distribution of the fuel. This means that good mixing has already occurred (because the gradients have faded) or, even more, that no mixing is occurring.

The potential core of the jet, which extends averagely for 10/20 diameters downstream, is surrounded by a mixing layer where, in the radial direction, the fuel concentration decreases quickly. CFD simulations show that mixing does not occur in the central core where the jet is supersonic. Only downstream, when the flow becomes subsonic, turbulent air-fuel mixing begins. String-like structures highlight the edges between high and low-concentration regions.

Figure 13 reports an example of SDR computed for an under-expanded methane jet.

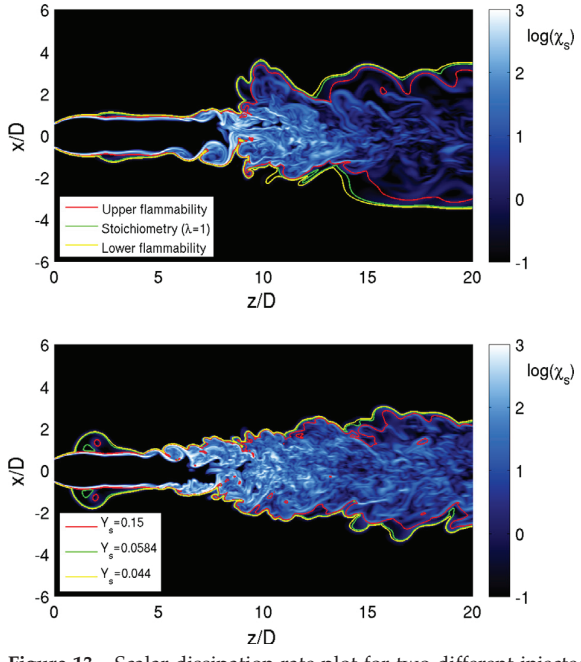

Figure 13. Scalar dissipation rate plot for two different injected fuels: N2 top and CH4 bottom. The isolines delimit zones where the fuel concentration is within the flammability limits or in stoichiometric conditions (reproduced with permission from Ref. [84]. Copyright 2014 Elsevier).

Some research used an SDR approach, concluding that a higher NPR favours a better and quicker air/fuel mixing [53,65,75]. This shows that NPR may substantially modify the mixing processes, which is not good news considering that high gaseous fuel injection pressures are typically not easily reachable due to intrinsic limitations in on-board gaseous fuel storage systems [114].

Achieving a quantitative estimation of the global mixture quality has relevant importance, especially with regard to the combustion process. Therefore, a statistical approach is commonly adopted to characterize the mixture obtained from the injection process. A mass-weighted probability density function (*PDF*) is usually calculated from the CFD results providing plots like the one in Figure 14.

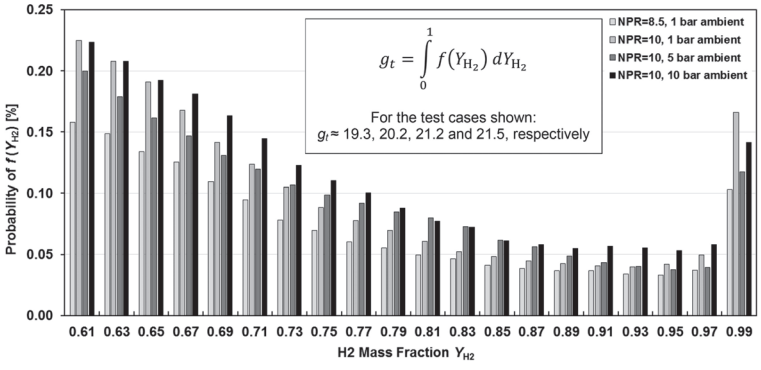

Figure 14. Probability density function computed to evaluate hydrogen mixture quality (reproduced with permission from Ref. [103]. Copyright 2016 Elsevier).

If the PDF function is integrated over different ranges of fuel concentration, it allows to estimate the percentage of lean, flammable and rich mixture [51,85,103]. This is important for evaluating the dynamics of the combustion process that follows the injection.

Turbulence effects are relevant in describing the structure of under-expanded jets far field. The common way to describe turbulence characteristics is to plot Q-criterion iso-surfaces or vorticity vectors; various authors did this on different kinds of jets [57,104,105].

Proper orthogonal decomposition (POD) was exploited by Vuorinen et al. [85] to project the turbulent flow field on basis functions that maximize the turbulent kinetic energy content for any subset of the base. The dominant structures indicate a helical mode and the spatial location and shown dynamics of the mode matches the previously existing picture of noise production.

The compressible vorticity transport equation rules vorticity evolution. Analysis of the driving forces to distort the streamwise vortices was performed by Li X et al. because it helps to understand the turbulent transition mechanisms [77]. The authors demonstrated that the dilatational and baroclinic terms, generally negligible in incompressible flows, are critical and play a key role in current under-expanded jets. The vorticity transport is not exclusively driven by vortex stretching but also by the compressibility and baroclinic effects.

The jets' self-similarity properties were also assessed. They can be estimated with the ratio of the radial penetration to the axial penetration. When the ratio is stable, it indicates that the jets reach a self-similarity [63].

Finally, Wu K. et al. focus on the simulation of the acoustic field of highly under-expanded jets to gain a deeper physical understanding of the noise generation mechanism [76].

6. Conclusions

In this review, a quick and, as far as possible, complete reference guide was presented in relation to the latest theoretical and experimental research activities regarding the investigation of under-expanded jets for application in advanced propulsion system.

Under-expanded jets are fluid flows that occur when a high-pressure fluid is suddenly released through a nozzle into a region of lower pressure. The term "under-expanded" specifically describes a condition where the fluid jet does not fully expand to match the surrounding pressure resulting in the formation of shock waves. Under-expanded jets are commonly encountered in various engineering applications, including rocket nozzles, gas and steam releases, supersonic exhaust from jet engines and during the injection of gaseous fuels in engine systems. Understanding the behaviour of under-expanded jets is now becoming crucial to develop clean and efficient combustion systems. For this reason, the most innovative experimental and numerical methods are used to study these jets.

Schlieren imaging is a broadly adopted technique for visualizing the overall jet development, and provides macroscopic information like jet penetration, cone angle, volume

and morphology. Local measurements of the jet velocity and fuel density are also possible via exploiting other techniques like PLIF and PIV.

Fluid-dynamic simulation of under-expanded jets is an important field of research. In dealing with a compressible flow, special attention must be paid to choosing discretization schemes with low numerical diffusion while ensuring computational stability. High-order schemes, like ENO or WENO, provide a proficient representation of these flows types but require structured grids that offer little versatility. On the contrary, flux splitting methods (like KNP/KT or AUSM+), together with high-order integration schemes, are widely used with unstructured grids and provide very good results. However, the high-computational demands represent a significant drawback of these approaches. Grids on the order of magnitude of 10–50 µm are required. Depending on the thermodynamic conditions, a real gas equation of state may be required to adequately represent critical conditions or, more generally, deviation from the ideal gas behaviour.

Both outwardly and inwardly injection devices have been the topic of scientific research. The former category seems to be the best choice due to the amount of fuel they can supply in a relatively short period.

Injection pressure is usually of the order of tens of bar due to an evident limitation related to the fuel storage on-board. The injection usually occurs at ambient pressure, while nozzle holes are of the order of the millimetre.

The Mach disc is undoubtedly the most studied feature of under-expanded jets. It strongly affects the flow field, the air–fuel entrainment, and its geometrical features (width and height) are related to the pressure ratio. The Mach disc dimensions are usually of the order of magnitude of a few millimetres.

Turbulent mixing only occurs downstream of the Mach disc and the so-called potential core, typically extending 10/20 diameters downstream.

POD decomposition, Q-criterion surfaces and vorticity plots help understand turbulence characteristics, while scalar dissipation rate theory and statistical evaluation of the mixing activity provide relevant information regarding the air–fuel mixture formation.

Finally, it can be stated that the research efforts in investigating under-expanded jets in advanced propulsion systems will be further directed towards developing injection devices capable of supplying the required fuel amount in the strict timings available during the engine cycle. Experimental observations should deepen the jet morphology, providing further visualisations depicting especially quantitative parameters for comparison with CFD simulations. The numerical methods adopted for studying under-expanded jets are resource-demanding. So, optimised approaches should be developed to reduce the associated computational cost, mainly because these models are expected to be embedded in whole engine simulations.

Author Contributions: Conceptualization, F.D.; methodology, F.D.; data curation, F.D.; writing—original draft preparation, F.D.; supervision, C.V. and A.D.V.; writing—review and editing, C.V. and A.D.V. All authors have read and agreed to the published version of the manuscript.

Funding: This research received no external funding

Data Availability Statement: No new data were created or analyzed in this study. Data sharing is not applicable to this article.

Conflicts of Interest: The authors declare no conflicts of interest.

Abbreviations

The following abbreviations are used in this manuscript:

CFD	Computational Fluid Dynamics
CNG	Compressed Natural Gas
CVC	Constant Volume Chamber

DI	Direct Injection
DNS	Direct Numerical Simulation
fps	frames per second
ICE	Internal Combustion Engines
KNP	Kurganov
KT	Kurganov and Tadmor
LED	Light Emitting Diode
LES	Large Eddy Simulation
$\dot{m}^*$	critical mass flow
NPR	Net Pressure Ratio
PDF	Probability Density Function
PECU	Programmable Electronic Control Unit
PFI	Port Fuel Injected
P_{inj}	injection pressure
p_∞	ambient pressure
P^*	critical pressure
PISO	Pressure Implicit Split Operator
PPM	Piecewise Parabolic Method
RANS	Reynolds-Averaged Navier–Stokes
TKE	Turbulent Kinetic Energy
TTL	Transistor–Transistor Logic
WENO	Weighted Essentially Non-Oscillatory

References

1. Joshi, A. *Review of Vehicle Engine Efficiency and Emissions*; SAE Technical Papers; SAE International: Warrendale, PA, USA, 2020; Volume 2020; pp. 1–29. [CrossRef]
2. IPCC. *Climate Change 2021: The Physical Science Basis. Contribution of Working Group I to the Sixth Assessment Report of the Intergovernmental Panel on Climate Change*; Masson-Delmotte, V., Zhai, P., Pirani, A., Connors, S.L., Péan, C., Berger, S., Caud, N., Chen, Y., Eds.; Cambridge University Press: Cambridge, UK, 2021; p. 3949.
3. International Energy Agency. *Tracking Transport 2020*; IEA: Paris, France, 2021.
4. International Energy Agency. *Net Zero by 2050: A Roadmap for the Global Energy Sector*; IEA: Paris, France, 2021; p. 224.
5. Li, F.; Wang, Z.; Wang, Y.; Wang, B. High-Efficiency and Clean Combustion Natural Gas Engines for Vehicles. *Automot. Innov.* **2019**, *2*, 284–304. [CrossRef]
6. Senecal, K.; Leach, F. *Racing Toward Zero: The Untold Story of Driving Green*; SAE International: Warrendale, PA, USA, 2021.
7. Sankesh, D.; Lappas, P. *Natural-Gas Direct-Injection for Spark-Ignition Engines—A Review on Late-Injection Studies*; SAE International: Warrendale, PA, USA, 2018. [CrossRef]
8. Nocivelli, L.; Sforzo, B.A.; Tekawade, A.; Yan, J.; Powell, C.F.; Chang, W.; Lee, C.F.; Som, S. *Analysis of the Spray Numerical Injection Modeling for Gasoline Applications*; SAE Technical Papers; SAE International: Warrendale, PA, USA, 2020. [CrossRef]
9. Zembi, J.; Mariani, F.; Battistoni, M.; Irimescu, A.; Merola, S. Numerical Investigation of Water Injection Effects on Flame Wrinkling and Combustion Development in a GDI Spark Ignition Optical Engine. In Proceedings of the SAE WCX Digital Summit, Virtual, 12–15 April 2021; SAE International: Warrendale, PA, USA, 2021. [CrossRef]
10. Oh, H.; Hwang, J.; Pickett, L.M.; Han, D. Machine-learning based prediction of injection rate and solenoid voltage characteristics in GDI injectors. *Fuel* **2022**, *311*, 122569. [CrossRef]
11. Allocca, L.; Montanaro, A.; Meccariello, G.; Duronio, F.; Ranieri, S.; De Vita, A. *Under-Expanded Gaseous Jets Characterization for Application in Direct Injection Engines: Experimental and Numerical Approach*; SAE Technical Papers; SAE International: Warrendale, PA, USA, 2020; Volume 2020; pp. 1–15. [CrossRef]
12. Yip, H.L.; Srna, A.; Chun, A.; Yuen, A.C.Y.; Kook, S.; Taylor, R.; Yeoh, G.; Medwell, P.; Chan, Q. A Review of Hydrogen Direct Injection for Internal Combustion Engines: Towards Carbon-Free Combustion. *Appl. Sci.* **2019**, *9*, 4842. [CrossRef]
13. Hajialimohammadi, A.; Honnery, D.; Abdullah, A.; Mirsalim, M.A. Time resolved characteristics of gaseous jet injected by a group-hole nozzle. *Fuel* **2013**, *113*, 497–505. [CrossRef]
14. Chiodi, M.; Berner, H.J.; Bargende, M. *Investigation on Different Injection Strategies in a Direct-Injected Turbocharged Cng-Engine*; SAE Technical Papers; SAE International: Warrendale, PA, USA, 2006. [CrossRef]
15. Yadollahi, B.; Boroomand, M. The effect of combustion chamber geometry on injection and mixture preparation in a CNG direct injection SI engine. *Fuel* **2013**, *107*, 52–62. [CrossRef]
16. Erfan, I.; Hajialimohammadi, A.; Chitsaz, I.; Ziabasharhagh, M.; Martinuzzi, R.J. Influence of chamber pressure on CNG jet characteristics of a multi-hole high pressure injector. *Fuel* **2017**, *197*, 186–193. [CrossRef]
17. Duronio, F.; Ranieri, S.; Montanaro, A.; Allocca, L.; De Vita, A. ECN Spray G injector: Numerical modelling of flash-boiling breakup and spray collapse. *Int. J. Multiph. Flow* **2021**, *145*, 103817. [CrossRef]
18. Fox, J.H. On the Structure of Jet Plumes. *AIAA J.* **1974**, *12*, 105–107. [CrossRef]

19. Doroudi, S. *Ansys Fluent Modelling of an Underexpanded Supersonic Sootblower Jet Impinging into Recovery Boiler Tube Geometries*; University of Toronto (Canada): Toronto, ON, Canada, 2015.
20. Knowles, K.; Saddington, A.J. A review of jet mixing enhancement for aircraft propulsion applications. *Proc. Inst. Mech. Eng. Part G J. Aerosp. Eng.* **2006**, *220*, 103–127. [CrossRef]
21. Orescanin, M.M.; Austin, J.M.; Kieffer, S.W. Unsteady high-pressure flow experiments with applications to explosive volcanic eruptions. *J. Geophys. Res. Solid Earth* **2010**, *115*. [CrossRef].
22. Von der Linden, J.; Kimblin, C.; McKenna, I.; Bagley, S.; Li, H.C.; Houim, R.; Kueny, C.S.; Kuhl, A.; Grote, D.; Converse, M.; et al. Standing shock prevents propagation of sparks in supersonic explosive flows. *Commun. Earth Environ.* **2021**, *2*, 195. [CrossRef]
23. Carcano, S.; Bonaventura, L.; Esposti Ongaro, T.; Neri, A. A semi-implicit, second-order-accurate numerical model for multiphase underexpanded volcanic jets. *Geosci. Model Dev.* **2013**, *6*, 1905–1924. [CrossRef]
24. Verhelst, S. Recent progress in the use of hydrogen as a fuel for internal combustion engines. *Int. J. Hydrogen Energy* **2014**, *39*, 1071–1085. . [CrossRef]
25. Onorati, A.; Payri, R.; Vaglieco, B.; Agarwal, A.; Bae, C.; Bruneaux, G.; Canakci, M.; Gavaises, M.; Günthner, M.; Hasse, C.; et al. The role of hydrogen for future internal combustion engines. *Int. J. Engine Res.* **2022**, *23*, 529–540. [CrossRef]
26. Kurnia, J.C.; Sasmito, A.P., Hydrogen Fuel Cell in Vehicle Propulsion: Performance, Efficiency, and Challenge. In *Energy Efficiency in Mobility Systems*; Sulaiman, S.A., Ed.; Springer: Singapore, 2020; pp. 9–26. [CrossRef]
27. Petrescu, R.V.V.; Machín, A.; Fontánez, K.; Arango, J.C.; Márquez, F.M.; Petrescu, F.I.T. Hydrogen for aircraft power and propulsion. *Int. J. Hydrogen Energy* **2020**, *45*, 20740–20764. [CrossRef]
28. Depcik, C.; Cassady, T.; Collicott, B.; Burugupally, S.P.; Li, X.; Alam, S.S.; Arandia, J.R.; Hobeck, J. Comparison of lithium ion Batteries, hydrogen fueled combustion Engines, and a hydrogen fuel cell in powering a small Unmanned Aerial Vehicle. *Energy Convers. Manag.* **2020**, *207*, 112514. [CrossRef]
29. Abdel-Rahman, A. A review of effects of initial and boundary conditions on turbulent jets. *WSEAS Trans. Fluid Mech.* **2010**, *4*, 257–275.
30. Donaldsion, C.; Snedeker, R. A study of free jet impingement. *J. Fluid Mech.* **1971**, *45*, 281–319. [CrossRef]
31. Saddington, A.J.; Lawson, N.J.; Knowles, K. An experimental and numerical investigation of under-expanded turbulent jets. *Aeronaut. J.* **2004**, *108*, 145–152. [CrossRef]
32. John, J. *Gas Dynamics*; Prentice Hall PTR: Hoboken, NJ, USA, 1984.
33. Dam, N.J.; Rodenburg, M.; Tolboom, R.A.L.; Stoffels, G.G.M.; Huisman-Kleinherenbrink, P.M.; ter Meulen, J.J. Imaging of an underexpanded nozzle flow by UV laser Rayleigh scattering. *Exp. Fluids* **1998**, *24*, 93–101. [CrossRef]
34. Saad, M. *Compressible Fluid Flow*; Prentice-Hall: Hoboken, NJ, USA, 1985.
35. EWAN, B.C.R.; MOODIE, K. Structure and Velocity Measurements in Underexpanded Jets. *Combust. Sci. Technol.* **1986**, *45*, 275–288. [CrossRef]
36. Keith, T.G.; John, J.E. *Gas Dynamics*; Pearson Education, Inc.: Upper Saddle River, NJ, USA, 2006.
37. Zucker, R.D.; Biblarz, O. *Fundamentals of Gas Dynamics*; John Wiley & Sons: Hoboken, NJ, USA, 2002.
38. Antsupov, A. Properties of Underexpanded and Overexpanded Supersonic Gas Jets. *Sov. Phys. Tech. Phys.* **1974**, *19*, 234 – 238.
39. Hatanaka, K.; Saito, T. Influence of nozzle geometry on underexpanded axisymmetric free jet characteristics. *Shock Waves* **2012**, *22*, 427–434. [CrossRef]
40. Addy, A.L. Effects of axisymmetric sonic nozzle geometry on Mach disk characteristics. *AIAA J.* **1981**, *19*, 121–122. [CrossRef]
41. Dong, Q.; Li, Y.; Song, E.; Fan, L.; Yao, C.; Sun, J. Visualization research on injection characteristics of high-pressure gas jets for natural gas engine. *Appl. Therm. Eng.* **2018**, *132*, 165–173. [CrossRef]
42. Zhao, J.; Liu, W.; Liu, Y. Experimental investigation on the microscopic characteristics of underexpanded transient hydrogen jets. *Int. J. Hydrogen Energy* **2020**, *45*, 16865–16873. [CrossRef]
43. Ni, Z.; Dong, Q.; Wang, D.; Yang, X. Visualization research of natural gas jet characteristics with ultra-high injection pressure. *Int. J. Hydrogen Energy* **2022**, *47*, 32473–32492. [CrossRef]
44. Settles, G.S. *Schlieren and Shadowgraph Techniques: Visualizing Phenomena in Transparent Media*; Springer Science & Business Media: Berlin/Heidelberg, Germany, 2001.
45. Panigrahi, P.K.; Muralidhar, K. *Schlieren and Shadowgraph Methods in Heat and Mass Transfer*; Springer: Berlin/Heidelberg, Germany, 2012; Volume 2.
46. Kook, S.; Le, M.K.; Padala, S.; Hawkes, E.R. Z-type Schlieren Setup and its Application to High-Speed Imaging of Gasoline Sprays. In Proceedings of the SAE International Powertrains, Fuels and Lubricants Meeting, Kyoto, Japan, 30 August–2 September 2011; SAE International: Warrendale, PA, USA, 2011. [CrossRef]
47. Montanaro, A.; Allocca, L.; De Vita, A.; Ranieri, S.; Duronio, F.; Meccariello, G. Experimental and Numerical Characterization of High-Pressure Methane Jets for Direct Injection in Internal Combustion Engines. In Proceedings of the SAE Powertrains, Fuels & Lubricants Meeting, Kraków, Poland, 22–24 September, 2020; SAE International: Warrendale, PA, USA, 2020. [CrossRef]
48. Samsam-Khayani, H.; Chen, B.; Kim, M.; Kim, K.C. Visualization of supersonic free jet flow structures subjected to various temperature and pressure ratio conditions. *Opt. Lasers Eng.* **2022**, *158*, 107144. [CrossRef]
49. Yu, J.; Hillamo, H.; Vuorinen, V.; Sarjovaara, T.; Kaario, O.; Larmi, M. *Experimental Investigation of Characteristics of Transient Low Pressure Wall-Impinging Gas Jet*; Institute of Physics Publishing: Bristol, UK, 2011; Volume 318. [CrossRef]

50. Yu, J.; Vuorinen, V.; Kaario, O.; Sarjovaara, T.; Larmi, M. Visualization and analysis of the characteristics of transitional underexpanded jets. *Int. J. Heat Fluid Flow* **2013**, *44*, 140–154. [CrossRef]
51. Sakellarakis, V.D.; Vera-Tudela, W.; Doll, U.; Ebi, D.; Wright, Y.M.; Boulouchos, K. The effect of high-pressure injection variations on the mixing state of underexpanded methane jets. *Int. J. Engine Res.* **2021**, *22*, 2900–2918. [CrossRef]
52. Deshmukh, A.Y.; Falkenstein, T.; Pitsch, H.; Khosravi, M.; van Bebber, D.; Klaas, M.; Schroeder, W. Numerical Investigation of Direct Gas Injection in an Optical Internal Combustion Engine. *SAE Int. J. Engines* **2018**, *11*, 353–378. [CrossRef]
53. Yu, J.; Vuorinen, V.; Kaario, O.; Sarjovaara, T.; Larmi, M. Characteristics of High Pressure Jets for Direct Injection Gas Engine. *Int. J. Fuels Lubr.* **2013**, *6*, 149–156. [CrossRef]
54. Schulz, C.; Sick, V. Tracer-LIF diagnostics: Quantitative measurement of fuel concentration, temperature and fuel/air ratio in practical combustion systems. *Prog. Energy Combust. Sci.* **2005**, *31*, 75–121. [CrossRef]
55. Kirchweger, W.; Haslacher, R.; Hallmannsegger, M.; Gerke, U. Applications of the LIF method for the diagnostics of the combustion process of gas-IC-engines. *Exp. Fluids* **2007**, *43*, 329–340. [CrossRef]
56. Banholzer, M.; Vera-Tudela, W.; Traxinger, C.; Pfitzner, M.; Wright, Y.; Boulouchos, K. Numerical investigation of the flow characteristics of underexpanded methane jets. *Phys. Fluids* **2019**, *31*, 056105. [CrossRef]
57. Thawko, A.; van Hout, R.; Yadav, H.; Tartakovsky, L. Flow field characteristics of a confined, underexpanded transient round jet. *Phys. Fluids* **2021**, *33*. [CrossRef]
58. Xiao, C.N.; Fond, B.; Beyrau, F.; T'Joen, C.; Henkes, R.; Veenstra, P.; van Wachem, B. Numerical Investigation and Experimental Comparison of the Gas Dynamics in a Highly Underexpanded Confined Real Gas Jet. *Flow Turbul. Combust.* **2019**, *103*, 141–173. [CrossRef]
59. Duronio, F.; Mascio, A.D.; Villante, C.; Anatone, M.; Vita, A.D. ECN Spray G: Coupled Eulerian internal nozzle flow and Lagrangian spray simulation in flash boiling conditions. *Int. J. Engine Res.* **2023**, *24*, 1530–1544. [CrossRef]
60. Hamzehloo, A.; Aleiferis, P.G. Large Eddy Simulation of Near-Nozzle Shock Structure and Mixing Characteristics of Hydrogen Jets for Direct-Injection Spark-Ignition Engines. In Proceedings of the 10th International Conference on Heat Transfer, Fluid Mechanics and Thermodynamics, Orlando, FL, USA, 14–16 July 2014.
61. Rahantamialisoa, F.N.; Zembi, J.; Miliozzi, A.; Sahranavardfard, N.; Battistoni, M. *CFD Simulations of Under-Expanded Hydrogen Jets under High-Pressure Injection Conditions*; Institute of Physics: Bristol, UK, 2022; Volume 2385. [CrossRef]
62. Verrière, J.; Kopriva, J.E. *Simulations of an Underexpanded Round Jet Using the Lattice-Boltzmann Method*; American Institute of Aeronautics and Astronautics Inc.: Reston, VA, USA, 2021. [CrossRef]
63. Kopriva, J.E.; Laskowski, G.M.; Polidoro, F.; Li, Y.; Jammalamadaka, A.; Nardari, C. *Lattice-Boltzmann Simulations of an Underexpanded Jet from a Rectangular Nozzle with and without Aft-Deck*; American Institute of Aeronautics and Astronautics Inc.: Reston, VA, USA, 2019. [CrossRef]
64. Ren, Z.; Wen, J.X. Numerical characterization of under-expanded cryogenic hydrogen gas jets. *AIP Adv.* **2020**, *10*. [CrossRef]
65. Buttay, R.; Lehnasch, G.; Mura, A. Analysis of small-scale scalar mixing processes in highly under-expanded jets. *Shock Waves* **2016**, *26*, 193–212. [CrossRef]
66. Quimby, D.; Jacobs, G.B. *Large Eddy Simulation of a Supersonic Underexpanded Jet with a High-Order Hybrid WENO-Z/central Scheme*; American Institute of Aeronautics and Astronautics Inc.: Reston, VA, USA, 2016. [CrossRef]
67. Su, H.; Cai, J.; Qu, K.; Pan, S. Numerical simulations of inert and reactive highly underexpanded jets. *Phys. Fluids* **2020**, *32*. [CrossRef]
68. Greenshields, C.J.; Weller, H.G.; Gasparini, L.; Reese, J.M. Implementation of semi-discrete, non-staggered central schemes in a colocated, polyhedral, finite volume framework, for high-speed viscous flows. *Int. J. Numer. Methods Fluids* **2010**, *63*, 1–21. [CrossRef]
69. Versteg, H.; Malalasekera, W. *An introduction to Computational Fluid Dynamics: The Finite Volume Method*, 2nd ed.; Pearson Education: London, UK, 2007.
70. Di Angelo, L.; Duronio, F.; De Vita, A.; Di Mascio, A. Cartesian Mesh Generation with Local Refinement for Immersed Boundary Approaches. *J. Mar. Sci. Eng.* **2021**, *9*, 572. [CrossRef]
71. Kurganov, A.; Tadmor, E. New High-Resolution Central Schemes for Nonlinear Conservation Laws and Convection-Diffusion Equations. *J. Comput. Phys.* **2000**, *160*, 241–282. [CrossRef]
72. Kurganov, A.; Noelle, S.; Petrova, G. Semidiscrete Central-Upwind Schemes for Hyperbolic Conservation Laws and Hamilton–Jacobi Equations. *SIAM J. Sci. Comput.* **2001**, *23*, 707–740. [CrossRef]
73. van Leer, B. Towards the ultimate conservative difference scheme. II. Monotonicity and conservation combined in a second-order scheme. *J. Comput. Phys.* **1974**, *14*, 361–370. [CrossRef]
74. Jin, Y.; Yao, W. *LES Investigation of Real-Fluid Effect on Underexpanded Jets*; American Institute of Aeronautics and Astronautics Inc.: Reston, VA, USA, 2021. [CrossRef]
75. Duronio, F.; Montanaro, A.; Ranieri, S.; Allocca, L.; De Vita, A. Under-Expanded Jets Characterization by Means of CFD Numerical Simulation Using an Open FOAM Density-Based Solver. In Proceedings of the 15th International Conference on Engines & Vehicles, Napoli, Italy, 12–16 September 2021; SAE International: Warrendale, PA, USA, 2021. [CrossRef]
76. Wu, K.; Li, X.; Yao, W.; Fan, X. *Three-Dimensional Numerical Study of the Acoustic Properities of a Highly Underexpanded Jet*; AIAA American Institute of Aeronautics and Astronautics: Reston, VA, USA, 2015. [CrossRef]

77. Li, X.; Yao, W.; Fan, X. Large-eddy simulation of time evolution and instability of highly underexpanded sonic jets. *AIAA J.* **2016**, *54*, 3191–3211. [CrossRef]
78. Vuorinen, V.; Wehrfritz, A.; Yu, J.; Kaario, O.; Larmi, M.; Boersma, B.J. Large-eddy simulation of subsonic jets. *J. Phys. Conf. Ser.* **2011**, *318*, 032052. [CrossRef]
79. Vuorinen, V.; Keskinen, J.P.; Duwig, C.; Boersma, B.J. On the implementation of low-dissipative Runge–Kutta projection methods for time dependent flows using OpenFOAM®. *Comput. Fluids* **2014**, *93*, 153–163. [CrossRef]
80. Vuorinen, V.; Larmi, M.; Schlatter, P.; Fuchs, L.; Boersma, B.J. A low-dissipative, scale-selective discretization scheme for the Navier–Stokes equations. *Comput. Fluids* **2012**, *70*, 195–205. [CrossRef]
81. Modesti, D.; Pirozzoli, S. A low-dissipative solver for turbulent compressible flows on unstructured meshes, with OpenFOAM implementation. *Comput. Fluids* **2017**, *152*, 14–23. [CrossRef]
82. Hamzehloo, A.; Aleiferis, P.G. Numerical modelling of transient under-expanded jets under different ambient thermodynamic conditions with adaptive mesh refinement. *Int. J. Heat Fluid Flow* **2016**, *61*, 711–729. [CrossRef]
83. Sun, G.; Wu, G.; Liu, C.J. Numerical Simulation of Supersonic Flow with Shock Wave using Modified AUSM Scheme. *Int. J. Nonlinear Sci. Numer. Simul.* **2006**, *7*, 329–332. [CrossRef]
84. Vuorinen, V.; Wehrfritz, A.; Duwig, C.; Boersma, B.J. Large-eddy simulation on the effect of injection pressure and density on fuel jet mixing in gas engines. *Fuel* **2014**, *130*, 241–250. [CrossRef]
85. Vuorinen, V.; Yu, J.; Tirunagari, S.; Kaario, O.; Larmi, M.; Duwig, C.; Boersma, B.J. Large-eddy simulation of highly underexpanded transient gas jets. *Phys. Fluids* **2013**, *25*, 016101. [CrossRef]
86. Hamzehloo, A.; Aleiferis, P.G. LES and RANS modelling of under-expanded jets with application to gaseous fuel direct injection for advanced propulsion systems. *Int. J. Heat Fluid Flow* **2019**, *76*, 309–334. [CrossRef]
87. Deshmukh, A.Y.; Bode, M.; Pitsch, H.; Khosravi, M.; Bebber, D.v.; Vishwanathan, G. Characterization of Hollow Cone Gas Jets in the Context of Direct Gas Injection in Internal Combustion Engines. *SAE Int. J. Fuels Lubr.* **2018**, *11*, 353–377. [CrossRef]
88. Bartolucci, L.; Cordiner, S.; Mulone, V.; Rocco, V. Natural Gas Stable Combustion under Ultra-Lean Operating Conditions in Internal Combustion Engines. *Energy Procedia* **2016**, *101*, 886–892. [CrossRef]
89. Hamzehloo, A.; Aleiferis, P. Large eddy simulation of highly turbulent under-expanded hydrogen and methane jets for gaseous-fuelled internal combustion engines. *Int. J. Hydrogen Energy* **2014**, *39*, 21275–21296. [CrossRef]
90. De Vita, M.; Duronio, F.; De Vita, A.; De Berardinis, P. Adaptive Retrofit for Adaptive Reuse: Converting an Industrial Chimney into a Ventilation Duct to Improve Internal Comfort in a Historic Environment gas expansion. *Sustainability* **2022**, *14* 3360. [CrossRef]
91. Zhu, H.; Battistoni, M.; Manjegowda Ningegowda, B.; Nadia Zazaravaka Rahantamialisoa, F.; Yue, Z.; Wang, H.; Yao, M. Thermodynamic modeling of trans/supercritical fuel sprays in internal combustion engines based on a generalized cubic equation of state. *Fuel* **2022**, *307*, 121894. [CrossRef]
92. Li, X.; Zhou, R.; Yao, W.; Fan, X. Flow characteristic of highly underexpanded jets from various nozzle geometries. *Appl. Therm. Eng.* **2017**, *125*, 240–253. [CrossRef]
93. Anaclerio, G.; Capurso, T.; Torresi, M.; Camporeale, S.M. *Numerical Characterization of Hydrogen Under-Expanded Jets: Influence of the Nozzle Cross-Section Shape*; Institute of Physics: Bristol, UK, 2022, Volume 2385. [CrossRef]
94. Bonelli, F.; Viggiano, A.; Magi, V. A numerical analysis of hydrogen underexpanded jets under real gas assumption. *J. Fluids Eng. Trans. ASME* **2013**, *135*. [CrossRef]
95. Kaario, O.; Vuorinen, V.; Hulkkonen, T.; Keskinen, K.; Nuutinen, M.; Larmi, M.; Tanner, F.X. Large eddy simulation of high gas density effects in fuel sprays. *At. Sprays* **2013**, *23*, 297–325. [CrossRef]
96. Pope, S.B. *Turbulent Flows*; Cambridge University Press: Cambridge, UK, 2001.
97. Weickert, M.; Teike, G.; Schmidt, O.; Sommerfeld, M. Investigation of the LES WALE turbulence model within the lattice Boltzmann framework. *Comput. Math. Appl.* **2010**, *59*, 2200–2214. [CrossRef]
98. Huang, S.; Li, Q.S. A new dynamic one-equation subgrid-scale model for large eddy simulations. *Int. J. Numer. Methods Eng.* **2010**, *81*, 835–865.
99. Yoshizawa, A; Horiuti, K. A statistically-derived subgrid-scale kinetic energy model for the large-eddy simulation of turbulent flows. *J. Phys. Soc. Jpn.* **1985**, *54*, 2834–2839. [CrossRef]
100. Munday, D.; Gutmark, E.; Liu, J.; Kailasanath, K. Flow structure and acoustics of supersonic jets from conical convergent-divergent nozzles. *Phys. Fluids* **2011**, *23*, 116102,
101. Garnier, E.; Adams, N.; Sagaut, P. *Large Eddy Simulation for Compressible Flows*; Springer Science & Business Media: Berlin/Heidelberg, Germany, 2009.
102. Rana, Z.A.; Thornber, B.; Drikakis, D. Transverse jet injection into a supersonic turbulent cross-flow. *Phys. Fluids* **2011**, *23*, 046103.
103. Hamzehloo, A.; Aleiferis, P.G. Gas dynamics and flow characteristics of highly turbulent under-expanded hydrogen and methane jets under various nozzle pressure ratios and ambient pressures. *Int. J. Hydrogen Energy* **2016**, *41*, 6544–6566. [CrossRef]
104. Duronio, F.; Ranieri, S.; Mascio, A.D.; Vita, A.D. Simulation of high pressure, direct injection processes of gaseous fuels by a density-based OpenFOAM solver. *Phys. Fluids* **2021**, *33*, 066104.
105. Duronio, F.; Montanaro, A.; Allocca, L.; Ranieri, S.; De Vita, A. Effects of Thermodynamic Conditions and Nozzle Geometry in Gaseous Fuels Direct Injection Process for Advanced Propulsion Systems. In Proceedings of the WCX SAE World Congress Experience, Detroit, MI, USA, 18–20 April 2020; SAE International: Warrendale, PA, USA, 2022. [CrossRef]

106. Banholzer, M.; Müller, H.; Pfitznery, M. *Numerical Investigation of the Flow Structure of Underexpanded Jets in Quiescent Air Using Real-Gas Thermodynamics*; American Institute of Aeronautics and Astronautics Inc.: Reston, VA, USA, 2017. [CrossRef]
107. Traxinger, C.; Banholzer, M.; Pfitzner, M. Real-Gas Effects and Phase Separation in Underexpanded Jets at Engine-Relevant Conditions. In Proceedings of the 2018 AIAA Aerospace Sciences Meeting, Kissimmee, FL, USA, 8–12 January 2018. [CrossRef]
108. Rahantamialisoa, F.; Battistoni, M.; Miliozzi, A.; Sahranavardfard, N.; Zembi, J. *Investigations on Hydrogen Injections Using a Real-Fluid Approach*; SAE International: Warrendale, PA, USA, 2023. [CrossRef]
109. Yosri, M.R.; Talei, M.; Gordon, R.; Brear, M.; Lacey, J. *A Numerical Simulation of an Under-Expanded Jet Issued from a Prototype Injector*; The University of Queensland: Brisbane, Australia, 2020. [CrossRef]
110. Bartolucci, L.; Cordiner, S.; Mulone, V.; Scarcelli, R.; Wallner, T.; Swantek, A.; Powell, C.; Kastengren, A. Gaseous jet through an outward opening injector: Details of mixing characteristic and turbulence scales. *Int. J. Heat Fluid Flow* **2020**, *85*, 108660. [CrossRef]
111. Cao, W.; Zhou, Z.; Zhou, W.; Xu, S.; Xiao, Q.; Cao, W.; Jiao, F.; Zhang, Y.; Yu, S.; Xu, S. The flow field behaviours of under-expansion jet flame in premixed hydrogen/air explosion venting. *Int. J. Hydrogen Energy* **2022**, *47*, 10420–10430. [CrossRef]
112. Duronio, F.; Di Mascio, A.; De Vita, A.; Innocenzi, V.; Prisciandaro, M. Eulerian–Lagrangian modeling of phase transition for application to cavitation-driven chemical processes. *Phys. Fluids* **2023**, *35*, 053305.
113. Förster, F.J.; Baab, S.; Steinhausen, C.; Lamanna, G.; Ewart, P.; Weigand, B. Mixing characterization of highly underexpanded fluid jets with real gas expansion. *Exp. Fluids* **2018**, *59*. [CrossRef]
114. Verhelst, S.; Sierens, R. Hydrogen engine-specific properties. *Int. J. Hydrogen Energy* **2001**, *26*, 987–990. [CrossRef]

materials

MDPI

Article

Mechanisms of Gravitational Influence on Weld Pool Behavior and Weld Bead Performance in Variable Polarity Plasma Arc Welding across Different Welding Position

Jingbo Liu [1,2], Fan Jiang [1,3,*], Shujun Chen [1], Bin Xu [1,2,4], Guokai Zhang [1], Wei Cheng [3] and Xinqiang Ma [3]

[1] Engineering Research Center of Advanced Manufacturing Technology for Automotive Components Ministry of Education, Faculty of Materials and Manufacturing, Beijing University of Technology, Beijing 100124, China; liujbbjut@163.com (J.L.); sjchen@bjut.edu.cn (S.C.); xubin2019@bjut.edu.cn (B.X.); gkzhang@bjut.edu.cn (G.Z.)
[2] Joining and Welding Research Institute, Osaka University, Osaka 567-0047, Japan
[3] Laser Institute, Qilu University of Technology (Shandong Academy of Sciences), Jinan 250353, China
[4] State Key Laboratory of Advanced Welding and Joining, Harbin Institute of Technology, Harbin 150001, China
* Correspondence: jiangfan@bjut.edu.cn; Tel.: +86-13720087645

Abstract: This article comprehensively explores the cross-scale effects of gravity on macroscopic flow formation and weld bead formation in variable polarity plasma arc welding. Gravity-induced changes in welding direction were achieved through welding at different spatial positions. The properties of the weld bead were investigated at various spatial locations. Additionally, an elemental tracing technique was employed to study the internal flow behavior of molten metal. In the flat welding position, there is an observable trend of increasing grain size in the welded bead, accompanied by a significant expansion of the coarse grain zone. Consequently, the properties of the weld bead in the flat position are inferior to those achieved in the vertical welding position. This phenomenon can be attributed to the accumulation of molten metal at the exit side of the keyhole, resulting in temperature accumulation. Research indicates that the internal flow within the weld pool plays a critical role in causing this phenomenon. The study's findings reveal the presence of two distinct vortex flow patterns within the weld pool: one aligned with the welding direction and the other directed towards the interior of the weld pool. Particularly noteworthy is the substantial expansion of the flow channel area in the flat welding position, which significantly amplifies the impact of internal flow. This enhanced flow intensity inevitably leads to the increased buildup of molten metal at the keyhole exit side. These studies lay the groundwork for achieving high-quality and controllable spatial-position welding.

Keywords: molten metal; flow behavior; three-dimensional flow; grain size; flow channel

Citation: Liu, J.; Jiang, F.; Chen, S.; Xu, B.; Zhang, G.; Cheng, W.; Ma, X. Mechanisms of Gravitational Influence on Weld Pool Behavior and Weld Bead Performance in Variable Polarity Plasma Arc Welding across Different Welding Position. *Materials* **2023**, *16*, 6457. https://doi.org/10.3390/ma16196457

Academic Editors: Vasily Novozhilov and Cunlu Zhao

Received: 21 August 2023
Revised: 14 September 2023
Accepted: 26 September 2023
Published: 28 September 2023

1. Introduction

Variable polarity plasma arc (VPPA) welding gained widespread application in the field of aluminum alloy structural connections due to its cathode cleaning effect and concentrated arc energy characteristics [1–6]. Compared to traditional arc welding techniques, VPPA welding, with its unique keyhole welding mode, effectively eliminates porosity, resulting in superior welding quality and properties of welding bead [7]. Consequently, VPPA welding exhibits special adaptability in areas requiring high-quality welds, such as aerospace and large ship manufacturing [8]. However, the intricate welding mode associated with keyhole also constrains the development of VPPA welding technology [9]. The presence of keyhole makes the flow of molten metal within the weld pool more complex, which could lead to weld pool collapse and welding instability [10]. In practical engineering applications, as workpiece volumes increase, operations such as flipping or moving become challenging. Therefore, repositioning the welding torch for flat welding position becomes unavoidable. Many scholars propose that vertical welding is the optimal

position for VPPA welding, as it allows molten metal to flow and solidify more effectively within the weld pool, resulting in high-quality welds [11,12]. However, during flat welding, the change in gravity direction disrupts force equilibrium, potentially increasing welding process instability and affecting the properties of welding bead [13]. Hence, investigating the influence of gravity on the molten metal in the flat VPPA welding becomes crucial.

Several scholars conducted research on the properties of VPPA-welded beads [14,15]. Cai et al. pointed out that the properties of VPPA-welded beads surpass those of traditional arc-welded beads [16]. Yan et al. investigated the influence of different torch angles on bead performance, highlighting that adjusting the flow behavior of molten metal and enhancing the performance of VPPA-welded beads in the transverse welding configuration can be achieved by altering the torch angle [17]. However, transverse welding is more adjustable due to evident gravitational differences, which contrasts with horizontal welding. In the case of horizontal welding, as gravity acts on the pool's exit side and is challenging to optimize through changes in welding parameters or other conditions, exploring the flow behavior and properties of VPPA welding in the horizontal position holds significant importance for the successful industrial application of this advanced technique. During the welding process, the flow and solidification of molten metal significantly influence the properties of welded beads, thereby impacting the properties of welding beads [18–20].

Numerous scholars conducted research on VPPA welding in different welding positions. Maintaining the flow behavior of molten metal is considered a key factor in ensuring welding stability [21,22], making the study of molten metal flow within the weld pool crucial [23–25]. Wu et al. established a multi-factor-coupled model through simulation to investigate the influence of different driving forces on the weld pool flow behavior during keyhole welding [26]. They pointed out that arc shear force and arc pressure are the main driving forces that induce directed flow of molten metal within the weld pool. Liu et al. utilized oxidized wires in the welding process to release oxide particles and track their flow behavior [27]. They confirmed that in vertical welding, gravity assists in better guiding the flow of molten metal towards solidification at the rear of the weld pool, with flow occurring from the keyhole front side to the rear side. Morisada et al. used metallic tungsten as a tracer particle to capture the flow behavior of the weld pool during flat welding [28]. The material flow was obtained by three-dimensional visualization through X-ray radiography. Ahn et al. used metal tungsten particles and an X-ray system to capture internal flow patterns of the weld pool, identifying arc shear force as the primary driving force during welding [29]. However, due to the significantly higher density of metal tungsten particles compared to molten metal, this method may not accurately reflect internal flow dynamics. In order to obtain the flow trajectory of the metallic material, Mugada et al. characterized the flow behavior of the base material by incorporating copper metal into it to trace the flow trajectory of copper metal [30]. However, this approach is only applicable to solid-state joining processes, as introducing copper into the molten pool during arc welding would compromise its stability. Yan et al. employed elemental tracing, adding Cu elements to form Al-Cu compounds during welding, and tracked their flow behavior within the weld pool [31]. Al-Cu compounds naturally exist in both the pool and weld, providing a more precise representation of internal flow dynamics. Nevertheless, the mentioned studies mainly focused on macroscopic pool flow, lacking research on microstructural performance, particularly the cross-scale impact of flow-induced microstructural changes in properties of welding bead.

This study focuses on examining the variations in the mechanical properties of welded beads at different welding positions, and aims to analyze and discuss the underlying reasons for these differences based on flow behavior. Specifically, the investigation delves into the gravitational influence on the internal flow dynamics and properties of aluminum alloy VPPA welding. To capture the flow patterns within the weld pool, the elemental tracer method was employed. Leveraging three-dimensional reconstruction techniques, the study unveiled the flow patterns within the spatial domain of the weld pool. Furthermore, the study explored the mechanism through which gravity influences the flow of molten metal

during the variable polarity plasma arc welding process. The outcomes of this research provide valuable insights for enhancing the horizontal welding process of aluminum alloy VPPA welding.

2. Materials and Methods

2.1. Common Experimental Setup and Welding Conditions

The experimental design for VPPA welding is illustrated in Figure 1. The welding system parameters include welding current, plasma gas, and shielding gas, set at 140/170 A (EN/EP), 4 L/min, and 20 L/min, respectively, as shown in Figure 1a. Both the plasma gas and shielding gas used are argon. The welding torch traverse speed and filler wire feed speed are 15 cm/min and 100 cm/min, respectively. The experimental setup is positioned in two spatial orientations: flat and vertical. In the flat position, the plate is parallel to the ground, the torch is perpendicular to the plate, and gravity is perpendicular to the direction of the weld, as shown in Figure 1. In the vertical position, the torch maintains its position relative to the base metal, while the plate surface is perpendicular to the ground, and gravity is opposing the direction of the weld. Furthermore, the side forming the weld seam corresponds to the keyhole rear side, with the opposite side being the front wall of the pool. The keyhole entry side, which comes into direct contact with the arc, represents the top side, and the keyhole exit corresponds to the bottom of the keyhole.

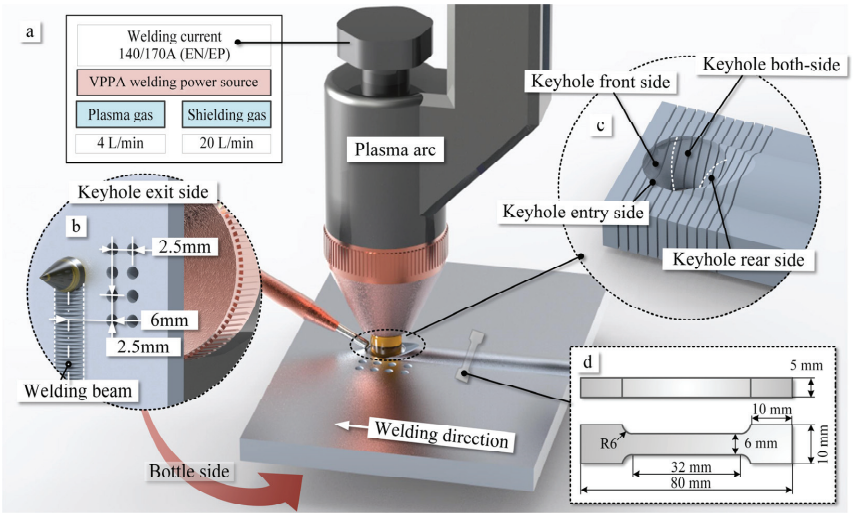

Figure 1. Schematic diagram of the experimental VPPA welding system. (**a**) Schematic diagram of the VPPA welding system. (**b**) Distribution of temperature measurement points on both sides of the weld pool. (**c**) Schematic diagram of the keyhole wall. (**d**) Schematic diagram of the sampling position.

The base material chosen is a 5052-aluminum alloy with dimensions of 5 mm × 200 mm × 200 mm. In order to minimize experimental errors during both the in-process and post-welding stages of wall welding, filler wire ER5183 with the same chemical composition as the base material was used for the structural performance experiments. The detailed chemical composition of the selected material is provided in Table 1.

Table 1. Chemical composition of base metal and feed wire (wt.%).

Material	Mg	Mn	Cr	Si	Fe	Zn	Cu	Al
5A06	5.80~6.80	0.50~0.80	-	≤0.40	≤0.40	≤0.20	≤0.10	Bla.
ER5183	4.50	0.70	0.15	≤0.40	≤0.40	≤0.25	≤0.10	Bla.
ER2319	0.02	0.20	-	0.20	≤0.40	≤0.10	5.80	Bla.

2.2. Mechanical Properties of Welding Bead

To assess the strength of weld beads and understand the influence of internal flow within the weld pool on mechanical properties, weld bead specimens were cut across the welding direction, as depicted in Figure 1d. Following corrosion, the cross-sections of the weld beads were captured using laser confocal microscopy, allowing measurement of grain size and distribution. For testing mechanical properties, specimens with specific dimensions were employed, as shown in Figure 1d. The fracture surfaces of tension tests were obtained using scanning electron microscopy Quanta 650 FEG (Thermo Fisher Scientific, Waltham, MA, USA), allowing measurement of elongation and tensile strength of the welded beads.

2.3. Measurement of Molten Metal Flow in the Weld Pool

To capture the flow behavior within the weld pool, the elemental tracing method and axial tomography method were applied. The elemental tracing method involved the introduction of compounds into the weld pool capable of characterizing molten metal flow. The axial tomography method facilitated the three-dimensional reconstruction of these characterized elemental compounds, as depicted in Figure 2. Similar to the attributes of the welding base material, filler wire ER2319 was utilized, with the unique inclusion of the element Cu, as depicted in Table 1. Additionally, the chosen Cu element can readily form compounds with Al. These selected compounds were etched using Keller reagent. Among the composed compounds, the grain boundaries of the Al-Cu compound have the highest energy, resulting in their preferential corrosion, as shown in Figure 2d, when the etching process is controlled for a fixed duration. By doing so, the distribution of the Al-Cu compound at different welding pool sections could be preserved, facilitating the tracking of internal flow within the weld pool. Furthermore, when ER5183 filler wire, similar in composition to the base material, was added, it was used for assessing structural and mechanical properties, as depicted in Figure 2c. Due to the absence of Cu in ER5183, there is no occurrence of the black region corresponding to Al-Cu compounds.

Through laser confocal microscopy, a sequential imaging of cross-sectional slices of solidified weld pool keyholes was performed, enabling the axial tomography of oxide compounds, as shown in Figure 2b. Rapid shutdown of the welding power source was achieved by cutting off the supply of arc and shielding gas from the welding machine. This method efficiently induced the instantaneous oxidation and solidification of the molten metal within the weld pool, preserving the state of the weld pool keyhole during welding. For the observation of Al-Cu compound distribution, a total of 11 cross-sections were cut from the front to back of the keyhole, as illustrated in Figure 2a. The dimensions of the keyhole are 12 mm in length and 10 mm in width. Each cut piece measures 5 mm × 15 mm × 1 mm, as shown in Figure 2a. Employing this approach, the distribution of the Al-Cu compound in the current piece can be obtained. Each etched piece was photographed using laser confocal microscopy, as shown in Figure 2d. Based on the acquired distribution of Al-Cu compounds, a three-dimensional reconstruction yields the compound distribution within the weld pool keyhole. Furthermore, the origin of the coordinate system is set at the edge of the weld pool, where the filler wire is introduced into the pool. The x-direction represents the opposite direction of welding, the y-direction points toward the side wall of the pool, and the z-direction indicates the depth of the weld pool.

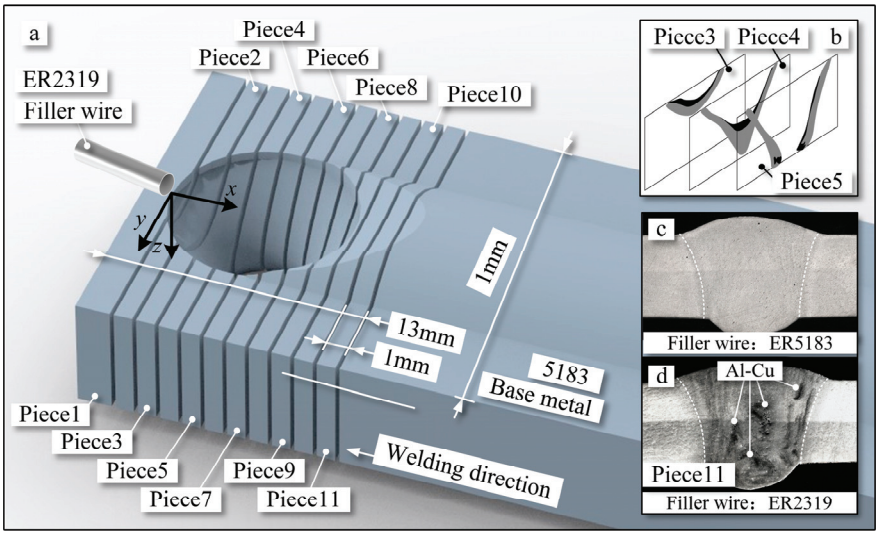

Figure 2. Schematic illustration of keyhole and weld pool pieces. (**a**) Schematic illustration of weld pool pieces. (**b**) Schematic diagram of slice reconstruction. (**c**) Results of cross-sectional corrosion of the weld seam with ER5183 filler wire. (**d**) Results of cross-sectional corrosion of weld seam with ER2319 filler wire.

2.4. Measurement of Temperature Distribution in the Weld Pool

Thermocouples were positioned on one side of the weld pool because in both flat and vertical positions, the molten metal flow within it is symmetrical, as shown in Figure 1. Temperatures were measured at distances of 6 mm and 8.5 mm from the weld seam edge. Multiple thermocouple measurement points and repeated experiments were employed to minimize the impact of errors on the experimental results.

3. Results

3.1. Properties of Welding Bead

Figure 3 illustrates the properties of the welded bead during vertical welding. Figure 3a–d,f depicts the properties at different positions of the welding bead during the vertical welding position. The top side corresponds to the side away from gravity. There are variations in grain distribution across different zones. The base metal (BM) displayed compressed grains oriented in line with the rolling direction, indicative of its manufacturing process. In both the heat-affected zone (HAZ) and weld bead (WB), a characteristic as-cast solidification structure was evident, characterized by the presence of equiaxed grains. A parallel observation was made on the top side, except for the HAZ, as shown in Figure 3a,c,d,f. In the weld bead center (CWB), the presence of a coarser-grained zone, such as the columnar-to-equiaxed transition, was noted. Its area was measured to be 26.6 mm^2. During vertical welding, the CWB exhibits a droplet-shaped pattern, with a wider area near the weld root and a narrower area near the weld crown. For the vertical position, the crown height and root penetration were measured to be 1.8 mm and 1.1 mm, respectively.

The grain distribution pattern during the flat welding position is similar to that during the vertical welding position, as shown in Figures 3e and 4e. Properties at different positions of the welding bead during the vertical welding position are depicted in Figure 4a–d,f. The coarse-grained zone in flat welding is also concentrated in the center of the weld, with an area of 46.2 mm^2. During flat welding, the CWJ shows a square distribution, evenly spread across the center of the weld pool. However, in the flat welding position, the size of the area near the weld root is larger than that in vertical welding. The central coarse-grained

zone in flat welding is larger than that in vertical welding. For the flat position, the crown height and root penetration were measured to be 0.7 mm and 2.3 mm, respectively.

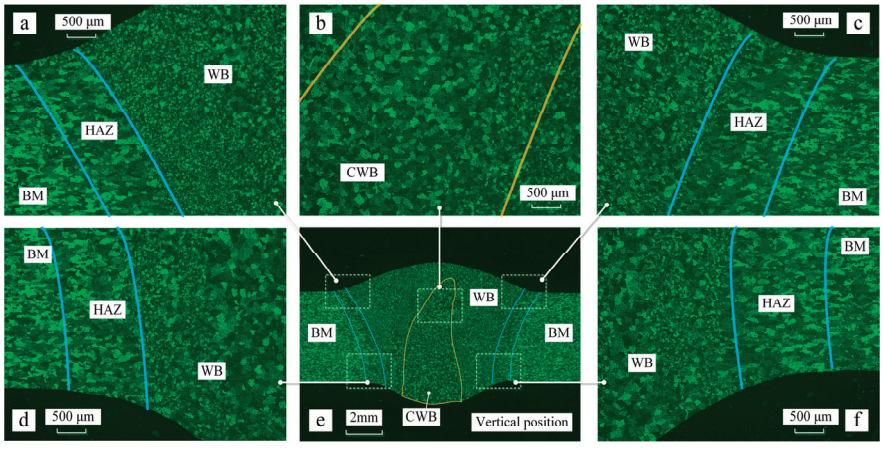

Figure 3. Properties of the welding bead in the vertical position. (**a**) Properties of the part of the welding bead on the upper left side. (**b**) Properties of the part of the welding bead on the middle side. (**c**) Properties of the part of the welding bead on the upper right side. (**d**) Properties of the part of the welding bead on the lower left side. (**e**) Properties of the welding bead. (**f**) Properties of the part of the welding bead on the lower right side.

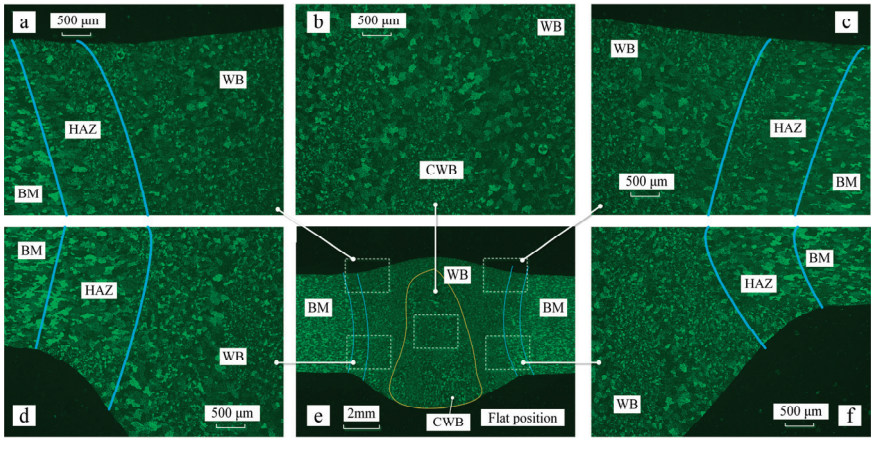

Figure 4. Properties of the welding bead in the flat position. (**a**) Properties of the part of the welding bead on the upper left side. (**b**) Properties of the part of the welding bead on the middle side. (**c**) Properties of the part of the welding bead on the upper right side. (**d**) Properties of the part of the welding bead on the lower left side. (**e**) Properties of the welding bead. (**f**) Properties of the part of the welding bead on the lower right side.

The grain size was determined using the standard linear intercept method, which is the primary technique for determining grain size. The grain sizes on the lower side of the welded bead were almost the same. However, the grain sizes varied with the welding position within the range of error. The grain size of the base material was around 88 μm, as showed in Figure 5a. For vertical welding position, the sizes of the HAZ, WB, and CWB were measured to be 106 μm, 66 μm, and 126 μm, respectively. In contrast, for flat welding, these sizes were 110 μm, 70 μm, and 156 μm, respectively. The grain sizes increased by 3.7%,

6%, and 23.8% for the HAZ, WB, and CWB, respectively, during flat welding. Particularly, in the vertical welding position, the average grain size in the weld center was larger than the average grain size in the weld bead by 20 μm, while in flat welding, this difference increased to 46 μm. The variation in grain size at the center of the welded bead was smaller compared to the flat welding position.

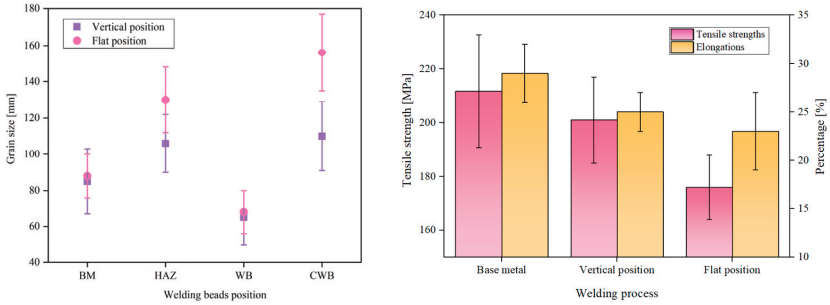

Figure 5. (**a**) Grain size of the welding bead. (**b**) The tensile strength and elongation of welds.

Furthermore, the mechanical properties of the welded bead were measured, as shown in Figure 5b. Five samples were taken for each welding position. For vertical welding, the tensile strength of the weld bead was 202 MPa, and for flat welding, it was 176 MPa. Both values were lower than the tensile strength of the base material (213 MPa). The tensile strength during flat welding was significantly lower than that during vertical welding. The elongation of the base material was 28%, while for vertical and flat welding, the elongation rates were 25% and 23%, respectively. The elongation rates of both welding positions were slightly lower than that of the base material, and the elongation rate in flat welding was still lower than that in the vertical welding position.

The SEM images of the tensile fracture surfaces at different welding positions are shown in Figure 6. The tensile result of the base material serves as a reference. The fracture surfaces exhibit extensive tearing, dimples, and clear indications of fracture, as depicted in Figure 6a. The reference outcome from the BM displays a fracture surface exhibiting numerous tears and dimples, indicative of a quasi-cleavage fracture. In both vertical position and BM, equiaxial dimples manifest on the fracture surface of the welded bead, depicted in Figure 6a,b. Conversely, in the case of the flat welding position, torn dimples become apparent. All these instances exhibit ductile fracture characteristics under tensile testing conditions. Notably, within the flat welding position, specimens fractured at the HAZ of the welds, whereas the BM and vertical position experienced random fractures.

3.2. Internal Flow Behavior within the Weld Pool

During vertical welding position, the distribution of the Al-Cu compound within the weld pool keyhole is depicted in Figure 7. Pieces 1 to 11 represent cross-sections along the welding direction of the keyhole. Pieces 1 to 4 correspond to the keyhole front side of the weld pool, as shown in Figure 7a–d. In these figures, the red zones denote the flow channels, while the blue areas indicate the Al-Cu compound. In Figure 7a, the filler wire is introduced into the weld pool, and upon its melting, it becomes mixed with the molten metal generated from the base material. As the welding progresses, molten metal is continually conveyed into the weld pool. The metal flows along the edges of the keyhole, moving from the keyhole entry side to the keyhole exit side, as illustrated in Figure 7b–d.

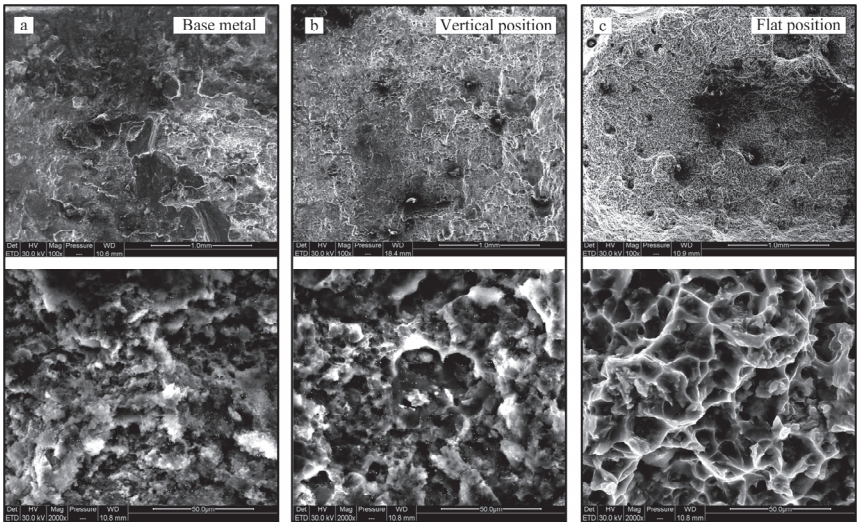

Figure 6. SEM fractography of the fractured surfaces. (**a**) Base metal. (**b**) Vertical position. (**c**) Flat position.

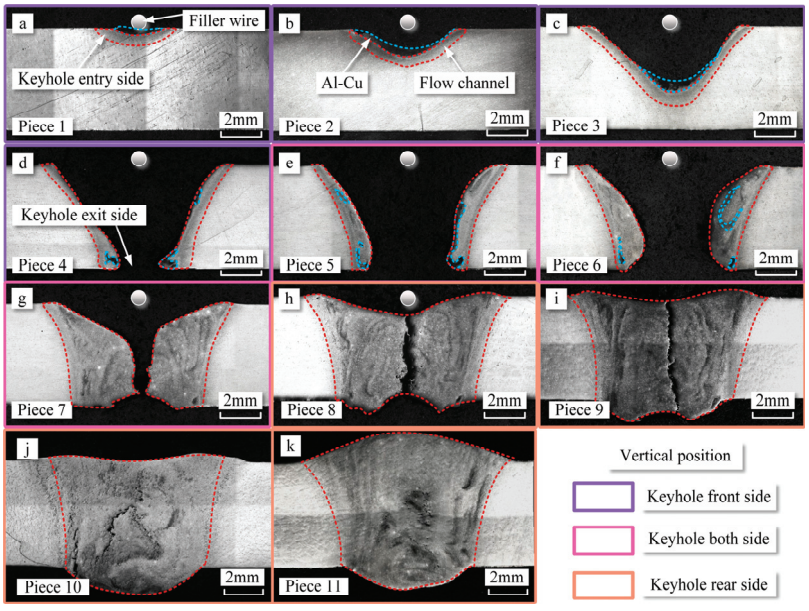

Figure 7. The internal flow behavior of molten metal in the vertical position. (**a**) Piece 1. (**b**) Piece 2. (**c**) Piece 3. (**d**) Piece 4. (**e**) Piece 5. (**f**) Piece 6. (**g**) Piece 7. (**h**) Piece 8. (**i**) Piece 9. (**j**) Piece 10. (**k**) Piece 11.

While the flow on either side of the weld is not perfectly symmetric in actual welding, the overall flow channels are quite consistent along both sides of the weld. To facilitate the comparison of the changes in flow channels from the front wall to the rear wall of the weld pool, the actual area is calculated as half of the flow channel area. This study focuses on both a vertical and flat position, making the flow of molten metal relatively symmetric on both sides of the weld pool. The flow channel areas for Piece 1 to Piece 4 are 3.78 mm^2,

4.31 mm^2, 4.84 mm^2, and 5.46 mm^2, respectively. The flow channel area at the front wall increases by 44%.

From Pieces 1 to 6, the welding direction is reversed, which corresponds to the primary direction of molten metal flow. The observation of metal flow within the weld pool keyhole is based on differences in the distribution of Al-Cu compounds. After extraction, a schematic representation of this process is illustrated in Figure 8. The accumulation of Al-Cu compounds in the black zone occurs on the surface of the weld pool, consistently remaining near the bottom of the current piece, as shown in Figure 8a–c. Tracing elements on the same side exhibit continuity. As a result, the depths of the weld pool front wall in Pieces 3 and 4 from the keyhole entry side are 0.25 mm and 0.76 mm, respectively, as depicted in Figure 4c,d. Within the flow channel, Al-Cu compounds exhibit an alternating arrangement, forming a regularly patterned vortex street phenomenon.

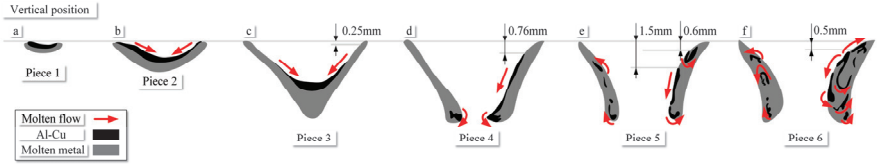

Figure 8. Schematic illustration of molten metal flow in the vertical position (**a**) Piece 1. (**b**) Piece 2. (**c**) Piece 3. (**d**) Piece 4. (**e**) Piece 5. (**f**) Piece 6.

Pieces 5 to 7 represent sections of the keyhole on both sides, as depicted in Figure 7e–g. Moving from the keyhole front side to both sides, the area of the flow channel gradually increases. Al-Cu compound near the keyhole front side flow along the wall surface. In the weld pool sidewall, some Al-Cu compounds exhibit flow from the wall surface into the interior of the weld pool. Al-Cu compounds flow along the pool wall to the keyhole exit side and generate vortices within the pool interior at the bottom, as shown in Figure 8d–f. Furthermore, with the increase in the flow channel area, internal flow also occurs within the pool wall, as depicted in Figure 8e,f. Al-Cu compounds contribute to the inward flow. In Piece 7, near the keyhole rear side, the diffusion of Al-Cu compounds extends throughout the entire interior surface of the pool wall. The flow channel areas for Pieces 5 to 7 are 5.78 mm^2, 7.36 mm^2, and 13.74 mm^2, respectively. The largest flow channel in the weld pool sidewall is 137.77% larger than that in the front wall.

Particularly, due to the method of arc disruption used to capture the keyhole's morphology during welding, the weld pool keyhole exhibits cracks when suddenly losing heat input, as illustrated in Figure 7h. An interesting phenomenon was observed in the weld pool sidewall: the tracing elements at a depth of 0.6 mm from the wall's surface exhibit bifurcation. Some tracing elements create vortices flowing inward along the wall, while another group flows toward the keyhole exits side, generating a second vortex.

Pieces 8 to 11 correspond to sections of the keyhole rear side, as illustrated in Figure 7h–k. The flow channel areas for Pieces 8 to 11 are 19.44 mm^2, 23.13 mm^2, 24.80 mm^2, and 28.26 mm^2, respectively. The largest flow channel in the keyhole rear side is 106% larger than that in the keyhole on both sides. However, the flow channel area on the keyhole rear side only increases by 45%. From Piece 8 to Piece 11, as the solidification zone shifts to the keyhole rear side, the weld bead's crown and root form gradually. The specific flow patterns within the weld pool are challenging to discern. However, their distribution patterns can be easily obtained. Al-Cu compounds are distributed across the entire keyhole rear side. After the formation of the weld bead, when the molten metal fully solidified, Al-Cu compounds are predominantly distributed throughout the cross-section, as shown in Figure 9. It can be observed that within the keyhole rear side, Al-Cu compounds are uniformly distributed at its center. However, as solidification progresses, Al-Cu compounds primarily distribute across the entire surface of the keyhole rear side.

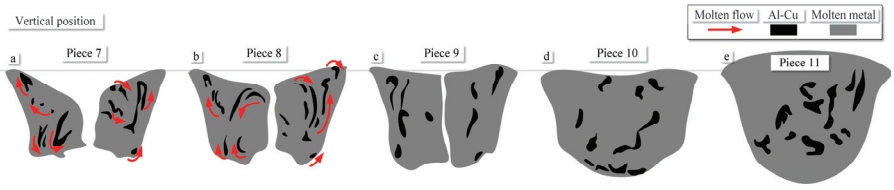

Figure 9. Schematic illustration of molten metal flow in the vertical position. (**a**) Piece 7. (**b**) Piece 8. (**c**) Piece 9. (**d**) Piece 10. (**e**) Piece 11.

During the flat position, the distribution of the Al-Cu compound in the weld pool cavity is shown in Figure 10. In these figures, the red zones denote the flow channels, while the blue areas indicate the Al-Cu compound. Similar to the vertical welding position, Pieces 1 to 4 represent the keyhole front side, as shown in Figure 10a–d. The flow channel areas for Piece 1 to Piece 4 are 3.75 mm^2, 4.54 mm^2, 4.99 mm^2, and 5.2 mm^2, respectively, indicating an increase in area by 38%. The difference in flow channel areas for the same slices compared to vertical welding is only 8%. Al-Cu compound accumulates on the surface of the weld pool, which is consistent with the vertical welding position.

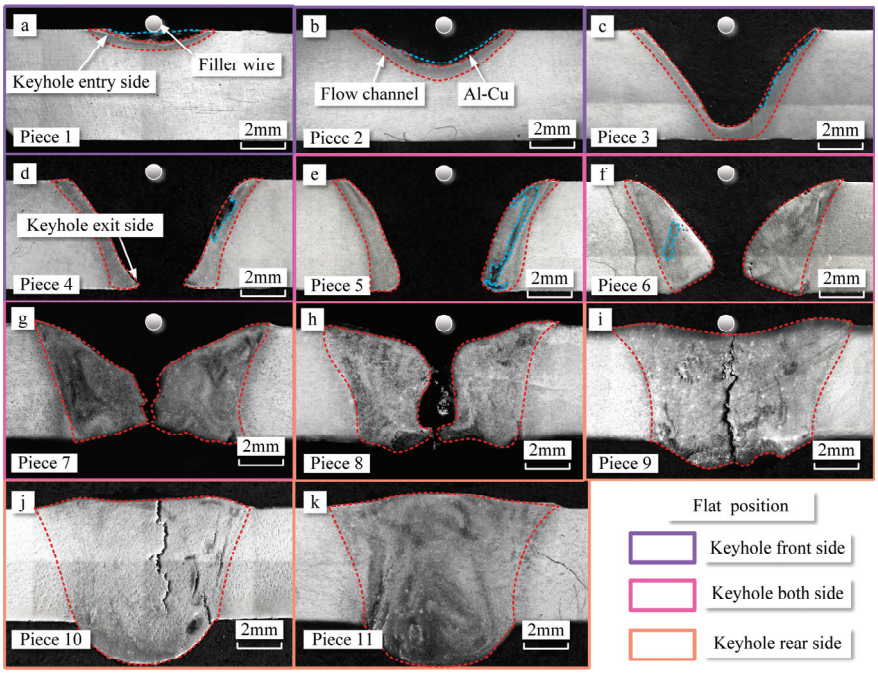

Figure 10. The internal flow behavior of molten metal in the flat position. (**a**) Piece 1. (**b**) Piece 2. (**c**) Piece 3. (**d**) Piece 4. (**e**) Piece 5. (**f**) Piece 6. (**g**) Piece 7. (**h**) Piece 8. (**i**) Piece 9. (**j**) Piece 10. (**k**) Piece 11.

The distribution schematic of the Al-Cu compound in the weld pool cavity during flat welding is shown in Figure 11. The Al-Cu compound adheres to the weld pool surface and flows along the front wall of the pool, moving from the welding entry side to the keyhole exit side. Flow towards the interior of the pool occurs at the junction between the front wall and the side wall, as shown in Figure 11d,e. Additionally, inward vortices appear at positions towards the exit side of the pool. Along the side wall of the pool, the flow channel areas for Pieces 5 to 7 are 6.02 mm^2, 9.5 mm^2, 16.12 mm^2, and 16.13 mm^2, respectively,

exhibiting a 167% increase in flow channel area from the keyhole front side to the both-side wall. Correspondingly, these areas in vertical welding at the respective positions increased by 16.2%, 64.3%, 119%, and 173.39%, indicating a significant increase in flow channel size during flat welding at the same piece positions.

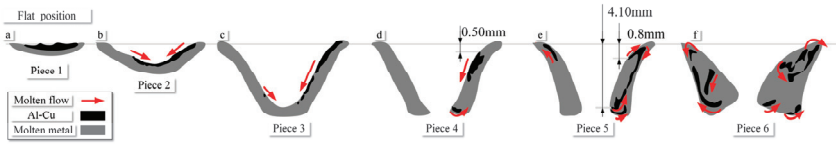

Figure 11. Schematic illustration of molten metal flow in the flat position. (**a**) Piece 1. (**b**) Piece 2. (**c**) Piece 3. (**d**) Piece 4. (**e**) Piece 5. (**f**) Piece 6.

Near the exit side of the keyhole exit side, vortices also emerge, causing the inward flow of Al-Cu towards the interior of the pool. Simultaneously, the sudden increase in the flow channel on the side wall causes earlier diffusion of the Al-Cu compound. During flat position, a separation point on the side wall of the pool is discovered at a depth of 0.8 mm. The first internal vortex appears here, followed by a second vortex towards the exit side, as depicted in Figure 11e.

In the position of flat welding, for the keyhole rear side, the flow channel areas for Pieces 8 to 11 are 17.4 mm^2, 22.94 mm^2, 24.12 mm^2, and 28.1 mm^2, respectively, as depicted in Figure 12e. The changes in flow channels at the rear wall are relatively small. These areas, corresponding to the vertical welding's respective positions, were reduced by 10%, 0.8%, 2.7%, and 0.5%. The variations in flow channels at the keyhole rear side are minor. After the formation of the weld, the Al-Cu compound is primarily distributed near the exit side of the cross-section, showing significant differences compared to vertical welding.

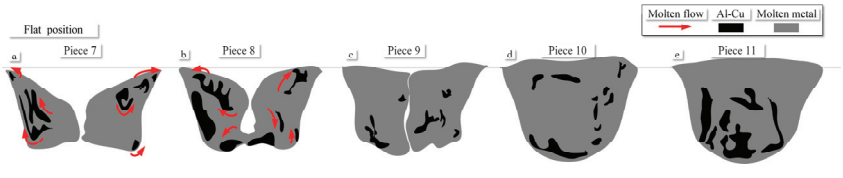

Figure 12. Schematic illustration of molten metal flow in the flat position. (**a**) Piece 7. (**b**) Piece 8. (**c**) Piece 9. (**d**) Piece 10. (**e**) Piece 11.

3.3. Temperature Distributions on the Weld Pool Surfaces

Temperature variation in HAZ of the weld seam at different welding positions is illustrated in Figure 13. The temperature change at 6 mm from the weld seam is depicted in Figure 13a, where the maximum temperatures for the top and bottle side of the flat position are 521 °C and 492 °C, respectively. The maximum temperature difference between the top and bottle side of the flat position is 29 °C. In contrast, for the vertical position, the maximum temperatures for the top and bottle side of the weld pool are 500 °C and 458 °C, respectively, resulting in a maximum temperature difference of 42 °C between the top and bottle sides. Consequently, the temperature difference between the top and bottle sides of the weld is smaller in the flat position compared to vertical welding. Notably, both for vertical and flat position welding, the temperature on the top side of the weld is higher than that on the bottle side. Moreover, the temperatures on both sides of the flat position are higher than the corresponding sides of the vertical position.

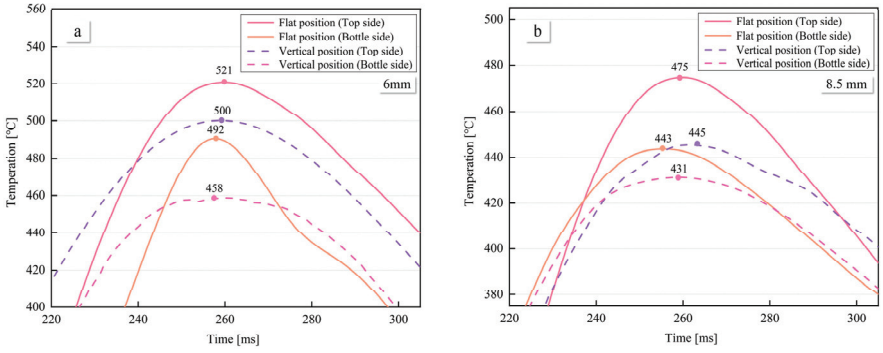

Figure 13. The average temperature distribution on the top and bottle side of the heat-affected zone of the weld pool. (**a**) The average temperature distribution of the weld pool at a distance to weld seam canter of 6 mm. (**b**) The average temperature distribution of the weld pool at a distance to weld seam canter of 8.5 mm.

The temperature change at 8.5 mm from the weld seam is shown in Figure 13b, where the maximum temperatures for the top and bottle side of the flat position are 466 °C and 443 °C, respectively, resulting in a temperature difference of 23 °C. For the vertical position, the temperature difference between the front and back sides is 27 °C. The lower temperatures and temperature differences at 8.5 mm compared to 6 mm are attributed to the increased distance from the weld pool.

4. Discussion

In VPPA welding, the flow patterns of the weld pool, temperature distribution, and grain distribution are illustrated in Figure 14. The distribution of grains on the left and right sides of the weld pool is similar during both vertical and flat welding, as shown in Figure 14. This similarity arises from the uniform distribution of the arc's effect on both sides of the keyhole. However, variations in temperature differences along the keyhole front side and rear side in different welding positions lead to differences in grain growth.

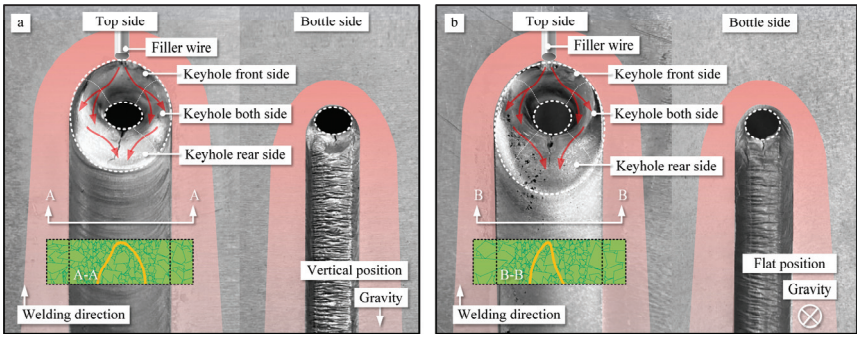

Figure 14. Schematic diagrams of weld pool flow patterns, temperature distributions and grain distributions at different welding positions. (**a**) Vertical position. (**b**) Flat position.

For the free growth model, the grain size is described by the following formula:

$$d = \frac{4\delta}{\Delta T_f \Delta S_f} \tag{1}$$

where d, ΔT_f, δ, and ΔS_f represent the grain size, undercooling, interfacial energy, and entropy of fusion, respectively. It means that at a clear ΔS_f, which is inversely proportional

to grain size, the grains begin to develop freely from these. This model claims that grain growth is solely temperature-dependent and independent of time.

According to this model, it indicates that grains begin to grow freely under a specific degree of undercooling, and their size is inversely proportional to the diameter. Based on this model, grain growth is independent of time and solely dependent on temperature. In the flat position, due to the overall higher temperature of the weld pool compared to vertical welding, and the smaller temperature difference between the top and bottle of the weld pool, the cooling rate is slower. This leads to larger grain sizes in flat welding. However, the excessively high temperature distribution results in slower grain production, further contributing to reduced mechanical properties of the welded bead. Consequently, the tensile elongation and tensile strength of the welded bead in flat welding are lower than those in vertical welding.

In the vertical welding position, the zone of coarse grain near the keyhole exit side is smaller, whereas in the flat welding position, the area of coarse grains is larger and concentrated in the middle. This phenomenon can be attributed to the temperature differential inherent in vertical welding processes, wherein the temperature gradient between the upper and lower regions of the molten metal is pronounced, resulting in accelerated solidification at the exit side of the keyhole. Variations in temperature distribution across distinct welding positions can be attributed to disparities in the dynamics of the weld pool, which, in turn, are influenced by gravitational changes. These gravitational alterations consequently impact grain distribution.

The flow of molten metal is reconstructed through the process of sectioning and three-dimensional reconstruction of the weld pool, as illustrated in Figure 15. Along the x-direction, which corresponds to the opposite direction of welding, spanning from the region proximate to the welding wire to the far side, encompassing weld pool pieces 1 through 12, the reconstructed sections offer a comprehensive insight into the internal dynamics of the molten metal within the keyhole's leading edge, side walls, as well as the accumulation at the rear side of the keyhole. The motion of the molten metal is driven by a diverse array of forces, which encompass shear forces, gravity, arc pressure, Lorentz forces, Marangoni forces, and others, as extensively discussed in reference [32]. Among these, the dominant forces driving the flow in the weld pool are the arc shear forces, gravity, and arc pressure [33]. Hence, this study primarily delves into the discussion of the three aforementioned key driving forces and their effects on various flow behaviors.

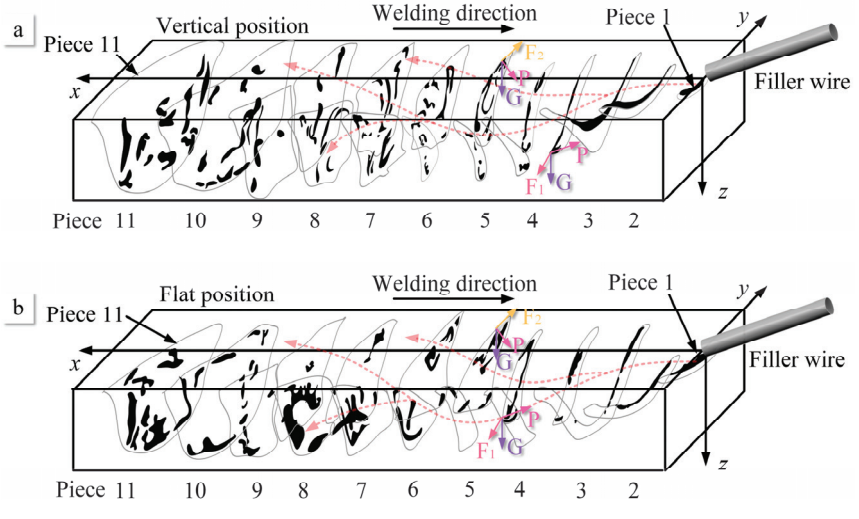

Figure 15. Three-dimension reconstruction of the weld pool pieces. (**a**) Vertical position. (**b**) Flat position.

The arc shear force is a result of the directed flow of the plasma arc, causing the molten metal to flow. Due to the distinctive shape of the weld pool with a wide keyhole entry side and a narrow keyhole exit side, there exists a countercurrent flow of the plasma arc within the pool. This countercurrent flow generates two opposite deflections on the weld pool walls: one directed towards the entrance side of the pool (F1) and the other towards the exit side of the pool (F2), as depicted in Figure 15. According to the simulation results by Wu et al., it was found that the arc shear force directed towards the keyhole exit side is smaller than that directed towards the keyhole entry side [31]. Gravity (G) acts vertically downward towards the horizontal ground and is considered the second most influential factor affecting the flow in the weld pool. Arc pressure (p) points from the liquid surface towards the center of the pool, as demonstrated by Wu et al.'s research [33]. However, due to the presence of the conical keyhole, the direction of arc pressure at different positions on the weld pool's wall varies. Specifically, this results in opposing directions of arc pressure at the keyhole entry side and the keyhole exit side.

The primary flow pattern of the molten metal within the weld pool involves flowing from the keyhole front side to the keyhole both side and then towards the keyhole rear side. At the front wall of the weld pool, the narrowness of the flow channels confines the movement of the molten metal due to applied forces, as illustrated in Figure 16a. The blue arrows show the flow behavior at the surface of the molten pool and the red arrows show the flow behavior inside the molten pool. On the upper side of the weld pool, the effects of gravity and arc pressure on the front wall are more significant than the arc shear force F1. As a result, the molten metal flows from the keyhole front side to the keyhole exit side. Simultaneously, near the keyhole both-side wall, the direction of the gravitational and arc shear force components on the lower side of the weld pool aligns, thus causing the molten metal to flow towards the exit side of the pool. Due to the similarity in the flow channels on the front side of the keyhole, the differences in flow patterns between the vertical and flat welding positions are relatively small. Gravity has a minor impact on the flow of molten metal on the front wall of the weld pool.

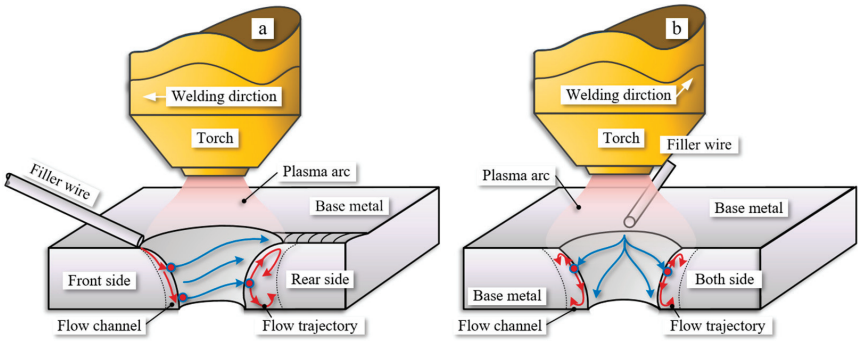

Figure 16. Schematic of the molten metal flow inside the VPPA weld pool. (**a**) Vertical position. (**b**) Flat position.

The flow patterns of molten metal on the keyhole both-side wall can be divided into two types: the first involves the flow from the sidewalls to the rear wall of the pool, while the second pertains to the occurrence of internal vortex flow. Vortex flows are observed at two positions within the weld pool: one near the entrance side and the other near the exit side of the pool, as shown in Figure 16b. The vortex flow near the keyhole entry side is a result of the combined effects of gravitational force and arc pressure, causing a portion of the molten metal along the pool wall to undergo inward convection. On the other hand, the vortex flow near the exit side is attributed to the limited liquid wall area, leading to an accumulation of molten metal in this zone. The forces at this location, including gravity, arc

shear force, and arc pressure, all direct towards the interior of the pool, thus enhancing the prominence of the vortex flow.

In the flat position, the influence of gravity drives the molten metal to flow more towards the keyhole exit side than towards the keyhole rear side, as indicated in Piece 6 of Figure 15. As a result, the disparity in the flow channel area within the weld pool is considerably more conspicuous in the flat welding position when juxtaposed with the vertical position. Furthermore, this phenomenon precipitates the earlier onset of internal convection within the weld pool during flat welding operations. In the context of VPPA welding, the existence of internal vortices instigated by the prevailing driving forces amplifies the active agitation of molten metal within the weld pool. This phenomenon, in turn, plays a pivotal role in augmenting the defect mitigation and enhancing the microstructural performance of VPPA welding when contrasted with alternative welding methodologies.

Due to the further expansion of the flow channels at the keyhole rear side, the internal flow within the weld pool becomes challenging to track. However, the internal vortices within it can still be discerned. Based on my previous research, two opposing flow patterns exist for the molten metal at the rear side: one flowing towards the exit side of the pool and the other flowing towards the entry side [27]. Therefore, in conjunction with the results of this experiment, it can be observed that there are two types of internal vortices within the rear wall of the weld pool. One type flow towards the keyhole entry of the pool and generates an internal vortex that flows inward, while the other type flows towards the keyhole exit side and forms an inward vortex near the keyhole exit side, as shown in Figure 16a. This flow behavior aligns with the simulation results by Wu et al. [26]. The combined effects of arc shear force, arc pressure, and gravity lead to a clockwise internal vortex near the keyhole entry side. Conversely, due to the directions of arc shear force, arc pressure, and gravity all pointing towards the exit side of the pool at the keyhole rear side, a counterclockwise vortex is induced near the bottom of the weld pool. Therefore, in the rear wall of VPPA welding, particularly near the weld seam, two opposing vortices are observed. The change in the direction of gravity results in a difference in the accumulation zones of the two vortices. In vertical welding, oxides are uniformly distributed across the entire rear wall of the weld pool. However, in flat welding, oxides tend to accumulate more at the keyhole rear side near exit side.

Furthermore, there exists a Karman vortex street in the welding direction. By analyzing the cross-sectional view along the welding direction, Yan et al. discovered alternating occurrences of oxides within the weld seam [31]. Hence, it is evident that a Karman vortex street exists within the internal flow of the weld pool, which is particularly noticeable in the rear wall of the weld pool. Therefore, the theoretical model for the internal flow within the weld pool essentially encompasses two types of vortices. One type emerges as a Karman vortex street along the path from the front wall of the weld pool through the side wall to the rear wall, extending into the gradually solidifying zone. The axis of this vortex aligns parallel to the axis of the welding torch. The second type occurs along the direction from the entrance of the weld pool towards the exit, forming a vortex.

During the flat welding process, the notable expansion of flow channels exacerbates the internal vortex flow within the molten metal. Moreover, in the context of flat welding, there is a heightened propensity for the molten metal to gravitate towards the keyhole exit side. Consequently, this leads to a more substantial accumulation of metal and a higher temperature distribution at the keyhole exit side, thereby resulting in a reduced cooling rate for the molten metal within this region. In the course of flat welding, these intricate interplays among these factors cumulatively yield a conspicuous increase in grain size and the enlargement of coarse grain zones. The collective consequence of these intricate phenomena manifests as a marked deterioration in mechanical performance.

5. Conclusions

This study investigates the differences in the internal flow behavior of molten metal affected by gravity during VPPA welding, as well as the reasons for the resulting differences in temperature distribution and mechanical properties of the welded beads.

1. Within the weld pool, two types of vortex currents exist: one along the direction of welding and the other directed towards the base metal zone inside the weld pool. The presence of these vortex currents ensures thorough mixing of the molten metal within the pool, contributing to improved mechanical properties. This phenomenon is induced by the shear force, arc pressure, and gravity. Gravity can exacerbate the buildup of molten metal on the keyhole exit side.
2. Compared to the vertical position, flat position welding exhibits larger flow channels within the weld pool, especially along the sides of the keyhole. This results in more active internal vortex currents during flat welding. The increase in channel area during flat welding is attributed to heat accumulation.
3. During flat position, due to the influence of gravity, molten metal accumulates on one side of the keyhole exit, leading to elevated temperatures at the exit. This results in a larger zone with coarser grains on the exit side, consequently leading to inferior mechanical properties compared to the vertical welding position.

This research reveals critical characteristics of the internal flow behavior of molten metal at different positions during VPPA welding and demonstrates the significant impact of gravity on molten metal flow and material properties. These findings contribute to the optimization of VPPA welding processes, particularly in spatial locations, to enhance welding quality.

Author Contributions: Conceptualization, J.L. and F.J.; methodology, B.X.; software, G.Z.; validation, B.X. and G.Z.; investigation, J.L.; resources, S.C.; data curation, J.L.; writing—original draft preparation, J.L.; writing—review and editing, J.L. and F.J.; supervision, X.M.; project administration, W.C.; funding acquisition, F.J. and S.C. All authors have read and agreed to the published version of the manuscript.

Funding: This work was supported by the National Natural Science Foundation of China (Grant Nos. U1937207, 52005014 and 52275302), the Major Science and Technology Innovation Project of Shandong Province (Grant No. 2020JMRH0504), Jinan Innovation Team Project (Grant No. 2021GXRC066) and Quan Cheng Scholars Construction Project (Grant No. D03032), State Key Laboratory of Advanced Welding and Joining, Harbin Institute of Technology (Grant No. AWJ-21M24). It was also supported by the China Scholarship Council for one year study at Osaka University (202206540024).

Institutional Review Board Statement: Not applicable.

Informed Consent Statement: Not applicable.

Data Availability Statement: Data is contained within the article.

Conflicts of Interest: The authors declare no conflict of interest.

References

1. Lang, R.; Han, Y.; Bai, X.; Hong, H. Prediction of the Weld Pool Stability by Material Flow Behavior of the Perforated Weld Pool. *Materials* **2020**, *13*, 303. [CrossRef]
2. Wang, Y.; Cong, B.; Qi, B.; Chen, X.; Yin, Y.; Lin, S. Influence of low-pulsed frequency on arc profile and weld formation characteristics in double-pulsed VPTIG welding of aluminium alloys. *J. Manuf. Process.* **2020**, *58*, 1211–1220. [CrossRef]
3. Wu, D.; Chen, H.; Huang, Y. Monitoring of weld joint penetration during variable polarity plasma arc welding based on the keyhole characteristics and PSO-ANFIS. *Mater. Process. Technol.* **2017**, *239*, 113–124. [CrossRef]
4. Wu, D.; Ishida, K.; Tashiro, S.; Nomura, K.; Hua, X.; Ma, N.; Tanaka, M. Dynamic keyhole behaviors and element mixing in paraxial hybrid plasma-MIG welding with a gap. *Int. J. Heat Mass Transf.* **2023**, *200*, 123551–123562. [CrossRef]
5. Liu, Z.; Cui, S.; Luo, Z.; Zhang, C.; Wang, Z.; Zhang, Y. Plasma arc welding: Process variants and its recent developments of sensing, controlling and modeling. *J. Manuf. Process.* **2016**, *23*, 315–327. [CrossRef]
6. Wu, C.; Jia, C.; Chen, M. A control system for keyhole plasma arc welding of stainless-steel plates with medium thickness. *Welding J.* **2010**, *89*, 89–101.

7. Sun, L.; Sun, X.; Guo, B.; Zhou, W.; Li, Z. Unified modeling and kinetic analysis of the near-cathode region and hot cathode in atmospheric-pressure arc discharges. *Phys. Fluids* **2022**, *34*, 067120. [CrossRef]
8. Wu, D.; Chen, J.; Liu, H.; Zhang, S.; Chen, S. Weld penetration in situ prediction from keyhole dynamic behavior under time-varying VPPAW pools via the OS-ELM model. *Int. J. Adv. Manuf. Technol.* **2019**, *104*, 3929–3941. [CrossRef]
9. Jiang, Y.; Xu, B.; L, Y.; Liu, C.; Liu, M. Experimental analysis on the variable polarity plasma arc pressure. *Chin. J. Mech. Eng.* **2011**, *24*, 607–611. [CrossRef]
10. Kazuya, I.; Tashiro, S.; Nomura, K.; Wu, D.; Tanaka, M. Elucidation of arc coupling mechanism in plasma-MIG hybrid welding process through spectroscopic measurement of 3D distributions of plasma temperature and iron vapor concentration. *J. Manuf. Process.* **2022**, *77*, 743–753. [CrossRef]
11. Wang, Y.; Cong, B.; Qi, B.; Yang, M.; Lin, S. Process characteristics and properties of AA2219 aluminum alloy welded by double pulsed VPTIG welding. *J. Mater. Process. Technol.* **2019**, *266*, 255–263. [CrossRef]
12. Pan, J.; Yang, L.; Hu, S. Numerical analysis of keyhole formation and collapse in variable polarity plasma arc welding. *Int. J. Heat Mass Transfer* **2017**, *109*, 1218–1228. [CrossRef]
13. Wu, D.; Nguyen, A.; Tashiro, S.; Hua, X.; Tanaka, M. Elucidation of the weld pool convection and keyhole formation mechanism in the keyhole plasma arc welding. *Int. J. Heat Mass Transf.* **2019**, *131*, 920–931. [CrossRef]
14. Wu, D.; Tashiro, S.; Hua, X.; Tanaka, M. Coupled mechanisms of the keyhole, energy transfer and compositional change associated with the variable polarity plasma arc process. *J. Phys. D Appl. Phys.* **2021**, *54*, 115204–115214. [CrossRef]
15. Sun, X.; Qi, B.; Jiang, Z.; Zeng, C.; Cong, N. Refined weld microstructure and enhanced joint mechanical property of 1460 Al-Li alloys via double-pulsed variable polarity TIG arc welding. *J. Manuf. Process.* **2022**, *82*, 738–749. [CrossRef]
16. Cai, D.; Han, S.; Yan, D.; Luo, Z.; Wang, H.; Zhang, Y. Microstructure and fatigue behavior of variable polarity plasma arc welded Al-6.2Mg alloys. *J. Mater. Process. Technol.* **2019**, *269*, 128–134. [CrossRef]
17. Yan, Z.; Chen, S.; Jiang, F.; Zhang, W.; Huang, N. Study and optimization against the gravity effect on mechanical property of VPPA horizontal welding of aluminum alloys. *J. Manuf. Process.* **2019**, *46*, 109–117. [CrossRef]
18. Wang, H.; Yang, C.; Wei, Y.; Lin, S.; Shen, H. Study of keyhole closure and analysis of microstructure and mechanical performance of weld joints for variable polarity vertical up plasma arc welding process. *Sci. Technol. Weld. Join.* **2006**, *3*, 315–340. [CrossRef]
19. Lefebvre, F.; Ganguly, S.; Sinclair, I. Micromechanical aspects of fatigue in a MIG welded aluminium airframe alloy: Part 1. Microstructural characterization. *Mater. Sci. Eng. A* **2005**, *397*, 338–345. [CrossRef]
20. Lefebvre, F.; Sinclai, I. Micromechanical aspects of fatigue in a MIG welded aluminium airframe alloy: Part 2. *Mater. Sci. Eng. A* **2005**, *407*, 265–272. [CrossRef]
21. Xiao, L.; Fan, D.; Huang, J.; Tashiro, S.; Tanaka, M. 3D Numerical Study of External Axial Magnetic Field-Controlled High-Current GMAW Metal Transfer Behavior. *Materials* **2020**, *13*, 5792. [CrossRef]
22. Ebrahimi, A.; Babu, A.; Kleijn, C.R.; Hermans, M.J.M.; Richardson, I.M. The Effect of Groove Shape on Molten Metal Flow Behaviour in Gas Metal Arc Welding. *Materials* **2021**, *14*, 7444. [CrossRef]
23. Pan, J.; Hu, S.; Yang, L.; Chen, S. Numerical analysis of the heat transfer and material flow during keyhole plasma arc welding using a fully coupled tungsten–plasma–anode model. *Acta Mater.* **2016**, *118*, 221–229. [CrossRef]
24. Shoichi, M.; Yasushi, T. Effect of Magnetic Field on Flows and Temperature Distribution of Molten Pool in Electromagnetic Controlled Molten Pool Welding Process. *J. Jpn. Weld. Soc.* **2015**, *84*, 244–250. [CrossRef]
25. Lu, H.; Xing, J.; Xing, L. Arc morphology and weld pool flowing in A-MAG welding process. *Trans. China Weld. Inst.* **2014**, *10*, 36–43.
26. Wu, D.; Tashiro, S.; Hua, X.; Tanaka, M. Analysis of the energy propagation in the keyhole plasma arc welding using a novel fully coupled plasma arc-keyhole-weld pool model. *Int. J. Heat Mass Transf.* **2019**, *141*, 604–614. [CrossRef]
27. Liu, J.; Jiang, F.; Xu, B.; Zhang, G.; Chen, S. Physical mechanism of material flow and temperature distribution in keyhole plasma arc welding at initial unstable stage. *Phys. Fluids* **2023**, *35*, 033115. [CrossRef]
28. Morisada, Y.; Fujii, H.; Kawahito, Y.; Nakata, K.; Tanaka, M. Three-dimensional visualization of material flow during friction stir welding by two pairs of x-ray transmission systems. *Scr. Mater.* **2011**, *65*, 1085–1088. [CrossRef]
29. Hemmesi, K.; Mallet, P.; Farajian, M. Numerical evaluation of surface welding residual stress behavior under multiaxial mechanical loading and experimental validations. *Int. J. Mech. Sci.* **2020**, *168*, 105127. [CrossRef]
30. Mugada, K.; Adepu, K. Influence of ridges shoulder with polygonal pins on material flow and friction stir weld characteristics of 6082 aluminum alloy. *J. Manuf. Process.* **2018**, *32*, 625–634. [CrossRef]
31. Yan, Z.; Chen, S.; Jiang, F.; Huang, N.; Zhang, S. Material flow in variable polarity plasma arc keyhole welding of aluminum alloy. *J. Manuf. Process.* **2018**, *36*, 480–486. [CrossRef]
32. Anh, N.; Tashiro, S.; Hanh, B.; Manabu, T. Experimental investigation on the weld pool formation process in plasma keyhole arc welding. *J. Phys. D Appl. Phys.* **2017**, *51*, 015204. [CrossRef]
33. Wu, D.; Tashiro, S.; Wu, Z.; Nomura, K.; Hua, X.; Tanaka, M. Interactive phenomena in hybrid KPAW-PGMAW. *Weld. J.* **2019**, *99*, 5. [CrossRef]

applied sciences

MDPI

Article

Internal Flow Prediction in Arbitrary Shaped Channel Using Stream-Wise Bidirectional LSTM

Jaekyun Ko †, Wanuk Choi † and Sanghwan Lee *

Department of Mechanical Convergence Engineering, Hanyang University, Seoul 04763, Republic of Korea; rhworbs1124@hanyang.ac.kr (J.K.); dhksdnr2003@hanyang.ac.kr (W.C.)
* Correspondence: shlee@hanyang.ac.kr
† These authors contributed equally to this work.

Abstract: Deep learning (DL) methods have become the trend in predicting feasible solutions in a shorter time compared with traditional computational fluid dynamics (CFD) approaches. Recent studies have stacked numerous convolutional layers to extract high-level feature maps, which are then used for the analysis of various shapes under differing conditions. However, these applications only deal with predicting the flow around the objects located near the center of the domain, whereas most fluid-transport-related phenomena are associated with internal flows, such as pipe flows or air flows inside transportation vehicle engines. Hence, to broaden the scope of the DL approach in CFD, we introduced a stream-wise bidirectional (SB)-LSTM module that generates a better latent space from the internal fluid region by additionally extracting lateral connection features. To evaluate the effectiveness of the proposed method, we compared the results obtained using SB-LSTM to those of the encoder–decoder(ED) model and the U-Net model, as well as with the results when not using it. When SB-LSTM was applied, in the qualitative comparison, it effectively addressed the issue of erratic fluctuations in the predicted field values. Furthermore, in terms of quantitative evaluation, the mean relative error (MRE) for the x-component of velocity, y-component of velocity, and pressure was reduced by at least 2.7%, 4.7%, and 15%, respectively, compared to the absence of the SB-LSTM module. Furthermore, through a comparison of the calculation time, it was found that our approach did not undermine the superiority of the neural network's computational acceleration effect.

Keywords: deep learning (DL); computational fluid dynamics (CFD); convolutional neural network (CNN); encoder–decoder (ED); recurrent neural network (RNN); long short-term memory (LSTM)

Citation: Ko, J.; Choi, W.; Lee, S. Internal Flow Prediction in Arbitrary Shaped Channel Using Stream-Wise Bidirectional LSTM. *Appl. Sci.* **2023**, *13*, 11481. https://doi.org/10.3390/app132011481

Academic Editors: Vasily Novozhilov and Cunlu Zhao

Received: 19 September 2023
Revised: 14 October 2023
Accepted: 17 October 2023
Published: 19 October 2023

1. Introduction

Engineering advancements in computational fluid dynamics (CFD) have facilitated the comprehension of flow and object–flow interactions. However, even if the pre-processing for numerical simulation, such as mesh generation, the differentiation of governing equations, boundary condition setting, and solver algorithms, is implemented in advance, the high computational cost of calculating the flow and post-processing the results has become an issue. This poses a significant problem for fluid mechanics engineers who need to conduct numerous experiments under diverse conditions.

Hence, neural network (NN) models have emerged as a viable alternative to address the aforementioned issues, particularly in cases where a substantial amount of data has been generated through CFD simulation. NN models [1,2] are trained by adopting the supervised learning strategy, which uses a dataset of paired inputs and the corresponding target obtained through numerous CFD processes. Specifically, various NN structures are designed according to the data type, such as a fully connected (FC) NN for a sampled point set [3], a graph neural network (GNN) for an unstructured grid [4,5], or a convolutional neural network (CNN) [6] for a structured grid [7].

Among these approaches, the CNN-based framework has a well-structured usage environment, demonstrating particular strength in constructing deep NNs [8,9]. Hence,

it is widely used for the interpolation of other types of data in a structured grid [10,11] or when using domain transformation [12]. For instance, Zhang et al. [13] introduced AeroCNN-2, in which the drag and lift coefficients are predicted based on the shape of the airfoil. Viquerat et al. [14] proposed VGG-like networks [15] that can forecast drag forces for arbitrary shapes. Liu et al. [16] presented Shock-Net, which detects shocks in flow and is three times faster than traditional non-deep-learning methods. Deng et al. [17] proposed Vortex-Net, which identifies vortices in shorter execution times with performance similar to that of the instantaneous vorticity deviation (IVD) method [18]. MS et al. [19] introduced a composite CNN-RNN architecture to estimate the viscosity from flow sequences. Liu et al. [20] designed Metric-Net to select a key time step for simulations.

Moreover, accelerating flow generation using DL methods has also become a mainstream research area. In certain instances, researchers have focused on replacing the spatial information processing of the fluid solver with CNNs. For example, Tompson et al. [21] proposed FluidNet, which accelerates the Eulerian fluid simulation by utilizing a CNN to solve a sparse linear system instead of the Euler equation. Xiao et al. [22] presented a CNN-based Poisson solver that employs a hierarchical structure to efficiently represent large sparse matrices. In addition, researchers have examined the combination of recurrent neural networks (RNNs) to learn temporal information from sequential data. Wiewel et al. [23] proposed a long short-term memory (LSTM)-CNN solver to predict the pressure field during the simulation, which is 100 times faster than a regular pressure solver. Hou et al. [24] proposed U-Net-LSTM, which combines U-Net and LSTM to learn the unsteady flow around a submarine, and they showed results with a higher resolution than those of other CNN-LSTM-based data-driven simulators. However, the problem of a model yielding critical errors upon encountering boundary conditions not previously included in the training dataset [25,26] has not been addressed yet.

As a result, research has actively focused on obtaining flow fields through the encoder–decoder (ED) structure to predict steady-state or averaged flows for various shapes and conditions. Guo et al. [1] demonstrated that a fully convolutional NN with an ED model can effectively learn laminar flow data around a car shape inside a rectangular channel. Ribeiro et al. [27] proposed a U-Net model that incorporates skip connections into the ED model to enhance the accuracy in predicting laminar flow results. On the basis of the aforementioned studies, methods have been introduced to predict solutions for Reynolds-averaged Navier–Stokes (RANS) flows around a cylinder [11] or over airfoil shapes [28,29]. Zhou et al. [30] further utilized parameterized boundary information as the input domain through an FC layer. Nonetheless, most of the datasets used by these models are external or the internal flow fields share similarities with the external flow. Notably, these datasets contain an arbitrarily shaped object that is positioned near the center of the channel, with the walls at the top and bottom ends of the input domain remaining parallel.

Therefore, in this study, we created a novel dataset containing various channel shapes and evaluated the training feasibility of the baseline models. Throughout different experiments, it was demonstrated that the baseline models could not properly learn internal flows, such as pipe flows. To solve this problem, we introduced a stream-wise bidirectional (SB)-LSTM module to learn the lateral connections for each pixel. The SB-LSTM module can be easily attached to existing models, thereby effectively increasing the internal flow learning ability. The proposed SB-LSTM module reduced the mean relative error (MRE) of the x-component of velocity, y-component of velocity, and pressure during evaluations by at least 2.7%, 4.7%, and 15%, respectively.

To the best of our knowledge, the proposed approach is the first method to predict a flow in arbitrarily shaped channels with flow separation and corner vortices and ensures high performance. The contributions of this study are summarized as follows.

- An SB-LSTM module is proposed to capture important physical properties of internal flows, whereby model performance is significantly improved by simply connecting the module in the latent space.

- Qualitative and quantitative evaluations conducted on various channel structures demonstrate the excellent performance of the proposed method compared with that of baseline models.

2. Methodology

In this section, we first explain the process of dataset generation, illustrate the structure of the proposed SB-LSTM, and then define the loss function used for training.

2.1. Arbitrary Channel Shape Generation

In the case of an external flow, there are no major issues in analyzing it by moving the object so that the center of mass is located in the middle of the CFD solving domain. However, in the case of internal flows, where the pipe interacts across the entire domain, the flow pattern changes depending on the order in which they are connected. Since the fully convolutional network produces feature maps only with partial information of the entire image, there can be issues in learning internal flow datasets that have the mentioned characteristics.

We suggest a data generation method to test the learning capabilities. This method allows for the independent generation of the top and bottom surfaces and also allows for the cross-sectional area of the pipe to vary through a distribution function. Additionally, it allows for the presence of steps and bumps at random positions within the domain.

For this, two serial pipes biased up and down from the center were joined together as in Figure 1. Each serial pipe was constructed by connecting a rectangle aligned with the inlet velocity direction and the space between them in a linear manner. We did not use Bezier curves or sine functions when designing the shape because the flow flowed parallel to the wall without flow separation or vortex generation along this function shape. Examples created through this method are shown in Figure 2.

Figure 1. Example of upper and lower serial pipe in dataset.

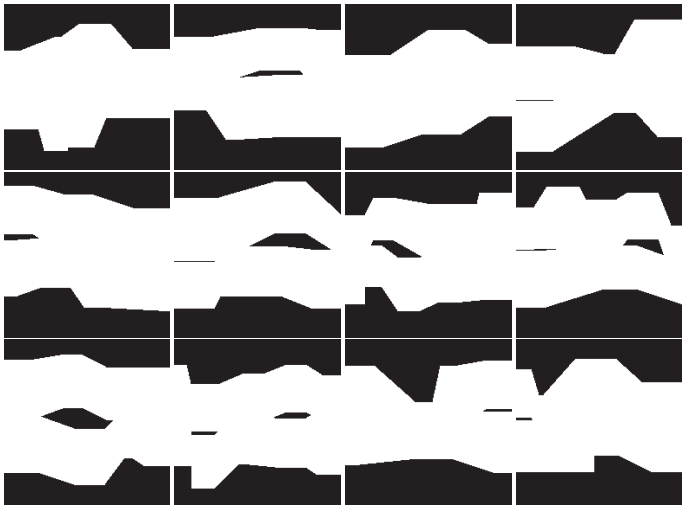

Figure 2. Samples of generated channel.

By configuring the pipe as above, we created different flow rates over converging and diverging channels, bumps and cavities at the walls, and objects in the channels. The height H, width W, and the x and y positions of each pipe were chosen as the independent variables to be determined before constructing a biased serial pipe, using discrete uniform and normal distributions. Detailed specifications are shown in Figures 3 and 4.

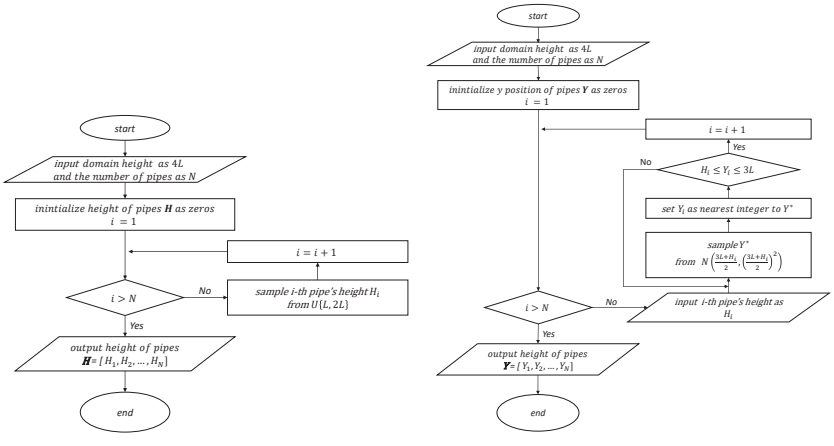

(**a**) (**b**)

Figure 3. Flow diagram for determination of the height and y positions of rectangles consisting of lower serial pipes. From left to right: (**a**) height, (**b**) y position. The superscript * represents a variable used as an intermediate step to determine the actual value.

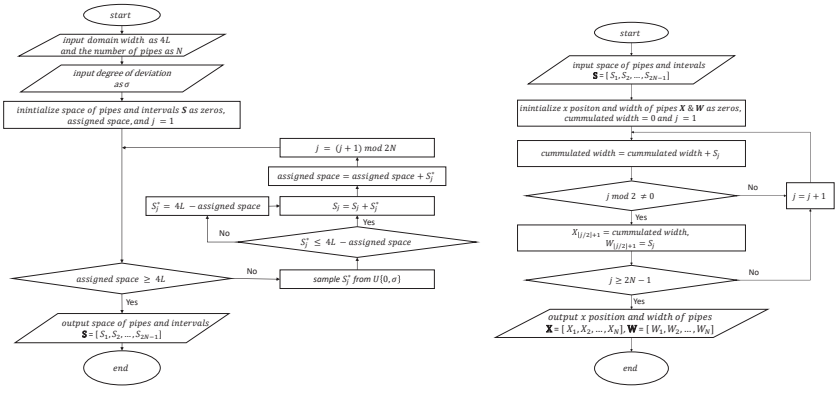

(**a**) (**b**)

Figure 4. Flow diagram for determination of the Width and x positions of rectangles consisting of lower serial pipes. From left to right: (**a**) spaces of pipes and intervals, (**b**) x position and width of pipes. The superscript * represents a variable used as an intermediate step to determine the actual value.

The size of the domain used in the experiment was set to 192×192. The number of pipes was selected by generating a random integer between three and seven, and the hyperparameter σ was set to 20. In addition, to create a higher serial pipe, the lower serial pipe was inverted in the y-direction, following the aforementioned procedure.

2.2. Target Field Data Generation

An open-source CFD tool, OpenFOAM [31], was employed to generate a target dataset. For mesh generation, a domain with a channel shape of 192 × 192 was converted into the 3D 192 mm × 192 mm × 1 mm domain of the voxel file that was obtained through the method explained in Section 2.1. The voxel file was finally converted into an STL file and the mesh was created by cutting out the basic domain generated by blockMesh to match the shape of the channel using an STL file, without the refinement process.

In our problem setup, when gravity is neglected, a fluid with kinematic viscosity ν of 1×10^{-4} m^2/s enters the channel from the left side as a uniform flow with an x-component velocity u_{inlet} of 1×10^{-3} m/s. The fluid then flows through the 2D channel, where the velocity at the boundaries and the pressure gradient in the normal direction are zero. Finally, the fluid exits through the right side of the channel, where the gauge pressure p is equal to 0 *Pa*. Based on these boundary conditions, the continuity and momentum equations are expressed as follows:

$$\nabla \cdot V = 0 \tag{1}$$

$$(V \cdot \nabla)V = -\nabla P + \nu \nabla^2 V \tag{2}$$

$$P = \frac{p}{\rho_0}, \tag{3}$$

where ∇, V, P, and ρ_0 denote the *del* operator, velocity vector, kinematic pressure, and constant mass density of the fluid, respectively. Our models were set to the laminar because our inlet velocity was low enough. To generate the target data, the SIMPLE algorithm [32] was used for the CFD solution. During post-processing, the corner vortex region near the wall was calculated as the region of interest (RoI) to compare the accuracy at the region. A sample set of fields in the target data is shown in Figure 5, where the channel region is highlighted in black to enhance the distinction between the wall and fluid regions.

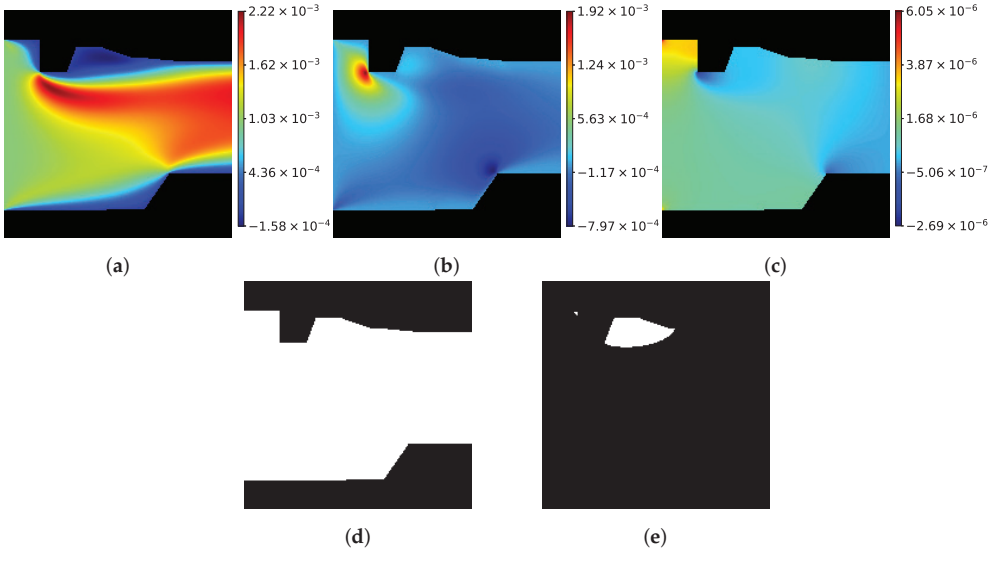

Figure 5. Sample set of target field data. From left to right: (**a**) x-component velocity, (**b**) y-component velocity, (**c**) kinematic pressure, (**d**) all fluid region, (**e**) corner vortex region.

2.3. Stream-Wise Bidirectional LSTM

The deformation of objects in previous internal flow prediction studies only has a small impact on the distribution of field values, and the overall pattern of the field does

not change significantly. However, the data generated through the above method undergo significant changes depending on the shape of the entire domain. Therefore, if a fully convolutional neural network is used for inference and training, problems arise.

To solve the problems of the existing network model, a module was designed based on bidirectional LSTM, which has shown strength in filling in words through context in natural language processing [33]. Generally, when dealing with dynamic data in deep learning, LSTM has been mainly used for time series data learning [34]. However, there have been studies using the concept of bidirectional LSTM for character inference within images in the field of image processing [35,36] The SB-LSTM module was inspired by this CNN-RNN combined approach.

The SB-LSTM module was designed to take the compressed latent geometry space as input and produce a feature map that includes the relationships between the forward and backward sequences of the feature space. While an encoder with convolutional layers can contract the input and extract high-level features, it does not include information about the lateral connections between pixels [37]. This means that global features related to the shape and flow direction of the channels are not well preserved in latent space when using only an encoder. To address this, the authors propose using bidirectional LSTM at the latent space to learn the directional relationships between pixels.

The entire process of the SB-LSTM module is depicted in Figure 6. The latent geometry space of size $H \times W \times C$, denoting the height, width, and channel, respectively, is first rearranged in the stream-wise direction (along the width axis) through a flattening process. This results in W divided components, each represented as a 1D matrix of size $C \times H$. Second, each serial vector Z_i continuously updates the cell state and hidden state of the forward LSTM, which are initialized to zero with a size equal to $C \times H$, and returns an output $Z^{'}_{f,i}$, where i denotes the index of each input vector. Consequently, this allows us to obtain the output $Z^{'}_{f,i}$, which contains information on the feature spaces sequentially passing along the flow direction to the i-th point. Similarly, Z_i is used to update the cell and hidden states of the backward LSTM from the outlet to the inlet direction, outputting $Z^{'}_{b,i}$. Third, the forward and backward hidden states at the i-th latent position are combined to create a set of new serial vectors containing the expected lateral relation along all separated areas. Since vectors from the forward and backward LSTM are aggregated together, the length of the output vector becomes $2C \times H$. Finally, the output is repeated H times in the vertical direction in order to share the same information among the latent spaces that are involved in the flattening process. In summary, the proposed SB-LSTM module addresses the local limitations of the latent space in the existing encoder by generating global features through bidirectional LSTM. This makes it suitable for the analysis of internal flows on arbitrary channel shapes. The effect of the module is thoroughly analyzed in Section 3.

2.4. Network with Stream-Wise Bidirectional LSTM

The integration of the SB-LSTM module in the network is explained using the example of a module with SB-LSTM applied to U-Net [27], used later in the experiments. The structural overview of U-Net with SB-LSTM is shown in Figure 7. In the middle part of the structure, where encoding ends, the latent space not only serves as an input for X2Nearest Neighbor interpolation, indicated by the blue arrow, for the first decoding process, but also acts as an input for SB-LSTM to extract additional lateral connection information. To adjust the size for application in the network, 1×1 convolution and nearest neighbor interpolation have been added to the path for SB-LSTM. The added lateral information is concatenated with the latent space and used as an input for the convolution operation in the decoding process, along with the latent space of the original path. The detailed process of the operation of this network is described below.

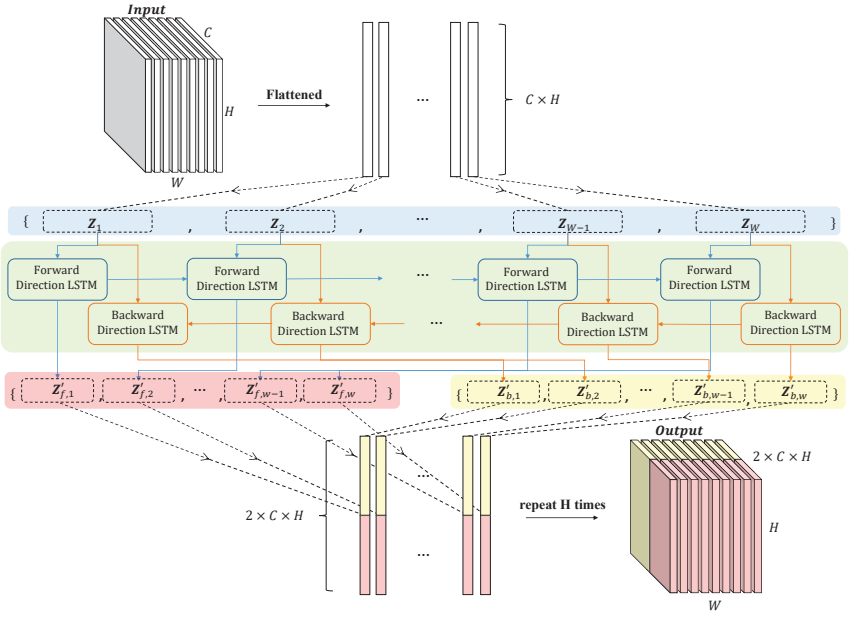

Figure 6. Structural overview of the proposed SB-LSTM module.

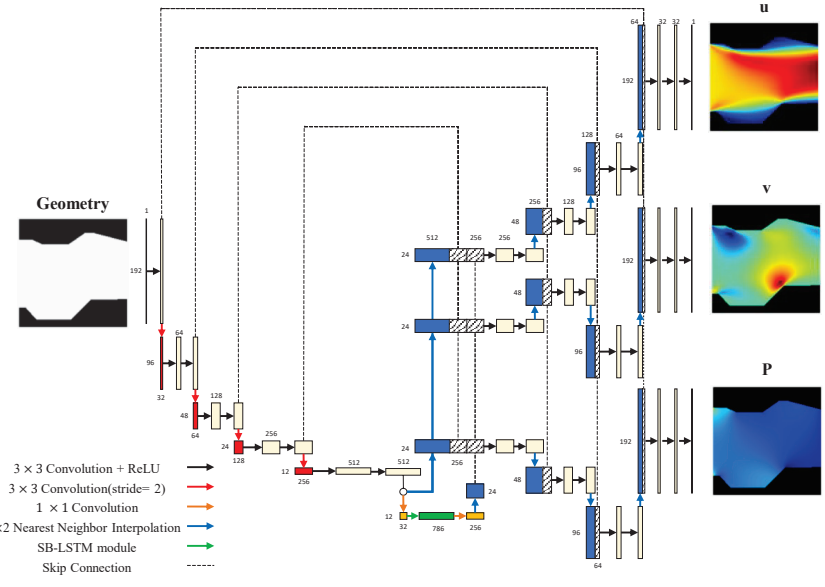

Figure 7. Structural overview of the proposed U-Net with SB-LSTM.

Given an input channel shape with dimensions of 192 × 192 × 1, denoting the height, width, and channel, respectively, the model first expands the number of channels to 32 using a 3 × 3 convolutional layer with a rectified linear unit (ReLU) activation function. Then, a 3 × 3 convolutional layer with a stride of two downsamples the height and width by half and increases the number of channels to 64 using two 3 × 3 convolutional layers with ReLU, which yields a 96 × 96 × 64 sized feature map. The same process is applied to the feature map until it reaches the size of 12 × 12 × 512. At the latent space, the number of

channels is reduced to 32 using a 1×1 convolutional layer and the compressed information is fed into the SB-LSTM module. After receiving the geometrical connection features from the SB-LSTM module, the channels are decreased to 256 using a 1×1 convolutional layer. The height and width are then upsampled using nearest neighbor interpolation with a scale factor of two. We have selected nearest neighbor interpolation to utilize the relations of adjacent pixels for a continuous upsampling process. The feature map shortly before the SB-LSTM module is also upsampled and both outputs are concatenated channel-wise. Moreover, the feature map from the encoder with the same spatial size is also aggregated to provide channel shape information. Two 3×3 convolutional layers with ReLU are then sequentially used for feature extraction and channel size reduction. This mechanism is applied repeatedly until the shape of the final output becomes $192 \times 192 \times 32$. Finally, a 3×3 convolutional layer is used to adjust the number of channels from 32 to 1. To predict u, v, and P, three decoders with the same architecture are employed, all sharing the features extracted by the SB-LSTM module.

2.5. Loss Function

Since the velocity x-component u, velocity y-component v, and pressure P consist of continuous values, the prediction of each field is similar to a regression task. Hence, the proposed model is trained by minimizing the difference between the predicted and target field at each pixel and the loss function is formulated as

$$Loss = \frac{1}{HW} \sum_{i}^{H} \sum_{j}^{W} \left(\| u_{pred_{i,j}} - u_{target_{i,j}} \|_1^1 + \| v_{pred_{i,j}} - v_{target_{i,j}} \|_1^1 + \| P_{pred_{i,j}} - P_{target_{i,j}} \|_1^1 \right), \quad (4)$$

where $\| \cdot \|_1^1$ represents the mean absolute error (MAE) and subscripts i and j denote the positions of the row and column, respectively.

3. Experiments

3.1. Dataset and Pre-Processing

A total of 5000 channel shapes were created through the process described in Section 2.1. The 5000 samples were then flipped upside down to double the quantity to 10,000. For all shapes, the samples were used as input into the NN, where pixels inside the binary array indicated the wall and fluid regions by 0 and 1, respectively. The data values obtained using the CFD tool in the domain were converted into target data by assigning the simulation results at the center position of each pixel set in the fluid region to an empty array with dimensions of 192×192. As a result, we constructed a dataset with 10,000 sets of an input channel shape and corresponding target fields. For the training, validation, and test datasets, we randomly selected and divided the generated samples into 8000, 1000, and 1000 cases, respectively.

During pre-processing, channel normalization was applied to the target field. Each pixel was divided by the standard deviation obtained from corresponding fluid regions to generate non-dimensional values. The pre-processing task is expressed as follows:

$$u^* = \frac{u}{u_{std}}, \quad v^* = \frac{v}{v_{std}}, \quad P^* = \frac{P}{P_{std}}. \quad (5)$$

3.2. Comparison Methods

The effectiveness of the SB-LSTM module was evaluated on two baseline models, ED and U-Net. These two models were adopted because they were used to train internal flow datasets in [1] and [27] and have also been referenced in many other papers regarding obtaining steady state solutions. ED consists of an encoder and decoder, and U-Net is an extension of ED with skip connections. In both models, the SB-LSTM module is attached at the latent space, and the structural comparison of the four different methods is depicted in Figure 8.

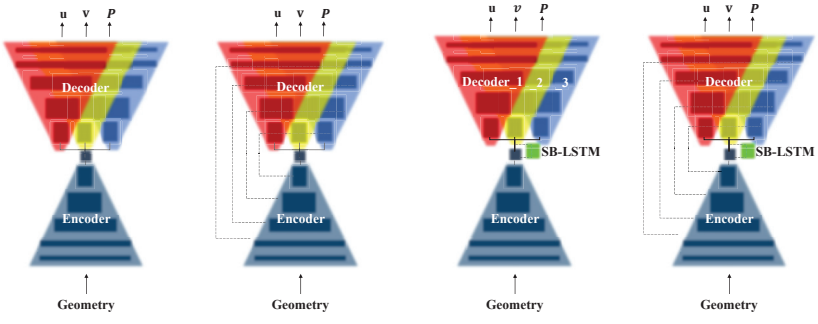

(**a**) (**b**) (**c**) (**d**)

Figure 8. Structural comparison of four different methods. From left to right: (**a**) ED, (**b**) U-Net, (**c**) ED with SB-LSTM, (**d**) U-Net with SB-LSTM.

Moreover, the number of model parameters of the four different methods is listed in Table 1. In both ED and U-Net, the model capacity is increased to 4,348,192 parameters with relative increment ratios of 34.67% and 22.60%, respectively. The significant growth in parameters occurs due to the use of the fully connected operation in the input gate, output gate, and forget gate of LSTM. Furthermore, since the network that we use utilizes two LSTM models, one for backward and one for forward processing, the increase in the number of parameters mentioned earlier is doubled. Despite the larger model capacity, overfitting did not occur during training and the models with the SB-LSTM module showed better performance, which is comprehensively analyzed in Sections 4.1–4.3.

Table 1. Number of model parameters for the four different methods.

Method	Number of Model Parameters
ED	12,540,227
U-Net	14,890,307
ED with SB-LSTM	16,888,419
U-Net with SB-LSTM	19,238,499

3.3. Implementation Details

In the experiments, we used the Adam optimizer [38] ($\beta_1 = 0.5$, $\beta_2 = 0.999$). The learning rate was initialized to 1×10^{-4} and the batch size was set to 64. All methods were trained for 200 epochs and evaluated at each epoch. Using the cosine annealing algorithm [39] as the learning rate scheduler, the learning rate gradually decayed to 1×10^{-6}. The PyTorch framework [40] and two NVIDIA RTX 3090 GPUs with 24 GB of RAM, 48 GB in total, were used for the implementation. The official code can be found in the following link: https://github.com/choiwanuk/SB-LSTM, accessed on October 19 2023.

4. Results and Discussion

4.1. Training History

To demonstrate whether the learning progressed well under the above conditions, we plotted four graphs that contained the history of the training and validation loss of the comparison methods. As illustrated in Figure 9, the baseline models, i.e., ED and U-Net, converged well, eventually showing lower validation loss compared to training loss. For methods with the SB-LSTM module, they also exhibited well-trained curve features where no overfitting problems occurred despite the model parameter increase. During the training process, the model with SB-LSTM attached showed a faster decrease in loss per epoch.

While the baseline methods did not show a decrease in loss from around 125 epochs, the attached models maintained a steady decrease.

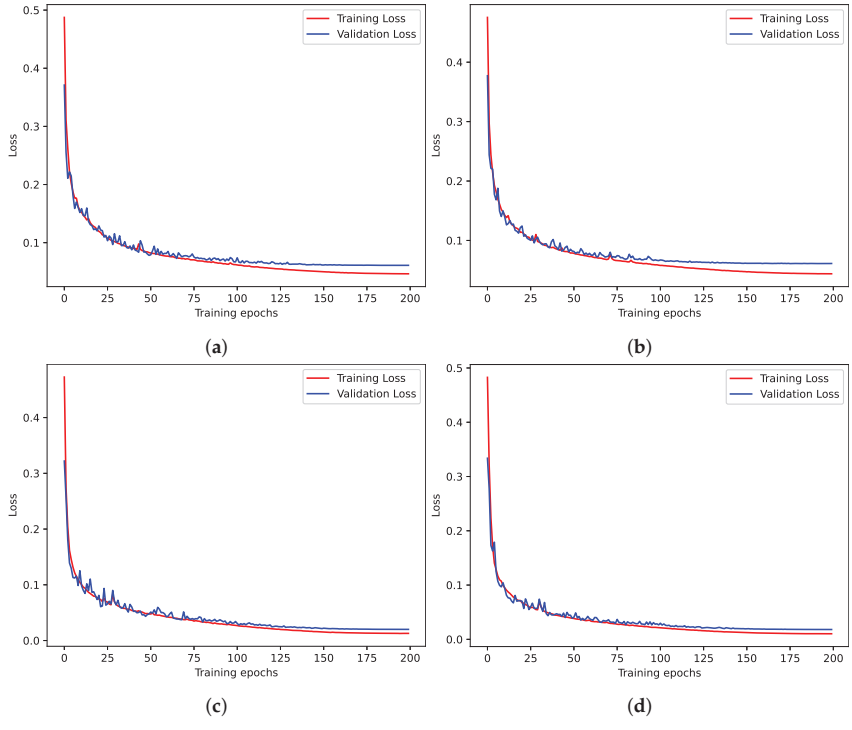

Figure 9. Training history of four different methods. From top left to bottom right: (**a**) ED, (**b**) U-Net, (**c**) ED with SB-LSTM, (**d**) U-Net with SB-LSTM.

4.2. Qualitative Evaluations

The target field predictions of the four different models are visualized in Figures 10–14. The representative data in each figure are for cases with a nearly constant vertical cross-sectional area, converging, diverging, converging–diverging, and diverging–converging, respectively. The colorbar range was determined by calculating the minimum and maximum values of predictions and targets for each case. In this section, the focus is mainly on the differences between the models with and without the SB-LSTM module, as the differences between the models that include the SB-LSTM module are not clearly visible within the range that encompasses the results of all four models. The qualitative comparison between models with SB-LSTM is visualized in Figures A1–A5 of Appendix A.

As shown in Figure 10, both the ED and U-Net models encountered a problem with a sudden discontinuity appearing in the u field at approximately three quarters of the width from the inlet in the x-direction. This indicates that the models struggled to accurately estimate the flow rate near the outlet of the channel shape. The issue with the v field was not as severe in this interval, instead appearing as a blurry error in the form of a thin line. As for the P field, as it approached the inlet from the outlet, the predicted value deviated more and there was a sudden change in value at around one quarter of the width from the inlet in the x-direction. Additionally, in Figures 11 and 12, it can be observed that the error in the predicted value increases as u approaches the outlet and P approaches the inlet.

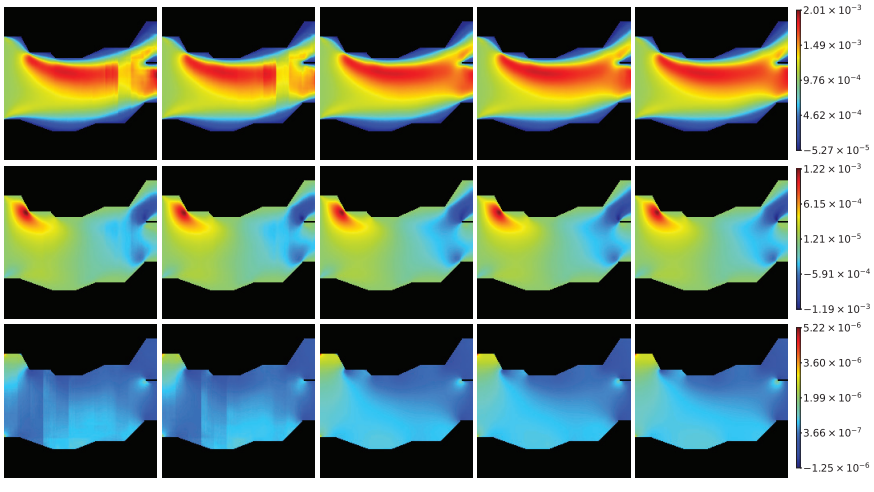

Figure 10. Qualitative results of four different methods. From top to bottom: u, v, P. From left to right: (**a**) ED, (**b**) U-Net, (**c**) ED with SB-LSTM, (**d**) U-Net with SB-LSTM, (**e**) target.

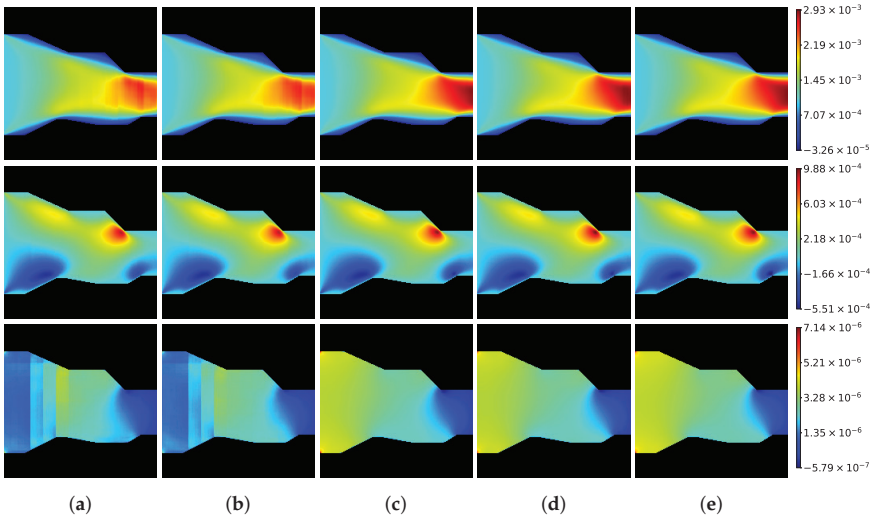

Figure 11. Qualitative results of four different methods. From top to bottom: u, v, P. From left to right: (**a**) ED, (**b**) U-Net, (**c**) ED with SB-LSTM, (**d**) U-Net with SB-LSTM, (**e**) target.

These limitations are observed in the convolutional neural network (CNN) components of ED and U-Net. The structure of the CNN is inspired by the visual cortex in animals [41,42] and it thus has the ability to learn and generate high-level feature maps. However, a drawback of the fully convolutional network is that it only considers information within the receptive field range. This means that if the necessary information for the prediction of the target value is outside of this range, the learning process may be flawed and solutions may be generated from irrelevant features. Consequently, when u and P move away from the fixed boundary condition, the results may show tendencies that are not present in the training dataset, as seen in Figure 14, where u suddenly increases despite there being no possibility for a further speed increase.

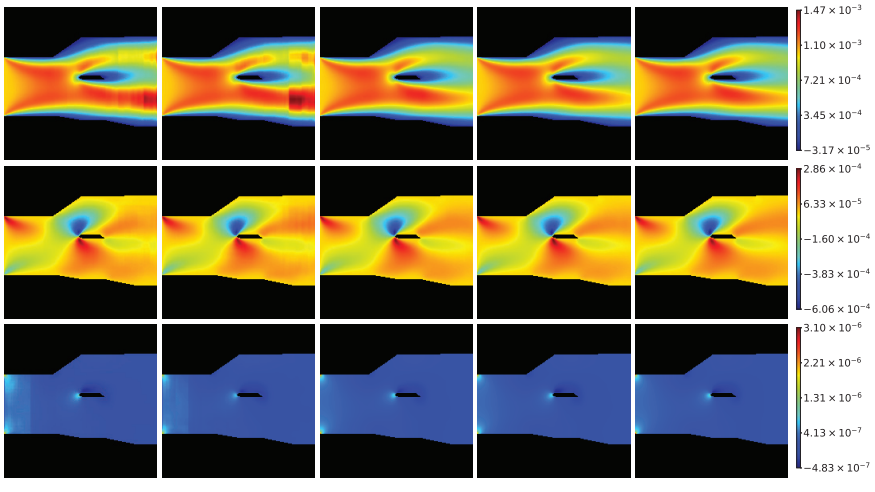

Figure 12. Qualitative results of four different methods. From top to bottom: u, v, P. From left to right: (**a**) ED, (**b**) U-Net, (**c**) ED with SB-LSTM, (**d**) U-Net with SB-LSTM, (**e**) target.

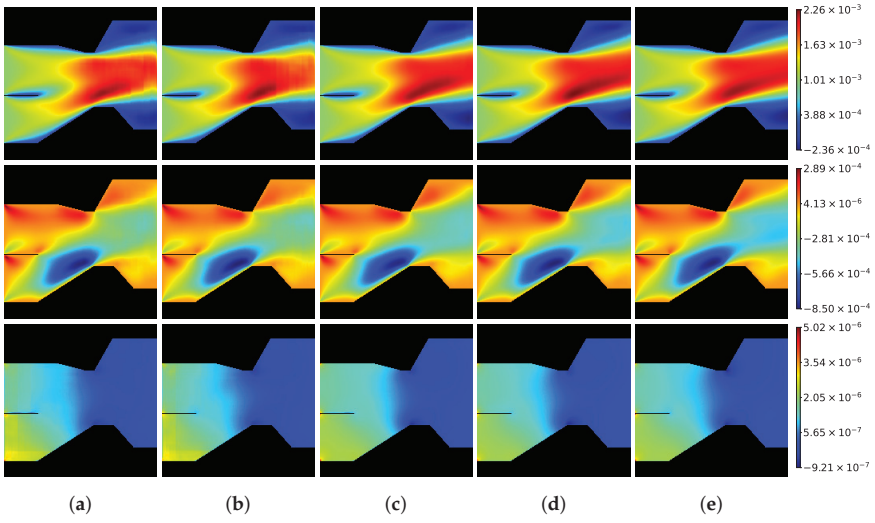

Figure 13. Qualitative results of four different methods. From top to bottom: u, v, P. From left to right: (**a**) ED, (**b**) U-Net, (**c**) ED with SB-LSTM, (**d**) U-Net with SB-LSTM, (**e**) target.

The proposed network, when combined with the SB-LSTM module, produced convincing results without encountering these types of issues in all the cases that were included in our test dataset. This confirms that not only errors related to patterns that deviate from fluid physics were successfully addressed, as shown in Figures 10–12 and 14, but also the resolution of the rows in Figure 13 was improved. This result can only be achieved by providing and receiving the appropriate features for estimation through lateral connections during the forward process using the attached SB-LSTM module. In other words, this demonstrates that the neural network that we designed possesses a structure that effectively learns the information to transfer during the backpropagation process. In addition to the above results, a qualitative evaluation related to the direction of LSTM in the SB-LSTM

module is described in Appendix B, along with Figure A6 on the training histories and Figure A7 on the results of the network depending on the direction setting of LSTM.

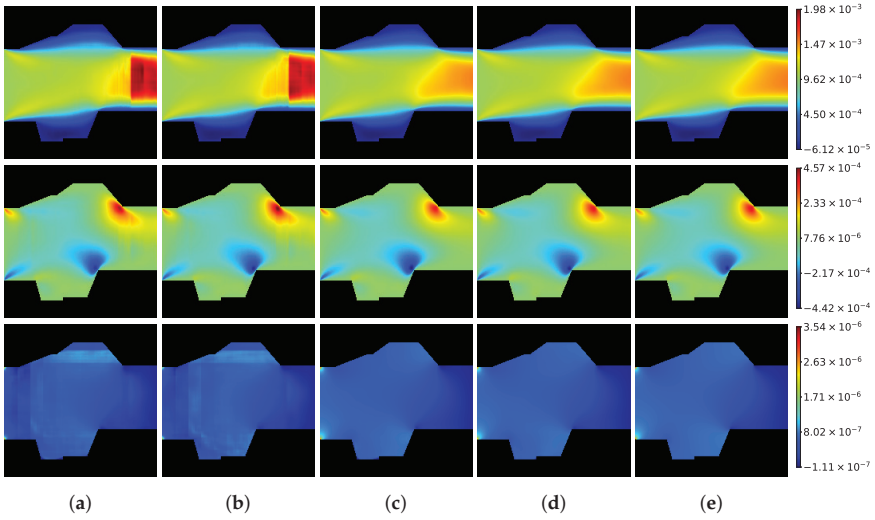

Figure 14. Qualitative results of four different methods. From top to bottom: u, v, P. From left to right: (**a**) ED, (**b**) U-Net, (**c**) ED with SB-LSTM, (**d**) U-Net with SB-LSTM, (**e**) target.

4.3. Quantitative Evaluations

4.3.1. Mean Relative Error

To quantify and compare the performance of the models, the mean relative error between the prediction and ground truth was calculated for two areas, the entire channel region and the corner vortex region generated near the wall, using the formula in Equation (6):

$$MRE(\alpha, \delta) = \frac{1}{N} \sum_{l=1}^{N} \frac{\sum_{i=1}^{Nx} \sum_{j=1}^{Ny} |\alpha_{ij} - \hat{\alpha}_{ij}| \delta_{ij}}{\sum_{i=1}^{Nx} \sum_{j=1}^{Ny} |\alpha_{ij}| \delta_{ij}}. \quad (6)$$

where α, δ, N, i, j, and $\hat{}$ denote a scalar field variable, binary field values of the RoI, the number of test datasets, the index values of the width and height axes, and the predicted value, respectively. Table 2 summarizes the mean relative error for each RoI of each model. In the table, the best performance results are shown in bold, and the second-best performance results are underlined for emphasis. U-Net with SB-LSTM showed the best performance for all metrics, followed by ED with SB-LSTM, which showed the second-best performance for all metrics. Note that there was a significant improvement in the case of P prediction compared to the decrease in the error rate of the u and v values. This demonstrates the effective performance improvement of internal flow learning with the SB-LSTM module. These findings align with previous studies that have shown that the U-Net structure outperforms the ED structure in original image processing and flow prediction.

Table 2. Quantitative comparisons of mean relative error between four different methods, with ↓ indicating that lower is better. The best result is highlighted in **bold** and the second-best result is underlined.

Method	*MRE* (All) (↓)			*MRE* (Corner) (↓)		
	u	***v***	***P***	***u***	***v***	***P***
ED	4.099%	10.200%	20.524%	54.007%	48.999%	35.241%
U-Net	4.056%	10.102%	20.962%	53.675%	48.794%	35.183%
ED with SB-LSTM	1.370%	5.591%	5.019%	30.738%	31.814%	15.831%
U-Net with SB-LSTM	**1.195%**	**5.212%**	**4.524%**	**30.350%**	**29.102%**	**13.724%**

4.3.2. Mean Absolute Error along Height Axis in Entire Channel

To analyze the characteristics of the errors of the models in Section 4.2, the mean absolute error along the height axis was calculated for each width position for the entire test data set using Equation (7).

$$MAE(\alpha, i) = \frac{1}{N}\sum_{l=1}^{N}\sum_{j=1}^{Ny}\left|\alpha_{ij} - \hat{\alpha}_{ij}\right|\delta_{ij}. \tag{7}$$

The calculated results are visualized in Figure 15. In the graph, U-Net with SB-LSTM shows the lowest error at all width positions, followed by ED with SB-LSTM, which has the next lowest error. Regardless of the presence or absence of the SB-LSTM module, the error of all models tends to increase as the predicted regions move further away from the boundary, with the boundary condition set to a fixed value. More attention should be given to models trained without the SB-LSTM module because of the periodic and significant increase in error in the stream-wise case. These peaks occur with exactly the same spacing and position, regardless of whether they are close to or far from the fixed boundary conditions in all width ranges of u, v, and P. This indicates that the error observed in Section 4.2 is occurring throughout the entire area, suggesting a problem with the approach of learning using a fully connected NN. However, when the SB-LSTM module is added, the error increases linearly without sharp changes. This confirms that the SB-LSTM module helps to address the issues that arise during the training of internal flows with the existing model.

4.4. Computation Time

To evaluate the impact of the SB-LSTM module on the prediction time in deep learning, two comparisons were conducted. First, the time required for a deep learning model with the SB-LSTM module attached was compared with that of the deep learning model without the module. Second, the time required for the SB-LSTM model was compared with that of the conventional CFD calculation method. The calculation time was measured using the RTX 3090 GPU for the deep learning models, whereas a single core of the AMD Ryzen 5 5600G CPU was used for CFD calculations. In both tests, the average computation times were measured by performing the calculation on 1000 pieces of test data. In this study, the time required to solve the SIMPLE algorithm solver using the CFD method was measured utilizing a time command in Linux. The average calculation time was 1.16811 seconds. In the case of surrogate models, the experiment was set up to examine the impact of different batch sizes. A total of 12 experiments were conducted, with batch sizes of 1, 10, and 100. The results of each experiment are summarized in Table 3.

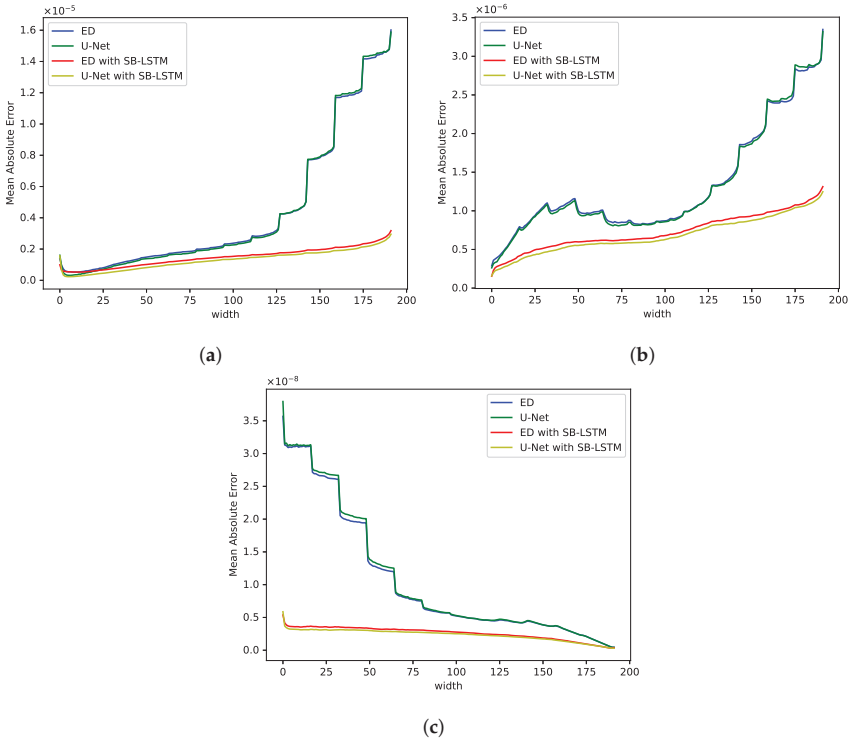

Figure 15. Figure of mean absolute error for each component of the models used in the experiment. From top left to bottom right: (**a**) u, (**b**) v, (**c**) P.

Table 3. Comparison of average computational time of four different methods in GPU environment.

Method	Batch Size	Average Computation Time (s)	Inference Speed Acceleration Ratio
ED	1	3.4044×10^{-3}	493.80
	10	2.0150×10^{-3}	834.3
	100	1.8760×10^{-3}	896.11
U-Net	1	4.4070×10^{-3}	381.46
	10	2.6121×10^{-3}	643.58
	100	2.4786×10^{-3}	678.25
ED with SB-LSTM	1	4.2567×10^{-3}	394.93
	10	2.2202×10^{-3}	757.1
	100	1.9821×10^{-3}	876.39
U-Net with SB-LSTM	1	4.9103×10^{-3}	342.36
	10	2.8264×10^{-3}	594.78
	100	2.5271×10^{-3}	665.23

For a batch size of one, the calculation time for the model with the SB-LSTM module was 0.8×10^{-3} seconds longer than that for the ED model and 0.5×10^{-3} s longer than that for the U-Net model, compared to the model without the SB-LSTM module. Although this is small considering that the CPU time required was 1.611 s, the SB-LSTM module can be considered inefficient in terms of calculation time as it took an additional 23% and 11% of the time compared to the baseline models. However, the additional time was due to the sequential calculation of the LSTM within the SB-LSTM module, which accounts for a large

portion of the total time when the batch size is one. As the batch size increases, the speedup value becomes comparable to that of the existing model.

5. Conclusions

This study was designed to determine whether the encoder–decoder or the U-Net structure, used for flow prediction, provides fast and acceptable results in learning internal flows compared to the existing CFD under various conditions. To this end, instead of generating arbitrary shapes between unchanged parallel walls, as in the existing method, we experimented with shapes created by simply joining serial pipes and CFD data corresponding to these shapes.

The existing neural networks exhibit problems in predicting flows from various patterns of shapes with different flow rates generated through the above method. To solve this problem, we proposed adding a module to the existing bottleneck part, to increase the learning capability through a spatial recurrent neural network that goes beyond the receptive field of the existing structure to capture information in the surrounding area, thereby solving the problems of the existing network, such as discontinuity in predicted values. When calculating the mean relative error in the region of interest, there was a decrease of at least 2.7% in the x-component of velocity, 4.7% in the y-component of velocity, and 15% in pressure, both in the overall area and the vortex corner region. Similarly, when comparing the computational time with the CFD method and the baseline model, this method was effective in terms of computational time.

During this research, the following shortcomings were discovered. In addition to evaluating the x-velocity and y-velocity used in the experiment as independent indicators, monitoring was also conducted on the direction created by both features. However, the directional plot did not align smoothly along the streamline; rather, it slightly jumped out like noise compared to the actual data flow. As a result, it seems necessary to conduct further research to force the interdependence between velocity fields, in addition to independently adjusting each data value.

Regarding follow-up studies, the dataset used in this work had a constant to fixed boundary condition. Therefore, follow-up flow prediction studies can add boundary condition information to the initial state of LSTM to study the effect of various boundary conditions. Additionally, flow prediction studies can be conducted for pipe shapes with a non-fixed domain size, taking advantage of the strengths of LSTM in language modeling.

Author Contributions: Conceptualization, J.K. and W.C.; methodology, J.K. and W.C.; software, J.K. and W.C.; validation, J.K. and W.C.; formal analysis, J.K. and W.C.; investigation, J.K. and W.C.; resources, J.K. and W.C.; data curation, J.K. and W.C.; writing—original draft preparation, J.K. and W.C.; writing—review and editing, J.K., W.C. and S.L.; visualization, J.K. and W.C.; supervision, S.L.; project administration, S.L. All authors have read and agreed to the published version of the manuscript.

Funding: This research received no external funding.

Institutional Review Board Statement: Not applicable.

Informed Consent Statement: Not applicable.

Data Availability Statement: Publicly available datasets were analyzed in this study. These data can be found here: [https://drive.google.com/file/d/1FY-TQfmuadkNOFuSsg1CbuB-kJ2I8612/view]. accessed on 19 October 2023.

Conflicts of Interest: The authors declare no conflict of interest.

Appendix A. Qualitative Evaluation of SB-LSTM Attached Model

This section demonstrates that the SB-LSTM module does not interfere with the characteristics of existing models. To visualize the differences in the results of models with SB-LSTM attached, the same procedure as in Section 4.2 was used to plot the two models,

with the ground truth as a reference. The absolute error is also plotted below to visually confirm the points where there are differences.

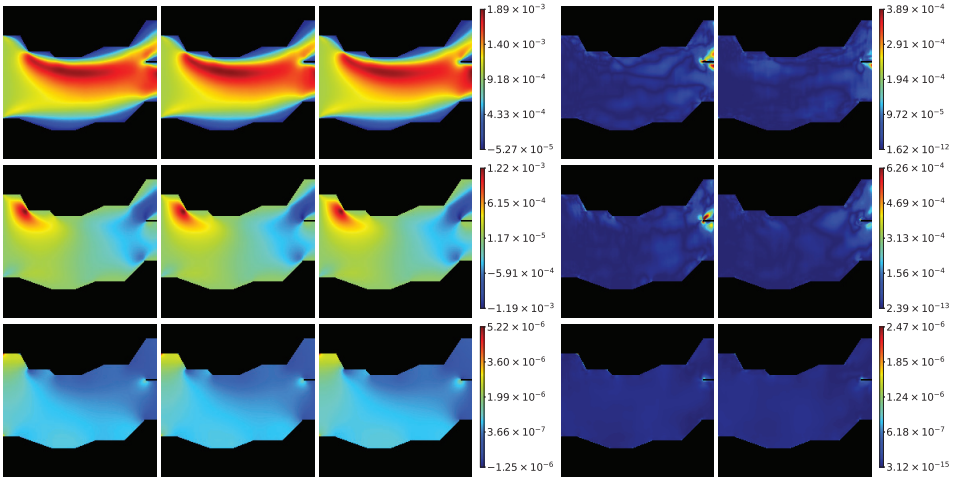

Figure A1. Qualitative results of four different methods. From top to bottom: u, v, P. From left to right: (**a**) ED with SB-LSTM, (**b**) U-Net with SB-LSTM, (**c**) ground truth, (**d**) absolute error of ED with SB-LSTM, (**e**) absolute error of U-Net with SB-LSTM.

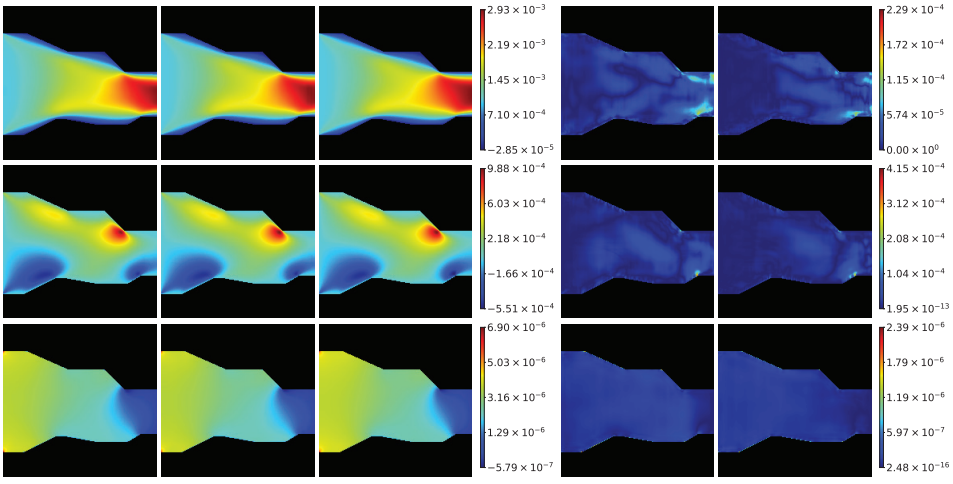

Figure A2. Qualitative results of four different methods. From top to bottom: u, v, P. From left to right: (**a**) ED with SB-LSTM, (**b**) U-Net with SB-LSTM, (**c**) ground truth, (**d**) absolute error of ED with SB-LSTM, (**e**) absolute error of U-Net with SB-LSTM.

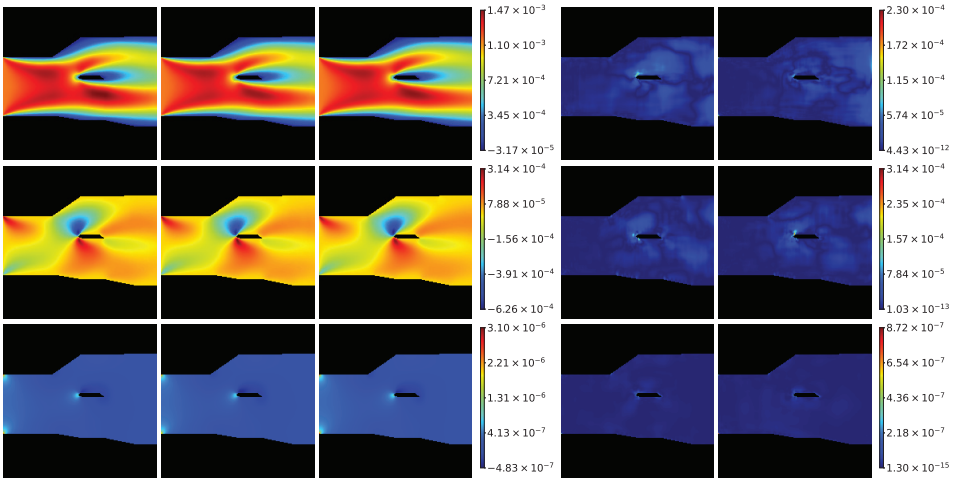

Figure A3. Qualitative results of four different methods. From top to bottom: u, v, P. From left to right: (**a**) ED with SB-LSTM, (**b**) U-Net with SB-LSTM, (**c**) ground truth, (**d**) absolute error of ED with SB-LSTM, (**e**) absolute error of U-Net with SB-LSTM.

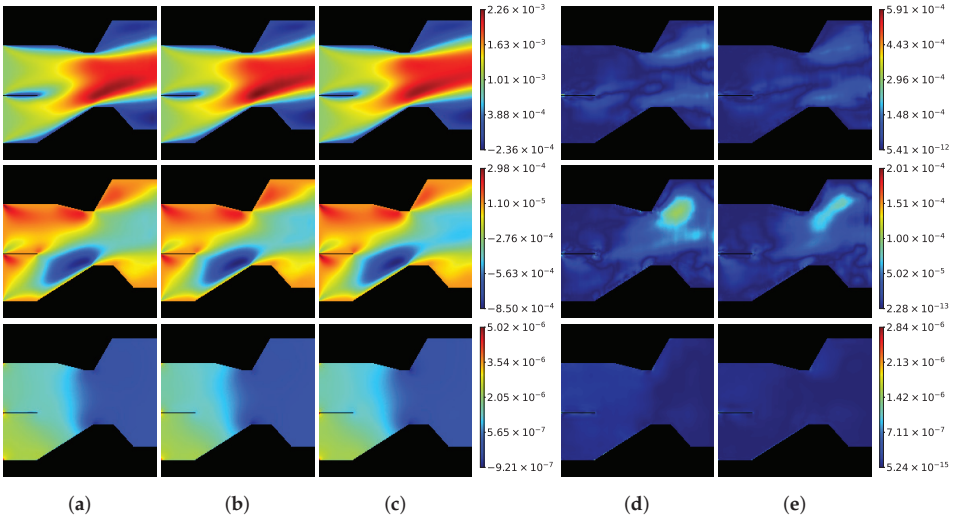

Figure A4. Qualitative results of four different methods. From top to bottom: u, v, P. From left to right: (**a**) ED with SB-LSTM, (**b**) U-Net with SB-LSTM, (**c**) ground truth, (**d**) absolute error of ED with SB-LSTM, (**e**) absolute error of U-Net with SB-LSTM.

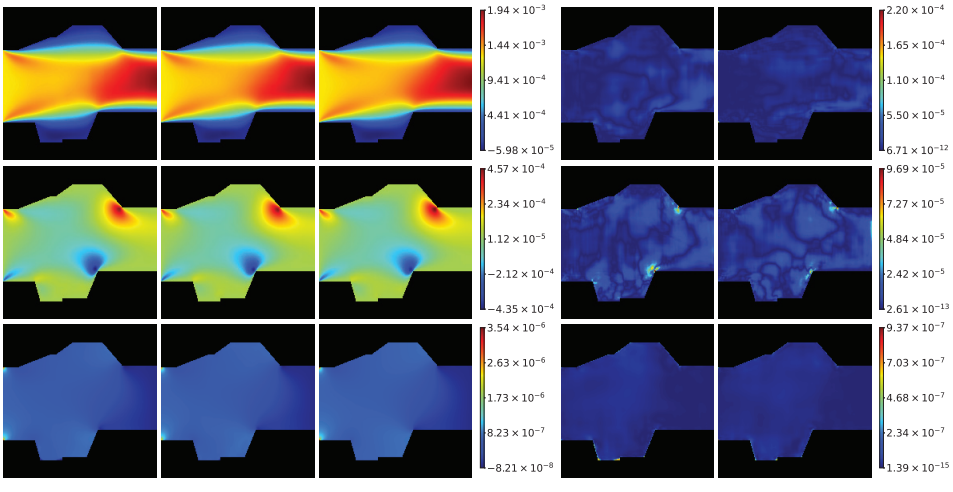

(**a**) (**b**) (**c**) (**d**) (**e**)

Figure A5. Qualitative results of four different methods. From top to bottom: u, v, P. From left to right: (**a**) ED with SB-LSTM, (**b**) U-Net with SB-LSTM, (**c**) ground truth, (**d**) absolute error of ED with SB-LSTM, (**e**) absolute error of U-Net with SB-LSTM.

We comprehensively evaluated the error plots of the cases visualized above, and we observed that the overall error value was lower in models with skip connections, and the errors occurring at the channel boundaries also decreased. This is the same as the difference shown in learning between the U-Net structure and the ED structure in [27].

Appendix B. Comparison of Learning According to Lateral Connection Direction

The results of an additional experiment are included to examine the impact of directionality in the latent space on learning. In this experiment, we replaced the LSTM in the SB-LSTM module with a unidirectional LSTM to investigate the difference in learning. The only difference between the two experiments was the sequential process direction in the latent space, using either forward LSTM or backward LSTM for the experimental condition. The number of parameters in both experiments was the same. The training was conducted using the same hyperparameters as in the previous experiment.

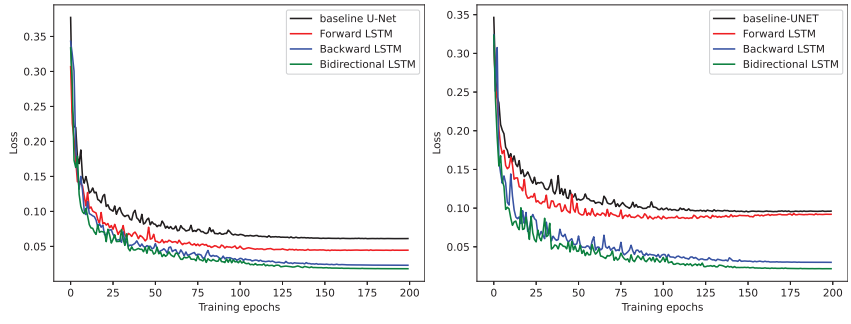

(**a**) (**b**)

Figure A6. Comparison of validation loss from LSTM with different directions. From left to right: (**a**) average loss, (**b**) pressure loss.

When LSTM was added, there was a common effect that sudden discontinuous intervals of values, as shown in Figures 10 and 14, disappeared in the case of velocity

prediction. However, in the case of pressure, the effect showed a significant difference depending on the direction, as shown in Figure A6. Upon analyzing the validation curve of the pressure in the training history, it was observed that even though the same number of learnable parameters was used, the forward LSTM overfitted after 90 epochs, whereas the learning of the backward LSTM was similar to that of the bidirectional LSTM. This indicates that simply adding LSTM does not guarantee improved performance. When incorporating a lateral connection, it is important to establish a pathway to receive the necessary information during supervised learning. An example result is as follows.

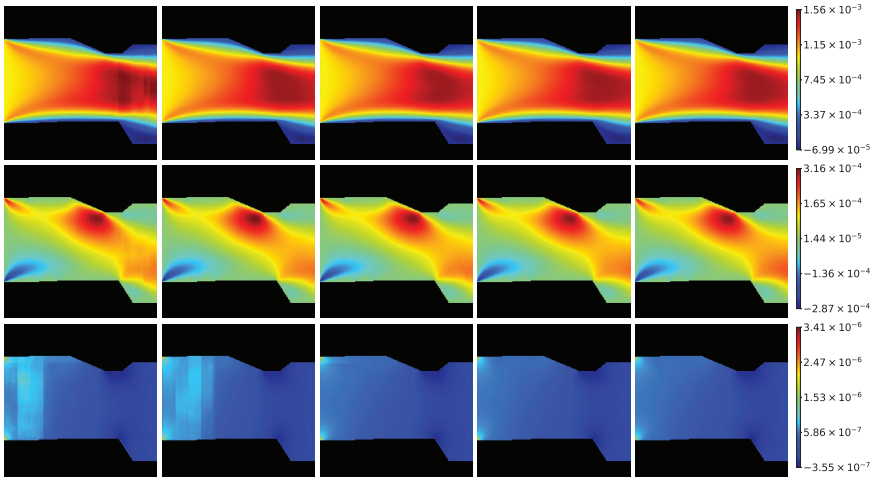

(**a**) (**b**) (**c**) (**d**) (**e**)

Figure A7. Qualitative results of four different methods. From top to bottom: u, v, P. From left to right: (**a**) U-Net, (**b**) U-Net with FLSTM, (**c**) U-Net with BLSTM, (**d**) U-Net with SB-LSTM, (**e**) target.

References

1. Guo, X.; Li, W.; Iorio, F. Convolutional neural networks for steady flow approximation. In Proceedings of the 22nd ACM SIGKDD International Conference on Knowledge Discovery and Data Mining, San Francisco, CA, USA, 13–17 August 2016; pp. 481–490.
2. Ozaki, H.; Aoyagi, T. Prediction of steady flows passing fixed cylinders using deep learning. *Sci. Rep.* **2022**, *12*, 447. [CrossRef] [PubMed]
3. Mao, Z.; Jagtap, A.D.; Karniadakis, G.E. Physics-informed neural networks for high-speed flows. *Comput. Methods Appl. Mech. Eng.* **2020**, *360*, 112789. [CrossRef]
4. Pfaff, T.; Fortunato, M.; Sanchez-Gonzalez, A.; Battaglia, P.W. Learning mesh-based simulation with graph networks. *arXiv* **2020**, arXiv:2010.03409.
5. Sanchez-Gonzalez, A.; Godwin, J.; Pfaff, T.; Ying, R.; Leskovec, J.; Battaglia, P. Learning to simulate complex physics with graph networks. In Proceedings of the International Conference on Machine Learning, PMLR, Virtual, 13–18 July 2020, pp. 8459–8468.
6. LeCun, Y.; Bottou, L.; Bengio, Y.; Haffner, P. Gradient-based learning applied to document recognition. *Proc. IEEE* **1998**, *86*, 2278–2324. [CrossRef]
7. Peng, J.Z.; Aubry, N.; Zhu, S.; Chen, Z.; Wu, W.T. Geometry and boundary condition adaptive data-driven model of fluid flow based on deep convolutional neural networks. *Phys. Fluids* **2021**, *33*, 123602. [CrossRef]
8. Zhou, D.X. Universality of deep convolutional neural networks. *Appl. Comput. Harmon. Anal.* **2020**, *48*, 787–794. [CrossRef]
9. Rusch, T.K.; Bronstein, M.M.; Mishra, S. A survey on oversmoothing in graph neural networks. *arXiv* **2023**, arXiv:2303.10993.
10. Chen, J.; Hachem, E.; Viquerat, J. Graph neural networks for laminar flow prediction around random two-dimensional shapes. *Phys. Fluids* **2021**, *33*, 123607. [CrossRef]
11. Portal-Porras, K.; Fernandez-Gamiz, U.; Ugarte-Anero, A.; Zulueta, E.; Zulueta, A. Alternative artificial neural network structures for turbulent flow velocity field prediction. *Mathematics* **2021**, *9*, 1939. [CrossRef]
12. Gao, H.; Sun, L.; Wang, J.X. PhyGeoNet: Physics-informed geometry-adaptive convolutional neural networks for solving parameterized steady-state PDEs on irregular domain. *J. Comput. Phys.* **2021**, *428*, 110079. [CrossRef]
13. Zhang, Y.; Sung, W.J.; Mavris, D.N. Application of convolutional neural network to predict airfoil lift coefficient. In Proceedings of the 2018 AIAA/ASCE/AHS/ASC Structures, Structural Dynamics, and Materials Conference, Kissimmee, FL, USA, 8–12 January 2018; p. 1903.

14. Viquerat, J.; Hachem, E. A supervised neural network for drag prediction of arbitrary 2D shapes in laminar flows at low Reynolds number. *Comput. Fluids* **2020**, *210*, 104645. [CrossRef]
15. Simonyan, K.; Zisserman, A. Very deep convolutional networks for large-scale image recognition. *arXiv* **2014**, arXiv:1409.1556.
16. Liu, Y.; Lu, Y.; Wang, Y.; Sun, D.; Deng, L.; Wang, F.; Lei, Y. A CNN-based shock detection method in flow visualization. *Comput. Fluids* **2019**, *184*, 1–9. [CrossRef]
17. Deng, L.; Wang, Y.; Liu, Y.; Wang, F.; Li, S.; Liu, J. A CNN-based vortex identification method. *J. Vis.* **2019**, *22*, 65–78. [CrossRef]
18. Haller, G.; Hadjighasem, A.; Farazmand, M.; Huhn, F. Defining coherent vortices objectively from the vorticity. *J. Fluid Mech.* **2016**, *795*, 136–173. [CrossRef]
19. MS, V.M.; Menon, V. Measuring Viscosity of Fluids: A Deep Learning Approach Using a CNN-RNN Architecture. In Proceedings of the First International Conference on AI-ML Systems, Bangalore, India, 21–23 October 2021; pp. 1–5.
20. Liu, Y.; Lu, Y.; Wang, Y.; Sun, D.; Deng, L.; Wan, Y.; Wang, F. Key time steps selection for CFD data based on deep metric learning. *Comput. Fluids* **2019**, *195*, 104318. [CrossRef]
21. Tompson, J.; Schlachter, K.; Sprechmann, P.; Perlin, K. Accelerating eulerian fluid simulation with convolutional networks. In Proceedings of the International Conference on Machine Learning. PMLR, Sydney, Australia, 6–11 August 2017; pp. 3424–3433.
22. Xiao, X.; Zhou, Y.; Wang, H.; Yang, X. A novel CNN-based Poisson solver for fluid simulation. *IEEE Trans. Vis. Comput. Graph.* **2018**, *26*, 1454–1465. [CrossRef]
23. Wiewel, S.; Becher, M.; Thuerey, N. Latent space physics: Towards learning the temporal evolution of fluid flow. In *Proceedings of the Computer Graphics Forum*; Wiley Online Library: Hoboken, NJ, USA, 2019; Volume 38, pp. 71–82.
24. Hou, Y.; Li, H.; Chen, H.; Wei, W.; Wang, J.; Huang, Y. A novel deep U-Net-LSTM framework for time-sequenced hydrodynamics prediction of the SUBOFF AFF-8. *Eng. Appl. Comput. Fluid Mech.* **2022**, *16*, 630–645. [CrossRef]
25. Lino, M.; Fotiadis, S.; Bharath, A.A.; Cantwell, C.D. Current and emerging deep-learning methods for the simulation of fluid dynamics. *Proc. R. Soc. A* **2023**, *479*, 20230058. [CrossRef]
26. Hasegawa, K.; Fukami, K.; Murata, T.; Fukagata, K. CNN-LSTM based reduced order modeling of two-dimensional unsteady flows around a circular cylinder at different Reynolds numbers. *Fluid Dyn. Res.* **2020**, *52*, 065501. [CrossRef]
27. Ribeiro, M.D.; Rehman, A.; Ahmed, S.; Dengel, A. DeepCFD: Efficient steady-state laminar flow approximation with deep convolutional neural networks. *arXiv* **2020**, arXiv:2004.08826.
28. Bhatnagar, S.; Afshar, Y.; Pan, S.; Duraisamy, K.; Kaushik, S. Prediction of aerodynamic flow fields using convolutional neural networks. *Comput. Mech.* **2019**, *64*, 525–545. [CrossRef]
29. Thuerey, N.; Weißenow, K.; Prantl, L.; Hu, X. Deep learning methods for Reynolds-averaged Navier–Stokes simulations of airfoil flows. *AIAA J.* **2020**, *58*, 25–36. [CrossRef]
30. Zhou, H.; Xie, F.; Ji, T.; Zhang, X.; Zheng, C.; Zheng, Y. Fast transonic flow prediction enables efficient aerodynamic design. *Phys. Fluids* **2023**, *35*, 026109. [CrossRef]
31. Weller, H.G.; Tabor, G.; Jasak, H.; Fureby, C. A tensorial approach to computational continuum mechanics using object-oriented techniques. *Comput. Phys.* **1998**, *12*, 620–631. [CrossRef]
32. Patankar, S. *Numerical Heat Transfer and Fluid Flow, Series on Computational Methods in Mechanics and Thermal Sciences*; Hemisphere Publ.: New York, NY, USA, 1980.
33. Park, H.; Park, J. Assessment of word-level neural language models for sentence completion. *Appl. Sci.* **2020**, *10*, 1340. [CrossRef]
34. Ding, Y.; Ye, X.W.; Guo, Y. A multistep direct and indirect strategy for predicting wind direction based on the EMD-LSTM model. *Struct. Control. Health Monit.* **2023**, *2023*, 4950487. [CrossRef]
35. Shivakumara, P.; Tang, D.; Asadzadehkaljahi, M.; Lu, T.; Pal, U.; Hossein Anisi, M. CNN-RNN based method for license plate recognition. *Caai Trans. Intell. Technol.* **2018**, *3*, 169–175. [CrossRef]
36. Sun, Q.; Lee, S.; Batra, D. Bidirectional beam search: Forward-backward inference in neural sequence models for fill-in-the-blank image captioning. In Proceedings of the IEEE Conference on Computer Vision and Pattern Recognition, Honolulu, HI, USA, 21–26 July 2017; pp. 6961–6969.
37. Visin, F.; Kastner, K.; Cho, K.; Matteucci, M.; Courville, A.; Bengio, Y. ReNet: A Recurrent Neural Network Based Alternative to Convolutional Networks. *arXiv* **2015**, arXiv:cs.CV/1505.00393.
38. Kingma, D.P.; Ba, J. Adam: A method for stochastic optimization. *arXiv* **2014**, arXiv:1412.6980.
39. Loshchilov, I.; Hutter, F. SGDR: Stochastic Gradient Descent with Warm Restarts. *arXiv* **2016**, arXiv:cs.LG/1608.03983.
40. Paszke, A.; Gross, S.; Massa, F.; Lerer, A.; Bradbury, J.; Chanan, G.; Killeen, T.; Lin, Z.; Gimelshein, N.; Antiga, L.; et al. PyTorch: An Imperative Style, High-Performance Deep Learning Library. In Proceedings of the Advances in Neural Information Processing Systems (NIPS), Vancouver, BC, Canada, 8–14 December 2019; Volume 32, pp. 8026–8037.
41. Hubel, D.H.; Wiesel, T.N. Receptive fields and functional architecture of monkey striate cortex. *J. Physiol.* **1968**, *195*, 215–243. [CrossRef] [PubMed]
42. Fukushima, K. Neocognitron: A self-organizing neural network model for a mechanism of pattern recognition unaffected by shift in position. *Biol. Cybern.* **1980**, *36*, 193–202. [CrossRef] [PubMed]

applied sciences

MDPI

Article

A Numerical Study on the Influence of Transverse Grooves on the Aerodynamic Performance of Micro Air Vehicles Airfoils

Zhiping Li [1], Yueren Zuo [1], Haideng Zhang [2,*], Long He [1], Enbo Sun [3], Yuhan Long [3], Lifu Zhang [3] and Peng Zhang [4]

[1] Research Institute of Aero-Engine, Beihang University, Beijing 102206, China; zzz6582@163.com (Y.Z.)
[2] College of Aeronatutics and Aerospace, Airforce Engineering University, Xi'an 710038, China
[3] School of Mechanical Engineering, Xi'an Jiaotong University, Xi'an 710049, China; sunenbo@stu.xjtu.edu.cn (E.S.); zlf18226172956@163.com (L.Z.)
[4] Aeronautical Engineering Institute, Civil Aviation University of China, Tianjin 300300, China; zp_sunshine@buaa.edu.cn
* Correspondence: zhanghaideng@126.com

Abstract: Micro Air Vehicles (MAVs) airfoils usually operate at low Reynolds number conditions, where viscous drag will consume a large amount of propulsion power. Due to the small dimensions, many drag reduction methods have failed, resulting in limited current research. To develop an effective method of reducing viscous drag, transverse grooves were placed on the surface of MAVs airfoils in this study, and a numerical investigation was implemented to uncover the corresponding flow control law as well as the mechanism. Research has shown that transverse grooves have an impact on the drag and lift of airfoils. For drag, properly sized transverse grooves have the effect of reducing drag, but under high adverse pressure gradients or when the continuous arrangement of grooves is excessive, the optimal drag reduction effect achieved by the grooves is weakened, and even the drag increases due to the significant increase in pressure difference. In severe cases, it may also cause strong flow separation, which is not conducive to MAV flight. For lift, the boundary vortex in the groove has the ability to reduce the static pressure near the groove. However, high adverse pressure gradients or too many grooves will thicken the boundary layer and increase the blockage effect, resulting in a large static pressure on the grooved side of the airfoil (with an increase in drag). From the perspective of circulation, the static pressure changes on the suction and pressure surfaces have opposite effects on lift. Considering the comprehensive aerodynamic performance of the airfoil, we designed a high lift-to-drag ratio airfoil with grooves, which increased the lift-to-drag ratio by 33.747% compared to the smooth airfoil. Based on the conclusions, we proposed preliminary design criteria for grooved airfoils, providing guidance for subsequent research and applications.

Keywords: MAV airfoil; low Reynolds number; transverse grooves; aerodynamic performance

Citation: Li, Z.; Zuo, Y.; Zhang, H.; He, L.; Sun, E.; Long, Y.; Zhang, L.; Zhang, P. A Numerical Study on the Influence of Transverse Grooves on the Aerodynamic Performance of Micro Air Vehicles Airfoils. *Appl. Sci.* **2023**, *13*, 12371. https://doi.org/10.3390/app132212371

Academic Editors: Vasily Novozhilov, Junhong Park and Cunlu Zhao

Received: 2 October 2023
Revised: 2 November 2023
Accepted: 14 November 2023
Published: 15 November 2023

1. Introduction

By virtue of smaller size and lower speed (<15 cm, 10–20 m/s [1]), Micro Air Vehicles (MAVs) are more portable, more covert, and quieter. Consequently, they have extensive applications in both military and civilian contexts [2,3]. In comparison to rotary-wing and flapping-wing configurations, fixed-wing MAVs, characterized by their higher lift–drag ratios, offer the greatest endurance [4] for a given mass. However, fixed-wing MAVs often operate within low Reynolds number flow regimes, where flow is predominantly governed by viscous drag, leading to a substantial depletion of propulsion energy.

To mitigate drag and enhance airfoil performance, researchers have undertaken extensive investigations from both active and passive control perspectives. These techniques include plasma actuation [5–7], drag-reducing riblets [8–10], flexible wings [11–13], and airfoil optimization [14–16]. Although having been proven effective in controlling the flow of airfoils, most of these techniques are still not perfect in reducing the viscous drag

of small-scale airfoils owing to complicated structures, extra energy cost, or shortage of drag reduction ability. At present, the mainstream research direction in improving the aerodynamic performance of MAVs is focused on airfoil shape, such as directly modifying individual geometric parameters of the airfoil or changing the profile through machine learning and other means. For example, O'meara et al. [17] modified the chord length of the airfoil to suppress the generation of separation bubbles at low Reynolds numbers. Mueller et al. [18] systematically studied the influence of leading-edge geometry on the flight performance of micro air vehicles through wind tunnel tests and made optimizations. Hosseini et al. [19] used machine learning to obtain the optimal configuration of two airfoils placed in series in the incoming flow, and Gad-el-Hak et al. [20] directly optimized the geometric shape of the airfoil using genetic algorithms. However, these methods can only target specific airfoils and have a long research period. In contrast, the modeling method [21,22] can quickly be designed for different working conditions. Then, to develop modeling flow control techniques characterized by a simple structure, low cost, and strong ability of drag reduction seems essential to improve the aerodynamic performance of MAVs airfoils.

Characterized by a simple structure and low manufacturing cost, transverse grooves have been proven efficient in reducing the drag near a solid surface. Transverse grooves represent surface structures that are recessed into the wall and extend perpendicularly to the mainstream flow. Their shapes mimic the occurring dunes found in low-entropy forms in the natural world, typically adopting a V-shape [23]. NASA has proposed the "Micro-Air Bearings" theory (MABS) to elucidate the drag reduction mechanism of this approach [24], such as in Figure 1. In this theory, the stable boundary vortices generated in the grooves act analogously to bearings, rotating and replacing the friction between fluid and the wall with that of the fluid and vortex to reduce viscous drag. Moreover, NASA [24] also pointed out that low-speed flow near the wall will stagnate on the windward side of the groove head and separate on the leeward side (Figure 1, right), resulting in pressure drag. Finally, the drag reduction effect of the transverse groove depends on the difference between the reduced viscous drag and the increased pressure drag.

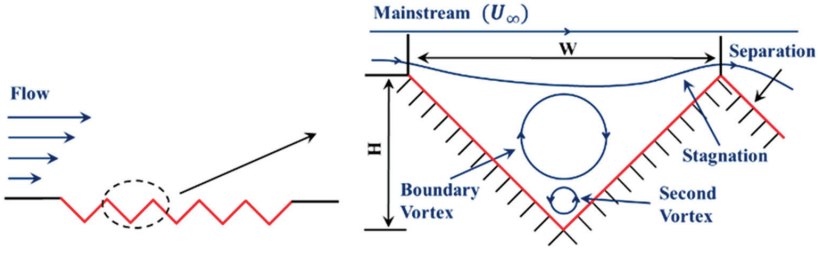

Figure 1. Transverse grooves and MABS theory.

Subsequently, a quantity of experiments and numerical simulation studies conducted by scholars reaffirmed this theory [25–27]. Following these developments, transverse grooves have been widely used in the field of engineering. For instance, Wang et al. [28] designed grooves on Mixed Flow Fans, achieving a reduction of approximately 38% in turbulent energy near the leading edge and a simultaneous reduction in noise. Liu et al. [29] introduced transverse grooves within petroleum pipelines, effectively reducing velocity gradients near the wall and obtaining a drag reduction benefit of 3.21% in a water tunnel. Furthermore, Lufthansa Group [30] applied grooved thin films to a Boeing 777 aircraft, resulting in a reduction of approximately 1% in drag, which means annual fuel savings of approximately 370 tons per aircraft per year. In addition, in 2022, Li et al. [31] combined their work with previous research results to derive a mathematical relationship between the size of transverse grooves and their drag reduction rate. This drag reduction model reduced the design cycle of transverse grooves greatly.

Based on the previous findings, it can be concluded that the transverse grooves may be effective in reducing the viscous drag of MAVs airfoils. Since the flow structures of low-Reynolds number MAVs airfoils are quite different from that of traditional large-Reynolds number flow conditions, it is believed that the influence of transverse grooves on the MAVs airfoils must be different from that on traditional airfoils. However, there is a paucity of relevant research regarding the application of transverse grooves on the airfoils of MAVs. To help establish a transverse groove-based viscous drag reduction technique, this paper applies transverse grooves to MAVs airfoils, and the impact of groove placement strategies on low-Reynolds number airfoil aerodynamic performance as well as the underlying physical mechanisms were numerically investigated. Section 2 introduces how to arrange grooves at different positions on the NACA2412 low-speed airfoil based on the drag-reduction model, as well as the numerical simulation methods used. Sections 3 and 4 respectively outlines research on the position and range of groove arrangement, and provides potential physical mechanisms behind the changes in aerodynamic parameters through the analysis of velocity and vorticity fields. Finally, a grooved airfoil with optimal aerodynamic performance, characterized by the highest lift–drag ratio, was designed. Based on the above conclusions, we propose preliminary design criteria for grooved MAV airfoils (Section 4). Section 5 summarizes the entire article.

2. Simulation Setup

2.1. Geometric Model Selection

In order to approximate the authentic operating conditions of low-altitude flight for MAVs, numerical simulations employed air as the flowing material, with an environmental temperature of 298.15 K and an atmospheric pressure of 1 atm. For fixed-wing MAVs, the selections of airfoils often lean towards well-established low-speed airfoils. Therefore, the NACA2412 airfoil (chord length, c = 100 mm) was chosen. This particularly non-symmetric airfoil exhibits superior aerodynamic performance even during low-speed flight [32]. The typical Reynolds number for MAVs is on the order of 10^5 [11]. Considering that the chord length was 100 mm, finally, the incoming velocity was set as 15 m/s, and the Reynolds number for the airfoil was approximately 1.03×10^5, which conformed to the operational conditions of MAVs. The primary objective of this study was to employ transverse grooves to reduce viscous drag, and as such, the grooves were placed in regions of the airfoil surface where pressure drag was slight. To investigate the influence of adverse pressure gradients (APG) on flow, Clauser [33] defined the Clauser parameter β to quantify the magnitude of adverse pressure gradients, as depicted in Equation (1).

$$\beta = \frac{\delta^*}{\tau_w}\frac{dP}{dx} \tag{1}$$

In Equation (1), δ^* represents the displacement thickness of the boundary layer, τ_w denotes the local shear stress, and dP/dx represents the pressure gradient along the streamwise direction (positive for adverse pressure gradients and negative for favorable pressure gradients). This parameter was employed in our study to assess the extent of adverse pressure gradients. Figure 2 illustrates the distribution of β on the suction and pressure surfaces of the NACA2412 airfoil under the aforementioned flight conditions. Due to the tendency for airfoil flow separation at low angles of attack (AOA) under low Reynolds numbers [11], the angle of attack of the airfoil in Figure 2 is merely 2 degrees.

It can be observed that near the airfoil leading and trailing edges, both the suction and pressure surfaces exhibit high values of β, indicating the presence of large pressure drag in these regions ($\beta > 2$ [34]). To minimize interference and facilitate research, the chord length of the airfoil was evenly divided into four segments, spanning from 20% to 80% of the chord length, and sequentially designated as the "Front(F)," "Middle(M)," "Rear(R)," and "Tail(T)" sections. Grooves would be positioned on the corresponding suction and pressure surfaces in these designated locations, as depicted in Figure 3. The adverse pressure gradient in these areas was not significant.

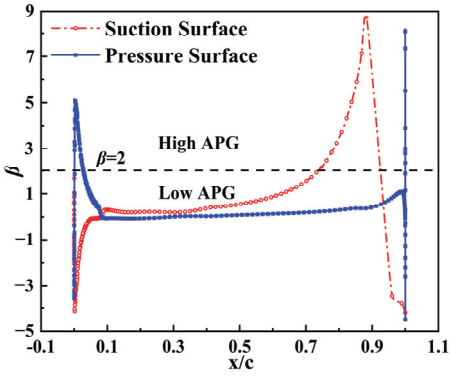

Figure 2. Distribution of β on the NACA2412 airfoil surface.

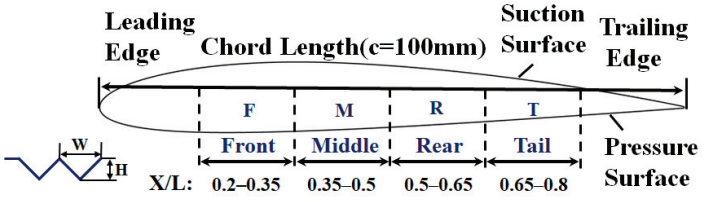

Figure 3. Surface position division of NACA2412 airfoil.

For the transverse V-shaped symmetrical grooves, the most critical geometric parameters are aspect ratio (W/H) and depth (H) (shown in Figure 1). When the aspect ratio of the groove is approximately 2, the boundary vortex structure within the groove is most stable, which is conducive to drag reduction [35]. The selection of groove depth was guided by the Transverse Groove Drag Reduction Model [31], which builds upon the stability of boundary vortices, deriving quantitative relationships among the local Reynolds number, groove dimensions, and drag reduction rate from the vortex dynamics. It allows to directly obtain the groove depth corresponding to the highest drag reduction rate based on the local Reynolds number. The derivation process did not fully consider the impact of strong turbulence, and the model only has high accuracy at low Reynolds numbers ($1.09 \times 10^4 - 5.44 \times 10^5$), which is suitable for the working condition in our research. Due to the fact that the kinematic condition for boundary vortex stability, i.e., the induced velocity equals the migration velocity, is still valid, and the research operating conditions are within the scope of the literature, in subsequent research, all grooves maintained the aspect ratio of 2, and the grooves' initial depths were collectively determined by the local Reynolds number and the Transverse Groove Drag Reduction Model. Furthermore, taking into account the research findings on the influence of adverse pressure gradients on the reduction of drag [36–38], a slight adjustment was made to the initial depths of the grooves based on the Clauser parameter β. Specifically, we conducted flow simulations on inclined plates and extended the relationship between slip velocity, dimensionless velocity, depth of grooves, and β. Finally, the new slip velocity was reintroduced into the drag reduction equation, and the optimal drag reduction size of the groove under the adverse pressure gradient was obtained. This adjustment ultimately yielded the groove depths utilized in the study.

2.2. Solving Methods for Flow Simulations

The principle of fluid dynamics necessitates adherence to three fundamental conservation laws: the law of mass conservation, the law of momentum conservation (expressed

through the Navier–Stokes equations), and the law of energy conservation. Their respective mathematical expressions are denoted by Equations (2)–(4):

$$\frac{\partial \rho}{\partial t} + \frac{\partial}{\partial x_i}(\rho u_i) = S_m \tag{2}$$

$$\frac{\partial}{\partial t}(\rho u_i) + \frac{\partial}{\partial x_j}\left(\rho u_i u_j\right) = -\frac{\partial p}{\partial x_i} + \frac{\partial \tau_{ij}}{\partial_{x_j}} + \rho g_i + F_i \tag{3}$$

$$\frac{\partial(\rho T)}{\partial t} + div(\rho u T) = div\left(\frac{k}{C_p} grad T\right) + S_T \tag{4}$$

In the provided equation, ρ represents fluid density, t denotes time, x_i represents the length in the i-direction, u_i corresponds to the velocity components in the i-direction, and S_m stands for a user-defined source term. The variable p signifies the static pressure of the fluid element, τ_{ij} denotes the stress tensor on the element's surface, g_i and F_i respectively represent the gravitational force and external volumetric forces in the i-direction, C_p is the specific heat capacity, T represents the static temperature, k is the fluid heat transfer coefficient, and S_T accounts for internal heat generation within the fluid and viscous dissipation. These conservation equations, along with various other fluid dynamic equations, collectively form a set of nonlinear partial differential equations using numerical methods to approximate analytical solutions.

When simulating the flow near the grooves, DeGroot et al. [39] conducted a comparative analysis between the numerical methods of Reynolds Averaged Navier–Stokes (RANS) and Direct Numerical Simulation (DNS). The findings revealed that the RANS method not only was cost-effective but also met the required accuracy. Furthermore, the work by Wokoeck et al. [40] demonstrated that, in comparison with experimental results, the RANS method also could effectively simulate the realistic flow around airfoils. Consequently, in this study, the RANS approach was employed for flow simulation computations. Within the RANS, the velocity is decomposed into time-averaged velocity and instantaneous velocity, introducing Reynolds stress terms in the equations. It is necessary to employ turbulence models to close the system of equations. Shome et al. [41] compared the experimental results and evaluated the accuracy of the k-omega SST model in predicting parameters such as airfoil pressure, lift, and drag coefficient at low Reynolds numbers, believing that it is suitable for MAVs. Combining their research and considering the sensitivity of the k-omega SST model to flow separation and the capability to accurately capture near-wall flow characteristics [42], it was selected for the numerical simulation.

The transport equations of the model are as follows, where P_k and P_ω are the generating terms, and k and ω are turbulent kinetic energy and dissipation coefficient, respectively.

$$\frac{\partial k}{\partial t} + u_j \frac{\partial k}{\partial x_j} = \frac{1}{\rho} P_k - \beta \prime k\omega + \frac{1}{\rho}\frac{\partial}{\partial x_j}\left[\left(\mu + \frac{\mu_t}{\sigma_k}\right)\frac{\partial k}{\partial x_j}\right] \tag{5}$$

$$\frac{\partial \omega}{\partial t} + u_j \frac{\partial \omega}{\partial x_j} = \frac{1}{\rho} P_\omega - \beta\omega^2 + \frac{1}{\rho}\frac{\partial}{\partial x_j}\left[\left(\mu + \frac{\mu_t}{\sigma_\omega}\right)\frac{\partial \omega}{\partial x_j}\right] \tag{6}$$

Subsequently, the accuracy of the numerical simulation method was validated in the following sections.

2.3. Computational Domain and Boundary Conditions

For an airfoil, a sufficiently large C-shaped computational domain can effectively mitigate the adverse impact of boundary conditions on the flow [43]. Therefore, the computational domain was established as depicted in Figure 4, with the airfoil positioned at the center of the domain. The shortest distance from the airfoil trailing edge to each boundary of the computational domain was 15 times the chord length, fully satisfying the computational requirements [44]. The size of the fixed wing MAV is relatively small,

and we consider that its airfoil has little variation in spanwise direction. Therefore, a two-dimensional grid was used, and the calculation was also two-dimensional.

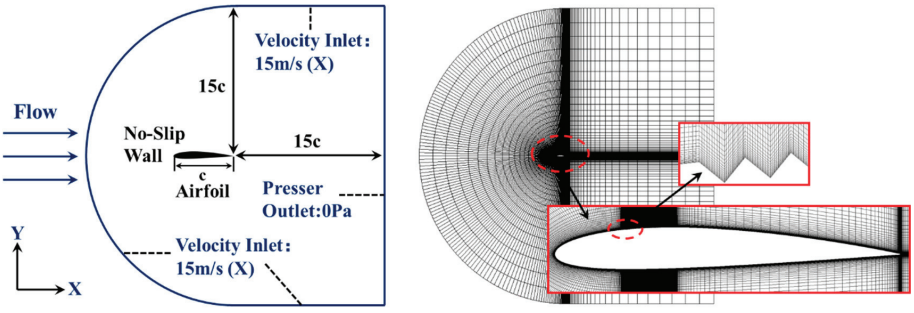

Figure 4. Schematic representation of the computational domain grid and boundary conditions.

In Figure 4, the inlet velocity was set at 15 m/s, the outlet pressure was maintained at 0 Pa (gauge pressure), and the airfoil surfaces were treated as no-slip wall boundaries. Structured quadrilateral grids were generated using the commercial software ICEM 18.2, with a first-layer grid height of 0.001 mm (the y^+ value less than 1), aiming to fulfill the computational requirements of the k-omega SST model while accurately capturing geometric variations in the normal direction of grooves. Additionally, uniform grid refinement was implemented in the streamwise direction of the grooves to ensure the accuracy of the flow simulation near the grooves. Ultimately, the mesh achieved a minimum angle of 43.3 degrees and a Jacobian Ratio minimum value of 0.876, indicating that the mesh exhibits favorable orthogonality and possesses overall high quality. This meticulously crafted mesh was employed for pressure-based implicit computations using the RANS method within the commercial software Fluent 18.2. Due to the selected cruising state for the calculation conditions and stable flow, we adopted a steady state calculation.

2.4. Validation of Grid Independence and Computational Accuracy

In order to enhance computational efficiency while ensuring accuracy, grid independence validation was conducted. Figure 5 presents the relative variation in total drag of the airfoil under different levels of grid refinement. It can be observed that when the number of grid cells exceeds 100,000, the relative change in drag remains below 0.5%. Consequently, the grid with approximately 100,000 total nodes was ultimately chosen for the subsequent accuracy validation of simulation, with grid cell counts ranging from 800,000 to 1.2 million in cases where the airfoil featured grooves.

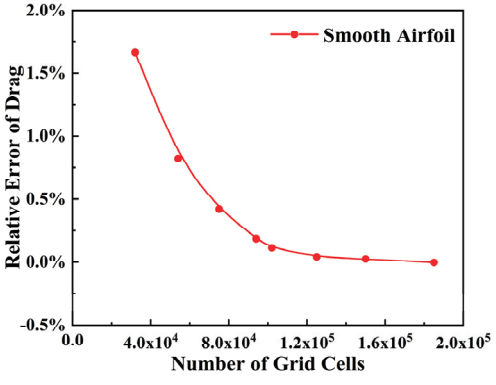

Figure 5. Validation of grid independence.

Figure 6 illustrates the lift coefficients of the airfoil at various angles of attack using the numerical methods mentioned above and compares them with the experimental results of the NACA2412 airfoil at low Reynolds numbers [45].

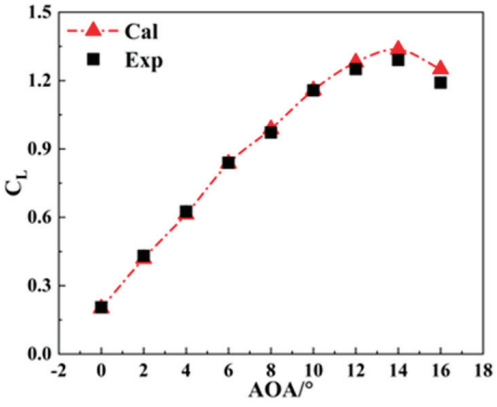

Figure 6. Validation of computational accuracy.

It can be observed that within the range of 0 to 16 degrees of angle of attack, the computational results exhibit a notable agreement with the experimental data. Particularly noteworthy is the fact that the deviation in lift coefficient for cases with small angles of attack does not exceed 1%. This confirms that the numerical computation and grid partitioning methods employed in this study can exactly reflect the aerodynamic performance of the airfoil. Therefore, the simulation methods were adopted for subsequent research.

3. Effect of Grooves Position on Aerodynamic Performance of Airfoil

In order to improve the flight performance of MVAs, it is imperative to increase the battery capacity while concurrently reducing the energy consumption per unit time of propulsion. The former is intricately linked to the lift coefficient of the airfoil, whereas the latter is contingent upon the drag coefficient of the airfoil. The expressions for the lift coefficient and drag coefficient are delineated in Equations (7) and (8), as follows:

$$C_L = \frac{L}{\frac{1}{2}\rho|V|^2 c} \tag{7}$$

$$C_D = \frac{D}{\frac{1}{2}\rho|V|^2 c} \tag{8}$$

In the equations, "L" represents lift, "D" denotes drag, and "c" stands for the characteristic length of the airfoil. The comprehensive impact of both lift and drag on aerodynamic performance is expressed through the airfoil lift–drag ratio (C_L/C_D). To contrapuntally distribute grooves over a wide range, it is significant to investigate the influence of groove placement. Consequently, we positioned grooves on both the suction and pressure surfaces corresponding to the front, middle, rear, and tail sections, as illustrated in Figure 3, to systematically explore their aerodynamic performance. The depths of the grooves are determined collectively by the local Clauser parameter (β), the local Reynolds number, and the drag reduction model (Li et al.) [31]. When the span is within 5 mm, we assume that the local Reynolds number and β remain relatively constant, and the groove depth (H) in this segment remains consistent. The specific groove depths for each segment are illustrated in Figure 7. The number of grooves is the range divided by the width (rounded off).

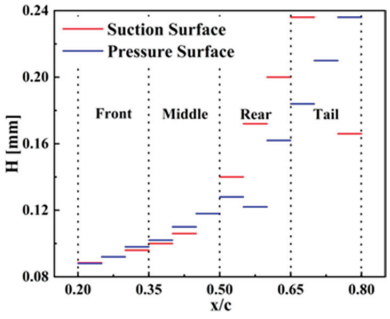

Figure 7. Depth of grooves at different positions on the airfoil surface.

We placed these transverse grooves on various segments of the airfoil suction and pressure surfaces, as depicted in Figure 3. The aerodynamic performance parameters of the airfoil are presented in Figure 8. In this figure, the blue dashed line represents the data corresponding to the smooth airfoil without grooves for reference.

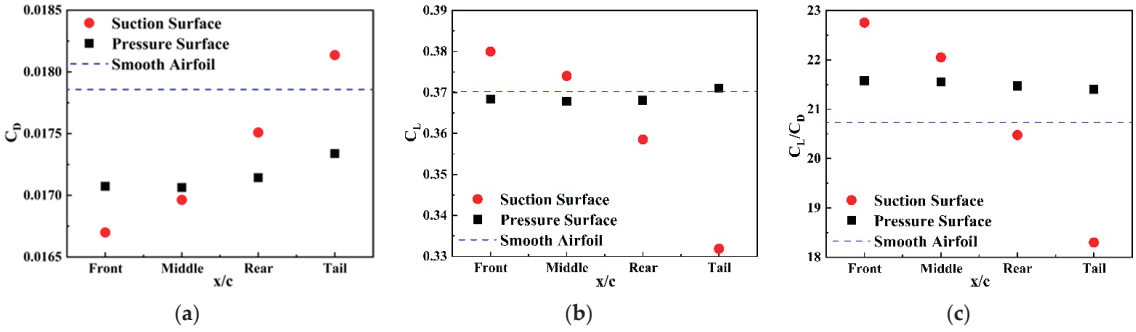

Figure 8. Effect of grooves at different positions on aerodynamic parameters of airfoils: (**a**) C_D; (**b**) C_L; and (**c**) C_L/C_D.

From Figure 8a, it is evident that in most cases, the airfoil with grooves experiences a significant reduction in drag coefficient. Moreover, regardless of whether the grooves are placed on the suction or pressure surface, those positioned closer to the leading edges result in a lower drag coefficient for the airfoil. Therefore, in subsequent designs, it is advisable to place grooves close to the front portion of the airfoil. In comparison to the suction surface, grooves on the pressure surface exhibit relatively similar drag reduction capabilities across different positions, with variations occurring primarily in the rear section. In terms of drag reduction effectiveness, placing grooves on the front section of the suction surface yields the smallest drag coefficient and the highest drag reduction rate. Additionally, when grooves are positioned in the middle section of the suction surface, the drag coefficient of the airfoil is still lower than that corresponding to the pressure surface. However, when grooves are positioned in the rear section of the suction surface, their drag reduction capabilities notably diminish compared to the grooves in the same location on the suction surface. And when grooves are placed in the tail section of the suction surface, the drag reduction effect rapidly deteriorates, so much so that the drag coefficient even surpasses that of the smooth airfoil, which is detrimental to flight. This observation indicates that after placing grooves in positions characterized by significant adverse pressure gradients (as illustrated in Figure 2), the benefits of grooves in reducing viscous drag can no longer offset the increase in pressure-induced drag, leading to a rapid increase in overall drag. Consequently, this region was avoided when subsequently arranging the grooves.

From the perspective of lift coefficient (Figure 8b), when grooves are placed on the pressure surface, the change in the airfoil lift coefficient is little, with variations not exceeding 1% in magnitude compared to the smooth airfoil. However, when grooves are positioned on the pressure surface, there is a more pronounced alteration in the lift coefficient. When grooves are located on the front section of the suction surface, there is a substantial increase in the airfoil lift coefficient. In contrast, when grooves are situated in the middle section, although the lift coefficient remains higher than that of the smooth airfoil, the increment is less than half of that observed in the front section. Furthermore, when grooves are placed in the rear or tail section of the suction surface, the aerodynamic performance of the airfoil deteriorates rapidly, causing the lift coefficient to drop below that of the smooth airfoil.

Due to the relatively stable lift coefficient and drag coefficient, as depicted in Figure 8c, there is little variation in the lift–drag ratio when grooves are placed at different locations on the pressure surface. These results exhibit higher lift–drag ratios greater that of the smooth airfoil, and indicate that the aerodynamic performance of the airfoil can experience a modest improvement when appropriately sized grooves are placed on any segment of the pressure surface. For grooves on the suction surface, owing to the smaller drag coefficient and larger lift coefficient, the airfoil lift–drag ratio can be significantly enhanced when grooves are positioned in the front and middle segments. The effects of placing grooves on the rear and tail segments of the suction surface, conversely, lead to a rapid deterioration in the airfoil aerodynamic performance, especially in the tail section. On the whole, the variations in the drag coefficient largely align with the trends observed in groove-induced drag reduction under adverse pressure gradients [37,38], where groove drag reduction rate becomes greater under mild adverse pressure gradients (Figure 2, Front and Middle sections of the suction surface), but deteriorates as the adverse pressure gradient approaches a strong magnitude ($\beta = 2$) (Figure 2, Rear and Tail sections of the suction surface). Due to the absence of significant pressure gradients on the pressure surface, the drag reduction effects observed in various segments are similar. In order to investigate the reasons behind the impact of grooves at different locations on the suction surface on the lift coefficient, Figure 9 compares the pressure distributions near the suction surface.

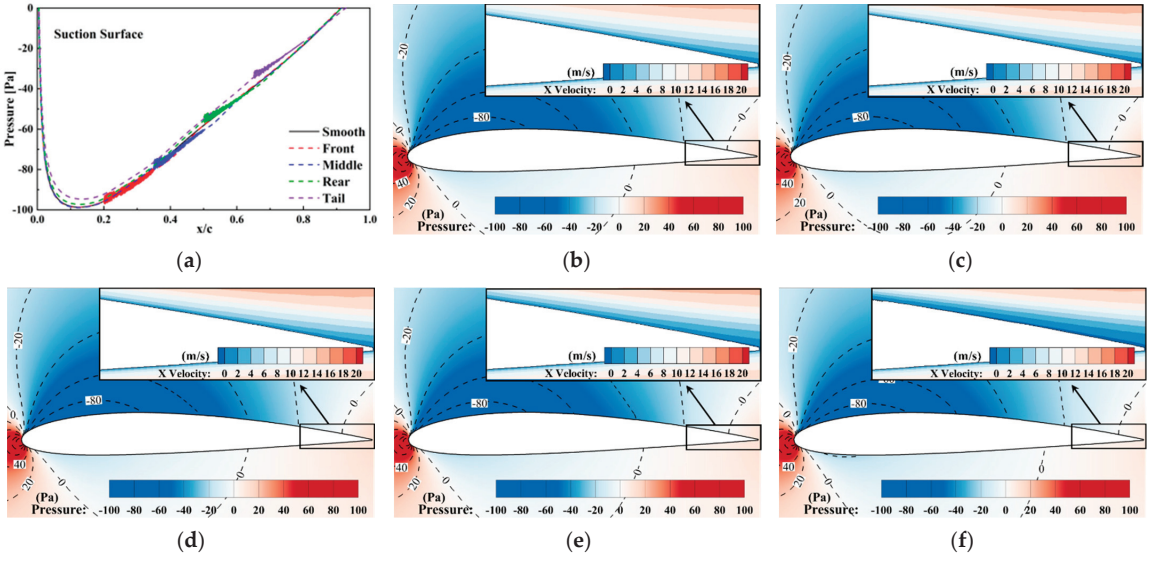

Figure 9. Pressure distribution of airfoils (suction surface grooves): (**a**) Pressure on suction surfaces; (**b**) smooth airfoil; (**c**) front section; (**d**) middle section; (**e**) rear section; and (**f**) tail section.

The pressure contours in Figure 9b–f show that the grooves on the suction surface have almost no effect on the pressure distribution near the pressure surface. As illustrated in Figure 9a, when grooves are positioned in the front or middle section of the airfoil, the pressure distribution on the suction surface closely resembles that of the smooth airfoil, with pressure values reduced only in the vicinity of the grooves and their downstream regions. This is evident in Figure 9c,d as an expansion of the deep blue region (pressure below −80 Pa) compared to the smooth airfoil (Figure 9b). The source of this pressure drop is the stable rotating vortex in the groove. The high-energy vortex in the groove injects momentum into the low-energy fluid near it, causing an increase in radial velocity and pressure drop [46,47]. So, this phenomenon only occurs in the grooves and their downstream vicinity. The pressure drop on the suction surface implies an increase in lift, resulting in an increase in the lift coefficient. Conversely, when grooves are placed in the rear or tail section of the suction surface, as indicated by the green and purple dashed lines in Figure 9a, the overall pressure on the suction surface increases. This is because arranging grooves in areas with high adverse pressure gradients such as the rear or tail section can quickly thicken the boundary layer near the rear of the suction surface (as shown in the enlarged image of Figure 9e,f, where the blue low-speed area near the airfoil increases), which strengthens the blockage effect and increases the overall pressure on the suction surface. In Figure 9e,f, this is manifested as a reduction in the blue regions representing low pressure to varying degrees, signifying a decrease in lift and a substantial drop in the lift coefficient.

4. Effect of Grooves Range on Aerodynamic Performance of Airfoil

Purposefully arranging appropriately sized grooves on the front or middle section of the suction surface, as well as on the front, middle, rear, or tail section of the pressure surface, can enhance the aerodynamic performance of the airfoil. However, the mere simultaneous placement of these grooves on the same airfoil does not guarantee the attainment of maximum aerodynamic benefits at low Reynolds numbers. It remains uncertain whether grooves situated on the rear section contribute to the aerodynamic performance of the airfoil due to the interactions among the grooves when the range of groove placement on the suction surface is extensive. To address these issues and ultimately design an airfoil with the highest lift–drag ratio, an investigation into the impact of widely placed grooves on the airfoil surface is imperative.

Because of the severe deterioration of airfoil aerodynamics resulting from the tail section grooves on the suction surface, we restricted the large-range grooves to the front-middle and front-middle-rear sections of the suction surface. Grooves on the pressure surface can be continuously positioned in the front-middle, front-middle-rear, and front-middle-rear-tail sections. After arranging these grooves, the aerodynamic parameters of the airfoil were as depicted in Figure 10.

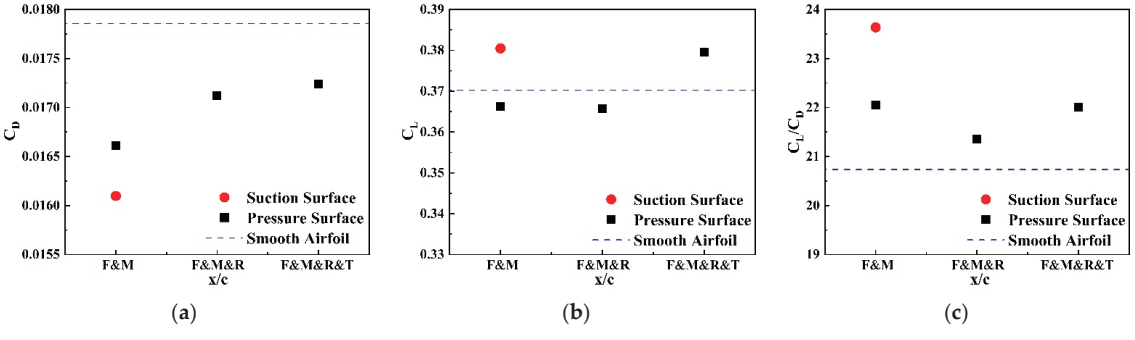

Figure 10. Effect of grooves at different ranges (continuous) on aerodynamic parameters of airfoils: (**a**) C_D; (**b**) C_L; and (**c**) C_L/C_D.

Comparing with Figure 8, in most cases, the lift–drag ratios of the airfoils were dramatically improved with the large-range of grooves (Figure 10c). For instance, when grooves are placed in the front-middle section of the suction surface, the drag coefficient decreased to 0.016 and the lift coefficient increased to 0.381, resulting in an increased lift–drag ratio of the airfoil to 23.635 (smooth airfoil: 20.733). From both a drag reduction and lift enhancement perspective, this project is markedly superior to the sole placement of grooves in one segment of the suction surface. Analyzing the trends of the black dots in Figure 10c, it can be observed that when large-range grooves are positioned on the pressure surface, airfoil with grooves placed in the front-middle section and front-middle-rear-tail section exhibit higher lift coefficients compared to only one section. The lift coefficient increases from around 21.5 to 22. However, for the grooves in the front-middle-rear section on the pressure surface, although their lift–drag ratios show improvement compared to the smooth airfoil, they remain lower than the grooves placed solely in the front section of the pressure surface. This phenomenon is attributed to the unexpected fact that as the number of grooves increases on the airfoil, the drag coefficient actually rises (in the front-middle-rear-tail section project, the increase in lift-to-drag ratio is mainly owed to an increase in the lift coefficient).

To understand why a large number of grooves can weaken the overall drag reduction effect, an exploration of the underlying reasons is imperative. Moreover, it is noteworthy that Figure 10 lacks data for the scenario where grooves are placed in the front-middle-rear section on the suction surface. This omission is due to the emergence of strong non-steady-state phenomena during calculations. As depicted in Figure 11, the overall drag coefficient is elevated and exhibits continuous fluctuations, rendering the calculation results challenging to analyze comprehensively.

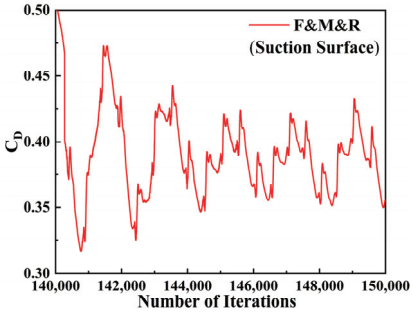

Figure 11. Drag coefficient changes with the number of iterations.

In order to investigate the reasons for the increase in drag coefficient and why the above non-steady-state phenomena occured, we analyzed the velocity and vorticity contours of the flow.

Comparing Figure 12a–c, it becomes evident that when grooves are extensively placed on the suction surface, certain separation structures manifest near the grooves that are unlikely to appear at high Reynolds numbers and low angles of attack. For instance, when grooves are arranged on the front-middle section (Figure 12b) or front-middle-rear section (Figure 12c) of the suction surface, wavy, low-speed regions (depicted in blue) appear in proximity to the grooves. In the enlarged local images, it is evident that there are obvious shedding vortices near the grooves. In the case of the front-middle section, this tendency is less conspicuous; however, when grooves are positioned in the front-middle-rear section, this separation phenomenon extensively occurs near the rear portion of the suction surface. Moreover, the wake region exhibits heightened instability, characterized by the expansion of the blue low-speed region at the trailing edge and the rapid curvature of streamlines. When grooves are exclusively placed in the front section of the suction surface (Figure 12a), almost no such phenomenon is observed. This elucidates why, when

grooves are arranged on the front-middle-rear section of the suction surface, the drag coefficient exhibits significant fluctuations with iteration steps. Furthermore, a comparison between Figure 12d,e reveals that when grooves are positioned on the front-middle section of the pressure surface, the blue low-speed region near the rear part of the pressure surface enlarges. This implies an increase in boundary layer thickness near the rear, resulting in elevated drag, aligning with the trends observed in the black dots of Figure 8a. This phenomenon also increases the static pressure on the pressure surface, resulting in an increase in the overall lift coefficient of the airfoil, as shown in Figure 10b. In contrast, when grooves are placed on the front-middle-rear-tail section of the pressure surface, not only does the boundary layer near the tail thicken, but the wake also exhibits mild instability, with minor deviations observed in streamlines near the trailing edge.

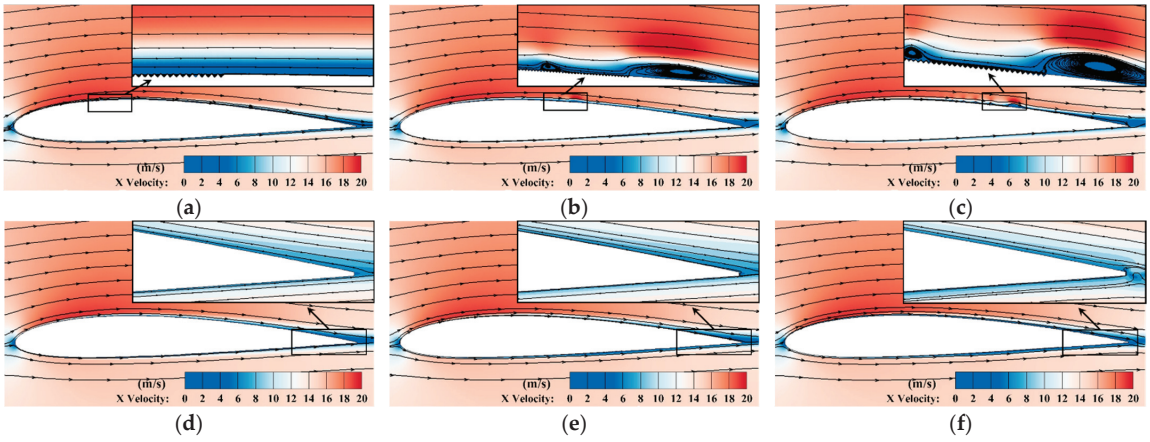

Figure 12. Velocity contours of airfoils with grooves arranged in different ranges (suction surface grooves: (**a**,**b**), pressure surface grooves: (**d**–**f**): (**a**) front section; (**b**) front-middle section; (**c**) front-middle-rear section; (**d**) smooth airfoil; (**e**) front-middle-rear section; and (**f**) front-middle-rear-tail section.

From Figure 13, the vorticity near the grooves increases to varying degrees, indicated by the proliferation of regions with strong vorticity (depicted in red). When grooves are only placed in the front section of the suction surface, the change in vorticity distribution is slight. However, when grooves are positioned in the front-middle section of the suction surface, mild fluctuations in vorticity distribution are observed in the vicinity of the airfoil midsection (Figure 13c), but the duration is not long, indicating the onset of weaker flow separation. When grooves are arranged in the front-middle-rear section of the suction surface, a series of detached, bubble-like structures form near the rear part of the suction surface (Figure 13c). This demonstrates the evolution and rupture of separation bubbles, causing highly unstable flow. In Figure 13e,f, when grooves are extensively placed on the pressure surface, the vorticity intensity on the pressure surface increases, particularly near the trailing edge. This signifies an augmented turbulence level. Because the diffusion rate of turbulent vortices greatly exceeds that of viscous vortex diffusion, the boundary layer thickness increases, leading to an elevation in the drag coefficient.

To mitigate the impact of increased turbulence levels, the possibility of discontinuously placing grooves on the airfoil surface was explored. Figure 14 provides a comparative analysis of the variation in aerodynamic parameters of airfoils when grooves are positioned in the front-middle-rear-tail section, front-middle-tail section, and middle-rear section of the suction surface, and the middle-rear section of the pressure surface.

It can be observed that when grooves are absent on the rear section or front-tail section of the pressure surface, the drag coefficient is lower than that of the grooves placed in the front-middle-rear-tail section of the pressure surface. When grooves are positioned on the

middle-rear section of the suction surface, the airfoil drag coefficient is lower than that of the smooth airfoil but remains higher than the grooves placed in the front-middle section of the suction surface. From the perspective of lift coefficient, the intermittent placement of grooves leads to an overall reduction in the lift coefficient. However, due to a more significant reduction in drag coefficient, grooves in the front-middle-tail section of the pressure surface yield the highest lift–drag ratio.

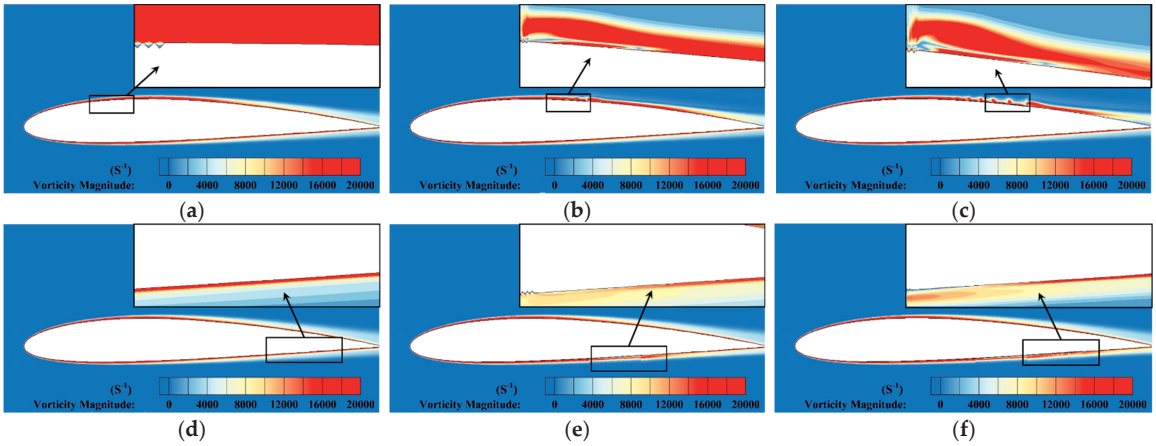

Figure 13. Vorticity contours of airfoils with grooves arranged in different ranges (suction surface grooves: (**a**,**b**), pressure surface grooves: (**d**–**f**): (**a**) front section; (**b**) front-middle section; (**c**) front-middle-rear section; (**d**) smooth airfoil; (**e**) front-middle-rear section; and (**f**) front-middle-rear-tail section.

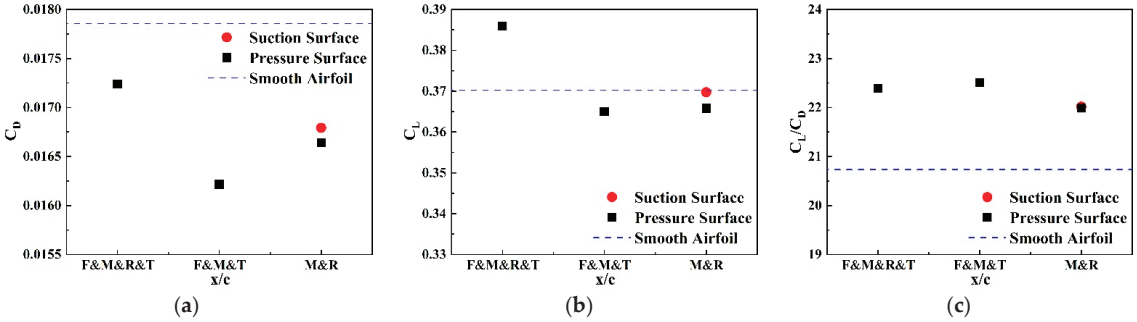

Figure 14. Effect of grooves at different ranges (discontinuous) on aerodynamic parameters of airfoils: (**a**) C_D; (**b**) C_L; and (**c**) C_L/C_D.

From the velocity contours near the airfoil in Figure 15, it can be observed that when grooves are intermittently placed on the front-middle-tail section of the pressure surface, the overall velocity distribution of the airfoil is similar to that of a smooth airfoil without grooves. Due to the reduced interaction between grooves, the wake becomes significantly more stable (as evidenced by the reduced streamline deflection in Figure 15c). In the locally enlarged image of Figure 15f, the distribution of vortices near the pressure surface is more uniform than when the grooves are continuously placed in the front-middle-rear-tail section of the pressure surface (Figure 15e), resulting in a thinner boundary layer and greater stability in the wake region. Consequently, there is a substantial reduction in the drag coefficient. But at the same time, the thinner boundary layer highlights the ability of the grooves themselves to reduce static pressure, resulting in a decrease in static pressure on the pressure surface and a decrease in lift coefficient. From the perspective

of comprehensive aerodynamic performance, arranging grooves in the front-middle-tail section of the pressure surface will still increase the lift–drag ratio.

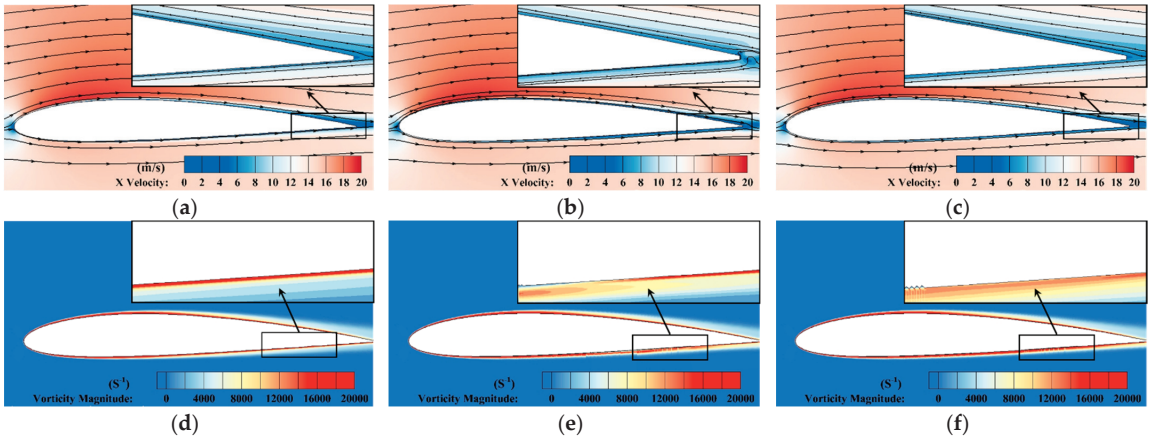

Figure 15. Velocity (upper) and vorticity (lower) contours of airfoils with grooves arranged on the pressure surface: (**a**,**d**) smooth airfoil; (**b**,**e**) front-middle-rear-tail section; and (**c**,**f**) front-middle-tail section.

Based on the analysis above, it is evident that by introducing grooves in the front-middle section of the suction surface and the front-middle-tail section of the pressure surface, one can achieve their respective maximum lift–drag ratios. Therefore, the ultimate choice was made to simultaneously incorporate appropriately sized grooves in both the front-middle section of the suction surface and the front-middle-tail section of the pressure surface and then compare their aerodynamic performance with airfoils that have grooves solely on the suction or pressure surface.

As depicted in Figure 16, when grooves are simultaneously incorporated in both the front-middle section of the suction surface and the front-middle-tail section of the pressure surface of the airfoil, there is a substantial reduction in the overall drag coefficient of the airfoil. Furthermore, the lift coefficient is extremely higher compared to airfoils with grooves on only one surface. The combination of lower drag coefficient and higher lift coefficient results in a remarkable enhancement of the lift–drag ratio, increasing from 20.733 for the smooth airfoil to 27.730. This represents an approximately 33.75% improvement in aerodynamic performance, which can greatly improve the endurance of MAVs.

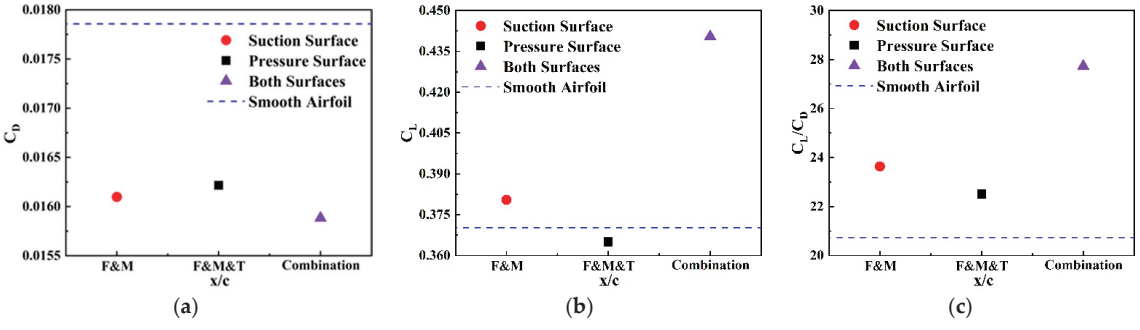

Figure 16. Aerodynamic performance of single or double-grooved airfoils: (**a**) C_D; (**b**) C_L; and (**c**) C_L/C_D.

Based on the above conclusions, we summarize the preliminary design criteria for grooved MAV airfoil: the grooves should be arranged as far as possible in the low adverse

pressure gradient region of the airfoil surface ($\beta < 0.5$), such as near the leading edge. This is because under high adverse pressure gradient, the effect of grooves on drag reduction and lift increase becomes weak, and it is also easy to cause separation, resulting in flight instability. On the other hand, with low pressure gradient, too large a range of grooves can quickly increase the thickness of the boundary layer, offsetting the aerodynamic benefits brought by the grooves. Adopting a discontinuous arrangement at the rear of the airfoil can reduce this effect, further improving the lift-to-drag ratio of the airfoil. These theories have certain guiding significance for the design of grooved airfoils, but the quantification of parameters requires further research in our follow-up work.

5. Conclusions

This study focused on the low-speed NACA2412 airfoil as the research subject, employing numerical simulation techniques to investigate the feasibility of implementing transverse grooves as a drag-reduction structure on the airfoil of the MAV. Additionally, it conducted an analysis of the physical mechanisms underlying the influence of various groove placement schemes at low Reynolds numbers on the lift–drag ratio of the airfoil. Based on the rules, we have designed a grooved airfoil with a high lift–drag ratio and proposed preliminary design criteria for grooved MAV airfoils that have a certain guiding significance for subsequent research. The specific research findings are as follows:

(1) The grooves near the leading edge of the airfoil exhibit lower drag, with the lowest drag coefficient decreasing from 0.0179 to 0.0167 compared to the smooth airfoil. As the groove position moves backwards, the unfavorable pressure gradient will reduce the drag-reduction effect of the grooves. The grooves on the pressure surface have a slight impact on the lift coefficient of the airfoil, whereas the grooves on the suction surface cause a significant change in the lift coefficient. At the front, the ability of the grooves themselves to reduce static pressure will reduce the static pressure on the suction surface and increase lift. As the groove position moves back, the thickening of the boundary layer causes an increase in static pressure on the suction surface, resulting in a decrease in the lift coefficient from 0.380 to 0.332 (smooth airfoil: 0.370). Therefore, the relationship between the lift–drag ratio and groove position is similar to the lift coefficient.

(2) When grooves are widely deployed on the suction surface of the airfoil, grooves positioned in the front-middle section yield the best aerodynamic performance (low β). In contrast, excessive grooves on the suction surface can cause airflow separation, and the degree of separation is positively correlated with the range and the local adverse pressure gradient. When significant separation occurs, it results in a series of separated bubbles causing disorder flow, which will be detrimental to the flight of MAV. On the pressure surface, widespread grooves will thicken the boundary layer, ultimately leading to increased drag and lift. Intermittently placing groove on the airfoil can reduce mutual interference between grooves, reducing this impact.

(3) Simultaneously introducing grooves in both the front-middle section of the suction surface and the front-middle-tail section of the pressure surface of the airfoil has yielded the optimal aerodynamic performance, a 33.747% increase in lift-to-drag ratio. This result confirms the effectiveness of the application of transverse grooves on MAVs, and we have also given preliminary design criteria: do not arrange grooves in high adverse pressure gradient areas ($\beta > 0.5$), and under low adverse pressure gradients, discontinuous arrangements of large-scale grooves should be adopted at the rear of the airfoil.

Author Contributions: Conceptualization, Z.L., Y.Z., H.Z. and L.H.; Data curation, Y.Z.; Formal analysis, Z.L., Y.Z. and H.Z.; Funding acquisition, Z.L., P.Z.; Investigation, Y.Z.; Methodology, Y.Z. and H.Z.; Project administration, Z.L.; Software, Y.Z.; Supervision, Z.L., P.Z. and H.Z.; Validation, Y.Z.; Writing—original draft, Y.Z.; Writing—review & editing, H.Z., P.Z., L.H., E.S., Y.L. and L.Z. All authors have read and agreed to the published version of the manuscript.

Funding: This research was funded by the National Natural Science Foundation of China (No. 52176032), National Science and Technology Major Project (2017-||-0005-0016), Natural Science Foundation of Tianjin Municipal Science and Technology Commission (Youth Program No. 22JCQNJC00050).

Institutional Review Board Statement: Not applicable.

Informed Consent Statement: Not applicable.

Data Availability Statement: Data are contained within the article.

Conflicts of Interest: The authors declare no conflict of interest.

References

1. Davis, W.R. Micro UAV. In Proceedings of the Presentation to 23rd AUVSI Symposium, Orlando, FL, USA, 15–19 July 1996.
2. Hassija, V.; Saxena, V.; Chamola, V. Scheduling drone charging for multi-drone network based on consensus time-stamp and game theory. *Comput. Commun.* **2020**, *149*, 51–61.
3. Serokhvostov, S.V. Ways and technologies required for MAV miniaturization. In Proceedings of the European Micro Air Vehicle Conference (EMAV'08), Braunschweig, Germany, 8–10 July 2008.
4. Keennon, M.; Grasmeyer, J. Development of two MAVs and vision of the future of MAV design. In Proceedings of the AIAA International Air and Space Symposium and Exposition: The Next 100 Years, Dayton, OH, USA, 14–17 July 2003; p. 2901.
5. Goeksel, B.; Greenblatt, D.; Rechenberg, I.; Nayeri, C.; Paschereit, C. Steady and unsteady plasma wall jets for separation and circulation control. In Proceedings of the 3rd AIAA Flow Control Conference, San Francisco, CA, USA, 5–8 June 2006; p. 3686.
6. Göksel, B.; Greenblatt, D.; Rechenberg, I.; Kastantin, Y.; Nayeri, C.N.; Paschereit, C.O. Pulsed plasma actuators for active flow control at MAV Reynolds numbers. In Proceedings of the Active Flow Control: Papers Contributed to the Conference "Active Flow Control 2006", Berlin, Germany, 27–29 September 2006; Springer: Berlin/Heidelberg, Germany, 2007; pp. 42–55.
7. Rizzetta, D.P.; Visbal, M.R. Numerical investigation of plasma-based control for low-Reynolds-number airfoil flows. *AIAA J.* **2011**, *49*, 411–425.
8. Radmanesh, M.; Samani, I.; Amiriyoon, A.; Tavakoli, M.R. The effects of rectangular riblets on rectangular micro air vehicles for drag reduction. *Proc. Inst. Mech. Eng. Part G J. Aerosp. Eng.* **2017**, *231*, 364–373. [CrossRef]
9. Viswanath, P.R. Aircraft viscous drag reduction using riblets. *Prog. Aerosp. Sci.* **2002**, *38*, 571–600.
10. Nafar-Sefiddashti, M.; Nili-Ahmadabadi, M.; Saeedi-Rizi, B.; Pourhoseini, J. Visualization of flow over a thick airfoil with circular cross-sectional riblets at low Reynolds numbers. *J. Vis.* **2019**, *22*, 877–888.
11. DeLuca, A.M.; Reeder, M.F.; Freeman, J.A.; Ol, M.V. Flexible-and rigid-wing micro air vehicle: Lift and drag comparison. *J. Aircr.* **2006**, *43*, 572–575. [CrossRef]
12. Hu, H.; Tamai, M.; Murphy, J.T. Flexible-membrane airfoils at low Reynolds numbers. *J. Aircr.* **2008**, *45*, 1767–1778.
13. Ifju, P.; Jenkins, D.; Ettinger, S.; Lian, Y.; Shyy, W.; Waszak, M. Flexible-wing-based micro air vehicles. In Proceedings of the 40th AIAA Aerospace Sciences Meeting & Exhibit, Reno, NV, USA, 14–17 January 2002; p. 705.
14. Tuncer, I.H.; Kaya, M. Optimization of flapping airfoils for maximum thrust and propulsive efficiency. *AIAA J.* **2005**, *43*, 2329–2336. [CrossRef]
15. Desert, T.; Moschetta, J.M.; Bezard, H. Aerodynamic design of a Martian micro air vehicle. In Proceedings of the 7th European Conference for Aeronautics and Aerospace Sciences, Milan, Italy, 3–6 July 2017.
16. Bellman, M.; Straccia, J.; Morgan, B.; Maschmeyer, K.; Agarwal, R. Improving genetic algorithm efficiency with an artificial neural network for optimization of low Reynolds number airfoils. In Proceedings of the 47th AIAA Aerospace Sciences Meeting Including the New Horizons Forum and Aerospace Exposition, Orlando, FL, USA, 5–8 January 2009; p. 1096.
17. O'meara, M.M.; Mueller, T.J. Laminar separation bubble characteristics on an airfoil at low Reynolds numbers. *AIAA J.* **1987**, *25*, 1033–1041.
18. Mueller, T.J.; Torres, G.E. *Aerodynamics of Low-Aspect Ratio Wings at Low Reynolds Numbers with Applications to Micro Air Vehicle Design and Optimization*; University of Notre Dame: Notre Dame, IN, USA, 2001.
19. Hosseini, N.; Tadjfar, M.; Abba, A. Configuration optimization of two tandem airfoils at low Reynolds numbers. *Appl. Math. Model.* **2022**, *102*, 828–846. [CrossRef]
20. Gad-el-Hak, M. Micro-air-vehicles: Can they be controlled better? *J. Aircr.* **2001**, *38*, 419–429. [CrossRef]
21. Xia, Q.; Wang, Z.; Ren, Y.; Sun, B.; Yang, D.; Feng, Q. A reliability design method for a lithium-ion battery pack considering the thermal disequilibrium in electric vehicles. *J. Power Sources* **2018**, *386*, 10–20. [CrossRef]
22. Malozyomov, B.V.; Martyushev, N.V.; Sorokova, S.N.; Efremenkov, E.A.; Qi, M. Mathematical Modeling of Mechanical Forces and Power Balance in Electromechanical Energy Converter. *Mathematics* **2023**, *11*, 2394. [CrossRef]
23. Guan, C.; Hasi, E.; Zhang, P.; Tao, B.; Liu, D.; Zhou, Y. Parabolic dune development modes according to shape at the southern fringes of the Hobq Desert, Inner Mongolia, China. *Geomorphology* **2017**, *295*, 645–655. [CrossRef]
24. Bushnell, D. Turbulent drag reduction for external flows. In Proceedings of the 21st Aerospace Sciences Meeting, Reno, Nevada, 10–13 January 1983; p. 227.
25. Ahmadi-Baloutaki, M.; Carriveau, R.; Ting DS, K. Effect of free-stream turbulence on flow characteristics over a transversely-grooved surface. *Exp. Therm. Fluid Sci.* **2013**, *51*, 56–70. [CrossRef]

26. Wang, B.; Wang, J.; Zhou, G.; Chen, D. Drag reduction by microvortexes in transverse microgrooves. *Adv. Mech. Eng.* **2014**, *6*, 734012. [CrossRef]
27. Walsh, M.J. Drag characteristics of V-groove and transverse curvature riblets. In Proceedings of the Symposium on Viscous Flow Drag Reduction, Dallas, TX, USA, 24–25 September 1980.
28. Wang, J.; Nakata, T.; Liu, H. Development of mixed flow fans with bio-inspired grooves. *Biomimetics* **2019**, *4*, 72. [CrossRef]
29. Liu, W.; Ni, H.; Wang, P.; Zhou, Y. An investigation on the drag reduction performance of bioinspired pipeline surfaces with transverse microgrooves. *Beilstein J. Nanotechnol.* **2020**, *11*, 24–40. [CrossRef]
30. Dvorchak, M.J.; Clouser, M.L.; Harbourne, A.D. AEROSPACE UV CURED Coatings; Yesterday, Today & Tomorrow. In Proceedings of the RadTech 2020 UV & EB Technical Conference Proceedings, Orlando, FL, USA, 8–11 March 2020.
31. Li, Z.; He, L.; Zheng, Y. Quasi-Analytical Solution of Optimum and Maximum Depth of Transverse V-Groove for Drag Reduction at Different Reynolds Numbers. *Symmetry* **2022**, *14*, 342. [CrossRef]
32. Prabhakar, A.; Ohri, A. CFD analysis on MAV NACA 2412 wing in high lift take-off configuration for enhanced lift generation. *J. Aeronaut Aerosp. Eng.* **2013**, *2*, 2. [CrossRef]
33. Clauser, F.H. Turbulent boundary layers in adverse pressure gradients. *J. Aeronaut. Sci.* **1954**, *21*, 91–108. [CrossRef]
34. Monty, J.P.; Harun, Z.; Marusic, I. A parametric study of adverse pressure gradient turbulent boundary layers. *Int. J. Heat Fluid Flow* **2011**, *32*, 575–585. [CrossRef]
35. Li, Z.; He, L.; Zuo, Y.; Meng, B. Analytic Solution of Optimal Aspect Ratio of Bionic Transverse V-Groove for Drag Reduction Based on Vorticity Kinetics. *Aerospace* **2022**, *9*, 749. [CrossRef]
36. Jones, E.M. *An Experimental Study of Flow Separation over a Flat Plate with 2D Transverse Grooves*; The University of Alabama: Tuscaloosa, AL, USA, 2013.
37. Truong, T.V.; Pulvin, P. Influence of wall riblets on diffuser flow. *Appl. Sci. Res.* **1989**, *46*, 217–227. [CrossRef]
38. Nieuwstadt, F.T.; Wolthers, W.; Leijdens, H.; Krishna Prasad, K.; Schwarz-van Manen, A. The reduction of skin friction by riblets under the influence of an adverse pressure gradient. *Exp. Fluids* **1993**, *15*, 17–26. [CrossRef]
39. De Groot, C.T.; Wang, C.; Floryan, J.M. Drag reduction due to streamwise grooves in turbulent channel flow. *J. Fluids Eng.* **2016**, *138*, 121201. [CrossRef]
40. Wokoeck, R.; Krimmelbein, N.; Ortmanns, J.; Ciobaca, V.; Radespiel, R.; Krumbein, A. RANS simulation and experiments on the stall behaviour of an airfoil with laminar separation bubbles. In Proceedings of the 44th AIAA Aerospace Sciences Meeting and Exhibit, Sacramento, CA, USA, 9–12 July 2006; p. 244.
41. Shome, B.; Radle, M. *Assessment of Transitional Model for Prediction of Aerodynamic Performance of Airfoils at Low Reynolds Number Flow Regime*; SAE Technical Paper; SAE International: Warrendale, PA, USA, 2013.
42. Menter, F.R. Two-equation eddy-viscosity turbulence models for engineering applications. *AIAA J.* **1994**, *32*, 1598–1605. [CrossRef]
43. Wang, J.; Zhang, C.; Wu, Z.; Wharton, J.; Ren, L. Numerical study on reduction of aerodynamic noise around an airfoil with biomimetic structures. *J. Sound Vib.* **2017**, *394*, 46–58. [CrossRef]
44. Mathey, F. Aerodynamic noise simulation of the flow past an airfoil trailing-edge using a hybrid zonal RANS-LES. *Comput. Fluids* **2008**, *37*, 836–843. [CrossRef]
45. Matsson, J.E.; Voth, J.A.; McCain, C.A.; McGraw, C. Aerodynamic performance of the NACA 2412 airfoil at Low Reynolds Number. In Proceedings of the 2016 ASEE Annual Conference & Exposition, New Orleans, LA, USA, 26–29 June 2016.
46. Sunu, P.W.; Wardana, I.N.; Sonief, A.A.; Hamidi, N. The effect of wall groove numbers on pressure drop in pipe flows. *Int. J. Fluid Mech. Res.* **2015**, *42*, 119–130. [CrossRef]
47. Li, Z.; Zuo, Y.; Lu, H.; He, L.; Meng, B. Numerical study on the influence of top and valley shape of the transverse groove on the drag reduction rate. *J. Theor. Appl. Mech.* **2023**, *61*, 741–754. [CrossRef]

energies

MDPI

Article

Universal Form of Radial Hydraulic Machinery Four-Quadrant Equations for Calculation of Transient Processes

Zdravko Giljen * and Miloš Nedeljković

Department for Hydraulic Machinery and Energy Systems, Faculty of Mechanical Engineering, University of Belgrade, Kraljice Marije 16, 11120 Belgrade, Serbia; mnedeljkovic@mas.bg.ac.rs
* Correspondence: zgiljen@gmail.com

Abstract: Suter curves for the *Wh* and *Wm* characteristics and four-quadrant (4Q) diagrams of 11 radial pump–turbine models with different specific speeds (*nq* = 24.34, 24.8, 27, 28.6, 38, 41.6, 41.9, 43.83, 50, 56, and 64.04) are presented for the first time in this paper, as well as Suter curves for two pump models (*nq* = 25 and 41.8) previously published in the literature. All of these curves were analyzed to establish a certain universal law of behavior, depending on the specific speed. To determine such a law, a fitting procedure using regression and spline methods was carried out. This paper provides details of a research plan and structures (including data collection for four-quadrant diagrams for pump–turbine and pump models under different specific speeds *nq*), a procedure for re-calculating four-quadrant diagrams of the models as Suter curves for the *Wh* and *Wm* characteristics, definitions of the optimal points for pump and turbine operating modes in pump–turbine models under different specific speeds, and the development of numerical models in MATLAB to obtain a universal equation for the *Wh* and *Wm* characteristics. The scientific contribution of this paper is that it is the first to publish original mathematical curves using universal equations for the *Wh* and *Wm* characteristics of radial pumps and pump–turbines. The applicability of the equations is demonstrated by considering a pumping station in which two radial pumps were installed, for which the calculation of transient processes was performed using a numerical model developed in MATLAB by the authors. The transition process results are compared for two cases: first, when input data in the numerical model are used with the values of the Suter curves for the *Wh* and *Wm* characteristics obtained by re-calculating the four-quadrant operating characteristics (Q_{11}, n_{11}, M_{11}) at a given specific speed, and second, when the values of the Suter curves for the *Wh* and *Wm* characteristics are obtained from the universal equations.

Keywords: universal equations for *Wh* and *Wm* characteristics; hydraulic transient calculation; radial hydraulic machinery; influence of the specific speed; method of characteristics

Citation: Giljen, Z.; Nedeljković, M. Universal Form of Radial Hydraulic Machinery Four-Quadrant Equations for Calculation of Transient Processes. *Energies* **2023**, *16*, 7736. https://doi.org/10.3390/en16237736

Academic Editors: Vasily Novozhilov and Cunlu Zhao

Received: 13 October 2023
Revised: 13 November 2023
Accepted: 15 November 2023
Published: 23 November 2023

1. Introduction

This paper describes a method for obtaining universal equations with all needed formulas, namely, initial, intermediate, and final diagrams of the four-quadrant working characteristics (Q_{11}, n_{11}, M_{11}) and their transition from *H/H**–*Q/Q**, *M/M**–*Q/Q** diagrams to an *n/n**–*Q/Q** diagram, thus giving *H* and *M* curves with various positive and negative percentages, which can then be transformed into Suter diagrams.

The aim of this paper is to analyze the possibility that there exists a certain law governing the behavior of Suter curves for various specific speed values.

As a classical example, the transition from *H/H**–*Q/Q**, *M/M**–*Q/Q** diagrams to the *n/n** – *Q/Q** diagram is presented, which provides the curves of *H* and *M* with various percentages. The mentioned diagrams were taken from the classical literature [1,2] and then transformed into Suter diagrams. This example considers a pump with *nq* = 25 (35); the original pump is a double-suction pump, where 25 corresponds to the impeller and

35 to the complete machine. Not much data on four-quadrant pump curves can be found in the literature, except for three specific speeds.

A modification of the formulas for re-calculating the four-quadrant characteristics Q_{11}, n_{11}, M_{11} into Suter curves is made [3–5], and the optimal point for the pump–turbine operating mode in pump–turbine models for different nq values is defined. The method for re-calculating the four-quadrant (4Q) characteristics Q_{11}, n_{11}, M_{11} into Suter curves (applied in [5]) is then analyzed. Consequently, for the first time, Suter curves for pump–turbine models (11 models at different specific speeds nq) are presented in this paper, which are used to determine the existence of a general law for their form in an attempt to obtain universal curves depending on the specific speed.

For the data analysis and determination of the best-fitting curve, regression and spline methods are utilized.

Experimental research focused on determining the four-quadrant curve characteristics (Q_{11}, n_{11}, M_{11}) carried out in the pump–turbine installations of laboratories in Vienna, Austria, and Wuhan, China are presented. The laboratory in Vienna has one pump–turbine installed, while the laboratory in Wuhan has two pump–turbines. The diagrams obtained according to the measurements are presented in the form of Suter curves for the optimal wicket gate openings (the conducting apparatus) for 11 radial pump–turbine models (which the first author personally collected and re-calculated), together with one Suter curve for the radial pump model from [4]. Diagrams with Suter curves for pumps and pump–turbines with various values of nq were obtained from the universal Suter equation, for which the authors of this paper developed a numerical model in MATLAB 2023b.

In terms of the innovative and academic value of this paper, a large number of Suter four-quadrant curves for pump–turbines and pumps with different specific rotation speeds are presented for the first time, as well as a methodology for analyzing the curves, in order to obtain a general law for the shape of the curves under different values of nq. The primary goal of this paper was to obtain a universal Suter curve for pump–turbines and pumps based on 11 sets of Suter curves for pump–turbines and two sets of Suter curves for pumps. The experimental four-quadrant curves faithfully describe the operating regimes of pump–turbines and pumps, representing a valid basis for analysis focused on their dependence on the specific rotation speed nq. Statistical processing of the approximation results for the experimental curves was conducted to obtain universal mathematical relationships with sufficient accuracy, so no major deviation in the results of the calculation of transition regimes was observed. The derived universal mathematical model for four-quadrant operating curves is simple enough for future practical applications, as its programming is not too complex and it is easy to use. The scientific contribution of this work is reflected in the definition of a methodology for the determination of universal (general or generalized) equations for the working curves of pump–turbines and pumps considering the influence of specific rotation speeds, defining a general law as a new mathematical model for such curves. The professional contribution of this paper is reflected in the application of the derived model to practical cases in order to test the validity of the model and analyze relevant deviations.

2. Literature Review

The subject of this research is the four-quadrant curves of turbomachines. In order to calculate transient processes in systems with turbomachinery, four-quadrant curves for the machine are required. We mainly consider the curves previously detailed in [2–4,6]. In [4], curves are given for only three specific speeds: nq = 25 (35), 147, and 261 (one radial, one semi-axial, and one axial turbomachine).

System designers use the curves most closely describing the analyzed machine, even without interpolation. Of course, many approximations can be used to calculate transient fluid phenomena, almost all of which have already been studied (with respect to unsteady friction, sound speed, fluid–structure interactions, and so on); however, with regard to the

wider knowledge that has been obtained, a thorough analysis of various specific speeds (and their impacts) has not yet been published in the literature.

A technique for determining the complete operating characteristics of a hydraulic machine, such as a centrifugal pump or turbine, together on a single diagram has been described in [1]. The characteristics of modern pumps, with high head and high efficiency, were analyzed and presented. The use of these complete characteristics to predict the behavior of the machine during the transient process was discussed and the analytical background was presented. The assumptions involved were explored and experimental checks of their validity were offered. By comparing the possible operating conditions of a hydraulic turbine and a centrifugal pump installation, it soon became clear that pumps are subject to much wider and more involved variations than turbines, especially during the transient states of starting, stopping, or emergency operations.

In [6], the complete characteristics of pumps at certain specific speeds [1800, 7600, and 13,500 (gpm), or 25 (35), 147, and 261 (SI units)] were presented, with the basic test data for the three pumps provided by Prof. Hollander at the California Institute of Technology. A method for creating complete pump characteristics from data obtained during model tests was described. Three sets of pump characteristics were compared, and the effects of certain specific speeds on hydraulic transient processes due to pump disconnection from the network or pump stoppage were determined. The conditions of the transient processes that occur in the radial flow pump, mixed flow pump, and axial flow pump were described. The authors described that, in most cases, complete pump characteristics are not available and incomplete pump characteristics can be extended according to homologous pump laws or similarity laws [5]. The most important connection between a model and a prototype of a pump or turbine is the relations defined by the similarity laws; from these relations, the equations for Q, H, and M can be derived, which are used during the conversion of data from four-quadrant curves to Suter curves. It is considered that, if the specific speed of the pump under study is approximately the same as the available pump characteristics, the results of the water hammer will be satisfactory for most engineering purposes. Furthermore, although some of the data obtained during the tests will not fit the curves obtained according to the homologous laws, this does not mean that those data are incorrect, but only that the pump during the test did not follow the homologous laws under certain abnormal operations. It was stated that only by using more test data can the average characteristic of the pumps be obtained.

In [3], the authors performed an analysis of transient processes caused by various pump operations, presented a procedure for storing pump characteristics in a digital computer system, developed boundary conditions, and solved a typical problem. They also provide a mathematical representation of the pump's working characteristics. The boundary conditions for load rejection of the pump were explained, as well as the equations for characteristics and the conditions of the boundary, which can be solved simultaneously to determine those conditions. Boundary conditions for more complex cases were developed and, in order to facilitate a better understanding of their implementation, a simple system with only one pump and a very short suction line was considered. A detailed analysis of the procedure for obtaining curves was also provided, indicating the relationships between variables (called pump characteristics). These curves have been presented in various forms suitable for graphical or computer analysis and, of all the methods proposed for storing pump characteristics in a digital computer, the method used by Marchal is considered the most suitable, with some modification. The authors also emphasized that although pump characteristic data in the pumping zone are usually available, relatively few data are available for the dissipation zone or the turbine operation zone.

Explanations related to transient processes and the causes of their occurrence have been provided in [4]. The authors explained that changes in the working state of the turbomachine are the result of non-stationary flow in the hydraulic system, and that this working condition can be caused by starting or stopping the centrifugal pump or by adjusting the load on the generator, which causes changes to occur at that time in the

hydraulic turbine. The authors explained how to apply the method of characteristics, using the dimensionless homologous characteristics of turbopumps. They also explained that the conditions for turbines can be described in the same way as for pumps; however, with turbine data, a set of characteristics may be required for each of the many wicket gate openings. The authors specified and analyzed four quantities related to the characteristics total dynamic head, discharge, shaft torque, and rotational speed. They stated two basic assumptions: the characteristics of the equilibrium state hold for the unstable state and, if the discharge and speed rotation change with time, their values at a given time determine the head and torque. They analyzed and explained the homologous relations in detail, noting that homologous theories assume that efficiency does not change with the size of the unit and that it is convenient to work with dimensionless characteristics h, β, v, and α.

Previously, the authors of this paper published two scientific papers dealing with the study and analysis of four-quadrant operating characteristics (Q_{11}, n_{11}, M_{11}) of pumps and pump–turbines, with the idea of determining whether a law exists [7,8].

In [9], the authors developed a mathematical model that describes the complete characteristics of a centrifugal pump. In this model, a non-linear functional relationship between the parameters of the characteristic operating points (COPs) and the specific speed is established. The main contribution of this paper is that it combines a mathematical model with a non-linear relationship to successfully predict the complete pump characteristics (CPCs) for a given specific speed. The authors verified the developed mathematical model through a case study, and the CPCs constructed according to the mathematical model derived in the paper were in agreement with the measured CPCs. Transient processes at pumping stations can be successfully simulated with the CPC prediction method proposed in this paper.

In [10], the authors analyzed the complete characteristics of centrifugal pumps and developed a machine learning model to calculate the complete characteristic curve and dimensionless head and torque curves from the quadrant III data set with high accuracy. To obtain a full characteristic curve based on a manufacturer's normal performance curve, the authors developed a machine learning model that predicts full and complete Suter curves using specific pump speeds from known parts of the Suter curve. They used this model to measure and predict the relationship between the data points of quadrant III and those of quadrants I, II, and IV of the centrifugal pump performance characteristic curve.

In [11], the authors analyzed a low-specific speed centrifugal pump with impeller eccentricity based on the N-S equations, and simulated the operation of the pump using the RNG k-e model. The authors studied the change in force induced by the fluid with respect to the eccentricity of the impeller, as well as the non-stationary characteristics of the flow of the internal flow field of the centrifugal pump under different flow conditions and rotation speeds. Furthermore, they performed a detailed analysis of the relationship between the force induced by the fluid of the impeller and the characteristics of the internal flow field. A significant contribution of this paper is that it provides important reference values for an accurate understanding of the principle defining the excitation of the internal flow of a centrifugal pump.

In [12], the authors simulated a centrifugal pump with a low specific speed under eccentric mounting conditions using the RNG k-e turbulence model. The authors studied the force induced by the fluid of the impeller of a centrifugal pump with a complex vortex. The main part of the research involved investigating the influences of different flow rates, impeller eccentricity, and vortex ratios on the impeller force induced by the fluid. An important observation in this paper is that the results calculated considering the eccentricity of the impeller were closer to the experimental data than the results calculated when not considering the eccentricity. This paper provides an important reference for centrifugal pump design and vibration in the fluid–structure interaction (FSI).

In [13], based on the basic shapes of the head and power curves in the normal operating zone, the authors described the disadvantages of using a specific speed and presented an improved method for selecting appropriate data from the four quadrants.

In [9], the authors discussed a new method that uses the inherent operating characteristics of a centrifugal pump to predict complete pump characteristics (CPCs). The authors also developed a mathematical model that describes the complete characteristics of a centrifugal pump. They performed measurements for a larger number of CPCs and determined a non-linear functional relationship between the parameters of characteristic operating points (COPs) and specific speeds. By combining a mathematical model with a non-linear relationship, they successfully predicted CPCs for given specific speeds.

In [14], the authors developed a method for fitting a complex pump characteristic curve with large deviations and unevenly spaced data points, using a cubic uniform B-spline. The authors proved, in this work, that the new method works well when considering the precise construction of data in a wide area into a smooth curve. No disturbances caused by random errors were observed during testing.

In [15], the authors simulated the complete characteristic curve of a reversible pump–turbine based on surface fitting, applying the moving least squares (MLS) approximation for this procedure. The authors also analyzed the influence of the MLS parameters, as well as the following parameters: the coefficient of the weighting function, the number of points in the support domain, and the scale of the radius of the support domain. They also analyzed how these parameters affect the calculation results.

In [16], the authors developed a method for determining three-dimensional internal characteristics based on computational fluid dynamics (CFD) in order to quickly and accurately obtain the Suter curves of double-suction centrifugal pumps. This method includes three-dimensional modeling, setting of pump operating conditions, simulation of the pump flow field, and transformation of the results. The main contribution of this method is that, through the use of CFD technology, the relationships between the flow, speed, head, and torque can be precisely calculated under certain pump operating conditions.

In [17], the authors studied the four-quadrant characteristics of the operating curves of a centrifugal pump, using experimental and numerical approaches during testing. A wide range of centrifugal pump flow rates was analyzed in their CFD calculations. They analyzed the behavior of the pump in four quadrants during transient regimes, and concluded that the results of numerical simulations based on two turbulence models of the equation were in good agreement with the experimental results.

In [18], the authors performed a theoretical and experimental investigation of the transient characteristics of a centrifugal pump in two operating modes: starting and stopping. A numerical model based on the method of characteristics was used to analyze the dynamic characteristics of the pump. The authors concluded that the dynamic characteristics of the pump showed significant deviation from the steady-state characteristics; thus, the developed numerical model could be applied to analyze purely non-stationary cases.

In [19], the authors compared the results obtained by using test equipment and numerical methods for a model of a mixed-flow diffusion pump and concluded that there was extremely good agreement between them. They also confirmed that the behavior of a four-quadrant mixed-flow diffusion pump can be reliably simulated by applying the CFD method. They successfully applied the numerically calculated behavior of the four quadrants during the calculation of the water hammer.

In [20], the authors developed an innovative theoretical approach to predict the flow rate and pressure at the best efficiency point (BEP) for pump and turbine modes based on the principle of conformity of characteristics between the runner and the spiral case. The main contribution of this paper was the derivation of a theoretical formula for the characteristics of the impeller in turbine mode. For this derivation, the Euler equation of roto machinery was used, as well as the ratio of speeds at the inlet and outlet of the runner. The method developed in this paper was verified by experiments with three types of pumps in the pump and turbine mode, which gave good results.

In [21], the authors developed an improved method with which the complete characteristics of a centrifugal pump can be obtained. For this method, based on the normal performance curve, a conversion formula of complete characteristics was established. Using

this newly developed method, the complete characteristic curves of the centrifugal pump 14SA-10 were obtained.

In [22], the authors developed a method for predicting complete pump curves using only normal operation data, along with curves from other machines with similar specific speeds. To model the complete curves, the authors used a trigonometric series and conducted particle swarm optimization (PSO) for fitting of the coefficients. The authors simulated a pump shutdown, compared the obtained results with the results of laboratory tests, and verified the differences using a modeled curve and a similar curve.

In [23], the authors made a significant contribution by developing a three-dimensional Cartesian coordinate system with relative flow angle, specific velocity, and *Wh* (or *Wm*) value as independent variables, then interpolated these values with a bicubic polynomial to develop a three-dimensional surface visual model for forecasting CPCs. Another significant contribution of this paper is that the predicted curves basically matched the measured data.

In [24], the authors developed a new formula for adjusting complete pump characteristics (CPCs) using the least squares method taking into account the specific speed, the relative flow angle, and the characteristic parameters corresponding to the condition of zero flow as independent variables.

In [25], based on an analysis of the full characteristic curve of the pump and using the all-purpose formula and nearest neighbor methods, the authors developed a method for obtaining discrete numerical data of the full characteristic curve of pumps with different specific speeds. The authors also determined that, according to similarity theory, it is theoretically feasible to perform numerical reconstruction of the full pump characteristic curve and that the full characteristic curves of pumps with different specific speeds are very different. For pumps of the same type, the difference between characteristic curves is small, and these curves are very similar after curve numbering.

In [26], the authors performed full testing of the four-quadrant performance considering a hydraulic model of the reactor cooling liquid of an ACP100 pump through a reduced speed test. The obtained data for the four-quadrant curves were complete, and the data were effective for further pump transition processes and the calculation of transient thermal–hydraulic characteristics of the entire cooling system of the reactor.

In [27], the authors developed a method for the prediction of the complete characteristics of a Francis pump–turbine. To develop this method, they used Euler equations and speed triangles on the runner, and obtained a mathematical model that describes the complete characteristics of the Francis pump–turbine. The main contribution of this work was that they combined the developed mathematical model with regression analysis of characteristic operating points (COPs) in order to predict complete characteristic curves for arbitrary specific speeds.

In [28], the authors analyzed how modifications to the runner can have different effects on a centrifugal pump operating in the pump and turbine mode. They used the CFD method to obtain the hydraulic performance of a low-specific speed centrifugal pump operating in both modes and experimentally verified the obtained results. They compared the turbine and the pump and concluded that the pump showed more obvious head variation. The obtained results have great significance for improving the hydraulic performance in both pump and turbine modes, through modification of the geometry of the runner.

In [29], using the finite volume method (ANSIS CFKS) and two-way test equipment, the authors analyzed the unsteady characteristics of the internal flow and the time–frequency characteristics of the pressure fluctuations of the pump as a turbine (PAT) after the shutdown process. The authors made a significant contribution by revealing the characteristics of the transient discharge during the process of a mixed flow pump as a turbine failing. This research is very important for the safe transient operation of a pump as a turbine.

3. Previous Personal Research

Experimental Research

The authors of this paper performed experiments to determine four-quadrant characteristic curves (n_{11}, Q_{11}, M_{11}) at laboratories with pump–turbine installations in Vienna, Austria (Institute for Energy Systems and Thermodynamics, Vienna University of Technology), and Wuhan, China (State Key Laboratory of Water Resources and Hydropower Engineering Science, Wuhan University). The laboratory in Vienna has one pump–turbine with nq = 41.6, while the laboratory in Wuhan has two pump–turbines, both with nq = 38, where the geometric profiles of the blades of the runners and input edges are different. During his time in these laboratories, the author performed measurements of different operating modes in the four quadrants of pump–turbines under both stationary and non-stationary conditions.

At the laboratory in Vienna, the author was introduced to the complete installation of the pump–turbine model (e.g., upper and lower pressure tanks, supply and discharge pipelines, pre-turbine shutter), as well as the complete measurement system, including the positions of instruments for measuring pressure along the inlet and outlet pipelines, spiral casing, and draft tube, along with instruments for measuring the number of revolutions, the torque on the turbine shaft, the power of the generator, the opening of the wicket gates of the conducting apparatus, and the displacement of the piston rod of the servomotor. The author was also introduced to the equipment in the control room, where the data measured at the pump–turbine were collected, processed, and converted from analog to digital, and the measurement of operating points on four-quadrant characteristic curves was monitored.

While measuring the pump–turbine installation with nq = 41.6 at the laboratory in Vienna from 22 October 2012 to 26 October 2012, the author participated in the installation of the measurement equipment and the process of measuring around 100 measurement points on two four-quadrant curves for the two openings of the blades of the conducting apparatus, as well as in the analysis of the obtained results. The measurements were made in the steady state throughout the entire area of the four-quadrant characteristic curves: pumping mode, braking-energy dissipation, turbine mode up to the line of runout and continuation in braking mode, reversible pumping mode, and start in pumping mode. During these measurements, the laboratory staff and the author examined the pump–turbine in all four quadrants for the two openings of the blades of the conducting apparatus (12 and 22 mm) and recorded about 100 measurement points. This was a unique opportunity for the author to become familiar with the complete measurement process of the pump–turbine model and to monitor and analyze the changes in physical quantities and phenomena that occur during the operation of the pump–turbine. It is very important to understand how complex the process is in the physical sense of the pump–turbine operation in all four operating modes: normal (negative rotation speed, positive torque, negative discharge), energy dissipation (negative rotation speed, positive torque, positive discharge), normal turbine (positive rotation speed, positive torque, positive discharge), and reverse pump (positive rotation speed, negative torque, negative discharge). During the measurements, the author had a unique opportunity to personally experience what happens to a turbomachine when it passes through all four working quadrants. There is significant instability and chaos during the transition from pump mode to turbine mode (zone of energy dissipation: discharge, torque, and speed of rotation change sign and direction), and it is difficult to measure the torque, discharge, and speed of rotation in this operating mode. A similar situation occurs during the transition from turbine mode to pump mode (reversible pump mode: discharge, torque, and a number of revolutions change sign and direction), with instability and chaos similarly occurring, making it very difficult to measure torque, discharge, and speed of rotation in this operating mode.

A photograph of Christian Bauer of the Vienna University of Technology, Zdravko Giljen (as a PhD student), and Bernhard List of Voith is presented in Figure 1. Figure 2 shows a photograph taken at the laboratory in Vienna, with a display of the complete

pump–turbine installation on the computer. During the test, the laboratory staff did not provide any technical data (e.g., related to what types of equipment were used to obtain the flow rate, head, torque, and so on) to the author; thus, such data are not presented in this paper.

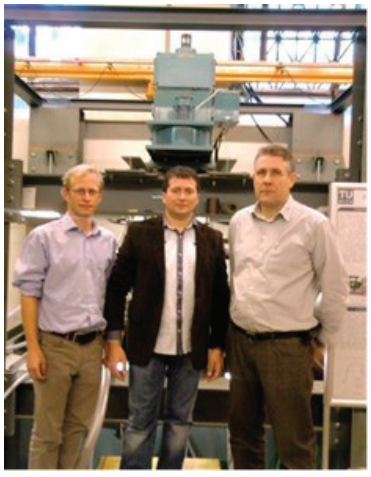

Figure 1. Left to right: Christian Bauer of the Vienna University of Technology, Zdravko Giljen (a PhD student), and Bernhard List of Voith.

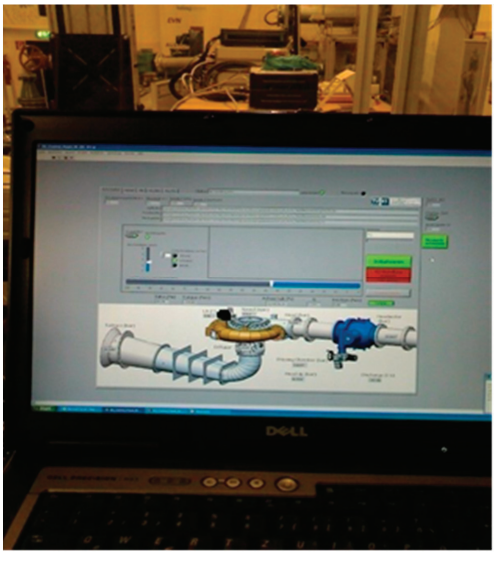

Figure 2. Laboratory at the University of Vienna: display of complete pump–turbine installation on the computer.

The author also made an official visit to the State Key Laboratory of Water Resources and Hydropower Engineering Science, Wuhan University, China, from 29 February 2016 to 29 March 2016, at the invitation of Yongguang Cheng, director of the laboratory's Research Section on the Safety of Hydropower Systems. On the test bench, pump–turbines were driven through four-quadrant operations, and the four-quadrant characteristics were tested

for two models of pump–turbines under stationary and non-stationary conditions. Measurements were made over the entire area of the four-quadrant diagram: pump mode, braking, turbine mode to the line of runout and continuation in braking mode, reversible pump mode, and start in pump mode. Subsequently, the author analyzed the obtained data, which were made dimensionless for the obtained Suter curves, and then conducted numerical experiments regarding the transient phenomena (1D) in a system with such machines.

While performing measurements, the author learned how complex the process is in the physical sense during the operation of the pump–turbine in all four modes, as well as how much instability and chaos there is during the transition from pump mode to turbine mode (zone of energy dissipation: discharge, torque, and speed of rotation change sign and direction) and how difficult it is to measure torque, discharge, and speed of rotation in this operating mode. The experimental platform in the laboratory consisted of nine parts: recycled water, excitation protection, speed control, frequency disguise, monitoring, load, measurement, model unit, and diversion system equipment. While developing his doctoral dissertation, the author analyzed the results obtained during the transition process on two pump–turbine models installed in this laboratory, as well as the process of data transformation from four-quadrant pump–turbine characteristic curves to Suter curves. During this period, the author became familiar with the complete installation of two pump–turbines at the State Key Laboratory in Wuhan (upstream reservoir, supply pipeline, upstream branch, installation of two pump–turbine models, downstream branch, surge chamber, downstream pipeline, downstream reservoir), as well as the equipment in the control room, where the data were collected. The process was monitored in the control room while, in the adjacent room, devices were used to process and convert all measurement signals and positions from analog to digital, and the measurements of working points on the four-quadrant characteristic curves in stationary and non-stationary conditions were monitored. The author then analyzed these obtained results. A photograph of Yongguang Cheng and Linsheng Xia of the State Key Laboratory with Zdravko Giljen (as a PhD student) is presented in Figure 3.

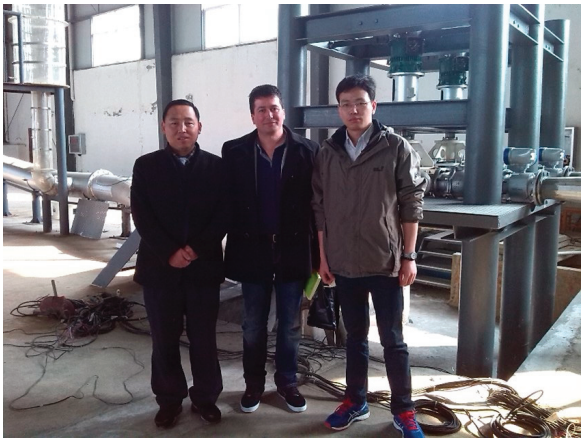

Figure 3. State Key Laboratory, Wuhan, China: (left to right) Yongguang Cheng, Zdravko Giljen, and Linsheng Xia.

The experimental platform at the laboratory in Wuhan consists of nine parts, as shown in Figure 4: recycled water, excitation protection, speed control, frequency disguise, monitoring, load, measurement, model unit, and diversion system equipment. The recycled water equipment includes cisterns, tanks, backwater channels, pumps, water pipes, valves, electromagnetic flow meters, transformers, distribution equipment, and other auxiliary equipment. Excitation protection equipment includes a generator motor excitation device

(generator, automatic registering devices, generator protection devices). The speed control equipment includes a speed controller, tester, digital cylinder actuators, valve controllers, and so on. The frequency disguise equipment includes drive and commutation components. The monitoring equipment includes a local control unit, host computer system, monitoring system software, and industrial TV monitors. The load equipment includes a 4 × 20 kW front-loaded cabinet. The measurement equipment includes a data logger, vibration tester data, and various sensors. The model unit equipment includes four models working as a head pump–turbine and generator motor. The diversion system equipment includes upper/lower reservoirs, inlet/outlet pressure pipelines, a surge chamber, and other components. During this test, the laboratory staff did not provide any technical data on what equipment was used to obtain the flow rate, head, torque, and so on to the author; thus, such data are not presented in this paper.

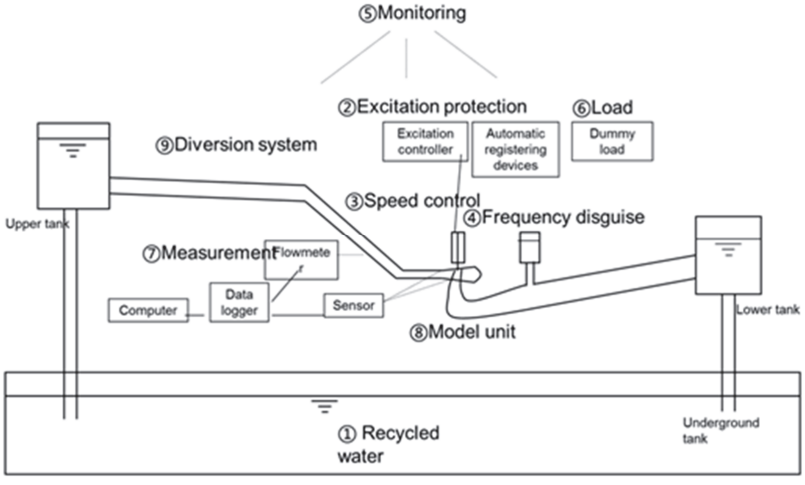

Figure 4. Scheme of experimental platform at State Key Laboratory, Wuhan, China.

4. Investigation of Analytical Connection in Data for Working Curves Given in Four Quadrants for 11 Pump–Turbine Models and 2 Pump Models

The authors of this paper conducted data collection, research, and analysis of four-quadrant diagrams for pump–turbine and pump models under different specific speeds *nq*, then studied and conducted the re-calculation of four-quadrant diagrams for 11 models of pump–turbines into Suter curves. The Suter curve for one pump model (*nq* = 25 radial pump) was derived from [2] and another model (*nq* = 41.8 radial pump) from [5]. The authors collected 11 sets of four-quadrant characteristic curves for models of radial pump–turbines (developed in laboratories in China, America, Russia, and Austria), 5 of which were obtained from the State Key Laboratory of Water Resources and Hydropower Engineering Science at Wuhan University and Yongguang Cheng.

From the four-quadrant diagrams for the 11 radial pump–turbine models with *nq* = 24.34, 24.8, 27, 28.6, 38, 41.6, 41.9, 43.83, 50, 56, and 64.04, the values for the characteristic unit speed of rotation, $n_{11} = \frac{nD_1}{\sqrt{H}}$; unit discharge, $Q_{11} = \frac{Q}{{D_1}^2\sqrt{H}}$; and unit moment, $M_{11} = \frac{M}{{D_1}^3\sqrt{H}}$ were determined, according to four-quadrant curves for various openings of the wicket gates of the conducting apparatus of the 11 models. Then, the authors calculated the degree of efficiency of these curves, and the optimum point with the highest degree of efficiency for the pump and turbine mode was determined for each model, and data for H^*, Q^*, and M^* from the optimal points were taken for the pumping mode and used for further data re-calculation. Then, the authors calculated the values of H, Q, and M for each point on the four-quadrant curves. After this, the values for the dimensionless head,

$h = \frac{H}{H^*}$; dimensionless moment, $\beta = \frac{M}{M_*}$; dimensionless speed of rotation, $\alpha = \frac{n}{n_*}$; and dimensionless discharge variable, $v = \frac{Q}{Q_*}$ were calculated—this refers to the procedure for converting four-quadrant curves to Suter curves. Suter diagrams show the curves of the characteristic head, $W_{h(\theta)} = \frac{h}{\alpha^2+v^2}$, and characteristic moment, $W_{m(\theta)} = \frac{\beta}{\alpha^2+v^2}$, expressed as functions of the angle θ, defined by $\theta = arctg\frac{\alpha}{v}$ [30].

After re-calculating the four-quadrant curves to Suter curves for all openings of wicket gates of the conducting apparatus for the 11 radial pump–turbine models, as shown in single diagrams in Figures 5 and 6, Suter curves for the optimal opening of the wicket gates of the conducting apparatus for one model of the radial pump (nq = 25) were derived from [2], and those for another radial pump model (nq = 41.8) were derived from [5].

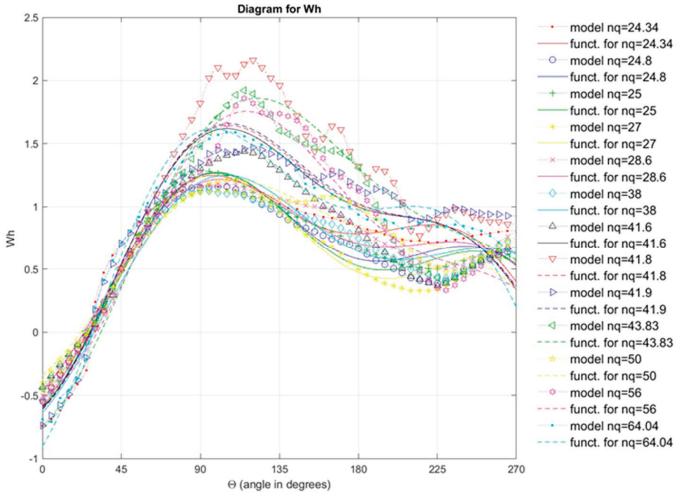

Figure 5. Comparison of Suter curves for the *Wh* characteristic obtained by re-calculating model curves Q_{11}, n_{11}, M_{11} with Suter curves obtained from the universal equation (11 pump–turbine and 2 pump models).

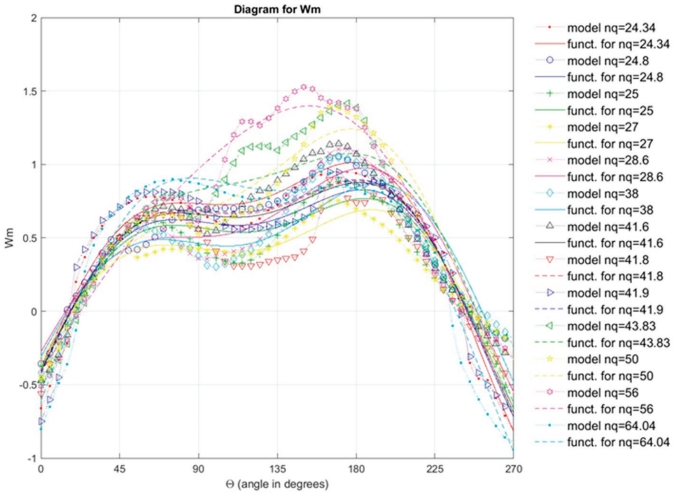

Figure 6. Comparison of Suter curves for the *Wm* characteristic obtained by re-calculating model curves Q_{11}, n_{11}, M_{11} with Suter curves obtained from the universal equation (11 pump–turbine and 2 pump models).

The parameters of the various pump–turbines are as follows: China: nq = 24.34, opening 24 mm; USA (Bad Creek): nq = 24.8, opening 26 mm; Serbia (Bajina Basta): nq = 27, opening 24 mm; USA: nq = 28.6, opening 18°; China: nq = 38, opening 24°; Vienna, Austria: nq = 41.6, opening 36 mm; China: nq = 41.9, opening 20°; Russa: nq = 43.83, opening 28 mm; China: nq = 50, opening 20.03°; China: nq = 56, 40 mm; and Russia: nq = 64.04, opening 16 mm.

The parameters for the pumps are as follows: nq = 25 [2] and nq = 41.8 [5].

Figures 5 and 6 show diagrams with 13 Suter curves for the *Wh* and *Wm* characteristics, of which 11 are for pump–turbine models and 2 are for pump models. According to a detailed analysis of the structure of the curves, the authors concluded that, in the following steps, they should observe Suter curves for pump–turbines and pumps together. Based on this, universal equations for the *Wh* and *Wm* characteristics could be obtained from a numerical model developed in MATLAB. A variant of this numerical model is detailed below (regression procedure: least squares method; interpolation procedure: spline method) [31], and the obtained results are shown in various diagrams.

4.1. Details of the Procedure and Variants

The aim of this study was to analyze the four-quadrant operating characteristics (Q_{11}, n_{11}, M_{11}), with the idea of determining whether a law exists. It is well known that the operating curves (Q_{11}, n_{11}, M_{11}) are stable in pump mode and turbine mode, and data for those regimes have been studied in more detail than data for the complete four-quadrant characteristic curves.

The authors of this paper, based on the data of Suter curves for 11 pump–turbine models—along with the data for one pump model from [5] and another pump model from [2]—used MATLAB to develop a numerical model using polynomial regression to obtain universal equations for the *Wh* and *Wm* characteristics, in order to analyze the existence of a more general law for the obtained curves depending on the specific speed nq. The process of developing the model consisted of the following steps.

Step one: All 13 Suter curves (each curve separately for both the *Wh* and *Wm* characteristics) for 11 pump–turbine models and 2 pump models with theta ranging from 0° to 360° were passed through the second-order Fourier function, as shown in Figures 7–9 for *Wh* and Figures 10–12 for *Wm*. Diagrams for all Suter curves passed through the Fourier function are not shown in order to not overload this paper with a large number of diagrams; instead, diagrams for six Suter curves (with nq = 24.34, 24.8, 25, 28.6, 38, and 1.6) regarding the *Wh* and *Wm* characteristics are shown.

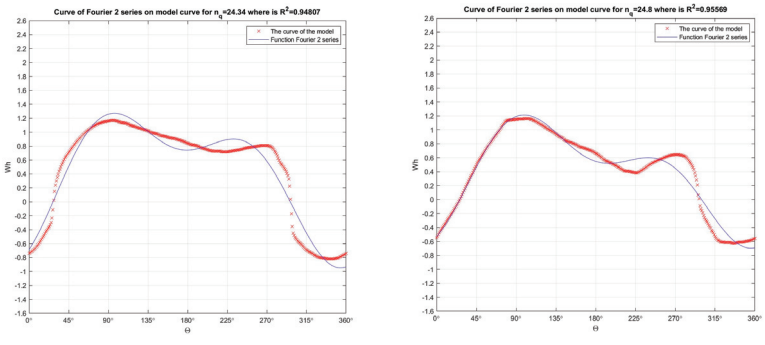

Figure 7. In the numerical model developed in MATLAB, second-order Fourier functions were passed through Suter curves (obtained by re-calculating the model curves Q_{11}, n_{11}, M_{11}) for nq = 24.34 (R^2 = 0.94807) and nq = 24.8 (R^2 = 0.95569) for the *Wh* characteristic.

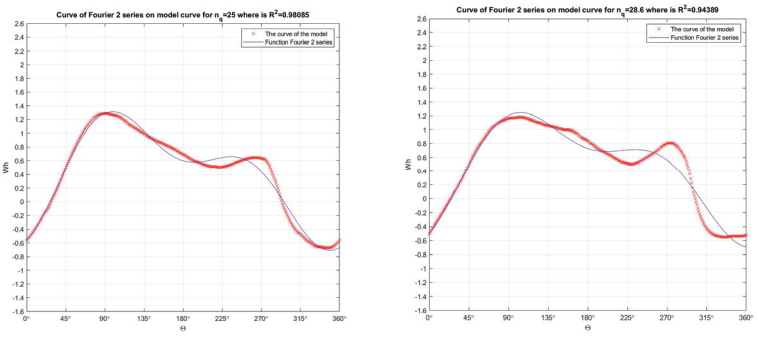

Figure 8. In the numerical model developed in MATLAB, second-order Fourier functions were passed through Suter curves (obtained by re-calculating the model curves Q_{11}, n_{11}, M_{11}) for nq = 25 (R^2 = 0.98085) and nq = 28.6 (R^2 = 0.94389) for the *Wh* characteristic.

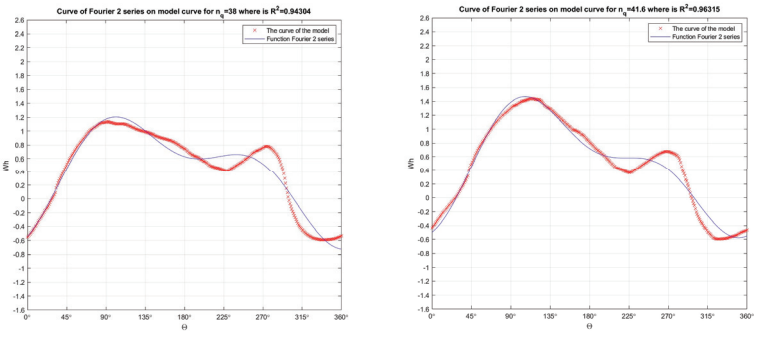

Figure 9. In the numerical model developed in MATLAB, second-order Fourier functions were passed through Suter curves (obtained by re-calculating the model curves Q_{11}, n_{11}, M_{11}) for nq = 38 (R^2 = 0.94304) and nq = 41.6 (R^2 = 0.96315) for the *Wh* characteristic.

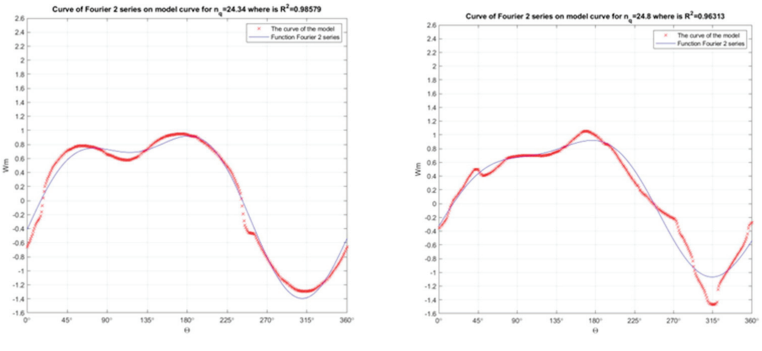

Figure 10. In the numerical model developed in MATLAB, second-order Fourier functions were passed through Suter curves obtained by re-calculating model curves Q_{11}, n_{11}, M_{11}, with nq = 24.34 (R^2 = 0.98579) and nq = 24.8 (R^2 = 0.96313), for the *Wm* characteristic.

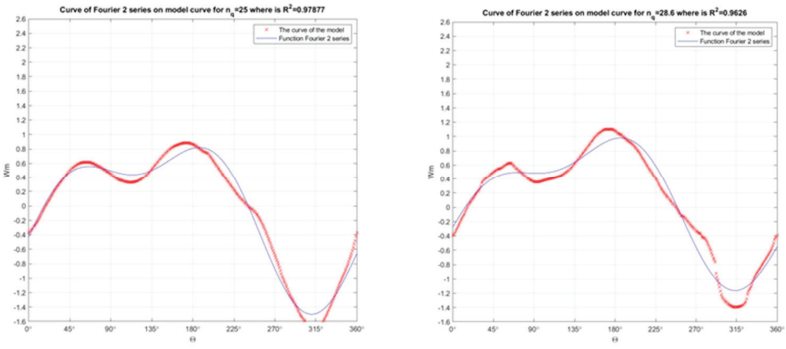

Figure 11. In the numerical model developed in MATLAB, second-order Fourier functions were passed through Suter curves obtained by re-calculating model curves Q_{11}, n_{11}, M_{11}, with nq = 25 (R^2 = 0.97877) and nq = 28.6 (R^2 = 0.9626), for the *Wm* characteristic.

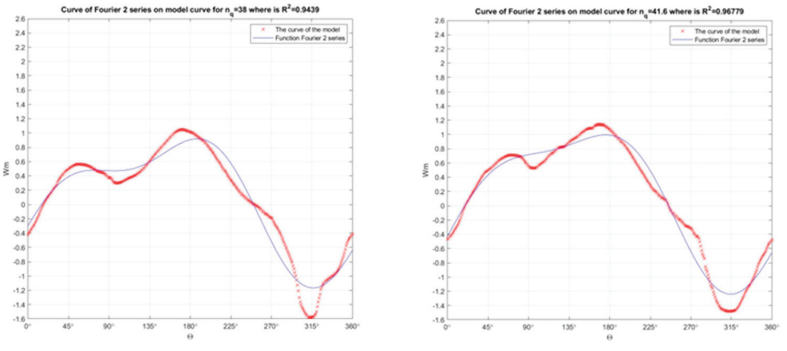

Figure 12. In the numerical model developed in MATLAB, second-order Fourier functions were passed through Suter curves obtained by re-calculating model curves Q_{11}, n_{11}, M_{11}, with nq = 38 (R^2 = 0.9439) and nq = 41.6 (R^2 = 0.96779), for the *Wm* characteristic.

Step two: The coefficients a_0, a_1, a_2, b_1, b_2, and w were taken from the 13 second-order Fourier functions through which the 13 Suter curves were passed (11 pump–turbine models and 2 pump models) separately for the *Wh* and *Wm* characteristics of each curve. Then, the values for these coefficients were grouped on separate diagrams. The diagrams for *Wh* are shown in Figures 13–15, and those for *Wm* in Figures 16–18, where the values of the coefficients from the second-order Fourier functions are shown depending on the specific speed *nq*. A polynomial of order 9 was passed through the values of the coefficients listed on these diagrams, and each polynomial shows the dependence of the coefficients on the specific speed *nq*.

Step 3: The dependence between the values of the coefficients (a_0, a_1, a_2, b_1, b_2, w) and the specific speed *nq* (for 11 pump–turbine models and 2 pump models) was determined by polynomial regression (using the polynomial of order 9) through the numerical model developed in MATLAB.

Step 4: Based on the developed numerical model, universal equations for the *Wh* and *Wm* characteristics were obtained depending on the specific speed. These universal equations were expressed in the numerical model with the second-order Fourier equation, depending on the specific speed.

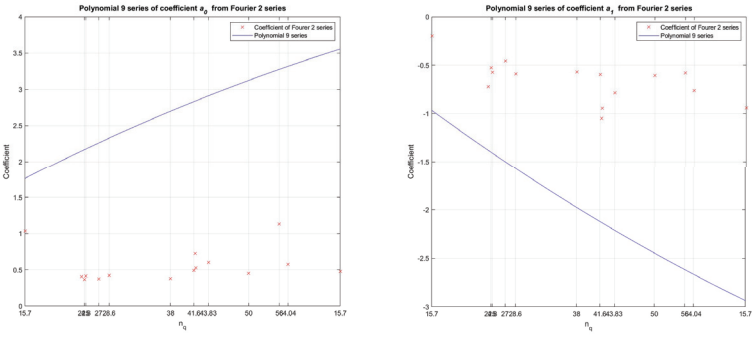

Figure 13. Through polynomial regression (with a polynomial of order 9) in the numerical model developed in MATLAB, the dependence between the values of coefficients a_0, a_1 (from the second-order Fourier function) and specific speed nq (11 pump–turbine models and 2 pump models) was determined for the *Wh* characteristic.

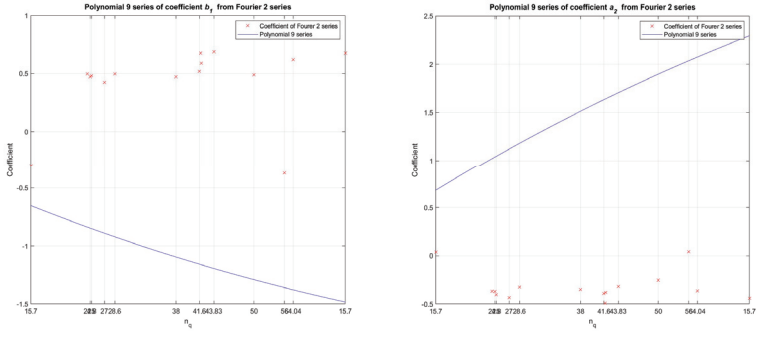

Figure 14. Through polynomial regression (with a polynomial of order 9) in the numerical model developed in MATLAB, the dependence between the values of coefficients b_1, a_2 (from the second-order Fourier function) and specific speed nq (11 pump–turbine models and 2 pump models) was determined for the *Wh* characteristic.

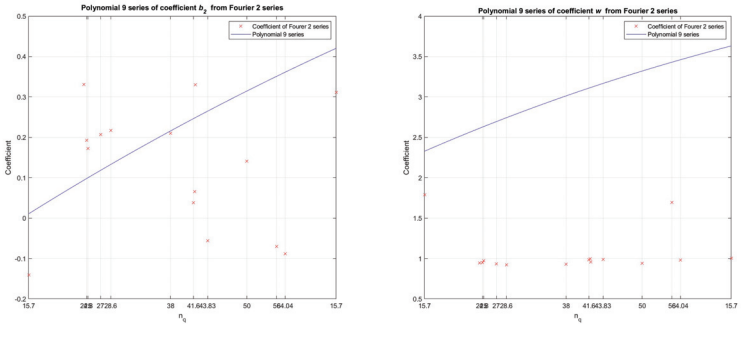

Figure 15. Through polynomial regression (with a polynomial of order 9) in the numerical model developed in MATLAB, the dependence between the values of coefficients b_2, w (from the second-order Fourier function) and specific speed nq (11 pump–turbine models and 2 pump models) was determined for the *Wh* characteristic.

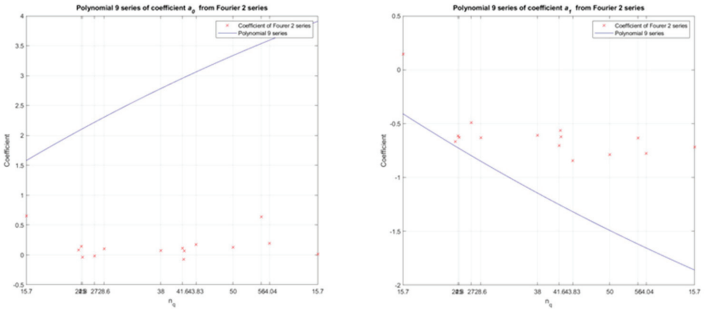

Figure 16. By polynomial regression (with a polynomial of order 9) in the numerical model developed in MATLAB, the dependence between the values of coefficients a_o, a_1 (from the second-order Fourier function) and specific speed *nq* (11 pump–turbine models and 2 pump models) was determined for the *Wm* characteristic.

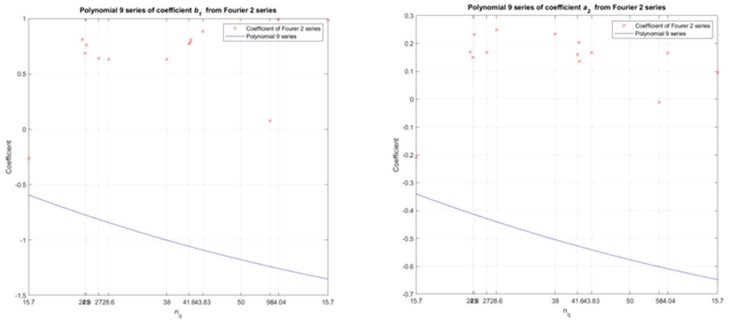

Figure 17. By polynomial regression (with a polynomial of order 9) in the numerical model developed in MATLAB, the dependence between the values of coefficients b_1, a_2 (from the second-order Fourier function) and specific speed *nq* (11 pump–turbine models and 2 pump models) was determined for the *Wm* characteristic.

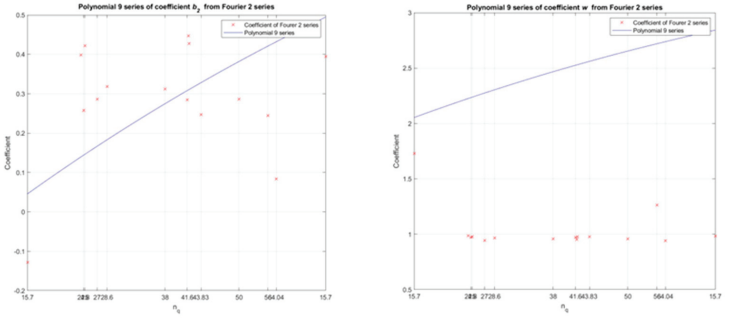

Figure 18. By polynomial regression (with a polynomial of order 9) in the numerical model developed in MATLAB, the dependence between the values of coefficients b_2, w (from the second-order Fourier function) and specific speed *nq* (11 pump–turbine models and 2 pump models) was determined for the *Wm* characteristic.

Step 5: Based on the developed numerical model, from the universal equations, the authors obtained values for the *Wh* and *Wm* characteristics for 13 Suter curves at different specific speeds *nq* and compared them with the values for the *Wh* and *Wm* characteristics in the 13 Suter curves obtained by re-calculating the model curves with different specific

speeds *nq* (for the 11 pump–turbine models and 2 pump models). In particular, the authors compared the Suter curves for the *Wh* and *Wm* characteristics with those obtained through re-calculation of the Suter curves obtained from the universal equations. In order to not overload this paper with a large number of diagrams, diagrams for six Suter curves are presented in Figures 19–21 for the *Wh* characteristic and six in Figures 22–24 for the *Wm* characteristic (*nq* = 24.34, 24.8, 25, 27, 28.6, and 64.04). Figures 5 and 6 show the Suter curves for the *Wh* and *Wm* characteristics, respectively, obtained from the re-calculated model and from the universal equation (for 11 pump–turbine models and 2 pump models).

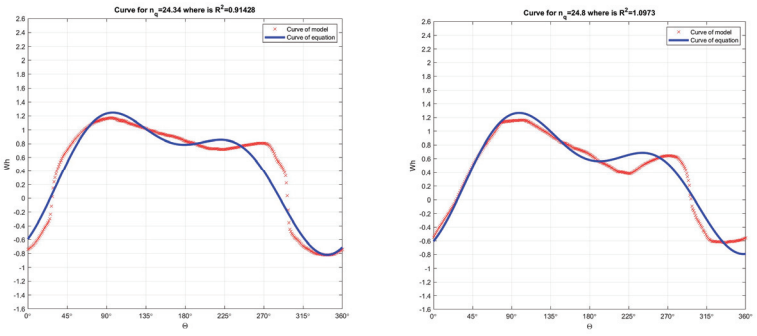

Figure 19. Comparison of Suter curves for the *Wh* characteristic obtained by re-calculating model curves Q_{11}, n_{11}, M_{11} with Suter curves obtained from universal equation, *nq* = 24.34 and 24.8.

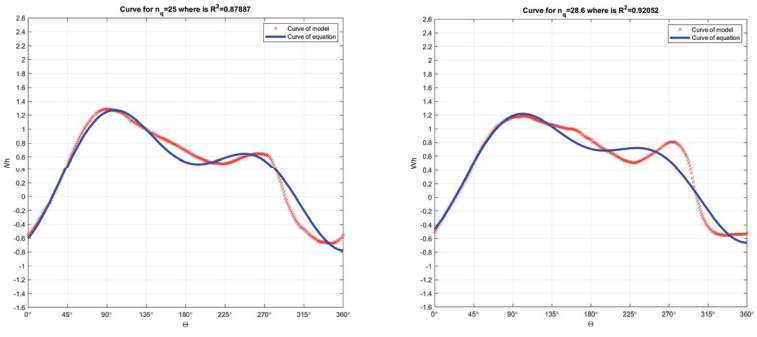

Figure 20. Comparison of Suter curves for the *Wh* characteristic obtained by re-calculating model curves Q_{11}, n_{11}, M_{11} with Suter curves obtained from universal equation, *nq* = 25 and 28.6.

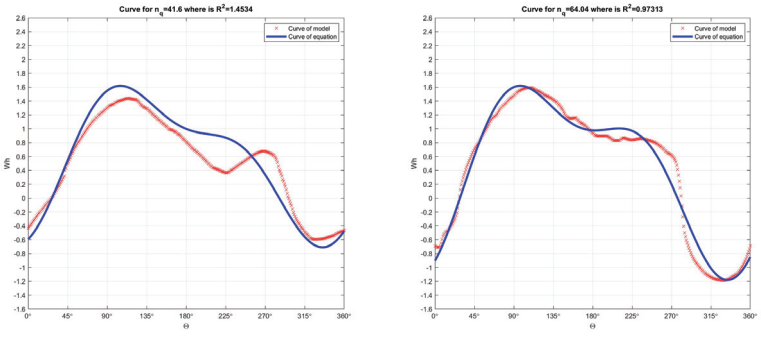

Figure 21. Comparison of Suter curves for the *Wh* characteristic obtained by re-calculating model curves Q_{11}, n_{11}, M_{11} with Suter curves obtained from universal equation, *nq* = 41.6 and 64.04.

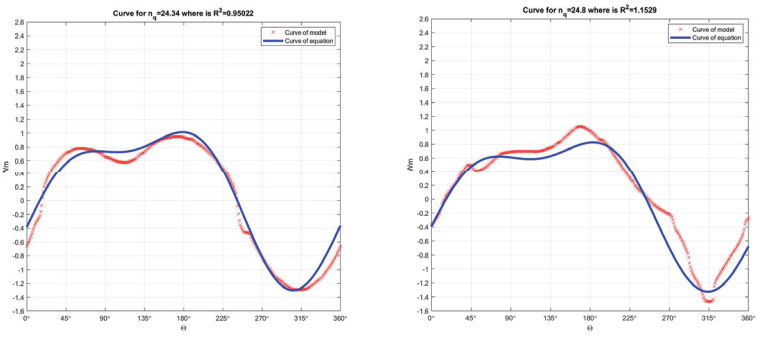

Figure 22. Comparison of Suter curves for the *Wm* characteristic obtained by re-calculating model curves Q_{11}, n_{11}, M_{11} with Suter curves obtained from the universal equation, *nq* = 24.34 and 24.8.

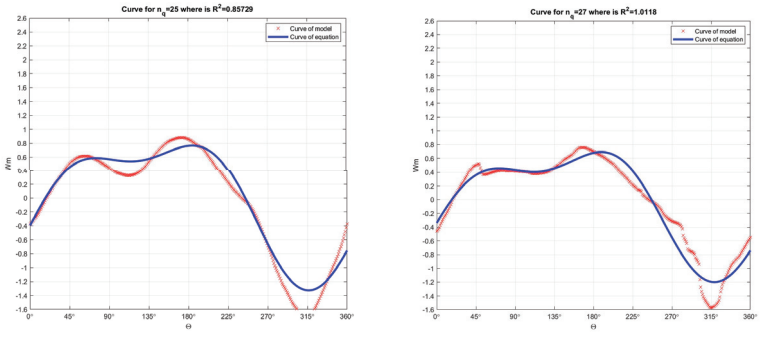

Figure 23. Comparison of Suter curves for the *Wm* characteristic obtained by re-calculating model curves Q_{11}, n_{11}, M_{11} with Suter curves obtained from universal equation, *nq* = 25 and 27.

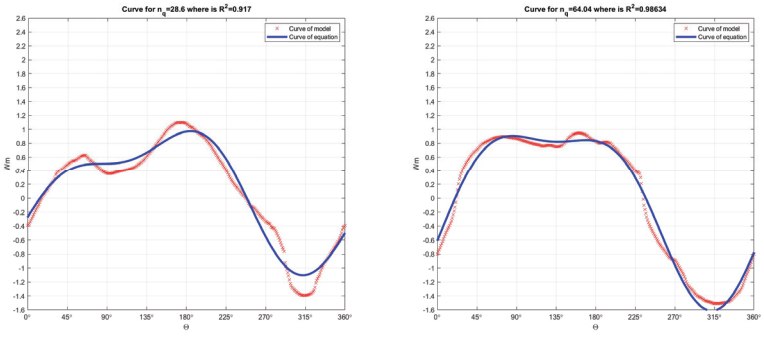

Figure 24. Comparison of Suter curves for the *Wm* characteristic obtained by re-calculating model curves Q_{11}, n_{11}, M_{11} with Suter curves obtained from the universal equation, *nq* = 28.6 and 64.04.

MATLAB was used to develop a numerical model for calculating the transient processes in a pumping plant where two pumps are installed (using the method of characteristics; MOC). As input data for this numerical model, the authors used the Suter curves for the *Wh* and *Wm* characteristics, which were obtained by re-calculating the model curves Q_{11}, n_{11}, M_{11} for different values of the specific speed, as well as the Suter curves for the *Wh* and *Wm* characteristics obtained from universal equations under various specific speed values.

In order to more reliably and precisely unite all values from the experimental four-quadrant curves for different values of *nq* in the universal equation for the *Wh* and *Wm* characteristics, we utilized a fitting method. The focus of this paper is on the simple

derivation and practical application of equations for data fitting, and we should be aware that there are theoretical aspects of regression that are of practical importance. For example, some statistical assumptions are inherent in the linear least squares procedure: each x has a fixed value, is not random, and is known without error; the y values are independent random variables, and all have the same variance; and y values for a given x must be normally distributed. As polynomial regression in MATLAB is applied in this paper, the authors developed a numerical model for performing polynomial regression on a large set of points on four-quadrant curves of pump and pump–turbine models under different values of *nq*. The least squares criterion can easily be extended to fitting data up to higher-order polynomials. For example, in this paper, the authors fit the experimental data from four-quadrant curve pumps and pump–turbines using a ninth-order polynomial, which gave very good results; this is why the authors decided to use this fitting method. For this case, we see that the problem of determining the least squares regression of polynomials of the ninth order is equivalent to solving a system of 10 simultaneous linear equations. This analysis can be easily extended to a more general case. In this way, we recognize that determining the coefficients of an m-order polynomial is equivalent to solving a system of $m + 1$ simultaneous linear equations.

As can be clearly seen from Figures 7–12, some coefficients of determination R^2 were not ideal and some localized error results were large; in the following part, we give recommendations and measures to address this issue. In this paper, the second-order Fourier function was used for passing through the Suter curves (obtained by re-calculating the model curves Q_{11}, n_{11}, M_{11}) under different *nq*, and the values of coefficient of determination R^2 were not ideal. During the development of this paper, we trialed many different types of functions (Fourier functions of order 2, 3, 4, 5, 6, 7, and 8; polynomials of order 1, 2, 3, 4, 5, 6, 7, 8, and 9; and Gaussian functions of order 1, 2, 3, 4, and 5) and many combinations of these functions. We also performed many analyses for all values of the coefficient of determination R^2 for all combinations of functions, and the best results were obtained with the combination of the second-order Fourier function and polynomial of order 9, which is why the values obtained with these two functions are presented. The authors recommend that researchers who would like to conduct further research in this area analyze other mathematical tools that can enhance the fitting process and obtain better values for the coefficient of determination R^2. All of the above explains why the polynomial regression (with polynomials of order 9) did not work well, and why we chose a fit with higher accuracy for the coefficients of the second-order Fourier function. This also explains why the polynomial curves in Figures 13–18 appear to be far from the samples. The results presented in this paper represent the maximum reached during the process of researching these issues, which was conducted over the past few years. It is encouraging that, while there were some deviations (according to the diagrams for some coefficients and R^2 values), this does not mean the approximations of *Wh* and *Wm* are bad in the engineering sense, as these coefficients have very little effect on the final parameters being investigated. According to our assessment, the error was about 3%, which is not of great importance in engineering practice. The final conclusion is that the calculation method provided at the end of this paper with the comparison diagrams is proof that, even with larger deviations of some coefficients, the transient calculation results remain very similar.

4.2. Universal Equation for Wh Characteristic Depending on nq Obtained from the Developed Numerical Model in MATLAB with Second-Order Fourier Function

The universal equation for the *Wh* characteristic was obtained from the numerical model developed in MATLAB, presented in the form:

$$W_{h,} = f(nq,\theta). \quad (1)$$

The universal equation for the *Wh* characteristic with respect to the second-order Fourier function is as follows:

$$Wh = a_0 + a_1 \cdot cos(\theta \cdot w) + b_1 \cdot sin(\theta \cdot w) + a_2 \cdot cos(2 \cdot \theta \cdot w) + b_2 \cdot sin(2 \cdot \theta \cdot w) \quad (2)$$

The coefficients in the universal equation are expressed using polynomials of order 9:

$$a_0 = c_1 \cdot {n_q}^9 + c_2 \cdot {n_q}^8 + c_3 \cdot {n_q}^7 + c_4 \cdot {n_q}^6 + c_5 \cdot {n_q}^5 + c_6 \cdot {n_q}^4 + c_7 \cdot {n_q}^3 + c_8 \cdot {n_q}^2 + c_9 \cdot n_q + c_{10}$$

$$a_1 = c_1 \cdot {n_q}^9 + c_2 \cdot {n_q}^8 + c_3 \cdot {n_q}^7 + c_4 \cdot {n_q}^6 + c_5 \cdot {n_q}^5 + c_6 \cdot {n_q}^4 + c_7 \cdot {n_q}^3 + c_8 \cdot {n_q}^2 + c_9 \cdot n_q + c_{10}$$

$$b_1 = c_1 \cdot {n_q}^9 + c_2 \cdot {n_q}^8 + c_3 \cdot {n_q}^7 + c_4 \cdot {n_q}^6 + c_5 \cdot {n_q}^5 + c_6 \cdot {n_q}^4 + c_7 \cdot {n_q}^3 + c_8 \cdot {n_q}^2 + c_9 \cdot n_q + c_{10}$$

$$a_2 = c_1 \cdot {n_q}^9 + c_2 \cdot {n_q}^8 + c_3 \cdot {n_q}^7 + c_4 \cdot {n_q}^6 + c_5 \cdot {n_q}^5 + c_6 \cdot {n_q}^4 + c_7 \cdot {n_q}^3 + c_8 \cdot {n_q}^2 + c_9 \cdot n_q + c_{10}$$

$$b_2 = c_1 \cdot {n_q}^9 + c_2 \cdot {n_q}^8 + c_3 \cdot {n_q}^7 + c_4 \cdot {n_q}^6 + c_5 \cdot {n_q}^5 + c_6 \cdot {n_q}^4 + c_7 \cdot {n_q}^3 + c_8 \cdot {n_q}^2 + c_9 \cdot n_q + c_{10}$$

$$w = c_1 \cdot {n_q}^9 + c_2 \cdot {n_q}^8 + c_3 \cdot {n_q}^7 + c_4 \cdot {n_q}^6 + c_5 \cdot {n_q}^5 + c_6 \cdot {n_q}^4 + c_7 \cdot {n_q}^3 + c_8 \cdot {n_q}^2 + c_9 \cdot n_q + c_{10}.$$

The values of the coefficients in the universal equation for the *Wh* characteristic, obtained from the numerical model developed in MATLAB based on the procedure described in this paper, are listed in Table 1.

Table 1. Values of coefficients specified in the universal equation for the *Wh* characteristic.

a_0 (c_1)	a_0 (c_2)	a_0 (c_3)	a_0 (c_4)
0.000000000082657281479101800	−0.000000029061457403003900	0.000004456379729293060 0	−0.000390851128806932 0000
a_0 (c_5)	a_0 (c_6)	a_0 (c_7)	a_0 (c_8)
0.021587807156691600	−0.7779210582576410	18.268604739268900	−269.24654067798700
a_0 (c_9)	a_0 (c_{10})	a_1 (c_1)	a_1 (c_2)
2256.073852668840	−8170.186565443250	−0.000000000035748269872097 40	0.000000013284959440729400
a_1 (c_3)	a_1 (c_4)	a_1 (c_5)	a_1 (c_6)
−0.000002153938639444960 0	0.000199742030177702 0000	−0.011660699346564100	0.4438125887830780
a_1 (c_7)	a_1 (c_8)	a_1 (c_9)	a_1 (c_{10})
−10.995720789290900	170.69105909768900	−1503.076337278080	5703.007866291280
b_1 (c_1)	b_1 (c_2)	b_1 (c_3)	b_1 (c_4)
−0.000000000075456939999082 80	0.000000025845257002692800	−0.000003855126002467060 0	0.000328448676289226 0000
b_1 (c_5)	b_1 (c_6)	b_1 (c_7)	b_1 (c_8)
−0.017601498848716700	0.6148165821380630	−13.985903630865500	199.60428369467500
b_1 (c_9)	b_1 (c_{10})	a_2 (c_1)	a_2 (c_2)
−1619.808788457710	5686.005279970290	0.000000000048535010149848 70	−0.000000017313106387755800
a_2 (c_3)	a_2 (c_4)	a_2 (c_5)	a_2 (c_6)
0.000002699043141492700 0	−0.000241155677305153 0000	0.013595507151620100	−0.5009101639852780
a_2 (c_7)	a_2 (c_8)	a_2 (c_9)	a_2 (c_{10})
12.042905981970900	−181.84512743002200	1561.180298581870	−5788.854265185760
b_2 (c_1)	b_2 (c_2)	b_2 (c_3)	b_2 (c_4)
−0.000000000001273837193401 39	0.000000000325499336592069	−0.000000026925857748338 5	−0.000000060851430274008 6
b_2 (c_5)	b_2 (c_6)	b_2 (c_7)	b_2 (c_8)
0.000160991178062167	−0.0123557610666339	0.463796303315559	−9.65109389182705
b_2 (c_9)	b_2 (c_{10})	w (c_1)	w (c_2)
106.113132649951	−478.811119088044	0.000000000076173836797593 40	−0.000000026492013127284700
w (c_3)	w (c_4)	w (c_5)	w (c_6)
0.000004016506974174600	−0.000348161206399576 0000	0.019000243595516300	−0.6763948591316100
w (c_7)	w (c_8)	w (c_9)	w (c_{10})
15.691961350241300	−228.50130238754600	1892.295034951600	−6775.282084470940

4.3. Universal Equation for Wm Characteristic Depending on nq Obtained from the Developed Numerical Model in MATLAB with Second-Order Fourier Function

The universal equation for the *Wm* characteristic obtained from the numerical model developed in MATLAB is presented in the form:

$$W_m = f(nq,\theta). \tag{3}$$

The universal equation with respect to the second-order Fourier function is as follows:

$$Wm = a_0 + a_1 \cdot cos(\theta \cdot w) + b_1 \cdot sin(\theta \cdot w) + a_2 \cdot cos(2 \cdot \theta \cdot w) + b_2 \cdot sin(2 \cdot \theta \cdot w). \tag{4}$$

The coefficients in the universal equation for the *Wm* characteristic are expressed using polynomials of order 9:

$$a_0 = c_1 \cdot {n_q}^9 + c_2 \cdot {n_q}^8 + c_3 \cdot {n_q}^7 + c_4 \cdot {n_q}^6 + c_5 \cdot {n_q}^5 + c_6 \cdot {n_q}^4 + c_7 \cdot {n_q}^3 + c_8 \cdot {n_q}^2 + c_9 \cdot n_q + c_{10}$$

$$a_1 = c_1 \cdot {n_q}^9 + c_2 \cdot {n_q}^8 + c_3 \cdot {n_q}^7 + c_4 \cdot {n_q}^6 + c_5 \cdot {n_q}^5 + c_6 \cdot {n_q}^4 + c_7 \cdot {n_q}^3 + c_8 \cdot {n_q}^2 + c_9 \cdot n_q + c_{10}$$

$$b_1 = c_1 \cdot {n_q}^9 + c_2 \cdot {n_q}^8 + c_3 \cdot {n_q}^7 + c_4 \cdot {n_q}^6 + c_5 \cdot {n_q}^5 + c_6 \cdot {n_q}^4 + c_7 \cdot {n_q}^3 + c_8 \cdot {n_q}^2 + c_9 \cdot n_q + c_{10}$$

$$a_2 = c_1 \cdot {n_q}^9 + c_2 \cdot {n_q}^8 + c_3 \cdot {n_q}^7 + c_4 \cdot {n_q}^6 + c_5 \cdot {n_q}^5 + c_6 \cdot {n_q}^4 + c_7 \cdot {n_q}^3 + c_8 \cdot {n_q}^2 + c_9 \cdot n_q + c_{10}$$

$$b_2 = c_1 \cdot {n_q}^9 + c_2 \cdot {n_q}^8 + c_3 \cdot {n_q}^7 + c_4 \cdot {n_q}^6 + c_5 \cdot {n_q}^5 + c_6 \cdot {n_q}^4 + c_7 \cdot {n_q}^3 + c_8 \cdot {n_q}^2 + c_9 \cdot n_q + c_{10}$$

$$w = c_1 \cdot {n_q}^9 + c_2 \cdot {n_q}^8 + c_3 \cdot {n_q}^7 + c_4 \cdot {n_q}^6 + c_5 \cdot {n_q}^5 + c_6 \cdot {n_q}^4 + c_7 \cdot {n_q}^3 + c_8 \cdot {n_q}^2 + c_9 \cdot n_q + c_{10}.$$

The values of the coefficients in the universal equation for the *Wm* characteristic obtained from the numerical model developed in MATLAB based on the procedure described in this paper are listed in Table 2.

Table 2. Values of coefficients specified in universal equation for the *Wm* characteristic.

a_0 (c_1)	a_0 (c_2)	a_0 (c_3)	a_0 (c_4)
0.000000000070017065867877730	−0.000000025015831555089 80	0.000003904738113736460	−0.000349191266686 3700
a_0 (c_5)	a_0 (c_6)	a_0 (c_7)	a_0 (c_8)
0.01969645197701400	−0.725829938836100	17.44890963741950	−263.3977401451720
a_0 (c_9)	a_0 (c_{10})	a_1 (c_1)	a_1 (c_2)
2260.388398637760	−8377.01350286527	−0.000000000009179203466987 76	0.000000003909054868417 79
a_1 (c_3)	a_1 (c_4)	a_1 (c_5)	a_1 (c_6)
−0.000000712669136566865	0.0000731932114855007	−0.00467292530266516	0.192408755177559
a_1 (c_7)	a_1 (c_8)	a_1 (c_9)	a_1 (c_{10})
−5.10821796821765	84.2463622056342	−782.004920168192	3104.72992929313
b_1 (c_1)	b_1 (c_2)	b_1 (c_3)	b_1 (c_4)
−0.000000000071407591907090 90	0.000000024518617769369 50	−0.000003666867803655490	0.0003132713588738140
b_1 (c_5)	b_1 (c_6)	b_1 (c_7)	b_1 (c_8)
−0.01683554373832690	0.589704417617438	−13.44994606400680	192.3971195389380
b_1 (c_9)	b_1 (c_{10})	a_2 (c_1)	a_2 (c_2)
−1564.118084049990	5496.89652832734	−0.000000000024738354288418 50	0.000000008573899770384 72
a_2 (c_3)	a_2 (c_4)	a_2 (c_5)	a_2 (c_6)
−0.000001293799012428200	0.0001114657248249200	−0.00603673362973466	0.212934147809491
a_2 (c_7)	a_2 (c_8)	a_2 (c_9)	a_2 (c_{10})
−4.88728990817866	70.3140700082219	−574.701954526231	2029.92561253025
b_2 (c_1)	b_2 (c_2)	b_2 (c_3)	b_2 (c_4)
0.000000000015326038956346 40	−0.000000005345978109828 02	0.000000813923958668984	−0.000070953583298 0723

Table 2. *Cont.*

b_2 (c_5)	b_2 (c_6)	b_2 (c_7)	b_2 (c_8)
0.00390090711682261	−0.140186188779757	3.29082695837552	−48.6175747114795
b_2 (c_9)	b_2 (c_{10})	w (c_1)	w (c_2)
409.662879623748	−1496.85732924952	0.000000000037258250849151 30	−0.000000013072371125036 80
w (c_3)	w (c_4)	w (c_5)	w (c_6)
0.000002001304912505130	−0.0001753365232788030	0.00967969358670688	−0.348859201252643
w (c_7)	w (c_8)	w (c_9)	w (c_{10})
8.19843384947085	−120.9703220724220	1015.016628204550	−3679.33688058800

5. Application of Universal Equations for *Wh* and *Wm* for Calculation of Transient Processes in Radial Hydraulic Machinery

For validation purposes, we consider a pumping plant in which two pumps are installed. The complete technical data of the plant are listed in Table 3, and a schematic representation is shown in Figure 25. The data for the pumping station were taken from [3]. The transient processes taking place in the pumping plant during load rejection of pumps were calculated using a numerical model developed by the authors in MATLAB.

Table 3. Technical characteristics of components of pumping station.

Pipe 1 Discharge (Q_1)	Pipe 1 Wave Speed (a_1)	Pipe 1 Friction Factor (f_1)	Pipe 1 Diameter (D_{1p})
0.5 m^3/s	900 m/s	0.01	0.75 m
Pipe 1 Length (L_1)	Pipe 2 Discharge (Q_2)	Pipe 2 Wave speed (a_2)	Pipe 2 Friction factor (f_2)
450 m	0.5 m^3/s	1100 m/s	0.012
Pipe 2 Diameter ($D_{2\,p}$)	Pipe 2 Length (L_2)	Pump efficiency (η)	Pump moment of inertia (WR^2)
0.75 m	550 m	0.84	16.85 kg·m^2
Pump rated speed of rotation (n^*)	Pump rated head (H^*)	Pump rated discharge (Q^*)	
1100 rpm	60 m	0.25 m^3/s	

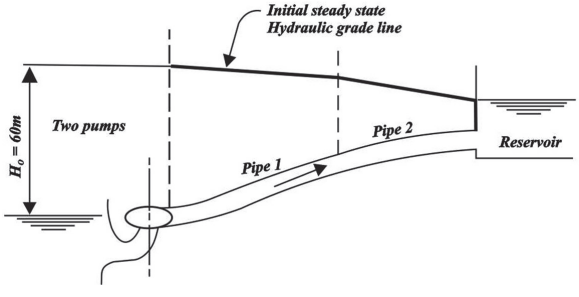

Figure 25. Schematic representation of components of pumping station.

As input data for the numerical model, we used the Suter curves for the *Wh* and *Wm* characteristics obtained by re-calculating the model curves Q_{11}, n_{11}, M_{11} and the Suter curves obtained from universal equations for different values of the specific speed *nq* (11 radial pump–turbine models with *nq* = 24.34, 24.8, 27, 28.6, 38, 41.6, 41.9, 43.83, 50, 56, and 64.04; and two radial pump models with *nq* = 25 and 41.8).

The transient process calculation results are presented visually in Figures 26–28. These diagrams show the changes in head, discharge, and speed of rotation during transient processes in the pump station (connection pump and pipe 1), and comparisons of the obtained results under the 13 specific speeds *nq*.

From Figure 26, it can be seen that the pressure drop at the connection between the pump and pipeline 1 occurred 2 s after the start of the transient process and, for all 13 speeds, this minimum pressure had approximately the same value (around 6 m.w.c.). Meanwhile, the maximum pressure occurred between 5 and 11 s after the beginning of the transient process. The maximum pressure value at the connection between the pump and pipeline 1 differed under the 13 speeds, varying in the range of 80 to 138 m.w.c. This clearly indicates the influence of the specific speed *nq* on the change in pressure at the connection. One of the main objectives of this work is to demonstrate the influence that the specific speed has on the transient process at the pump station.

Figure 27 shows the change in discharge during the transient process at the pump station (connection pump and pipe 1), comparing the obtained results for 13 specific speeds.

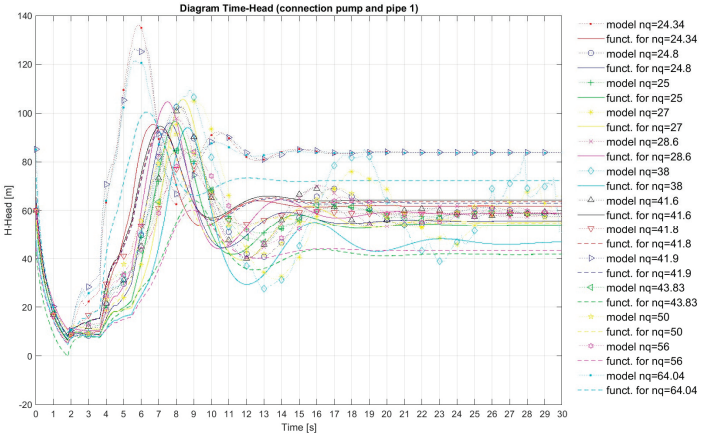

Figure 26. Change in head during transient processes at pump station (connection pump and pipe 1): comparison of obtained results for 13 specific speeds *nq*.

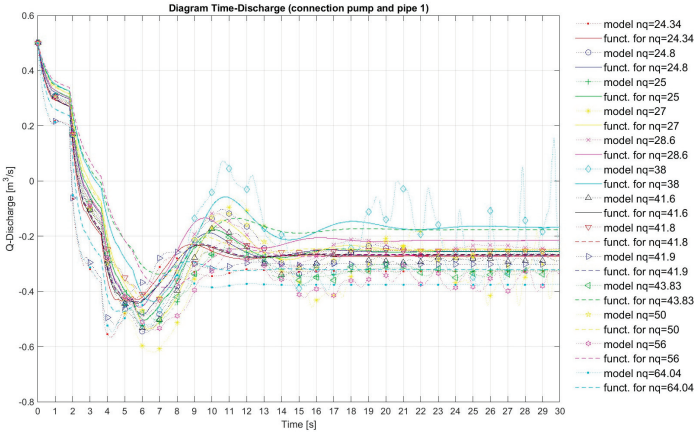

Figure 27. Change in discharge during transient process at pump station (connection pump and pipe 1): comparison of obtained results for 13 specific speeds *nq*.

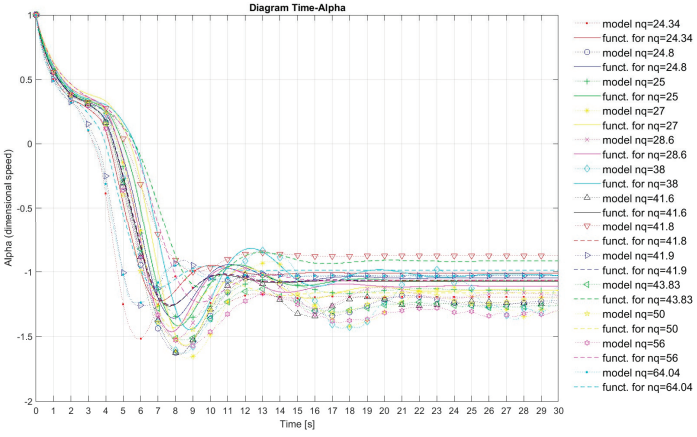

Figure 28. Change in dimensionless speed during transient processes at the pump: comparison of obtained results for 13 specific speeds *nq*.

From Figure 27, it can be seen that the discharge drop at the connection between the pump and pipeline 1 occurred between 4 and 8 s after the beginning of the transient process. In that time interval, the discharge had the lowest value and was approximately the same for all 13 specific speeds, around -0.55 m^3/s. The maximum discharge occurred between 9 and 13 s after the beginning of the transient process and the values under the 13 specific speeds varied in the range of -0.38 to 0.11 m^3/s, which clearly indicates the influence of the specific speed *nq* on the change in discharge at the connection between the pump and pipeline 1.

The diagram presented in Figure 28 shows the change in dimensionless speed during the transient process of the pump, comparing the results obtained for the 13 specific speeds. It can be seen that the drop in rotation speed of the pump occurred between 5.5 and 9.0 s after the beginning of the transient process. In this time interval, the speed of rotation had the lowest value, and the minimum value for the 13 specific speeds varied in the range of -1.2 to -1.80 (dimensionless speed). The maximum speed of rotation occurred between 9.5 and 14 s after the beginning of the transient process, and the value for the 13 specific speeds varied in the range of -1.1 to -0.8 (dimensionless speed). This clearly indicates the influence of specific speed on the change in speed of rotation at the pump during the transient process at the pump station.

The most important objective of this paper is to show how well the results obtained through the calculation of the transient process at the pump station matched (i.e., when shown together in Figures 26–28) for all 13 specific speeds.

6. Conclusions

Universal equations for the *Wh* and *Wm* characteristics depending on the specific speed *nq* were obtained for the first time, through the use of a numerical model developed in MATLAB. The final expressions of the equations, as well as the model used to obtain them, were developed by the authors using the second-order Fourier function to fit the data.

Comparisons of the results obtained when calculating the transient process at a pumping plant under 13 specific speeds are shown in Figures 26–28. For each of the 13 specific speeds, the values for the Suter curves for the *Wh* and *Wm* characteristics were obtained by re-calculating the model characteristics Q_{11}, n_{11}, M_{11}, and from the universal equations for the *Wh* and *Wm* characteristics. Then, the data for the Suter curves were used as input data for the numerical model in order to calculate the transient process at this pump station. In the first case, the set of points for the measured diagram was entered as a separate file outside the numerical model developed in MATLAB. In the second case, the values obtained from the universal equations for the *Wh* and *Wm* characteristics were entered

(these equations are included in the numerical model). A comparison of the calculated results demonstrated that the universal equations for the *Wh* and *Wm* characteristics provide almost the same results as the exact data.

Finally, the main highlight of this paper is that the numerical model developed in MATLAB to obtain universal equations for the *Wh* and *Wm* characteristics is original and has not been presented in any previous paper. Furthermore, for the first time, we describe the application of the results obtained from the universal equations for the *Wh* and *Wm* characteristics in the numerical model for calculating the transient process in a pump station. Finally, we showed that there exists a small error between the values (head, discharge, and rotation speed) obtained through the calculation of the transient process. Notably, when comparing inlet values for *Wh* and *Wm* characteristics obtained from the universal equation and the experimental model test data for different values of *nq*, they differed by less than 3%.

Author Contributions: Conceptualization, Z.G. and M.N.; data curation, Z.G. and M.N.; formal analysis, Z.G. and M.N.; funding acquisition, Z.G. and M.N.; investigation, Z.G. and M.N.; methodology, Z.G. and M.N.; project administration, Z.G. and M.N.; resources, Z.G. and M.N.; software, Z.G. and M.N.; supervision, Z.G. and M.N.; validation, Z.G. and M.N.; visualization, Z.G. and M.N.; writing—original draft, Z.G. and M.N.; writing—review and editing, Z.G. and M.N. All authors have read and agreed to the published version of the manuscript.

Funding: This research received no external funding.

Data Availability Statement: The data of this paper is available through e-mail via authors.

Acknowledgments: Special research was carried out on the two pump–turbine models at the State Key Laboratory of Water Resources and Hydropower Engineering Science, Wuhan University, China, which provided the Q_{11}, n_{11}, and M_{11} 4Q characteristic data. The help provided by Yongguang Cheng, director of the laboratory's Research Section on the Safety of Hydropower Systems, is gratefully acknowledged. Special research was also carried out on the pump–turbine model at the Laboratory of the Institute for Energy Systems and Thermodynamics, Vienna University of Technology, Austria, which provided the Q_{11}, n_{11}, and M_{11} 4Q characteristic data. The help provided by Christian Bauer, head of the university's Institute for Energy Systems and Thermodynamics, Department of Fluid Flow Machinery, is gratefully acknowledged.

Conflicts of Interest: The authors declare no conflict of interest.

Nomenclature

a_1	wave speed in pipe 1 (m/s)
a_2	wave speed in pipe 2 (m/s)
ANSIS CFKS	finite volume method
BEP	best efficiency point
COPs	characteristic operating points
CPCs	complete pump characteristics
CFD	computational fluid dynamics
D_1	inlet diameter of runner (m)
D_{1p}	diameter of pipe 1 (m)
D_{2p}	diameter of pipe 2 (m)
FSI	fluid–structure interaction
L_1	length of pipe 1 (m)
L_2	length of pipe 2 (m)
MLS	moving least squares
f_1	friction factor in pipe 1 (-)
f_2	friction factor in pipe 2 (-)
H	head (m)
H^*	rated head (m)
M	shaft moment (Nm)
M^*	rated shaft moment (Nm)

M_{11}	unit moment (-)
MOC	method of characteristics
n_q	specific speed (-)
n	speed of rotation (rpm, min^{-1})
n^*	rated speed of rotation (rpm, min^{-1})
n_{11}	unit speed of rotation (-)
P_{11}	unit power (-)
PSO	particle swarm optimization
PAT	pump as a turbine
Q	discharge (m^3/s)
Q^*	rated discharge (m^3/s)
Q_{11}	unit discharge (-)
Q_1	discharge in pipe 1 (m^3/s)
Q_2	discharge in pipe 2 (m^3/s)
RNG	re-normalization group k-ε model
Wh	characteristic head (-)
Wm	characteristic moment (-)
v	dimensionless discharge variable (-)
h	dimensionless head (-)
α	dimensionless speed of rotation (-)
β	dimensionless moment (-)
θ	angle (^{o})
η	pump efficiency (-)
WR^2	pump moment of inertia ($\text{kg}\cdot\text{m}^2$)

References

1. Knapp, R.T. Complete Characteristics of Centrifugal Pumps and Their Use in the Prediction of Transient Behavior. *Trans. ASME* **1937**, *59*, 683–689. [CrossRef]
2. Stepanoff, A.J. *Radial–Und Axialpumpen*; Springer (GmbH): Berlin/Heidelberg, Germany, 1959.
3. Chaudhry, M.H. *Applied Hydraulic Transients*; Van Nostrand Reinhold Company: New York, NY, USA, 1979.
4. Wylie, E.B.; Streeter, V.L. *Fluid Transients in Systems*; Prentice Hall: New York, NY, USA, 1993.
5. Thorley, A.R.D.; Chaudry, A. Pump characteristics for transient flow analysis. In *Proceedings of the BHR Group Conference Series, Publication No. 19*; Mechanical Engineering Publications Limited: London, UK, 1996.
6. Donsky, B. Complete pump characteristics and the effects of specific speeds on hydraulic transients. *Basic. Eng. Trans. ASME* **1961**, *83*, 685–699. [CrossRef]
7. Giljen, Z.; Nedeljkovic, M.; Cheng, Y.G. Analysis of four-quadrant performance curves for hydraulic machinery transient regimes. In Proceedings of the 17th International Conference on Fluid Flow Technologies, Budapest, Hungary, 4–7 September 2018; Paper No 98. pp. 1–8.
8. Giljen, Z.; Nedeljkovic, M. Radial hydraulic machinery four-quadrant performance curves dependent on specific speed and applied in transient calculations. In Proceedings of the 29th IAHR Symposium on Hydraulic Machinery and Systems, Kyoto, Japan, 16–21 September 2018; Paper No 224. pp. 1–10. Available online: https://iopscience.iop.org/article/10.1088/1755-1315/240/4/042002 (accessed on 28 March 2019).
9. Li, H.; Lin, H.; Huang, W.; Li, J.; Zeng, M.; Ma, J.; Hu, X. A New Prediction Method for the Complete Characteristic Curves of Centrifugal Pumps. *Energies* **2021**, *14*, 8580. [CrossRef]
10. Yu, J.; Akoto, E.; Degbedzui, D.K.; Hu, L. Predicting Centrifugal Pumps' Complete Characteristics Using Machine Learning. *Processes* **2023**, *11*, 524. [CrossRef]
11. Zhou, W.; Yu, D.; Wang, Y.; Shi, J.; Gan, B. Research on the Fluid-Induced Excitation Characteristics of the Centrifugal Pump Considering the Compound Whirl Effect. *Facta Univ. Ser. Mech. Eng.* **2023**, *21*, 223–238. [CrossRef]
12. Zhou, W.; Wang, Y.; Li, C.; Zhang, W.; Wu, G. Analysis of Fluid-Induced Force of Centrifugal Pump Impeller with Compound Whirl. *Alex. Eng. J.* **2020**, *59*, 4247–4255. [CrossRef]
13. Walters, T.W.; Dahl, T.; Rogers, D. Pump Specific Speed and Four Quadrant Data in Water hammer Simulation—Taking Another Look" auxiliary data files. In Proceedings of the ASME 2020, Pressure Vessels and Piping Conference, Online, 3 August 2020; Volume 4.
14. Zhang, L.; Xu, H.; Yu, Y.H. Fitting method for pump complex characteristic curve based on B-spline. *Drain. Irrig. Mach.* **2007**, *25*, 50–53.
15. Shao, W.Y.; Zhang, X. A new simulation method of complete characteristic curves of reversible pump turbine moving least square approximation. *J. Hydroelectr. Eng.* **2004**, *23*, 102–106.

16. Wang, L.; Li, M.; Wang, F.J.; Wang, J.B.; Yao, C.G.; Yu, Y.S. Study on three-dimensional internal characteristics method of Suter curves for double-suction centrifugal pump. *J. Hydraul. Eng.* **2017**, *48*, 113–122.
17. Gros, L.; Couzinet, A.; Pierrat, D.; Landry, L. Complete pump characteristics and 4-quadrant representation investigated by experimental and numerical approaches. In Proceedings of the ASME-JSME-KSME 2011 Joint Fluids Engineering Conference, Hamamatsu, Japan, 24–29 July 2011; Volume 1, pp. 359–368.
18. Thanapandi, P.; Prasad, R. Centrifugal pump transient characteristics and analysis using the method of characteristics. *Int. J. Mech. Sci.* **1995**, *37*, 77–89. [CrossRef]
19. Höller, S.; Benigni, H.; Jaberg, H. Investigation of the 4-Quadrant behaviour of a mixed flow diffuser pump with CFD-methods and test rig evaluation. *IOP Conf. Ser. Earth Environ. Sci.* **2016**, *49*, 032018. [CrossRef]
20. Huang, S.; Qiu, G.; Su, X.; Chen, J.; Zou, W. Performance prediction of a centrifugal pump as turbine using rotor-volute matching principle. *Renew. Energy* **2017**, *108*, 64–71. [CrossRef]
21. Wan, W.; Huang, W. Investigation on complete characteristics and hydraulic transient of centrifugal pump. *J. Mech. Sci. Technol.* **2011**, *25*, 2583–2590. [CrossRef]
22. Lima, G.M.; Luvizotto Júnior, E. Method to estimate complete curves of hydraulic pumps through the polymorphism of existing curves. *J. Hydraul. Eng.* **2017**, *143*, 04017017. [CrossRef]
23. Hu, X.Y.; Yu, B.; Guo, J.; Wang, S.K. Visualization for predictable model of complete characteristic curve of pump. *Fluid Mach.* **2012**, *3*, 37–39.
24. Zhu, M.L.; Zhang, X.H.; Zhang, Y.H.; Wang, T. Study on prediction model of complete characteristic curves of centrifugal pumps. *J. Northwest Sci-Tech. Univ. Agric. For. Nat. Sci. Ed.* **2006**, *4*, 143–146.
25. Yang, Y.S.; Dong, R.; Jing, T. Influence of Full Characteristic Curve on Pump-off Water Hammer and Its Protection. *China Water Wastewater* **2010**, *26*, 63–66.
26. Huang, B.; Wu, P.; Liu, X.S.; Feng, X.D.; Yang, S.; Wu, D.Z. Four-quadrant Full Characteristic Model Test of the ACP100 Reactor Coolant Pump. *Fluid Mach.* **2020**, *48*, 8–11.
27. Huang, W.; Yang, K.; Guo, X.; Ma, J.; Wang, J.; Li, J. Prediction Method for the Complete Characteristic Curves of a Francis Pump-Turbine. *Water* **2018**, *10*, 205. [CrossRef]
28. Dai, C.; Dong, L.; Lin, H.; Zhao, F. A Hydraulic Performance Comparison of Centrifugal Pump Operating in Pump and Turbine Modes. *J. Therm. Sci.* **2020**, *29*, 1594–1605. [CrossRef]
29. Wang, W.; Guo, H.; Zhang, C.; Shen, J.; Pei, J.; Yuan, S. Transient characteristics of PAT in micro pumped hydro energy storage during abnormal shutdown process. *Renew. Energy* **2023**, *209*, 401–412. [CrossRef]
30. Suter, P. Representation of pump characteristics for calculation of water hammer. In *Sulzer Technical Review*; Research No. 66; Sulzer Brothers Limited: Winterthur, Switzerland, 1966; pp. 45–48.
31. Canale, R.P.; Chapra, S.C. *Numerical Methods for Engineers*; McGraw-Hill Education: New York, NY, USA, 2015.

fluids

MDPI

Article

Prediction of Flow Properties of Porous Triply Periodic Minimal Surface (TPMS) Structures

Saúl Piedra, Arturo Gómez-Ortega and James Pérez-Barrera *

CONAHCYT-Centro de Ingeniería y Desarrollo Industrial (CIDESI), Av. Playa Pie de la Cuesta No. 702, Santiago de Querétaro, Querétaro 76125, Mexico; saul.piedra@cidesi.edu.mx (S.P.); arturo.gomez@cidesi.edu.mx (A.G.-O.)
* Correspondence: james_pe_ba@hotmail.com or james.perez@cidesi.edu.mx

Abstract: The flow through geometrically complex structures is an important engineering problem. In this work, the laminar flow through Triply Periodic Minimal Surface (TPMS) structures is numerically analyzed using Computational Fluid Dynamics (CFD) simulations. Two different TPMS structures were designed, and their porosity was characterized as a function of the isovalue. Then, CFD simulations were implemented to compute the pressure drop by systematically varying the flow velocity and the porosity of the structure. A Darcy–Forchheimer model was fitted to CFD results to calculate the inertial and permeability coefficients as functions of the porosity. These types of results can be very useful for designing fluid flow applications and devices (for instance, heat exchangers), as well as for integrating these TPMS structures since the flow can be very well estimated when using the porous medium model.

Keywords: triply periodic minimal surfaces; Darcy–Forchheimer porous media model; computational fluid dynamics

Citation: Piedra, S.; Gómez-Ortega, A.; Pérez-Barrera, J. Prediction of Flow Properties of Porous Triply Periodic Minimal Surface (TPMS) Structures. *Fluids* **2023**, *8*, 312. https://doi.org/10.3390/fluids8120312

Academic Editors: Vasily Novozhilov, Cunlu Zhao and D. Andrew S. Rees

Received: 5 October 2023
Revised: 21 November 2023
Accepted: 23 November 2023
Published: 29 November 2023

1. Introduction

The flow through porous media is an important engineering problem since many industrial processes need a liquid to flow through (or to be extracted from) natural or man-made porous structures as part of the productive process. These processes pose a challenge since the fluid permeates the interstitial (or pore) space available between the solid matter, thus making it difficult for fluid flow. In addition, this occurs depending on the particular features of the medium. These and other related phenomena have been treated by a combination of experimental and theoretical approaches, therefore resulting in the proposal of several simplified models (currently known as porous media models) that try to take into account the complexity of the medium's geometry through a few characteristic parameters. Porous media models allow for the assessment of the qualitative and quantitative behavior of the flow that moves through geometrically complex structures, and they can be used without the need for detailed and computationally expensive numerical simulations or with experimental observations and measurements that are hard to achieve.

The pioneering model by Darcy considers a linear relation between the macroscopic pressure gradient that occurs through the media and the resulting average velocity of the fluid. In this model, the two characteristic parameters of importance are porosity (understood as the ratio of void space to total volume) and permeability (which is dependent on pore shape, connectivity, and flow features). Although this model has been proven to be valid only for very small Reynolds numbers, its conceptual simplicity has served as the basis for more complete models. One such of these models was proposed by Forchheimer [1], in which a quadratic inertial term was used to modify Darcy's model.

This improved model, known as the Darcy–Forchheimer (DF) model, has been used to describe the fluid flow through porous media in different situations. For instance, Tosco et al. [2] performed 2D pore-scale flow simulations for Newtonian and non-Newtonian

fluids, and they concluded that the DF model can accurately describe the flow behavior for both kinds of fluids when using only two macroscopic parameters for the Newtonian case and three for non-Newtonian fluids. In [3], the authors also studied the flow of a non-Newtonian (viscoelastic) fluid, whereby they considered the Cattaneo–Christov heat transfer through a DF porous medium over a linear stretching surface. In a more recent publication, Hayat et al. [4] analyzed the flow through a DF porous medium over an inclined stretching surface, which included the consideration of mixed convection, heat transfer, and chemical reactions. As demonstrated by latter references, the interest of the scientific community in this kind of system includes the analysis of flows through a DF porous medium alongside different physical phenomena, such as magnetohydrodynamics [5,6], homogeneous–heterogeneous chemical reactions [7], mass transfer [8], and nanofluids [9], to name a few. Some works have even combined several of these phenomena to consider multiphysics in their analysis [10–13]. One interesting application of the DF model corresponds to the analysis and characterization of biological systems [14,15]. Takhanov [16] recorded a detailed literature review of this model and its derivation by using both micro- and macroscale approaches and established a range of validity with experimental data. In their work, the authors stated that this model can be derived at the continuum scale from Navier–Stokes equations, whereas, in a microscopic view, a porous medium is thought as an array of parallel or series of capillary tubes, for which simple analytical solutions can be applied. Regardless of the approximation used, the author assessed the validity of the model using previously published experimental data for consolidated and unconsolidated porous media, as well as for rock fractures.

Additive manufacturing (AM), most commonly known as 3D printing, comprises a set of seven families of different technologies that are used to fabricate prototypes and devices in a layer-by-layer manner. The rapid technological growth of AM provides engineers with almost unlimited freedom of design, as well as a set of advantages over traditional manufacturing techniques, such as the possibility to build lightweight structures [17], topologically optimized parts [18], and part consolidation [19,20], all of which are based on the fact that AM allows for the printing of complex structures easily. In particular, Triply Periodic Minimal Surface (TPMS) structures fabricated by AM are promising complex structures for the enhancement of different applications in which fluid flow is involved. In this sense, the fluid flow through TPMS-based structures has been reported previously, although most of the studies regarding this have focused on the heat transfer properties of these structures [21,22]. A detailed summary of these investigations can be found in [23]. TPMS structures have also raised interest in biological applications [24] and tissue engineering [25].

Recently, several papers have considered TPMS structures as porous media. For instance, Rathore et al. [26] performed pore-scale simulations through four different TPMS structures when using different approaches. They achieved this by considering the TPMS structures in the following ways: (1) as a zero-thickness wall; (2) as the interface between a solid and a fluid; and (3) as a porous medium, which was modeled by an extended Darcy model. Through their simulations, the authors characterized the flow through the four TPMS structures by varying the flow velocity for a single porosity value of 32%. They found that the extended Darcy porous medium model was appropriate for estimating the pressure drop, and this was achieved by considering a cubic behavior for the average velocity. In their work, Ali et al. [27] studied the flow properties of lattice and TPMS structures with a constant porosity of 80%, and they calculated their permeability using Darcy's law. Zeng and Wang [28] proposed a method through which to construct low porosity, TPMS-based isotropic, porous structures, and they compared their structures with a graphite porous material. As a result, the authors proposed an analytical model for the permeability of the structures based on the Hagen–Poiseuille equation and Darcy's law. Zou et al. [29] designed, 3D printed, and experimentally assessed the permeability of several TPMS structures with the constant hydrostatic head technique, as well as by fitting the results to a Darcian model.

Since TPMS structures are geometrically complex, and as highly precise AM technologies are limited to small printing volumes, the use of this kind of structures has been researched to be applied in heat sinks for electronic devices, in which high heat dissipation, large surface areas, and low-pressure drops are desirable. In this sense, Al-ketan et al. [30] designed, simulated, and assessed the thermal performance of TPMS-based heat sinks under forced convection conditions, and they 3D printed some structures to assess their manufacturability. Although the thermal performance increased, there were defects when fabricating the sinks, and these left their study in a proof-of-concept situation. In their work, Passos [31] integrated several TPMS structures into counterflow heat exchangers (HXs) and numerically investigated and compared their performance against a traditional flat plate HX. Li et al. [32] proposed and simulated a heat exchanger design to be used in a supercritical CO_2 Brayton cycle using TPMS structures and compared its thermal and fluid flow features against a printed circuit heat exchanger. They concluded that their design promotes turbulent flows and, thus, increases heat transfer by 30–80%. As can be seen, the use of TPMS in HXs is still an ongoing, active branch of research.

As demonstrated, interest in TPMS structures as porous media has been limited to studies involving just a few porosity values and linear porous media models. In this work, we investigated the flow characteristics through geometrically complex structures by systematically varying their porosity using Computational Fluid Dynamics (CFD) simulations in a channel flow. The analysis of the pressure drop due to the presence of the TPMS structures, varying the inlet flow velocity, leads to the conclusion that the flow through the selected structures behaves as a Darcy–Forchheimer porous medium, whose parameters, namely porosity, permeability, and Forchheimer coefficient were characterized numerically. Given that the fluid flow analysis is an important aspect of heat exchanger design (alongside the heat transfer physics), this work contributes by providing a simplified model for calculating the pressure drop along these structures, which can be seamlessly integrated into the conventional heat exchanger design process.

2. Design of Triply Periodic Minimal Surface (TPMS) Structures

Among the complex structures that can be 3D printed, TPMS, which are smooth surfaces with zero mean curvature and that separate space into two regions of the same volume [33], have garnered attention for applications in structural mechanics [34–36], heat transfer [37,38], and biomedical devices [39,40]. This attention is due to their mathematical simplicity and highly tailorable geometric properties, which directly affect different effective physical properties.

TPMS are mathematically defined by level-set equations of the form $F(x, y, z) = t$, where t is known as the isovalue. For $t = 0$, the level-set surface separates space into two regions of the same volume. If $t \neq 0$, the surface offsets so that one of the regions becomes larger while the other one becomes smaller in the same amount. Consequently, the isovalue directly influences the solid volume fraction (or, equivalently, the porosity) of the structure. This type of equation defines a skeletal structure, but squaring the equation results in defining a sheet-based structure.

In this paper, we analyze two TPMS sheet-based structures: The Schwarz Primitive and Schoen I-graph Wrapped Package (IWP) structures, which are defined by the following equations:

$$\text{Primitive:} \quad \cos\tilde{x} + \cos\tilde{y} + \cos\tilde{z} = t, \tag{1}$$

$$\text{IWP:} \quad 2(\cos\tilde{x}\cos\tilde{y} + \cos\tilde{y}\cos\tilde{z} + \cos\tilde{x}\cos\tilde{z}) - (\cos 2\tilde{x} + \cos 2\tilde{y} + \cos 2\tilde{z}) = t, \tag{2}$$

where $\tilde{x} = \dfrac{2\pi x}{a}$, $\tilde{y} = \dfrac{2\pi y}{a}$ and $\tilde{z} = \dfrac{2\pi z}{a}$, a being the unit cell size. Figure 1 shows four sheet-based TPMS structures, including the two used in this study.

Despite their evident applications, software for designing and integrating TPMS into usable devices is still scarce. Although there are a few commercial [41] and open-source options [42–45] recently made available, the former tends to be costly, whereas the latter is

limited in some fundamental aspects, such as the necessity to use third-party software to integrate TPMS into arbitrary geometries.

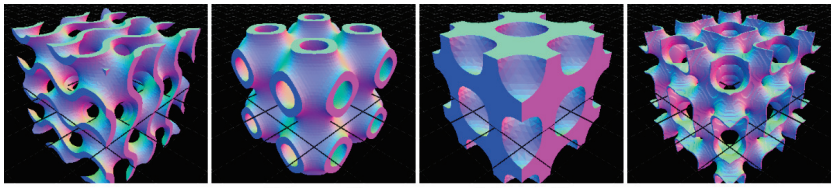

Figure 1. Examples of TPMS sheet-based structures generated using the MaSMaker [46] source code. All these structures separate space into two regions of equal volume.

In this paper, MaSMaker v1.0 [46] was used to generate the two TPMS-based structures of interest for studying their behavior as porous media. To characterize the flow through these structures, several cubic unit cells with varying porosity were designed for both structures. Because MaSMaker produces an STL file, the designed structures underwent preprocessing to ensure compatibility with CFD simulation software. This preprocessing involved repairing the triangulated surface in MeshMixer v3.5 [47], followed by a solidification procedure executed in FreeCAD v0.21.1 [48], ultimately allowing their integration into the computational domain of interest.

3. Mathematical Model and Numerical Implementation

The computational domain comprises a parallelepiped channel ($60 \times 10 \times 10$ mm^3) through which a laminar flow occurs, with a solid TPMS structure (IWP, Schwarz Primitive) immersed within (see Figure 2a). The TPMS unit cells, designed within a volume of $10 \times 10 \times 10$ mm^3, are positioned 10 mm from the inlet flow within the parallelepiped domain. Air, characterized by standard constant properties, serves as the working fluid for all reported simulations. As air passes through the structure, the flow and pressure drop along the channel are disturbed due to the presence of the TPMS. This phenomenon is governed by the mass conservation and balance of momentum equations for a laminar, Newtonian, and incompressible flow in a steady state:

$$\nabla \cdot \mathbf{u} = 0, \tag{3}$$

$$(\mathbf{u} \cdot \nabla)\mathbf{u} = -\frac{1}{\rho}\nabla p + \frac{\mu}{\rho}\nabla^2 \mathbf{u}, \tag{4}$$

where $\mathbf{u}$ and p are the velocity and pressure fields, and ρ and μ are the mass density and dynamic viscosity of the fluid, respectively. The governing equations were discretized using the Finite Volume Method (FVM) implemented in the ANSYS Fluent software [49], where a pressure-based steady solver and a laminar model were selected for solving the governing equations. The Semi-Implicit Method for Pressure-Linked Equations (SIMPLE) algorithm was used for pressure-velocity coupling. The convective terms were discretized using a second-order upwind scheme, while the diffusive terms were approximated using a central differences scheme. The implemented boundary conditions are depicted in Figure 2a. A constant velocity is imposed at the entrance of the channel as the inlet boundary condition, a fixed outlet pressure is applied at the end of the channel, and periodic boundary conditions are enforced in the lateral walls to mitigate their effect, considering that only one unit cell is used in the simulations.

In Figure 2b, an example of the polyhedral surface mesh constructed over the TPMS structure is displayed. A poly-hexahedral volume mesh was constructed, and a central slice of the mesh for the channel with the IWP structure is shown in Figure 2c. This type of mesh predominantly consists of orthogonal cells, resembling a structured mesh

in the bulk of the flow, and offers a good approximation of the geometry near the TPMS structure using a conformal unstructured mesh. To capture the flow inside the pores, appropriate refinements were applied close to the structures. The minimum and maximum cell lengths were defined as 0.02 mm and 0.4 mm, respectively. The constructed meshes achieved acceptable geometrical metrics, with a maximum skewness of 0.72 and a minimum orthogonal quality of 0.23. The convergence of the simulations was ensured by monitoring the resulting residuals, with a value smaller than 10^{-6} indicating a converged solution. Additionally, the mass balance at the inlet and outlet of the channel was computed to guarantee mass conservation throughout the system. The Reynolds number based on the width of the channel (w) and inlet velocity (U) was used for describing the flow regime, $Re = \frac{Uw}{\nu}$.

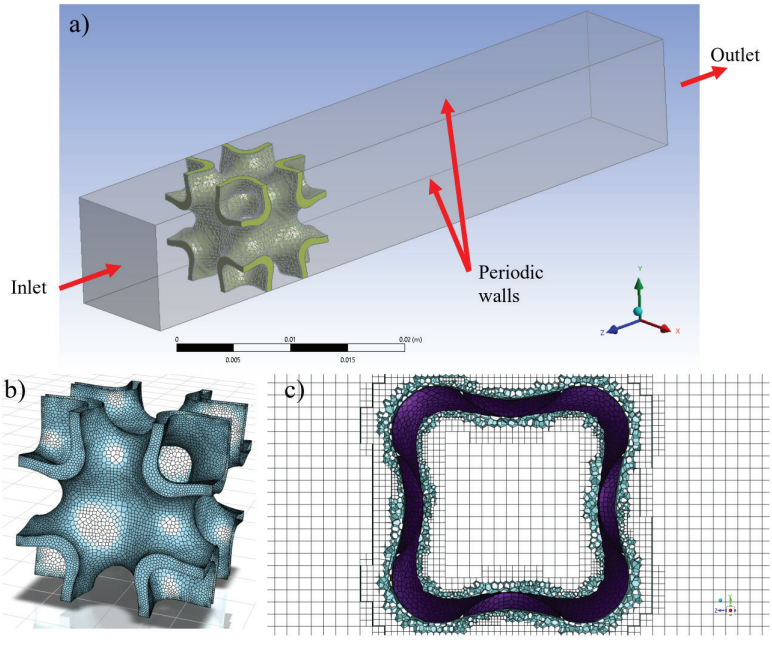

Figure 2. (**a**) Physical model and (**b**,**c**) examples of the computational mesh for the IWP structure.

A mesh sensitivity study was conducted to ensure the consistency of the simulations. The analysis was based on the calculation of pressure drop as a function of the computational mesh size for the IWP structure with $t = 0.7$ and Re = 200. First, a coarse mesh with acceptable metrics (orthogonality, skewness, and aspect ratio) was constructed. Then, mesh refinement tools were applied to generate finer grids. Table 1 lists the grids used for the sensitivity analysis along with their corresponding pressure drop results. Notably, grids 3, 4, and 5 exhibited negligible differences in pressure drop. Consequently, computational simulations for all cases were performed using the sizing parameters of grid 4. This allowed for a reduction in computational time while ensuring consistent results for each simulation.

To ensure the physical reliability of the computational mesh, one can assume that when the computational domain is discretized into small control volumes, and the flow is laminar, the variables within each control volume undergo gradual changes. For the case of the velocity change within a mesh cell, this condition is met if the Reynolds number based on the control volume scale is small ($Re_{cv} = zw/\nu < 1$). With this assumption, the Re_{cv} was calculated for each control volume based on its size and velocity, revealing that in around 85% of the total control volumes, it is less than 1.

Table 1. Mesh sensitivity analysis results.

Grid	Cells	$\Delta p/L$ (Pa/m)
1	102253	389.14
2	258222	405.34
3	345876	410.10
4	431847	409.45
5	760027	411.95

4. Results and Discussion

4.1. TPMS Structures Design and Porosity Characterization

TPMS structures were designed in MaSMaker [46], with variations in the isovalue (t). As the porosity of the structure depends on t, the initial step in modeling such structures as porous mediums involves characterizing the relationship between porosity and the isovalue. For this purpose, Schwarz "P" (also known as Primitive) and IWP structures were designed in MaSMaker for different values of t. Using Blender software [50], the volume fraction can be calculated for each structure, and a polynomial fit can be determined to relate the volume fraction (V_f) to the isovalue (t).

In Figure 3, the results illustrating the relationships between t and the volume fraction are presented for both TPMS structures. It is important to mention that each structure has its own topological features. Since our focus is on cases with open and connected porosities allowing fluid passage, the volume fraction range for the two selected structures was restricted to those depicted in Figure 3. The continuous black line represents the best fifth-grade polynomial fit for the resulting relation, calculated using the equation:

$$t = aV_f^5 + bV_f^4 + cV_f^3 + dV_f^2 + eV_f + f. \tag{5}$$

The coefficients of the polynomial fit and their respective coefficients of determination R^2 for each TPMS are presented in Table 2. Using this characterization, the porosity ($\phi = 1 - V_f$) of the structures can be directly computed to model them as porous media.

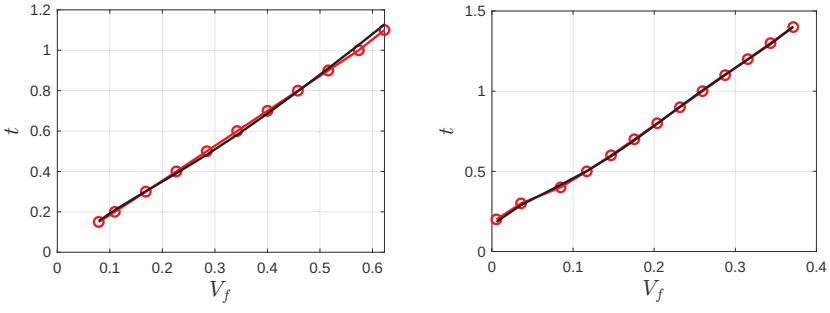

(**a**) Schwarz "P" (**b**) Schoen "IWP"

Figure 3. Isovalue as a function of the volume fraction (V_f) for (**a**) Schwarz "P" and (**b**) Schoen IWP structures. The porosity, ϕ, is related to the volume fraction by $\phi = 1 - V_f$. The red points represent the original data fitted using a fifth-grade polynomial, depicted by the black line.

Table 2. Coefficients for the polynomial fit to compute the isovalue as a function of the volume fraction (Equation (5)).

TPMS	a	b	c	d	e	f	R^2
Primitive	17.03	−34.93	26.9	−8.89	2.83	−0.025	0.99
IWP	746.2	−744.3	260.2	−35.49	4.56	0.16	0.98

4.2. Mean Flow Characteristics

As an initial exploration, the flow through the TPMS structures was examined. In Figure 4, streamlines depicting the flow are presented for the Schwarz "P" structure with $\phi = 0.83$. It is evident that at low Reynolds numbers (Re = 10), the velocity increases along the central part of the channel, resulting in smooth streamlines that nearly fill the structure channel. At higher Reynolds numbers (Re = 300), recirculations develop at the lateral sides of the structure. The vortices within the Schwarz "P" cell contribute significantly to the pressure drop along the cell, as the flow passing through the structure is confined to the center of the cell.

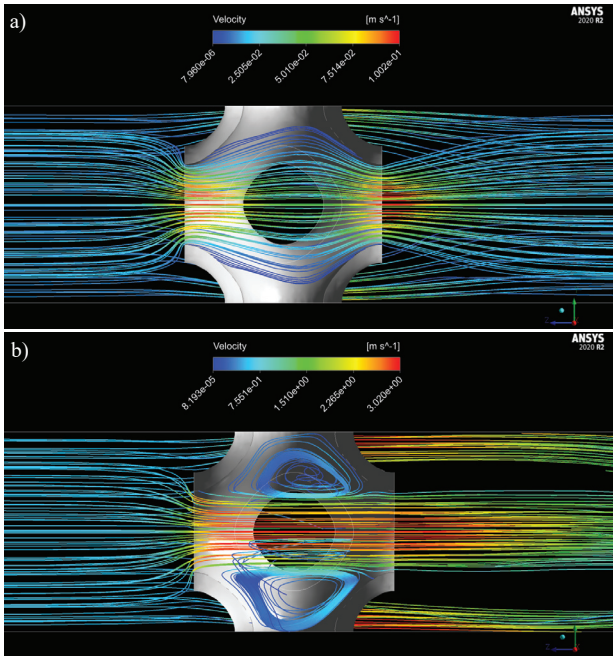

Figure 4. Streamlines of the flow through the Schwarz "P" structure ($\phi = 0.83$): (**a**) Re = 10, (**b**) Re = 300.

Streamlines of the flow through the IWP structure are illustrated in Figure 5. As observed, the flow is divided by the channels of the TPMS and smoothly passes through the structure. Specifically, at a low Reynolds number (Re = 10), two symmetrical separated streams can be seen flowing through the central part of the structure. However, at higher Reynolds numbers (Re = 300), the inertial effects of the flow disturb and mix these streams. Under these conditions, the mixing could be advantageous for the application of this type of structure in heat and mass transfer processes.

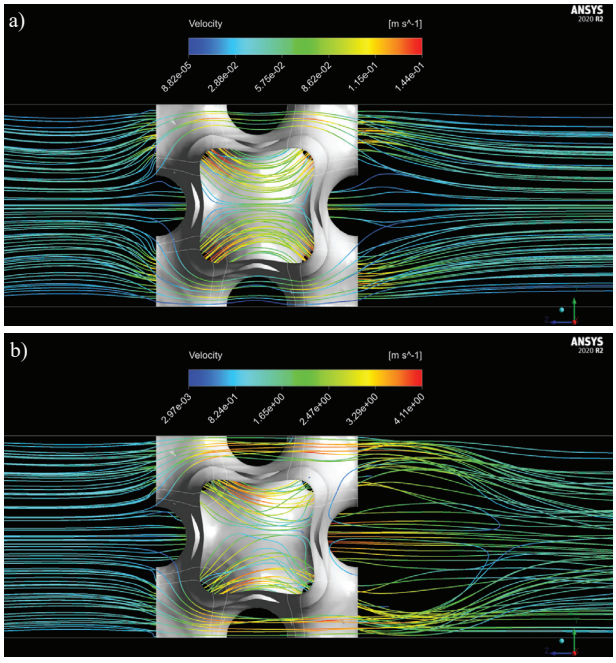

Figure 5. Streamlines of the flow through IWP structures ($\phi = 0.79$): (**a**) Re = 10, (**b**) Re = 300.

4.3. Modeling the TPMS Structures as Porous Media

The primary objective of this study is to demonstrate how the flow through TPMS structures can be effectively modeled using the Darcy–Forchheimer porous medium model. The aim is to develop relations that enable the computation of pressure drop as a function of porosity and mean flow velocity exclusively. This, in turn, facilitates the straightforward estimation of mean flow characteristics when employing these structures for engineering applications.

The Darcy–Forchheimer model proves to be a common choice for describing fluid flow through porous media, especially when inertial effects are substantial in comparison to diffusive effects. The model amalgamates Darcy's law, asserting that the average flow velocity of a fluid through a porous medium is proportional to the pressure gradient, with an additional term accounting for resistance due to inertia and viscous drag at higher flow rates. Thus, the Darcy–Forchheimer equation takes the form of a two-coefficient parameter model:

$$\frac{\Delta p}{L} = \frac{\mu}{k} U + \frac{c_F \rho}{\sqrt{k}} U^2, \tag{6}$$

where Δp is the pressure drop through a porous medium with length L, k is the permeability of the medium in the direction of the u component of the velocity, and c_F is the Darcy–Forchheimer coefficient, which is a measure of the resistance of the flow through the porous medium. This resistance considers both viscous drag and inertial effects. The Darcy–Forchheimer coefficient's value depends on various parameters, including porosity, geometric features of the porous medium, and fluid flow conditions. Consequently, a comprehensive understanding of the TPMS structure and its fluid flow characteristics is essential for the accurate application of the Darcy–Forchheimer model.

Computational simulations were systematically conducted, varying the porosity of the structures through the isovalue, t, and the inlet stream velocity. In Figure 6, the circle markers represent the pressure drop along the TPMS structures as a function of velocity for different values of t. The continuous lines depict the second-grade polynomial fit

applied to each series. Notably, at higher velocities or, equivalently, high *Re*, the pressure drop for Primitive structures is significantly higher (approximately 10 times) than for their IWP counterparts. This discrepancy arises from fluid recirculations within the Primitive structure, as illustrated in Figure 4.

As evident, the second-grade polynomial effectively fits the data obtained from the numerical simulations for all cases. This suggests the potential applicability of the Darcy–Forchheimer model to both TPMS structures.

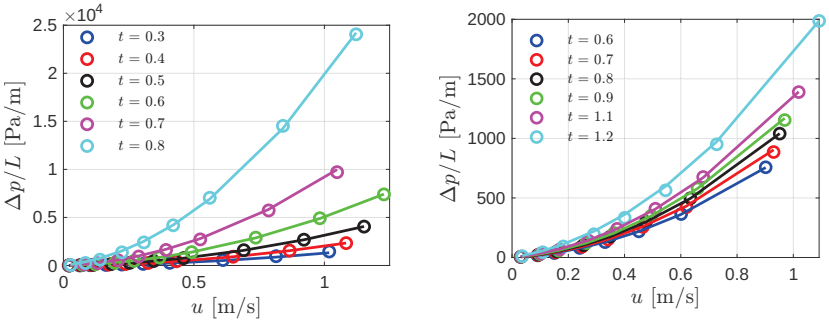

(**a**) Schwarz "P" (**b**) Schoen "IWP"

Figure 6. Pressure drop as a function of the velocity for (**a**) the Primitive and (**b**) IWP structures. Circle markers correspond to the pressure drop computed from the CFD simulations, whereas the continuous lines represent the second-grade polynomial fit.

The next step involves fitting the Darcy–Forchheimer model to the pressure drop predictions obtained from CFD simulations. Subsequently, the permeability and Forchheimer coefficients are computed for each porosity value. In the case of the Primitive structure, the results for permeability and the Darcy–Forchheimer coefficient as functions of porosity are presented in Figure 7. Clearly, there exists a discernible relationship between porosity, permeability, and the Forchheimer coefficient.

Numerous equations have been proposed for different porous media to calculate permeability as a function of porosity [51]. For instance, the Kozeny-Carman equation stands out as one of the most widely recognized relations [52]. Similar to the current study, in [53], the authors examined the pressure drop as a function of velocity for lattice structures. Subsequently, they employed a modified Ergun equation to compute the permeability of the lattices. However, they reported that neither the Ergun equation nor any of its various modifications found in the literature could accurately predict both permeability and the Forchheimer coefficient. In this case, it was also found that the classical correlations are not feasible for predicting the Darcy–Forchheimer model coefficients to compute the pressure drop through these kinds of structures. Nevertheless, other models have been proposed for relating the permeability with porosity [51], for instance, power law regressions. Following this idea, for the Primitive structure, power law relations were computed for both permeability and Forchheimer coefficient according to:

$$k(\phi) = a\phi^b; \qquad c_F(\phi) = d\phi^e, \tag{7}$$

where a, b, c and d are constant coefficients used to fit the power law.

The power law fits for permeability, and Forchheimer coefficients are plotted as continuous lines in Figure 7a,b, respectively. The resulting coefficients of the power laws are reported in Table 3. Notably, the power laws fit very well with the values of k and c_F computed from the numerical simulations. The correlation coefficient (R^2) for permeability and Forchheimer coefficients power law fits are 0.982 and 0.994, respectively.

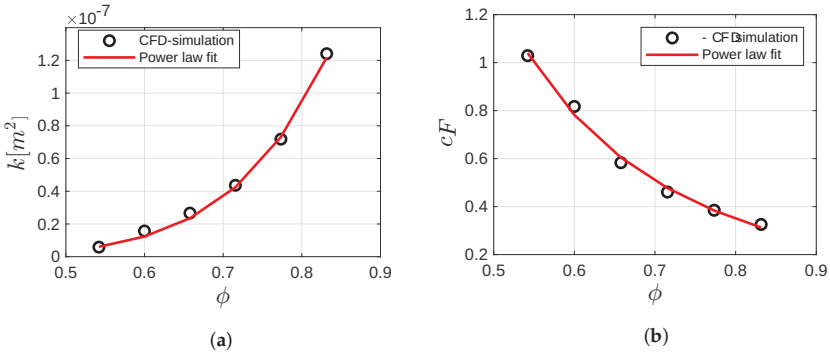

Figure 7. (**a**) Permeability and (**b**) Forchheimer coefficient as a function of the porosity for the Primitive structure.

Table 3. Coefficients for fitting the power laws for k and c_F.

	k		C_F	
TPMS	a	b	d	e
Primitive	4.439×10^{-7}	7.015	0.1865	−2.806
	d	e	f	C_F
IWP	1.005×10^{-6}	0.4505	-7.971×10^{-7}	≈0.25

For the IWP structure, it was found that it is also possible to fit a power law for calculating the permeability as a function of the porosity. The results are shown in Figure 8. In this particular case, due to the geometric features of the IWP structure, the power law added an extra constant term:

$$k(\phi) = d\phi^e + f. \tag{8}$$

The term f is necessary since, at lower porosities, the IWP structure design features isolated void spaces through which the fluid cannot flow. Consequently, permeability under such circumstances approaches zero. In Figure 8, the permeability as a function of porosity is presented, with circle markers indicating results obtained from CFD simulations. The continuous red line represents the power law proposed in Equation (8). Notably, the power law aligns well with the simulation results, yielding a coefficient of determination $R^2 = 0.98$. Regarding the Forchheimer coefficient, it was determined that within the porosity range analyzed in this study, a constant value of 0.25 suffices for predicting pressure drop using the Darcy–Forchheimer model.

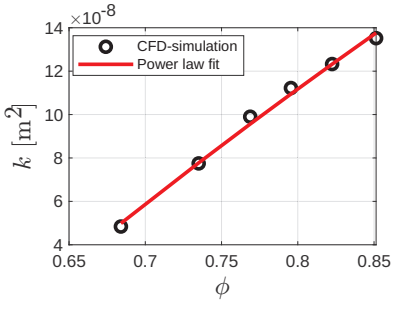

Figure 8. Permeability as a function of the porosity for the IWP structure.

Finally, the Darcy–Forchheimer model was used to compute the pressure drop as a function of the stream velocity varying the isovalue, for both structures. The permeability

and Forchheimer coefficients were directly calculated by the proposed power law equations (Equations (7) and (8)). In Figure 9, the pressure drop computed by the porous media model is compared with the results from the CFD simulations for both the Primitive and IWP structures. In this case, the circle markers are the CFD results, and the continuous lines are the prediction calculated by the Darcy–Forchheimer model. Notably, the model exhibits good agreement with the simulations within the range of porosity and flow velocity analyzed. For the Primitive and IWP structures, the mean error of the computed pressure drop by Equation (7) relative to CFD calculations is approximately 11% and 5%, respectively.

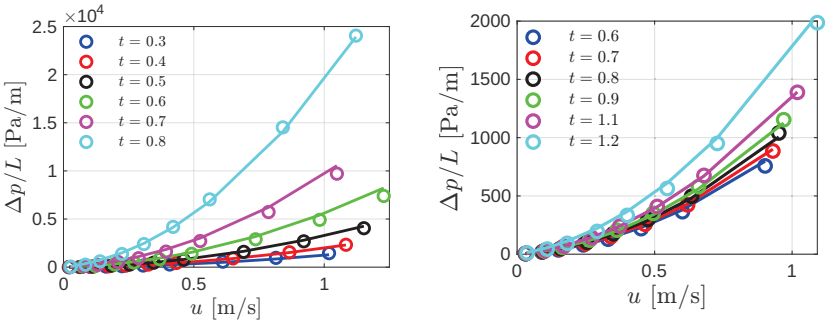

(**a**) Schwarz "P" (**b**) Schoen "IWP"

Figure 9. Pressure drop as a function of the velocity for (**a**) the Primitive and (**b**) IWP structures. Circle markers are the pressure drop computed from the CFD simulations, whereas the continuous lines are the pressure drop calculated using the Darcy–Forchheimer model coupled with the proposed power law relations for permeability and Forchheimer coefficient.

5. Conclusions

In this paper, the fluid flow analysis through two different TPMS structures was presented. The studied structures were designed, preprocessed, and geometrically characterized to establish a relationship between the volume fraction and the isovalue. It was found that a fifth-grade polynomial adequately fits both variables for both structures. Computational simulations were conducted to characterize the flow inside the Primitive and IWP structures under laminar regimes. The main features of the mean flow were discussed for both structures, revealing that the Primitive structure promotes the occurrence of fluid recirculations inside the cell at high Reynolds numbers. Pressure drop as a function of the stream velocity was also computed for different structure porosities. The Primitive structure exhibits a larger pressure drop, approximately ten times larger than the IWP structure, attributed to the earlier mentioned fluid recirculations. Subsequently, it was demonstrated that the flow inside both structures can be modeled by the Darcy–Forchheimer equation for a porous medium. A key result of this investigation is the proposal of power laws to calculate the permeability and Forchheimer coefficient as functions of the porosity for the analyzed structures. Power law equations have been widely employed to describe the permeability of porous media [52]. The proposed relations enable direct computation of the pressure drop along the structures using a porous media model. The mean errors between the pressure drop computed from the Darcy–Forchheimer model and that from the CFD simulations were 11% and 5% for the Primitive and IWP structures, respectively. These results can be utilized in the early stages of the design process for components in fluid flow applications based on TPMS since the pressure drop can be easily calculated only by establishing the porosity of the structure and the mean flow velocity.

Given that the design of heat exchangers requires knowledge of both the pressure drop and the convective heat transfer coefficient in the system, this study contributes to the design process for these devices. The presented results can serve as a basis for the design of heat transfer applications, provided that correlations for the Nusselt number (or,

equivalently, the convective heat transfer coefficient) are known for the TPMS structures considered, which is still an open problem.

Author Contributions: Conceptualization, S.P.; methodology, S.P.; software, S.P.; validation, S.P. and J.P.-B.; formal analysis, S.P.; investigation, S.P., A.G.-O. and J.P.-B.; writing—original draft preparation, S.P.; writing—review and editing, A.G.-O. and J.P.-B.; visualization, S.P. and J.P.-B.; supervision, A.G.-O. and J.P.-B.; project administration, S.P. and J.P.-B. All authors have read and agreed to the published version of the manuscript.

Funding: Publication of this research was funded through CONAHCYT's project No. 322615—"F003 Desarrollo de tecnología incremental y disruptiva en sistemas de enfriamiento 2023–2024".

Data Availability Statement: The data presented in this study are available from the corresponding author upon reasonable request.

Acknowledgments: The authors acknowledge support from CONAHCYT's project No. 321159 "Laboratorio Nacional de Investigación en Tecnologías del Frío". S. Piedra, A. Gómez-Ortega, and J. Pérez-Barrera thank the "Investigadoras e Investigadores por México" program from CONAHCYT. Support from the National Cooperative for Additive Manufacturing (CONMAD-CIDESI) is acknowledged.

Conflicts of Interest: The authors declare no conflict of interest. The funding sponsors had no role in the design of the study; in the collection, analyses, or interpretation of data; in the writing of the manuscript, and in the decision to publish the results

Abbreviations

The following abbreviations are used in this manuscript:

AM	Additive Manufacturing
CFD	Computational Fluid Dynamics
DF	Darcy–Forchheimer
FVM	Finite Volume Method
SIMPLE	Semi-Implicit Method for Pressure-Linked Equations
TPMS	Triply Periodic Minimal Surface

Nomenclature

a	Unit cell size (m)
c_F	Forchheimer coefficient
k	Permeability (m^2)
μ	Dynamic viscosity (kg m^{-1} s^{-1})
ν	Kinematic viscosity, μ/ρ (m^2 s^{-1})
p	Pressure field (N m^{-2})
ϕ	TPMS porosity, $1 - V_f$
Re	Reynolds number, Uw/ν
ρ	Mass density (kg m^{-3})
t	Isovalue of the TPMS
$\mathbf{u}$	Vector velocity field (m s^{-1})
U	Inlet flow velocity (m s^{-1})
V_f	TPMS Solid volume fraction
w	Width of the channel (m)

References

1. Forchheimer, P. Wasserbewegung durch boden. *Z. Vereins Dtsch. Ingenieure* **1901**, *45*, 1782–1788.
2. Tosco, T.; Marchisio, D.L.; Lince, F.; Sethi, R. Extension of the Darcy-Forchheimer Law for Shear-Thinning Fluids and Validation via Pore-Scale Flow Simulations. *Transp. Porous Media* **2013**, *96*, 1–20. [CrossRef]
3. Hayat, T.; Haider, F.; Muhammad, T.; Alsaedi, A. Darcy-Forcheimer flow with Cattaneo-Christov heat flux and homogeneous-hetegoreneous reactions. *PLoS ONE* **2017**, *12*, e0174938. [CrossRef] [PubMed]
4. Hayat, T.; Haider, F.; Alsaedi, A. Darcy-Forchheimer flow with nonlinear mixed convection. *Appl. Math. Mech.* **2020**, *41*, 1685–1696. [CrossRef]

5. Majdeed, A.; Zeeshan, A.; Noori, F.M. Numerical study of Darcy-Forchheimer model with activation energy subject to chemically reactive species and momentum slip of order two. *AIP Adv.* **2019**, *6*, 045035. [CrossRef]
6. Abbas, A.; Jeelani, M.B.; Alharthi, N.H. Magnetohydrodynamic Effects on Third-Grade Fluid Flow and Heat Transfer with Darcy-Forchheimer Law over and Inclined Exponentially Stretching Sheet Embedded in a Porous Medium. *Magnetochemistry* **2022**, *8*, 61. [CrossRef]
7. Khan, M.I.; Hayat, T.; Alsaedi, A. Numerical analysis for Darcy-Forchheimer flow in presence of homogeneous-heterogeneous reactions. *Results Phys.* **2017**, *7*, 2644–2650. [CrossRef]
8. Hayat, T.; Haider, F.; Muhammad, T.; Alsaedi, A. An optimal study for Darcy-Forchheimer flow with generalized Fourier's and Ficl's laws. *Results Phys.* **2017**, *7*, 2878–2885. [CrossRef]
9. Hayat, T.; Haider, F.; Muhammad, T.; Alsaedi, A. On Darcy-Forchheimer flow of viscoelastic nanofluids: A comparative study. *J. Mol. Liq.* **2017**, *233*, 278–287. [CrossRef]
10. Rasool, G.; Khan, W.A.; Bilal, S.M.; Khan, I. MHD Squeezed Darcy-Forchheimer nanofluid flow between two *h*-distance apart horizontal plates. *Open Phys.* **2020**, *18*, 1100–1107. [CrossRef]
11. Tlili, I.; Shahmir, N.; Ramzan, M.; Kadry, S.; Kim, J.Y.; Nam, Y.; Lu, D. A novel model to analyze Darcy Forchheimer nanofluid flow in a permeable medium with Entropy generation analysis. *J. Taibah Univ. Sci.* **2020**, *14*, 916–930. [CrossRef]
12. Ullah, M.Z.; Serra-Capizzano, S.; Baleanu, D. A Numerical Simulation for Darcy-Forchheimer Flow of Nanofluid by a Rotating Disk With Partial Slip Effects. *Front. Phys.* **2020**, *7*, 219. [CrossRef]
13. Rao, D.P.C.; Thiagarajan, S.; Kumar, V.S. Heat Transfer in Darcy-Forchheimer Flow of Tangent Hyperbolic Fluid Over and Inclined Plate with Joule Heating. *J. Appl. Math. Comput. Mech.* **2021**, *20*, 31–40. [CrossRef]
14. Grillo, A.; Carfagna, M.; Federico, S. The Darcy-Forchheimer Law for Modelling Fluid Flow in Biological Tissues. *Theor. Appl. Mech.* **2014**, *41*, 283–322. [CrossRef]
15. Grillo, A.; Carfagna, M.; Federico, S. Non-Darcian flow in a fibre-reinforced biological tissues. *Meccanica* **2017**, *52*, 3299–332. [CrossRef]
16. Takhanov, D. Forchheimer Model for Non-Darcy Flow in Porous Media and Fractures. Master's Thesis, Imperial College London, London, UK, 2011.
17. Plocher, J.; Panesar, A. Review on design and structural optimisation in additive manufacturing: Towards next-generation lightweight structures. *Mater. Des.* **2019**, *183*, 108164. [CrossRef]
18. Arredondo-Soto, M.; Cuan-Urquizo, E.; Gómez-Espinosa, A. A Review on Tailoring Stiffness in Compliant Systems, via Removing Material: Cellular Materials and Topology Optimization. *Appl. Sci.* **2021**, *11*, 3538. [CrossRef]
19. Schmelzle, J.; Kline, E.V.; Dickman, C.J.; Reutzel, E.W.; Jones, G.; Simpson, T.W. (Re)Designing for Part Consolidation: Understanding the Challenges of Metal Additive Manufacturing. *J. Mech. Des.* **2015**, *137*, 111404. [CrossRef]
20. Yang, S.; Tang, Y.; Zhao, Y.F. A new part consolidation method to embrace the design freedom of additive manufacturing. *J. Manuf. Process.* **2015**, *20*, 444–449. [CrossRef]
21. Attarzadeh, R.; Rovira, M.; Duwig, C. Design analysis of the "Schwartz D" based heat exchanger: A numerical study. *Int. J. Heat Mass Transf.* **2021**, *177*, 121415. [CrossRef]
22. Attarzadeh, R.; Attarzadeh-Niaki, S.H.; Duwig, C. Multi-objective optimization of TPMS-based heat exchangers for low-temperature waste heat recovery. *Appl. Therm. Eng.* **2022**, *212*, 118448. [CrossRef]
23. Yeranee, K.; Rao, Y. A Review of Recent Investigations on Flow and Heat Transfer Enhancement in Cooling Channels Embedded with Triply Periodic Minimal Surfaces (TPMS) . *Energies* **2022**, *15*, 8994. [CrossRef]
24. Coimbra, J.C.; Martins, M.A.; Oliveira, P.S.; Minim, L.A. The potential use of a gyroid structure to represent monolithic matrices for bioseparation purposes: Fluid dynamics and mass transfer analysis via CFD. *Sep. Purif. Technol.* **2021**, *254*, 117594. [CrossRef]
25. Shi, J.; Wei, F.; Chouraki, B.; Sun, X.; Wei, J.; Zhu, L. Study on Performance Simulation of Vascular-like Flow Channel Model Based on TPMS Structure. *Biomimetics* **2023**, *8*, 69. [CrossRef] [PubMed]
26. Rathore, S.S.; Mehta, B.; Kumar, P.; Asfer, M. Flow Characterization in Triply Periodic Minimal Surface (TPMS)-Based Porous Geometries: Part I–Hydrodynamics. *Transp. Porous Media* **2023**, *146*, 669–701. [CrossRef]
27. Ali, D.; Ozalp, M.; Blanquer, S.B.; Onel, S. Permeability and fluid flow-induced wall shear stress in bone scaffolds with TPMS and lattice architectures: A CFD analysis. *Eur. J. Mech. B/Fluids* **2020**, *79*, 376–385. [CrossRef]
28. Zeng, C.; Wang, W. Modeling method for variable and isotropic permeability design of porous material based on TPMS lattices. *Tribol. Int.* **2022**, *176*, 107913. [CrossRef]
29. Zou, S.; Mu, Y.; Pan, B.; Li, G.; Shao, L.; Du, J.; Jin, Y. Mechanical and biological properties of enhanced porous scaffolds based on triply periodic minimal surfaces. *Mater. Des.* **2022**, *219*, 110803. [CrossRef]
30. Al-Ketan, O.; Ali, M.; Khalil, M.; Rowshan, R.; Khan, K.A.; Abu Al-Rub, R.K. Forced Convection Computational Fluid Dynamics Analysis of Architected and Three-Dimensional Printable Heat Sinks Based on Triply Periodic Minimal Surfaces. *J. Therm. Sci. Eng. Appl.* **2020**, *13*, 021010. [CrossRef]
31. Passos, A.G.P. Laminar Flow and Heat Transfer in Triply Periodic MINIMAL Surfaces. Master's Thesis, Instituto Superior Técnico, Universidade de Lisboa, Lisboa, Portugal, 2019.
32. Li, W.; Yu, G.; Yu, Z. Bioinspired heat exchangers based on triply periodic minimal surfaces for supercritical CO_2 cycles. *Appl. Therm. Eng.* **2020**, *179*, 115686. [CrossRef]

33. Yan, C.; Hao, L.; Yang, L.; Hussein, A.Y.; Young, P.G.; Li, Z.; Li, Y. *Triply Periodic Minimal Surface Lattices Additively Manufactured by Selective Laser Melting*, 1st ed.; 3D Printing Technology Series; Academic Press: Cambridge, MA, USA, 2021. [CrossRef]
34. Jin, M.; Feng, Q.; Fan, X.; Luo, Z.; Tang, Q.; Song, J.; Ma, S.; Nie, Y.; Jin, P.; Zhao, M. Investigation on the mechanical properties of TPMS porous structures fabricated by laser powder bed fusion. *J. Manuf. Process.* **2022**, *76*, 559–574. [CrossRef]
35. Wang, H.; Tan, D.; Liu, Z.; Yin, H.; Wen, G. On crashworthiness of novel porous structure based on composite TPMS structures. *Eng. Struct.* **2022**, *252*, 113640. [CrossRef]
36. Sun, Q.; Sun, J.; Guo, K.; Wang, L. Compressive mechanical properties and energy absorption characteristics of SLM fabricated Ti6Al4V triply periodic minimal surface cellular structures. *Mech. Mater.* **2022**, *166*, 104241. [CrossRef]
37. Qureshi, Z.A.; Elnajjar, E.; Al-Ketan, O.; Al-Rub, R.A.; Al-Omari, S.B. Heat transfer performance of a finned metal foam-phase change material (FMF-PCM) system incorporating triply periodic minimal surfaces (TPMS). *Int. J. Heat Mass Transf.* **2021**, *170*, 121001. [CrossRef]
38. Oh, S.H.; Ha, J.W.; Park, K. Adaptive Conformal Cooling of Injection Molds Using Additively Manufactured TPMS Structures. *Polymers* **2022**, *14*, 181. [CrossRef] [PubMed]
39. Savio, G.; Rosso, S.; Meneghello, R.; Concheri, G. Geomteric Modeling of Cellular Materials for Additive Manufacturing in Biomedical Field: A Review. *Appl. Bionics Biomech.* **2018**, *2018*, 14. [CrossRef] [PubMed]
40. Dong, Z.; Zhao, X. Application of TPMS structure in bone regeneration. *Eng. Regen.* **2021**, *2*, 154–162. [CrossRef]
41. nTopology. 2021. Next-Generation Engineering Design Software. Windows. nTop. Available online: https://www.ntop.com/ (accessed on 4 October 2023).
42. Karakoç, A. RegionTPMS—Region based triply periodic minimal surfaces (TPMS) for 3-D printed multiphase bone scaffolds with exact porosity values. *SoftwareX* **2021**, *16*, 100835. [CrossRef]
43. Al-Ketan, O.; Al-Rub, R.K.A. MSLattice: A free software for generating uniform and graded lattices based on triply periodic minimal surfaces. *Mater. Des. Process. Commun.* **2020**, *3*, e205. [CrossRef]
44. Maskery, I.; Parry, L.A.; Padrão, D.; Hague, R.J.M.; Ashcroft, I.A. FLatt Pack: A research-focussed lattice design program. *Addit. Manuf.* **2022**, *49*, 102510. [CrossRef]
45. Perez-Boerema, F.; Barzegari, M.; Geris, L. A flexible and easy-to-use open-source tool for designing functionally graded 3D porous structures. *Virtual Phys. Prototyp.* **2022**, *3*, 682–699. [CrossRef]
46. Tenorio-Suárez, M.I.; Gómez-Ortega, A.; Canales, H.; Piedra, S.; Pérez-Barrera, J. MaSMaker: An open-source, portable software to create and integrate maze-like surfaces into arbitrary geometries. *SoftwareX* **2022**, *19*, 101203. [CrossRef]
47. Autodesk. Meshmixer: Free Software for Making Awesome Stuff (Version 3.5). Windows. Autodesk, Inc. 2020. Available online: https://meshmixer.com/ (accessed on 4 October 2023).
48. Riegel, J.; van Havre, W.M.Y. FreeCAD: Your Own 3D Parametric Modeler (Version 0.21.1). Windows. The FreeCAD Team. 2021. Available online: https://meshmixer.com/ (accessed on 4 October 2023).
49. ANSYS, Inc. ANSYS Fluent User's Guide, (Version 2020 R2). Windows. ANSYS, Inc. 2020. Available online: https://www.ansys.com/ (accessed on 4 October 2023).
50. Community, B.O. *Blender—A 3D Modelling and Rendering Package*; Blender Foundation, Stichting Blender Foundation: Amsterdam, The Netherlands, 2023.
51. Schulz, R.; Ray, N.; Zech, S.; Rupp, A.; Knabner, P. Beyond Kozeny–Carman: Predicting the Permeability in Porous Media. *Transp. Porous Med.* **2019**, *130*, 487–512. [CrossRef]
52. Hommel, J.; Coltman, E.; Class, H. Porosity-Permeability Relations for Evolving Pore Space: A Review with a Focus on (Bio-)geochemically Altered Porous Media. *Transp. Porous Med.* **2018**, *124*, 589–629. [CrossRef]
53. Mishra, A.; Korba, D.; Kaur, I.; Singh, P.; Li, L. Prediction and Validation of Flow Properties in Porous Lattice Structures. *J. Fluids Eng.* **2023**, *145*, 041402. [CrossRef]

applied sciences

MDPI

Article

The Experiments and Stability Analysis of Hypersonic Boundary Layer Transition on a Flat Plate

Yanxin Yin [1,2], Yinglei Jiang [3,4], Shicheng Liu [3,4] and Hao Dong [3,4,*]

[1] Department of Mechanics, School of Mechanical Engineering, Tianjin University, Tianjin 300072, China; xinye624@163.com
[2] China Academy of Launch Vehicle Technology, Beijing 100076, China
[3] College of Aerospace Engineering, Nanjing University of Aeronautics and Astronautics, Nanjing 210016, China; jiangyl01@nuaa.edu.cn (Y.J.); liushicheng@nuaa.edu.cn (S.L.)
[4] Key Laboratory of Unsteady Aerodynamics and Flow Control, Ministry of Industry and Information Technology, Nanjing University of Aeronautics and Astronautics, Nanjing 210016, China
* Correspondence: donghao@nuaa.edu.cn

Abstract: Experimental and linear stability theory (LST) investigation of boundary layer transition on a flat plate was conducted with a flow of Mach number 5. The temperature distributions and second-mode disturbances on the flat plate surface at different unit Reynolds number (Re_{unit}) values were captured by infrared thermography and PCB technology, respectively, which revealed the transition location of the flat-plate boundary layer. The PCB sensors successfully captured the second-mode disturbances within the boundary layer initially at a frequency of about 100 kHz, with a gradually expanding frequency range as the distance travelled downstream increased. The evolution characteristics of the second-mode instabilities were also investigated by LST and obtained for the second mode, ranging from 100 to 250 kHz. The amplitude amplification factor (N-factor) of the second-mode instabilities was calculated by the e^N method. The N-factor of the transition location in the wind tunnel experiment predicted by LST is about 0.98 and 1.25 for $Re_{unit} = 6.38 \times 10^6$ and 8.20×10^6, respectively.

Keywords: hypersonic boundary layer; transition; LST; e^N method; infrared thermography

Citation: Yin, Y.; Jiang, Y.; Liu, S.; Dong, H. The Experiments and Stability Analysis of Hypersonic Boundary Layer Transition on a Flat Plate. *Appl. Sci.* **2023**, *13*, 13302. https://doi.org/10.3390/app132413302

Academic Editor: Francesca Scargiali

Received: 6 November 2023
Revised: 9 December 2023
Accepted: 14 December 2023
Published: 16 December 2023

1. Introduction

The flow regime within the boundary layer, whether laminar or turbulent, significantly influences surface friction and heat exchange. The friction and heat flux of the turbulent boundary layer are approximately 3~5 times higher than those observed in the laminar boundary layer [1]. Accurate and efficient prediction of boundary layer transition is crucial for enhancing the safety and payload capacity of hypersonic vehicles. Consequently, the precise determination of the transition location in the hypersonic boundary layer is of paramount importance for the meticulous design of the entire aerospace vehicle, especially concerning the thermal protection system (TPS). Nevertheless, due to the inherently highly nonlinear characteristics, the transition of the hypersonic boundary layer remains a formidable challenge in the realm of fluid mechanics [2,3].

In contrast to the incompressible boundary layer, hypersonic boundary layer transition is influenced by two mechanisms: second-mode instability and crossflow instability. Mack [4,5] initially identified the second-mode instability using linear stability analysis to explore the hypersonic flat-plate boundary layer. Subsequent experiments have successfully measured the second mode, and the results align closely with theoretical predictions from linear stability theory (LST) [6–8]. Currently, wind tunnel experiments continue to play a crucial role in advancing our understanding of hypersonic boundary layer transition. Zhao et al. [9] studied the influence of different total temperatures on the basic flow and transition position of the boundary layer under the same Mach number and unit Reynolds

number freestream conditions and pointed out the significance of ensuring consistent total temperature of the inflow in wind tunnel experiments. With the advancement of measurement technology, some instantaneous measurement methods that have high spatial and temporal resolution, such as PCB [10,11] and ALTP [12], are used for identifying the disturbance modal in the boundary layer. Infrared thermography appears to be a potential tool for investigating boundary layer transitions. Borg et al. [13] employed IR technology to study the boundary layer transition of HIFiRE-5b at a freestream Mach number 6. The findings suggest that IR can clearly depict high- and low-temperature streaks in the streamwise direction on the model surface and capture the transition process. In addition to surface disturbance measurements, some flow visualization techniques are used to capture the process of boundary layer transition, too. Yao et al. [14] used infrared thermography and wall pressure tests to obtain the turning position and the development and interaction law of unstable modes of a flat delta wing in a hypersonic wind tunnel. Xu et al. [15] successfully captured the process of the second-mode wave growth and breaking into turbulence in the boundary layer of a conical surface using NPLS technology and found that a single forward-facing step (FFS) could suppress the second-mode wave and delay the cone's hypersonic boundary layer transition at AOA 0. Zhu et al. [16] used the Rayleigh scattering technique to successfully capture second modes of rope waves in the boundary layer of a flared cone and found that the amplitude of the second mode decays before transition to turbulence. Liu et al. [17] used infrared thermography to study the effect of different roughness elements on the transition of a flat plate at Mach number 6, with a special study of the roughness element wake vortex structure. In addition to wind tunnel experiments, due to the development of computer computing power, many researchers have begun to use direct numerical simulation (DNS) to study the sensitivity of the hypersonic boundary layer of the flat plate and the propagation of disturbance [18,19].

Various theoretical analysis techniques, including linear stability theory (LST) and parabolized stability equations (PSE), have been employed for the investigation and prediction of hypersonic boundary layer transition. Saric [20] conducted a comprehensive examination of hypersonic boundary layer transition prediction, emphasizing the potential applicability of the e^N method for predicting two-dimensional hypersonic transition locations in his work [21]. Additionally, Chen et al. [22] explored boundary layer transition on a cone and plate at Mach number 3.5 using the e^N method. Their results indicate that when $N = 10$, the theoretical results are in excellent agreement with the transition data obtained by the experiments. Juliano et al. [23] investigated the influence of the noise environment on Hifire-5 elliptic cone transition in the wind tunnel and found that $N = 3.5$ in the case of noise, and $N = 8$ in the quiet freestream condition. Su et al. [24] improved the e^N method while considering the modal transformation; the results show that by neglecting the disturbance decay between the two instability modes, the proposed strategy provides more accurate results than existing strategies. LST method has also been applied to other studies on boundary layer stability. Zhu et al. [25] used wind tunnel experiment and stability analysis to study the nonlinear interaction between high-frequency and low-frequency modes on porous surfaces. It was found that the suppression of near wall disturbances by porous surfaces changed the spatial distribution characteristics of fundamental resonance disturbances, broke the phase-locked relationship, and suppressed the instability of fundamental oblique waves. At the same time, the study also found that porous surfaces greatly suppressed aerodynamic heating and delayed the transition position. Chen et al. [26] developed a linear stability analysis method under thermochemical nonequilibrium conditions, which extends the scope of application of linear stability. In a recent study, Klothakis et al. [27] employed the direct simulation Monte Carlo (DSMC) method to computationally analyze the steady laminar flow over a semi-infinite flat plate. The obtained results demonstrated a favorable agreement with corresponding solutions derived from boundary layer considerations. Following this, the researchers conducted a comparative examination of the linear stability characteristics between the DSMC-generated basic flow and those derived from classical Navier–Stokes-based profiles. The findings revealed

a slight increase in stability for flows obtained through the DSMC method when compared to their Navier–Stokes counterparts.

In this study, experimental investigations were conducted to examine hypersonic boundary layer transition on a flat plate, employing infrared (IR) thermography and PCB technology. Additionally, linear stability analysis was employed to calculate the growth rate of the second-mode instability in the boundary layer across various Reynolds numbers. The primary focus of this paper centers on characterizing the transition position observed in the experiments, along with analyzing the growth rate and amplitude of disturbances within the hypersonic boundary layer. Furthermore, the determination of the *N*-factor at the transition location of the flat plate in the NHW hypersonic wind tunnel was performed using the e^N method.

2. Experiment Facility and Model

2.1. Wind Tunnel

The experimental investigations were carried out by using the hypersonic wind tunnel (NHW) at Nanjing University of Aeronautics and Astronautics. This wind tunnel operates in a blow-down and vacuum-suction mode, allowing for a variable operating Mach number ranging from 4 to 8 through adjustments to the corresponding Laval nozzle, as shown in Figure 1. The wind tunnel is equipped with five sets of axisymmetric Laval nozzles, each with a 500 mm diameter, enabling the provision of a stable flow field at Mach number 5 for approximately 8 s during experimental procedures. Optical accessibility is facilitated by two optical windows on each side of the plenum chamber, suitable for schlieren imaging. Additionally, a rectangular window situated above the plenum chamber serves as an optical access point for high-speed cameras or infrared cameras.

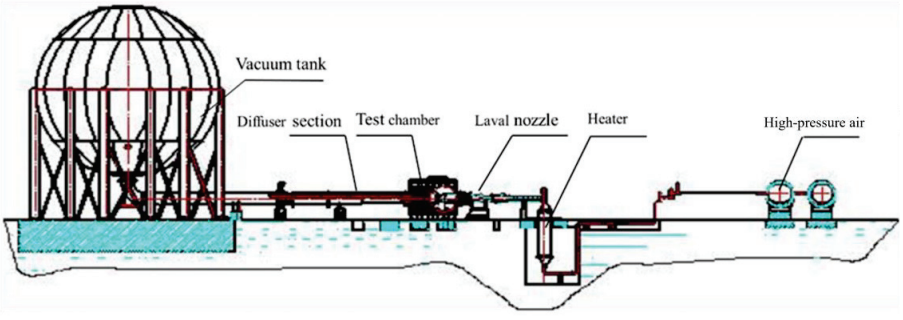

Figure 1. Sketch of NHW wind tunnel.

2.2. Experiment Model

Figure 2 displays a photograph of the flat-plate model positioned within the wind tunnel at a zero angle of attack. The primary structure of the model is constructed from stainless steel to guarantee adequate stiffness. Positioned centrally within the model is an embedded polyether ether ketone (PEEK) component. PEEK is a high-temperature-resistant, high-strength resin material with excellent insulation performance. By utilizing the insulation performance of PEEK material, the strength of high-speed airflow and wall friction can be well reflected on the surface temperature of the model, making it convenient for monitoring by infrared thermal imagers. In addition, PEEK also has a high infrared emissivity, making the results monitored by the infrared thermal imager highly accurate, which makes it very suitable for the application of IR thermography. Juliano et al. [23] used infrared thermal imaging technology to study the surface transition phenomenon of the HIFiRE-5 model made of polyether ether ketone (PEEK) material under Ma = 6 conditions. The experimental results showed that the infrared thermal image can clearly display the high- and low-temperature bands flowing towards the model surface and can capture the transition process. The Mach 5 freestream direction is from left to right. The

infrared camera (FLIR T630sc, FLIR Systems Inc, American) observes the flat plate from the upper observation hole with a zinc selenide (ZnSe) window. The detailed flow conditions in experiment are shown in Table 1; Ma, P_0, T_0, and Re/m are the freestream Mach number, freestream stagnation pressure, freestream stagnation temperature, and freestream unit Reynolds number, respectively. The unit Reynolds number is changed by adjusting the total pressure of the freestream flow. Three freestream flow conditions with different Reynolds numbers were set up to study the effect of unit Reynolds number on transition Reynolds number.

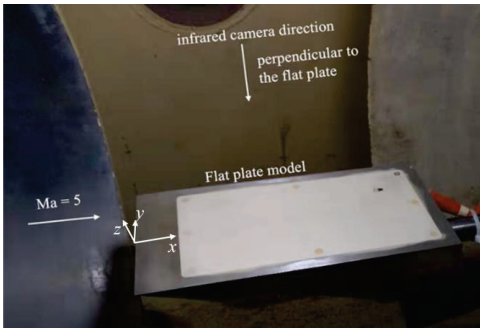

Figure 2. Schematic diagram of flat-plate installation in wind tunnel.

Table 1. Flow condition.

Flow Condition		P_0/kPa	T_0/K	Re/m/10^6
Ma = 5	Case1	200.1	501	2.52
	Case2	490.5	491	6.38
	Case3	729.9	539	8.20

2.3. Heat Flux Calculating

In this experiment, the heat flux distribution on the surface of the plate was obtained by solving the one-dimensional inverse heat-transfer equation [28]. The surface temperature of the model was recorded by IR image. A constant initial temperature was assumed through the PEEK. According to the one-dimensional heat conduction equation,

$$\frac{\partial T}{\partial t} = \alpha \frac{\partial^2 T}{\partial y^2} \tag{1}$$

where α is the thermal diffusivity, which is related to the materials. In Equation (1), the time term adopts the first-order forward difference, and the space term adopts the second-order central difference scheme. The finite difference scheme is presented as follows:

$$\frac{T_{i+1,j} - T_{i,j}}{\triangle t} = \frac{\alpha(T_{i,j-1} - 2T_{i,j} + T_{i,j+1})}{(\triangle y)^2} \tag{2}$$

Δy takes the appropriate value to ensure the numerical stability. Utilizing the temperature distribution within the PEEK model, the heat flux for individual pixels at each time step is computed through the application of Fourier's law, as expressed below [28]:

$$q = -k\frac{\partial T}{\partial y} \tag{3}$$

The dimensionless Stanton number (St) is derived from the surface heat flux by utilizing the freestream parameters.

$$St = \frac{q}{\rho_\infty U_\infty C_p (T_0 - T_w)} \tag{4}$$

where the subscript ∞ represents the freestream condition. C_p, T_0, and T_w represent the constant pressure specific heat, flow total temperature, and wall temperature, respectively.

2.4. Numerical Setup

In this investigation, two-dimensional, compressible Navier–Stokes equations are solved utilizing an upwind finite-volume formulation. The transition model employed in all simulations is the *k*-*ω* SST model, introduced by Menter [29] to address certain limitations within the realm of two-equation turbulence models. The *k*-*ω* SST model integrates the advantages of Wilcox's *k*-*ω* model [30] for capturing turbulent flow near the wall and the characteristics of the k-ε model in regions far from the wall. This integration is achieved through a coupling function, ensuring the conservation of compressible equations for turbulent kinetic energy and specific dissipation rate, respectively.

$$\frac{\partial(\rho k)}{\partial t} + \frac{\partial(\rho u_j k)}{\partial x_j} = \tau_{ij}\frac{\partial u_j}{\partial x_j} - \beta^* k\omega + \frac{\partial}{\partial x_j}\left[\rho(\nu + \sigma_k \nu_T)\frac{\partial k}{\partial x_j}\right] \tag{5}$$

and

$$\begin{array}{l} \frac{\partial(\rho\omega)}{\partial t} + \frac{\partial(\rho u_j \omega)}{\partial t} = \frac{\gamma}{\nu_T}\tau_{ij}\frac{\partial u_j}{\partial x_j} - \beta\omega^2 + \frac{\partial}{\partial x_j}\left[\rho(\nu + \sigma_\omega \nu_T)\frac{\partial \omega}{\partial x_j}\right] \\ +2(1-F_1)\frac{\rho\sigma_{\omega 2}}{\omega}\frac{\partial k}{\partial x_j}\frac{\partial \omega}{\partial x_j} \end{array} \tag{6}$$

where β, β^*, γ, σ_k, and σ_{w2} are closure constant coefficients.

The model is completed by the kinematic viscosity limitation of the following form:

$$\nu_T = \frac{k}{\max\left(\omega, \frac{\Omega F_2}{a_1}\right)} \tag{7}$$

where Ω is the vorticity magnitude, a constant coefficient, and a function with asymptotic behavior. Boundary conditions on a smooth wall are as follows:

$$k_\omega = 0, \omega_w = 10\frac{6\nu}{\beta_1 y^2} \tag{8}$$

with β_1 being a constant coefficient.

The numerical calculation model conditions are the same as the experimental conditions, with a length of 0.5 m and a height of 0.1 m. First, we calculate the number of grids to 200 × 150; the height of the first layer of grid on the wall is 1×10^{-5} m, satisfying y^+ less than 1. The schematic diagram of the grid is shown in Figure 3. The incoming flow boundary condition is the pressure far field, the outlet is the pressure outlet boundary condition, and the upper and front areas of the plate are set with symmetric boundary conditions.

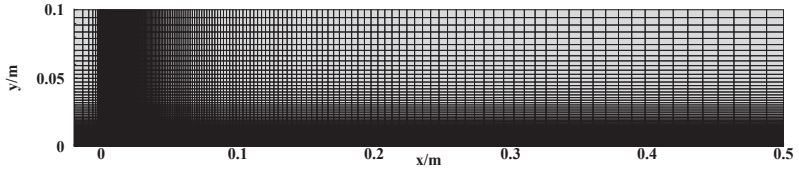

Figure 3. Schematic diagram of flat-plate mesh division and boundary conditions.

2.5. Linear Stability Theory

Linear stability theory (LST) is established under the assumption of small perturbations [4], and under this assumption, the perturbation can be written in the form of the sum of the basic flow and the perturbation quantity:

$$p(x, y, z, t) = \overline{p}(x, y) + p'(x, y, z, t) \tag{9}$$

In hypersonic boundary layer, p (x, y, z, t) represents u, v, w, ρ, and T. The basic flow field is obtained by solving the Blasius equation. It is assumed that the flow in the boundary layer is a parallel flow, and the small perturbation p' can be written in the form of the traveling wave as follows:

$$p'(x, y, z, t) = p(y)e^{i(\alpha x + \beta z - \omega t)} + c.c. \tag{10}$$

where α, β, and ω are the streamwise wave number, the spanwise wave number, and the frequency, respectively. In addition, *c.c.* represents the conjugate complex number. The generalized eigenvalue problem can be obtained by putting Equation (2) into the wave equation and ignoring the second-order small quantities. The eigenvalue is the streamwise growth rate, and the eigenvector represents the disturbance shape along the wall normal. In spatial mode, β and ω are real numbers, and α is an imaginary number:

$$\alpha = \alpha_r + i\alpha_i \tag{11}$$

The real part represents the wave number of the disturbance, and the imaginary part represents the disturbance growth rate. When $\alpha_i < 0$, the disturbance is unstable along the flow direction.

In the realm of laminar–turbulent transition (LST) analysis, a widely applied approach involves the computation of the N-factor using a semi-empirical method known as the e^N method. The determination of the N- factor is calculated by the following formula [23]:

$$N = -\int_{x_0}^{x} \alpha_i dx \tag{12}$$

where x_0 represents the flow direction position where the disturbance wave first begins to be unstable, and x_0 is different at different frequencies. In general, the NT in a low-speed wind tunnel is generally 6~9, while in a hypersonic wind tunnel, the divergence of N_T is quite large. In the case of hypersonic flow, the N- factor as the transition criterion needs to be determined by wind tunnel experiments.

2.6. Steady Base Flow

The calculation of the stability equation requires a high-precision basic flow field. For the flat-plate boundary layer, the basic flow field can be obtained by calculating the compressible boundary layer equation [31]. Wall temperature, Prandtl number, and specific heat ratio are assumed to be constant. The viscosity coefficient adopts the Sutherland viscosity law.

$$\begin{aligned} &(\rho\mu f'')' + \tfrac{1}{2} f f'' = 0 \\ &\tfrac{1}{2} c_p \cdot f g' + \tfrac{1}{\mathrm{Pr}} \cdot (\kappa \cdot g' \cdot \rho) + \rho\mu \cdot Ec \cdot (f'')^2 = 0 \\ &\rho = \tfrac{1}{g} \end{aligned} \tag{13}$$

In this paper, the laminar boundary layer flow should be obtained for LST analysis by solving the compressible boundary layer equation. For solving the differentia equations, the physical quantities are nondimensionalized by the free flow parameters and reference length. The dimensionless compressible boundary layer equations are as follows, where *Ec*, *k*, and Pr are the Eckert number, thermal conductivity, and Prandtl number, respectively. In

this work, we consider the boundary layer of a perfect gas with Prandtl number Pr = 0.71 and specific heat ratio γ = 1.4, and the viscosity law satisfies the Sutherland's law.

The mean flow variables of the boundary layer at different unit Reynolds numbers are given in Figure 4. As the unit Reynolds number increases, the boundary layer thickness gradually diminishes.

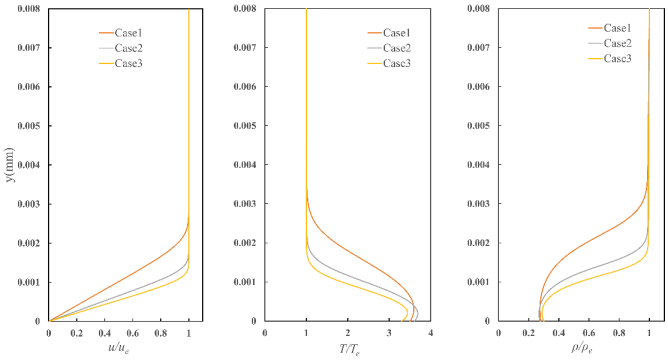

Figure 4. Comparation of mean flow variables at x = 0.1 m.

3. Experimental Results and Stability Analyses

3.1. IR Results

Figure 5 shows the surface temperature distribution of a flat plate under different unit Reynolds numbers. At a lower Reynolds number (Figure 5a), the temperature at the leading edge of the flat plate is the highest and gradually decreases downstream. With the increase in Reynolds number (Figure 5b,c), the plate surface shows a different temperature distribution, and there is an obvious temperature difference along the flow direction. It can be seen from the IR image that the transition region presents an irregular "wavy shape". Willems et al. [32] also found this "wavy" transition non-uniformity in the study of the boundary layer transition of the flat plate and concluded that it may be caused by the natural incoming flow and the disturbance non-uniformity of the forefront of the flat plate.

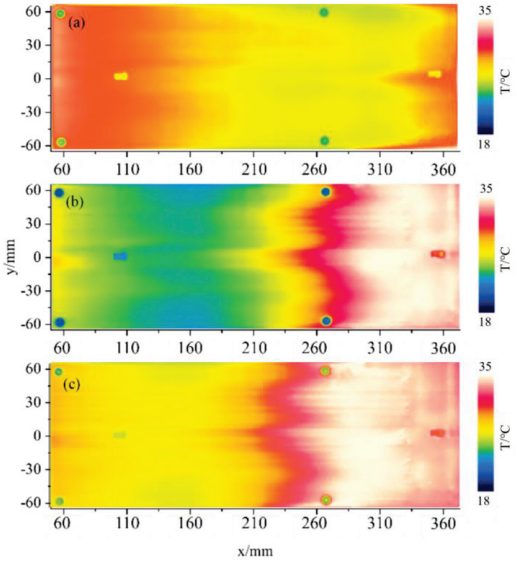

Figure 5. Surface temperature distribution of a flat plate under different unit Reynolds numbers: (**a**) $Re_{unit} = 2.56 \times 10^6$; (**b**) $Re_{unit} = 6.38 \times 10^6$; (**c**) $Re_{unit} = 8.20 \times 10^6$.

The mean Stanton number distributions calculated from IR images are shown in Figure 6. The black and red dashed lines represent the Stanton numbers for the flat-plate boundary layer in all laminar and turbulent states, respectively. The curve of discrete points in the Figure 6 shows the distribution of mean Stanton numbers along the x-direction calculated from the wind tunnel experiments, where the surface of a flat plate develops from laminar flow through turning to turbulence. In the transition region, the Stanton number increases rapidly and reaches the value for turbulent flow. In the case of a lower unit Reynolds number (Figure 6a), limited by the length of the plate, the IR images only capture the beginning of the BL transition. With the increase in the unit Reynolds number, the transition position moves upstream, whereas the transition Reynolds number increases, and the complete laminar transition to turbulent processes can be observed. As a comparison, the results of full laminar flow and full turbulence are also given as a reference. The calculation results of infrared thermal imaging are in good agreement with the calculation results in the laminar flow area, and the change of the flow direction Stanton number is within the range of laminar flow and turbulence.

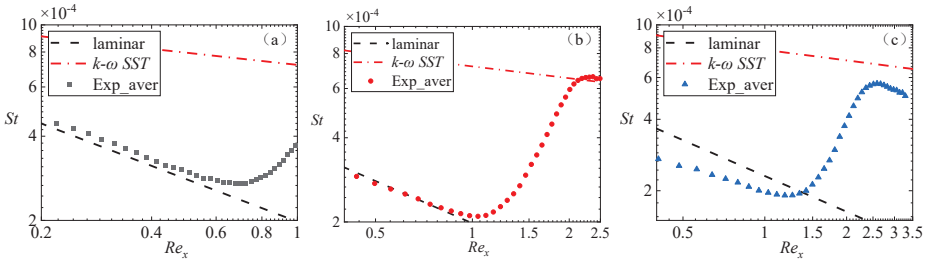

Figure 6. Mean Stanton number distribution of plate flow direction under different unit Reynolds numbers: (**a**) $Re_{unit} = 2.56 \times 10^6$; (**b**) $Re_{unit} = 6.38 \times 10^6$; (**c**) $Re_{unit} = 8.20 \times 10^6$.

Figure 7 represents the transition Reynolds number distribution at different spanwise positions under different unit Reynolds numbers. Moreover, the transition Reynolds number calculated by the compressibility-modified transition model γ-Reθt [33] (shown as CC in the Figure 7) is given. It can be found that for the lower unit Reynolds number (Figure 7a), the transition Reynolds number is also relatively small; with the increase in the unit Reynolds number of the freestream, the transition Reynolds number increases accordingly. In addition, it also shows that the spanwise distribution of transition position on the surface of the flat plate is uneven, and the spanwise distribution of transition Reynolds number increases with the increase in the unit Reynolds number, similarly as in Figure 5. In this paper, the unit Reynolds number has a great influence on the transition Reynolds number, whereas some wind tunnel experiments show the opposite results. A more in-depth investigation is warranted to explore the impact of unit Reynolds number on the transition Reynolds number.

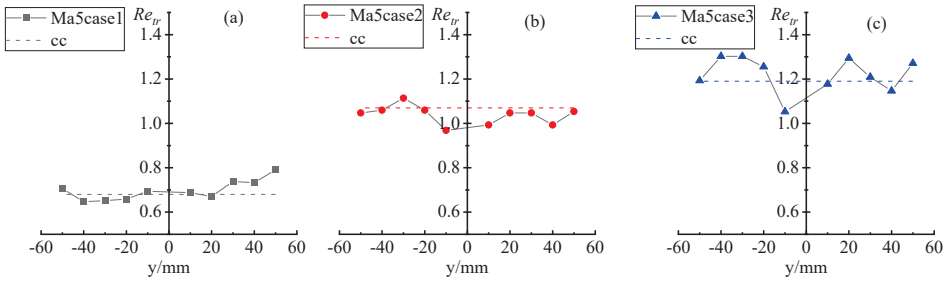

Figure 7. Transition Reynolds number distribution of plate spanwise at different unit Reynolds numbers: (**a**) $Re_{unit} = 2.56 \times 10^6$; (**b**) $Re_{unit} = 6.38 \times 10^6$; (**c**) $Re_{unit} = 8.20 \times 10^6$.

3.2. Instability Characteristics along Streamwise Direction

The inhouse LST code written by FORTRAN used in this paper is shown in reference [34]. Figure 8 illustrates the variations in disturbance growth rates within the ω-β plane at Rex = 6.5 × 10^5 under the freestream conditions of case 3. Two distinct modes coexist in the boundary layer—the lower frequency corresponds to the first mode, while the higher frequency characterizes the second mode. Notably, the bandwidth of the first mode surpasses that of the second mode. The diagram emphasizes the prevalence of the second mode in the hypersonic boundary layer, notably featuring a predominantly two-dimensional disturbance. Conversely, the first mode, exhibiting the highest amplification, predominantly occurs near β = 0.8, signifying its three-dimensional perturbation nature.

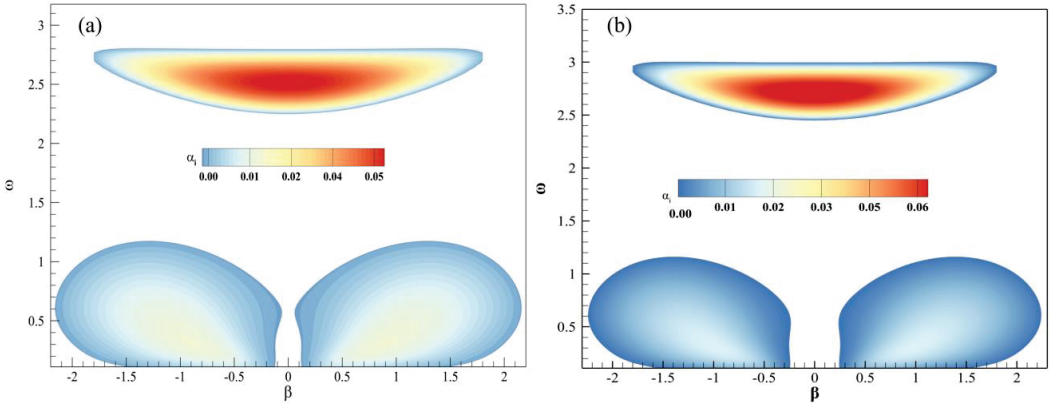

Figure 8. Growth rate in ω-β plane: (**a**) Re_{unit} = 6.38 × 10^6; (**b**) Re_{unit} = 8.20 × 10^6.

The evolution of instability waves along the streamwise direction was obtained and analyzed. Figure 9 shows the PSDs of the boundary layer instability waves at several streamwise positions under different unit Reynolds numbers by PCB.

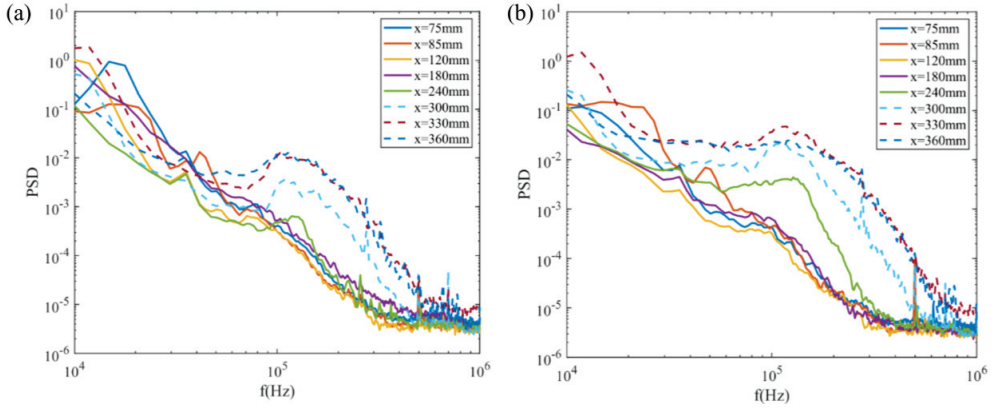

Figure 9. Comparison of PCB-measured spectra along the streamwise direction: (**a**) Re_{unit} = 6.38 × 10^6; (**b**) Re_{unit} = 8.20 × 10^6.

As illustrated in Figure 9, for a unit Reynolds number (Re_{unit}) of 6.38 × 10^6, the absence of a discernible peak characterizing second-mode waves in the power spectral density (PSD) before the streamwise location of x = 180 mm indicates that second-mode disturbances have not yet developed, signifying a laminar boundary layer state at this location. However, a subtle peak with broadband characteristics around 100 kHz emerges

in the PSD at x = 240 mm, suggesting the initiation and growth of second-mode waves. Subsequently, the PSD of the second mode remains consistent between x = 330 mm and x = 360 mm, indicating saturation of the second-mode disturbances. In the case of a higher unit Reynolds number, i.e., $Re_{\mathrm{unit}} = 8.20 \times 10^6$, the peak in the PSD at the streamwise location of x = 240 mm surpasses that of $Re_{\mathrm{unit}} = 6.38 \times 10^6$, indicating the earlier appearance and growth of second-mode disturbances before x = 240 mm. Beyond x = 330 mm, the energy associated with second-mode waves exhibits a gradual increase and disperses into neighboring frequency domains, signaling the imminent breakdown of second-mode waves and the transition of the boundary layer.

According to previous studies, when the Ma > 4, the second-mode wave is more unstable, always leading to transition. Figure 10 shows the evolution of the growth rate of second-mode disturbances in different frequencies along the flow direction by LST. The second modes at different frequencies start to grow from different stations, and the high-frequency modes usually begin to arise and grow at first. Figure 10b indicates that, at the same unit Reynolds number condition, the higher frequency of the second mode wave can achieve a higher growth rate than that at low frequency. However, due to the attenuation of the high-frequency disturbance, it develops to a very short distance in the direction of flow, as shown in Figure 11. As the high-frequency modes begin to decay, the low-frequency modes in the boundary layer begin to appear and grow along the flow direction. Although the growth rate of lower-frequency disturbance is smaller than that of higher frequency, it usually becomes key to promote transition because of its larger propagation distance in the boundary layer.

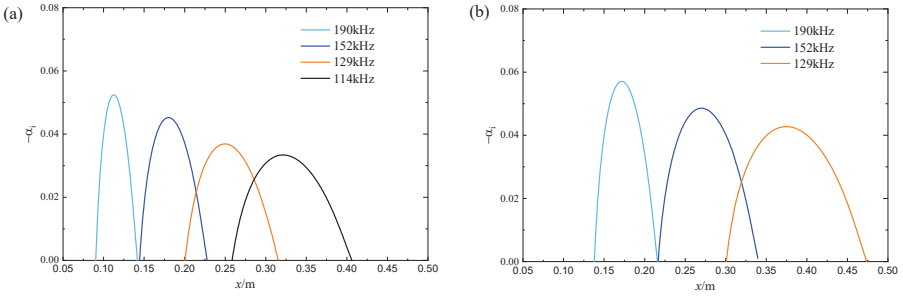

Figure 10. The growth rate of second-mode waves along flow directions predicted by LST: (**a**) $Re_{\mathrm{unit}} = 6.38 \times 10^6$; (**b**) $Re_{\mathrm{unit}} = 8.20 \times 10^6$.

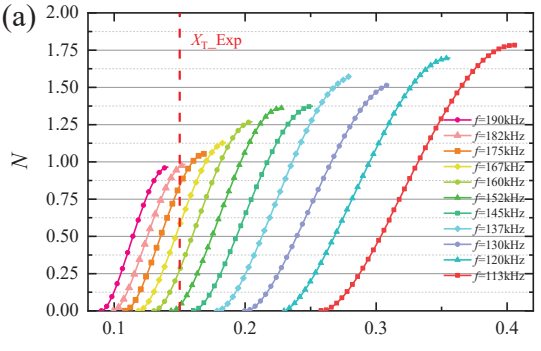

Figure 11. *Cont.*

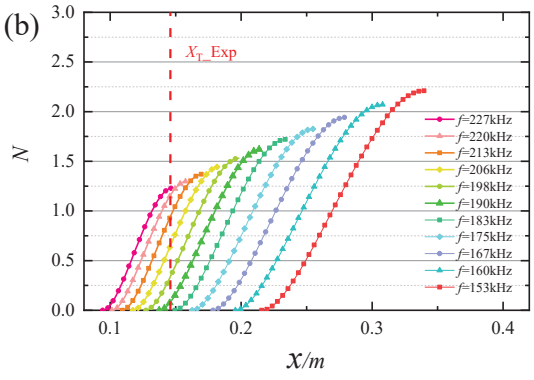

Figure 11. *N*-factor predicted by LST: (**a**) $Re_{\text{unit}} = 6.38 \times 10^6$; (**b**) $Re_{\text{unit}} = 8.20 \times 10^6$.

As is shown in Figure 10, with the increase in the unit Reynolds number, the initial position of disturbance growth at the same frequency gradually moves backward. Under the condition of $Re_{\text{unit}} = 2.52 \times 10^6$ (Figure 10a), the second mode of 190 kHz in the boundary layer decreases. Moreover, the growth rate of the disturbance is higher than that in the case of a low unit Reynolds number and moves further forward.

3.3. e^N Method

The distribution of *N*-factor of a range of representative frequency disturbances along the flow direction is shown in Figure 11. The *N*-factor is sensitive to frequency and freestream unit Reynolds number. Because of the larger propagation distance in the boundary layer of relatively low-frequency disturbance, it is easier to reach a larger *N*- factor, as suggested in Figure 10. Because the transition position of the plate in the experiment is obviously "wavy", the transition position calculated by the transition model γ-Reθt is used as the "average" transition position of the flat plate in the experiment. The red dashed line in Figure 10 represents the transition position obtained from the heat flow in the experiment. The *N*-factors of the transition location of two cases of unit Reynolds numbers are 0.98 and 1.25, respectively. Figure 12 illustrates the eigenfunction of two cases with different unit Reynolds numbers at x = 130 mm. There is no significant difference between the shape function of flow velocity u and temperature under the two experiments conditions. The normal distance of disturbance decreases with the increase in the unit Reynolds number.

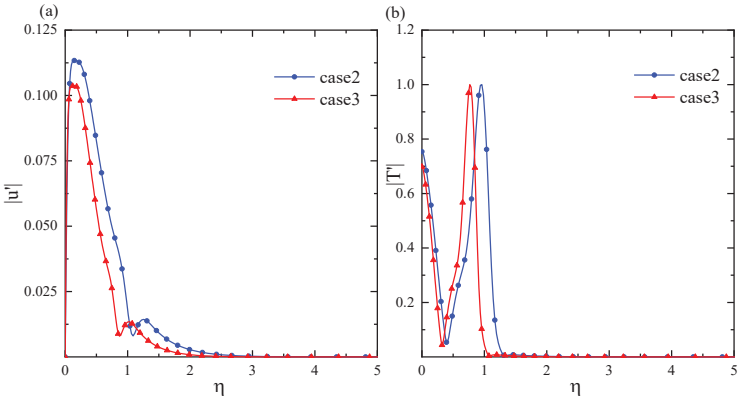

Figure 12. Eigenfunction predicted by LST at x = 130 mm. (**a**) xxx Eigenfunction of stream-wise velocity (**b**) Eigenfunction of Temperature.

4. Discussion

This study systematically examined the instability characteristics of the hypersonic boundary layer over a flat plate at a zero angle of attack, employing a combined approach of experimental analysis and linear stability analysis. The compression modification formula was fitted using the modified γ-Reθt model and the experimental results of the flat plate in a hypersonic wind tunnel. The validation results show that the predictions of the modified γ-Reθt model are more in line with the experimental results, which verifies the correctness of the modified γ-Reθt model. The application of PCB technology and infrared thermography facilitated the characterization of instability waves and enabled the calculation of the Stanton number along the streamwise direction. Additionally, the e^N method was implemented to determine the *N*-factor at the transition location within the wind tunnel. The conclusions derived from this study are outlined as follows:

(1) The transition model based on compressibility correction can better predict the transition position of the hypersonic boundary layer, and the simulation results are in good agreement with the experimental results. Moreover, the freestream unit Reynolds number has a great effect of the transition Reynolds number of the flat-plate boundary layer. As the unit Reynolds number increases, the transition position moves forward, and the transition Reynolds number also increases;

(2) The LST results show that the first mode and the second mode are both present in the hypersonic boundary layer at the Mach number 5. Combined with the PCB results of the experiments, the second-mode frequency range predicted by the LST matches the frequencies measured in the experiments, with a second-mode frequency range from 100 to 250 kHz;

(3) The *N*-factor of wind tunnel transition location predicted by LST is about 0.98 and 1.25 for $Re_{\text{unit}} = 6.38 \times 10^6$ and 8.20×10^6, respectively. With the increase in the unit Reynolds number, although the transition position moves forward, the *N*- factor of the transition position increases due to the increase in the magnification of the disturbance.

Author Contributions: Conceptualization, H.D.; validation, S.L.; formal analysis, Y.J.; investigation, S.L.; data curation, Y.J.; writing—original draft, Y.Y.; funding acquisition, H.D. All authors have read and agreed to the published version of the manuscript.

Funding: This research was funded by the National Numerical Wind-Tunnel (No. 2021-ZTNNW-QT00-50042, No. 2020-DY01-001), the National Natural Science Foundation of China (No. 11872208).

Institutional Review Board Statement: Not applicable.

Informed Consent Statement: Not applicable.

Data Availability Statement: Data is contained within the article.

Conflicts of Interest: The authors declare no conflict of interest.

Abbreviations

f	Frequency
Ma	Mach number
Pr	Prantl number
p	Pressure
Re	Reynolds number
u	Velocity
T	Temperature
ρ	Density
x, y, z	Cartesian coordinates

q	Heat flux
St	Stanton number
LST	Liner stability theory
α	Streamwise wave number
$-\alpha i$	Spatial amplification rate
γ	Ratio of specific heat
ω	Angular frequency
β	Spanwise wave number
Cp	Specific heat capacity
T_0	Stationary temperature
$T\infty$	Freestream temperature
$U\infty$	Freestream velocity
$\rho\infty$	Freestream density
k	Heat conductivity
PEEK	Poly-ether-ether-ketone

References

1. Marineau, E.C.; Grossir, G.; Wagner, A.; Leinemann, M.; Radespiel, R.; Tanno, H.; Chynoweth, B.C.; Schneider, S.P.; Wagnild, R.M.; Casper, K.M. Analysis of second-mode amplitudes on sharp cones in hypersonic wind tunnels. *J. Spacecr. Rocket.* **2019**, *56*, 307–318. [CrossRef]
2. Jianqiang, C.; Guohua, T.; Yifeng, Z.; Guoliang, X.U.; Xianxu, Y.; Cheng, C. Hypersonic boundary layer transition: What we know where shall we go. *Acta Aerodyn. A Sin.* **2017**, *35*, 311–337.
3. Quintanilha, H.; Paredes, P.; Hanifi, A.; Theofilis, V. Transient growth analysis of hypersonic flow over an elliptic cone. *J. Fluid Mech.* **2022**, *935*, A40. [CrossRef]
4. Mack, L.M. *Boundary-Layer Linear Stability Theory*; California Inst of Tech Pasadena Jet Propulsion Lab: Pasadena, CA, USA, 1984.
5. Mack, L.M. Linear stability theory and the problem of supersonic boundary-layer transition. *AIAA J.* **1975**, *13*, 278–289. [CrossRef]
6. Laurence, S.J.; Wagner, A.; Hannemann, K. Experimental study of second-mode instability growth and breakdown in a hy-personic boundary layer using high-speed schlieren visualization. *J. Fluid Mech.* **2016**, *797*, 471–503. [CrossRef]
7. Estorf, M.; Radespiel, R.; Schneider, S.; Johnson, H.; Hein, S. Surface-pressure measurements of second-mode instability in quiet hypersonic flow. In Proceedings of the 46th AIAA Aerospace Sciences Meeting and Exhibit, Reno, NV, USA, 7–10 January 2008; p. 1153.
8. Wendt, V.; Simen, M.; Hanifi, A. An experimental and theoretical investigation of instabilities in hypersonic flat plate boundary layer flow. *Phys. Fluids* **1995**, *7*, 877–887. [CrossRef]
9. Zhao, J.S.; Liu, S.; Zhao, L.; Zhang, Z. Numerical study of total temperature effect on hypersonic boundary layer transition. *Phys. Fluids* **2019**, *31*, 114105. [CrossRef]
10. Zhang, C.; Shi, Z. Nonlinear wave interactions in a transitional hypersonic boundary layer. *Phys. Fluids* **2022**, *34*, 114106. [CrossRef]
11. Cheng, J.; Huang, R.; Liu, W.; Wu, J. Influence of Single Roughness Element on Hypersonic Boundary-Layer Transition of Cone. *AIAA J.* **2023**, *61*, 3210–3218. [CrossRef]
12. Thele, M.; Selcan, C.; Sander, T.; Rödiger, T.; Mundt, C. Bluntness-Dependent Hypersonic Boundary-Layer Modes' Excitation. *J. Spacecr. Rocket.* **2022**, *59*, 1613–1622. [CrossRef]
13. Borg, M.P.; Kimmel, R.L. Ground test of transition for HIFiRE-5b at flight-relevant attitudes. *J. Spacecr. Rocket.* **2018**, *55*, 1329–1340. [CrossRef]
14. Yao, S.; Duan, Y.; Yang, P.; Wang, L.; Zhao, X.; Min, C. Experimental study of hypersonic boundary layer transition on a flat plate delta wing. *Exp. Therm. Fluid Sci.* **2020**, *112*, 109990. [CrossRef]
15. Xu, X.; Yi, S.; Han, J.; Quan, P.; Zheng, W. Effects of steps on the hypersonic boundary layer transition over a cone at 10° angle-of-attack. *Phys. Fluids* **2022**, *34*, 034114. [CrossRef]
16. Zhu, Y.; Zhang, C.; Chen, X.; Yuan, H.; Wu, J.; Chen, S.; Lee, C.; Gad-El-Hak, M. Transition in hypersonic boundary layers: Role of dilatational waves. *AIAA J.* **2016**, *54*, 3039–3049. [CrossRef]
17. Liu, S.; Wang, M.; Dong, H.; Xia, T.; Chen, L.; Zhao, A. Infrared thermography of hypersonic boundary layer transition induced by isolated roughness elements. *Mod. Phys. Lett. B* **2021**, *35*, 2150500. [CrossRef]
18. Nakagawa, K.; Tsukahara, T.; Ishida, T. DNS Study on Turbulent Transition Induced by an Interaction between Freestream Turbulence and Cylindrical Roughness in Swept Flat-Plate Boundary Layer. *Aerospace* **2023**, *10*, 128. [CrossRef]
19. Zhou, T.; Liu, Z.; Lu, Y.; Wang, Y.; Yan, C. Direct numerical simulation of complete transition to turbulence via first-and second-mode oblique breakdown at a high-speed boundary layer. *Phys. Fluids* **2022**, *34*, 074101. [CrossRef]
20. Saric, W.; Reshotko, E.; Arnal, D. *Hypersonic Laminar-Turbulent Transition*; AR-3l9; AGARD: Seine, France, 1998.
21. Mason, W.H. *Fundamental Issues in Subsonic/Transonic Expansion Corner Aerodynamics*; AIAA Paper; American Institute of Aeronautics and Astronautics: Reston, VA, USA, 1993; p. 0649.

22. Chen, F.J.; Malik, M.R.; Beckwith, I.E. Boundary-layer transition on a cone and flat plate at mach 3.5. *AIAA J.* **1989**, *27*, 687–693. [CrossRef]
23. Juliano, T.J.; Paquin, L.; Borg, M.P. Measurement of HIFiRE-5 boundary-layer transition in a Mach-6 quiet tunnel with infrared thermograph. In Proceedings of the 54th AIAA Aerospace Sciences Meeting, San Diego, CA, USA, 4–8 January 2016; p. 0595.
24. Tao, S.; Su, C.; Huang, Z. Improvement of the e N method for predicting hypersonic boundary-layer transition in case of modal exchange. *Acta Mech. Sin.* **2023**, *39*, 122416. [CrossRef]
25. Zhu, W.; Shi, M.; Zhu, Y.; Lee, C. Experimental study of hypersonic boundary layer transition on a permeable wall of a flared cone. *Phys. Fluids* **2020**, *32*, 011701. [CrossRef]
26. Chen, X.L.; Fu, S. Linear stability analysis of hypersonic boundary layer on a flat-plate with thermal-chemical non-equilibrium effects. *Acta Aerodyn. Sin.* **2020**, *38*, 316–325.
27. Klothakis, A.; Quintanilha Jr, H.; Sawant, S.S.; Protopapadakis, E.; Theofilis, V.; Levin, D.A. Linear stability analysis of hypersonic boundary layers computed by a kinetic approach: A semi-infinite flat plate at $4.5 \leq M\infty \leq 9$. *Theor. Comput. Fluid Dyn.* **2022**, *36*, 117–139. [CrossRef]
28. Boyd, C.F.; Howell, A. *Numerical Investigation of One-Dimensional Heat-Flux Calculations*; Technical Report NSWCDD/TR-94/114; Dahlgren Division Naval Surface Warfare Center: Silver Spring, MD, USA, 1994.
29. Menter, F.R. Two-equation eddy-viscosity turbulence models for engineering applications. *AIAA J.* **1994**, *32*, 1598–1605. [CrossRef]
30. Chedevergne, F. A double-averaged Navier-Stokes k–ω turbulence model for wall flows over rough surfaces with heat transfer. *J. Turbul.* **2021**, *22*, 713–734. [CrossRef]
31. White, F.M. *Viscous Fluid Flow*, 3rd ed.; McGraw-Hill Series in Mechanical Engineering; McGraw-Hill Higher Education: New York, NY, USA, 2006.
32. Willems, S.; Gülhan, A.; Steelant, J. Experiments on the effect of laminar–turbulent transition on the SWBLI in H2K at Mach 6. *Exp. Fluids* **2015**, *56*, 49. [CrossRef]
33. Menter, F.R.; Langtry, R.B.; Likki, S.R.; Suzen, Y.B.; Huang, P.G.; Völker, S. A correlation-based transition model using local variables—Part I: Model formulation. *J. Turbomach.* **2006**, *128*, 413–422. [CrossRef]
34. Guo, X.; Tang, D.; Shen, Q. Boundary layer stability with multiple modes in hypersonic flows. *Mod. Phys. Lett. B* **2009**, *23*, 321–324. [CrossRef]

energies

MDPI

Article

Experimental Investigation of the In-Cylinder Flow of a Compression Ignition Optical Engine for Different Tangential Port Opening Areas

Mitsuhisa Ichiyanagi [1,*], Emir Yilmaz [1], Kohei Hamada [2], Taiga Hara [2], Willyanto Anggono [3] and Takashi Suzuki [1]

[1] Department of Engineering and Applied Sciences, Sophia University, Tokyo 102-8554, Japan; yilmaz@sophia.ac.jp (E.Y.); suzu-tak@sophia.ac.jp (T.S.)
[2] Graduate School of Science and Technology, Sophia University, Tokyo 102-8554, Japan; k-hamada-3c8@eagle.sophia.ac.jp (K.H.); t-hara-5d1@eagle.sophia.ac.jp (T.H.)
[3] Mechanical Engineering Department, Petra Christian University, Surabaya 60236, Indonesia; willy@petra.ac.id
* Correspondence: ichiyanagi@sophia.ac.jp

Abstract: The push for decarbonization of internal combustion engines (ICEs) has spurred interest in alternative fuels, such as hydrogen and ammonia. To optimize combustion efficiency and reduce emissions, a closer look at the intake system and in-cylinder flows is crucial, especially when a hard-to-burn fuel, such as ammonia is utilized. In port fuel injection ICEs, airflow within cylinders profoundly affects combustion and emissions by influencing the air–fuel mixing phenomenon. Adjusting intake port openings is an important factor in controlling the in-cylinder airflow. In previous experiments with a transparent cylinder, tangential and helical ports demonstrated that varying the helical port's opening significantly impacts flow velocities, swirl ratios, and swirl center positions (SCPs). In this study, we used a particle image velocimetry technique to investigate how the tangential port's opening affects intake and in-cylinder flows. Flow velocities were assessed at different planes near the cylinder head, evaluating streamline maps, turbulent kinetic energy (TKE), and SCPs. Under the given experimental conditions, swirl flows were successfully generated early in the compression stroke when the tangential port opening exceeded 25%. Our findings emphasize the importance of minimizing TKE and SCP variation for successful swirl flow generation in engine cylinders equipped with both tangential and helical ports.

Keywords: in-cylinder flow; PIV; swirl flow; swirl center position; turbulent kinetic energy

Citation: Ichiyanagi, M.; Yilmaz, E.; Hamada, K.; Hara, T.; Anggono, W.; Suzuki, T. Experimental Investigation of the In-Cylinder Flow of a Compression Ignition Optical Engine for Different Tangential Port Opening Areas. *Energies* **2023**, *16*, 8110. https://doi.org/10.3390/en16248110

Academic Editors: Vasily Novozhilov and Cunlu Zhao

Received: 7 November 2023
Revised: 11 December 2023
Accepted: 15 December 2023
Published: 17 December 2023

1. Introduction

Carbon-free fuels, such as hydrogen and ammonia, are promising options for sustainable propulsion, particularly for the urgent need for decarbonization in the transportation industry. Previous experimental studies on hydrogen- [1] and ammonia [2,3] -fueled engines have revealed the necessity of a different approach to intake systems. Ammonia is considered to be a "hard to burn" fuel due to its high latent heat of vaporization and slow laminar burning velocity [2]. Higher intake air temperatures were found to be necessary for the combustion process to take place. This increase in the intake air temperature affects the air-to-fuel ratio, and thus the air–fuel mixing phenomenon [3]. It is also widely acknowledged that droplet atomization and achieving a homogenous air–fuel mixture before the start of combustion is crucial for high combustion efficiency. With the utilization of alternative fuels, further analysis of in-cylinder flow is vital as the density and viscosity of these alternative fuels are different to conventional internal combustion engine (ICE) fuels. In [4,5], fuel inside the combustion chamber was less susceptible to atomization due to higher momentum and longer break-up times for liquid droplets, resulting in soot production, which deposits inside the combustion chamber. It was shown that the generation of turbulence inside the cylinders improved the atomization of the fuel droplets as well as the

promotion of rapid air–fuel mixing, which resulted in better performance and a reduction in hazardous emissions. In [6], it was shown that a high swirl intensity affects engine combustion and emissions by reducing the combustion period, reducing soot generation, and CO_2 emissions. In [7], the researchers investigated the influence of swirl flow on heat transfer in a diesel engine cylinder and reported a 4–12% increase in heat transfer due to the increased swirl ratio at different operating conditions of the engine. In [8], it was shown that higher heat transfer was a consequence of increasing the swirl ratio, which enhanced the power performance by 5.79% and improved the fuel consumption as well. Furthermore, the influences of the following factors on swirl flows inside cylinders were investigated: the shape of the piston bowl [9–11], the shapes and configurations of intake ports [12–15], the volume flow rates of air from the intake ports [16–20], and so forth.

In a conventional engine cylinder, there are two types of intake ports, these being the helical port and the tangential port. These ports deliver intake air with different characteristics. Computational fluid dynamics (CFD) has been used to predict the flow characteristics of these intake ports [19–22]. In [19], the results indicated that flows within the helical port have higher velocities than those within the tangential port, and flows entering into the combustion chamber from the helical port generate intense local vortical structures. On the other hand, those from the tangential port induced a significant amount of momentum with no particular vortical structure. However, airflow was diverted by the cylinder walls to generate a swirling structure on the scale of the cylinder bore. Moreover, as the various ports were throttled, there was a significant interaction between the flows from these two ports, which could result in a non-monotonic variance in swirl generation. In particular, CFD simulations revealed that the variances in swirl flow were considerably more complex when the tangential port was throttled.

In experimental analyses, there are several methods to measure gas flows inside engine cylinders, such as the hot-wire anemometry [22] and laser Doppler velocimetry [23], which are known for their excellent temporal and spatial resolutions. However, since these methods measure only one point in a flow field, it is difficult to measure flow velocities in the entire engine cylinder. Therefore, the particle image velocimetry (PIV) technique has garnered attention in terms of measuring flow velocities simultaneously at multiple points inside the engine cylinders without interfering with the flow fields [12,24–37]. In [30], the PIV technique was applied during the compression stroke to a light-duty optical diesel engine. They evaluated the swirl center positions (SCPs) in the x–y plane depending on the inclination of the rotation axis and the piston bowl's inclination angle. They reported that the piston geometry effect might be more responsible than the intake flow effect for the tilting of SCPs. However, PIV measurements took place only during the compression stroke and in conditions where measurement planes were close to each other. Thus, it is somewhat hard to grasp the effects of the z-axis during the piston's reciprocating motion. In [28], a swirl control vane was used inside the helical and the tangential ports to change the swirl ratio to 2.2, 3.5, and 4.5, and it was found that a single dominant swirl flow structure tilts with respect to the cylinder axis. Their study also focused only on the compression stroke, where the eccentricity of the swirl center also caused in-cylinder flow to be asymmetric, which lowered the swirl ratio. In our previous studies, we measured the flow velocity inside cylinders when changing the engine speed and the opening area of helical ports under both the motored- and the fired-engine conditions [14,15,34,35]. We found that by changing the helical port's opening areas, SCPs do not shift significantly, and airflow velocities do not change with an increase in engine speed. In addition, as the helical port's opening area was increased, the swirl ratio was reduced, which lowered the turbulent intensity. Thus, our attention shifted to the tangential port instead, which is the main focus of the present study; there being only a few studies where the tangential port's effect was investigated experimentally. In [19], the researchers developed a computational model to simulate intake flow and its effect on in-cylinder swirl and flow structures by using different throttle angles in both the tangential and helical ports. However, this study was mainly focused on

the intake stroke. Therefore, in this study the effect of tangential port opening areas, along with their influence on compression stroke and swirl formation was investigated.

The authors have focused on the utilization of ammonia as a carbon-free fuel in conventional ICEs. The aim is to develop an ICE that can be powered solely with ammonia. However, due to its chemical properties, ammonia is considered to be hard-to-burn fuel in conventional ICEs. Thus, the authors have conducted co-combustion experiments using an ammonia–gasoline fuel mixture [3]. However, the results have shown that the percentage of ammoniain the fuel mixture can only be increased up to 67% without losing significant power output. Thus, in order to improve ammonia's flame retardancy and increase its ratio in the fuel mixture, the authors shifted their focus on the intake system to investigate the formation of swirl flow and turbulence inside the cylinder. The investigation focused on the intake port opening areas, which is considered to be an effective method resulting in minimal changes to a conventional ICE. In the present study, the PIV technique was applied to a commonly arranged intake–exhaust port four-stroke engine, at three different measurement planes to investigate the influence of the tangential port's opening area on swirl flow generation. The PIV measurements took place during the intake and compression strokes, in order to obtain a broader perspective on swirl flow generation. The helical port's opening area was set to 100% throughout the experiments, whereas the tangential port's opening area was changed using several kinds of gaskets. The data obtained from the PIV experiments were used to calculate spatially averaged velocities and TKE. Three-dimensional coordinates of SCPs were calculated, where the tilting of SCPs became clear with the piston's reciprocating motion and the tangential port's opening areas. It was found that swirl flows were successfully formed when the tangential port's opening area was 25% or more. In addition, a preliminary relationship was found between the calculated TKE and swirl flow generation, where low variances of TKE and SCPs in in-cylinder flows led to the successful formation of swirl flow.

2. Experimental Setup and Methodology

2.1. Experimental Apparatus

Figure 1 illustrates the experimental apparatus based on the optical single cylinder diesel engine, and Table 1 provides the specification of the PIV system, which was similar to our previous studies [14,15,34,35].

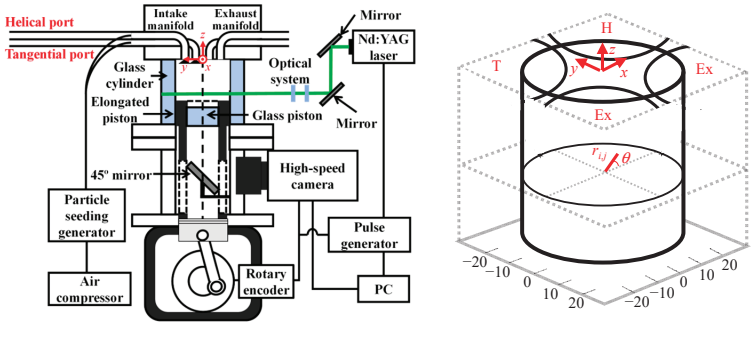

(**a**) (**b**)

Figure 1. (**a**) Experimental apparatus and (**b**) location of each port on the cylinder head and its coordinates. Units are mm.

Table 1. Experimental engine and equipment specification.

Equipment Name	Equipment Details
Laser	Mesa-PIV (Amplitude Japan, Tokyo, Japan) Nd:YAG, Double pulse, 532 nm
Particle seeding generator	PivSolid3 (PIVTEC GmbH, Göttingen, Germany)
Tracer particle	Silica (SiO_2) particles, 4.65 μm
High-speed camera	FASTCAM SA5 (Photron Ltd., Tokyo, Japan) Spatial resolution: 696 × 704 pixels Temporal resolution: 15 kHz
Air compressor	ACP-25SLA (Takagi Co., Ltd., Niigata, Japan)

An optical four-valve engine with two intake ports and two exhaust ports was used during the PIV experiments. For the intake ports, the tangential port and the helical port were connected to the cylinder head of the engine as shown in Figure 2. The tangential port had a straight port which generated an airflow along the cylinder wall resulting in large-scale swirl flow. On the other hand, the helical port was highly tilted with a spiral structure before entering the cylinder, creating a small-scale swirl flow. The bore, stroke, and cavity sizes were 85 mm, 96.9 mm, and 51.6 mm, respectively.

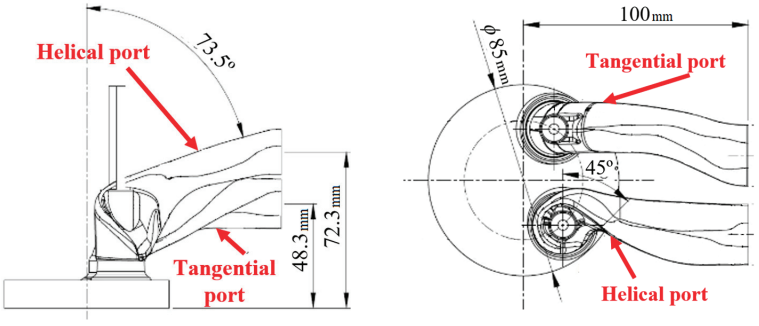

Figure 2. (**a**) Side view and (**b**) top view of the helical and tangential intake ports.

For visualization inside the cylinder, the cylinder was made of transparent quartz glass and the cavity of the piston was made of sapphire glass. The PIV system had a mirror underneath the piston allowing observation inside the cylinder. Since the sapphire glass was used only in the cavity, the observable area was limited to the cavity part of the piston in the present study. From the relationship between the position of the piston and the laser light sheet, the visible crank angle (CA) was between 70 deg.CA and 290 deg.CA. For the light source, a double pulse Nd:YAG laser (Mesa-PIV, Amplitude Japan, Tokyo, Japan) was used, which radiated light with a wavelength of 532 nm. The laser light created a 1 mm thickness light sheet by passing through the cylindrical and condenser lenses. This laser light sheet was irradiated horizontally into the glass cylinder. The height of the laser light sheet was set in parallel orientation and at distances of 10 mm, 20 mm, and 30 mm below the cylinder head to capture particle images in the upper part of the engine cylinder. For the tracer particles, silica (SiO_2) with an average diameter of 4.65 μm was used. These particles were directed into the intake port by using a particle seeding generator (PivSolid3, PIVTEC GmbH) with an air compressor (ACP-25SLA, Takagi Co., Ltd., Niigata, Japan). When the engine was started, the tracer particles were flown into the cylinder during the intake stroke. The mirror underneath the piston reflected the scattered light inside the cylinder to the high-speed CMOS camera (FASTCAM SA5, Photron Ltd., Tokyo, Japan) to capture the tracer particle images. The high-speed CMOS camera was set at a frame rate of 15,000 frames per second and the images were captured with a spatial resolution

of 696 × 704 pixels. Images taken from this camera were analyzed using commercial software (FtrPIV, version 3.2.0.0, Flowtech Research Inc., Kanagawa, Japan) to calculate the velocity vectors of the swirl flows. In the present study, the interrogation and search window sizes were 16 × 16 pixels and 33 × 33 pixels, respectively, which overlapped by 50%. The engine, the high-speed CMOS camera, and the laser were synchronized via the pulse generator using the signal for every two deg.CA of output from the rotary encoder set in the engine. When the pulse generator received the signal from the rotary encoder once, both the laser and the camera were operated twice, which made it possible to capture of two images with a time interval of 10 μs. The error in the PIV measurements was focused on the calculation velocity of the tracer (SiO_2) particles. The particle flow velocity was obtained from the ratio between particles displacement, Δx, and the time interval, Δt. A measurement uncertainty at a 95% confidence interval was calculated by combining the bias and precision indices as described in [38]. For the present study, four different error factors were considered, namely α (magnification), Δx (displacement of particles), Δt (time interval), and δu (variation of velocity based on the measurement principle). The calculation result revealed a measurement uncertainty of 1.7%, according to which the present PIV system was considered to be accurate.

2.2. Experimental Conditions

The experimental conditions in the present study are summarized in Table 2. For the helical port, all the gaskets had the same size of a 100% opening area. For the tangential port, five different gaskets were prepared to change the opening areas to 0%, 25%, 50%, 75%, and 100%. For the evaluation of swirl flows at different measurement planes, velocities were measured at 10 mm, 20 mm, and 30 mm below the cylinder head (which corresponds to $z = -10$ mm, -20 mm, and -30 mm, respectively). Our previous study revealed that engine speed had a minor effect on swirl flow generation [20], thus, it was set to 1000 rpm.

Table 2. Experimental conditions.

Engine speed	1000 rpm
Measurement plane	$z = -10$ mm, -20 mm, -30 mm
Opening area of helical port	100%
Opening area of tangential port	0%, 25%, 50%, 75%, 100%

2.3. Evaluation Technique for Swirl Center Position

SCPs of flows inside engine cylinders do not stay in a fixed position but vary with each CA, which is affected by flows from the intake ports and so forth. Our successive studies developed an evaluation technique for SCPs using PIV measurements, which was based on the algorithms proposed in [29,30]. For any fixed arbitrary lattice point, $P_{i,j}$, in an in-plane velocity field, the following gamma function, $\Gamma(P_{i,j})$, was calculated, which indicates the average sine of the angle, θ_l, between the vectors connecting the point to all other interrogation window centers and those to the measured velocities [37]:

$$\Gamma(P_{i,j}) = \frac{1}{N}\sum_{l=1}^{N}\sin(\theta_l) \tag{1}$$

where N is the total number of lattice points in each measurement plane [29,30]. The first candidates for the SCP were determined as the lattice point with an absolute value of Γ of more than 0.85.

The swirl ratio, S_R, was calculated using the PIV measurements according to the following equation, which is the ratio of the swirl flow's angular velocity to the engine's angular velocity:

$$S_R = \frac{1}{\omega} \times \frac{1}{N}\sum_{i=1}^{N}\frac{V_{i,j}\cdot\cos\theta - U_{i,j}\cdot\sin\theta}{r_{i,j}} \tag{2}$$

where ω is the engine angular velocity [rad/s], $r_{i,j}$ is the distance between the cylinder center and any lattice point [m], θ is the angle of the cylinder center and any lattice point (Figure 1b) [rad], $U_{i,j}$ and $V_{i,j}$ are the velocities in the x and y directions [m/s], respectively. The second candidates for the SCP were determined as the lattice point with an S_R of more than 0.55. Finally, the intersections of both candidates were calculated, and the lattice point with the smallest velocity among the intersections was determined as the SCP.

2.4. Evaluation Technique for Turbulent Kinetic Energy

TKE, k, is a parameter that shows the strength of the turbulence of a flow, which is the magnitude of deviation from the average flow velocity. In the present study, TKE was calculated using PIV measurements according to the following equation:

$$k = \frac{1}{N}\sum_{l=1}^{N}\frac{\left(u'^2 + v'^2\right)}{2} \tag{3}$$

where u' and v' were the velocities obtained by subtracting the ensemble-averaged velocity from the instantaneous velocities in the x and y directions [m/s], respectively. When its deviation is large, k becomes large, which means that a mixing action with a surrounding fluid was promoted. In the case of a diesel engine, a large k means the promotion of the mixture of air and fuel.

3. Results and Discussion

3.1. Evaluation of the Velocity Vector and Streamline Maps

Figure 3 shows the ensemble-averaged velocity vector maps at $z = -10$ mm and -30 mm. Figure 4 shows the streamline maps, which were calculated using the results from Figure 3. The velocity vector calculations and streamline maps at $z = -20$ mm are omitted since the results were similar to those at $z = -10$ mm. In the present study, intake stroke was defined from 70 deg.CA to 180 deg.CA, due to the visibility constraints mentioned in the previous section. The compression stroke was divided into three periods, these being 180 deg.CA to 216 deg.CA (early period), 216 deg.CA to 254 deg.CA (middle period), and 254 deg.CA to 290 deg.CA (latter period). Table 3 shows the matching of the case numbers and port opening area. The results for 254 deg.CA were omitted since they were observed to be similar to those at 216 deg.CA. For example, the velocity vector map at 70 deg.CA under the condition of a 0% opening area was expressed as "1A". Similarly, the streamline map results at 216 deg.CA with a 75% opening area were expressed as 3I. As depicted in Figures 3 and 4, the location of the tangential port is shown as *T*, that of the helical port is shown as *H*, and that of the exhaust ports is shown as *Ex*. The origin coordinate (0, 0) indicates the cylinder center. The SCPs are plotted as white dots, which were calculated using Equation (1), and are shown in Figure 3. The analyses of in-cylinder flows were divided into intake and compression stroke cases in the next sections.

Table 3. Case expressions for the tangential port opening area.

deg.CA	Case No
70	1
180	2
216	3
290	4

Opening Area %	Velocity Vector	Streamline Map
0	A	F
25	B	G
50	C	H
75	D	I
100	E	J

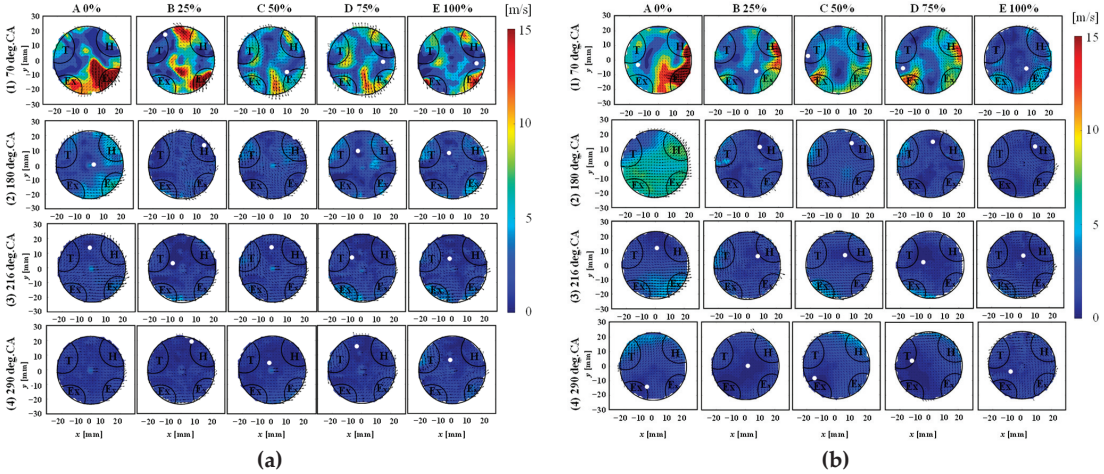

Figure 3. Ensemble-averaged velocity vector map at 70 deg.CA, 180 deg.CA, 216 deg.CA, and 290 deg.CA at (**a**) $z = -10$ mm and (**b**) -30 mm under conditions of five different opening areas.

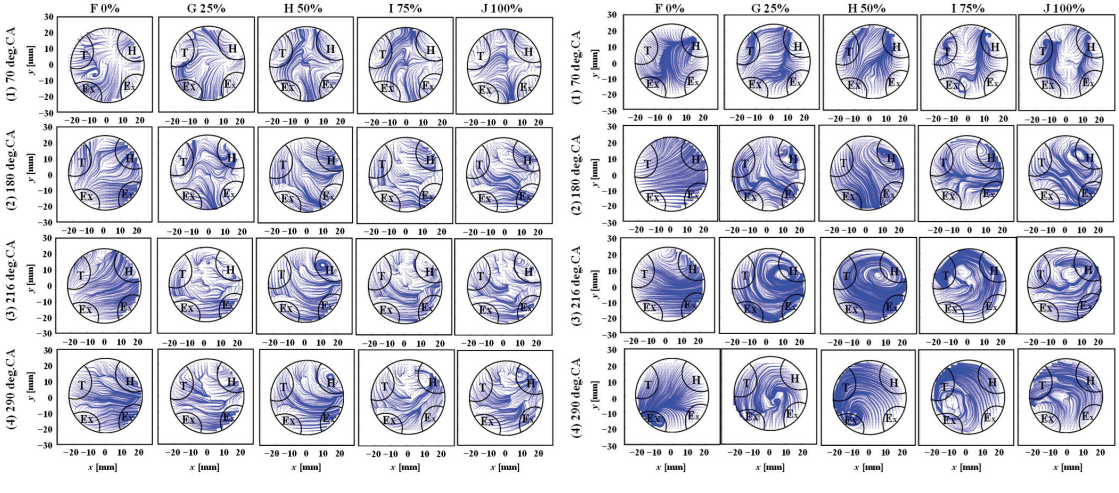

Figure 4. Streamline map at 70 deg.CA, 180 deg.CA, 216 deg.CA, and 290 deg.CA at (**a**) $z = -10$ mm and (**b**) -30 mm under conditions of five different opening areas.

3.1.1. Intake Stroke

In view of the ensemble-averaged velocity vector maps, at both measurement planes ($z = -10$ mm & -30 mm), it was calculated that the magnitudes of velocities in 1A–1E (during the intake stroke) were larger than those in 2A–4E (during the compression stroke), as shown in Figure 3. In addition, during the intake stroke in each measurement plane, regardless of the port opening areas, streamlines were found to be complicated for each opening area, as shown in Figure 4. This was an indication that the swirl flows were not formed during the intake stroke. In the present study, these types of flows are called "complicated flow".

3.1.2. Compression Stroke

From the piston's reciprocating motion, during the compression stroke, the $z = -30$ mm measurement plane shows the earlier results of the in-cylinder flow. Thus, Figure 4b needs to be analyzed prior to Figure 4a. Focusing on the cases with flows only from the helical port (2F–4F), it was observed that the streamlines in 2F–3F had curved lines; however, the SCPs could not be visualized clearly. This was an indication of the continuation of complicated flows. However, as the piston moved upwards, in case 4F, swirl-like flow was observed during the latter period of the compression stroke, as shown in Figure 4b. The SCP for case 4F was calculated as $(x, y) = (-4.6$ mm, -14.7 mm). These results make it clear that the initial swirl-like flows were formed towards the end of the compression stroke when the intake air was directed only from the helical port. There was a possibility that a part of the swirl flow (defined as "swirl-like flow") was formed in the cavity, and was caused by the collision of both flows from the tangential and the helical port.

Similarly, at the $z = -30$ mm measurement plane, as the tangential port opening area was increased, the streamlines at the beginning of the compression stroke (in 2G–2J) were still observed to be complicated flow. Consequently, as the piston moved upwards (in 3G–4J) successful formation of swirl flows was observed. In 4G, 4H, 4I, and 4J SCPs were calculated to be $(x, y) = (1.5$ mm, 0.0 mm), $(-14.9$ mm, -8.6 mm), $(-12.0$ mm, 3.4 mm), and $(0.6$ mm, -3.6 mm), respectively. This was apparently the result of the tangential port's effect on the generation of swirl flows from the middle period of the compression stroke. In addition, from our previous studies, we observed that swirl flows were formed at $z = -40$, -60, and -80 mm under the condition of a 100% opening area for both the helical and tangential ports [15]. Combining the results of the previous and the present study, it can be said that swirl flow was successfully formed 30 mm below the engine cylinder ($z = -30$ mm), with tangential port's opening area of 25% and above, during the compression stroke.

When the focus is moved up to the measurement plane at $z = -10$ mm, in cases 2G–2J, the streamlines were still observed to be complicated flow, similar to those in the -30 mm plane, as shown in Figure 4a. However, those in 3G–4J had curved lines, in which SCPs were still visible. For instance, for the 4I and 4J cases, SCPs were calculated as $(x, y) = (-3.1$ mm, 15.4 mm) and $(-0.8$ mm, 6.5 mm), respectively. Based on these findings, it is evident that when the tangential port opening areas were 25% or more, as the mixture flow moved upwards inside the engine cylinder, swirl-like flows were maintained. Even though SCPs were not highly apparent, by using both intake ports simultaneously the swirl-like flows continued their effect, which is beneficial for more a homogenous air–fuel mixture to achieve higher combustion efficiency. Table 4 summarizes the classification of flows formed under each condition of the opening areas at each measurement period.

Table 4. Classification of flow formed for each opening area of the tangential port and each period at (**a**) $z = -10$ mm and (**b**) -30 mm (×: complicated flow, ▲: swirl-like flow, ●: swirl flow).

(a)					
CASE	**0%**	**25%**	**50%**	**75%**	**100%**
70 deg.CA	×	×	×	×	×
180 deg.CA	×	×	×	×	×
216 deg.CA	×	▲	▲	▲	▲
290 deg.CA	×	▲	▲	▲	▲
(b)					
CASE	**0%**	**25%**	**50%**	**75%**	**100%**
70 deg.CA	×	×	×	×	×
180 deg.CA	×	×	×	×	×
216 deg.CA	×	●	●	●	●
290 deg.CA	▲	●	●	●	●

3.1.3. Swirl Ratio

Figure 5a,b illustrates swirl ratio calculated based on the cylinder center, under each tangential opening area at −10 mm and −30 mm, respectively. During the first half of the intake stroke (70 deg.CA—125 deg.CA), results from both measurement planes showed similar tendencies, where a 0% opening area case showed values smaller than zero, meaning an opposite direction of swirl flow generation. However, this swirl flow was diminished rather quickly as the swirl ratio changed to positive values towards the end of first half of the intake stroke. In addition, tangential port opening areas of 25% and above showed a sinusoidal trend, where swirl ratio values were becoming high and low consequently. Thus, in general, it can be said that the formation of swirl flow was not successful during the intake stroke.

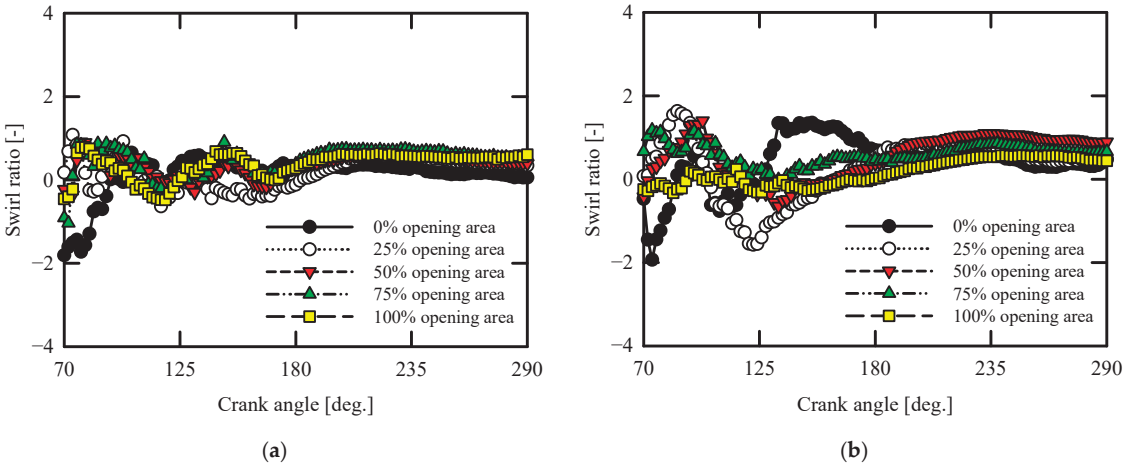

Figure 5. Time evolution of swirl ratios calculated from the cylinder center position at (**a**) $z = -10$ mm and (**b**) −30 mm under five different opening area conditions.

During the compression stroke (from 180 deg.CA and onwards), both measurement planes' swirl ratio values showed a somewhat steady level. It also became clear that at $z = -30$ mm the swirl ratio values were higher than those of $z = -10$ mm. This could be interpreted as the in-cylinder air flow velocities in the −10 mm plane becoming slower due to the interference induced by flows returning from the cylinder head. In addition, the sequential order of the swirl ratio values was different at the $z = -10$ mm when compared to $z = -30$ mm plane. At −30 mm, a tangential port opening area of 50% showed the highest value, whereas at −10 mm the highest value was attained under the 100% case. The sequential orders of the swirl ratios for the −10 mm and −30 mm measurement planes were 100% > 75% > 50% > 25% > 0%, and 50% > 75% > 100% > 25% > 0%, respectively. At both measurement planes, for the 0% case (air flow only from the helical port), swirl ratio values showed a decreasing trend. This is thought to be related to the higher in-cylinder velocities attained during the intake stroke from the helical port, causing complicated flow inside the engine cylinder, rather than forming swirl flow. By looking at these results, it became clear that to generate a swirl ratio, the tangential and helical ports need to be used simultaneously.

3.2. Evaluation of Spatially Averaged Velocity and Turbulent Kinetic Energy

For the investigation of factors that induced the classification of flows, spatially averaged velocities and TKE were evaluated at $z = -10$ mm and −30 mm, as shown in Figures 6 and 7, respectively. For each case, TKE was calculated using Equation (3). As shown in Figures 6 and 7, during the compression stroke, the spatially averaged velocities and TKE were asymptotic to about 1–2 m/s and about 1–3 m^2/s^2, respectively. Although

there were three kinds of flows, as shown in Table 4, large differences in averaged velocities or TKE were not observed during the compression stroke. Thus, it became clear that the intake stroke affected the formation of in-cylinder flows the most, which was also supported by the large variances of TKE during the intake stroke when compared to the compression stroke at various measurement planes.

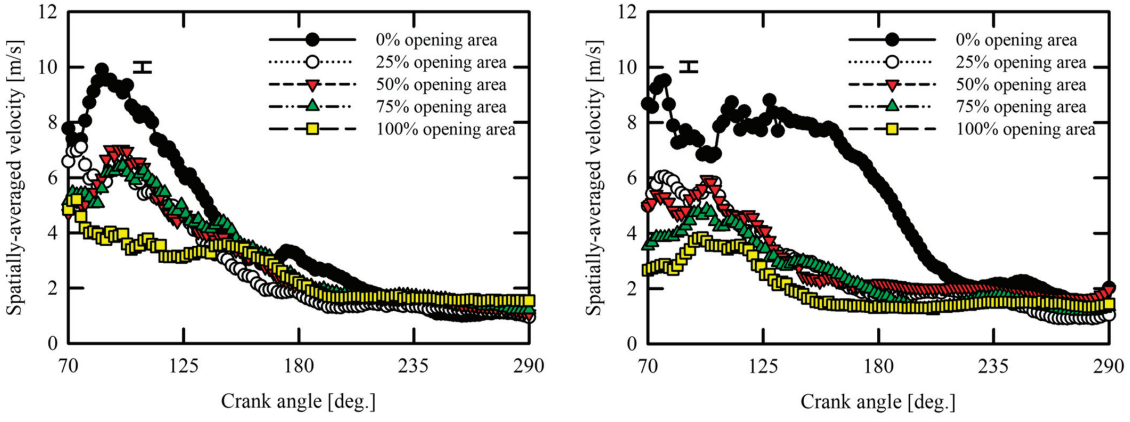

Figure 6. Time evolution of spatially averaged velocity at (**a**) $z = -10$ mm and (**b**) -30 mm under conditions of five different opening areas. The error bar corresponds to a 95% confidence interval.

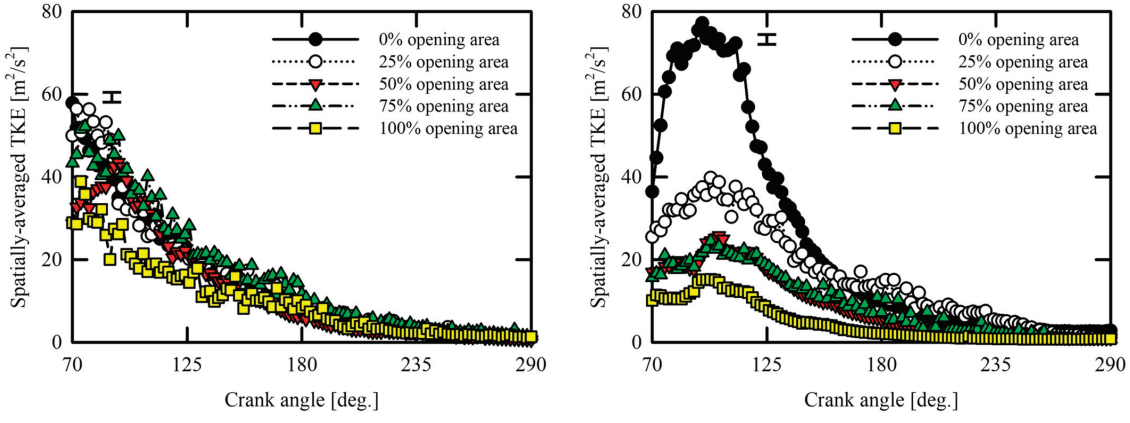

Figure 7. Time evolution of spatially averaged TKE at (**a**) $z = -10$ mm and (**b**) -30 mm under conditions of five different opening areas. The error bar corresponds to a 95% confidence interval.

At the $z = -10$ mm measurement plane, during the intake stroke (from 70 deg.CA to 180 deg.CA), the order of averaged velocities depending on the tangential port area was calculated to be 0% > 25% ≈ 50% ≈ 75% > 100%, as shown in Figure 6a. Similar results were also apparent for TKE, as shown in Figure 7a, with the exception of the 0% opening area case being similar to 25%, 50%, and 75%. The reasoning behind this was thought to be the similarities between the structure and turbulence of flows; TKE was roughly proportional to the averaged velocity. Thus, orders of both magnitudes were expected to be roughly the same. However, as the opening area of the tangential port was increased, averaged velocities decreased due to the interference between the flows along the cylinder

wall caused by the tangential port and the vertical flow caused by the helical port. In addition, under the condition of a 100% opening area, TKE was smaller than for the 25–75% opening area cases, due to the aforementioned interference flows induced by the opening of both ports. Thus, the order of TKE at the $z = -10$ mm measurement plane was different from the spatially averaged velocities.

For the results at the $z = -30$ mm measurement plane, spatially averaged velocities showed similar results when compared to the $z = -10$ mm measurement plane, with an exception for the 75% opening area case, which briefly showed higher averaged velocities between 125 deg.CA and 180 deg.CA when compared to the 50% opening case. Thus, the order of spatially averaged velocities was 0% > 25% > 50% ≈ 75% > 100%, as shown in Figure 6b. The averaged order of TKE was also calculated to be 0% > 25% > 50% ≈ 75% > 100%, as shown in Figure 7b. It was also found that under the condition of a 0% opening area, TKE was about twice that of the 25% opening area. This high TKE value for the 0% opening area case is thought to be the reason why there was no formation of swirl flow, as mentioned before (see cases 1F–4F in Figure 4b).

Furthermore, variances of TKE during the intake and compression strokes are listed in Table 5 (a) and (b), respectively. During the intake stroke, at $z = -10$ mm, TKE variances were calculated to be the highest. At this period, there was no formation of swirl flow under all tangential port opening areas. Similarly, at $z = -30$ mm under the condition of a 0% opening area, TKE variance was calculated to be high, with no formation of swirl flow. Conversely, when TKE variances became smaller during the compression stroke (at $z = -30$ mm), swirl flows were formed, as already shown in Figure 4b. From these results, it became clear that almost no swirl flow was formed when the TKE variances were large. Meaning that, in order to generate swirl flow, TKE variances needs to be small, which was achieved by using both the tangential and helical ports at the same time.

Table 5. Variances of TKE averaged during (**a**) the intake and (**b**) the compression strokes under conditions of five different opening areas. The unit is m^4/s^4.

(a)					
CASE	**0%**	**25%**	**50%**	**75%**	**100%**
$z = -10$ mm	180.0	219.9	136.3	151.7	59.9
$z = -30$ mm	563.0	73.6	36.3	24.7	18.3
(b)					
CASE	**0%**	**25%**	**50%**	**75%**	**100%**
$z = -10$ mm	4.7	4.4	2.2	6.2	3.7
$z = -30$ mm	4.5	15.1	1.4	5.3	0.2

3.3. Evaluation of Swirl Center Positions

For further investigation of the classification of flows, SCPs at $z = -10$ mm, -20 mm, and -30 mm under the conditions of five different opening areas were evaluated using the technique described in Section 2.3. Figure 8a shows the SCP maps in the x–y plane during the intake stroke between 70 deg.CA and 180 deg.CA, whereas Figure 8b shows the latter period of the compression stroke between 254 deg.CA and 290 deg.CA

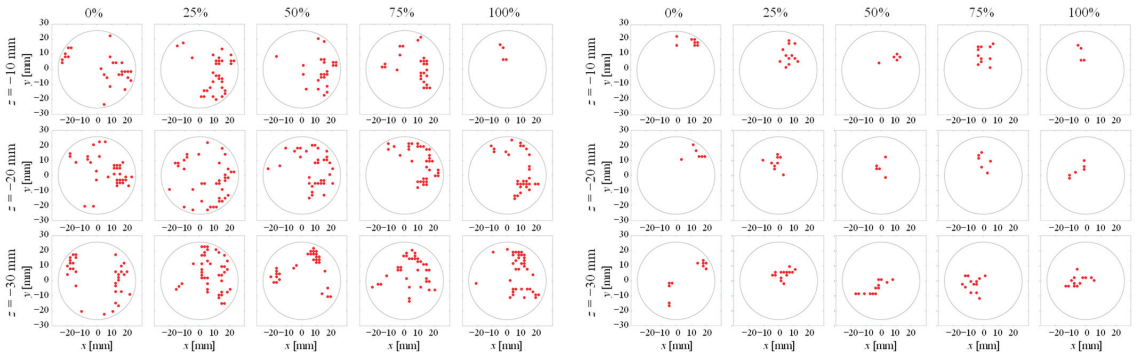

Figure 8. (**a**) SCP maps during the intake stroke and (**b**) the latter period of the compression stroke in the *x*–*y* plane under conditions of five different opening areas.

During the intake stroke, it was observed that SCPs tend to be dispersed regardless of the measurement plane and the opening area. Since these results correspond to 1F–2J of Figure 4b, it was considered that these dispersions of SCPs were induced by the formation of complicated flow as TKE variances were also high. Thus, no clear correlation could be made for the formation of swirl flow during the intake stroke.

During the latter period of the compression stroke, it was more apparent that SCPs were concentrated within a certain region at all measurement planes. However, SCPs differed depending on opening area conditions of the tangential port, as shown in Figure 8b. Similar to the results given in cases 4F–4J of Figure 4a,b, corresponding to $z = -10$ mm and -30 mm, respectively, swirl like flows were observed at $z = -10$ mm, whereas swirl flows were formed at -30 mm during the latter period of the compression stroke.

From the viewpoint of the quantitative evaluation, the variances of SCPs were calculated at $z = -10$ mm and -30 mm. Intake stroke results are given in Table 6 (a), and the latter period of the compression stroke results are given in Table 6 (b). During the intake stroke, SCP variances were larger than those during the latter period of the compression stroke under the conditions of 25–100% opening areas. This was due to the higher in-flow velocities induced during the intake stroke, causing high variances for the exact location of SCPs for each case.

Table 6. Variances of SCPs averaged during (**a**) the intake stroke and (**b**) the latter period of the compression stroke under conditions of five different opening areas. The units are mm^2.

(a)					
CASE	**0%**	**25%**	**50%**	**75%**	**100%**
$z = -10$ mm	180.0	219.9	136.3	151.7	59.9
$z = -30$ mm	563.0	73.6	36.3	24.7	18.3
(b)					
CASE	**0%**	**25%**	**50%**	**75%**	**100%**
$z = -10$ mm	4.7	4.4	2.2	6.2	3.7
$z = -30$ mm	4.5	15.1	1.4	5.3	0.2

For the latter period of the compression stroke, Table 6 (b), SCP variances were lowered as these flows corresponded to swirl-like or swirl flows. However, SCPs changed depending on the measurement plane and the tangential port's opening area. Thus, from a qualitative evaluation perspective, the relationship between the SCPs and the flow structure is unclear.

In order to have a clearer idea, the proper orthogonal decomposition (POD) and MODE calculations will be implemented to further understand the in-cylinder flow structure.

Figure 9 shows the SCP locations averaged during the latter period of the compression stroke, at (a) the x–z plane and (b) the y–z plane. It should be noted that these values are averaged results, in which some cases of SCP locations differed due to in-cylinder air flow. As already shown in Figure 1b, both intake ports were located at the positive region in the y direction ($x > 0$ and $y > 0$ for the helical port, and $x < 0$ and $y > 0$ for the tangential port). Thus, it is considered that the in-cylinder flow was formed with the tilt of the SCP, due to the locations of the intake ports and the interference between the flows induced from them depending on the piston's position in the z-axis. In Figure 9a, for the 0% opening area case, it was observed that SCPs were centered towards the positive x direction at all measurement planes, where the helical port was located. As the tangential port's opening area was increased, with the piston's upward movement (from −30 mm to −10 mm), SCPs were shifted towards the center. For the analyses in the y direction (Figure 9b), since both intake ports were located in a positive y direction, under all opening areas, SCPs were located towards the positive region of the y direction.

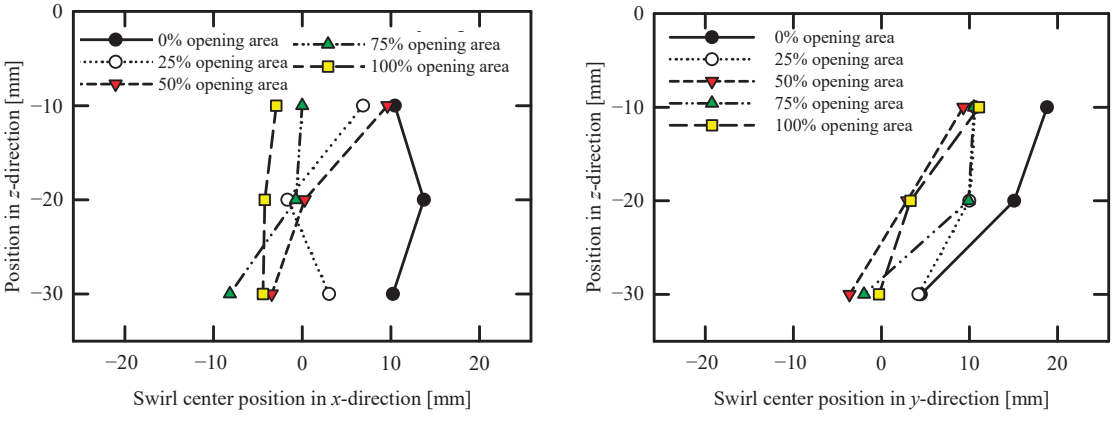

Figure 9. (**a**) SCPs averaged from 254 deg.CA to 290 deg.CA (latter period) in the x–z plane and (**b**) the y–z plane under conditions of five different opening areas.

Summarizing the above, in an engine when both tangential and helical ports were used, it was expected to observe complicated or swirl-like flows when the SCP variances were relatively large. In contrast, swirl flows were formed when SCP variances were relatively small, which was induced by the higher opening areas of the tangential port.

4. Conclusions

For a four-valve diesel engine, the effects of the opening area of the tangential port on the in-cylinder swirl flow were investigated, where the opening areas were changed to 0%, 25%, 50%, 75%, and 100% using different gaskets. The present study measured the velocities in a transparent engine cylinder in three different measurement planes, at $z = -10$ mm, −20 mm, and −30 mm, by using the PIV technique. The gathered experimental data were used to evaluate velocity vectors, streamline maps, spatially averaged TKE, and SCPs in three-dimensional coordinates. Important conclusions obtained from the present study are summarized below:

1. The velocity vector and the streamline maps were evaluated using the obtained velocities through PIV measurements. In the case of the 0% opening area, during intake stroke, complicated flows were observed at $z = -10$ mm, −20 mm and −30 mm, where variances of TKE and SCPs were large. During the compression stroke, com-

plicated flows were also observed at $z = -10$ mm and -20 mm measurement planes. At the latter period of the compression stroke, swirl-like flows started to form at $z = -30$ mm.

2. In the case of opening areas of 25% or more (flows from both ports), during intake stroke, similar tendencies were observed in the cases where only the helical port was used, where no swirl flow generation was observed. After the first half of the compression stroke, swirl-like flows were observed at $z = -10$ and -20 mm and swirl flows were successfully formed at $z = -30$ mm.
3. Swirl ratios were calculated from the center of the engine cylinder for each tangential port opening area. Calculations showed that, during the intake stroke, a sinusoidal pattern was apparent in the swirl ratios, meaning proper swirl flow was not formed. On the other hand, during the compression stroke, as the tangential port opening areas increased, swirl ratio also increased and reached to a steady level for cases when the tangential port opening was 25% and above.
4. The spatially averaged TKE and its variances were evaluated using the obtained velocities. During the compression stroke, large differences in TKE were not observed, thus a comparison cannot be made. However, during the intake stroke differences in the TKE were apparent depending on the measurement planes and the size of the opening areas. It was concluded that, during the intake stroke, as the variances of TKE became larger, complicated or swirl-like flows were formed. As these variances started to become smaller, swirl flows started to form.
5. SCPs and their variances were evaluated using the obtained velocities. SCPs were not clear during the intake stroke. However, for cases with an opening area of 25% or more, SCPs were observed clearly during the compression stroke. A tilting motion of SCPs was also observed in the x–y planes in the z direction during the compression stroke. The SCP variances under the conditions that form complicated or swirl-like flows were larger than those under the conditions that form swirl flows. It was concluded that swirl flows were successfully formed when the variances of SCPs were relatively low.

As the next step of this study, the know-how on the swirl flow formation will be applied to a modified diesel engine with a high compression ratio, which is fueled by an ammonia–gasoline mixture. In this setup, the fuel mixture of ammonia–gasoline will be used in a port injection method. Subsequent experiments will be conducted to validate the outcomes presented in this paper through ammonia–gasoline co-firing.

Author Contributions: Conceptualization, M.I. and T.S.; data curation, M.I., K.H. and T.H.; formal analysis, M.I.; funding acquisition, M.I. and T.S.; investigation, M.I., E.Y., K.H., T.H., W.A. and T.S.; methodology, M.I. and T.S.; project administration, M.I. and T.S.; resources, M.I. and T.S.; software, K.H. and T.H.; supervision, M.I. and T.S.; validation, M.I., E.Y. and T.S.; visualization, M.I., E.Y. and T.S.; writing—original draft, M.I., E.Y., K.H. and T.H.; writing—review and editing, M.I., E.Y., W.A. and T.S. All authors have read and agreed to the published version of the manuscript.

Funding: This research was funded by the Japan Society for the Promotion of Science, Grants-in-Aid for Scientific Research (No. 19K04244).

Data Availability Statement: Data will be available from the corresponding author upon reasonable request. All other data supporting this study are available within the article.

Acknowledgments: The authors thank Yoseph A. Salim and Shunya Aoyagi for their technical support.

Conflicts of Interest: The authors declare no conflict of interest.

References

1. Shadidi, B.; Najafi, G.; Yusaf, T. A Review of Hydrogen as a Fuel in Internal Combustion Engines. *Energies* **2021**, *14*, 6209. [CrossRef]

2. Mounaim-Rousselle, C.; Mercier, A.; Brequigny, P.; Dumand, C.; Bouriot, J.; Houille, S. Performance of ammonia fuel in a spark assisted compression ignition engine. *Int. J. Eng. Res.* **2021**, *23*, 781–792. [CrossRef]
3. Yilmaz, E.; Ichiyanagi, M.; Zhang, Q.; Guo, B.; Aratake, N.; Kodaka, M.; Shiraishi, H.; Okada, T.; Suzuki, T. Investigation of intake air temperature effect on co-combustion characteristics of NH_3/gasoline in naturally aspirated high compression ratio engine with sub-chamber. *Sci. Rep.* **2023**, *13*, 11649. [CrossRef] [PubMed]
4. Brijesh, P.; Sreedhara, S. Exhaust emissions and its control methods in compression ignition engines: A review. *Int. J. Automot. Technol.* **2013**, *14*, 195–206. [CrossRef]
5. Bari, S.; Hossain, S.N.; Saad, I. A review on improving airflow characteristics inside the combustion chamber of CI engines to improve the performance with higher viscous biofuels. *Fuel* **2020**, *264*, 116769. [CrossRef]
6. Yoon, S.; Lee, S.; Kwon, H.; Lee, J.; Park, S. Effects of the swirl ratio and injector hole number on the combustion and emission characteristics of a light duty diesel engine. *Appl. Therm. Eng.* **2018**, *142*, 68–78. [CrossRef]
7. Broatch, A.; Olmeda, P.; Garcia, A.; Salvador-Iborra, J.; Warey, A. Impact of swirl on in-cylinder heat transfer in a light-duty diesel engine. *Energy* **2017**, *119*, 1010–1023. [CrossRef]
8. Wang, G.; Yu, W.; Li, X.; Su, Y.; Yang, R.; Wu, W. Study on dynamic characteristics of intake system and combustion of controllable intake swirl diesel engine. *Energy* **2019**, *180*, 1008–1018. [CrossRef]
9. Prasad, B.V.; Sharma, C.S.; Anand, T.N.; Ravikrishna, R.V. High swirl-inducing piston bowls in small diesel engines for emission reduction. *Appl. Energy* **2011**, *88*, 2355–2367. [CrossRef]
10. Subramanian, S.; Rathinam, B.; Lalvani, J.; Annamalai, K. Piston Bowl Optimization for Single Cylinder Diesel Engine Using CFD. *SAE Tech. Pap.* **2016**. [CrossRef]
11. Jena, A.; Singh, H.; Agarwal, A.K. Effect of Swirl Ratio and Piston Geometry on the Late-Compression Mean Air-Flow in a Diesel Engine. *SAE Tech. Pap.* **2021**. [CrossRef]
12. Rebault, J.; Vernet, J.A.; Lindgren, B.; Alfredsson, P.H. A study using PIV of the intake flow in a diesel engine cylinder. *Int. J. Heat Fluid Flow.* **2016**, *62*, 56–67. [CrossRef]
13. Abo-Elfadl, S.; Mohamed, A.A.E. Enhancement of swirl generation in diesel engine cylinder by using combinations of twisted tape and guide vanes with shrouded valve. *J. Eng. Sci.* **2018**, *46*, 33–45.
14. Aljarf, S.; Singh, H.; Ndizeye, G.; Ichiyanagi, M.; Suzuki, T. Effect of a dual air inlet port of the 4-valve CI engine on the swirl flow generated at the bottom region of the cylinder using the PIV technique. *Mech. Eng. J.* **2021**, *8*, 20-00392. [CrossRef]
15. Ichiyanagi, M.; Saito, R.; Sawamura, Y.; Ndizeye, G.; Gotama, G.J.; Anggono, W.; Suzuki, T. Effects of intake flow on in-cylinder swirl flow under motoring and firing conditions for CI engines using PIV measurements. *J. Eng. Sci. Technol.* **2021**, *16*, 3600–3619.
16. Furuno, S.; Iguchi, S.; Oishi, K.; Inoue, T. The Effects of 'Inclination Angle of Swirl Axis' on Turbulence Characteristics in a 4-Valve Lean-Burn Engine with SCV. *SAE Trans.* **1990**, *99*, 2248–2254.
17. Huang, R.F.; Yu, J.H.; Yeh, C.N. Manipulating tumble and swirl flows in cylinder of a motored four-valve engine by inlet deflection valve. *J. Mech.* **2008**, *24*, 333–345. [CrossRef]
18. Kim, Y.; Han, Y.; Lee, K. A study on the effects of the intake port configurations on the swirl flow generated in a small D.I. diesel engine. *J. Therm. Sci.* **2014**, *23*, 297–306. [CrossRef]
19. Perini, F.; Miles, P.C.; Reitz, R.D. A comprehensive modeling study of in-cylinder fluid flows in a high-swirl, light-duty optical diesel engine. *Comput. Fluids* **2014**, *105*, 113–124. [CrossRef]
20. Anggono, W.; Ichiyanagi, M.; Saito, R.; Gotama, G.J.; Cornelius, C.; Kreshna, R.; Suzuki, T. Airflow characteristics investigation of a diesel engine for different helical port openings and engine speeds. *J. Eng. Technol. Sci.* **2021**, *53*, 210306. [CrossRef]
21. Bari, S.; Saad, I. CFD modelling of the effect of guide vane swirl and tumble device to generate better in-cylinder air flow in a CI engine fuelled by biodiesel. *Comput. Fluids* **2013**, *84*, 262–269. [CrossRef]
22. Zhijun, W.; Zhen, H. In-cylinder swirl formation process in a four-valve diesel engine. *Exp. Fluids* **2001**, *31*, 467–473. [CrossRef]
23. Kook, S.; Bae, C.; Miles, P.C.; Choi, D.; Bergin, M.; Reitz, R.D. The Effect of Swirl Ratio and Fuel Injection Parameters on CO Emission and Fuel Conversion Efficiency for High-Dilution, Low-Temperature Combustion in an Automotive Diesel Engine. *SAE Tech. Pap.* **2006**. [CrossRef]
24. Deslandes, W.; Dupont, A.; Baby, X.; Charnay, G.; Boree, J. PIV Measurements of Internal Aerodynamic of Diesel Combustion Chamber. *SAE Trans.* **2003**, *112*, 2067–2073.
25. Deslandes, W.; Dumont, P.; Dupont, A.; Baby, X.; Charnay, G.; Boree, J. Airflow Cyclic Variances Analysis in Diesel Combustion Chamber by PIV Measurements. *SAE Tech. Pap.* **2004**. [CrossRef]
26. Cosadia, I.; Boree, J.; Charnay, G.; Dumont, P. Cyclic variances of the swirling flow in a diesel transparent engine. *Exp. Fluids* **2006**, *41*, 115–134. [CrossRef]
27. Stansfield, P.; Wigley, G.; Justham, T.; Catto, J.; Pitcher, G. PIV analysis of in-cylinder flow structures over a range of realistic engine speeds. *Exp. Fluids* **2007**, *43*, 135–146. [CrossRef]
28. Petersen, B.; Miles, P.C. PIV measurements in the swirl-plane of a motored light-duty diesel engine. *SAE Int. J. Engines* **2011**, *4*, 1623–1641. [CrossRef]
29. Okura, Y.; Higuchi, K.; Urata, Y.; Someya, S.; Tanahashi, M. Measurement of in-cylinder turbulence in an internal combustion engine using high speed particle image velocimetry. *Trans. Jpn. Soc. Mech. Eng. B* **2013**, *79*, 2193–2206. (In Japanese) [CrossRef]

30. Zha, K.; Busch, S.; Miles, P.C.; Wijeyakulasuriya, S.; Mitra, S.; Senecal, P.K. Characterization of Flow Asymmetry during the Compression Stroke Using Swirl-Plane PIV in a Light-Duty Optical Diesel Engine with the Re-entrant Piston Bowl Geometry. *SAE Int. J. Engines* **2015**, *8*, 1837–1855. [CrossRef]
31. Zhuang, H.; Hung, D.L.S.; Yang, J.; Tian, S. Investigation of swirl ratio impact on in-cylinder flow in an SIDI optical engine. *J. Eng. Gas Turbines Power* **2016**, *138*, 081505. [CrossRef]
32. Garcia-Oliver, J.M.; Garcia, A.; Gil, A.; Pachano, L. Study of air flow interaction with pilot injections in a diesel engine by means of PIV measurements. *SAE Int. J. Engines* **2017**, *10*, 740–751. [CrossRef]
33. Perini, F.; Zha, K.; Busch, S.; Kurtz, E.; Peterson, R.C.; Warey, A.; Reitz, R.D. Piston geometry effects in a light-duty, swirl-supported diesel engine: Flow structure characterization. *Int. J. Engine Res.* **2018**, *19*, 1079–1098. [CrossRef]
34. Aljarf, S.; Singh, H.; Ichiyanagi, M.; Suzuki, T. In-cylinder gas flow characteristics study of CI engine under motoring and pre-ignition firing conditions using a high-speed PIV. *Alex. Eng. J.* **2022**, *61*, 6441–6455. [CrossRef]
35. Aljarf, S.; Singh, H.; Baiju, V.; Ichiyanagi, M.; Suzuki, T. Experimental investigation of swirl motion of in-cylinder flow in CI engine under firing condition due to pre-injection using PIV and POD techniques. *Automot. Engine Technol.* **2023**, *8*, 73–93. [CrossRef]
36. Ikeda, Y. The Interaction between In-Cylinder Turbulent Flow and Flame Front Propagation in an Optical SI Engine Measured by High-Speed PIV. *Energies* **2022**, *15*, 2783. [CrossRef]
37. The Visualization Society of Japan. *PIV Handbook*, 1st ed.; Morikita Publishing Co., Ltd.: Tokyo, Japan, 2002.
38. Graftieaux, L.; Michard, M.; Grosjean, N. Combining PIV, POD and vortex identification algorithms for the study of unsteady turbulent swirling flows. *Meas. Sci. Technol.* **2001**, *12*, 1422–1429. [CrossRef]

energies

MDPI

Article

Numerical Modeling of Two-Phase Flow inside a Wet Flue Gas Absorber Sump

Nejc Vovk † and Jure Ravnik *,†

Faculty of Mechanical Engineering, University of Maribor, 2000 Maribor, Slovenia; nejc.vovk@um.si
* Correspondence: jure.ravnik@um.si
† These authors contributed equally to this work.

Abstract: A numerical model of a flue gas scrubber sump is developed with the aim of enabling optimization of the design of the sump in order to reduce energy consumption. In this model, the multiphase flow of the continuous phase, i.e., water, and the dispersed phase, i.e., air bubbles, is considered. The air that is blown in front of the agitators, as well as the influence of the flow field of the agitators on the distribution of the dispersed phase and the recirculation pumps as outlet, is modeled. The bubble Sauter mean diameter is modeled using the population balance model. The model is used to analyze operating parameters such as the bubble retention time, the average air volume fraction, bubble Sauter mean diameter, the local distribution of the bubble size and the amount of air escaping from the pump outlets at two operating points. The purpose of the model is to simulate the two-phase flow in the sump of the flue gas scrubber using air dispersion technology with a combination of spargers and agitators, which, when optimized, reduces energy consumption by 33%. The results show that the homogeneity of air is lower in the bottom part of the absorber sump and that the amount of air escaping through recirculation pipes equals 1.2% of the total air blown into the absorber sump. The escaping air consists mainly of bubbles smaller than 6 mm. Additional operating point results show that halving the magnitude of the linear momentum source lowers the air retention, as well as the average homogeneity of the dispersed air.

Keywords: flue gas scrubbing; air dispersion; numerical model; OpenFoam; energy savings

Citation: Vovk, N.; Ravnik, J. Numerical Modeling of Two-Phase Flow inside a Wet Flue Gas Absorber Sump. *Energies* **2023**, *16*, 8123. https://doi.org/10.3390/en16248123

Academic Editors: Vasily Novozhilov and Cunlu Zhao

Received: 24 November 2023
Revised: 11 December 2023
Accepted: 14 December 2023
Published: 18 December 2023

1. Introduction

Flue gas desulfurization methods with the aim of reducing the impact on human health have been known since the early days [1]. The first ideas relating to the removal of sulfur dioxide (SO_2) from flue gases emerged in England around 1850, where the consequences of the industrial revolution began to manifest themselves not only as economic indicators but also as a serious threat to human health.

Throughout history, numerous flue gas desulfurization technologies have been developed [2,3], primarily aimed at cleaning emissions from coal-fired power plants and metallurgical plants. It was found that certain additives in water improve the ability to remove SO_2 from flue gases. The first studies were carried out on the solubility of SO_2 in a solution of water and lime, which showed improved properties in terms of flue gas cleaning. Nowadays, most modern flue gas desulfurization plants are based on the wet limestone process [4]. The reason for this is that limestone is abundant in nature and can be processed cost-effectively for use in FGD plants.

The first larger FGD plants were built in England in the early 20th century. At the beginning, the technology was based on the spraying of water from the river Thames into the flue gas counter flow. The effluent, which contained absorbed SO_2, was channeled back into the Thames and posed a significant threat to the river's ecosystem. Later improvements included the addition of lime to the river water before spraying, which increased the alkalinity of the water and, thus, the proportion of neutral $CaSO_3$ in the wastewater. This

measure improved the problem of acidic emissions into the Thames. Another improvement concerned the modification of the scrubber itself. A sump was built below the flue gas inlet of the absorber, in which the wastewater was retained. The purpose of the absorber sump was to extend the retention time of the wastewater so that more time was available for the reaction of SO_2 to form $CaSO_3$. Finally, interest arose in converting $CaSO_3$ into a usable form and in dewatering the obtained byproduct for sale on the market. The proposed method involved the oxidation of $CaSO_3$ into $CaSO_4 \cdot H_2O$, also known as gypsum. This conversion only partially compensates for the high operating costs of FGD plants, as the gypsum produced as a byproduct is not necessarily of high quality [5] and can rarely be used as a load-bearing material [6]. Additional treatment can improve the mechanical properties of byproduct gypsum [7,8].

There is little literature on the numerical modeling of a real FGD absorber sump, as the numerical modeling of flue gas scrubbers mainly focuses on the optimization of the absorption process of SO_2 from flue gases into liquid droplets. Arif et al. [9] conducted a Euler–Lagrangian analysis of FGD absorbers using Lagrangian tracking of droplets generated on absorber spray levels. They concluded that the inlet flue gas velocity distribution has a major influence on the efficiency of the FGD absorber. A similar approach was adopted by Marocco et al. [10], who modeled the absorption of SO_2 from flue gas into liquid droplets using two-film theory. They reported good agreement with the experimental results in terms of flue gas temperature measurements, absorber pressure drop and the overall efficiency of SO_2 removal. Qu et al. [11,12] investigated the effects of different droplet diameters, as well as spray injections and spray morphologies, on the efficiency of FGD absorbers. Flue gas scrubbing strongly depends on the droplet diameter, as larger droplets reduce the absorption rate of SO_2, and smaller droplets evaporate faster preventing absorption.

Regarding the modeling of the absorber sump, the aim of numerical modeling is to optimize the air dispersion using different combinations of spargers and agitators (mixers) [13], which can be included in a dynamic model of an FGD plant [14]. Gomez et al. [15] created a detailed numerical model of an FGD plant using the Euler–Euler approach, which includes both the scrubber section and the absorber sump. By implementing chemical kinetics, including gypsum formation models, they gained detailed insights into actual limestone consumption. The latter is also dependent on the actual limestone dissolution rate [16]. To model the effects of agitators on air dispersion in different aeration systems, either direct modeling with the MRF approach is used or the agitator flow field is modeled as a linear momentum source [17].

The capability of numerical modeling of process plants has been strongly influenced throughout history by the development of multiphase flow modeling and available hardware. For a thorough description of all chemical and physical phenomena inside the FGD absorber and the absorber sump, especially with regard to the modeling of SO_2 absorption, O_2 absorption, droplet drying, etc., advanced CFD approaches must be used [18–20].

Society has been confronted with exponential growth in production capacities for decades. In order to satisfy all needs, energy production must follow suit, which is not possible without ecological consequences. Today, these consequences can be divided into an increase in the concentration of carbon dioxide in the atmosphere—a direct consequence of the use of fossil fuels—and the rapid depletion of natural resources—a direct consequence of consumerism. It seems that the environmental measures taken by industrialized countries are primarily aimed at the former. Decision makers see the solution primarily in reducing the use of fossil fuels and replacing them with renewable sources.

One of the consequences of these measures is increasing globalization, which is pushing industrialized countries into greater dependence on countries that are rich in natural resources needed for the transition to renewable energy sources. One example of this is the solarization of the power system based on photovoltaics, which has led to an increased demand for silicon-based semiconductor materials, most of which are produced in China.

European countries are forced by their own regulations to rely on developing countries, which strengthens their competitiveness in the global market.

Current environmental policy, particularly in relation to greenhouse gas emissions, has not yet shown the improvements for which it was designed. This is partly due to the lack of global consensus and partly due to the interests of countries and companies whose success is based on maximizing consumption and, therefore, production. At this point, it becomes clear why environmental regulations are predominantly focused in one direction. Any measure to drastically reduce consumption can have disastrous consequences for a modern country in today's economic system, as the general indicator of a country's prosperity is expressed in the buying power of the population and, consequently, in production growth. The fact remains that we only have a finite supply of natural resources and that it is crucial for a sustainable existence to utilize them properly.

Due to these concerns, we developed a numerical model of an FGD absorber sump with the aim of improving the energy consumption characteristics of FGD systems.

2. Flue Gas Scrubbing

2.1. Physical Background

The desulfurization of flue gases from a thermal power plant is carried out using the wet calcite process to clean the flue gases of SO_2, which is a byproduct of the combustion of sulfur-containing coal [21]. The technology shown in Figure 1 requires the construction of a process building called a flue gas scrubber. Its main objective is to absorb SO_2 into liquid droplets that are sprayed into the flue gas counter current as it flows towards the top of the scrubber, into the stack. The droplets are generated on the spray levels in the upper part of the absorber. The liquid consists of water and dissolved limestone, which binds SO_2 and produces $CaSO_3$. Droplets of absorbed SO_2 fall to the bottom of the absorber, into the absorber sump. The main task of the absorber sump is to maintain the conditions for the formation of a stable product. This is achieved by the further oxidation of $CaSO_3$ to $CaSO_4$ (gypsum), which forms crystals when supersaturated in water. The resulting suspension is circulated from the sump to the spray levels by the so-called recirculation pumps. Oxidation takes place by blowing air directly into the absorber sump. The aim is to achieve a homogeneous distribution of air in the absorber sump with the smallest possible mean bubble diameter in order to maximize the transfer of oxygen from the bubbles into the surrounding liquid. The numerical model of the absorber sump presented here is based on technology that requires the use of a combination of air spargers and agitators to ensure a homogeneous distribution of air bubbles in the absorber sump.

2.2. Scrubber (Absorber) Design

The flue gas enters from the side and is then diverted to the outlet at the top of the scrubber. Next to the FGD absorber, there is normally a separate building housing the recirculation pumps. The diameter of the recirculation pipe must be dimensioned so that the minimum required suspension velocity is achieved to prevent gypsum or limestone particles from settling. A mist eliminator must be installed in the upper part of the absorber to prevent additional process water loss.

Figure 2a shows the CAD model of the considered FGD absorber. The absorber sump has the following tasks:

- The air dispersion required for the forced oxidation of $CaSO_3$ is achieved by a combination of agitators and air spargers. An example of agitators with corresponding air spargers in a reference project at the Trbovlje Thermal Power Plant (TET) (Slovenia) is shown in Figure 2b. The design of the sump in TET is different from the design we investigated in this study. Instead of a single sparger on the agitator, air is blown into three points in front of the agitator, as shown in the figure.
- The suspension of gypsum and limestone particles to prevent them from settling, thus eliminating the risk of a solid layer forming at the bottom of the absorber sump. The

appropriate suspension conditions also create a suitable environment for the growth of gypsum crystals when supersaturation is reached.

- Ensuring volume and, thus, sufficient time for chemical reactions and the absorption of oxygen into the surrounding liquid.

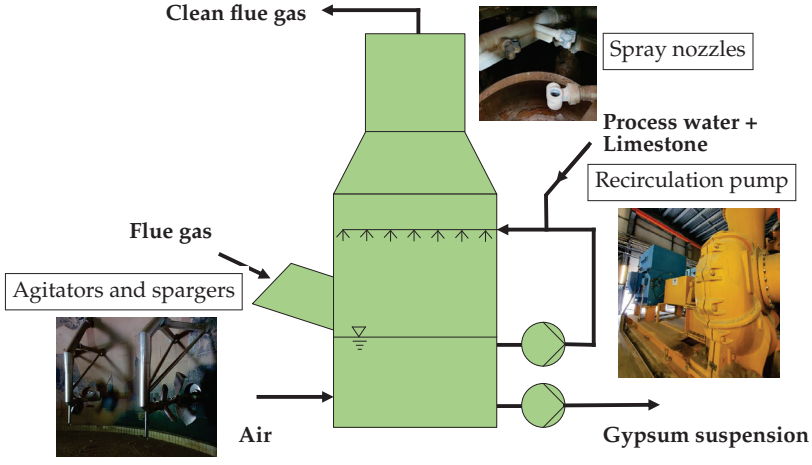

Figure 1. Flow diagram of wet flue gas desulfurization with the main equipment. The flue gas enters the absorber from the side and is diverted upwards. The limestone suspension is sprayed into the counter flow. The gypsum suspension is collected at the bottom of the absorber sump and pumped to a dewatering system.

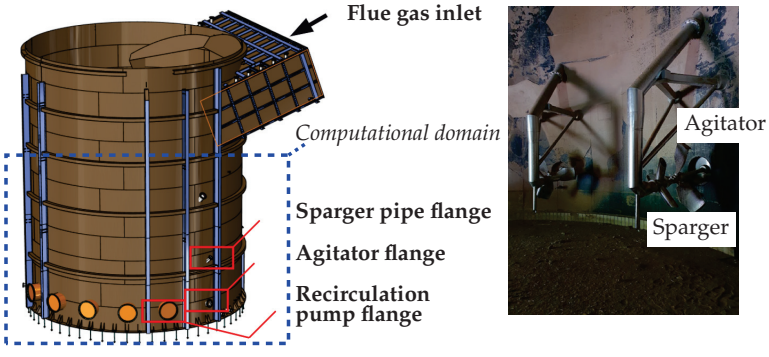

Figure 2. Construction of an FGD absorber sump with agitators and spargers. (**a**) CAD model of the absorber sump with a flue gas inlet duct. In the lower part, the flanges for the installation of the main equipment are also visible. The blue dotted line shows the domain considered in the numerical model. The CAD model was visualized using Solidworks 2023 software. (**b**) Agitators and spargers inside of the FGD absorber sump in a reference project. In this case, the oxidation air is blown into three points in front of the agitator.

3. Methods

3.1. Governing Equations

Open-source software OpenFoam version 11 [22] was used to simulate the multiphase flow in the absorber sump. The URANS approach was adopted to model the unsteady, turbulent, two-phase flow of the continuous and dispersed phases. The compressible continuity equation for an arbitrary phase (φ) is expressed as

$$\frac{\partial(\alpha_\varphi \rho_\varphi)}{\partial t} + \nabla \cdot (\alpha_\varphi \rho_\varphi \mathbf{u}_\varphi) = 0, \tag{1}$$

and the compressible momentum equation is expressed as

$$\frac{\partial}{\partial t}\alpha_\varphi \rho_\varphi \mathbf{u}_\varphi + \mathbf{u}_\varphi(\nabla \cdot \alpha_\varphi \mathbf{u}_\varphi \rho_\varphi) = -\alpha_\varphi \nabla p + \nabla \cdot \mathbf{T}_\varphi + \alpha_\varphi \rho_\varphi \mathbf{g} + \mathbf{m}_\varphi + \mathbf{s}_{m,\varphi}. \tag{2}$$

The governing equations are connected by volume fraction

$$\alpha_{\varphi,i} = \frac{V_{i,\varphi}}{V_i}, \tag{3}$$

for phase φ in cell i. In Equations (2) and (3), ρ is the density, $\mathbf{u}$ is the velocity vector, p is the pressure and $\mathbf{g}$ is the vector of the gravitational constant. The term $\mathbf{s}_{m,\varphi}$ represents all additional momentum sources for the φ phase. The additional local momentum source is represented by the agitator. The term $\mathbf{m}_\varphi$ covers the momentum transfer between the phases and requires the modeling of the forces acting on a bubble. The term $\nabla \cdot \mathbf{T}_\varphi$ is the divergence of the stress tensor, where the latter is defined for compressible fluids as

$$\mathbf{T}_\varphi = 2\mu \mathbf{D}_\varphi - \frac{2}{3}\mu(\nabla \cdot \mathbf{u}_\varphi)\mathbf{I}. \tag{4}$$

In Equation (4), $\mathbf{D}$ is the deformation tensor, which is defined as

$$\mathbf{D}_\varphi = \frac{1}{2}\Big((\nabla \otimes \mathbf{u}_\varphi) + (\nabla \otimes \mathbf{u}_\varphi)^\top\Big). \tag{5}$$

For turbulence modeling purposes, the k-Omega SST Sato [23] and k-Epsilon [24] turbulence models were used for the continuous and dispersed phases, respectively.

The population of bubbles in the absorber sump is polydisperse. The reason for the varying size is bubble breakup in areas with high shear flow (agitator area) and coalescence in areas with low shear flow (in the upper part of the absorber sump). The development of the bubble size is described by the population balance model [25] as

$$\frac{\partial N_j}{\partial t} = \nabla \cdot (\mathbf{u}_d N_j) = H_j, \tag{6}$$

where N_j is the number concentration of bubbles in size group j, and $\mathbf{u}_d$ is the velocity vector of the dispersed phase. Breakup and coalescence are modeled by the term H_j as the source/sink of the bubbles in size group j. The proportion of the individual size groups is given by

$$f_j = \frac{\alpha_j}{\alpha_d}, \tag{7}$$

where α_j is the volume fraction of air bubbles that correspond to size group j so that $\alpha_d = \sum_j^n \alpha_j$ and $\sum_j^n f_j = 1$ always holds for n size groups.

3.2. Boundary Conditions

The geometry of the numerical model of the FGD absorber sump is shown in Figure 3. The boundary conditions on the free surface are relatively complex. There, a mixed boundary condition must be defined for the velocity of the continuous phase so that inflow is allowed and outflow is not allowed. For velocity components that are tangential to the free surface (u_x, u_y), a free slip condition must be employed:

$$\frac{\partial u_{x,y}}{\partial z} = 0. \tag{8}$$

A no-slip boundary condition for the velocity and a Neumann boundary condition with zero gradient for the pressure are defined at the wall. Wall functions are used for turbulent variables, as the mesh size in the region close to the wall fulfills $30 < y^+ < 300$.

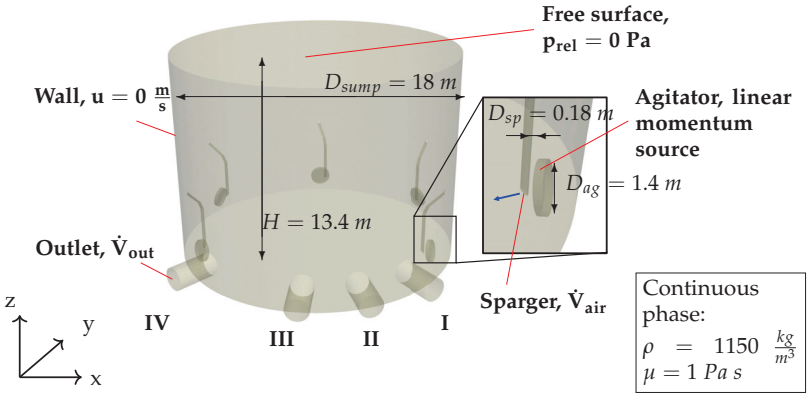

Figure 3. Boundary conditions of the absorber sump numerical model. Agitators are modeled as a linear momentum source. The free surface enables the outlet of the dispersed phase and the inlet of the continuous phase. The direction of the air inlet is marked with a blue arrow.

The air enters the computational domain through a sparger. A fixed volume fraction of the air and a fixed value for the turbulent variables are defined. The direction of the air inlet is marked with a blue arrow.

In the present numerical model, the agitators are modeled as a linear momentum source. The momentum source is calculated based on the agitator flange axial force, which is provided by the agitator manufacturer as

$$\mathbf{s}_{m,\varphi,agitator} = \frac{F_{axial}}{V_{agitator}}, \tag{9}$$

where $V_{agitator}$ denotes the volume taken by the rotating agitator blades.

The key simplifications of the absorber sump for numerical modeling are summarized as follows:

- A mixed boundary condition that enables the inflow of the continuous phase and the outflow of the dispersed phase is applied on the free surface. Since free surface modeling was outside the scope of this research, the applied simplification was allowed.
- The influence of the agitators on the flow field inside of the absorber sump is modeled as a local linear momentum source, since obtaining the exact geometry of the agitator blades can be challenging. The applied linear momentum source was calculated based on the agitator flange axial force provided by the agitator manufacturer.
- The geometry was simplified so that measurement equipment inside of the absorber sump was omitted from the geometry creation.

3.3. Submodels

To model the interaction between the continuous and dispersed phases, we included the following submodels, as available in the OpenFOAM CFD package [26]. The forces are accounted for in the momentum equation (Equation (3)) as the sum of the below forces per unit volume as $\mathbf{m}_{\varphi,i} = 1/V_i \cdot \Sigma_q \mathbf{F}_{i,q}$, where q represents the type of force submodel, as presented below.

Drag force between air bubbles and liquid inside of the absorber sump is calculated as

$$\mathbf{F}_D = -C_D \alpha_d \rho_c \frac{3}{4 d_p} |\mathbf{u}_d - \mathbf{u}_c| (\mathbf{u}_d - \mathbf{u}_c), \tag{10}$$

where subscripts d and c represent the dispersed and continuous phases, respectively; d_p is the local bubble diameter; and C_D is drag coefficient, which is calculated as

$$C_D = \frac{24}{Re}\left(1 + 0.1Re^{3/4}\right). \tag{11}$$

Shear induced lift force acts on a particle traveling with a relative velocity in a shear flow field of viscous fluid and is calculated as

$$\mathbf{F}_L = -C_L \alpha_d \rho_c (\mathbf{u}_d - \mathbf{u}_c) \times (\nabla \times \mathbf{u}_c), \tag{12}$$

where C_L is the lift coefficient calculated using the model proposed by Tomiyama et al. [27].

Turbulent dispersion force is modeled as proposed by Burns et al. [28]:

$$\mathbf{F}_{TD} = -C_D \alpha_d \frac{\nu_{t,c}}{Sc_t}\left(\frac{\nabla \alpha_d}{\alpha_d} - \frac{\nabla \alpha_c}{\alpha_c}\right), \tag{13}$$

where $\nu_{t,c}$ is the turbulent viscosity of the continuous phase, C_D is the drag coefficient given in Equation (11) and Sc_t is the turbulent Schmidt number.

Virtual mass force is applicable when one phase accelerates through the surrounding phase. The force is calculated as

$$\mathbf{F}_{VM} = C_{VM} \alpha_d \rho_c \left(\frac{D\mathbf{u}_c}{Dt} - \frac{D\mathbf{u}_d}{Dt}\right), \tag{14}$$

where C_{VM} is a virtual mass coefficient and equals 0.5. In Equation (14), D denotes the total derivative.

Wall lubrication force occurs when the dispersed phase flows along a wall. The force vector points in a direction normal to the wall. It is calculated as

$$\mathbf{F}_{WL} = C_{WL} \alpha_d \rho_c |\mathbf{u}_c - \mathbf{u}_d|_{||}^2 \mathbf{n}, \tag{15}$$

where $|\mathbf{u}_c - \mathbf{u}_d|_{||}$ denotes the magnitude of the relative velocity of phases tangential to the wall (or $|\mathbf{u}_c - \mathbf{u}_d|_{||} = |(\mathbf{u}_c - \mathbf{u}_d) - \mathbf{n}((\mathbf{u}_c - \mathbf{u}_d) \cdot \mathbf{n})|$), and $\mathbf{n}$ is the wall-normal vector. C_{WL} is the wall lubrication force coefficient and is calculated as proposed by Antal et al. [29].

4. Results

4.1. Validation

For the numerical modeling of an FGD absorber sump, a mesh with hexagonal elements was created, as shown in Figure 4.

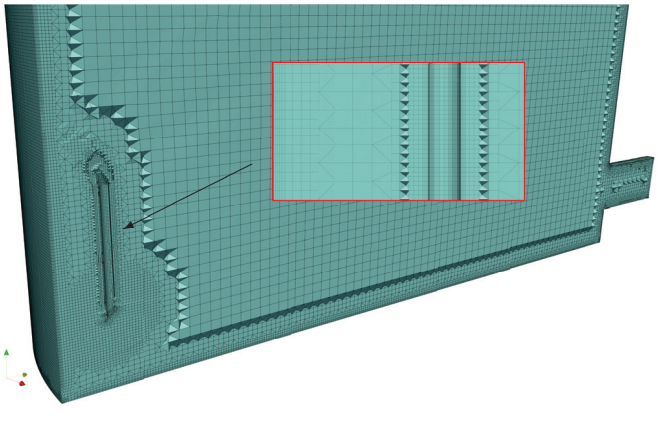

Figure 4. Hexagonal mesh of the FGD absorber sump with refinement regions.

A refinement region was created in the sparger and agitator area, as well as the pump outlet area. Wall element thickness was set to 10 mm.

A mesh independence study was conducted to validate the numerical model. Homogeneity profiles and the bulk air volume fraction were compared for four meshes (0.4×10^6, 0.7×10^6, 2.3×10^6 and 3.0×10^6 cells) with varying element sizes. For the unsteady simulation, we set the maximum Courant number to be equal to 1, and the time step was calculated accordingly. First-order numerical schemes were used for both temporal and spatial discretization. The bulk air volume fraction, which is, from the engineering standpoint, the most important parameter, with respect to the number of cells in a mesh is shown in Figure 5. We observed clear convergence of the results, since the results do not significantly change between the 2.3 and 3 million meshes.

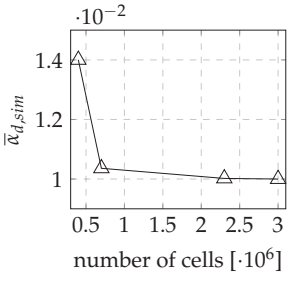

Figure 5. Comparison of bulk air volume fraction for four meshes (0.4×10^6, 0.7×10^6, 2.3×10^6 and 3.0×10^6 cells) with varying element sizes.

Homogeneity of air dispersion was also compared for all meshes. We evaluated the homogeneity based on variance [1], calculated as

$$\sigma^2(\tilde{h}) = \frac{1}{A_{\tilde{h}}} \int_{A_{\tilde{h}}} \left(\frac{\alpha}{\overline{\alpha}_d} - 1 \right)^2 dA, \tag{16}$$

where $A_{\tilde{h}}$ is the surface area of a cross-sectional plane at a non-dimensional height of absorber sump $\tilde{h} = z/H$. Figure 6a shows that the homogeneity is lower in the bottom part of the absorber sump, where air spargers are located. This is expected, since near the sparger inlets, the air bubbles are not yet dispersed properly.

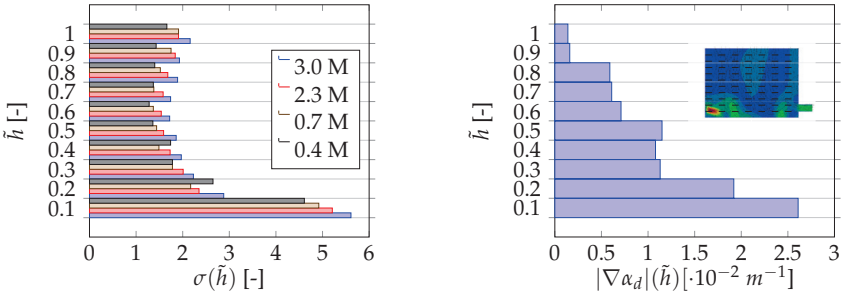

(**a**) (**b**)

Figure 6. In the lower part of the absorber sump, there is a greater discrepancy in terms of homogeneity between meshes. This can be attributed to a higher gradient of all quantities in this area. (**a**) Homogeneity of the dispersed air along the height of the absorber sump for different meshes. (**b**) The gradient magnitude of the dispersed air volume fraction along the height of the absorber sump with the 3 million mesh.

In the lower part of the absorber sump, there is a greater discrepancy in terms of homogeneity between meshes. This can be attributed to a higher gradient of all quantities in this area, as shown in Figure 6b. The gradient of the air volume fraction along the height

of the absorber sump was taken as the average gradient along profiles (inset of Figure 6b). The mesh independence study showed satisfactory results, so all subsequent calculations were carried out with the 2.3×10^6 cell mesh.

4.2. Simulation Results

The results were visualized using open-source ParaView 5.10 software. The parameters of the simulation, such as the air inflow ($\dot{V}_d$), were selected in accordance with the relative air–$CaSO_3$ ratio ($\lambda = 1.5$). This parameter means that the total amount of air blown into the absorber sump is 150% of the air required under stoichiometric conditions for the oxidation of the total produced $CaSO_3$.

The simulation showed that the bulk volume fraction of dispersed air in the absorber sump is equal to $\overline{\alpha}_{d,sim} = 0.010$. Using $\bar{t}_d = \overline{\alpha}_{d,sim} V_{sump} / \dot{V}_d$, we can determine the average retention time of air in the sump with the volume (V_{sump}) and the air inflow ($\dot{V}_d$).

The distribution of air at different heights in the absorber sump is shown in Figure 7. We can observe the air plume at the inlets of the spargers at $\tilde{h} = 0.1$ and the merging of the plumes towards the upper parts of the absorber sump. We also observe a higher air volume fraction at the first recirculation pump on the left side, indicating a higher escape rate of air through the recirculation pump.

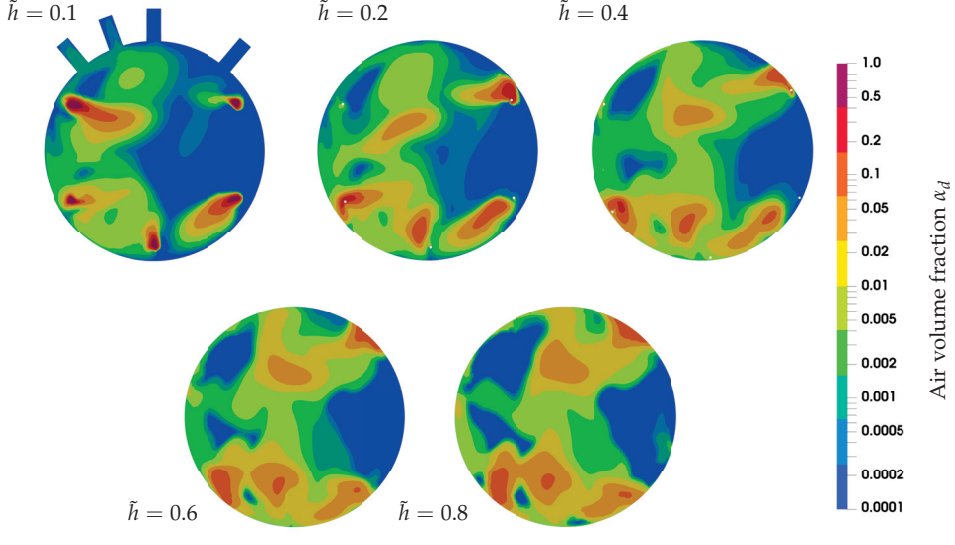

Figure 7. Contours of the air volume fraction at different heights ($\tilde{h} = z/H$) of the absorber sump. We can observe the air plume at the inlets of the spargers and the merging of the plumes towards the upper parts of the absorber.

The 3D contours of the air volume fraction are shown in Figure 8. The escape of the air is also visible here. This phenomenon should be avoided, since the escaped air has a significantly lower retention time than the air moving through the absorber sump. The 3D representation shows the bulk movement of the air.

The population balance model allows us to analyze the local size of the bubbles in the absorber sump. The size groups are distributed as shown in Table 1.

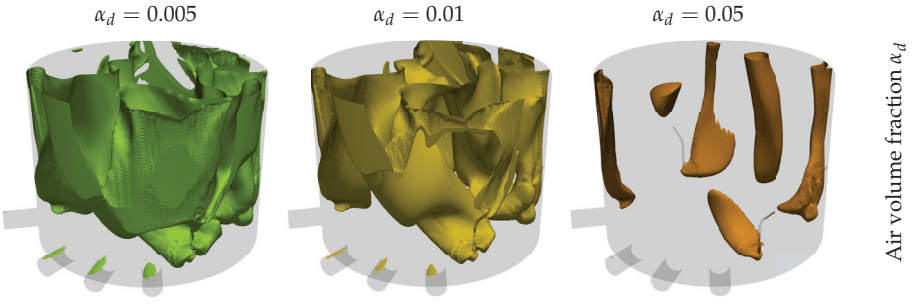

Figure 8. The 3D contours of the air volume fraction show the movement of air through the absorber sump.

Table 1. Dispersed-phase size groups.

Size Group j	Diameter Range (mm)
1	<3
2	3...6
3	6...10
4	10...30
5	30...180

The maximum size of the bubbles (size group 5) was determined by the size of the internal diameter of the air sparger. The minimum size (size group 1) was determined empirically by taking the critical Weber number [1] as

$$We = \frac{d^3 r^2 \rho_c}{\sigma_{st}}, \tag{17}$$

where d is the agitator diameter, r is the rotation speed and σ_{st} is the surface tension. The intermediate sizes are distributed in the lower part of the bubble size spectrum. We can evaluate the average size of the bubbles by calculating the Sauter mean diameter [25], which is defined as

$$d_{32} = \left(\sum_j \frac{f_j}{d_j} \right)^{-1} \tag{18}$$

and equals 7.0 mm for the dispersion of air inside the absorber sump. The local air bubble sizes are shown in Figure 9.

We see that only the smallest bubbles (3...6 mm) escape through the pump outlets, as well as a small amount of the largest bubbles, because of the proximity of the sparger inlet. Immediately after the air enters the absorber sump, a strong reduction in bubble size is observed, which can be attributed to the high shear flow in the area of the agitator and the resulting strong bubble breakup. In the upper part of the absorber sump, the coalescence of the bubbles has a major influence on the bubble size, as a higher proportion of larger bubble size groups can be observed here. The latter is more illustratively shown in Figure 10, where average bubble size (Sauter mean diameter) is plotted against the height of the absorber sump.

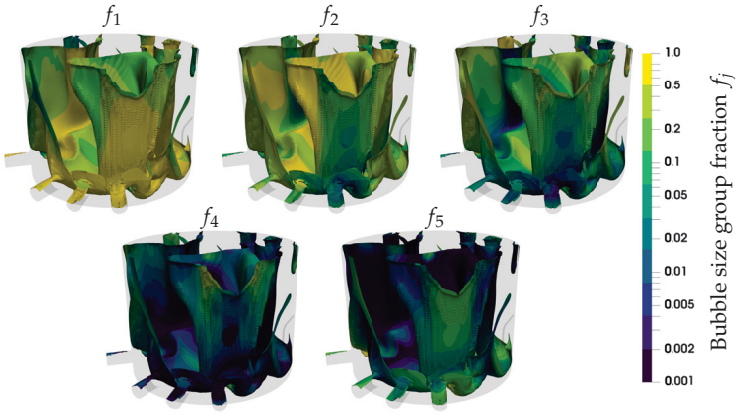

Figure 9. Contours of the bubble size group fractions on the isosurface of the air volume fraction ($\alpha_d = 0.001$). We can see that only the smallest bubbles escape through the pump outlets, as well as a small amount of the largest bubbles, because of the proximity of the sparger inlet. In the upper part, the coalescence of the bubbles has a large influence on the bubble size, as a higher proportion of larger size groups is observed.

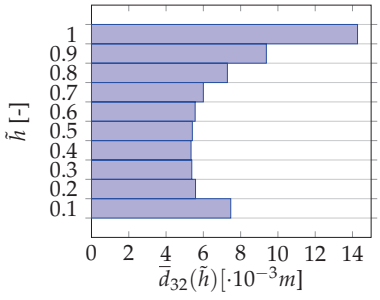

Figure 10. Average bubble Sauter mean diameter along the height of the absorber sump. In the upper part of the absorber sump, the coalescence of the bubbles has a major influence on the bubble size, as a larger average bubble size is observed there.

A more detailed analysis of the retention time of the air bubbles was carried out by analyzing the path lines of the air bubbles moving through the absorber sump. The retention time of a single air bubble traveling along the path line (**s**) was calculated using a path integral as follows:

$$\mathbf{u}(\mathbf{s}) = \frac{d\mathbf{s}}{dt} \rightarrow t_r = \oint_{\mathbf{s}} \frac{d\mathbf{s}}{\mathbf{u}}. \tag{19}$$

By evaluating multiple bubble path lines, a bubble retention time probability function was obtained in non-dimensional form as $\tilde{t}_r = t_r / \bar{t}_r$, as shown in Figure 11. The probability function is expressed by normal distribution as

$$f(\tilde{t}_r) = \frac{1}{\sigma_{dev}\sqrt{2\pi}} \exp\left[-\frac{1}{2}\left(\frac{\tilde{t}_r - \bar{\tilde{t}}_r}{\sigma_{dev}}\right)^2\right], \tag{20}$$

where $\bar{\tilde{t}}_r$ is the average non-dimensional bubble retention time, and σ_{dev} is its standard deviation.

We find that the maximum of the probability function is just below $\tilde{t}_r = 1$, which implies a good agreement with the calculation of the average retention time based on the bulk volume fraction ($\alpha_{d,sim}$). We also observe a relatively large scatter of bubble retention

times due to the wide range of bubble diameters, as shown in Figure 11. Figure 12 shows the air volume fraction contours at the pump outlets of the absorber sump as a result of the flow field induced by recirculation pumps.

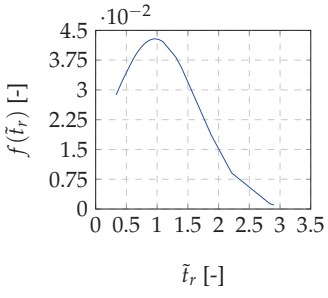

Figure 11. Bubble retention time probability function. We observe that the maximum of the probability function is around $\tilde{t}_r = 1$, which implies a good agreement with the average retention time calculated based on the bulk volume fraction ($\alpha_{d,sim}$). We also observe relatively scattered bubble retention times, which can be attributed to the wide range of bubble diameters.

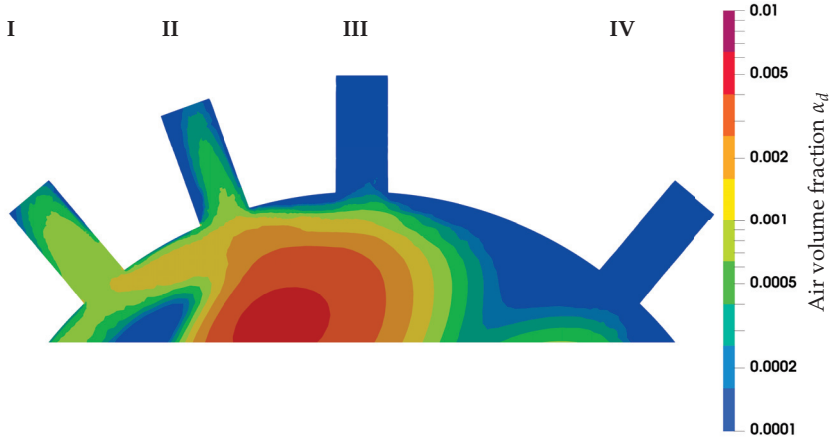

Figure 12. Contours of the air volume fraction at the pump outlets. The largest amount of air escapes through pump outlet no. I. The reason for this lies in the orientation of the agitators, which cause a circular movement of the liquid in the absorber sump, due to which the air plume from the sparger flows directly towards pump outlet no. I.

The total amount of air escaping through the pump outlets accounts for 1.2% of the total air blown into the absorber sump for forced oxidation. Pump outlet no. IV has the least effect on the air distribution in the absorber sump.

4.3. Simulation Results with Lower Linear Momentum Source

An additional operating point was simulated in order to check the FGD absorber sump air dispersion capabilities at lower agitator power. For this simulation, the linear momentum source used to model the influence of the agitators was halved. A comparison of the main process parameters is shown in Table 2.

The bulk air volume fraction is lower in the case of a lower momentum source, which is expected. This is due to the air being pushed further towards the center of the absorber sump in the case of the baseline operating point. This phenomenon is better visualized in Figure 13.

Table 2. Comparison of the FGD absorber sump air dispersion capabilities at two operating points.

	Baseline	Lower Linear Momentum Source
Bulk air vol. frac. ($\overline{\alpha}_d$ [−])	0.010	0.008
Average homogeneity ($\overline{\sigma}$ [−])	2.15	2.50
Sauter mean diam. (d_{32} [mm])	7.0	7.3
Average escaped air (%)	1.2	0.8

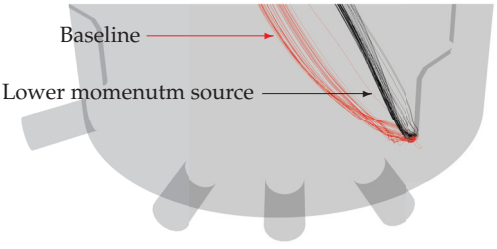

Figure 13. The air is being pushed further towards the center of the absorber sump in the case of the baseline operating point. This is due to a higher fluid velocity caused by a higher linear momentum source from the agitator.

The observed phenomenon also affects the escapement of air, as the lower levels of escape are observed in the case of the lowered momentum source.

The remaining process parameters showed no significant change when switching to a lower linear momentum source. The air dispersion is around 15% more homogeneous in the case of the baseline operating point, although it could not entirely be attributed to a lower momentum source. The Sauter mean diameter shows practically no significant difference when comparing the two operating points. However, in real operation, the lower agitator rotor speed would create a lower shear flow and would decrease the rate of bubble breakup in the agitator area. This observation indicates that it would be beneficial to obtain the agitator blade geometry and model the influence of the agitators with the MRF approach.

Table 3 presents a concise overview of the merits and demerits associated with employing numerical modeling in the context of an FGD absorber sump. It highlights the cost-saving aspect of simulations, allowing for efficient exploration of different configurations and providing detailed insights into sump operations. However, it emphasizes the necessity for rigorous model calibration and validation processes to ensure accuracy, especially given the complexity of mathematical modeling involved.

Table 3. Merits and demerits of numerical modeling.

Merits	Demerits
Cost savings	Need for model calibration
Quick testing of various configurations	Complex mathematical modeling
Detailed insights into sump operation	Extensive data on operating conditions required
Enables assessment of failure scenarios	Need for model validation

5. Conclusions

Numerical simulation of an FGD absorber sump is able to provide insights into the behavior of the continuous and dispersed phases inside the sump. We have demonstrated that the retention time of the air can be determined in two ways: based on the average volume fraction of the dispersed phase in the sump and by analyzing the path lines of the individual liquid elements (bubbles) leaving the sparger. We found that the retention time deviation of individual bubbles can be large, which is due to a large bubble diameter range. Finally, we analyzed the escape of air through the outlets of the recirculation pumps. We found that the total amount of escaping air is equal to 1.2% of the total air blown into the

absorber sump. The escaping air consists mainly of bubbles smaller than 6 mm and is not necessarily lost. On the way through the recirculation pipeline, a transfer of oxygen into the surrounding liquid continues to take place. However this phenomenon should be avoided, since the escaped air has a significantly lower retention time.

A comparison between the two operating points showed that lowering the magnitude of the linear momentum source used for the modeling of agitators results in lower homogeneity and lower air retention time in the absorber sump. However, the Sauter mean diameter of the bubbles changes little between the two operating points. This points to the fact that obtaining the exact geometry of the agitators and modeling their influence with the MRF approach are crucial for the detailed optimization of FGD absorber sumps.

Given the results of the numerical model, optimization of the air spargers can be considered. We observed that the lower part of the absorber sump contains a non-negligible proportion of bubbles larger than 30 mm. Optimization of the air spargers must aim to reduce the bubble diameter at the outlet of the air sparger. Optimization should be carried out in such a way that the pressure drop of the air sparger increases only minimally. The developed numerical model presented in this paper is able to facilitate such optimization and help design the optimal sump.

The technology under consideration requires a flow rate of air blown into the absorber sump with a relative air–$CaSO_3$ ratio of $\lambda = 1.5$. However, older technology often operates with a relative ratio equal to $\lambda = 2.5$. In order to fulfill the tender requirements, air turbo-blowers with corresponding motor drives are installed, which enable operation with $\lambda = 2.5$. By controlling the inlet and diffuser blades of the turbo-blower, the operating point can be lowered to $\lambda = 1.5$, resulting in a reduction in power consumption of 33%.

The distribution of the dispersed phase and its homogeneity were also determined by numerical calculations. It is important to emphasize that we only modeled the influence of the agitators as a linear momentum source and therefore did not consider the exact geometry of the agitator blades for which the MRF approach would be used. Consequently, the magnitude of the shear stress in the lower part of the absorber sump is lower than it would be if the actual geometry of the agitator blades and the MRF approach were used. In real operation, this increases the proportion of the smallest bubbles and, consequently, the potential escape of air through the outlets of the recirculation pumps. Modeling the agitators as a linear momentum source is a good solution in this case, as obtaining the exact geometry of the agitator blades can be challenging.

The numerical analysis carried out in this study opens up many possibilities for further work. The next stage of numerical modeling of the absorber sump involves the introduction of models for oxygen absorption and the calculation of the mass transfer coefficient. This would allow us to directly determine the amount of oxygen absorbed. By introducing chemical reaction modeling, we could gain insight into the actual amount of oxygen used for forced oxidation. Similar to the absorption process, chemical reactions (oxidation) also take time. Modern and advanced CFD methods already allow for the modeling of chemical reactions, which enables a more precise optimization of the absorber sump and provides more accurate insights into the physical and chemical processes that take place in the absorber sump.

Author Contributions: Conceptualization, J.R.; methodology, N.V.; software, N.V.; validation, N.V.; formal analysis, N.V.; investigation, N.V.; resources, N.V.; data curation, N.V.; writing—original draft preparation, N.V.; writing—review and editing, J.R.; visualization, N.V.; supervision, J.R.; project administration, J.R.; funding acquisition, J.R. All authors have read and agreed to the published version of the manuscript.

Funding: This research was funded by Slovenian research and Innovation Agency (ARIS) grant number P2-0196.

Institutional Review Board Statement: Not applicable.

Data Availability Statement: The data presented in this study are available on request from the corresponding author. The data are not publicly available due to large file size.

Conflicts of Interest: The authors declare no conflict of interest.

Abbreviations

The following abbreviations are used in this manuscript:

FGD	Flue gas desulfurization
CFD	Computational fluid dynamics
MRF	Moving reference frame
CAD	Computer-aided design
URANS	Unsteady Reynolds-averaged Navier–Stokes

Nomenclature

The following variables and subscripts are used in this manuscript:

Variable	Meaning	Subscipt	Meaning
α	volume fraction	φ	phase
ρ	density	α	mass
t	time	m	momentum
$\mathbf{u}$	velocity vector	j	size group
σ	bubble size deviation	d	dispersed phase
p	pressure	x, y	x and y direction
$\mathbf{T}$	stress tensor	out	outlet
$\mathbf{g}$	gravitational vector	air	air at the inlet
$\mathbf{m}$	momentum vector	rel	relative
$\mathbf{s}_m$	momentum source vector	i	cell
V	volume	D	drag
μ	dynamic viscosity	p	particle
$\mathbf{D}$	deformation tensor	c	continuous phase
$\mathbf{I}$	identity matrix	L	lift
N	number concentration	TD	turbulent dispersion
H	source/sink of bubbles	t	turbulent
f	proportion of the individual size group of bubbles	VM	virtual mass
n	total number of size groups	WL	wall lubrication
x, y, z	directions	$\|\|$	tangential
H	height of the absorber sump	rgh	without the hydrostatic contribution
$\dot{V}$	flow rate	sim	simulation
F	force magnitude	r	retention
$\mathbf{F}$	force vector	sp	sparger
C	submodel coefficient	q	type of force submodel
d	diameter		
Re	Reynolds number		
ν	kinematic viscosity		
Sc	Schmidt number		
$\mathbf{n}$	normal vector		
σ_{dev}	standard deviation		
$\tilde{h}$	non-dimensional height		
A	cross-sectional area		
λ	relative air–$CaSO_3$ ratio		
We	Weber number		
r	rotation speed		
σ_{st}	surface tension		
$\mathbf{s}$	pathline vector		
Co	Courant number		
D	Diameter		

References

1. Mersmann, A.; Kind, M.; Stichlmair, J. *Thermal Separation Technology*; Springer: Berlin/Heidelberg, Germany, 2011. [CrossRef]
2. Córdoba, P. Status of Flue Gas Desulphurisation (FGD) Systems from Coal-Fired Power Plants: Overview of the Physic-Chemical Control Processes of Wet Limestone FGDs. *Fuel* **2015**, *144*, 274–286. [CrossRef]
3. de Salazar, R.O.; Ollero, P.; Cabanillas, A.; Otero-Ruiz, J.; Salvador, L. Flue Gas Desulphurization in Circulating Fluidized Beds. *Energies* **2019**, *12*, 3908. [CrossRef]
4. Srivastava, R.K.; Jozewicz, W. Flue Gas Desulfurization: The State of the Art. *J. Air Waste Manag. Assoc.* **2001**, *51*, 1676–1688. [CrossRef] [PubMed]
5. Poullikkas, A. Review of Design, Operating, and Financial Considerations in Flue Gas Desulfurization Systems. *Energy Technol. Policy* **2015**, *2*, 92–103. [CrossRef]
6. Tesárek, P.; Drchalová, J.; Kolísko, J.; Rovnaníková, P.; Černý, R. Flue Gas Desulfurization Gypsum: Study of Basic Mechanical, Hydric and Thermal Properties. *Constr. Build. Mater.* **2007**, *21*, 1500–1509. [CrossRef]
7. Jian, S.; Yang, X.; Gao, W.; Li, B.; Gao, X.; Huang, W.; Tan, H.; Lei, Y. Study on Performance and Function Mechanisms of Whisker Modified Flue Gas Desulfurization (FGD) Gypsum. *Constr. Build. Mater.* **2021**, *301*, 124341. [CrossRef]
8. Navarrete, I.; Vargas, F.; Martinez, P.; Paul, A.; Lopez, M. Flue Gas Desulfurization (FGD) Fly Ash as a Sustainable, Safe Alternative for Cement-Based Materials. *J. Clean. Prod.* **2021**, *283*, 124646. [CrossRef]
9. Arif, A.; Stephen, C.; Branken, D.; Everson, R.; Neomagus, H.; Piketh, S. Modeling Wet Flue Gas Desulfurization. In Proceedings of the Conference of the National Association for Clean Air (NACA 2015), Bloemfontein, South Africa, 1–2 October 2015.
10. Marocco, L.; Inzoli, F. Multiphase Euler–Lagrange CFD Simulation Applied to Wet Flue Gas Desulphurisation Technology. *Int. J. Multiph. Flow* **2009**, *35*, 185–194. [CrossRef]
11. Qu, J.; Qi, N.; Li, Z.; Zhang, K.; Wang, P.; Li, L. Mass Transfer Process Intensification for SO_2 Absorption in a Commercial-Scale Wet Flue Gas Desulfurization Scrubber. *Chem. Eng. Process. Process. Intensif.* **2021**, *166*, 108478. [CrossRef]
12. Qu, J.; Qi, N.; Zhang, K.; Li, L.; Wang, P. Wet Flue Gas Desulfurization Performance of 330 MW Coal-Fired Power Unit Based on Computational Fluid Dynamics Region Identification of Flow Pattern and Transfer Process. *Chin. J. Chem. Eng.* **2021**, *29*, 13–26. [CrossRef]
13. Xiang, L.; Sun, X.; Wei, X.; Wang, G.; Boczkaj, G.; Yoon, J.Y.; Chen, S. Numerical Investigation on Distribution Characteristics of Oxidation Air in a Lime Slurry Desulfurization System with Rotary Jet Agitators. *Chem. Eng. Process. Process. Intensif.* **2021**, *163*, 108372. [CrossRef]
14. Kallinikos, L.; Farsari, E.; Spartinos, D.; Papayannakos, N. Simulation of the Operation of an Industrial Wet Flue Gas Desulfurization System. *Fuel Process. Technol.* **2010**, *91*, 1794–1802. [CrossRef]
15. Gómez, A.; Fueyo, N.; Tomás, A. Detailed Modelling of a Flue-Gas Desulfurisation Plant. *Comput. Chem. Eng.* **2007**, *31*, 1419–1431. [CrossRef]
16. De Blasio, C.; Salierno, G.; Sinatra, D.; Cassanello, M. Modeling of Limestone Dissolution for Flue Gas Desulfurization with Novel Implications. *Energies* **2020**, *13*, 6164. [CrossRef]
17. Höhne, T.; Mamedov, T. CFD Simulation of Aeration and Mixing Processes in a Full-Scale Oxidation Ditch. *Energies* **2020**, *13*, 1633. [CrossRef]
18. Lerotholi, L.; Everson, R.C.; Koech, L.; Neomagus, H.W.J.P.; Rutto, H.L.; Branken, D.; Hattingh, B.B.; Sukdeo, P. Semi-Dry Flue Gas Desulphurization in Spray Towers: A Critical Review of Applicable Models for Computational Fluid Dynamics Analysis. *Clean Technol. Environ. Policy* **2022**, *24*, 2011–2060. [CrossRef]
19. Zhang, G.; Li, Y.; Jin, Z.; Dykas, S.; Cai, X. A Novel Carbon Dioxide Capture Technology (CCT) Based on Non-Equilibrium Condensation Characteristics: Numerical Modelling, Nozzle Design and Structure Optimization. *Energy* **2024**, *286*, 129603. [CrossRef]
20. Zhang, G.; Yang, Y.; Chen, J.; Jin, Z.; Dykas, S. Numerical Study of Heterogeneous Condensation in the de Laval Nozzle to Guide the Compressor Performance Optimization in a Compressed Air Energy Storage System. *Appl. Energy* **2024**, *356*, 122361. [CrossRef]
21. Bricl, M. Cleaning of Flue Gases in Thermal Power Plants. *J. Energy Technol.* **2016**, *9*, 45.
22. Weller, H.G.; Tabor, G.; Jasak, H.; Fureby, C. A Tensorial Approach to Computational Continuum Mechanics Using Object-Oriented Techniques. *Comput. Phys.* **1998**, *12*, 620–631. [CrossRef]
23. Sato, Y.; Sadatomi, M.; Sekoguchi, K. Momentum and Heat Transfer in Two-Phase Bubble Flow—I. Theory. *Int. J. Multiph. Flow* **1981**, *7*, 167–177. [CrossRef]
24. Launder, B.; Spalding, D. The Numerical Computation of Turbulent Flows. *Comput. Methods Appl. Mech. Eng.* **1974**, *3*, 269–289. [CrossRef]
25. Lehnigk, R.; Bainbridge, W.; Liao, Y.; Lucas, D.; Niemi, T.; Peltola, J.; Schlegel, F. An Open-source Population Balance Modeling Framework for the Simulation of Polydisperse Multiphase Flows. *Aiche J.* **2022**, *68*, e17539. [CrossRef]
26. Silva, L.; Lage, P. Development and Implementation of a Polydispersed Multiphase Flow Model in OpenFOAM. *Comput. Chem. Eng.* **2011**, *35*, 2653–2666. [CrossRef]
27. Tomiyama, A.; Tamai, H.; Zun, I.; Hosokawa, S. Transverse Migration of Single Bubbles in Simple Shear Flows. *Chem. Eng. Sci.* **2002**, *57*, 1849–1858. [CrossRef]

28. Burns, A.; Frank, T.; Ian, H.; Shi, J.M. The Favre Averaged Drag Model for Turbulent Dispersion in Eulerian Multi-Phase Flows. In Proceedings of the Conference on Multiphase Flow, ICMF2004, Yokohama, Japan, 30 May–4 June 2004; Volume 392.
29. Antal, S.; Lahey, R.; Flaherty, J. Analysis of Phase Distribution in Fully Developed Laminar Bubbly Two-Phase Flow. *Int. J. Multiph. Flow* **1991**, *17*, 635–652. [CrossRef]

fluids

MDPI

Article

The Influence of Two-Dimensional Temperature Modulation on Floating Droplet Dynamics

Alexander Nepomnyashchy and Ilya Simanovskii *

Department of Mathematics, Technion-Israel Institute of Technology, Haifa 32000, Israel; nepom@technion.ac.il
* Correspondence: yuri11@inter.net.il; Tel.: +972-544-378318

Abstract: We investigate the dynamics and instabilities of a droplet that floats on a liquid substrate. The substrate is cooled from below. In the framework of the slender droplet approximation and the precursor model, the problem is studied numerically. Oscillatory and stationary regimes of thermocapillary convection have been observed. The influence of a two-dimensional spatial inhomogeneity of temperature on the droplet dynamics is investigated. The two-dimensional spatial temperature inhomogeneity can suppress oscillations, changing the droplet's shape. In a definite region of parameters, the two-dimensional spatial modulation can lead to the excitation of periodic oscillations. The influence of the Biot number on the shape of the droplets is studied.

Keywords: interfacial phenomena; oscillatory instabilities; droplets

Citation: Nepomnyashchy, A.; Simanovskii, I. The Influence of Two-Dimensional Temperature Modulation on Floating Droplet Dynamics. *Fluids* **2024**, *9*, 6. https://doi.org/10.3390/fluids9010006

Academic Editors: Manolis Gavaises and D. Andrew S. Rees

Received: 20 October 2023
Revised: 13 December 2023
Accepted: 21 December 2023
Published: 25 December 2023

1. Introduction

The motion of a viscous liquid droplet on a *solid* substrate, which contradicts the nonslip condition, has been studied extensively during the past few decades [1,2]. The exploration of the dynamic phenomena (specifically, the difference between the static and dynamic contact angles and the existence of the dynamic contact angle hysteresis) led to essential progress in the understanding of interfacial phenomena.

Droplets on a *liquid* substrate ("liquid lenses") are very important in various branches of engineering, including microfluidics [3], chemical engineering [4], environment protection [5], etc. Nevertheless, their dynamics has still attracted less attention.

The dynamics and instabilities of nonisothermal floating droplets are of special interest. Oscillatory convective motions, generated by the thermocapillary effect and buoyancy, have been observed in some experiments [6–8]. Recently, the influence of the homogeneous heating or cooling of the liquid substrate on the stability of a thin floating droplet under microgravity conditions has been studied in [9]. A number of instability modes leading to droplet oscillations, droplet decomposition or the substrate layer's rupture were revealed. The observed instabilities of droplets are reminiscent of longwave deformational instabilities in two-layer films [10].

In various applications (e.g., in microfluidic devices), it can be necessary to move a droplet in a controllable way. The simplest way to influence the dynamics of a droplet is a temperature inhomogeneity that creates a thermocapillary motion. Typically, the droplet is advected by the thermocapillary flow in a liquid layer in the direction opposite to the surface temperature gradient, but there is a contribution to the droplet velocity due to the thermocapillary stresses on the droplet interfaces and due to the shear in the substrate liquid [11]. The direction of motion can be different depending on the details of the generated convective flow [6] and the droplet shape [12]. Moreover, the direction of the flow can change periodically with time due to the laser heating of a droplet [6,7]. Experiments on droplet evaporation where the buoyancy–thermocapillary convection caused by the evaporative cooling creates hydrothermal waves [8] and leads to the droplet disintegration [13] can also be mentioned.

In the present work, the dynamics of a droplet on a liquid substrate *cooled from below* under the action of *a two-dimensional* spatial temperature modulation is studied. The results of numerical simulations carried out in the framework of the longwave approximation and the precursor model are presented. The novelty of the present investigation is as follows. We show that a two-dimensional spatial temperature modulation can significantly change the shape of the droplet and oscillation features. Specifically, the two-dimensional spatial inhomogeneity of the temperature can *suppress* oscillations, leading to the formation of steady droplets. In a definite region of parameters, the two-dimensional spatial modulation can lead to the *excitation* of the specific type of periodic oscillations. For the first time, the influence of the Biot number on the shape of the droplet is studied.

The structure of this paper is as follows. We give the formulation of the problem in Section 2. The action of the two-dimensional spatial modulation of temperature on nonlinear stationary droplets is considered in Section 3. Droplet oscillations generated by an oscillatory thermocapillary instability in the presence of two-dimensional temperature modulation are described in Section 4. The influence of gravity on the droplet dynamics is discussed in Section 5. The influence of the Biot number on the shape of droplets is considered in Section 6. Some concluding remarks are presented in Section 7.

2. Formulation of the Problem

We consider a droplet of liquid 2 that floats on the layer of liquid 1, and both are in contact with the gas phase 3 (see Figure 1). Later on, we do not consider any processes in fluid 3: at the gas/liquid interface, the viscous stresses are neglected. The heat transfer is described using the heat exchange coefficient q. The mth fluid has density ρ_m, dynamic viscosity η_m and thermal conductivity κ_m, $m = 1, 2$.

The contact angles on the triple line surrounding the droplet are determined by the balance of interfacial tensions σ_{12}, σ_{23} and σ_{13} between the corresponding fluids according to the Neumann triangle construction [14]. The droplet exists in two cases: (i) when the spreading coefficient $S = \sigma_{13} - \sigma_{12} - \sigma_{23} < 0$ (*partial wetting*); (ii) when $S > 0$ but only a small part of fluid 2 is spread between fluids 1 and 3 forming an ultrathin film (*pseudo-partial wetting*) due to the attractive interaction of those fluids through the film of fluid 2 (positive *Hamaker constant* A).

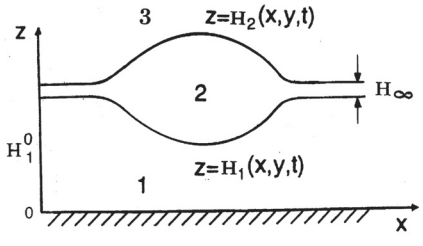

Figure 1. Geometric configuration of the region and coordinate axes.

In the present paper, we consider the thermocapillary convection in a floating droplet. The temperature of the gas phase is $T_g = const$, and the temperature of the solid substrate is a function of horizontal coordinates, $T_s = T_s(x, y)$. Assuming that the temperature differences in the system are not too large, we disregard the dependence of liquid parameters on the temperature, with only one exception: because we are interested in the investigation of the thermocapillary convection, we take into account the thermocapillary stresses proportional to derivatives of the interfacial tensions with respect to the temperature. The interfacial tension coefficients on the lower and upper surfaces of the droplet, $\sigma_1 \equiv \sigma_{12}$ and $\sigma_2 \equiv \sigma_{23}$, are assumed to be linear functions of temperature T: $\sigma_1 = \sigma_1^0 - \alpha_1 T$ and $\sigma_2 = \sigma_2^0 - \alpha_2 T$, where α_1 and α_2 are constants. It is assumed that $|\alpha_1 T| \ll \sigma_1$ and $|\alpha_2 T| \ll \sigma_2$; therefore, we disregard that dependence in the relations that contain the inter-

facial tensions as a whole, i.e., in the stress balances on the triple line and in the expressions for Laplace pressures.

The description of the temporal evolution of the triple line surrounding the droplet is technically difficult (see [15]). In [16], *the precursor model* was suggested for the description of a floating droplet: the interface between fluids 1 and 3 outside the droplet is replaced by an ultrathin precursor layer of fluid 2 (see Figure 1). The latter model describes the droplet on the liquid substrate as a *two-layer film*. The same equations are used in the whole region, but outside the droplet, where the top layer is ultrathin, the corresponding *disjoining pressure* is taken into account. Let us emphasize that the latter approach can be applied both in the case of pseudo-partial wetting and partial wetting, because macroscopically both cases are identical. In the present paper, we apply that approach for the description of the dynamics of a nonisothermal floating droplet.

Far from the droplet, the equilibrium thickness of layer 1 is H_1^0, and the thickness of the precursor film is H_∞. The deformable interfaces are described by equations $z = H_1(x, y, t)$ and $z = H_2(x, y, t)$. The gravity acceleration is g.

Later on, we consider a *slender* droplet, i.e., where the slopes of both droplet's interfaces are small. Also, we assume that the characteristic horizontal scale of the interface deformations is large as compared to the characteristic vertical size of the droplet and the substrate. Those assumptions allow us to apply the mathematical model governing the longwave dynamics of nonisothermal liquid layers that has been derived using the lubrication approximation [17] (see also [10,18,19]). In the framework of the longwave approach, the shapes of the interfaces $z = H_1$ and $z = H_2$ depend on the scaled horizontal coordinates $X = \epsilon x$ and $Y = \epsilon y$, $\epsilon \ll 1$, rather than on x and y. Also, it is assumed that they depend on the scaled time variable $\tau = \epsilon^2 t$. A comprehensive description of the longwave approach can be found in the review paper [20].

We present the problem in the nondimensional form using the equilibrium thickness of the lower layer, H_1^0, as the vertical length scale. The choice of the horizontal scale L^* is arbitrary [19]. We choose

$$\tau^* = \frac{\eta_1 (L^*)^4}{\sigma_1^0 (H_1^0)^3} \tag{1}$$

as a time scale and

$$p^* = \frac{\sigma_1^0 H_1^0}{(L^*)^2} \tag{2}$$

as a pressure scale.

The nondimensional parameters of the problem are as follows. We define the *local* Marangoni number as

$$M(X, Y) = \frac{\alpha_1 (T_s(X, Y) - T_g)}{\sigma_1^0} \left(\frac{L^*}{H_1^0} \right)^2, \tag{3}$$

which is *a function* of X and Y rather than a number. Also, we shall use the *mean* Marangoni number

$$\bar{M} = \frac{\alpha_1 (\bar{T}_s - T_g)}{\sigma_1^0} \left(\frac{L^*}{H_1^0} \right)^2, \tag{4}$$

where $\bar{T}_s$ is a characteristic mean temperature of the substrate.

The other nondimensional parameters of the problem are defined as follows:

$$Bi = \frac{q H_1^0}{\kappa_2} \tag{5}$$

is the Biot number, $\eta = \eta_1/\eta_2$, $\kappa = \kappa_1/\kappa_2$, $\sigma = \sigma_2^0/\sigma_1^0$, $\alpha = \alpha_2/\alpha_1$ and $\rho = \rho_2/\rho_1$.

In the framework of the lubrication approximation, the velocity and pressure fields are *enslaved* to the deformations of interfaces. The temporal evolution of those deformations is governed by the volume conservation equations [18]:

$$h_{1\tau} + \nabla \cdot \mathbf{q}_1 = 0,\ h_{2\tau} + \nabla \cdot \mathbf{q}_2 = 0, \tag{6}$$

$$\mathbf{q}_1 = f_{11}\nabla p_1 + f_{12}\nabla p_2 + \mathbf{q}_1^T,\ \mathbf{q}_2 = f_{21}\nabla p_1 + f_{22}\nabla p_2 + \mathbf{q}_2^T, \tag{7}$$

where $h_j = H_j/H_1^0$, $p_j = P_j/p^*$ and $j = 1, 2$.

The expressions for pressures,

$$p_1 = -\nabla^2 h_1 - \sigma\nabla^2 h_2 + w_1(h_1, h_2), \tag{8}$$

$$p_2 = -\sigma\nabla^2 h_2 + w_2(h_1, h_2), \tag{9}$$

include the contributions of the Laplacian pressures, hydrostatic pressures and disjoining pressures. Because the thickness of liquid layer 1 is always macroscopic, we can neglect the contribution of w_1. In layer 2, we apply the following expression for the disjoining pressure:

$$w_2 = \frac{a}{(h_2 - h_1)^3}\left[1 - \left(\frac{h_\infty}{h_2 - h_1}\right)^3\right], \tag{10}$$

where a is the nondimensional Hamaker constant, which is related to the dimensional Hamaker constant A as follows:

$$a = \frac{A(L^*)^2}{6\pi\sigma_1^0(H_1^0)^4}, \tag{11}$$

and $h_\infty = H_\infty/H_1^0$ (for details, see [16,21]).

The expressions for mobilities f_{ij}, $i, j = 1, 2$, are

$$f_{11} = -\frac{1}{3}h_1^3,\ f_{12} = -\frac{1}{2}h_1^2(h_2 - h_1),$$

$$f_{21} = \frac{1}{6}h_1^3 - \frac{1}{2}h_1^2 h_2,\ f_{22} = (h_2 - h_1)\left[h_1^2\left(\frac{1}{2} - \frac{\eta}{3}\right) + h_1 h_2\left(-1 + \frac{2\eta}{3}\right) - \frac{\eta}{3}h_2^2\right].$$

The nondimensional expressions for the rates of the thermocapillary flows are

$$\mathbf{q}_1^T = -\frac{h_1^2}{2}\nabla\{M[1 + d(\alpha\kappa - Bih_1)]\}, \tag{12}$$

$$\mathbf{q}_2^T = -\frac{\eta\alpha\kappa}{2}h_2^2\nabla(Md) +$$

$$\frac{(2h_2 - h_1)h_1}{2}\nabla\{M[-1 + Bih_1 d - \alpha\kappa(1 - \eta)d]\}, \tag{13}$$

where

$$d = [\kappa + Bi(1 - \kappa)h_1 + Bi\kappa h_2]^{-1}. \tag{14}$$

Note that in the absence of gravity, a liquid layer with a deformable interface is subject to a monotonic Marangoni instability for arbitrary $\bar{M} > 0$, i.e., by any heating from below [22]. That instability is not saturable, and it leads to the rupture of the substrate layer. The temperature disturbance caused by the droplet acts as "a seed" of instability. Therefore, in the presence of the temperature gradient, one can expect the existence of a stable configuration containing a droplet on a layer flat on the infinity only if $\bar{M} < 0$, i.e., by cooling from below.

In the present work, we consider nonlinear regimes of the thermocapillary convection in the case of a spatially periodic temperature modulation of the local Marangoni number,

$$M(X,Y) = \bar{M}\left(1 + \delta_X \sin\frac{2\pi X}{L} + \delta_Y \sin\frac{2\pi Y}{L}\right) = \bar{M} - \Delta_X \sin\frac{2\pi X}{L} - \Delta_Y \sin\frac{2\pi Y}{L}, \quad (15)$$

where $\bar{M} < 0$, $\delta_X \geq 0$, $\Delta_X = |\bar{M}|\delta_X \geq 0$, $\delta_Y \geq 0$ and $\Delta_Y = |\bar{M}|\delta_Y \geq 0$. Note that the change in the sign of δ_X or δ_Y is obtained by a translation $X \to X + L/2$ or $Y \to Y + L/2$, correspondingly. Because of the symmetry of the problem with respect to the transformations $X \to Y$ and $Y \to X$, it is sufficient to consider the case $\delta_Y \geq \delta_X$.

The problem governed by Equations (6)–(10) and (12)–(15) has been solved numerically with some initial conditions. The evolution equations were discretized using central differences for spatial derivatives and solved using an explicit scheme. Periodic boundary conditions have been applied on the boundaries of the computational region $L \times L$.

The computations have been performed in the region $L \times L = 240 \times 240$ using the grid 80×80. Some additional simulations on the grids 100×100 and 120×120 did not reveal any qualitative changes.

Computations have been performed for the system of fluorinert FC70 (liquid 1) and silicon oil 10 (liquid 2). This system was used in microgravity experiments (see, e.g., [23]). We applied the following set of liquid parameters that was formerly used in simulations of the thermocapillary instability in two-layer systems [19]: $\eta = 3.04$, $\kappa = 0.522$, $\alpha = 2$, $\rho = 0.482$, $\sigma = 2.6$. $h_- = 1.02$, $h_+ = 1$, $R = 60$, $h_\infty = 0.01$, $Bo = 0$ and $Bi = 20$. The value of a_2 is chosen equal to 3×10^{-6} (see [9]).

3. Manipulation by a Stationary Droplet

In this section, we describe the shape of a stationary droplet in the limit of large τ.

3.1. The Case of Axisymmetric Initial Conditions

It is known that in the absence of gravity and the thermocapillary effect, both interfaces of an equilibrium droplet are spherical caps. The exact formulas that follow from the balance of interfacial tensions on the triple line are given in [24]. In the longwave limit, these interfaces become paraboloids with constant values of $d^2h_1/dr^2 > 0$ and $d^2h_2/dr^2 < 0$, where r is the radial coordinate. When a temperature gradient across the substrate layer is applied, the temperature on both droplet interfaces becomes inhomogeneous; therefore, the thermocapillary convection is developed both in the droplet and in the substrate. If the initial conditions with an axisymmetric drop shape are applied and $\Delta_X = \Delta_Y = 0$, for sufficiently small values of $|\bar{M}|$ the droplet is stationary and axisymmetric in the limit $\tau \to \infty$. The shapes of isolines for $h_1(X,Y)$ and $h_2(X,Y)$, which are determined by equations $\mathbf{q}_1 = 0$ and $\mathbf{q}_2 = 0$, look perfectly circular, despite the violation of the rotational symmetry by the periodic boundary conditions [9]. Note that in contradistinction to the case of an isothermal droplet, both d^2h_1/dr^2 and d^2h_2/dr^2 are negative, except the vicinity of the triple line. Indeed, when the terms $\mathbf{q}_1^T$ and $\mathbf{q}_2^T$ caused by the inhomogeneities of the interfacial temperatures are dominant in the expressions (7) for flow rates, the system tends to minimize those inhomogeneities. The temperature of the interface between the substrate and the droplet is nearly constant when the ratio $h_2(r)/h_1(r)$ is nearly constant.

Let us take the steady round droplet [9] ($\bar{M} = -2$; $\Delta_X = \Delta_Y = 0$) as the initial condition and consider its evolution under the action of two-dimensional temperature modulation ($\bar{M} = -2$; $\Delta_X = \Delta_Y = 0.1$). In the case $\Delta_X = \Delta_Y \equiv \Delta$, the Marangoni number field (15) can be written as

$$M(X,Y) = \bar{M} + \tilde{M}(X,Y),\ \tilde{M}(X,Y) = -2\Delta \sin\frac{\pi(X+Y)}{L}\cos\frac{\pi(X-Y)}{L}.$$

Thus, the substrate temperature inhomogeneity has the shape of a square pattern. The function $\tilde{M}(X,Y)$ is symmetric with respect to axes $X = L/4$, $X = 3L/4$, $Y = L/4$ and

$Y = 3L/4$. It changes its sign on the lines $Y = L - X$ and $Y = X \pm L/2$. Near the diagonal $Y = X$, it is negative for $X < L/2$ and positive for $X > L/2$. Under the action of the thermocapillary stresses, the liquid in the droplet moves slowly towards the region $X < L/2, Y < L/2$, changing its shape and height. The intermediate stages of the evolution of the initially round droplet are presented in Figure 2. A change in the droplet's shape is visible between Figure 2a,c. At $\tau \geq 200{,}000$, the equilibration takes place. Finally, we obtain the steady droplet with the maximum, shifted along the axis $Y = X$ to the region $X < L/2$, where the local value of $|M|$ is higher (i.e., into the cooler part of the region). Figure 3 shows a snapshot of the fields of (a) $h_2(X, Y, \tau)$ and (b) $h_1(X, Y, \tau)$ at the equilibrium stage. The droplet is not round anymore, but it keeps the symmetry with respect to the axis $Y = X$.

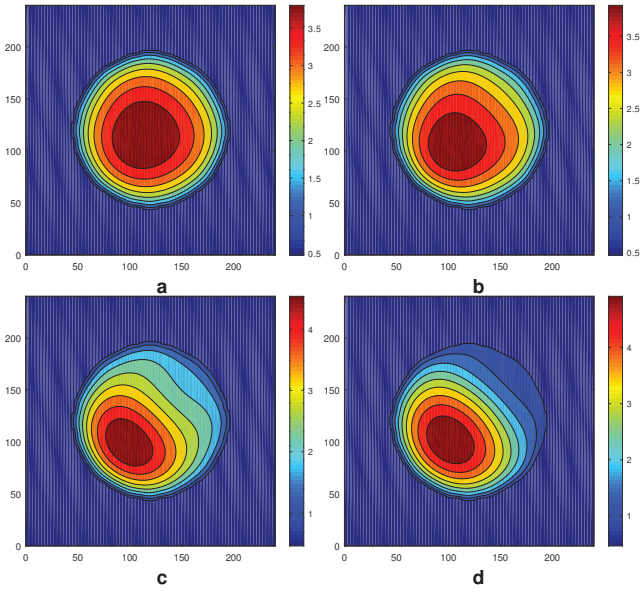

Figure 2. The fields of $h_2(X, Y, \tau)$ for $\bar{M} = -2$, $\Delta_X = \Delta_Y = 0.1$, $Bo = 0$ and $Bi = 20$: (**a**) $\tau = 750$; (**b**) $\tau = 1500$; (**c**) $\tau = 4500$; (**d**) τ = 10,000.

Let us consider now the action of an increased temperature modulation, $\Delta_X = \Delta_Y = 0.5$, on the initially round steady droplet. The intermediate states of the evolution of the initially round droplet under the action of two-dimensional temperature modulation are presented in Figure 4. As in the previous case, in the early stages the liquid in the droplet moves to the left bottom part of the computational region (Figure 4a,b). A visible change in the droplet's shape takes place between Figure 4a,c. One can see the division of the droplet and the creation of two satellites that are symmetric with respect to the axes $Y = X$ (see Figure 4e,f). With an increase in time (at $\tau \geq 100{,}000$), the further evolution of the droplet and the equilibration takes place. Finally, we obtain a steady droplet with the maximum significantly shifted along the axis $Y = X$ to the region $X < L/2$. A snapshot of the fields of (a) $h_2(X, Y, \tau)$ and (b) $h_1(X, Y, \tau)$ at the equilibrium stage is shown in Figure 5 and the corresponding shapes of interfaces are presented in Figure 6. The droplet keeps the symmetry with respect to the axis $Y = X$. One can see that the droplet becomes much shorter in the direction of the axis $Y = X$ (see Figure 5). Let us note that the droplet is significantly higher than that obtained in the case $\Delta_X = \Delta_Y = 0.1$ (cf. Figures 3 and 5).

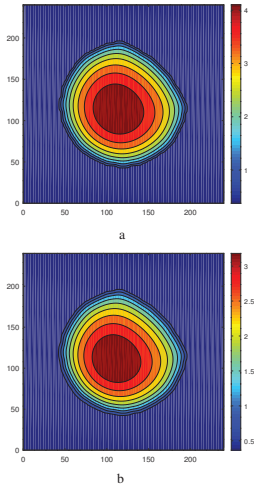

Figure 3. A snapshot of the fields of $h_2(X, Y, \tau)$ and $h_1(X, Y, \tau)$ for $\bar{M} = -2$, $\Delta_X = \Delta_Y = 0.1$, $Bo = 0$, $Bi = 20$ and $\tau = 1 \times 10^6$.

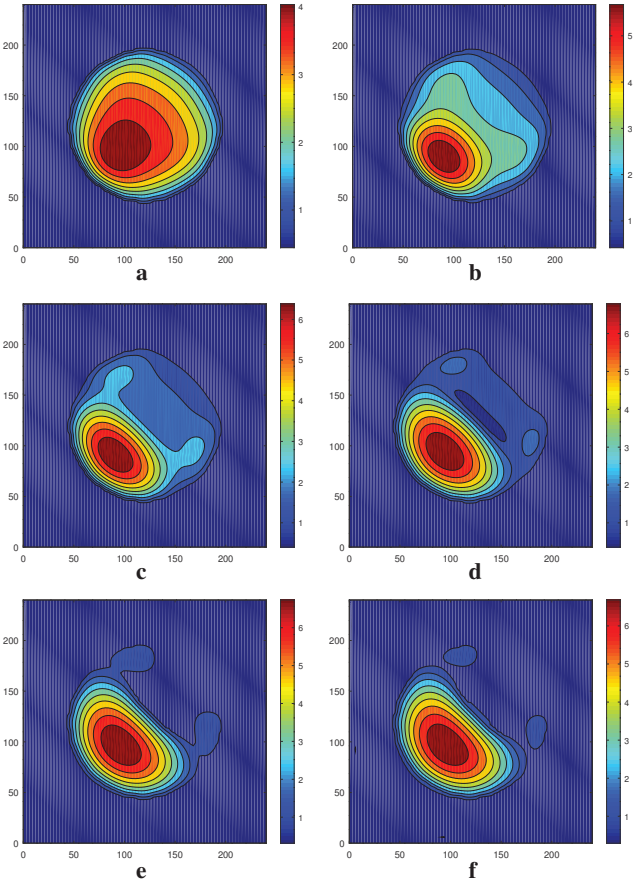

Figure 4. The fields of $h_2(X, Y, \tau)$ for $\bar{M} = -2$, $\Delta_X = \Delta_Y = 0.5$, $Bo = 0$ and $Bi = 20$: (**a**) $\tau = 500$; (**b**) $\tau = 1500$; (**c**) $\tau = 2500$; (**d**) $\tau = 5000$; (**e**) $\tau = 8000$ (**f**) $\tau = 9500$.

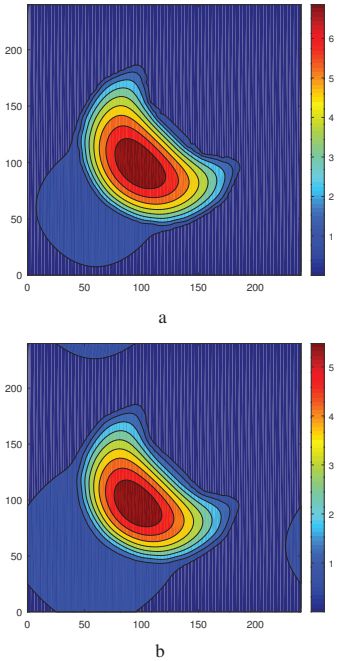

Figure 5. A snapshot of the fields of $h_2(X, Y, \tau)$ and $h_1(X, Y, \tau)$ for $\bar{M} = -2$, $\Delta_X = \Delta_Y = 0.5$, $Bo = 0$, $Bi = 20$ and $\tau = 1 \times 10^6$.

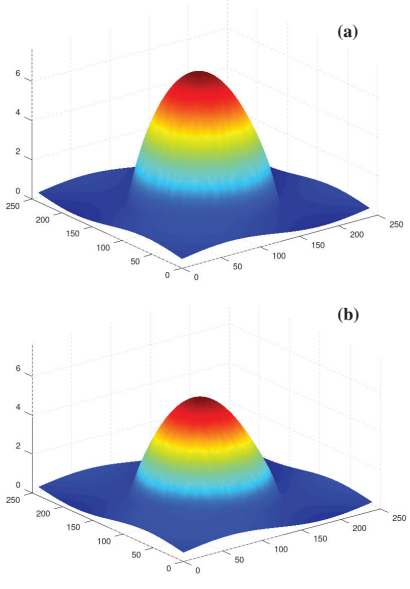

Figure 6. The shapes of (**a**) $h_2(X, Y, \tau)$ and (**b**) $h_1(X, Y, \tau)$ for $\bar{M} = -2$, $\Delta_X = \Delta_Y = 0.5$, $Bo = 0$, $Bi = 20$ and $\tau = 1 \times 10^6$.

Under the action of the asymmetric field $M(X, Y)$ ($\Delta_X = 0.1; \Delta_Y = 0.5$) on the steady round droplet, the symmetry of the initially round droplet is broken. A snapshot of the fields of (a) $h_2(X, Y, \tau)$ and (b) $h_1(X, Y, \tau)$ is shown in Figure 7, and the shapes of the

interfaces are presented in Figure 8. Now, there is no symmetry with respect to the axis $Y = X$ (cf. Figures 3 and 7).

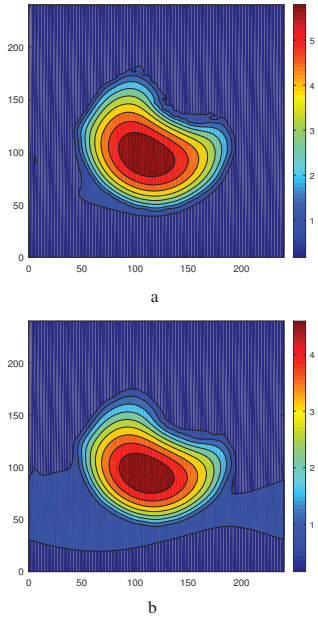

Figure 7. A snapshot of the fields of $h_2(X, Y, \tau)$ and $h_1(X, Y, \tau)$ for $\bar{M} = -2$, $\Delta_X = 0.1, \Delta_Y = 0.5$, $Bo = 0$, $Bi = 20$ and $\tau = 1 \times 10^6$.

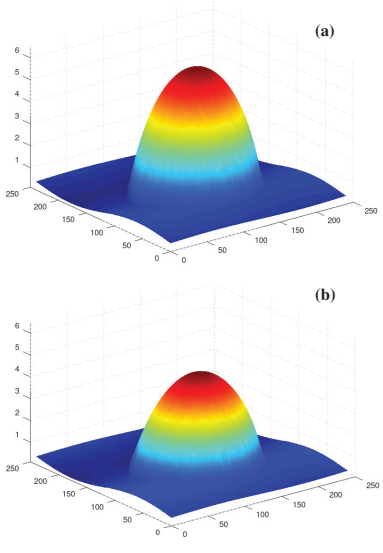

Figure 8. The shapes of (**a**) $h_2(X, Y, \tau)$ and (**b**) $h_1(X, Y, \tau)$ for $\bar{M} = -2$, $\Delta_X = 0.1, \Delta_Y = 0.5$, $Bo = 0$, $Bi = 20$ and $\tau = 1 \times 10^6$.

3.2. The Case of Nonaxisymmetric Initial Conditions

Let us take now the steady droplet with the maximum, shifted to the left part of the computational region (see Figure 3 in [25]), as the initial conditions and consider

its evolution under the action of two-dimensional temperature modulation ($\bar{M} = -2$; $\Delta_X = \Delta_Y = 0.1$). Despite the symmetry of the spatial temperature modulation, we obtain an asymmetric steady state. A snapshot of the fields of (a) $h_2(X, Y, \tau)$ and (b) $h_1(X, Y, \tau)$ is shown in Figure 9, and the shapes of the interfaces are presented in Figure 10.

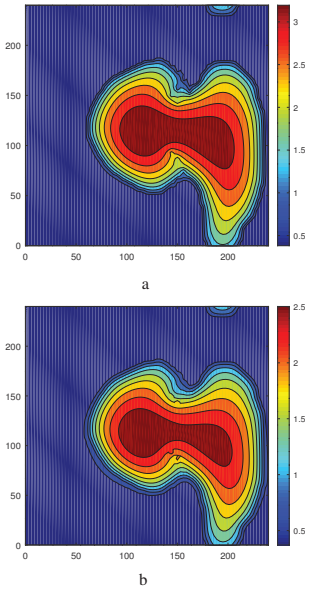

Figure 9. A snapshot of the fields of (**a**) $h_2(X, Y, \tau)$ and (**b**) $h_1(X, Y, \tau)$ for $\bar{M} = -2$, $\Delta_X = \Delta_Y = 0.1$, $Bo = 0$, $Bi = 20$ and $\tau = 1 \times 10^6$.

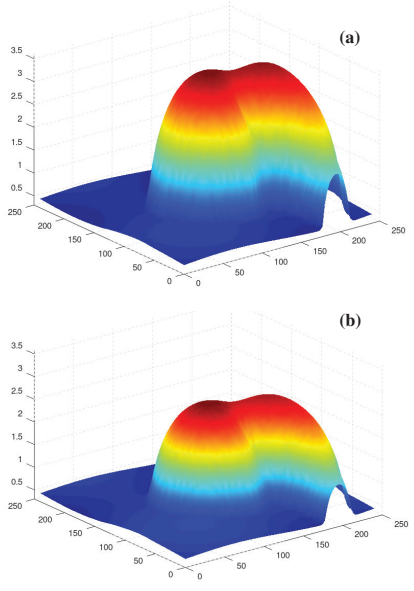

Figure 10. The shapes of (**a**) $h_2(X, Y, \tau)$ and (**b**) $h_1(X, Y, \tau)$ for $\bar{M} = -2$, $\Delta_X = \Delta_Y = 0.1$, $Bo = 0$, $Bi = 20$ and $\tau = 1 \times 10^6$.

4. Droplet Oscillations

It has been shown in [9] that in the case of a homogeneous cooling from below, the droplet becomes oscillatory unstable with an increase in $\bar{M}$ (see Figure 11). That instability is similar to that formerly found in a system of two flat liquid layers [10]. Let us note that oscillatory Marangoni instabilities for cooling from below have also been observed in some other problems (see [26]).

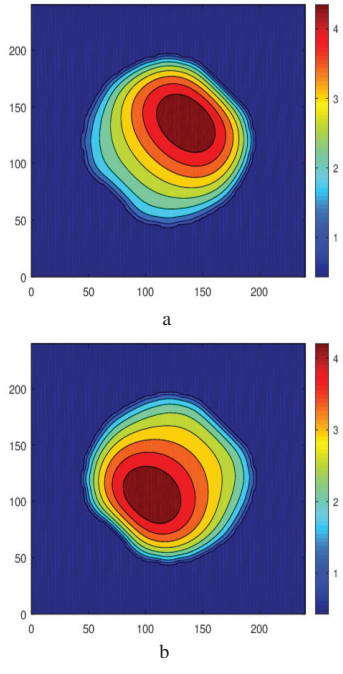

Figure 11. A snapshot of the fields of $h_2(X, Y, \tau)$ for $\bar{M} = -2.5$, $Bi = 20$ and $\Delta_X = \Delta_Y = 0$: (**a**) $\tau = 7 \times 10^5$; (**b**) $\tau = 7.15 \times 10^5$.

In the course of oscillations, the droplet keeps the symmetry with respect to the axis $Y = X$. Also, the oscillations are characterized by the symmetry

$$h_m(X, Y, \tau + T/2) = h_m(L - Y, L - X, \tau), \; m = 1, 2, \tag{16}$$

where T is the period of oscillations. In other words, after the half-period, the shape of the droplet is reflected with respect to the axis $X + Y = L$. Therefore, the quantities

$$h_{max,m}(\tau) = \max h_m(X, Y, \tau)$$

and

$$h_{min,m}(\tau) = \min h_m(X, Y, \tau)$$

are periodic in time with the period $T/2$. The temporal evolution of $h_{max,1}$ and $h_{max,2}$ is shown in Figure 12.

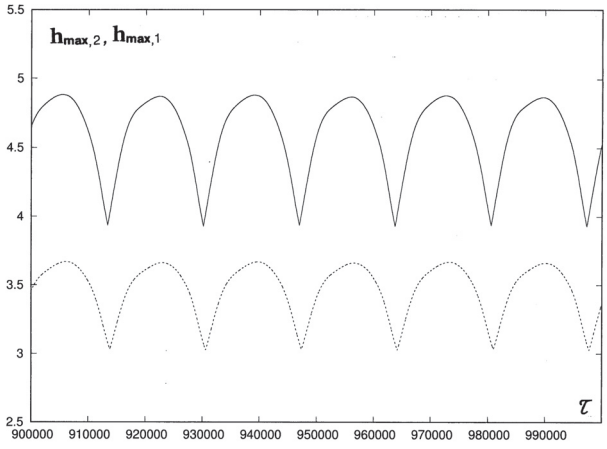

Figure 12. The oscillations of $h_{max,2}(\tau)$ (solid line) and $h_{max,1}(\tau)$ (dashed line) for $\bar{M} = -2.5$ and $Bi = 20$.

Below, we discuss the influence of the substrate temperature modulation on the oscillatory regime.

4.1. Suppression of Oscillations

Let us take the oscillatory droplet (see Figures 11 and 12) ($\bar{M} = -2.5$; $\Delta_X = \Delta_Y = 0$) as the initial conditions and consider its evolution under the action of two-dimensional spatial temperature modulation ($\bar{M} = -2.5$; $\Delta_X = \Delta_Y = 0.1$). Under the action of the symmetric field $M(X, Y)$, the oscillations are suppressed and the steady state develops in the system. The transient process from the periodic oscillations to the steady droplet is shown in Figure 13, and the intermediate stages of the evolution at different instants of time are presented in Figure 14. One can see that the symmetry of the droplet is broken. Finally, a steady *asymmetric* droplet is observed in the system. A snapshot of the fields of (a) $h_2(X, Y, \tau)$ and (b) $h_1(X, Y, \tau)$ at the equilibrium stage is shown in Figure 15, and the corresponding shapes of the interfaces are presented in Figure 16.

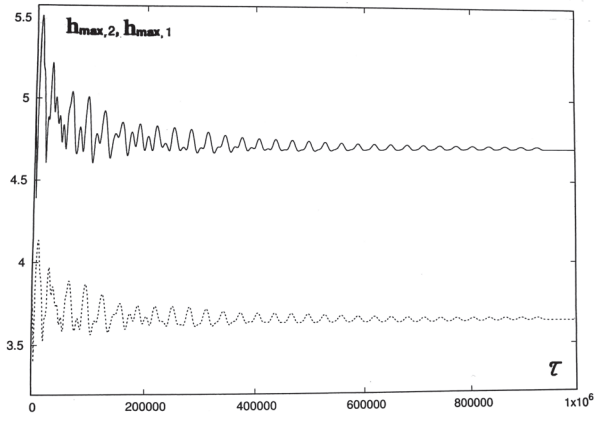

Figure 13. The oscillations of $h_{max,2}(\tau)$ (solid line) and $h_{max,1}(\tau)$ (dashed line) for $\bar{M} = -2.5$, $\Delta_X = \Delta_Y = 0.1$, $Bo = 0$ and $Bi = 20$.

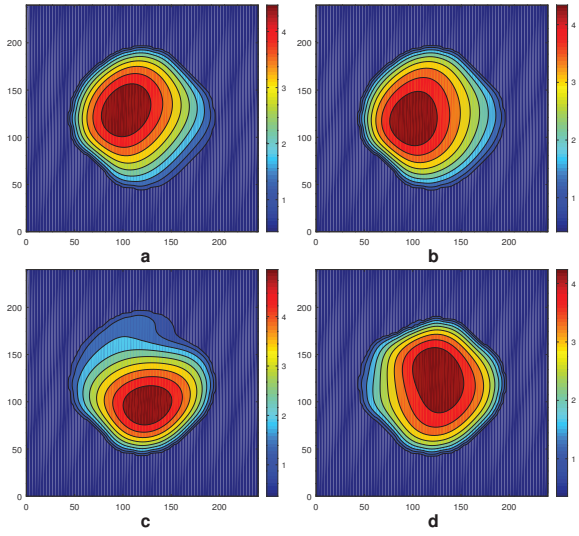

Figure 14. The fields of $h_2(X, Y, \tau)$ for $\bar{M} = -2.5$, $\Delta_X = \Delta_Y = 0.1$, $Bo = 0$ and $Bi = 20$: (**a**) $\tau = 500$; (**b**) $\tau = 1500$; (**c**) τ = 10,000; (**d**) τ = 20,000.

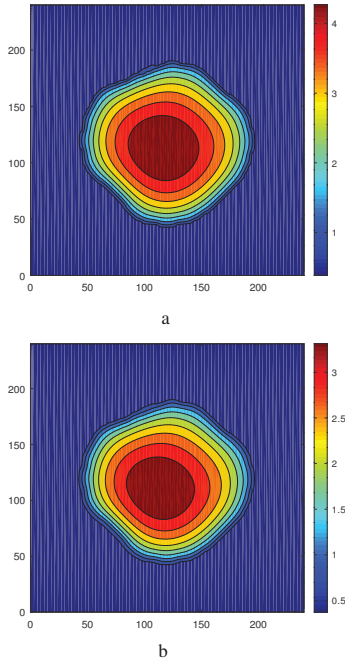

Figure 15. A snapshot of the fields of (**a**) $h_2(X, Y, \tau)$ and (**b**) $h_1(X, Y, \tau)$ for $\bar{M} = -2.5$, $\Delta_X = \Delta_Y = 0.1$, $Bo = 0$, $Bi = 20$ and $\tau = 1 \times 10^6$.

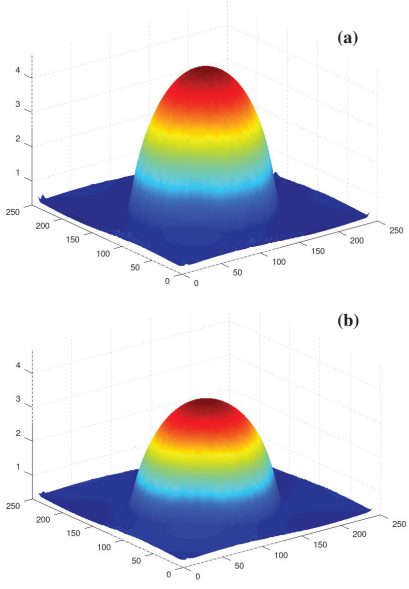

Figure 16. The shapes of **(a)** $h_2(X, Y, \tau)$ and **(b)** $h_1(X, Y, \tau)$ for $\bar{M} = -2.5$, $\Delta_X = \Delta_Y = 0.1$, $Bo = 0$, $Bi = 20$ and $\tau = 1 \times 10^6$.

Let us consider the influence of asymmetric field $M(X, Y)$ on the oscillatory regime presented in Figures 11 and 12—we take $\Delta_X = 0.1$ and $\Delta_Y = 0.5$ ($M = -2.5$). In this case, the oscillations are also suppressed and the asymmetric steady droplet develops in the system. A snapshot of the fields of (a) $h_2(X, Y, \tau)$ and (b) $h_1(X, Y, \tau)$ is presented in Figure 17, and the shapes of the interfaces are shown in Figure 18. The sharp corners in Figure 18 present the connection of the droplet with the neighbor droplet and are created by the crossing of the interfaces with the plane $X = 0$, which cuts the droplet. One can see that the shape of the droplet is rather smooth.

4.2. Excitation of Oscillations

Surprisingly, we observed *an excitation* of oscillations for $\bar{M} = -2$, i.e., in the case where in the absence of modulation the round droplet is stable, when we apply an asymmetric field $M(X, Y)$ ($\Delta_X = 0.1$, $\Delta_Y = 0.5$) on the asymmetric steady droplet with the maximum, shifted to the left part of the computational region (see Figure 3 in [25]). In this case, periodic oscillations with essentially different adjacent maxima develop in the system (see Figure 19); the period of oscillations T = 69,420. Snapshots of the fields $h_2(X, Y, \tau)$ at different instants of time are presented in Figure 20. The small and big maxima of $h_{max,j}(\tau)$, $j = 1, 2$, correspond to different spatial points. Let us note that because the different maxima are in the points with different values of $M(X, Y)$, there is no reason for them to be equal. Since we consider the region with periodic boundary conditions, one can see the appearance of a finger that meets the fingers of the neighbor drops at the boundary of the computational region. The combination and the recombination of the droplet with its neighbors could be the origin of the oscillations. The shapes of interfaces, corresponding to Figure 20b, are shown in Figure 21. A diagram of the regimes in the plane (δ_X, δ_Y) for $\bar{M} = -2$ is presented in Figure 22. One can see that bistability takes place at several points.

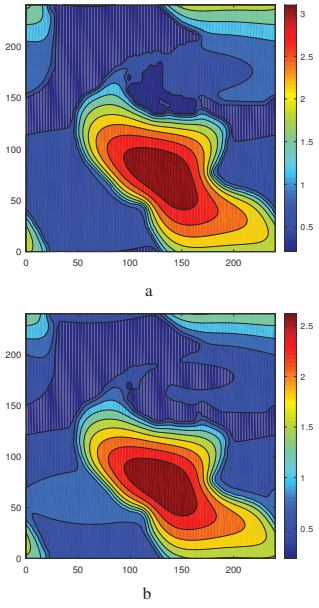

Figure 17. A snapshot of the fields of (**a**) $h_2(X, Y, \tau)$ and (**b**) $h_1(X, Y, \tau)$ for $\bar{M} = -2.5$, $\Delta_X = 0.1$, $\Delta_Y = 0.5$, $Bo = 0$, $Bi = 20$ and $\tau = 1 \cdot 10^6$.

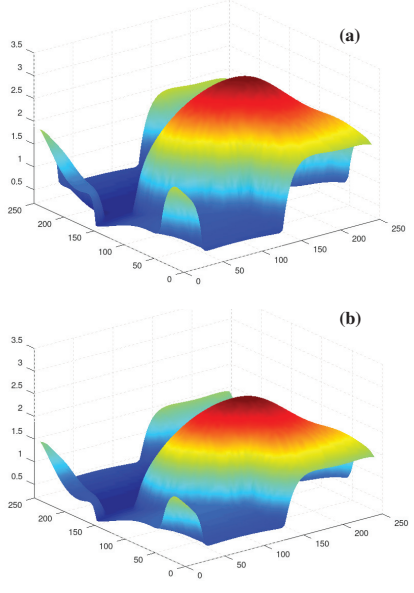

Figure 18. The shapes of (**a**) $h_2(X, Y, \tau)$ and (**b**) $h_1(X, Y, \tau)$ for $\bar{M} = -2.5, \Delta_X = 0.1, \Delta_Y = 0.5$, $Bo = 0$, $Bi = 20$ and $\tau = 1 \times 10^6$.

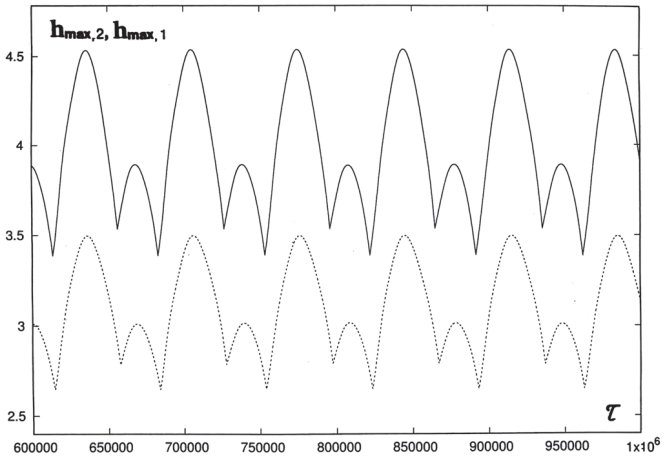

Figure 19. The oscillations of $h_{max,2}(\tau)$ (solid line) and $h_{max,1}(\tau)$ (dashed line) for $\bar{M} = -2$, $\Delta_X = 0.1$, $\Delta_Y = 0.25$, $Bo = 0$ and $Bi = 20$.

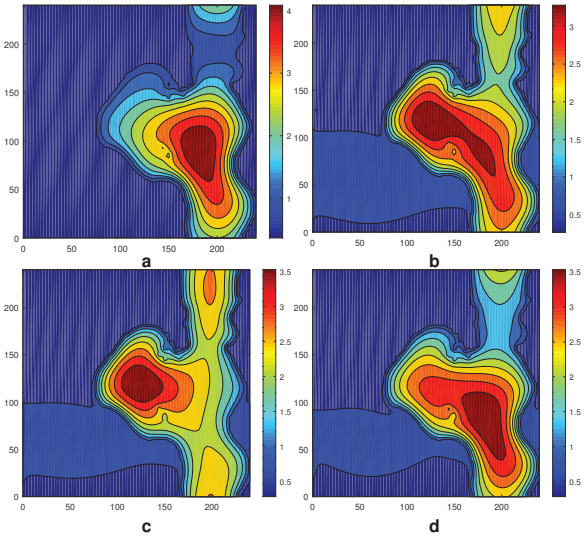

Figure 20. The fields of $h_2(X, Y, \tau)$ for $\bar{M} = -2$, $\Delta_X = 0.1, \Delta_Y = 0.25$, $Bo = 0$ and $Bi = 20$: (**a**) $\tau = 9.15 \times 10^5$; (**b**) $\tau = 9.3 \times 10^5$; (**c**) $\tau = 9.35 \times 10^5$; (**d**) $\tau = 9.5 \times 10^5$.

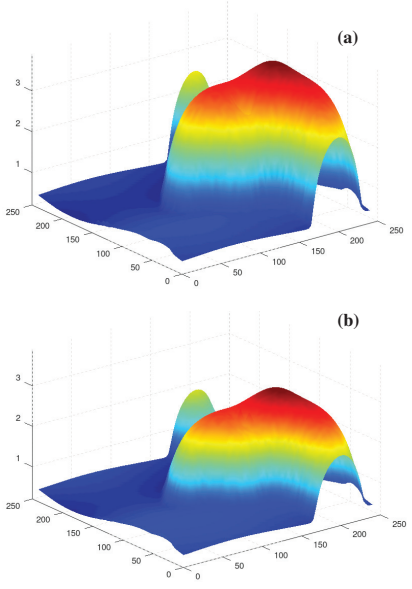

Figure 21. The shapes of (**a**) $h_2(X, Y, \tau)$ and (**b**) $h_1(X, Y, \tau)$ for $\bar{M} = -2$, $\Delta_X = 0.1$, $\Delta_Y = 0.25$, $Bo = 0$, $Bi = 20$ and $\tau = 9.3 \times 10^5$.

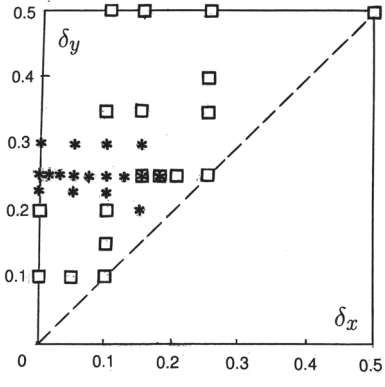

Figure 22. Diagram of regimes on the plane (δ_X, δ_Y) for $M = -2$, $Bo = 0$ and $Bi = 20$: empty square, stationary pattern; asterisk, oscillatory flow.

Let us take the oscillatory flow presented in Figures 19 and 20a as the initial condition and consider its evolution at the larger values of $|\bar{M}|$. With an increase in $|\bar{M}|$, periodic oscillations with different adjacent maxima become of a rather complex form; the amplitude of oscillations grows and the period of oscillations decreases (cf. Figure 23 ($T = 52{,}940$) and Figure 19 ($T = 69{,}420$)). At $\bar{M} \leq -2.92$, quasiperiodic oscillations develop in the system (see Figure 24).

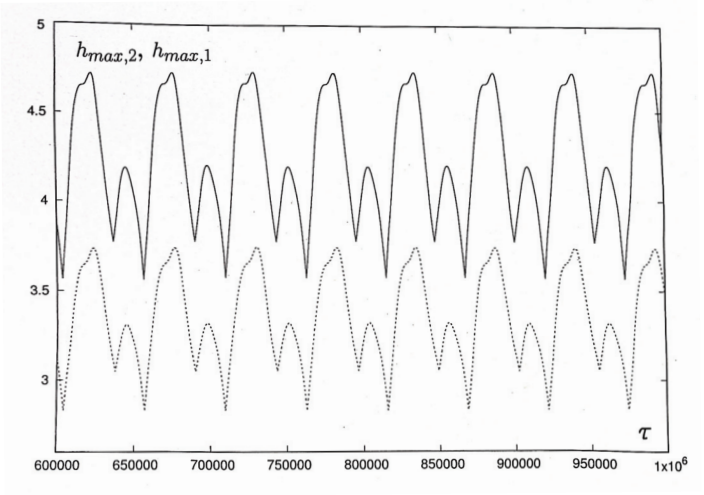

Figure 23. The oscillations of $h_{max,2}(\tau)$ (solid line) and $h_{max,1}(\tau)$ (dashed line) for $\bar{M} = -2.825$, $\Delta_X = 0.1$, $\Delta_Y = 0.25$, $Bo = 0$ and $Bi = 20$.

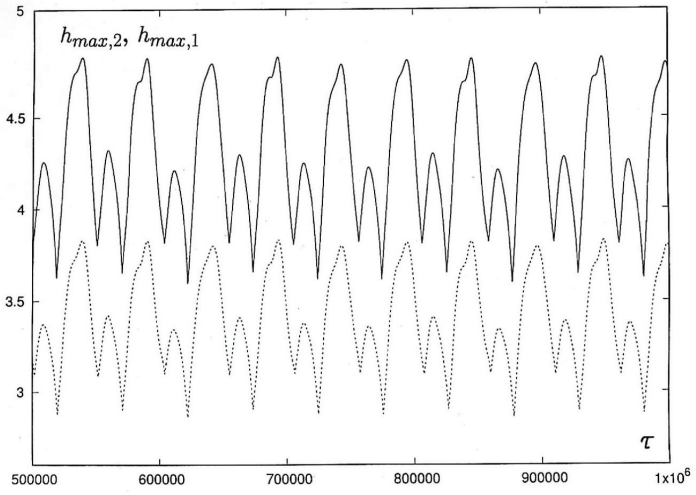

Figure 24. The oscillations of $h_{max,2}(\tau)$ (solid line) and $h_{max,1}(\tau)$ (dashed line) for $\bar{M} = -2.925$, $\Delta_X = 0.1$, $\Delta_Y = 0.25$, $Bo = 0$ and $Bi = 20$.

5. The Influence of Gravity on the Droplet Dynamics

Now, let us consider the action of gravity on the droplets. If we take the stationary droplet obtained under the action of the symmetric field $M(X, Y)$ ($\bar{M} = -2, \Delta_X = \Delta_Y = 0.1$) as the initial condition (see Figure 3), under the action of gravity ($Bo = 0.1$), the droplet is essentially flattened. The intermediate stages of the evolution of the initially round droplet are presented in Figure 25. Under the action of the thermocapillary flow in the substrate directed along the axis $Y = X$, the droplet changes its shape and height. The isolines and the shapes of the interfaces, corresponding to the final equilibrium state, are shown in Figures 26 and 27 (cf. Figures 3 and 26). The droplet still keeps the symmetry with respect to axis $Y = X$.

Under the action of gravity ($Bo = 0.05$) on the asymmetric stationary droplet shown in Figure 7 ($\bar{M} = -2$, $\Delta_X = 0.1$; $\Delta_Y = 0.5$), we obtain the asymmetric significantly flattened droplet (cf. Figures 7 and 28).

Let us take as initial conditions the periodic oscillations presented in Figures 19 and 20a. Under the action of sufficiently small gravity ($Bo = 0.01$), oscillations are suppressed and the steady droplet develops in the system. A snapshot of the fields of (a) $h_2(X, Y, \tau)$ and (b) $h_1(X, Y, \tau)$ is shown in Figure 29. The height of the droplet is essentially lower than that obtained in the absence of gravity (cf. Figures 20a and 29a).

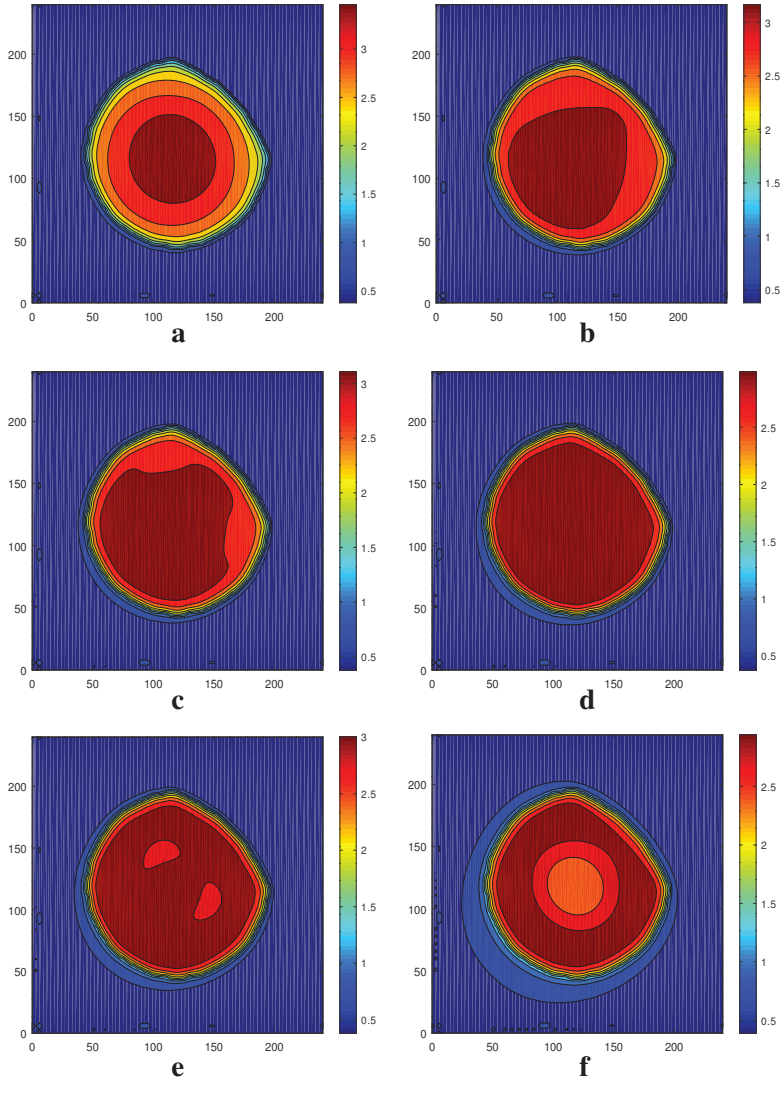

Figure 25. The fields of $h_2(X, Y, \tau)$ for $\bar{M} = -2$, $\Delta_X = \Delta_Y = 0.1$, $Bo = 0.1$ and $Bi = 20$: (**a**) $\tau = 250$; (**b**) $\tau = 450$; (**c**) $\tau = 500$; (**d**) $\tau = 650$; (**e**) $\tau = 850$ (**f**) $\tau = 2500$.

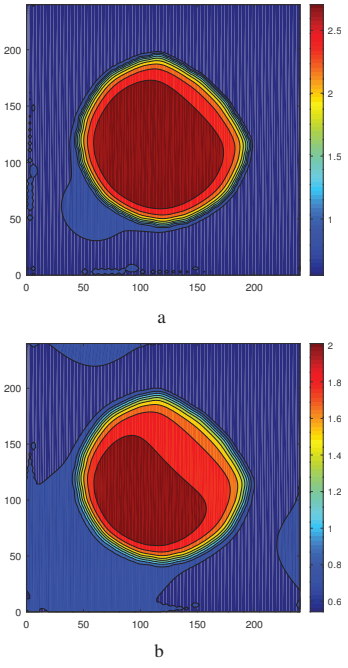

Figure 26. A snapshot of the fields of $h_2(X, Y, \tau)$ and $h_1(X, Y, \tau)$ for $\bar{M} = -2$, $\Delta_X = \Delta_Y = 0.1$, $Bo = 0.1$, $Bi = 20$ and $\tau = 1 \times 10^6$.

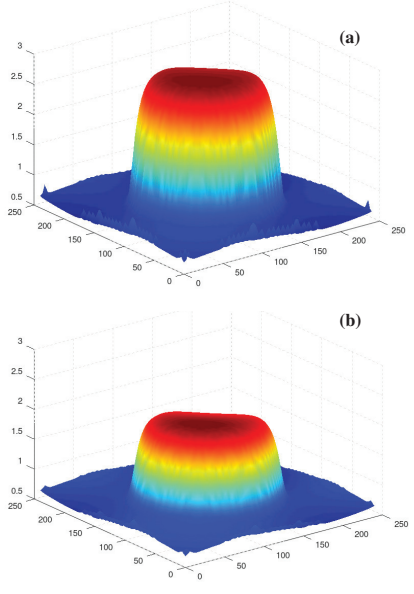

Figure 27. The shapes of (**a**) $h_2(X, Y, \tau)$ and (**b**) $h_1(X, Y, \tau)$ for $\bar{M} = -2$, $\Delta_X = \Delta_Y = 0.1$, $Bo = 0.1$, $Bi = 20$ and $\tau = 1 \times 10^6$.

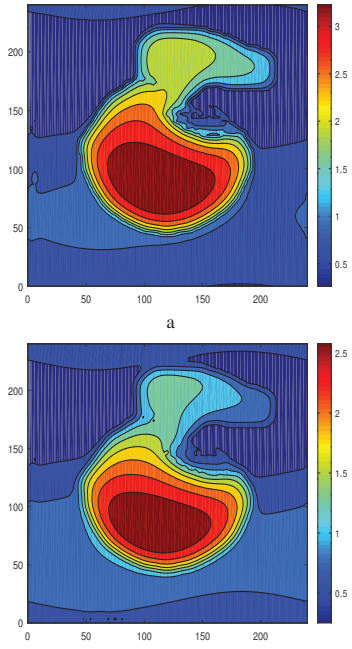

Figure 28. A snapshot of the fields of $h_2(X, Y, \tau)$ and $h_1(X, Y, \tau)$ for $\bar{M} = -2$, $\Delta_X = 0.1$, $\Delta_Y = 0.5$, $Bo = 0.05$, $Bi = 20$ and $\tau = 1 \times 10^6$.

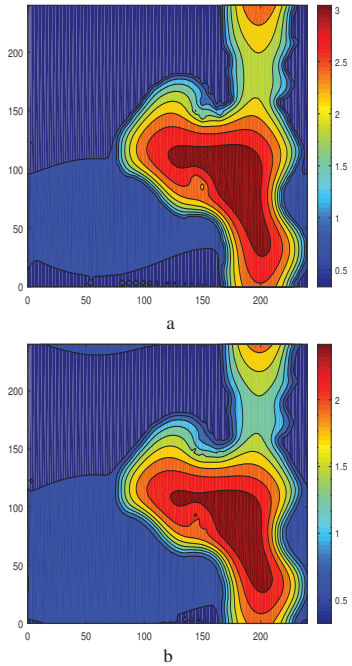

Figure 29. A snapshot of the fields of $h_2(X, Y, \tau)$ and $h_1(X, Y, \tau)$ for $\bar{M} = -2$, $\Delta_X = 0.1$, $\Delta_Y = 0.25$, $Bo = 0.01$, $Bi = 20$ and $\tau = 1 \times 10^6$.

6. The Influence of the Biot Number on the Shape of the Droplet

Let us consider the influence of the Biot number Bi on the shape of droplets. We take the stationary droplet obtained under the action of the symmetric field $M(X, Y)$ ($\bar{M} = -2$, $\Delta_X = \Delta_Y = 0.1$) as the initial conditions (see Figure 3). With a decrease in Bi, under the action of the thermocapillary flow in the substrate directed along the axis $Y = X$, the droplet is completely destroyed, and we obtain a square pattern. A snapshot of the field $h_2(X, Y, \tau)$, corresponding to the final equilibrium state for a sufficiently small value of Bi, is shown in Figure 30. The pattern keeps the symmetry with respect to axis $Y = X$. The shape of the upper interface is presented in Figure 31. The similar patterns generated by the bottom temperature modulation have been obtained in two-layer films [27].

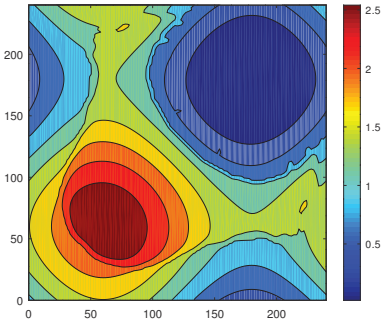

Figure 30. A snapshot of the field of $h_2(X, Y, \tau)$ for $\bar{M} = -2$, $\Delta_X = \Delta_Y = 0.1$, $Bo = 0$, $Bi = 0.1$ and $\tau = 1 \times 10^6$.

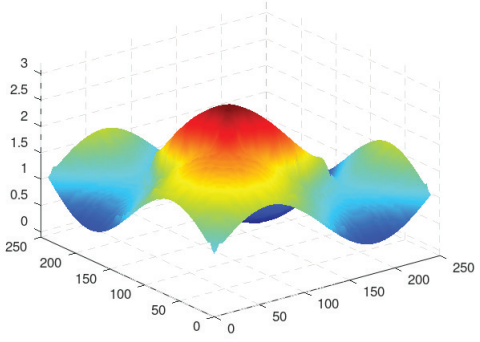

Figure 31. The shape of the interface $h_2(X, Y, \tau)$ for $\bar{M} = -2$, $\Delta_X = \Delta_Y = 0.1$, $Bo = 0$, $Bi = 0.1$ and $\tau = 1 \times 10^6$.

Let us note that the same steady regime has been obtained from the other initial conditions when a droplet of liquid 2 with a Gaussian shape was imposed on a flat layer of liquid 1.

The redistribution of the liquids in the droplet and in the substrate along the axis $Y = X$ with the maximum shifted to the region $X < L/2$ also takes place for sufficiently small values of $\bar{M}$ ($\bar{M} = -0.1$, $\Delta_X = \Delta_Y = 0.1$, $Bi = 0.5$). The intermediate stages of the evolution of the field $h_2(X, Y, \tau)$ at different instants of time are presented in Figure 32. A snapshot of the field $h_2(X, Y, \tau)$ and the corresponding shape of the upper interface at the final equilibrium state are shown in Figures 33 and 34.

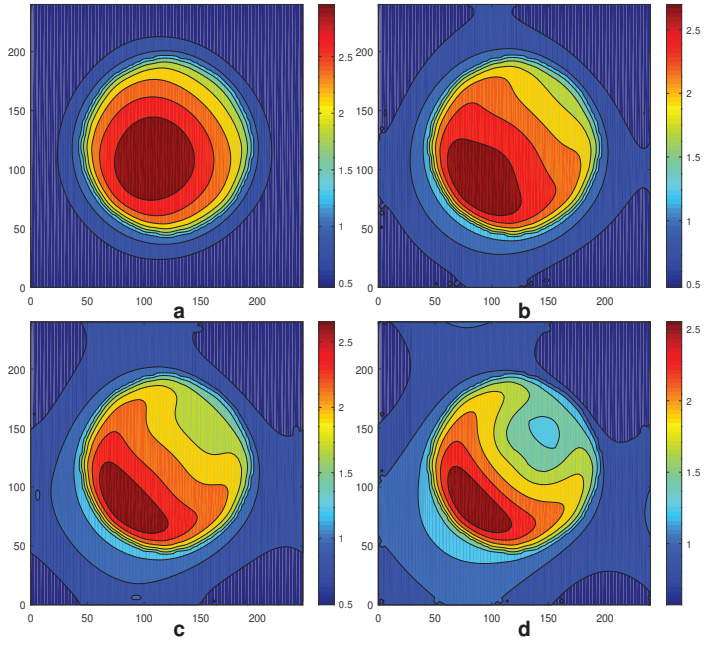

Figure 32. The fields of $h_2(X, Y, \tau)$ for $\bar{M} = -0.1$, $\Delta_X = \Delta_Y = 0.1$, $Bo = 0$ and $Bi = 0.5$: (**a**) $\tau = 10{,}000$: (**b**) $\tau = 25{,}000$; (**c**) $\tau = 40{,}000$; (**d**) $\tau = 80{,}000$.

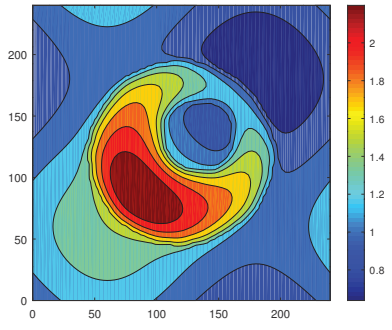

Figure 33. A snapshot of the field of $h_2(X, Y, \tau)$ for $\bar{M} = -0.1$, $\Delta_X = \Delta_Y = 0.1$, $Bo = 0$, $Bi = 0.5$ and $\tau = 1 \times 10^6$.

Now, let us take as initial conditions the periodic oscillations presented in Figures 19 and 20a. With a decrease in Bi (at $Bi \leq 18.95$), oscillations are suppressed and the steady asymmetric droplet develops in the system. A snapshot of the field of $h_1(X, Y, \tau)$ is shown in Figure 34. Let us note that the asymmetric droplet has also been obtained for sufficiently small values of $\bar{M}$ and Bi ($\bar{M} = -0.17$, $\Delta_X = 0.1$, $\Delta_Y = 0.25$, $Bi = 0.95$). The isolines and the shape of the upper interface, corresponding to the final equilibrium state, are shown in Figures 35 and 36. One can see that the symmetry with respect to axis $Y = X$ is broken.

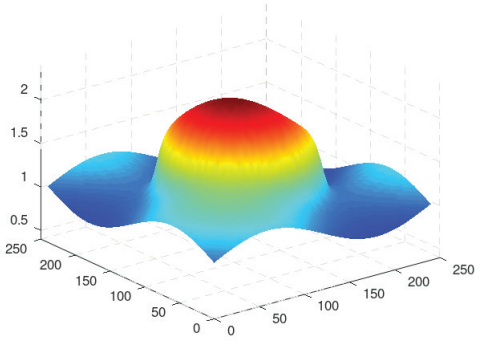

Figure 34. The shape of the interface $h_2(X, Y, \tau)$ for $\bar{M} = -0.1$, $\Delta_X = \Delta_Y = 0.1$, $Bo = 0$, $Bi = 0.5$ and $\tau = 1 \times 10^6$.

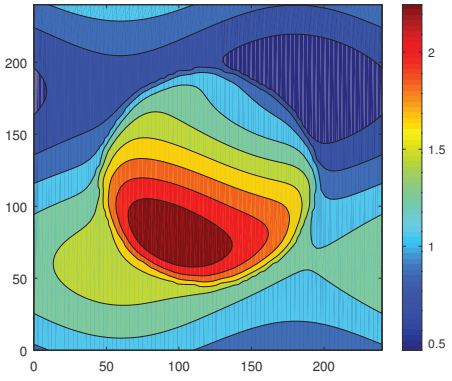

Figure 35. A snapshot of the field of $h_2(X, Y, \tau)$ for $\bar{M} = -0.17$, $\Delta_X = 0.1$, $\Delta_Y = 0.25$, $Bo = 0$, $Bi = 0.95$ and $\tau = 1 \times 10^6$.

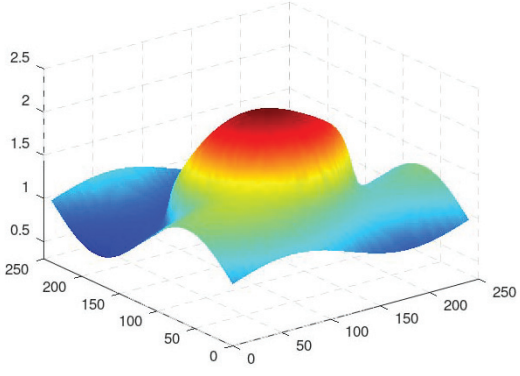

Figure 36. The shape of the interface $h_2(X, Y, \tau)$ for $\bar{M} = -0.17$, $\Delta_X = 0.1, \Delta_Y = 0.25$, $Bo = 0$, $Bi = 0.95$ and $\tau = 1 \times 10^6$.

7. Conclusions

The dynamics of a droplet on a liquid substrate in the case of an inhomogeneous cooling from below has been investigated. The problem is studied numerically in the framework of the longwave approximation and the precursor model.

It is shown that a two-dimensional spatial inhomogeneity of the substrate temperature creates more diverse flow regimes than a one-dimensional temperature inhomogeneity.

The nonhomogeneous cooling creates a disbalance of thermocapillary stresses that leads to the redistribution of the liquids in the droplet and in the substrate. It is found that the droplet can be stationary or subject to oscillations caused by an oscillatory Marangoni instability. The two-dimensional spatial inhomogeneity of the temperature enhances the oscillatory instability threshold, and it can *suppress* oscillations, leading to the formation of steady droplets. In a definite region of parameters, the two-dimensional spatial modulation can lead to the *excitation* of the specific type of periodic oscillations with different adjacent maxima. A diagram of regimes in the plane (δ_X, δ_Y) has been constructed. The bistability in several points has been obtained. The gravity flattens the droplet and suppresses oscillations.

The influence of the Biot number on the shape of the droplet has been studied. The smaller the *Bi*, the stronger the inhomogeneities of the temperature on the free surface and, thus, the stronger the action of the thermocapillary effect. Square patterns similar to those generated by the bottom temperature modulation in two-layer films have been obtained.

Author Contributions: A.N. and I.S. wrote the paper together. All authors have read and agreed to the published version of the manuscript

Funding: This research was supported by the Israel Science Foundation (grant No. 843/18).

Data Availability Statement: Data are contained within the article.

Conflicts of Interest: The authors declare no conflict of interest.

References

1. de Gennes, P.G. Wetting: Statics and dynamics. *Rev. Mod. Phys.* **1985**, *57*, 827. [CrossRef]
2. de Gennes, P.G.; Brochard-Wyart, F.; Quérxex, D. *Capillarity and Wetting Phenomena: Drops, Bubbles, Pearls, Waves*; Springer: Berlin/Heidelberg, Germany, 2004.
3. Labanieh, L.; Nguyen, T.N.; Zhao, W.A.; Kang, D.K. Floating droplet array: An ultrahigh-throughput device for droplet trapping, real time analysis and recovery. *Micromachines* **2015**, *60*, 1469–1482. [CrossRef] [PubMed]
4. Yamini, Y.; Rezazadeh, M.; Seidi, S. Liquid-phase microextraction—The different principles and configurations. *TRAC—Trends Anal. Chem.* **2019**, *112*, 264–272. [CrossRef]
5. Ju, G.; Yang, X.; Li, L.; Cheng, M.; Shi, F. Removal of oil spills through a self-propelled smart device. *Chem. Asian J.* **2019**, *14*, 2435–2439. [CrossRef] [PubMed]
6. Rybalko, S.; Magome, N.; Yoshikawa, K. Forward and backward laser-guided motion of an oil droplet. *Phys. Rev. E* **2004**, *70*, 046301. [CrossRef] [PubMed]
7. Song, C.; Moon, J.K.; Lee, K.; Kim, K.; Pak, H.K. Breathing, crawling, budding, and splitting of a liquid droplet under laser heating. *Soft Matter* **2014**, *10*, 2679–2684. [CrossRef] [PubMed]
8. Buffone, C. Formation, stability and hydrothermal waves in evaporating liquid lenses. *Soft Matter* **2019**, *15*, 1970–1978. [CrossRef]
9. Nepomnyashchy, A.; Simanovskii, I. Droplets on the liquid substrate: Thermocapillary oscillatory instability. *Phys. Rev. Fluids* **2021**, *6*, 034001. [CrossRef]
10. Nepomnyashchy, A.A.; Simanovskii, I.B. Marangoni instability in ultrathin two-layer films. *Phys. Fluids* **2007**, *19*, 122103. [CrossRef]
11. Greco, E.F.; Grigoriev, R.O. Thermocapillary migration of interfacial droplets. *Phys. Fluids* **2009**, *21*, 042105. [CrossRef]
12. Yakshi-Tafti, E.; Cho, H.J.; Kumar, R. Droplet actuation on a liquid layer due to thermocapillary motion: Shape effect. *Appl. Phys. Lett.* **2010**, *96*, 264101. [CrossRef]
13. Keiser, L.; Bense, H.; Colinet, P.; Bico, J.; Reyssat, E. Marangoni bursting: evaporation induced emulsification of binary mixtures on a liquid layer. *Phys. Rev. Lett.* **2017**, *118*, 074504. [CrossRef]
14. Neumann, F. *Vorlesungen über die Theorie der Capllarität*; Teubner: Leipzig, Germany, 1894.
15. Kriegsmann, J.J.; Miksis, M.J. Steady motion of a drop along a liquid interface. *SIAM J. Appl. Math.* **2003**, *64*, 18. [CrossRef]
16. Craster, R.V.; Matar, O.K. On the dynamics of liquid lenses. *J. Colloid Interface Sci.* **2006**, *303*, 503–516. [CrossRef] [PubMed]
17. Pototsky, A.; Bestehorn, M.; Merkt, D.; Thiele, U. Morphology changes in the evolution of liquid two-layer films. *J. Chem. Phys.* **2005**, *122*, 224711. [CrossRef] [PubMed]
18. Nepomnyashchy, A.A.; Simanovskii, I.B. Effect of gravity on the dynamics of non-isothermic ultra-thin two-layer films. *J. Fluid Mech.* **2010**, *661*, 1–31. [CrossRef]
19. Nepomnyashchy, A.; Simanovskii, I. Nonlinear Marangoni waves in a two-layer film in the presence of gravity. *Phys. Fluids* **2012**, *24*, 032101. [CrossRef]
20. Oron, A.; Davis, S.H.; Bankoff, S.G. Long-scale evolution of thin liquid films. *Rev. Mod. Phys.* **1997**, *69*, 931. [CrossRef]

21. Pototsky, A.; Oron, A.; Bestehorn, M. Vibration-induced flotation of a heavy liquid drop on a lighter liquid film. *Phys. Fluids* **2019**, *31*, 087101. [CrossRef]
22. Sternling, C.V.; Scriven, L.E. On cellular convection driven by surface tension gradients: Effects of mean surface tension and surface viscosity. *J. Fluid Mech.* **1964**, *19*, 321–340.
23. Géoris, P.; Hennenberg, M.; Lebon, G.; Legros, J.C. Investigation of thermocapillary convection in a three-liquid-layer systems. *J. Fluid Mech.* **1999**, *389*, 209–228. [CrossRef]
24. Princen, H.M. Shape of interfaces, drops, and bubbles. In *Surface and Colloid Science*; Matijevic, E., Ed.; Wiley: New York, NY, USA, 1969; Volume 2, p. 1.
25. Nepomnyashchy, A.; Simanovskii, I. Marangoni instabilities of droplets on the liquid substrate under the action of a spatial temperature modulation. *J. Fluid Mech.* **2022**, *936*, A26. [CrossRef]
26. Nepomnyashchy, A.; Simanovskii, I.; Legros, J.C. *Interfacial Convection in Multilayer Systems*, 2nd ed.; Springer: New York, NY, USA, 2012.
27. Nepomnyashchy, A.; Simanovskii, I. The influence of two-dimensional temperature modulation on nonlinear Marangoni waves in two-layer films. *J. Fluid Mech.* **2018**, *846*, 944–965. [CrossRef]

fluids

MDPI

Brief Report

Multiple Steady States in Laminar Rayleigh–Bénard Convection of Air

Julien Carlier *,† and Miltiadis V. Papalexandris †

Institute of Mechanics, Materials and Civil Engineering, Université Catholique de Louvain, 1348 Louvain-la Neuve, Belgium; miltos@uclouvain.be
* Correspondence: julien.carlier@uclouvain.be
† These authors contributed equally to this work.

Abstract: In this article, we report on numerical simulations of laminar Rayleigh–Bénard convection of air in cuboids. We provide numerical evidence of the existence of multiple steady states when the aspect ratio of the cuboid is sufficiently large. In our simulations, the Rayleigh number is fixed at $Ra = 1.7 \times 10^4$. The gas in the cube is initially at rest but subject to random small-amplitude velocity perturbations and an adverse temperature gradient. When the flow domain is a cube, i.e., the aspect ratio is equal to unity, there is only one steady state. This state is characterized by the development of a single convective roll and by a symmetric normalized temperature profile with respect to the mid-height. On the contrary, when the aspect ratio is equal to 2, there are five different steady states. Only one of them exhibits a symmetric temperature profile and flow structure. The other four steady states are characterized by two-roll configurations and asymmetric temperature profiles.

Keywords: natural convection; low-Mach-number flow; convective instabilities; multiple steady states

Citation: Carlier, J.; Papalexandris, M.V. Multiple Steady States in Laminar Rayleigh–Bénard Convection of Air. *Fluids* **2024**, *9*, 7. https://doi.org/10.3390/fluids9010007

Academic Editors: Vasily Novozhilov and Cunlu Zhao

Received: 9 November 2023
Revised: 18 December 2023
Accepted: 23 December 2023
Published: 26 December 2023

1. Introduction

Rayleigh–Bénard convection (RBC) constitutes a common configuration of convective heat transfer and has been studied extensively over the years. The classical RBC problem involves a fluid between two horizontal solid boundaries which are maintained at uniform but different temperatures. The temperature at the bottom boundary is higher than in the top one and, therefore, convective motions are developed by the interplay between the buoyancy and gravity forces. A review of numerical and experimental studies of turbulent RBC can be found in [1].

RBC is characterized by three dimensionless numbers, the Rayleigh and Prandtl numbers and the aspect ratio, Γ. For cuboids, Γ is the width-to-height ratio, whereas for circular cylinders it is the diameter-to-height ratio. In the past, several authors have studied the influence of the aspect ratio on RBC [2–4]. Regarding steady states, Gelfgat [5] numerically studied RBC in rectangular enclosures just above the instability threshold and showed that multiple steady states can be obtained, depending on the perturbation of the initial condition. In the experimental study [6] of laminar RBC of water in cylindrical domains with large aspect ratios, it was reported that five different steady states can develop. Subsequently, the authors of [7] studied experimentally and numerically the RBC of water in a cylindrical domain and constructed a bifurcation diagram of the solution branches in terms of the Rayleigh number and in the range of $Ra = 2 \times 10^3$ and $Ra = 3 \times 10^4$. In [8], a more extensive bifurcation diagram was proposed for water in cylindrical geometries with $\Gamma = 2$ and for the same range of Ra. Also, the authors of [9] considered the 2D laminar RBC of air in a square and proposed a stochastic approach for the final steady state in terms of the initial condition. In the same study, the authors predicted that the most probable steady state arising from a low-wave-number perturbation is a single-roll configuration. Further, the authors of [10] conducted numerical simulations of turbulent RBC in a cylindrical

domain ($Ra = 10^8$, $Pr = 10^3$ and $\Gamma = 0.5$) and predicted that multiple states can also be developed in that turbulent regime. Multiple states in natural convection have also been observed in settings different than the classical RBC. Examples include rectangular cavities with heated vertical walls [11] and natural convection of Bingham fluids [12].

With regard to classical RBC, the vast majority of studies on multiple steady states have focused on cylindrical domains whereas steady-state solutions in cuboids have received much less attention. However, it is well known that the shape of the container plays a significant role in the flow patterns developed in RBC [13].

The objective of this article is to provide numerical evidence of the existence of multiple steady states in laminar Rayleigh–Bénard convection in cuboids with large aspect ratio. In order to compute the various steady states, the initial condition that we consider is that of a fluid at rest in which we superimpose different random small-amplitude perturbations and an adverse temperature gradient. Herein, we present results for domains with two different aspect ratios Γ, namely, $\Gamma = 1$ (cube) and $\Gamma = 2$.

2. Governing Equations

We consider the natural convection of air enclosed in a cuboid. The system of governing equations is the low-Mach-number approximation of the compressible Navier–Stokes–Fourier equations [14,15]. In dimensionless form, this system reads

$$\frac{\partial \rho}{\partial t} + \nabla \cdot (\rho \boldsymbol{u}) \;=\; 0\,, \tag{1}$$

$$\frac{\partial \rho \boldsymbol{u}}{\partial t} + \nabla \cdot (\rho \boldsymbol{u}\boldsymbol{u}) \;=\; -\nabla p' + \frac{1}{Re}\nabla \cdot (\mu \boldsymbol{S}) + Ri\, y \nabla \rho\,, \tag{2}$$

$$c_p \frac{\partial \rho T}{\partial t} + c_p \nabla \cdot (\rho \boldsymbol{u} T) \;=\; \frac{\gamma - 1}{\gamma}\frac{dp_0}{dt} + \frac{1}{Re\, Pr}\nabla \cdot (\lambda \nabla T)\,. \tag{3}$$

The various flow variables and thermophysical properties are non-dimensionalized by those of a reference state of the working gas. The reference physical parameters are denoted by the subscript r.

In the above equations, ρ, $\boldsymbol{u} = (u, v, w)$ and T stand, respectively, for the density, velocity vector and temperature of the working fluid. Further, γ is the adiabatic ratio, and p_0 is the first-order term of the low-Mach-number expansion of the pressure which is referred to as the "thermodynamic pressure" [15]. In closed domains of fixed volume V, as in the present study, p_0 is evaluated by combining the expression for the (constant) mass of the working medium, $m = \int \rho dV$, with its equation of state. In our study, air is treated as a perfect gas, $p_0 = \rho T$. Therefore, in dimensionless form we have that

$$p_0 \;=\; \frac{\int \rho dV}{\int \frac{1}{T} dV}\,. \tag{4}$$

Also p' stands for the piezometric pressure [16,17], $p' \;=\; p + \rho Riy$ with p being the sum of the dynamic and bulk-viscous pressures [18]. In (2), y is the spatial coordinate in the vertical direction and opposite to gravity, and $\boldsymbol{S}$ is twice the deviatoric part of the strain-rate tensor, $\boldsymbol{S} = (\nabla \boldsymbol{u} + \nabla \boldsymbol{u}^\top) - \frac{2}{3}(\nabla \cdot \boldsymbol{u})\boldsymbol{I}$, with $\boldsymbol{I}$ being the identity matrix. Further, c_p, μ, and λ stand, respectively, for the specific heat capacity under constant pressure, dynamic viscosity and thermal conductivity of the gas. The transport coefficients μ and λ are assumed to follow a Sutherland-type law. In dimensionless form, the presumed law reads

$$\mu(T) \;=\; T^{0.7}\,, \qquad \lambda(T) = T^{0.7}\,. \tag{5}$$

With regard to the left-hand side of the energy Equation (3), we have used the fact that, for a perfect gas, the specific enthalpy is given by $h_s = c_p T + const$. Moreover, β is the thermal expansion coefficient; for a perfect gas, $\beta = 1/T$.

The top and bottom walls of the domain are maintained at temperatures T_c and T_h, respectively, with $T_h > T_c$. For non-dimensionalization purposes, the height of the domain, H, is the reference length and $T_r = (T_h + T_c)/2$ is the reference temperature. Then, the reference thermodynamic state is that at T_r and the initial thermodynamic pressure p_0. Also, the free-fall velocity, u_{ff}, serves as the reference velocity, $u_{\mathrm{ff}} = \sqrt{gH\beta_r\Delta T}$ with $\beta_r = 1/T_r$ and ΔT the difference between the fixed temperatures at the bottom and top walls, $\Delta T = T_h - T_c$. Then, the free-fall time, $t_{\mathrm{ff}} = H/u_{\mathrm{ff}}$, is set as the reference time scale of the problem in hand. The relevant dimensionless groups are the Rayleigh (Ra), Prandtl (Pr), Reynolds (Re) and Richardson (Ri) numbers,

$$Ra = \frac{g\beta_r\Delta T H^3}{\nu_r\alpha_r}, \quad Pr = \frac{\nu_r}{\alpha_r}, \quad Re = \frac{Hu_{\mathrm{ff}}}{\nu_r}, \quad Ri = \frac{gH}{u_{\mathrm{ff}}^2}, \tag{6}$$

with $\alpha_r = \frac{\lambda_r}{\rho_r\, c_{p_r}}$ being the thermal diffusivity of air at the reference state, $\nu_r = \frac{\mu_r}{\rho_r}$ the reference kinematic viscosity and g the gravitational acceleration.

The governing system (1)–(3) is integrated numerically via the time-accurate algorithm for low-Mach-number flows [15]. This algorithm is based on a second-order accurate predictor–corrector scheme for integration in time. Further, it involves a projection method for the evaluation of the piezometric pressure p'. The projection step amounts to taking the divergence of the momentum equation which, in conjunction with the continuity equation, leads to a constant-coefficient Poisson equation for p'. This Poisson equation is then discretized and solved numerically via a linear-system solver. Discretization of spatial derivatives is performed via second-order centered differences. The algorithm is implemented in a collocated grid arrangement because this arrangement offers ease of implementation and straightforward applicability to curvilinear coordinate systems. In order to avoid the problem of pressure odd–even decoupling that is often encountered in such grids, the algorithm is supplemented with a flux-interpolation technique [15] which is the generalization of the original scheme [19] to variable-density flows.

This algorithm has been implemented in a parallel code in C/C++ and uses the PETSc suite of data structures and routines [20]. Parallelization is performed via a Message Passing Interface (MPI). Also, the Poisson equation for p' is solved with the PETSc routine of PFMG which is a parallel semicoarsening multigrid solver. Validation tests of the algorithm and comparisons with numerical results and experimental data can be found in [15,21], respectively. In the past, this algorithm has been used in numerical studies of forced [22] and natural [23] convection and in a variety of simulations of reacting flows.

3. Numerical Setup

As mentioned above, the computational domain is a cuboid. Its width is denoted by W and is the same in the horizontal (x and z) directions. Thus, the aspect ratio of the domain is given by $\Gamma = W/H$. Herein, we present results for two different cases. In case 1, the flow domain is a cube, i.e., $\Gamma = 1$. In case 2, the aspect ratio is increased to $\Gamma = 2$. In both cases, the height of the domain is set at $H = 2.25$ cm.

All boundaries of the domain are no-slip rigid walls. The side walls are adiabatically isolated whereas the top and bottom walls are maintained at uniform temperatures, $T_c = 298.15$ K and $T_h = 313.5$ K, respectively. Accordingly, the bottom–top temperature difference is $\Delta T = 15.35$ K, while the reference temperature is $T_r = 305.8$ K. For air at T_r, the Prandtl number is $Pr = 0.73$. With regard to reference values, the free-fall velocity is $u_{\mathrm{ff}} = 0.11$ m/s, the free-fall time is 0.21 s, and the product between the thermal expansion and temperature difference is $\beta_r\Delta T = 0.05$. With these values, the Rayleigh number is $Ra = 1.7 \times 10^4$, which corresponds to the supercritical but laminar regime. It is also worth adding that the total temperature variation ΔT is in the order of 5% of the reference temperature T_r. This means that the total variation of the density is also close to 5%, while the total variation of the viscosity μ is approximately 4%. Such variations are not a priori

negligible. Accordingly, for purposes of computational accuracy, we opted to employ the low-Mach-number equations in our numerical study.

In terms of initial conditions, we assume that the gas is at rest and impose a linear temperature profile between T_h and T_c. The initial thermodynamic pressure p_0 is 1 bar. Also, as noted above, we apply random perturbations to the initial zero-velocity field. The amplitude of the applied perturbations is quite small, namely, 1% of the free-fall velocity u_{ff}. On the other hand, the initial temperature profile is left unperturbed.

Regarding grid resolution, we have employed a mesh size of 60^3 cells. The mesh is refined in the near-wall regions and stretched away from the walls following a hyperbolic tangent distribution. The height of the largest computational cell Δy (which is located in the center of the domain) is $\Delta y = 0.022\,H$. This mesh conforms to the resolution criteria [24–26] in the bulk and the near-boundary regions for direct numerical simulations of turbulent RBC at $Ra = 10^6$. Since this mesh is sufficiently fine to resolve all turbulent scales of RBC at $Ra = 10^6$, then we can safely assume that it can also resolve all the flow structures of the cases of laminar convection treated herein, in which $Ra = 1.7 \times 10^4$. Moreover, we have performed simulations with a coarser grid, consisting of 30^3 cells, and observed only very minor differences in the numerical results. This is another indication that the mesh of 60^3 cells is appropriate for the purposes of our study.

Each simulation is first conducted for a time period of 600 t_{ff}, before assuming that a steady state has been reached. This time period is sufficient to wash out all transient effects. Subsequently, each simulation is run for an additional period of 400 t_{ff}. In all cases, it has been confirmed that the flow profiles remained constant during this additional period.

4. Results and Discussion

With regard to notation, the horizontal-area (xz) average of a generic quantity U is denoted by $\langle U \rangle$. Also, U' is the deviation of U from $\langle U \rangle$ in horizonal planes. Results for the thermal field are shown in terms of the normalized temperature, $\theta = (T - T_r)/\Delta T$. In order to compute multiple steady states, we have performed several simulations of the two cases by solving the low-Mach-number Equations (1)–(3) with different random perturbations of the initial condition of the velocity field. In other words, for each simulation, a separate field of random velocity perturbations is generated.

4.1. Case 1: Aspect Ratio $\Gamma = 1$

According to our numerical experiments, only one steady state is developed when the aspect ratio is equal to unity. In Figure 1, we have plotted the profile of the area-averaged normalized temperature $\langle \theta \rangle$ for this case. We can readily deduce that the profile is practically symmetric with respect to the mid-height. In principle, the profile cannot be completely symmetric due to the variation of the fluid properties (density, viscosity and conductivity) with the temperature. However, as mentioned above, the total (bottom-to-top) variation of the temperature ΔT is in the order of 5% and therefore the variations of ρ, μ and λ with T are approximately linear. Consequently, the emerging profile of $\langle \theta \rangle$ is practically symmetric.

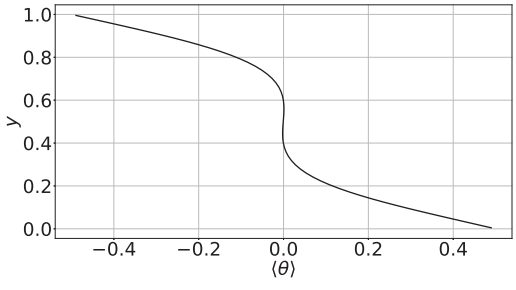

Figure 1. Case 1, aspect ratio $\Gamma = 1$; profile of the area-averaged normalized temperature $\langle \theta \rangle$.

In Figure 2, we present plots of the streamlines colored by θ for case 1. We observe that the flow is organized into a single large roll which is aligned in one horizontal direction. Also, the streamlines are practically symmetric with respect to the vertical (yz) mid-width plane. As mentioned above, this is due to the small variation of the fluid properties with temperature.

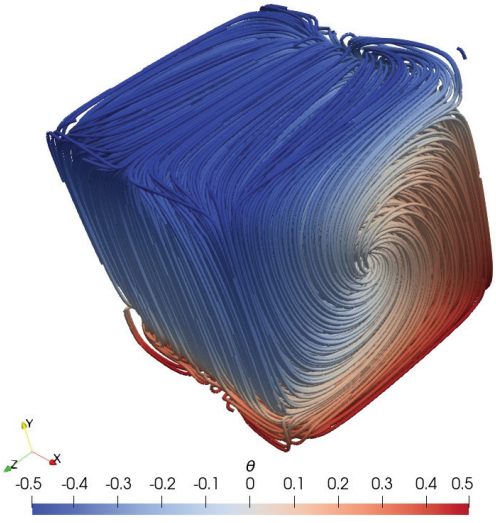

Figure 2. Case 1, streamlines colored by the normalized temperature θ.

In the context of our study we also performed a simulation of this case by invoking the Boussinesq approximation. According to it, ρ is constant and equal to ρ_r everywhere in the governing system except for the gravity term in (2) in which $\frac{\partial \rho}{\partial y} = -\beta_r \rho_r \frac{\partial T}{\partial y}$. Also, λ and μ are constant. Our simulation with the Boussinesq approximation produced nearly identical results for $\langle \theta \rangle$ and the streamlines.

In fact, the only discernible non-Boussinesq effect in our simulation based on the low-Mach-number Equations (1)–(3) is a non-zero mean vertical velocity $\langle v \rangle$. Its presence is explained as follows. The mass flux $\langle \rho v \rangle$ is decomposed according to $\langle \rho v \rangle = \langle \rho \rangle \langle v \rangle + \langle \rho' v' \rangle$. For steady flow, $\langle \rho v \rangle = 0$; thus, $\langle v \rangle = -\langle \rho' v' \rangle / \langle \rho \rangle$. In general, $\langle v \rangle$ is not zero. In Figure 3, we present profiles of $\langle v \rangle$ for case 1, by solving the low-Mach-number Equations (1)–(3), i.e., without the Boussinesq approximation. According to this figure, the amplitude of $\langle v \rangle$ is small, albeit non-zero, and peaks at mid-height. On the other hand, under the Boussinesq approximation ρ', hence $\langle v \rangle$, are zero.

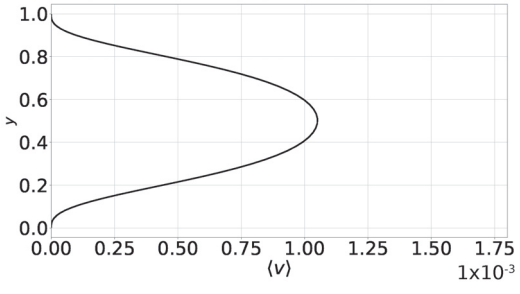

Figure 3. Case 1, profile of the area-averaged vertical velocity $\langle v \rangle$. The establishment of a vertical velocity component is the only discernible non-Boussinesq effect.

4.2. Case 2: Aspect Ratio $\Gamma = 2$

In this section, we examine the case that corresponds to the higher aspect ratio, $\Gamma = 2$. By considering different random perturbations on the initial velocity, we were able to compute five different steady states. The profiles of $\langle\theta\rangle$ for case 2 are shown in Figure 4. Therein, the various steady solutions are referred to as '2a', '2b' and so on.

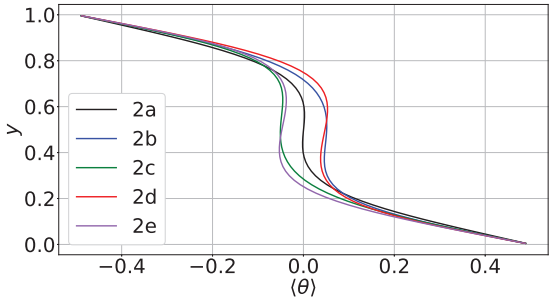

Figure 4. Case 2, aspect ratio $\Gamma = 2$: profiles of $\langle\theta\rangle$ for the 5 different steady states. These states are referred to as '2a', '2b' and so on.

In the steady state 2a, the profile of $\langle\theta\rangle$ is practically symmetric with respect to the mid-height and close to those in case 1. However, the profiles of the other four steady states are asymmetric and shifted either to the left or to the right, i.e., they are shifted either towards the cold top wall or the warmer bottom one. This asymmetry has been observed in different types of natural convection [11,12] and is associated with the development of more than one convective structure in domains with high aspect ratio. More specifically, this asymmetry is a result of the particular orientation of the flow structures. Our simulations confirm that this is true in classical RBC as well.

We further note that the profiles of $\langle\theta\rangle$ are not monotonic but exhibit overshoots at the edges of the thermal boundary layers. Such overshoots have already been predicted in simulations of turbulent RBC [3,27]. In laminar RBC, we attribute these overshoots to the strong ascending and descending plumes which bring substantial amounts of warm gas near the top wall and cold gas near the bottom one, respectively. But since the flow is not turbulent, thermal mixing is not strong enough to reduce the temperature gradients in the bulk of the domain, thereby resulting in such overshoots.

Next, we examine the flow structures in the five different steady states. In Figure 5, we present the streamlines for the steady state 2a, colored by the normalized temperature θ. The flow is organized into a single large roll which is aligned in one horizontal direction. Further, similarly to the $\langle\theta\rangle$ profile, the streamlines are symmetric with respect to the vertical mid-width plane.

In Figure 6, we have plotted the streamlines of the steady states 2b and 2c. In these states, the flow is organized into two large counter-rotating rolls. These rolls have different sizes but are both aligned in a diagonal plane. The particular diagonal plane of alignment may vary, depending on the perturbation of the initial condition for the velocity. As a result, the streamlines are no longer symmetric with respect to the mid-width plane, which in turn explains the shift of the corresponding $\langle\theta\rangle$ profiles. Globally, the flow patterns in 2b and 2c are the same but with opposite direction of rotation of the large rolls.

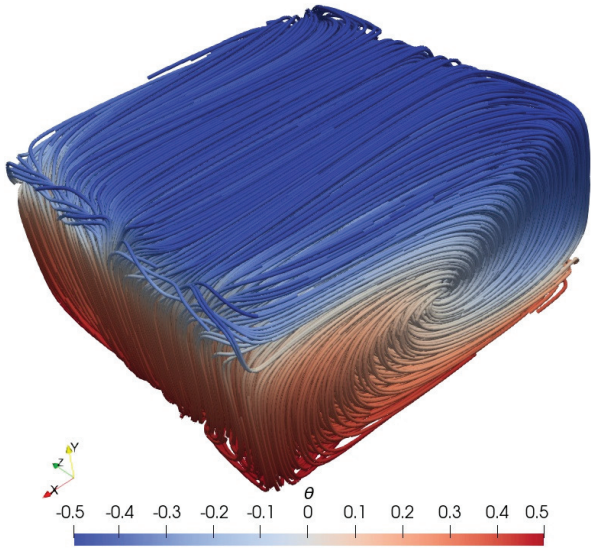

Figure 5. Case 2, streamlines colored by the normalized temperature θ for the steady state 2a.

Plots of the streamlines of the steady states 2d and 2e are presented in Figure 7. According to these plots, the flow is organized again into two large counter-rotating rolls. However, these rolls now have equal sizes and are aligned in a horizontal direction, instead of being aligned in a diagonal plane. Further, the flow patterns in 2d and 2e are the same, but with opposite direction of rotation of the large rolls. Upon comparison of the plots in Figures 6 and 7, we infer that in the steady states 2b and 2d, in which the $\langle\theta\rangle$ profile is shifted towards the hot bottom wall, the fluid in contact with the side walls is mostly hot whereas in the other two states, 2c and 2e, the $\langle\theta\rangle$ profile is shifted towards the top cold wall while the fluid in contact with the side walls is mostly cold.

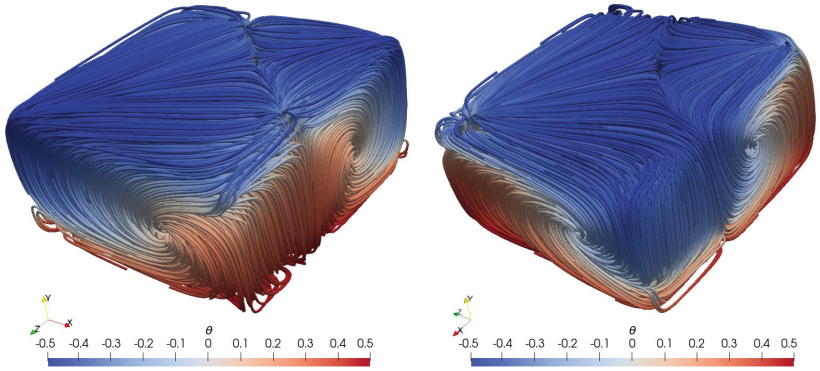

Figure 6. Case 2, streamlines colored by the normalized temperature θ for the steady states: (**a**) 2b and (**b**) 2c.

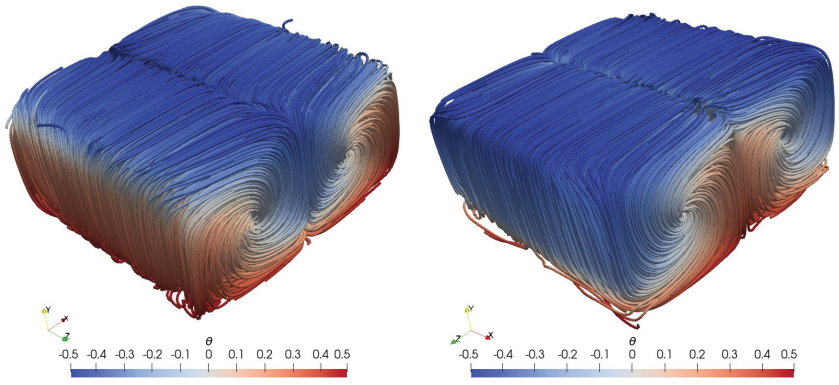

Figure 7. Case 2, streamlines colored by the normalized temperature θ for the steady states (**a**) 2d and (**b**) 2e.

Additional information about the differences between the emerging steady states can be obtained by examining the profiles of the area-averaged horizontal velocity $\bar{u} = \sqrt{\langle u \rangle^2 + \langle w \rangle^2}$. The plots of $\bar{u}$ for the steady states of case 2 are shown in Figure 8. Globally, these profiles are M-shaped, with a local minimum near the mid-height and two peaks at $y \approx 0.2$ and $y \approx 0.8$, respectively. As with the other flow variables, only the profile of the single-roll state 2a is symmetric. In the other four states, the profiles are asymmetric and the peak values are different. More specifically, in the two-roll states 2b and 2d (whose $\langle \theta \rangle$ profile is shifted towards the hot bottom wall), the highest peak is the lower one. As will be shown below, the same is true for the vertical velocity component. This in turn implies that, in 2b and 2d, convective motions and heat transfer are stronger in the lower part of the domain.

On the contrary, in the two-roll states 2c and 2e (whose $\langle \theta \rangle$ profile shifted towards the top cold wall), the highest peak of $\bar{u}$ is the upper one. In these states, the vertical velocity also peaks at the top part of the domain. Therefore, in steady states 2c and 2e, convective motions are stronger in the upper part of the domain.

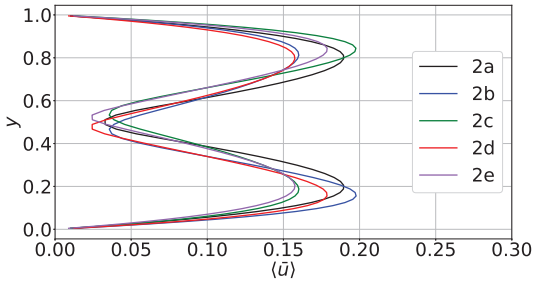

Figure 8. Case 2, profiles of the area-averaged horizontal velocity $\bar{u}$ for the 5 different steady states.

Plots of the mean vertical velocity component, $\langle v \rangle$, are presented in Figure 9. According to those, the values of $\langle v \rangle$ are the highest in states 2d and 2e, i.e., when the flow is organized in two rolls aligned in a horizontal direction. Next, in descending order, are the values of $\langle v \rangle$ in cases 2b and 2c which are characterized by two rolls aligned in a diagonal plane. Finally, the smallest values are predicted in the single-roll state 2a. As mentioned above, these observations imply that the flow arrangement of cases 2d and 2e exhibits the strongest convective motions.

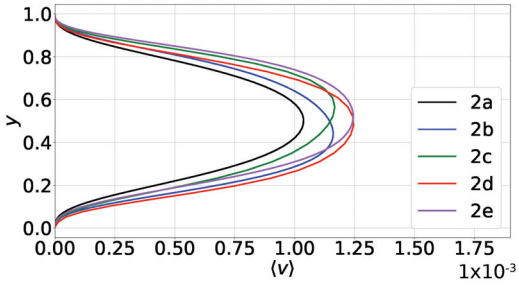

Figure 9. Case 2, profiles of the area-averaged vertical velocity $\langle v \rangle$. The establishment of a vertical velocity component is the only discernible non-Boussinesq effect.

Next, we present results for the Nusselt number. The area-averaged Nusselt number Nu_y is given by

$$Nu_y = \underbrace{\sqrt{Ra\,Pr} < \rho\, v\, \theta >}_{Nu_{\text{conv}}} - \underbrace{< \lambda \frac{\partial \theta}{\partial y} >}_{Nu_{\text{diff}}} . \tag{7}$$

In the above equation, Nu_{conv} represents the convective contribution and Nu_{diff} the diffusive one. At steady state, Nu_y should be constant and equal to the *global* Nusselt number. This was indeed predicted by our simulations. The profiles of Nu_{conv} and Nu_{diff} are shown in Figure 10a and Figure 10b, respectively. We observe that Nu_{diff} takes small negative values near the center of the domain. This is due to the fact that the profiles of $\langle \theta \rangle$ are not monotonic but instead exhibit two overshoots.

As expected, the profile of Nu_{conv} in steady state 2a is symmetric whereas in states 2b and 2d the profile is shifted downwards. This further corroborates that in 2b and 2d, convective heat transfer is stronger in the lower part of the domain. The opposite is true for the steady states 2c and 2e, i.e., the Nu_{conv} profile is shifted upwards because convection is stronger in the upper part of the domain. These findings are in accordance with the predicted velocity profiles. Further, from the plots of Figure 10 we infer that the states 2d and 2e (characterized by two rolls aligned in a horizontal direction) have the highest Nusselt number, whereas the single-roll state 2a has the lowest one.

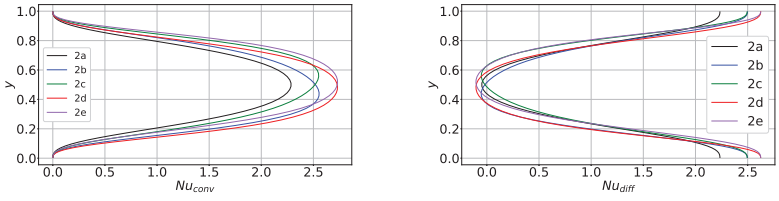

Figure 10. Case 2, profiles of the Nu_y components. (**a**) convective component, (**b**) diffusive component.

For this case, we also performed a simulation by invoking the Boussinesq approximation. The results were once again very similar to those based on the low-Mach-number Equations (1)–(3). More specifically, the only discernible non-Boussinesq effect is the establishment of a non-zero mean velocity component $\langle v \rangle$, as shown in Figure 9. Meanwhile, under the Boussinesq approximation, $\langle v \rangle$ is exactly zero.

Finally, it is worth adding that a given random perturbation of the initial condition for the velocity does not always result in the same steady state with and without the Boussinesq approximation. Accordingly, in order to compute the various steady solutions

with the Boussinesq approximation, we had to employ different random perturbations than those in the simulations without it. This implies that even though non-Boussinesq effects are not significant in the steady states, such effects can play a role in the transient regime, i.e., during the formation and growth of the convective structures. More specifically, the variation of the fluid properties with the temperature can favor the establishment of one steady state over another.

5. Conclusions

In this article, we presented a numerical study of the different steady states in laminar Rayleigh–Bénard convection in cuboids. In the case of a cube, our simulations predicted a single steady state: the flow is organized in a single convective roll and the mean flow variables are symmetric with respect to the mid-height. On the other hand, for aspect ratio $\Gamma = 2$, there are five different steady states. One of them consists of a single-roll configuration whereas in two other steady states, the flow is organized in a two-roll configuration with rolls of different sizes that are aligned in one diagonal plane. In the remaining two states, the flow is organized in two rolls of equal size that are aligned in one horizontal direction. In the two-roll configurations, the profiles of the area-averaged flow variables are asymmetric with respect to the mid-height and the convective motions are stronger either in the lower or upper part of the domain. The states with two rolls of equal size exhibit the strongest convective motions and highest Nusselt number, whereas the single-roll configuration has the lowest Nusselt number. Finally, the only noticeable non-Boussinesq effect is the development of a vertical velocity component which only mildly enhances the intensity of fluid motion in the bulk.

Author Contributions: Conceptualization, J.C. and M.V.P.; methodology, J.C. and M.V.P.; software, J.C.; validation, J.C. and M.V.P.; formal analysis, J.C. and M.V.P.; investigation, J.C. and M.V.P.; resources, M.V.P.; data curation, J.C.; writing—original draft preparation, J.C. and M.V.P.; writing—review and editing, J.C. and M.V.P.; visualization, J.C.; supervision, M.V.P.; project administration, M.V.P.; funding acquisition, M.V.P. All authors have read and agreed to the published version of the manuscript.

Funding: The authors gratefully acknowledge the financial support provided by the Belgian Federal Public Service Economy under the Energy Transition Fund, project SFP-LOCA.

Data Availability Statement: Data are contained within the article.

Conflicts of Interest: The authors declare no conflicts of interest.

References

1. Chillà, F.; Schumacher, J. New perspectives in turbulent Rayleigh-Bénard convection. *Eur. Phys. J. E* **2012**, *35*, 58. [CrossRef] [PubMed]
2. Wagner, S.; Shishkina, O. Aspect-ratio dependency of Rayleigh-Bénard convection in box-shaped containers. *Phys. Fluids* **2013**, *25*, 085110. [CrossRef]
3. Yigit, S.; Poole, R.J.; Chakraborty, N. Effects of aspect ratio on laminar Rayleigh-Bénard convection of power-law fluids in rectangular enclosures: A numerical investigation. *Int. J. Heat Mass Tran.* **2015**, *91*, 1292–1307. [CrossRef]
4. Wang, Q.; Verzicco, R.; Lohse, D.; Shishkina, O. Multiple states in turbulent large-aspect-ratio thermal convection: what determines the number of convection rolls? *Phys. Rev. Lett.* **2020**, *125*, 074501. [CrossRef] [PubMed]
5. Gelfgat, A.Y. Different modes of Rayleigh-Bénard instability in two- and three-dimensional rectangular enclosures. *J. Comput. Phys.* **1999**, *156*, 300–324. [CrossRef]
6. Hof, B.; Lucas, P.G.J.; Mullin, T. Flow state multiplicy in convection. *Phys. Fluids* **1999**, *11*, 2815–2817. [CrossRef]
7. Ma, D.-J.; Sun, D.-J.; Yin, X.-Y. Multiplicty of steady states in cylindrical Rayleigh-Bénard convection. *Phys. Rev. E* **2010**, *74*, 037302. [CrossRef]
8. Borońska, K.; Tuckerman, L.S. Extreme multiplicity in cylindrical Rayleigh-Bénard convection. II. Bifurcation diagram and symmetry classification. *Phys. Rev. E* **2010**, *81*, 036321. [CrossRef]
9. Venturi, D.; Wan, X.; Karniadakis, G.E. Stochastic bifurcation analysis of Rayleigh-Bénard convetion. *J. Fluid Mech.* **2010**, *650*, 391–413. [CrossRef]
10. Silano, G.; Sreenivasan, X.R.; Verzicco, R. Numerical simulations of Rayleigh-Bénard convection for Prandtl numbers between 10^{-1} and 10^4 and Rayleigh numbers between 10^5 and 10^9. *J. Fluid Mech.* **2010**, *662*, 409–446. [CrossRef]

11. Erenburg, V.; Gelfgat, A.Y.; Kit, E.; Bar-Yoseph, P.Z.; Solan, A. Multiple states, stability and bifurcations of natural convection in a rectangular cavity with partially heated vertical walls. *J. Fluid Mech.* **2003**, *492*, 63–89. [CrossRef]
12. Yigit, S.; Poole, R.J.; Chakraborty, N. Effects of aspect ratio on natural convection of Bingham fluids in rectangular enclosures with differentially heated horizontal walls heated from below. *Int. J. Heat Mass Tran.* **2015**, *80*, 727–736. [CrossRef]
13. Shishkina, O. Rayleigh-Bénard convection: The container shape matters. *Phys. Rev. Fluids* **2021**, *6*, 090502. [CrossRef]
14. Paolucci, S. Filtering of sound from the Navier–Stokes equations. *Tech. Rep. SAND* **1982**, *SAND*, 82–8257.
15. Lessani, B.; Papalexandris, M.V. Time-accurate calculation of variable density flows with strong temperature gradients and combustion. *J. Comput. Phys.* **2006**, *212*, 218–246. [CrossRef]
16. Hong, W.; Walker, D.T. Reynolds-averaged equations for free-surface flows with application to high-Froude-number jet spreading. *J. Fluid Mech.* **2000**, *417*, 183–209. [CrossRef]
17. Antoniadis, P.D.; Papalexandris, M.V. Numerical study of unsteady, thermally-stratified shear flows in superposed porous and pure-fluid domains. *Int. J. Heat Mass Tran.* **2016**, *96*, 643–659. [CrossRef]
18. Papalexandris, M.V. On the applicability of Stokes' hypothesis to low-Mach-number flows. *Contin. Mech. Therm.* **2020**, *32*, 1245–1249. [CrossRef]
19. Rhie, C.M.; Chow, W.L. Numerical study of the turburlent flow past an airfoil with trailing edge separation. *AIAA J.* **1983**, *21*, 1525–1532. [CrossRef]
20. Balay, S.; Abhyankar, S.; Adams, M.; Brown, J.; Brune, P.; Buschelman, K.; Dalcin, L.; Dener, A.; Eijkhout, V.; Gropp, W.; et al. PETSc Users Manual. *Technical Report ANL-95/11-Revision 3.11, Argonne National Laboratory*; Argonne National Lab. (ANL): Argonne, IL, USA, 2019.
21. Georgiou, M.; Papalexandris, M.V. Numerical study of turbulent flow in a rectangular T-junction. *Phys. Fluids* **2017**, *29*, 065106. [CrossRef]
22. Georgiou, M.; Papalexandris, M.V. Direct numerical simulation of turbulent heat transfer in a T-junction. *J. Fluid Mech.* **2018**, *845*, 581–614. [CrossRef]
23. Marichal, J.; Papalexandris, M.V. On the dynamics of the large scale circulation in turbulent convection with a free-slip upper boundary. *Int. J. Heat Mass Tran.* **2021**, *183*, 122220. [CrossRef]
24. Shishkina, O.; Stevens, R.; Grossmann, S.; Lohse, D. Boundary layer structure in turbulent thermal convection and its consequences for the required numerical resolution. *New J. Phys.* **2010**, *12*, 075022. [CrossRef]
25. Grötzbach, G. Spatial resolution requirements for direct numerical simulation of the Rayleigh-Bénard convection. *J. Comput. Phys.* **1983**, *49*, 214–264. [CrossRef]
26. Stevens, R.; Verzicco, R.; Lohse, D. Radial boundary layer structure and Nusselt number in Rayleigh-Bénard convection. *J. Fluid Mech.* **2010**, *643*, 495–507. [CrossRef]
27. Horn, S.; Shishkina, O.; Wagner, C. On non-Oberbeck-Boussinesq effects in three-dimensional Rayleigh-Bénard convection in glycerol. *J. Fluid Mech.* **2013**, *724*, 175–202. [CrossRef]

fluids

MDPI

Review

From Navier to Stokes: Commemorating the Bicentenary of Navier's Equation on the Lay of Fluid Motion

Aldo Tamburrino [1,2]

[1] Department of Civil Engineering, University of Chile, Santiago 8370448, Chile; atamburr@ing.uchile.cl
[2] Advanced Mining Technology Center, University of Chile, Santiago 8370448, Chile

Abstract: The article presents a summarised history of the equations governing fluid motion, known as the Navier–Stokes equations. It starts with the work of Castelli, who established the continuity equation in 1628. The determination of fluid flow resistance was a topic that involved the brightest minds of the 17th and 18th centuries. Navier's contribution consisted of the incorporation of molecular attraction effects into Euler's equation, giving rise to an additional term associated with resistance. However, his analysis was not the only one. This continued until 1850, when Stokes firmly established the boundary conditions that must be applied to the differential equations of motion, specifically stating the non-slip condition of the fluid in contact with a solid surface. With this article, the author wants to commemorate the bicentennial of the publication of "*Sur les Lois du Mouvement des Fluides*" by Navier in the Mémoires de l'Académie Royale des Sciences de l'Institut de France.

Keywords: Navier–Stokes equation; fluid flow resistance; viscosity; non-slip boundary condition

Citation: Tamburrino, A. From Navier to Stokes: Commemorating the Bicentenary of Navier's Equation on the Lay of Fluid Motion. *Fluids* **2024**, *9*, 15. https://doi.org/10.3390/fluids9010015

Academic Editors: D. Andrew S. Rees, Vasily Novozhilov and Cunlu Zhao

Received: 7 November 2023
Revised: 21 December 2023
Accepted: 30 December 2023
Published: 6 January 2024

1. Introduction

This year marks the 200th anniversary since the article "*Sur les Lois du Mouvement des Fluides*" by Claude Louis Marie Henri Navier was published in the Mémoires de l'Académie Royale des Sciences de l'Institut de France. As Navier's work is part of the foundations of fluid mechanics, the author considers it appropriate to commemorate it in a journal devoted to fluids and their motion. This article presents a summary of Navier's contribution to the controversial problem of fluid resistance to motion, which engaged the brightest minds in mathematics, physics, and engineering from the 18th until the mid-19th centuries, when the work of Stokes definitively consolidated what we now identify as the Navier–Stokes equations.

Before presenting how Navier introduced the resistance of motion, it is interesting to mention some of his biography, taken from McKeon (1981) [1]. Navier was born in Dijon on 10 February 1785, and died on 21 August 1836, in Paris. His father was a lawyer for the Legislative Assembly in Paris during the French Revolution and died in 1793, leaving him under the guardianship of his great-uncle Emiland Gauthey, chief engineer of the Corps of Bridges and Roads of Paris, who educated and prepared him to enter the École Polytechnique in 1802, where he had Joseph Fourier as professor of analysis (calculus), who would become his protector and later, friend. In 1804, Navier entered the École des Ponts et Chaussées, graduating in 1806. It is important to mention Navier's passage through both schools: In the first, he acquired a rigorous mathematical and theoretical education, while in the second, he received an orientation to the practice of engineering. Navier would know how to take advantage of this complementary education. A few months after his graduation, his great-uncle passed away, and the administration of the Corps of Bridges and Roads commissioned Navier in 1807 to edit Gauthey's manuscripts, which were published between 1809 and 1816. From 1819, Navier oversaw the applied mechanics courses at the École des Ponts et Chaussées. In parallel with the edition of his great-uncle's engineering manuscripts, from 1807 to 1820, he made mathematical analysis a fundamental

tool of civil engineering. The combination of these two skills, theoretical-analytical and practical application to engineering, was fundamental to the contributions he made in solid mechanics (elasticity) and fluid mechanics [2].

2. The Problem of the Motion of Fluids

Arbitrarily, and just to establish a starting point, we can say that modern hydraulics began as an experimental science in Italy in the 16th century, becoming more theoretical in the following century. Benedetto Castelli (c.1577–c.1644) is one of its best exponents by presenting the equation of continuity in his treatise *Della misura delle acque correnti* in 1628. Although the propositions established by Castelli in his treatise had already been indicated by Leonardo da Vinci a century earlier, he did not divulge them, so they remained unknown until the codices with his works began to be rediscovered and known. Leonardo did not form disciples, unlike Galileo Galilei, who was able to form a school, with Benedetto Castelli being one of his most accomplished students. The continuity equation for a steady-state regime is stated on page 8 of the 1639 edition of the book that the author had access to [3], and it is shown in the lines within the rectangle in Figure 1. A loose translation of the text is "if two pipes with unequal velocity in the same amount of time, discharge the same amount of water, the size of the first to the size of the second will have a reciprocal proportion to the velocity of the second to the velocity of the first". That is, if the flow discharged in two pipes is the same, then $A_1 : A_2 = V_2 : V_1$, with the subindexes 1 and 2 denoting each of the conduits.

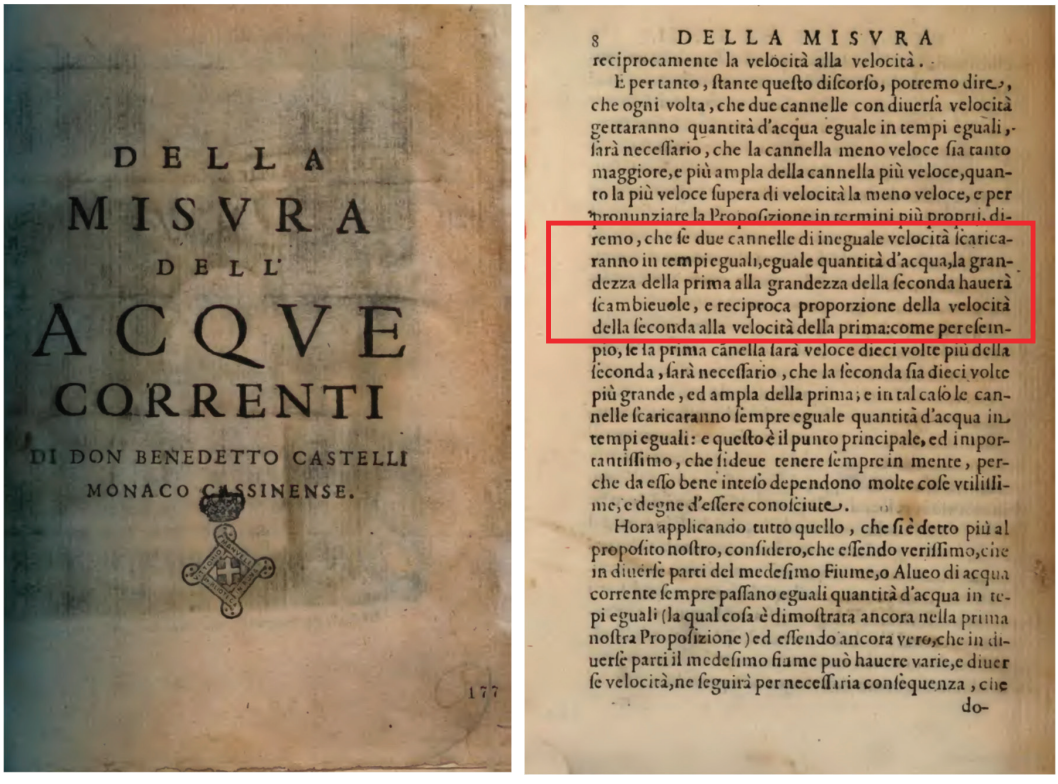
DELLA
MISVRA
DELL'
ACQVE
CORRENTI
DI DON BENEDETTO CASTELLI
MONACO CASSINENSE.

177

8 DELLA MISVRA

reciprocamente la velocità alla velocità.

E per tanto, ſtante queſto diſcorſo, potremo dire, che ogni volta, che due cannelle con diuerſa velocità gettaranno quantità d'acqua eguale in tempi eguali, ſarà neceſſario, che la cannella meno veloce ſia tanto maggiore, e più ampla della cannella più veloce, quanto la più veloce ſupera di velocità la meno veloce, e per pronunziare la Propoſizione in termini più propri, diremo, che ſe due cannelle di ineguale velocità ſcaricaranno in tempi eguali, eguale quantità d'acqua, la grandezza della prima alla grandezza della ſeconda hauerà ſcambieuole, e reciproca proporzione della velocità della ſeconda alla velocità della prima: come per eſempio, ſe la prima cannella ſarà veloce dieci volte più della ſeconda, ſarà neceſſario, che la ſeconda ſia dieci volte più grande, ed ampla della prima; e in tal caſo le cannelle ſcaricaranno ſempre eguale quantità d'acqua in tempi eguali: e queſto è il punto principale, ed importantiſſimo, che ſi deue tenere ſempre in mente, perche da eſſo bene inteſo dependono molte coſe vtiliſſime, e degne d'eſſere conoſciute.

Hora applicando tutto quello, che ſi è detto più al propoſito noſtro, conſidero, che eſſendo veriſſimo, che in diuerſe parti del medeſimo Fiume, o Alueo di acqua corrente ſempre paſſano eguali quantità d'acqua in tepi eguali (la qual coſa è dimoſtrata ancora nella prima noſtra Propoſizione) ed eſſendo ancora vero, che in diuerſe parti il medeſimo fiume può hauere varie, e diuerſe velocità, ne ſeguirà per neceſſaria conſequenza, che

do-

Figure 1. First publication in which the continuity equation is presented. Edition of 1639 of Benedetto Castelli's work. On the eighth page, it is indicated that $A_1 : A_2 = V_2 : V_1$.

In the 16th and 17th centuries, a drastic change in scientific thinking took place, paving the way for the Scientific Revolution. Some of the key changes during this period included an emphasis on empirical observation and experimentation, leading to the rejection of the prevailing Aristotelian worldview. Additionally, there was a shift towards using mathematics as a tool to describe and understand natural phenomena, the development of the scientific method, the invention of the printing press enabling the dissemination of scientific ideas, and the exploration and expansion of empirical knowledge. The era also witnessed the development of new tools and instruments and posed challenges to established religious and political authorities due to scientific discoveries and new ideas. This transformative period culminated in 1687 with the publication of Newton's *Philosophiæ Naturalis Principia Mathematica* [4]. As a reflection of this change, known as the Scientific Revolution, the Royal Society of London for Improving Natural Knowledge was created in 1662, and the Académie des Sciences de Paris was established in 1666 [5]. The development of physics required better mathematical tools. At the end of the 16th century, the French mathematician François Viète (1540–1603) wrote the first work on symbolic algebra, introducing the use of letters to represent quantities [6]. Another significant contribution was made by René Descartes (1596–1650), who reduced geometry to equations [7]. This process peaked with Newton and Leibniz, who established modern calculus. It is important to keep in mind that, at that time, the concepts of momentum and energy were not yet well established. Regarding the driving force that puts bodies in motion, in the 18th century, the focus (and result of its application) varied, depending on the school or doctrine to which the researcher adhered. Thus, the Cartesians indicated that it was momentum, the Newtonians the variation of momentum, and the Leibnizians the conversion of vis morta to vis viva (a concept that we now associate with energy). It was Pierre Varignon (1654–1722) who, applying the calculus developed by Leibniz to the mechanics presented by Newton, analytically determined the exit velocity through an orifice based on the concept of momentum, with an expected error coefficient of $\sqrt{2}$ [8]. In 1738, Daniel Bernoulli (1700–1782) published *Hydrodynamica, sive de viribus et motibus fluidorum commentarii* [9] (Figure 2), in which he used what we call nowadays the energy approach for the first time to address the problem and correctly obtain Torricelli's expression for discharge through an orifice. The English translations of Daniel Bernoulli's *Hydrodynamica* and Johann Bernoulli's *Hydraulica* were published in 1969 in a single book by Dover Publications Inc. Following Leibniz, whose formulation of energy concepts was based on the fall of particles, the energy conservation applied by Bernoulli considers only the terms associated with what we now call kinetic energy (*vis viva*, "living forces") and potential energy (*vis morta*, associated with pressure or weight).

Jean Le Rond D'Alembert (1717–1783) demonstrated the conservation of "living forces" and in 1744 published *Traité de l'équilibre et du mouvement des fluide*s, in which he formally proved the results of Bernoulli. In this work, he considered that the equilibrium that exists between the "parts" of fluids, despite the difference in pressures, is due to the adhesion between particles, and in Chapter IV he asks: "Is this force purely passive, that is, only due to the roughness of the fluid particles that touch each other, or is it an active force that tends to unite these particles and bring them closer together?" [10] (p. 37). In 1768, in the first part of volume 5 of *Opuscules Mathématiques*, D'Alembert published the article *Paradoxe proposé aux Géometres sur la Resistance des Fluides*, in which he demonstrated that the force due to the motion of an incompressible fluid over an axisymmetric obstacle, whose geometry of the half facing the flow is equal to the rear, is zero. Unable to explain the reason for this result, he concluded the article by writing that it is a "singular paradox that I leave for geometers to clarify" [11].

Significant advances to Newtonian dynamics were made by Leonard Euler (1707–1783). Newton's work basically referred to particle dynamics in one dimension. In 1750, Euler presented the equations for the generalised motion in the three spatial dimensions, which were published in 1752 in an article titled *Découverte d'un nouveau principe de mécanique* [12], in which he extended the second law of Newton to a continuous medium. In 1757, the

works presented in 1755 were published in the *Mémoires de l'Académie Royale des Sciences et Belles-Lettres de Berlin*. The Mathematics section presents three works by Euler: *Principes généraux de l'état de l'équilibre des fluids* [13], *Principes généraux du mouvement des fluids* [14], and *Continuation des Recherches sur la théorie du mouvement des fluids* [15]. In the second of these, Euler derives the components in the three spatial directions of the equation of motion of the ideal fluid, currently known as the Euler equation (Figure 3). Joseph-Louis Lagrange (1736–1813), among his many contributions to mathematics and physics, in his *Mémoire sur la théorie du mouvement des fluids* [16], uses the potential function to describe the motion of fluids.

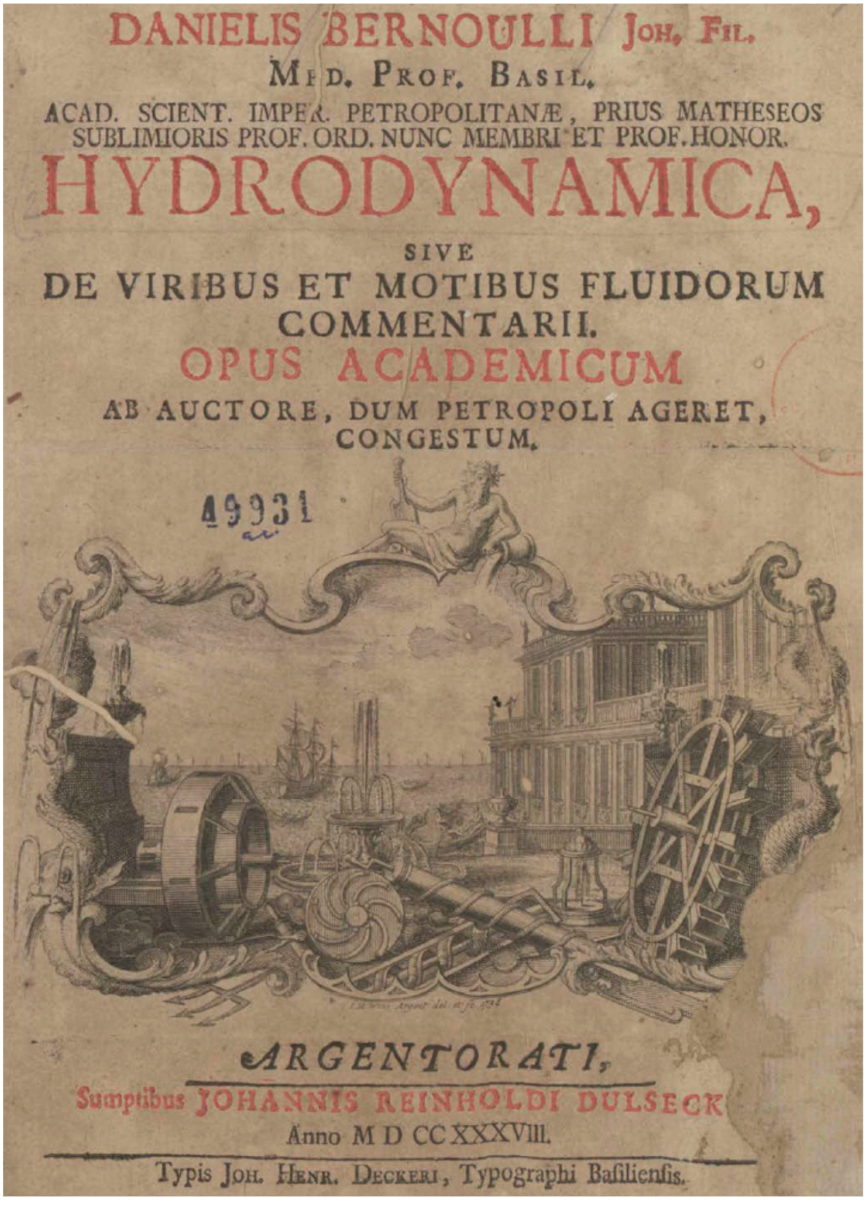

Figure 2. First page of the first edition (1738) of Daniel Bernoulli's *Hydrodynamica*.

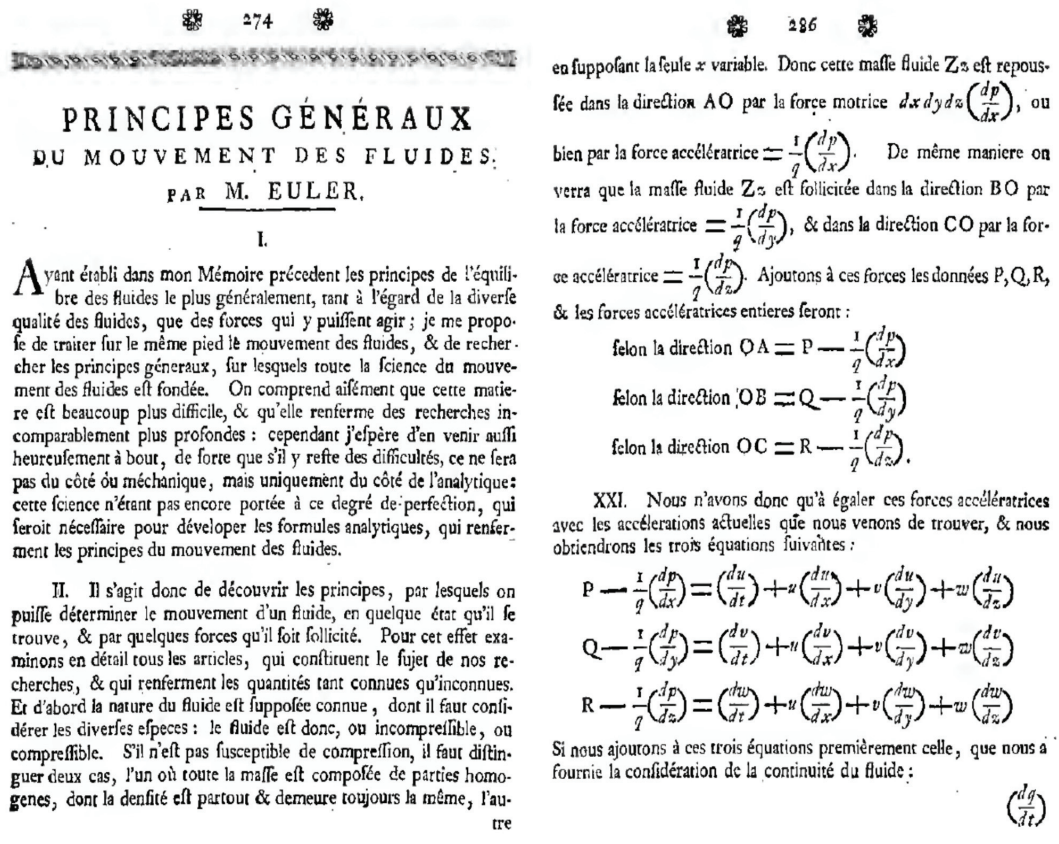

274

PRINCIPES GÉNÉRAUX
DU MOUVEMENT DES FLUIDES.
PAR M. EULER.

I.

Ayant établi dans mon Mémoire précedent les principes de l'équilibre des fluides le plus généralement, tant à l'égard de la diverſe qualité des fluides, que des forces qui y puiſſent agir ; je me propoſe de traiter ſur le même pied le mouvement des fluides, & de rechercher les principes généraux, ſur lesquels toute la ſcience du mouvement des fluides eſt fondée. On comprend aiſément que cette matiere eſt beaucoup plus difficile, & qu'elle renferme des recherches incomparablement plus profondes : cependant j'eſpère d'en venir auſſi heureuſement à bout, de ſorte que s'il y reſte des difficultés, ce ne ſera pas du côté ou méchanique, mais uniquement du côté de l'analytique: cette ſcience n'étant pas encore portée à ce degré de perfection, qui ſeroit néceſſaire pour développer les formules analytiques, qui renferment les principes du mouvement des fluides.

II. Il s'agit donc de découvrir les principes, par leſquels on puiſſe déterminer le mouvement d'un fluide, en quelque état qu'il ſe trouve, & par quelques forces qu'il ſoit ſollicité. Pour cet effet examinons en détail tous les articles, qui conſtituent le ſujet de nos recherches, & qui renferment les quantités tant connues qu'inconnues. Et d'abord la nature du fluide eſt ſuppoſée connue, dont il faut conſidérer les diverſes eſpeces : le fluide eſt donc, ou incompreſſible, ou compreſſible. S'il n'eſt pas ſuſceptible de compreſſion, il faut diſtinguer deux cas, l'un où toute la maſſe eſt compoſée de parties homogenes, dont la denſité eſt partout & demeure toujours la même, l'autre

286

en ſuppoſant la ſeule x variable. Donc cette maſſe fluide $Z\omega$ eſt repouſſée dans la direction AO par la force motrice $dx\,dy\,dz\left(\frac{dp}{dx}\right)$, ou bien par la force accélératrice $= \frac{1}{q}\left(\frac{dp}{dx}\right)$. De même maniere on verra que la maſſe fluide $Z\omega$ eſt ſollicitée dans la direction BO par la force accélératrice $= \frac{1}{q}\left(\frac{dp}{dy}\right)$, & dans la direction CO par la force accélératrice $= \frac{1}{q}\left(\frac{dp}{dz}\right)$. Ajoutons à ces forces les données P, Q, R, & les forces accélératrices entieres ſeront :

$$\text{ſelon la direction OA} = P - \frac{1}{q}\left(\frac{dp}{dx}\right)$$
$$\text{ſelon la direction OB} = Q - \frac{1}{q}\left(\frac{dp}{dy}\right)$$
$$\text{ſelon la direction OC} = R - \frac{1}{q}\left(\frac{dp}{dz}\right).$$

XXI. Nous n'avons donc qu'à égaler ces forces accélératrices avec les accélerations actuelles que nous venons de trouver, & nous obtiendrons les trois équations ſuivantes :

$$P - \frac{1}{q}\left(\frac{dp}{dx}\right) = \left(\frac{du}{dt}\right) + u\left(\frac{du}{dx}\right) + v\left(\frac{du}{dy}\right) + w\left(\frac{du}{dz}\right)$$
$$Q - \frac{1}{q}\left(\frac{dp}{dy}\right) = \left(\frac{dv}{dt}\right) + u\left(\frac{dv}{dx}\right) + v\left(\frac{dv}{dy}\right) + w\left(\frac{dv}{dz}\right)$$
$$R - \frac{1}{q}\left(\frac{dp}{dz}\right) = \left(\frac{dw}{dt}\right) + u\left(\frac{dw}{dx}\right) + v\left(\frac{dw}{dy}\right) + w\left(\frac{dw}{dz}\right)$$

Si nous ajoutons à ces trois équations premièrement celle, que nous a fournie la conſidération de la continuité du fluide :

$$\left(\frac{dq}{dt}\right)$$

Figure 3. Euler's article presented in 1755 and published in 1757 where the equations that currently bear his name are derived. In the figure, the left image corresponds to first page of the article and in the right side is the page with the equations of motion for an ideal fluid. P, Q, R correspond to the components along x, y, z of the body force field per unit mass, and q is the fluid density.

3. Structure of the Matter: Continuum or Atomic?

D'Alembert, Euler, and Lagrange made extensive use of differential equations, using the calculus tools developed up to that time. This meant that they considered matter as a continuous medium. However, this assumption generated some problems, for example, when trying to explain the deformation of solids or the vortices and eddies in what we now know as turbulent flows. This development of hydrodynamics, called "analytical mechanics", contrasts with what would later be called "physical mechanics", which was based on the interaction of molecules [17] (p. 361). This division continued to be present in the teaching of mechanics at the École Polytechnique at the end of the 19th century, as shown by Boussinesq in his *Leçons Synthétiques de Mécanique Générale servant d'Introduction au Cours de Mécanique Physique* (Synthetic Lessons of General Mechanics serving as an Introduction to the Course of Physical Mechanics), printed in 1889 [18]. Boussinesq was a defender of physical mechanics and indicated that rational (or analytical) mechanics was insufficient for the study of the most important phenomena and that the "material points" that arise from the atomic hypothesis for the constitution of matter allow us to explain the behaviour of matter by considering the interaction between them, as indicated in the first lesson of his *Leçons Synthétiques* [18].

The idea that matter was composed of atoms was not new. Already in the 5th century BC, the presocratic philosophers Leucippus of Miletus and his disciple Democritus of

Abdera had proposed it. The ideas of Leucippus and Democritus were reformulated in the philosophy of Epicurus (c.341–c.270 BC), and the atomistic physics derived from it was presented by the Roman poet and philosopher Lucretius (98–55 BC) in his verse work *De Rerum Natura* (On the Nature of Things). Rodríguez-Navas, in his Spanish translation, in prose, published in 1892, says, "Deliberately, no doubt, Lucretius did not use the word 'atom' even once in his entire extensive poem, which encompasses the subject most thoroughly studied in all his work" [19] (p. 4). The conception that matter is made up of atoms or fundamental particles was transmitted through the centuries and commented on, modified, or questioned by different authors, including Galileo Galilei (1564–1642), Thomas Hobbes (1588–1679), Robert Boyle (1627–1691), Robert Hooke (1635–1703), Christiaan Huygens (1629–1695), and Isaac Newton (1642–1727). Of the aforementioned, Boyle, Hooke, and Newton considered that heat was associated with the vibration of atoms or basic particles. Atomism was not free from detractors, especially for religious reasons, such as those made by St. Dionysius of Alexandria (3rd century) and with great force in the period 1660–1700, when it began to be considered with a more scientific than philosophical approach. The Parliament of Paris decreed in 1624 that those who supported or taught atomism would be subject to the death penalty [20]. Chapter 4 of Whyte's book (reference [20]) contains a chronological table, which has been the basis for what is presented here regarding the development of atomistic ideas.

Concerning the forces between basic particles, Newton postulates in his *Philosophiæ naturalis principia mathematica* [4] that they can be either attractive or repulsive (the latter being distinct from gravitational), and he demonstrates Boyle's law for gases by considering that the force of repulsion is inversely proportional to the distance between the centers of the particles (Proposition XXIII, Theorem XVIII of Book 2; [21]). Newton does not write $pV =$ constant but instead does so descriptively, without equations. Another important contribution regarding the forces of interaction between particles was made by the Croatian Rudjer Josip Bošković (1711–1787, also called Ruggero Giuseppe Boscovich), who published two important works related to the atomic (or molecular) structure of matter: In 1745, *De Viribus Vivis Dissertatio*, and in 1758, *Theoria Philosophiæ Naturalis*, with a revised and improved edition in 1763. In them, he postulates the existence of attractive and repulsive forces between atoms (or molecules), depending on the distance between them. If the atoms are far enough apart, the force is Newtonian attraction (proportional to the inverse square of the distance), but when they are very close, it is repulsive, asymptotically tending to an infinite value as the separation approaches zero. Between these two extreme behaviors, the force is finite and oscillates between attraction and repulsion. Figure 4 shows the graphical representation of these forces, taken from Boscovich's publications of 1745 and 1758 [22,23].

Pierre Simon Laplace (1749–1827) considers the molecular structure of matter and presents it in his successive editions of *Exposition du Système du Monde* (1796 [24], 1799 [25], and 1808 [26]), in each of which he improves his arguments. In a publication from 1805, he explains capillary rise through a molecular approach [27] (p. 1) and indicates that these molecular attraction forces "are insensible to sensible distances". This idea of molecular forces whose spatial action is very limited is refined in the third edition of his *Exposition*, in which he includes a chapter titled "*On molecular attraction*", where he reinforces the idea that molecular forces are "sensible only to imperceptible distances". The molecules are subject to an attraction force that decreases extremely rapidly [26] (p. 316) and to one that opposes it, due to heat, which also has the effect of decreasing their viscosity or intermolecular adhesion [26] (p. 317).

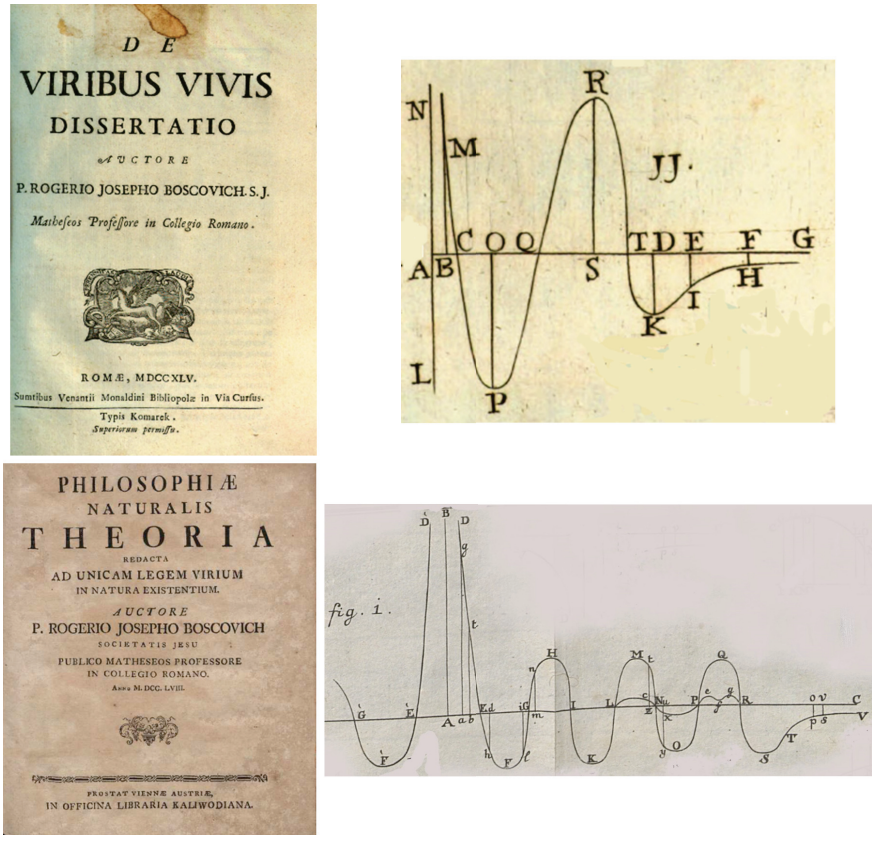

Figure 4. Intermolecular forces of attraction (below the horizontal line in the graphs) and repulsion (above the horizontal line), according to Boscovich. The vertical line NAL in the upper figure and BA in the lower one corresponds to a distance equal to zero between the centers of the particles or molecules, and the repulsive force becomes infinitely large. As the separation increases, the force oscillates between repulsion and attraction. When the particles are far enough apart, they are subject to attractive forces, like a Newtonian gravitational model (Boscovich, 1745 and 1758).

4. Navier's Equation

With the concepts of intermolecular forces presented above, Navier approached the study of fluid motion. Navier deduced and presented his equation for incompressible fluids in two articles. The first, published in 1821 in the *Annales de Chimie et de Physique* (Figure 5), titled *Sur les Lois des mouvemens des fluides, en ayant egard à l'adhesion des molecules* [28], does not detail the algebraic deduction of the term associated with flow resistance. The momentum equations that Navier arrived at are presented in Figure 6, where X, Y, and Z correspond to the components of the body force, which, a few lines later, he considers to be gravitational. Note that in the notation of the time, there was no differentiation between the partial derivative $\partial u/\partial x, \ldots$ and the total derivative $du/dx, \ldots$. It is interesting to see that the terms associated with molecular resistance (those that accompany the ε coefficient) are not presented in reduced form, resulting when using the continuity equation. For example, with modern notation, the term in parentheses for the component along x can be written as:

$$3\frac{\partial^2 u}{\partial x^2} + \frac{\partial^2 u}{\partial y^2} + \frac{\partial^2 u}{\partial z^2} + 2\frac{\partial^2 v}{\partial x \partial y} + 2\frac{\partial^2 w}{\partial x \partial z} = \frac{\partial^2 u}{\partial x^2} + \frac{\partial^2 u}{\partial y^2} + \frac{\partial^2 u}{\partial z^2} + 2\frac{\partial}{\partial x}\left(\frac{\partial u}{\partial x} + \frac{\partial v}{\partial y} + \frac{\partial w}{\partial z}\right) \quad (1)$$

reducing to $\nabla^2 u$ when the continuity equation is imposed for an incompressible fluid:

$$3\frac{\partial^2 u}{\partial x^2} + \frac{\partial^2 u}{\partial y^2} + \frac{\partial^2 u}{\partial z^2} + 2\frac{\partial^2 v}{\partial x \partial y} + 2\frac{\partial^2 w}{\partial x \partial z} = \frac{\partial^2 u}{\partial x^2} + \frac{\partial^2 u}{\partial y^2} + \frac{\partial^2 u}{\partial z^2} = \nabla^2 u \tag{2}$$

Navier's first application of his equations corresponds to the flow generated by a pressure gradient in a very long (in the x-direction), rectangular cross-section pipe that is inclined, such that "all the fluid molecules move parallel to each other". The fluid is initially at rest, so the solution depends on (y, z, t). The boundary condition corresponds to zero velocity at the wall, which Navier justifies with the argument "...there exists an extremely thin layer of motionless fluid against solid walls, or these walls are formed by the very substance of the fluid, which would have solidified". For any given time, the resulting velocity distribution occupies a couple of lines of the page, and for $t \to \infty$, it reduces to the expression presented in Figure 7. In that equation, ζ represents the hydraulic head and λ represents the length of the pipe. ε is the coefficient of molecular attraction, which Navier rigorously deduced and presented in his article published in 1823 [29].

In order to compare his theoretical result with experimental data, Navier determined the average velocity for a rectangular pipe with sides b and c using the theoretical expression for velocity distribution obtained from the equations of motion (Figure 7). He compared his result with the data taken by Girard, presented in l'Académie de France in 1816 and published in 1818 [30].

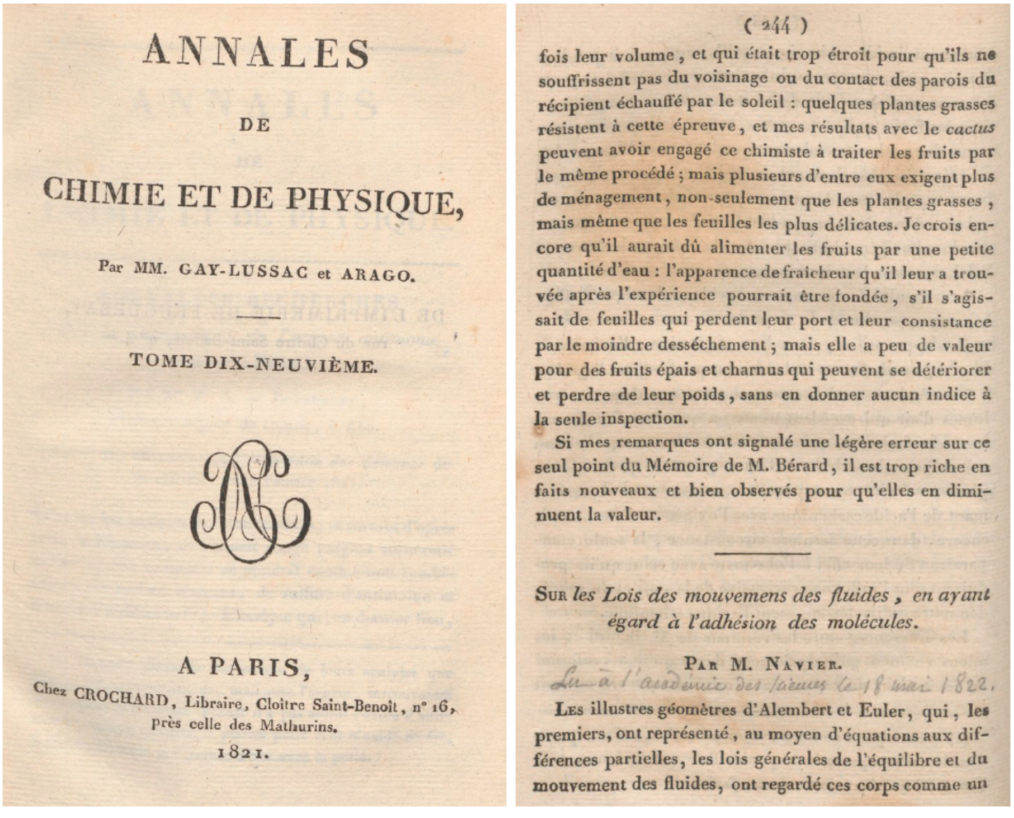

ANNALES

DE

CHIMIE ET DE PHYSIQUE,

Par MM. GAY-LUSSAC et ARAGO.

TOME DIX-NEUVIÈME.

A PARIS,

Chez CROCHARD, Libraire, Cloître Saint-Benoît, n° 16,
Près celle des Mathurins.

1821.

(244)

fois leur volume, et qui était trop étroit pour qu'ils ne souffrissent pas du voisinage ou du contact des parois du récipient échauffé par le soleil : quelques plantes grasses résistent à cette épreuve, et mes résultats avec le *cactus* peuvent avoir engagé ce chimiste à traiter les fruits par le même procédé ; mais plusieurs d'entre eux exigent plus de ménagement, non-seulement que les plantes grasses, mais même que les feuilles les plus délicates. Je crois encore qu'il aurait dû alimenter les fruits par une petite quantité d'eau : l'apparence de fraîcheur qu'il leur a trouvée après l'expérience pourrait être fondée, s'il s'agissait de feuilles qui perdent leur port et leur consistance par le moindre desséchement ; mais elle a peu de valeur pour des fruits épais et charnus qui peuvent se détériorer et perdre de leur poids, sans en donner aucun indice à la seule inspection.

Si mes remarques ont signalé une légère erreur sur ce seul point du Mémoire de M. Bérard, il est trop riche en faits nouveaux et bien observés pour qu'elles en diminuent la valeur.

SUR *les Lois des mouvemens des fluides, en ayant égard à l'adhésion des molécules.*

PAR M. NAVIER.

Lu à l'académie des sciences le 18 mai 1822.

LES illustres géomètres d'Alembert et Euler, qui, les premiers, ont représenté, au moyen d'équations aux différences partielles, les lois générales de l'équilibre et du mouvement des fluides, ont regardé ces corps comme un

Figure 5. First article by Navier in which the flow resistance due to intermolecular forces are presented (Navier, 1821).

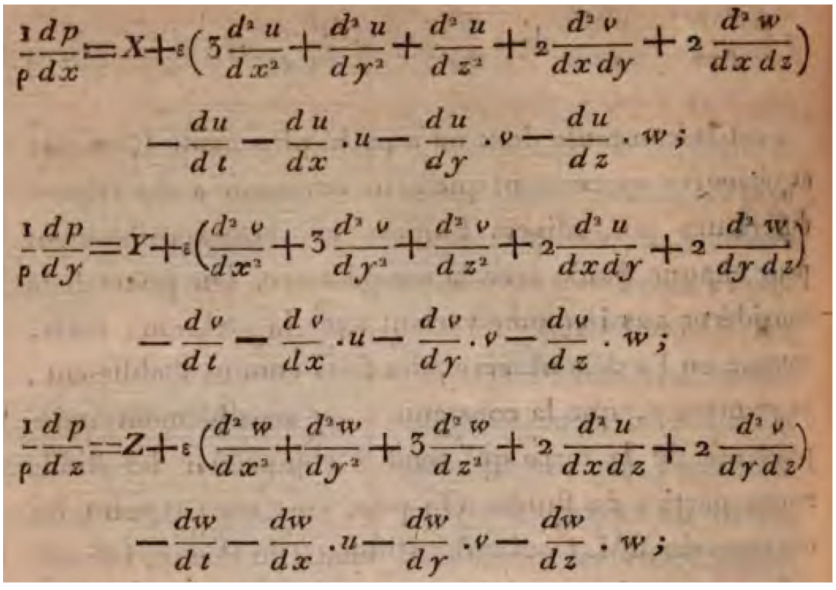

$$\frac{1}{\rho}\frac{dp}{dx} = X + \varepsilon\left(3\frac{d^2u}{dx^2} + \frac{d^2u}{dy^2} + \frac{d^2u}{dz^2} + 2\frac{d^2v}{dx\,dy} + 2\frac{d^2w}{dx\,dz}\right) - \frac{du}{dt} - \frac{du}{dx}.u - \frac{du}{dy}.v - \frac{du}{dz}.w;$$

$$\frac{1}{\rho}\frac{dp}{dy} = Y + \varepsilon\left(\frac{d^2v}{dx^2} + 3\frac{d^2v}{dy^2} + \frac{d^2v}{dz^2} + 2\frac{d^2u}{dx\,dy} + 2\frac{d^2w}{dy\,dz}\right) - \frac{dv}{dt} - \frac{dv}{dx}.u - \frac{dv}{dy}.v - \frac{dv}{dz}.w;$$

$$\frac{1}{\rho}\frac{dp}{dz} = Z + \varepsilon\left(\frac{d^2w}{dx^2} + \frac{d^2w}{dy^2} + 3\frac{d^2w}{dz^2} + 2\frac{d^2u}{dx\,dz} + 2\frac{d^2v}{dy\,dz}\right) - \frac{dw}{dt} - \frac{dw}{dx}.u - \frac{dw}{dy}.v - \frac{dw}{dz}.w;$$

Figure 6. Momentum equations according to Navier (1821).

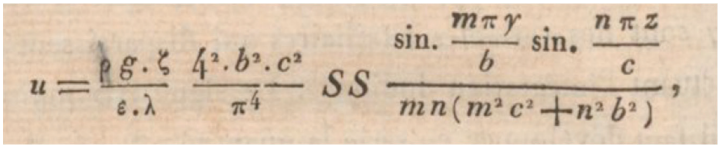

$$u = \frac{\rho g.\zeta}{\varepsilon.\lambda}\,\frac{4^2.b^2.c^2}{\pi^4}\,SS\,\frac{\sin.\frac{m\pi y}{b}\sin.\frac{n\pi z}{c}}{mn(m^2c^2+n^2b^2)},$$

Figure 7. Velocity distribution for a flow in a rectangular section pipe (with sides *b* and *c*), obtained by Navier in his article of 1821. *SS* corresponds to the double summation over *n* and *m*, both of them being odd numbers. There is an error in the equation, which is pointed out at the end of the Annales (p. 448) since the density ρ should not be in the equation.

On 18 March 1822, Navier presented his *Mémoire sur les Lois du Mouvenment des Fluides* at the Académie Royale des Sciences in Paris, which was published in the Volume VI, corresponding to 1823, but issued in 1827, of the Mémoires de l'Académie des Sciences de l'Institut de France [29] (Figure 8). In this work, Navier considers the fluid as incompressible and consisting of "a set of material points, or molecules, located at very small distances from each other, and capable of changing almost freely their relative positions". The pressure exerted on the fluid "and penetrating into the interior of the body", "tends to bring the parts closer, which resist this action by repulsive forces that are established between neighbouring molecules". In the hydrostatic condition, "each molecule is in equilibrium, subject to these repulsive forces and external forces, such as gravity, which may act on it". Furthermore, "the actions exerted from molecule to molecule within bodies vary with the distance between the molecules", so that if the distance between them is reduced, a repulsive force is generated, and if it is increased, an attractive force is created. When the fluid is in motion, Navier considers that "two molecules that approach each other repel with greater force, and two molecules that move away from each other repel with less force", so that "the repulsive actions of the molecules increase or decrease in an amount proportional to the velocity with which the molecules approach or separate from each other". These same forces also act between the molecules of the fluid and those of the walls of the solid that contains them.

MÉMOIRES
DE
L'ACADÉMIE ROYALE DES SCIENCES
DE L'INSTITUT
DE FRANCE.

ANNÉE 1823.

TOME VI.

PARIS,
CHEZ FIRMIN DIDOT, PÈRE ET FILS, LIBRAIRES,
RUE JACOB, N° 24.

1827.

MÉMOIRE

SUR LES LOIS DU MOUVEMENT DES FLUIDES;

PAR M. NAVIER.

Lu à l'Académie royale des Sciences; le 18 mars 1822.

I. *Notions préliminaires.*

Les géomètres représentent, au moyen d'équations aux différences partielles, les conditions générales de l'équilibre et du mouvement des fluides. Ces équations ont été déduites de divers principes, qui supposent tous que les molécules du fluide sont susceptibles de prendre les unes par rapport aux autres des mouvements quelconques, sans opposer aucune résistance, et de glisser sans effort sur les parois des vases dans lesquels le fluide est contenu. Mais les différences considérables, ou totales, que présentent dans certains cas les effets naturels avec les résultats des théories connues, indiquent la nécessité de recourir à des notions nouvelles, et d'avoir égard à certaines actions moléculaires qui se manifestent principalement dans les phénomènes du mouvement. On sait, par exemple, que, dans le cas où l'eau s'écoule hors d'un vase par un long tuyau d'un petit diamètre, le cal-

Figure 8. Second article by Navier regarding the laws of fluid motion. Here, Navier elaborates in detail on the intermolecular attraction forces that give rise to the term associated with flow resistance.

For the hydrostatic equilibrium condition, Navier analyses the interaction between two neighbouring molecules, M and M' (Figure 9), with coordinates (x, y, z) and $(x+\alpha, y+\beta, z+\gamma)$, so that the distance between them is $\rho = \sqrt{\alpha^2+\beta^2+\gamma^2}$. It is necessary to note that in the article, ρ is used interchangeably to indicate the distance between the two molecules M and M' as well as to designate the density of the fluid. By designating $f(\rho)$ as the force between the two molecules and $f(\rho)\delta\rho$ as the moment of $f(\rho)$ between the two molecules, the moment on molecule M resulting from the action of the 8 molecules surrounding it in an arrangement as indicated in Figure 9, turns out to be (using the current notation for partial derivatives):

$$\frac{8f(\rho)}{\rho}\left(\frac{\partial\delta x}{\partial x}\alpha^2+\frac{\partial\delta y}{\partial y}\beta^2+\frac{\partial\delta z}{\partial z}\gamma^2\right) \tag{3}$$

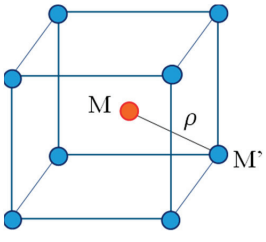

Figure 9. Scheme for the analysis of intermolecular force interaction.

In the static condition, where there is a balance between the pressure force and the repulsive forces, the following holds true:

$$p = \frac{4\pi}{3}\int_0^\infty \rho^3 f(\rho)d\rho \tag{4}$$

Then, Navier relates the pressure to body forces for the hydrostatic condition, which in modern notation is written as $\nabla p = \rho \vec{f}_m$, where $\vec{f}_m$ is the body force vector (per unit mass) and in this case ρ denotes the fluid density.

Once the static problem is solved, Navier addresses the case where the fluid is in motion, which induces other forces of molecular interaction, and "the main objective of the work is to find analytical expressions for these forces". To do this, he considers that there is a relative motion between the molecules M and M', whose velocities are, respectively, (u, v, w) and

$$\left(u + \frac{\partial u}{\partial x}\alpha + \frac{\partial u}{\partial y}\beta + \frac{\partial u}{\partial z}\gamma,\ v + \frac{\partial v}{\partial x}\alpha + \frac{\partial v}{\partial y}\beta + \frac{\partial v}{\partial z}\gamma,\ w + \frac{\partial w}{\partial x}\alpha + \frac{\partial w}{\partial y}\beta + \frac{\partial w}{\partial z}\gamma\right),$$

obtaining that the moment of the forces resulting from the mutual action of M and M' is given by

$$\begin{array}{l}\frac{f(\rho)}{\rho^2}\left[\alpha\left(\frac{\partial u}{\partial x}\alpha + \frac{\partial u}{\partial y}\beta + \frac{\partial u}{\partial z}\gamma\right) + \beta\left(\frac{\partial v}{\partial x}\alpha + \frac{\partial v}{\partial y}\beta + \frac{\partial v}{\partial z}\gamma\right) + \gamma\left(\frac{\partial w}{\partial x}\alpha + \frac{\partial w}{\partial y}\beta + \frac{\partial w}{\partial z}\gamma\right)\right]\times \\ \left[\alpha\left(\frac{\delta\partial u}{\partial x}\alpha + \frac{\delta\partial u}{\partial y}\beta + \frac{\delta\partial u}{\partial z}\gamma\right) + \beta\left(\frac{\delta\partial v}{\partial x}\alpha + \frac{\delta\partial v}{\partial y}\beta + \frac{\delta\partial v}{\partial z}\gamma\right) + \gamma\left(\frac{\delta\partial w}{\partial x}\alpha + \frac{\delta\partial w}{\partial y}\beta + \frac{\delta\partial w}{\partial z}\gamma\right)\right]\end{array} \quad (5)$$

From the interaction between two molecules, given by the previous expression, Navier obtains the result for the eight molecules surrounding it, which is presented in Figure 10.

$$\begin{aligned}&\frac{8 \cdot f(\rho)}{\rho^2}\Bigg\{\left(\frac{du}{dx}\frac{\delta du}{dx}\alpha^4 + \frac{du}{dy}\frac{\delta du}{dy}\alpha^2\theta^2 + \frac{du}{dz}\frac{\delta du}{dz}\alpha^2\gamma^2\right) + \\ &\left(\frac{dv}{dy}\frac{\delta du}{dx}\alpha^2\theta^2 + \frac{dv}{dx}\frac{\delta du}{dy}\alpha^2\theta^2\right) + \\ &\left(\frac{dw}{dz}\frac{\delta du}{dx}\alpha^2\gamma^2 + \frac{dw}{dx}\frac{\delta du}{dz}\alpha^2\gamma^2\right) + \\ &\left(\frac{du}{dx}\frac{\delta dv}{dy}\alpha^2\theta^2 + \frac{du}{dy}\frac{\delta dv}{dx}\alpha^2\theta^2\right) + \\ &\left(\frac{dv}{dx}\frac{\delta dv}{dx}\alpha^2\theta^2 + \frac{dv}{dy}\frac{\delta dv}{dy}\theta^4 + \frac{dv}{dz}\frac{\delta dv}{dz}\theta^2\gamma^2\right) + \\ &\left(\frac{dw}{dy}\frac{\delta dv}{dz}\theta^2\gamma^2 + \frac{dw}{dz}\frac{\delta dv}{dy}\theta^2\gamma^2\right) + \\ &\left(\frac{du}{dx}\frac{\delta dw}{dz}\alpha^2\gamma^2 + \frac{du}{dz}\frac{\delta dw}{dx}\alpha^2\gamma^2\right) + \\ &\left(\frac{dv}{dy}\frac{\delta dw}{dz}\theta^2\gamma^2 + \frac{dv}{dz}\frac{\delta dw}{dy}\theta^2\gamma^2\right) + \\ &\left(\frac{dw}{dx}\frac{\delta dw}{dx}\alpha^2\gamma^2 + \frac{dw}{dy}\frac{\delta dw}{dy}\theta^2\gamma^2 + \frac{dw}{dz}\frac{\delta dw}{dz}\gamma^4\right)\Bigg\}\end{aligned}$$

Figure 10. Resultant on molecule M of the moments of the forces from the surrounding molecules (Navier, 1823).

As mentioned, the expression in Figure 10 corresponds to the effect that the surrounding molecules have on one molecule. To consider all the molecules in the fluid, it is necessary to integrate over the entire flow domain, which can be considered infinite in

terms of the dimensions associated with the molecules. This integration is facilitated by working in spherical coordinates, resulting in:

$$\varepsilon = \frac{8\pi}{30}\int_0^\infty \rho^4 f(\rho)d\rho \tag{6}$$

In the determination of the value of ε, Navier indicates that the sum of moments was considered twice, so the numerical coefficient of Equation 6 must be divided by 2. Navier repeats the analysis for the case of molecules that are in contact with the solid wall (which he denotes m), with an interaction force $F(\rho)$, resulting in:

$$E = \frac{4\pi}{6}\int_0^\infty \rho^2 F(\rho)d\rho \tag{7}$$

E is a constant that must be determined experimentally and depends on the nature of the wall and the fluid, and it can be considered "as a measure of their reciprocal action". After analysing the dynamic equilibrium and a lot of algebra, Navier obtained the set of differential equations that, according to him, govern the motion of incompressible fluids (Figure 11, where P, Q, and R are the components of the body force per unit volume, i.e., $(\mathrm{P},\mathrm{Q},\mathrm{R}) = \rho\vec{f}_m\Big)$, and considering the gravity force field, in current notation, is written as:

$$g_x - \frac{\partial p}{\partial x} = \rho\left(\frac{\partial u}{\partial t} + u\frac{\partial u}{\partial x} + v\frac{\partial u}{\partial y} + w\frac{\partial u}{\partial z}\right) - \varepsilon\left(\frac{\partial^2 u}{\partial x^2} + \frac{\partial^2 u}{\partial y^2} + \frac{\partial^2 u}{\partial z^2}\right) \tag{8}$$

$$g_y - \frac{\partial p}{\partial y} = \rho\left(\frac{\partial v}{\partial t} + u\frac{\partial v}{\partial x} + v\frac{\partial v}{\partial y} + w\frac{\partial v}{\partial z}\right) - \varepsilon\left(\frac{\partial^2 v}{\partial x^2} + \frac{\partial^2 v}{\partial y^2} + \frac{\partial^2 v}{\partial z^2}\right) \tag{9}$$

$$g_z - \frac{\partial p}{\partial z} = \rho\left(\frac{\partial w}{\partial t} + u\frac{\partial w}{\partial x} + v\frac{\partial w}{\partial y} + w\frac{\partial w}{\partial z}\right) - \varepsilon\left(\frac{\partial^2 w}{\partial x^2} + \frac{\partial^2 w}{\partial y^2} + \frac{\partial^2 w}{\partial z^2}\right) \tag{10}$$

$$\mathrm{P} - \frac{dp}{dx} = \rho\left(\frac{du}{dt} + u\frac{du}{dx} + v\frac{du}{dy} + w\frac{du}{dz}\right) - \varepsilon\left(\frac{d^2u}{dx^2} + \frac{d^2u}{dy^2} + \frac{d^2u}{dz^2}\right),$$

$$\mathrm{Q} - \frac{dp}{dy} = \rho\left(\frac{dv}{dt} + u\frac{dv}{dx} + v\frac{dv}{dy} + w\frac{dv}{dz}\right) - \varepsilon\left(\frac{d^2v}{dx^2} + \frac{d^2v}{dy^2} + \frac{d^2v}{dz^2}\right),$$

$$\mathrm{R} - \frac{dp}{dz} = \rho\left(\frac{dw}{dt} + u\frac{dw}{dx} + v\frac{dw}{dy} + w\frac{dw}{dz}\right) - \varepsilon\left(\frac{d^2w}{dx^2} + \frac{d^2w}{dy^2} + \frac{d^2w}{dz^2}\right).$$

Figure 11. Equations for the motion of fluids obtained by Navier (1823).

Note that in the previous equations, the coefficient ε is unknown since it depends on the intermolecular force $f(\rho)$, of which it is only known that it decreases very rapidly with distance, so its range of action is very small ("they are insensible to sensible distances", as Laplace wrote). It is also known that "this constant has different values for different fluids and varies significantly for each fluid with temperature" and that it is "sensibly independent" of pressure [28] (p. 251).

Regarding the boundary conditions, Navier indicates that fluid molecules in contact with the wall cannot move in the normal direction to it, so for a wall in the XY plane, it must satisfy:

$$Eu + \varepsilon\frac{\partial u}{\partial z} = 0 \quad , \quad Ev + \varepsilon\frac{\partial v}{\partial z} = 0 \tag{11}$$

Similarly, for walls in the XZ and YZ planes:

$$Eu + \varepsilon\frac{\partial u}{\partial y} = 0 \quad , \quad Ew + \varepsilon\frac{\partial w}{\partial y} = 0 \tag{12}$$

$$Ev + \varepsilon \frac{\partial v}{\partial x} = 0 \quad , \quad Ew + \varepsilon \frac{\partial w}{\partial x} = 0 \tag{13}$$

In the case of a free surface, $E = 0$. The boundary conditions given by Equations (11)–(13) are now called "Navier's conditions", allow for slip velocity at the wall, and are applied, for example, in modelling the flow of superhydrophobic fluids.

Navier concludes his work by applying the obtained equations to three cases: (i) Flow in a straight rectangular pipe, (ii) flow in a straight circular pipe, and (iii) flow with a free surface in a rectangular channel. For all three cases, the boundary conditions he uses are those given in the preceding equations. The problems in pipes are transient; the flow starts from rest and asymptotically reaches the steady state. The flow of case (i) is the same as that solved in his 1821 publication [28], but at that time, the boundary conditions applied were not Navier's conditions but non-slip conditions at the walls.

5. Viscosity

Before continuing, it is worth reviewing the history of the word and concept of fluid viscosity. It is common in introductory fluid mechanics courses to present the property "viscosity" based on a flow with parallel streamlines (Figure 12) and postulating the proportionality between the shear stress (τ) applied to an element of fluid and its rate of angular deformation ($d\alpha/dt$, which is demonstrated to be equal to the velocity gradient du/dy). The proportionality coefficient corresponds to dynamic viscosity. This is how it is shown, for example, in the texts by White [31] (pp. 22–23), Massey [32] (pp. 21–24), and Munson et al. [33] (pp. 14–15), where it is stated that $\tau \sim d\alpha/dt$. Directly in the form as Newton proposed it, that is $\tau \sim du/dy$, it is presented, among others, in the texts by Granger [34] (pp. 41–43), Streeter et al. [35] (pp. 8–9), and Shames [36] (pp. 10–12).

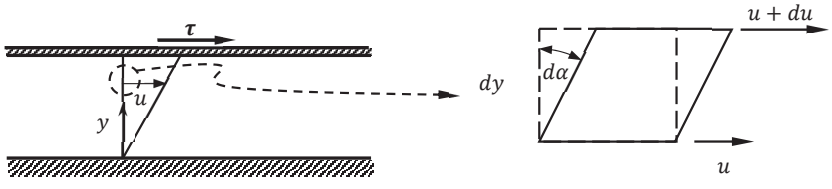

Figure 12. A typical scheme used to introduce the concept of viscosity in standard introductory fluid mechanics courses. Usually, $\tau \sim d\alpha/dt$ or $\tau \sim du/dy$ is postulated.

Newton, in the first edition of 1687 of his *Principia* [4], as in later editions, did not propose the parallel straight-line motion shown in Figure 12, but instead established the proportionality between shear stress and velocity gradient in the part of his *Principia* concerning the circular motion of fluids. In Book II, Section IX (Figure 13), he postulated that "the resistance arising from the lack of lubricity in the parts of a fluid is, other things being equal, proportional to the velocity with which the parts of the fluid separate from each other" [21].

Note that Newton does not mention the word "viscosity" or "viscous", but instead refers to the "lubricity" of fluid particles. According to the Online Etymology Dictionary, www.etymonline.com (accessed on 1 September 2023), the word "viscosity" was first recorded in English in the early 15th century and comes from the Old French "*viscosité*", which was recorded in the 13th century, or directly from Medieval Latin (6th–14th centuries) "*viscositatem/viscositas*", a word that, in turn, comes from Late Latin (3rd–6th centuries) "*viscosum*", which means "sticky". This last word comes from Latin "*viscum*", which refers to mistletoe, a semi-parasitic plant that grows on the branches of certain trees and whose fruit is a berry containing a sticky (or viscous) pulp. In Spanish (https://iedra.es/, accessed on 1 September 2003), the first recorded use of the word "*viscoso*" (sticky) in a dictionary is in 1570, in Cristóbal de las Casas' "*Vocabulario de las dos lenguas Toscana y Castellana*" [37], and the word "*viscosidad*" is first recorded in 1617 in John Minsheu's "*Vocabularium Hispanicum*

Latinum et Anglicum copiossisimum". The Royal Spanish Academy (*Real Academia Española*), founded in 1713, records both words in its first edition of "*Tomo Sexto del Diccionario de la Lengua Castellana*", printed in 1739 [38] (p. 437 and 438), with the meaning of "sticky matter or humour" for viscosity and "sticky or glutinous" for viscous.

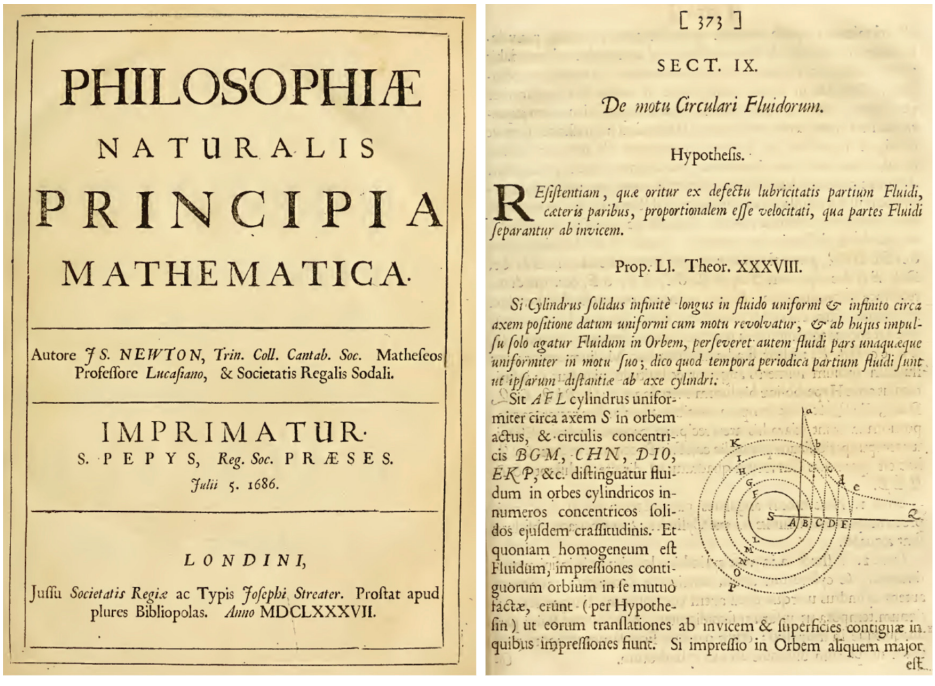

PHILOSOPHIÆ
NATURALIS
PRINCIPIA
MATHEMATICA.

Autore *J S. NEWTON*, *Trin. Coll. Cantab. Soc.* Matheſeos Profeſſore *Lucaſiano*, & Societatis Regalis Sodali.

IMPRIMATUR.
S. PEPYS, *Reg. Soc.* PRÆSES.
Julii 5. 1686.

LONDINI,

Juſſu *Societatis Regiæ* ac Typis *Joſephi Streater*. Proſtat apud plures Bibliopolas. *Anno* MDCLXXXVII.

[373]

SECT. IX.

De motu Circulari Fluidorum.

Hypotheſis.

Reſiſtentiam, quæ oritur ex defectu lubricitatis partium Fluidi, ceteris paribus, proportionalem eſſe velocitati, qua partes Fluidi ſeparantur ab invicem.

Prop. LI. Theor. XXXVIII.

Si Cylindrus ſolidus infinite longus in fluido uniformi & infinito circa axem poſitione datum uniformi cum motu revolvatur, & ab hujus impulſu ſolo agatur Fluidum in Orbem, perſeveret autem fluidi pars unaquæque uniformiter in motu ſuo; dico quod tempora periodica partium fluidi ſunt ut ipſarum diſtantiæ ab axe cylindri.

Sit *AFL* cylindrus uniformiter circa axem *S* in orbem actus, & circulis concentricis *BGM*, *CHN*, *DIO*, *EKP*, &c. diſtinguatur fluidum in orbes cylindricos innumeros concentricos ſolidos ejuſdem craſſitudinis. Et quoniam homogeneum eſt Fluidum, impreſſiones contiguorum orbium in ſe mutuò factæ, erunt (per Hypotheſin) ut eorum tranſlationes ab invicem & ſuperficies contiguæ in quibus impreſſiones fiunt. Si impreſſio in Orbem aliquem major eſt

Figure 13. First edition (1687) of Newton's Principia. First page of the book and page corresponding to Section IX of Book II "On the circular motion of fluids", where he postulates, using current language and notation, that $\tau \sim du/dy$.

The first use of the term viscosity with a physical meaning was by Wiedemann in 1856, in a study related to the flow induced by electrolysis in saline solutions, using the expression Zähigkeitconstante der Flüssigkeiten, "viscosity constant of liquids" [39] (Figure 14). Note that neither Cauchy [40], nor Poisson [41], nor Saint-Venant [42], nor Stokes [43] used the word "viscosity" in their publications on the equations of fluid motion. Stokes, in his work, expresses "The amount of internal friction of water depends on the value of μ", without explicitly defining what the coefficient μ is. More than 20 years later, the use of the term viscosity could even harm the publication of an article. This is reflected in one of the letters from the extensive correspondence between Saint-Venant and Boussinesq. In a letter dated 12 July 1868, the septuagenarian Saint-Venant advises the young Boussinesq, regarding a manuscript that the latter wanted to publish, to avoid using "viscosity" in the title and other places in the work, as that would give the reviewer arguments to make comments and thus make it difficult to accept the article, suggesting that he "change the title, for example, to: The influence of internal and external friction (or tangential actions) on the motion of fluids". Promptly, on 14 July, Boussinesq replied, "I think I must tell you at once that there is no opposition to you in my manuscript dealing with the friction of fluids. . .I use the term friction everywhere instead of the term viscosity" [44]. Note that as late as 1886, it seemed appropriate to define viscosity, as did Reynolds in his article "On the Theory of Lubrication . . ." [45] (pp. 164–165), where he defined "the coefficient of viscosity, or, commonly, the viscosity of the fluid" as "the shearing stress divided by the rate of distortion".

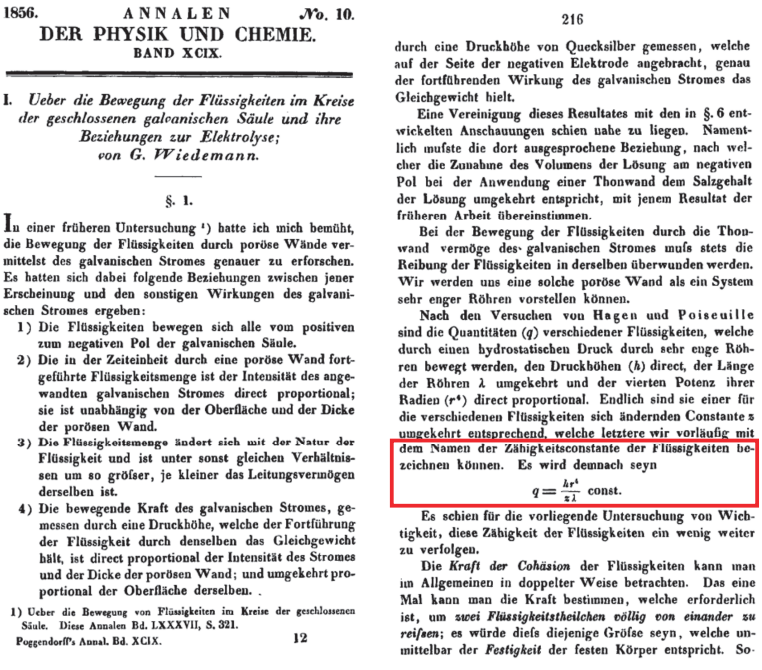

1856. ANNALEN №. 10.
DER PHYSIK UND CHEMIE.
BAND XCIX.

I. *Ueber die Bewegung der Flüssigkeiten im Kreise der geschlossenen galvanischen Säule und ihre Beziehungen zur Elektrolyse;*
von G. Wiedemann.

§. 1.

In einer früheren Untersuchung [1]) hatte ich mich bemüht, die Bewegung der Flüssigkeiten durch poröse Wände vermittelst des galvanischen Stromes genauer zu erforschen. Es hatten sich dabei folgende Beziehungen zwischen jener Erscheinung und den sonstigen Wirkungen des galvanischen Stromes ergeben:

1) Die Flüssigkeiten bewegen sich alle vom positiven zum negativen Pol der galvanischen Säule.
2) Die in der Zeiteinheit durch eine poröse Wand fortgeführte Flüssigkeitsmenge ist der Intensität des angewandten galvanischen Stromes direct proportional; sie ist unabhängig von der Oberfläche und der Dicke der porösen Wand.
3) Die Flüssigkeitsmenge ändert sich mit der Natur der Flüssigkeit und ist unter sonst gleichen Verhältnissen um so gröfser, je kleiner das Leitungsvermögen derselben ist.
4) Die bewegende Kraft des galvanischen Stromes, gemessen durch eine Druckhöhe, welche der Fortführung der Flüssigkeit durch denselben das Gleichgewicht hält, ist direct proportional der Intensität des Stromes und der Dicke der porösen Wand; und umgekehrt proportional der Oberfläche derselben.

1) Ueber die Bewegung von Flüssigkeiten im Kreise der geschlossenen Säule. Diese Annalen Bd. LXXXVII, S. 321.

durch eine Druckhöhe von Quecksilber gemessen, welche auf der Seite der negativen Elektrode angebracht, genau der fortführenden Wirkung des galvanischen Stromes das Gleichgewicht hielt.

Eine Vereinigung dieses Resultates mit den in §. 6 entwickelten Anschauungen schien nahe zu liegen. Namentlich mufste die dort ausgesprochene Beziehung, nach welcher die Zunahme des Volumens der Lösung am negativen Pol bei der Anwendung einer Thonwand dem Salzgehalt der Lösung umgekehrt entspricht, mit jenem Resultat der früheren Arbeit übereinstimmen.

Bei der Bewegung der Flüssigkeiten durch die Thonwand vermöge des galvanischen Stromes mufs stets die Reibung der Flüssigkeiten in derselben überwunden werden. Wir werden uns eine solche poröse Wand als ein System sehr enger Röhren vorstellen können.

Nach den Versuchen von Hagen und Poiseuille sind die Quantitäten (q) verschiedener Flüssigkeiten, welche durch einen hydrostatischen Druck durch sehr enge Röhren bewegt werden, den Druckhöhen (h) direct, der Länge der Röhren λ umgekehrt und der vierten Potenz ihrer Radien (r^4) direct proportional. Endlich sind sie einer für die verschiedenen Flüssigkeiten sich ändernden Constante z umgekehrt entsprechend, welche letztere wir vorläufig mit dem Namen der Zähigkeitsconstante der Flüssigkeiten bezeichnen können. Es wird demnach seyn

$$q = \frac{hr^4}{z\lambda} \text{ const.}$$

Es schien für die vorliegende Untersuchung von Wichtigkeit, diese Zähigkeit der Flüssigkeiten ein wenig weiter zu verfolgen.

Die *Kraft der Cohäsion* der Flüssigkeiten kann man im Allgemeinen in doppelter Weise betrachten. Das eine Mal kann man die Kraft bestimmen, welche erforderlich ist, um *zwei Flüssigkeitstheilchen völlig von einander zu reifsen*; es würde diefs diejenige Gröfse seyn, welche unmittelbar der *Festigkeit* der festen Körper entspricht. So-

Figure 14. Wiedemann's article (1856) where the term viscosity is introduced for the first time with a clear physical meaning. The first appearance of the term is in the box in the figure and denoted by the letter z. The equation shown corresponds to the flow rate q in a Poiseuille flow, where h denotes the pressure gradient, r the radius of the tube, and L the length of the tube. The value of the constant, const $= \pi/8$, is easily obtained from the solution of the Navier–Stokes equation and is one of the first applications made in basic fluid mechanics courses.

6. The Other Equations of Fluid Motion

The equation presented by Navier in 1822 was rederived at least four more times: By Cauchy in 1823, Poisson in 1829, Saint-Venant in 1837, and Stokes in 1845. Each of the authors of the new derivations ignored or criticised the development of their predecessors, justifying the conceptual foundations of their own deduction [2]. It is interesting to note the close relationship between the development of equations governing fluid motion and those for elastic solids. Developed for one material, the concepts were applied to the other, which in practice means replacing displacements of molecules (solids) with displacements per unit time (fluids). Darrigol's work [2] presents this parallel development in a lively manner (using current vector and index notation). Without going into further detail regarding the deductions made by the different authors, the equations governing fluid motion obtained by them are presented below. The following subsections take the article by Darrigol as their main reference.

6.1. Augustin-Louis Cauchy (1789–1857)

On 30 September 1822, Cauchy presented the results of his study at the Académie Royale des Sciences in Paris, and a summary was published in 1823 in the Bulletin des Sciences by the Société Philomathique de Paris [40] (Figure 15). In his work, Cauchy analysed Navier's work regarding the restoring forces of a solid subject to dilation and flexion. According to Navier, two types of restoring forces are required, but Cauchy concluded that the second was not necessary if it was considered that the first was not perpendicular to the section on which it acted. In other words, the pressure does not act normal to the surface; that is, there are normal and tangential stresses whose resultant is a stress ("pressure") not perpendicular to

the surface. Although other authors such as Coulomb, Young, and Navier had considered the presence of what we now call shear stresses in certain beam-breaking problems, Cauchy was the first to propose an elasticity theory based on a general definition of internal stresses. Cauchy demonstrated three fundamental theorems of elasticity, which in current language are: (i) the stress tensor is a second-rank tensor (σ_{ij} 3×3 matrix), (ii) the stress tensor is symmetrical ($\sigma_{ij} = \sigma_{ji}$), and (iii) the resultant of the forces acting on a volume element, per unit volume, is given by $\partial\sigma_{ij}/\partial x_j$.

To apply the ideas developed for solid bodies to fluids, Cauchy considered an infinitesimal element of "solidified fluid", on whose surfaces normal and tangential stresses, τ_{ij}, act. In his work, Cauchy proposed a constitutive law with two constants, which we now call viscosity and second coefficient of viscosity.

6.2. Siméon-Denis Poisson (1781–1840)

Like Navier and Cauchy, Poisson studied both the behaviour of elastic solids and the movement of fluids. In his article read in 1828 and published in 1829 [17], Poisson followed Navier's line to obtain the equations of elasticity, considering molecular attraction forces, with some differences. For example, he did not use the method of moments but directly summed the molecular forces acting on a particular molecule. In another paper, read on 12 October 1829, at the Académie des Sciences de Paris and published in 1831 in the Journal de l'École Polytechnique [41] (Figure 16), he considered that a fluid element is subject to shear stresses during its movement, which spontaneously relax very rapidly, alternating the fluid in rapid states of stress and relaxation. He supposed that the stresses on the fluid element are proportional to the rate of deformation, analogous to his assumption that the stresses acting on an isotropic elastic solid body element are proportional to the deformation.

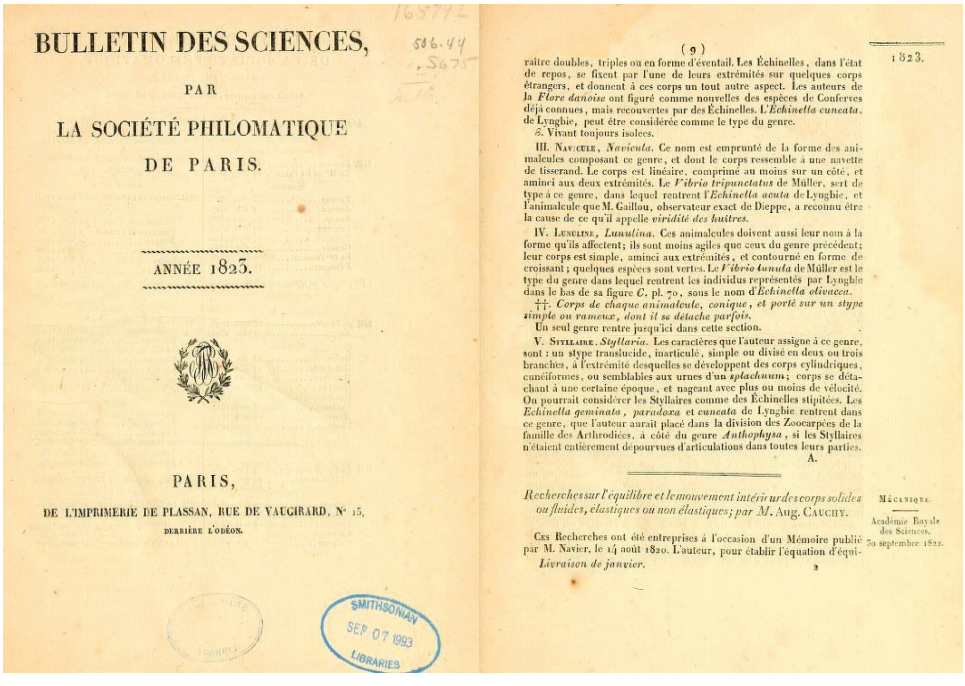

BULLETIN DES SCIENCES,

PAR

LA SOCIÉTÉ PHILOMATIQUE

DE PARIS.

ANNÉE 1823.

PARIS,

DE L'IMPRIMERIE DE PLASSAN, RUE DE VAUGIRARD, N° 15,

DERRIÈRE L'ODÉON.

raître doubles, triples ou en forme d'éventail. Les Échinelles, dans l'état de repos, se fixent par l'une de leurs extrémités sur quelques corps étrangers, et donnent à ces corps un tout autre aspect. Les auteurs de la *Flore danoise* ont figuré comme nouvelles des espèces de Conferves déjà connues, mais recouvertes par des Échinelles. L'*Echinella cuneata*, de Lyngbie, peut être considérée comme le type du genre.

S. Vivant toujours isolées.

III. Navicule, *Navicula*. Ce nom est emprunté de la forme des animalcules composant ce genre, et dont le corps ressemble à une navette de tisserand. Le corps est linéaire, comprimé au moins sur un côté, et aminci aux deux extrémités. Le *Vibrio tripunctatus* de Müller, sert de type à ce genre, dans lequel rentrent l'*Echinella acuta* de Lyngbie, et l'animalcule que M. Gaillou, observateur exact de Dieppe, a reconnu être la cause de ce qu'il appelle *viridité des huîtres*.

IV. Lunuline, *Lunulina*. Ces animalcules doivent aussi leur nom à la forme qu'ils affectent; ils sont moins agiles que ceux du genre précédent; leur corps est simple, aminci aux extrémités, et contourné en forme de croissant; quelques espèces sont vertes. Le *Vibrio lunula* de Müller est le type du genre dans lequel rentrent les individus représentés par Lyngbie dans le bas de sa figure *C*, pl. 70, sous le nom d'*Echinella olivacea*.

$\frac{4}{11}$. *Corps de chaque animalcule, conique, et porté sur un stype simple ou rameux, dont il se détache parfois.*

Un seul genre reste jusqu'ici dans cette section.

V. Stylaire, *Stylaria*. Les caractères que l'auteur assigne à ce genre, sont : un stype translucide, inarticulé, simple ou divisé en deux ou trois branches, à l'extrémité desquelles se développent des corps cylindriques, cunéiformes, ou semblables aux urnes d'un *splachnum*; corps se détachant à une certaine époque, et nageant avec plus ou moins de vélocité. On pourrait considérer les Stylaires comme des Échinelles stipitées. Les *Echinella geminata*, *paradoxa* et *cuneata* de Lyngbie rentrent dans ce genre, que l'auteur aurait placé dans la division des Zoocarpées de la famille des Arthrodiées, à côté du genre *Anthophysa*, si les Stylaires n'étaient entièrement dépourvues d'articulations dans toutes leurs parties.

A.

Recherches sur l'équilibre et le mouvement intérieur des corps solides ou fluides, élastiques ou non élastiques; par M. Aug. Cauchy.

Mécanique.

Académie Royale des Sciences. 30 septembre 1822.

Ces Recherches ont été entreprises à l'occasion d'un Mémoire publié par M. Navier, le 14 août 1820. L'auteur, pour établir l'équation d'équi-

Figure 15. The first page of the summary of Cauchy's work, read on 30 September 1822, at the Royal Academy of Sciences in Paris. The summary was published in 1823 and begins by stating that he was inspired by a paper published in 1820 by Navier regarding the equilibrium condition of an elastic solid plane.

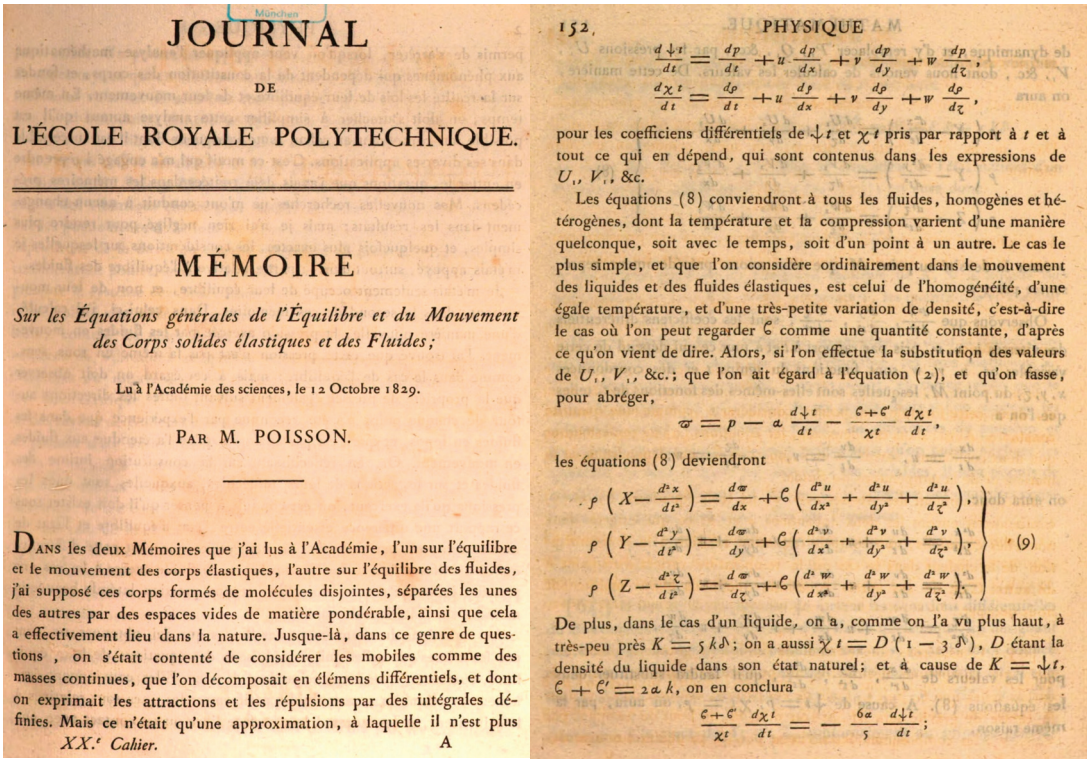

JOURNAL

DE

L'ÉCOLE ROYALE POLYTECHNIQUE.

MÉMOIRE

Sur les Équations générales de l'Équilibre et du Mouvement des Corps solides élastiques et des Fluides;

Lu à l'Académie des sciences, le 12 Octobre 1829.

PAR M. POISSON.

DANS les deux Mémoires que j'ai lus à l'Académie, l'un sur l'équilibre et le mouvement des corps élastiques, l'autre sur l'équilibre des fluides, j'ai supposé ces corps formés de molécules disjointes, séparées les unes des autres par des espaces vides de matière pondérable, ainsi que cela a effectivement lieu dans la nature. Jusque-là, dans ce genre de questions, on s'était contenté de considérer les mobiles comme des masses continues, que l'on décomposait en élémens différentiels, et dont on exprimait les attractions et les répulsions par des intégrales définies. Mais ce n'était qu'une approximation, à laquelle il n'est plus

XX.e Cahier. A

152. PHYSIQUE

$$\frac{d\downarrow t}{dt} = \frac{dp}{dt} + u\frac{dp}{dx} + v\frac{dp}{dy} + w\frac{dp}{dz},$$

$$\frac{d\chi t}{dt} = \frac{d\rho}{dt} + u\frac{d\rho}{dx} + v\frac{d\rho}{dy} + w\frac{d\rho}{dz},$$

pour les coefficiens différentiels de $\downarrow t$ et χt pris par rapport à t et à tout ce qui en dépend, qui sont contenus dans les expressions de $U,$, $V,$, &c.

Les équations (8) conviendront à tous les fluides, homogènes et hétérogènes, dont la température et la compression varient d'une manière quelconque, soit avec le temps, soit d'un point à un autre. Le cas le plus simple, et que l'on considère ordinairement dans le mouvement des liquides et des fluides élastiques, est celui de l'homogénéité, d'une égale température, et d'une très-petite variation de densité, c'est-à-dire le cas où l'on peut regarder $\mathcal{C}$ comme une quantité constante, d'après ce qu'on vient de dire. Alors, si l'on effectue la substitution des valeurs de $U,$, $V,$, &c.; que l'on ait égard à l'équation (2), et qu'on fasse, pour abréger,

$$\varpi = p - a\frac{d\downarrow t}{dt} - \frac{\mathcal{C}+\mathcal{C}'}{\chi t}\frac{d\chi t}{dt},$$

les équations (8) deviendront

$$\left.\begin{aligned} \rho\left(X - \frac{d^2x}{dt^2}\right) &= \frac{d\varpi}{dx} + \mathcal{C}\left(\frac{d^2u}{dx^2} + \frac{d^2u}{dy^2} + \frac{d^2u}{dz^2}\right), \\ \rho\left(Y - \frac{d^2y}{dt^2}\right) &= \frac{d\varpi}{dy} + \mathcal{C}\left(\frac{d^2v}{dx^2} + \frac{d^2v}{dy^2} + \frac{d^2v}{dz^2}\right), \\ \rho\left(Z - \frac{d^2z}{dt^2}\right) &= \frac{d\varpi}{dz} + \mathcal{C}\left(\frac{d^2w}{dx^2} + \frac{d^2w}{dy^2} + \frac{d^2w}{dz^2}\right). \end{aligned}\right\} \quad (9)$$

De plus, dans le cas d'un liquide, on a, comme on l'a vu plus haut, à très-peu près $K = 5k\Delta$; on a aussi $\chi t = D(1 - 3\Delta)$, D étant la densité du liquide dans son état naturel; et à cause de $K = \downarrow t$, $\mathcal{C} + \mathcal{C}' = 2a\,k$, on en conclura

$$\frac{\mathcal{C}+\mathcal{C}'}{\chi t}\frac{d\chi t}{dt} = -\frac{6a}{5}\frac{d\downarrow t}{dt};$$

Figure 16. Article by Poisson in which he derives the equations of fluid motion and presents in the set of Equation (9). X, Y, and Z correspond to the body forces (components of gravity), the term ϖ is defined in the previous equation and corresponds to the pressure plus terms associated with the compressibility of the fluid. β is the coefficient that we currently associate with viscosity.

6.3. Adhémar Jean Claude Barré de Saint-Venant (1797–1886)

Saint-Venant is known in the field of hydraulics for his deduction of the equations that bear his name that describe gradually varied transient flow in open channels (published in 1871 [46]), but his contributions in other aspects of fluid mechanics, including his visionary conception of turbulence and particularly the idea of turbulent viscosity (which he transmitted to Boussinesq, who found expressions for them), often go unnoticed or simply ignored. With a strong mathematical background, he sought to reconcile engineering applications and scientific support with the state of knowledge at the time regarding the physics of solids and fluids, based on the concept of molecular structure of matter. There is little doubt that he developed vector calculus in 1832, but it was only published in 1851 in class notes (*Principes de mécanique fondés sur la cinématique*) used in courses taught at the Institut Agronomique. Usually, Grassmann receives credit as the inventor of vector calculus due to the work published in 1844 [47]. At his death, at the age of 89, Saint-Venant had published around 160 articles, and several more were published posthumously. His main interest, as well as his greatest contributions, was in the area of elasticity.

In the edition of 19 April 1834, of *L'Institut, Journal Général des Sociétés et Travaux Scientifiques de la France et de l'Étranger*, two abstracts of Saint-Venant's work read in the session of April 14 are presented [48]. The first, in a short paragraph, refers to a general mechanics problem related to kinetic energy and work. The second abstract occupies almost an entire column of the magazine and is a review of studies on fluid dynamics, which mentions, among other topics, the demonstration of the existence of parallel pressures

(resulting from friction) and normal to the direction of fluid movement. According to Darrigol [2], the complete work was never published. In 1843, Saint-Venant published a note to the 1834 work, in which he gives some details of the ideas developed almost a decade earlier [42]. In the note, he establishes that there is a proportionality between the differences in normal and tangential pressures, corresponding to the Navier's ε or Poisson's β coefficient, as seen in Figure 17. Consistent with his denomination of "pressure" to what is currently called "stress", he uses the letter p instead of τ. Note that the notation used by Saint-Venant is the same used now to indicate the direction of stress and the normal to the surface on which it acts, i.e., $p_{ij} = \tau_{ij}$. The note ends with the paragraph identified with 7 (Figure 17), where he states that "The solution is undoubtedly not yet complete, because the above does not establish that ε is the same at all points". This comment, which may seem erroneous to us if we consider that ε is associated with viscosity, is not so when we pay attention to some paragraphs of other articles by Saint-Venant. For example, in his summary of *L'Institut*, he says: "the molecules, when passing each other, necessarily follow undulating trajectories, and the oscillations of their individual movements around the mean movement explain the internal friction of the fluids, which is essential to take into account, as well as the inequality between the pressures in a direction parallel and in a direction normal to the movements" [48]. In a footnote to the 1843 publication in *Compte Rendu des Séances de l'Académie des Sciences* of the article from 1834, Saint-Venant considered it important to clarify that "partial irregularities in the movement of a fluid require taking faces of a certain extension to have averages that vary regularly" [42] (p. 1242), that is, values of velocities and stresses averaged over the surface of the face are considered in the faces of the volume element. These irregularities in the movement, which could not be deduced from the Navier's equation, arise from the observation of experiments in pipes and channels of an undulating or oscillatory motion, which we now associate with turbulence. In another article, published in 1838 [49], three pages long but with a long title: "Memoir on the Calculation of the Effects of Steam Engines, which contains general equations of the steady or periodic flow of fluids, taking into account their expansions and their temperature changes and without assuming that they move in parallel sections or by independent filaments", Saint-Venant refers to the work of ordinary friction and the work of extraordinary friction, the latter determined by the swirling of fluid ("*tournoiement du fluide*"), especially in places where the flow section increases abruptly. In this way, it is possible to glimpse that Saint-Venant's ε coefficient includes what, in modern language, we call molecular viscosity and eddy viscosity. It would be Boussinesq who would develop this idea in depth (which he undoubtedly discussed with his mentor Saint-Venant) and present it in his "*Essai sur la Théorie des Eaux Courantes*" in 1877 [50]. On page 7 of that essay, he writes, "M. de Saint-Venant seems to have been the first to point out the influence of vortex agitation on the coefficient of internal friction". Later on, on the same page, he indicates that "everything we know leads us to infer that it must increase the coefficient of this proportionality (ε) with the dimensions of the cross sections". Saint-Venant reasserted this idea when he wrote in 1851 that "this can be explained to some extent by noting that fluid layers do not move parallel to each other with regularly graded velocities from one to another, and that disruptions, vortices, and other complicated or oblique movements, which must influence the magnitude of friction greatly, are formed and developed even more in larger sections" [51] (p. 49). In a note from 1846 regarding the "retarding forces" of liquid motion, Saint-Venant indicates that internal friction depends on both the relative velocities of fluid particles and the dimensions of the section and distance to the wall. He concludes by saying, "this is what we can suspect from known facts that are difficult to explain in any other way" [52].

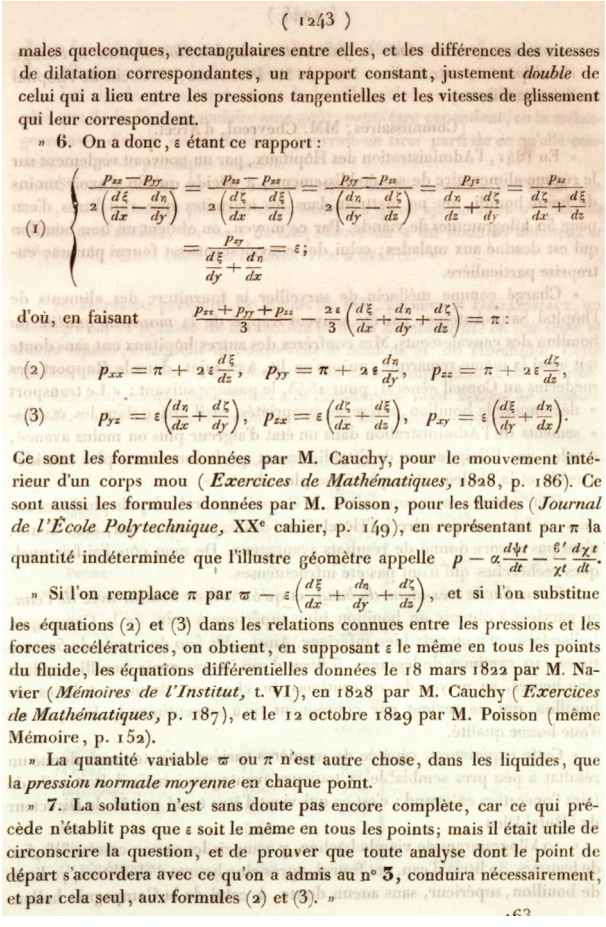

(1243)

males quelconques, rectangulaires entre elles, et les différences des vitesses de dilatation correspondantes, un rapport constant, justement *double* de celui qui a lieu entre les pressions tangentielles et les vitesses de glissement qui leur correspondent.

» **6.** On a donc, ε étant ce rapport :

$$(1)\quad \left\{ \begin{aligned} &\frac{p_{xx}-p_{yy}}{2\left(\frac{d\xi}{dx}-\frac{d\eta}{dy}\right)} = \frac{p_{xx}-p_{zz}}{2\left(\frac{d\zeta}{dx}-\frac{d\xi}{dz}\right)} = \frac{p_{yy}-p_{zz}}{2\left(\frac{d\eta}{dy}-\frac{d\zeta}{dz}\right)} = \frac{p_{yz}}{\frac{d\eta}{dz}+\frac{d\zeta}{dy}} = \frac{p_{zx}}{\frac{d\zeta}{dx}+\frac{d\xi}{dz}} \\ &\qquad = \frac{p_{xy}}{\frac{d\xi}{dy}+\frac{d\eta}{dx}} = \varepsilon ; \end{aligned} \right.$$

d'où, en faisant $\dfrac{p_{xx}+p_{yy}+p_{zz}}{3} - \dfrac{2\varepsilon}{3}\left(\dfrac{d\xi}{dx}+\dfrac{d\eta}{dy}+\dfrac{d\zeta}{dz}\right) = \pi$:

$$(2)\qquad p_{xx} = \pi + 2\varepsilon\frac{d\xi}{dx}, \quad p_{yy} = \pi + 2\varepsilon\frac{d\eta}{dy}, \quad p_{zz} = \pi + 2\varepsilon\frac{d\zeta}{dz},$$

$$(3)\qquad p_{yz} = \varepsilon\left(\frac{d\eta}{dx}+\frac{d\zeta}{dy}\right), \quad p_{zx} = \varepsilon\left(\frac{d\zeta}{dx}+\frac{d\xi}{dz}\right), \quad p_{xy} = \varepsilon\left(\frac{d\xi}{dy}+\frac{d\eta}{dx}\right).$$

Ce sont les formules données par M. Cauchy, pour le mouvement intérieur d'un corps mou (*Exercices de Mathématiques*, 1828, p. 186). Ce sont aussi les formules données par M. Poisson, pour les fluides (*Journal de l'École Polytechnique*, XX^{e} cahier, p. 149), en représentant par π la quantité indéterminée que l'illustre géomètre appelle $p - \alpha\frac{d\psi t}{dt} - \frac{6'}{\chi t}\frac{d\chi t}{dt}$.

» Si l'on remplace π par $\varpi - \varepsilon\left(\frac{d\xi}{dx}+\frac{d\eta}{dy}+\frac{d\zeta}{dz}\right)$, et si l'on substitue les équations (2) et (3) dans les relations connues entre les pressions et les forces accélératrices, on obtient, en supposant ε le même en tous les points du fluide, les équations différentielles données le 18 mars 1822 par M. Navier (*Mémoires de l'Institut*, t. VI), en 1828 par M. Cauchy (*Exercices de Mathématiques*, p. 187), et le 12 octobre 1829 par M. Poisson (même Mémoire, p. 152).

» La quantité variable ϖ ou π n'est autre chose, dans les liquides, que la *pression normale moyenne* en chaque point.

» **7.** La solution n'est sans doute pas encore complète, car ce qui précède n'établit pas que ε soit le même en tous les points; mais il était utile de circonscrire la question, et de prouver que toute analyse dont le point de départ s'accordera avec ce qu'on a admis au n° **3**, conduira nécessairement, et par cela seul, aux formules (2) et (3). »

Figure 17. Page from Saint-Venant's explanatory note to his work of 1834 (Saint-Venant, 1843) where he relates normal and tangential stresses to the deformations of the fluid element. (ξ, η, ζ) correspond to the velocities in the (x, y, z) directions.

Undoubtedly, Saint-Venant's contributions to hydrodynamics were transcendent, although his surname does not accompany the names of the equation of motion or the modelling of turbulence. The comments reproduced in the previous paragraph must be understood in the context of the knowledge that existed about fluid motion until the first three-quarters of the 19th century. Deductions, compatible with the molecular approach, led to equations of motion that presented two problems (in addition to the impossibility of finding a general solution to the differential equations, due to the presence of non-linear terms): A theoretical and an empirical one. The theoretical problem corresponds to the boundary condition that must be imposed: Is there or is there not slip of the fluid molecules in contact with the wall? The empirical problem is due to the fact that the results obtained from the application of the equations of motion only agreed with measurements made in capillary tubes or very small-diameter tubes. In larger-size channels and pipes, the flow rate and resistance did not match the theoretical result. In addition, a pattern of motion was observed that was not rectilinear but with "undulating trajectories" and the presence of vortices that, according to Saint-Venant, generated extraordinary internal friction (in opposition to the ordinary friction that was present for rectilinear flow). It would be necessary to wait for Reynolds to establish the difference between what we currently call

laminar flow and turbulent flow, as well as the equations that govern the latter. But Saint-Venant already understood that he had to consider average quantities and that the internal resistance coefficient, ε, depended on both fluid properties (due to molecular attraction forces) and the flow and geometry of the channel. In current language, we would say that $\varepsilon = \mu + \mu_T$, i.e., the coefficient of internal friction (as Saint-Venant would say) has a viscous component and a turbulent component (μ_T). It was Boussinesq who published expressions for ε in 1877, and undoubtedly, they had been discussed with Saint-Venant. In general form, according to Boussinesq, ε depends on the position (y, z) in the flow section and is given by:

$$\varepsilon = \rho g A \frac{\sigma}{\chi} \pi_0 F\left(\frac{\chi y}{\sigma}, \frac{\chi z}{\sigma}\right) \tag{14}$$

where ρ is the density of the fluid, g is the acceleration due to gravity, σ is the flow area, χ is the wetted perimeter, π_0 is the mean velocity value at the wall, and F is a functional relationship that depends on $\chi y/\sigma$ and $\chi z/\sigma$. A is a coefficient that depends on the size of the wall roughness, is almost independent of π_0 and slowly varies with the hydraulic radius [50] (p. 51). The dimensions of A are $\mathrm{L}^{-2}\mathrm{T}$.

Thus, we can see that Saint-Venant's contribution goes far beyond the deduction of the equation of motion of fluids. Combining his acute analytical and observational skills, physical principles, and theory, he was able to anticipate what turbulence modelling would become by conceiving that local resistance to motion depends on both molecular factors and the integral properties of the flow. The success of the master can be seen through the work of his protégé, J. Boussinesq, who successfully applied Navier's ideas to turbulent flow, considering average variables and a variable viscosity.

6.4. George Gabriel Stokes (1819–1903)

As we have seen, the equation of motion for fluids appears to be an exclusive creation of French minds, a result of the solid mathematical training provided at the École Polytechnique, which sought to generate advanced knowledge in mathematical physics in the context of engineering applications [2]. The interest of English scientists of that time was in astronomy or mathematics, and only tangentially in hydrodynamics or elasticity. The contributions of people such as George Airy (1801–1892), George Green (1793–1841), or Phillip Kelland (1808–1879), especially in the field of wave theory, were only by-products of their main interests. In this environment, we find Stokes, whose training was in mathematics.

The first article that appears in *Mathematical and Physical Papers by George Gabriel Stokes*, Vol. 1, published in 1880, which compiles Stokes' work taken from the original publications "with additional notes by the author", is titled "*On the steady motion of incompressible fluids*", was read on 25 April 1842, and originally published in Vol. VII of *Transactions of the Cambridge Philosophical Society* [53,54]. The article considers two-dimensional irrotational flow "where the stream-lines are a system of similar ellipses or hyperbolas having the same centre, or a system of equal parabolas having the same axis" [54] (p. 446). When discussing the case of hyperbolas, he considers the discharge through an orifice from one fluid-filled tank to another, indicating the experimental result that the fluid "has a tendency to keep within a channel of its own, instead of spreading out" [54] (p. 447). In this way, Stokes is the first to relate the equations governing irrotational flow (Euler's equations) with surfaces of discontinuity. But perhaps even more interesting is when he writes, "I have not proved that the fluid must move in this system of lines . . . there may be perhaps different modes of permanent motion; and of these some may be stable, and others unstable. There may even be no stable mode of motion possible, in which case the fluid would continue in perpetually eddying motion". It is thus that Stokes, in 1842, introduced the concept of hydrodynamic stability, which is now commonly used in fluid mechanics and hydraulics.

On 14 April 1845, Stokes presented to the Cambridge Philosophical Society the work for which he is most recognised today: "*On the Theories of Internal Friction in Fluids and the Equilibrium and Motion of Elastic Solids*", in which he derived the equations of motion of a compressible or incompressible Newtonian fluid [43]. Interestingly, he does not explicitly

mention viscosity, although he does say that "the amount of internal friction of water depends on the value of μ". The deduction that Stokes makes is not as direct as we commonly do in fluid mechanics courses. First, he considers the relative displacement between two points P and P' of the fluid and concludes that the most general movement is composed of translation, rotation, "uniform dilation", and "displacement movements" (angular deformation). He breaks down pressure into two terms, one corresponding to the pressure in a state of equilibrium and the other associated with motion, which he demonstrates is independent of angular velocity and must depend on "residual relative velocities", e', e'', e''', where the primes indicate the three axes of extension or coordinate directions, i.e., with our current notation, $e' = \partial u/\partial x$, $e'' = \partial v/\partial y$, $e''' = \partial w/\partial z$. The pressure acting in the direction of each of the axes is given by $p + p'$, $p + p''$, and $p + p'''$, with p being the pressure in the state of equilibrium and those with primes corresponding to motion in the respective directions. The pressures in the directions perpendicular to the x, y and z axes must be functions of the residual relative velocities, so those must be taken into account:

$$p' = \phi(e', e'', e'''); \quad p'' = \phi(e'', e''', e'); \quad p''' = \phi(e''', e', e'') \tag{15}$$

where "$\phi(e'$, e'', e''') denotes a function of e', e'' and e''' that is symmetric with respect to the last two quantities. The problem now is to determine, under what may appear to be the most probable hypothesis, the form of the function ϕ". Stokes considers a linear relationship between p' and e', obtaining $p' = Ce'$, $p'' = C'e'$, $p''' = C'''e'$. Invoking the symmetry previously indicated, $C'' = 0$ and $C' = -C$ are obtained. Then, without further explanation, Stokes considers $C = -2\mu$, obtaining:

$$p' = -2\mu e'; \quad p'' = -2\mu e''; \quad p''' = -2\mu e''' \tag{16}$$

If the fluid, in addition to moving, is subjected to a dilation (compressible fluid), the expression for p' turns out to be:

$$p' = \frac{2}{3}\mu\left(e'' + e''' - 2e'\right) + \kappa\left(e' + e'' + e'''\right) \tag{17}$$

Similar expressions are obtained for p'' and p'''. The next step for Stokes was to determine the "oblique pressure, or the resultant of the normal pressure and the tangential action, on any plane". Finally, in terms of the cubic dilation rate 3δ, the normal and tangential stresses acting on the surfaces of an element of fluid are given by:

$$3\delta = \frac{\partial u}{\partial x} + \frac{\partial v}{\partial y} + \frac{\partial w}{\partial z} \tag{18}$$

$$\left.\begin{array}{ccc} P_1 = p - 2\mu\left(\frac{\partial u}{\partial x} - \delta\right), & P_2 = p - 2\mu\left(\frac{\partial v}{\partial y} - \delta\right), & P_3 = p - 2\mu\left(\frac{\partial w}{\partial z} - \delta\right) \\ T_1 = -\mu\left(\frac{\partial v}{\partial z} + \frac{\partial w}{\partial y}\right), & T_2 = -\mu\left(\frac{\partial w}{\partial x} + \frac{\partial u}{\partial z}\right), & T_3 = -\mu\left(\frac{\partial u}{\partial y} + \frac{\partial v}{\partial x}\right) \end{array}\right\} \tag{19}$$

Writing the above stresses using the notation commonly used today, we have: $P_1 = \tau_{xx}, P_2 = \tau_{yy}, P_3 = \tau_{zz}, T_1 = \tau_{zy} = \tau_{yz}, T_2 = \tau_{zx} = \tau_{xz}, T_3 = \tau_{xy} = \tau_{yx}$. For an incompressible fluid, $\delta = 0$, and the normal stresses reduce to thermodynamic pressure.

The following comment that Stokes made regarding μ is of interest: "We also see that it is necessary to suppose μ to be positive, otherwise the tendency of the forces would be to increase the motion of the parts of the fluid, and the equilibrium of the fluid would be unstable" [55] (p. 296). It is noteworthy that, according to Stokes, a positive value of the coefficient μ must be assumed. Nowadays, no one would doubt that viscosity must be positive and that it is not an assumption. With the additional assumptions that μ must be constant and independent of pressure, and that the fluid is homogeneous, Stokes arrives at the equation of motion of Newtonian fluids, whose component in the x direction is presented in Figure 18. Equation (12) of Stokes' article corresponds to the

case of compressible fluid, and Equation (13) to that of an incompressible fluid. In these equations, X is the x-component of the body force per unit mass (generally due to the gravitational field, g_x), and $Du/Dt = \partial u/\partial t + \vec{V}\cdot\nabla u$.

The year following his presentation at the Cambridge Philosophical Society, Stokes submitted an article to the British Association for the Advancement of Science titled "*Report on Recent Researches in Hydrodynamics*" [55], summarizing the results of his 1845 work along with those previously obtained by Navier, Cauchy, Poisson, and Saint-Venant. Stokes refers to the contributions of these authors and his own regarding the non-perpendicularity of "pressures" on the surfaces of a moving fluid volume element, decomposing each of these "pressures" into three components (one normal and two tangential) that we now call stresses. Stokes also notes that, despite having different assumptions in their derivations, all five authors arrive at an equation of motion with the same form, featuring a frictional resistance proportional to $\nabla^2\vec{V}$.

The next problem to be solved is that of boundary conditions, and "the method of proceeding will be different depending on whether the boundary surface is considered to be a free surface, the surface of a solid, or the surface of separation of two fluids, and it will be necessary to consider these cases separately ..." [43] (p. 298). Without going into detail about the boundary conditions for the different cases, it is interesting to note that Stokes considers that there is no slip of the flow in contact with the wall, "The condition that occurred first to me for this case was that a film of fluid immediately in contact with the solid has no relative motion to the surface of the solid" [43] (p. 299). However, when comparing the result calculated from the formula for flow rate obtained from his equations with the experiments of Bossut and Dubuat, he found "that the formula did not agree at all with the experiment". This led him to include a slip velocity U, so the velocity distribution $w(r)$ that he obtains in a cylindrical pipe of radius a is given by:

$$w = \frac{\rho g \sin\alpha}{4\mu}\left(a^2 - r^2\right) + U \tag{20}$$

It is clear that Stokes was not convinced by Equation (20), as stated in his report to the British Association for Advancement of Science in 1846 [55], where he indicates that "Dubuat established, as a result of his experiments, that when the velocity of water flowing through a pipe is less than a certain amount, the water adjacent to the surface of the pipe is at rest". Stokes also specifies that the no-slip condition agrees with the experimentation of Coulomb, who conducted experiments with a metal disc that oscillated slowly about an axis passing perpendicular to its centre: The resistance to movement was the same whether the surface of the disc was clean, coated with grease (to reduce friction), or had sand adhered to it. This result is consistent with the assumption that the fluid in contact with the surface has no relative velocity with respect to it [55] (p. 19). The no-slip condition would be definitively established with his experiments on pendulum oscillation. In his 1850 publication, he states, "I will assume, ..., that the velocity of a fluid particle will be the same, both in magnitude and direction, as that of the solid particle with which it is in contact. The agreement of the results thus obtained with observation is shown to be very satisfactory" [56] (p. 15).

Nowadays, it is known that, strictly speaking, there is slip at the solid–liquid interface, and "Navier's condition" is valid. Defining the "slip length" as $b = \varepsilon/E$, where ε and E are the coefficients resulting from the interaction force between fluid molecules and between fluid molecules and the solid wall, respectively (Equations (11)–(13)). In general, b is on the order of a nanometer [57], so the no-slip condition can be safely used without any significant loss of accuracy for flows developed at scales such as those used in the experiments carried out in the 18th and 19th centuries. However, only 10 years after Stokes established the no-slip condition, it was questioned. In 1860, Helmholtz and von Piotrowski [58] claimed to have found evidence of slip of a liquid flowing over a solid boundary. Their work was followed by a series of articles, both in favor of and against the conclusions published

in 1860 [59]. Navier's condition was first associated with the superhydrophobicity of the solid surface by Ronceray in 1911 in experiments with capillaries coated with paraffin [60]. Research in the second half of the 20th century definitively established that slip length is related to wettability and surface roughness [61–63]. The validity of Navier's condition is not questioned in micro and nanofluidics [63,64].

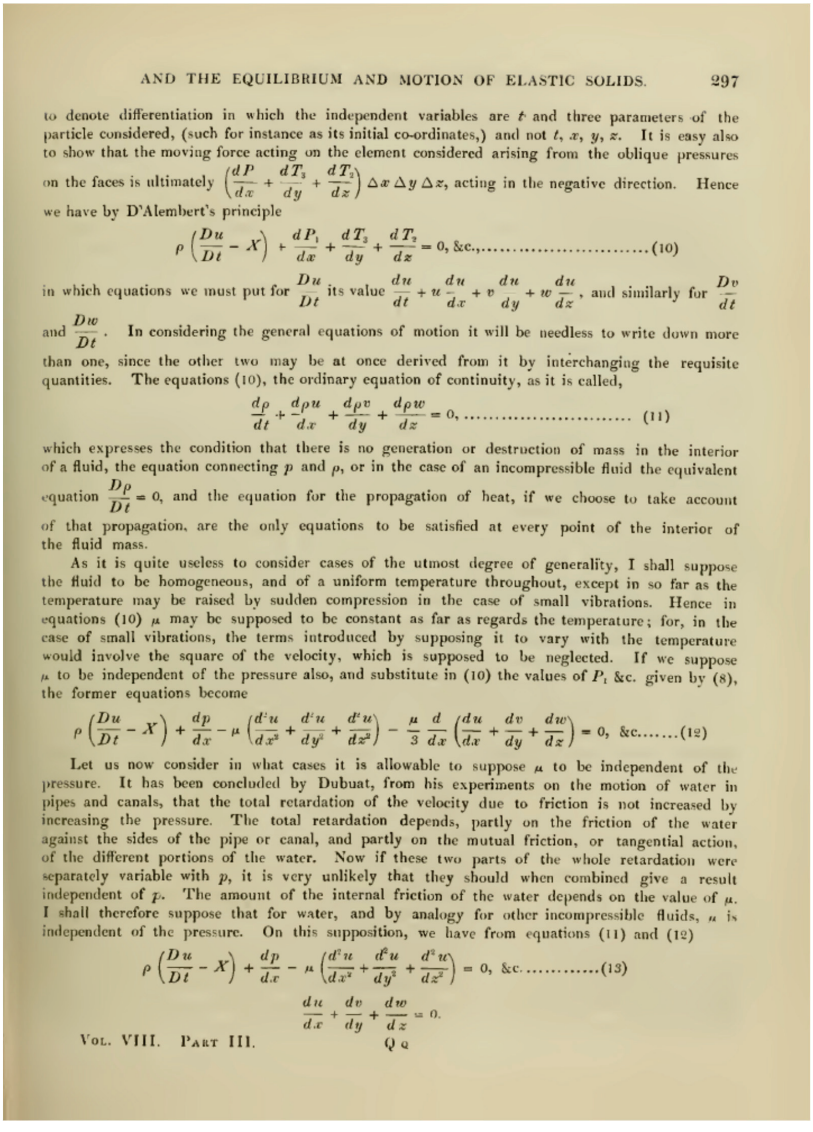

AND THE EQUILIBRIUM AND MOTION OF ELASTIC SOLIDS. 297

to denote differentiation in which the independent variables are t and three parameters of the particle considered, (such for instance as its initial co-ordinates,) and not t, x, y, z. It is easy also to show that the moving force acting on the element considered arising from the oblique pressures on the faces is ultimately $\left(\frac{dP}{dx} + \frac{dT_3}{dy} + \frac{dT_2}{dz}\right)\Delta x\,\Delta y\,\Delta z$, acting in the negative direction. Hence we have by D'Alembert's principle

$$\rho\left(\frac{Du}{Dt} - X\right) + \frac{dP_1}{dx} + \frac{dT_3}{dy} + \frac{dT_2}{dz} = 0, \text{ \&c.,} \quad \ldots\ldots\ldots\ldots\ldots\ldots\ldots\ldots (10)$$

in which equations we must put for $\frac{Du}{Dt}$ its value $\frac{du}{dt} + u\frac{du}{dx} + v\frac{du}{dy} + w\frac{du}{dz}$, and similarly for $\frac{Dv}{dt}$ and $\frac{Dw}{Dt}$. In considering the general equations of motion it will be needless to write down more than one, since the other two may be at once derived from it by interchanging the requisite quantities. The equations (10), the ordinary equation of continuity, as it is called,

$$\frac{d\rho}{dt} + \frac{d\rho u}{dx} + \frac{d\rho v}{dy} + \frac{d\rho w}{dz} = 0, \quad \ldots\ldots\ldots\ldots\ldots\ldots\ldots\ldots (11)$$

which expresses the condition that there is no generation or destruction of mass in the interior of a fluid, the equation connecting p and ρ, or in the case of an incompressible fluid the equivalent equation $\frac{D\rho}{Dt} = 0$, and the equation for the propagation of heat, if we choose to take account of that propagation, are the only equations to be satisfied at every point of the interior of the fluid mass.

As it is quite useless to consider cases of the utmost degree of generality, I shall suppose the fluid to be homogeneous, and of a uniform temperature throughout, except in so far as the temperature may be raised by sudden compression in the case of small vibrations. Hence in equations (10) μ may be supposed to be constant as far as regards the temperature; for, in the case of small vibrations, the terms introduced by supposing it to vary with the temperature would involve the square of the velocity, which is supposed to be neglected. If we suppose μ to be independent of the pressure also, and substitute in (10) the values of P_1 &c. given by (8), the former equations become

$$\rho\left(\frac{Du}{Dt} - X\right) + \frac{dp}{dx} - \mu\left(\frac{d^2u}{dx^2} + \frac{d^2u}{dy^2} + \frac{d^2u}{dz^2}\right) - \frac{\mu}{3}\frac{d}{dx}\left(\frac{du}{dx} + \frac{dv}{dy} + \frac{dw}{dz}\right) = 0, \text{ \&c.} \ldots\ldots (12)$$

Let us now consider in what cases it is allowable to suppose μ to be independent of the pressure. It has been concluded by Dubuat, from his experiments on the motion of water in pipes and canals, that the total retardation of the velocity due to friction is not increased by increasing the pressure. The total retardation depends, partly on the friction of the water against the sides of the pipe or canal, and partly on the mutual friction, or tangential action, of the different portions of the water. Now if these two parts of the whole retardation were separately variable with p, it is very unlikely that they should when combined give a result independent of p. The amount of the internal friction of the water depends on the value of μ. I shall therefore suppose that for water, and by analogy for other incompressible fluids, μ is independent of the pressure. On this supposition, we have from equations (11) and (12)

$$\rho\left(\frac{Du}{Dt} - X\right) + \frac{dp}{dx} - \mu\left(\frac{d^2u}{dx^2} + \frac{d^2u}{dy^2} + \frac{d^2u}{dz^2}\right) = 0, \text{ \&c.} \ldots\ldots\ldots\ldots (13)$$

$$\frac{du}{dx} + \frac{dv}{dy} + \frac{dw}{dz} = 0.$$

Figure 18. Page from Stokes' 1845 article in which he presents his derivation of the equations governing fluid motion. Equation (12) corresponds to the component along x for a compressible fluid, and Equation (13) for an incompressible fluid.

Finally, and just as an anecdotal fact, in his 1850 article, Stokes indicates that the results associated with the effect of friction on the oscillation of a pendulum can be characterised by a single constant, which he calls the "friction index" and denotes as μ'. The friction index is determined for various fluids and is defined as $\mu' = \mu/\rho$, which corresponds to

what we now know as kinematic viscosity. Stokes says that in the solution of the equations of motion, μ always appears divided by ρ, so the use of μ' is more convenient. In addition, the friction index has the advantage that its units are "the square of a line divided by a time", so it is easier to adapt to different systems of units [56] (p. 17).

7. Conclusions

Thus, we can close the history of the development of the equations governing fluid motion and present it to commemorate the bicentenary of the publication of Navier's landmark work. A long story that in this article arbitrarily began in 1628, with the establishment of the continuity equation by Benedetto Castelli and that culminated two hundred years later with the work of Navier, remade with different visions or emphases by Cauchy, Poisson, Saint-Venant, and Stokes, great thinkers ("geometers" in the language of D'Alembert), that helped to reinterpret and rigorously formalise the concept of internal friction in fluids. Using all the baggage of available scientific knowledge and mathematical tools of their time, Navier incorporated flow resistance in the equation of fluid motion, making an enormous impact on the development of fluid dynamics foundations. His contribution was so important that his surname, together with Stokes, is associated with the equation of fluid motion. The great contribution of the latter was to elucidate the correct boundary condition that must be imposed when integrating the equations of fluid motion for the flows of interest in the 19th century. However, a few decades later, Navier's conditions would be redeemed, and they are currently applied in micro and nanofluidic, as well as in flows on superhydrophobic surfaces. However, in the author's opinion, Saint-Venant's contribution has not been sufficiently recognised.

In this article, experimental work has only been sporadically mentioned to the extent that it contradicted the result obtained from theory. Although Bossut, Dubuat, and Girard have been mentioned, there are many others who contributed with their measurements to validate and, perhaps more importantly, to question the theoretical results. Only the discussion of the correct boundary condition generated controversy that took more than half a century to resolve. Navier and Stokes considered both the no-slip condition and the existence of a relative velocity of the fluid with respect to the solid wall. This discussion arose when trying to reconcile theory with measurements. To address the experimental aspect provides enough material for another article, both in terms of measurements and flow visualisation, which announced a new field of study related to instabilities and turbulence.

Finally, it should not be forgotten that the mathematical complexity of the Navier–Stokes differential equations is such that it constitutes one of the seven unsolved Millennium Prize Problems. These problems were proposed by the Clay Mathematics Institute, with a prize of one million dollars to anyone who solves one of them. The formal statement of the problem is formulated in mathematical language on the Institute's website, https://www.claymath.org/ (accessed on 1 August 2023), and basically consists of demonstrating the existence of differentiable solutions, in three dimensions, for any physically valid initial condition value.

Funding: This research received no external funding.

Data Availability Statement: No new data were created or analyzed in this study.

Acknowledgments: The author acknowledges the project ANID AFB230001 and the Department of Civil Engineering, University of Chile. This article is mostly a translation of "A 200 años de la contribución de Navier a la determinación de la resistencia del flujo de fluidos (200 years after Navier's contribution to the determination of fluid flow resistance)" written by the author and originally published in Spanish by the Chilean Society of Hydraulic Engineering (SOCHID) in *Revista de la Sociedad Chilena de Ingeniería Hidráulica*, 2022, Vol. 37, No. 2, pp. 3–38. www.sochid.cl/publicaciones-sochid/revista-sochid (Accessed on 27 November 2023). Permission for publication in Fluids was granted by SOCHID.

Conflicts of Interest: The author declares no conflict of interest.

References

1. McKeon, R.M. Navier, Claude-Louis-Marie-Henri. In *Dictionary of Scientific Biography*; Gillispie, C.C., Ed.; Charles Scribner's Sons: New York, NY, USA, 1981; Volume 10, pp. 2–5.
2. Darrigol, O. Between Hydrodynamics and Elasticity Theory: The First Five Births of the Navier-Stokes Equation. *Arch. Hist. Exact Sci.* **2002**, *56*, 95–150. [CrossRef]
3. Castelli, B. *Della Misura dell'Acque Correnti*; Per Francesco Caualli: Roma, Italy, 1639.
4. Newton, I. *Philosophiæ Naturalis Principia Mathematica*; Printer S. Pepys, Printing of the Royal Society: London, UK, 1687.
5. Spencer, J.B.; Brush, S.G.; Osler, M.J. "Scientific Revolution". Encyclopedia Britannica. Available online: https://www.britannica.com/science/Scientific-Revolution (accessed on 18 September 2022).
6. Busard, H.L.L. François Viète. In *Dictionary of Scientific Biography*; Gillispie, C.C., Ed.; Charles Scribner's Sons: New York, NY, USA, 1981; Volume 14, pp. 18–25.
7. Mahoney, M.S. Descartes: Mathematics and Physics. In *Dictionary of Scientific Biography*; Gillispie, C.C., Ed.; Charles Scribner's Sons: New York, NY, USA, 1981; Volume 10, pp. 55–61.
8. Rouse, H.; Ince, S. *History of Hydraulics*; Dover Publications, Inc.: New York, NY, USA, 1963.
9. Bernoulli, D. *Hydrodynamica, Sive de Viribus et Motibus Fluidorum Commentarii*; Printer: Johan Heinrich Deckeri: Basilea, Switzerland, 1738.
10. D'Alembert, J.L.R. *Traité de L'équilibre et du Mouvement des Fluides*; Imprimerie de Jean-Baptiste Coignard: Paris, France, 1744.
11. D'Alembert, J.L.R. Paradoxe proposé aux Géometres sur la Resistance des Fluides. In *Opuscules Mathématiques*; Tome V; Première Partie, Imprimerie de Chardon: Paris, France, 1768; pp. 132–138.
12. Euler, L. Découverte d'un nouveau principe de mécanique. In *Mémoires de l'Académie Royale des Sciences et des Belles-Lettres de Berlin*; Tome VI; Chez Haude et Spenee: Berlin, Germany, 1752; pp. 185–217.
13. Euler, L. Principes généraux de l'état de l'équilibre des fluids. In *Mémoires de l'Académie Royale des Sciences et des Belles-Lettres de Berlin*; Tome XI; Chez Haude et Spenee: Berlin, Germany, 1757; pp. 217–273.
14. Euler, L. Principes généraux du mouvement des fluids. In *Mémoires de l'Académie Royale des Sciences et des Belles-Lettres de Berlin*; Tome XI; Chez Haude et Spenee: Berlin, Germany, 1757; pp. 274–315.
15. Euler, L. Continuation des Recherches sur la théorie du mouvement des fluids. In *Mémoires de l'Académie Royale des Sciences et des Belles-Lettres de Berlin*; Tome XI; Chez Haude et Spenee: Berlin, Germany, 1757; pp. 316–361.
16. Lagrange, J.-L. Mémoire sur la théorie du mouvement des fluids. In *Nouveaux Mémoires de l'Académie Royale des Sciences et des Belles-Lettres de Berlin*; 1781. Also, In *Oeuvres de Lagrange*, Tome IV; Imprimeur Gauthier-Villars: Paris, France; pp. 695–748.
17. Poisson, S.D. Mémoire sur l'équilibre et le mouvement des corps élastiques. In *Mémoires de l'Académie des Sciences de l'Institut de France*; Tome VIII; Read in the Meeting of l'Académie de Paris on 14 April 1828; Bachelier, Imprimeur-Libraire: Paris, France, 1829; pp. 357–570.
18. Boussinesq, J. *Leçons Synthétiques de Mécanique Générale Servant d'Introduction au Cours de Mécanique Physique*; Gauthier-Villars et Fils, Imprimeurs-Libraires: Paris, France, 1889.
19. Lucrecio. *Naturaleza de las Cosas*, Prose version in Spanish of "*De rerum natura*", translated by Manuel Rodríguez-Navas; Printed by Agustín Avrial; Imprenta de la Compañía de Impresores y Libreros: Madrid, Spain, 1892.
20. Whyte, L.L. *Essay on Atomism: From Democritus to 1960*; Wesleyan University Press: Middletown, CT, USA, 1961.
21. Newton, I. *Sir Isaac Newton's Mathematical Principles of Natural Philosophy and His System of the World*; Translated into English by Andrew Motte in 1729. The translations revised, and supplied with an historical and explanatory appendix, by Florian Cajori. Volume One: The Motion of Bodies. Eighth Printing; University of California Press: Berkeley, CA, USA, 1974.
22. Boscovich, R.J. *De Vitribus Vivis Dissertatio*; Impresor Komarek: Roma, Italy, 1745.
23. Boscovich, R.J. *Philosophiæ Naturalis Theoria*; Prostat Viennæ Austriæ, in Officina Libraria Kaliwodiana: Viena, Austria, 1758.
24. Laplace, P.S. *Exposition du Système du Monde*; Imprimerie du Cercle-Social: Paris, France, 1796; 2 volumes.
25. Laplace, P.S. *Exposition du Système du Monde*, 2nd ed.; Imprimerie de Crapelet: Paris, France, 1798.
26. Laplace, P.S. *Exposition du Système du Monde*, 3rd ed.; Chez Courcier: Paris, France, 1808.
27. Laplace, P.S. Sur l'Action Capillaire. In *Supplément au Dixième Livre du Traité de Mécanique Céleste*; Tome Quatrième; Chez Courcier: Paris, France, 1805; pp. 1–50.
28. Navier, C.L. Sur les Lois des mouvemens des fluides, en ayant egard à l'adhesion des molecules. *Ann. Chim. Phys.* **1821**, *19*, 244–260, Errata in p. 448.
29. Navier, C.L. Sur les Lois du Mouvement des Fluides. *Mémoires L'Académie des Sci. L'institut Fr.* **1823**, *6*, 389–416, Read in the Académie Royale des Sciences on 18 March 1822.
30. Girard, M. Mémoire sur le mouvement des fluides dans les tubes capillaires, et l'influence de la température sur ce movement. In *Mémoires des Sciences Mathématiques et Physiques de l'Institut de France*; Années 1813, 1814, 1815; Chez Firmin Didot: Paris, France, 1818; pp. 249–380, Read in l'Académie, on 30 April 30 and 6 Mai 1816.
31. White, F.M. *Mecánica de Fluidos*; Fifth edition in Spanish; Mc Graw Hill: Madrid, Spain, 2004.
32. Massey, B. *Mechanics of Fluids*, 8th ed.; Taylor & Francis: New York, NY, USA, 2006.
33. Munson, B.R.; Young, D.F.; Okiishi, T.H.; Huebsch, W.W. *Fundamentals of Fluid Mechanics*, 6th ed.; John Wiley & Sons, Inc.: Jefferson City, MO, USA, 2009.
34. Granger, R.A. *Fluid Mechanics*; Dover Publications, Inc.: New York, NY, USA, 1995.

35. Streeter, V.L.; Wylie, E.B.; Bedford, K.W. *Mecánica de Fluidos*; Ninth edition in Spanish Edición; Mc Graw Hill: Santafé de Bogotá, Colombia, 1999.
36. Shames, I.H. *Mecánica de Fluidos*; Third edition in Spanish; Mc Graw Hill: Santafé de Bogotá, Colombia, 2001.
37. de las Casas, C. *Vocabvlario de las Dos Lengvas Toscana y Castellana*; Printed in Casa de Alonso: Sevilla, Spain, 1576.
38. Real Academia Española. *Diccionario de la Lengua Castellana*; Tomo Sexto que contiene las letras S, T, U, V, X, Y, Z; Imprenta de la Real Academia Española: Madrid, España, 1739.
39. Wiedemann, G. Ueber die Bewegung der Flüssigkeiten im Kreise der geschlossenen galvanischen Säule und ihre Beziehungen zur Elektrolys. *Ann. Phys. Chem.* **1856**, *175*, 177–233. [CrossRef]
40. Cauchy, A. Recherches sur l'équilibre et le mouvement intérieur des corps solides ou fluides, élastiques on non élastiques. *Bull. des Sci. par la Société Philomatique de Paris* **1823**, 9–13, Imprimerie de Plassan: Paris, France.
41. Poisson, S.D. Mémoire sur les équations générales de l'équilibre et du mouvement des corps solides élastiques et des fluids. *J. L'École Polytech.* **1831**, *Tome XIII*, 1–174, Read in the meeting of l'Académie des Sciences de Paris on 12 October 1829.
42. Saint-Venant, A. Note à joindre au Mémoire sur la dynamique des fluides. *Compte Rendu Séances L'académie Sci.* **1843**, *17*, 1240–1244, Presented on 14 April 1834.
43. Stokes, G.G. On the Theories of the Internal Friction of Fluids in Motion, and of the Equilibrium and Motion of Elastic Solids. *Trans. Camb. Philos. Soc.* **1845**, *8*, 287–317.
44. Hager, W.H.; Hutter, K.; Castro-Orgaz, O. Correspondence between de Saint-Venant and Boussinesq 5: Viscosity and hydraulic resistance. *Comptes Rendus. Mécanique* **2021**, *349*, 145–166. [CrossRef]
45. Reynolds, O. On the Theory of Lubrication and its Application to Mr. Beauchamp Tower's Experiments, including an Experimental Determination of the Viscosity of Olive Oil. *Philos. Trans. R. Soc. Lond.* **1886**, *177*, 157–234.
46. Saint-Venant, A. Théorie du mouvenment non permanenl des eaux, avec application aux crues des rivières et à l'introduction des marées dans leur lit. *Compte Rendu Séances L'académie Sci.* **1871**, *63*, 147–154, (deduction of equations) and; pp. 237–249 (application).
47. MacTutor. Adhémar Jean Claude Barré de Saint-Venant. *MacTutor History of Mathematics.* Available online: https://mathshistory.st-andrews.ac.uk/Biographies/Saint-Venant/ (accessed on 3 October 2023).
48. Saint-Venant, A. L'Institut. *J. Général Sociétés Trav. Sci. Fr. L'Etranger.* **1834**, *49*, 126.
49. Saint-Venant, A. Mémoire sur le Calcul des efféts des machines à vapeur; contenant des équations générales de l'écoulement permanent ou périodique des fluides, en tenant compte de leurs dilatations et de leurs changements de température et sans supposer qu'ils se meuvent par tranches parallèles, ni par filets indépendants. *Compte Rendu Séances L'Académie Sci.* **1838**, *6*, 45–47.
50. Boussinesq, J. Essai sur la Théorie des Eaux Courantes. *Mémoires Présentés par Divers. Savants a L'Académie des Sci.* **1877**, *23*, 1–680.
51. Saint-Venant, A. *Formules et Tables Nouvelles pour la Solution des Problems Relatifs aux eaux Courantes*; Imprimé par E. Thunot et Cie: Paris, France, 1851; Also, in *Annales des Mines*; Quatrième Série **1851**, *20*, 183–357.
52. Saint-Venant, A. Note sur la détermination expérimentale des forces retardatrices du movement des liquids. *Comptes Rendus Hebd. Séances L'Académie Sci.* **1846**, *22*, 306–309.
53. Stokes, G.G. *Mathematical and Physical Papers by George Gabriel Stokes*; The University Press: Cambridge, UK, 1880; Volume 1.
54. Stokes, G.G. On the Steady Motion of Incompressible Fluids. *Trans. Camb. Philos. Soc.* **1842**, *7*, 439–453.
55. Stokes, G.G. Report on Recent Researches in Hydrodynamics. In Proceedings of the Sixteenth Meeting of the British Association for the Advancement of Science, Southampton, UK, 10–15 September 1846; Richard and John E. Taylor, Printers. Oxford University Press: London, UK, 1847; pp. 1–20.
56. Stokes, G.G. On the Effect of the Internal Friction of Fluids on the Motion of Pendulums. *Trans. Camb. Philos. Soc.* **1850**, *9*, 8–106.
57. Rothstein, J.P. Slip on Superhydrophobic Surfaces. *Annu. Rev. Fluid Mech.* **2010**, *42*, 89–109. [CrossRef]
58. Helmholtz, H.; von Piotrowski, G. Über Reibung tropfbarer Flüssigkeiten. *Sitzungsberichte Kais. Akad. Wiss.* **1860**, *40*, 607–658.
59. Vinogradova, O.I. Slippage of water over hydrophobic surfaces. *Int. J. Miner. Process.* **1999**, *56*, 31–60. [CrossRef]
60. Ronceray, M.P. Recherches sur l'écoulement dans les tubes capillaires. *Ann. Chim. Phys.* **1911**, *22*, 107–125.
61. Schnell, E. Slippage of water over nonwettable surfaces. *J. Appl. Phys.* **1956**, *27*, 1149–1152. [CrossRef]
62. Churaev, N.V.; Sobolev, V.D.; Somov, A.N. Slippage of liquids over lyophobic solid surfaces. *J. Colloid Interface Sci.* **1984**, *97*, 574–581. [CrossRef]
63. Lauga, E.; Brenner, M.P.; Stone, H.A. Microfluidics: The non-slip boundary condition. In *Springer Handbook of Experimental Fluid Mechanics*; Tropea, C., Yarin, A.L., Foss, J.F., Eds.; Springer: Berlin, Germany, 2007; pp. 1210–1240.
64. Cheng, J.-T.; Giordano, N. Fluid flow through nanometer-scale channels. *Phys. Rev. E* **2002**, *65*, 031206-1–031206-5. [CrossRef]

materials

MDPI

Article

Modeling of the Flow Field and Clad Geometry of a Molten Pool during Laser Cladding of CoCrCuFeNi High-Entropy Alloys

Dachuan Tian [1], Chonggui Li [1,*], Zhiguo Hu [1], Xintong Li [1], Yajun Guo [1], Xiaosong Feng [2], Zhenhai Xu [3], Xiaoguang Sun [4] and Wenge Li [5]

[1] School of Materials Science and Engineering, Shanghai University of Engineering Science, Shanghai 201620, China
[2] Shanghai Aerospace Equipment Manufacturer Co., Ltd., Shanghai 200245, China
[3] National Key Laboratory for Precision Hot Processing of Metals, Harbin Institute of Technology, Harbin 150001, China
[4] Technical Engineering Department, CRRC Qingdao Sifang Co., Ltd., Qingdao 266111, China
[5] Institute for Marine Materials Science and Engineering, Shanghai Maritime University, Shanghai 201306, China
* Correspondence: chongguili@sues.edu.cn

Abstract: A flow field analysis was performed in this research using the ANSYS Fluent module, and a dynamic heat source employing UDF was constructed using the DEFINE_PROFILE macro. A VOF model was developed to track the volume fraction of each fluid throughout the computational domain as well as the steady-state or transient condition of the liquid–gas interface in the free liquid surface area. To determine the distribution state and regularity of the molten pool flow field, the flow field velocity was calculated iteratively by linking the Simple algorithm with the horizontal set method. The molten pool was concave, indicating that the key hole was distributed narrowly. Inserting cross-sections at different depths yielded the vector distribution of the molten pool flow velocity along the depth direction. We set up monitoring sites along the molten pool's depth direction and watched the flow change over time. We investigated the effects of the process parameters on the flow field's vector distribution.

Keywords: laser cladding; molten pool flow; high-entropy alloys; clad geometry; simulation

Citation: Tian, D.; Li, C.; Hu, Z.; Li, X.; Guo, Y.; Feng, X.; Xu, Z.; Sun, X.; Li, W. Modeling of the Flow Field and Clad Geometry of a Molten Pool during Laser Cladding of CoCrCuFeNi High-Entropy Alloys. *Materials* **2024**, *17*, 564. https://doi.org/10.3390/ma17030564

Academic Editors: Vasily Novozhilov and Cunlu Zhao

Received: 16 November 2023
Revised: 10 December 2023
Accepted: 17 January 2024
Published: 25 January 2024

1. Introduction

304 stainless steel has great corrosion resistance, can be used in most acidic situations for a long time, and has a high strength and toughness [1–3]. It can also survive the erosion caused by various corrosive media at room temperature, such as oxidation, alkalinity, and high temperature, and is, thus, widely used in food processing equipment, pressure vessels, chemical equipment, medical equipment, building decorations, car parts, and in other sectors. However, the low hardness and poor wear resistance of 304 stainless steel severely limit its industrial applications [4]. As a result, the application of a high-entropy protective coating to the surface of stainless steel can significantly extend the service life of severe wear strips under high-temperature settings. There have been few studies on how to improve the performance of 304 stainless steel with high-entropy alloy coatings.

High-entropy alloys are significantly better than conventional metals because of their high hardness, high toughness, and high thermal stability as well as their good wear resistance, corrosion resistance, and other factors [5]. Under some special conditions, high-entropy alloys can even break the limits of existing materials, so they have become a hot spot within the development of material science [6–8]. Therefore, the preparation of a high-entropy protective coating on the surface of stainless steel could effectively extend the service life of severe wear strips under high-temperature conditions.

The process parameters typically used have a significant impact on the shape and coating quality of the final clad layer. The parameters of the laser cladding process include the laser power, scanning speed, defocus amount, protective gas, and so on. The laser power determines the temperature and depth of the covered area, which usually needs to be adjusted according to the material type and thickness. The scanning speed affects the speed of movement on the material's surface and affects the thickness and compactness of the cladding layer. Goodarzi et al. [9] analyzed the influence of laser cladding process parameters on the geometry of the composite layer and analyzed the cladding results, concluding that the laser power and cladding speed are the main parameters in controlling the width of the cladding layer. Hofman et al. [10] used a novel method to determine the envelope geometry. The correlation between the observable melt pool characteristics and dilution was investigated using this model. Different combinations of the cladding speed, laser power (distribution), and substrate temperature were simulated. The simulation results were compared to the experimental results with high agreement. Benarji et al. [11] performed a finite element analysis of the L-MD to understand the thermal behavior governing the microstructural features (grain size and morphology). The input parameters of the L-MD were the effects of the scanning rate, powder feeding rate, and laser power on the cladding height and width and the variation in the solidification rate and temperature gradient under various process parameters. The composite width and height increased significantly with the laser power and the powder feeding rate but decreased with the scanning rate.

The laser melting process involves a high-temperature melting and rapid cooling process, which results in a harsh environment that is difficult to monitor. The laser cladding process is accompanied by a variety of heat exchanges, such as heat conduction, heat convection, and heat radiation, and the thermal change is difficult to analyze through experiments, so the use of a numerical model that reproduces the physical process can reduce the experimental period and cost [12]. Afshari et al. [13] used finite element techniques to simulate the laser cladding process to assess the effects of the scanning rate and laser power on the changes in the microstructure, geometry, and temperature of Inconel 718. It was shown that by increasing the scanning rate and decreasing the laser power, the height and length decreased, as the heat transfer to the sample was faster than its temperature rise speed. Hao et al. [14] constructed an adaptive cladding layer and mobile heat source models through an inverse modeling method, which realized the temperature distribution of laser cladding with different process parameter combinations, and they verified the effectiveness of the proposed model through the numerical and experimental results. Khomenko et al. [15] developed a new, coupled kinetic model of heat transfer and coagulation for optimizing microstructures in laser additive manufacturing applications. Their developed model had a fairly good agreement with the experimental data. In this paper, the influence of the processing parameters on the orbital macroscopic and microscopic parameters are analyzed. A method for changing the average crystal size and simultaneously preserving the orbital height and width is proposed.

2. Mathematical Modeling of Single-Track Laser Cladding

2.1. Model Building and Meshing

The cuboid model developed in this study was established using the ICEM CFD module in the ANSYS 18.2 software, as shown in Figure 1. The lower layer was a stainless-steel substrate, and the powder layer reflow field in the upper layer became an area of free liquid level change. Because the substrate powder is basically symmetrical in the actual cladding process, it could be divided from the symmetry surface, and half of the model could be built to reduce the calculation amount in the simulation process. After establishing the basic model, the six faces of the model needed to be named to impose the boundary conditions on each face using the Fluent 18.2 software. After naming the six sides of the model, the edges were linearly cut at the absolute value through the Blocking module. The closer the mesh is to the molten pool, the denser the mesh division is, so the

edges of the near seam area needed to be divided into more nodes, and each segment was 0.1 mm. The partition grid could be previewed in Pre-mesh. The model had 100,560 units. If the preview grid met the requirements, the formal grid was generated through the Load from the Blocking module, and the model was exported. The process parameters of this simulation test are shown in Table 1. The total time step calculated by the simulation was 1 s, and the sub-time step was 0.001 s.

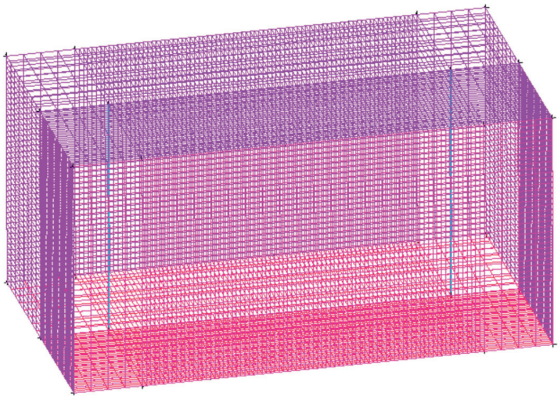

Figure 1. Model geometry and grid.

Table 1. Laser cladding process parameters.

Number	Laser Power (W)	Scanning Speed (mm/s)	Defocusing Amount (mm)	Spot Radius (mm)
1	2000	10	40	1
2	2500	10	40	1
3	3000	10	40	1
4	2500	5	40	1
5	2500	15	40	1

2.2. The User-Defined Function (UDF) Loads the Heat Source Model

The UDF is a user−defined function that can be passed to the solver, and is essentially a set of macros, each with its own role. The compilation of the UDF can complete many of Fluent's dynamic processes, such as the loading of heat sources. The wall heat source of the laser cladding process is not static but moves along the direction of the laser scan. Firstly, the heat flux density of the laser heat source is not uniformly distributed (it can be Gaussian, biellipsoidal, annular heat source distribution, etc.); secondly, the heat source sweeps across the plane, changing the heated area in the space. In this scenario, the heating surface could not be simply defined as a constant heat flux density, and the UDF must specify the thermal wall surface to simulate the scanning heating of the heat source. This simulation applied a dynamic heat source by writing a UDF via the DEFINE_PROFILE macro.

When using the attenuation heat source model to solve the problem, a heat source outside the molten pool is present. The heat generation area in the molten pool is larger the closer it is to the thermal escape surface, while the heat generation area outside the molten pool is smaller. However, this is inconsistent with reality. Therefore, a Gaussian rotating heat source model with the heat flow changing with the depth was selected. The function expression is shown in the following equation [16]:

$$q(x,y,z) = \frac{3MQ}{\pi H\left(1-\frac{1}{e^3}\right)} \exp\left(-\frac{3M}{\log\left(\frac{H}{z}\right)}\left(x^2+y^2\right)\right) \quad (1)$$

where H is the heat source height, Q is the heat input rate, and M is the heat source concentration coefficient.

The heat source concentration coefficient M is a function of the heat source radius correlation, as follows:

$$M = \frac{3}{R_0} \tag{2}$$

2.3. The Underlying Assumptions of the Model

Fluid movement is a complex physical process in practical problems. There are many factors affecting the viscosity and compressibility of a fluid. In the process of laser melting, the interaction process between the laser beam and the powder layer and substrate is also a complex process. Therefore, to simulate the model, certain assumptions must be made:

1. This article ignored the thermal recoil pressure of metal evaporation and the influence of the protective gas on the free interface of the melting tank.
2. The influences of the surface tension of the molten pool and the recoil pressure on the morphology and flow of the molten pool were considered.
3. The liquid in question was an incompressible Newtonian liquid, and the molten pool liquid exhibited laminar flow. The material was isotropic, and its heat did not vary with the position.

3. The Volume of Fluid (VOF) Model and the Simple Algorithm

3.1. VOF Model

To simplify the model, we only considered the melting tank and air phases. The numerical analysis of the interface between two insoluble fluids is typically handled using the Lagrangian and Euler methods [17]. Compared with the Lagrangian method, the Euler method addresses the significant interface deformation that occurs during laser melting. The Euler method encompasses several techniques, including the phase field method, the horizontal set method, and the diffuse reflection interface method. The selected method was the VOF method. The VOF model was used to divide the fluid into small cells (or grids) and define the volume fraction within each cell, representing the proportion of the volume containing a substance in that cell to the total volume. Then, the volume fraction within each cell was updated by calculating the mass and momentum transfer between each of the phases in the fluid. The velocity, pressure, and other physical parameters of the fluid were also calculated.

The VOF model was used to introduce the air-phase volume fraction α_g and the alloy-liquid-phase volume fraction α_A. the following constraints also needed to be met for the two-phase volume fraction:

$$\alpha_g + \alpha_A = 1 \tag{3}$$

The interface between the two phases can be tracked by solving the continuity equation for their volume fraction, as described in the following equation [18]:

$$\frac{1}{\rho_A}\left[\frac{\partial}{\partial t}(\rho_A \alpha_A) + \nabla\cdot(\rho_A \alpha_A \vec{v})\right] = S_{\alpha_g} + \sum_{\alpha_A=1}^{n} \left(\dot{m}_{gA} - \dot{m}_{Ag}\right) \tag{4}$$

where ρ_A is the alloy liquid density, $\vec{v}$ is the fluid flow rate, $\dot{m}_{gA}$ is the mass transfer from the gas phase to the alloy liquid phase, and $\dot{m}_{Ag}$ is the mass transfer from the alloy liquid phase to the gas phase.

According to the volume fraction of one phase, it is possible to determine the corresponding phase of cell. This can be achieved as follows:

$$\alpha_A = 1 \; -- \text{ Liquid phase} \tag{5}$$

$$0 < \alpha_A < 1 \; -- \text{ Air and liquid border} \tag{6}$$

$$\alpha_A = 0 \; -- \text{Gaseous phase} \tag{7}$$

However, it is difficult to solve the complex discontinuity fluid problem. In order to solve the problem of discontinuity interface crossing, we used the horizontal set method in conjunction with the VOF model. The VOF model was coupled with the horizontal set method in laser cladding to investigate the flow behavior of the melting tank. This was achieved by tracking the liquid–gas interface between the air and the melting tank. The horizontal set method (level set) is a technique for analyzing curve or surface evolution. It was first proposed by Osher and Sethian in 1988. Since then, it has become a popular technique in the fields of computational fluid mechanics, image processing, and geometric modeling. The scalar function (horizontal set function) is used to define the position and shape of the fluid interface. The fluid interface is represented by the isosurface of the horizontal set function, as shown in Figure 2. The interface of the two phases is indicated by the red ellipse. The simulation of the motion and deformation of the fluid interface can be simulated by evolving the level set function. The evolution of the level set function is described by a partial differential equation, or the level set equation, a partial differential equation that uses curvature flow to drive its evolution. The equation for the horizontal set can apply force on a fluid interface or curve, causing it to move along the gradient direction and adjust its shape based on the curvature.

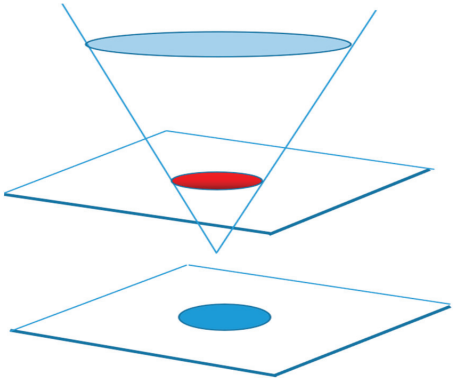

Figure 2. Schematic diagram of the level set.

3.2. Simple Algorithm

Solving the three major control equations in fluid mechanics, namely the mass equation, the momentum equation, and the energy equation (the generalized N-S equation), is a challenging task. The difficulty in solving the N-S equation mainly arises from the following three points: (1) the N-S equation contains three velocity field equations, namely Ux, Uy, and Uz, but it lacks the corresponding pressure equation. (2) The momentum equation is also obtained through the continuous equation constraint as the three velocity field equations are solved. (3) In the case of incompressible isothermal flow, the density and temperature remain constant and cannot be determined through the equation of state. To address the computational challenges with the N-S algorithm, the Simple algorithm was used for this simulation. The Simple algorithm [19] is an iterative method used to solve the pressure and velocity components of the N-S equation. The algorithm's core involves two steps: (1) deriving the pressure equation from the momentum equation and the continuity equations and (2) correcting the velocity field to satisfy the continuity equation. The process is as follows:

1. The velocity field is first solved by the momentum equation, where the velocity does not satisfy the following continuous equation:

$$MU = -\nabla p \tag{8}$$

2. The pressure field is solved by Poisson's ratio with the following formula:

$$\nabla \cdot \left(A^{-1}\nabla p\right) = \nabla \cdot \left(A^{-1}H\right) \tag{9}$$

3. After obtaining the pressure field, the velocity field can satisfy the continuous equation.

4. The Force of the Molten Pool

4.1. Recoil Pressure of the Molten Pool

During the process, the metal liquid will vaporize when it reaches boiling point. This will create a reverse pressure on the molten pool, causing its surface to sink. The laser can then directly hit the bottom of the pit to create a thin and narrow shape of the molten pool. This process continues until the recoil pressure reaches a dynamic balance with the surface tension and gravity of the liquid metal. The pressure resulting from the recoil acts on the wall surface of the hole perpendicular to the air–liquid interface. Semak V. proposed the recoil pressure model [20] as follows:

$$P_r = 0.54P_0 \exp\left(\Delta H_v \frac{T - T_b}{RTT_b}\right) \tag{10}$$

In the formula, P_0 is the ambient pressure, ΔH_v is the evaporative and latent heat of the material, T is the Spoon hole wall temperature, T_b is the boiling point of the material, and R is the ideal gas constant.

4.2. Heat Buoyancy of the Molten Pool

The buoyancy of the pool thermal energy is typically combined with natural or forced convection and is influenced by several factors, including the welding parameters, material properties, environmental conditions, etc. During the melting process, the flow rate of the molten pool is slow, and the flow area is small; thus, the Boussinesq assumption is used. The Boussinesq assumption is based on the buoyancy effect of a small change in fluid density, which creates a buoyancy perpendicular to the density gradient. This buoyancy can be calculated by introducing a term called the Boussinesq approximation:

$$F = -\rho_0 \beta (T - T_0) g \tag{11}$$

In the formula, ρ_0 is the density of fluid, β is the volume expansion system, and T_0 is the reference temperature.

4.3. The Surface Tension of the Molten Pool

During laser melting, the flow behavior of the molten pool is largely dependent on the magnitude and direction of the surface tension. The surface tension flow is caused by a surface tension gradient. As the temperature increases, the surface tension constantly decreases, and the two are negatively correlated. When the temperature gradient is generated, the surface tension gradient of the molten pool also follows. Therefore, the calculation of the surface tension can be simplified using the following equation:

$$\sigma = \sigma_m^0 + \frac{d\sigma}{dT}(T - T_m) \tag{12}$$

where σ_m^0 is the surface tension of the pure metal at the melting point, and T_m is the melting point of the metal.

5. Results and Discussion

5.1. Dynamic Evolution of the Flow Field of Laser-Coated High-Entropy Alloys

The morphology of the power of 2500 W and the surface flow velocity vector distribution with a scanning speed of 10 mm/s are shown in Figure 3a. The temperature range was 301–1671 K, which corresponded to the room temperature and the melting temperature of the metal substrate. The molten pool was concave, resembling a spoon with a wide top and narrow bottom. The material was rapidly vaporized by the laser, producing a pressure that emitted the molten metal and formed a spoon-shaped hole. The laser melted and evaporated the surface of the material. If the evaporation speed is large enough, the steam recoil pressure can overcome the tension of the liquid metal surface and liquid gravity, causing the molten pool in the liquid metal at the laser zone to become concave and form a small pit. The beam acted directly at the bottom of the pit, causing the metal to melt and gasify further. The high-pressure vapor then forced the liquid metal around the molten pool, deepening the hole. This process continued until a hole was formed in the liquid metal. The temperature at the center of the molten pool was the highest, and it spread to all sides. When the metal vapor pressure generated by the laser beam in the hole reached equilibrium with the surface tension and gravity of the liquid metal, a stable hole was formed without further deepening. The maximum flow rate was observed at the center of the molten pool due to the combined action of the recoil pressure and surface tension, gradually decreasing towards the periphery. When the flow rate of the molten pool decreased to a certain extent, the liquid metal moved from the center of the laser beam to the periphery of the molten pool due to the negative temperature coefficient of the surface tension. As a result, the flow rate of the molten pool rose again, exhibiting a wave-like pattern.

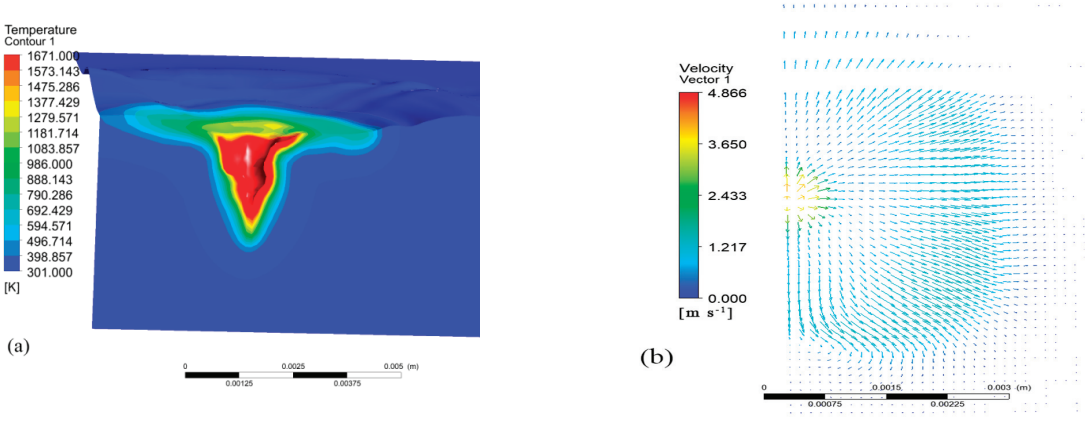

Figure 3. (**a**) Morphology of the molten pool; (**b**) vector distribution of flow velocity on the surface of the molten pool.

5.2. Distribution of Molten Pool Flow Fields at Different Depths

In order to study the flow field distribution within the steady-state melting tank, this simulation observed the symmetrical cross-section of the molten pool. Monitoring points A, B, C, and D were selected at different depths of the molten pool, and the velocity change curve over time is shown in Figure 4. It is evident that the molten pool had a flow rate of 0 before t = 0.001 s, indicating its initial formation at this time. The flow rate of the molten pool increased over time and reached its peak at t = 0.006 s. Subsequently, the monitoring point gradually decreased, with a faster decline rate closer to the bottom of the molten pool. The laser's rapid heating caused a decrease in the molten pool temperature gradient and the liquid surface tension, resulting in a sudden decrease in the flow rate of the detection

point at t = 0.003 s. The decrease was closer to the bottom of the molten pool. The maximum flow rate decreased as the molten pool depth increased. This was due to the greater friction force between the unmelted substrate and the molten pool fluid, which hindered the liquid flow as the pool approached the bottom. The flow rate in the upper part of the molten pool exceeded both the recoil pressure and the surface tension.

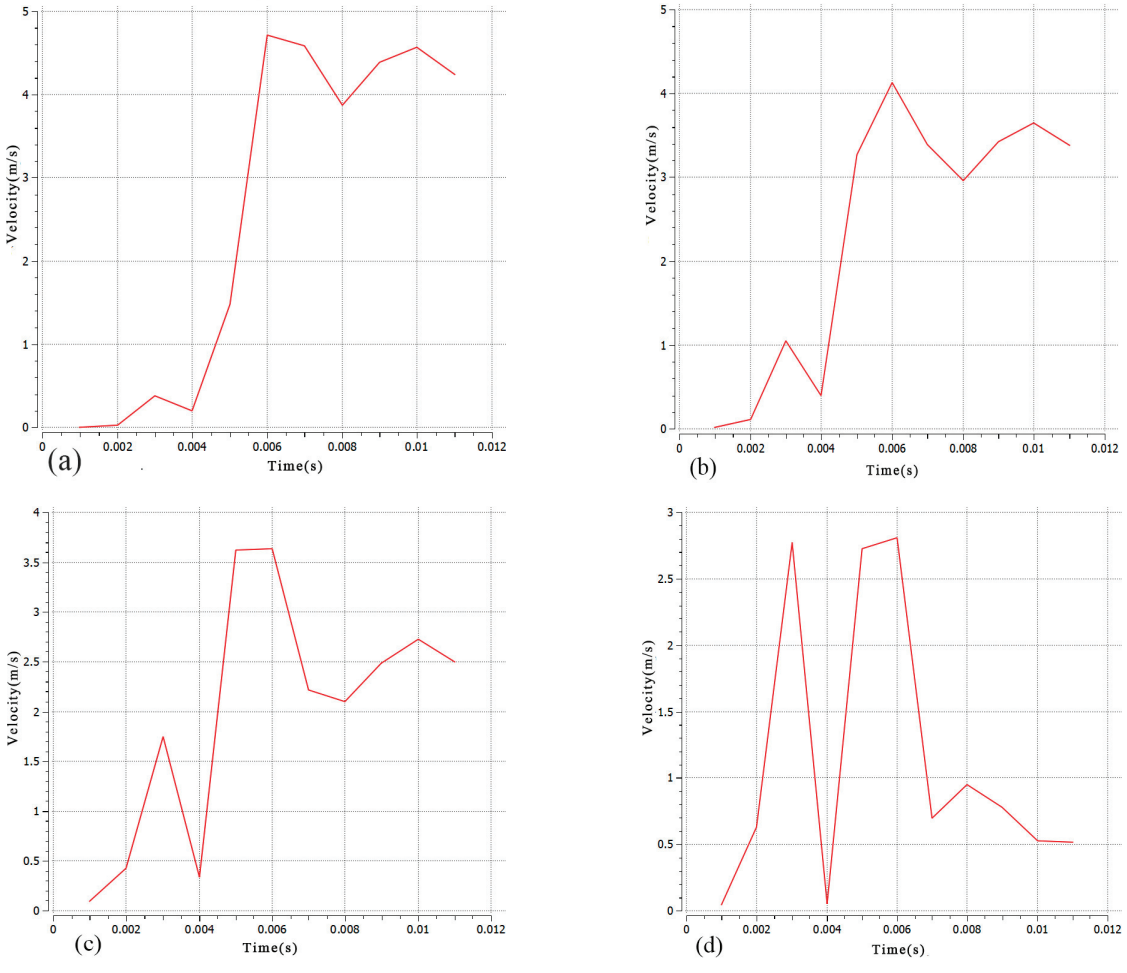

Figure 4. Time process curves of vector at the molten pool center in the depth direction (**a**–**d**).

To investigate the distribution of the flow field inside the molten pool, we obtained the velocity vector distribution of the molten pool flow along the depth direction, as shown in Figure 5. As the section depth decreased, the overall velocity of the molten pool slowed significantly, and the wavy velocity distribution caused by the surface tension gradually disappeared. The surface tension of the molten pool section increased as it approached the heat source due to its proximity to the heat source and the higher temperature. Each section of the molten pool had an upward flow trend, which weakened as the section depth decreased continuously.

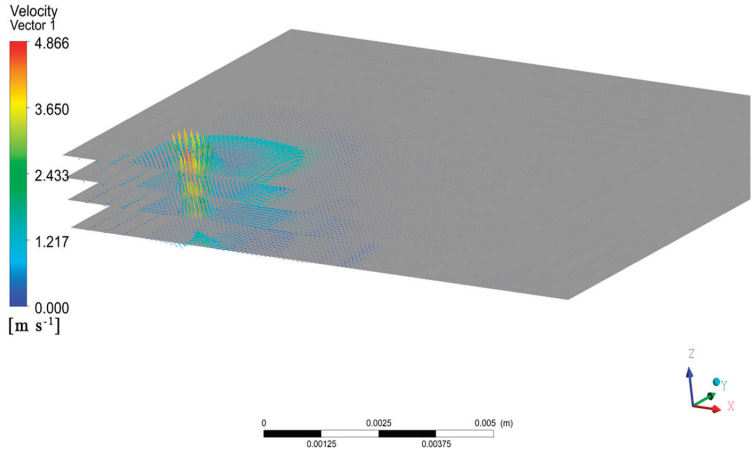

Figure 5. Distribution of molten pool flow fields with different depth cross-sections.

A plane perpendicular to the laser scanning direction was inserted at the center of the molten pool, and its flow rate distribution vector is shown in Figure 6. On the far-left-hand side of the vector distribution map, there is a symmetric line on the symmetry surface. This line reflects the flow rate distribution at the center of the molten pool. The molten pool had vortices of varying sizes distributed along the symmetry line. The flow rate of the molten pool corresponded to the distribution of the molten pool flow field in different cross-sections. This distribution was affected by the large surface tension and recoil pressure, causing the vortex at the bottom and closer to the center of the pool to have a greater flow rate. Technical terms are explained when first used.

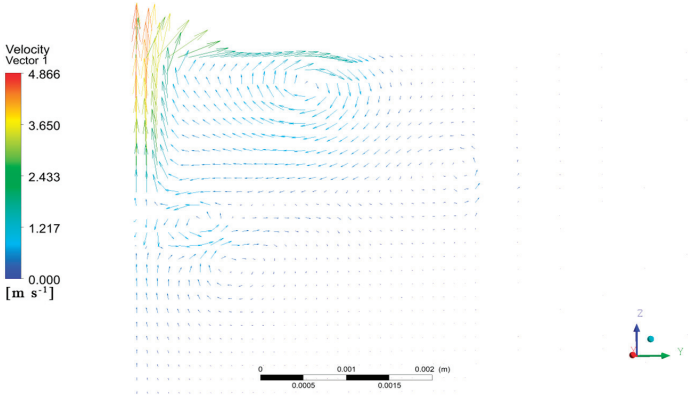

Figure 6. Vector maps of fluid velocity on longitudinal plane of molten pool.

5.3. Effect of Laser Power on the Flow Field of Laser-Coated High-Entropy Alloys

The convection within the molten pool occurred primarily in the cross-section parallel to the laser scanning direction, specifically at the symmetric surface. In order to study the influence of the laser power on the molten pool flow field, three molten pool flow fields with laser powers of 2000 W, 2500 W, and 3000 W, all with a scanning speed of 10 mm/s, were selected for comparison, as shown in Figure 7.

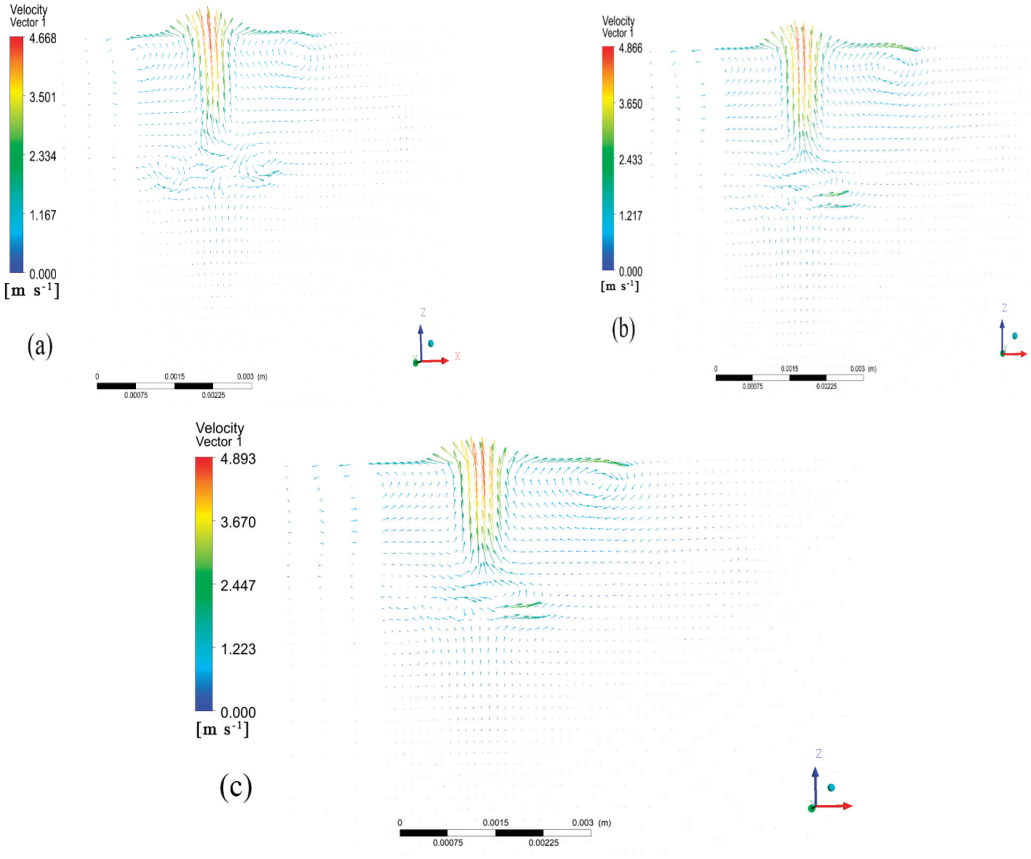

Figure 7. Vector maps of fluid velocity on the symmetry plane of molten pool at different laser powers: (**a**) p = 2000 W, (**b**) p = 2500 W, (**c**) p = 3000 W.

The molten pool exhibited the highest flow rate at its top and the lowest at its bottom. At the bottom and top of the molten pool, two symmetrical vortices appeared on the left and right, respectively. The center of the molten pool is where the vortices intersected. The left vortex was primarily sustained by the residual heat from the scanning and the heat conduction from the front end. As a result, the flow vector distribution was diluted, and the maximum flow rate was lower than that of the right vortex. As the laser cladding power increased, the highest flow velocity in the molten pool also increased gradually. This was due to the fact that the laser cladding process was mainly affected by the recoil pressure and the liquid surface tension. As the laser power increased, the temperature of the hole surface also increased. This, in turn, increased the recoil pressure and liquid surface tension, enhanced the convection effect, and increased the flow velocity in the molten pool. At 2000 W, the vortex flow at the bottom of the molten pool was more pronounced. As the power increased, the temperature gradient difference at the bottom of the molten pool gradually decreased, weakening the convection at the bottom and resulting in a more stable flow field.

5.4. Effect of Scanning Speed on the Flow Field of Laser-Coated High-Entropy Alloys

The speed at which the scanning is conducted has an impact on the flow field of the high-entropy alloy melting cell during laser melting. An experiment was conducted using a laser power of 2500 W at three different speeds: 5 mm/s, 10 mm/s, and 15 mm/s.

Figure 8 shows the distribution of the flow field and the velocity vectors at the interface of the molten pool. As the scanning speed increased, the heat input decreased, resulting in a smaller temperature gradient in the molten pool. Therefore, the size of the molten pool constantly decreased. Simultaneously, the increase in the scanning speed reduced the heat accumulation at the back end, causing the left vortex to continuously decrease. The maximum flow rates of the molten pool, as calculated from CFD-POST, were 3.5 m/s, 4.6 m/s, and 4.8 m/s, respectively. As the velocity of the laser sweep surface increased, the maximum flow velocity in the molten pool also increased. This was due to the heat accumulation decreasing, resulting in a reduction in the heat absorption per unit time. As a result, the temperature gradient increased, which in turn increased the inner surface tension of the molten pool, driving more intense convection at the top of the molten pool. The velocity vector at the bottom of the molten pool decreased as the scanning speed increased. At a speed of 5 mm/s, a vortex was clearly visible at the bottom of the molten pool. At a scanning speed of 15 mm/s, the convection effect at the bottom of the molten pool was negligible, and the fluid flow rate stabilized. A scanning speed that is too fast reduces the heat input, resulting in a smaller temperature gradient at the bottom of the molten pool and a decrease in the surface tension, which in turn leads to a smaller bottom flow rate.

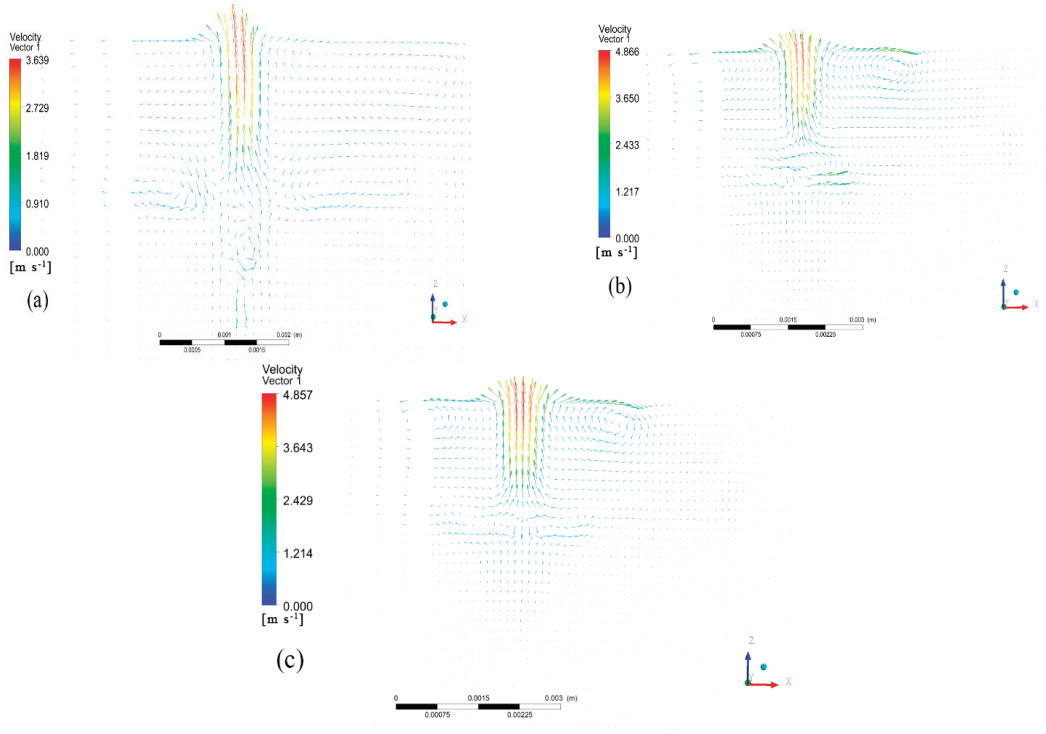

Figure 8. Vector maps of fluid velocity on the symmetry plane of molten pool under different scanning speeds: (**a**) v = 0.005 m/s, (**b**) v = 0.01 m/s, (**c**) v = 0.015 m/s.

5.5. Comparison with the Other Numerical Simulations

Grange et al. [21] established a three-dimensional finite element model of Inconel 738 laser coating that considered the temperature, stress, and flow fields. The molten pool flow vector map at the interface was plotted, as shown in Figure 9. The molten pool had a wide keyhole shape at the top and narrowed at the bottom, and the maximum flow rate of the molten pool was at the top, and the flow rate decreased as the depth decreased.

Compared to the simulation results presented here, the distribution of the fluid vectors in the molten pool was in agreement.

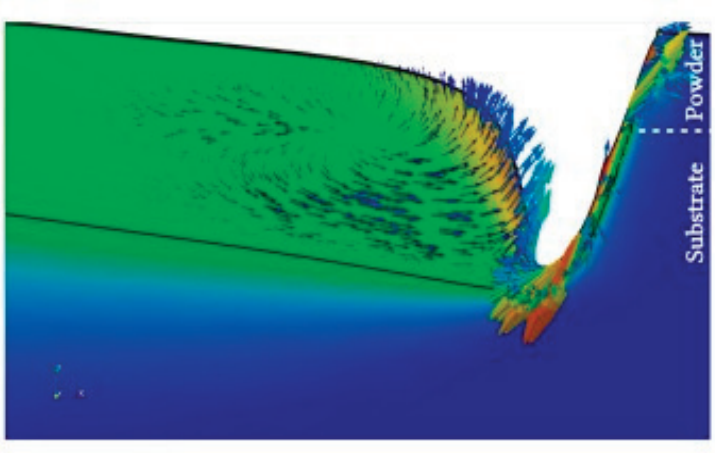

Figure 9. Flow velocity distribution at the pool interface [21].

6. Conclusions

This paper presented an analysis of the flow law of fluid inside the molten pool under different processing parameters of the laser cladding flow field. It also investigated the influence law of the laser power and scanning speed on the flow field. The main conclusions are as follows:

1. At t = 0.001 s, the pool was formed. At t = 0.003 s, the flow rate suddenly decreased and then increased and reached a peak at t = 0.006 s. The molten pool exhibited a keyhole effect due to the recoil pressure, resulting in a wide and narrow hole. The surface flow velocity vector of the molten pool decreased initially and then increased in waves. Along the depth direction, the flow velocity at the top of the pool was much higher than at the bottom of the pool.
2. With decreasing the depth of the molten pool in different cross-sections, the overall flow rate of the molten pool slowed down. The wavy distribution shape gradually disappeared, and the molten pool had an upward flow trend. The trend became more intense closer to the top of the molten pool.
3. The velocity of the flow in the molten cell increased with the increase in the laser power, and the maximum flow velocity appeared at the top of the molten pool. When the laser power was low, there was a noticeable eddy current at the bottom of the melting pool. As the eddy current gradually dissipated, the flow rate at the bottom of the melting pool gradually stabilized.
4. With an increase in the scanning speed, the size of the melting pool decreased. Additionally, the left and bottom vortices of the melting pool also decreased, while the bottom flow velocity of the melting pool gradually decreased and the apical flow velocity increased.

Author Contributions: D.T.: conceptualization, methodology, software, writing—original draft, visualization, investigation. C.L.: conceptualization, methodology, software, writing—original draft, writing—review and editing. Z.H.: supervision, formal analysis, software, validation. X.L.: visualization, investigation. Y.G.: visualization, investigation. X.F.: writing—review and editing. Z.X.: writing—review and editing. X.S.: writing—review and editing. W.L.: writing—review and editing. All authors have read and agreed to the published version of the manuscript.

Funding: This work was financially supported by the National Natural Science Foundation of China (51402189) and Class III Peak Discipline of Shanghai—Materials Science and Engineering (High-Energy Beam Intelligent Processing and Green Manufacturing).

Data Availability Statement: The data presented in this study are available on request from the corresponding author.

Acknowledgments: Thanks to Chonggui Li, Zhihuo Hu, Xintong Li, Yajun Guo, Xiaosong Feng, Zhenhai Xu, Xiaoguang Sun, and Wenge Li for the help with data calibration.

Conflicts of Interest: Author Xiaosong Feng was employed by the company Shanghai Aerospace Equipment Manufacturer Co., Ltd. Author Xiaoguang Sun was employed by the company Technical Engineering Department, CRRC Qingdao Sifang Co., Ltd. The remaining authors declare that the research was conducted in the absence of any commercial or financial relationships that could be construed as a potential conflict of interest.

References

1. Taiwade, R.V.; Patil, A.P.; Ghugal, R.D.; Patre, S.J.; Dayal, R.K. Effect of welding passes on heat affected zone and tensile properties of AlSi 304 stainless steel and chrome-manganese austenitic stainless steel. *ISIJ Int.* **2013**, *53*, 102–109. [CrossRef]
2. Brunelli, K.; Gottardello, S.; Napolitani, E.; Bianco, B.D.; Bertocello, R.; Magrini, M.; Dabalà, M. The effect of surface treatment with atmospheric pressure plasma jet, generated by air, on corrosion properties of AISI 304L stainless steel. *Mater. Chem. Phys.* **2012**, *136*, 1073–1080. [CrossRef]
3. Bak, S.H.; Abro, M.A.; Lee, D.B. Effect of hydrogen and strain-induced martensite on mechanical properties of AISI 304 stainless steel. *Metals* **2016**, *6*, 169. [CrossRef]
4. Junior, F.A.D.; Ferreira, R.A.S.; Lima, R.R.D. Study for Performance Increase of a Extractor Device by Steel Replacement of AISI 304 Steel for AISI 420 Steel. *Materials* **2022**, *15*, 280. [CrossRef]
5. Edalati, P.; Fuji, M.; Edalati, K. Superfunctional high-entropy alloys and ceramics by severe plastic deformation. *Rare Met.* **2023**, *42*, 3246–3268. [CrossRef]
6. Bhardwaj, V.; Zhou, Q.; Zhang, F.; Han, W.C.; Du, Y.; Hua, K.; Wang, H.F. Effect of Al addition on the microstructure, mechanical and wear properties of TiZrNbHf refractory high entropy alloys. *Tribol. Int.* **2021**, *160*, 107031. [CrossRef]
7. Miracle, D.B.; Senkov, O.N. A critical review of high entropy alloys and related concepts. *Acta Mater.* **2017**, *122*, 448–511. [CrossRef]
8. Tsai, C.W.; Chen, Y.L.; Tsail, M.H.; Tsail, K.Y.; Chang, S.Y.; Yeh, J.W.; Yeh, A.C. Deformation and annealing behaviors of high-entropy alloy Al0. *5CoCrCuFeNi. J. Alloys Compd.* **2009**, *486*, 427–435. [CrossRef]
9. Goodarzi, D.M.; Pekkarinen, J.; Salminen, A. Analysis of laser cladding process parameter influence on the clad bead geometry. *Weld. World* **2017**, *61*, 883–891. [CrossRef]
10. Hofman, J.T.; De Lange, D.F.; Pathiraj, B.; Meijer, J. FEM modeling and experimental verification for dilution control in laser cladding. *J. Mater. Process. Technol.* **2011**, *211*, 187–196. [CrossRef]
11. Benarji, K.; Ashwin, P. Numerical simulation and experimental study on austenitic stainless steel by laser assisted metal deposition (L-MD). *Mater. Today Proc.* **2021**, *39*, 1497–1502. [CrossRef]
12. Tamanna, N.; Crouch, R.; Naher, S. Progress in numerical simulation of the laser cladding process. *Opt. Lasers Eng.* **2019**, *122*, 151–163. [CrossRef]
13. Afshari, M.; Hamzekolaei, H.G.; Mohammadi, N.; Yazdanshenas, M.; Hamounpeyma, M.; Afshari, H. Investigating the effect of laser cladding parameters on the microstructure, geometry and temperature changes of Inconel 718 superalloy using the numerical and experimental procedures. *Mater. Today Commun.* **2023**, *35*, 106329. [CrossRef]
14. Hao, M.; Sun, Y. A FEM model for simulating temperature field in coaxial laser cladding of TI6AL4V alloy using an inverse modeling approach. *Int. J. Heat Mass Transf.* **2013**, *64*, 352–360. [CrossRef]
15. Khomenko, M.D.; Makoana, N.W.; Mirzade, F.K.; Pityana, S. Coupled heat transfer, fluid flow and solidification kinetics for laser additive manufacturing applications. *J. Manuf. Process.* **2021**, *67*, 611–618. [CrossRef]
16. Gusarov, A.V.; Kruth, J.P. Modelling of radiation transfer in metallic powders at laser treatment. *Int. J. Heat Mass Transf.* **2005**, *48*, 3423–3434. [CrossRef]
17. Shyy, W.; Udaykumar, H.S.; Rao, M.M. *Computational Fluid Dynamics with Moving Boundaries*; CRC Press: Boca Raton, FL, USA, 1995.
18. Alnaimat, F.; El Kadi, K.; Mathew, B. CFD investigation of R134a and Propane condensation in square microchannel using VOF model: Parametric study using steady state solution. *Therm. Sci. Eng. Prog.* **2023**, *38*, 101662. [CrossRef]
19. Koshizuka, S.; Shibata, K.; Kondo, M.; Matsunaga, T. *Moving Particle Semi-Implicit Method: A Meshfree Particle Method for Fluid Dynamics*; Academic Press: Cambridge, MA, USA, 2018.

20. Le, T.N.; Lo, Y.L. Effects of sulfur concentration and Marangoni convection on melt-pool formation in transition mode of selective laser melting process. *Mater. Des.* **2019**, *179*, 107866. [CrossRef]
21. Grange, D.; Queva, A.; Guillemot, G.; Bellet, M.; Bartout, J.D.; Colin, C. Effect of processing parameters during the laser beam melting of Inconel 738: Comparison between simulated and experimental melt pool shape. *J. Mater. Process. Technol.* **2021**, *289*, 116897. [CrossRef]

fluids

MDPI

Review

The Chimera Revisited: Wall- and Magnetically-Bounded Turbulent Flows

Nils Tångefjord Basse

RISE Research Institutes of Sweden, Brinellgatan 4, 504 62 Borås, Sweden; nils.basse@ri.se

Abstract: This review is a first attempt at bringing together various concepts from research on wall- and magnetically-bounded turbulent flows. Brief reviews of both fields are provided: The main similarities identified are coherent (turbulent) structures, flow generation, and transport barriers. Examples are provided and discussed.

Keywords: wall-bounded non-ionised turbulent flows; magnetically-bounded fusion plasmas; coherent structures; flow generation; transport barriers; logarithmic and wake regions; core turbulence; high Reynolds number transition

Citation: Basse, N.T. The Chimera Revisited: Wall- and Magnetically-Bounded Turbulent Flows. *Fluids* **2024**, *9*, 34. https://doi.org/10.3390/fluids9020034

Academic Editors: Vasily Novozhilov and Cunlu Zhao

Received: 25 November 2023
Revised: 20 January 2024
Accepted: 27 January 2024
Published: 30 January 2024

1. Introduction

1.1. Turbulent Flows in Fluids and Plasmas

Turbulent flow in fluids, i.e., liquids and gases, has been studied since long before da Vinci's contributions [1]; usage of the term "turbulence" can be traced back to da Vinci [2], although consistent usage of the nomenclature did not occur until the early twentieth century [3]. In contrast, plasmas, i.e., ionised gases, were discovered much later and named by Langmuir in 1928 [4]. Over the following decades, it was found that turbulence is as important in plasmas as in fluids; see [5] and references therein. Plasmas can also be described as fluids and their behaviour in electromagnetic (EM) fields is termed magnetohydrodynamics (MHD) [6]. Broader efforts to treat fluids and plasmas together exist [7–9], but direct comparisons are scarce. Common phenomena in the turbulent flows of fluids and plasmas have previously been identified, such as momentum transport caused by velocity fluctuations. With this review, we aim to provide more details on known similarities and discover new shared mechanisms, thereby providing impetus for novel research directions. We aim to facilitate cross-pollination between turbulent flow research in fluids and plasmas.

As representatives of fluids and plasmas, we choose two types of turbulent flows:

- Fluids: wall-bounded [10].
- Plasmas: magnetically-bounded [11].

Wall- and magnetically-bounded turbulent flows have likely not been systematically associated for several reasons, e.g., (i) the plasma physics (PP) community first and foremost focuses on links with astrophysical plasmas and (ii) the fluid mechanics (FM) community does not systematically consider parallel efforts in the PP community. However, FM research, for example, the Kolmogorov 1941 (K41) energy cascade [12,13], has been used for PP turbulence studies. Other concrete examples are covered in [14,15].

This review is personal in the sense that it is a result of my own "voyage through turbulence" [16], transitioning from PP to FM research. My journey began in academic PP research (1997–2005), where I also had contact with K41 and energy/enstrophy cascades for two- and three-dimensional flows. Moving to industrial FM research (2006–2023), my focus was on wall-bounded turbulent flows, e.g., turbulent mixing of gases, two-phase flow, flow noise (acoustics), and thermofluids. This review is an attempt to synthesise my experience, but there is a risk of not referring to the latest research, particularly for PP, as

I have not been active in the field since 2005. Wall- and magnetically-bounded flows are treated, but cross-disciplinary efforts have also included unbounded flows, e.g., similarities between turbulence on mm and Mpc scales [17,18]. However, those results are outside the scope of the present review.

1.2. Motivation behind the Review

The transport barrier (TB) concept was introduced to FM by Prandtl as the laminar/turbulent boundary layer (LBL/TBL) [16,19,20], where the LBL constitutes an edge transport barrier (ETB) using nomenclature from magnetic confinement fusion PP. The boundary layer (BL) is characterised by mean velocity shear and molecular (LBL)/turbulent (TBL) viscosity. The ETB was first identified in magnetically confined fusion plasmas in 1982 [21] and led to the naming of the high (H) confinement mode as opposed to the previously known low (L) confinement mode.

In 1995, uniform momentum zones (UMZs), regions where the streamwise momentum is close to being constant, were discovered [22]. The UMZs are separated by internal shear layers. That year, internal transport barriers (ITBs) were discovered in two magnetically confined fusion experiments [23,24].

In this review, we will attempt to link the LBL and ETB concepts and the UMZ and ITB concepts, for the first time to the best of our knowledge. In addition to the LBL/ETB and UMZ/ITB similarities, other observations that prompted this review include the following:

- Increasing core fluctuations for pipe flow high Reynolds number (*Re*) transitions (we use *Re* without subscript as a general term; later in the review, two specific definitions, the bulk and friction Reynolds number, are defined using subscripts) [25] is similar to controlled confinement transitions in fusion plasmas [26,27]
- Travelling wave solutions in pipe flow [28] are reminiscent of the magnetic field structure (islands) in fusion plasmas

In order to avoid copyright issues, figures from cited papers will be discussed but not shown. This unfortunately makes the review more difficult to read, but open-source versions of most references can be found online.

The review is organised as follows: Sections 2 and 3 consist of primers (in the spirit of *The Los Alamos Primer* [29]) on the wall- and magnetically-bounded turbulent flows, respectively. In Section 4 transport barriers are treated in general and Section 5 focuses on comparing turbulent flows in the core region. An overview of important concept similarities and differences follows in Section 6. A discussion is presented in Section 7 and we conclude in Section 8.

2. Wall-Bounded Turbulent Flows

In FM, there are two main ways to treat wall-bounded turbulent flows; one is the statistical approach and the other is a dynamical systems viewpoint [30]. An important difference is that the (traditional) statistical approach considers turbulent flows with a high *Re*, whereas the dynamical systems analysis is limited to a lower *Re*. We will focus on the statistical point of view below but will discuss the dynamical systems approach in Section 2.16. Research on the laminar–turbulent pipe flow transition [31] introduces a third perspective: linear or nonlinear hydrodynamic stability. This has been deemed out of scope for this review and will not be covered.

Canonical, i.e., standard, wall-bounded flows include zero pressure gradient (ZPG) TBLs, channels, and pipes [32]. In the following, we focus on pipe flow but will also address features of other canonical flows.

The coordinates are usually named (i) streamwise (x along the flow), (ii) wall-normal (y perpendicular to the wall), and (iii) spanwise (z parallel to the wall and perpendicular to the streamwise direction).

We assume the no-slip and no-penetration boundary conditions (BCs) [33], i.e., the velocity at the wall is zero and the walls are impermeable.

2.1. Transition from Laminar to Turbulent Flow

To define the bulk Reynolds number Re_D, where $D = 2R$ is the pipe diameter and R is the pipe radius, the area-averaged streamwise mean flow velocity U_m is used:

$$Re_D = \frac{DU_m}{\nu_{\text{kin}}}, \tag{1}$$

where ν_{kin} is the kinematic molecular viscosity.

At a certain Re_D ($\sim$2000), the laminar to turbulent transition takes place [16,34], associated with a steepening of the edge velocity gradient. However, the transition is gradual with Re_D; as it increases, turbulent puffs are observed first, which are turbulence regions separated by laminar regions. Turbulent puffs either decay or split, both with very long timescales. As Re_D increases further, the turbulent patches increase in size and become what is called slugs, before turbulent flow fills the entire pipe [31].

2.2. The Boundary Layer Concept

Both velocity (momentum) and temperature (heat) BLs exist in wall-bounded laminar and turbulent flows [20]. The concepts are analogous, with a region of (velocity/temperature) gradients close to the wall and another region of (almost) constant values toward the pipe axis. The thermal BL can either be coupled to the velocity field or not depending on the conditions, e.g., assumptions on density, dynamic viscosity, specific heat capacity, and thermal conductivity.

2.3. The Turbulent/Non-Turbulent Interface

In addition to a BL close to the wall, TBLs also have a turbulent/non-turbulent interface (TNTI) at the free-stream boundary where the TBL ends [35–37].

The TNTI was identified in [35] through experiments and characterised as a thin fluid layer where viscous forces dominate, denoted as the "laminar superlayer"; this layer is thought to be a wrinkled sheet of viscous vortical fluid. The mean and fluctuating vorticity propagate through this (wrinkled) layer to the non-turbulent (irrotational) region. The thickness of the layer is of the order of the Kolmogorov length:

$$\eta_K = \left(\frac{\nu_{\text{kin}}^3}{\varepsilon} \right)^{1/4}, \tag{2}$$

where ε is the dissipation rate of k, the turbulent kinetic energy (TKE) per unit mass.

Direct numerical simulations (DNSs) of TBLs were presented in [36], where a small peak in the spanwise vorticity and an associated small jump in streamwise velocity were observed at the TNTI. The interfacial layer was found to have an inertia-viscous double structure:

- A turbulent sublayer, with a thickness l_I (between the interface and vorticity peak) of the order of the Taylor microscale:

$$\lambda_T \approx \sqrt{10\nu_{\text{kin}}\frac{k}{\varepsilon}} \tag{3}$$

- An outer boundary (superlayer), thickness l_S (width of vorticity peak) of the order of the Kolmogorov length scale η_K.

The length scale of the turbulent sublayer l_I is longer than the length scale of the outer boundary l_S.

The analysis shows that the TNTI acts as a barrier in both directions: Exterior irrotational fluctuations are damped/filtered at the interface and internal rotational fluctuations are also blocked at the TNTI, which remains sharp.

Velocity jumps at the TNTI and inside the TBL were studied experimentally in [37] and were found to have similar characteristics. The velocity jump height was found to be

constant for $y/\delta_{99} > 0.5$, i.e., far from the wall, with larger jumps closer to the wall. Here, δ_{99} is the (99%) TBL width, where δ corresponds to R in a pipe. The internal layers are regions of high shear, which are thought to bind large-scale motions (LSM); see Section 2.7. The jump thickness δ_w is observed to scale with the (local) Taylor microscale: $\delta_w \approx 0.4\lambda_T$. The internal layers are observed to move away from the wall, with a faster layer velocity further from the wall. It is conjectured that shear layers are generated not only at the wall but away from the wall as well.

2.4. Mean Turbulent Flow

The mean flow is in the streamwise direction, with three main wall-normal regions: the viscous sublayer closest to the wall, the logarithmic (log) layer, and the wake region toward the pipe axis [10,38]. Sometimes the terms inner (outer) layer are used for the regions close to (far away) from the wall, respectively.

2.5. Fluctuating Turbulent Flow

Streamwise velocity fluctuations have a peak close to the wall (the inner peak) and a second peak in the log region, which becomes more prominent with increasing Re (the outer peak). The inner peak has a fixed wall-normal position (normalised to the viscous length scale), but it is under discussion if it has a maximum or continues to increase with Re. The attached eddy model (AEM) [39,40] leads to structures increasing in size from the wall toward the pipe axis, also as a (streamwise and spanwise, but not wall-normal) log law, but decreasing toward the pipe axis as opposed to the mean streamwise flow [41].

Streamwise velocity fluctuations are usually higher than both the wall-normal and spanwise fluctuations; energy transfer takes place from the streamwise to the wall-normal and spanwise fluctuations [20].

2.6. Turbulence Models

Turbulence models attempt to close the equations of motion, e.g., by introducing a turbulent (eddy) viscosity; for the simplest algebraic model, the turbulent viscosity is proportional to the mixing length, which is a concept introduced by Prandtl [42,43]. The turbulent shear (streamwise/wall-normal) Reynolds stress (RS) τ_{xy} is then equal to the product of the dynamic turbulent viscosity μ_t and the mean velocity gradient $\mathcal{S} = |\partial U/\partial y|$:

$$\tau_{xy} = \mu_t \times \left| \frac{\partial U}{\partial y} \right| = n_f \nu_t \times \mathcal{S}, \tag{4}$$

where n_f is the fluid density and ν_t is the kinematic turbulent viscosity: $\nu_t \gg \nu_{\text{kin}}$. The turbulent RS represents the turbulent transport of momentum to the wall due to velocity fluctuations.

2.7. Turbulent Structures

Turbulence consists of smaller structures in the inner layer, whereas both small and large structures coexist in the outer layer. The structures can be sorted into four different groups [44]:

- Sublayer (near-wall) streaks generated by streamwise vortices; [31]
- Hairpin or Λ vortices;
- Vortex packets or LSM;
- Even larger structures, called (i) very large scale motions (VLSMs) in pipe flow and (ii) superstructures in boundary layers.

The hairpin or Λ vortices are vorticity structures with a "head" and two "feet"; the head is typically further downstream than the feet, i.e., the vortices are leaning in the streamwise direction.

There is an ongoing discussion on the interaction between structures—whether large structures in the outer layer are superimposed onto inner layer structures or if the mechanism involves amplitude modulation [45,46]. There is also a discussion about whether

the large structures are "active" or "passive", i.e., whether they contribute to the turbulent shear RS or not [47].

Proper orthogonal decomposition is an area of research that has traditionally been included in the statistical approach, yet also contains elements from the dynamical systems viewpoint [48]; e.g., proper orthogonal decomposition has been used to analyse radial and azimuthal modes of VLSM [44].

2.8. Minimal Flow Unit

A minimal flow unit (MFU) was identified [49], which is a minimum structure size needed to sustain small-scale turbulence close to the wall. This was done using DNS to isolate small structures in the inner layer.

The spanwise MFU $\lambda_z^+ = \lambda_z u_\tau / \nu_{\text{kin}} \approx 100$, where "+" indicates normalisation by the viscous length scale ν_{kin}/u_τ. Here, u_τ is the friction velocity. The spanwise MFU matches the value widely observed for the spacing of sublayer streaks and streamwise vortices. The streamwise MFU was observed to be $\lambda_x^+ \approx 250$–350, which is of the same order as experimental observations of vortices near a wall. Turbulence statistics are in good agreement with simulations covering the entire cross-section below a wall-normal distance $y^+ = 40$; near-wall turbulence can be sustained indefinitely for a layer width of this size.

Subsequent work on MFUs [50] found two different streamwise MFUs:

- $\lambda_x^+ \simeq 200$–300: quasi-streamwise vortices;
- $\lambda_x^+ \simeq 600$–700: near-wall streaks.

2.9. Turbulent Length Scales

We already introduced the Kolmogorov and Taylor length scales in Section 2.3. Two other useful scales can be added; the first is the mixing length (as mentioned in Section 2.6):

$$\ell_m = \sqrt{\frac{\nu_t}{\mathcal{S}}}, \tag{5}$$

and the second is the length scale of larger eddies:

$$L = \frac{k^{3/2}}{\varepsilon}, \tag{6}$$

see [25] and the associated Supplementary Information for more details.

The Kolmogorov scale is the smallest scale and L is the largest scale. The Taylor and mixing length scales are intermediate (meso), with the Taylor length being shorter than the mixing length.

For the log law region, we can write the following:

$$\mathcal{S} = |\partial U/\partial y| = \frac{u_\tau}{\ell_m}, \tag{7}$$

and define a length scale associated with the mean velocity gradient:

$$L_U = U/\mathcal{S} = \frac{U}{|\partial U/\partial y|}, \tag{8}$$

which can be used to rewrite the mean velocity gradient as

$$\mathcal{S} = U/L_U = \frac{u_\tau}{\ell_m} \tag{9}$$

Two other length scales have also previously been mentioned: the largest (outer) scale δ (or R) in Section 2.3 and the small (inner) viscous length scale in Section 2.8. The ratio between these scales defines the friction Reynolds number:

$$Re_\tau = \frac{\delta u_\tau}{\nu_{\text{kin}}} = \frac{u_\tau}{2U_m} Re_D \tag{10}$$

From these length scales, it has been argued that mixed scaling can be relevant, i.e., combinations of the inner and outer length scales; for example, [33]:

$$y_m = \sqrt{\frac{y}{\delta} y^+} = \frac{y^+}{\sqrt{Re_\tau}} = \frac{y}{\delta}\sqrt{Re_\tau} \tag{11}$$

2.10. Uniform Momentum Zones

The first type of internal TBL observed was the UMZ, with nearly constant streamwise momentum separated by thin viscous-inertial shear layers [22]. In the shear layers, spanwise vorticity is lumped into strongly vortical regions, i.e., a collection of vortices. This interpretation differs from the picture in [35], where the TNTI was interpreted as a continuous vortex sheet.

Later observations in TBLs have continued to study the UMZ structure and the intense vorticity in the shear layers [51]. The number of UMZs increases proportionally to $\log(Re_\tau)$ and the UMZ thickness increases with increasing distance from the wall. The structures generating the UMZ behave consistently with the AEM: hairpin packets are shown to create a zonal-like organisation.

A UMZ vortical fissure (VF) model was presented in [52] and validated against DNS simulations of channel flow. The UMZs are segregated by narrow fissures of concentrated vorticity, with a discrete number of fissures (internal shear layers) across the TBL. The model has two primary domains, (i) an inertial domain and (ii) a subinertial domain; the theoretical basis for the inertial layer (far from the wall) is more solid than for the subinertial layer (near-wall). A fixed fissure width gives the best match to DNS and the jump in streamwise velocity is proportional to u_τ. The wake is not taken into account for the modelled mean velocity. The internal VFs are allowed to be repositioned (from an initial master profile) and a momentum exchange mechanism is necessary:

- The outward flux of vorticity is connected with the inward flux of momentum;
- The VF characteristic velocity is recalculated as follows:
  - If the VF moves farther from (toward) the wall, there is momentum loss (gain) compared to the master profile
- The outermost VF is not allowed to move and exchange momentum.

The momentum exchange mechanism, i.e., where VFs gain (lose) momentum when they are displaced toward (away) from the wall, is consistent with a variation of the streamwise/wall-normal turbulent RS:

$$\frac{1}{n_f}\frac{\mathrm{d}\tau_{xy}}{\mathrm{d}y} = \overline{v\omega_z} - \cancelto{0}{\overline{w\omega_y}}, \tag{12}$$

where the overbar is time-averaging and ω_z is the spanwise vorticity. The last right-hand side term is zero because only wall-normal VF movement is considered.

An alternative concept to the UMZ model, a momentum transport barrier (MTB) model, was published in [53].

2.11. Quiescent Core

For turbulent channel flow, what is known as the quiescent core was experimentally identified and characterised [54]. The quiescent core is a large UMZ, which can cover up to 40–45% of the channel; it can be approximated by regions where the mean velocity is above 95 % of the centreline (CL) mean velocity: $U > 0.95U_{CL}$. The interface has a jump in streamwise velocity, and sometimes—but not always—a vorticity peak. Inside the core UMZ, the streamwise velocity varies only weakly. The core UMZ is meandering (moves around), can reach the wall, and be streamwise-separated (breakup). The core UMZ has low TKE, i.e., it is weakly turbulent (quiescent).

A two-state model of the TBL (extendable to internal flows) is presented in [55] to capture the log law and law of the wake regions. The new model has a log law state and

a free stream state, with a velocity jump at their interface. The concept of mean flow can be applied to streamwise turbulence as well. One drawback of the model is that it does not take the viscous region close to the wall into account. The model is calibrated against measurements and the position of the interface is fitted to a Gaussian distribution that is independent of Re_τ. The resulting velocity jumps and deviations of the fit from the log law are also independent of Re_τ, except for pipe flow below $Re_\tau = 3400$, which is interesting and may be related to the high Re transition region for pipe flow [25].

Open channel flow was studied in [56] using DNS, and it was concluded that: "The virtual absence of a wake region and of corrective terms to the log-law in the present flow leads us to conclude that deviations from the log-law observed in internal flows are likely due to the effects of the opposing walls, rather than the presence of a driving pressure gradient." Thus, the law of the wake may only exist due to TBL interactions.

2.12. Uniform Thermal Zones

After the identification of UMZ, uniform thermal zones (UTZs) have been found, which consist of regions of relatively uniform temperature separated by thermal interface layers [57]. The analysis was conducted on DNS simulations of transcritical channel flow. An analogy was made between UMZ and momentum internal interface layers (MIILs) and UTZ and thermal internal interface layers (TIILs). Thus, the two types of zones are related to velocity (momentum) and temperature (heat) fields. A local heat transfer peak is expected in the TIILs. The MIILs and TIILs were found to be at similar but not identical locations, i.e., not collocated.

A model of UTZ and TIILs was published in [58], and constructed along the same lines as the UMZ model in [52]. The nomenclature is slightly modified compared to [57]; here, the uniform thermal zones are called uniform temperature zones and the TIILs are named thermal fissures (TF). The heat model (UTZ/TF) is combined with the momentum model (UMZ/VF) and calibrated against DNS simulations of channel flow. As for the momentum model, the TFs can move (from an original master profile) and exchange heat as they move in the wall-normal direction. If a TF moves toward (away from) the wall, its temperature increases (decreases), respectively. The finding in [57] that VF/TF (MIIL/TIIL) are correlated but not coincident is confirmed in [58].

It is important to note that temperature is a passive scalar [59] (when buoyancy is neglected), i.e., it does not affect the dynamics of the fluid.

2.13. Uniform Concentration Zones

Experiments have identified a third type of uniform zone (UZ), uniform concentration zones (UCZs) [60]. As is the case for temperature, concentration is also a passive scalar.

In both shear and shear-free flows, ramp–cliff (RC) structures have been identified for passive scalars, i.e., a slow increase (ramp) followed by a fast decrease (cliff) [61]. These structures have also been said to have a "saw-tooth appearance" with plateaus separated by cliffs [62]. From an interpretation of experiments, the RC structures can be understood as large counter-rotating structures that form a saddle point associated with converging–diverging separatrices, as discussed in [63]. The cliff (or front) occurs at the diverging separatrix, which inclines close to the direction of the principal axis of strain. If the passive scalar is temperature, the front is the separation between warm and cold fluids entrained in the counterflowing structures. In aircraft measurements, inverse cliff–ramp (CR) structures have been considered as signatures of the Kelvin–Helmholtz instability [64].

2.14. Uniform Momentum and Temperature Zones

The simultaneous existence of both UMZ and UTZ has been reported for both stably and unstably stratified turbulent flow by analysis of large eddy simulations (LESs) [65,66]. In [65], the stably stratified planetary boundary layer (PBL) was treated; it was found that UMZ and UTZ are "closely, but not perfectly related". Unstable stratified channel flow was covered in [66], where it was found that "Conditional averaging indicates that both UMZ

and UTZ interfaces are associated with ejections of momentum and warm updrafts below the interface and sweeps of momentum and cool downdrafts above the interface."

2.15. Turbulence Control

Methods for classical flow control—up to around the year 2000—have been covered in [67]. Methods can be active or passive, e.g.,

1. Passive: riblets, surface treatment, tripping, and shaping;
2. Active: suction, blowing, and wall cooling/heating.

Here, the purpose can be to modify the transition to turbulence, decrease friction (pressure drop), enhance heat transfer, and reduce acoustic noise [68].

More recent work included turbulence suppression due to pulsatile driving of pipe flow [69]. The work was inspired by the human cardiovascular system, where blood flow in the aorta is an example of pulsating flow. By comparing experiments and DNS, it is demonstrated that both turbulence and turbulent drag can be reduced significantly in pulsating flow.

In recent years, machine learning (ML) has become a more powerful tool for both turbulence simulation and control [70]. The method can be seen as a fourth pillar, complementing theory, experiments, and simulations.

2.16. Dynamical Systems Viewpoint

For the dynamical systems approach, we focus on invariant solutions to the Navier–Stokes equations (NSE) as defined in [71]:

"Here by 'invariant solutions' or 'exact coherent structures', we mean compact, time-invariant solutions that are set-wise invariant under the time evolution and the continuous symmetries of the dynamics. Invariant solutions include equilibria, travelling waves, periodic orbits, and invariant tori. Note in particular that the closure of a relative periodic orbit is an invariant torus."

The first exact coherent state (ECS) or travelling wave (TW) solution to the NSE was identified theoretically in [72], followed by multiple efforts, both with theoretical [28,73–76] and experimental [30,77,78] focus.

For pipe flow, it has been found that the ECS originates in saddle-node bifurcations at Re_D down to around 400 [79]. The TWs consist of a certain number of azimuthally and radially separated streaks; for example, threefold azimuthal symmetry: six outer (high speed) streaks and three inner (low speed) streaks. The TWs lead to the transport of slow fluid toward the centre and the transport of fast fluid toward the wall.

Additional TW solutions were constructed in [28] by "mixing three key flow structures—2-dimensional streamwise rolls, streaks and 3-dimensional streamwise-dependent waves—in the right way". This is in line with what has been termed the self-sustaining process (SSP); see [80] and references therein. Here, it is proposed that edge turbulence is maintained (against viscosity) by a cycle of rolls, streaks, and waves.

Another process has been proposed for core turbulence [81], which involves inertial ECS, in contrast to the viscous ECS for the SSP. It is interesting to notice the appearance of "Kelvin's cat's-eyes vortex pattern" inside the VF; see Figures 9 and 12 in [81].

A main obstacle to a direct link between the dynamical and statistical approaches involves identifying invariant solutions for high *Re*. Experimental support for the existence of these solutions has come from [30], where the ECS is shown to have an impact of up to $Re_D = 35{,}000$.

Other theoretical ECS solutions have been investigated in parallel; we refer to related work, focusing on the relative periodic orbit (RPO) framework [71,82–84]. The two types of ECS solutions can be summarised as follows:

- TW: A fixed velocity profile moving in the streamwise direction with a constant phase speed.

- RPO: Time-dependent velocity profiles that repeat exactly after a certain time period and streamwise length; in addition, these orbits may also have azimuthal rotations.

A dynamical systems approach has also been pursued in laminar–turbulent transition [31] studies; as mentioned, TWs have been identified for Re_D lower than the observed transition. It has also been shown that spatially localised RPOs can experience a series of bifurcations leading to transient chaos.

3. Magnetically Bounded Turbulent Flow

For the material on PP, we focus on commonalities with FM; therefore, many specific features have been disregarded. Of course, this entails a risk of leaving out important topics. An example of what is left out involves specific issues related to EM fields and plasma currents.

A note on units: In PP, temperature is usually denoted using units of energy, where 1 eV corresponds to around 11,600 K. Another convention to keep in mind is that for PP, density has the units of particle density (number of particles per volume), whereas in FM, mass density is used (mass per volume).

3.1. Magnetic Field Structure

A plasma consists of charged particles (electrons and ions), which need to be confined within a toroidal shape to enable fusion. Since charged particles follow magnetic field lines (with superimposed gyroradii), the method of confinement is to construct closed magnetic field surfaces.

The basic shape of a magnetic confinement device is a torus, with coordinates (i) toroidal (the "long" way around a torus), (ii) radial, and (iii) poloidal (the "short" way around a torus).

Concerning pipe flow, the corresponding coordinates are toroidal/streamwise, radial/wall-normal, and poloidal/spanwise.

Additional (a) perpendicular and (b) parallel coordinates refer to the directions perpendicular (cross-field) and parallel to the magnetic field. These are different from—but related to—the toroidal, radial, and poloidal coordinates.

We focus on cases from tokamaks [85] but include material on stellarators and heliotrons [86] when relevant.

For these machine types, the main toroidal magnetic field is generated by external planar coils. A main difference between tokamaks and stellarators/heliotrons is how the poloidal magnetic field is created. In tokamaks, it is created by a toroidal current induced through transformer action, but in stellarators/heliotrons, it is created by modular (non-planar) coils. For stellarators, the modular coils are predominantly poloidal; for heliotrons, the modular coils are mainly toroidal. This implies that the plasma current in tokamaks is much higher than in stellarators/heliotrons, which has important implications for, e.g., current-driven instabilities, steady-state operations, and machine complexities.

All machine types treated herein generate an MHD equilibrium with nested magnetic surfaces. The boundary is named the last closed flux surface (LCFS), which is denoted as a separatrix if it includes one or more "X-points", which are points with zero (null) poloidal field. Plasmas can also be bound by physical limiters. We use the term "magnetically-bounded" for plasmas that are bounded by a separatrix, i.e., where the LCFS is not in contact with physical surfaces. The region between the separatrix and the physical wall is called the scrape-off layer (SOL), where magnetic field lines are open and intersect the wall. Divertors intersect the open field lines from the separatrix and are used for particle and heat exhaust.

The winding number of magnetic field lines is called the safety factor in tokamaks due to its importance for plasma stability:

$$q = \frac{\mathrm{d}\phi}{\mathrm{d}\theta}, \tag{13}$$

where ϕ is the toroidal angle and θ is the poloidal angle. Traditionally, another definition has been used in stellarators/heliotrons:

$$\iota = \frac{\iota}{2\pi} = \frac{1}{q} \tag{14}$$

Typically, q-profiles in tokamaks have a minimum $q_{\min}$ close to the axis and increase toward the plasma edge. For stellarators/heliotrons, the ι-profile is often more flat. We define the magnetic shear as follows:

$$s = \frac{r}{q}\frac{\partial q}{\partial r}, \tag{15}$$

where r is the minor radius measured from the magnetic axis.

Thus, tokamaks have high shear and stellarators/heliotrons have low shear.

The magnetic field decreases from the centre of the torus outward, inversely proportional to the major radius R, which can lead to particle trapping due to the magnetic mirror effect. For tokamaks, these are called banana orbits and are centred on the outboard midplane (the low field side). For stellarators/heliotrons, the particles are helically trapped.

3.2. Turbulence and Improved Confinement Regimes

As mentioned, the purpose of the magnetic field is confinement; the plasma also needs to have a sufficiently high temperature for the ions to fuse and release energy. Two timescales can be used to quantify energy and particle confinement, namely the energy confinement time τ_E and the particle confinement time τ_p. These timescales indicate how efficient the confinement of energy (temperature) and particles (density) is.

Another way of gauging confinement quality is β, which is the plasma pressure normalised to the magnetic pressure. β can be defined using the total (B), toroidal (B_ϕ), or poloidal (B_θ) magnetic field. As the plasma pressure increases, the centre of the magnetic axis is displaced radially outward, an effect called the Shafranov shift.

If transport is only taking place due to thermal motion (Coulomb collisions), with curvature effects included, it is called neoclassical transport [87]. However, in reality, much larger transport is observed perpendicular to the magnetic field, which is called anomalous transport [88].

Anomalous transport is caused by turbulence, e.g., microinstabilities driven by the ion (ITG) or electron (ETG) temperature gradient or by trapped electrons, such as the trapped electron mode (TEM). The smallest turbulent scale is due to ETG, the medium scale is due to TEM, and the largest scale is due to ITG. Instabilities driven by density or temperature gradients are called drift waves (DW). Even larger scale (macroscopic) MHD instabilities can be driven by, e.g., current, pressure, or fast particles. Often instabilities can be ballooning, which means that—due to curvature effects—their growth rate is larger on the outer side of the torus compared to the inner side. Turbulence can lead to the formation of streamers, first identified in nonlinear gyrokinetic simulations of ETG turbulence [89,90], and followed by theoretical predictions for ITG turbulence [91]. Streamers are radially elongated mesoscale vortices centred on the outboard midplane; they lead to enhanced cross-field transport, thereby degrading confinement.

A main effort in the fusion community is to understand and reduce anomalous transport to improve confinement and obtain more efficient fusion reactions.

One way to control anomalous transport is by the external heating of electrons and ions; for example, by ion or electron cyclotron resonance heating (ICRH/ECRH) or by neutral beam injection (NBI). The plasma current can be manipulated using both external heating and current drive methods, e.g., lower hybrid current drive (LHCD).

The plasma state can experience either gradual confinement improvements or sudden bifurcations to improved confinement regimes; sometimes, improved confinement is associated with instabilities, such as edge localised modes (ELMs), leading to bursts of the

cross-field transport of particles and energy. Other improved confinement regimes can be associated with coherent modes that regulate transport and avoid ELMs.

3.3. Length Scales

An important group of length scales is associated with the Larmor radius, which is the gyration distance of charged particles around the magnetic field:

$$\rho_j = \frac{m_j v_\perp}{e_j B} = \frac{v_\perp}{\omega_{cj}}, \tag{16}$$

where the subscript j represents electrons (e) or ions (i), m_j is the mass, $v_\perp$ is the velocity perpendicular to the magnetic field, e_j is the charge, and $\omega_{cj} = e_j B/m_j$ is the cyclotron frequency. Here, we can relate the velocity to temperature by assuming two degrees of freedom:

$$v_\perp^2 = 2v_{Tj}^2, \tag{17}$$

which leads to:

$$\rho_j = \sqrt{2}\frac{m_j v_{Tj}}{e_j B} = \sqrt{2}\frac{v_{Tj}}{\omega_{cj}} \tag{18}$$

For scaling purposes, the ion Larmor radius normalised to the minor radius of the machine ($r = a$) is used:

$$\rho^* = \frac{\rho_i}{a}, \tag{19}$$

and for turbulence modelling, the ion Larmor radius at the electron temperature is used:

$$\rho_s = \sqrt{2}\frac{m_i v_{Te}}{e_i B} \tag{20}$$

Scale lengths were mentioned previously in Section 2.9; we generalise the notation to write the scale length L_x of a quantity x as

$$L_x = \frac{x}{|\mathrm{d}x/\mathrm{d}r|} = (|\mathrm{d}(\ln x)/\mathrm{d}r|)^{-1} \tag{21}$$

Equation (9) can be reformulated for electron density fluctuations ($x = n_e$):

$$\frac{n_e}{L_{ne}} = \frac{\delta n_e}{\rho_s}, \tag{22}$$

where δn_e denotes density fluctuations (corresponding to the friction velocity) and ρ_s denotes the typical scale of the density fluctuations (corresponding to the mixing length). For DWs, the density fluctuations saturate at this level:

$$\frac{\delta n_e}{n_e} = \frac{\rho_s}{L_{ne}} \sim \frac{1}{k_\perp L_{ne}}, \tag{23}$$

where $k_\perp \sim 1/\rho_s$ is the perpendicular wavenumber of the density fluctuations.

Microscales are on the order of the (ion/electron) Larmor radius, from sub-mm to mm scales, depending on temperature and magnetic field strength. Macroscales are on the order of the machine minor radius and mesoscales are between micro- and macroscales; an example of a mesoscale phenomenon is streamers, and we will encounter other mesoscale structures later.

An effect known as turbulence spreading, originally theoretically predicted in [92], occurs for inhomogeneous turbulence [93]: "Turbulence spreading is a process of turbulence self-scattering by which locally excited turbulence spreads from the place of excitation to other places." This is not related to the K41 paradigm, which deals with homogeneous turbulence.

3.4. Rational Safety Factors and Transport

If $q = m/n$ is a rational number (m and n both integers), then the magnetic field line returns to the initial position after m toroidal and n poloidal rotations. For a fixed toroidal angle, this corresponds to a poloidal mode number m, and for a fixed poloidal angle, it corresponds to a toroidal mode number n.

Since the magnetic field line paths constitute a Hamiltonian system, rational values of the safety factor correspond to resonant tori, which are unstable against perturbations according to the Kolmogorov–Arnold–Moser (KAM) theorem [94]. Perturbations can lead to the formation of magnetic islands or ergodic regions.

A classical example of instabilities is sawtooth crashes (relaxations) for $q < 1$, where heat and particles are ejected from the core plasma due to magnetic reconnection [95]: "Magnetic reconnection is a topological rearrangement of the magnetic field that converts magnetic energy to plasma energy." The periodic core temperature collapse is due to an instability that has an $m = n = 1$ structure, corresponding to $q = 1$.

Enhanced transport has been observed for q-profiles at or close to low-order rationals in the Rijnhuizen Tokamak Project (RTP) [96,97]. Transport barriers for the electron temperature were observed as temperature steps that could be controlled by the deposition location of external electron heating. A "q-comb" model was constructed to model the transport barriers as low electron heat conductivity at low-order rationals, possibly due to the formation of magnetic island chains.

As for the RTP, similar behaviour has been observed in the Wendelstein 7-Advanced Stellarator (W7-AS) [98,99]. Here, reduced transport was also found to be associated with low-order rationals.

3.5. Magnetic Islands Caused by Instabilities or Topology

In both tokamaks and stellarators/heliotrons, magnetic islands can be caused by instabilities as mentioned above, e.g., global Alfvén eigenmodes (GAE) [100] and tearing modes [101]. These islands can be either non-rotating ("locked") or rotating.

In addition, natural magnetic islands can exist in stellarators/heliotrons. An example is from the W7-AS and Wendelstein 7-X (W7-X) stellarators, where islands form for

$$\iota = \frac{n}{m} = \frac{5}{m}, \tag{24}$$

the constant "5" being due to the fact that the machines have a five-fold toroidal symmetry. The five field periods are also flip-symmetric, leading to ten identical sections. For W7-AS, the standard divertor configuration (SDC) is $m = 9$ [102], whereas for W7-X, it is $m = 5$ [103], with the change due to ι-profile differences. Thus, W7-X has larger islands with lower poloidal mode numbers compared to W7-AS.

The natural magnetic islands can be used to form a separatrix and an associated island divertor. This also enables detachment, which is a state where a large fraction of the power is dissipated by volume radiation before it reaches the physical wall. This is a potential exhaust solution under reactor conditions since the heat flow will be intercepted before reaching the divertor target plates, leading to significantly reduced fluxes at the targets.

3.6. $E \times B$ Flow Shear Decorrelation

A mechanism to reduce turbulent transport by velocity shear has been theoretically identified in [104] (earlier theoretical efforts can be found in [105]) and reviewed along with experimental evidence in [14]. It causes eddy stretching, which leads to eddies losing coherence (breakup), i.e., energy transfer from large scales (low wavenumbers) to small scales (high wavenumbers). It is called sheared $E \times B$ flow and is generated by the radial electric field E_r, which results from the radial force balance (ignoring the RS term):

$$E_r = \frac{1}{n_i Z_i e} \frac{\mathrm{d}p_i}{\mathrm{d}r} + v_{\phi i} B_\theta - v_{\theta i} B_\phi, \tag{25}$$

where the "i" subscript refers to ions (dominating compared to electrons), p is the pressure, Z is the charge state, e is the electronic charge, v_ϕ is the toroidal velocity, and v_θ is the poloidal velocity. Suppression of turbulence takes place if the shearing rate $\omega_{E\times B}$ is larger than the maximum linear growth rate $\gamma_{\max}$ of the relevant instability:

$$\omega_{E\times B} = \frac{RB_\theta}{B_\phi}\frac{\partial}{\partial \mathrm{r}}\left(\frac{E_r}{RB_\theta}\right) > \gamma_{\max} \tag{26}$$

The shearing rate increases with shear in the radial electric field $\partial E_r/\partial r$, so the regions where the radial electric field changes rapidly as a function of radius are the regions where turbulence is suppressed most efficiently. $E \times B$ shearing is a mean flow effect on turbulence, which affects not only the turbulence amplitude but also the "phase angle between an advected fluctuation and the advecting flow" [14]. Shear suppression is a universal, self-regulating process between shear flow and transport. Turbulence reduction leads to steepened gradients (temperature, density), which increases the pressure gradient, which in turn increases the flow shear and reduces turbulence further.

In addition to the shearing rate criterion, three additional requirements have to be fulfilled:

- The shear flow must be stable.
- Turbulence must remain in the flow shear region for longer than an eddy turnover time [10].
- Dynamics should be 2D.

These requirements are often met in fusion plasmas, but rarely in non-ionised fluids; some exceptions are mentioned in [14], e.g., stratospheric geostrophic flow and perhaps the laminar phase between bursts of turbulence for wall-bounded flows.

3.7. Transport Barriers

In this section, we provide a brief overview of the different TB variants in fusion plasmas: (i) ETB [21,106], (ii) ITB [23,24,107,108], and (iii) both ETB and ITB [109].

3.7.1. ETB

As mentioned in the introduction, the first ETB was identified in 1982 in the axially symmetric divertor experiment (ASDEX) tokamak [21]. For NBI power above a certain threshold, an L-H-mode transition was obtained. This was possible for diverted plasmas but not for limited plasmas. Apart from the power threshold, the H-mode could only be accessed for a safety factor at the edge $q_a > 2.6$.

The improved H-mode confinement was seen as an increased poloidal β (β_θ) and an increase in the electron density and temperature. Bursts of $H_\alpha - D_\alpha$ emissions were observed in the H-mode and were later identified as ELM signatures.

The H-mode ETB is quite robust and has steep density and temperature gradients inside the LCFS. $E \times B$ flow shear is part of the prerequisite for the H-mode, along with suitable edge plasma conditions which may vary between different machine designs. As of now, there is no comprehensive, predictive theory-based model for ETB formation and spatial structure.

ELMs generated by the large pressure gradients created in ETBs can often degrade or even destroy the barrier. Some methods exist to stabilise instabilities; for example, applying an external magnetic field or operating variants of H-modes with quasi-coherent (QC) or edge harmonic oscillations (EHO), which provide increased particle transport through the barrier without significantly increasing the energy transport.

3.7.2. ITB

As mentioned in the introduction, the first ITBs were identified in 1995 in two tokamaks, the tokamak fusion test reactor (TFTR) [23] and the Doublet III-D (DIII-D) [24].

For both machines, the most important component in achieving an ITB was in obtaining reversed magnetic shear, which was obtained by creating a hollow current density profile. This was achieved through a combination of current ramping and NBI, taking advantage of the fact that the current diffusion time is much longer than the rise time of the plasma current.

The ITB led to reduced particle and ion thermal transport in the plasma core where reversed shear was created. The high-pressure gradient generated a strong off-axis bootstrap current, which helped to maintain the hollow current density profile. Electron thermal transport was also reduced but not as significantly as ion thermal transport. The ion thermal diffusivity and electron particle diffusivity decreased to levels close to or below the neoclassical level.

MHD modes can exist outside the ITB and limit the obtainable β.

ITBs in tokamaks were reviewed in [107]. It was found that low or reversed magnetic shear in combination with large $E \times B$ shear flows are essential ITB ingredients, where magnetic shear stabilises high-n ballooning modes and $E \times B$ shear stabilises medium- to long-wavelength turbulence, i.e., ion thermal transport and particle transport. It is possible to have high electron thermal transport even with ITBs. The q value at 95% of the magnetic flux, q_{95}, is found to be important for magnetic stability, and $q_{\min}$ has been seen to correlate with the ITB foot. The Shafranov shift can have a stabilising effect on turbulence called α-stabilisation. ITBs can exist with equal ion (T_i) and electron (T_e) temperatures, as well as for cases where $T_i < T_e$ or $T_e < T_i$, depending on the plasma density and external heating method.

Throughout the rest of this section, we will summarise the results from the most recent review [108], which covers both tokamak and helical (in our case: stellarators/heliotrons) plasmas. A systematic approach is applied, with an ITB definition being a (radial) discontinuity of temperature, flow velocity, or density gradient.

ITBs are characterised by three parameters:

1. Normalised temperature gradient $R/L_T = R \times |\nabla T|/T$ (large value: weak, small value: strong).
2. Location $r_{\mathrm{ITB}}/a = \rho_{\mathrm{ITB}} = (\rho_{\mathrm{shoulder}} + \rho_{\mathrm{foot}})/2$ (large value: large, small value: small).
3. Width $W/a = \rho_{\mathrm{foot}} - \rho_{\mathrm{shoulder}}$ (large value: wide, small value: narrow).

Here, $L_T = T/|\nabla T|$ is the temperature scale length, "shoulder" is at the top of the steep gradient, and "foot" is at the bottom of the steep gradient.

The key elements for ITB formation are summarised as follows:

- Radial electric field shear ($E \times B$ flow shear).
- Magnetic shear.
- Rational surface and/or magnetic islands.

It is instructive to write the equations relating radial fluxes (particle, momentum, electron/ion heat) and gradients (density, toroidal rotation, temperature). For the particle flux, Γ, we write the following:

$$\frac{\Gamma(r)}{n_e} = -\left[\frac{D\nabla n_e}{n_e} - v_{\mathrm{conv}}\right], \tag{27}$$

where D is the diffusion coefficient, n_e is the electron density, and v_{conv} is the convection velocity. For the momentum flux, P_ϕ, we write the following:

$$\frac{P_\phi(r)}{m_i n_e} = -\nu_\perp \nabla v_\phi + v_{\mathrm{pinch}} v_\phi + \Gamma_\phi^{\mathrm{resi}}, \tag{28}$$

where m_i is the ion mass, $\nu_\perp$ is the perpendicular kinematic viscosity, v_{pinch} is the momentum pinch velocity, and $\Gamma_\phi^{\mathrm{resi}}$ is the radial flux due to residual stress [110,111]. We note

that Equation (28)—when disregarding the two final right-hand side terms—has the same structure as Equation (4). For the electron and ion heat flux ($Q_{e,i}$), we write the following:

$$\frac{Q_{e,i}(r)}{n_e} = -\frac{\chi_{e,i}\nabla T_{e,i}}{m_i}, \tag{29}$$

with the electron and ion thermal diffusivity $\chi_{e,i}$. To cite [108]: "When the density, velocity, and temperature gradient become large due to the decrease in the diffusion coefficient, D, viscosity, $\mu_\perp$, and thermal diffusivity, $\chi_{e,i}$, the region in the plasma is called the transport barrier." We will use "diffusion coefficient" as a collective term for D, $\mu_\perp$ and $\chi_{e,i}$. An ITB can be defined as a bifurcation in the flux-gradient relationship, which causes a discontinuity in the density/velocity/temperature gradient for a given particle/momentum/heat flux, leading to the formation of a discontinuity in the gradient with radius.

The ITB foot (point) often follows integer q values, typically $q = 1$ ($\rho \sim 0.3$), $q = 2$ ($\rho \sim 0.5$), and $q = 3$ ($\rho \sim 0.7$); this is valid for positive or weakly reversed magnetic shear, but not for strongly reversed magnetic shear. Sometimes ITBs are also observed for half-integer q values. For reversed magnetic shear, an ITB appears when $q_{\min}$ crosses a rational surface.

Experiments using resonant magnetic perturbations (RMPs) to produce magnetic islands were carried out in the large helical device (LHD) to distinguish the role of magnetic islands and rational surfaces. It was found that [108]: "This experiment supports the idea that the magnetic island at the rational surface contributes to the transition from the L-mode to the ITB rather than to the rational surface itself". A reduction of transport inside magnetic islands has been observed, close to what is called the "O-point", as opposed to the previously mentioned X-point. There is a reduction in turbulence (and transport) at the boundary of magnetic islands and the pressure profile is flat in the O-point inside the islands.

Important observed differences between tokamak and helical plasmas include the following:

- Ion barriers are the most significant for tokamaks, whereas electron barriers are more significant for helical devices.
- Simultaneous ion/electron barriers have been seen in tokamaks but not in helical devices.
- In general, magnetic shear is negative for helical devices, but both positive and negative for tokamaks.
- Differences in particle transport: There is a clear density barrier for tokamaks; the barrier disappears at higher densities in helical devices. But it exists for both when pellet injection is used.
- The toroidal angular velocity is higher for tokamaks.
- The sign of the impurity pinch is the opposite: It is inward for tokamaks (impurity accumulation) and outward for helical systems.
- ITBs are more variable for tokamaks due to the freedom of the current profile (magnetic shear), which is restricted in helical devices
- Radial electric field:
    1. Helical: Mainly generated by poloidal velocity.
    2. Tokamak: Significant contribution from toroidal rotation.

Non-locality of ITB plasmas has been observed, e.g., coupling between the inside and the outside of the ITB. The curvature of the ion temperature ($\partial^2 T_i/\partial r^2$) has been linked with ITB stability, where a convex (concave) curvature means a less (more) stable ITB, respectively.

3.7.3. Both ETB and ITB

It was already demonstrated in [24] that an ITB can coexist with both L- and H-mode edges, where an ITB with an H-mode edge is a double barrier (DB), i.e., an ETB and an

ITB. Non-locality has also been observed for this type of DB, where the ITB formation takes place simultaneously with the L-H transition [108].

Multiple barriers have been reviewed in [109] and we present a summary of this work throughout the rest of the section.

The leading mechanisms for stabilisation are as follows: (i) $E \times B$ flow shear and (ii) a reduction of growth rates due to α-stabilisation. The combination of ETB and ITB is useful if it can

- Increase the plasma volume with reduced transport.
- Lead to improved stability against MHD modes.
- For tokamaks: Improve the bootstrap current fraction for steady-state operation.

On the other hand, potential drawbacks include the following:

- ITB degradation due to the ETB, e.g., reduction of rotation shear and pressure gradient at the ITB location.
- High density at the ETB can reduce NBI penetration efficiency.
- ELMs can lead to the flattening of ITB temperature gradients.

An example where the barriers lead to additive beneficial effects is the quiescent double barrier (QDB) mode in DIII-D, where an ITB is combined with a quiescent H-mode (QH), which has an EHO.

3.8. Zonal Flows

We will now review zonal flows (ZFs) based on the material in [15,108,112–117].

ZFs are azimuthally symmetric band-like $E \times B$ shear flows with mode numbers $n = m = 0$. They are mesoscale electric field fluctuations with zero mean frequency and finite radial wave number k_r. ZFs are flows that are driven by turbulence, e.g., turbulent shear RS [118] or DW. Due to their structure, ZFs are benign repositories for free energy and do not drive radial (energy or particle) transport. ZFs vary rapidly in the radial direction. For toroidal plasmas having a strong toroidal magnetic field (valid assumption in this review), ZFs are predominately poloidally directed with velocities $v_\theta = -E_r/B$ and $v_\phi = -2qv_\theta \cos\theta$. The convention is that $\theta = 0^\circ$ at the outboard midplane and increases in the counterclockwise direction.

ZFs differ from mean $E \times B$ shear flows (see Section 3.6); mean shear flows are generated as a result of the ion radial force balance and ZF shear flows are driven by turbulence. Mean shear flows can persist without turbulence, whereas ZF shear flows cannot. This is reflected in the different radial electric fields:

- The radial electric field from ZFs is oscillatory, complex, consists of small structures, and is driven exclusively by nonlinear wave interaction processes.
- The mean radial electric field evolves on transport timescales and is driven by, e.g., heating, fuelling, and momentum input, which determine equilibrium profiles, and in turn, regulate the radial force balance.

The mean and ZF shear flows can interact, e.g., mean flows can suppress ZFs through turbulence decorrelation. Both flow types can tilt and break turbulent eddies.

ZFs shear or quench turbulence to extract energy from it, leading to a self-regulating mechanism with a predator-prey system of turbulent energy (prey) and ZF energy (predator). In that sense, ZFs can shift (delay) the onset of turbulence, often referred to as the "Dimits shift" [119].

ZFs have been linked to rational ι values, e.g., in the H-1 National Facility (H-1NF), which was a 3-field period heliac. ZFs were found at two locations (due to reversed shear), where $\iota = 7/5$.

Because of the 3D nature of shear flow physics, several RS terms can contribute to ZF generation, e.g., radial–parallel, radial–perpendicular, and radial–poloidal.

ZFs are not Landau (wave)-damped but mainly collisionally damped due to friction between trapped and circulating ions; they increase with decreasing collisionality.

The energy partition between ZFs and turbulence is key for plasma confinement: A large fraction of ZFs results in better confinement. To understand the process, one can write the ratio of ZFs and turbulence as follows:

$$\zeta = V^2/N = \frac{\gamma_L/\alpha}{\gamma_{\text{damp}}/\alpha} = \gamma_L/\gamma_{\text{damp}}, \tag{30}$$

where V is the ZF intensity, N is the turbulence energy, γ_L is the DW (turbulence) linear growth rate, α is a coupling constant between ZFs and DWs, and γ_{damp} is the flow-damping of ZFs due to collisionality. The ratio ζ increases with improved confinement since the damping rate decreases.

ZFs may take the role of a trigger for confinement transitions, possibly at the L-H transition. An interaction between mean and zonal flows may also exist; e.g., the mean $E \times B$ flow exists before the transition, and the additional effect of ZFs triggers the transition itself.

In nature, the Jovian belts/zones and the terrestrial jet stream have been given as examples of ZFs.

Finally, we mention zonal fields, which involve the generation of structured magnetic fields from turbulence, i.e., a magnetic counterpart to ZFs. They were theoretically predicted in [120] and experimentally detected in [121]. The magnetic field structures, also with $n = m = 0$ and the finite radial wave number, can be generated by DW turbulence and may have a back-reaction on turbulence via magnetic shearing.

3.9. Geodesic Acoustic Modes

We proceed with a review of geodesic acoustic modes (GAMs) based on material in [113–115,117].

In many respects, GAMs are similar to ZFs. GAMs also have mode numbers $n = m = 0$, but they couple to pressure/density fluctuations with $m = \pm 1$ (poloidal mode number) and $n = 0$. These fluctuations are poloidally asymmetric, being highest at the top and bottom of the tokamak plasmas. For stellarators/heliotrons, the highest fluctuation is not at the top and bottom but follows the helical pitch. For completeness, we note that there is also a magnetic component with $m = \pm 2$ and $n = 0$. GAMs have velocities $v_\theta = -E_r/B$ and $v_\phi = q^{-1} v_\theta \cos\theta$.

GAMs have a finite frequency as opposed to ZFs, which have zero frequency. The GAM frequency scales with the square root of the temperature; this can be derived from the single-fluid ideal (all dissipative processes neglected) MHD [122]:

$$\omega_{\text{GAM}}^2 = \frac{2c_s^2}{R^2}\left(1 + \frac{1}{2q^2}\right), \tag{31}$$

where:

$$c_s = \sqrt{\gamma(T_e + T_i)/m_i} \tag{32}$$

is the speed of sound and $\gamma = 5/3$ is the specific heat ratio.

GAMs are both Landau-damped ($\propto \exp(-q^2)$) and collisionally damped; zero frequency ZFs are not Landau-damped, but only collisionally damped. Due to the differences in Landau damping and magnetic configuration in tokamaks and helical devices, GAMs are mainly found at the edge of tokamaks and in the low ι core region of stellarators/heliotrons. Generally, it has also been observed that GAMs are stronger (and have been observed more often) in tokamaks than helical devices.

GAMs can be driven directly from the poloidally symmetric $m = 0$ component of the turbulent shear RS, similar to ZFs: "Since both the GAM and the ZF are driven by turbulence there is the issue of competition in the nonlinear transfer leading to the dominance of one or other mode" [117]. However, ZFs and GAMs can coexist and transitions between ZFs and GAMs have also been observed.

Both ZFs and GAMs have comparable radial correlation lengths, which are mesoscale, as also found for streamers.

The response of ZFs and GAMs to fluctuations is different: ZFs are incompressible (slow response) and GAMs are compressible (fast response).

Usually, GAMs are not observed in H-mode.

The impact of GAMs on transport can be summarised as follows:

- No direct radial energy or particle transport is observed.
- Oscillatory flow shearing occurs.
- GAMs act as an energy sink through Landau damping or dissipation.
- They modulate cross-field transport through pressure fluctuations (GAMs are rarely contiguous and stable).

Finally, we will present quotes from [117] on the relationship between GAMs and magnetic islands:

- "The interaction of GAMs with MHD modes (static and rotating) is multi-fold. An island chain may create a GAM-like oscillation, or it may enhance and/or entrain a natural edge GAM, or it may suppress and destroy the natural GAM."
- "At the extreme, the velocity shearing associated with the GAM can also restrict the island radial structure and thus limit the growth of the MHD mode."
- "The flow and turbulence behaviour can be divided into three distinct spatial regions: inside the island separatrix, around the island boundary, and spatially (radially) well away from the island chain."

3.10. Blobs

Blobs are filaments generated by edge plasma turbulence with enhanced levels of particles and heat aligned along magnetic field lines in the SOL [123]. There are intermittent eruptions of plasma and heat into the SOL, leading to the radial motion of blobs. They exhibit 'ballooning', with more transport at the outboard midplane. The fluctuation level and turbulence-driven transport (the number of events) increase with β and collisionality. Blobs have an asymmetric waveform over time, where the rise time is fast and the decay is slow; their total duration is around 25 ms.

A theory on blob creation based on the breakup of streamers due to velocity shear was experimentally validated in [124]. These streamers are located outside the separatrix, so in that sense, they are different from the streamers previously mentioned. A possible mechanism for the shear flow generation is the interchange instability, which is "very similar in nature to the Rayleigh-Taylor instability in fluid dynamics" [86]. More blobs are observed in the L-mode than in the H-mode.

4. Transport Barriers

4.1. General

For FM TBs, the edge BLs or core internal interface layers (IILs) both result from the momentum balance of the NSE and the energy equation for thermal barriers. For FM, the question is: Is there a phenomenon analogous to the magnetic field in PP—perhaps ECS?

TBs for PP are associated with both mean $E \times B$ shear turbulence suppression and properties of the confining magnetic field, e.g., magnetic islands.

In general, both particle and heat TBs contribute to an increased pressure gradient, whereas the momentum TB results in a steeper velocity gradient.

4.2. Edge

The LBL concept from FM seems to be equivalent to the ETB of PP associated with the H-mode. For FM, the steeper velocity gradient for turbulent flow is associated with the domination of inertial forces over viscous forces quantified by Re. For PP, the H-mode is associated with an external power threshold, magnetic field effects, and mean $E \times B$ shear flow.

We collect the edge TB cases in Table 1, which shows that the LBL and the H-mode (ETB) have a low edge radial flux, i.e., a TB, whereas the TBL and the L-mode have a high edge radial flux.

Table 1. Relationship between the fluid/plasma state and the edge radial flux.

Edge State	Edge Diffusion Coefficient	Edge Gradient	Edge Radial Flux
FM: TBL	Large (ν_t)	Steep	High
FM: LBL	Small (ν_{kin})	Moderate	Low
PP: L-mode	Large	Moderate	High
PP: H-mode (ETB)	Small	Steep	Low

4.3. Internal

For FM, the wake in TBLs [38] can be modelled as a velocity jump or an internal shear layer [55]. For TWs, a step in the axial velocity profile was observed; see Figures 21 (and 22) in [28]. This is very similar to ITB profiles in PP and is a central observation of this review. Thus, the wake can be interpreted as an ITB, possibly related to the quiescent core observed for channel flow [54].

We present the core TB cases in Table 2, where we use the IIL term for FM. Diffusion coefficients are affected by RS-driven flows and structures (TWs/magnetic islands) for both FM and PP. This is in contrast to the edge TBs, where the FM and PP mechanisms are different.

Table 2. Relationship between the fluid/plasma state and the core radial flux.

Core State	Core Diffusion Coefficient	Core Gradient	Core Radial Flux
FM: No IIL	Large	Moderate	High
FM: With IIL	Small	Steep	Low
PP: No ITB	Large	Moderate	High
PP: With ITB	Small	Steep	Low

5. Core Turbulence

In PP, turbulence during controlled confinement transitions has been studied by modifying the magnetic field structure [26,27]. It was found that core turbulence increased for degraded confinement.

It has been speculated that a similar phenomenon occurs during the high *Re* transition in pipe flow [25]. Here, increased core turbulence was observed with increasing Re_τ, leading to the question: does low (high) Re_τ for pipe flow correspond to good (bad) confinement in PP? Perhaps this points to the existence of a stronger (larger) wake for low Re_τ.

A Possible Reinterpretation of the High Reynolds Number Transition Region

The log law region is associated with large turbulent structures and extends further inwards for higher *Re*. It can be argued that the high *Re* transition corresponds to the log law/wake transition region being pushed toward the core or even collapses at sufficiently high *Re*. The loss of this IIL/ITB leads to higher levels of core turbulence since the quiescent core is reduced or disappears and is replaced with structures from the log law region. This is also reflected in an increasing turbulent length scale at the transition [25]. The proposed mechanism implies that turbulence in pipe flow ends up similar to open channel flow for sufficiently high *Re* [56]. The transition from localised to expanding turbulence for the laminar–turbulent transition is associated with regions where the TKE production-to-

dissipation ratio, $\mathcal{P}/\varepsilon > 1$ [31], which corresponds to the non-equilibrium high *Re* state detailed in [25].

6. An Overview of Concepts

In this section, we provide an appraisal of the similarities, differences, and question marks we have identified so far.

6.1. Similarities

Possible FM/PP-related flow phenomena are presented in Table 3.

Regarding coherent (turbulent) structures, ECS and VLSM in FM can be considered counterparts of magnetic field structures in PP, such as magnetic islands associated with rational surfaces or MHD phenomena.

Flow generation by RS has been observed as ZFs in PP and we argue that a similar mechanism is at play in FM.

As discussed, the IILs (momentum, heat, concentration) and ITBs have strong similarities. And the wake in FM can be likened to an ITB as proposed above. It is remarkable that the FM VF/TF model (Sections 2.10 and 2.12) is almost identical to the q-comb model for PP (Section 3.4).

Finally, we have a separate table entry for RC structures observed for passive scalars and their similarity to sawtooth crashes in PP, which are magnetic reconnection events associated with particle and heat ejection from the plasma core.

Table 3. Proposed analogies between FM and PP: structures, flow, and TBs.

	FM	**PP**
	ECS, VLSM	Magnetic islands, MHD
	RS-driven flow	RS-driven ZF
	IIL	ITB
	Wake	ITB
	RC structures	Sawtooth crashes

The laminar–turbulent transition in FM can be correlated with confinement transitions in PP; see Table 4. Here, laminar flow is denoted as H-mode (low turbulence level) and turbulent flow as L-mode (high turbulence level). In PP, dithering between L- and H-mode can be thought of as collections of closely spaced ELMs [125,126], similar to puffs in FM. The relationship between increasing *Re* in FM and worse confinement in PP is consistent with the findings presented in Section 5.

Table 4. Proposed analogies between FM and PP: laminar–turbulent and confinement transitions.

FM	**PP**	**Edge Radial Flux**
Laminar flow	H-mode	Low
Laminar regions Laminar–turbulent transition	No ELMs H-L transition	Low
Turbulent puffs Laminar–turbulent transition	ELMs H-L transition	High
Turbulent flow	L-mode	High

The mixing length concept from FM (Section 2.9) was adopted in PP (Section 3.3). Apart from that, it is difficult to compare important length scales; relevant micro-, meso- and macro-scales exist for both FM and PP, but other scales can also have an impact, so a direct correspondence is not obvious.

Both FM and PP can be considered as (quasi-) 2D, where the symmetry-breaking coordinate is streamwise for FM and toroidal (or parallel) for PP. Both FM and PP streamwise/toroidal turbulent structures can be extremely long, i.e., tens of pipe diameters for FM (VLSM) and tens of meters for PP.

Cross-scale interaction between turbulent structures is important in both FM [45] and PP [108,127].

6.2. Differences

Since we have compared pipe flow and toroidal devices, an obvious difference is the curvature. But we should mention that curved pipes and linear plasma machines exist and could be interesting to bring into this comparison.

The inboard/outboard asymmetry observed for PP, e.g., streamers, does not have a direct correspondence with FM. The closest would be the asymmetric TW identified in [76], where the TW only occupied half of the pipe.

Another important difference is the existence of EM fields for PP, which are not present for FM. Thus, phenomena that can only be caused by EM fields are not relevant to our comparison. The associated twisted magnetic field lines in PP do not have a counterpart in FM; however, helical TWs exist with a similar structure [76].

The physical wall for FM, leading to no-slip and no-penetration BCs, is non-existent at the separatrix for PP, where the conditions are free-slip and penetrable. The additional SOL for PP does not have an equivalent for FM; the only way to have fluid phenomena inside the wall is by use of image vorticity [128] placed in nonphysical regions to satisfy the impermeable BC [129] (pun intended).

6.3. Question Marks

Particle mirror trapping in PP is caused by the magnetic field and there is no direct process like this in FM. The closest might be the rolls–streaks–waves SSP mentioned in Section 2.16.

Plasma shaping effects are important in PP, e.g., the GAM dependency on vertical plasma elongation. Many other shaping parameters exist, such as triangularity, inverse aspect ratio, and the Shafranov shift. Shaping also impacts FM flows, but this has not been explored in detail yet.

The MFU in FM (Section 2.8) may correspond to microscales in PP; here, additional investigations should be carried out (if they have not been carried out already?) to determine whether self-sustaining cycles exist in the plasma edge.

7. Discussion

Objectives in FM and PP can be different, but for both fields, an understanding is needed, regardless of whether an effect has to be minimised or maximised.

Examples of quantities of importance for the two fields include:

- FM: Drag (pressure drop) and heat transfer.
- PP: Confinement: Cross-field anomalous transport of particles and heat.

7.1. Possible Universal Turbulent Flow Mechanisms

To some extent, we agree with the "chimera" view of turbulence proposed by Saffman [130] ("Finally, we should not altogether neglect the possibility that there is no such thing as 'turbulence'. That is to say, it is not meaningful to talk of the properties of a turbulent flow independently of the physical situation in which it arises. In searching for a theory of turbulence, perhaps we are looking for a chimera. Turbulent phenomena of many types exist, and each one of practical importance can be analysed or described to any required degree of detail by the expenditure of sufficient effort. So perhaps there is no 'real turbulence problem', but a large number of turbulent flows and our problem is the self-imposed and possibly impossible task of fitting many phenomena into the Procrustean bed of a universal turbulence theory. Individual flows should then be treated on their

merits and it should not necessarily be assumed that ideas valid for one flow situation will transfer to others. The turbulence problem may then be no more than one of cataloguing, The evidence is against such an extreme point of view as many universal features seem to exist, but cataloguing and classifying may be a more useful approach than we care to admit."), but would argue that common ingredients do exist. These ingredients will change in importance, depending on the specific situation, but will always exist. If we continue using the chimera metaphor, this would be a chimera with the same body parts but different proportions. Traditional ingredients are:

- Geometry;
- BCs.

And what has been argued in this review are the additional (FM/PP) ingredients:

- ECS/magnetic islands;
- RS-driven (zonal) flows;
- IILs/ITBs.

There is an interplay between the ingredients, and some ingredients are less clear than others; for example, whether the RS-driven flow in FM and PP can be thought of as the same phenomenon. For the L-H transition in PP, "The picture is thus of an close interaction among sheared flows, eddy structures, RS, and ZFs across the confinement transition" [117].

In Figure 1, we present a sketch that consists of the identified FM/PP ingredients. The arrows are meant to indicate the general sequence, but drawing such a picture opens up a wide range of new questions, which will be addressed in [131].

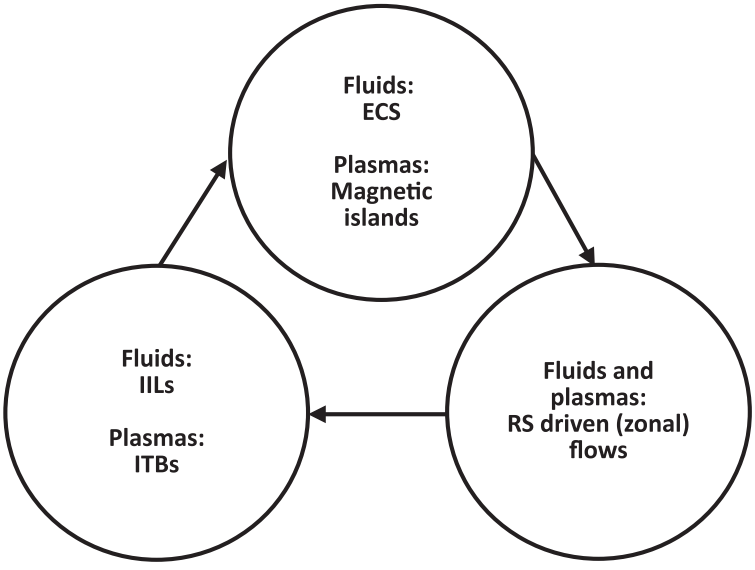

Figure 1. Proposed common FM/PP process.

7.2. Nomenclature Pertaining to Radial Fluxes

There are different names to describe the manifestations of low or high radial fluxes in FM and PP; see Table 5. But the underlying mechanisms are the same, i.e., perpendicular/cross-field transport of momentum, particles, and heat.

Table 5. Manifestations of low and high radial fluxes.

State	Radial Flux	Manifestations
FM: Laminar flow	Low	Small pressure drop Low heat transfer
FM: Turbulent flow	High	Large pressure drop High heat transfer
PP: Improved confinement (L-mode with ITB) (H-mode with/without ITB)	Low	Long energy and particle confinement times
PP: Degraded confinement (L-mode without ITB)	High	Short energy and particle confinement times

7.3. Proposal for New Research Program

We recommend the initiation of specific cross-disciplinary efforts in model-building for both the FM and PP communities to take advantage of progress in both fields.

An experimental FM approach would be to build a simple device to test e.g., ZF generation from RS without EM fields. This could either be a linear or toroidal device, where shape effects, such as those found in PP, could be tested using, for example, elliptical pipes.

In general, cross-disciplinary work should cover all the similarities, differences, and question marks mentioned above, but focus on the question marks.

We end this section with three quotes on interesting avenues to take:

- Ref. [14]: "A simple, direct demonstration of shear suppression, ideally in a controlled neutral-fluid experiment, is a desirable direction for future work."
- Ref. [15]: "Finally, it must be said that the greatest opportunities for future research on zonal flows lie in the realm of experiment. Particular challenges include the simultaneous study, correlation, and synthesis of generation dynamics in real space (i.e., via vorticity transport) and k-space (i.e., via nonlinear mode coupling), and the development of methods to control zonal flows. More generally, future experiments must emphasize challenging the theory and confronting it with stressful quantitative tests."
- Ref. [117]: "A range of high quality diagnostics have been used in the study of ZFs, but, often lacking are comprehensive sets of simultaneous measurements of the flow oscillations, their structure (as well as their sidebands to confirm the ZFO or GAM identity), together with high-k measurements of the ambient flow and density turbulence, its properties and structure."

  (Here, ZFO are ZF oscillations.)

8. Conclusions

We presented a comparative study of wall- and magnetically-bounded turbulent flows to identify possible cross-disciplinary similarities. The most important common phenomena found are coherent (turbulent) structures, shear Reynolds stress flow generation, and transport barriers.

Exact coherent structures found in fluid mechanics appear to have many similarities with magnetic islands in fusion plasmas, which are associated with rational values of the winding number of the magnetic field lines.

Zonal flows in fusion plasmas create radial velocity shear, which is also seen between uniform momentum zones in non-ionised turbulent flows.

To the best of our knowledge, this is the first time the uniform momentum zones in fluid mechanics have been compared to internal transport barriers in magnetically confined fusion plasmas.

We propose that the following phenomena are common (universal) ingredients for both non-ionised fluids and magnetically confined fusion plasmas:

- Exact coherent states/magnetic islands.
- Shear Reynolds stress-driven (zonal) flows.
- Internal interface layers (momentum, heat, concentration)/internal transport barriers.

The improved understanding has been used to reinterpret transport barriers and core turbulence.

An additional potential similarity is between ramp–cliff structures in passive scalar flows and sawtooth crashes caused by magnetic reconnection in fusion plasmas.

Finally, we propose a new cross-disciplinary experimentally based research program to test the ideas we have put forth.

A note of caution: Cross-disciplinary research is notoriously difficult to carry out and to gauge since one will be an outsider in some fields and risk being seen as a crackpot in others. This naturally leads to the disclaimer that all misunderstandings and errors are mine.

Funding: This research received no external funding.

Data Availability Statement: Data availability does not apply to this article as no new data were created or analysed.

Acknowledgments: Tak til C.V.Jørgensen for "Alverdens turbulens".

Conflicts of Interest: The author declares no conflicts of interest.

References

1. Marusic, I.; Broomhall, S. Leonardo da Vinci and fluid mechanics. *Annu. Rev. Fluid Mech.* **2021**, *53*, 1–25. [CrossRef]
2. Colagrossi, A.; Marrone, S.; Colagrossi, P.; Le Touzé, D. Da Vinci's observation of turbulence: A French-Italian study aiming at numerically reproducing the physics behind one of his drawings, 500 years later. *Phys. Fluids* **2021**, *33*, 115122. [CrossRef]
3. Schmitt, F.G. Turbulence from 1870 to 1920: The birth of a noun and of a concept. *C. R. Mec.* **2017**, *345*, 620–626. [CrossRef]
4. Langmuir, I. Oscillations in ionized gases. *Proc. Natl. Acad. Sci. USA* **1928**, *14*, 627–637. [CrossRef] [PubMed]
5. Kadomtsev, B.B. *Plasma Turbulence*; Academic Press: London, UK, 1965.
6. Goedbloed, J.P.H.; Poedts, S. *Principles of Magnetohydrodynamics: With Applications to Laboratory and Astrophysical Plasmas*; Cambridge University Press: Cambridge, UK, 2004.
7. National Research Council. *Plasmas and Fluids*; National Academies Press: Washington, DC, USA, 1986.
8. Choudhuri, A.R. *The Physics of Fluids and Plasmas: An Introduction for Astrophysicists*; Cambridge University Press: Cambridge, UK, 1998.
9. Special Topic: Turbulence in Plasmas and Fluids. Available online: https://publishing.aip.org/publications/journals/special-topics/phf/turbulence-in-plasmas-and-fluids/ (accessed on 29 January 2024).
10. Pope, S.B. *Turbulent Flows*; Cambridge University Press: Cambridge, UK, 2000.
11. Horton, W. *Turbulent Transport in Magnetized Plasmas*, 2nd ed.; World Scientific: Singapore, 2017.
12. Kolmogorov, A.N. The local structure of turbulence in incompressible viscous fluid for very large Reynolds numbers (Russian). *Dokl. Akad. Nauk SSSR* **1941**, *30*, 301–305.
13. Frisch, U. *Turbulence: The Legacy of A. N. Kolmogorov*; Cambridge University Press: Cambridge, UK, 1995.
14. Terry, P.W. Suppression of turbulence and transport by sheared flow. *Rev. Mod. Phys.* **2000**, *72*, 109–165. [CrossRef]
15. Diamond, P.H.; Itoh, S.-I.; Itoh, K.; Hahm, T.S. Zonal flows in plasma—A review. *Plasma Phys. Control. Fusion* **2005**, *47*, R35–R161. [CrossRef]
16. Davidson, P.A.; Kaneda, Y.; Moffatt, K.; Sreenivasan, K.R. (Eds.) *A Voyage through Turbulence*; Cambridge University Press: Cambridge, UK, 2011.
17. Basse, N.P. Density fluctuations on mm and Mpc scales. *Phys. Lett. A* **2005**, *340*, 456–460. [CrossRef]
18. Basse, N.P. A study of multiscale density fluctuation measurements. *IEEE Trans. Plasma Sci.* **2008**, *36*, 458–461. [CrossRef]
19. Prandtl, L. Über Flüssigkeitsbewegung bei sehr kleiner Reibung. In *Verhandlungen des III*; Internationalen Mathematiker-Kongresses: Heidelberg, Germany, 1905; pp. 484–491.
20. Schlichting, H.; Gersten, K. *Boundary-Layer Theory*, 8th ed.; Springer: Berlin/Heidelberg, Germany, 2000.
21. Wagner, F.; Becker, G.; Behringer, K.; Campbell, D.; Eberhagen, A.; Engelhardt, W.; Fussmann, G.; Gehre, O.; Gernhardt, J.; Gierke, G.V. et al. Regime of improved confinement and high beta in neutral beam heated divertor discharges of the ASDEX tokamak. *Phys. Rev. Lett.* **1982**, *49*, 1408–1412. [CrossRef]

22. Meinhart, C.D.; Adrian, R.J. On the existence of uniform momentum zones in a turbulent boundary layer. *Phys. Fluids* **1995**, *7*, 694–696. [CrossRef]
23. Levinton, F.M.; Zarnstorff, M.C.; Batha, S.H.; Bell, M.; Bell, R.E.; Budny, R.V.; Bush, C.; Chang, Z.; Fredrickson, E.; Janos, A. et al. Improved confinement with reversed magnetic shear in TFTR. *Phys. Rev. Lett.* **1995**, *75*, 4417–4420. [CrossRef]
24. Strait, E.J.; Lao, L.L.; Mauel, M.E.; Rice, B.W.; Taylor, T.S.; Burrell, K.H.; Chu, M.S.; Lazarus, E.A.; Osborne, T.H.; Thompson, S.J. et al. Enhanced confinement and stability in DIII-D discharges with reversed magnetic shear. *Phys. Rev. Lett.* **1995**, *75*, 4421–4424. [CrossRef] [PubMed]
25. Basse, N.T. An algebraic non-equilibrium turbulence model of the high Reynolds number transition region. *Water* **2023**, *15*, 3234. [CrossRef]
26. Zoletnik, S.; Basse, N.P.; Saffman, M.; Svendsen, W.; Endler, M.; Hirsch, M.; Werner, A.; Fuchs, C.; W7-AS Team. Changes in density fluctuations associated with confinement transitions close to a rational edge rotational transform in the W7-AS stellarator. *Plasma Phys. Control. Fusion* **2002**, *44*, 1581–1607. [CrossRef]
27. Basse, N.P.; Michelsen, P.K.; Zoletnik, S.; Saffman, M.; Endler, M.; Hirsch, M. Spatial distribution of turbulence in the Wendelstein 7-AS stellarator. *Plasma Sources Sci. Technol.* **2002**, *11*, A138–A142. [CrossRef]
28. Wedin, H.; Kerswell, R.R. Exact coherent structures in pipe flow: Travelling wave solutions. *J. Fluid Mech.* **2004**, *508*, 333–371. [CrossRef]
29. Serber, R. *The Los Alamos Primer: The First Lectures on How to Build an Atomic Bomb*; University of California Press: Berkeley, California, USA, 2020.
30. Dennis, D.J.C.; Sogaro, F.M. Distinct organizational states of fully developed turbulent pipe flow. *Phys. Rev. Lett.* **2014**, *113*, 234501. [CrossRef]
31. Avila, M.; Barkley, D.; Hof, B. Transition to turbulence in pipe flow. *Annu. Rev. Fluid Mech.* **2023**, *55*, 575–602. [CrossRef]
32. Smits, A.J.; McKeon, B.J.; Marusic, I. High-Reynolds number wall turbulence. *Annu. Rev. Fluid Mech.* **2011**, *43*, 353–375. [CrossRef]
33. McKeon, B.J. The engine behind (wall) turbulence: Perspectives on scale interactions. *J. Fluid Mech.* **2017**, *817*, P1. [CrossRef]
34. Reynolds, O. An experimental investigation of the circumstances which determine whether the motion of water shall be direct or sinuous and the law of resistance in parallel channels. *Phil. Trans. R. Soc.* **1883**, *174*, 935–982.
35. Corrsin, S.; Kistler, A.L. *Free-Stream Boundaries of Turbulent Flows*; NACA Report 1244; National Advisory Committee for Aeronautics: Washington, DC, USA, 1955.
36. Ishihara, T.; Ogasawara, H.; Hunt, J.C.R. Analysis of conditional statistics obtained near the turbulent/non-turbulent interface of turbulent boundary layers. *J. Fluids Struct.* **2015**, *53*, 50–57. [CrossRef]
37. Eisma, J.; Westerweel, J.; Ooms, G.; Elsinga, G.E. Interfaces and internal layers in a turbulent boundary layer. *Phys. Fluids* **2015**, *27*, 055103. [CrossRef]
38. Coles, D. The law of the wake in the turbulent boundary layer. *J. Fluid Mech.* **1956**, *1*, 191–226. [CrossRef]
39. Townsend, A.A. *The Structure of Turbulent Shear Flow*, 2nd ed.; Cambridge University Press: Cambridge, UK, 1976.
40. Marusic, I.; Monty, J.P. Attached eddy model of wall turbulence. *Annu. Rev. Fluid Mech.* **2019**, *51*, 49–74. [CrossRef]
41. Marusic, I.; Monty, J.P.; Hultmark, M.; Smits, A.J. On the logarithmic region in wall turbulence. *J. Fluid Mech.* **2013**, *716*, R3. [CrossRef]
42. Prandtl, L. Bericht über Untersuchungen zur ausgebildeten Turbulenz. *Z. Angew. Math. Mech.* **1925**, *5*, 136–139. [CrossRef]
43. Prandtl, L. Bericht über neuere Turbulenzforschung. In *Hydraulische Probleme*; VDI-Verlag: Berlin, Germany, 1926.
44. Smits, A.J. Some observations on Reynolds number scaling in wall-bounded flows. *Phys. Rev. Fluids* **2020**, *5*, 110514. [CrossRef]
45. Marusic, I.; Baars, W.J.; Hutchins, N. Scaling of the streamwise turbulence intensity in the context of inner-outer interactions in wall turbulence. *Phys. Rev. Fluids* **2017**, *2*, 100502. [CrossRef]
46. Andreolli, A.; Gatti, D.; Vinuesa, R.; Örlü, R.; Schlatter, P. Separating large-scale superposition and modulation in turbulent channels. *J. Fluid Mech.* **2023**, *958*, A37. [CrossRef]
47. Deshpande, R.; de Silva, C.M.; Marusic, I. Evidence that superstructures comprise self-similar coherent motions in high Reynolds number boundary layers. *J. Fluid Mech.* **2023**, *969*, A10. [CrossRef]
48. Berkooz, G.; Holmes, P.; Lumley, J.L. The proper orthogonal decomposition in the analysis of turbulent flows. *Annu. Rev. Fluid Mech.* **1993**, *25*, 539–575. [CrossRef]
49. Jiménez, J.; Moin, P. The minimal flow unit in near-wall turbulence. *J. Fluid Mech.* **1991**, *225*, 213–240. [CrossRef]
50. Hwang, Y. Near-wall turbulent fluctuations in the absence of wide outer motions. *J. Fluid Mech.* **1991**, *723*, 264–288. [CrossRef]
51. de Silva, C.M.; Hutchins, N.; Marusic, I. Uniform momentum zones in turbulent boundary layers. *J. Fluid Mech.* **2016**, *786*, 309–331. [CrossRef]
52. Cuevas Bautista, J.C.; Ebadi, A.; White, C.M.; Chini, G.P.; Klewicki, J.C. A uniform momentum zone-vortical fissure model of the turbulent boundary layer. *J. Fluid Mech.* **2019**, *858*, 609–633. [CrossRef]
53. Aksamit, N.O.; Haller, G. Objective momentum barriers in wall turbulence. *J. Fluid Mech.* **2022**, *941*, A3. [CrossRef]
54. Kwon, Y.S.; Philip, J.; de Silva, C.M.; Hutchins, N.; Monty, J.P. The quiescent core of turbulent channel flow. *J. Fluid Mech.* **2014**, *751*, 228–254. [CrossRef]
55. Krug, D.; Philip, J.; Marusic, I. Revisiting the law of the wake in wall turbulence. *J. Fluid Mech.* **2017**, *811*, 421–435. [CrossRef]
56. Pirozzoli, S. Searching for the log law in open channel flow. *J. Fluid Mech.* **2023**, *971*, A15. [CrossRef]

57. Yao, M.X.; Sun, Z.; Scalo, C.; Hickey, J.-P. Vortical and thermal interfacial layers in wall-bounded turbulent flows under transcritical conditions. *Phys. Rev. Fluids* **2019**, *4*, 084604. [CrossRef]
58. Ebadi, A.; Cuevas Bautista, J.C.; White, C.M.; Chini, G.; Klewicki, J. A heat transfer model of fully developed turbulent channel flow. *J. Fluid Mech.* **2020**, *884*, R7. [CrossRef]
59. Warhaft, Z. Passive scalars in turbulent flows. *Annu. Rev. Fluid Mech.* **2000**, *32*, 203–240. [CrossRef]
60. Eisma, J.; Westerweel, J.; van de Water, W. Do coherent structures organize scalar mixing in a turbulent boundary layer? *J. Fluid Mech.* **2021**, *929*, A14. [CrossRef]
61. Sreenivasan, K.R.; Antonia, R.A.; Britz, D. Local isotropy and large structures in a heated turbulent jet. *J. Fluid Mech.* **1979**, *94*, 745–775. [CrossRef]
62. Shraiman, B.I.; Siggia, E.D. Scalar turbulence. *Nature* **2000**, *405*, 639–646. [CrossRef] [PubMed]
63. Antonia, R.A.; Chambers, A.J.; Britz, D.; Browne, L.W.B. Organized structures in a turbulent plane jet: Topology and contribution to momentum and heat transport. *J. Fluid Mech.* **1986**, *172*, 211–229. [CrossRef]
64. Wroblewski, D.E.; Coté, O.R.; Hacker, J.M.; Dobosy, R.J. Cliff–ramp patterns and Kelvin–Helmholtz billows in stably stratified shear flow in the upper troposphere: Analysis of aircraft measurements. *J. Atmos. Sci.* **2007**, *64*, 2521–2539. [CrossRef]
65. Heisel, M.; Sullivan, P.P.; Katul, G.G.; Chamecki, M. Turbulence organization and mean profile shapes in the stably stratified boundary layer: Zones of uniform momentum and air temperature. *Bound.-Layer Meteorol.* **2023**, *186*, 533–565. [CrossRef]
66. Salesky, S.T. Uniform momentum and temperature zones in unstably stratified turbulent flows. *J. Fluid Mech.* **2023**, *958*, A7. [CrossRef]
67. Gad-el-Hak, M. *Flow Control*; Cambridge University Press: Cambridge, UK, 2006.
68. Gad-el-Hak, M. Coherent structures and flow control: Genesis and prospect. *Bull. Pol. Acad. Tech.* **2019**, *67*, 411–444. [CrossRef]
69. Scarselli, D.; Lopez, J.M.; Varshney, A.; Hof, B. Turbulence suppression by cardiac-cycle-inspired driving of pipe flow. *Nature* **2023**, *621*, 71–74. [CrossRef]
70. Vinuesa, R. Perspectives on predicting and controlling turbulent flows through deep learning. *arXiv* **2023**, arXiv:2310.04054.
71. Budanur, N.B.; Short, K.Y.; Farazmand, M.; Willis, A.P.; Cvitanović, P. Relative periodic orbits form the backbone of turbulent pipe flow. *J. Fluid Mech.* **2017**, *833*, 274–301. [CrossRef]
72. Nagata, M. Three-dimensional finite-amplitude solutions in plane Couette flow: Bifurcation from infinity. *J. Fluid Mech.* **1990**, *217*, 519–527. [CrossRef]
73. Waleffe, F. Homotopy of exact coherent structures in plane shear flows. *Phys. Fluids* **2003**, *15*, 1517–1534. [CrossRef]
74. Faisst, H.; Eckhardt, B. Travelling waves in pipe flow. *Phys. Rev. Lett.* **2003**, *91*, 224502. [CrossRef] [PubMed]
75. Schneider, T.M.; Eckhardt, B.; Vollmer, J. Statistical analysis of coherent structures in transitional pipe flow. *Phys. Rev. E* **2007**, *75*, 066313. [CrossRef] [PubMed]
76. Pringle, C.; Kerswell, R.R. Asymmetric, helical and mirror-symmetric travelling waves in pipe flow. *Phys. Rev. Lett.* **2007**, *99*, 074502. [CrossRef] [PubMed]
77. Hof, B.; van Doorne, C.W.H.; Westerweel, J.; Nieuwstadt, F.T.M.; Faisst, H.; Eckhardt, B.; Wedin, H.; Kerswell, R.R.; Waleffe, F. Experimental observation of nonlinear traveling waves in turbulent pipe flow. *Science* **2004**, *305*, 1594–1598. [CrossRef]
78. Jäckel, R.; Magacho, B.; Owolabi, B.E.; Moriconi, L.; Dennis, J.C.; Loureiro, J.B.R. Coherent organizational states in turbulent pipe flow at moderate Reynolds numbers. *Phys. Fluids* **2023**, *35*, 045127. [CrossRef]
79. Paranjape, C.S.; Yalnuz, G.; Duguet, Y.; Budanur, N.B.; Hof, B. Direct path from turbulence to time-periodic solutions. *Phys. Rev. Lett.* **2023**, *131*, 034002. [CrossRef] [PubMed]
80. Waleffe, F. On a self-sustaining process in shear flows. *Phys. Fluids* **1997**, *9*, 883–900. [CrossRef]
81. Montemuro, B.; White, C.M.; Klewicki, J.C.; Chini, G.P. A self-sustaining process theory for uniform momentum zones and internal shear layers in high Reynolds number shear flows. *J. Fluid Mech.* **2020**, *901*, A28. [CrossRef]
82. Cvitanović, P.; Gibson, J.F. Geometry of turbulence in wall-bounded shear flows: Periodic orbits. *Phys. Scr.* **2010**, *2010*, 014007. [CrossRef]
83. Cvitanović, P. Recurrent flows: The clockwork behind turbulence. *J. Fluid Mech.* **2013**, *726*, 1–4. [CrossRef]
84. Cvitanović, P.; Artuso, R.; Mainieri, R.; Tanner, G.; Vattay, G. *Chaos: Classical and Quantum*; Niels Bohr Institute: Copenhagen, Denmark, 2020. Available online: https://ChaosBook.org (accessed on 29 January 2024).
85. Wesson, J. *Tokamaks*, 2nd ed.; Oxford University Press: Oxford, UK, 1997.
86. Wakatani, M. *Stellarator and Heliotron Devices*; Oxford University Press: Oxford, UK, 1998.
87. Hinton, F.L.; Hazeltine, R.D. Theory of plasma transport. *Rev. Mod. Phys.* **1976**, *48*, 239–308. [CrossRef]
88. Carreras, B.A. Progress in anomalous transport research in toroidal magnetic confinement devices. *IEEE Trans. Plasma Sci.* **1997**, *25*, 1281–1321. [CrossRef]
89. Jenko, F.; Dorland, W.; Kotschenreuther, M.; Rogers, B.N. Electron temperature gradient driven turbulence. *Phys. Plasmas* **2000**, *7*, 1904–1910. [CrossRef]
90. Dorland, W.; Jenko, F.; Kotschenreuther, M.; Rogers, B.N. Electron temperature gradient turbulence. *Phys. Rev. Lett.* **2000**, *85*, 5579–5582. [CrossRef] [PubMed]
91. Diamond, P.H.; Champeaux, S.; Malkov, M.; Das, A.; Gruzinov, I.; Rosenbluth, M.N.; Holland, C.; Wecht, B.; Smolyakov, A.I.; Hinton, F.L.; et al. Secondary instability in drift wave turbulence as a mechanism for zonal flow and avalanche formation. *Nucl. Fusion* **2001**, *41*, 1067–1080. [CrossRef]

92. Garbet, X.; Laurent, L.; Samain, A.; Chinardet, J. Radial propagation of turbulence in tokamaks. *Nucl. Fusion* **1994**, *34*, 963–974. [CrossRef]
93. Singh, R.; Diamond, P.H. When does turbulence spreading matter? *Phys. Plasmas* **2020**, *27*, 042308. [CrossRef]
94. Ott, E. *Chaos in Dynamical Systems*; Cambridge University Press: Cambridge, UK, 2000.
95. Zweibel, E.G.; Yamada, M. Magnetic reconnection in astrophysical and laboratory plasmas. *Annu. Rev. Astron. Astrophys.* **2009**, *47*, 291–332. [CrossRef]
96. Lopes Cardozo, N.J.; Hogeweij, G.M.D.; de Baar, M.; Barth, C.J.; Beurskens, M.N.A.; De Luca, F.; Donné, A.J.H.; Galli, P.; van Gelder, J.F.M.; Gorini, G.; et al. Electron thermal transport in RTP: Filaments, barriers and bifurcations. *Plasma Phys. Control. Fusion* **1997**, *39*, B303–B316. [CrossRef]
97. Hogeweij, G.M.D.; Lopes Cardozo, N.J.; de Baar, M.R.; Schilham, A.M.R. A model for electron transport barriers in tokamaks, tested against experimental data from RTP. *Nucl. Fusion* **1998**, *38*, 1881–1891. [CrossRef]
98. Brakel, R.; Anton, M.; Baldzuhn, J.; Burhenn, R.; Erckmann, V.; Fiedler, S.; Geiger, J.; Hartfuß, H.J.; Heinrich, O.; Hirsch, M.; et al. Confinement in W7-AS and the role of radial electric field and magnetic shear. *Plasma Phys. Control. Fusion* **1997**, *39*, B273–B286. [CrossRef]
99. Brakel, R.; W7-AS Team. Electron energy transport in the presence of rational surfaces in the Wendelstein 7-AS stellarator. *Nucl. Fusion* **2002**, *42*, 903–912. [CrossRef]
100. Weller, A.; Geiger, J.; Werner, A.; Zarnstorff, M.C.; Nührenberg, C.; Sallander, E.; Baldzuhn, J.; Brakel, R.; Burhenn, R.; Dinklage, A. et al. Experiments close to the beta-limit in W7-AS. *Plasma Phys. Control. Fusion* **2003**, *45*, A285–A308. [CrossRef]
101. Fitzpatrick, R. *Tearing Mode Dynamics in Tokamak Plasmas*; IOP Publishing: Bristol, UK, 2023.
102. McCormick, K.; Grigull, P.; Baldzuhn, J.; Feng, Y.; Fiedler, S.; Giannone, L.; Hartfuß, H.; Herrmann, A.; Hildebrandt, D.; Hirsch, M. et al. Core-edge studies with boundary island configurations on the W7-AS stellarator. *Plasma Phys. Control. Fusion* **1999**, *41*, B285–B304. [CrossRef]
103. Feng, Y.; Jakubowski, M.; König, R.; Krychowiak, M.; Otte, M.; Reimold, F.; Reiter, D.; Schmitz, O.; Zhang, D.; Beidler, C.D. et al. Understanding detachment of the W7-X island divertor. *Nucl. Fusion* **2021**, *61*, 086012. [CrossRef]
104. Biglari, H.; Diamond, P.H.; Terry, P.W. Influence of sheared poloidal rotation on edge turbulence. *Phys. Fluids B* **1990**, *2*, 1–4. [CrossRef]
105. Lehnert, B. Short-circuit of flute disturbances at a plasma boundary. *Phys. Fluids* **1966**, *9*, 1367–1372. [CrossRef]
106. Gohil, P. Edge transport barriers in magnetic fusion plasmas. *C. R. Phys.* **2006**, *7*, 606–621. [CrossRef]
107. Wolf, R.C. Internal transport barriers in tokamak plasmas. Plasma Phys. *Control Fusion* **2003**, *45*, R1–R91. [CrossRef]
108. Ida, K.; Fujita, T. Internal transport barrier in tokamak and helical plasmas. *Plasma Phys. Control. Fusion* **2018**, *60*, 033001. [CrossRef]
109. Gohil, P. Dynamics of the formation, sustainment and destruction of transport barriers in magnetically contained fusion plasmas. *Plasma Phys. Control. Fusion* **2002**, *44*, A37–A61. [CrossRef]
110. Zhao, K.J.; Chen, Z.P.; Shi, Y.; Diamond, P.H.; Dong, J.Q.; Chen, Z.Y.; Ding, Y.H.; Zhuang, G.; Liu, Y.B.; Zhang, H.Q. et al. Enhancements of residual Reynolds stresses by magnetic perturbations in the edge plasmas of the J-TEXT tokamak. *Nucl. Fusion* **2020**, *60*, 106030. [CrossRef]
111. Rice, J. *Driven Rotation, Self-Generated Flow, and Momentum Transport in Tokamak Plasmas*; Springer: Berlin/Heidelberg, Germany, 2022.
112. Gonçalves, B.; Hidalgo, C.; Pedrosa, M.A.; Orozco, R.O.; Sánchez, E.; Silva, C. Role of turbulence on edge momentum redistribution in the TJ-II stellarator. *Phys. Rev. Lett.* **2006**, *96*, 145001. [CrossRef]
113. Itoh, K.; Itoh, S.-I.; Diamond, P.H.; Hahm, T.S.; Fujisawa, A.; Tynan, G.R.; Yagi, M.; Nagashima, Y. Physics of zonal flows. *Phys. Plasmas* **2006**, *13*, 055502. [CrossRef]
114. Fujisawa, A. A review of zonal flow experiments. *Nucl. Fusion* **2009**, *49*, 013001. [CrossRef]
115. Zhao, K.J.; Dong, J.Q.; Li, J.Q.; Yan, L.W. A brief review: Experimental investigation of zonal flows and geodesic acoustic modes in fusion plasmas. *Plasma Sci. Technol.* **2018**, *20*, 094006. [CrossRef]
116. Nishizawa, T.; Almagri, A.F.; Anderson, J.K.; Goodman, W.; Pueschel, M.J.; Nornberg, M.D.; Ohshima, S.; Sarff, J.S.; Terry, P.W.; Williams, Z.R. Direct measurement of a toroidally directed zonal flow in a toroidal plasma. *Phys. Rev. Lett.* **2019**, *122*, 105001. [CrossRef] [PubMed]
117. Conway, G.D.; Smolyakov, A.I.; Ido, T. Geodesic acoustic modes in magnetic confinement devices. *Nucl. Fusion* **2022**, *62*, 013001. [CrossRef]
118. Diamond, P.H.; Kim, Y.-B. Theory of mean poloidal flow generation by turbulence. *Phys. Fluids B* **1991**, *3*, 1626–1633. [CrossRef]
119. Dimits, A.M.; Bateman, G.; Beer, M.A.; Cohen, B.I.; Dorland, W.; Hammett, G.W.; Kim, C.; Kinsey, J.E.; Kotschenreuther, M.; Kritz, A.H. et al. Comparisons and physics basis of tokamak transport models and turbulence simulations. *Phys. Plasmas* **2000**, *7*, 969–983. [CrossRef]
120. Gruzinov, I.; Das, A.; Diamond, P.H.; Smolyakov, A. Fast zonal field dynamo in collisionless kinetic Alfven wave turbulence. *Phys. Lett. A* **2002**, *302*, 119–124. [CrossRef]
121. Fujisawa, A.; Itoh, K.; Shimizu, A.; Nakano, H.; Ohshima, S.; Iguchi, H.; Matsuoka, K.; Okamura, S.; Minami, T.; Yoshimura, Y.; et al. Experimental evidence of a zonal magnetic field in a toroidal plasma. *Phys. Rev. Lett.* **2007**, *98*, 165001. [CrossRef]
122. Freidberg, J.P. *Ideal MHD*; Cambridge University Press: Cambridge, UK, 2014.

123. Garcia, O.E. Blob transport in the plasma edge: A review. *Plasma Fusion Res.* **2009**, *4*, 019. [CrossRef]
124. Bisai, N.; Banerjee, S.; Zweben, S.J.; Sen, A. Experimental validation of universal plasma blob formation mechanism. *Nucl. Fusion* **2022**, *62*, 026027. [CrossRef]
125. Basse, N.P.; Zoletnik, S.; Saffman, M.; Baldzuhn, J.; Endler, M.; Hirsch, M.; Knauer, J.P.; Kühner, G.; McCormick, K.; Werner, A.; et al. Low- and high-mode separation of short wavelength turbulence in dithering Wendelstein 7-AS plasmas. *Phys. Plasmas* **2002**, *9*, 3035–3049. [CrossRef]
126. Basse, N.P.; Zoletnik, S.; Antar, G.Y.; Baldzuhn, J.; Werner, A.; W7-AS Team. Characterization of turbulence in L- and ELM-free H-mode Wendelstein 7-AS plasmas. *Plasma Phys. Control. Fusion* **2003**, *45*, 439–453. [CrossRef]
127. Maeyama, S.; Watanabe, T.-H.; Nakata, M.; Nunami, M.; Asahi, Y.; Ishizawa, A. Multi-scale turbulence simulation suggesting improvement of electron heated plasma confinement. *Nat. Commun.* **2022**, *13*, 3166. [CrossRef] [PubMed]
128. Saffman, P.G. *Vortex Dynamics*; Cambridge University Press: Cambridge, UK, 1992.
129. Boatto, S.; Crowdy, D. Point-vortex dynamics. In *Encyclopedia of Mathematical Physics*; Françoise, J.-P., Naber, G.L., Tsun, T.S., Eds.; Academic Press: Cambridge, MA, USA, 2006; pp. 66–79.
130. Saffman, P.G. Problems and progress in the theory of turbulence. In *Structure and Mechanics of turbulence, II*; Fiedler, H., Ed.; Lecture Notes in Physics; Springer: Berlin/Heidelberg, Germany, 1978; Volume 76, pp. 274–306.
131. Basse, N.T. On control of turbulent flows in fluids and plasmas: Self-sustaining and -regulating processes. *Inventions* **2024**, *In preparation*.

MDPI AG
Grosspeteranlage 5
4052 Basel
Switzerland
Tel.: +41 61 683 77 34

MDPI Books Editorial Office
E-mail: books@mdpi.com
www.mdpi.com/books

Academic Open
Access Publishing

mdpi.com

ISBN 978-3-7258-1466-4